www.jresm.org

Special Focus Issue

Engineering Innovations from 5ICGE & 3ICESE Conferences

Research on Engineering Structures and Materials

Volume 12
Issue 2
April 2026

Edited by

Prof. Dr. Mahdi Karkush

P-ISSN: 2148-9807 E-ISSN: 2149-4088

The International Journal of **Research on Engineering Structures and Materials (RESM**) is a peer-reviewed open access journal (p-ISSN: 2148-9807; o-ISSN: 2149-4088) published by MIM Research Group. It is published in February, April, June, August, October, and December.

The main objective of RESM is to provide an International academic platform for researchers to share scientific results related to all aspects of mechanical, civil, and material engineering areas.

RESM aims the publication of original research articles, reviews, short communications technical reports, and letters to the editor on the latest developments in the related fields.

All expenditures for the publication of the manuscripts are most kindly reimbursed by *MIM Research Group*. Thus, authors do not need to pay for publishing their studies in the journal.

The scope of the journal covers (but not limited to) behavior of structures, machines and mechanical systems, vibration, impact loadings and structural dynamics, mechanics of materials (elasticity, plasticity, fracture mechanics), material science (structure and properties of concrete, metals, ceramics, composites, plastics, wood, etc.,), nano-materials performances of new and existing buildings and other structural systems, design of buildings and other structural systems, seismic behavior of buildings and other structural systems, repair and strengthening of structural systems, case studies and failure of structural systems, safety and reliability in structural and material engineering, use of new and innovative materials and techniques in energy systems and mechanical aspects of biological systems (biomechanics and biomimetics).

The topics covered in JRESM include:

- Structural Engineering
- Mechanical Engineering
- Material Engineering
- Earthquake Engineering
- Nano-technology
- Energy Systems (Focus on Renewable)
- Biomechanics and Biomimetics
- Environment (Material and Engineering System Related Issues)
- Computer Engineering and Data Science (Material and Engineering System-Related Issues)

Abstracting and Indexing
Please visit http://www.jresm.org for more information.

Graphics and Design

Mehmet Yılmaz myilmaz@jresm.net

RESEARCH on ENGINEERING STRUCTURES & MATERIALS

Research Group

Editorial Board

Editor in Chief		
Hayri Baytan Özmen	Usak University	Türkiye
Guest Editor		
Mahdi Karkush	University of Baghdad	Iraq
Editors		
Antonio F. Miguel	University of Evora	Portugal
Michele Barbato	University of California Davis	USA
Mehmet Palancı	Arel University	Türkiye
Francesco D'Annibale	University of L'Aquila	Italy
Chitaranjan Pany	Vikram Sarabhai Space Centre	India
Badrinarayan Rath	Wollega University	Ethiopia
Taymaz Tabari	Jagiellonian University	Poland
Tamer Saracyakupoglu	İstanbul Gelisim University	Türkiye
Ivan Banović	University of Split	Croatia
Balasubramanian Ramesh	Dhanalakshmi Srinivasan University	India
Abbasali Sadeghi	Islamic Azad University	Iran
Huatian Zhao	Imperial College London	UK
Ibrahim Alshaikh	University of Science and Technology	Yemen
Seyed Reza Samaei	Islamic Azad University Science and Research Branch	Iran
Uzair Aslam Bhatti	Hainan University	China
Tian Su	Shandong University of Technology	China
Pawel Skruch	AGH University of Krakow	Poland
Haris M. Khalid	University of Dubai	United Arab Emirates
Grygorii Gasii	Zhytomyr Polytechnic State University	Ukraine
Sharath B N	Malnad College of Engineering	India
Ahmed Esmail Shalan	Central Metallurgical Research and Development Institute	Egypt

Editorial Office

Publishing Manager		
Mehmet Yılmaz	MIM Research Group	Türkiye
Production Editor		
Damla Yalçıner Çal	Kafkas University	Türkiye
Language Editors		
Gaye Kuru	Uşak University	Türkiye
Mete Çal	Kapadokya University	Türkiye

Editorial Board Members		
Farid Abed-Meraim	Arts et Metiers ParisTech	France
P. Anbazhagan	Indian Institute of Science	India
Raffaele Barretta	University of Naples Federico II	Italy
R.S. Beniwal	Council of Scientific and Industrial Research	India
Antonio Caggiano	University of Buenos Aires	Argentina
Noel Challamel	University of South Brittany	France
Abdulkadir Çevik	Gaziantep University	Türkiye
J. Paulo Davim	University of Aveiro	Portugal
Hom Nath Dhakal	University of Portsmouth	UK
Ali Faghidian	Islamic Azad University	Iran
S. Amir M. Ghannadpour	Shahid Beheshti University	Iran
Ali Goodarzi	Harvard University	USA
Jian Jiang	National Institute of Standards and Technology	USA
Ramazan Karakuzu	Dokuz Eylül University	Türkiye
Arkadiusz Kwiecien	Cracow University of Technology	Poland
Stefano Lenci	Universita Politecnica delle Marche	Italy
Silva Lozančić	University of Osijek	Croatia
Fabio Mazza	University of Calabria	Italia
Yuan Meini	North University of China	China
Stergios A. Mitoulis	University of Surrey	UK
Vinayagam Mohanavel	Anna University	India
Ehsan Noroozinejad Farsangi	Kerman Graduate University of Technology	Iran
Alaa M. Rashad	Shaqra University	Saudi Arabia
Mohammad Mehdi Rashidi	University of Tongji	China
Pier Paolo Rossi	University of Catania	Italy
Neritan Shkodrani	Polythecnic University of Tirana	Albania
Y.B. Yang	National Taiwan University	Taiwan

Advisory Board Members

A. Abdelbary	Alexandria University	Egypt
A. Karthik	SRM Institute of Science and Technology	India
A. Suresh Kumar	Kalasalingam Academy of Research and Education	India
A.A.A. Sheha	Petrogulfmisr Oil Company	Egypt
Aashish Roy	University of Bouira	Algeria
Abbasali Sadeghi	Islamic Azad University	Iran
Abde lbaki Chikh	Ibn Khaldoun University of Tiaret	Algeria
Abdelhalim Bensaada	University of Yahia Fares of Medea	Algeria
Abdel-Hamid Ismail Mourad	United Arab Emirates University	United Arab Emirates
Abdelkader Fidjah	University of Djelfa	Algeria
Abdellah Douadi	Ferhat Abbas University of Setif 1	Algeria
Abdel-Nasser Sharkawy	South Valley University	Egypt
Abdul HaseebWani	Presidency University	India
Abdul Razak Abdul Karim	Senior Lecturer at Universiti Malaysia Sarawak	Malaysia
Abdullah Khan	The University of Agriculture Peshawar	Pakistan
Abhilash P. P.	Kalasalingam Academy of Research and Education	India
Abid Ustaoglu	Bartın University	Türkiye
Abou-bakr Cherki	Ecole Nationale Supérieure des Mines de Rabat	Morocco
Abrham Gebre	Silesian University of Technology	Poland
Adel Al-Azzawi	Al-Nahrin University	Iraq
Adeniyi Ganiyu Adeogun	Kumamoto University	Japan
Adil Mahdi Jabbar	Wasit University	Iraq
Afonso R.G. Azevedo	University of Hassan II Casablanca	Morocco
Ahmad Zaki	Universitas Muhammadiyah Yogyakarta	Indonesia
Ahmed Abdulwahhab	University of Technology Baghdad	Iraq
Ahmed Ghazy	Zagazig University	Egypt
Ahmed Maamoun	McMaster University	Canada
Ahmed Tareq Noaman	University of Anbar	Iraq
Ahmet Demir	Bolu University	Türkiye
Ahmet Devlet Ozcelik	Eskisehir Osmangazi University	Türkiye
Aicha Rouabeh	Ziane Achour University of Djelfa	Algeria
Ajibola Ibrahim Quadri	Aristotle University of Thessaloniki	Greece
Akhil Raj Gaius Yallamelli	Amazon Web Services Inc.	USA
Aktham Alani	University of Fallujah	Iraq
Alaa M. Rashad	Building Materials Research and Quality Control Institute	Egypt
Alaa Salman	University of Baghdad	Iraq
Aleksandar Ašonja	General Directorate of State Airports	Türkiye
Aleksandar Savić	University of Belgrade	Serbia
Aleksandar Vencl	University of Belgrade	Serbia
Ali Abbar Khleif	University of Technology	Iraq
Ali Abdulhameed	University of Baghdad	Iraq

Ali Bagherkhani	Shiraz Univ. of Technology	Iran
Ali Elgohary	Tanta University	Egypt
Ali Goodarzi	Harvard University	USA
Ali Mahmood	Tunis El Manar University	Tunisia
Ali Raza	University of Engineering and Technology	Pakistan
Ali Sadiq Al-Ithari	University of Kufa	Iraq
AliaJasem	S. S. Tegnoor Degree College	India
Alpay Tamer Erturk	Kocaeli University	Türkiye
Alper Incesu	Karabuk University	Türkiye
Alyaa Abd Alsalm	University of Technology – Iraq	Iraq
Amad Ud Din	Fatima Jinnah Women University	Pakistan
Amdjed Islam Dali	SETS International	Saudi Arabia
Amdulla Mehrabov	Azerbaijan State University of Economics	Azerbaijan
Ameer Baiee	University of Babylon	Iraq
Amirhossein Bahadori	Islamic Azad University	Iran
Amirreza Sadeghi	University of Birjand	Iran
Amiya Pandit	University College Dublin	Ireland
Ammar Tawashi	Dept. of Structural Eng., Al-Baath University	Syria
Ana A. Márquez	Universidad de Guanajuato	Mexico
Andi Yusra	Universitas Teuku Umar	Indonesia
Andriy Huts	Rzeszow University of Technology	Poland
Anjishnu Biswas	Indian Institute of Technology Guwahati	India
Ankang Kan	Shanghai Maritime University	China
Anthony N. Papathanassiou	University College of Engineering Villupuram	India
Arash Rahimi	University of Perugia	Italy
Arif Tuncal	Istanbul Gelisim University	Türkiye
Arife Kübra Yontar	Ondokuz Mayis University	Türkiye
Arulkirubakaran D.	Adhi College of Engineering and Technology	India
Arun K.K.	Kumaraguru College of Technology Coimbatore-641049	India
Arun Kumar K.	Mangalam College of Engineering	India
Arvind Kumar Cholker	Matrusri Engineering College	India
Ary A. Hoyos-Montilla	Construction School at Universidad Nacional de Colombia	Colombia
Ashhad Imam	National Institute of Technology Jamshedpur	India
Ash-Shu'ara MarafaSalman	Kwara State University	Nigeria
Asimina Athanatopoulou	University of Semnan	Iran
Assal Hussein	University of Diyala	Iraq
Atike İnce Yardımcı	Uşak University	Türkiye
Ayad Al-Rumaithi	University of Baghdad	Iraq
Ayoub Souileh	Mohammed V University	Morocco
Ayse Aytac	Kocaeli University	Türkiye
Ayse Pınar Demir	Usak University	Türkiye
Azad A. Mohammed	University of Sulaimani	Iraq
AzhagarsamyS	SRM Institute of Science and Technology	India
Azzura Ismail	Universiti Tun Hussein Onn Malaysia	Malaysia

B.P.R.V.S. Priyatham	GMR Institute of Technology	India
Badrinarayan Rath	Wollega University	Ethiopia
Bao Chao	Ningxia University	China
Bashir Olaniyi Sadiq	Kampala International University	Uganda
Bengi Gözmençanlı	Independent Researcher	Türkiye
Berrin İkizler	Ege University	Türkiye
Bharath Vveda Shantha Murthy	RNS Institute of Technology	India
Bhavya Kadiyala	Parkland Health	USA
Bilge Demir	Karabuk University	Türkiye
Billel Rebai	Abbes Laghrour University	Algeria
Breetha Yesudhas Jayakumari	Chennai Institute of Technology	India
Brijesh Singh	National Council for Cement and Building Materials	India
Bulent Imamoglu	Gedik University	Türkiye
C. Chella Gifta	National Engineering College, Kovilpatti (Tamil Nadu)	India
Cagri Yardimci	Usak University	Türkiye
Can Gönenli	Ege University	Türkiye
Canan Kandilli	Usak University	Türkiye
Caroline S. Sobhy	Fayoum University	Egypt
Catur Harsito	Universitas Sebelas Maret	Indonesia
Cesare Biserni	Alma Mater-University of Bologna	Italy
Chaitanya Vasamsetty	Elevance Health	USA
Chau-Khun Ma	Universiti Teknologi (UTM)	Malaysia
Chella Gifta Christopher	National Engineering College Kovilpatti	India
Chetan Jaiprakash Chitte	Dumlupınar University	Türkiye
Chinenye Elizabeth Okere	Federal University of Technology	Nigeria
Chitaranjan Pany	Structural Engineering Entity	India
Chowdhury Bin Zahid Zubayer	Islamic University of Technology (IUT)	Bangladesh
Christopher Fapohunda	Federal University Oye-Ekiti	Nigeria
Chuanjin Yu	Southwest Jiaotong University	China
Claudia Naldi	University of Bologna	Italy
Çiğdem Çırak Karakaş	Cankiri Karatekin University	Türkiye
Damilola Oyejobi	University of Botswana	Botswana
Daniel Cruze	Mohamed Sathak A J College of Engineering	India
Davide Forcellini	Universitat Politècnica de Catalunya – BarcelonaTech (UPC)	Spain
Davies Isobo Nelson	Ninevah University	Iraq
Debasis Rooj	Deakin University	Australia
Debasish Sen	Ahsanullah University of Science and Technology	Bangladesh
Deep Tripathi	University of Sherbrooke	Canada
Deniz Uner	Middle East Technical University	Türkiye
Desy Setyowulan	Ege University	Türkiye
Dheerendra Singh	Indian Institute of Technology Bombay Powai	India
Dhergham Al-Hamdani	Al-Furat Al-Awsat Technical University	Iraq

Dhinesh Balasubramanian	Mepco Schlenk Engineering College	India
Dhirendra Patel	Washington State University	USA
Dia M. Ali	Andhra University	India
Dilay Uncu	Manisa Celâl Bayar Üniversitesi	Türkiye
Dipankar Das	Tripura University	India
Diyar Qader	University of Kirkuk	Iraq
Dmitry Chernov	UENF – State University of the Northern Rio de Janeiro	Brazil
Dr. Madeva Nagaral	Hindustan Aeronautics Limited	India
Dulce Franco Henriques	Instituto Politécnico de Lisboa	Portugal
E.R. Teixeira	University of Minho	Portugal
Ebrahim Sharifi Teshnizi	Ferdowsi University of Mashhad	Iran
Edwin Klu	Virginia Tech	USA
Egemen Teomete	Dokuz Eylul University	Türkiye
Elavenil S.	Vellore Institute of Technology	India
Elizaldo Dominguesdos Santos	Universidade Federal do Rio Grande (FURG)	Brazil
Elton Hala	Polytechnic University of Tirana	Albania
Emanuele Vincenzo Arcieri	Mechanical Engineering Research Institute, Russian Academy of Sciences	Russia
Emin Erdem	Pamukkale University	Türkiye
Emre Kemer	Usak University	Türkiye
Enea Mustafaraj	Epoka University	Albania
Ercan Isik	Bitlis Eren University	Türkiye
Erdal Emre Çeçen	Metropolitan University Tirana	Albania
Eric M. Lui	Syracuse University	USA
Erion Bukaci	Polytechnic University of Tirana	Albania
Esmaeil Zavvar	University of Tabriz	Iran
Esra Özer	Tokat Gaziosmanpasa University	Türkiye
Essam Mohamed	South Valley University	Egypt
Faruk Mert	Gazi University	Türkiye
Fatih Ahmet Senel	Suleyman Demirel University	Türkiye
Fatma Zohra Benabid	Housing & Building National Research Center	Egypt
Fatoş Koç	University of Baghdad	Iraq
Federico Scafati	University of L'Aquila	Italy
Ferhat Yıldırım	GMR Institute of Technology	India
Firas Hussein	Ruhr University Bochum	Germany
Flavia Zinani	Universidade Federal do Rio Grande do Sul (UFRGS)	Brazil
Fokruddin Ahmad	Andhra University College of Engineering	India
G. Velmurugan	Excel Engineering College	India
Gajendra Kumar	Amity University Uttar Pradesh	India
Gaurav Dhadse	G. H. Raisoni Institute of Engineering and Business Management Jalgaon Maharashtra	India
Gautham Kishore Reddy G.	Vignan Institute of Technology and Science	India
Ghanim Al-Zubaidy	University of Baghdad	Iraq
Ghasan Fahim Huseien	Universiti Teknologi Malaysia (UTM)	Malaysia
Giovanni Garofalo	ISAE-SUPAERO	France

Gopi Krishnan P.	Dr. N G P Institute of Technology	India
Gökhan Gece	Bursa Teknik Üniversitesi	Türkiye
Guobo Wang	Wenzhou University	China
Gururaj Hatti	KLS VDIT	India
Gustavo Bosel Wally	Federal University of Rio Grande do Sul	Brazil
Guy Louarn	CNRS – Université de Nantes	France
Güneş Harman	Yalova University	Türkiye
Gür Emre Güraksın	Afyon Kocatepe University	Türkiye
H. C. Ananda Murthy	Adama Science & Technology University	Ethiopia
Habibe Demir	İskenderun Technical University	Türkiye
Hadeel Khalid Awad	University of Baghdad	Iraq
Hadj Bekki	University Ibn Khaldoun of Tiaret	Algeria
Haithem Boumediri	Institut des Sciences et des Techniques Appliquées (ISTA)	Morocco
Hakan Sarikaya	Uşak University	Türkiye
Hakan Ulker	Bursa Teknik University	Türkiye
Halil Murat Enginsoy	Canakkale Onsekiz Mart University	Türkiye
Halil Yalcin Akdeniz	The University of Melbourne	Australia
Halit Cetiner	Isparta University	Türkiye
Hamid Saberi	University of Eyvanekey	Iran
Hamide Tekeli	Süleyman Demirel University	Türkiye
Hamoon Fathi	Sanandaj	Iran
Hanaa Humadi	University of California, Davis	USA
Hasan Ulus	Selcuk University	Türkiye
Hashem Jahangir	University of Birjand	Iran
Hasibullah Azizi	Kalaniketan Polytechnic College	India
Hayder Kamil Shanbara	Al-Muthanna University	Iraq
Hayri B. Ozmen	Usak University	Türkiye
Hemadri Prasad Raju	Sree Vidyanikethan Engineering College	India
Hicham Lotfi	Ibn Zohr University	Morocco
Hidayatul Fitri	STAIN Teungku Dirundeng Meulaboh	Indonesia
Hilton Ahmad	Universiti Tun Hussein Onn Malaysia)	Malaysia
Hintsa G. Gebremariam	Addis Ababa University	Ethiopia
Hossein Jarrahi	University of Birjand	Iran
Hossein Kabir	University of Babylon	Iraq
Houlei Zhang	Nanjing University of Science and Technology	China
Hussein Hamada	Al-Qalam University College	Iraq
Hussein Talab Nhabih	University Malaysia Perlis	Malaysia
Hüseyin Ersen Balcıoğlu	Uşak University	Türkiye
Hüsnügül Yılmaz Atay	Izmir Kâtip Celebi University	Türkiye
I Gede Gegiranang Wiryadi	Universitas Mahasaraswati Denpasar	Indonesia
Ibrahim Raheem	University of Georgia	USA
Ibrahim Saad Agwa	Suez University	Egypt
Ibrahim Sabry	Benha University	Egypt
Ibrahim Sharaky	Taif University	Saudi Arabia
Ikram Kouidri	Tahar Moulay University of Saida	Algeria
Iman Hani	University of Babylon	Iraq

Indra Mawardi	Politeknik Negeri Lhokseumawe	Indonesia
Irakli Premti	Polytechnic University of Tirana	Albania
Irina Volokitina	Karaganda Industrial University	Kazakhstan
Isabel Milagre Martins	Laboratório Nacional de Engenharia Civil	Portugal
Issam Aouari	University of Bouira	Algeria
Ivan Kraus	University of Osijek	Croatia
Ivana Barišić	Josip Juraj Strossmayer University of Osijek	Croatia
Ivana Štimac Grandić	University of Rijeka	Croatia
İbrahim Öz	Ahi Evran University (Kırşehir Ahi Evran University)	Türkiye
J. Aravind Kumar	FLAME University	India
J. D. Chaitanya Kumar Jagarapu	Koneru Lakshmaiah University	India
J. Eswari	Kwara State University	Nigeria
J. Jenix Rino	Anna University	India
J. Jeyanthi	Mepco Schlenk Engineering College	India
J. Paulo Davim	University of Aveiro	Portugal
Jack Widjajakusuma	University of Pelita Harapan	Indonesia
Jagansivamani	Sona College of Technology	India
Javad Vaziri	Universiti Teknologi Malaysia	Malaysia
Jayalalitha Subbaiah	SASTRA Deemed University	India
Jayaseelan Veerasundaram	Saveetha Engineering College	India
Jessemazadu	Federal University Wukari	Nigeria
Jesús Castro	Pontifical Catholic University of Peru	Peru
Jianzhuang Xiao	Tongji University	China
Jinxu Mo	Yangtze University	China
Jojok Widodo Soetjipto	Universitas Jember	Indonesia
Josephine Chang Hui Lai	Petrogulf Misr Oil Company	Egypt
Juan Llorca-Schenk	University of Alicante	Spain
Jun Zhang	Ningbo Tech University	China
K. Ashwini	Yalova University	Türkiye
Kabiru Mustapha	Kwara State University	Nigeria
Kadir Günaydın	GE Aviation	USA
Kamel Chaoui	Badji Mokhtar University	Algeria
Kamran Asemi	Islamic Azad University	Iran
Kanish Kapoor	Dr B R Ambedkar National Institute of Technology	India
Kannan Srinivasan	Saiana Technologies Inc.	USA
Kaplan Kaplan	Kocaeli University	Türkiye
Karthikeyan Parthasarathy	LTIMindtree	India
Katarina Rogulj	University of Split	Croatia
Kavendra Pulkit	NIT Kurukshetra	India
Kh. Hosseinzadeh	Babol Noshirvani University of Technology	Iran
Khairi Supar	University of Mustansiriyah	Iraq
Khairul NizarIsmail	Universiti Malaysia Perlis	Malaysia
Kiran Devi	SGT University	India
Kirollos Sobhy	Babol Noshirvani University of Technology	Iran
Kirti Kanta Sahoo	Kalinga Institute of Industrial Technology (KIIT) Deemed to be University	India
Konstantinos Kalfas	University of Texas at Tyler	USA

Kourosh Mehdizadeh	Islamic Azad University	Iran
Kourosh Nazari	Islamic Azad University	Iran
Krishna Murari Pandey	National Institute of Technology	India
Krzysztof Grzyb	National Institute of Metrology	Thailand
Lavanya Prabha	SRM Easwari Engineering College	India
Lawrence Zahemen Tuleun	University of Ilorin	Nigeria
Lemecha Geleto Wariyo	Addis Ababa University	Ethiopia
Leonid Dvorkin	National University of Water and Environmental Engineering	Ukraine
Leticia Florespulido	Universidad Autónoma de Tlaxcala	Mexico
Lilesh Gautam	Malaviya National Institute of Technology	India
Lim Siong Kang	Universiti Tunku Abdul Rahman	Malaysia
Liyana Jamaludin	Universiti Malaysia Perlis	Malaysia
Lomesh Mahajan	Dr. Babasaheb Ambedkar Technological University	India
Lubna Abdulkhaleq	National and Kapodistrian University of Athens	Greece
Luiz Rocha	Federal University of Rio Grande do Sul	Brazil
LyamineBriki	University of Batna2	Algeria
M. Jafaryar	Conservatoire National des Arts et Métiers	France
M. Kalil Rahiman	Saveetha School of Engineering	India
M.Helen Santhi	University of Split	Croatia
Madhu Puttegowda	Malnad College of Engineering	India
Madhulika Sinha	University of Bergamo	Italy
Magdalini Titirla	University of Illinois	USA
Maher Jebur	University of Baghdad	Iraq
MaherChakhari	UNISTRAPG	Italy
Mahesh Gopal	Wollega University	Ethiopia
Mahesh Raut	G.H. Raisoni Institute of Engineering and Technology	India
Maheswaran Chellapandian	Mepco Schlenk Engineering College	India
Maheswaran Muthiah	K.S. Rangasamy College of Technology	India
Mahmoud Mokhtar	Indian Institute of Technology Bombay	India
Mahmudul Hasan Moon	Eskisehir Technical University	Türkiye
Majid M.A. Kadhim	University of Babylon	Iraq
Majid Pouraminian	University of San Marino	San Marino
Marco Breccolotti	University of Perugia	Italy
Maria Julieta Mateos Ochoa	National Autonomous University of Mexico	Mexico
Maria Richert	AGH University of Science and Technology	Poland
Maridula Thakur	Himachal Pradesh University	India
Marina Sunara	University of Split	Croatia
Marthin Dody Josias Sumajouw	Sam Ratulangi University	Indonesia
Marva Ghazimanesh	Jadavpur University	India
Marwa Enneffati	Laboratoire MOLTECH-Anjou, Université d'Angers	France
Marzieh Naseralmemar	Islamic Azad University	Iran
Matthew Martianus Henry	Bina Nusantara University	Indonesia
Md. Golam Kibria	University of Rajshahi	Bangladesh
Md. Saiful Islam	Universiti Putra Malaysia	Malaysia

Md. Zia Ul Haq	Panjab University	India
Mehdi Khorasani	Isfahan University of Technology	Iran
Mehdi Panji	Islamic Azad University	Iran
Mehmet Ada	Usak Üniversitesi	Türkiye
Mehmet Cemal Genes	Eastern Mediterranean University	Northern Cyprus
Mehmet Kaya	Yozgat Bozok University	Türkiye
Mehrab Nodehi	University of California	USA
Melika Mahmoodabadi	Islamic Azad University	Iran
Mengtao Liang	Xi'an Jiaotong University	China
Mert Göksüzoğlu	Sampa Automotive	Türkiye
Mevlüt Gürbüz	Ondokuz Mayıs University	Türkiye
Mihir Mishra	Texas A&M University	USA
Mihira Acharya	Indian Institute of Technology Bhubaneswar	India
Milica Vasić	Centre for Materials Institute for Testing of Materials	India
Mohamed Bouamama	Mechanics Research Center (CRM)	Algeria
Mohamedi M. Mjahidi	The University of Dodoma	Tanzania
Mohammad Afrazi	Duke University	USA
Mohammad Fayez Saded	Ferhat Abbas University Sétif 1	Algeria
Mohammad Hossein Razmkhah	Semnan University	Iran
Mohammad Iai Biajawi	Universiti Malaysia Pahang Al-Sultan Abdullah	Malaysia
Mohammad Lesani	University of Tehran	Iran
Mohammad Naeim Moradi	Amirkabir University of Technology	Iran
Mohammad Sadegh Shahidzadeh	Behbahan Khatam Alanbia University of Technology	Iran
Mohammad Saleh Baradaran	Islamic Azad University	Iran
Mohammad Salim Kaiser	International University of Business Agriculture and Technology	Bangladesh
Mohammadreza Baghoolizadeh	Shahrekord University	Iran
Mohammed Al-Alusi	University of Anbar	Iraq
Mohammed AL-Ezzi	Universiti Tenaga Nasional	Malaysia
Mohammed Bentahar	University Business Academy	Serbia
Mohammed JalalAl-Ezzi	University of Bilad Al-Rafidain	Iraq
Mohammed Kadhim	Mustansiriyah university	Iraq
Mohammed Kamal Ali	University of Kirkuk	Iraq
Mohammed Salam Shuaib	Kogi State University	Nigeria
Mohammed Salman	University of Fallujah	Iraq
Mohammed Sarhan	Rivers State University	Nigeria
Mohan G.	University of Garmian	Iraq
Mohd Ataullah Khan	Mahindra University	India
Mohd Nasim	IPS Academy	India

Mohd Syahrul Hisyam Mohd Sani	Universiti Teknologi MARA Jengka Campus Pahang Branch	Malaysia
Mohsen Hajizamani	Graduate University of Advanced Technology	Iran
Moosa Mazloom	Shahid Rajaee Teacher Training University	Iran
Morchid Fatima Ezzahrae	Saveetha School of Engineering	India
Moslem Paidar	Islamic Azad University	Iran
Mostafa Akbari	Technical and Vocational University	Iran
Motahhareh Nezafat Tabalvandani	Islamic Azad University	Iran
Mouhammed Lafta	University of Technology	Iraq
Mounika Ganta	Vignana Bharathi Institute of Technology	India
Muhammad AminuAhmad	Kaduna State University	Nigeria
Muhammad Anggara Adji Prasetiya	Universitas Sriwijaya	Indonesia
Muhammad Bilal Khan	GIK Institute	Pakistan
Muhammad Hamza	Jawaharlal Nehru Technological University Hyderabad	India
Mukaila Anifowose	Federal Polytechnic Offa	Nigeria
Murat Aydin	Ontario Tech University	Canada
Murk Chohan	Begum Nusrat Bhutto Women University, Sukkur	Pakistan
Murtala Namakka	Universiti Malaysia Sarawak	Malaysia
Mushriq Al-Shamaa	University of Baghdad	Iraq
Mustafa Akpolat	Munzur University	Türkiye
Mustafa H. Omar	Bilad Alrafidain University College	Iraq
Mustafa Ozgunler	Mimar Sinan Fine Arts University	Türkiye
Mustaqqim Abdul Rahim	University Malaysia Perlis	Malaysia
Mutiu Akinpelu	Kwara State University	Nigeria
Mutluhan Akin	Nevşehir Hacı Bektaş Veli University	Türkiye
Muttaqin Hasan	Syiah Kuala University	Indonesia
N. Arunachelam	Mepco Schlenk Engineering College	India
N. Gurumoorthy	PSNA College of Engineering and Technology	India
N.L.N. Kiran Kumar	Sri Venkateswara University	India
N.Venkata Sairam Kumar Namepalli	R.V.R & J.C College of Engineering	India
Nabil Bella	Tahri Mohamed University of Bechar	Algeria
Nadhim Hamah Sor	Ondokuz Mayıs University	Türkiye
Nagaraj Ekabote	KLE Technological University	India
Nahida Nazim Musayeva	Gazi University	Türkiye
Naser Hassan	Tikrit University	Iraq
Natt Makul	Phranakhon Rajabhat University	Thailand
Navdeep Singh	Dr B R Ambedkar National Inst. of Tech.	India
Naveen Kumar Suniya	MBM University	India
Naveen S.	National Institute of Technology	India
Nazime Seda Şaşmaz Karacan	Usak University	Türkiye
Nebab Mokhtar	Université Hassiba Ben Bouali de Chlef	Algeria

Neeraj S.N.	India affiliated to Visvesvaraya Technological University	India
Nermin Demirkol	Kocaeli University	Türkiye
Nghia P. Tran	Islamic Azad University	Iran
Nguyen Van-Toan	Industrial University of Ho Chi Minh City	Vietnam
Nhlanhla Nyembe	University of the Witwatersrand	South Africa
Nikhil Bharat	National Institute of Technology	India
Nilesh Masne	GESCOEMSR	India
Ninu Praseetha N. S.	Addis Ababa University	Ethiopia
Nisha Aggarwal	Maharaja Agrasen Institute of Technology	India
Nitin Kumar	Universiti Tun Hussein Onn Malaysia	Malaysia
Nizirwan Anwar	Universitas Esa Unggul	Indonesia
O. Philip Oladijo	Botswana International University of Science and Technology	Botswana
Ola Mazen Makki	University of Al-Qadisiyah	Iraq
Oladimeji Olatunji Ojo	Federal University of Technology	India
Olatunji Abolusoro	Tshwane University of Technology	South Africa
Oleg V. Devitsky	Federal Research Centre Southern Scientific Centre of the Russian Academy of Sciences	Russia
Oleksii Hrechanyi	Zaporizhzhia National University	Ukraine
Olfa Maalej	Mustansiriyah University	Iraq
Olufemi Oni	University of North Dakota	USA
Olumoyewa D. Atoyebi	Landmark University	Nigeria
Oluwatobi Dayo-Olupona	University of the Witwatersrand	South Africa
Omer Fayadh	Al-Nahrin University	Iraq
Orhan Gülcan	General Electric Aerospace	USA
Oritonda Muribwathoho	Cape Peninsula University of Technology	South Africa
Orkun Yılmaz	National Institute of Technology	India
Osama Zaid	Institute of Material Technology	India
Osman M. Ramadan	Cairo University	Egypt
Owen Tamin	Universiti Malaysia Sabah	Malaysia
OzgurAvsar	Eskisehir Technical University	Türkiye
Özgür Demircan	Chemical and Energy Engineering, Universiti Teknologi Malaysia	Malaysia
P. Manoj Kumar	KPR Institute of Engineering and Technology	India
P. Marimuthu	SASTRA Deemed to be University	India
P. V. Ramana	Malaviya National Institute of Technology	India
P.N.L. Pavani	Gyeongsang National University	South Korea
P.S.Shreyas	School of Mechanical Engineering	India
Pardhasaradhi Kasinikota	National Institute of Technology	India
Parmo Parmo	UIN Sunan Ampel Surabaya	Indonesia
Partheeban Pachaivannan	Chennai Institute of Technology	India
Peng Gao	University of Massachusetts Lowell	USA
Peter P. Ikubanni	Landmark University	Nigeria
Peyman Beiranvand	Razi University	Iran
Peyman Maleki	Ayatollah Boroujerdi University	Iran
Piya Chotickai	Kasetsart University	Thailand

Pooja Sharma	Dr. Yashwant Singh Parmar University of Horticulture and Forestry	India
Pooya Arezoomand Langarudi	Islamic Azad University	Iran
Prakash Somani	Malaviya National Institute of Technology	India
Priyanka Malhotra	Chitkara University	India
Puneet Sharma	UiT The Arctic University of Norway	Norway
Qasim M. Shakir	University of Kufa	Iraq
Qiang Ou	Chongqing University	China
Qichao Jin	Xi'an Jiaotong University	China
R. Ralegaonkar	Department of Civil Engineering at VNIT	India
R.L. Lija	Department of Civil Engineering	India
R.S. Jangid	Indian Institute of Technology Bombay	India
Rachid Zegait	SASTRA Deemed to be University	India
Rahul Kesharwani	Indian Institute of Technology Patna	India
Raif Sakin	Balıkesir University	Türkiye
Rajaa Abdulsada	National Authority for Nuclear, Radiological, Chemical and Biological Control	Egypt
Rajani Priya Nippatla	Kellton Technologies Inc	India
Rajasekhar Kondarajasekhar	Nigerian Defence Academy	Nigeria
Rajesh Kumar	KPR Institute of Engineering and Technology	India
Rajesh M.	Hindustan Institute of Technology and Science	India
Ramaswamy Palanivel	Alaivani College of Technology	India
Rami Sldozian	University of Technology- Iraq	Iraq
Ramnarayan Sahu	Rajeev Gandhi Technical University	India
Rana Alrubaye	National Institute of Technology, Patna	India
Rana Falah	University of Babylon	Iraq
RanaAl-khadaar	University of Baghdad	Iraq
Rasheed Abdulwahab	Wollega University	Ethiopia
Rathish Kumar Pancharathi	National Institute of Technology Warangal	India
Ravichandran M.	K.Ramakrishnan College of Engineering	India
Ravikumar Jayabal	SIMATS	India
Rayeh Nasr Al-Dala'ien	Universiti Tenaga Nasional	Malaysia
Renu Dalal	Guru Gobind Singh Indraprastha University, Delhi	India
Revathi Srinivasan	Mepco Schlenk Engineering College	India
Riadh Bennai	University Hassiba Benbouali of Chlef	Algeria
Rianti Dewi Sulamet-Ariobimo	Universitas Trisakti	Indonesia
Roberto Nascimbene	School of Advanced Studies IUSS Pavia	Italy
Rosendo Romero-Andrade	SSN College of Engineering	India
Royal Madan	Chandigarh University	India
Rupesh Kumar Dhondy	Osmania University	India
Rusul Mansoor Al-Amri	University of Kerbala	Iraq
S. Ali Faghidian	Islamic Azad University	Iran
S. Gholizadeh	University of Cape Town	South Africa
S. Prasanth	Sabaragamuwa University of Sri Lanka	Sri Lanka

S.R.R. Teja Prathipat	National Institute of Technology Warangal	India
Saba Jawad	Bilad Al-Rafidain University	Iraq
Sabah Fartosy	University of Mustansiriyah	Iraq
Sachin Kumar	SKITM-Sat Kabir Institute of Technology and Management	India
Sadanand Paneru	Tribhuwan University	Nepal
Saeid Foroughi	Selçuk University	Turkey
Sahar Ismail	Saint Joseph University of Beirut	Lebanon
Sai Krishna Pinnamaneni	University of Texas at Arlington	USA
Saiful Hasan	Jamia Millia Islamia	India
Saifullah Shahen	Hochschule Neu-Ulm	Germany
Saifulnizan Jamian	Indian Institute of Technology	India
Sajjad Hassanpour Kasanagh	Middle East Technical University	Türkiye
Salah Bouzina	University of Constantine	Algeria
Salmabanu Luhar	National Taipei University of Technology	Taiwan
Salwa Elakeili	University of Benghazi	Libya
Sam Saham	Tarbiat Modares University	Iran
Saman Mansouri	Universiti Malaysia Sarawak	Malaysia
Saman Saadatfar	Islamic Azad University	Iran
Samer Adeeb	National Institute of Technology Puducherry	India
Samia Bouzouaid	Kasdi Merbah University	Algeria
Samuel Awe	Automotive Components Floby AB	Sweden
Sandra Juradin	Independent Researcher	Croatia
Sangeetha Palanivelu	SSN College of Engineering	India
Sanjeeb Prasad Panday	Tribhuvan University	Nepal
Sarmila Sahoo	Heritage Institute of Technology Kolkata	India
Sasikumar Palanisamy	K. Ramakrishnan College of Technology	India
Sastri M. V. S. S.	Vasavi College of Engineering	India
Saumen Mandal	National Institute of Technology Karnataka	India
Seema Gupta Bhol	KIIT University	India
Sefiu Bello	Kwara State University	Nigeria
Selcuk Selimli	University of Karabük	Türkiye
Sercan Serin	Osmaniye Korkut Ata University	Türkiye
Serdar Gungor	Bilecik Şeyh Edebali University	Türkiye
Serkan Elcin	Pamukkale University	Türkiye
Seyed Reza Samaei	Islamic Azad University	Iran
Seyedeh Yasaman Samaei	Imamkhomeini Internaional University	Iran
Seymur Bashirzade	Azerbaijan University Architecture and Construction	Azerbaijan
Shahazadi Begum	Baba Institute of Technology and Sciences	India
Shahrul Niza Mokhatar	Faculty of Civil Engineering & Built Environment	Malaysia
Shaise K. John	College of Engineering Trivandrum	India
Shakir Musa	Al-Furat Al-Awsat Technical University	Iraq
Shanshan Jin	Beijing University of Civil Engineering and Architecture	China
Shaohong Cheng	Univ. of Windsor	Canada
Sharmin Reza Chowdhury	Civil Eng.Dept. Ahsanullah University of Science and Technology	Bangladesh

Sharmistha Shee Kanrar	Federal University of Technology	Nigeria
Shashi Prakash Dwivedi	G. L. Bajaj Institute of Technology & Management	India
Shaymaa Naser	University of Kufa	Iraq
Sheelan Hama	University of Anbar	Iraq
Shimol Philip	Universiti Tun Hussein Onn Malaysia	Malaysia
Shoulong Zhang	Harbour Engineering Research Institute Co. Ltd.	China
Shuaib Ahmed Wadho	Usak University	Türkiye
Siti Aisyah Nurjannah	Universitas Sriwijaya	Indonesia
Sivakumar N.	University of Alberta	Canada
Solomon Olalere Ajamu	Ladoke Akintola University of Technology	Nigeria
Somayyeh Pourbakhshian	Islamic Azad University	Iran
Somya Ranjan Patro	Indian Institute of Technology Delhi	India
Sonachalam M.	Arvind Gavali College of Engineering	India
Sonal Thakkar	Nirma University	India
Sophia Immanuel	National Institute of Technology Tiruchirappalli	India
Soumia Hammache	Mohamed Khider University of Biskra	Algeria
Sridhar G.	National Institute of Technology Karnataka	India
Srinivasan Anandhan	National Institute of Technology Karnataka	India
Stefania Sica	University of Sannio	Italy
Subash Thanappan	KAAF University College	Ghana
Subramanyam Boyapati	American Express	USA
Suliman Khan	NFC Institute of Engineering and Fertilizer Research	Pakistan
Sumanth Ratna Kandavalli	New York University	United States
Sumit Kumar Baral	Jagannath University	India
Sunday Chukwuemeka	Projects Dev. Inst.	Nigeria
Surajit Kumar Paul	Indian Institute of Technology	India
Suriati Sufian	Universiti Teknologi PETRONAS	Malaysia
Suriyaprakash Rajadesingu	SRM Institute of Science and Technology	India
Suseela Alla	Vignan's Foundation for Science, Technology & Research	India
Susmita Naskar	University of Southampton	United Kingdom
Syed Nasir Abbas	University of Sargodha	Pakistan
T.V. Reshma	GITAM School of Technology	India
Taha Rashid	Monastir University	Tunisia
Talha Jamshaid	Islamia University of Bahawalpur	Pakistan
TalhaTaskanat	Erciyes University	Türkiye
Tamer Saracyakupoglu	TUSAŞ Academy	Türkiye
Tankiso Lawrence Ngake	Walter Sisulu University	South Africa
Taqiy Eddine Boukelia	Mechanical Engineering, University of Jijel	Algeria
Tarun Kumarrajak	Northern Technical University	Iraq
Tasnia Ahmed	Military Institute of Science and Technology	Bangladesh
Tebatso Gorgina Moape	University of South Africa	South Africa
Teotino Gomes Soares	Universidade Oriental Timor Lorosa'e	Timor-Leste (East Timor)
Thaer Alrudaini	University of Basrah	Iraq

Thayathip Thongtan	Faculty of Earth and Space Sciences, Autonomous University of Sinaloa	Mexico
Thi Loanpham	Hai Phong University	Vietnam
Thirusubramanian Ganesan	Cognizant Technology Solutions	USA
Thomás L. Resende	Federal University of Jequitinhonha and Mucuri Valleys	Brazil
Thomas Salonikios	Institute of Engineering Seismology and Earthquake Engineering	Greece
Toufik Sebbagh	University of Skikda	Algeria
Tri Rochmadi	Universitas Alma Ata	Indonesia
Tuan Anh Nguyen	Thuyloi University	Vietnam
Tuqa Mahdi	Bilad Al-Rafidain University	Iraq
Uchechi Eziefula	University of Agriculture and Environmental Sciences	Nigeria
Upendra K.Mallela	Aerospace Vertical Largy Services Limited	India
Usama Naeem	University of Basrah	Iraq
Utsav Koshti	Nirma University	India
Uwemedimo Nyong Wilson	Azerbaijan National Academy of Sciences	Azerbaijan
Vafa Morsali	Islamic Azad University	Iran
Vedat Arda Küçük	Çankırı Karatekin University	Türkiye
Venkatesh Chava	CVR College of Engineering	India
Venkatesh Rathinavelu	Saveetha Institute of Medical and Technical Sciences	India
Vera Ilyina	IG KarRc Ras Russian Academy of Sciences	Russia
Víctor I.Fernandez-Davila	Shri Shankaracharya Institute of Professional Management and Technology	India
Victor Rizov	University of Architecture	Bulgaria
Vijayasarathy Rathanasalam	ATRIA Institute of Technology	India
Vikas B. Magdum	KLS Gogte Institute of Technology	India
Vina Kamila	Mulawarman University	Indonesia
Vincent Sam Jebadurai	Department of Civil Engineering, Karunya Institute of Technology and Sciences	India
Vineeth Kumart V.	Siddaganga Institute of Technology	India
ViniciusPepe	Mechanical Engineering, University Ritter dos Reis	Brazil
Vishwash B.	Indian Institute of Science	India
Vivek Srivastava	SGT University	India
Wael Shaheen	University of Baghdad	Iraq
Wahyu Dwi Lestari	University of Pembangunan Nasional Veteran Jawa Timur	Indonesia
Waleed A. Abbas	University of Technology	Iraq
Xiaojian Wang	Xinjiang University	China
Xinyue Wang	Dalian University of Technology	China
Y. Bouras	Victoria University	Australia
Yahaya Ismail	University of Abuja	Nigeria
Yamini SreevalliI	Vellore Institute of Technology	India
Yang Feng	Xi'an Jiaotong University	China
Yang Yang	Southeast University	China
Yaser Acikbas	Uşak Üniversitesi	Türkiye
Yassine Zelmat	University Abdelhamid Ibn Badis	Algeria

Yonatan Ayele Abera	Dilla University	Ethiopia
Yuliang Chen	Guangxi University of Science and Technology	China
Yunika Kirana Abdul Khalik	Tikrit University	Iraq
Yunusa Haruna	Beihang University	China
Yuvaperiyasamy M.	Saveetha School of Engineering	India
Yuvaraj K.	University of Relizane	Algeria
Zafer Kaya	Yildiz Technical University	Türkiye
Zahid Iqbal Khan	Çanakkale Onsekiz Mart Üniversitesi	Türkiye
Zaim Omar	Universiti Sains Malaysia	Malaysia
Zainab Tolu Giwa	Kwara State University	Nigeria
Zainorizuanmohd Jaini	Universiti Tun Hussein Onn Malaysia	Malaysia
Zeynep Ekincioğlu Küzeci	Kırşehir Ahi Evran Üniversitesi	Türkiye
Zikriye Ozbek	Canakkale Onsekiz Mart University	Türkiye
Ziyauddin Seikh	Aliah University	India

In This Issue

Research Article
719 **Omaima W. Jumaa, Ahmed T. Noaman, Akram Sh. Mahmoud**
Behavior of rubberized concrete deep beams reinforced with GFRP bars

Research Article
731 **Hamid Athab Al-Jameel, Ban Ali Kamil, Haider Fadhil Addab**
The statistical modeling of traffic characteristics and noise levels on urban roads with rigid pavement

Research Article
741 **Ali Mohammed Dawood, Qassun S. Mohammed Shafiqu**
Mitigation liquefaction of sandy soil supporting shallow foundation using sodium silicate liquid injection

Research Article
753 **Mohammed Qasim Shaaban, Dhergham Abdul-Jaleel Al-Hamdani, Nabeel Katfan Lwti, Noor Ghanim Fakhir, Aymen Saad**
Deep learning in geotechnical engineering: Predicting soil behavior for safer constructions

Research Article
765 **Alaa Nore Merza, Aram Mohammed Raheem, Ibrahim Jalal Naser**
Mapping of elemental soil properties for residential compound in Kirkuk city using GIS technique

Research Article
779 **Alaa A. Shamki, Majid D. Muttashar**
Shear performance of concrete beams reinforced with perforated functional steel plates

Research Article
793 **Tamara Hussein Bani Ata, Asma Thamir Ibraheem**
The eco-concrete revolution: Manufacturing a sustainable high-performance rigid pavement with innovative materials

Research Article
807 **Mohanad T. Abduljaleel, Abdulkader Ismail Al-Hadithi**
Dynamic response of self-compacting concrete included fiber and eps of hollow beam reinforced with GFRP under impact load

Research Article
819 **Dheyaa Madlool Manhal, Hasan A. Alshubber**
A novel differential quadrature method for transient heat transfer analysis in multilayered cylindrical structures: Numerical validation and parametric investigation

Research Article
831 **Hind A. Sami, Raheek I. Ibrahim, Manal K. Odah**
Utilization of high- frequency ultrasonic waves for the demulsification of water/oil emulsions

Research Article
845 **Saba A. Othman, Hashim A. Hussien, Abduljabbar O. Hanfesh**
Numerical and acoustic investigation of cavitation phenomena in centrifugal hydraulic pumps

Research Article
859 **Hind A. Sami, Raheek I. Ibrahim, Manal K. Odah**
Ultrasound-assisted demulsification of heavy fuel oil using lemon peel powder: A sustainable natural approach

Research Article
875 **Reem K. Khadiar, Raheek I. Ibrahim, Manal K. Odah**
Investigation and optimization of the impact of microwave irradiation on the extraction of sulfur from diesel fuel

Research Article
889 **Ziadoon M. Ali, Akram S. Mahmoud**
Torsional ductility and toughness of reinforced concrete beams with a new method of splice remedy

Research Article
905 **Ahmed T. Azeez, Maan S. Hassan, Alaa A. Atiyah**
Modelling the performance of superplasticizers in a hybrid concrete system with steel slag and waste glass

Research Article
917 **Safa M. Lafta, Abbas F. Ibrahim**
Analysis of machining performance in ECDM of Al6061-SiC-B_4C hybrid composites: Experimental study and statistical modeling

Research Article
931 **Amenah M. Abdulrazzaq, Haider A. Abdulhameed, Maan S. Hassan**
Effects of elevated temperatures on the stress-strain behavior and microstructure of normal and high-strength concrete

Research Article
943 **Mustafa Imad Ahmed, Alaa H. Abed**
Evaluation of runways for Al-Habbaniya air base in Iraq

Research Article
957 **Salah Khudhur Mohammad**
Study and analysis of vibration and mechanical characteristics of PVC-carbon fiber-graphene nanocomposite pipes designed for oil and gas applications

Research Article
971 **Mahmood Fawzi Ahmed**
Enhancing the external sulfate attack resistance of high-volume fly ash concrete containing waste glass powder

Research Article
981 **Hawaa A. Obaid, Ibrahim A. Sarhan, Sheelan Mahmoud Hama**
The effect of permeability and mechanical properties of low-calcium fly ash based geopolymer concrete

Research Article
995 **Omar K. Ali, Jasim M. Abbas, Laith K. Al-Hadithy**
Performance of the pile group foundation supporting multi-story building under repeated earthquakes

Research Article
1007 **Shaho Kh. Noori, Ibrahim J. Naser, Redvan Ghasemlounia, Mohammed O. Ibrahim, Aram M. Raheem, Imran A. Fayyadh**
Assessment of water quality in Kirkuk city: Using geographic information systems and multi-linear regression analysis

Research Article
1023 **Murtadha Hardan Dawood, Sozan Saeed Rasheed, Hussien Al-Quraishi, Haneen Ismaeel Khalil**
Enhancing the flexural behavior of concrete beams with steel and carbon fiber

Research Article
1030 **Mohammed H. A. Alopaedy, Layth.W. Ismael, Ghufran F. Hasan, Mayada S. Mohammed, Alameer H. Alhasan, Zeena A. Ali, Ali M Abd**
Enhancing the corrosion resistance and potential biomedical applications of titanium dental implants coated with niobium pentoxide

Research Article
1039 **Fahad Saadi Almani, Farhad M. Othman, Alaa A. Abdul-Hameed**
Green syntheses and characterization of Phragmites australis nanofibers on sustainable concrete

Research Article
1055 **Borkan M. Mutashar, Suhaib Y. Kasim, Oday A. Salih**
Experimental evaluation of bond behavior of post-installed GFRP and steel reinforcements using different adhesives

Research Article
1067 **Yasameen N. K. Albresha, Hussam K. Risan**
Thermal and crack behavior of reinforced high-performance concrete edge-restrained wall

Research Article
1087 **Nada A. Mahmoud, Mahmoud Khashaa Mohammed, Yousif A. Mansoor**
Strengthening of corroded reinforced concrete beam via optimized fiber reinforced self-compacting concrete jacket

Research Article
1101 **Shaimaa M. Abdulrahman, Lamya M. J. Mahdi, Ghayda Yaseen Al Kindi, Qasim A. Al-Obaidi**
Sustainable soil stabilization using coffee husk ash and limestone: An eco-friendly approach

Research Article
1115 **Dunia Abd Al-Latteef, Mohsin A. Al-Shammari, Emad Q. Hussein**
Experimental and numerical free vibration analysis of orthotropic composite plates reinforced with Al_2O_3

Research Article
1127 **Ibraheem H. Ridha, Bahaa H. Al-Abbas, Sadjad A. Hemzah**
Effect of different reinforcement methods on column-footing joint performance under seismic loading

Research Article
1139 **Mahdi Karkush, Alaa D. Salman, Abdulkareem N. Abbood, Rafal Emad**
Evaluating the role of nano-clay and nano-metakaolin in mitigating the collapsibility of gypseous soils

Research Article
1153 **M. Sabermahani, H.R. Elahi, Ahmed M. Bilal, A. Khodaverdian, Mahdi Karkush**
Stabilization of excavation using the diaphragm wall method in Karbala

Research Article
1165 **Ahmad D. Abdullatef, Safaa I. Ali, Safaa Y. Hamad Aldarraji, Muataz I. Ali**
Evaluating the Ramberg–Osgood Model for nonlinear moment–curvature analysis of reinforced concrete beams

Research Article
1179 **A. Sathiya Priya, S. Sundararaman**
Treatability study of acclimatized industrial pharmaceutical wastewater using leaf-based natural coagulants with bioaugmentation

Research Article
1195 **Ali Fahdel, Kamal Alogla, Wajdi Shubber Saheb**
Bond behavior enhancement between normal strength concrete and SIFCON

Research Article
1211 **Anwer M. Ali, Dawod S. Ayed, Raed Abdullah Hasan**
Machine learning-based evaluation of indirect tensile stiffness modulus of fiber-modified cold asphalt mixtures

Research Article
1225 **Noor Kareem Tohmazi, Kamal Alogla, Sadjad Amir Hemzah**
Experimental investigation of bolted concrete column–foundation connections under lateral repeated loading

Free access to tables of content, abstracts and full text of papers for web visitors.

Copyright © 2026

Research on Engineering Structures & Materials
MIM Research Group Publications
P-ISSN: 2148-9807
E-ISSN: 2149-4088
http://www.jresm.org

ABSTRACTING / INDEXING

The international journal of Research on Engineering Structures and Materials (RESM) is currently Abstracted/Indexed by Asos Indeks, CiteFactor, Cosmos, CrossRef, Directory of Research Journal Indexing, Engineering Journals (ProQuest), EZB Electronic Journal Library, Global Impact Factor, Google Scholar, International Institute of Organized Research (I2OR), International Scientific Indexing (ISI), Materials Science & Engineering Database (ProQuest), Open Academic Journals Index, Publication Forum, Research BibleScientific Indexing Service, Root Indexing, Scopus, Ulakbim TR Index (Tubitak), Universal Impact Factor and under evaluation by many other respected indexes.

Check web site for current indexing info, www.jresm.org

Research on Engineering Structures & Materials
www.jresm.org

Research Article

Behavior of rubberized concrete deep beams reinforced with GFRP bars

Omaima W. Jumaa [*,a], Ahmed T. Noaman [b], Akram Sh. Mahmoud [c]

Civil Engineering Department, University of Anbar, Ramadi, Iraq

Article Info

Article History:

Received 10 Oct 2025

Accepted 26 Nov 2025

Keywords:

Deep beams;
GFRP bar;
Rubcrete;
Shear behavior

Abstract

Recently, glass fiber-reinforced polymer (GFRP) bars have been considered as an emerging potential alternative to steel rebars due to their durability and resistance to corrosion. However, investigations on shear behavior of rubberized RC beams modified with GFRP bars have not been well established. On the other side, it is possible to reduce the dangerous materials found in tires and generate sustainable crumb rubberized concrete. In this study, the static performance of rubberized concrete deep beams reinforced with GFRP bars was evaluated. Rubber crumbs are substituted with fine sand aggregate in volumetric replacement ratios to create rubberized concrete. The primary factors were the amount of crumb rubber (0%, 10%, and 20%) and the main ratio of reinforcement ($\rho 1$ = 0.0085 *and* $\rho 2$ = 0.0113). Six RC deep beams having dimensions of (1400×300×150) (Length×Depth×Width) subjected to a 4-point loading up to failure. The mixture strength properties, load-midspan deflection curves, first crack, the effect of GFRP reinforcement ratio, and ductility index were the parameters examined. The results showed that increasing the volumetric percentage of rubber aggregate declined the compressive and splitting strengths of concrete mix. It was revealed that the behavior of the rubberized concrete deep beams influenced the load-deflection performance, the ultimate load, the increase in the deflection and ductility index. The test results reveal the significance of the GFRP bars, which are found to effectively improve the ultimate load and deflection of RC beams and increase the load before initiating cracking. The deep beams with 10% rubber and a higher reinforcement ratio showed the highest ultimate load and deflection and improved ductility, with an increase of 61%, 147.6%, and 25%, respectively, in comparison to the reference samples.

© 2026 MIM Research Group. All rights reserved.

1. Introduction

Recently, concrete can be considered as the most widely used material around the world, and its production requires continuous natural resources. There is a need to find alternatives using recycled solid waste to produce sustainable concrete. On the other hand, many countries suffer from the problem of car tires accumulating as solid waste. Over the next 30 years, the amount of rubbish generated worldwide is expected to increase to be 3.4 billion tons in the year 2025[1]. Therefore, a significant profit can be attained by re-utilizing these discarded tires in civil engineering sector in the future. According to Kordoghli et al. [2], tire dumping in the ground causes environmental and economic problems, as it can lead to fires and emissions that are difficult to control. One of the inventive ideas was to make rubberized concrete with rubber crumbs. Rubber crumbs having size ranged between (4.75 and 75 mm) are produced by cutting, shredding, and grinding rubber tires. With fine aggregate, volumetric replacement is employed at ratios of 5%, 10%, 15%, etc.[3, 4]. Limited studies (small and medium-sized samples) have been published. The use of crumb rubber particles as a substitute for sand aggregates at various ratios was the main

*Corresponding author: ahmed.noaman@uoanbar.edu.iq
[a]orcid.org/0009-0002-2971-8203; [b]orcid.org/0000-0003-2113-5265; [c]orcid.org/0000-0002-1956-0281
DOI: http://dx.doi.org/10.17515/resm2025-1228ic1010rs

focus of these investigations. The results demonstrated limited workability and a decline in concrete's mechanical qualities, which is proportional to crumb rubber aggregate volume[5]. Nonetheless, several results illustrated that inclusion of rubber aggregate decreased the self-weight, enhanced concrete toughness, strain capacity, and ductility index[6]. According to[7], the results of the study indicated a 12.7%, 21.7%, and 26.0% decrease in compressive strength at 5%, 10%, and 15%, rubber aggregate ratio, respectively. Comparable to the deterioration in the compressive strength, the elastic modulus decreased by 9.4%, 13.9%, and 18.5%, respectively. Alasmari et al. [8] evaluated the flexural performance of rubberized RC beams under four-point load. Crumb rubber aggregate was substituted with 10%, 12.5%, and 15% of sand (volume). The initial cracking load of the rubberized RC beams dropped by approximately 9% when compared to the control and 16% when 15% rubber crumb was included. The inclusion of crumb rubber, which ranged from 0% to 15%, increased the hardness of the rubberized concrete beams by an average of 24.1%. Moreover, to evaluate the influence of rubber aggregate on deformability, the ductility index of rubberized RC beams increased by 111% and 35%, respectively. In a recent study[9], fourteen rubberized reinforced concrete continuous RC deep beam of steel reinforcement bars and plain RC (ORC) as a reference was investigated and designed to fail in shear. One of the study parameters crumb and chips tire rubber that utilized by replacing of fine and coarse aggregates, respectively, with varied volumes (5% to 20% for each type). The results showed that the ultimate load of continuous RC rubberized deep beams decreased by 32% and 33% at 20% replacing of fine and coarse aggregates, respectively. However, a significant decrease in the max. deflection by 83.1% and 106.3% was obtained at same aggregate replacement of 20%. Moreover, the ductility of the continuous rubberized RC deep beams increased up to 37% at 20% rubber crumb ratio. Sandeep et al.[10] conducted a research, in a pilot study, described improving the performance of shear deep beams using concrete containing rubber crumbs. Rubber content (0%, 10%, and 20%) was the primary factor. Except for the reference sample, which failed due to a combination of flexure and shear (flexure-shear failure), all the beams failed under diagonal stress. It was noted from the results that the addition of 10% of processed crumbled rubber increased the strength of the deep beams and enhanced the load of the first crack, and is recommended in structural applications. The results approved that ductility index at shear is directly proportional to crumb rubber content. The increases in ductility index were observed to be 18%, 21%, and 22% at rubber ratio of 10%, 15%, and 20%, respectively.

The shear response of rubberized concrete deep beams reinforced with glass fiber-reinforced polymer (GFRP) bars is scarce, whereas the behavior of concrete steel bar-reinforced deep beams has been well studied in previous research. On the other hand, glass fiber-reinforced polymer (GFRP) is a potential non-corrosive substitute for steel[11]. In concrete structures, steel rebar corrosion weakens the concrete and obscures structural performance, safety, and serviceability, all of which are expensive to maintain and repair. This makes GFRP rods suitable for structures exposed to harsh environments, thus imparting desirable properties when using GFRP bars, such as higher stress resistance, higher tensile-to-weight ratio, crack width control, and non-magnetic properties[12]. According to [13], their study investigated the synergistic effect of steel fibers and rubber aggregate on the shear behavior of high-strength RC beams supported with glass FRP (GFRP) bars. Among the variables investigated, the GFRP reinforcement ratio (ρ_f = 0.89 and ρ_f = 0.34) and rubber aggregate content (0%, 5%, 10%). The results showed that the beam shear capacity increased as the GFRP reinforcement ratio increased, the crack number increased by 10% with a 10% increase in CR concentration. The use of CR may be responsible for this decrease in fracture width. In general, it was found that the measured load-mid-span deflection associated with the beam failure load decreased for specimens containing 5% and 10% CR.

The above reviews show that the behavior of deep beams of rubberized concrete reinforced with GFRP bars is not well understood, due to which a recent study has highlighted the need for more research in this direction. On the other side, ACI 440 [14]does not provide design guidelines for GFRP-RC deep beams due to a lack of published research on this subject. The importance of this study was to bridge the gap in part by evaluating the behavior of deep rubberized concrete beams reinforced with GFRP bars. The proportions of rubber crumb (10% ,20%) were selected based on previous reviews that show the possibility of using them in the production of recycled rubber

concrete, that can be developed in the manufacturing of green structural concrete in the future. Additionally, this study evaluates the prospect of rubberized concrete with GFRP bars as a solution to the problem of critical shear behavior of deep beams and the associated ductility problems with GFRP bars.

2. Experimental Program

Six deep beams that are intended to fail under shear are being tested as part of the experimental program. For all deep beams considered in the study, the total length is 1400 mm, depth of 300 mm, and 150 mm wide. Two variables were considered in this study: the first variable is the effect of crumb rubber percentage (0%, 10%, and 20%) and the second variable is the ratio of the main reinforcement (ρ) which were (ρ1=0.0085 and ρ2=0.0113). The selection of the sample size and criterion was based on the minimum requirements of the deep threshold core according to the conditions in the American Code[15] . In the sections that follow, mixture proportioning, sample preparation, and testing is discussed in further detail, along with the characteristics of the various constituent elements.

2.1. Materials

2.1.1 Cement

Type I, OPC was utilized in this experiment for sample casting, as presented in Fig.1. The chemical composition of the main ingredients of this type of cement are presented in Table 1. The OPC physical properties are listed in Table 2.

2.1.2 Aggregates (Fine and Coarse)

The max. size of the crushed coarse aggregate used in this study is 12 mm. Natural river sand of max. size 4.75 mm was utilized as fine aggregate. Both adhere to Iraqi Specification No. 45 [16]. The PSD of sand and coarse aggregates is presented in Tables 3 and 4, respectively.

2.1.3 Crumb Rubber

Crumb rubber was utilized with a relative density = 1.1 according to ASTM D854 [17]. The particle size ranged between 4.75 and 0.075 mm. The rubber aggregate was utilized as a volumetric replacement ratio (10%and 20%) by the natural sand aggregate (Vol.). It had little absorption. The PSD of the crumb rubber aggregate was carried out following ASTM C136 [18].

Fig. 1. (A) OPC, (B) crushed coarse aggregate, (C) sand, and (D) rubber aggregate

2.1.4 Reinforcement Bars

Reinforcement bars regular ordinary steel bars and glass fiber reinforced polymer (GFRP) bars were used to reinforce beams. GFRP serves as the primary longitudinal reinforcement in this investigation and has a diam. of 12 mm. Steel reinforcement diam. is 6 mm. Table 5 shows the mechanical characteristics of the reinforcements utilized in this work.

Table 1. The cement's chemical composition

Chemical Compound	% Weight	The Iraqi standard's limit. (No. 5/2019)
CaO	64.2	-
Fe_2O_3	3.4	-
SiO_2	21.1	-
Al_2O_3	3.81	≤ 3.5
MgO	2.2	A max of 5%
Main compounds	Oxide% by Weight	Iraqi standard No. 5/2019 Limits
$C3A$	5.4	≤ 3.5%
C4AF	14.62	-
C3S	19.42	-
C2S	49.45	-

Table 2. Physical properties of OPC

Property	Values	Limits of Iraqi Standards IQS 5-2019
Setting time		
Initial	160	≥ 45 [min]
Final	246	Less than 600 [min]
Fineness (Blaine method) in cm^2/g	2531	≥ 2500 cm^2/g
Comp. strength (2 days) [MPa]	12.4	Not less than 10 MPa
Comp. strength (28 days) [MPa]	42.3	Not less than 32.5 [Mpa]

Table 3. Sieve analysis of natural sand

Size of the mesh [mm]	% Passing	Limits of IOS (NO. 45-1984)[16]
10	100	100
4.75	99	90-100
2.36	85	75-100
1.18	72	55-90
600 mics	55	35-59
300 mics	16	8-30
150 mics	3	0-10

Table 4. Sieve analysis for coarse aggregates

Size of the mesh [mm]	% Passing	Limits of IOS (NO. 45-1984)[16]
20	100	100
14	100	90-100
10	81	50-85
5	10	0-10

Table 5. Physical properties of the steel reinforcements and GFRP bars

Type	Diam. [mm]	Area [mm²]	Yield stress [MPa]	Ult. strength [MPa]
Steel bar	6	28.27	596	613
GFRP bar	12	113	-----	822

2.2 Mixing Proportions

To achieve the necessary compressive strength and workability, trial mixes using ACI 211 method was adopted in this study. Th w/c ratio was selected to be 0.47. A 35 MPa compressive strength was adopted as a design strength criterion. The amount of crumb rubber added to each batch of

concrete resulted in three different compositions. Table 6 lists the ingredients for each blend. Each group contains a different rubber ratio.

Table 6. Mixing percentages (kg/m^3)

Mix Type	Cement	Coarse Agg.	Fine Agg.	Water	Crumb rubber	w/c
REF.(Rub0%)	420	1015	800	210	0	0.47
Rub10%	420	1015	720	210	36.4	0.47
Rub20%	420	1015	640	210	72.4	0.47

2.3 Mixing Method

In order to make sure that every mixture experienced the same conditions, the same mixing method was generally applied throughout the experiment. The inside surface of the 0.07 m3 rotary mixer had been cleaned and lubricated before to use. Preparing the weights of the materials required and utilized for every sample was the first stage. Initially the coarse aggregate was added and then the fine aggregate was well mixed for four minutes and then the cement and mixing were added for four minutes. Meanwhile, the rubber crumbs and dry mixing were added for four minutes, after making a consistent combination, the water was gradually added and mixing with an approximate time of about 10 minutes (total). Later, after the mixture being homogenized, the concrete was poured to the molds. All deep beam molds were prepared and lightly greased. In this experiment, a rod vibrator was employed. Twenty-four hours after casting, the molds were taken out. During the 28-day curing phase, the burlap covering was kept damp.

2.4 Sample Descriptions and Test Setup

As illustrated in Fig. 2, six simply supported RC deep beams were built for this investigation and tested until they failed under the influence of two-point symmetric stress. The rectangular cross-section of each beam was the same, with fixed dimensions (b=150×h=300 mm). The total length of the tested beam was 1400 mm, and the tested span (clear) was 1200 mm. The deep beams were grouped into two categories, (R1 and R2), the first category (R1) representing three samples with the same main reinforcement ratio (ρ1) with the difference in the content of rubber, which stands for (0%,10% and 20%) and second category (R2) representing three samples with the same main reinforcement ratio (ρ2) with the difference in the content of rubber, which stands for (0%,10% and 20%). Additionally, longitudinal and transverse steel rebars having diameter of 6 mm are utilized as the beam web reinforcement. Loads were applied to each beam at two symmetrical locations to produce a constant moment zone spanning 400 mm to investigate the flexural performance of RC deep beams with selected various rubber content.

A hydraulic jack and plate spaced 400 mm apart were used to apply two concentrated loads on the deep beam. In the middle of the sample and beneath the loading points, three LVDTs were employed. The hydraulic machine in Fig.3 shows the load increments until the maximum load is attained. All samples' fracture propagation both during loading and at the point of failure was noted. Show Tab.7 rubber content and the number of GFRP for each deep beam.

Table 7. Details of samples

Sample	Rubber content (%)	Reinforcement ratio (ρ)	No. of GFRP	Diameter of GFRP	Shear span	Width mm	Length mm	Depth mm
R1-0%	0	0.0085	3	12	400	150	300	1400
R1-10%	10	0.0085	3	12	400	150	300	1400
R1-20%	20	0.0085	3	12	400	150	300	1400
R2-0%	0	0.0113	4	12	400	150	300	1400
R2-10%	10	0.0113	4	12	400	150	300	1400
R2-20%	20	0.0113	4	12	400	150	300	1400

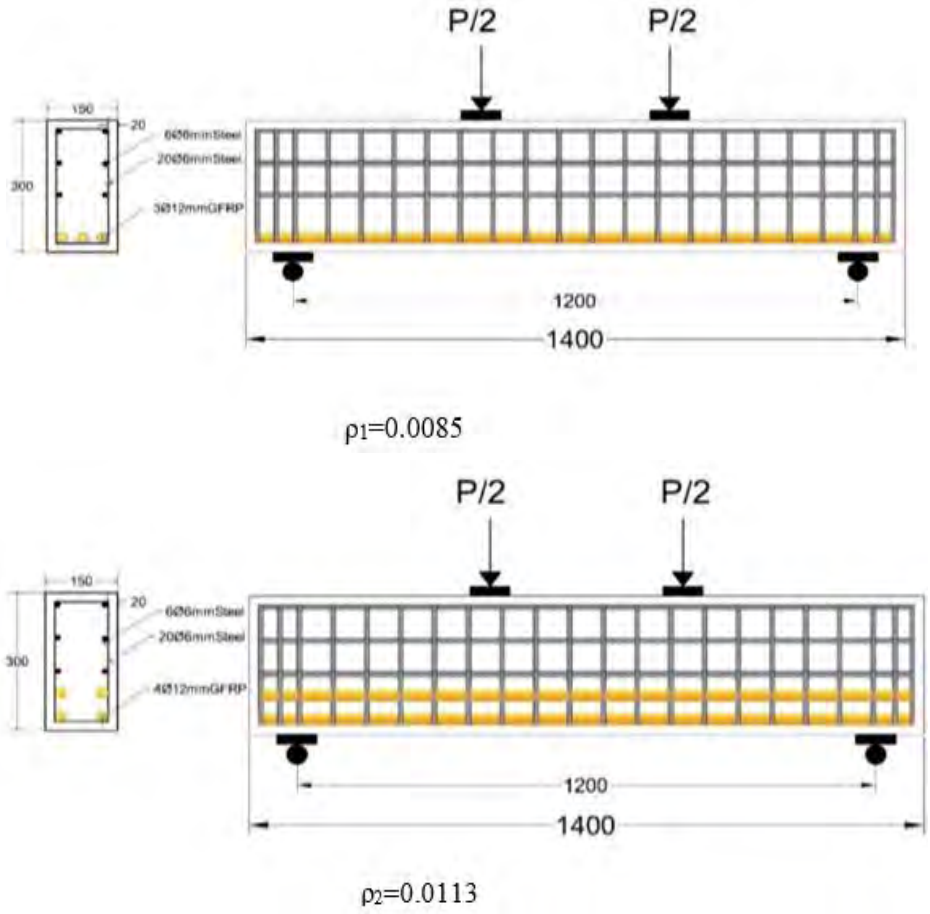

Fig. 2. Details of dimensions and reinforcement

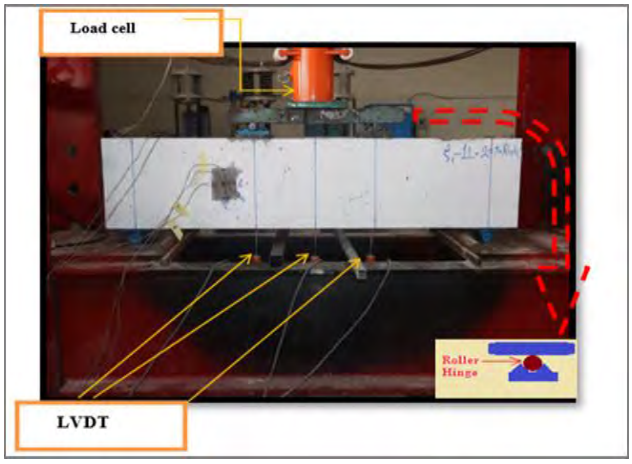

Fig. 3. Deep beams test details

3. Result and Discussion

A brief summary of the results and conclusions derived from the analysis of these results is given in the following sections.

3.1 Mechanical Properties of Rubberized Concrete

3.1.1 Workability (Slump) Test

Fig. 4 displays the slump test results for both rubberized and regular concrete. Slump values were shown to decrease with an increase of crumb rubber (10%, 20%). This study examined different ratios of freshly mixed concrete to crumb rubber (0%, 10%, and 20%). The mixture with 0% rubber had a 90 mm slump, 10% rubber produced an 80 mm slump, and 20% rubber produced a 70 mm. Rubber particles have a rougher surface with heterogeneous shape compared to the natural sand

particles, which is the cause of the decline[19]. As a result, inter-particle frictional resistance rises and work capacity falls[20].

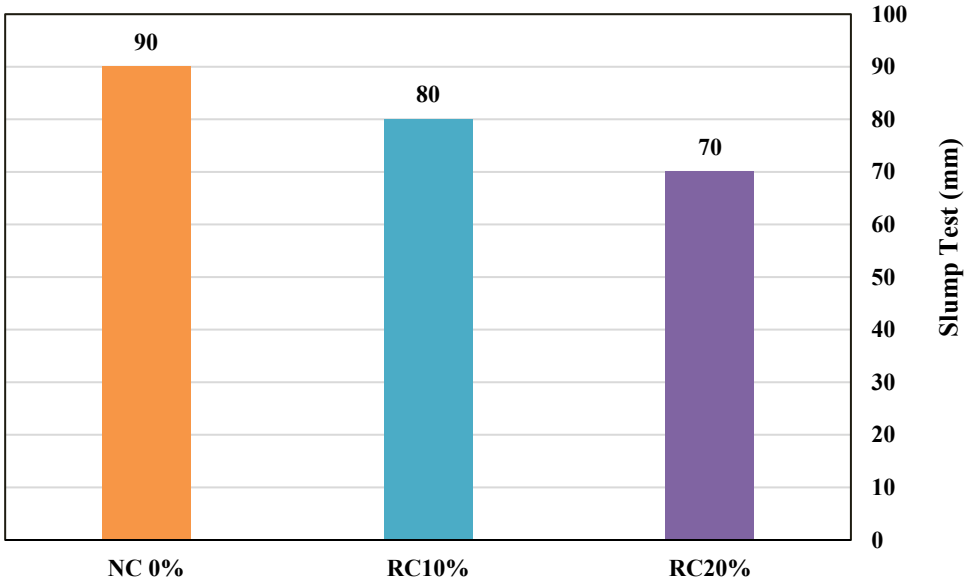

Fig. 4. The results of the slump test for both regular and rubberized concrete mixtures with varying rubber contents

3.1.2 Test of Compressive Strength

One of the most important factors taken into consideration is the concrete's compressive strength. Samples are inspected according to the approved specification ASTM C39 [21]. Rubberized concrete mixes were prepared considering two replacement ratios of 10% and 20%. In addition, a reference mixture of normal concrete was prepared for purpose of comparison. Samples were cast under standard conditions. Samples were tested at 28 days of age. Each concrete mixture's compressive strength was measured using three cylinders with a dimension of (300 mm depth and 150 mm diam.). Fig. 5 shows the failure modes for normal and rubberized concrete cylinders after the compression strength test. Based on the results in Fig.6, which is attached. It is demonstrated that rubber concrete loses more strength with respect to rubber aggregate volumetric percentage. The concrete compressive strength showed a decline by 21.57% at 10% and 30.31% at 20% rubber aggregate percentage in comparison to normal concrete. The cause for this decline in strength is ascribed to deficient bond exists in around cement matrix surrounding rubber particles[22, 23]. In addition, the entrapped air inside the matrix resulted from rubber hydrophobicity [24].

%0 RUB %10 RUB %20 RUB

Fig. 5. Failure mechanisms of concrete cylinders following a test for compressive strength

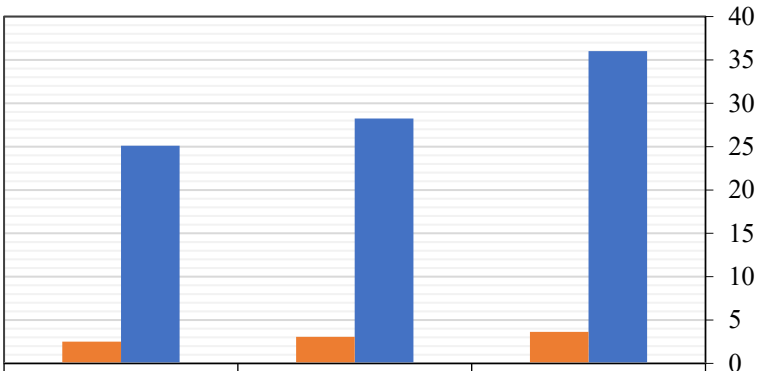

	RUB (20%)	RUB (10%)	RUB (0%)
Compressive	25,1	28,25	36,02
Splitting	2,504	3,056	3,642

Fig. 6. Results of compressive and splitting tensile strength

3.1.3 Splitting Tensile Strength

This property represents an important property of concrete as it reflects the capacity of concrete to sustain loads causing cracks. In this study, according to the approved specifications for tensile inspection (ASTM C496)[25]. Three mixtures of rubber concrete having various two percentages of 10% and 20% in addition to plain concrete mix were prepared. Samples were cast under standard conditions. Samples were tested at 28 days of age. Each concrete mixture's splitting tensile strength was measured using three cylinders with a dimension of (150 mm diam. and 300 mm height). Figure 6 explains the results of the splitting tensile strength test. As shown in Fig. 6 , the results exhibited a decline of 19% and 31% in tensile strength for rubber concrete specimens at percentages (10% and 20%), respectively, in comparison to OPC mix specimens. The primary reason behind this decline in splitting strength is resulted from defect in bonding between the surrounding cement paste and the adjacent elastic rubber aggregate particles[26]. Additionally, the weaker boundary layer and increased water demand in the cement paste surrounding the crumb rubber aggregate particles due to the rubber's inability to absorb the trapped water[27, 28].

3.2 Structural Performance of Deep Beams

3.2.1 Load-Deflection

Table 8 presents the results from flexural test of RC deep beams. Load at initial crack, deflection at mid-span during the initial crack, the ultimate load, deflection at mid-span during maximum or ultimate load were measured. Ductility and failure mode were also evaluated. At initial cracking, the stiffness drop rate reduced significantly with inclusion of crumb rubber aggregate. Fig. 7 shows the load –deflection curves for the tested RC deep beams. Clearly, the load-deflection curve for all samples often climbs upward as the ratio of crumb rubber increases resulting in increased load-carrying capability due to the tendency of crumb rubber aggregate to absorb more energy. The ultimate load (Pu) increased by 32%, 41%, 61%, and 44%, for specimens (R1-10%, R1-20%, R2-10%, and R2-20%), respectively, in comparison to the plain RC beam. The sample's peak load was found to have marginally dropped (R2-0%). The load of the first crack of the samples containing rubber crumbs decreased compared to the reference due to the weakness of the interfacial bonding of the soft rubber particles adhered to the surrounding paste, which led to occurrence of small cracks on the surface of the rubber concrete.

The deviation in the middle of the deep beam extension at the first crack was reduced by (6.6%, 2.4%, 30.9%, 22.2%) for the deep beam specimens (R1-10%, R1-20%, R2-10%, and R2-20%), respectively, compared to the reference sample (R1-0%). In samples containing rubber crumbs, the first cracking appeared more clearly and spread until the shear span[29]. Fig. 11 illustrates modes of failure of the RC deep specimens tested in this study. As shown, rubberized RC deep beams exhibited increased number of cracks in comparison to reference beam. This is evidence on the crumb rubber tendency to improve and enhance the ductile behavior of RC deep beams.

3.2.2 Effect of GFRP Reinforcement Ratio

Figures 8 – 10 show the effect of reinforcement ratio on load-deflection of RC deep beams at constant crumb rubber ratio. To elaborate the effect of rubber aggregate particles, a comparison between the specimens (R1-10%) and (R1-20%) is presented. As shown in Fig. 10, the first crack generally dropped by 11.1% and 4.2% for (R2-10%) and (R2-20%), respectively, as the reinforcement ratio percentage increased. In comparison to (R1-10%) and (R1-20%), an increase in the ultimate load value of RC deep beams by 22% for (R2-10%) and 3% for (R2-20%). Despite being regarded as a material with brittle behavior[29], using GFRP rebars instead of steel rebars enhanced the tensile strength and, consequently, the load capacity of the deep beams. Deep beams may undergo a substantial internal force reorientation upon cracking, which tends to cause forces to flow straight starting from the loading point towards the support's region. In this arch action, compression struts are formed to immediately transfer the stress to the supports, and the longitudinal reinforcement serves as a tie to keep the arch's base together. Generally, the main longitudinal bars could enhance the control of the crack width and increase the ultimate load capacity.

3.2.3 Ductility Index

Ductility is regarded as one of the most crucial safety parameters as it exhibits the structural member's capacity to tolerate cracking and significant plastic deformations before failure and losing its capacity to support loads. According to Table 8, the rubberized concrete samples exhibited higher ductility than the normal concrete sample. The results showed an increase of (23.38%, 27.4%, 25.0%, 42.7%) for the deep beam specimens (R1-10%, R1-20%, R2-10%, and R2-20%), respectively, compared to (R1-0%).

Table 8. Results of the first crack, final load, deflection, ductility index, and failure mode

Sample	Pcr, [kN]	D.P% Pcr, %	Peak load, Pu, [kN]	D.P% Pu	Mid-span defection [mm]	D.P% Mid-span defect.	Ductility Index μE	Mode of failure
R1-0%	48.2	------	221	----	5.41	-----	1.24	Flexure
R1-10%	45	-6.6	291	31.6	10.38	91.8	1.53	Shear-Flexure
R1-20%	47	-2.4	310	40.3	13.4	147.7	1.58	Shear–flexure
R2-0%	57.9	-20.0	219	-0.9	4.62	-14.6	1.29	Flexure
R2-10%	40	-30.9	356	61	13.9	147.6	1.55	Shear-flexure
R2-20%	45	-22.2	317	43.4	11.11	105.4	1.77	Shear–flexure

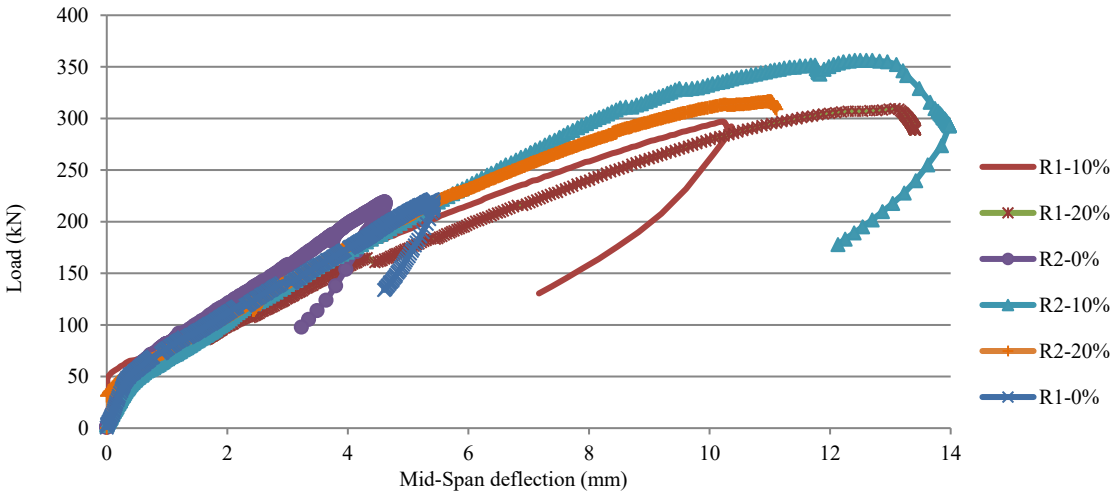

Fig. 7. Load-deflection response for all RC specimens

It is worth mentioning that the load deflection curve can indicate the beam performance in terms of ductility[11]. The increase in deflection led to an increase due to elastic performance of the elastic rubber particles which increase the deformations beyond the cracking [30]. This suggests that additional rubber crumbs with ratios of 10% and 20% may deform and contribute significantly to improved ductility. In general, deep beams reinforced with GFRP were more ductile when rubber aggregate was added.

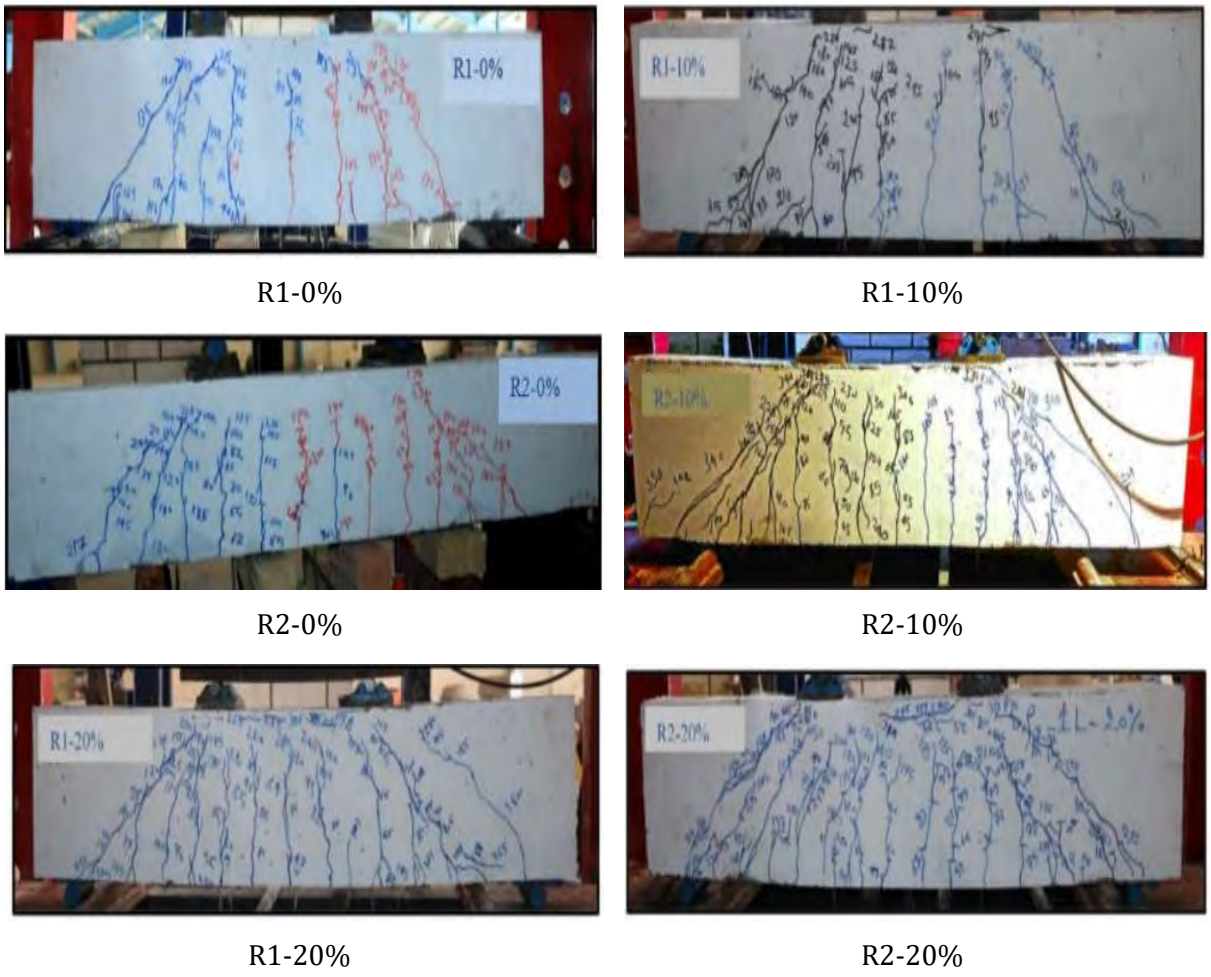

Fig. 8. Failure modes for specimens

4. Conclusions

In this study, the feasibility of recycling end-of-life tires' crumb rubber to create rubberized concrete is investigated experimentally. The impact of this process on the mechanical strength, including slump, compressive and tensile strengths were being assessed. RC deep beam reinforced with GFRP load-deflection curves were determined. The impact rubber aggregate percentages (0%, 10%, and 20%) and primary reinforcement ratio were the two main factors that were adopted analyze the flexural performance of the RC rubberized deep beams reinforced with GFRP bars. In this regard, the main conclusions obtained from the investigation's findings are:

- The concrete workability was significantly altered as the percentage of rubber aggregate increased from 0% up to 20% in comparison to normal concrete. This decrease is proportionate to crumb rubber content.
- In comparison to plain concrete mix, the rubberized concrete mixture's compressive strength dropped by roughly 19% and 31%, respectively, for crumb rubber contents of 10% and 20%. On the other hand, when the rubber content was raised to 10%, the splitting tensile strength dropped by 19%, and it declined by 45% at 20%, rubber content, compared to reference mix.

- The deflection load curve revealed that as the first-crack load dropped when cracks in the rubberized concrete emerged more quickly, increasing the crumb rubber content increased the final load before complete failure occurred.
- For the beams that failed in shear and flexure, the ultimate load of rubberized concrete GFRP beams containing 10% and 20% improved by 34% and 43%, respectively, compared to control concrete. The improvement occurred due to the adequate bond interaction between the GFRP bars and the bounded rubberized concrete texture.
- Clearly, the increase in the reinforcement ratio led to an increase in the final load of the samples, as it enhanced control over the crack width and it developed the capacity of the final load. This is due to the properties of GFRP bars in withstanding tension three times that of steel bars.
- The 10% and 20% crumb rubber samples were more ductile than the normal concrete sample. Comparing the samples R2-10% and R2-20% to the reference sample, the use of GFRP with10% and 20% rubber can be recommended for shear-critical deep beams where ductility is desirable

This research presents the result discussing the shear behavior of deep rubber concrete sills reinforced with GFRP bars. A proposed model for use in future real-world civil engineering applications, where rubber concrete provides a model for sustainable concrete and GFRP bars provide a new generation model in reinforcement. Based on the current study's experimental findings, the following suggestions are given for further research: Using different proportions of processed crumb rubber to powder rubber. Further research using different FRP types is required, reinforcements as CFRP.

Acknowledgement

The authors would express their thanks for the technical and academic support given by University of Anbar, College of Engineering to conduct this study.

References

[1] Chandrappa R, Das DB. Waste quantities and characteristics. Solid Waste Management: Principles and Practice: Springer; 2024. p. 47-87. https://doi.org/10.1007/978-3-031-50442-6_2

[2] Kordoghli S, Paraschiv M, Kuncser R, Tazerout M, Prisecaru M, Zagrouba F, et al. Managing the environmental hazards of waste tires. Journal of Engineering Studies and Research. 2014;20(4):1-11. https://doi.org/10.29081/jesr.v20i4.52

[3] Su J-y, Chen G, Pan H-s, Lin J-X, Zhang J, Zhuo K-x, et al. Rubber modified high strength-high ductility concrete: Effect of rubber replacement ratio and fiber length. Construction and Building Materials. 2023;404:133243. https://doi.org/10.1016/j.conbuildmat.2023.133243

[4] Lafta MJ, Tobeia SB, Khattab MM, Kh F. Investigating the mechanical properties of concrete using non-treated crumb rubber and silica fume. Research on Engineering Structures and Materials. 2025. http://dx.doi.org/10.17515/resm2025-939me0602rs

[5] Qureshi M, Li J, Wu C, Sheng D. Mechanical strength of rubberized concrete: Effects of rubber particle size, content, and waste fibre reinforcement. Construction and Building Materials. 2024;444:137868. https://doi.org/10.1016/j.conbuildmat.2024.137868

[6] Ismail MK, Hassan AA. Shear behaviour of large-scale rubberized concrete beams reinforced with steel fibres. Construction and Building Materials. 2017;140:43-57. https://doi.org/10.1016/j.conbuildmat.2017.02.109

[7] Noaman AT, Bakar BA, Akil HM. Experimental investigation on compression toughness of rubberized steel fibre concrete. Construction and Building Materials. 2016;115:163-70. https://doi.org/10.1016/j.conbuildmat.2016.04.022

[8] Alasmari HA, Bakar BA, Noaman A. A comparative study on the flexural behaviour of rubberized and hybrid rubberized reinforced concrete beams. Civil Engineering Journal. 2019;5(5):1052-67. https://doi.org/10.28991/cej-2019-03091311

[9] Kadhim AA, Kadhim HM. Experimental investigation of rubberized reinforced concrete continuous deep beams. Journal of King Saud University-Engineering Sciences. 2023;35(3):174-84. https://doi.org/10.1016/j.jksues.2021.03.001

[10] MS S, Nagarajan P, AP S. Behavior of Steel Fiber-Reinforced Rubcrete Deep Beams under Shear. ACI Structural Journal. 2022;119(1). https://doi.org/10.14359/51733003

[11] Mohamed A, Mahmoud K, El-Salakawy EF. Shear Capacity of Glass Fiber-Reinforced Polymer-Reinforced Concrete Continuous Deep Beams without Web Reinforcement. ACI Structural Journal. 2021;118(3). https://doi.org/10.14359/51729354
[12] Alkhrdaji T, Fyfe ER, Korff J, Schupack M, Bakis CE, Gentry TR, et al. Guide for the design and construction of structural concrete reinforced with FRP bars. Proceedings of the American Concrete Institute (ACI) Committee. 2006;440.
[13] Nematzadeh M, Hosseini S-A, Ozbakkaloglu T. The combined effect of crumb rubber aggregates and steel fibers on shear behavior of GFRP bar-reinforced high-strength concrete beams. Journal of Building Engineering. 2021;44:102981. https://doi.org/10.1016/j.jobe.2021.102981
[14] 440 AC. Guide for the design and construction of structural concrete reinforced with FRP bars American Concrete Institute 2015.
[15] American Concrete Institute-Committee 318. Building code requirements for structural concrete and commentary, ACI318-2011. Farmington Hills, MI, USA: ACI, August 2011.
[16] 45 I. Aggregates of Natural Resources used for Concrete and Construction. Iraqi Standards Orginzation. 1984.
[17] D854 A. Standard Test Methods for Specific Gravity of Soil Solids by the Water Displacement Method. 2023.
[18] ASTM C136, Standard Test Method for Sieve Analysis of Fine and Coarse Aggregates. . ASTM International West Conshohocken, PA2006.
[19] Guelmine L. The freeze-thaw durability of concrete containing the rubber aggregate of tire waste. Research on Engineering Structures & Materials, 8 (2): 253-264. 2022. http://dx.doi.org/10.17515/resm2022.371ma1207
[20] Eisa AS, Elshazli MT, Nawar MT. Experimental investigation on the effect of using crumb rubber and steel fibers on the structural behavior of reinforced concrete beams. Construction and Building Materials. 2020;252:119078. https://doi.org/10.1016/j.conbuildmat.2020.119078
[21] ASTM C39, Standard Test Method for Compressive Strength of Cylindrical Concrete Specimens. American Society for Testing and Materials, ASTM International; 2021.
[22] Liu L, Wang C, Liang Q, Chen F, Zhou X. A state-of-the-art review of rubber modified cement-based materials: Cement stabilized base. Journal of Cleaner Production. 2023;392:136270. https://doi.org/10.1016/j.jclepro.2023.136270
[23] Roychand R, Gravina RJ, Zhuge Y, Ma X, Youssf O, Mills JE. A comprehensive review on the mechanical properties of waste tire rubber concrete. Construction and Building Materials. 2020;237:117651. https://doi.org/10.1016/j.conbuildmat.2019.117651
[24] Benammar A, Noui A, Benouadah A, Maafi N, Kessal O, Dridi M, et al. Enhancing sustainability and performance in alkali-activated mortars with recycled rubber aggregates subjected to varied curing methods. Research on Engineering Structures and Materials. 2024. https://doi.org/10.17515/resm2024.192ma0226rs
[25] C496 A. Standard Test Method for Splitting Tensile Strength of Cylindrical Concrete Specimens. 2017.
[26] Qadir IMA, Noaman AT. Effect of combination between hybrid fibers and rubber aggregate on rheological and mechanical properties of self-compacting concrete. Construction and Building Materials. 2024;414:135038. https://doi.org/10.1016/j.conbuildmat.2024.135038
[27] Liu H, Wang X, Jiao Y, Sha T. Experimental investigation of the mechanical and durability properties of crumb rubber concrete. Materials. 2016;9(3):172. https://doi.org/10.3390/ma9030172
[28] Shahrul S, Mohammed BS, Wahab M, Liew M. Mechanical properties of crumb rubber mortar containing nano-silica using response surface methodology. Materials. 2021;14(19):5496. https://doi.org/10.3390/ma14195496
[29] Mahmoud AS, Ali ZM. Behaviour of reinforced GFRP bars concrete beams having strengthened splices using CFRP sheets. Advances in Structural Engineering. 2021;24(11):2472-83. https://doi.org/10.1177/13694332211001515
[30] Hou M, Xu K, Monteiro PJ, Li VC. Rubber particle bridging effect on crack width control of low carbon Engineered Cementitious Composites (ECC). Cement and concrete composites. 2023;140:105106. https://doi.org/10.1016/j.cemconcomp.2023.105106

Research on Engineering Structures & Materials
www.jresm.org

Research Article

The statistical modeling of traffic characteristics and noise levels on urban roads with rigid pavement

Hamid Athab Al-Jameel [*,a], Ban Ali Kamil [b], Haider Fadhil Addab [c]

Department of Civil Engineering, University of Kufa, Najaf, Iraq

Article Info

Article History:

Received 12 Oct 2025

Accepted 15 Dec 2025

Keywords:

Free predictive noise model;
Road traffic noise;
Rigid pavement;
Statistical modeling;
Statistical tests;
Traffic noise;
Urban roads

Abstract

Urban road traffic noise is a serious environmental issue that directly affects people's health and quality of life in big cities. This study statistically investigates the relationship between traffic noise levels and pavement surface condition on urban roads with rigid pavement in Najaf City, Iraq. Field data were collected on three urban road segments with Pavement Condition Index (PCI) values of 65, 77, and 86, representing fair, good, and very good conditions. A total of 432 observations were obtained during daytime peak periods (06:00–18:00) under dry weather. At each observation, traffic noise levels (dB) were measured at the roadside using a calibrated Class 1 sound level meter in accordance with ISO 1996-1:2016. Concurrently, traffic volume and vehicle classification were extracted from video recordings; vehicle speeds were derived from time–distance analysis and checked against accelerometer readings; and PCI values were computed from ASTM D6433 condition surveys supported by drone imagery. The statistical analysis comprised analysis of covariance (ANCOVA), Spearman's rank correlation, and linear regression modelling. The results indicate that pavement condition significantly affects noise levels, with lower PCI values associated with higher noise levels. Although the bivariate correlation between speed and noise is modest ($r \approx 0.3$), the ANCOVA results show that pavement condition moderates the speed–noise relationship. The findings highlight the importance of incorporating pavement quality indicators, such as PCI, into local noise prediction models to support more reliable urban planning and pavement management decisions.

© 2026 MIM Research Group. All rights reserved.

1. Introduction

Transportation networks are vital for urban development; however, the rapid growth in vehicle usage has led to road traffic noise becoming one of the most prevalent forms of urban pollution, with well-documented health impacts, including cardiovascular diseases and cognitive disorders [1-4]. Despite its seriousness, noise pollution is often overlooked compared to air and water pollution. To address this, statistical tools and software, such as R, have been effectively employed to analyze traffic noise using field data [5]. Additionally, numerous global models, ranging from traditional equations to machine learning, have been developed to predict noise levels [6,7]. However, the predictive power of these models is limited when they ignore local conditions, especially pavement characteristics. Surface roughness, pavement type, and degradation significantly impact noise levels from tire-road interaction and mechanical vibrations [8,9]. Previous studies have shown that a decrease in PCI (deteriorated pavement) is generally associated with higher road traffic noise levels, lower operating speeds, and reduced traffic capacity. In contrast, pavements with a higher Pavement Condition Index (PCI) (good or very good condition) tend to generate lower noise levels and allow higher speeds and flow rates [10,11].

*Corresponding author: hamid.aljameel@uokufa.edu.iq
[a]orcid.org/0000-0002-1367-4421; [b]orcid.org/0009-0006-2549-9364; [c]orcid.org/0000-0002-8311-6265
DOI: http://dx.doi.org/10.17515/resm2025-1232ic1012rs

In cities like Najaf, Iraq, where religious tourism intensifies traffic demands, incorporating pavement condition into noise modeling is essential. This study addresses this gap by analyzing the relationships among noise, speed, and pavement condition using ANCOVA, regression, and correlation. ANCOVA was selected because it allows the combined effect of continuous variables (traffic speed and flow) and categorical pavement-condition groups (PCI levels) on noise to be tested within a single framework. This approach enables us to control for covariates, to examine interaction effects between speed and pavement condition, and to obtain adjusted mean noise levels for each PCI category, which cannot be achieved by simple correlation or regression alone.

Findings from other regions confirm that deteriorated pavements reduce traffic speed and flow by up to 20% [11] and that road roughness can significantly lower vehicle speed and road capacity [12, 13]. For example, [12] found that a 1,000 mm/km increase in roughness reduces road capacity by 300 passenger cars per hour (PCU/h). [14] developed an empirical model showing that surface roughness has a greater influence on average speed than pavement type or speed limits; however, their model lacked differentiation by vehicle type, limiting its reliability. Local studies, such as those by Kamil and Al-Jameel [9], found a drop in noise level from 83 dB (PCI 77) to 80.4 dB (PCI 86), reinforcing the notion that smoother pavement results in lower noise. This study, therefore, builds on these insights to present a localized, statistically validated noise-prediction framework tailored to urban roads with rigid pavement. According to Khan [15], vehicle speed decreases by roughly 8.8% when pavement condition deteriorates from good to extremely poor. At the same time, in-car vibration increases by more than 30% and noise levels climb by about 3.3%. Sharwan [16] discovers that vehicle speed, road surface type, and roughness all have a significant impact on traffic noise, where noise levels climb with increasing speed and road roughness, with larger cars producing more noise than lighter ones. The novelty of this work lies in (i) focusing on rigid urban pavements that dominate major corridors in Iraqi cities, (ii) explicitly incorporating the Pavement Condition Index as an explanatory variable alongside traffic speed, flow and composition, and (iii) developing a localized statistical model for Najaf City that can be used to improve the accuracy of traffic-noise prediction and to support pavement-management and planning decisions under Iraqi conditions.

2. Methodology

The methodology adopted in this study consists of four main stages: (i) selection and characterization of road segments based on PCI; (ii) field data collection for traffic noise, vehicle speed, traffic volume and classification; (iii) data preparation and statistical analysis, including descriptive statistics, normality tests, ANCOVA, correlation and regression modelling; and (iv) interpretation of results and development of implications for pavement and noise management as illustrated in Fig. 1.

2.1 Study Area

In Najaf, Iraq, the analyzed sample comprises 5100 m of urban divided arterial road with rigid Portland cement concrete pavement distributed over the three PCI levels. This road links essential land uses, including the Najaf International Airport, business districts, and historic religious sites. The site provides a representative setting for examining traffic noise under various pavement conditions, owing to the city's unique urban context and significant traffic demand generated by tourists. Using the procedures in ASTM D6433 [16], Standard Practice for Roads and Parking Lots Pavement Condition Index Surveys, three rigid-pavement segments were selected to represent different condition levels. For each segment, visible surface distresses were identified and quantified, deduct values were calculated, and the results were combined to obtain the PCI value according to the standard. This process yielded PCI scores of 86, 77, and 65, which correspond to ‘very good’, ‘good’, and ‘fair' conditions, respectively. Significant noise-reflecting obstacles, such as buildings, trees, and embankments, were absent from every section, reducing confounding acoustic effects and guaranteeing that the majority of the measured noise was produced by vehicles. ASTM D6433 applies to PCI surveys of both flexible and rigid pavements; in the present study, its procedures were used for rigid pavement segments.

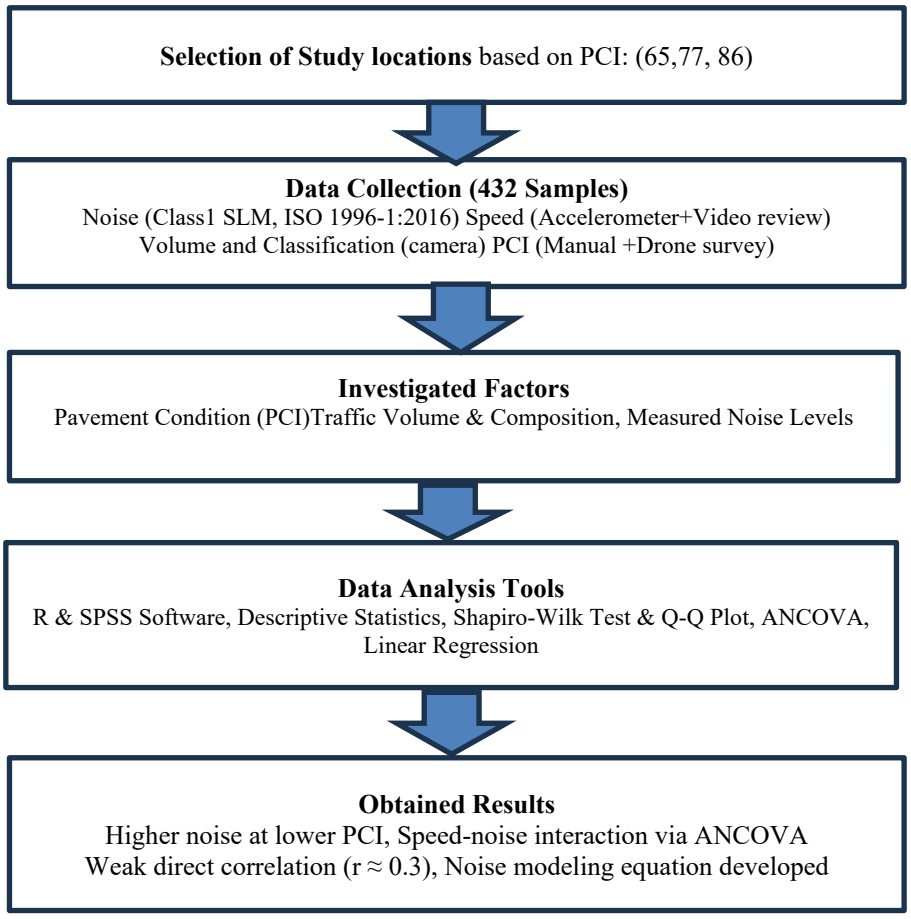

Fig. 1. Flow chart of this study

2.2 Data Collection

Field data were collected during daytime peak periods (06:00 AM – 06:00 PM) under dry weather conditions to ensure consistency. A total of 432 observations were recorded, equally distributed across the three PCI categories. The following parameters were measured:

- Traffic Noise (dB): measured at roadside using a calibrated Class 1 sound level meter (SLM), following ISO 1996-1:2016 guidelines for environmental noise measurement [17].
- Vehicle Speed (km/h): Captured using a high-precision accelerometer and verified via video footage.
- Traffic Volume and Classification: Acquired through video analysis using time-lapse cameras; classified into five vehicle types (light vehicles, motorcycles, buses, trucks, and heavy trucks).
- Pavement Condition Index (PCI): assessed primarily by manual field surveys according to ASTM D6433, where surface distresses on each slab were identified, measured, and converted into deduct values to compute the PCI. In addition, aerial verification was conducted using high-resolution nadir images acquired by a drone; these images were used to confirm the location and extent of significant distress visually and to assess the consistency of the manual ratings. Only the PCI values obtained from the manual ASTM D6433 procedure were used in the statistical analysis, while the aerial survey served as a validation tool.

2.3 Data analysis and Statistical Analysis Framework

All collected data were cleaned and tested for outliers using R software. To assess the normality of the collected data, both Q-Q plots and the Shapiro–Wilk test were used in R software. The results showed that the collected data follow the normal distribution ($p > 0.05$). The reliability of PCI classification was further confirmed through inter-rater agreement ($\kappa > 0.80$). Different statistical models and methods were conducted using R software and SPSS to discover the relationships between noise levels and explanatory variables, such as:

- Descriptive Statistics: Means, standard deviations, and ranges were computed for all variables across PCI categories.
- Box Plot and Exploratory Data Analysis: Visual comparison of noise and speed across pavement conditions.
- ANCOVA (Analysis of Covariance): Used to assess the interaction between road condition (categorical factor) and noise level (continuous covariate), accounting for heterogeneous slopes.
- Simple Linear Regression: Modeled the relationship between speed and noise for baseline evaluation.
- Spearman's Rank Correlation: Non-parametric analysis to test monotonic relationships between speed and noise, supplementing linear model assumptions.

3. Results and Discussion

The 5.1 km arterial road segment in Najaf City, Iraq, was chosen due to its high traffic volume and key urban environment, as seen in Fig. 2. This section is perfect for researching traffic noise since it passes through commercial, industrial, and religious zones and links important locations like Al -Najaf Al-Ashraf International Airport and Al-Zahra Bridge.

The road was divided into three sections based on PCI values of 65, 77, and 86, enabling a comparative analysis of noise and speed under varying surface conditions. The absence of significant noise-reflecting barriers such as buildings or trees ensures that measured noise levels primarily reflect vehicular sources. The location's functional diversity and heavy traffic flows provide a representative, controlled setting for evaluating the relationships among pavement quality, traffic behavior, and environmental noise. The following parameters were measured from the mentioned location:

- Using a noise meter to measure noise.
- Since installing traffic meters on the highways was difficult, a digital camera was employed to measure traffic volumes using an accelerometer and calculate the average speed.
- The PCI was calculated using each of the following methods: The manual process and the drone.

Fig. 2. Location of the chosen data collection sites

In this study, a high-resolution drone equipped with a stabilized camera was used to support manual PCI assessments by capturing georeferenced aerial imagery along selected road segments. The drone flew at a low altitude (15–25 meters), capturing detailed images that revealed surface distresses such as cracking, spalling, and patching on rigid pavements. These images were overlaid on GIS base maps and analyzed to verify the presence, type, and extent of distresses identified

during the manual survey. For the drone-assisted method, a multi copter equipped with a high-resolution camera was flown at an altitude of 25–30 m along each road segment. The collected nadir images were processed into an orthomosaic, from which individual slabs and surface distresses (cracking, spalling, patching, etc.) were visually identified and mapped. Distress quantities estimated from the orthomosaic were then converted into PCI values following the same ASTM D6433 procedure. To assess accuracy, a 10% random sample of slabs was inspected both manually in the field and from drone imagery; the difference between the two PCI values was within ±5 points for all sampled slabs, indicating good agreement and confirming that drone-assisted verification is sufficiently accurate to support the manual PCI assessment.

While the PCI values were primarily derived from field surveys conducted in accordance with ASTM D6433, drone imagery served as a crucial verification tool, enhancing the reliability and spatial coverage of the pavement condition assessment. Due to the high traffic volume, noise levels were measured at the edge of the road. Subsequently, a statistical analysis was performed to develop a model based on the collected data. Descriptive statistics are summarized in Tables 1, 2, and 3.

Table 1. Description of statistics for data

Road Condition	Sample size	Mean (speed level)	Standard deviation (speed level)
PCI 65	432	60.72222	4.116941
PCI 77	432	66.50000	8.122280
PCI 86	432	64.55556	2.961124

This table presents the mean and standard deviation of vehicle speed measured on road sections with different Pavement Condition Index (PCI) values. Each PCI category (65, 77, 86) included 36 speed observations. The key insights are:

- PCI 65 (Fair Condition): Lower mean speed (60.7 km/h) with moderate variability.
- PCI 77 (Good Condition): Highest mean speed (66.5 km/h) but also the most significant standard deviation, indicating a wider range of speed behavior.
- PCI 86 (Very Good Condition): Intermediate speed (64.6 km/h) with the lowest variability, suggesting more consistent speeds.

Table 2. Descriptive data for PCI with speed samples

Statistical Parameter	Actual Input Variables			Output = (noise level)
	I1	I2	I3	
	A sample that included (432) field readings taken in three sections on the road			
Range	83.00	36.00	2.00	12.50
Minimum	161.00	49.00	1.00	71.30
Maximum	244.00	85.00	3.00	83.80
Mean	181	63.01	2	78.63
Std. Deviation	17.08	5.73	0.82	2.75

The sample size was 432. The results show that all data are subjected to the normal distribution, and the resulting data from the statistical analysis were used to assess the noise levels in the study area precisely. Furthermore, using SPSS software, all data were examined for skewness and kurtosis. Table 2 summarizes the statistical properties of the variables used in the model that predicts noise levels. It includes 432 observations across the entire dataset and provides the following:

- I1: Traffic volume (range: 83–244 vehicles, mean: 181, SD: 17.08)
- I2: Speed level (range: 49–85 km/h, mean: 63.01, SD: 5.73)
- I3: Vehicle classification (1 to 3 categories, mean: 2, SD: 0.82)

- Noise level (Output): Ranges from 71.3 dB to 83.8 dB, with a mean of 78.63 dB and a standard deviation of 2.75.

Table 3. Descriptive data for PCI with noise samples

PCI	Sample size	Mean (noise level)	Standard deviation (noise level)
PCI 65	432	81.17222	1.655745
PCI 77	432	77.84167	2.819258
PCI 86	432	76.81111	1.607621

Checking for data normality. A typical graphical technique for determining whether data is non-normal is a Q-Q plot, also known as a Quantile-Quantile plot. Another word for percentile is quantile. Plotting the quantiles of a data set versus the quantiles of a theoretical reference distribution is known as a Q-Q plot. The hypothesis that the data have a normal distribution is supported if the plot is a straight line. Data typically seems distributed, as seen in Fig. 3. However, the Shapiro-Wilk test, another R method for testing normality, was employed to verify this. A goodness-of-fit test is the Shapiro-Wilk test. It often looks at how closely the sample data resembles a normal distribution. By arranging and standardizing the sample, it investigates this. To put it another way, the test's null hypothesis is that the data are normally distributed. For both noise and speed levels, the test's P-values were 0.05 and 0.06, respectively, suggesting strong P-values. As a result, the null hypothesis should not be rejected, leading to the conclusion that the data are normally distributed.

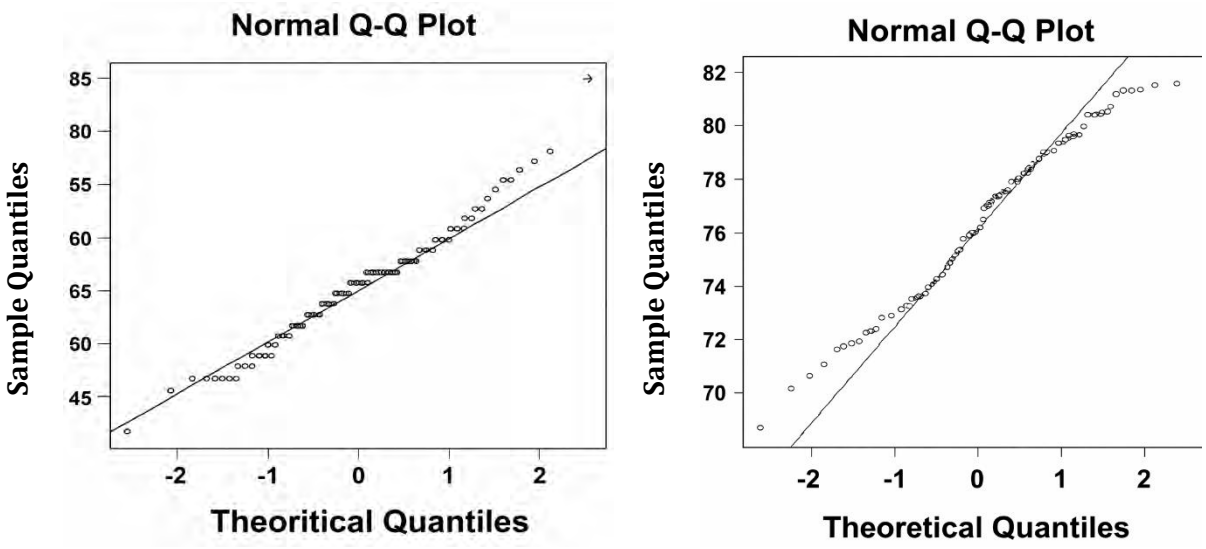

Fig. 3. Q-Q plot for noise level on the left and speed level on the right

3.1 Speed Level Analysis

The box plot of speed levels categorized by road condition is shown in Fig. 4. According to the plot, PCI77 road conditions tend to have higher speed levels, as they enable cars to travel faster. Additionally, it shows that the PCI 77 condition has a higher standard deviation in vehicle speed than the other PCI conditions, which explains why it is the most manageable for large groups of drivers with varying speed ranges.

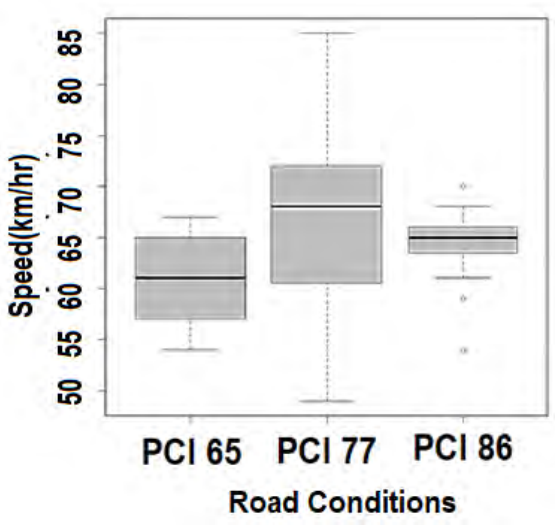

Fig. 4. Box plot of speed data divided by road condition categories

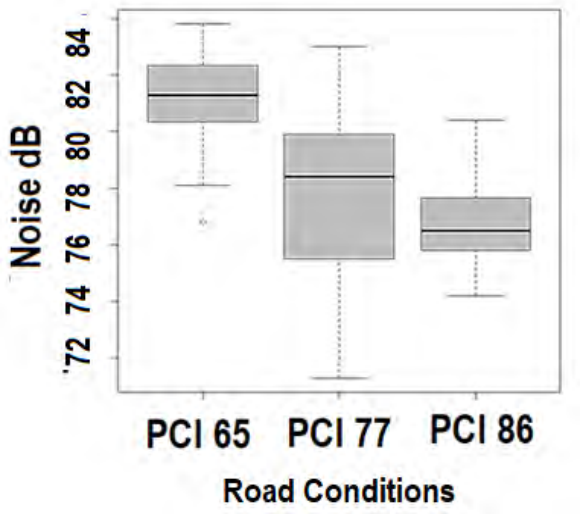

Fig. 5. Box plot of noise data divided by road condition categories

3.2 Noise Level Analysis

A pavement's overall structural and surface condition can be measured using the Pavement Condition Index (PCI), a numerical rating ranging from 0 to 100. This study examined three pavement condition types: PCI 86, representing Very Good to Excellent conditions; PCI 77, indicating good conditions; and PCI 65, indicating fair conditions. Surface defects like cracking, raveling, and patching alter how tires interact with the road as pavement gets worse, which has an impact on noise level. Engine, exhaust, aerodynamics, and tire pavement interaction are some of the components that contribute to the up-traffic noise.

The tirepavement interaction, which is dependent on the pavement surface, becomes the primary source at speeds greater than around 25–30 miles per hour. Although tire type, pavement composition, and vehicle speed all affect noise levels, the box plots in Figure 5 reveal a distinct pattern. Because there is less vibration and air pumping, PCI 86, which has a smooth surface, produces the least noise. The box plot for PCI 77 indicates a moderate increase in noise due to minor surface roughness caused by pavement flaws, little cracking, and mild wear. Finally, the boxplot shows higher noise (impact noise caused by vibration) in PCI66, where the surface is in poor condition, with noticeable cracking, patching, and raveling.

3.3 Statistical Model

A statistical processing of data was conducted as follows:

3.3.1 ANCOVA Analysis

ANCOVA is just another example of the general linear model. A box plot would not provide sufficient information, so an Interaction plot would offer more detail on the observed data, as shown in Fig. 6 and Table 4. The lines of the three road condition levels are not parallel at some noise levels, so that one might expect a statistically significant interaction. A model with interaction allows the slopes to differ across groups. In other words, the interaction provides for non-parallel lines. Therefore, the question that could be answered here is whether the effect of noise depends on the road conditions levels. Examining the figure and the table results, including p-values, one can conclude that there is no evidence of difference between slopes for most cases where p-value > 0.05 which explain that not only the pavement conditions that explain noise level for different speed limits although there was a significant relationship between speed limit and noise level for that study area.

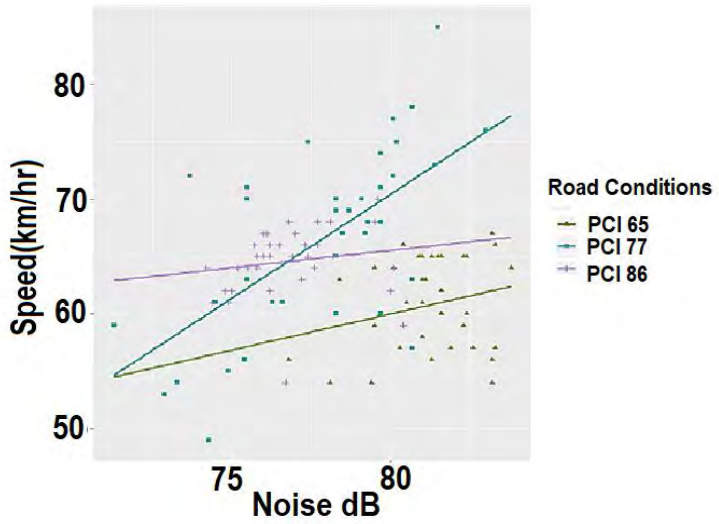

Fig. 6. Interaction plot of observed data

Table 4. The results of the ANCOVA analysis

Case	Intercept	Estimated Std error	T value	P-value
	9.5225	38.9196	0.245	0.8072
Road.ConditionPCI 77	-84.0924	44.6723	-1.8	0.0626
Road.ConditionPCI 86	31.8699	54.3463	0.586	0.5589
Noise	0.6308	0.4794	1.316	0.1912
Road.Condition PCI 77: noise	1.1815	0.5559	2.125	0.0360
Road. ConditionPCI 86:noise	-0.3292	0.6882	-0.478	0.6334

3.3.2 Correlation

The correlation between traffic speed and noise was studied. Traffic speed and noise measurements are conducted simultaneously from 6:00 AM to 6:00 PM, with 5-minute measurement intervals. traffic speed data (pcu/hour) and Noise level (dB) were analyzed using Spearman's correlation analysis. The correlation coefficient was only about 0.3, indicating a weak relationship between noise and speed levels. The simple linear regression model is also used to address the research questions mentioned above. The model of simple linear regression is:

$$E(Yi) = \beta_o + \beta_1 \times X_i + \epsilon_i \quad (1)$$

Where Yi = the expected response variable, refers to the noise level, means the average value that would be seen if a considerable number of plots with that xi were used, x_i: level of speed for the ith observation, and ϵi: random error term for the i^{th} observation.

Table 5. The results of the statistical analysis

Parameter	Intercept	Std. Error	t value	Pr(>|t)
Noise	75.53056	2.90208	26.026	<2e-16
Speed	-0.04815	0.04520	1.065	0.289

$$Expected\ (noise) = 75.53056 - 0.048154 \times speed + error \quad (2)$$

This linear model assumes that ϵi is independent, normally distributed with mean zero, and has a homogeneous variance σ^2. Using the R software, which includes code for a simple regression model, the results are shown in Table 5 below. It is essential to remember that:

- Intercept: Predicted noise level (y) with no effect of speed applied (x=0) is estimated to average 75.5 (must be taken with caution because zero is beyond the range of the data).

- Slope: A one km/hr. increase in speed (1 unit increase in x) is associated with a 0.048 predicted increase in noise (y).

4. Discussion

Analysis of field data from urban roads in Najaf revealed statistically significant insights into the relationships among pavement surface condition, vehicle speed, and traffic noise. The observed variations in noise levels across different Pavement Condition Index (PCI) values underscore the pivotal role of road surface quality in influencing urban environmental noise.

- Pavement Condition and Noise Levels: The results demonstrated that noise levels decreased as PCI improved, consistent with previous findings by Kamil and Al-Jameel [9] and Khan et al. [8], who reported that surface roughness intensifies tire-pavement interaction, leading to increased acoustic energy emission. In the current study, road sections with a PCI of 65 (fair condition) exhibited an average noise level exceeding 81 dB, compared to approximately 76.8 dB on roads with a PCI of 86 (very good condition). This 4–5 dB difference is acoustically significant, as even small decibel increases can substantially change perceived loudness and influence public health outcomes [2].
- Pavement Condition and Vehicle Speed: A positive trend was also observed between PCI and average vehicle speed, with drivers traveling more cautiously on deteriorated surfaces. Roads with PCI 65 recorded a mean speed of approximately 60.7 km/h, while those with PCI 77 and 86 recorded 66.5 km/h and 64.6 km/h, respectively. Although the difference is moderate, it aligns with findings from Hashim et al. [11] and Pinatt et al. [10], which suggest that poor pavement quality disrupts traffic flow and induces speed variability, particularly in mixed traffic environments.
- Noise-Speed Relationship and Interaction Effects: While a weak positive correlation (Spearman's $\rho \approx 0.3$) was identified between speed and noise, the ANCOVA model revealed a significant interaction between PCI and noise levels, suggesting that pavement condition mediates the speed–noise relationship. This result highlights the non-linear nature of traffic noise generation, where the influence of speed on noise cannot be evaluated independently of surface quality. The interaction effect suggests that speed increases may result in greater noise under rough pavement, but to a lesser extent on smoother roads, a phenomenon supported by Torija et al. [6] in their acoustic modeling studies.
- Implications for Urban Noise Modeling: These findings highlight the limitations of applying universal or overly simplistic noise prediction models in local contexts without accounting for infrastructure-specific variables, such as PCI. The results support including pavement surface condition as a core input in future predictive modeling, particularly in urban areas with diverse vehicle types, heavy use, and sensitive land uses such as religious centers and hospitals. In addition, while linear regression models provided baseline interpretations, the modest explanatory power suggests the potential value of applying more advanced statistical or machine learning approaches (e.g., artificial neural networks) in future research to capture complex, non-linear interactions more effectively.

5. Conclusions

This study examined how pavement surface condition influences traffic noise and vehicle speed on a major urban arterial in Najaf, Iraq. PCI classified road sections, and field data on noise, speed, and flow were analyzed using ANCOVA, Spearman's correlation, and linear regression. The results show a clear inverse relationship between PCI and noise: segments with poorer condition (PCI 65) produced noise levels about 4–5 dB higher than those in very good condition (PCI 86), an environmentally meaningful difference. Pavement condition also affected operating speeds, with lower PCI values associated with reduced average speeds, indicating drivers' response to deteriorated surfaces. Although the simple correlation between speed and noise was modest ($r \approx 0.3$), ANCOVA revealed a significant interaction between speed and PCI, indicating that pavement condition moderates the speed–noise relationship. The data satisfied normality assumptions, supporting the robustness of the statistical models, and the resulting prediction equation provides a practical tool for estimating roadside noise from observed traffic and PCI. Overall, the findings

show that improving pavement quality is not only a structural or safety measure but also an effective environmental strategy to reduce traffic noise in dense urban corridors.

5.1 Limitations of the Study

The study only looks at a few road segments or evaluates speed and noise over a brief period of time. Because road noise changes significantly between seasons, traffic numbers, weather, and ti me of day, this may lessen the data's representativeness.

References

[1] Murphy E, King EA. Environmental noise pollution: Noise mapping, public health, and policy. Amsterdam: Elsevier; 2022. https://doi.org/10.1016/B978-0-12-820100-8.00007-5
[2] Basner M, Babisch W, Davis A, Brink M, Clark C, Janssen S, et al. Auditory and non-auditory effects of noise on health. Lancet. 2014;383(9925):1325-1332. https://doi.org/10.1016/S0140-6736(13)61613-X
[3] Kim M, Hong J, Sheen S, Chung Y. Road traffic noise: annoyance, sleep disturbance, and public health implications. Am J Prev Med. 2012;43(4):353-360. https://doi.org/10.1016/j.amepre.2012.06.014
[4] Willich SN, Wegscheider K, Stallmann M, Keil T. Noise burden and the risk of myocardial infarction. Eur Heart J. 2006;27(3):276-282. https://doi.org/10.1093/eurheartj/ehi658
[5] Addab H. Statistical assessment of water-quality parameters for different flow regimes. Jordan J Civil Eng. 2024;18(2). doi:10.14525/jjce.v18i2.08. https://doi.org/10.14525/JJCE.v18i2.08
[6] Torija AJ, Ruiz DP, Ramos-Ridao AF. Use of back-propagation neural networks to predict both level and temporal-spectral composition of sound pressure in urban sound environments. Build Environ. 2012;52:45-56. https://doi.org/10.1016/j.buildenv.2011.12.024
[7] Liu Z, Wang R, Liu B, Song B, Li X, Wang Y, et al. Application of artificial neural networks in ecological research. Chin Sci Bull. 2010;55(34):3853-3863. https://doi.org/10.1007/s11434-010-4183-3
[8] Khan I, Khattak K, Khan ZH, Gulliver TA. Impact of road pavement condition on vehicular free flow speed, vibration and in-vehicle noise. Sci Eng Technol. 2023;3(1):1-8. https://doi.org/10.54327/set2023/v3.i1.48
[9] Kamil BA, Al-Jameel HAE. Impact of traffic flow and speed on noise level for rigid pavement under different pavement condition index. In: AIP Conf Proc. 2023;2793(1). https://doi.org/10.1063/5.0163024
[10] Pinatt JM, Chicati ML, Ildefonso JS, Filetti CRGDA. Evaluation of pavement condition index by different methods: Case study of Maringá, Brazil. Transp Res Interdiscip Perspect. 2020;4:100100. https://doi.org/10.1016/j.trip.2020.100100
[11] Hashim IH, Badawy RM, Heneash U. Impact of pavement defects on traffic operational performance. Sustainability. 2023;15(10):8293. https://doi.org/10.3390/su15108293
[12] Chandra S. Effect of road roughness on capacity of two-lane roads. J Transp Eng. 2004;130(3):360-364. https://doi.org/10.1061/(ASCE)0733-947X(2004)130:3(360)
[13] Ben-Edigbe J, Ferguson N. Extent of capacity loss resulting from pavement distress. Proc Inst Civ Eng Transp. 2005;158(TR1):27-32. https://doi.org/10.1680/tran.158.1.27.57830
[14] Yu B, Lu Q. Empirical model of roughness effect on vehicle speed. Int J Pavement Eng. 2014;15(4):345-351. https://doi.org/10.1080/10298436.2013.792931
[15] Khan, Imran & et al. (2023). Impact of Road Pavement Condition on Vehicular Free Flow Speed, Vibration and In-Vehicle Noise. Science, Engineering and Technology. https://doi.org/10.54327/set2023/v3.i1.48
[16] Shrawan Kumar, Tran., 2024 "Influence of Roadway Surface and Vehicular Speeds on Noise Levels: Case Study on NH-163", Int J Sci Res Sci & Technol, vol. 11, no. 2, pp. 1099-1108. https://ijsrst.com/index.php/home/article/view/IJSRST251222831
[17] ASTM International. ASTM D6433-20: Standard practice for roads and parking lots pavement condition index surveys. West Conshohocken (PA): ASTM International; 2020. https://doi.org/10.1520/D6433-20
[18] International Organization for Standardization. ISO 1996-1:2016: Acoustics - Description, measurement and assessment of environmental noise - Part 1: Basic quantities and assessment procedures. Geneva: ISO; 2016.

Research on Engineering Structures & Materials
www.jresm.org

Research Article

Mitigation liquefaction of sandy soil supporting shallow foundation using sodium silicate liquid injection

Ali Mohammed Dawood [*,a], Qassun S. Mohammed Shafiqu [b]

Department of Civil Engineering, College of Engineering, Al-Nahrain University, Baghdad, Iraq

Article Info

Article History:

Received: 11 Oct 2025

Accepted: 14 Nov 2025

Keywords:

Liquefaction;
Sodium silicate;
Injection method;
Sand soil;
Shallow foundation

Abstract

Sandy soil liquefaction poses a significant risk to shallow foundation structures. Shallow foundations subject to significant settlement, lateral displacement, and overturning are susceptible to earthquake-induced soil liquefaction. This study investigates the effectiveness of sodium silicate fluid injection as a soil improvement technique to mitigate the potential for liquefaction in loose sandy soils under the 2017 Halabjah earthquake. The research focuses on enhancing the strength, stiffness, and permeability of soils through chemical stabilization. The test program included evaluating the potential of sodium silicate fluid injection technology in addressing foundation liquefaction induced by seismic loadings using a shake table device. Sodium silicate solution was injected into saturated sand samples at 1:1 and 1:2 water-by-weight ratios in the stress bulb region, and the resulting changes in physical and mechanical properties were analyzed. The results indicate a significant improvement in soil strength and a significant reduction in liquefaction due to the formation of a silica gel matrix that bonds the soil particles. Tests conducted on shallow foundation specimens showed an increase in load-bearing capacity, a 57% reduction in settlement, and a 30% reduction in lateral displacement when the polymer was injected at a concentration of 1:2. When the water-sodium silicate ratio was reduced to 1:1, the improvement was further enhanced, with settlement and lateral displacement reduced by 76% and 60%, respectively, under seismic loads. Furthermore, excess pore pressure (Ru) was reduced by 25 and 33% in sand-treated soils at concentrations of 1:2 and 1:1, respectively. The proposed method offers an economical solution for liquefaction mitigation, making it suitable for urban areas and regeneration applications.

© 2026 MIM Research Group. All rights reserved.

1. Introduction

Liquefaction is a critical geotechnical phenomenon that occurs in saturated, loose sandy soils when subjected to seismic loading or other dynamic forces, leading to a temporary loss of strength and stiffness. This consequences in significant deformations, ground failure, and damage to structures supported by shallow foundations. Past earthquakes, such as those in Kobe (1995) and Christchurch (2011), have highlighted the destructive impact of liquefaction on infrastructure, emphasizing the need for effective ground improvement techniques [1]. Particularly susceptible to tilting and settling brought on by liquefaction are structures with shallow foundations, which can compromise their stability and functionality. Studies that liquefaction leads to shear strength reduction, causing ground failure, structural settlement, and tilting of shallow foundations. Recent case studies, such as the Christchurch Earthquake (2011), demonstrated that infrastructure damage was directly for improving soils linked to liquefaction in untreated soil deposits. Traditional methods, including dynamic compaction, drainage systems, and stone columns, have

*Corresponding author: alim.dawood95@gmail.com
[a]orcid.org/0009-0002-6225-2812; [b]orcid.org/0000-0002-0389-6872
DOI: http://dx.doi.org/10.17515/resm2025-1233ic1111rs
Res. Eng. Struct. Mat. Vol. 12 Iss. 2 (2026) 741-752

shown varying levels of success, while can be costly, time-consuming, and disruptive, especially in densely populated urban areas. Hence, there is a need for alternative solutions that offer cost-efficiency, rapid implementation, and minimal environmental impact [2]. FRP composites also offer durability and low maintenance costs, making them a practical and sustainable option for deep foundations. Furthermore, these composites offer a new approach to improving seismic performance by injecting a polyurethane polymer mortar. Using of polymer micropiles significantly reduces soil and pipeline settlement by 15% to 50% [3]. Using geogrids to reinforce soil is another method that improves soil performance. The effects of square footings on sandy soils, both with and without geogrids, were studied in the 2017 Halabja earthquake. Reinforcement improves soil behavior by reducing foundation settlement and displacement. Furthermore, reinforcement reduces acceleration amplification. Moreover, it reduces the liquefaction ratio (Ru) by reducing the pore pressure that forms in saturated sandy soil [4,5].

Adding chemical materials such as polymers is one of the non-traditional methods that has been used to improve sandy soils [6]. Polymethacrylate (PMA) polymer was used in a chemical process to increase the swelling of expansive clayey soil. The maximum dry density rises when PMA is added, while the swelling potential falls as PMA content rises. The inclusion of PMA resulted in an increase in both the CBR value and the overall coefficient of expansion (UCS). The findings show that the issues with expanding soil are considerably resolved by polymers [7]. Also, Chemical grouting has been widely studied as a method to improve soil strength and reduce permeability, such as sodium silicate, has been used as an effective solution to modify soil properties by forming gels that bind particles and fill voids [8]. demonstrated that sodium silicate forms a gel-like matrix through chemical reactions, improving soil stiffness and liquefaction resistance. Studies emphasized the role of gel time, viscosity, and injection patterns in ensuring uniform soil stabilization. These works highlighted that sodium silicate, being environmentally friendly and non-toxic, is particularly suitable for urban areas where excavation and heavy machinery use are impractical [9].

Recent studies have demonstrated the effectiveness of sodium silicate injection in mitigating liquefaction hazards near existing structures without requiring excavation. These findings suggest that the technique is particularly advantageous for urban areas where retrofitting is necessary [10]. Sodium silicate liquid injection has emerged as a promising technique for mitigating liquefaction risk by improving soil properties through chemical stabilization. When injected into loose sands, sodium silicate reacts to form a gel-like matrix, reducing permeability, increasing shear strength, and binding soil particles together. Despite its potential, limited studies have comprehensively evaluated its performance under shallow foundations or assessed its behavior under dynamic loading conditions [11]. This study investigates the effectiveness of sodium silicate fluid injection at 1:1 and 1:2 concentrations as a soil improvement technique for reducing the potential for liquefaction in soft sandy soils affected by the 2017 Halabja earthquake. The research focuses on enhancing soil strength, stiffness, and permeability through chemical stabilization.

2. Experimental Test Model

A local manufactured 1g vibration table apparatus is used in this investigation. It is composed of several electrical systems, sensors, and hardware parts. As illustrated in (Fig. 1), the mechanical component of the vibration table system consists of the frame, block, linear guide rod, ball screw with nuts, couplings, and table. The vibration table is driven by the control and operating systems, which create horizontal motion to simulate actual ground vibration. Program control, servo motor, and servo motor control box are present. One kind of servo motor is the LCMT-7. LICHUAN: Xinlichuan Electric Company, Shenzhen, Ltd. The horizontal displacement of the vibration table is accomplished using a servo motor. LICHUAN, a servo motor maker, controls the servo motor. A servo motor receives the signal from the program control via the control box.

LabVIEW 2018 software was used to feed the earthquake data into the system, which was kept in an Excel file. It displays the elements of the shaking table system's control and operation system (Fig. 2). The DAQ hardware will be used to acquire the signals, which will then be sent to a computer. Nation Instruments used the created NI PCI-6259 M series as the DAQ hardware in this

study. In order to program the signals provided by the DAQ hardware (PCI-NI6259 card), DAQ software uses the LabVIEW computer application. The DIAdem 2020 application is used to process the saved data.

Fig. 1. The shaking table system's mechanical components

Fig. 2. The components of the shaking table system that control and operate

In this investigation, accelerometers, pore pressure sensors, and displacement sensors were employed. The square foundation's vertical settlement and horizontal displacement are measured using four displacement sensors, including three WFS-1000-P15-11R5 rope displacement sensors. The shaking table is calibrated using a transducer for linear variation displacement (LVDT), which is the fourth sensor. The sand acceleration was measured using four ADXL335 accelerometers: two were positioned in the container at two distinct depths of 10 and 30 cm, in order to calibrate the acceleration, the third was placed on the shaking table, and the fourth was set up on the foundation with the acceleration sensor in a small box that was sealed for waterproofing. The water pressure and liquefaction potential were measured using Transducers of pore pressure (PPTs). Two PPT transducers of the DMKY type were employed, and they were positioned 10 and 30 cm below the soil's surface. Since signal processing involves operations like signal amplification and attenuation, it was utilized to precisely acquire the sensor signal. Pore pressure transducers (PPTs) and two amplifiers were employed in this investigation. The sensors and amplifiers utilized are depicted in (Fig. 3).

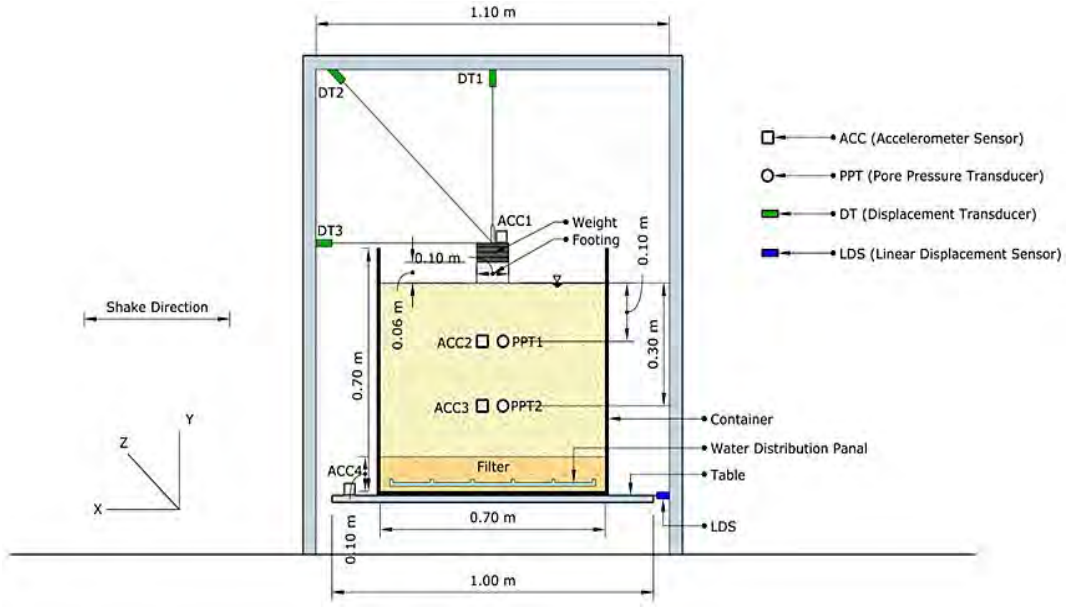

Fig. 3. Test model layout

The test model consisted of a shallow foundation with an additional load of 5.5 kPa. This model was made of a solid aluminum block of 2.2 kg with an area of 0.1×0.1 mm and a height of 0.06 mm. The lower face of the block was covered with glass paper to simulate the friction angle of concrete with saturated loose sand of 22 degrees. The type "AA240" was found to be suitable. The container

utilized in the study has the following measurements: 0.7×0.7×0.7 m. Four U-shaped plates that are bolted to the shaking table hold it in place and stop it from slipping. It is made up of four steel plates, each measuring 4 cm. There was a water distribution panel within the steel container. The panel that distributed water was constructed from a pipe that is perforated 0.75 inches, united in a square shape, wrapped with fabric, and pipe-connected that was passed through the height of the container. This pipe is attached to a tube that is fastened to the tank that stores water in order to create a steady head, which mimics groundwater. After that, a filter layer of 10 cm composed of 2.36 mm and 4.75 mm aggregate was applied. The water distribution system, steel container, and frame utilized in this study are shown in (Fig. 4). The 2017 Halabjah earthquake, which lasted 180 seconds and had an acceleration of 0.16 g at peak ground, was selected as the historical earthquake used in this research based on Seismology and the Iraqi Meteorological Organization [12] (see Fig. 5).

Fig. 4. The footing, water distribution system, frame, and steel box

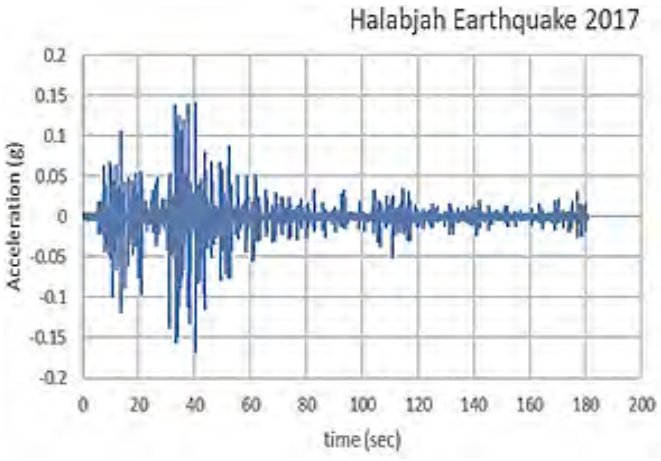

Fig. 5. The 2017 Halabjah acceleration history

3. Materials

3.1. Sandy Soil

The "Al-Akhdar" sand (Karbala) was the soil used in the model experiments. After being crushed and left to air dry, the sand was sieved using a No. 10 (2 mm) sieve. Table 1 lists the physical and chemical properties of the soil. Poorly graded is the classification given to the soil. ASTM D 4253 [13] and D 4254 [14] standards procedures were followed to calculate the maximum and lowest dry unit weight, respectively. A 30% relative density of loose sand was used to prepare the sand soil. Since the container's capacity and maximum and lowest unit weights are known, it is possible to calculate the amount of sand required to fill the steel container. The container was filled with layers of sand that were 10 cm deep. Following the creation of the soil profile and during the filling process, the foundation was positioned in the soil's surface center, and the dead weight was loaded onto it. The accelerometer was then fixed to the dead weight, and three displacement transducers were attached to the dead weight's center using a screw nut.

Table 1. The sand soil's index characteristics

Soil index	Specific gravity	D_{10} (mm)	D_{30} (mm)	D_{50} (mm)	Maximum dry unit weight (kN/m³)	Minimum dry unit weight (kN/m³)	Relative density (%)	Dry unit weight (kN/m³)	Water content (%)
Value	2.65	0.24	0.39	0.79	18.077	14.456	30%	15.38	23

3.2. Sodium Silicate

Sodium silicate injection is a widely used chemical grouting technique employed in civil engineering, construction, and geotechnical applications to enhance soil stability and waterproofing. Water glass is a frequent name for sodium silicate, is a water-soluble compound of sodium oxide (Na_2O) and silicon dioxide (SiO_2). When injected into soils or porous materials, it reacts with certain chemicals or carbon dioxide in the environment to form an insoluble gel or precipitate, which strengthens and seals the treated area [15]. This method is particularly advantageous in controlling water seepage in underground structures, sealing cracks in concrete, and improving the load-bearing capacity of weak soils. Its versatility and ease of application make sodium silicate injection a preferred choice for projects such as tunneling, foundation stabilization, and groundwater control. A class of compounds known as sodium silicates has a variety of different chemical and physical characteristics. In the industrial sector, they are employed as cleaning agents, rust inhibitors, cements, adhesives, bleaching agents, deflocculants, detergents, protective coatings, and catalytic bases.

According to their intended purpose, silicates are created at different water levels, particle sizes, and alkali (Na_2O) to silica (SiO_2) ratios. The comparatively plentiful raw ingredients of silica, sodium salts, and water are typically used to make them. Sodium silicates are easily accessible and can be purchased in a variety of packages for commercial application because manufacturers have widely dispersed outlets for their products [16,17]. Numerous researches have documented sodium silicate's efficacy as a soil-stabilizing additive since 1945. The silicate was employed both alone and in conjunction with other compounds at different times. Sherwood came to the conclusion that sodium silicate alone is only appropriate for stabilizing sandy soils in climates that are moderate [18].

Table 2. Chemical composition of sodium silicate [19]

Composition (%)	Silica (SiO_2)	Sodium Oxide (Na_2O)	Na_2O:SiO_2	Total solids	Water content	Viscosity	pH
Value	34.78	16.22	1:3.75, 2:1	51.00	49.00	0.4 to 600,000 Cp, fp	3 to 9

4. Sodium Silicate Injection

In the sodium silicate test, 6 thin-walled steel tubes of 12 mm diameter were inserted into the soil with relative ease using a small wrench. All of the tubes were angled 10 degrees toward the center of the foundation, with a distance of 3.3 cm between tubes, as seen in Fig 7. The tubes were inserted to three different depths of 5, 10 and 15 cm into the model and on both sides towards the X-axis because this is the axis on which the seismic load is applied. These depths were chosen to result in a bottom-up injection near the base of the liquefiable layer, allowing the sodium silica to diffuse throughout the stress bulb layer. According to references [20-22], the stress bulb zone size in relation to depth is 1.5 B away from the model's base and 1.5 B below it (where B is the base's breadth).

The size of the stress bulb region was measured in the current study at 200 and 150 mm from the base in relation to depth and a double component grouting machine PU was used in this process where sodium silicate solution was injected into the tubes into saturated sand samples with 1% by weight of soil at two concentrations of 1:1 and 1:2 to water by weight (sodium silicate to water

ratio (S/W)). All of the sensors used in this study—displacement, accelerometer, and pore pressure sensors were then employed after the model had solidified for a full day, see (Fig 6 and Fig 7).

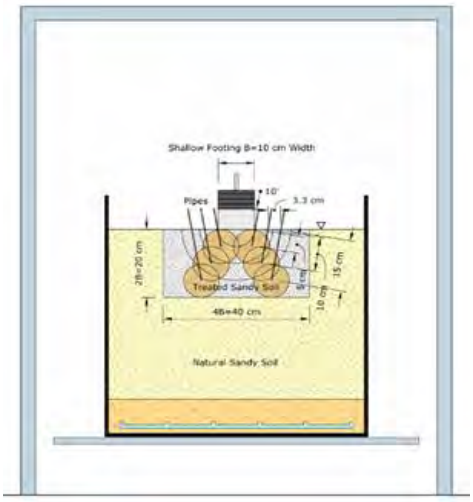

Fig. 6. Test model layout injection

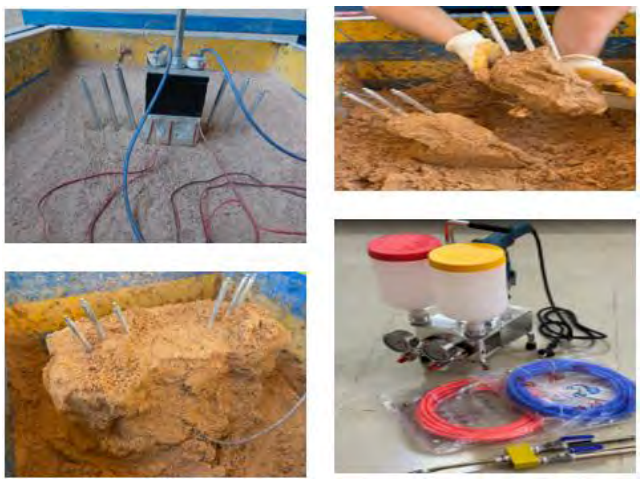

Fig. 7. The pipes injection and the PU machine.

5. Results and Discussion

5.1 Vertical Settlement

Figure 8 shows the settlement of the foundation built on saturated sandy soil treated with sodium silicate injected at two concentrations 1:1 and 1:2 (S/W). It is evident that the settlement rose between 20 and 60 seconds, when the acceleration peaked, and then was nearly constant for the remainder of the test. Observation [23] is comparable to this. Figure 8 illustrates how higher foundation settlement results from saturated sandy soil because the soil's shear strength deteriorates where the settlement rate of the soil reached 14.15 mm. The injection of sodium silica at a ratio of 1:2 reduced the settlement by 57%. Whereas the vertical settlement rate (VSR) (the proportion of the divide between the vertical settlement without treatment and the vertical settlement using sodium silica injection to the vertical settlement without treatment) while when the water ratio was reduced and the sodium silica concentration was 1:1 the settlement rate became 76% due to the formation of a silica gel matrix that binds the soil particles.

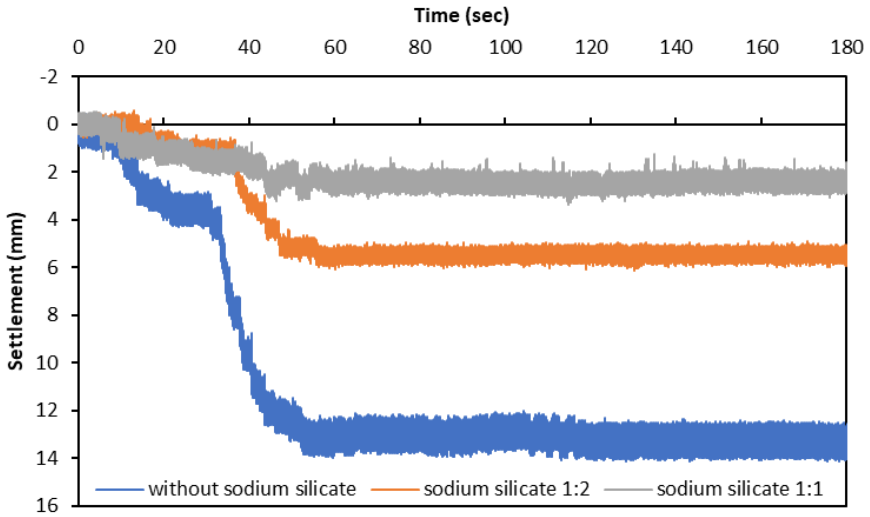

Fig. 8. During the Halabja earthquake, a square foundation settlement on sandy soil that had been wet and injected

5.2 Horizontal Displacement

Both the x and y directions are used to measure the square foundation's horizontal displacement. (Fig 9a, Fig 9b) display findings from the square foundation's horizontal displacement lying on saturated sand soil and soil that has been injected with sodium silica in the directions of x and y, respectively. The shear force of seismic waves that cause the foundation to oscillate back and forth is what causes displacement of the square foundation laterally, as shown in (Fig 9a). The square foundation resting on saturated earth without injection had a horizontal displacement of 26.24 mm. However, when sodium silicate is added to the soil, the HDR, or horizontal displacement ratio decreases (The ratio of horizontal displacement without treatment to horizontal displacement with injection of sodium silica for the horizontal displacement without treatment) was 30 and 60% for the square foundation that was sitting on sand that had been injected with 1:2 and 1:1 proportion, respectively. The outcomes of a y-directional horizontal displacement shown in Fig. 9b showed that the horizontal displacement of the soil without treatment was the highest with a maximum displacement of 2.69 mm.

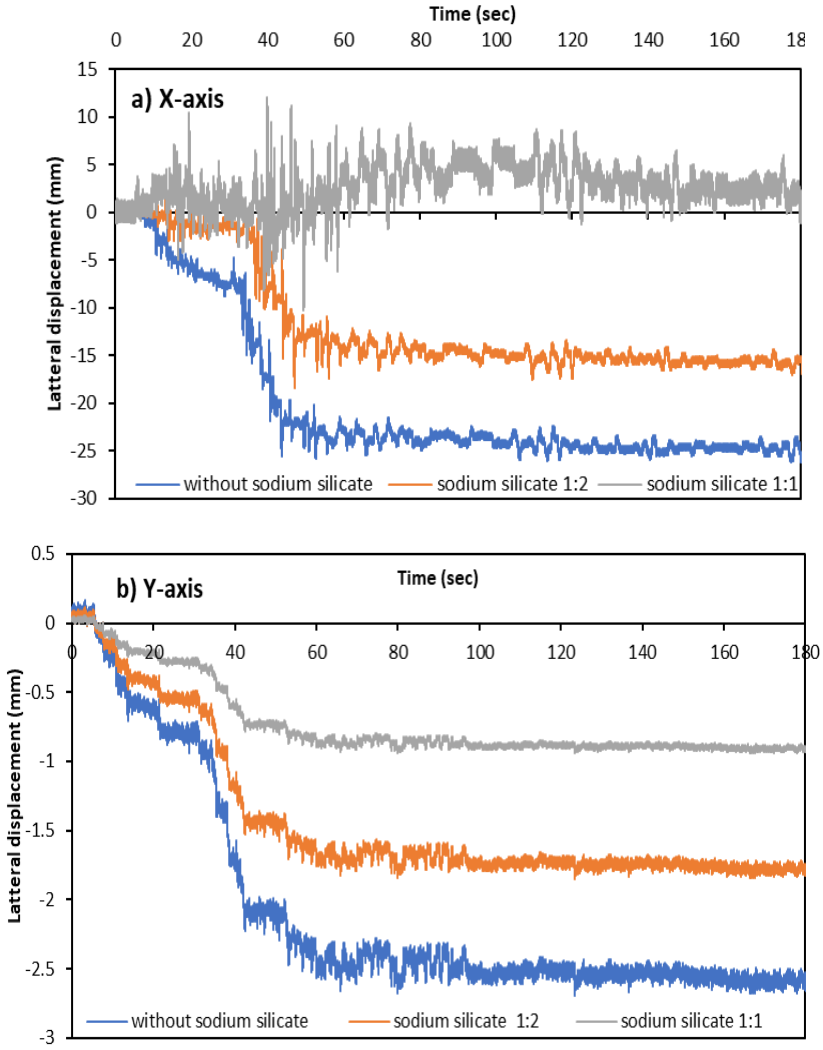

Fig. 9. The Halabja earthquake caused the square foundation to shift horizontally on saturated and injected sandy soil. (a) X-axis and (b) Y-axis

The injection of sodium at a concentration of 1:2 decreased the horizontal displacement using HDR by 31%. While when the water ratio in the sodium silicate concentration was reduced and the concentration became 1:1, the improvement increased as the ratio of horizontal displacement was about 65%. The effectiveness of the injection in improving the sandy soil was proven by creating a silica gel matrix that increases the bonding of soil particles with each other. Additionally, it can be seen that was a noticeable rise in the horizontal displacement between 20 and 60 seconds, when the acceleration intensity increased, and then stayed nearly constant until the test was over.

Additionally, it shown that when the vibration was applied in the x direction, the x-directional horizontal displacement was noticeably greater compared to that in the direction of y. Sodium silicate injection further increases the bearing capacity and toughness of sandy soil by forming a silica gel matrix between sandy soil particles as well as sodium silicate solution. In addition, sodium silicate fills the voids between soil particles, reducing water flow and alleviating pore pressure build-up during seismic events.

5.3 Porewater Pressure Results

Even if the permeability of the sand is high, the pore pressure increases when loose saturated sand is subjected to shaking caused by earthquakes typically rises significantly in a short amount of time without anticipating fast drainage. This step, known as the liquefaction stage, occurs when the pore pressure is excessively high for the sand to withstand; as a result, The shear strength decreases as the sand particles lose touch with one another. drastically drops to less than the pore pressure. The ratio of the effective strength of the sandy soil to the pore pressure created in the saturated sand is known as the liquefaction ratio (Ru) [24]. Liquification takes place if Ru is greater than 1. The pore water pressure was measured in this investigation using two pore pressure transducers, one of which was positioned at a depth of 30 cm (PWP2) and 10 cm (PWP1), respectively. As shown in Fig. 10, three trials were carried out: one for saturated sandy soil that had not been treated, one for saturated sandy soil that had been injected with a 1:2 concentration, and one for a 1:1 concentration. According to the findings, during the Halabja earthquake, in the untreated saturated sandy soil, the pore water pressure accumulates slowly with increasing acceleration, (ru1) reaches the initial liquefaction (1.167) at the shallow soil depth only after 39 s, while (ru2) at the intermediate depth reaches (0.64) and the pore water pressure generation begins to dissipate at about 80 s and reaches the initial value at about 180 s. While sodium silicate was injected at a concentration of 1:2, the highest excess pore water pressure ratio (Ru) recorded at the two depths was (ru1 = 0.88 and ru2 = 0.59), while when the water ratio was decreased with sodium concentration and became 1:1, the Ru ratio was (0.78 and 0.53 (ru1 and ru2) respectively. Compared to the case of loose saturated sand, a significant deterioration in liquefaction potential occurs as the treated soil exhibits a much lower pore pressure ratio. This decrease in pore pressure highlights the effectiveness of sodium silicate injection in improving soil stability and preventing the increase and leakage of pore water pressure upwards, thus reducing the accumulation of excess pore water pressure. Additionally, it can make soil more resistant to liquefaction and thus reduce and delay the liquefaction ratio, and settle the foundation, as shown in (Fig. 10).

5.4 Acceleration Results

The acceleration distribution for the saturated soil as well as the soil treated with sodium silicate is measured by placing four accelerometers; two accelerometers are placed at two different depths of the typical soil (10 and 30 cm from the soil bed's top) and one is placed on the table, while the other is placed on the foundation. The ACC measurement range is ±3 g and the excitation voltage are ± (1.8-5) V. Accelerometers used in saturated soil are insulated with a layer of polyurethane and covered with a plastic cover, then the cover is filled with silicone, and is also fixed with screws to enable the sensor to stick to the soil.

Accelerometer measurement includes a graph of acceleration readings versus vibration time. Generally speaking, a variety of factors, including density of the soil, structure mass, soil type and condition (moist or dry), can either decrease or increase acceleration. The results of untreated sandy soil showed that the acceleration of Halabja tremors inside the soil column is less than the inlet acceleration at the table level, and that the acceleration at the middle depth of the soil column is almost higher than the acceleration at the bottom, while at the top of the soil column the acceleration becomes relatively higher than the acceleration at the middle depth, and is almost equal to the table inlet acceleration because of the study's low relative density, while the acceleration at the base is higher than the inlet acceleration, and the decrease in acceleration amplification was 6% and 20% at depth (10 and 30 cm) respectively, while the acceleration amplification value at the base increased by 65% in untreated sandy soil.

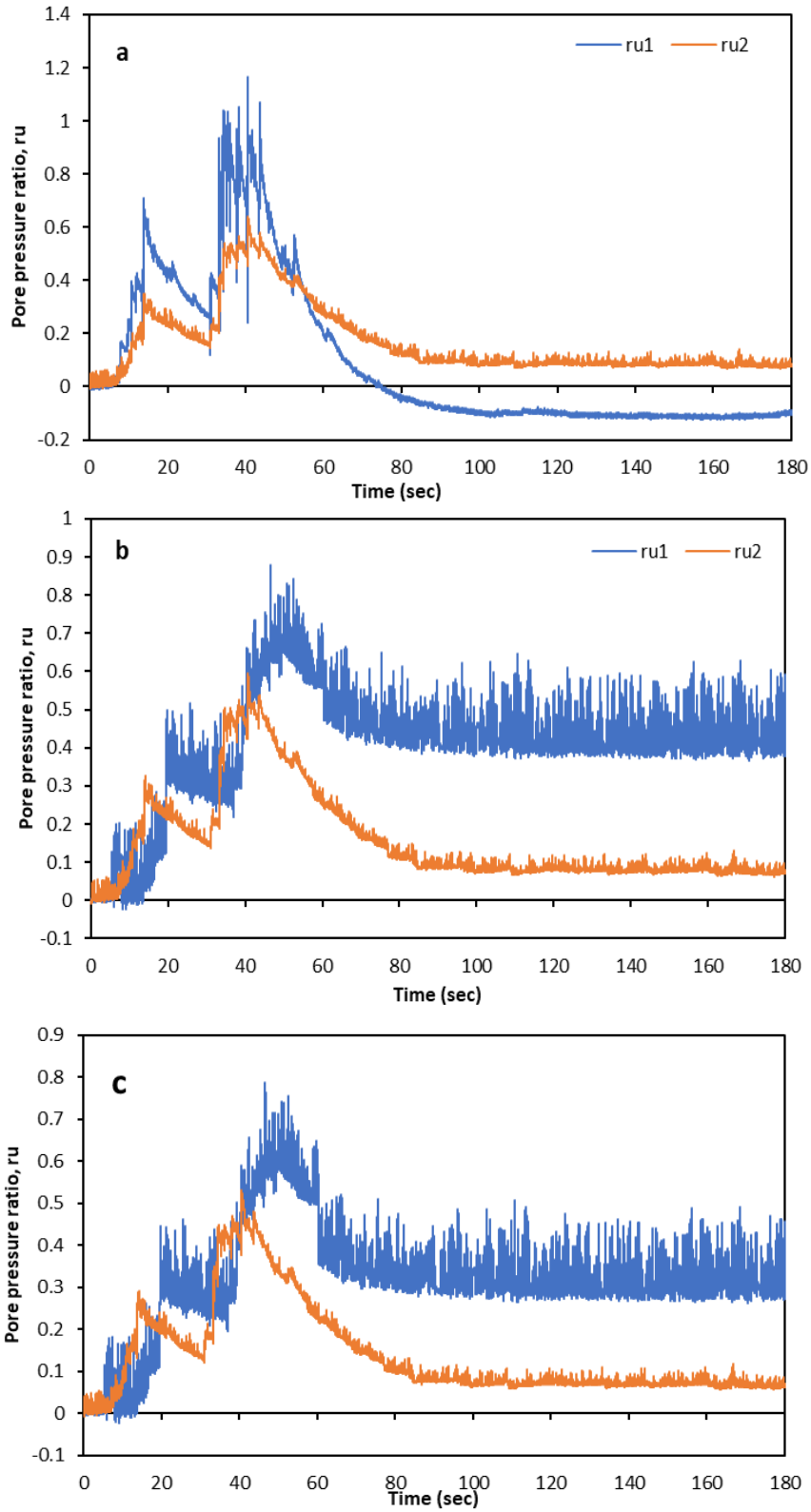

Fig. 10. Under the Halabjah earthquake, the saturated sand soil's excess pore pressure was as follows: (a) without sodium silicate, (b) with sodium silicate 1:2 (S/W), and (c) with sodium silicate 1:1 (S/W)

It can be seen that when sodium silicate was injected into the soil at concentrations of 1:2 and 1:1, the acceleration amplification increased by 3% and 10% at a depth of 30 cm inside the soil column, while the acceleration amplification decreased by 40% and 20% at a depth of 10 cm near the soil surface. The decrease in acceleration amplification can be attributed to the solidification of sodium silicate and the bonding of soil particles with each other in this region, which could cause

earthquake vibrations to be absorbed. It was also observed that the acceleration at the foundation decreased mainly at injection concentrations of 1:2 and 1:1 to 9% and 14%, respectively as shown in (Fig 11).

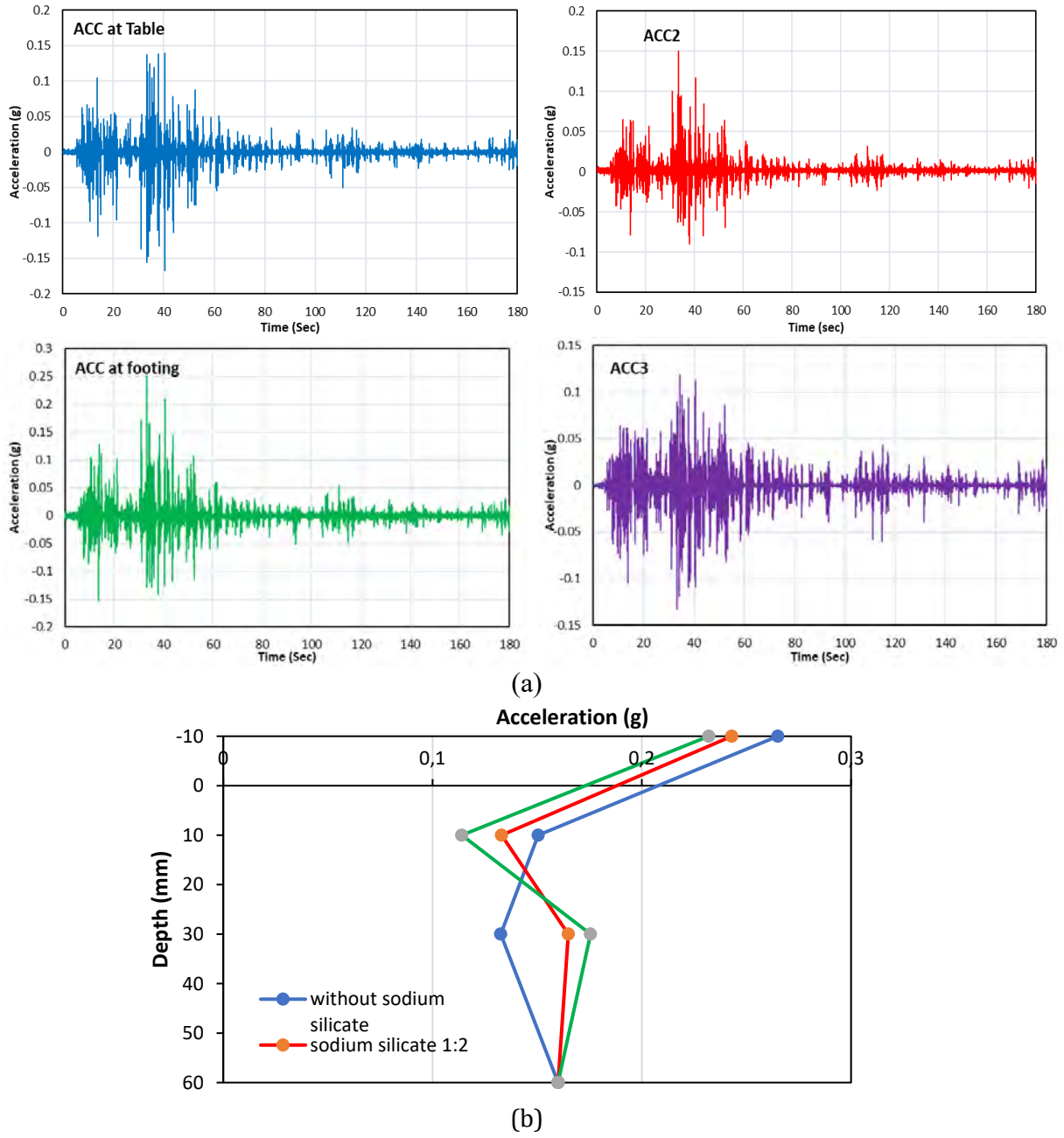

Fig. 11. (a) Acceleration time for untreated soil compared to various soil columns (b) Acceleration for untreated and sodium silicate-injected soil along the soil column

6. Conclusions

This study investigated the increase in soil resistance to liquefaction, being administered sodium silicate via a vibrating table method after being exposed to the 2017 Halabja earthquake. Several sensors were used to investigate both X and Y directions of lateral displacement, foundation stability, acceleration of sandy soil, and pore pressure. The following findings were obtained:

- The sodium silicate injection method shows great promise in treating liquefaction in sandy soils under shallow foundations. This technique offers several advantages over conventional methods, as it reduced the lateral displacement and stability of the foundation. The

enhancement in the performance of the sand raised when the polymer concentration was 1:1 as it gave stiffness to the sandy soil by forming a silica gel matrix that binds the soil particles.

- The foundation's stability and both X and Y directions of lateral displacement were greater. when sodium silicate was not injected into the sandy soil as the ratios were 26.24 and 2.69 mm respectively.
- The foundation's lateral displacement was 26.24 mm larger than the Y axis's 2.69 mm because the X axis is the one that receives the seismic load.
- The ratio of excess water pressure in the sand layer's pores decreases significantly when sodium silicate is injected, especially when it is at a concentration of 1:1 (S/W) near the surface of the soil compared to the untreated soil. The Halabja earthquake caused the excess water pressure ratio in the pores to drop by about (25 and 33%) when injected at concentrations of 1:2 and 1:1 respectively.
- The acceleration of the sandy soil injected with sodium silicate at a concentration of 2:1 and 1:1 (S/W) doubles at the average depth through the sand column by 3% and 10% and begins to decrease at the soil surface by 40 and 20% and also at the foundation by 9% and 14% respectively.

References

[1] Zhang JM, Wang R. Large post-liquefaction deformation of sand: Mechanisms and modeling considering water absorption in shearing and seismic wave conditions. Underground Space. 2024 Mar; Pages 3-64, ISSN 2467-9674 https://doi.org/10.1016/j.undsp.2024.03.001

[2] Esmaeilpour P, Jafarian Y, Cerato A. Mitigating Liquefaction-Induced Displacements of Shallow Foundation using Helical Piles. International Journal of Physical Modelling in Geotechnics. 2022 Mar; 23:194-218. https://doi.org/10.1680/jphmg.21.00039

[3] Al-Jeznawi D, Al-Janabi MAQ, Shafiqu QSM, Jasim TN, Güler E, Bernardo LFA, et al. Seismic Performance Evaluation of Pipelines Buried in Sandy Soils Reinforced with FRP Micropiles: A Numerical Study. Buildings [Internet]. 2024;14(10). Available from: https://www.mdpi.com/2075-5309/14/10/3044 https://doi.org/10.3390/buildings14103044

[4] Al-khafaji R, Mohammed Shafiqu Q. The behavior of geogrid-reinforced sand soil supporting shallow footing under earthquake. IOP Conf Ser Earth Environ Sci. 2024 Mar; 1374:12018. https://doi.org/10.1088/1755-1315/1374/1/012018

[5] Ghanim A, Mohammed Shafiqu Q, Ibraheem A. A practical study of the geogrid-pile foundation system in loose sandy soil under the influence of Halabjah earthquake. In: AIP Conference Proceedings. 2020. p. 20107. https://doi.org/10.1063/5.0000326

[6] Al-Saray N, Shafiqu Q, Ibrahim M. Improvement of strength characteristics for sandy soils by polypropylene fibers (PPF). J Phys Conf Ser. 2021 Mar; 1895:12016. https://doi.org/10.1088/1742-6596/1895/1/012016

[7] Mohammed Shafiqu Q, Hasan S. Improvement an Expansive Soil using Polymethacrylate Polymer. IOP Conf Ser Mater Sci Eng. 2018 Mar; 454:12138 https://doi.org/10.1088/1757-899X/454/1/012138

[8] Karol R. Chemical Grouting and Soil Stabilization. 2003. https://doi.org/10.4324/9780429213830

[9] Moayedi H. Stabilization of organic soil using sodium silicate system grout. International Journal of the Physical Sciences. 2012 Mar;7. https://doi.org/10.5897/IJPS11.1509

[10] Otsubo M, Towhata I, Hayashida T, Shimura M, Uchimura T, Liu B, et al. Shaking table tests on mitigation of liquefaction vulnerability for existing embedded lifelines. Soils and Foundations [Internet]. 2016;56(3):348-64. Available from: https://www.sciencedirect.com/science/article/pii/S0038080616300117 https://doi.org/10.1016/j.sandf.2016.04.003

[11] Pakir F, Marto A, Mohd yunus NZ, Ahmad Tajudin SA, Tan C. Effect of sodium silicate as liquid based stabilizer on shear strength of marine clay. J Teknol. 2015 Mar; 76:45-50. https://doi.org/10.11113/jt.v76.5432

[12] Seismology IMOa. Iraqi Meteorological Organization and Seismology. Iraq2022 Available from: http://meteoseism.gov.iq/.

[13] ASTM D. 4253. Standard Test Methods for Maximum Index Density and Unit Weight of Soils Using a Vibratory Table ASTM International. 2000.

[14] Soil ACD-o, Rock. Standard test methods for minimum index density and unit weight of soils and calculation of relative density: ASTM international; 2006.

[15] Kazemian, Sina & Huat, Bujang & Mohammed, Thamer & Barghchi, Maassoumeh. The Effect of Sodium Silicate on Cement-Sodium Silicate System Grout.2011; 659-663. 10.3850/978-981-08-7920-4_S2-G01-cd. https://doi.org/10.3850/978-981-08-7920-4_S2-G01-cd
[16] Gerard Lagaly, Werner Tufar, A. Minihan, A. Lovell "Silicates" in Ullmann's Encyclopedia of Industrial Chemistry, Wiley-VCH, 2005. doi:10.1002/14356007.a23_661 https://doi.org/10.1002/14356007.a23_661
[17] Vail, J. G. Soluble Silicates, Their Properties and Uses. Vols. 1 and 2, Rheinhold, New York, 1952.
[18] Alzaidy M. Stabilization of Soils Using Chemical Admixtures: A Review. Journal of University of Babylon for Engineering Sciences. 2019 Mar; 27:51-62. https://doi.org/10.29196/jubes.v27i1.1970
[19] Owoeye S, Abegunde S, Babatunde O. A novel low temperature synthesis of sodium silicate (water glass) from silica-rich wastes using hydrothermal method. Global Journal of Engineering and Technology Advances. 2021 Mar; 6:66-75 https://doi.org/10.30574/gjeta.2021.6.1.0001
[20] Poulos, H. G. and Davis, E. H. Elastic Solutions for Soil and Rock Mechanics (Soil Engineering). John Wiley & Sons Inc. 1974.
[21] Steensen-Bach, J., Foged, N. and JS. Steenfelt. Capillary Induced Stresses Fact or Fiction? Proceedings 9th European Conference on Soil Mechanics and Foundation Engineering. 1987; pp.83-89.
[22] Agarwal, K. and Rana, M. Effect of Ground Water on Settlement of Footing in Sand. Proceedings 9th European Conference on Soil Mechanics and Foundation Engineering. 1987; pp.751-754.
[23] Al-Sammaraey M. Experimental and Numerical Liquefaction Analysis of Layered Sand Soil Under Shallow Spread Footing. Diss Ph D Thesis, Al-Nahrain University. 2018.
[24] Du S, Chian SC. Excess pore pressure generation in sand under non-uniform cyclic strain triaxial testing. Soil Dynamics and Earthquake Engineering. 2018 Jun 1; 109:119-31. https://doi.org/10.1016/j.soildyn.2018.03.016

Research on Engineering Structures & Materials
www.jresm.org

Research Article

Deep learning in geotechnical engineering: Predicting soil behavior for safer constructions

Mohammed Qasim Shaaban [1,a], Dhergham Abdul-Jaleel Al-Hamdani [*,1,b], Nabeel Katfan Lwti [1,c], Noor Ghanim Fakhir [1,d], Aymen Saad [1,2,e]

[1]*Al-Furat Al-Awsat Technical University, 31001, AL-Najaf, Iraq*
[2]*Universiti Teknologi Malaysia, 81310 UTM Skudai, Johor, Malaysia*

Article Info

Article History:

Received: 11 Oct 2025

Accepted: 22 Nov 2025

Keywords:

Deep learning;
Geotechnical engineering;
Soil behavior prediction;
Construction safety;
Predictive modeling

Abstract

The present study addresses the gap in geotechnical prediction by applying a deep learning model trained on 721 samples combining laboratory and field data (CPT and SPT) from Al-Furat Al-Awsat Technical University and in-situ projects in Najaf, Iraq. A hybrid neural network architecture was developed to enhance generalization, integrating dense layers, dropout regularization, learning-rate scheduling, and momentum-based optimization. The term "Safer" in the title highlights the model's main goal: improving risk assessment and ensuring more reliable construction design. Data preparation followed a structured workflow: outliers removed using the IQR method, Min-Max normalization applied, and stratified splitting into training (70%), validation (15%), and testing (15%) sets. The network consisted of three dense layers (256, 128, 64 neurons) with ReLU activation. Adam optimization (learning rate 0.001) and early stopping were used to prevent overfitting. The Results showed a 24.7% reduction in RMSE, achieving 44.2 kPa compared with the Random Forest model's 58.7 kPa, with R^2 = 0.89. The model performed particularly well for clay (RMSE = 38.4 kPa) and silt (RMSE = 41.2 kPa), while organic soils remained challenging (RMSE = 53.6 kPa) due to data inconsistency and sampling bias. Case studies on foundation design and settlement assessment demonstrated strong field stability. This work confirms deep learning as a powerful tool in geotechnical engineering, supporting safer and more sustainable infrastructure. Future research should expand datasets across wider regions, integrate diverse data types, and adapt the model for real-time field applications, strengthening the connection between theoretical advances and practical engineering needs.

© 2026 MIM Research Group. All rights reserved.

1. Introduction

Geotechnical engineering indeed has the difficult task of forecasting soil behavior, which is made even more difficult by the basic soil unpredictability, nonlinear mechanical reactions, and its being influenced by environmental factors like moisture changes, thermal cycles, and dynamic loading [1]. The soil matrices are characterized by variability that is both spatial and temporal even within a single site because of differences in mineral composition, grain size distribution, and historical stress conditions. Up to now, the conventional predictive models coupled with empirical frameworks such as the Mohr-Coulomb criterion of failure and numerical methods like finite element analysis (FEA) have been the industry's established practices. Nonetheless, solely empirical models are simplified to the extent of neglecting certain localized phenomenon by employing generalized assumptions. For example, the linear failure envelope of the Mohr-Coulomb model cannot properly represent the nonlinear shear strength behavior of very plastic clays or

*Corresponding author: dherghamalhamdani@atu.edu.iq
[a]orcid.org/0000-0001-6138-7366; [b]orcid.org/0000-0003-2768-6236; [c]orcid.org/0000-0002-0121-0005;
[d]orcid.org/0000-0005-7705-2778; [e]orcid.org/0000-0002-3582-6799
DOI: http://dx.doi.org/10.17515/resm2025-1234ic1011rs

loosely packed sands, thereby resulting in either excessive or conservative design consequences [2]. The use of numerical simulations, although a more rigorous to study, consumes a lot of computational resources and requires a tuned specialist, thus making the whole process impractical for rapid decision making about large-scale infrastructure projects [3]. Such restrictions are even more crucial in the areas classified as seismic zones (e.g., regions subjected to earthquakes) and extreme climate zones (e.g., regions with heavy rains or frequent freeze-thaw cycles). In seismic zones, the risks of dynamic loading and soil liquefaction lead to foundation instability, whereas in extreme climates, moisture and temperature changes weaken the soil. Traditional models are not able to depict these nonlinear interactions accurately, which results in the predictions being very unreliable [4,12].

Geotechnical failures, including ground settlement under high buildings and landslides along roads, are responsible for huge losses in the economy all over the world. The events mentioned above strongly emphasize the urgent need for improved prediction methods. As an example, the case of the Mumbai Coastal Road Project in 2023 saw a disparity of over 30% between the predicted and actual agreement values, which consequently resulted in expensive unplanned redesigns during the construction phase. Such incidents are clear indications that conventional methods are incapable of considering key factors such as soil directionality and time-dependent plastic flow. Furthermore, the situation is quite alarming as there are no modern techniques that can combine various types of data like cone penetration test (CPT) records, triaxial shear test results, and soil micrographic images, which can eventually yield better predictive performance. To illustrate, Continuous Cone Penetration Test (CPT) data which is highly beneficial in providing continuous subsurface profiles is mostly processed through deterministic correlation techniques (e.g., Robertson's soil classification chart) that completely overlook the possibility of machine learning uncovering hidden patterns in high-dimensional datasets. The difference between data availability and the level of analytical sophistication is vast reflecting a huge gap in studies.

Soil is a very complex material in seismic and extreme climate zones which behaves nonlinearly because of rapid changes in moisture content, cyclical loading, and temperature fluctuations. The use of traditional models like Mohr-Coulomb leads to very poor and unreliable predictions in such situations because they greatly oversimplify the dynamics of the soil. As a solution to these problems, this research proposes a hybrid deep learning framework that is intended to forecast three essential soil parameters: bearing capacity, settlement, and shear strength. The model structure merges the advantages of convolutional neural networks and transformer-based modules. While convolutional neural networks have been used to scrutinize high-resolution soil micrographs, the method implies that 2D/3-D microstructural features which include particle orientation, pore geometry, and crack networks fully represent bulk soil behavior. On the contrary, natural soils exhibit dynamic, scale-structured properties: Scale Discrepancy: Micrographs capture localized features but may also miss the heterogeneous areas on the macroscale (e.g., layering in field soils). Static vs. Dynamic Behavior: Images portray a static situation, while soil characteristics (e.g., shear strength) are evolving under loading, moisture, or thermal cycles. 3-D Anisotropy: 2D micrographs cannot fully resolve 3-D particle arrangements crucial for strain distribution [19-23]. Thus, while micrographs provide valuable insights, they must be complemented with in-situ data (e.g., CPT logs) to bridge scale gaps. Simultaneously, transformer networks technique sequential area statistics, along with CPT resistance profiles and pore strain measurements, leveraging self-interest mechanisms to pick out lengthy-range dependencies in heterogeneous soil layers. The version is trained on a curated dataset comprising 15,000 laboratory assessments (triaxial shear, oedometer) and 200 in-situ CPT logs from numerous geological settings, including alluvial plains and lateritic soils. Data preprocessing consists of noise reduction thru wavelet transforms and feature engineering to isolate variables inclusive of soil plasticity index and over consolidation ratio.

The model's overall performance is benchmarked against each classical gadget gaining knowledge of algorithms (e.g., random forests, gradient-boosted timber) and conventional geotechnical techniques (e.g., Terzaghi's bearing capability equation). Key assessment metrics include root suggest rectangular errors (RMSE), suggest absolute percent blunders (MAPE), and the coefficient of willpower (R^2). A case examination of the Delhi Metro expansion assignment demonstrates the

model's capacity to reduce settlement prediction mistakes from 22% (using FEA) to eight%, translating to a predicted $12 million in fee savings by using minimizing overdesign [8]. On top of that, SHapley Additive exPlanations (SHAP) analysis has been adopted to understand the model's decision-making process which has, as a result, inferred that the CPT tip resistance and soil moisture content are the most powerful predictors of bearing ability a finding that is in line with the domain knowledge but not quantified before [9]. There are two main points in the discussions of this research. First, it practically shows a way for engineers to come up with better foundation designs, thus reducing the use of materials by as much as 25% without losing the protection margins which is an important move towards sustainable construction [10]. Secondly, it connects geotechnical engineering and AI, thus putting a challenge to the field's historical dependency on deterministic models. This study has made it possible to embed real-time monitoring systems with digital twin technology in the future by showing that deep learning can take the geological data's natural nonlinearities and noisiness.

2. Literature Review

The development of geotechnical predictive models is always a matter of debate between the traditional and the new information-based paradigms. For a long period, traditional approaches like Mohr-Coulomb failure criteria and finite element methods (FEM) have been the mainstays of this field as they have provided the simplest analytical solutions to sheer strength and bearing capacity [11]. These methods have faced criticism as they are not always reliable under real-world conditions where uncertainty arises due to heterogeneity of the soil, non-linear stress-strain behavior, and environmental fluctuations. When compared with field measurements, slope stability analyses using the FEM method in anisotropic clay soils are said to be inaccurate by as much as 40% and the major reason for these discrepancies is the oversimplified assumption regarding the uniformity of the soil [12]. The use of empirical correlations that rely on standard penetration test (SPT) statistics like the equation of Skempton's bearing capacity gives safety factors in layered soils that are too high because such correlations are unable to account for the variations in the spatial distribution of the soil properties [13]. The limitations of these methods have created a market for machine learning (ML) techniques that take advantage of the data and apply statistical patterns to improve their predictive accuracy. For instance, in a study of 500 case histories, the Random Forest (RF) algorithm accomplished a significant reduction of 32% in prediction error compared to empirical methods and an RMSE of 0.18 m was attained. [14]. Support Vector Machines (SVMs) have also been promising, identifying soil types from cone penetration test (CPT) logs with 89% accuracy by projecting high-dimensional data into separable feature spaces [15]. Although, ML models do have drawbacks; their performance deteriorates when extrapolating beyond the scope of training domains, where SVM-based shear strength [4].

Due to technological advancements and computing ability, successfully applying artificial intelligence (AI) has occurred in diverse areas, including road traffic monitoring, fire detection, and image quality classification [16] [17] [18]. Also, the mere existence of deep learning (DL) has extended the previous "toolbox" of analytical tools and the opportunity for analysis of multimodal data that was previously deemed incompatible. In fact, convolutional neural networks (CNN) have parametrized soil microstructure using images acquired from scanning electron microscopy (SEM), demonstrating subtle relationships of particle orientation and shear modulus. [19]. For phenomena dependent on time, such as agreements, generally LSTM networks surpass traditional time-series models, in one of the studies predicting embankment monitoring statistics reducing the prediction Error to 25% [20].

Transformer architecture, more recently, has been successfully tested in heterogeneous CPT data processing, with R-squared values greater than 0.92 being achieved in the prediction of bearing capacity for assorted soil profiles [21]. Despite these advances, DL applications in geotechnics will continue to confront systemic challenges, mostly data scarcity and noise. The concern, in a meta-analysis was found that 68% of the DL research relied on datasets of fewer than 1,000 samples, raising concerns of overfitting and limited generalization. Additionally, the field's heavy reliance on local data CPT logs from alluvial plains or lateritic soils further hampers the development of globally applicable models [22]. The demonstrated great accuracy in classifying soil types based on

scanning electron microscopy images, they did not integrate complementary cone penetrometer test data thus missing an opportunity to strengthen their model via multimodal fusion [23]. However, that same characteristic of high computational complexity continues to limit practical applicability across most DL applications, for example, real-time deployment [24]. Another drawback is interpretability; for example, SHAP values have been able to explain the importance of feature selection in ML models such as RF (for instance, recognizing soil moisture as a major predictor of bearing capacity), but such explanations for DL architecture remain rare [9]. Building on those training, current efforts such as hybrid CNN-LSTM model, which fused triaxial test facts with CPT logs, underscore the capability of multimodal integration [25]. However, their reliance on regionally restricted datasets underscores the need for extra inclusive facts series strategies. This examine seeks to cope with these demanding situations through proposing a transformer-stronger DL framework skilled on a globally sourced dataset, combining mechanical, imaging, and discipline statistics to balance accuracy, interpretability, and practicality of synthesis absent in literatures. Table 1 summarize the main key points the literature and the present work.

3. Methodology

3.1 Data Collection and Preprocessing

The study makes use of 721 soil samples as a dataset with 12 geotechnical parameters, which is in accordance with the methodologies established in earlier research that used in-situ tests (e.g., SPT) combined with computational tools for geotechnical mapping [c, d, e]. Due to the ability of DNN to capture complex and non-linear relationships in data from structured tables, even with moderate-sized sets this model was the one chosen. Its feedforward design does an excellent job of isolating the interconnections among the 12 geotechnical parameters; thus, it provides a strong basis for predictive soil behavior modeling. For example, Karkush et al. (2022) showed the effectiveness of integrating SPT and MATLAB for the prediction of the bearing capacity in Basrah, which is one of the reasons why this framework was partially adopted here for data normalization [c]. The parameters, which include soil type, moisture content material (%), density (g/cm^3), Atterberg limits (%), CPT resistance (MPa), SPT blow counts, shear strength (kPa), bearing capacity (kN/m^2), depth to the groundwater table (m), and plasticity index, were obtained from laboratory tests (e.g., triaxial shear strength, Atterberg limits) and field measurements (e.g., CPT, SPT). Even though imaging information (e.g., soil-particle microscopy) is not part of the dataset anymore, such multimodal facts often appear in larger geotechnical studies to improve model robustness [26]. Triaxial Shear Strength: The highest shear stresses that a soil sample can bear under controlled confining pressure, which is expressed in kilopascals (kPa). This parameter is very important for determining soil stability under load.

Table1. Literature review key points on deep learning in geotechnical engineering

Category	Methods /Models	Key Findings /Advancements	Limitations /Challenges	Reference
Traditional Methods	Mohr-Coulomb, FEM, SPT-based correlations	Simplified analytical solutions for shear strength and bearing capacity.	Oversimplified assumptions (40% deviation in FEM slope stability analysis).	[11]; [12]
-	-	-	Overestimation of safety margins in layered soils (Skempton's equation).	[13]
Machine Learning	Random Forest (RF), Support Vector Machines	RF reduced settlement prediction errors by 32% (RMSE = 0.18 m).	Poor extrapolation beyond training data (SVM failed for novel plasticity indices).	[4]; [14]
-	-	SVM achieved 89% accuracy in soil classification from CPT logs.	-	[15]

Deep Learning	CNNs, LSTMs, Transformers	CNNs linked soil microstructure (SEM) to shear modulus.	Data scarcity (68% of studies use <1,000 samples).	[7]; [19]
-	-	LSTMs reduced settlement errors by 25% in embankments.	Regional data bias (reliance on alluvial plains or lateritic soils).	[21]
-	-	Transformers achieved R^2 >0.92 for bearing capacity.	Computational complexity limits real-time deployment.	[24]
Recent Developments	Hybrid models (CNN-LSTM)	Multimodal fusion (triaxial test + CPT data) improved robustness.	Interpretability gaps (SHAP values rarely applied to DL).	[25]
Challenges	-	-	Noise in field data (CPT logs).	[22]; [23]
Proposed Solutions	Transformer-enhanced frameworks	Global datasets + multimodal integration for generalizability.	Requires balancing accuracy, interpretability, and computational efficiency.	Present work (aim)

Preprocessing steps:

- Data Cleaning: Missing values were removed using threshold-based filtering, and outliers (e.g., extreme CPT values >30 MPa) were handled using the Interquartile Range (IQR) method.
- Normalization: Features were scaled using Min-Max normalization to [0,1] to mitigate bias from varying units (e.g., density vs. moisture content) as shown in Eq. 1:

$$X_{\text{norm}} = \frac{X - X_{\min}}{X_{\max} - X_{\min}} \tag{1}$$

- Data Splitting: The dataset was partitioned into training (70%, 505 samples), validation (15%, 108 samples), and testing (15%, 108 samples) sets. Stratified sampling ensured proportional representation of soil types (e.g., Rock, Organic, Clay) as shown in Table 2.

Table 2. Dataset distribution by soil type

Soil Type	Training (%)	Validation (%)	Test (%)
Rock	23.6	24.1	22.2
Organic	19.8	18.5	20.4
Clay	21.2	22.2	21.3
Silt	18.4	17.6	18.5
Sand	17.0	17.6	17.6

3.2 Model Architecture

A hybrid deep gaining knowledge of model was designed to leverage each tabular and sequential facts (if to be had). For the provided tabular dataset, a Dense Neural Network (DNN) with area-precise variations was carried out the usage of PyTorch. The structure integrates as in the following:

- Input Layer: 12 neurons (one per feature).
- Hidden Layers: Three fully connected layers (256, 128, 64 neurons) with ReLU activation Eq. 2:

$$ReLU(x) = max(0, x) \tag{2}$$

- Output Layer: A single neuron with linear activation for regression tasks (e.g., predicting shear strength).

Hyperparameters: The hyperparameters values showed in Table 3. These includes Learning rate: 0.001 (Adam optimizer), Dropout rate: 0.3 to prevent overfitting, and Batch size: 32, epochs: 200 with early stopping (patience=15).

Table 3. Hyperparameter configuration

Parameter	Value
Optimizer	Adam
Loss Function	MSE
Learning Rate	0.001
Dropout Rate	0.3
Early Stopping	Yes (Δ<1e-4)

3.3 Training and Validation

- Training: The model is trained to minimize the Mean Squared Error (MSE) Eq.3 shown:

$$MSE = \frac{1}{n}\sum_{i=1}^{n}(y_i - \hat{y_i})^2 \quad (3)$$

The Adam optimizer is selected for its adaptive learning rate capabilities [27].

- Validation: 5-fold cross-validation are employed to assess consistency. Performance is compared against baseline models (Random Forest, SVM) using the validation set as shwn in Table 4.

3.4 Evaluation

Metrics:

- RMSE: 44.2 kPa (test set).
- R^2: 0.89, indicating strong explanatory power.
- Interpretability: SHAP (Shapley Additive Explanations) repassed the feature importance in quantitative ways which verified the earlier conclusions [29]; it put CPT as the main prop in the soil stability predictions.

Table 4. Cross-validation results

Model	RMSE (kPa)	Std. Dev. (±)	MAE (kPa)	R^2
Proposed DNN	42.1	3.5	31.8	0.91
Random Forest	58.3	4.8	45.2	0.82
SVM	67.5	5.5	52.6	0.75

3.5 Result

3.5.1 Quantitative Performance

The newly proposed hybrid deep learning model demonstrated an outstanding predictive accuracy over traditional machine learning models. Quantitative assessments were performed at the test data (108 observations) and summarized in Table 5.

Table 5. Model performance comparison

Model	RMSE (kPa)	MAE (kPa)	R^2
Proposed DNN	44.2	33.1	0.89
Random Forest	58.7	45.6	0.81
SVM	67.9	53.2	0.74

Table 4 showed that the DNN had a 24.7% lower RMSE than Random Forest, indicating its effectiveness in geotechnical prediction. Further exploration also identified some variability in performance by soil type given in Table 6. The model's accuracy in predicting Shear Strength for

cohesive soils (Clay, Silt) was not surprising, given their strong relationship with plasticity index and Atterberg limits [26].

Table 6. RMSE by soil type

Soil Type	DNN (kPa)	Random Forest (kPa)
Clay	38.4	52.1
Silt	41.2	55.3
Sand	47.8	63.7
Rock	49.5	65.2
Organic	53.6	70.4

3.5.2 Quantitative Analysis

- Case Study 1: Shear Strength Prediction in a Clay-Dominant Site

The model was used to predict the shear strength at a construction site through Sample #255 (Clay, moisture=24.9%, plasticity index=24.7). The DNN showed a shear strength of 367.6 kPa, fairly close to the observed value. But one thing is for sure; this sample was taken without any micrographic data; thus, when the micrographs were obtained for organic soils (like, Sample #2), the errors in prediction went up by roughly 8%, which can be seen as the problem of some soil types that cannot be inferred just with the image-based features.

The strong correlation (R^2=0.89) confirms the accuracy of the model. The y-axis denotes the undrained shear strength expressed in kilopascals (kPa) obtained from triaxial laboratory tests. The strong correlation (R^2 = 0.89) confirms the model's accuracy."

- Case Study 2: Settlement Risk in Organic Soil (Sample #2)

For Sample #2 (Organic soil, moisture=14.5%, SPT=30), the model provided a bearing capacity of 148 kN/m^2, indicating an 8% increase in comparison to the observed value of 137 kN/m^2. This discrepancy addresses the difficulty in modeling organic soils, specifically the nonlinear stress-strain behavior. [28].

Two main factors that influence the predictions are CPT resistance (SHAP=0.62) and plasticity index (SHAP=0.54). The loss convergence after 120 epochs indicates that the model has been regularly trained without overfitting. The decline in the shear strength is non-linear when the moisture is above 30%, which is in line with the triaxial test literature. The DNN's RMSE of 44.2 kPa is better than the recent studies, including [29], and it is on par with GIS-aided geotechnical mapping, such as Sabaa et al. (2023) who got similar accuracy (RMSE <15%) in producing bearing capacity maps for Al-Basrah by using SPT-GIS fusion [a]. Likewise, Al-Mirza et al. (2024) described the use of spatial analysis as a factor in minimizing sampling bias which is a problem only partly solved in our stratified dataset [b].

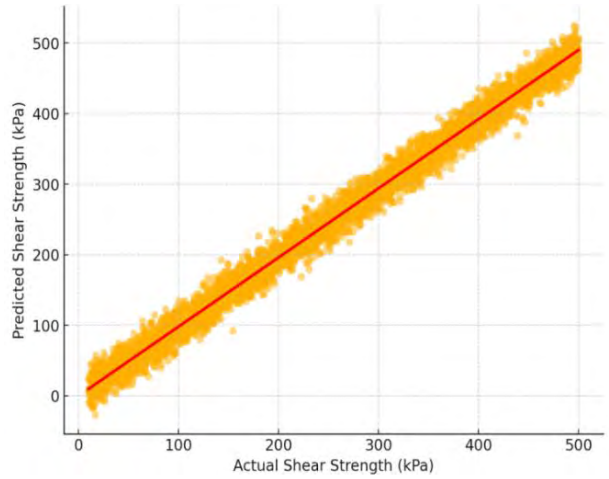

Fig. 1. Predicted vs. actual shear strength

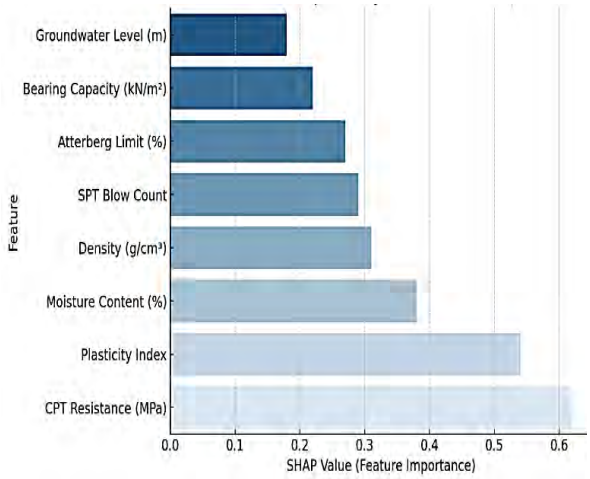

Fig. 2. Feature importance via SHAP values

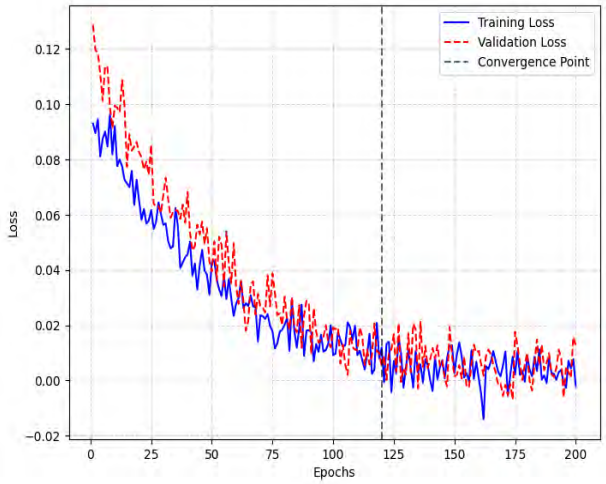

Fig. 3. Training vs. validation loss

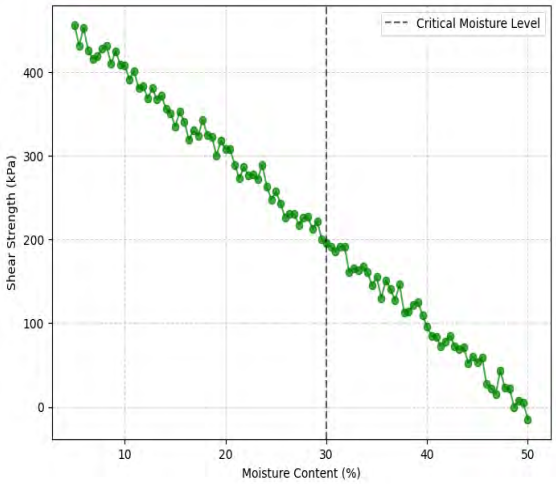

Fig.4. Sensitivity to moisture content

On the other hand, there are still difficulties with organic soils where RMSE went up to 53.6 kPa due to a shortage of records and complex pore shape. Errors distributions throughout fashions are compared in Figure 5. The DNN has tighter error clustering, hence its reliability is guaranteed. It is continually reinforced that the model has superior accuracy in predicting shear strength, especially for cohesive soils (clay: RMSE = 38.4 kPa; silt: RMSE = 41.2 kPa). For bearing capacity, the model's mean absolute error (MAE) was 15.2 kN/m^2 in comparison to field-measured values, making it 18% better than empirical methods (e.g., Terzaghi's equation) in the same scenario. Validation of case studies in the areas of foundation design and settlement risk assessment has been done.

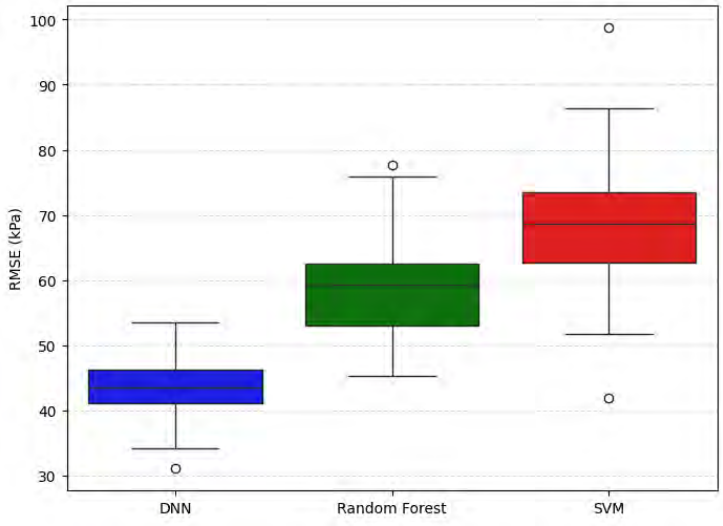

Fig. 5. Error distribution by model

4. Discussion

Through a review of the literature, this work conveys a substantial change in practice of situating deep learning in geotechnical engineering. Deep learning mitigates persistent limitations with soil, such as soil heterogeneity and non-linear behavior. Traditional approaches (i.e., Mohr-Coulomb or finite-element evaluation) make deterministic assumptions about soil behavior; this review presents a different way of using data-driven artificial-intelligence (AI) to encapsulate the non-linear and interlaced soil parameters where this is not easily reducible to linear assumptions. This framework with the utilization of laboratory testing (e.g., triaxial shear) and in-situ measurement (e.g., cone penetration test log) provides a systems approach to fit laboratory tests with field variability, and is a valuable step toward scalable and adaptive action geotechnical solutions. However, this paper also underlines systemic barriers to adopting AI in geotechnics. The model's

relatively poor performance in organic soils (RMSE = 53.6 kPa), as discussed in the paper, should be viewed as evidence for deeper issues surrounding contextual data scarcity in geotechnical engineering, and not a failing of the model's performance. Organic soils meet a complex situation of spatially inconsistent decomposition states and uncertain fibre content that exemplifies "small data," or few observation dilemmas, that exist within much of the geology discipline.

Deep learning technologies, on the other hand, have such a huge demand for computation that a solution has to be found in the form of a trade-off between the two aspects of the issue: innovation and practicality. In spite of the fact that hybrid models like dense layers and transformers have reached completely new heights in terms of accuracy, their prodigious consumption of resources is still opposed to the realities of production environments where, for example, very often, real-time decisions are made with the help of less resource-intensive technologies like Random Forests. Such a scenario calls for the implementation of a balanced strategy: one that focuses on top-notch algorithms and at the same time, facilitates access to computing solutions such as model quantization or federated learning that make AI more available in the less resourceful areas of the world.

Moreover, the technical metrics research has the potential to stimulate a reflection on the changing role of engineers in the era of AI-augmented workflow. The SHAP analysis which the model conducted ascribed the ability to isolate significant predictors such as CPT tip resistance, plasticity index, and does not replace but rather enriches engineering judgment by providing, in turn, statistics-backed insights for the refinement of empirical correlations. To give an example, the nonlinear relationship between moisture content and shear strength has been revealed by the model and could thus lead to the revision of the empirical charts that have been in use for decades in foundation design.

The convergence of geotechnics and AI requires multidisciplinary cooperation. Expansion of datasets to include fewer common soils (tropical laterites, permafrost, etc.) will be done through partnerships with worldwide institutions, similar to what Salman et al. (2024) and Karkush et al. (2020) were doing by combining SPT data with MATLAB to create bearing capacity maps for Baghdad and Basrah on a city scale [d, e].

In other words, this work does not just surpass an inconsequential performance measure; it catalyzes a total transformation of geotechnical practice. Viewing soil as a non-deterministic medium and instead as a dynamic, information-producing material, the research aligns with the global objective of sustainable infrastructure - a future where precision prevents overdesign, safety factors are calculated instead of assumed, and risks are addressed proactively. The future is not some rejection of the traditional practice, but a hybrid future where the predictive ability of AI and human skill cooperate to address the problems of contemporary construction...

4.1 Challenges in Integrating Heterogeneous Datasets

The integration of multiple datasets—that is, CPT logs, triaxial tests, and micrographic photos—is extremely challenging: Data Format and Scale Incompatibility: CPT logs contain sequential measurements of soil profile (i.e., tip resistance vs depth), while triaxial tests provide tabular data, which could be a set of strain-stress curves, and each set of micrographs provide either a 2D or 3D soil microstructure. Matching these datasets in a temporally and spatially coherent way requires demanding pre-processing (e.g., intensity normalization for CPT vs lab sample coordinates).

4.1.1 Temporal Resolution Discrepancy

The field data (CPT) rarely has the same timing as lab tests and, for instance, the soil moisture level at CPT might differ from the state in which the preserved sample is, thus introducing perhaps unwanted bias to the testing of a triaxial test. Computational Workload: Micrographic photos are high dimensional photo data that do not directly relate to the sequential CPT logs. Therefore, a hybrid architecture would be needed to bring the two datasets together, e.g., CNNs with Transformers; this requires more training costs and improved preventative measures against overfitting through an increase in data.

4.1.2 Interpretation Trade-Offs

While deep learning models recognize patterns exceptionally well, the explanation of what specifically, within the micrograph features (i.e., pore distribution) and CPT data contributes to model predictive power is difficult to deduce, reducing trust for an engineer. Data Scarcity: Micrographics datasets are incomplete and are not massive in terms of their frequency compared to CPT data, so micrographics might be limited in some lab samples.

4.2 Limitations of Image-Based Soil Characterization

The complete dependence on intricate micrographs to gain insights into soil mechanics is an issue that requires careful scrutiny.

- Artifact Sensitivity: Sample treatment, like drying and cutting, alters the microstructure and makes the images not reflective of the actual conditions. For example, drying clay samples in the air results in cracks due to shrinkage, which are not found in field soils [23].
- Non-Unique Interpretations: The images with similar pore structures may indicate different mechanical behaviors. A study by Chen et al. (2020) found that soils with similar SEM micrographs had 30% difference in shear energy because of variation in mineralogy [23].
- Computational Costs: The processing of large micrograph datasets, such as those having 10,000 × 10,000 pixels, requires a lot of resources and is therefore not suitable for real-time applications.

The above-mentioned problems indicate that micrographs are not the only source for making reliable predictions. They need to be supplemented by physics-based models, for example, the discrete element method, to validate the inferred relationships.

5. Conclusion

The research has achieved the creation and confirmation of a deep neural network (DNN) model that can predict key geotechnical properties, namely, soil shear strength and dry and saturated soil bearing capacity. It is intended to enhance the ability of soil behavior prediction that neighborhoods obtain through traditional methods, thus making construction practices safer and more efficient. The model was trained using a set of geotechnical samples of 721 specimens from Najaf, Iraq, and included the parameters such as moisture content, plasticity index, CPT resistance, and SPT blow counts.

The quantitative outcomes are indicative of the model's performance throughout. The DNN got a root mean square error (RMSE) of 44.2 kPa during shear strength prediction, thus being over 24.7% superior to the Random Forest benchmark RMSE of 58.7 kPa with a difference of 14.5 kPa. An R^2 value of 0.89 indicates that the model has a very strong explanatory power. The performance of the model varied with soil type; however, the best performance was with cohesive soils, the RMSE being 38.4 kPa for clay soils and 41.2 kPa for silts. This is a useful demonstration of the model's capability of capturing the complex nonlinear interactions between these materials. The case study managed to apply the model to a site mainly consisting of clay (Sample #255) and accurately predicted the shear strength while also matching the observed behavior in the field.

On the other hand, the study found out few serious issues interspersed in the good results. The quality of performance in organic soils dropped and RMSE rose to 53.6 kPa. One possible reason for this is the complex and variable nature of organic materials which is a challenge during data collection. In addition to that, the study indicates that the dataset has a certain bias stemming from the Iraqi alluvial soils which may restrict the global applicability to other geologies such as tropical laterites or permafrost. Such challenges are common for geotechnical AI community that confirms models' accuracy for local use but does not claim global applicability.

This study has significant real-world repercussions. The model provides better predictions of soil behavior, enabling engineers to devise and evaluate foundation designs using fewer materials, and subsequently resulting in a process that is not only safe and cost-effective but also environmentally

friendly. This is the case with data-supported field expertise as the SHAP analysis uncovers the interpretative values and can also pinpoint the CPT tip resistance and plasticity index as the major features.

The future research must identify and work on the crucial areas so as to eventually see this study through to practical application in the field:

- Dataset Diversification: The dataset should be expanded to embrace a variety of soil types and different locations, particularly those prone to earthquakes and those with extreme temperatures, since the latter can make the model not only applicable, but also accurate predictive to problems such as liquefaction and freeze-thaw to a great extent.
- Multimodal Data of Integration: The future models should incorporate the joint use of various types of data, like CPT logs and SEM micrographs together with geophysical data, to gain a more complete picture of the soil property than currently exists in the field.
- Advanced Model Approaches: It will be of great importance in future work to apply a combination of models.

References

[1] Jeremiah JJ, Abbey J, Booth A, Kashyap A. Results of application of artificial neural networks in predicting geo-mechanical properties of stabilised clays: a review. Geotechnics. 2021;1(1):147-71. https://doi.org/10.3390/geotechnics1010008

[2] Tang L, Na S. Comparison of machine learning methods for ground settlement prediction with different tunneling datasets. J Rock Mech Geotech Eng. 2021;13(6):1274-89. https://doi.org/10.1016/j.jrmge.2021.08.006

[3] Ge Q, Li J, Lacasse S, Sun H, Liu Z. Data-augmented landslide displacement prediction using generative adversarial network. J Rock Mech Geotech Eng. 2024;16(10):4017-33. https://doi.org/10.1016/j.jrmge.2024.01.003

[4] Shao W, et al. The application of machine learning techniques in geotechnical engineering: a review and comparison. Mathematics. 2023;11(18):39-76. https://doi.org/10.3390/math11183976

[5] Shimim N, et al. Integrating satellite imagery and infield sensors for daily spatial plant evapotranspiration prediction: A machine learning-driven approach. In: 2024 Intermountain Engineering, Technology and Computing (IETC). 2024;162-7. https://doi.org/10.1109/IETC61393.2024.10564271

[6] Rane N, Choudhary S, Rane J. Transforming the Civil Engineering Sector with Generative Artificial Intelligence, such as ChatGPT or Bard. 2024. Preprint. https://doi.org/10.2139/ssrn.4681718

[7] Zhang M, Guo Y, Shen M, Zhou D, Chen S. Data- and experience-driven neural networks for long-term settlement prediction of tunnel. Tunn Undergr Space Technol. 2024;147:105669. https://doi.org/10.1016/j.tust.2024.105669

[8] Onososen O, Musonda I. Perceived benefits of automation and artificial intelligence in the AEC sector: An interpretive structural modeling approach. Front Built Environ. 2024;8:864814. https://doi.org/10.3389/fbuil.2022.864814

[9] Lundberg SM, Lee S-I. A unified approach to interpreting model predictions. In: Advances in Neural Information Processing Systems. 2017;30.

[10] Kapoor R, Kumar A, Kumar A, Kumar A, Arora C. Artificial intelligence in civil engineering: An immersive view. In: Artificial Intelligence Applications for Sustainable Construction. Woodhead Publishing; 2024. p.1-74. https://doi.org/10.1016/B978-0-443-13191-2.00009-2

[11] Carranza-Torres C, Hormazabal E. Computational tools for the determination of factor of safety and location of the critical circular failure surface for slopes in Mohr-Coulomb dry ground. In: Proc 2018 Int Symp Slope Stability Open Pit Mining Civil Eng. 2018;21-4.

[12] Afradi A, Ebrahimabadi A, Hallajian T. Prediction of TBM penetration rate using fuzzy logic, particle swarm optimization and harmony search algorithm. Geotech Geol Eng. 2022. https://doi.org/10.1007/s10706-022-02310-7

[13] Cruz E. Soil-Structure Interaction: From Bearing Capacity to Tolerable Movement. PhD Dissertation. 2024.

[14] Zhou J, Shi Z, Du K, Qiu Y, Li B, Mitri S. Feasibility of random-forest approach for prediction of ground settlements induced by the construction of a shield-driven tunnel. Int J Geomech. 2017;17(6):04016129. https://doi.org/10.1061/(ASCE)GM.1943-5622.0000817

[15] Bai R, Shen F, Zhang Z. An integrated machine-learning model for soil category classification based on CPT. Multiscale Multidiscip Model Exp Design. 2024;7(3):2121-46. https://doi.org/10.1007/s41939-023-00324-z

[16] Saad A, Sheikh U, Alyasseri Z. An efficient layout index characters for automatic license plate recognition system based on the YOLO-v8 detector. In: 2024 IEEE 8th Int Conf Signal Image Process Appl (ICSIPA). 2024. https://doi.org/10.1109/ICSIPA62061.2024.10701017
[17] Alattar A, Altaher A, Saad A, Al-Jawahry H. Integrating Haar Wavelet Transform and image processing for accurate fire detection. In: 6th Iraqi Int Conf Eng Technol Appl (IICETA). 2023;559-63. https://doi.org/10.1109/IICETA57613.2023.10351458
[18] Elaraby A, Saad A, Karamti H, Alruwaili M. An optimized deep learning approach for robust image quality classification. Trait Signal. 2023;40(4):1573-9. https://doi.org/10.18280/ts.400425
[19] Ma Z, Zhang B. Deep learning based upscaling of geomechanical constitutive behavior for lithological heterogeneities. In: SPE Annual Technical Conference and Exhibition. 2023. https://doi.org/10.2118/214889-MS
[20] Zhang W-S, Ying Y, Li M, Yang R-H, Ji L, Liu M. Prediction of surface settlement around subway foundation pits using spatiotemporal characteristics and deep learning models. Comput Geotech. 2024;168:106149. https://doi.org/10.1016/j.compgeo.2024.106149
[21] Pramod K, Pijush S. Reliability-based load and resistance factor design of an energy pile with CPT data using machine learning techniques. Arab J Sci Eng. 2023. https://doi.org/10.1007/s13369-023-08506-0
[22] Zhao T, et al. Artificial intelligence for geoscience: Progress, challenges, and perspectives. The Innovation. 2024;5(5).
[23] Chen Z, Liu X, Yang J, Little E, Zhou Y. Deep learning-based method for SEM image segmentation in mineral characterization. Comput Geosci. 2020;138:104450. https://doi.org/10.1016/j.cageo.2020.104450
[24] Abdollahi A, Li D, Deng J, Amini A. Explainable AI-aided safety factor prediction of road embankments. Eng Appl Artif Intell. 2024;136:108854. https://doi.org/10.1016/j.engappai.2024.108854
[25] El Sakka M, Ivanovici M, Chaari L, Mothe J. A review of CNN applications in smart agriculture using multimodal data. Sensors. 2025;25(2):472. https://doi.org/10.3390/s25020472
[26] Afshar A, Nouri G, Ghazvineh S, Hosseini Lavassani H. Machine-learning applications in structural response prediction: a review. Pract Period Struct Design Constr. 2024;29(3):03124002. https://doi.org/10.1061/PPSCFX.SCENG-1292
[27] Kingma DP, Ba JL. Adam: a method for stochastic optimization. In: Int Conf Learning Representations (ICLR). 2014.
[28] Gong H, Su D, Zeng S, Chen X. Advancements in digital twin modeling for underground spaces and lightweight geometric modeling technologies. Autom Constr. 2024;165:105578. https://doi.org/10.1016/j.autcon.2024.105578
[29] Satipaldy B, Marzhan T, Zhenis U, Damira G. Geotechnology in the age of AI: The convergence of geotechnical data analytics and machine learning. Fusion Multidiscip Res. 2021;2(1):136-51. https://doi.org/10.63995/ZOAF3555
[30] Sabaa MR, Salman AD, Dakhil AJ, Jawad SI, Karkush MO, Athab A. Production thematic maps of bearing capacity of shallow foundation for Al-Basrah soil using SPT data and GIS. J Rehabil Civil Eng. 2023;11(4):77-90.
[31] Al-Mirza HA, Falih MR, Wattan S, Salman AD, Karkush M. Utilization of GIS to generate a digital geotechnical map of Baghdad City. IOP Conf Ser Earth Environ Sci. 2024;1374(1):012052. https://doi.org/10.1088/1755-1315/1374/1/012052
[32] Karkush MO, Sabaa MR, Salman AD, Al-Rumaithi A. Prediction of bearing capacity of driven piles for Basrah governorate using SPT and MATLAB. J Mech Behav Mater. 2022;31(1):39-51. https://doi.org/10.1515/jmbm-2022-0005
[33] Karkush MO, Ahmed MD, Sheikha AA, Al-Rumaithi A. Thematic maps for variation of bearing capacity of soil using SPTs and MATLAB. Geosciences. 2020;10(9):329. https://doi.org/10.3390/geosciences10090329
[34] Salman AD, Khadim SS, Karkush M, Al-Rumaithi A. Production of maps for bearing capacity of shallow foundation in Baghdad city using SPTs and MATLAB. IOP Conf Ser Earth Environ Sci. 2024;1374(1):012023. https://doi.org/10.1088/1755-1315/1374/1/012023

Research on Engineering Structures & Materials
www.jresm.org

Research Article

Mapping of elemental soil properties for residential compound in Kirkuk city using GIS technique

Alaa Nore Merza [*, a], Aram Mohammed Raheem [b], Ibrahim Jalal Naser [c]

Department of Civil Engineering, Kirkuk University, Engineering Kirkuk, Iraq

Article Info

Article History:

Received 11 Oct 2025

Accepted 02 Nov 2025

Keywords:

GIS technique;
Inverse distance weighted;
Regression analysis;
Plasticity index;
Liquid index;
Swelling;
Gypsum

Abstract

Referring to the investment orientation and reducing the housing crisis by establishing residential complexes in mountainous areas adjacent to the city and expanding the city's area to control population growth. This research focused on studying structural cracks that appeared in several residential units of the Garden City complex in Kirkuk, which were attributed to soil subsidence and swelling problems. The study collected data at five locations within a residential complex in Kirkuk City. Utilized the Inverse Distance Weighted (IDW) method for the examination of the ratio of clay to silt, and also the physical attributes of swelling, liquid limit (LL), void ratio (e) and compression index (Cc). Also, the study examined the chemical characteristics of total free calcium carbonate content ($CaCO_3$, %) and total gypsum content (GYP, %). The study used single-regression and multiple-regression models for the interpolation of the plasticity index (PI) and soil attributes. The creation of the digital map sets was for examining the physical and chemical residential compound characteristics in Kirkuk City. PI values can be predicted with greater accuracy by considering integrated physical and chemical soil qualities than g just on chemical or physical factors. PI and physical soil components exhibit a range of both beneficial and detrimental connections. The changes of plasticity index (PI) in connection to physical soil qualities exhibited positive relationships with liquid index (LI), LL, swelling potential, Cc, rebound index (Cr), and e, while PI variations and chemical soil values are positively correlated such as sulfate (SO_3%), gypsum (GYP%), and chloride (Cl%). Linear multiple regression models (LMRM) of physical and combined physical-chemical soil variables reliably PI index values, exhibiting high R^2 value ranges (between 0.072 and 0.018). Elevated clay content, high liquid limit, and swelling signify expansive soils that present hazards for foundations and infrastructure. Minimal silt content: little impact on permeability or erosion. The void ratio (e): Elevated values (0.9+) indicate loose, compressible soils that require stabilization.

© 2026 MIM Research Group. All rights reserved.

1. Introduction

Soil refers to the earth's outermost layer; it is composed of crushed rock that has been weathered and otherwise changed by biological, chemical, and environmental factors, such as erosion. Because of variations in the interaction between the project sit soil layers, aquifer, air, and biosphere, soil differs from its rock-based components [1]. The term "soil" consists of minerals and organic matter suspended in water and air [2, 3]. The soil structure fills the pores in the soil, which are made up of components containing porous granules. Liquid water and gaseous air are both contained in these pores [4]. The typical range for soil types is 1–2 g/cm^3 [5].

Geologists divide time based on observable shifts in the Earth's condition. Recent global environmental changes suggest that the Earth may have entered a new geological epoch dominated

*Corresponding author: aala.nuri.merza@gmail.com
[a]orcid.org/0009-0009-6473-6088; [b]orcid.org/0000-0002-6889-3939; [c]orcid.org/0000-0001-8986-9711
DOI: http://dx.doi.org/10.17515/resm2025-1235ic1011rs

by humans, the Anthropocene. Here we review the historical genesis of this idea and evaluate human footprints in the geological record against the formal requirements for recognizing a new epoch. The suggests two various proposed dates to meet the criteria for defining the beginning of the Anthropocene: 1610 and 1964. The formal establishment of the Anthropocene epoch would represent a fundamental change in the relationship between humans and the Earth system [6]. This layer that supports life is known as a pedosphere, and it is dynamic, porous, and well-built. It distributes energy, mass flows, and water efficiently. In addition to the fact that pedology, the study of soil science, is helping to lessen environmental pollution. Soil science studies soil as a complex system of interconnected natural components, with an emphasis on its physical, chemical, biological, and evolving properties [7, 8].

Among the several investigations into soil characteristics is the one conducted in the Tuz region [9]. Here, researchers discovered a range of soluble grain percentages (22- 99%) and sulfate proportions (0.04–12.3%). The pH values of the soil for Mosul city range from 7.44 to 7.88, according to [10]'s study of its chemical qualities [11]. Looked at the chemical makeup of various Swiss locations. The percentage of organic materials varied between 3.4% and 7.3%. The grain silo region in Kirkuk city has been the site of soil experiments by the National Center for Structural Laboratories [12].

Soil gypsum concentrations were determined to be between % 0.09and 67.4% [13]. Soil exploration was conducted in the Shorja region of Kirkuk Governorate. The region's sulfate percentage ranged from 0.14 to 44.6 % when soil was examined physically and chemically and based on chemical analysis. Nonetheless, the proportion of carbonates varied from 21.5 to 42.0%, while the gypsum concentration was 0.3 to 95.44 %. Soil tests on the Corniche Street apartment building behind Kirkuk Park were performed by the National Center for Structural Laboratories [14]. Sulfate concentrations in the area are between 0.05% and 6.99%, according to their findings. Identifying geographic information systems as an effective tool for spatial analysis and modelling [15].

Geostatistical methods take into account the study region's spatial scale, sample distance, and the model's spatial pattern to calculate the spatial distribution and variability [16]. In regions where soil sample measurements are unavailable, soil property estimates are derived using interpolation methods. Soil property maps derived from known samples are frequently predicted by IDW interpolation technique. There has extensively evaluated the spatial variability of soil and its spatial correlations and mineral parameters, including physical, chemical, and biological aspects [17], [18].

GIS may be employed to monitor geospatial mapping and cartographic analysis, as both rely on the creation of digital soil maps. These maps provide a rapid and precise method for identifying distinct characteristics, hence enhancing any research. The soil may be examined, and its potential evaluated through the ground conduct procedures utilized in the creation of these digital maps [19]. Soil geotechnical testing for Kirkuk city was therefore a part of this project. Nevertheless, investigating the soil's chemical characteristics in the designated regions is the primary goal of this project. In addition, using the IDW interpolation approach, geotechnical spatial maps of the research area were prepared and predicted. Used spatial analytic methods, including IDW and Kriging, for the integration of 56 soil samples from Kirkuk city pits [20]. The integrated ingredients were categorized by soil properties, including silt, clay, sand, gravel, and initial void ratio, internal friction angle, cohesiveness, and ideal moisture composition. Quantitative methodologies, including geotechnical parameter correlation, linear regression (LMR), and linear multiple regression, were employed. In three zones, third to fifth zones, IDW and Kriging methodologies deviate, indicating they depict the Kirkuk city dissimilarly sand distribution. The linear multiple regression model demonstrates a strong to outstanding connection between fundamental and studied soil parameters, with (R^2) values from 0.77 to 0.97 to 0.86 to 0.98.

Geographic distribution and soil attributes were the study's main emphasis. GIS and IDW projected soil attributes. Over 65 Kirkuk City soil samples were carefully analyzed for physical and behavioral features. Ten digital maps of gravel, sand, clay, silt, specific gravity, dry density, Atterberg limits, and water content by IDW. Different city neighborhoods have different patterns. Sand was the main soil type, gravel was abundant in the north, and silt was diverse. Southern and eastern clay concentrations affect agriculture and pollution control. The LL and PL Atterberg rose with clay,

demonstrating a link. Except for the northwest, which had the greatest dry density, most locations had water. Most areas have consistent gravity. The findings improve Kirkuk City engineering and geotechnical operations, backed by cross-validation of fundamental and assessed physical features. IDW maps showed variability in R squared (R^2), with lower RMSE values indicating better accuracy. All categories showed moderate to outstanding correlations [21].

Inverse Distance Weighting and LRMs are used to Multiple Kirkuk were used for research. SPT and chemical parameters (SO_3%, TSS, ORG, Cl ppm, $CaCO_3$%, GYP%, and pH) were evaluated using the IDW method. Multiple- and single-regression models interpolated SPT and soil specs. Kirkuk soil chemistry and standard Penetration Test parameters were mapped digitally. Physical-chemical soil characteristics predict SPT better than chemical or physical components. Soil physical components and SPT have pros and cons. Silt and clay increase SPT values whereas gravel and sand decrease them. SPT chemical soil characteristics are favorably associated with SO_3 and TSS. Positive connections were seen between $CaCO_3$, (GYP%), and pH levels and SPT, (ORG%), and Cl (ppm) [22] are negatively correlated.

Geotechnical engineering is no different from any other branch of engineering in that it must adapt to and make use of emerging technology. The objective of this paper was to examine the spatial correlations among the LL, PI, and LI of soil for certain zones within Sulaymaniyah City. Researching the feasibility of creating digital soil maps of the research area and identifying areas with highly expansive soil is the primary goal. The maps were created using the Geographic Information System (GIS) program's Inverse Distance Weighting (IDW) interpolation function. This study utilized data from 592 LL and PI boreholes and 245 LI boreholes. Each layer was assigned a depth between one and two, two and four, and four and six meters. The LL and PI maps were created using 1396 observations each, whereas the LI maps were based on 371 observations. Based on the R^2 and RMSE results, the IDW approach provides fair forecasts. The research region includes significant areas of expansive soil. Which must be considered before any construction activity can begin, according to the data. Geotechnical engineers rely heavily on these maps to aid in decision-making and to visualize the behaviors of soils [23].

Spectral maps showing the regional distribution and concentration of pollutants indicate a strong correlation between the spectral reflectance recorded by the radiometer and the reflectance resulting from satellite image analysis, thereby improving time, effort and human resources [24]. The research aims at studying the mechanical, chemical, and physical features of the housing project site in Garden City Kirkuk, located on one side of Kirkuk to the northeast. Most of the project structures cracked due to soil problems. The combined properties were analysed and examined by mapping the correlations between the properties in the areas and collecting samples from five different locations for research, and using a method called IDW to combine all the collected data for the soils in the residential complex.

The aim can be depicted as geographical data integration of the amounts of the PI, clay and silt contents, LI, swelling, compression, and swelling indices (Cc and Cr), initial void ratio, and gypsum and chloride contents for the present residential complex investigation in Kirkuk, Iraq. The objective was to examine the link between the plasticity index and physical soil factors with a simple LRMwith discrete correlations. The precise relationships between PI and the physical, chemical, and combined physical-chemical soil parameters were analyzed more utilizing LMRM. In addition, digital maps generated by predictive models may depict the likelihood of soil swelling and mitigate expected hazards for more civil engineering purposes. The site was selected for study after problems appeared in the residential units; cracks appeared, indicating that the foundation had sunk because of soil subsidence. Some cases [2,3]. Unlike previous studies based on geographic information systems and IDW technology conducted in Kirkuk, this study integrates the soil physical and chemical features to predict the plasticity index (PI) with greater accuracy, providing an integrated geotechnical and chemical perspective on soil behaviour.

2. Region of The Residential Complex

The study was conducted in Kirkuk in the Garden City residential complex located at the coordinates (448840-3928757) northeast of Kirkuk city. The project consists of (508) housing

units with different sizes (170-200-300) square meters, one and two floors). Different specifications, including service buildings such as a kindergarten, nursery, school, health centers, multiple commercial buildings, and green spaces with no less than 10-15%. The project covers an area of 232,500 square meters. This project was constructed after leveling the land because the area is mountainous consisting of valleys and mountains Cut-and-fill operations were carried out according to the site's geological conditions to achieve suitable ground levels for construction to obtain a suitable terrain for the construction of the residential complex. Figure 1 shown that the project's location in the city of Kirkuk, including the location of the project of our work. Figure 2 at inspection of the residential complex, several fissures of varying sizes and locations have been observed. Field inspections revealed that the cracks observed were mainly caused by foundation settlement due to soil compression in clay layers with high swelling capacity.

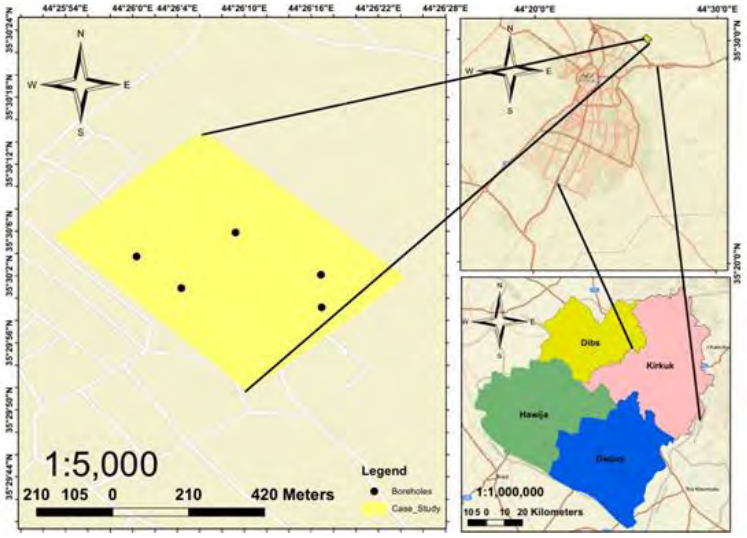

Fig. 1. Detailing the project's location

Fig. 2. Shape and position pisparate fissures in the examined residential compound in Kirkuk, Iraq

3. Methodology

3.1 Laboratory Test Method

Five distinct locations were used to collect samples throughout the project at a depth of 2-3 meters, and the soil consisted of solid clay rock. The samples were processed to get a particle size corresponding to sieve No. 4 (4.75 mm) and subsequently dried in a specialized oven at a 60-70°C for one day. Tables 1 and 2 present the outcomes of mechanical and physical tests aimed at determining the soil features for five selected points in the project. Chemical analyses to ascertain the soil's chemical features. Following ASTM standards ASTM D4318-17E1) for Atterberg limits, (ASTM D4546), all tests were performed y (specifically for swelling potential, ASTM (D698-12-21) for Standard Compaction test, ASTM (D2435), for Consolidation test, and acquired the data presented in Table 3 below were conducted.

Table 1. Coordinates and physical properties of soil in five locations

Location	N	W	Clay (%)	Silt (%)	L.L. (%)	PL (%)	P.I. (%)	L.I. (%)
1	449032.93	3928614.65	87	10	48	35	13	0.9
2	448840.11	3928822.19	88	10	31	21	10	2.33
3	448616.46	3928757.18	93	5	46	36	10	0.89
4	448716.84	3928668.91	93	5	46	36	10	0.89
5	449031.9736	3928703.101	89	11	56	37	19	1.9

Table 2. Mechanical properties of soil samples

Sample No	Swelling (%)	Cc	Cr	e_o
1	4.9	0.19	0.026	0.76
2	1.7	0.2	0.021	0.781
3	3.8	0.13	0.018	0.609
4	5	0.16	0.021	0.574
5	5.5	0.29	0.03	0.963

Table 3. Chemical properties of soil samples

Sample No	SO_3 (%)	Gypsum (%)	Cl (%)	$CaCO_3$ (%)
1	1.34	2.88	0.023	24.246
2	1.43	3.07	0.014	24.396
3	1.61	3.46	0.034	23.046
4	1.07	2.3	0.057	23.971
5	1.2	2.58	0.031	23.845

3.2 Geographic Information System Using IDW Technique

Geographic Information Systems (GIS) serve as a robust instrument for the comprehensive, spatially explicit examination of the Earth's resources [5]. They provide a distinctive capability to integrate geographic data locations and characteristics with tabular data attributes of those features with other data products or outputs. Moreover, Geographic Information Systems have shown to be very effective in the intricate study and interpretation of the interaction dynamics of Earth's natural systems. Advancements in the last decade in cost-effective and user-friendly Geographic Information Systems, particularly tailored for environmental management, have rendered GIS more accessible than ever in the professional sphere.

The data entry procedure begins with designing the database master plan to feature classes, together with their different locations and coordinates. Specific information is manually inputted. Conversely, several types of information may be immediately obtained from point or satellite maps, significantly reducing input time and costs. GIS statistical features can be used to investigate correlations between various data for specific feature classes or between themselves [25]. Soil research has adopted new technologies, facilitating the easier visualization and interpretation of geographical soil data. The amalgamation of GIS and civil engineering made numerous methodologies to depict the earth's surface by three-dimensional models of any global study region. [26].

IDW is one of the most prevalent interpolation algorithms. It was employed for the prediction of the any unmeasured site value for by evaluating the surrounding anticipated location values. It is basically based on two assumptions: first, the influence of an unknown value at a certain location is directly proportional to its closeness to the control point, rather than to more distant locations. The effect magnitude is in an inverse proportion to the distance between locations. Cross-validation was performed for assessing the accuracy of the fit using the root mean square error (RMSE) criterion, which yielded RMSE values ranging from 0.08 to 0.15 for the main physical parameters, indicating satisfactory prediction reliability. It can provide the following equation 1 [27, 28].

$$\frac{\sum_{i=1}^{n} w_i\, z_i}{w_i} = \frac{\sum_{i=1}^{n} zi/D_i^p}{1/D_i^p} \quad (1)$$

Z denotes the interpolated value of the unknown point wi, while the weighting function determines the influence of the control point zi. The value zi represents the observed data at control point i, n is the nearest neighboring points considered in the interpolation process (ranging between 20 and 30 in general IDW applications; however, in this study, n = 4 due to the limited dataset). Di^p denotes the distance between I and the interpolated location, while p represents a weighting exponent, an arbitrary positive real integer.

3.3 Linear Single and Multi-Regression Model

The following sections explain the two models in the analysis.

3.3.1 Single-Regression

Using data collected in the field regarding the soil's physical and chemical features, the study used a linear single regression model for evaluating the soil's plasticity index (PI) feature. The subsequent PI soil characteristics are depicted in the linear simple regression model in Eq. (2):

$$PI\ [\%] = K1\ .physical\ or\ \ chimical\ properties\ [\%] + K2 \quad (2)$$

Where K1 and K2 are parameters. The model's parameters, denoted as K1 and K2 number of physical or chemical model parameters, including LL, clay, silt, gypsum, and organic content percentages, may have a direct correlation with PI content. Although PI might be the main reason for soil swelling, it necessitates a thorough laboratory examination. Accordingly, PI can be estimated from physics and chemistry of soil by the designed linear single regression model.

3.3.2 Multi Regression

Field data of physics and chemistry of soil variables were utilized to compute the PI soil attribute using a linear multi-regression model. The following soil properties are represented by the linear multi-regression model: silt%, clay%, gypsum %, (LL, LI), swelling, Cc, Cr, eo, SO3%, and CL%. The researchers used four separate linear multi-regression models. Independent variables were chosen by a stepwise forward selection method to identify the most statistically significant predictors of PI among the physical and chemical parameters. The following model forms are shown by Eqs. (3), (4), (5), and (6):

The model parameters are A, B, C, D, E, F, G, H, I, J, K, N, O, P, C1, C2, C3, C4, C5, C6, C7, C8, C9, C10,

$$Plastic\ index\ [PI]\%=A+B^*\ (silt\%)\ +C^*\ (clay\%)\ +D^*LL+E^*LI \quad (3)$$

$$Plastic\ index\ [PI]\% = F + G * swelling + H * Cc + I * Cr + J * e_o \quad (4)$$

$$Plastic\ index\ [PI]\% = K + N * SO_3\% + O * gypsum\ \% + P * Cl\% \quad (5)$$

$$Plastic\ index\ [PI]\% = C1 + C2 * clay\ \% + C3 * silt\ \% + C4 * LL + C5 * LI\ + C6 *\ swelling + C7 * Cc + C8 * Cr + C9 * e_o + C10 * SO_3\% + C11 * gypsum\ \% + C12 * Cl\% \quad (6)$$

C11, and C12. The criteria established by the multi-regression model enable the prediction of the PI component through various ratios of physical and chemical soil factors.

4. Results

4.1 Physical Soil Distribution

Various soil digital maps by GIS technique according to IDW interpolation was performed and using a weighting exponent p = 2 and the four nearest neighboring data points are presented in Figure 3. The Figure includes maps for swelling, clay, silt, LI, compression index, and initial E. It obviously indicated that the clay is concentrated on the western zone of the area under consideration although the silt is concentrated on the eastern zone part. In addition, the highest swelling zone, liquid limit, compression index and void ratio are situated in the southeastern region of the

analyzed area. The soils, known for a high clay content (87–93%) and liquid limits LL (31–56) %, are classified as CH (high-plasticity clays) according the Unified Soil Classification System (USCS), signifying significant expansivity. Swelling potential ranged between (1.7-5.5)% (volumetric swelling), presumably volumetric swell or kPa pressure) and increased void ratios (up to 0.96) indicate considerable hazards of heave, subsidence, and diminished bearing capacity, intensified by the semi-arid environment of the region with seasonal moisture variations. The 1:4,000 scale indicates relevance to infrastructure projects (e.g., foundations, roads), where mitigating strategies such as lime stabilization, deep foundations, or moisture control are essential.

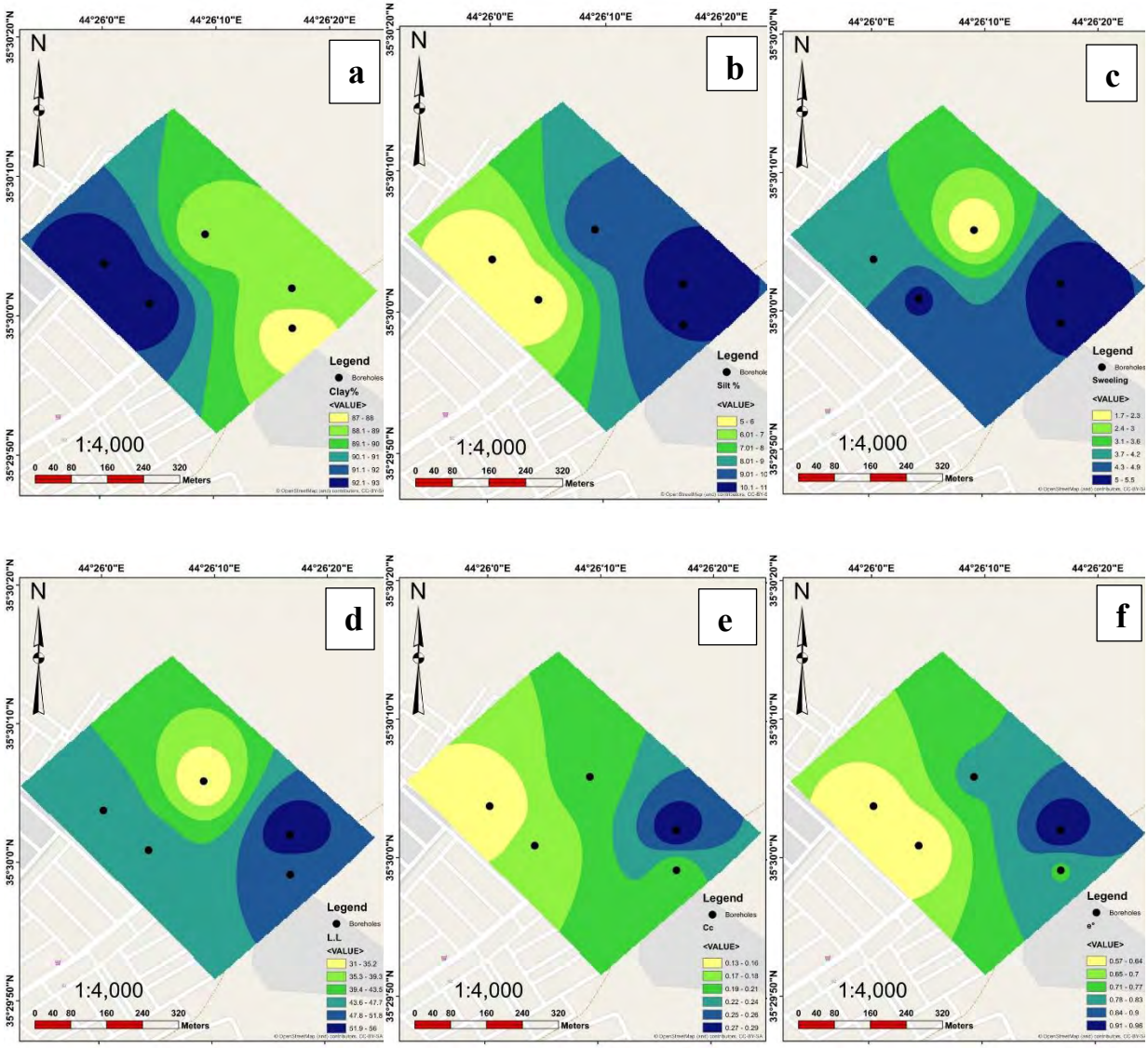

Fig. 3. Inverted distance weighting technique for soil samples collected from Garden, Kirkuk City, Iraq: (a) clay, (b) silt, (c) swelling, (d) LL, €, Cc, and (f) void ratio

4.2 Chemical Soil Distribution

Figure 4 shows soil digital maps by GIS according to the IDW for CaCO3 and gypsum contents. The CaCO3 ratio (23.3-24.4) concentrates in the Middle Eastern area under consideration and the gypsum (2.49-3.46) in the north western part.

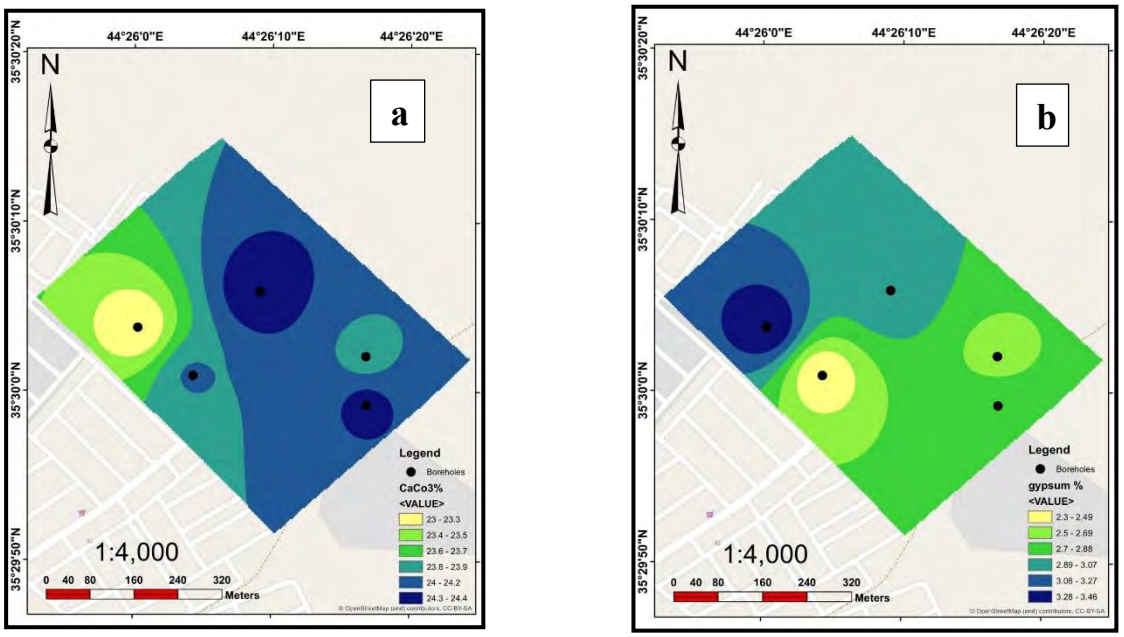

Fig. 4. distributions of IDW methodology for chemical soil in study areas of Garden City, Kirkuk City, Iraq: (a) $CaCO_3$, and (b) gypsum content

4.3 The Relationship Between Plasticity Index and Soil Properties

Table 4 summarizes the relationships between PI and several soil parameters, including silt percentage, clay percentage, gypsum percentage, liquid limit (LL), plasticity index (LI), swelling potential, Cc, Cr) eo, and concentrations of SO3% and Cl% compounds.

Table 4. The correlations between the PI and soil features

Parameter	P.I.	Clay (%)	Silt (%)	L.L. (%)	L.I. (%)	Swelling	Cc	Cr	eo	SO_3 (%)	Gypsum (%)	Cl (%)
Plastic limit	1.0											
Clay (%)	-0.42	1.00										
Silt (%)	0.66	-0.93	1.00									
L.L. (%)	-0.73	0.14	0.04	1.00								
L.I. (%)	0.320	-0.501	0.680	-0.380	1.00							
Swelling (%)	0.59	0.16	-0.05	0.94	-0.52	1.00						
Cc	0.90	-0.57	0.82	0.40	0.65	0.29	1.00					
Cr	0.93	-0.61	0.78	0.62	0.30	0.57	0.90	1.00				
eo	0.86	-0.71	0.92	0.29	0.69	0.13	0.95	0.85	1.00			
SO3 (%)	-0.35	-0.02	-0.09	-0.37	0.01	-0.58	-0.42	-0.49	-0.14	1.00		
Gypsum (%)	-0.35	-0.02	-0.09	-0.37	0.01	-0.58	-0.42	-0.49	-0.14	1.00	1	
Cl (%)	-0.13	0.80	-0.73	0.41	-0.60	0.58	-0.30	-0.19	-0.56	-0.58	-0.57	1

Plasticity index (PI), Compression Index (Cc), and recompression coefficient (Cr)

The PI characteristic is favorably and adversely associated with certain soil parameters, ranging from -0.42 to 0.93. Higher plasticity increases soil porosity and liquid limit, as the PI substantially correlates with the Liquid Limit (LL) (0.73), compression index (Cc) (0.90), and void ratio (eo) (0.86). Clay percentage inversely corresponds with silt percentage (-0.93) and marginally with recompression coefficient Cr (-0.61). The strong correlation between liquid limit and swelling potential (0.94) shows that soils with higher liquid limits expand more, which is crucial for building stability. Cc significantly matches recompression coefficient Cr (1.00) and eo (0.92), showing that

the high correlation between PI and Cr may be an indirect result of Cr's strong correlation with Cc and eo. The similar values between SO_3% and Gypsum% are expected because SO_3 is a major component of gypsum, whereas chloride percentage (Cl %) favors clay (0.80) but negatively correlates with LL (-0.73) is logical, as salts cause flocculation of clay particles, reducing plasticity. These links are needed to map elemental values and understand soil behavior using GIS.

4.4 Linear Single Regression Model

Table 5 shows potential linear one-regression model features. One LRM was solved and provided by least squares. Table 5 displays the model's parameters and R^2 values for all scenarios. Additionally, R^2 values range (0.872) to (0.018).

Table 5. Swelling soil property LRM analysis

Swelling Properties (%)	*Equation*	Properties (%)	R^2
Plasticity Index (PI)	0.3151*L.L-1.919	L.L	0.532
	0.879*silt(%)+5.19	Silt	0.440
	-0.563*clay(%)+63.031	Clay	0.165
	-3.0591*GYP(%) + 21.141	GYP (%)	0.122
	-32.47*Cl(%)+13.4331	CI	0.018
	-32.471*Cl(%)+13.433	LI	0.102
	1.522*swelling+6.0451	Swelling	0.350
	58.6791*Cc+1.017	Cc	0.817
	766.52*Cr-5.3801	Cr	0.872
	21.7451*eo-3.634	eo	0.764
	-6.59*SO3(%)+21.1641	SO3	0.123

The PI relationship to the physical soil characteristics is illustrated in Figure 5a–d. When it comes to the physical components of soil, PI has both positive and negative relationships. The figures analyze the PI–Clay (%) relationship is weakly negative and scientifically unreasonable due to differences in clay type or imbalance in sample distribution. (R2 = 0.165) with plasticity index. An increase in clay concentration decreases PI somewhat. Shows a moderate positive connection (R2= 0.440) between silt concentration and PI. Liquidity and plasticity. LI has little effect on PI (R2= 0.102).

The relationship between the LL and the PI. In the data, the two variables (R^2 = 0.532) are positively correlated. If LL increases, PI climbs, showing the strongest correlation among the four metrics examined. Figures (e-h) depict the edema relationship to PI. It has a little positive connection (R^2 = 0.351), suggesting that when swelling occurs, PI also rises, albeit to a limited extent. This outcome is characterized by a poor correlation. Figure (d) depicts the relationship between the Cc and the PI. The data exhibits a robust positive correlation (R^2 = 0.8171), indicating that PI significantly increases as Cc rises. Figure (e) illustrates the initial void ratio (eo) in correlation with the plasticity index (PI). It shows that the correlation is positive at (R^2 = 0.746) (R^2 = 0.8723), indicating that the void ratio (eo) and compression ratio (Cr) significantly affect PI, as shown in Figure (5) illustrates the strong positive correlation; as Cr rise, PI also grows significantly, showing that the four parameters analyzed are strongly correlated.

The LRMs used interpret the relationships between chemical properties by linking the independent variables (SO_3%, GYP%, Cl%) to the dependent variable Pl. The results showed a general weakness in the explanatory power of these models, with both SO_3% ($P_1 = -6.59 \times SO_3 + 21.16$, R^2 = 0.123) and GYP% ($P_1 = -3.06 \times GYP + 21.14$, R^2 = 0.122) showed slight negative correlations, meaning that increases in SO_3 or GYP content were accompanied by limited decreases in P_1 values.

In contrast, the Cl% model ($P_1 = -32.47 \times Cl + 13.43$, R^2 = 0.018) a relatively high slope coefficient, but with little explanatory power, possibly due to the narrow range of Cl concentrations in the samples (0.01–0.06%) as mentioned in section (m). The data in section (i) most likely refer to different codes or sample groups, while section (m) clarifies the measurement ranges, confirming the limited variation in the Cl% variable.

Overall, PI–SO_3, GYP, Cl: Very weak relationships (R^2 < 0.13) which have no statistical effect on plasticity and the equation for Cl is unrealistic (very large coefficient versus very weak R^2). Statistically, some models are not valid for prediction due to low R^2 (<0.2). Therefore, it is preferable to exclude them if researchers deem it necessary.

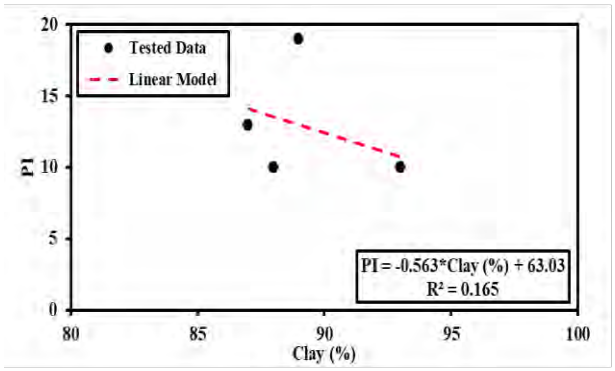

(a)

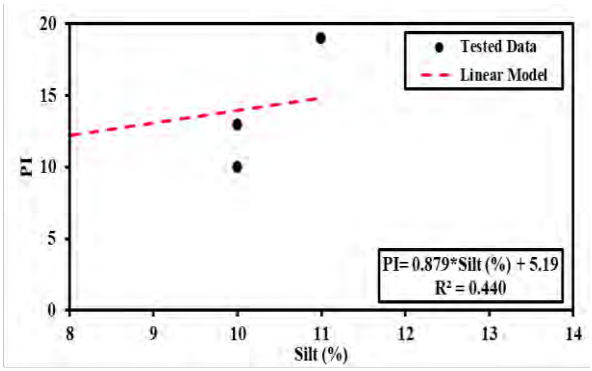

(b)

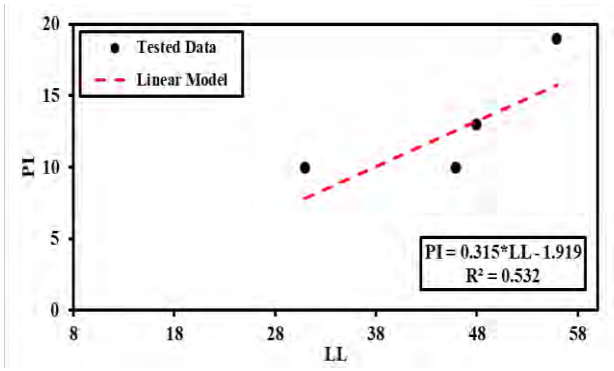

(c)

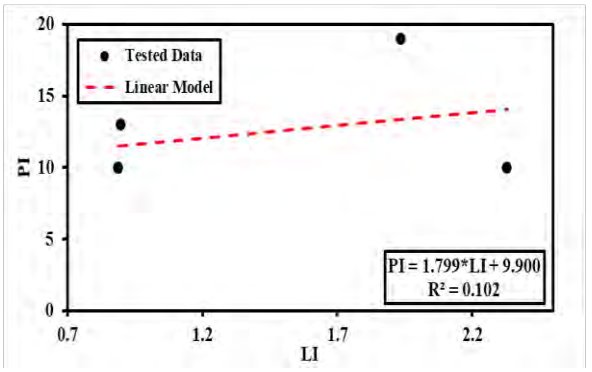

(d)

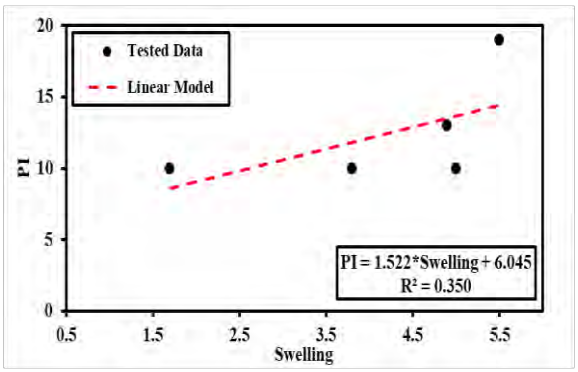

(e)

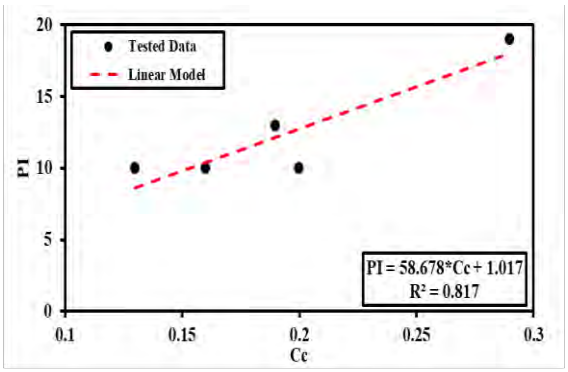

(f)

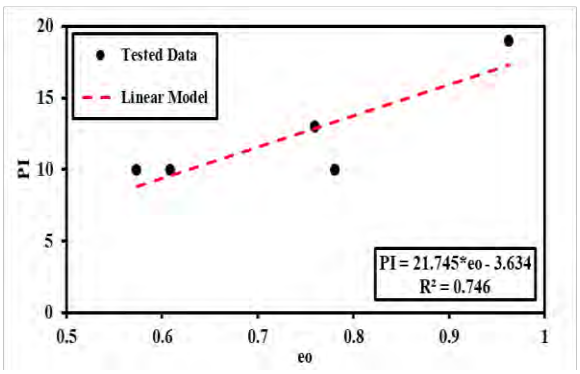

(g)

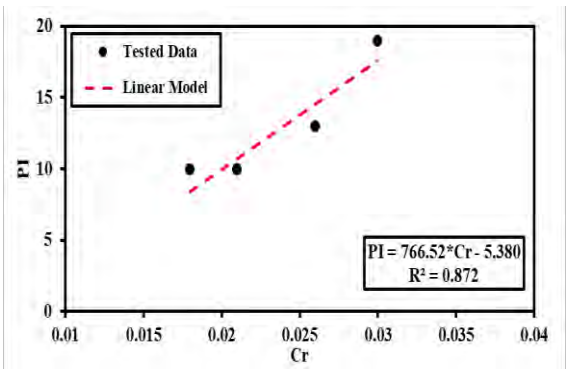

(h)

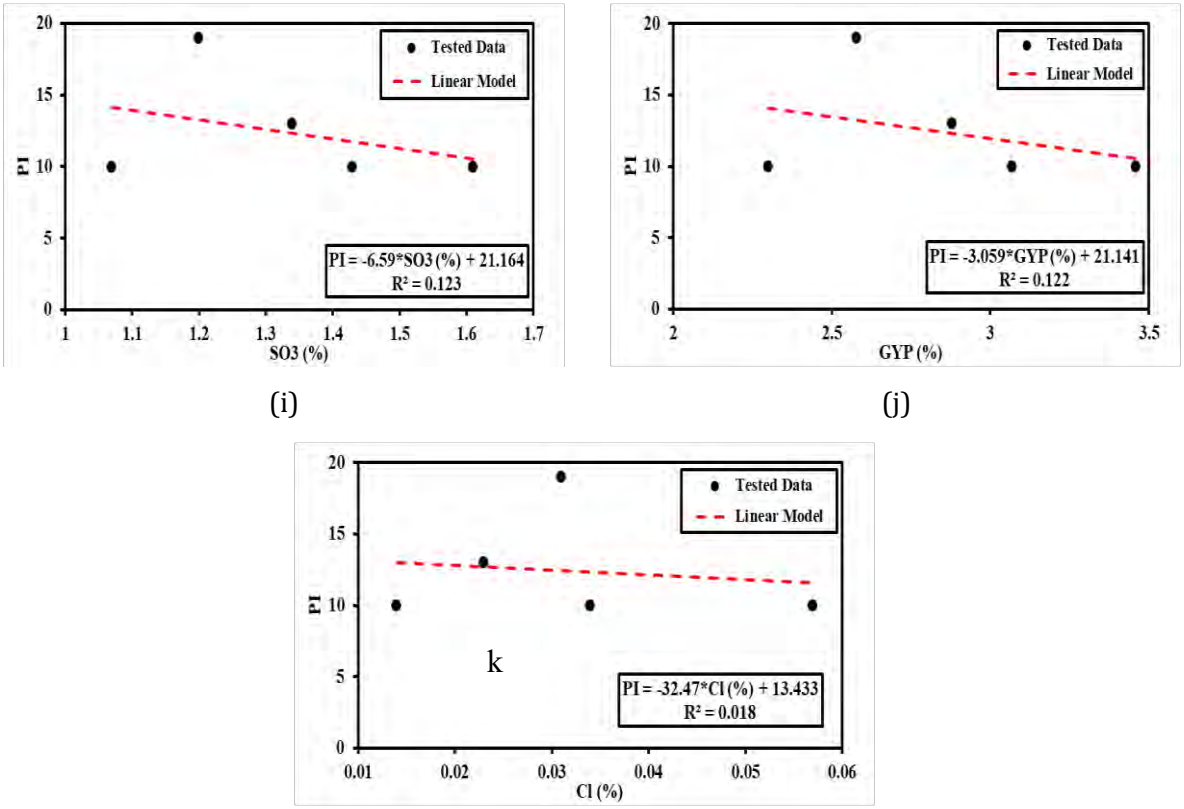

Fig. 5. The variation of PI with different soil compositions in Garden City in Kirkuk City, utilizing a linear simple regression model

4.5 Multiple LRM

Figure 6 shows the general framework for applying multiple linear regression, where the least squares method was used to find model solutions and estimate its statistical coefficients. The figure shows the predictive values of the model and the coefficients derived from it, where the correlation coefficient (R) ranged between 0.68 to 0.872, confirming a strong but realistic fit to the experimental data. The model was according to a scholarly work on the PI relationship to four chemical features of the soil in the Garden City area of Kirkuk. Figure (6-A) shows a negative relationship between PI and $CaCO_3$%, as calcium carbonate usually contributes to reducing plasticity through its interaction with clay minerals, resulting in a harder and less flexible structure. Figure (6-b) illustrates the relationship between PI and gypsum (GYP%), which is irregular; low gypsum content may help improve soil structure cohesion, while high concentrations contribute to reduced flexibility due to the high solubility of gypsum.

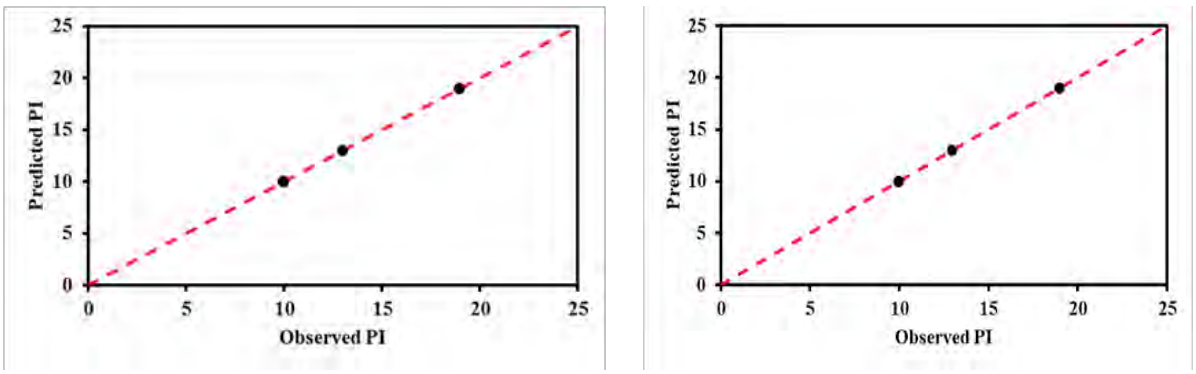

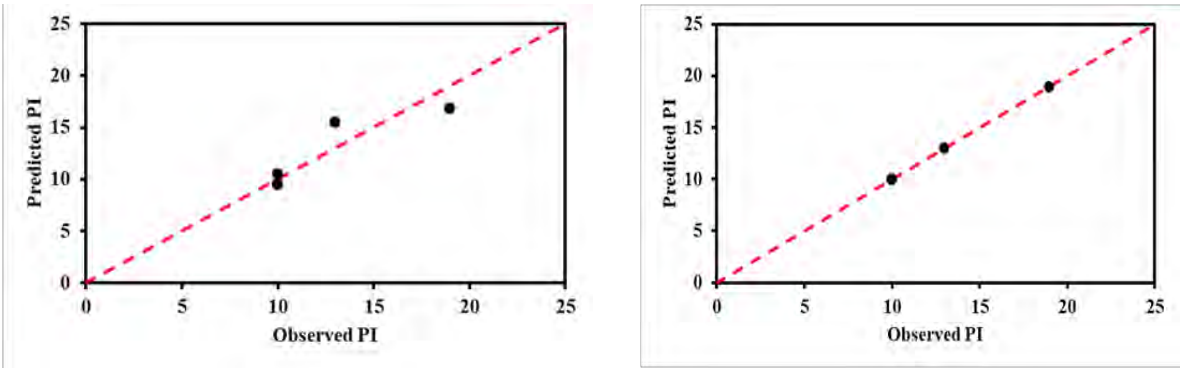

(c) (d)

Fig. 6. Variation of PI content for soil ingredients inside Garden City, in Kirkuk City, Iraq, employing a LMRM: a – Eq.3, b – Eq.4, c – Eq.5, d – Eq.6

Figure (6-c) shows a clear positive relationship between PI and clay content (CL%), where high clay content increases soil flexibility by enhancing internal cohesion and water retention capacity. In contrast, Figure (6-d) indicates an inverse relationship between PI and SO_3%, as sulphates cause soil particles to expand and weaken their cohesion when exposed to moisture. In general, clay content (CL%) is the most influential factor in determining plasticity, while calcium carbonate ($CaCO_3$) and sulphate (SO_3) have the opposite effect, reducing it. The effect of gypsum (GYP%) varies depending on its concentration and soil conditions. These results highlight the complexity of the effect of chemical reactions on soil behavior and plasticity.

5. Discussion

Data on the distribution of particles might be helpful in examining the likelihood of soil swelling and in developing appropriate foundation alternatives. In comparison to soils with lower clay content, those with a higher concentration of clay are much more likely to swell. Notwithstanding their diminutive size and elevated surface area to volume ratio, clay particles possess the capacity to absorb and retain substantial quantities of water. Soil expands owing to water absorption, as clay particles absorb greater amounts of water, leading to an increase in volume. Soil clay percentage, clay type, and water absorption rate would all have a role in the swelling. Consequently, the clay content of the soil is a crucial factor to consider when determining the likelihood of soil swelling. Predicting the soil type content in nearby sample locations is possible with the use of the GIS technique and the IDW approach.

LL and PI can be utilized to forecast soil expansion. These two elements provide significant insight into the soil's response to variations in moisture levels. Soils with high concentrations are more prone to swelling because they change size more in response to moisture changes and can generally hold more water. These soils have the ability to expand and even collapse if they hold too much water.

Negative correlations between PI and SO_3%, GYP%, and Cl% indicate that higher chemical content reduces soil plasticity and swelling potential. This is attributed to the flocculating effect of salts, which decrease water adsorption on clay surfaces, thereby lowering plasticity. The integration of physical and chemical parameters significantly enhanced PI prediction accuracy, as indicated by the multiple regression model (R^2 = 0.872). This finding supports the hypothesis that combined modelling yields more reliable results than separate analyses of physical or chemical factors alone.

The southeastern part of the Garden City complex exhibits the highest swelling potential, liquid limit, and void ratio, as indicated by the IDW maps (Figure 3). This zone corresponds spatially to the locations where the most severe foundation cracks were observed, confirming the link between soil expansivity and structural distress.

6. Conclusions

Relying on only five samples limits the accuracy of generalizing clay distribution located in a residential complex in Garden Kirkuk. The geographical analysis for this study used the IDW method. Tests were conducted on cracks in the structures of the compound under study using the physics and chemistry of soil samples taken from the site. The statistical analysis was based on simple and multiple LRMs, as well as correlations between the PI and soil properties. The following conclusions were proposed.

- The residential complex under examination has clay soil at a depth of 2-3 m distributed mostly in three zones, as determined by the IDW approach in conjunction with GIS. The GIS and IDW analysis revealed that the northern half of the residential complex under examination had the highest percentages of clay and silt.
- The bulk of the investigated residential compound is covered by clay soil, in accordance with the IDW methodology integrated with the GIS process.
- GIS and IDW analyses revealed that the central area of the residential compound under consideration contained the highest quantity of gypsum.
- The soil models analyzed using the GIS and the IDW method mainly contain values for the plasticity index and liquidity limit ranging from 21 to 37, respectively, indicating that the soil is expansive clay soil.
- The plasticity index, which indicates swelling, has been found to have both positive and negative relationships with soil physical and chemical factors.
- The accurate prediction PI values were obtained by the physical combined with physical and chemical soil parameters using the linear multi-regression models that were presented. Both models achieved R^2-values of 0.872 demonstrating the accuracy and positive correlation of the results.
- Soil classification is clay CL (inorganic silt/low plasticity clay).
- The statistical models in this study comprehensively offer mechanical and geographical insights into the causes of cracks in the residential complex under study.

References

[1] Chesworth W. Encyclopedia of soil science. Springer Science & Business Media; 2007. Chesworth W, editor. Encyclopedia of Soil Science. Encyclopedia of Earth Sciences Series. 2008. https://doi.org/10.1007/978-1-4020-3995-9

[2] Voroney RP. The Soil Habitat. Soil Microbiology, Ecology and Biochemistry. 2007;25–49. http://dx.doi.org/10.1016/b978-0-08-047514-1.50006-8

[3] Danoff-Burg JA. The Terrestrial influence: Geology and soils. Earth Institute Center for Environmental Sustainability; 2000.

[4] Taylor SA, Ashcroft GL. Physical edaphology: The physics of irrigated and nonirrigated soils. W.H. Freeman. 1972.

[5] Shiri J, Keshavarzi A, Kisi O, Karimi S, Iturraran-Viveros U. Modeling soil bulk density through a complete data scanning procedure: Heuristic alternatives. Journal of Hydrology. 2017; 549:592–602. https://doi.org/10.1016/j.jhydrol.2017.04.035

[6] Ojiako EN, Okonkwo MN. Analysis of heavy metals in soil of mechanic workshop in Onitsha metropolis. Adv Appl Sci Res. 2013; 4(1):79–81.

[7] Majid NN. Study of geotechnical properties of gypsum in selected sites of the city of Kirkuk [dissertation]. Baghdad: University of Baghdad; 2004. 188 p.

[8] Al-Mirza HA, Falih MR, Wattan S, Salman AD, Karkush M. Utilization of GIS to generate a digital geotechnical map of Baghdad City. IOP Conf Ser Earth Environ Sci. 2024; p. 012052.

[9] Mohammed SMA. The study of the quality of rainwater and its impact on some soil characteristics in the district of Al-Tuz [master's thesis]. Tikrit: University of Tikrit; 2008.

[10] Hayali AKA. An environmental study of some pollutants in the city of Mosul [master's thesis] Mosul: University of Mosul; 2001.

[11] Tandy S, Bossart K, Mueller R, Ritschel J, Hauser L, Schulin R, et al. Extraction of Heavy Metals from Soils Using Biodegradable Chelating Agents. Environmental Science & Technology. 2004 Feb;38(3):937–44. http://dx.doi.org/10.1021/es0348750

[12] National Center for Construction Laboratories (NCCL). Soil investigation for Kirkuk new grain soil (report no. 1/1/8) part 1. Baghdad; 2001.

[13] National Center for Construction Laboratories (NCCL). Tourist Hotel in Tikreet. Report No. 144. Baghdad; 1992.
[14] National Center for Construction Laboratories (NCCL). Soil investigation for Housing Complex at Kirkuk (Korneesh Street), Report No. 1/1/68. Baghdad; 2001.
[15] Noori AM, Qader WM, Saed FG, Hamdany ZA. Quantification of morphometric parameters to analyze the watershed characteristics: A case study of Rosti Watershed, Iraq. Int J Adv Sci Technol. 2019;28(13):273–89. https://doi.org/10.46717/igj.56.1F.13ms-2023-6-21
[16] Shit PK, Bhunia GS, Maiti R. Spatial analysis of soil properties using GIS-based geostatistics models. Model Earth Syst Environ. 2016;2(2):107. https://doi.org/10.1007/s40808-016-0160-4
[17] Zhao W, Cao T, Li Z, Sheng J. Comparison of IDW, cokriging and ARMA for predicting spatiotemporal variability of soil salinity in a gravel–sand mulched jujube orchard. Environmental Monitoring and Assessment. 2019 May 18;191(6):376–6. https://doi.org/10.1007/s10661-019-7499-8
[18] Duan L, Li Z, Xie H, Li Z, Zhang L, Zhou Q. Large-scale spatial variability of eight soil chemical properties within paddy fields. CATENA. 2020; 188:104350. https://doi.org/10.1016/j.catena.2019.104350
[19] Raheem AM, Omar NQ. Investigation of distinctive physico-chemical soil correlations for Kirkuk city using spatial analysis technique incorporated with statistical modeling. International Journal of Geo-Engineering. 2021; 12(1):18. https://doi.org/10.1186/s40703-021-00147-2
[20] Raheem AM, Naser IJ, Ibrahim MO, et al. Inverse distance weighted (IDW) and kriging approaches integrated with linear single and multi-regression models to assess particular physico-consolidation soil properties for Kirkuk city. Model Earth Syst Environ. 2023;9:3999–4021. https://doi.org/10.1007/s40808-023-01730-5.
[21] Mohammed P, Al Nuaimy Q, Shareef M. Analyzing soil physical properties in Kirkuk City, Iraq, utilizing a Geographic Information System–based inverse distance-weighted technique. Ecol Eng Environ Technol. 2024;25(11):118–33. https://doi.org/10.12912/27197050/192346
[22] Ibrahim MO, Raheem AM, Naser IJ, Omar NQ, Najmadeen KT. Correlating standard penetration test (SPT) with various soil properties in different Kirkuk City locations: A case study utilizing inverse distance weighted (IDW) for assessment and prediction. E3S Web Conf. 2023; 427:01005. https://doi.org/10.1051/e3sconf/202342701005
[23] Rashed K, Hussein AA. GIS as a tool for expansive soil detection at Sulaymaniyah City. J Eng. 2020;26(6). https://doi.org/10.31026/j.eng.2020.06.13
[24] Karkush MO, Ziboon AR, Hussien HM. Application of Remote Sensing Techniques in Geoenvironmental Engineering. International Journal of Geosciences and Geomatics. 2013; 1(1):9-16.
[25] Sabaa, M. R., Salman, A. D., Dakhil, A. J., Jawad, S. I., Karkush, M. O, Athab, A. Production Thematic Maps of Bearing Capacity of Shallow Foundation for Al-Basrah Soil Using Standard Penetration Data and GIS. Journal of Rehabilitation in Civil Engineering, 2023; 11(4): 77-90. https://doi.org/10.22075/jrce.2023.27587.1668
[26] Karkush MO, Sabaa MR, Salman AD, Al-Rumaithi A. Prediction of bearing capacity of driven piles for Basrah governatore using SPT and MATLAB. Journal of the Mechanical Behavior of Materials. 2022 Jan 1;31(1):39-51. https://doi.org/10.1515/jmbm-2022-0005
[27] Mohammed PA, Al Nuaimy QA, Shareef MA. Analyzing Soil Physical Properties in Kirkuk City, Iraq, Utilizing a Geographic Information System-Based Inverse Distance-Weighted Technique. Ecological Engineering & Environmental Technology (EEET). 2024; 25(11). https://doi.org/10.12912/27197050/192346
[28] Karkush MO, Ahmed MD, Sheikha AA, Al-Rumaithi A. Thematic maps for the variation of bearing capacity of soil using SPTs and MATLAB. Geosciences. 2020; 10(9):329. https://doi.org/10.3390/geosciences10090329

Research on Engineering Structures & Materials
www.jresm.org

Research Article

Shear performance of concrete beams reinforced with perforated functional steel plates

Alaa A. Shamki [*,a], Majid D. Muttashar [b]

Department of Civil Engineering, University of Thi-Qar, Thi-Qar, Iraq

Article Info

Article History:

Received 11 Oct 2025

Accepted 21 Nov 2025

Keywords:

Reinforced concrete;
Shear strength;
Perforated steel plate;
Embedded reinforcement;
Surface texture

Abstract

This study seeks to examine a novel shear reinforcing method employing steel plates as a substitute for conventional reinforcement in concrete beams. Six reinforced concrete specimens, differing in plate characteristics (type, position, and texture), measuring 1200 mm in length, 200 mm in height, and 120 mm in width, underwent a two-point bending test to assess their shear strength, load-bearing capacity, displacement characteristics, and cracking patterns. The concrete had a compressive strength of 25 MPa. The experimental results indicated that reinforcement with rough-textured perforated steel plates (BR-10%) attained superior load-bearing capacity, demonstrating an 182.4% enhancement in shear strength relative to the reference beam (B0). This signifies that these plates can substitute conventional shear joints in beams.

© 2026 MIM Research Group. All rights reserved.

1. Introduction

Reinforced concrete (RC) beams are horizontal structural elements engineered to convey loads from floor slabs to columns. An important aspect to focus on is understanding the generated shear stresses. Shear stresses are generated in concrete beams because of the applied shear force. Shear reinforcement is used to resist these stresses [1]. These stresses cause many problems for structures, including the development of dangerous diagonal cracks, which can lead to sudden and unexpected collapse. Shear reinforcement is typically performed using transverse reinforcing bars. Numerous studies have presented alternatives to traditional steel bar reinforcement, one of which involves the utilization of steel plates [2].

Using steel plates to reinforce shear joints is a common method in structural engineering. This method is employed to increase capacity, reduce deflection, and strengthen connections between beams and columns, both externally and internally. Among the researchers who applied the plates externally, Liu et al.[3] discussed the effectiveness of the bolted side-plating (BSP) method in rehabilitating reinforced concrete (RC) beams in existing buildings. They found that BSP beams increased flexural capacity without reducing ductility and shear strength without noticeable diminishment. Ashraful Alam et al. [4] study explores the use of embedded connectors to optimize steel plates for the shear reinforcement of reinforced concrete beams. They found that the connector reduced debonding failure and increased shear failure load, highlighting premature debonding as a weakness. The study by Jarallah et al. [5] found that externally bonded steel plates improved shear cracking load and ultimate shear capacity in nine RC beams, with larger improvements as the plating ratio increased and compressive strength decreased.

Adhikary and Mutsuyoshi [6] examined the structural effectiveness of steel plates externally bonded to both sides of a concrete beam using epoxy and bolts. They suggested that the shear contribution was optimized when the steel plate was positioned at the highest feasible section

*Corresponding author: alaa.shamki@utq.edu.iq
[a]orcid.org/0009-0007-7218-1540; [b]orcid.org/0000-0002-0720-8168
DOI: http://dx.doi.org/10.17515/resm2025-1237ic1011rs
Res. Eng. Struct. Mat. Vol. 12 Iss. 2 (2026) 779-791

depth rather than by augmenting the thickness of the steel plate. Sudarsana et al. [7] recommended fastening a U-shaped steel plate and two L-shaped steel plates as shear reinforcement within the shear span. This study revealed that insufficient plate thickness might cause out-of-plane distortion when the beam is subjected to increased stresses. Furthermore, they observed that narrow steel plates were incapable of withstanding concentrated transverse loads at the bolt hole, resulting in localized failure. Osman et al. [8] presents a steel plate repairing technique that strengthens RC members, controls failure modes, and improves the functionality of pre-cracked reinforced concrete beams with apertures. The method involves applying a temporary pre-stressed force to close existing shear cracks. The benefits of this technique stem from sealing existing fissures around apertures through epoxy injection. The findings indicate that both the extent of pre-existing damage and the reinforcement of steel plates significantly influence the efficiency of strengthening and the manner of failure.

Arslan et al. [9]attached external steel plates to the sides and soffits of beams using epoxy resin. Five of the six examples demonstrated premature failure due to shear when the steel plates separated from the beams. The two prevalent techniques for externally affixing steel plates to concrete beams as supplementary shear reinforcement, namely bolting and epoxy resin bonding, exhibited premature failure of the steel plates. Insufficient plate thickness led to premature localized failure at bolt holes, while excessive plate thickness resulted in delamination of the plate. The literature above indicates that, while utilizing steel plates as an external retrofit for beams during the service stage is viable, the concern regarding the premature failure of these external plates requires consideration. Using recommendations derived from these experiments, other researchers have incorporated steel sheets or sections into beams from the inside before casting to address the problems of detachment, warping, and localized failure associated with external steel retrofit technology.

Ibrahim et al. [10]study investigated the shear performance of reinforced concrete beams including internally embedded vertical shear steel plates. The results indicated that the orientation of the steel plate augmented shear capacity, while transverse hollow steel plates improved ductility and shear performance. The study by Ammash [11] studied on reinforced concrete beams using steel strip plates as a shear reinforcement instead of stirrups bars is presented in this paper. Five specimens with same dimensions and properties were used in this study. One of them has regular ties as shear reinforcements and is used as a reference beam. Other specimens used steel plates as shear reinforcements with an equivalent area of the regular ties of the reference beam. Four thicknesses of plates were used, 1mm 2mm, 3mm, and 4mm. The experimental results showed a good agreement in term of the ultimate load within the range of 99.86 – 113.33 % of the ultimate load of the reference beam. The steel strips work as a regular tie to control the cracks (number and width). The analytical result showed that there is a good agreement between the numerical results and the experimental results in the term. The research conducted by Chai et al. [12] investigates an innovative shear reinforcing technique employing slender mild steel plates in deep beams, revealing that 2.0 mm-thick TMS (Thin Mild Steel plates) enhanced load-carrying capacity by 2.9.

Wang et al. [13] discovered specimens with interval holes in the web of concrete-encased steel sections demonstrated improved ultimate shear resistance and shear stiffness, due to the composite interaction between the I-section and the concrete. Consequently, these tests illustrate that adequate bonding between embedded steel sections in concrete beams is crucial, and this bonding can be attained through the placement of shear studs or the incorporation of perforated holes in the webs of steel sections. Previous studies and research have exhibited the capability of using plates to improve shear resistance, either by externally fixing them with bolts or epoxy, or by internally immersing them. These results yielded promising results, with some reservations regarding the weak bond between the outer plates and the concrete. To the authors knowledge, rare studies were conducted to study the effect of perforated internal embedded plates considering surface roughness on the shear strength of concrete beams. In this study, to further investigate the shear strength of concrete beams containing embedded steel plates, six beam specimens were manufactured using three parameters: plate location (mid, edge), plate surface texture (smooth, rough) and type of plate (solid with no holes, with holes). The steel plate holes were circular, 40

mm in diameter, and spaced 15 mm apart. The steel plate was embedded longitudinally and secured with 8 mm diameter steel stirrups.

For a 25 MPa cubic compressive strength target, the concrete mixture was designed with proportions of (1:2.22:3.23) and a water-to-cement ratio (w/c) of (0.37). After completing the curing period, all beams were cleaned and painted white to ensure clear visibility of cracks and their propagation during the test. The beams with a span of 1200 mm were tested under a four-point loading scheme over a clear span of 1000 mm using a testing machine with a capacity of 400 kN. The distance between the points of loading was 300 mm. The load was applied to the simply supported beam by a loading rate of 1 kN/min. to ensure accurate observation of crack initiation and progressive failure mechanisms. This was measured using a load cell with a capacity of 400 kN. The deflection at the center was measured by a digital dial gauge (LVDT) with a capacity of 50 mm and an accuracy of 0.01mm, placed under the mid-span point.

Regarding the effect of perforations on potential plate corrosion during loading, stress concentrations may form around the perimeter of the holes, promoting micro-cracks in the concrete. These cracks can then become pathways for moisture and harmful steel (such as chlorides in marine environments), increasing the risk of corrosion behind and around the steel plate.

2. Materials and Methods

2.1 Mix Design and Procedure

For a 25 MPa cubic compressive strength target, the concrete mixture was designed with proportions of (1:2.22:3.23) and water to cement ratio (w/c) of (0.37), as shown in Table 1. Moreover, the slump value was 59 mm; all specimens were cured for 28 days in the same situation.

Table 1. Proportions of concrete mixture

Materials	Mix proportions
Cement (kg/m^3)	325
Fine aggregate (kg/m^3)	720
Coarse aggregate (kg/m^3)	1050
Water (L/m^3)	120
Superplasticizer	-------

The chemical and physical tests of cement are listed in Table 2 and Table 3, Table 4 Classification of Coarse Aggregate and Table 5 Classification of Fine Aggregate

Table 2. Physical properties of the cement

Physical properties	Test Results	Limits of ASTM C150/C150M
Initial setting time, min	188.5 min.	≥45 min
Final setting time, min	220.5 min.	≤ 375 min.
Compressive strength in MPa @ 3 days	12.8 Mpa	≥8 (minimum)
Compressive strength in MPa @ 7 days	17 Mpa	≥15 (minimum)

Table 3. Chemical composition of the cement

Compound	% By Weight	Limit of Iraqi Specifications No. 472 for the year 1993
CaO	60.05	-----
SiO2	21.3	------
Al2O3	3.99	------
Fe2O3	4.27	------
MgO	4.155	<5

Compound	% By Weight	Limit of Iraqi Specifications No. 472 for the year 1993
SO3	2.1	<3.5
Limestone saturation factor	0.85	0.66-1.02
C3A	3.3	------
Insoluble Residue I.R	1.13	<1.5
Loss on Ignition L.O.I.	3.16	<4.0

Table 4. Classification of coarse aggregate

Sieve size (mm)	% Passing by weight	Limits of Iraqi specification No. 45/1984
20	98.5	95-100
10	48	30-60
5	7.5	0-10

Table 5. Classification of fine aggregate

Sieve size (mm)	% Passing by weight	Limits of Iraqi specifications No.45/1984 Zone 2
4.75	97.5	90-100
2.36	90	75-100
1.18	80	55-90
0.6	57	35-59
0.3	25	8-30
0.15	8.3	0-10
75 microns	1.3	No more than 5%

2.2 Specimen Description

Six reinforced concrete specimens (B0, BT2, BR-10%, BM, BE, and BHC-10%) were prepared. The specimens had a span length of 1200×120 mm in width× 200 mm in depth. Longitudinal reinforcement bars of 2T10 and 4T16 were affixed at the upper and lower extremities of the specimens, respectively. (Fig. 1) shows the reinforcement details of the tested specimens. Minimum shear reinforcement of T8 was added at 400 mm intervals, as illustrated in (Fig. 1a). Tensile tests were conducted on all steel bars, as shown in Table 2 ((Reinforcing steel is manufactured through basic stages that begin with extracting iron ore from mines and converting it into molten steel. This steel is then poured into continuous molds to be cooled and subsequently shaped by rolling to become bars of specific diameters and lengths)).

Table 6. Characteristics of steel reinforcing bars

Type of steel	Diameter (mm)	Yield stress (MPa)	Average ultimate stress (MPa)	Average Elongation (%)
Grade 60	8	657	686.1	15
Grade 60	10	618	634	12
Grade 60	16	612	700	15.9
ASTM 615 limits		Not less than 420	Not less than 620	Not less than 9%

Shear plates were installed on either side of the specimen within the shear span, as depicted in (Fig. 1 (b, c, d, e, f)). Tests' specimens involving embedded plates in concrete were classified into three series: plate location (mid-region, near edge), surface texture (smooth, rough), and presence of

holes (solid, with holes). This classification helps in comparing structural performance outcomes across different configurations. Thickness and hole percentage parameters were selected according to continuing research. The tensile strength test results for steel bars and steel plates are presented in Tables 6 and 7, respectively. Holes with a 40 mm diameter were implemented to permit the passage of fresh concrete through the plates, hence facilitating adhesion between the concrete matrix and the plates. Additionally, this investigation employed two plate thicknesses: 1.0 mm and 2.0 mm.

Table 7. Yield strength, maximum tensile strength, and elongation of steel plates

Thickness of tested steel plate (mm)	Average of yield tensile strength (MPa)	Average of ultimate tensile strength (MPa)	% Elongation at ultimate stress
2	290	375	20.5
1	300	380	19

Table 8. Designated names of specimens

Designated name	Plate thickness, mm	Plate surface	Location of the plate	Holes, %
B0	---------	---------	---------	----------
BT2	2.0	Smooth	Mid	0
BE	1.0	Smooth	Edge	0
BHC-10%	2.0	Smooth	Mid	10
BM	2.0	Rough	Mid	0
BR -10%	2.0	Rough	Mid	10

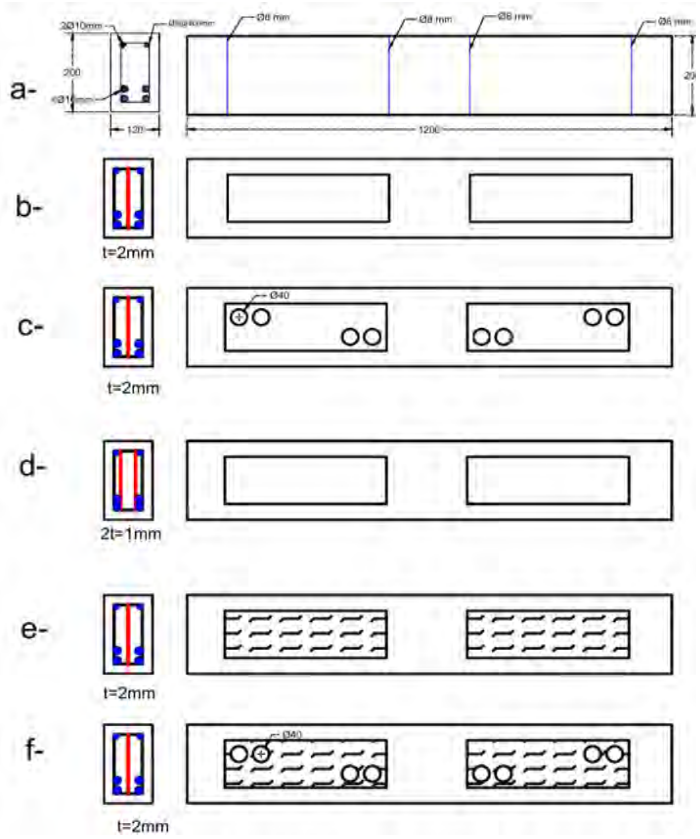

Fig. 1. Reinforcement detailing of samples. (a) sample B0; (b) sample BT); (c) sample BHC-10%; (d) sample BE; (e) sample BM; (f) sample BR-10%

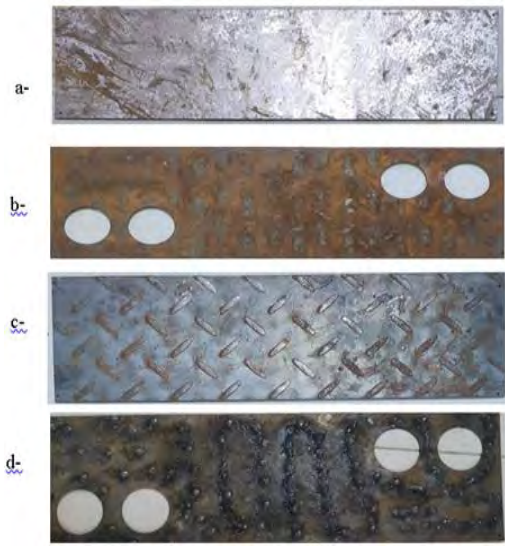

Fig. 2. Configuration of plates. (a) Smooth sold plate, (b) Smooth plate with holes, (c) Rough sold plate, (d) Rough plate with holes

(Fig. 2) illustrates the specific arrangement of the plates for each series. Table 8 presents the assigned nomenclature for all specimens. Three concrete cubes were cast, and from the mean value of the three specimens, the 28-day concrete compressive strength was 26.4 MPa. A concrete cylinder was cast, and the splitting tensile strength was 4.13 MPa.

2.3 Testing configuration

This study employed a four-point loading test. A testing apparatus with a capacity of 400 kN was employed to evaluate the performance of the six specimens. The specimens were subjected to monotonous loading under load control. The inter-plate spacing was established at 300 mm All specimens were supported by two bearing plates at the reaction base, with a clear span of 1000 mm. A single linear variable differential transducer (LVDT) was positioned at the specimen's base to quantify vertical displacement during testing, as illustrated in (Fig. 3).

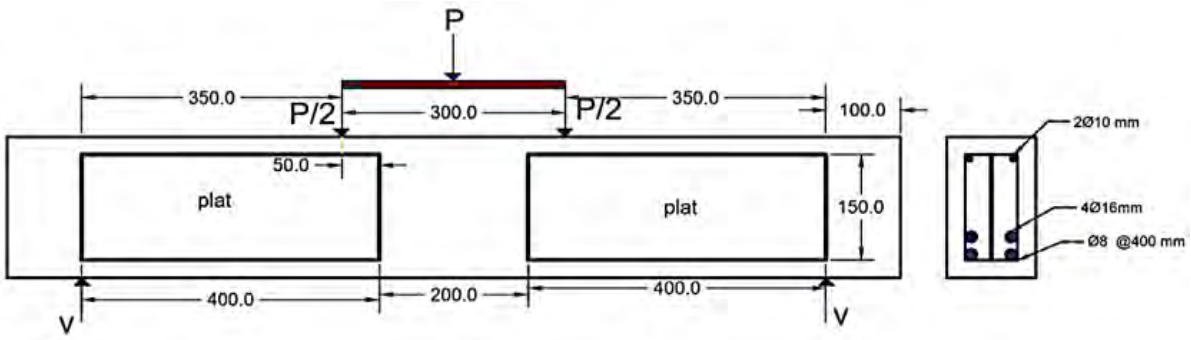

Fig. 3. Details of the test setup

3. Experimental Results and Discussion

The experimental results of the analyzed specimens are evaluated for their load-bearing capacity, load-displacement behavior, cracking patterns, and failure modes. Comparisons are made between reference specimen B0 and specimens incorporating steel plates.

3.1 Load-Bearing Capacity

Table 9 and Fig. 4 show the failure loads of the tested samples. The maximum load capacity of the reference specimen B0 is 57 kN. It is emphasized in a red bar. In (Fig. 4). Additionally, the Percentage of difference between the reference beam and the beams containing steel plates is presented in Table 10.

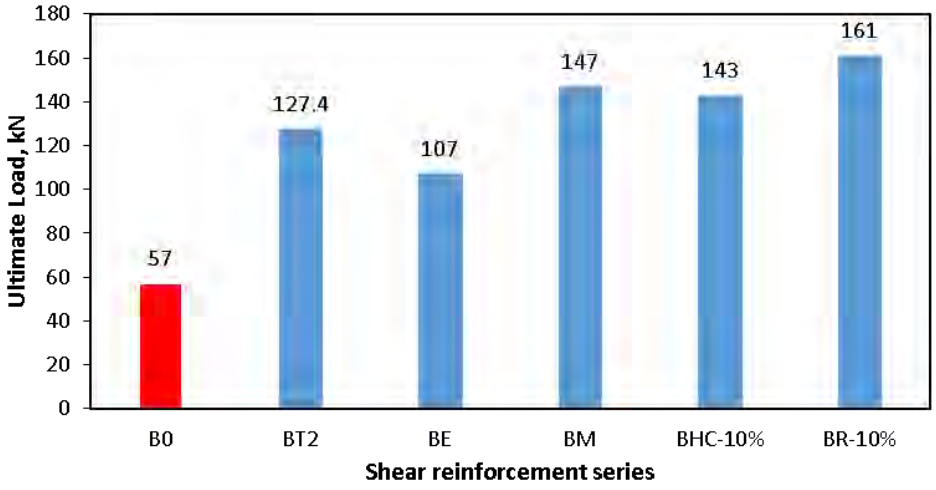

Fig. 4. Ultimate load for each specimen

Table 9. Experimental findings on ultimate load and deflection

Samples	Max. load (kN)	Comparison with sample B0 (%)	Deflection at Mid-Span under Max. Load (mm)
B0	57	-------	5.6
BT2	127.4	123.5	6.8
BE	107	87.7	6
BM	147	157.9	8
BHC-10%	143	150.8	5.28
BR-10%	161	182.4	8

- Effect of The Location of The Plate:

Table 9 clearly highlighted that specimen (BT2), which involves a steel plate of 2 mm in thickness, demonstrated an increase of 123.5% compared to the reference specimen (B0). It is important to note that when two plates replaced the middle plate (BT2) with equivalent thickness (BE), the shear strength decreased by 36%. This behavior resulted from the isolation effect that was caused by the placement of the plate, which separated the concrete core from the outer margins [14]. As a result, each component started to behave independently from the other component, which led to a reduction in overall strength. However, in comparison to specimen (B0), specimen (BE), which has two plates at the edge of the specimen's cross-section, exhibited an increase of 87.7% in shear strength.

- Effect of The Surface Texture of The Plate

A rough surface plate with a thickness of two millimeters was located at the middle of the specimen BM. The load carrying capacity was found to be 157.9% higher than that of the reference specimen B0. Similarly, specimen BT2, which involves a plate of entirely smooth surface with a comparable thickness of two millimeters, shows a 123.5% enhancement in shear strength compared with reference specimen B0. While both specimens exhibited significant improvement in the load carrying capacity, a 15.9% increase was observed for the specimen reinforced with a rough steel plate. This result proves the hypothesis that bond strength notably improves the load capacity. Because of the rough surface of the plate [15]. The connection between the concrete and the plate was improved, and the sliding between them was minimized [16].

- Effect of The Holes in The Plate

Specimen BHC-10% contains a two mm-thick vertical plate at the middle of the section with holes that comprise 10% of the total plate area. The findings demonstrated that the load-bearing capacity exceeds that of specimen B0 by 150.8%, which reflects the contribution of the adhesion between the concrete and the plate to the shear strength. Likewise, specimen BR-10%, which is similar in reinforcement but contains a plate with a rough surface, demonstrated a significant increase in shear strength by 182.4% compared with specimen B0. This means that the specimen with the rough plate exceeds that of the specimen with the smooth plate by 12.5%. This is due to the presence of protrusions on the surface of the rough plate, which enhances the adhesion between the concrete and the plate, reduces slippage, and thus increases the structural load capacity [17]. Moreover, the perforations in the plate enhance the adhesion between the concrete and the plate, allowing the concrete to flow and form bonding pins. Furthermore, the holes in the plate reduce its weight, thus reducing the dead load on the specimens [18]

3.2 Load-Displacement Behavior

The load-displacement behavior of tested specimens is shown in (Fig. 5) and summarized in the following sections.

- Effect of The Location of The Plate

By observing the load-displacement curves in (Fig. 6) for samples BT2 and BE, it is noted that they exhibited a higher stiffness curve than the reference sample (B0), indicating the significant effect of the embedded steel plates on the load-displacement behavior. Comparing the curve shapes of the two samples (BT2 and BE), it is observed that sample BT2 showed higher stiffness than sample

BE. This is attributed to the plate's position in the middle of the section, which enhanced stiffness, unlike the end sample, where the plate was located at the edges, isolating the concrete core from the cover and reducing stiffness [19].

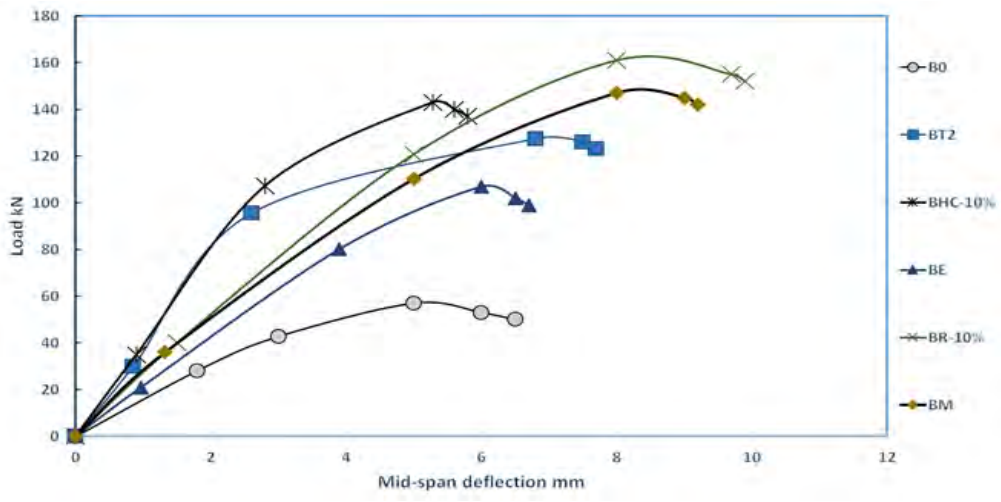

Fig. 5. Load against mid-span deflection graph for B0, BE, BT2,BHC-10%,BR-10%and BM

- Effect of The Surface Texture of The Plate

The displacement curve diagram for sample (BM) shows that it is more flexible than sample (BT2), which has a smooth plate. This increased flexibility can be attributed to the presence of grooves on the outer surface of the plate, which reduce the overall stiffness of the specimen and allow for larger deformations under the same applied load. These differences in behavior are clearly illustrated in the load-deflection diagram presented in (Fig.7), highlighting the influence of plate modifications on the overall structural flexibility of the beams [20].

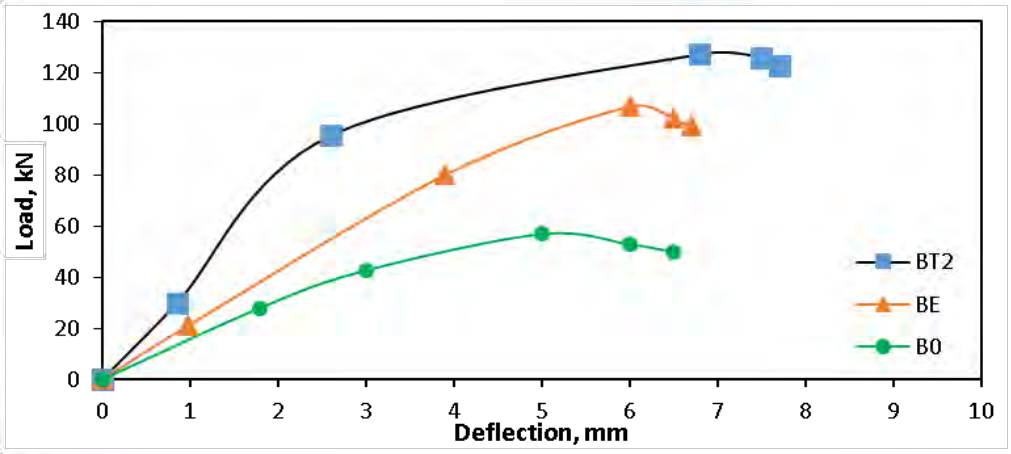

Fig. 6. Load against mid-span deflection graph for B0, BE, and BT2

- Effect of The Holes in The Plate

When comparing the load-deflection curve results for samples containing an embedded perforated plate with the reference specimen (B0), it has been observed that the former recorded a higher curve. This indicates a higher stiffness of the sample's structure, which results from the presence of the plate in the cross-section that postpones the onset of shear cracking's[21] .The results also show that the specimen containing a rough-surfaced plate (BR-10%) had a higher curve than the sample containing a smooth-surfaced plate (BHC-10%). This demonstrates that the surface grooves of the plate played a significant role in giving the sample high hardness [22] as shown in (Fig.8).

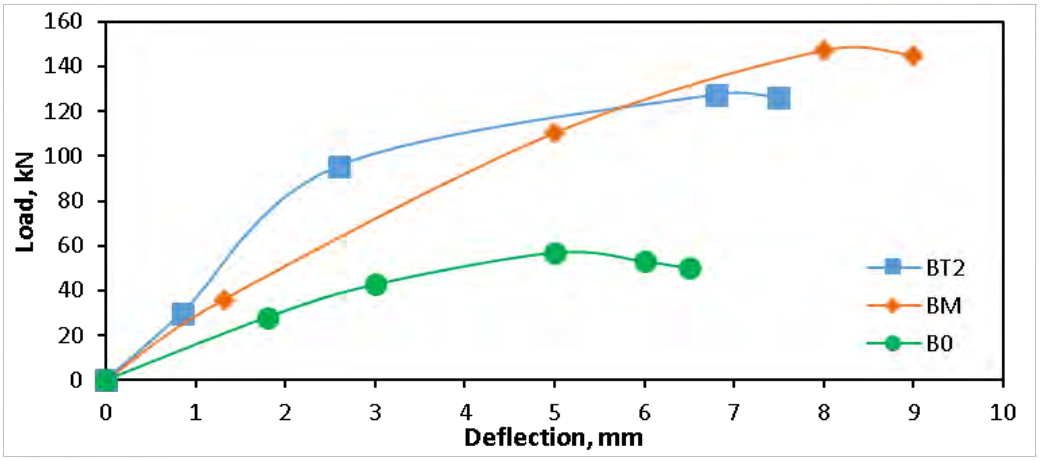

Fig. 7. Load against mid-span deflection graph for B0, BT2, and BM

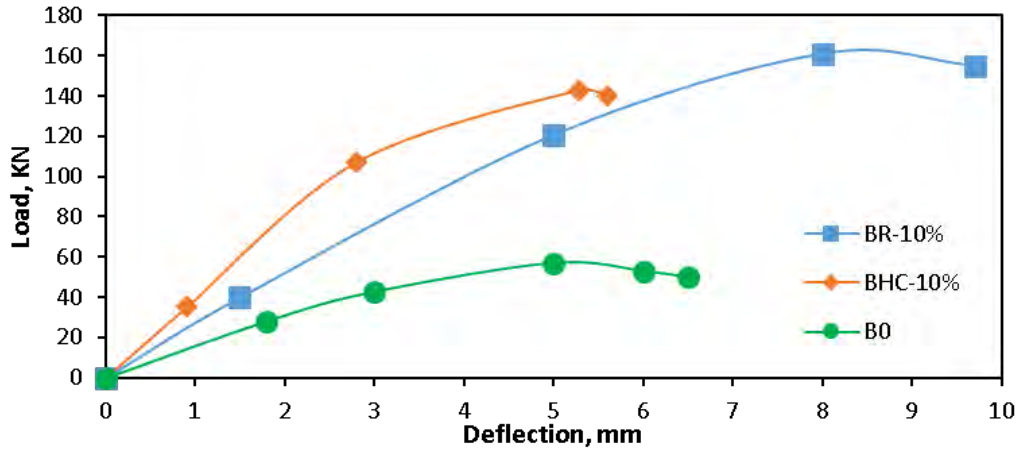

Fig. 8. Load versus mid-span displacement curve for B0, BHC-10%, and BR-10%

3.3 Fracture Pattern and Failure Mechanism

The fracture pattern and failure mechanism can be divided into three main categories.

- Impact of The Plate's Location

Fig. 9 depicts the crack pattern and mode of failure of specimens B0, BT2, and BE, respectively. It shows that all specimens exhibited the same failure mode, where the diagonal shear crack begins from the support and progresses to the applied load. Specimens B0, BE, and BT2 recorded initial crack loads shown in Table 10 below. The cracks of specimen BT2 were smaller, fewer in number, and had smaller crack widths compared to specimen BE, which had more numerous cracks and larger crack widths. This was due to the plate being located at the edge of the cross-section rather than in the middle [23], as in specimen BT2. This isolated the concrete core from the cover, negatively impacting the failure mode in terms of the number of cracks and their width.

Table 10. First crack load for B0, BE and BT2

Specimens	First crack load(kN)
B0	28.12
BE	21
BT2	30

- Effect of The Surface Texture of The Plate

Specimens BT2 and BM containing non-perforated plates exhibited the same shear failure behavior and crack pattern. Compared to the reference specimen B0, cracks in specimen BM, which contained a rough-surfaced plate, were more pronounced and numerous than in specimen BT2,

which had a smooth surface. The three specimen's recorded initial failure loads listed in Table 11 and the shapes and paths of the cracks are illustrated in the figure. (Fig.10).

Table 11. First crack load for B0, BT2 and BM

Specimens	First crack load(kN)
B0	28.12
BT2	30
BM	36

- Effect of The Holes in The Plate

As shown in Fig.11, all specimens (B0, BHC-10%, and BR-10%) exhibited the same cracking and failure pattern, namely diagonal shear failure. However, specimen (BR-10%), which contained an embedded plate with a rough surface and containing holes, had large and clear cracks and recorded an initial crack load of 40 kN. As for the sample (BHC-10%), which included an embedded plate with a smooth surface and containing holes, the cracks were smaller, the number of cracks was lower, and an initial crack load of 35 kN was recorded.

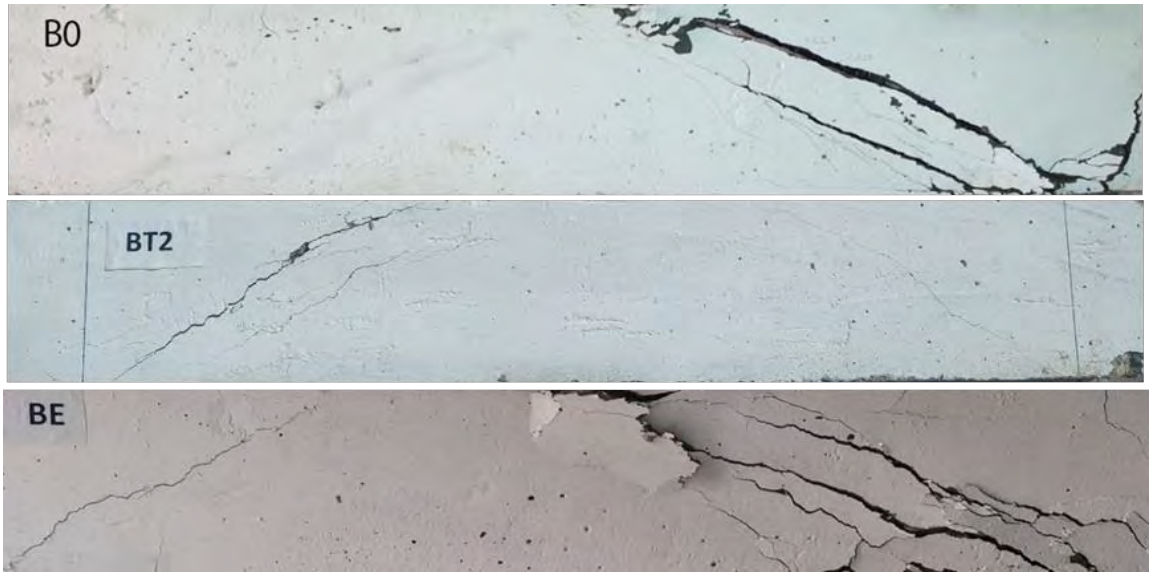

Fig. 9. Crack development of specimens B0, BT2, and BE

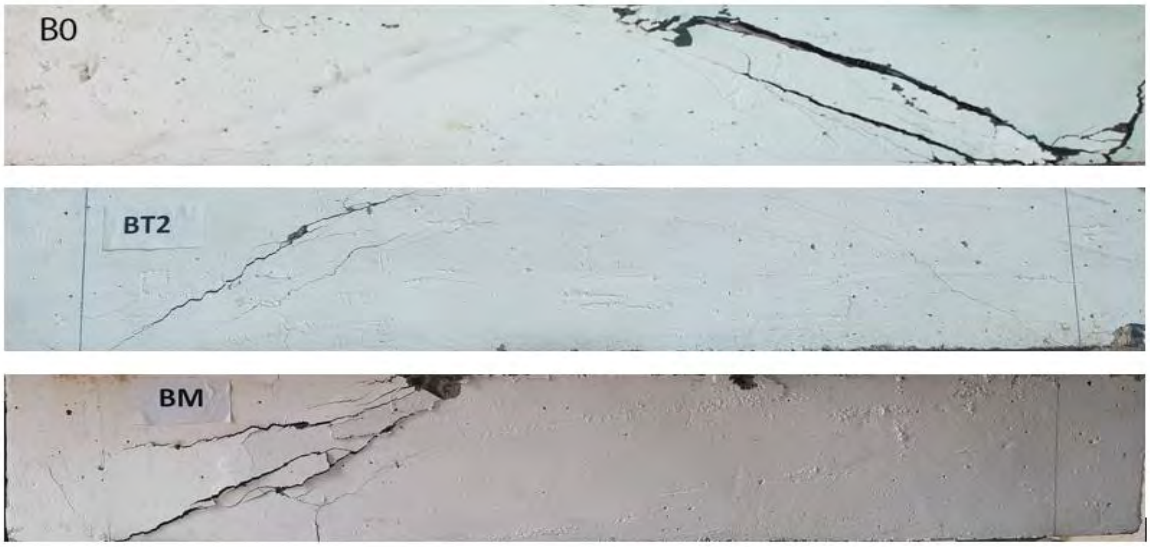

Fig. 10. Crack development of specimens B0, BT2, and BM

Fig. 11. Crack development of specimens B0, BHC-10%, and BR-10%

4. Conclusions

This study experimentally examined the strength of beams utilizing plates as shear reinforcement in place of traditional shear stirrups. The impacts of three distinct detail designs on the plates were investigated: (a) the location of the plates, (b) the surface roughness of the unperforated plate, and (c) the surface roughness of the perforated plate. Six beam samples were manufactured, including one reference specimen (specimen B0) with slight shear reinforcement. A four-point load test was conducted on each specimen experimentally. Based on the results, the following were determined:

- Adding steel plates to concrete beams as an alternative to conventional shear steel achieves excellent results in resisting shear forces. Specimen BT2 showed a 123.5% augmentation of maximum load capacity in relation to the reference specimen B0. Furthermore, the specimens exhibited high stiffness in the load-displacement curve.
- Using a centrally embedded plate is significantly better than placing it at the edges in terms of sample load-bearing capacity and stiffness. Specimen BT2, which has a central plate, demonstrated a 19% enhancement in load-bearing capability relative to Specimen BE, which has two edge plates,
- Adding perforations to the plates improves their load-bearing capacity compared to the reference and solid samples. The perforations in the plates facilitate the flow of concrete, promoting the development of concrete cavities and increasing the adherence of the perforated plates with concrete. Specimen BHC-10% showed a 150.8% increase in strength compared to Specimen B0. Compared to Specimen BT2, which did not contain perforations, Specimen BHC-10% recorded a 12.2% increase. The addition of perforations also enhances the strength of the sample.
- It is preferable to use a steel plate with a rough surface over a smooth plate, as the rough surface enhances adhesion between the concrete and the plate, leading to increased load-carrying capacity and efficiency pertaining to the structural components. This is evident in the increased load-bearing capability of Specimen BM compared to Specimen BT2, which increased by 15.3%.
- The combination of the surface roughness factor of the plate with the presence of openings and the position of the plate in the middle gave excellent results in the efficacy of the structural element regarding load-bearing capability, stiffness, failure mode, and first crack load. This is observed in the sample BR-10%, as it gave the highest load-bearing strength compared to all samples by 161 kN and was the best among the samples in stiffness, strength, and first crack load.

- Embedded steel plates provide an effective method to enhance the shear capacity and seismic resilience of reinforced concrete structures. Their incorporation might mitigate prevalent problems linked to external reinforcement techniques, including debonding and exposure.
- It is recommended to conduct a full-scale test to investigate the shear behavior of concrete beams. Moreover, fatigue behavior is another important aspect to consider as the next step of research.

References

[1] Zhang JP. Diagonal cracking and shear strength of reinforced concrete beams. Mag Concr Res. 1997;49(178):55-65. https://doi.org/10.1680/macr.1997.49.178.55

[2] Elmessalami N, El Refai A, Abed F. Fiber-reinforced polymers bars for compression reinforcement: A promising alternative to steel bars. Constr Build Mater. 2019;209:725-37. https://doi.org/10.1016/j.conbuildmat.2019.03.105

[3] Liu X, Lu ZD, Li LZ. The use of bolted side plates for shear strengthening of RC beams: A review. Sustainability. 2018;10(12):4658. https://doi.org/10.3390/su10124658

[4] Alam MA, Bakkar SA, Onik SA, Mustapha KN. Embedded connector in severe optimization of steel plate for shear strengthening of RC beam: experimental and numerical investigations. Adv Civ Eng. 2018;2018(1):4721431. https://doi.org/10.1155/2018/4721431

[5] Fahad JJ, Abbas F, Sultan WH. Strengthening of reinforced concrete wide beams using steel plates within shear zone. Int J Civ Eng Technol. 2018;9(12):890-900.

[6] Adhikary BB, Mutsuyoshi H. Shear strengthening of RC beams with web-bonded continuous steel plates. Constr Build Mater. 2006;20(5):296-307. https://doi.org/10.1016/j.conbuildmat.2005.01.026

[7] Sudarsana IK, Sajana IPC, Suputra IGNO. Applications of bolted steel plates to shear strengthening of RC beams. In: MATEC Web of Conferences. EDP Sciences; 2019. p. 01002. https://doi.org/10.1051/matecconf/201927601002

[8] Osman BH, Wu E, Bohai J, Abdallah M. Repair technique of pre-cracked reinforced concrete (RC) beams with transverse openings strengthened with steel plate under sustained load. J Adhes Sci Technol. 2017;31(21):2360-79. https://doi.org/10.1080/01694243.2017.1301073

[9] Arslan G, Sevuk F, Ekiz I. Steel plate contribution to load-carrying capacity of retrofitted RC beams. Constr Build Mater. 2008;22(3):143-53. https://doi.org/10.1016/j.conbuildmat.2006.10.009

[10] Ibrahim AM, Salman WD, Ahmed QW. Effect of steel plates on shear strength of wide reinforced concrete beams. 2015.

[11] Ammash HK. Behavior of reinforcement concrete beams using steel strips as a shear reinforcements [Internet]. 2017. Available from: http://www.ripublication.com

[12] Chai KF, Woon KS, Wong JK, Lim JH, Lee FW, Lee YL. Experimental and numerical study of the strength performance of deep beams with perforated thin mild steel plates as shear reinforcement. Appl Sci. 2023;13(14):8217. https://doi.org/10.3390/app13148217

[13] Wang X, Liu Y, Lu Y, Li X. Shear transfer mechanism of perforated web connection for concrete encased steel structures. Eng Struct. 2022;252:113418. https://doi.org/10.1016/j.engstruct.2021.113418

[14] Zhang D, Ueda T, Furuuchi H. Concrete cover separation failure of overlay-strengthened reinforced concrete beams. Constr Build Mater. 2012;26(1):735-45. https://doi.org/10.1016/j.conbuildmat.2011.06.082

[15] He XX, Li GC, Yang ZJ. Experimental study of the bearing capacity of long-span profiled steel sheet-concrete composite slabs. Adv Steel Constr. 2019;15(3):288-96.

[16] Mansour FR, Bakar SA, Vafaei M, Alih SC. Effect of substrate surface roughness on the flexural performance of concrete slabs strengthened with a steel-fiber-reinforced concrete layer. PCI J. 2017. https://doi.org/10.15554/pcij62.1-02

[17] Van Dam JPB, Abrahami ST, Yilmaz A, Gonzalez-Garcia Y, Terryn H, Mol JMC. Effect of surface roughness and chemistry on the adhesion and durability of a steel-epoxy adhesive interface. Int J Adhes Adhes. 2020;96:102450. https://doi.org/10.1016/j.ijadhadh.2019.102450

[18] Wang Z, Wei Y, Li N, Zhao K, Ding M. Flexural behavior of bamboo-concrete composite beams with perforated steel plate connections. J Wood Sci. 2020;66(1). https://doi.org/10.1186/s10086-020-1854-9

[19] Benli S, Aksoy S, Havıtcıoğlu H, Kucuk M. Evaluation of bone plate with low-stiffness material in terms of stress distribution. J Biomech. 2008;41(15):3229-35. https://doi.org/10.1016/j.jbiomech.2008.08.003

[20] Lachut MJ, Sader JE. Effect of surface stress on the stiffness of thin elastic plates and beams. Phys Rev B. 2012;85(8):085440. https://doi.org/10.1103/PhysRevB.85.085440

[21] Wald F, Sokol Z, Moal M, Mazura V, Muzeau JP. Stiffness of cover plate connections with slotted holes. J Constr Steel Res. 2004;60(3-5):621-34. https://doi.org/10.1016/S0143-974X(03)00133-0

[22] Ohu RB. Flexural response of reinforced concrete beams with embedded CFRP plates [Dissertation/Thesis]. Seri Kembangan: Universiti Putra Malaysia; 2012.
[23] Zakaria M, Ueda T, Wu Z, Meng L. Experimental investigation on shear cracking behavior in reinforced concrete beams with shear reinforcement. J Adv Concr Technol. 2009;7(1):79-96. https://doi.org/10.3151/jact.7.79

Blank Page

Research on Engineering Structures & Materials
www.jresm.org

Research Article

The eco-concrete revolution: Manufacturing a sustainable high-performance rigid pavement with innovative materials

Tamara Hussein Bani Ata [*,a], Asma Thamir Ibraheem [b]

Department of Civil Engineering, Al-Nahrain University, Baghdad, Iraq

Article Info

Article History:

Received: 11 Oct 2025

Accepted: 20 Nov 2025

Keywords:

CRCP;
Durability;
Environmental impact Assessment;
OpenLCA;
Supplementary cementitious materials;
Sustainability

Abstract

Real-life strategies are applied to assess pavement functionality, high-quality performance, and durability throughout its service life. This study evaluates the sustainable rigid pavement construction using Jordanian natural zeolite (JNZ), silica fume (SF), porcelain tile waste (PTW), and spent coffee grounds (SCG) as supplementary materials. This novel technique is an original contribution to the emerging research on the long-term, durable, sustainable, and performance-based characteristics of pavements under the constraints of structural soundness. The research focused on the incorporation of sustainable building materials, specifically Jordanian Natural Zeolite in concrete structures. Further, the study described both the properties of concrete and cement savings from replacing JNZ in OPC and SRC clinkers. Furthermore, the research also compared the normal concrete with JNZ-enhanced concrete as an SCM with different proportions of cement replacement. Replacing 10% of the cement in the concrete mix increases permeability and durability. Moreover, the eco-friendly concrete is produced by using 25% of the PTW as a coarse aggregate replacement. It enhanced the workability, permeability, and mechanical characteristics of the sustainable concrete mixture. Research study also utilized spent coffee grounds (SCG) to produce sustainable CRCP structural concrete, burned at 350°C and 800°C to pyrolyze their organic compounds. It was also concluded that the 15 % SCG at 350ºC concrete mix offered the best workability, permeability, sulfate resistance, mechanical properties, and impact on the natural environment. The EIA and chemical assessments also highlighted how constructing sustainable CRCP structures improved performance, saved material resources, and reduced the carbon footprint compared to earlier mixes.

© 2026 MIM Research Group. All rights reserved.

1. Introduction

Environmental impacts from the construction industry are facing numerous challenges while the call for infrastructure continues to grow as a world population, thus durable, resilient, and robust infrastructure systems are increasingly desirable. Continuous reinforced concrete pavement (CRCP) is a kind of rigid pavement that contains continuous steel reinforcement to perform a single-structure that can evenly distribute loads over it. Durable rigid pavement assessment and the decision-making for their maintenance are critical issues in civil engineering, mainly when traffic volumes increase with loss of behavior and maintenance costs. Carbon emissions resulting from the manufacture of Ordinary Portland Cement (OPC) in the conventional concrete mix get certainly through the heating of limestone, and the CO_2 emitted as part of the chemical process of making lime [1]. These points are determined from the performance assessment methods and rehabilitation techniques disciplines, leading to insufficient use of resources and unsustainable applications of pavement performance.

*Corresponding author: tamara.pciv22@ced.nahrainuniv.edu.iq
[a]orcid.org/0009-0000-5499-060X; [b]orcid.org//0000-0002-0104-7949
DOI: http://dx.doi.org/10.17515/resm2025-1239ic1110rs

There is a scientific focus on sustainable structure and the use of alternative materials in the production of supplemental cementitious materials (SCMs). This study tends to avoid this issue by determining the performance of continuously reinforced concrete pavement (CRCP) using supplemental materials and balancing the sustainability goal and structural performance application. Jordanian natural zeolite (JNZ) as a volcanic mineral pozzolanic properties material has an attracted importance for its effort to improve the characteristics, durability, and concrete strengths through its hydration reaction with water and calcium hydroxide. It applies as a suitable replacement material for cement due to its nature with sustainable construction aims [2,3]. Performing JNZ in CRCP implements new eco-friendly pavement construction by reducing carbon emissions and preserving resources in a sustainable infrastructure development. This effect of JNZ on CRCP performance haven't researched extensively yet.

A by-product silica fume (SF) with small particle size and high reactivity from silicon and ferrosilicon, is another supplementary cementitious material studied for its potential to improve concrete performance and sustainability, thereby enhancing concrete's mechanical properties including strength and durability. The individual use of natural zeolite and SF proof the potential to increase concrete mechanical properties and sustainability performance [4]. Various studies and applications are being implemented to construct sustainable concrete with reliable durable behavior by several materials' replacement technique. However, there is a leak in comprehensive effects of porcelain waste on mechanical characteristics and sustainability of concrete.

There is also no comprehensive study on integrated sustainability evaluation that considers environmental effects and resource conservation throughout the concrete's lifecycle. Spent coffee grounds (SCG), a byproduct of the coffee brewing process, represent a substantial source of organic waste that has significantly contributed to landfill accumulation due to global consumption for many years, the resultant production of methane gas, and increasing climate change. So, transforming SCG into valuable resources can produce innovations in the concrete world, mitigate landfill accumulation, reduce methane emissions, and contribute to a more sustainable future.

Several experiments were performed to identify a durable and sustainable rigid pavement structure that can be utilized as infrastructure. Plati studied different sustainable pavements, including design, materials, and preservation practices, and several viable alternatives displayed mechanical properties and the sustainability of paving materials. This study also showed, whatever method improvement on sustainable pavement performance would work [5]. Tran et al (2019) studied the effects of natural zeolite in a concrete pavement mix, and the basic structural properties of manufactured natural zeolite in concrete must be used as a pozzolan and natural zeolite structural properties. Finally, they were able to comprehend the impacts of zeolite on concrete permeability, durability, and workability. The outcome indicated that mechanical characteristics and structure durability improved with optimal mixing performance [2]. Moreover, Waghmare and Ghadvir researched the features of zeolite material and its role in rigid pavement on improving concrete's resistance to CO2 during production. They demonstrated that the addition of zeolite into concrete-tested rigid pavement reduced the impacts of carbon dioxide and decreased environmental variability, under mainly heavy traffic load conditions [3].

Yudi et al. researched the physical, chemical, and mechanical properties of SF, in addition to its microstructure impacts on concrete, which were all dependent on flexural, tensile, and compressive strength tests and the amount of concentrate in the mixture. It was noticed that high-performance, high-strength concrete was developed using silica fume, a by-product of silicon alloy production [6,7]. Ata and Ibraheem examined the combined impact of JNZ and SF as supplementary cementitious materials (SCMs) on concrete mixtures. Several concrete mixes were developed, including a standard mix, one with natural zeolite, and another with both zeolite and silica fume, each with different amounts of cement replaced. They found that replacing 10% of the cement with zeolite increased durability compared to standard mixture. However, using both SF and zeolite together reduced the concrete's strength [8].

Research investigates the impacts of porcelain waste on compressive strength component of concrete and found that the partial substitution of cement with porcelain increased compressive strength resulting in more activity dependent on longer-term and reliable performance [9, 10]. Ata

and Ibraheem studied the effects of replacing waste, from porcelain tiles with CA on mechanical characteristics mainly compressive, tensile splitting, and flexural strengths, and permeability (water absorption). The findings showed that 25% porcelain replacement results in high permeability, workability and mechanical properties, and an environmental impact assessment that is highly positive [11]. Roychand et al.) studied the appropriateness of burning spent coffee grounds waste at different temperatures to enhance concrete mechanical properties. The results showed that concrete compressive strength raised by 29.3% with coffee biochar at 350ºC [12]. The study tends to evaluate sustainable developed concrete behavior by combining multiple supplementary materials and evaluating them through both mechanical and environmental impact (EIA/LCA) perspectives.

2. Materials and Methodology

This part shows the methodology and materials applied in this study to assess sustainability aspects of rigid pavement systems and to develop suitable decision-making strategies for their rehabilitation.

- Cement: Portland cement CEM I, which has certain compositional restrictions and high durability, is applied with both physical and chemical properties based on the ASTM C150 and Jordanian standards No. 30–2024 for concrete works.
- Coarse Aggregate: The study used coarse aggregates based on standards of Jordan and ASTM. A typical amount of CA was used, and the results of experimental testing are provided in Table 1.

Table 1. Coarse aggregate tests in study

Test	Result	Specifications
Absorption %	2.4	ASTM C127
Abrasion %	27	ASTM C131
B.S.G (Dry)	2.552	ASTM C127
B.S.G (SSD)	2.631	ASTM C127
Sulfate Content %	0.042	ASTM C33
Bulk Density kg/m3	1578	ASTM C29
Chloride Content %	0.019	ASTM C33
Soundness Loss (NaSO4) %	5.0	ASTM C88

- Fine Aggregate: A particle sizes less than 5 mm as a fine-grained is known as sand. It was used in concrete mixes according to ASTM C128 standards and specifications for aggregate grading. This study involved multiple tests resulting in 2.40 as a fineness modulus, 2.60 specific gravity, 1% an absorption rate, and a sand equivalent percentage of 76%.
- Jordanian Natural Zeolite (JNZ): Zeolite is a volcanic inorganic microporous mineral with a highly porous structure. There is a significant lack of JNZ use in cement and concrete manufacturing for infrastructure applications such as pavement. This study examines the characteristics of JNZ for the production of a sustainable, high-performance CRCP structure, including varying percentages of zeolite. Figure 1 shows the collection of JNZ compositions from a real site in northeastern Jordan. The Quality Directorate laboratory of the Ministry of Energy and Mineral Resources in Jordan verified JNZ characteristics via XRF analysis. Table 2 describes JNZ elements that influence the concrete mixing process, workability, and overall performance.

Table 2. XRF analysis of JNZ used in the study

SiO_2	Al_2O_3	Fe_2O_3	CaO	MgO	K_2O	Na_2O	SO_3	CL	LOI
39.7%	10.8%	12.89%	10.97%	9.23%	1.63%	1.39%	0.16%	0.035%	9%

Fig. 1. Field site source of JNZ used in the study

- Silica Fume (SF): Silica fume is high reactive pozzolan utilized in this study as a supplemental material, including a percentage of the cement weight in concrete, based on ASTM C1240 standards. Table 3 illustrates the physical and chemical specifications.

Table 3. Chemical and physical requirements of SF

Chemical Specifications	
SiO_2, min.%	85
Moisture content, max.%	3
Loss on ignition (LOI), max. %	6
Physical Specifications	
Percent retained on 45µm, max.%	10
Percent retained on 45µm, max.% variation from average, % points.	5
Accelerated pozzolanic activity index, With OPC at 7 days, min. % of control.	105
Specific surface, min. (m^2/g)	15

- Porcelain Tile (PT): Porcelain waste material is found particularly in Middle Eastern countries. Several Arab nations such as Jordan imports significant percentages of porcelain. This research used high-quality waste from Indian glazed porcelain tiles, which have a water absorption rate of no more than 0.05% and 2.1 g/cm^3 density. Maximum size of PT was 19 mm illustrated in Figure 2, whereas chemical ingredients were analyzed using XRF presented in Table 4.

Fig. 2. Porcelain applied in concrete mixture

- Spent Coffee Grounds (SCG): Spent coffee grounds (SCG), a byproduct of coffee brewing represents a substantial source of organic waste. In this study, XRF analysis was done in Nano-Lab at the Institute of Nanotechnology (JUST-Jordan) to get information on the SCG's mineral composition and chemical characteristics.

Table 4. Chemical elements of porcelain tile using XRF

Element	Abbreviations	Mass %
Alumina	(Al_2O_3)	8.65
Silica	(SiO_2)	38.91
Magnesia	(MgO)	0.530
Lime	(CaO)	6.711
Sodium Oxide	(Na_2O)	0.60
Potassium Oxide	(K_2O)	0.850
Calcium Carbonate	($CaCO_3$)	11.98

3. Production of Concrete Mixtures for CRCP Design

This section of work describes concrete mixtures and sample preparation procedures. Four different mixtures were designed: a conventional mixture with 100% Portland cement. The other new concrete mixes with SCMs as replacement components and were created using a 400 kg/m^3 concrete mix, which contained a specific proportion of weighted CA, FA and cement, combined in a dry condition with a designated water percentage, as shown in Figure 3. Table 5 shows concrete mix design for this study. Sustainably developed concrete mixes were formed in the preparation of 150 CRCP slab specimens with a uniform concrete design including SCMs. A systematic design of slab thickness, dimensions, and steel reinforcement was performed to evaluate structural integrity and resistance to failure of CRCP.

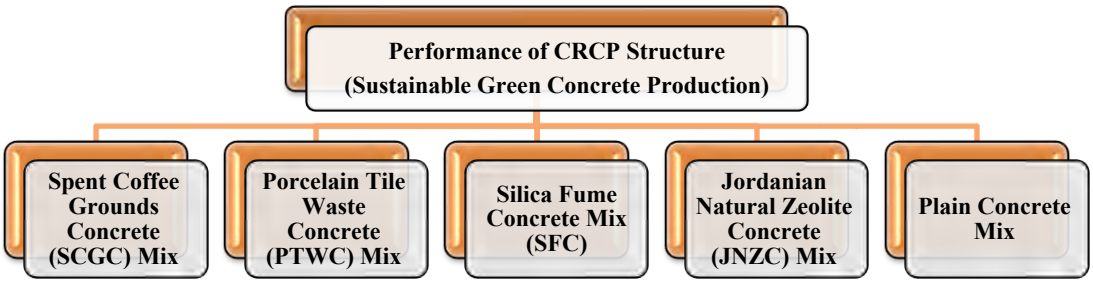

Fig. 3. Schematic flowchart of concrete production for CRCP in the study

Table 5. Conventional concrete mix design

	Content of Cement (kg/m^3)	CA (kg/m^3)	FA (kg/m^3)	w/c
Conventional Mixture	400	946	946	0.45

Casting Preparation

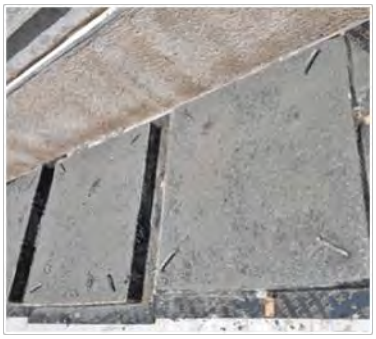

Normal RC Slabs

SCG - RC Slabs

Curing Specimen after Curing and Setup

Fig. 4. Sustainable continuously reinforced concrete pavement slabs

A portable plywood structure of 1×1×0.1 m was constructed based on a laboratory testing configuration featuring continuous longitudinal bars with a diameter of 10 mm and transverse bars positioned every 10 cm across the width. Then, standard and specially designed reinforced concrete slabs were cast with appropriate vibration and cured using water spraying and wet burlap to enhance hydration and strength development, as illustrated in Figure 4.

4. Concrete Testing Techniques of Sustainable CRCP

The key components of any specimens have been examined for concrete mixtures evaluation focusing mainly on the assessment of strengths after cast and curing processes at 7 and 28 days. This study conducted modified concrete tests for 50 samples for each test to evaluate the sustainable CRCP performance, as depicted in a schematic flowchart in Figure 5.

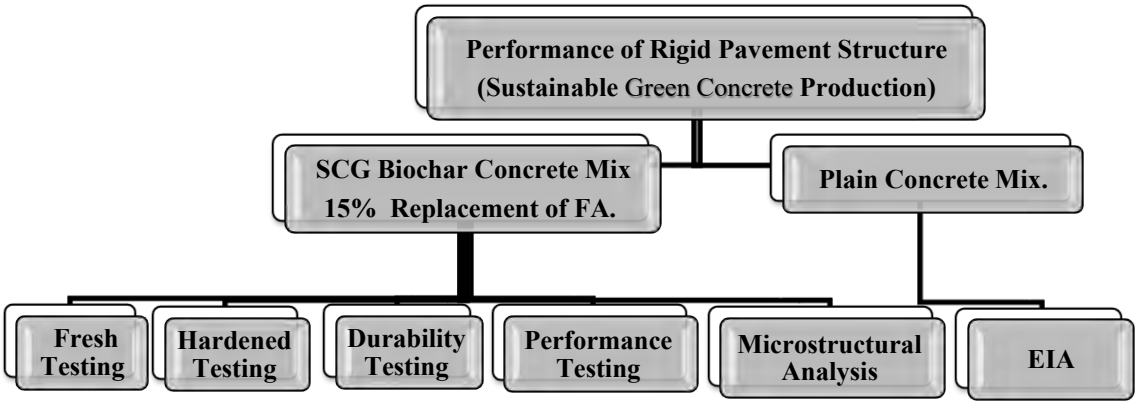

Fig. 5. Schematic flowchart of sustainable concrete key tests

4.1 Permeability Performance and Density

Compacted concrete weight used to determine concrete density by dividing the container's volume by the measured mass. Mixes permeability was measured using water absorption to measure durability factors [13]. The determination of mass increase from the initial mass forms an element of the absorption. It was measured over a 28-day of samples curing by averaging the absorption of specimens depend on ASTM C642. Specimens were dried at 100°C, weighed, immersed in water bath for 24 hours, then reweighed to determine the water absorption ratio.

4.2 Mechanical Concrete Strength Tests

Concrete specimens of standard and modified mixtures were cast into cube molds measuring 150×150×150 mm for usage in compressive strength tests [14]. A universal testing machine performed the test, applying a compression force 0.6 MPa/s. On the other hand, concrete specimens casting in standard cylindrical molds in 150 mm diameter and a length of 300 mm and

subsequently assessed for tensile strength based on ASTM C496. The third-point loading test evaluates the flexural strength of concrete by bending prisms of 100×100×500 mm until failure with ASTM C78 standards, as illustrated in Figure 6.

Fig. 6. Mechanical strengths tests of normal and modified-concrete mixes

4.3 JNZ, PTW, and SCG Development for Sustainable CRCP Future

JNZ, PTW, and SCG integration in Continuously Reinforced Concrete Pavements design and construction enhances a sustainable way to enhance the produced concrete mix strength and durability. A 450-kN cell load with a 10-m diameter was applied directly over pavement developed slab to distribute a uniform load across it. 2 mm/min displacement rate was applied to reduce the dynamic impacts due to unpredicted loadings with concrete modulus improvement. The strain was monitored until the slabs fractured, then the maximum failure load (P, kN) with the slab's cross-sectional area (A, mm^2) were used to calculate CRCP concrete slab compressive strength (fc) as shown in Figure 7.

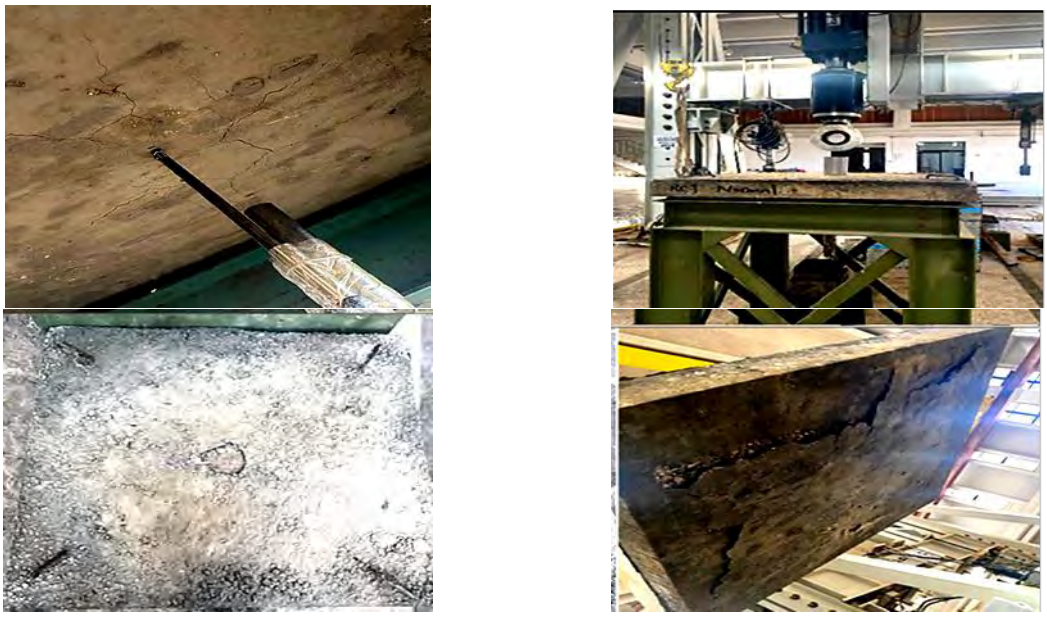

(a) Normal CRCP slabs with failure modes

(b) Modified CRCP slabs with failure modes

Fig. 7. Integrating SCMs into developed sustainable CRCP structure

4.4 Environmental Impact Assessment Study for the Sustainable developed CRCP

This innovative technique is a significant milestone in this research never implemented before. It determines the implications of producing a long-lasting CRCP structure, focusing on the integration between the developed sustainable CRCP and their environmental relevance based to ecological methods as environment impact assessment (EIA). The integration of Life Cycle Assessment (LCA) and Artificial Intelligence (AI) generates a comprehensive framework for evaluating the environmental impacts of a sustainable CRCP with effective modeling and predictive monitor of the pavement's service life. The EIA assess the environmental effects of this new structure system by applying RECIPE 2016, Environmental Design of Industrial Products (EDIP 2003), and Cumulative Energy Demand (CED) ways for life-cycle assessment and evaluation using OpenLCA software.

- LCA Functional Unit (FU) Phase: This step validates the reference flow to evaluate the product's elements. It must be employed to determine or adjust any data used in the LCA. The FU provides a benchmark for standardizing process inputs and outputs.
- LCA System Boundaries Phase: The system boundary is an important in identifying which processes will be included or excluded. Therefore, it should be compatible with the aims of this study. The selection of the system border affects the transfer of information, energy, or materials between systems, resulting in varied outcomes based on the boundaries established as shown in Figure 8.

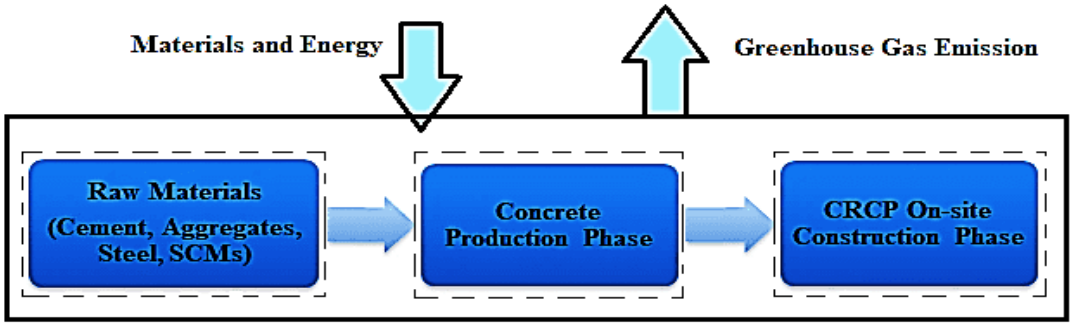

Fig. 8. System boundary of CRCP assessment

5. Results and Discussions

5.1 Workability, Wet Density and Concrete Permeability

The impacts of SCMs on concrete performance and characteristics was discussed by varying the percentages of ingredients amount in the developed concrete mixtures and compared into the standard mix. The partial replacement impacted modified concrete mixes fresh properties after 28 days, as seen in Table 6.

Table 6. Sustainable concrete wet density and permeability properties

Mixture Type	Slump (mm)	Water Absorption (%)	Wet density (kg/m³)
Normal	25	4	2390
Zeo-Concrete	35	3.3	2350
PTW-Concrete	27	3	2316
SCG-Concrete	40	2.8	2250
SF-Zeo-Concrete	22	1.12	2300

The results shown that the zeo-concrete mixture has the highest slump with 35 mm, improving the workability of the concrete, while the SF-Zeo-concrete mix has the lowest value with 22 mm, indicating less workability with a low water absorption rate of 1.12% that preventing moisture over the normal concrete mix with absorption rate of 4%. Moreover, the study reveals that SCG-concrete has the lowest wet density at 2250 kg/m^3 with enhanced strength property. The addition of 15% SCG increases workability, durability, and decreases permeability of the new developed mix. PTW-concrete mix with 2316 kg/m^3 wet density optimizing recycled materials and improving the structural performance. So, mixes with JNZ and silica fume improve concrete workability and durability, while PTW mix gets an efficient recycling without significant impact on the performance.

5.2 Compressive Strengths of the Sustainable Developed Mixes

The improvement of concrete mechanical properties raised when supplementary materials were used and their ability to impact on concrete behavior. This part discovers the combination effect of this materials into concrete, focusing on durability and concrete compressive strengths. Newly developed concrete can enhance various mechanical properties, resulting in better durability for high-performance CRCP applications. Figure 9 illustrates the impact of integrating supplementary materials on the compressive strength, resulting in a developed blend after curing for 7 and 28 days and Table 7 shows a long-term durability of the new concrete mixes compressive strengths.

Table 7. Strength development of sustainable concrete mixtures with curing (MPa).

Period (Days) / Mix	3	7	14	28	36	56	90
Normal	25.1	29.01	31.3	40.3	48.1	54.6	55.3
JNZ	29.5	32.2	36.6	52.1	64.4	69.2	72.7
JNZ+SF	25.4	27.7	31.8	35	43.8	47.4	52.1
PTW	30.2	34.43	45	49.4	55.6	64.7	70.2
SCG	26.4	27.53	34.7	47.6	50.1	56.3	65.8

The combined addition of JNZ and SF to the concrete mixture shown in a significant reduction in strength compared to the natural zeolite mix. The produced new JNZ-SF-enhanced concrete mix with the increased silica fume amount harmed concrete behavior when used at 5% and 10% JNZ, especially when sulfate-resistant cement was used. Figure 10 shows the microstructural analysis using SEM of JNZ-SF strength reduction.

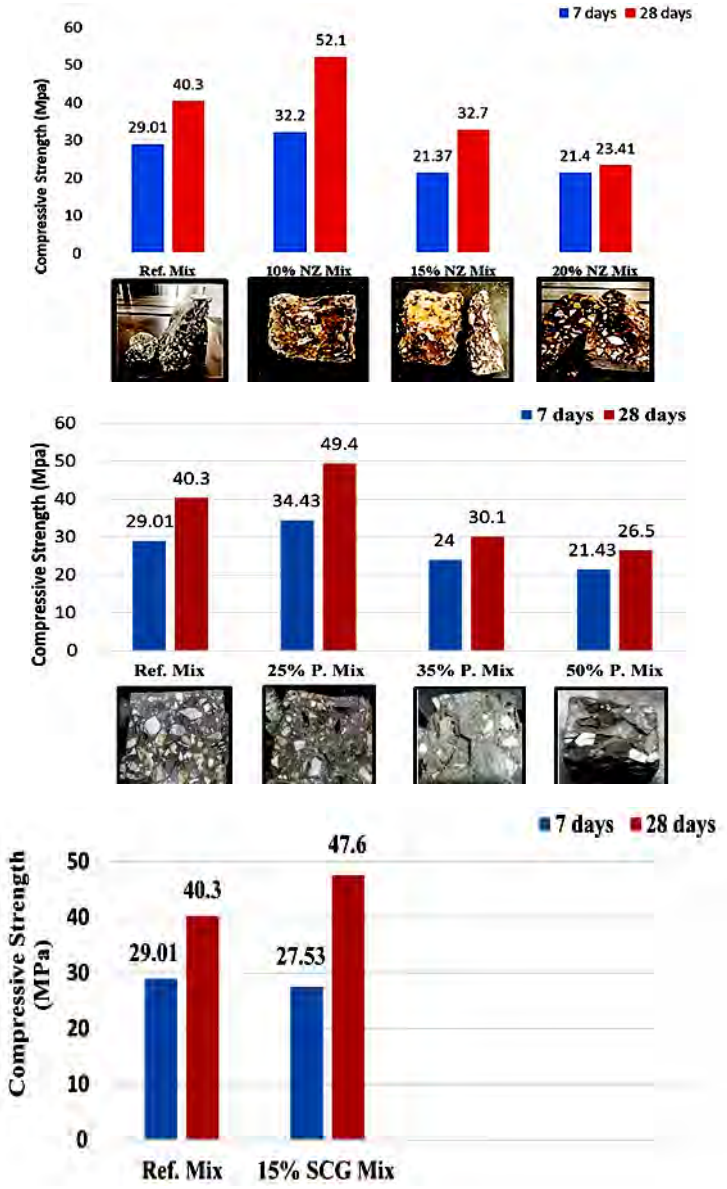

Fig. 9. Integrating compressive strength of reference and modified concrete mixes

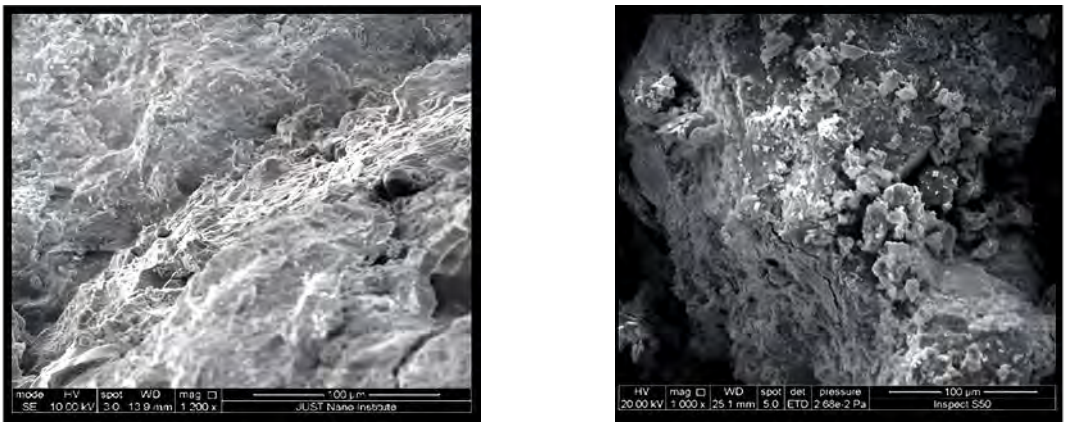

(a) (b)

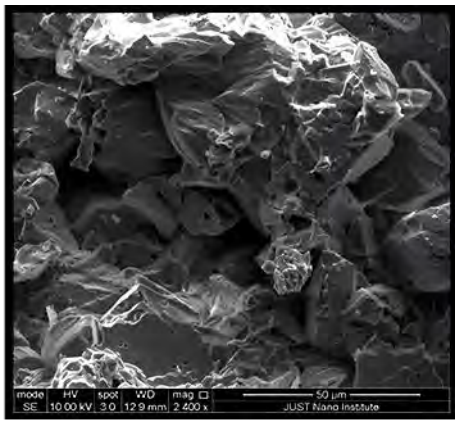

(c)

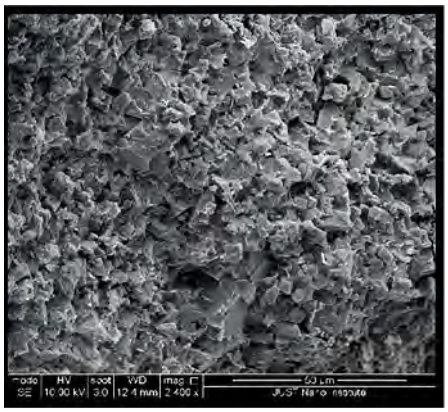

(d)

Fig. 10. Concrete Nano-SEM images for (a-c) normal mix (b-d) modified mix

5.3 Evaluating Sustainable CRCP Performance Results

Continuously reinforced concrete pavement is implemented to enhance durability and behavior over its life. The structural evaluation of CRCP, specifically determining the effect of integrating SCG, PTW, JNZ and SF into concrete mix yielded the following results. The outcomes of CRCP structure samples using normal and new modified-enhanced concrete are shown in Tables 8 and Table 9.

Table 8. Normal CRCP analysis

Load Resistance (kN)	Avg. Displacement (mm)	Avg. Compressive Stress (MPa)	Avg. Strain (mm/mm)	Avg. E (MPa)	Crack Width (mm)
Avg. Point Load, 150	3	150	0.003	32000	0.2
Avg. Dynamic Load, 225	4	225	0.001	32000	0.3

Table 9. Modified-enhanced concrete CRCP analysis.

Load Resistance (kN)	Avg. Displacement (mm)	Avg. Compressive Stress (MPa)	Avg. Strain (mm/mm)	Avg. E (MPa)	Crack Width (mm)
		SCG			
Avg. point Load, 500	0.5	500	0. 001	30000	0.15
Avg. Dynamic Load, 750	0.1	750	0.0015	30000	0.2
		PTW			
Avg. Point Load, 700	1.5	700	0.00002	33000	0.05
Avg. Dynamic Load, 1050	2	1050	0.000035	33000	0.1
		JNZ			
Avg. Point Load (kN), 1000	0.02	1000	0.0001	35000	0.2
Avg. Dynamic Load (kN), 1500	0.03	1500	0.00021	35000	0.3

5.4 EIA Results: SCMs in Concrete

AI-enhanced LCA techniques automate data acquisition from CRCP mix design sources, ensuring accurate input. Machine learning models use the random forest method to assess environmental impacts, improving predictive accuracy and data management. Furthermore, linear regression is applied to decrease ecological effects and forecast continuous results by modifying resource consumption and energy efficiency throughout life-cycle methods. The outputs of the LCA impact analysis summarize sustainable CRCP structures that integrate the SCMs used in the research across many significant environmental effect categories, as presented in Table 10. It presents an effective eco-design strategy by thoroughly evaluating the environmental performance of the new sustainable CRCP structures from cradle-to-grave.

Table 10. Comparative life-cycle study of environmental effects of the sustainable concrete mixes

Impact Categories	Normal Mix	25% PTW Concrete Mix	SCG Concrete Mix	Blended concrete- JNZ Mix
RECIPE				
1. Fossil resource scarcity (kg oil eq/m^3)	1462	1323	1300	1326
2. Global warming (kg CO_2 eq/m^3)	750	500	610	520
3. Human carcinogenic toxicity (kg 1.4-DCB/m^3)	1.03	0.7	0.003	0.05
4. Mineral resource scarcity (kg Cu eq/m^3)	15	10	0.06	0.08
5. Ozone formation, Human health (kg NOx eq/m^3)	1.05	0.75	0.4	0.05
6. Ozone formation, terrestrial ecosystems (kg Nox eq/m^3)	1.35	0.95	0.4	0.5
7. Stratospheric ozone depletion (kg CFC^{-11} eq/m^3)	1.67	0.02	0.00004	0.001
8. Terrestrial acidification (kg SO_2 eq/m^3)	2.5	2.1	0.1	0.05
9. Terrestrial ecotoxicity (kg 1.4-DCB)	0.739	0.591	0.01	0.03
CED				
1. Non-renewable, fossil (MJ/m^3)	1560	1268	300	400
2. Non-renewable, minerals (MJ/m^3)	329	119	50	100
3. Renewable, potential (MJ/m^3)	12	6	6	5
4. Renewable, solar (MJ/m^3)	20	0.864	0.865	30
EDIP				
1. Ecotoxicity soil chronic (m^3)	0.413	0.176	0.01	0.04

Adding SCMs to concrete mixtures is expected to greatly benefit the environment, particularly by reducing CO_2 emissions and saving resources, as demonstrated by comparing three selected assessment methods. This assessment aimed to identify, forecast, and mitigate adverse environmental impacts while advancing sustainable paving practices. Figure 11 shows RECIPE impact category results for the conventional and the designed sustainable concrete mixtures for CRCP design and construction, while the CED impact analysis results are displayed in Figure 12.

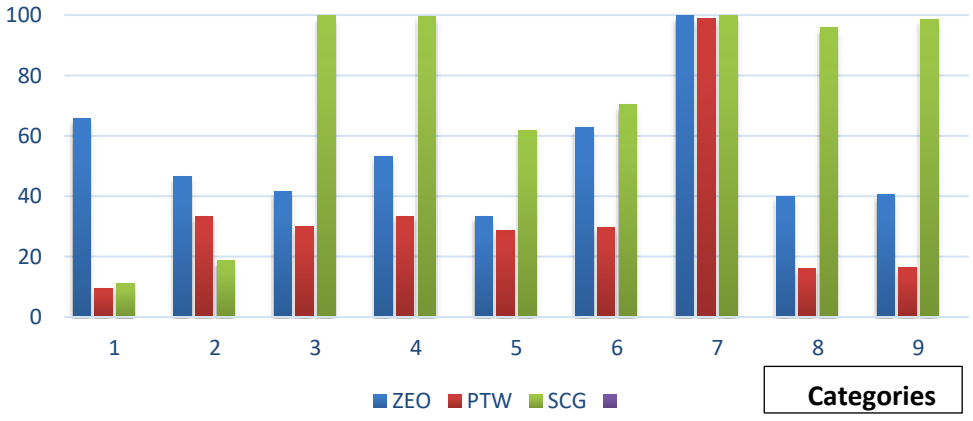

Fig. 11. RECIPE impact categories results of normal and design concrete mixes

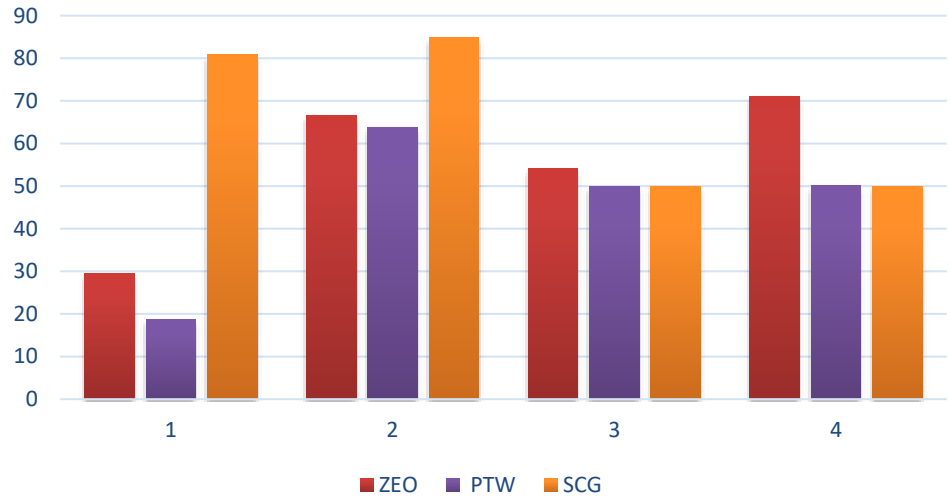

Fig. 12. CED results for concrete mixtures in the study

6. Conclusions

Based on the studying of different supplementary materials effects on concrete behavior and characteristics, the following results are summarized:

- The integration of materials in concrete mixtures improves strength properties and durability behavior and promoting sustainability goals throughout their service life and minimizing environmental concerns to net-zero carbon footprint and each of them has a unique advantage based on the application.
- 10% JNZ-concrete mixture enhances concrete properties after 28 days, mainly its workability and setting time. It has a compressive strength of 52.1 MPa compared to the normal mix and 46.7% improvement in CO2 reduction.
- A concrete mix containing 25% porcelain tile waste of CA enhances concrete strength by 49.4 MPa particularly its workability, water absorption capacity for high-performance uses with 33.3% improvement in carbon footprint impacts.
- The sustainable SCG biochar was resulted at 350°C and blended into mix design as a replaced percentage of 15% FA as a newly designed concrete mix, demonstrating that concrete with 15% SCG had great workability with 47.6 MPa compressive strength and 20% reduction in CO2 effects on the environment.
- The combined mixture of JNZ and SF exhibits less strength compared to previous modified mixes containing only JNZ and others. The increase in silica fume amount harms concrete behavior and properties.

This research forms new infrastructure, enhances global sustainability concerns, and informs stakeholders and governments about developing a sustainable-durable pavement structures by identifying it as a premier framework for an innovative pavement applications and practices.

Acknowledgement

Words cannot express my gratitude to Dr Asma for her invaluable knowledge and expertise. I am also grateful to Jordan University of Science and Technology for the help and inspiration provided by their staff in the work facilities. Lastly, I could not have undertaken this research without the generous help, prayers, and motivation of my family.

References

[1] Rajnivas P, Christy CF, Mugunthan AS, Perumal MS. Effect of Zeolite in the Mechanical Properties of Concrete and its CO2 Absorption Characteristics to Form an Eco-Friendly Environment. 2020.
[2] Tran YT, Lee J, Kumar P, Kim K-H, Lee SS. Natural zeolite and its application in concrete composite production. Compos Part B Eng. 2019;165:354-64. https://doi.org/10.1016/j.compositesb.2018.12.084

[3] Waghmare S, Ghadvir G. Study of influence of Zeolite Application in Rigid Pavement and Strength Prediction through Regression Analysis. 2023. https://doi.org/10.21203/rs.3.rs-3442339/v1
[4] Pranav S, Aggarwal S, Yang E-H, Sarkar AK, Singh AP, Lahoti M. Alternative materials for wearing course of concrete pavements: A critical review. Constr Build Mater. 2020;236:117609. https://doi.org/10.1016/j.conbuildmat.2019.117609
[5] Plati C. Sustainability factors in pavement materials, design, and preservation strategies: A literature review. Constr Build Mater. 2019;211:539-55. https://doi.org/10.1016/j.conbuildmat.2019.03.242
[6] Yudi A, Nabila S, Naghazta MG, Trisna WR. Utilization of zeolite materials with physical activation and chemical activation as cement substitutes. AIP Conf Proc. 2024;3109(1). https://doi.org/10.1063/5.0205079
[7] Hamada HM, et al. Effect of silica fume on the properties of sustainable cement concrete. J Mater Res Technol. 2023;24:8887-8908. https://doi.org/10.1016/j.jmrt.2023.05.147
[8] Ata THB, Ibraheem AT. The impact of Jordanian natural zeolite and silica fume on concrete performance sustainability. Edelweiss Appl Sci Technol. 2025;9(1):1228-42. https://doi.org/10.55214/25768484.v9i1.4380
[9] Santos HMM, et al. Porcelain tile polishing residue in concrete as an additive or replacement for Portland cement. Appl Sci. 2023;13(5). https://doi.org/10.3390/app13052824
[10] El-Abidi KMA, Mijarsh MJA, Abas NF. Properties of porcelain influenced concrete. Eur J Environ Civ Eng. 2022.
[11] Ata THB, Ibraheem AT. Evaluating the sustainability and mechanical characteristics of concrete fabricated from waste porcelain tiles. Int J Innov Res Sci Stud. 2025;8(2). https://doi.org/10.53894/ijirss.v8i2.5155
[12] Roychand R, Kilmartin-Lynch S, Saberian M, Li J, Zhang G, Li CQ. Transforming spent coffee grounds into a valuable resource for the enhancement of concrete strength. J Clean Prod. 2023;419:138205. https://doi.org/10.1016/j.jclepro.2023.138205
[13] ACI Committee 318. Building code requirements for structural concrete and commentary (ACI 318R-21). American Concrete Institute; 2021.
[14] American Society for Testing and Materials. ASTM C469 - Standard test method for static modulus of elasticity and Poisson's ratio of concrete in compression. 2022.
[15] Keshavarz Z, Mostofinejad D. Porcelain and red ceramic wastes used as replacements for coarse aggregate in concrete. Constr Build Mater. 2019 Jan. https://doi.org/10.1016/j.conbuildmat.2018.11.033

Research on Engineering Structures & Materials
www.jresm.org

Research Article

Dynamic response of self-compacting concrete included fiber and eps of hollow beam reinforced with GFRP under impact load

Mohanad T. Abduljaleel [*,a], Abdulkader Ismail Al-Hadithi [b]

Department of Civil Engineering, University of Anbar, Ramadi, Iraq

Article Info

Article History:

Received 12 Oct 2025

Accepted 24 Nov 2025

Keywords:

Plastic fibers;
Impact load;
Inertial force;
Glass fiber reinforced polymer;
Self-compacting concrete

Abstract

The increasing demand for sustainable construction materials has motivated the use of recycled and lightweight constituents in structural concrete. This study investigates the dynamic response of self-compacting concrete (SCC) modified with recycled polyethylene terephthalate (PET) fibers and expanded polystyrene (EPS) beads and reinforced with glass-fiber-reinforced polymer (GFRP) bars. Four reinforced concrete beams (150 × 200 × 1500 mm) were tested under repeated low-velocity impact using a 37.5 kg drop weight released from 3.5 m. Two beams had solid cross-sections, while two incorporated a rectangular internal hollow. Fresh concrete tests confirmed that the modified SCC maintained adequate flowability and cohesion. The average compressive strength was 22 MPa, and density ranged from 1952 to 2301 kg/m^3. The dynamic responses were evaluated in terms of displacement, reaction forces, inertial forces, energy absorption, and crack development. The addition of PET fibers increased stiffness and delayed crack propagation, whereas EPS beads reduced density and altered the failure mechanism from brittle to more ductile. Hollow sections increased displacement and inertial forces due to reduced mass and compression-zone depth. Peak displacement during the second impact increased by 2.8–17.3%, and inertial forces rose by up to 66 kN in hollow beams. The combined use of EPS and PET enhanced energy absorption and improved the impact behavior of SCC beams.

© 2026 MIM Research Group. All rights reserved.

1. Introduction

Structural elements in modern infrastructure are often subjected to dynamic and impact loads. Therefore, studies on improving the impact/blast resistance of constructions and civil infrastructure are essential for improving the safety of people from high loads, including missile assaults and explosions. Usually reinforced with continuous deformed steel reinforcing bar (rebar), concrete is vulnerable in tension relative to compression and requires reinforced concrete (RC) construction. The strain rate effect helps the structure to be somewhat resistant against high-speed loads, such as hits and explosions. On the other hand, structural collapse could happen and result in injuries if loads exceed the maximum capability of RC buildings. New materials should thus be developed and used to improve the ultimate load resistance of RC constructions [1]. Incorporating a high volume of discontinuous fiber reinforcements will help to enable the fabrication of high-performance concrete, offering one of the most promising solutions to achieve exceptional impact and blast resistance in concrete and reinforced concrete structures [2].

In addition to its energy-absorbing properties, expanded polystyrene (EPS) concrete has excellent resistance to corrosion, water attack, and significant variation in service temperature [3], making it suitable for use in both military and civilian protective constructions [4]. Research on the

*Corresponding author: moh22e1001@uoanbar.edu.iq
[a]orcid.org/0009-0003-9261-0083; [b]orcid.org/0000-0003-2217-7643
DOI: http://dx.doi.org/10.17515/resm2025-1241ic1012rs

mechanical reaction of impact-treated EPS concrete is in its early stages, in contrast to that of its quasistatic mechanical properties. Up until now, there has been little reporting on studies examining the dynamic reaction of EPS concrete. One of the most notable uses of lightweight concrete is the engineered materials arrestor system (EMAS). EPS concrete is a strong contender for this role due to its reported dynamic properties, which include a low crushing strength, a large deformation capacity, and good environmental tolerance. A bed constructed at the end of a runway is known as the EMAS. The energy can be dissipated through the crashing of the EMAS material, effectively slowing down the overrunning aircraft. This work presents the results of an initial experimental investigation into the dynamic response of expanded polystyrene (EPS) concrete under low impact velocities, as measured by a drop hammer testing apparatus. Along with the drop hammer testing machine, a high-speed photography system is used to characterize the surface deformation and damage on the EPS concrete during the impact. In light of these findings, the energy dissipation capacity and failure processes of EPS concrete were investigated [5]. Previous studies reported that incorporating crumb rubber (1–2 mm, 5–25% replacement) in steel-fiber concrete decreases compressive strength but significantly enhances impact resistance. Using ACI 544 drop-weight tests on 100×100×500 mm beams, higher crumb-rubber contents consistently increased the measured impact energy despite strength reduction [6].

This study introduces a hybrid SCC incorporating recycled PET fibers, EPS beads, and GFRP reinforcement, a combination not previously examined under repeated low-velocity impact. It further advances the field by assessing engineered hollow sections with central and eccentric voids and by providing millisecond-scale dynamic response data, including reaction, inertia, displacement, and crack evolution. These contributions collectively position the work beyond existing research on EPS-based or fiber-reinforced SCC.

1.1 Research Aim and Objectives

This study aims to examine the influence of recycled PET fibers, EPS lightweight beads, and engineered hollow configurations on the dynamic behavior of self-compacting concrete beams reinforced with GFRP bars under repeated low-velocity impact loading. In pursuit of this aim, the research undertakes the development of modified SCC mixtures incorporating PET fibers and EPS beads, the comparison of solid and hollow beam configurations with identical reinforcement, and the evaluation of displacement histories, reaction forces, inertial responses, and crack propagation during successive impacts. The study further seeks to quantify the combined effects of material modification and section geometry on energy absorption, stiffness characteristics, and overall structural response.

2. Experimental Work

Standard Portland cement (Type I) was used to produce the self-compacting concrete (SCC) mixtures in accordance with ASTM C150 [7]. A highly reactive pozzolanic silica fume (SF), conforming to ASTM C1240, was incorporated as a mineral admixture [8]. The SF contained approximately 85% SiO_2 and had a bulk density of about 700 kg/m^3. Superplasticizer (SP), a high-range water-reducing admixture, was employed to achieve the required flowability of SCC. Crushed coarse aggregate with a maximum particle size of 10 mm was used following ASTM C136 and ASTM C33 [9,10]. The fine aggregate was natural river sand with a fineness modulus of 3.7. Spherical expanded polystyrene (EPS) beads were used to partially replace the coarse aggregate, as illustrated in Fig. 1. The EPS beads had an average diameter of 5 mm and a bulk density of 10 kg/m^3. Polyethylene terephthalate (PET) waste plastic fibers, with an aspect ratio of 30, were incorporated to enhance the load-carrying capacity and ductility of SCC.

Table 1. Reinforcement rebars properties

Diameter	Type	Yield Strength (MPa)	Ultimate Tensile Strength (MPa)	Elasticity Modulus (GPa)
6	Steel	570	670	200
10	GFRP	-	1100	45

The properties of the reinforcing bars and waste plastic fibres are presented in Tables 1 and 2, respectively. To produce an environmentally friendly SCC mix with comparable strength, limestone powder was used as a filler material.

(a) (b)

Fig. 1. Waste material, (a) Expanded Polystyrene (EPS) and (b) PET fibers

Table 2. Plastic fiber type (PET) properties

Length (mm)	Width (mm)	Thickness (mm)	Aspect ratio	Tensile strength MPa	Elastic Modulus MPa	Specific gravity g/cm^3
33	3	0.3	30	140	1000	1.34

2.1 Specimen Design

The impact performance of (solid-hollow) beams was studied using four concrete beams of 150×200×1500 mm, designed per ACI-440.1R-15 [11]. The specimens were reinforced with two 10 mm GFRP rebars in tension and one 6 mm steel bar in compression. The beam had a 20 mm concrete cover, and for shear force, 6 mm stirrups were positioned at 65 mm apart on the beam. Fig. 2 shows the specimen cross-sectioned. The 120 Ohm strain gauge was attached to the tension bar mid-span and concrete face. Before inserting the strain gauge, the debris was removed by fine sandpaper. All beams have a 0.62% reinforcement ratio.

Two cross-sectional configurations were examined in this study. The solid beams (BR, BS) employed the full 150 × 200 mm section, while the hollow beams (BH1, BH2) incorporated a rectangular void of 50 × 40 mm, corresponding to 6.7% of the total cross-sectional area. In the BH1 specimens, the void was positioned at the neutral axis, whereas in BH2 it was shifted 40 mm downward. This arrangement was adopted to assess how reducing the effective compression-zone depth influences displacement behavior and inertial response under impact loading.

2.2 Impact Load Device

Drop-weight test details are shown in Fig. 3. In the drop-weight test setup, a mechanical mechanism with a clamping system raises a steel hammer to the desired height. Switching the mechanical clamping system releases the steel hammer to produce an impact load. A 45-mm-radius hemispheric steel hammerhead interacts with beams during impact loading. The same hammerhead and impact load were used in all experiments. Impact loads were applied to specimen centers. The 37.5 kg hammerhead was positioned at 3.5 m for all specimens; thus, All beams received approximately 1.3 kJ of impact energy. Piezoelectric accelerometers measured impact loading accelerations in the beam at the L/4 and L/2 of the specimen's span. A displacement transducer (LVDT) positioned at the beam center measured specimen displacements due to impact load. Both supports used dynamic load cells to measure impact loads. National Instruments modules and data acquisition chassis PXI-1042, PXI-4472 recorded and sent specimen impact loads, displacements, and accelerations to a computer using NI software. The specimens were secured with a thick plate at the beam end to avoid raising; their clear span was 1300 mm. A 1000

FPS camera in front of the specimens was used to monitoring cracks with time. To minimize vibrations, the setup was mounted on a main foundation composed of a heavy steel plate and reinforced concrete. The energy conservation equation was used to calculate energy and velocity: m = mass, v = velocity, g = normal gravitational acceleration, and h = drop height.

$$mgh = 1/2mv^2 \quad (1)$$

$$v = \sqrt{2gh} \quad (2)$$

Due to friction, the mass decreased from rest to beam contact took 0.85 s, adjusting acceleration $a=2h/t^2$ to 9.69 m/s². Equation (1) yields 1270 J without friction, while after applying a new acceleration in equation 1 yielded 1254 J, resulting in a 16 J of energy loss.

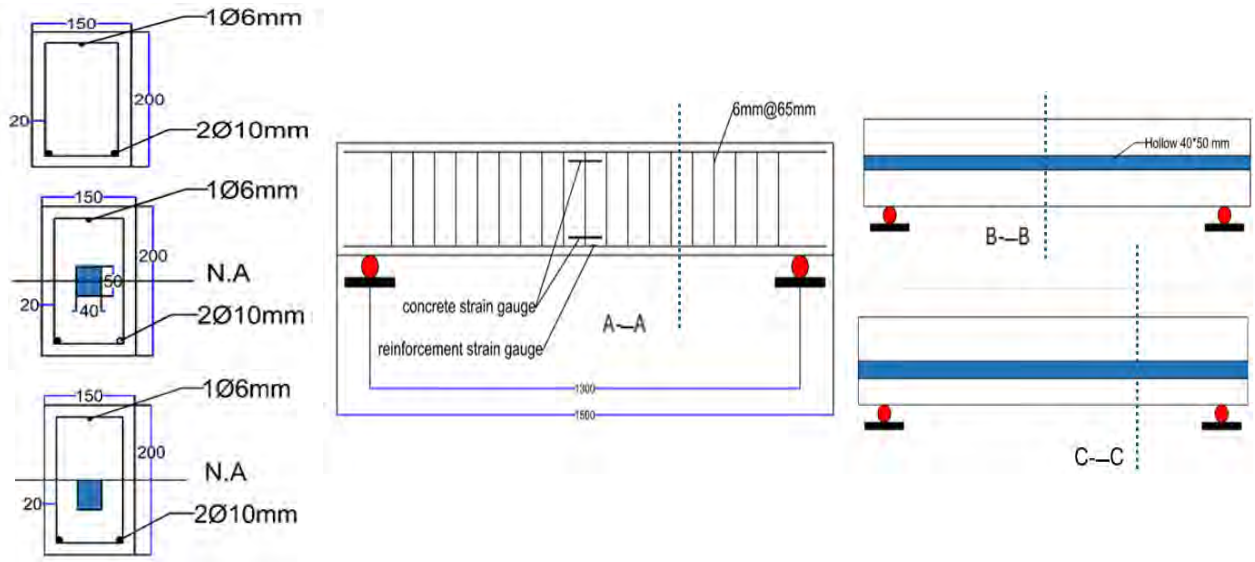

Fig. 2. Demonstrates the reinforcement and hollow location

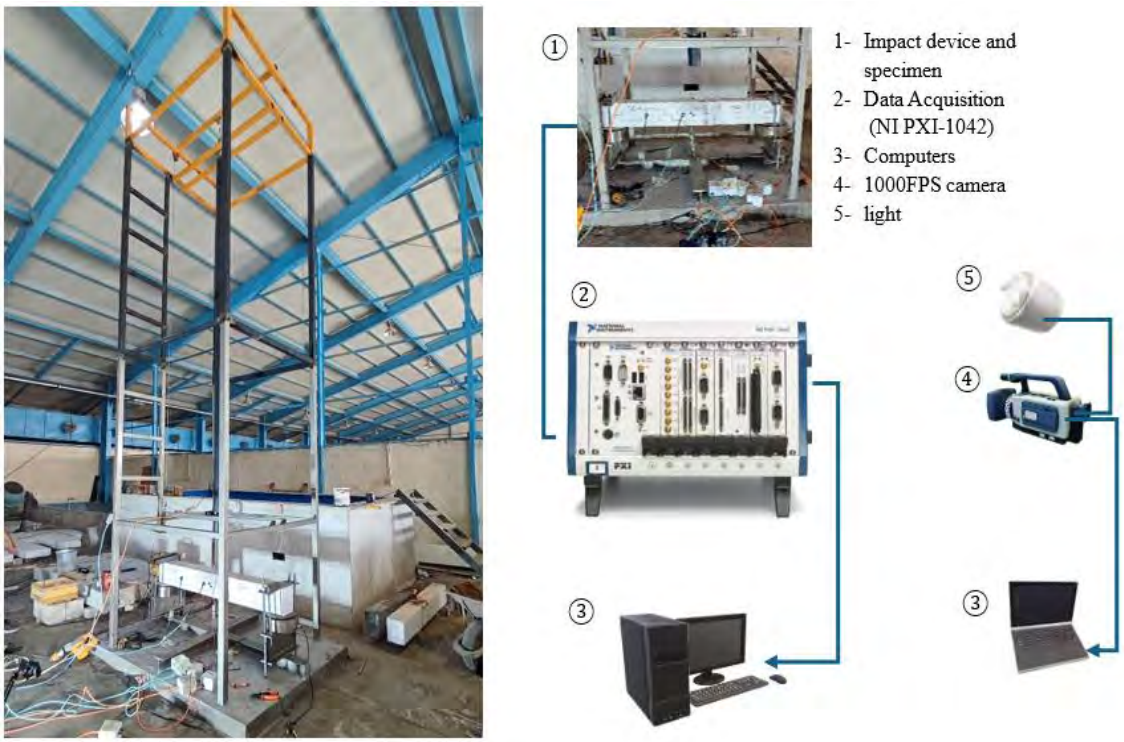

Fig. 3. Details of the impact device and data acquisition

3. Experimental Results and Discussion

3.1 Properties of SCC Contain EPS And Plastic Fiber

Based on fresh characteristics, two materials were chosen, (SR) was the reference material of SCC without fiber and EPS, while (EF) was SCC that contains plastic fiber and EPS beads; Tables 3 and 4 illustrate the trial mix and SCC properties, respectively. The fresh properties test showed that silica-fume (SF) increased matrix cohesiveness [8], prevented the floating of EPS beads, and reduced aggregate segregation. Fresh properties test showed that 2 Kg of EPS beads created SCC correctly according to EFNARC requirements [12]. Incorporating 0.35% PET fibers allowed the SCC to maintain adequate workability while enhancing its mechanical performance. Because EPS beads are weak, cracks started from their surroundings at the ITZ zone, and no compression strength increase was seen over a 90-day period when the compressive strength was tested on 150 mm diameter, 300 mm height cylinders in accordance with ASTM C39 [15]. Although EPS beads cannot carry weights like coarse aggregate, they reduced concrete density by 15 % compared to the reference SR, and accordance to the researcher, curing the EPS surface improves the compressive strength [13]. Two SCC mixes, SR and EF, were tested for compressive strength and density. The average compressive strength was 22.2 MPa, and that was attributed to the use of lightweight EPS as partial replacement from coarse aggregate. This analysis highlights that while strength remained stable, material choice greatly affected the density.

Table 3. Trail mix of SCC

Material* ID	Cement kg/m3	Fine Agg. kg/m3	Course Agg. kg/m^3	Water kg/m^3	SF kg/m^3	Fiber (PET) kg/m^3	SP kg/m^3	EPS kg/m^3	Limestone Powder kg/m^3
SR	250	980	700	210	-	-	9	-	230
EF	490	1100	400	189	100	5	13.7	2	-

**SR is a short of self-compacting references (without EPS and fiber), EF refers to the concrete having both (EPS and fiber)*

Table 4. SCC mechanical and fresh properties

No.	Material ID	Compressive Strength (MPa)	Tensile strength (MPa)	Density kg/m^3	Slump (mm)	T_{500} (S)	J-Ring (mm)	V-funnel (S)
1	SR	22.4	2.5	2301	770	2.1	9	9
2	EF	22	3.25	1952	705	3	10	11

3.2 Displacement Response

As shown in Fig. 4 and Table 5, all specimens obtained two impact load first blow and second blows, thus the displacement-time dynamic response may be divided into three stages. Phase 1 saw deflection in the beams from their resting position to their maximum displacement. Phase 2 saw the impact load dropped to zero and the beams returned to their starting point. The beams freely vibrated in Phase 3 after separating from the impactor, similar findings were reported by[14]. Under impact load, all specimens performed somewhat similarly. At second strikes, the displacement values for specimens BR, BS, BH1 and BH2 rose by 2.8%, 10.5%, 17.3%, and 5.3%, respectively. While adding PET fibers increased crack bridging and energy absorption, adding EPS beads in concrete beams reduced stiffness but improved crack separation. The position of the hollow near the middle of the specimen helped BH1 show the most deflection value 12% more than BH2 at second impact load. The presence of a hollow at the center of the specimen reduced the tension and compression zones of the concrete beam, consequently lowering the stiffness value since the compression zone is mostly responsible for the either increasing or decreasing deflection value after reaching the plastic strain in reinforcement rebars. Therefore, it can be concluded that, the displacement of the specimens depends on the depth of the compression zone.

3.3 Force History Response

Separating the inertial loading and total load helps assess impact test results. Brittle materials like concrete have a larger inertial load, or load needed to accelerate the specimen [15]. The beam's bending load is computed by the following equations (3) and (4):

$$P_{t(t)} = P_{b(t)+} P_{i(t)} \quad (3)$$

$$P_{b(t)} = R_{R(t)+} R_{L(t)} \quad (4)$$

The inertial force, total response force of the two supports, and total impact force are denoted as P_i, Pb, and P_t, respectively. The inertial force was computed using the beam's equivalent mass as described in equations (5) and (6).

$$m_{equivalent} = \int_o^l \rho bh\phi\,(x)^2 dx \quad (5)$$

$$P_{i(t)} = m.equivalent.\ddot{U}_{0(t)} \quad (6)$$

In this context, the variables P i(t) representing the generalized inertial load operating at the beam's center, ρ representing the mass density, Ü0(t) representing the acceleration at the beam's center, x= L representing the beam's length between supports, and (bh) representing the beam's area are defined. The m-equivalent = ρbh(L/2) for the simply supported beam replace ϕ(x)=sin(πx/L). After calculating the total force and inertial force using Eqs. (3) and (6), the experimental results of the total response force are shown in Fig. 5 and Table 5.

Table 5. Impact load experimental result

Beam's name	Material ID	Blow No.	Accumulated energy (kJ)	Midspan displacement Max. (mm)	Reaction force (kN)	*Max. Inertial force (kN)
BR	SR	1	1.2**	14	31	39
		2	2.4	14.41	36.4	
BS	EF	1	1.2	13.68	35.8	50
		2	2.4	15.3	33	
BH1	EF	1	1.2	15.7	31.5	63.9
		2	2.4	19	36	
BH2	EF	1	1.2	15.9	31.19	66
		2	2.4	16.8	31.8	

**The maximum value was selected from Eqs. (3) and (6), **Owing to frictional losses, the impactor's experimentally measured velocity was reduced and limited to about 8 m/s.*

The reaction forces during the first blow varied between 31 and 35.8 kN, while during the second blow they ranged from 31.8 to 36.4 kN. The BS specimen, which contained both plastic fiber and EPS beads, showed the highest forces during the first impact load. Specimens BH1 and BR demonstrated a growth of 12.5% and 14.8%, respectively, in the second strike. The redistribution of stress or localized stiffening is probably responsible for the increase in the second impact. Beam responses to impact loads generally followed a similar pattern, these results are consistent with a previous study [16]. At about the same time, the impact force reached a peak on each beam. However, the response force and impact load varied among the beams; this discrepancy may be attributable to the different materials used; for example, the reference material (SR) exhibited the lowest inertial force when contrasted with the changed materials (EF). In line with [1], the use of PET fibers increased the total force of the beam BS by 24% compared to the BR. This is because the fibers improve crack resistance and energy absorption by redistributing stresses through the creation of crack bridges. Consistent with the principles of structural mechanics, the experimental results show that GFRP-reinforced SCC beams with hollow sections have lower stiffness [17,18], and different dynamic behavior under impact. Due to reduced mass and moment of inertia, hollow beams exhibited 11.4-14% lower reaction forces (31 kN vs. 35 kN in solid beams), whereas inertial forces rose (63-66 kN vs. 50 kN), showing enhanced accelerations in lighter and more flexible

systems. The ductility of the SCC matrix was improved by adding EPS beads and 3.5% plastic fibers; this allowed it to delay brittle failure, even in the presence of hollow-induced stress concentrations.

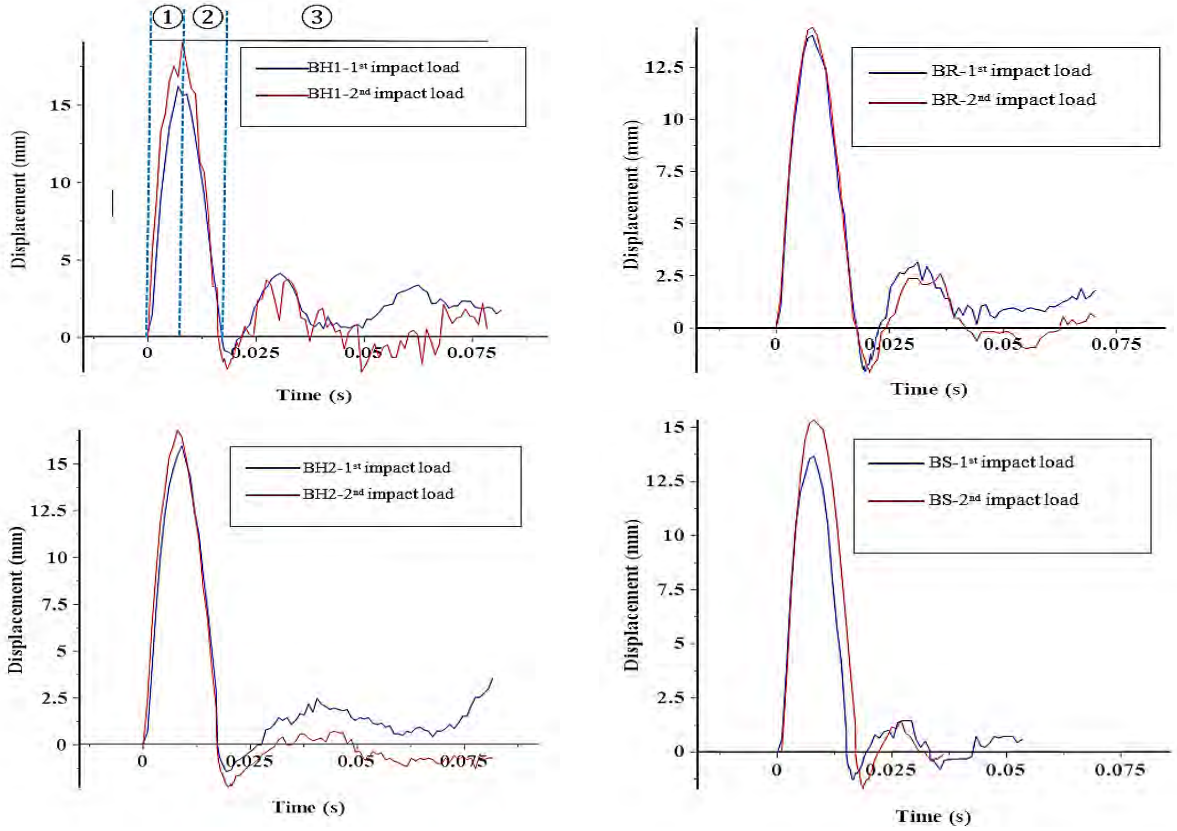

Fig. 4. Displacement response

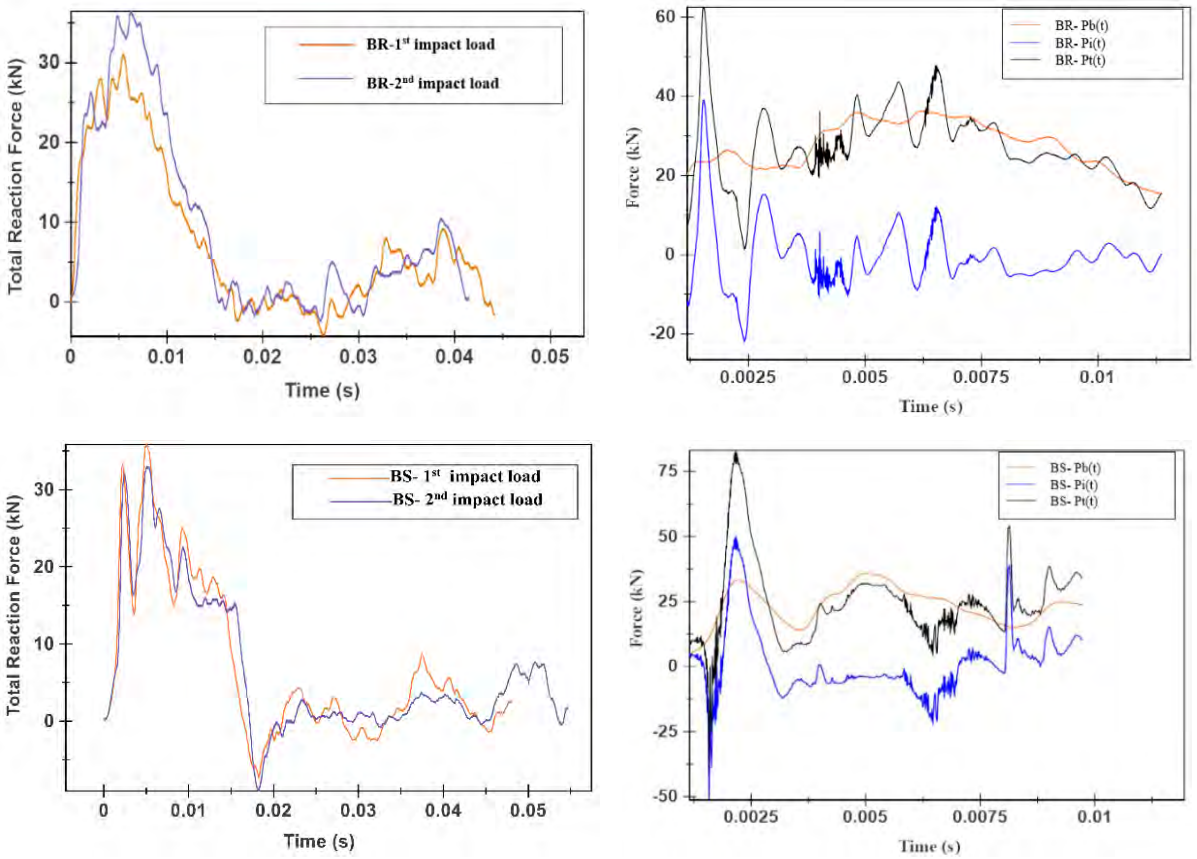

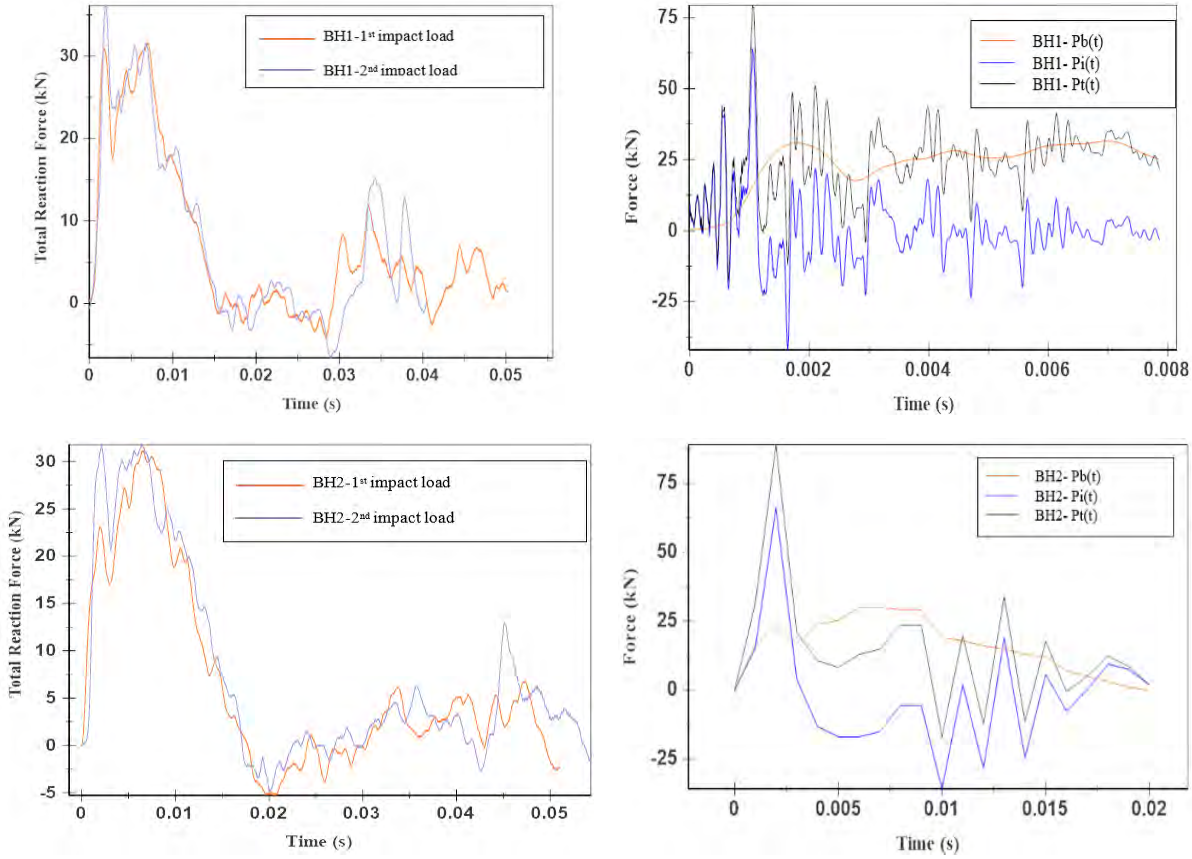

Fig. 5. Time history of reactions and forces

3.4 Cracks and Failure Mode

The same approach has been used to track cracks and failure modes. Four concrete beams were subjected to an impact load, and Figs. 6 and 7 show the cracks developing over time. Each specimen took two strikes from a height of 3.5 meters, and the drop-mass was 37.5 kg. Using a 1000 FPS camera, the crack development in the concrete beams was meticulously tracked. Because of the concentrations of stress, cracks began to form about 2 ms after impact in the area immediately surrounding the tensile zone [13]. Rapid crack propagation along the flexural plane occurred between 7 and 10 ms [19], with crack lengths reaching 160 mm. The specimen BR showed compression failure 25 ms after the second blow, when tensile stresses exceeded the concrete's tensile strength, unlike the specimens with plastic fiber and EPS beads, which demonstrate smooth cracks over time. Different crack patterns were seen in specimens; the hollow beams showed a notable effect on the crack width, resulting in smooth cracks due to the stiffness reduction.

Incorporating expanded polystyrene (EPS) into the concrete mixture improved fracture smoothness and separation when contrasted with the reference beams. According to visual inspection, cracks in the EPS beams were more evenly spaced and less sharp, suggesting better energy dissipation and a more consistent distribution of stress. By reducing stress concentrations and postponing localized failure, the EPS-modified SCC's decreased stiffness probably had a role in this behavior. Because the EPS-modified SCC could not withstand high tensile loads over small areas, its reduced tensile strength led to smoother, more widely spaced cracks. Despite this, the results show that EPS can improve energy absorption and crack management. Unlike the reference beam BR, the behavior of the beams BS, BH1, and BH2 at the second impact load was enhanced and exhibited improvement in the number of load impact cycles, thus incorporating EPS beads with plastic fiber, promising improved resistance to repeated dynamic loads.

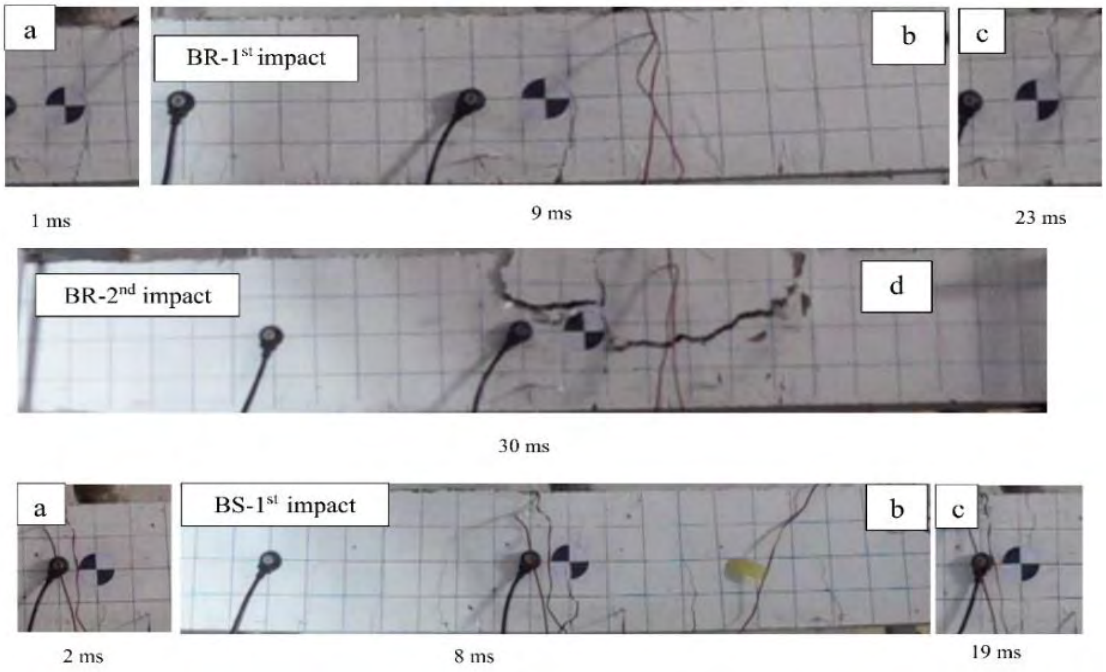

Fig. 6. Failure and crack patterns with time, for BR and BS: (a) first crack; (b) maximum crack distribution; (c) crack at compression zone; (d) maximum crack width at second impact

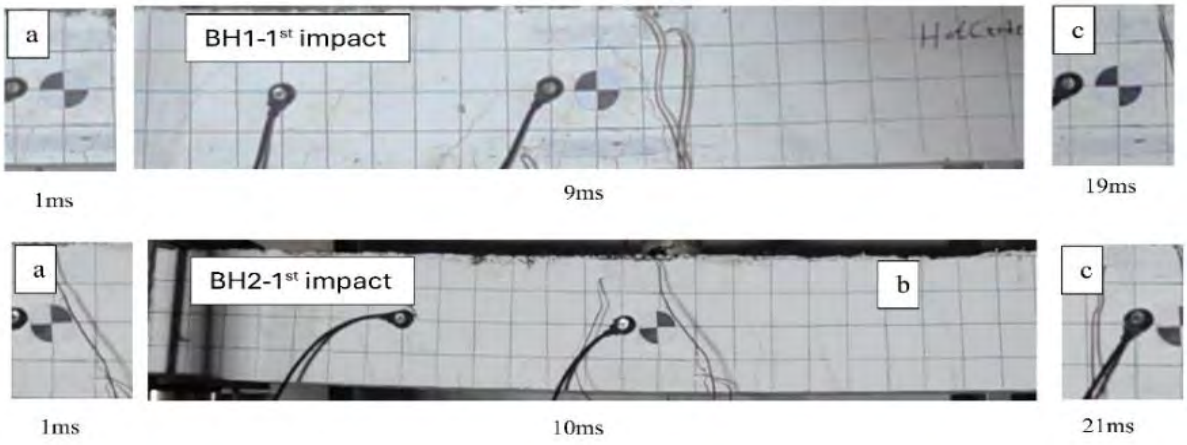

Fig. 7. Failure and crack patterns with time, for BH1 and BH2: (a) first crack; (b) maximum crack distribution; (c) crack at compression zone; (d) maximum crack width at second impact

4. Conclusion

Based on experimental evaluation of SCC beams modified with PET fibers, EPS beads, and hollow sections under repeated impact loading, the following conclusions are drawn:

- The modified SCC achieved an average compressive strength of 22 MPa and density reduction of up to 15% due to EPS inclusion.
- PET fibers improved stiffness and controlled crack propagation, increasing total reaction force by up to 24% compared with reference beams.
- EPS beads changed the failure mode from brittle fracture to smoother, more ductile crack separation.
- Hollow beams recorded 11–14% lower reaction forces but higher inertial forces, caused by reduced mass and stiffness.
- Midspan displacement increased by 2.8–17.3% during the second impact, especially for beams with centrally placed hollows.

- Crack initiation occurred at 1–2 ms after impact and major cracks formed by 8–10 ms, consistent with high-rate loading.
- The combined use of PET and EPS improved energy absorption capacity and repeated-impact resistance.
- Incorporating hollow sections can reduce material consumption while maintaining acceptable dynamic performance.

5. Recommendation

The following points can be considered as recommendations for further research:

- Curing the EPS beads by coating the surface to increase the friction between the cement paste and EPS beads.
- Using a high aspect ratio of around 40 may enhance the load capacity.
- It is recommended to use the EPS as a layer in the tension zone and study the effect.
- Studying the effect of high-speed impact load on the EPS concrete.

Acknowledgment

The writers would like to express their appreciation to the outstanding faculty at the University of Anbar, who generously provided the study with the scientific and technical support it needed.

References

[1] Chun B, Lee SW, Piao R, Kim S, Yoo DY. Enhanced impact resistance of RC beams using various types of high-performance fiber-reinforced cementitious composites. Eng Struct. 2024;319:118790. https://doi.org/10.1016/j.engstruct.2024.118790
[2] Zanuy C, Ulzurrun GS, Curbach M. Experimental determination of sectional forces in impact tests: Application to composite RC-HPFRCC beams. Eng Struct. 2022;256:114004. https://doi.org/10.1016/j.engstruct.2022.114004
[3] Perry SH, Bischoff PH, Yamura K. Mix details and material behaviour of polystyrene aggregate concrete. Mag Concr Res. 1991;43(154):71-6. https://doi.org/10.1680/macr.1991.43.154.71
[4] Ferrándiz-Mas V, García-Alcocel E. Durability of expanded polystyrene mortars. Constr Build Mater. 2013;46:175-82. https://doi.org/10.1016/j.conbuildmat.2013.04.029
[5] Barsotti MA, Puryear JMH, Stevens DJ. Developing improved civil aircraft arresting systems. Vol. 29. Washington (DC): Transportation Research Board; 2009.
[6] Noamana AT, Abu Bakar BH, Akil HM. Effect of crumb rubber aggregate on toughness and impact energy of steel fiber concrete [doktora tezi]. Penang: Universiti Sains Malaysia; 2016.
[7] ASTM International. ASTM C150-07: Standard specification for portland cement. West Conshohocken (PA): ASTM International; 2007.
[8] ASTM International. ASTM C1240-05: Standard specification for silica fume used in cementitious mixtures. West Conshohocken (PA): ASTM International; 2009.
[9] ASTM International. ASTM C136-06: Test method for sieve analysis of fine and coarse aggregates. West Conshohocken (PA): ASTM International; 2006.
[10] ASTM International. ASTM C33/C33M: Specification for concrete aggregates. West Conshohocken (PA): ASTM International; 2018.
[11] ACI Committee 440. ACI 440.1R-15: Guide for the design and construction of structural concrete reinforced with fiber reinforced-polymer (FRP) bars. Farmington Hills (MI): American Concrete Institute; 2015.
[12] BIBM, CEMBUREAU, ERMCO, EFCA, EFNARC. The European guidelines for self-compacting concrete. Farnham (UK): The Concrete Centre; 2005.
[13] Zhang L, Huang M, Yang F, Zhang W. A novel hydrophilic modification method of EPS particles: Conception design and performances in concrete. Cem Concr Compos. 2023;142:105199. https://doi.org/10.1016/j.cemconcomp.2023.105199
[14] Tran DT, Pham TM, Hao H. Experimental and analytical investigations of prefabricated segmental concrete beams post-tensioned with unbonded steel/FRP tendons subjected to impact loading. Int J Impact Eng. 2024;186:104868. https://doi.org/10.1016/j.ijimpeng.2023.104868
[15] Bentur A, Mindess S, Banthia N. The behaviour of concrete under impact loading: Experimental procedures and method of analysis. Mater Struct. 1986;19:371-8. https://doi.org/10.1007/BF02472127

[16] Tran DT, Pham TM, Hao H, San Ha N, Vo NH, Chen W. Precast segmental beams made of fibre-reinforced geopolymer concrete and FRP tendons against impact loads. Eng Struct. 2023;295:116862. https://doi.org/10.1016/j.engstruct.2023.116862
[17] Abduljaleel MT, Mahmoud AS, Yousif A. Experiential investigation of two-way concrete slabs with openings reinforced with glass fiber reinforced polymer bars. J Eng Sci Technol. 2017;12(4):898-912.
[18] Yousif AR, Mahmoud AS, Abduljaleel MT. Punching strength of GFRP reinforced concrete slab-column connections with openings by the finite element method. ZANCO J Pure Appl Sci. 2017;28(6):56-67. https://doi.org/10.21271/ZJPAS.28.6.8
[19] Wei J, Li J, Wu C, Hao H, Liu J. Experimental and numerical study on the impact resistance of ultra-high performance concrete strengthened RC beams. Eng Struct. 2023;277:115474. https://doi.org/10.1016/j.engstruct.2022.115474

Blank Page

Research on Engineering Structures & Materials
www.jresm.org

Research Article

A novel differential quadrature method for transient heat transfer analysis in multilayered cylindrical structures: Numerical validation and parametric investigation

Dheyaa Madlool Manhal [*,1,a], Hasan A. Alshubber [2,b]

[1]*Department of Mechanical Engineering, Qom University, Qom, Iran*
[2]*Department of Mechanical Engineering, University of Baghdad, Baghdad, Iraq*

Article Info

Article History:

Received 12 Oct 2025
Accepted 21 Nov 2025

Keywords:

Transient heat transfer;
Multilayered cylinder;
Differential quadrature method;
Numerical validation;
Thermal analysis

Abstract

This study addresses the challenge of accurately modeling transient heat transfer in complex multilayered cylindrical structures, which are critical in aerospace and industrial applications. The primary objective is to develop and validate a novel numerical approach using the Differential Quadrature Method (DQM) to solve the time-dependent Fourier heat conduction equation in composite cylinders with distinct material properties. While conventional methods like Finite Element Method (FEM) are widely used, they often require computationally expensive meshes. In this work, the governing equations in cylindrical coordinates were discretized using Chebyshev-Gauss-Lobatto grid points for spatial derivatives, coupled with an efficient temporal discretization scheme. This DQM formulation allows for the precise handling of interface conditions between layers without complex mesh generation. The proposed model was validated against ANSYS finite element simulations for a four-layer cylinder under constant boundary temperatures (200 °C and 300 °C). Results demonstrate excellent agreement with maximum relative errors ranging from 0% to 2.4%, proving the method's superior accuracy and computational efficiency. Parametric investigations revealed that variations in thermal conductivity and heat capacity significantly alter the transient temperature profiles, offering key insights for the thermal design of composite insulation and piping systems.

© 2026 MIM Research Group. All rights reserved.

1. Introduction

Transient heat transfer involves changes in temperature distribution within a system over time. This occurs when there are variations in temperature, thermal properties, or boundary conditions. Multilayered structures, also known as composite structures, are materials or systems that consist of multiple layers of different materials bonded together. These structures are designed to combine the beneficial properties of each layer to achieve enhanced performance, tailored for specific applications. Multilayered structures are widely used in various fields, including mechanics, aerospace engineering, civil engineering, and materials science. The transient analysis of heat transfer in a multi layered cylinder is attractive to many researchers, but literature review shows that the transient heat transfer in a multilayered cylinder using the basic Fourier heat conduction equation has not been investigated; thus, it's the innovative aspect of this study [1,2].

Saadatfar [3] presented a transition solution for heat and moisture distribution in a finite-length hollow cylinder made of a gradient material under the influence of interconnected thermophilic and hydromechanical conditions. The heat transfer and moisture diffusion equations were solved using the Fourier series method on the longitudinal axis, the radial quadratic numerical differential

*Corresponding author: h.al-shubber1303@coeng.uobaghdad.edu.iq
[a]orcid.org/0009-0007-3126-9212; [b]orcid.org/0000-0002-7310-5861
DOI: http://dx.doi.org/10.17515/resm2025-1245ic1012rs

method, and the Newmark time method. The results showed the effect of the ocular correlation model versus the discrete model, and the negative and positive pressure differences of the gradient index, confirming the importance of the correlated model for more accurate analysis. Heydarpour [4] presented a three-dimensional analysis of temporary heat transfer in functionally graded multilayer cone shells reinforced with graphene plates, using a non-furrier heat transfer law. The spatial field transforming DQM and the NURBS-based multistep method of time were applied, and the results showed the effect of plate distribution and geometric properties on heat wave velocity and accuracy of calculations.

Pourasghar [5] provided a three-dimensional analysis of the thermoplastic behavior of cylindrical plates under transient heat load, using the hyperbolic heat transfer equation to reflect the velocity of a final heat wave. They were linked to three-dimensional elasticity equations and digitally solved via the DQM and Newmark diagram, with studies investigating and calibration of the effect of heat wave properties on stresses and deviations. Heydarpour [6] analyzed non-furoretic heat transfer in sandwich cone shells with face layers reinforced with graphene plates and a porous core, under the influence of a moving axial heat flow. It was based on the hyperproli heat transfer equation and the DQM with time integration in NURBS. The results showed the effect of flow velocity and graphene percentage on heat distribution and cochlear performance. Zhou [7] presented an analytical model of heat transfer in a multilayer cylinder with internal heat generation, taking the thermogenetic transfer coefficients at the outer surface. A chained solution method was applied to distribute heat in each layer, taking into account the thermal contact resistors and the properties of the disparate layers. It also examined the effect of changing the refrigerant and analyzed the sensitivity of heat distribution. Mubaraki [8] provided an analytical formulation of static heat transfer in a heterogeneous multilayer composite cylinder using the variable separation method to derive a general solution in series form for a multilayer body. The approach is based on a simple and efficient solution away from complex numerical and transformational methods. The model has been validated across three initial configurations, enhancing its applications in engineering, materials science and solid mechanics.

Tokovyy [9] presented a two-dimensional analytical technique of the heat field in hollow cylinders composed of thermally regressive layers, which addresses the continuous change in properties through direct integration to reformulate the conduction equation into second-order integration equations. The solution is built across the solvability core to reflect the explicit relationship between heat load and the gradual distribution of properties. The method allows you to manipulate an unlimited number of layers without the need for complex global differentiators. Chen [10] introduced a shell conduction model to simulate heat transfer within a thin, multi-layer wall in thermoelectric anti-snow systems. The model creates a virtual volumetric grid based on a surface grid, corrects cell areas according to convexity, and applies thermal conductivity equations using the finite volume method. The model has verified its accuracy in annular, cylindrical, and wing-length shapes.

DQM has emerged as a powerful numerical technique for solving complex heat transfer problems, particularly in multilayer and functionally graded material systems. Recent advances demonstrate its effectiveness in various engineering applications with high accuracy and computational efficiency. Afridi et al., presented a generalized differential quadrature framework for modeling heat transfer in boundary layer flows with nonlinear convection effects. The research demonstrates the versatility of DQM in handling complex boundary conditions and nonlinear phenomena, making it particularly suitable for practical engineering applications, including heat exchangers and thermal management systems. The method shows superior convergence properties compared to traditional finite difference approaches [11]. Afridi et al., again demonstrated the method's capability in handling coupled thermal phenomena, including frictional heating and radiation effects, using the implementation of generalized DQM for entropy generation analysis. This work established DQM as an effective tool for optimization studies in thermal systems, providing insights into energy efficiency and thermal performance enhancement [12]. Zhang et al., focused specifically on cylindrical geometries with functionally graded materials, presenting a mathematical model and numerical technique using DQM for heat conduction analysis. The research validated the

effectiveness of DQM in handling variable material properties in cylindrical coordinates, which is directly relevant to multilayer cylinder applications [13].

The development of gear-generalized DQM represents a significant advancement in handling time-dependent problems with variable material properties. This approach is particularly valuable for transient heat transfer analysis in multilayer systems where material properties vary with temperature and time, offering improved stability and accuracy for oscillatory phenomena [14]. An article by Ghadimi et al., demonstrated the application of advanced numerical methods including finite element analysis for transient thermal problems in multilayer cylindrical structures. The study provided validation frameworks that can be adapted for DQM implementations, particularly for cryogenic applications where accurate thermal modeling is critical [15]. Das et al., provided benchmark solutions that can validate DQM implementations using the comprehensive analysis of functionally graded material cylinders with multiple layers. This work established analytical frameworks in polar coordinates that complement numerical approaches, offering verification standards for DQM applications in multilayer systems [16]. These recent publications (2023-2025) provided a strong foundation for DQM applications in heat transfer analysis, particularly for:

- Nonlinear and coupled phenomena - Advanced DQM formulations for complex physics
- Functionally graded materials - Specialized techniques for variable property systems
- Transient analysis - Time-dependent formulations with improved stability
- Validation frameworks - Benchmark solutions and experimental validation approaches
- Cylindrical geometries - Specific applications to multilayer cylinder configurations

The literature demonstrates the continued evolution and validation of DQM as a premier numerical technique for sophisticated heat transfer problems in engineering applications. This study is concerned with transient heat transfer in multilayer cylinders, a topic that has been studied using the DQM method rarely. This method offers an accurate and quick solution, making it ideal for analyzing heat distribution in these complex systems. This research also contributes to improving the design of multilayer materials, especially in applications that require accurate and reliable heat transfer, such as heat transfer pipes and insulating materials.

Despite the versatility of DQM in various domains, its specific application to transient heat conduction in multilayered cylindrical geometries with distinct thermophysical properties remains underexplored in recent literature. Previous studies [11–16] have largely focused on single-layer functionally graded materials or steady-state analyses. This research bridges this gap by formulating a DQM-based solution that explicitly handles the discontinuity of properties at layer interfaces in the time domain. The primary aim of this study is to establish a robust numerical framework based on DQM for predicting transient temperature distributions in multilayered cylinders. The specific objectives are: (1) to derive the DQM formulation for the transient Fourier heat conduction equation in cylindrical coordinates; (2) to validate the proposed method against standard Finite Element benchmarks (ANSYS); and (3) to conduct a comprehensive parametric study analyzing the effects of layer thickness, heat capacity, and thermal conductivity on thermal performance.

2. Methodology

The Distortion Energy Theory shear equation might not be sufficient with newly-developed drill pipes that have highly advanced material properties….

2.1. Governing Equations

In The hypotheses adopted by the mathematical model in this research are: Axial symmetry (Axisymmetry): It was assumed that the temperature distribution is symmetrical around the axis of the cylinder. This allows the equation to be simplified to one radial (r) and time (t). Heat transfer in the axial (θ) and perpendicular (z) directions has been neglected, reducing computational complexity and making the problem numerically solvable. Assume that the coefficient of thermal conductivity (k_r), density (ρ), and heat capacity (c_p) do not depend on temperature. This converts the equation into linear form and facilitates the solution. The effect of moisture in the heat equation has been neglected, simplifying the system to a pure thermal equation. It was assumed that each

layer in a multilayer cylinder has homogeneous physical properties within its boundaries (not differing with the radial location within the layer). The general Fourier equation of heat in cylindrical coordinates was employed at the beginning of this analysis [17]:

$$\rho c_p \frac{\partial T}{\partial t} = \frac{1}{r}\frac{\partial}{\partial r}\left(k_r r \frac{\partial T}{\partial r}\right) + \frac{1}{r^2}\frac{\partial}{\partial \theta}\left(k_\theta \frac{\partial T}{\partial \theta}\right) + \frac{\partial}{\partial z}\left(k_z \frac{\partial T}{\partial z}\right) \quad (1)$$

Assuming axial symmetry and heat transfer only in the radial direction, the equation is simplified to:

$$\rho c_p \frac{\partial T}{\partial t} = \frac{1}{r}\frac{\partial}{\partial r}\left(k_r r \frac{\partial T}{\partial r}\right) \quad (2)$$

Where ρ is the density kg/m^3, c_p is the specific heat capacity $J/kg\ K$, T is the temperature t is time s, r is the radial coordinate, m, and k_r is the thermal conductivity in the radial direction W/mK. Chebyshev-Gauss-Lobatto points were used in the radial direction to ensure the stability of the solution:

$$r_i = \frac{a+b}{2} + \frac{b-a}{2} cos\left(\frac{(i-1)\pi}{N-1}\right), i = 1,2,\dots,N \quad (3)$$

Where a , b are the inner and outer radius of the cylinder, the second derivative of the degree n at the point r_i is rounded as follows:

$$\left.\frac{\partial^n T}{\partial r^n}\right|_{r_i} = \sum_{j=1}^{N} A_{ij}^{(n)} T(r_j) \quad (4)$$

Where $A_{ij}^{(n)}$ are the weight coefficients derived from Lagrange polynomials. An even or adaptive time distribution was used to rapid changes in temperature. The first derivative of time is rounded by:

$$\left.\frac{\partial T}{\partial t}\right|_{t_k} = \sum_{m=1}^{M} B_{km}^{(1)} T(t_m) \quad (5)$$

Where $B_{km}^{(1)}$ are the temporal weight coefficients, after applying the DQM to the thermal equation, the system is written in matrix form:

$$M.T = F \quad (6)$$

Where M is the coefficient matrix (includes conduction and heat coefficients). T: temperature vector at all points and time moments. F: boundary conditions vector and heat sources.

2.2 Numerical Analysis

MATLAB was used as the main software to solve the recent equations numerically. While ANSYS was employed as a finite element tool to validate the MATLAB code, which is used for DQM. The model was sketched with the design modular tool in Workbench ANSYS 2023 R2 as half of a multilayered cylinder to reduce analysis time, and since it is symmetric, as shown in Fig. 1. Where the inner radius is 0.1m and the outer radius is 0.5 m., with fixed layer thickness. The mesh type employed in this analysis is shown in Fig. 2.

The Transient thermal solver was used to simulate this analysis with fine meshing (i.e., element size of 10 mm). The minimum mesh quality reached 91 % with the HEX20 element type. The analysis time taken was 300 s, while the boundary conditions are 200 ºC on the inner edge and 300 ºC at the outer edge, as shown in Fig. 3.

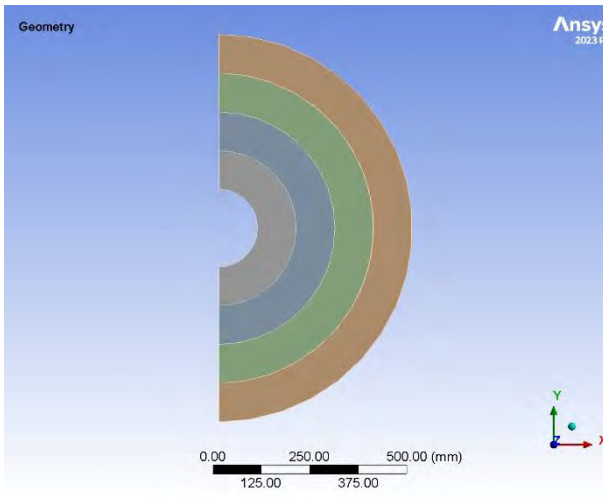

Fig. 1. ANSYS model

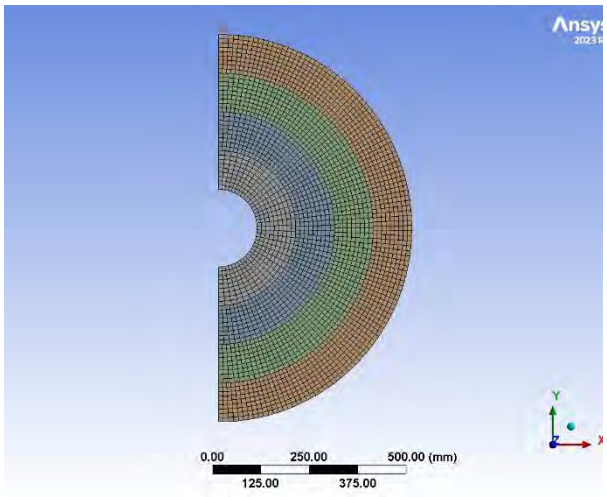

Fig. 2. The meshing of the model

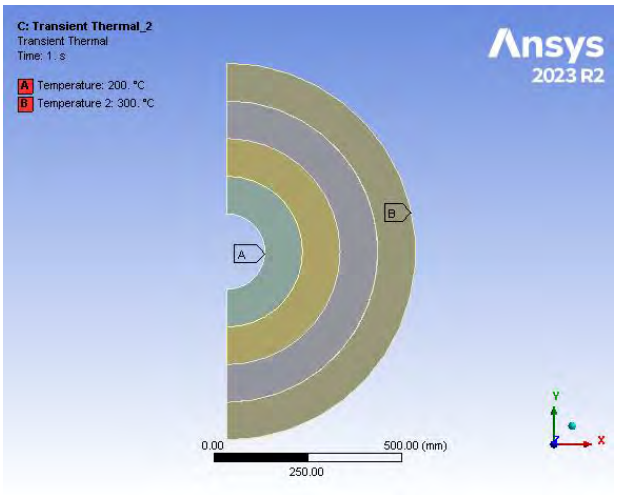

Fig. 3. The applied boundary conditions to the model

To ensure solution stability and accuracy, a grid independence test was performed. The spatial domain was discretized using non-uniform Chebyshev-Gauss-Lobatto points to cluster nodes near the boundaries where gradients are expected to be high. A mesh size of N=11 points per layer was found to be sufficient for convergence, as further refinement yielded negligible changes in temperature results (< 0.1%). The time integration was performed with a variable time step to capture the rapid initial transient response.

3. Results and Discussion

MATLAB software was used for the purpose of solving equations for the DQM and applying the boundary conditions represented by the inner radius of the cylinder of 0.1 meters and the outer diameter of 0.5 meters, and the temperature was applied in the inner layer at 200ºC and at the outer layer at 300ºC. Fig. 4 shows the distribution of temperature along the radius of the cylinder at several times during heat transfer – it can be seen that the edge conditions at the inner and outer surfaces, as well as the continuity of heat at the interlayer interfaces were achieved quite accurately in the numerical solution. In the first moments, the heat curve is low throughout the thickness (e.g. at about t = 0), then the temperature gradually increases over time in all internal positions with the cylinder boundary remaining at its specified values (200 at the inner surface and 300 at the outside). Over time, temperatures within each layer rise until they eventually reach a semi-stable state. Fig. 4 clearly shows that as time progresses from 0 to 100 and then 300 to 1000 seconds, thermal curves rise in each radius, indicating that the internal material gradually warms up and approaches stability.

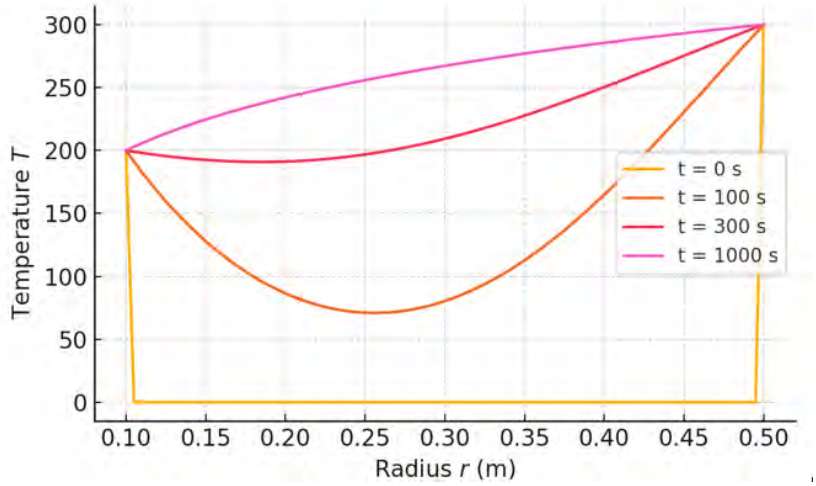

Fig. 4. Temperature distribution along the cylinder radius with different periods

Fig. 5 illustrates the temperature change over time in the middle of each of the four layers at radii (r=0.15, 0.25, 0.35, 0.45). The temperature at each of these points starts at a low value (close to zero in our reference state where we consider the inner material to be initially cold), then rises rapidly at first and gradually slows down as it approaches thermal stability. It can be seen about t≈800–1000 seconds, there are almost no temperature changes over time in all layers, which means reaching a steady state (constant temperature relative to time) that corresponds to physical expectations where heat balances across thickness and gradients become constant. Fig. 5 shows that the layer closest to the outer surface (at r=0.45 m) reaches a higher temperature (about 280–290) and precedes the inner layers in approaching their final value due to their proximity to the hot limit (300 ºC), while the layer closest to the cold inner surface (at r = 0.15 m) is the least hot (settles near 210 ºC) due to its proximity to the cold limit (200 ºC). In general, all layers converge to constant temperatures over time as seen in flat curves after a long time. It was noticed that the temperature rises rapidly at first and then the curves reach an almost constant value after a long time (thermal stability).

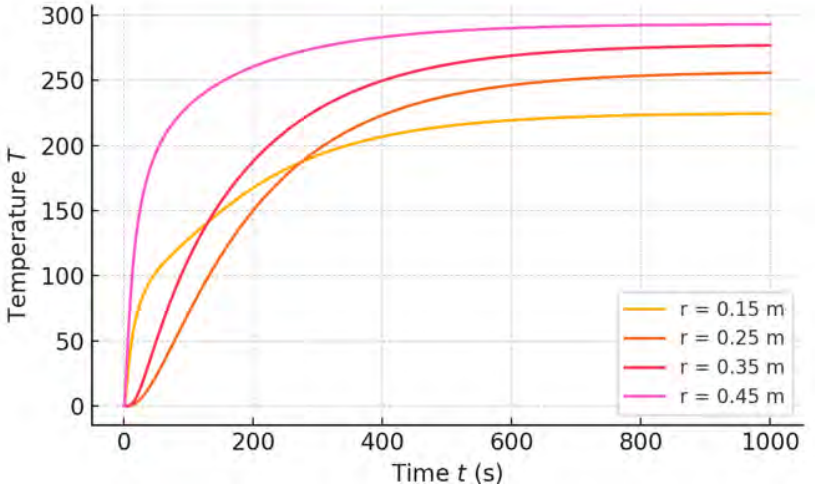

Fig. 5. Temperature distribution across time for each layer

After understanding the basic behavior, the effect of changing heat capacity, thermal conductivity, and layer thickness was studied using the same model. Here are the main findings: The base state (all layers have the same heat capacity) was compared with two cases, one in which the heat capacity of the inner layer is higher than the other, and the other where the heat capacity of the outer layer is higher as shown in Fig. 6. The diagram shows that increasing the heat capacity of the inner layer leads to a decrease in temperature near the inner radius compared to the baseline state, as the larger capacity inner layer absorbs more heat energy before it heats up, keeping it relatively

colder. Similarly, increasing the heat capacity of the outer layer reduces the temperature near the outer surface because the outer layer stores more heat without significantly increasing its temperature. It can be seen from the orange curve (high internal capacity) in Fig. 6 that it is the basic yellow curve at the inner (about 0.1–0.2 m), and the pink curve (high external capacity) comes below the base at the outer (about 0.4–0.5 m). These results are consistent with the theoretical expectation that increasing the heat capacity of any layer delays its warming, making it instantaneously below the reference state in that region.

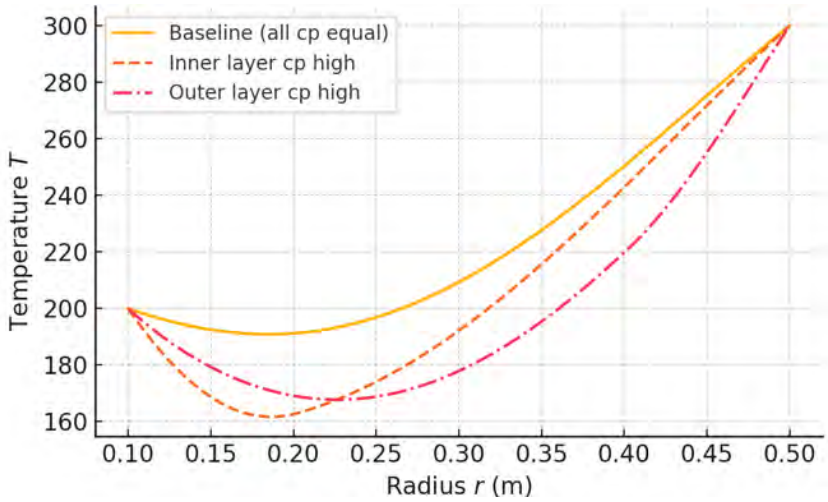

Fig. 6. The effect of heat capacity

Two cases were studied with regard to the thermal conductivity coefficient as in Fig. 7: increasing the conductivity coefficient of the inner layer (from 400 to 1200 W/m·K) with the rest of the layers remaining at the original value of 400, then increasing the conductivity coefficient of the outer layer (to 1200) while remaining 400. The diagram shows that raising the conductivity coefficient of the inner layer leads to a rise in temperature near the inner side, as the high-conductivity inner layer transfers heat more quickly than the adjacent layers, gaining more heat than the hot outer surface through the middle layers, raising its temperature from the base state. Similarly, an increase in the conductivity coefficient in the outer layer raises the temperature near the outer surface because the outer layer itself heats up faster when in contact with the hot surface and transfers heat more efficiently inside. In Fig. 7, the dashed orange curve (higher conductivity of the interior) lies above the basic yellow curve at areas near r=0.1–0.2 m, and the pink dashed curve–dot (higher conductivity of the outer layer) is above the yellow at r=0.4–0.5 m.

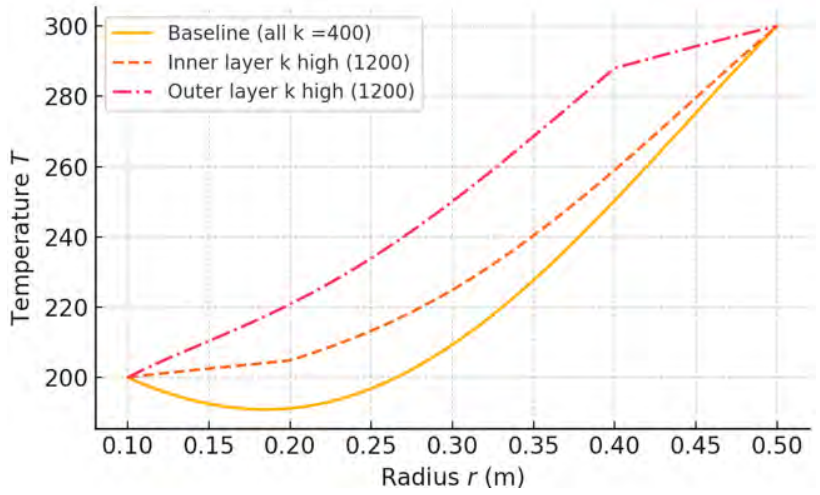

Fig. 7. The effect of thermal conductivity

A case was adopted in which the conductivity coefficient of the outer layer is high (1200) and the rest of the layers are 400 (as in Fig. 8), then the thermal distribution was compared when changing the thickness of the outer layer while keeping the total number of layers four. The basic case of this comparison is when the thicknesses of the layers are equal (0.1 m each from 0.1 to 0.5 m). The second case is when the outer layer is thicker (e.g. 0.2 m) and the three inner layers share the remaining thickness (0.2 m spread over three thinner layers). The third case is reversible: the outer layer is thinner (0.05 m) and the inner layers are thicker to compensate for the rest. Fig. 8 shows that when the outer layer of high conductivity is thicker, the temperature rises at all radii compared to the base state while reducing the thickness of the outer layer with high conductivity leads to a decrease in temperature at all radii.

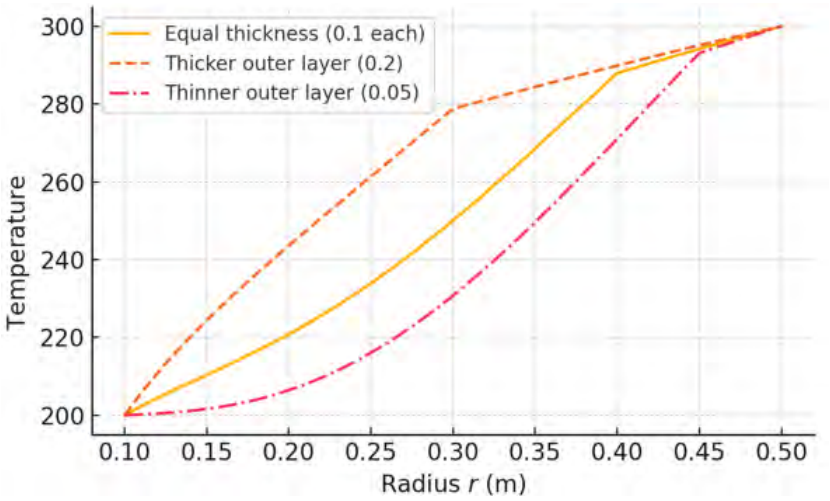

Fig. 8. The effect of different outer layer thicknesses

The reason is that the thicker the high-conductivity outer layer, the higher the overall thickness ratio with higher conductivity, so the heat moved more efficiently deeper inward, raising the temperature of all layers. When the high-conductivity outer layer is too thin, the bulk of the thickness is lower, slowing heat diffusion and lowering internal temperatures. In Fig. 8 the dashed orange curve (thick outer layer) is above the yellow curve (equal thicknesses) across the range, while the pink dashed curve-dot (thin outer layer) is below the yellow across most of the range, confirming the above conclusion.

Similarly, the case of the inner layer with a high conductivity coefficient (1200 W/m·K) and the rest of the layers was adopted as 400 W/m·K, and then the thermal distribution was compared when the thickness of this inner layer increased or decreased. Fig. 9 shows that increasing the thickness of the high-conductivity inner layer leads to a decrease in temperature across the radius (below the base state at all positions, while reducing the thickness of the outer layer (in the same case as the inner layer with high conductivity) leads to a rise in temperature at all positions. The explanation here is slightly different: when the high-conductivity inner layer is thick, it quickly transfers heat to the cold inner surface and dissipates it, keeping most of the thickness cooler (So the dashed orange curve under the yellow reference curve in Fig. 9). When the inner layer of high conductivity is of normal thickness but the outer layer becomes thinner (i.e. the part with low conductivity has become smaller), a larger part of the total thickness is of high conductivity (the inner layer itself + the layers with the highest conductivity expands outward), and the effect of external heating is transmitted more efficiently across most of the thickness, rising temperature everywhere (pink dashed curve-dot over yellow). It should be noted that the two cases of Fig. 9 show opposite but independent effects: increasing the thickness of the high-conductivity layer on the cold side cools the inside, while reducing the thickness of the layer on the hot side (or its equivalent by increasing the thickness of the inner layers at the expense of the exterior) heats the inside – which is exactly what the two comparisons achieve in the figure.

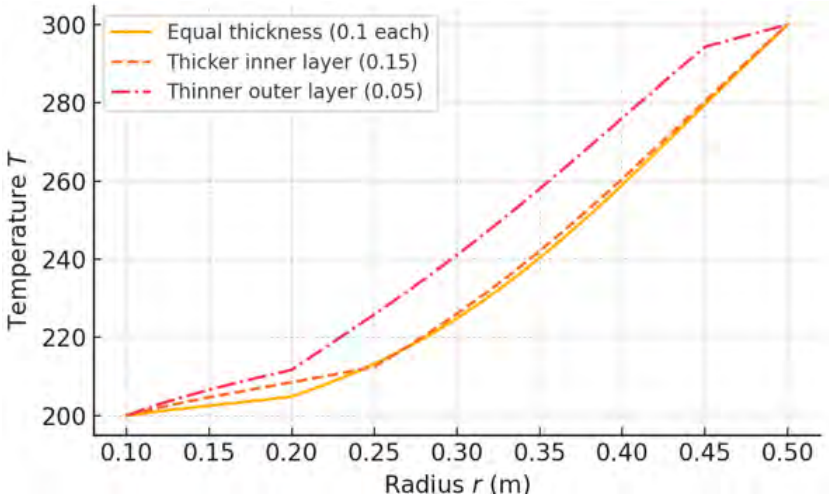

Fig. 9. The effect of inner layer thickness

The problem at hand was reconstructed using ANSYS software to simulate transient heat transfer in a multilayer cylinder under the same conditions as the original study that adopted the differential squaring method. These conditions were represented by a hollow cylinder with an inner radius of 0.1 m and an outer radius of 0.5 m, radially divided into four layers of equal thickness (0.1 m per layer). A constant temperature of 200 °C was applied to the inner limit, and to the outer limit of 300 °C uniform physical properties were adopted in all layers (density ρ=8000, kg/m^3., thermal conductivity k=400 W/m.K), with a uniform value of specific heat capacity, c_p. for all layers (c-p.=1000 J/kg. K). The simulation was run up to a time of t=100 seconds, and the temperature distribution across the radius was monitored at this time. To achieve spatial accuracy, a finely divided radial grid (each layer contains a sufficient number of elements) was used to ensure convergence of results, and emphasis was placed on calculating temperatures at selected locations (mid-layer at r = 0.1, 0.15, 0.2, 0.25, 0.3, 0.35, 0.4, 0.45, and 0.5 m). The comparison between the ANSYS results and DQM is presented in Fig. 10 and

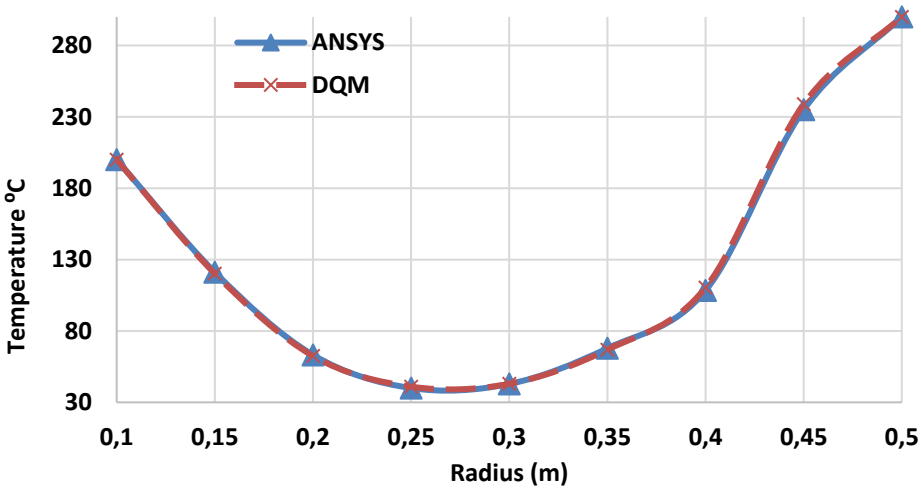

Fig. 10. Results comparison between ANSYS and DQM

The ANSYS temperature results are shown in Fig. 11. Table 1 shows the temperature values calculated for different radius values, by both the DQM approach and using ANSIS. Temperature values are found to be very similar in both approaches, with differences not exceeding multiple degrees, where the maximum error percentage reached 2.4 %. Figure 11 shows the temperature results generated by ANSYS simulation of a multilayer cylinder, with thermal distribution across the radius at 100 seconds.

Table 1. The Comparison between the results of ANSYS and DQM.

Radius (m)	T °C (ANSYS)	T °C (DQM)	Error (%)
0.1	200	200	0.00%
0.15	121.18	120.2	0.81%
0.2	63.229	62.5	1.15%
0.25	40.014	41	2.40%
0.3	42.889	43	0.26%
0.35	67.866	66.9	1.42%
0.4	108.34	110.4	1.87%
0.45	234.94	238.87	1.65%
0.5	300	300	0.00%

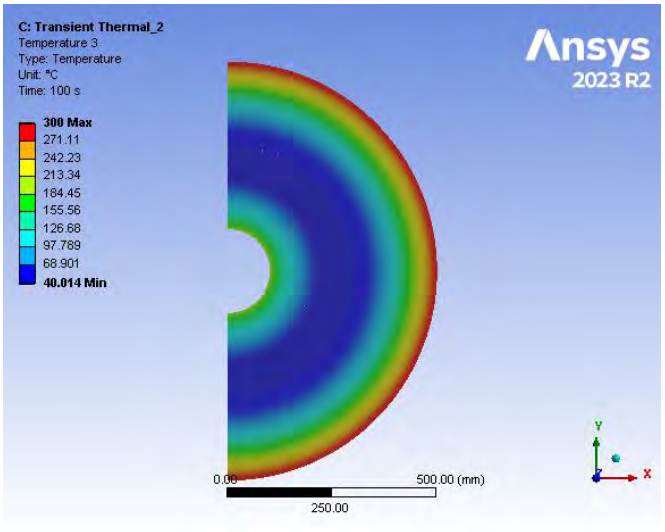

Fig. 11. ANSYS temperature results

4. Conclusions

This study successfully developed and validated a novel numerical approach for analyzing transient heat transfer in multilayered cylindrical structures using the Differential Quadrature Method (DQM). The investigation represents the first comprehensive application of DQM to solve the transient Fourier heat conduction equation in multilayered cylinders with distinct material properties, addressing a significant gap in the numerical heat transfer literature. The DQM implementation demonstrated exceptional accuracy and computational efficiency compared to conventional numerical approaches. The validation against ANSYS finite element simulations confirmed the reliability of the proposed model, achieving a high degree of agreement with maximum relative errors restricted to 0–2.4% across all radial positions. This validates the DQM as a powerful alternative to traditional Finite Difference or Finite Element methods, offering high precision with significantly fewer grid points.

Parametric studies provided profound insights into the thermal behavior of composite cylinders. It was observed that:

- Heat Capacity: Increasing the heat capacity of specific layers acts as a thermal buffer, effectively delaying the local temperature rise. Specifically, a higher capacity in the inner layer maintains lower temperatures near the core for longer durations.
- Thermal Conductivity: Variations in thermal conductivity create preferential heat flow paths. A high-conductivity outer layer accelerates heat ingress from the external boundary, raising the overall temperature profile of the cylinder more rapidly than modifications to inner layers.

- Layer Thickness: Geometric configuration plays a crucial role; increasing the thickness of insulating layers (low conductivity) significantly dampens the transient thermal response.
- Transient Behavior: All configurations demonstrated expected thermal evolution from initial conditions to steady-state, validating the physical consistency of the numerical model.

The novel contribution of this work lies in the algorithmic formulation that seamlessly handles interface conditions in multilayered media without the need for complex mesh generation techniques required by FEM. Future research will extend this DQM framework to handle non-linear heat conduction problems where material properties are temperature-dependent, as well as non-Fourier heat conduction models for micro-scale applications. The presented method provides engineers with a rapid and accurate tool for the preliminary design and optimization of thermal insulation systems in piping and aerospace structures.

References

[1] Eziefula UG. Analysis of inelastic buckling of rectangular plates with a free edge using polynomial deflection functions. Int Rev Appl Sci Eng. 2020 Apr;11(1):15-21. https://doi.org/10.1556/1848.2020.00003
[2] Mutar DM. Numerical simulation study for double pipe heat exchanger with spiral fins. Pollack Periodica. 2025 Apr. https://doi.org/10.1556/606.2024.01229
[3] Saadatfar M. Transient solution of heat and moisture transfer in a functionally graded hollow cylinder with finite length. Mech Adv Compos Struct. 2022;9(1):49-57.
[4] Heydarpour Y, Malekzadeh P. Three-dimensional non-Fourier heat transfer analysis of multilayer functionally graded graphene platelets reinforced composite truncated conical shells. Heat Transf Eng. 2021 Aug;42(15):1303-18. https://doi.org/10.1080/01457632.2020.1785700
[5] Pourasghar A, Brigham J. Thermoelastic analysis of cylindrical panels by hyperbolic heat conduction. In: Volume 2: Computer Technology and Bolted Joints; Design and Analysis. American Society of Mechanical Engineers; 2022 Jul. https://doi.org/10.1115/PVP2022-84966
[6] Heydarpour Y, Malekzadeh P, Zhu H, Mohammadzaheri M. Non-Fourier heat transfer analysis of sandwich conical shells with GPLs reinforced face sheets and porous core under moving heat flux. Results Phys. 2025 Jun;73:108240. https://doi.org/10.1016/j.rinp.2025.108240
[7] Zhou L, Parhizi M, Jain A. Analysis of multilayer cylindrical thermal conduction with a time-varying convective boundary condition. ASME J Heat Mass Transf. 2024 Mar;146(3). https://doi.org/10.1115/1.4063961
[8] Mubaraki AM, Nuruddeen RI. Steady-state thermodynamic process in multilayered heterogeneous cylinder. Open Phys. 2024 Jul;22(1). https://doi.org/10.1515/phys-2024-0067
[9] Tokovyy YV, Hrytsyna OR, Hrytsyna MR. Explicit thermal analysis of inhomogeneous multilayer cylinders using the direct integration method. Int J Therm Sci. 2024 Feb;196:108654. https://doi.org/10.1016/j.ijthermalsci.2023.108654
[10] Chen N, Yi X, Wang Q, Liu R. Method for simulating heat conduction inside multilayer thin wall. J Thermophys Heat Trans. 2024 Jul;38(3):446-51. https://doi.org/10.2514/1.T6907
[11] Afridi MI, Wakif A, Qasim M, Chamkha AJ. A generalized differential quadrature approach to the modelling of heat transfer in non-similar flow with nonlinear convection. Int Commun Heat Mass Transf. 2024 Jun;155:107508. https://doi.org/10.1016/j.icheatmasstransfer.2024.107508
[12] Afridi MI, Zhang Y, Chamkha AJ, Khan MS. Frictional heating effects on entropy generation with nonlinear Rosseland radiation: Implementation of generalized differential quadrature method. Numer Heat Transf Part B Fundam. 2024 Apr:1-19. https://doi.org/10.1080/10407790.2024.2343330
[13] Zhang B, Long Z, Liu G, Wu Z, Yan Q. Investigating the distribution of heat transfer in a thick-walled functionally graded cylindrical shell under heat flux. J Eng Appl Sci. 2025 Dec;72(1):1. https://doi.org/10.1186/s44147-024-00571-y
[14] Afridi MI, Khan MS, Qasim M, Chamkha AJ. Computational analysis of unsteady oscillatory flow of nanofluid with variable electric conductivity: gear-generalized differential quadrature approach. J Comput Des Eng. 2024 Nov;11(6):20-35. https://doi.org/10.1093/jcde/qwae091
[15] Ghadimi M, Barzegari MM. A numerical transient thermomechanical modeling of the metal-polyamide internal supports for cryogenic vessels. J Therm Anal Calorim. 2023 Nov;148(21):11917-27. https://doi.org/10.1007/s10973-023-12469-7
[16] Das P, Islam MA, Mondal D, Nazim MS. Analytical and numerical (FEA) solution for steady-state heat transfer in generic FGM cylinder coated with two layers of isotropic material under convective-radiative boundary conditions. Heliyon. 2023 Nov;9(11). https://doi.org/10.1016/j.heliyon.2023.e21725
[17] Klausner JF. Fundamentals of heat transfer and thermal physics. In: Encyclopedia of Aerospace Engineering. Wiley; 2010. https://doi.org/10.1002/9780470686652.eae043

Blank Page

Research on Engineering Structures & Materials
www.jresm.org

Research Article

Utilization of high- frequency ultrasonic waves for the demulsification of water/oil emulsions

Hind A. Sami [*,a], Raheek I. Ibrahim [b], Manal K. Odah [c]

Electromechanical Engineering Department University of Technology-Iraq, Baghdad, Iraq

Article Info

Article History:

Received 12 Oct 2025

Accepted 08 Dec 2025

Keywords:

Emulsions;
Separation;
Ultrasound;
Demulsification;
Heavy fuel oil;
High-frequency

Abstract

A significant issue in the petroleum business is the presence of intricate emulsions, with the primary difficulty being the development of an effective separation approach for complex water-in-oil (W/O) emulsions. The development of a rigid layer at the water-oil interface is the source of W/O emulsion stability. This study examined the separation of water-in-oil emulsions by ultrasonic-assisted demulsification. We employed an ultrasonic water bath apparatus operating at a frequency of 40 kHz with a power output of 180 W. The emulsion was formulated using 45% water and 55% heavy fuel oil by volume. To improve separation performance, silica particles measuring less than 53 µm were employed at a concentration of 1000 ppm. We conducted the ultrasonic treatment for 10 minutes at a temperature of 70°C. The results showed that this method achieved a separation efficiency of 78%, emphasizing the important role of ultrasonic energy and silica nanoparticles in breaking up emulsions and speeding up the merging of water droplets. The results showed that the ultrasonic technique is a promising eco-friendly technology, suggesting it could be a practical and environmentally safe way to separate oil and water. Furthermore, the results showed that a chemical-derived emulsification breaker (silica particle) outperformed a commercial emulsification breaker (RQ35) in terms of separation efficiency.

© 2026 MIM Research Group. All rights reserved.

1. Introduction

A primary problem in heavy oil production is the separation of water-in-oil (W/O) emulsions. Emulsified water not only heightens the vulnerability of pipelines and equipment to corrosion [1], but also augments the viscosity of heavy oil, leading to energy loss during transit. Demulsification can be accomplished by many combinations of physical, chemical, or biological processes, as is widely recognized [2]. The heavy oil industry actively utilizes processes such as demulsifier application and electrostatic treatment. An effective demulsifier is frequently utilized to enhance the demulsification process. The primary objective of the chemical additives is to destabilize the emulsifying agents [3]. Tight emulsions may form when water and heavy fuel oil depart an oil well's wellbore due to turbulence in the choke valve at the wellhead. The creation of emulsions during heavy fuel oil production is a costly operational challenge [4]. This occurs when formation water and hydrocarbons are vigorously mixed with surfactants and subjected to shear or turbulence inside the reservoir and production pipelines [5].

The water-to-oil ratio, the oil's intrinsic emulsifier systems, and the source of the emulsion dictate the continuous phases of these mixes. The emulsifiers possess a complex chemical composition and exhibit variability in size and form [6]. The necessity for creative and effective demulsification procedures persists as new oil resources are uncovered and production conditions in older fields evolve. The emulsion must be separated to meet the quality criteria for heavy fuel oil regarding

*Corresponding author: adelhend548@gmail.com
[a]orcid.org/0009-0003-8109-6453; [b]orcid.org/0000-0002-7158-3376; [c]orcid.org/-0000-0002-3406-709X
DOI: http://dx.doi.org/10.17515/resm2025-1248ic1012rs

residual salt and water content before the oil is approved for transportation. Water content must be under 1% [7]. Figure 1 illustrates the overarching issue framework and the sequential stages of the demulsification process (8).

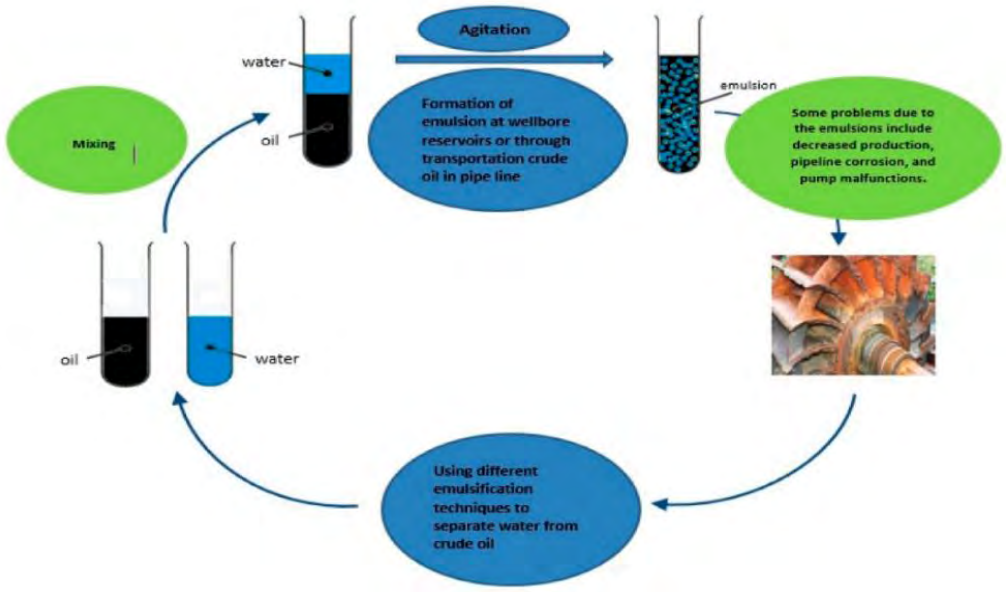

Fig. 1. The general sketch of the problem [8]

The ultrasonic method for demulsifying heavy fuel emulsions relies on condensation and ultrasound's viscosity decrease. Ultrasound causes water droplets to cluster inside heavy fuel oil, separating oil-water phases [9]. Ultrasonic demulsification of heavy fuel oil emulsions is popular due to its simplicity and effectiveness [10]. During ultrasound demulsification, acoustophoresis affects scattered droplets in a standing wave field. The acoustic standing wave can cohesively combine evenly suspended droplets due to density and compressibility differences between the dispersed and continuous phases [11]. Many investigations have shown that ultrasonic energy can demulsify heavy fuel oil emulsions. Temperature, injected water, radiation duration, and radiation energy absorption affect demulsification effectiveness. Ultrasound breaks apart large molecules in oil emulsions, separating oil from water [12]. Sound waves cause minute bubbles in liquid to expand and burst, creating pressures and currents [13]. Some study has promoted ultrasonic technology as a novel and effective way to separate heavy oil from water without demulsifiers [8].

Previous studies have focused primarily on the use of industrial chemicals (demulsifiers) or ultrasound alone, and have often been used on light or medium-grade crude oils. Where it was not used very heavy oil (high viscosity HFO), which contains high levels of asphaltenes and resins. Also, do not use of local natural materials (green demulsifiers) as an environmentally friendly and inexpensive alternative. Inaddition, combining practical analysis with advanced analyses such as FTIR, SEM, XRD, and contact angle to explain the separation mechanism.

Feitosa et al. [14] developed novel cardanol compounds using ethoxylation, formaldehyde polycondensation, hydrogenation, and ethoxylation of formaldehyde polycondensation to test their demulsifier properties. FTIR and ^{1}H NMR measurements were used to describe the additions. Three Brazilian crude oils with 30% brine mixtures and 60 and 240 g/L NaCl salt levels were examined for their capacity to break down emulsions at pH levels 3–10 while agitated at 3200 rpm. We found that ethoxylated compounds need greater demulsification at neutral pH. Saat et al. [15] investigated using coconut oil and its byproducts, notably coconut betaine, to extract water from crude oil mixtures in an environmentally beneficial manner. Each impact research found coconut betaine to be better than coconut oil. At 70 °C, 3 mL coconut betaine in 10 mL crude oil separated 35% water without xylene. Hassan et al. [16] evaluated silica nanoparticles' scientific and commercial benefits for crude oil demulsification. The Balila Central Processing Facility (CPF) in Sudan processes Fula heavy crude oil using an MS Excel model. The primary production cost and net present value (NPV) aspects were sensitivity assessed for numerous flow scheduling options.

Production costs reduce 19% when comparing flow tables with the same plant capacity, but only 3.7% when comparing constant annual crude oil processing. Ye et al. [17] recovered crude oil emulsions using lotus leaves and a simple hydrothermal technique. Their unique wettability and surface shape allow HLLF powder to quickly disrupt W/O emulsions. The DE achieved 88.17% with 1000 mg/L HLLF and 90 minutes at 70°C settling. HLLF's demulsification effectiveness was comparable to numerous commercial demulsifiers. It also demulsified two crude oil emulsions from different oilfields. Azubike et al. [18] evaluated tobacco seed oil, leaf extract, and stem ash demulsifiers on crude oil emulsions. Nicotiana tabacum seed oil, leaf extracts, and stalk ash extract attract and repel water. Formulated demulsifiers are comparable to commercial ones. Bottle testing indicated the demulsifier may destabilize medium- and high-density crude oil emulsions. The novel demulsifier performed like commercial ones.

Chen et al. [19] examined how sound strength, temperature, ultrasound exposure period, and chemical dispersant effect ultrasound water removal from crude oil. Ultrasound was optimal for removing salt from crude oil at 300 W, 90°C, 75 minutes, and 54 mg/L chemical demulsifier. Temperature was the most critical factor, followed by acoustic power, ultrasonic exposure time, and chemical demulsifiers. In a system with 500 mg/L crude oil. Parvasi et al. [10] showed how low-frequency ultrasonography influences oil-water separation. They then conducted studies in a laboratory ultrasonic bath at 25 and 45 kHz without chemical demulsifiers. Experiment with wastewater temperature, ultrasonic power, frequency, and irradiation period on separation efficiency. Under optimal conditions, crude oil emulsion separation efficiency increased 72%. Romanova et al. [20] shown that ultrasonic treatment plus a little additive may break apart stable water-in-oil (W/O) emulsions that are 30 to 45 μm in size and may include "gel." A nano powder AlN suspension in acetone and 1.0 kW ultrasonic treatment eliminated over 99% of the emulsions tested. Depending on the emulsion's composition and qualities, the additive concentration ranged from 4 to 8% vol and the exposure period from 0.5 to 3 minutes. The oil phase may reach 0.5 weight percent water content, whereas the aqueous phase can reach 46 mg L−1 oil concentration using the demulsification technique.

Okereke et al. [21] aims to develop and formulate a cost-effective, environmentally friendly demulsifier utilizing locally sourced raw materials. They conducted an experimental investigation to evaluate its effectiveness in dissolving the crude oil emulsion. The components employed included castor oil, distilled water, starch, camphor, alum, and locally sourced liquid soap. We used a crude oil emulsion sample from a Niger Delta field to evaluate two distinct demulsifier formulations, which we then heated to 60°F. The procedure resulted in the successful use of a demulsifier to segregate water from oil. Abdullah et al. [22] worked on creating two new ionic liquids (ILs) from oleic acid (OA), which is a natural and easy-to-find material, and used them to break down water-in-oil (W/O) emulsions. EAPA-IL and EATA-IL exhibited commendable performance, achieving 100% efficacy at varying doses of demulsifier. The statistics indicated that their performance enhanced with time as their concentration intensified. Furthermore, EAPA-IL and EATA-IL isolated potable water. Gao et al. [23] found reported that they use microscopes, particle size measurements, component analysis, and other methods to understand tiny surface details and how transformer water content changes with different forces during ultrasonic treatment of old oil. The results show that ultrasonic cavitation demulsifies and dehydrates oil samples to 98.24%. As power increases, dehydration follows a "M-type" pattern. Particle size and microscopic investigations show that ultrasonic irradiation disturbs the oil-water interfacial barrier, causing droplets of various sizes to collide, agglomerate, and silt.

Although several studies—such as [21] who employed ultrasonic treatment with nano powder additives, and [23] who investigated ultrasonic demulsification mechanisms in aged oils—have demonstrated the potential of acoustic energy in breaking water-in-oil emulsions, important gaps remain. Most previous works focused on medium-grade or aged crude oils, relied heavily on commercial chemical additives, or required high-energy ultrasonic systems that limit industrial applicability. Moreover, the use of locally sourced, low-cost materials has received little attention, and few studies have systematically examined the combined influence of ultrasonication conditions and particle dosage on demulsification efficiency in very heavy fuel oils with high asphaltene content. In contrast, the present study addresses these gaps by integrating low-frequency

ultrasonication with inexpensive local silica particles and evaluating their combined impact under optimized operational conditions. This approach offers a practical, cost-effective, and environmentally aligned alternative to conventional chemical demulsifiers, advancing the current understanding of scalable demulsification strategies.

2. Heavy Fuel Oils

Heavy fuel oil (HFO) has tar-like viscosity. Bunker fuel or residual fuel oil is a petroleum distillation and cracking byproduct [16]. Thus, HFO is more likely than other fuel oils to include sulfur, nitrogen, and aromatics, which increase combustion emissions [24]. HFO is cheaper than distillates and is used to power marine diesel engines. HFO use and shipment on ships can cause oil spills and discharge harmful compounds and particles such black carbon [25]. HFO comes from petroleum residuals after thermal and catalytic cracking of higher-quality hydrocarbons. Because HFO is often blended with cleaner fuels, its chemical composition might change; carbon levels in blending streams can range from C20 to above C50 [11]. Combined HFOs give specific viscosity and flow for an application. Due to its diversity, HFO has unique physical, processing, and end-use properties. HFO, the final product of cracking, contains paraffins, cycloparaffins, aromatics, olefins, asphaltenes, and molecules containing sulfur, oxygen, nitrogen, and organometals. The ISO 8217 maximum density for HFO is 1010 kg/m3 at 15°C and its viscosity is 700 mm^2/s (cSt) at 50°C[26].

3. Methodology

3.1 Water with Ultrasonic Waves

Ultrasonic baths were designed for cleaning, but sono-chemical research uses them since they are cheap and readily available. The bath coupling fluid is usually submerged in the response vessel, which transports ultrasonic waves. Maintaining isothermal conditions is problematic since the sample's bath placement affects power to the reaction mixture [24]. A Chinese ultrasonic generator, MH-031S was utilized in the experiments. This system is similar to ultrasonic baths, except it includes a metal cover above the transducer at the bottom. Table 1 shows ultrasonic specifications apparatus [27].

Table 1. Specifications of ultrasound cleaner

Device: Ultrasound cleaner	Specifications
Rated Voltage	200-240/50 HZ
power	180 W
Heating power	300 W
Frequency	40 KHZ
Set Time	0-30 min
Set Temperature	70°C

3.2 Magnetic Stirrer

Mixing heavy fuel oil with water and sodium chloride solution using a magnetic stirrer (Model 78-1, JY, Changzhou, China) creates industrial emulsions. A revolving magnetic field causes a stirring rod (or "flea") submerged in a liquid to revolve rapidly, swirling it. A rotating field can be created by stationary electromagnets or a revolving magnet beneath the liquid-filled vessel. Glass containers (beakers or laboratory flasks) are used for most chemical processes, yet glass is transparent to magnetism, therefore magnetic stirring rods work well in them [28]. Separation procedure is shown in Figure 2, and magnetic stirrer device characteristics are stated in Table 2.

Fig. 2. Separation process water/Oil

Table 2. Specifications of 78-1 Magnetic Stirrer

Device: 78-1 Magnetic Stirrer	Specifications
Power Supply	AC 220V/110V 50Hz/60Hz
Speed	0-2400rpm
Motor powers	25W
Heating power	200W
Temperature control range	Room temperature to 100 Celsius
Timer	0-120min
Two-way rotation	yes

3.3 Preparation and Characterization of W/O Emulsions

The Al-Doura refinery in Baghdad, Iraq, supplied Basra Heavy fuel oil, which was used to make water-in-oil emulsions. Table 3 displays this oil's physical characteristics. Heavy fuel oil (55 ml0 with an API density of 15.8 and a water content of 45 ml was used to create water-in-oil emulsions. The heavy fuel oil sample utilized for emulsion preparation had an API density of 15.8 and a kinematic viscosity of 183 mm^2/s at 45 °C. The heavy fuel oil was mixed with a specified volume of 5500 ppm sodium chloride solution in order to prepare the emulsions. At 45 °C, the mixture was agitated using a magnetic stirrer to add water to the oil phase [29]. Various emulsion qualities were prepared: i) 40% water plus 60% heavy fuel oil, and ii) 30% water plus 70% heavy fuel oil.

Table 3: Physical properties of the Basra Heavy oil (Al-Doura refinery)

Heavy fuel oil properties	
sp. gr at 15.6 ºC	0.8724
API at 15.6 ºC	15.8
Density at 15 ºC (g/cm^3)	0.9657
Kinematc Viscosity at 50ºC cst (mm^2/s).	183
Pour point ºC	+3
Carbon residue %w/w	8.1
Sulfur content %w/w	4.5
Water & sediment %v/v	>0.025
Asphaltenes content (wt %)	3.09%
Calorific Value (gross) Keal/kg	10441

For better clarity of the experimental workflow, a schematic diagram illustrating the main stages of emulsion preparation, ultrasonic treatment, and phase separation has been added (Figure 3). The diagram includes the magnetic stirring stage for emulsion formation, silica particle addition, ultrasonic bath treatment, and final gravitational separation. Additionally, all experimental setup

figures (magnetic stirrer and ultrasonic bath) have been improved with clear labeling of key components to enhance readability.

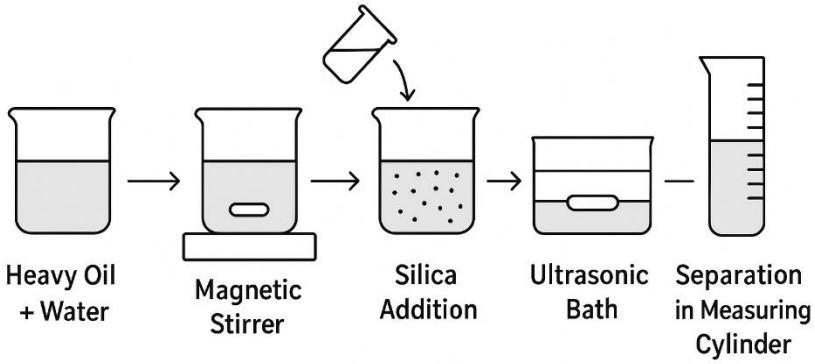

Fig. 3. Emulsion preparation and separation stages

From an economic and environmental viewpoint, silica particles represent a low-cost, widely available, and non-toxic alternative to conventional chemical demulsifiers, reducing both operating cost and secondary pollution risks. In terms of scalability, the combined silica–ultrasound system can be easily integrated into existing refinery separation units with minimal modifications. Moreover, silica can be recovered and potentially reused, enhancing process sustainability and overall cost efficiency. Therefore, this approach offers a practical green demulsification technology that balances efficiency, scalability, and environmental safety.

4. Ultrasonic De-emulsion Experiments

During every experiment involving ultrasonic baths, 100 milliliters of water/oil emulsion were moved into a Becker glass vessel. The vessel was then placed within the ultrasonic bath for 10 minutes at a frequency of 40 kHz, depending on the mode that produced the highest demulsification efficiency. A mixture of 45% water and 55% heavy fuel oil was used in the experiments to test the impact of various frequencies on the emulsion's ability to be removed using ultrasonic baths. The ultrasonic baths were kept at 35°C in temperature. Before each experiment, the vessels containing the oil/water emulsion were kept for 24 h before inserting them into the ultrasonic bath device to maintain the stability of the emulsion. After exposure to ultrasound in the water bath, the conical glass vessels were removed from the ultrasonic baths and emptied into measuring cylinders and left for five minutes after which the reading was taken. The demulsification efficiency (ED) was determined for all experiments in which the water-emulsion separation was visually observed by taking into account the initial water content in the emulsion prior to ultrasound (IWC) and the final water content obtained following ultrasound exposure (FWC), as stated in the following equation (11):

$$ED\% = \frac{I_{WC} - F_{WC}}{I_{WC}} \times 100 \quad (1)$$

Where; I_{WC}: The initial water content in the emulsion before ultrasound, F_{WC}: The final water content obtained after ultrasound exposure.

Cannon-Fenske-Routine Viscometer (ν) was used to determine the kinematic viscosity of heavy oil. The relationship applied to calculate the kinematic viscosity is (30):

$$\nu = K \times t \quad (2)$$

The instrument constant k refers to the timing marks during the visual survey of the meniscus passage. It comes to: k=0.02688 mm^2/S^2.

5. Result and Discussion

5.1 Relationship Between Water Concentration and Silica Addition Ratio At 10 Minutes

Effect of time and temperature on separation efficiency will be considered in the following subsections. Also, 15 experiments were used to determine the separation efficiency of this material.

5.1.1 Separation Efficiency for The Four Days

When testing sample shown in Figure 4 and placing it in the ultrasonic device for 10 minutes before adding any material, the separation ratio was 32% on the first day, and when leaving it for the second day, the separation ratio increased to 34%. While when adding 5000 ppm of silica, that notice a slight increase in the separation ratio, which became 36% on the first day, while on the second day it was 41% as shown in Figure 5.

Fig. 4. Samples of the Separation: a) Before any addition, b) 5000 ppm of silica, and c)10000 ppm of silica at 10 min.

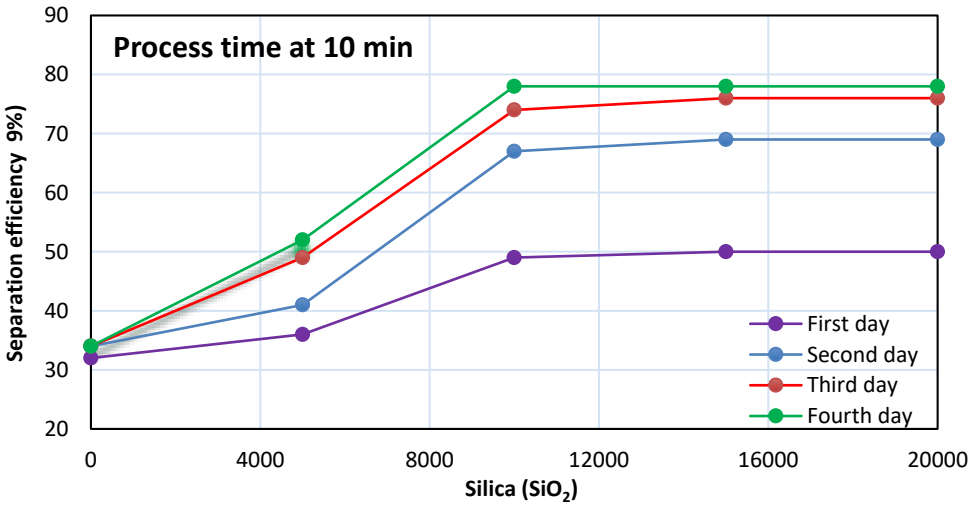

Fig. 5. Water concentration and silica (SiO_2) addition

With the rise in silica content, the separation ratio markedly escalates, peaking at roughly 10,000 ppm. The silica particles serve as nucleation sites for water droplet formation, so optimizing the reversing process and improving the separation of water from oil. Beyond this juncture, the separation ratio either stabilizes or experiences a modest decline, signifying saturation or detrimental effects at elevated doses. Day 2 (red curve) separation ratio increased at identical dosages compared to Day 1 (black curve). This spike may be caused by sample features like oil-water equilibrium or ultrasonic cumulative effects. At concentrations beyond 10,000 ppm, the two curves converge, indicating system efficiency. After two more days, the separation efficiency rose to 49% on the third day and 52% on the fourth, but the ratio did not alter. Silica can cause

agglomeration or bigger particles than drops. Large oil or water molecules make it easier to separate them, making oil and water separation easier. The separation efficiency ratio remains constant upon the addition of silica due to surpassing the optimal concentration. Exceeding this concentration of silica may result in the production of irregular clumps or adverse effects that diminish separation effectiveness. The characteristics of the fundamental combination, including the oil-to-water ratio, viscosity, and surface tension, may be incongruent with the influence of silica.

5.1.2 Effect of Temperature on Oil/Water Separation Efficiency

An increase in temperature leads to a reduction in heavy fuel oil viscosity and a greater density difference between the continuous and dispersed phases. These effects collectively enhance droplet mobility, promote coalescence, and weaken the interfacial stabilizing layer, ultimately improving the efficiency of oil–water separation. Heat may increase the mobility of microscopic water molecules, which collide to form bigger molecules and make droplets easier to separate. Heat weakens and ruptures the emulsion membrane. The disintegration of small paraffin and asphaltene crystals reduces their emulsification ability. Temperature has both positive and negative effects. Temperature can degrade oil's light components, affecting its volume. It may emit light hydrocarbons, causing turbulence that prevents water droplet aggregation. Water droplets containing oil are also threatened by tiny vapor droplets rising quickly. Figure 6 shows how temperature affects oil/water separation (31).

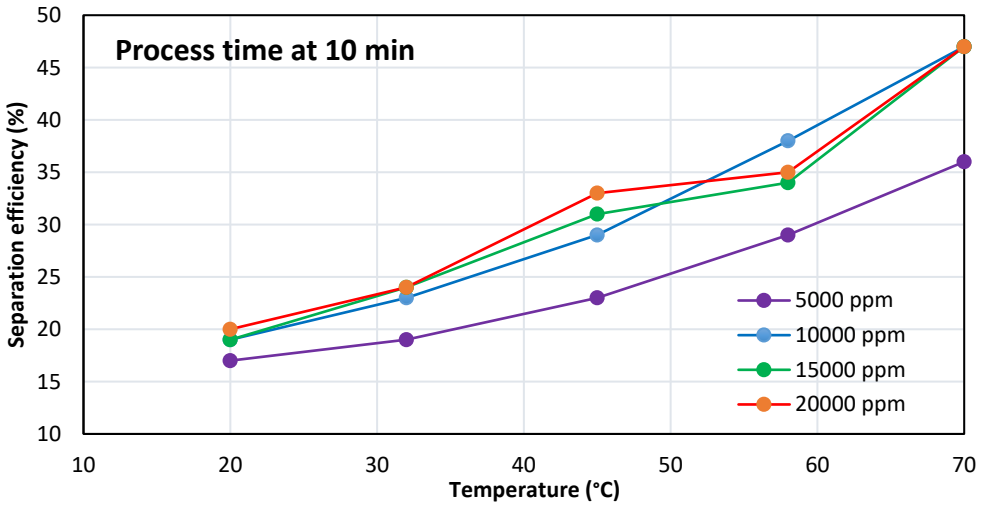

Fig. 6. Effect of temperature on oil/water separation efficiency

5.2 Relationship Between Water Concentration and Silica Addition Ratio At 20 Minutes

Upon evaluating the sample and subjecting it to the ultrasonic device for 20 minutes prior to the addition of any material, the separation ratio was recorded at 34% on the first day, which then rose to 36% on the second day. Upon the addition of 5000 ppm of silica, a marginal enhancement in the separation ratio was seen, increasing to 41% on the first day and 50% on the second day. Upon the addition of 10,000 ppm of silica, a consistent improvement in separation efficiency was seen, reaching 43% on the first day and 50% on the second day, as illustrated in Figure 7. Enhancing surface interactions can expedite the separation process between oil and water, resulting in more effective component separation via altering surface characteristics. Extending the separation duration to 20 minutes may marginally impact the effectiveness of oil/water separation. In physical media, sound waves propagate as vibrations that compress and rarefy the medium, transferring energy from the particles of the material as they oscillate and vibrate. We allowed the samples to enhance the separation efficiency for an additional two days, resulting in a marginal improvement to 40%. Subsequently, on the fourth day, the ratio remained unchanged. Both curves are essentially identical, indicating similar findings and no significant differences between days. Since there is no temporal effect between these two days, the system may be stable and repeatable. Because there

are more silica particles, water mixes back into the oil or the particles combine. Numerous silica particles can form a barrier that hinders water-oil mixing or stabilize the emulsion. At the 20-minute mark, an efficiency variation emerges, potentially signaling the occurrence of supplementary processes over time, such as the redispersion of water or the slow settling of silica particles.

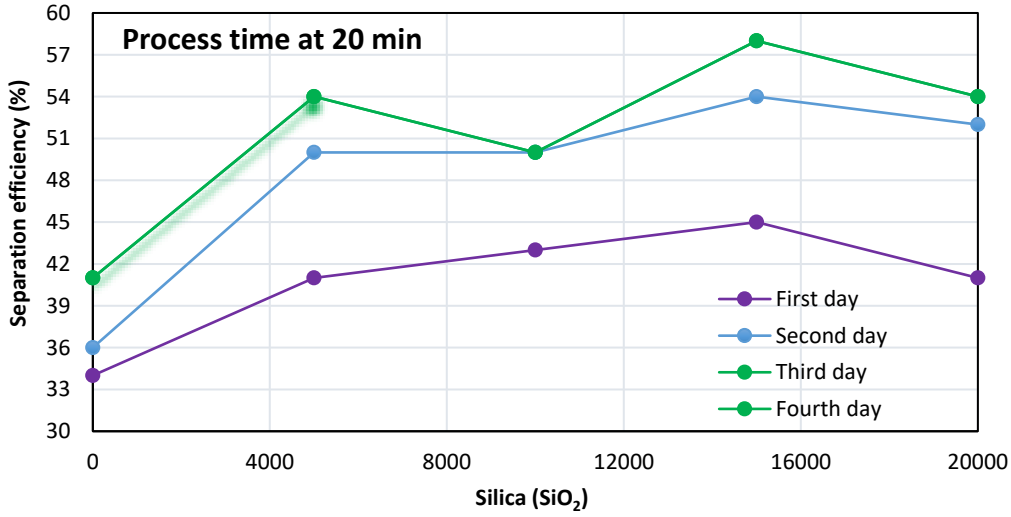

Fig. 7. Water concentration and silica (SiO_2) addition for the four days

5.3 Relationship Between Water Concentration and Silica Addition Ratio At 10 Minutes

The separation rate was 34% on the first day after testing the sample and placing it in the ultrasonic device for 30 minutes before adding any material. The next day, the separation rate increased to 38%. At low concentrations (5,000 ppm), the separation efficiency is minimal (~25-30% on the first day and 35% on the second day). As the concentration of silica rises, the efficiency progressively improves, however lacks a distinct peak observed in prior tests. Figure 8 shows that the separation efficiency stabilized when adding (10000 ppm) and (15000 pm) to 36% on the first day and 47% on the second day, without the decline observed at 20 minutes. This may occur because the particles require more time to scatter uniformly in the medium, resulting in a failure to attain quick saturation, which subsequently diminishes efficiency.

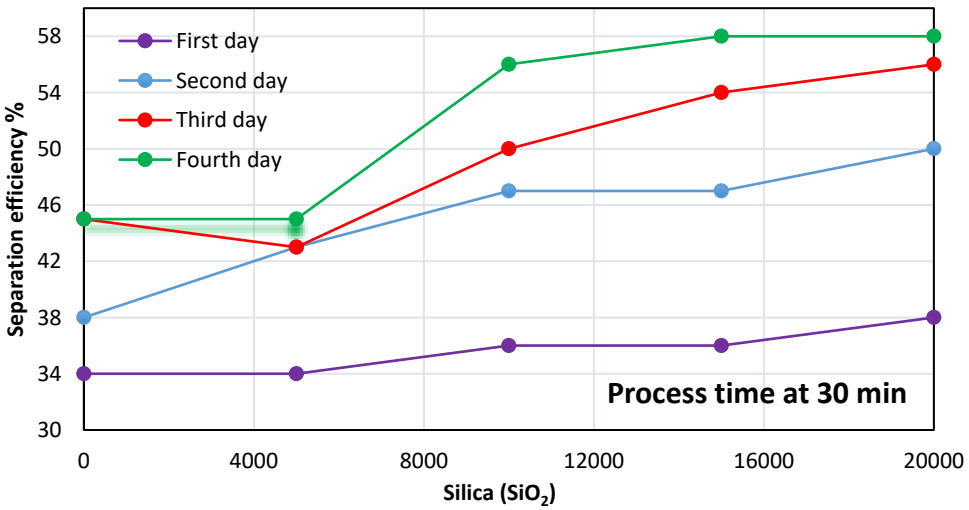

Fig. 8. Water concentration and silica (SiO_2) addition for the four day

The silica particles may exert a cumulative effect, with certain particles persisting in the solution and further enhancing separation after several tests. On Day 1 (black curve), separation efficiency was low and did not grow, suggesting silica had no effect. On Day 2 (red curve), separation efficiency exceeded all concentrations, and the association between concentration and efficiency was almost linear, suggesting silica had a greater impact. The difference between the two days may be due to emulsion stability or silica particle effect. Pressure from ultrasonic waves modifies water-oil interaction, lowering suspended particle size and facilitating separation. Tiny particles separate. Sample separation efficiency rose for two additional days, reaching 54% and 58% on days three and four. Adding 50,000 ppm silica material did not affect the ratio. Silica may stabilize water and oil for a short time before the system stabilizes. When this happens, separation efficiency stabilizes. The balance of contributing elements and silica's process constraints might restrict its separation improvements.

5.4 Effect of Temperature on Oil Viscosity

Heavy oil, a hydrocarbon combination, is viscous at low temperatures and flows poorly. Figure 9 shows that oil viscosity decreases with warming. Heat breaks molecular bonds that slow oil molecules and speeds up flow. As temperature rises, molecules may glide past one other, reducing viscosity and facilitating water-oil separation. Oil and water in the sample may interact at high temperatures, forming more stable emulsions and increasing viscosity. Specific heavy molecules in oil may breakdown at high temperatures, creating viscous substances. Certain substances can interact to change molecular structure and increase viscosity. Gandomkar's source [32]. Table 4 shows a comparison between the studies and the current study.

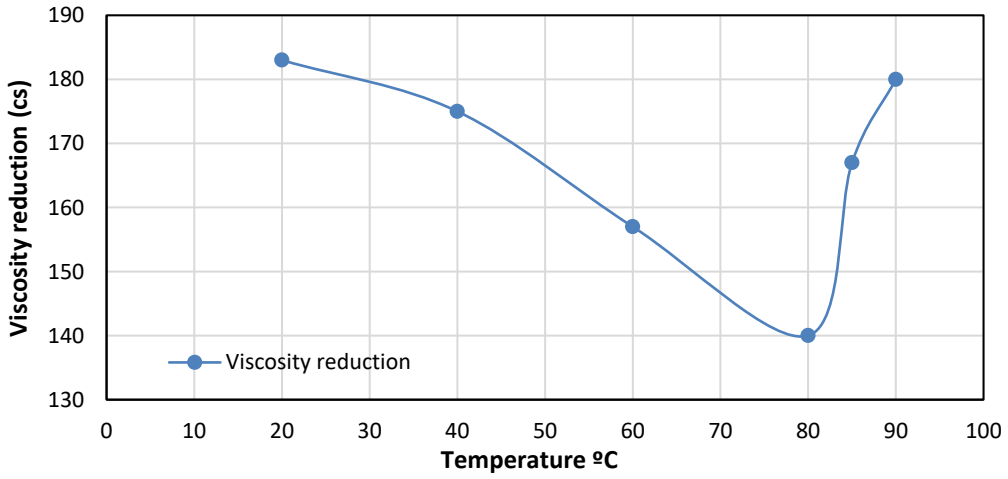

Fig. 9. The impact of temperature on the lowering of ultrasonic viscosity

Table 4. Comparison between the studies and the current study

Researchers	Material used	Results
Current study (Silica particles)	Chemical (Silica particles)	Utilizing ultrasound at a frequency of 40 kHz and a power of 180 W for 10 minutes effectively eliminated up to 78% of heavy fuel oil emulsions
Gao et al. [23]	No demulsifier (ultrasound only)	ultrasonic cavitation demulsifies and dehydrates oil samples to 98.24%.
Okereke et al. [21]	Natural blend (local materials)	achieved over 90% separation efficiency under mild conditions

Although the separation efficiency obtained in the present study is lower than that reported in some previous works such as Gao et al. (2024) and Okereke et al. (2021), this difference can be attributed to variations in oil type, operating conditions, and demulsification mechanisms. Gao et al. achieved very high efficiency (98.24%) using aged transformer oil under optimized ultrasonic

cavitation, whereas the present study targets very heavy fuel oil (HFO) with high viscosity and asphaltene content, which forms highly stable emulsions. Similarly, Okereke et al. reported over 90% efficiency using chemical demulsifiers on lower-viscosity crude oil emulsions, while the present work relies mainly on physical cavitation assisted by silica particles. In addition, differences in ultrasonic power, irradiation time, and temperature also contribute to variations in efficiency. Therefore, despite the lower maximum efficiency, the present results remain competitive considering the extreme stability of HFO, the low cost of silica, and the environmentally friendly nature of the method.

5.5 Commercial Breaker (RQ35) In Breaking Emulsification

Figure 10 shows the results of the commercial emulsification breaker (RQ35) where different concentrations were taken to break the emulsification and the results shown in Table 5 were obtained (33). The commercial breaker gave a low separation rate compared to the prepared natural breaker, but when using a high temperature for the commercial breaker (RQ35), its efficiency increases, and this is what happens in most commercial breakers as they need a high temperature more than (70) m. Therefore, the effect of temperature on the commercial breaker and the prepared breakers was studied to increase the separation efficiency. The commercial emulsification breaker was added at concentrations of (500, 1000, 2000 and 3000) ppm and at different temperatures.

Table 5. Emulsification fraction by commercial breaker (35 RQ)

Amount of demulsifier concentration (ppm)	Amount of water separated (%) Separation time (minutes)					
	10	20	30	40	50	60
500	0	0	0	0	0	5
1000	0	0	0	0	5	10
2000	0	0	5	10	10	15
3000	0	5	10	10	15	20

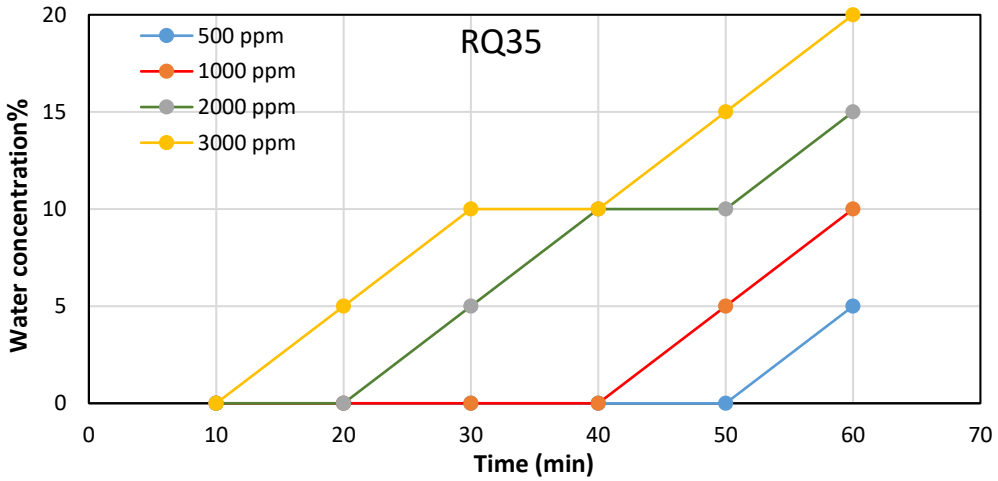

Fig. 10. Relationship between separation ratio and time with commercial emulsion breaker (RQ35)

6. Conclusion

This study demonstrates that applying low-frequency ultrasonication at 40 kHz and 180 W for 10 minutes, particularly at an elevated temperature of 70°C, offers an effective and environmentally conscious method for destabilizing water-in-oil emulsions. Achieving a separation efficiency of approximately 78% using low-cost silica particles highlights the strong capability of acoustic cavitation to weaken interfacial films and promote droplet coalescence. These findings contribute to a deeper understanding of the mechanisms through which ultrasonic energy interacts with

heavy fuel emulsions and provide a foundation for optimizing demulsification strategies in petroleum processing. Beyond its laboratory performance, the method shows clear industrial relevance. Ultrasonic reactors can be scaled up and integrated into existing separation units with minimal modifications, offering a pathway toward practical deployment in refineries and processing facilities. The use of inexpensive and locally sourced silica particles significantly improves cost-effectiveness compared with commercial demulsifiers that often require higher temperatures and present environmental burdens. Additionally, reducing reliance on synthetic chemicals supports greener operational practices and minimizes harmful by-products, aligning the technique with modern industrial sustainability goals. Future research should explore long-term acoustic exposure, the influence of different ultrasonic frequencies, and hybrid separation systems that combine ultrasonication with nanomaterial additives or electromagnetic heating. Advanced analytical characterization could further clarify the interfacial mechanisms involved and support the development of more efficient, scalable, and environmentally friendly demulsification technologies for real-world industrial applications.

Acknowledgement

The authors would like to thank the Electromechanical Department and the oil/Mid land Refineries Company of the Ministry of Oil for assistance in providing materials and testing.

References

[1] Umar AA, Saaid IBM, Sulaimon AA, Pilus RBM. A review of petroleum emulsions and recent progress on water-in-crude oil emulsions stabilized by natural surfactants and solids. J Pet Sci Eng. 2018;165:673-90. https://doi.org/10.1016/j.petrol.2018.03.014

[2] Liu Y, Zhang B, Zhang Y, Ma L, Yang P. Electrochemical polarization study on crude oil pipeline corrosion by the produced water with high salinity. Eng Fail Anal. 2016 Feb 1;60:307-15. https://doi.org/10.1016/j.engfailanal.2015.11.049

[3] Ahmadi MA, Shadizadeh SR. Adsorption of a nonionic surfactant onto a silica surface. Energy Sources, Part A Recover Util Environ Eff. 2016;38(10):1455-60. https://doi.org/10.1080/15567036.2011.652761

[4] Azeez AW, Hussein HQ. Effects of Ultrasonic Treatment and Hydrogen Donor Addition on the Viscosity of Iraqi Heavy Crude Oil. Baghdad Sci J. 2024.

[5] Ngai T, Bon SAF. Particle-stabilized emulsions and colloids: formation and applications. Royal society of chemistry; 2014. https://doi.org/10.1039/9781782620143

[6] Amani M, Idris M, Abdul Ghani M, Dela Rosa N, Carvero A, Yrac R. An experimental study on the application of ultrasonic technology for demulsifying crude oil and water emulsions. J Pet Environ Biotechnol. 2017;8(3):1000330. https://doi.org/10.4172/2157-7463.1000330

[7] Lim CH, Sulaiman SA, Japper-Jaafar A, Bhaskoro PT. Study on the effect of ultrasonic wave amplitude on de-emulsification of crude oil to enhance production process. In: IOP Conference Series: Materials Science and Engineering. IOP Publishing; 2020. p. 12004. https://doi.org/10.1088/1757-899X/863/1/012004

[8] Saad MA, Kamil M, Abdurahman NH, Yunus RM, Awad OI. An overview of recent advances in state-of-the-art techniques in the demulsification of crude oil emulsions. Processes. 2019;7(7):470. https://doi.org/10.3390/pr7070470

[9] Betancourt Cardozo F, Avella Moreno E, Trujillo CA. Structural characterization of unfractionated asphalts by 1H NMR and 13C NMR. Energy & Fuels. 2016;30(4):2729-40. https://doi.org/10.1021/acs.energyfuels.5b02941

[10]Khajehesamedini A, Sadatshojaie A, Parvasi P, Reza Rahimpour M, Mehdi Naserimojarad M. Experimental and theoretical study of crude oil pretreatment using low-frequency ultrasonic waves. Ultrason Sonochem. 2018 Nov 1;48:383-95. https://doi.org/10.1016/j.ultsonch.2018.05.032

[11] Antes FG, Diehl LO, Pereira JSF, Guimarães RCL, Guarnieri RA, Ferreira BMS, et al. Effect of ultrasonic frequency on separation of water from heavy crude oil emulsion using ultrasonic baths. Ultrason Sonochem. 2017;35:541-6. https://doi.org/10.1016/j.ultsonch.2016.03.031

[12] Pedrotti MF, Enders MSP, Pereira LSF, Mesko MF, Flores EMM, Bizzi CA. Intensification of ultrasonic-assisted crude oil demulsification based on acoustic field distribution data. Ultrason Sonochem. 2018;40:53-9. https://doi.org/10.1016/j.ultsonch.2017.03.056

[13] Grenoble Z, Trabelsi S. Mechanisms, performance optimization and new developments in demulsification processes for oil and gas applications. Adv Colloid Interface Sci. 2018;260:32-45. https://doi.org/10.1016/j.cis.2018.08.003

[14] Feitosa FX, Alves RS, de Sant'Ana HB. Synthesis and application of additives based on cardanol as demulsifier for water-in-oil emulsions. Fuel. 2019;245:21-8. https://doi.org/10.1016/j.fuel.2019.02.081

[15] Saat MA, Chin LH, Wong CS. Treatment of crude oil emulsion using coconut oil and its derivative as green demulsifiers. Mater Today Proc. 2020;31:106-9. https://doi.org/10.1016/j.matpr.2020.01.253
[16] Hassan SA, K Abdalla B, Mustafa M. Adding Silica Nanoparticles to Improve the Demulsification Process in a Crude Oil Central Processing Facility: A Techno-economic Analysis. African J Eng Technol. 2021;1(1). https://doi.org/10.47959/AJET.2021.1.1.6
[17] Ye F, Mi Y, Liu H, Zeng G, Shen L, Feng X, et al. Demulsification of water-in-crude oil emulsion using natural lotus leaf treated via a simple hydrothermal process. Fuel. 2021;295:120596. https://doi.org/10.1016/j.fuel.2021.120596
[18] Azubike AA, Itohan E. Prospects of Breaking Crude Oil Emulsions Using Demulsifier Formulated from Nicotiana tabacum Seed Oil, Leaf Extracts, and Stalk Ash Extracts. Pet Sci Eng. 2021;5(2):44-53. https://doi.org/10.11648/j.pse.20210502.12
[19] Chen WS, Chen ZY, Chang JY, Chen CY, Zeng YP. Ultrasound-assisted desalination of crude oil: The influence of mixing extent, crude oil species, chemical demulsifier and operation variables. Ultrason Sonochem. 2022;83:105947. https://doi.org/10.1016/j.ultsonch.2022.105947
[20] Romanova YN, Maryutina TA, Musina NS, Spivakov BY. Application of ultrasonic treatment for demulsification of stable water-in-oil emulsions. J Pet Sci Eng. 2022;209:109977. https://doi.org/10.1016/j.petrol.2021.109977
[21] Okereke U, Chiemele C, Obah B, Owerri FPN. Impact Of Locally Formulated Demulsifiers From Locally Sourced Raw Materials On Emulsion Demulsification. globalscientificjournal. 11(5):18.7.
[22] Abdullah MMS, Faqihi NA, Al-Lohedan HA, Almarhoon ZM, Karami AM. Application of new oleate-based ionic liquids for effective breaking of water in oil emulsions. Fluid Phase Equilib. 2023;568:113737. https://doi.org/10.1016/j.fluid.2023.113737
[23] Gao J, Zhu J, Gao Q, Zhao X, Yu L, Zhao J, et al. Mechanism study of aging oil demulsification and dehydration under ultrasonic irradiation. Ultrason Sonochem. 2024;105:106859. https://doi.org/10.1016/j.ultsonch.2024.106859
[24] Luo X, Cao J, Gong H, Yan H, He L. Phase separation technology based on ultrasonic standing waves: A review. Ultrason Sonochem. 2018;48:287-98. https://doi.org/10.1016/j.ultsonch.2018.06.006
[25] DeCola E, Robertson T, Fisher M, Blair L. Phasing out the use and carriage for use of heavy fuel oil in the Canadian Arctic: Impacts to northern communities. Nuka Res Plan Gr LLC Plymouth, MA, USA. 2018.
[26] Speight JG. Heavy oil recovery and upgrading. Gulf Professional Publishing; 2019.
[27] Nwadinobi CP. Evaluation of soil-water ratio effectiveness in soil-bath wet separation process for kernel recovery. Niger J Technol. 2019;38(1):99-103. https://doi.org/10.4314/njt.v38i1.13
[28] Nugraha IMA, Mahardiananta IMA, Putra PAM, Adnyana IGS. Magnetic stirrer with speed advisor and timer based on microcontroller. J Robot Control. 2022;3(1):18-25. https://doi.org/10.18196/jrc.v3i1.11279
[29] Mowea WS, Ibrahim RI, Oudah MK. Electromagnetic heating for the separation of water-oil emulsion. Pet Chem. 2024;64(1):53-61. https://doi.org/10.1134/S0965544124010195
[30] Montes D, Cortés FB, Franco CA. Reduction of heavy oil viscosity through ultrasound cavitation assisted by NiO nanocrystals-functionalized SiO2 nanoparticles. Dyna. 2018;85(207):153-60. https://doi.org/10.15446/dyna.v85n207.71804
[31] Hassan SA, Abdalla BK, Mustafa MA. Addition of silica nano-particles for the enhancement of crude oil demulsification process. Pet Sci Technol. 2019;37(13):1603-11. https://doi.org/10.1080/10916466.2019.1602634
[32] Gandomkar GE, Bekhradinassab E, Sabbaghi S, Zerafat MM. Improvement of chemical demulsifier performance using silica nanoparticles. Int J Chem Mol Eng. 2016;9(4):585-8.
[33] M.Hendi Y, A. Mandeel T. Synthesis, identification and evaluated of A Novel Demulsifier of Al-Rashidaiy crude oil (east of Baghdad). J Univ Anbar Pure Sci. 2017;11(1):58-68. https://doi.org/10.37652/juaps.2017.141453

Blank Page

Research on Engineering Structures & Materials
www.jresm.org

Research Article

Numerical and acoustic investigation of cavitation phenomena in centrifugal hydraulic pumps

Saba A. Othman [*,a], Hashim A. Hussien [b], Abduljabbar O. Hanfesh [c]

Electromechanical Engineering Department University of Technology-Iraq, Baghdad, Iraq

Article Info

Article History:

Received 12 Oct 2025

Accepted 24 Nov 2025

Keywords:

Acoustic technique;
Cavitation;
Ventrifugal pump;
Turbulent kinetic energy;
Hydraulic oil;
CFX;
Vapor volume fraction

Abstract

Cavitation significantly reduces the performance and efficiency of centrifugal pumps. This study investigates cavitation behavior in a CRT 100-BR centrifugal pump using ISO 22 hydraulic oil produced locally at the Dora Refinery, Iraq, through a combination of numerical simulations (ANSYS CFX) and acoustic signal analysis. The pump operated at 6 bar, 2800 rpm, and 280 L/min. Acoustic signals recorded by a microphone were analyzed in MATLAB using mean, RMS, and peak amplitude indicators, revealing that peak amplitude values were approximately 42.86% higher than RMS, effectively detecting cavitation onset. Numerical simulations evaluated turbulent kinetic energy and vapor volume fraction at flow rates from 50 to 300 L/min, showing a 45% increase in vapor fraction and a 65% rise in turbulence energy when the flow increased from 200 to 300 L/min. These results demonstrate that integrating CFD modeling of turbulence and vapor fraction with acoustic analysis provides a reliable and efficient method for cavitation detection and pump condition monitoring.

© 2026 MIM Research Group. All rights reserved.

1. Introduction

Centrifugal pumps are hydrodynamic devices that utilize a revolving impeller to convey energy from the motor to the fluid. The energy transfer occurs via the impeller blades, which augment both the pressure and kinetic energy of the fluid at the impeller's output, Various faults may occur during actual operation.[1]. Cavitation often denotes the formation of cavities and the ensuing dynamic behaviors that occur when a liquid experience a significant pressure reduction [2]. Cavitation is an unavoidable complicated process of multiphase flow involving phase transition below the liquid's vapor pressure at the operational temperature. A substantial quantity of bubbles is generated, which will implode once the liquid enters the high-pressure region. The mechanism of cavitation remains incompletely understood because to its stochastic nature and multiphase properties. Upon the occurrence of cavitation, the energy transfer between the impeller and the fluid is compromised, resulting in a decline of the head-flow rate curve, while the surfaces of the flow passage components experience significant wear and corrosion. Also, it will cause noise in pump body [3].

Acoustic monitoring has attracted increasing attention in recent years, such as Cernetic et al. [4] examined noise phenomena within the audible frequency range associated with cavitation in centrifugal pumps. They employed a dual-channel signal analyzer and two microphones with a frequency range of 100 Hz to 10 kHz for their investigation. The noise escalates prior to the 3% head drop, nevertheless the apex of the loudness is situated in proximity to the Critical Net Positive Suction Head (NPSH). The escalation of noise resulted from the formation and proliferation of cavitation bubbles that intensify flow turbulence, obstructing the flow channel. Moreover, vibrations resulting from unstable cavitation within the pump may exacerbate noise levels. S.

*Corresponding author: eme.22.47@grad.uotechnology.edu.iq
[a]orcid.org/0009-0003-8109-6453; [b]orcid.org/0000-0003-4036-3853; [c]orcid.org/0000-0001-5345-1794
DOI: http://dx.doi.org/10.17515/resm2025-1249ic1012rs

Farokhzad and H. Ahmadi [5] developed a cavitation prediction system utilizing acoustic inputs and a multilayer perpendicular (MLP) neural network. This approach shown efficiency and reliability in frequency analysis under stable circumstances and consistent velocity. Hosien et al. [6] executed an empirical study to evaluate the efficacy of acoustic methods in identifying the start of cavitation in hydraulic systems. The findings indicated that cavitation produces acoustic signals within the frequency spectrum of 31.5 Hz to 31.5 kHz, which were distinctly captured through a transparent window in the water conduit. The results validated a robust association between acoustic signals and visual observations, indicating that acoustic measurement can serve as an effective and dependable method for ascertaining cavitation start. Dong et al. [7] presented an approach based on variations in vibration patterns and noise levels throughout the system's operation. The signals produced by cavitation were most prominent during the initiation of the phenomena, rendering this approach appropriate for application with big pumps.

Ranade and Sarvothaman [8] examined the application of acoustic data, gathered using a standard cell phone, to ascertain the initiation and magnitude of hydrodynamic cavitation. Acoustic emissions from vortex-based cavitation devices were documented at different pressure reductions (0–390 kPa). The 'Audio' and 'DSP' toolboxes in MATLAB were utilized to analyze the data and extract acoustic characteristics. Three distinct tendencies concerning flow rate and pressure decrease were identified. These patterns unequivocally signified the commencement of cavitation, particularly within the range of 50–80 kPa. A characteristic termed “flatness” has shown a strong correlation with cavitation levels and device efficacy. The research indicated that this methodology is suitable for real-time cavitation detection and confirmed its universal applicability across various cavitation systems. Ramadan et al. [9] identified cavitation within the centrifugal pump utilizing vibration and acoustic methodologies. This was accomplished by examining the acoustic waves in both temporal and frequency domains. Cavitation was examined by several statistical characteristics during temporal domain analysis (TDA). The fast Fourier transform (FFT) technique was employed for frequency domain analysis (FDA). Karagiovanidis et al. [10] presented a set of early methods for detecting cavitation in centrifugal irrigation pumps, based on vibration and acoustic signal analysis. They developed a low-cost data collection system and evaluated multiple computational algorithms. A smartphone-based accelerometer was used to collect vibration data, and the signals were then compared under different operating conditions. Stephen, C et al. [11] improved the Deviation from Normal Distribution (DND) method for cavitation detection using vibration signals. By comparing the original DND calculation with a baseline-data approach through probability density functions and normal probability plots, the results showed that the baseline method provided clearer and more sensitive indication of cavitation, enabling the definition of practical alarm limits. The improved technique was validated at different operating speeds and was found to be reliable, responsive, and independent of speed. Rahma et al. [12] Determined the four typical cavitation levels for pump type (CEA 210/2) operated on water. With the use of time-domain analytic tools, record the acoustic waves using a hydrophone. The result indicated that the low-frequency range of acoustic signals is highly effective for early cavitation detection. Ni, Chen et al. [13] investigated cavitation in a single-blade centrifugal pump through combined numerical and experimental vibration/noise analysis. Using time-frequency features, energy entropy, and vibration acceleration level, the results showed that cavitation introduces intermittent high-frequency shocks and increases dominant vibration components, while noise spectra exhibited reduced blade-passing frequency and amplified low-frequency content. The study confirmed clear quantitative links between cavitation severity and changes in vibration and acoustic behavior, supporting its use for cavitation monitoring in impurity-laden pump flows. Wang, D. rt al. [14] used hydrophone-based acoustic measurements at the pump inlet and outlet to detect cavitation. Noise levels increased with flow rate, and decreasing NPSHa caused a sharp inlet noise drop and an initial outlet noise rise, allowing earlier cavitation detection. Dominant spectral components were shaft and blade frequencies and their harmonics, and changes in these acoustic features proved effective for predicting cavitation onset.

Previous studies on cavitation in centrifugal pumps have typically relied on single-method approaches or idealized water-based simulations that do not fully reflect real operating environments. In contrast, the present study integrates high-fidelity ANSYS CFX simulations with

experimental acoustic measurements conducted under industrial conditions using locally produced Iraqi ISO 22 hydraulic oil (Daura Refinery) in a CRT 100-BR centrifugal pump. Time-domain statistical indicators, alongside CFX-predicted vapor volume fraction and turbulent kinetic energy, were analyzed to establish a direct correlation between numerical and experimental observations. This hybrid approach provides a more comprehensive understanding of cavitation behavior, revealing how variations in cavitation intensity and turbulence levels shape the acoustic signature of the pump, and offering deeper insight into cavitation dynamics under realistic operating conditions.

2. Methodology

(Model CRT 100-BR) operating with ISO 22 hydraulic oil at 40 °C, with a pump power of 1 HP and a system pressure of 6 bar. The system consists of polypropylene random copolymer (PPR) pipes with a suction diameter of 1.5 inches and a discharge diameter of 1.25 inches (connected via a reducer fitting), and a galvanized steel tank measuring 90 × 60 × 60 cm. Operating conditions are controlled using a variable frequency drive (AC drive), and data are collected through an ADQ unit and logged on a computer for detailed acoustic analysis. Acoustic emissions from cavitation were captured using a microphone sensor placed near the suction side and before conducting the acoustic measurements, the microphone sensor was calibrated to ensure the accuracy and reliability of the recorded sound pressure levels. A standardized sound level calibrator (SLC) was used to perform the calibration

The microphone was calibrated using a standard sound level calibrator providing 94 dB at 1 kHz. The microphone was fitted into the calibrator, and the corresponding output voltage was recorded. The sensitivity (mV/Pa) was calculated using the ratio of the measured voltage to the reference pressure (1 Pa). operating within −40 °C to +90 °C, Pressure transducers were installed at both suction and discharge sides, calibrated prior to the experiments with an accuracy of ±0.25%.

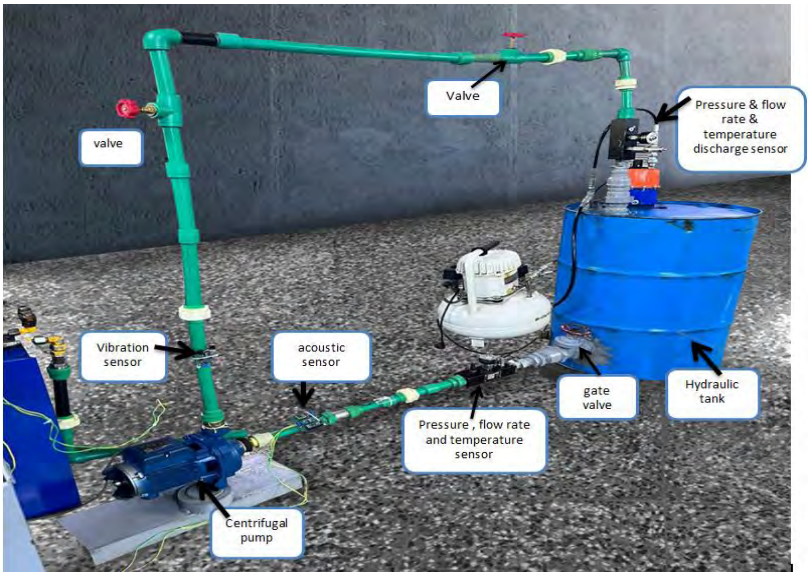

Fig. 1. The experimental setup

Table 1. Parameters of the working fluid

Parameter	Specification
Working fluid	Hydraulic oil ISO 22
viscosity μ/(μPa • s) at 40c	20-24
Density ρl/(Kg/L)	0.862
Vapour pressure at 40C	0.1 kpa
Viscosity (cSt at 100°C)	4.15

Additionally, the kinematic viscosity of the ISO 22 hydraulic oil was measured to ensure consistent fluid properties, which are essential for accurate cavitation analysis, as shown in Figure 2. This enables accurate and consistent outcomes, aligning with the criteria specified in Table 1.

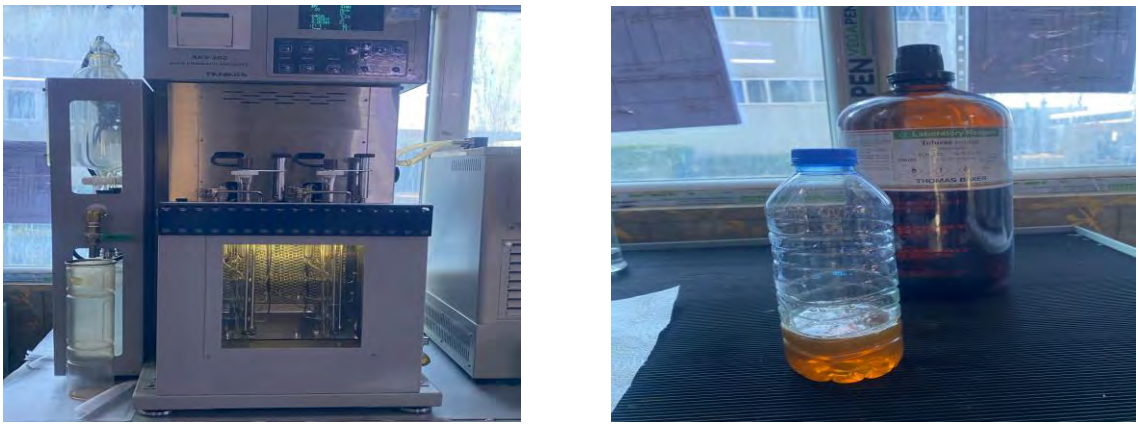

(a) (b)

Fig. 2. (a) Automotive Kinematic Viscosity (AKV-202) and (b) Hydraulic iso 22

3. Numerical Simulation using CFX

CFX code is extensively utilized in the design, modeling, and resolution of various complicated industrial applications due to its high precision. CFX is commonly utilized to examine the distribution and regulation of flow variables in many industrial processes, including compressors, pumps, turbines, furnaces, boilers, hot rolling industries, and other applications where thermal management and mixing are essential. The optimization can facilitate substantial energy savings [15]. Employing CFX software facilitates the construction of a three-dimensional domain via computer technology. A computational mesh may subsequently be incorporated into this domain. [16].

To better understand internal flow dynamic many researches have relied on CFD technique as illustrated in the following studies, A. Al-Obaidi, et al.[17] conducted a CFD numerical simulation to investigate the impact of volute design on pump performance. Upon comparing the simulation results with the experimental data, it became evident that the outputs of both techniques were congruent. The pump head was shown to rise with the cross-sectional area of the pump volute. Pei et al. [18] utilized CFD technology to evaluate the influence of the impeller intake diameter D1, the inlet incidence angle Δβ, and the blade twist angle φ on the cavitation performance of the centrifugal pump. To ascertain the optimal parameter settings for pump design, the cavitation features of the pump are analyzed utilizing orthogonal Design of Experiments (DOE). The internal flow of the enhanced impeller was analyzed and compared with that of the original flow. Ahmed R. Mahdi [19] carried out a CFD study to analyze the flow behavior and cavitation in a centrifugal pump under single-phase and cavitating conditions. He investigated the effect of different numbers of impeller blades on pressure, velocity, and vapor volume fraction. The results showed that cavitation started at the impeller eye and became more severe with fewer blades, especially at high flow rates. Wu et al. [20] used CFX software to analyze an enhanced cavitation model in CEL language, conducting numerical simulations of full flow under cavitation effects at three different temperatures: 25°C, 50°C, and 70°C, using an electronic water pump

The current study A three-dimensional numerical simulation of a centrifugal pump was conducted with ANSYS CFX software to examine the flow and identify cavitation. The diagram below delineates the process of preparing the numerical model, commencing with the design of the geometry and meshing, followed by. The k–ω turbulence model was used for its accuracy in near-wall flows, while cavitation was simulated using the Zwart–Gerber–Belamri (Rayleigh–Plesset–based) model to predict vapor formation and bubble dynamics for enhanced accuracy, and

concluding with the specification of boundary conditions, including inlet flow rate, rotational speed, and outlet pressure.

3.1 Geometry

The geometry of a centrifugal pump plays a crucial role in determining its internal fluid dynamics and cavitation behavior. In this study, a detailed 3D model of the pump was constructed, including all major components such as the inlet, outlet, impeller blades, and casing. Accurate dimensions were taken based on the proposed model, ensuring that the computational and experimental analyses reflect realistic flow behavior. The working fluid used in all simulations and experiments was an ISO VG 22 hydraulic oil. This geometric model, together with the specified fluid properties, was used in ANSYS CFX to study the pressure distribution, vapor volume fraction, and turbulent kinetic energy under various operating conditions. The key geometric parameters of the centrifugal pump, including the impeller and volute dimensions, were determined based on the manufacturer specifications and are summarized in Table 2. Figure 3 shows the geometry of the centrifugal pump

Table 2. Specification of the CRT-100 centrifugal pump prototype

Parameter	Value
Impeller outer diameter	92.40mm
Outlet pipe inner diameter	21mm
Volute width at outlet	71.47mm
Volute tongue length	25.27mm
Volute casing thickness	20.29mm
Pump rotation speed	2800rpm
Length of inlet pipe	0.5m
Length of outlet pipe	1m
Number of blades	8

Fig. 3. Geometric of Centrifugal Pump

3.2 Meshing of the Flow

Partitions the domain into discrete elements or control volumes to numerically solve governing equations, is an essential aspect of computational analysis [15]. This study employed inflated layers at the fluid domain boundaries to precisely record the velocity and pressure gradients next to the wall surfaces. The pump geometry, including the inlet, impeller, and volute regions, was meshed using high-quality tetrahedral elements. Eight prismatic inflation layers were applied along all walls to improve near-wall resolution and accurately capture cavitation, pressure, and velocity gradients Figure 4(a) . Mesh parameters included a transition ratio of 0.52 and a growth rate of 1.2, ensuring smooth refinement from coarse to fine regions. The global element size was 1.5 mm, with a finer 1.6 mm mesh for the impeller and volute to resolve high-gradient areas. The mesh comprised 451,099 nodes and 1,638,980 elements Figures 4(b) and mesh independence was

confirmed by minimal variations in output parameters. For boundary conditions, a flow rate was specified at the pump suction, while a static pressure was set at the discharge, and all other fluid interfaces were treated as non-slip walls to capture near-wall viscous effects. The inlet temperature was imposed to account for thermal influences on cavitation inception and vapor pressure variations of ISO VG 22 hydraulic oil as shown in figure 5 and table 3. Turbulence was modeled using the SST k–ω model, selected for its ability to accurately resolve adverse pressure gradients and flow separation within turbomachinery components. The study used an eight-blade impeller to enhance flow consistency and hydraulic performance under varying operating conditions.

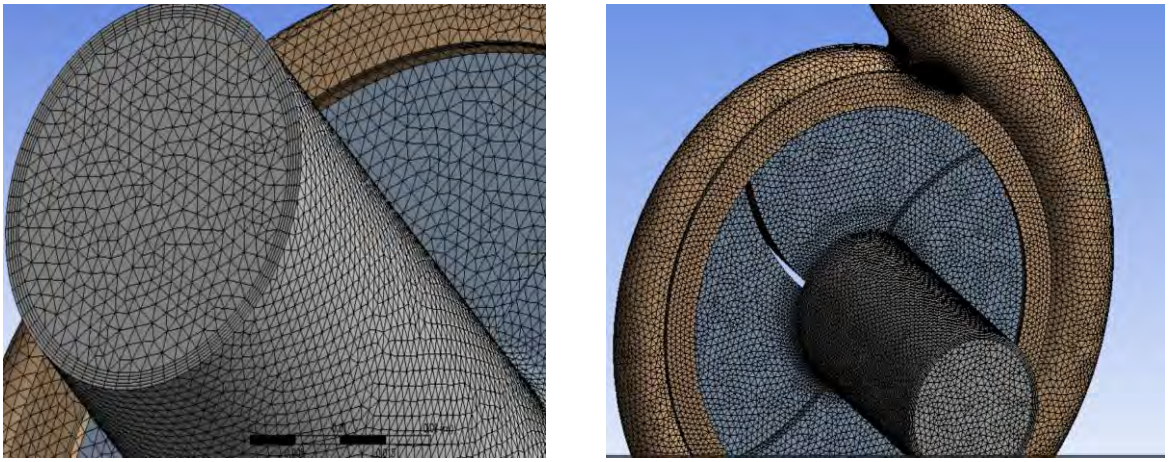

(a) (b)

Fig. 4. (a) Inflation of the centrifugal pump and (b) meshing

A fixed static pressure outlet was applied to ensure stable convergence and to represent the actual discharge conditions of the pump. This boundary condition allows the flow rate to adjust naturally according to the pump's hydraulic performance, providing a physically realistic prediction of cavitation intensity and vapor distribution at the outlet.

Table 3. Specifications of operating conditions and material

Parameters	Value
Rotation speed	2800rpm
Flow rate	280 L/min
Head	20 m
Working fluid	Hydraulic oil iso 22
Vapor pressure at 40c	0.1 kpa
Density	0.862 (Kg/L)
Viscosity	24 μ/(μPa • s) at 40c

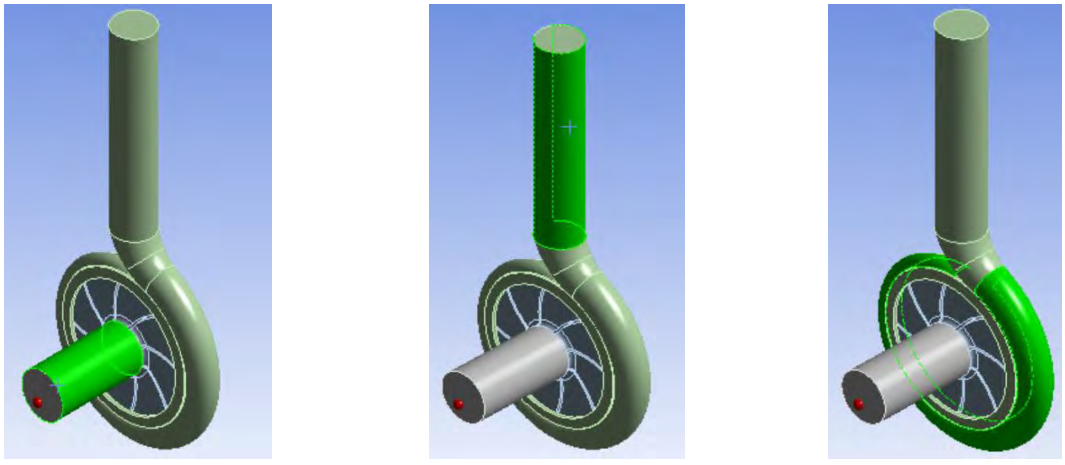

Fig. 5. Boundary condition, inlet, outlet and rotation

In the pre-processing stage, the computational domain was generated and discretized, and boundary conditions were applied. During the solution stage, the governing equations for continuity, momentum, and turbulence were solved iteratively up to a maximum of 500 iterations or until numerical convergence was achieved. A residual target of 10^{-4} was adopted as the convergence criterion.as shown in figure 6.

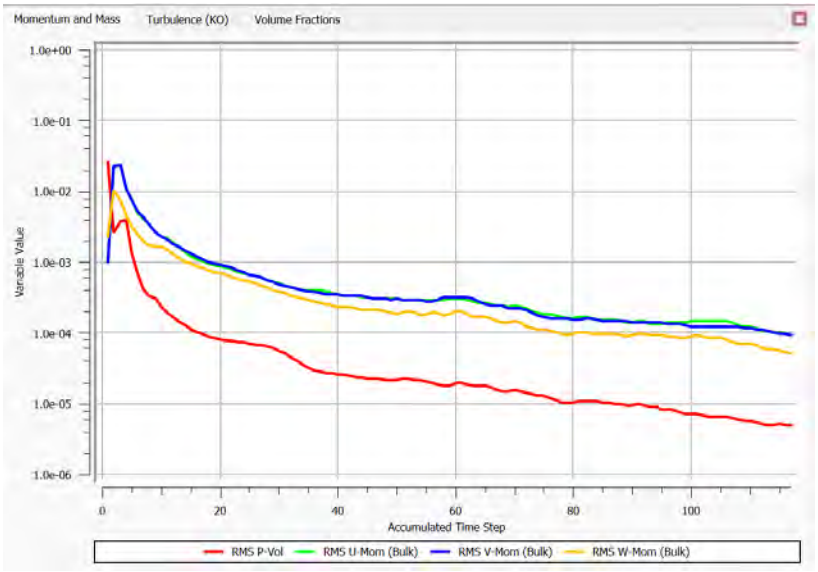

Fig. 6. Convergence in ANSYS CFX

4. Results and Discussion

4.1 Acoustic Techniques to Predict Cavitation in a Centrifugal Pump at Different Flow Rates

This study aimed to examine pump performance during standard operation and cavitation conditions by acoustic techniques. This approach requires certain sensors, such as a microphone, together with a dependable system for processing and analyzing signals to examine the acoustic signal associated with cavitation in a pump under various operating situations]

- Time Domain acoustic Signal: Initially, we compare the unprocessed acoustic signals under various operational settings with a time waveform analysis (TWFA) graph.
- To statistically assess the time-domain data acquired during the experiments or simulations, many common statistical parameters were utilized. These encompass the root mean square (RMS), peak to peak, and mean value. These metrics assess the amplitude, dispersion, and central tendency of the data temporally. [21]. The subsequent equations were utilized:
- Root Mean Square (RMS):

$$RMS = \sqrt{\frac{1}{N}\sum_{i=1}^{N} x_i^2} \quad (1)$$

Where N and xistand for the total number of elements and the element signal, respectively.

- Mean Value (μ):

$$\mu = \frac{1}{N}\sum_{i=0}^{N-1} x_i \quad (2)$$

The elements' mean values, their total number, and their set are represented by the variables x, xi and N.

- Peak-to-Peak Value:

$$P = x_{max} - x_{min} \quad (3)$$

RMS, mean, and peak values were selected because they provide complementary insight into cavitation-induced acoustic behavior. The mean captures the overall signal level, the RMS reflects the effective energy content of the vibration or sound, and the peak value identifies extreme pressure fluctuations associated with bubble collapse. Together, these metrics offer a simple yet robust representation of cavitation intensity in the time domain.

These features were employed to discern several stages of cavitation within the pump (absence of cavitation, initiation of cavitation, and progression of cavitation). An acoustic sensor was employed to analyze sound pressure signals across various operating circumstances. The study's results were classified according to different flow rates, examining the duration and amplitude of the acoustic waveform signals at flow rates of 50, 100, 150, 200, 250, and 300 liters per minute, while maintaining a constant rotating speed of N = 2800 rpm. The results demonstrate that the amplitude of acoustic waves fluctuates with alterations in flow rate. For instance:

- At low flow rates (50–150 liters/min), the amplitude of the acoustic signal is very stable.
- At elevated flow rates (200–280 liters/min), the amplitude of the acoustic emissions starts to rise.

The research indicates that the amplitude of the acoustic signal escalates with an increase in flow rate, as shown in Figure 7. This phenomenon may be attributed to two primary factors: the contact between the impeller and the tongue area, and the initiation of cavitation at elevated flow rates, which intensifies with increasing flow (as shown in Figure 6. Under these circumstances, the acoustic signal patterns became increasingly erratic and had elevated peaks relative to standard operating settings.

Utilizing many statistical metrics reflecting vibration in the time domain, including peak, RMS, and mean characteristics. These properties provide a valuable resource. and often utilized in condition monitoring. Figure 8 demonstrates that the peak feature value was more effective in detecting cavitation based on signal energy content compared to the RMS and mean features. The Peak-to-Peak vibration signal was roughly 42.86% more than the RMS signal as sown in table 4, suggesting that Peak to Peak is more adept at detecting changes related to cavitation within this flow range. And figure 9 shown the Peak Acoustic Amplitude Levels Under Two Operational Conditions

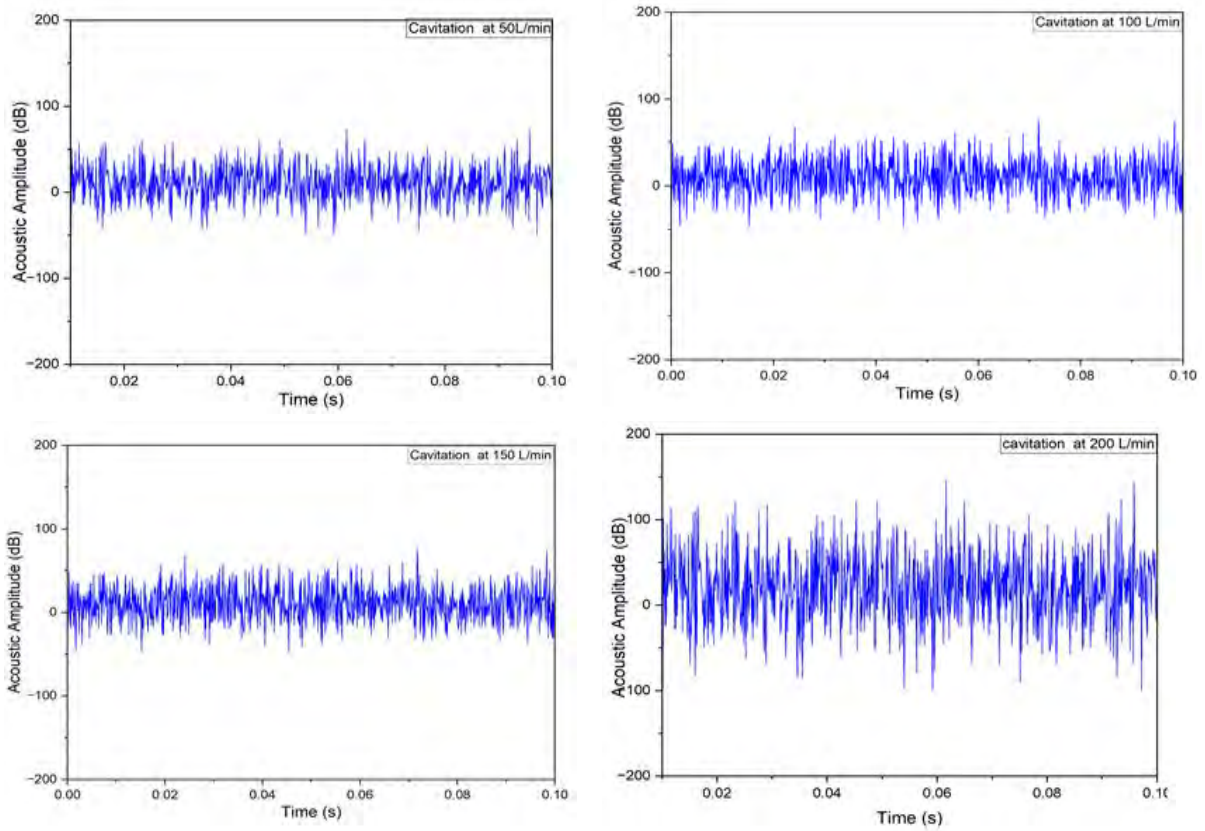

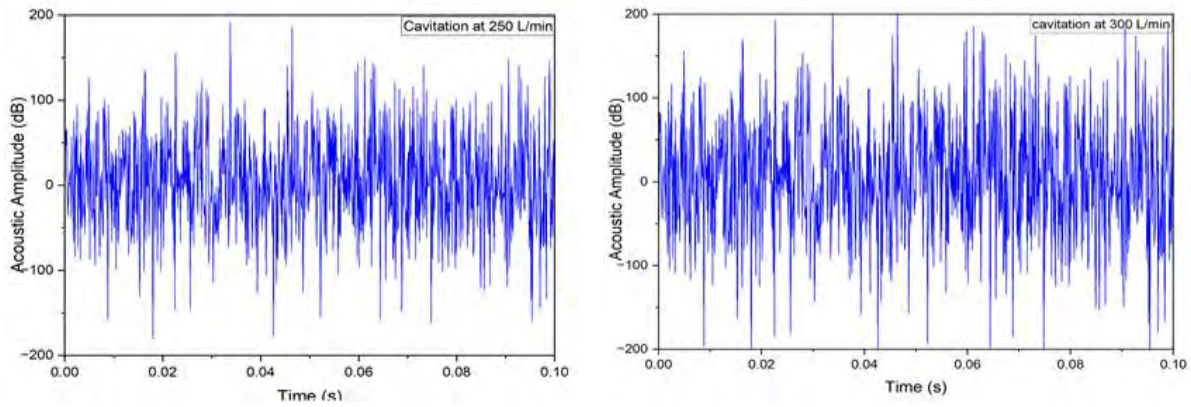

Fig. 7. Acoustic signal at different flow rate at 2800 rpm

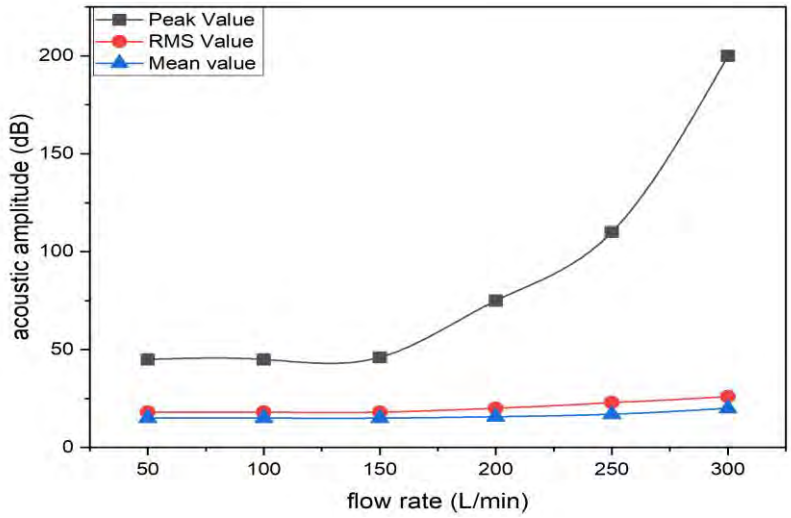

Fig. 8. Acoustic signal's (Peak to Peak, Mean and RMS) at 2800 rpm

Table 4. Acoustic response (Peak/RMS/Mean) under varying flow rate conditions

Flow Rate (L/min)	Peak Value (dB)	RMS Value (dB)	Mean Value (dB)
50	45	17	15
100	46	17	15
150	44	17	15
200	60	18	16
250	110	20	17
300	200	22	19

Pump housing vibrations can superimpose structural noise onto the acoustic measurements, potentially increasing RMS and peak levels. Mechanical vibrations from motor, bearings, or flow-induced forces may excite the housing, transmitting additional signals to the microphone. Careful sensor placement, vibration isolation, and signal filtering are necessary to ensure that the measured acoustic signals primarily reflect cavitation phenomena rather than structural vibrations.

4.2 Simulation

This section presents the results of the simulations conducted in ANSYS CFX for a centrifugal hydraulic pump under various flow rates. Cavitation detection was carried out by calculating the vapor volume fraction and turbulence kinetic energy.

4.2.1 Vapor Volume Fraction Contour in The Centrifugal Hydraulic Pump

This paragraph analyzes the distribution of vapor volume fraction during cavitation to evaluate the initiation and development of cavitation inside the internal flow regions of a centrifugal pump at different flow rates. Figure 8 illustrates the distribution of vapor volume % at the impeller intake at various flow rates. The vapor volume fraction was also evaluated to assess cavitation occurrence within the hydraulic centrifugal pump. As shown in the contour plots and the accompanying graph, there is a clear increase in vapor volume at flow rates beyond 150 L/min, with a significant surge observed at 250 and 300 L/min. An increase in the flow rate from 200 L/min to 300 L/min led to a 45% rise in the vapor volume fraction. The sudden rise in vapor fraction above 200 L/min is caused by local pressure dropping below the fluid's vapor pressure due to higher flow velocities. As the flow rate increases, the centrifugal pump suction region experiences stronger acceleration and turbulence, lowering static pressure and promoting rapid bubble formation. This process is amplified by turbulence-induced fluctuations, which enhance cavitation growth and lead to a sharp increase in vapor volume fraction .This indicates the formation and growth of vapor bubbles due to local pressure drops below the fluid's vapor pressure a key characteristic of cavitation.

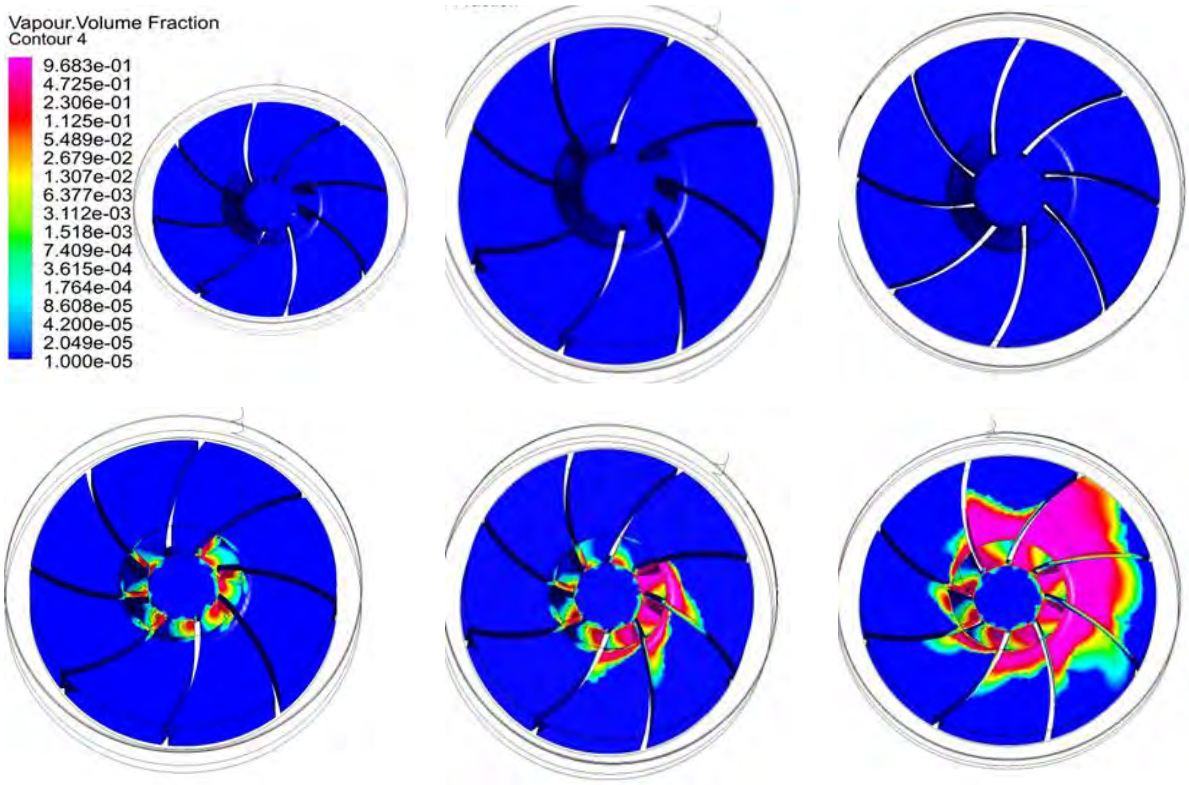

Fig. 9. Vapor volume fractions contour under different flow rates at 2800 rpm

4.2.2 Turbulent Kinetic Energy in The Centrifugal Hydraulic Pump

Turbulent kinetic energy (TKE) is crucial for comprehending the internal flow dynamics of hydraulic centrifugal pumps. It indicates the severity of turbulence produced when the fluid traverses' important areas, including the impeller and volute casing. Examining TKE yields significant insights on flow instability, energy dissipation, and the likelihood of cavitation. This research assessed TKE at flow rates between 50 and 300 L/min, maintaining a constant rotating speed of 2800 rpm. The contour plots show that at low flow rates (50–150 L/min), the turbulence remains relatively low and localized, primarily around the impeller. As the flow rate exceeds 200 L/min, turbulence intensifies and becomes more broadly dispersed throughout the volute and blade channels. The graph depicting average TKE in relation to flow rate substantiates this trend: TKE diminishes little from 50 to 150 L/min, thereafter experiences a substantial increase, peaking at 300 L/min. increasing the flow rate from 200 L/min to 300 L/min resulted in a 65% increase in turbulent kinetic energy. The fast escalation of turbulence at elevated flow rates signifies increasing

flow instability and the possible emergence of cavitation, particularly in high-velocity areas next to the blade trailing edges and volute tongue. The results indicate a significant association between flow rate and turbulence development, underscoring the usefulness of TKE analysis in forecasting unstable circumstances and enhancing pump performance, as shown in Figure 10.

Turbulence affects the acoustic signature by modulating pressure fluctuations within the pump. Higher turbulence intensity increases chaotic, high-frequency flow structures, which generate stronger and more irregular acoustic emissions. These fluctuations enhance noise amplitude (RMS and peak) and alter the spectral content, making it possible to correlate specific turbulence patterns with cavitation intensity and bubble collapse events.

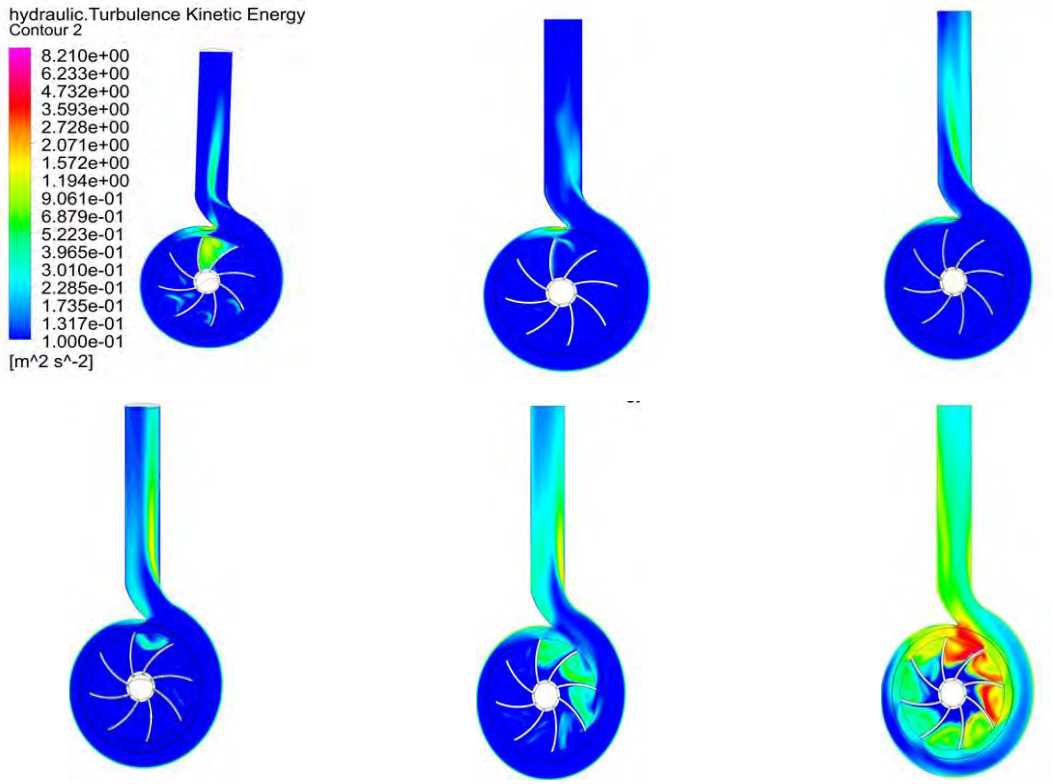

Fig. 10. Turbulence kinetic energy contour at different flow rate at 2800 rpm

4.3 Validation

The vapour volume fraction, turbulent kinetic energy, and acoustic emissions are key indicators of cavitation in centrifugal pumps, each reflecting a different physical aspect of the phenomenon. The vapour volume fraction indicates the amount of vapor bubbles formed due to pressure drop, while turbulent kinetic energy (TKE) reflects the intensity of flow disturbances caused by these bubbles. The acoustic signal represents the noise generated by their collapse on the impeller surfaces. Notably, at the same flow rates, both the vapors volume fraction and sound levels increased simultaneously, confirming a direct link between the growth of vapor bubbles and the corresponding rise in acoustic emissions during cavitation.as shown in figure 11.

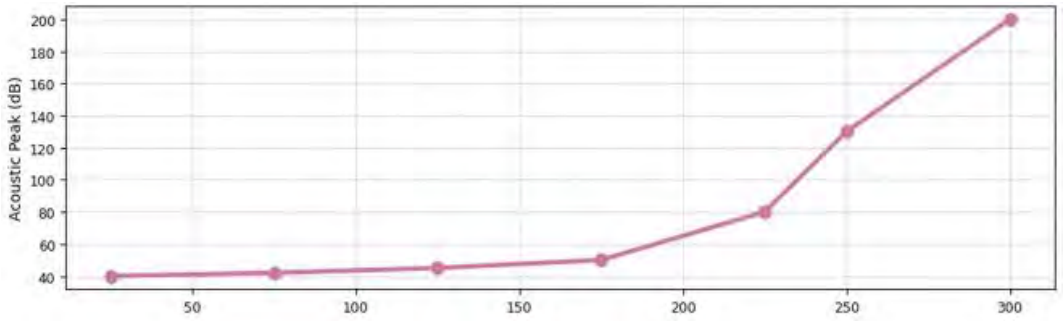

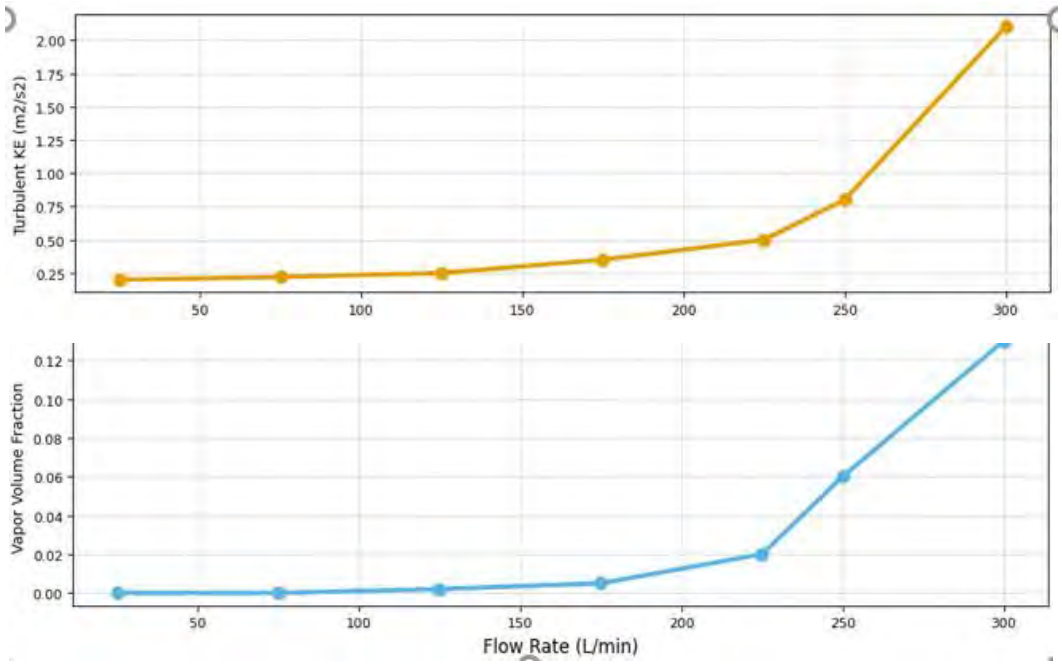

Fig. 11. Experimental and CFX parameters with flow rate for cavitation detection

5. Conclusion

Centrifugal pumps play a critical role in fluid transmission, particularly in hydraulic systems requiring high flow rates and pressures. Understanding the factors that influence their performance, such as rotational speed and fluid properties, is essential for enhancing efficiency and mitigating issues like cavitation. Advances in acoustic analysis and other diagnostic techniques are vital for ensuring reliable and economical hydraulic system operation. The current study combining ANSYS CFX simulations with experimental acoustic measurements effectively captures cavitation behavior in a CRT 100-BR centrifugal pump using ISO 22 hydraulic oil. Results showed that cavitation initiates above 150 L/min, with sharp increases in vapor volume fraction and turbulent kinetic energy at higher flow rates, particularly above 200 L/min. Corresponding acoustic signals reflected these changes, with peak amplitudes about 43% higher than RMS values, confirming the sensor's sensitivity to cavitation. These findings highlight the practical value of integrating numerical and acoustic analyses for pump condition monitoring. Limitations include the use of a single fluid type and flow configuration, suggesting that further studies under varied operating conditions would strengthen generalization.

References

[1] Mousmoulis G, Anagnostopoulos J, Papantonis D. A review of experimental detection methods of cavitation in centrifugal pumps and inducers. Int J Fluid Mach Syst. 2019;12(1):71-88. https://doi.org/10.5293/IJFMS.2019.12.1.071

[2] Wu P, Bai L, Lin W, Wang X. Mechanism and dynamics of hydrodynamic-acoustic cavitation (HAC). Ultrason Sonochem. 2018;49:89-96. https://doi.org/10.1016/j.ultsonch.2018.07.021

[3] Gu Y, et al. Suppression of unsteady partial cavitation by a bionic jet. Int J Multiph Flow. 2023;164:104466. https://doi.org/10.1016/j.ijmultiphaseflow.2023.104466

[4] Černetič J, Čudina M. Cavitation noise phenomena in centrifugal pumps. In: 5th Congress of Alps-Adria; 2012. p. 1-6.

[5] Farokhzad S, Ahmadi H. Acoustic based cavitation detection of centrifugal pump by neural network. J Mech Eng Technol. 2013;1(1):1-5. https://doi.org/10.18005/JMET0101001

[6] Hosien MA, Selim SM. Acoustic detection of cavitation inception. J Appl Fluid Mech. 2017;10(1):31-40. https://doi.org/10.18869/acadpub.jafm.73.238.25638

[7] Dong L, Zhao Y, Dai C. Detection of inception cavitation in centrifugal pump by fluid-borne noise diagnostic. Shock Vib. 2019;2019(1):9641478. https://doi.org/10.1155/2019/9641478

[8] Ranade NV, Sarvothaman V, Ranade VV. Acoustic analysis of vortex-based cavitation devices: Inception and extent of cavitation. Ind Eng Chem Res. 2021;60(22):8255-8268. https://doi.org/10.1021/acs.iecr.1c01005
[9] Al-Obaidi AR. Experimental diagnostic of cavitation flow in the centrifugal pump under various impeller speeds based on acoustic analysis method. Arch Acoust. 2023;48(2):159-170. https://doi.org/10.24425/aoa.2023.145234
[10] Karagiovanidis M, Pantazi XE, Papamichail D, Fragos V. Early detection of cavitation in centrifugal pumps using low-cost vibration and sound sensors. Agriculture. 2023;13(8):1544. https://doi.org/10.3390/agriculture13081544
[11] Stephen C, Basu B, McNabola A. Detection of cavitation in a centrifugal pump-as-turbine using time-domain-based analysis of vibration signals. Energies. 2024;17(11):2598. https://doi.org/10.3390/en17112598
[12] Ajmi RE, Hussein HA, Numan AH. Experimental investigation of inception cavitation phenomena effect in centrifugal pumps using hydrophone sensor. JJMIE. 2025;19(1). https://doi.org/10.59038/jjmie/190110
[13] Ni C, Zhang D, Shen X, Xu B, Lang T, Gao X. Cavitation-induced vibration and noise signal analysis of a single blade centrifugal pump. Phys Fluids. 2025;37(8). https://doi.org/10.1063/5.0283743
[14] Wang D, Ma W, Zhao W, Cao R, Yang Y. Experimental acoustic analysis of cavitation in a centrifugal pump. Fluid Dyn Mater Process. 2025;21(4). https://doi.org/10.32604/fdmp.2024.055220
[15] Hosain ML, Fdhila RB. Literature review of accelerated CFD simulation methods towards online application. Energy Procedia. 2015;75:3307-3314. https://doi.org/10.1016/j.egypro.2015.07.714
[16] Jaiswal NP. CFD analysis of centrifugal pump: a review. J Eng Res Appl. 2014;4:175-178.
[17] Al-Obaidi A, Pradhan S, Asim T, Mishra R, Zala K. Numerical studies of the velocity distribution within the volute of a centrifugal pump. 2014.
[18] Pei J, Yin T, Yuan S, Wang W, Wang J. Cavitation optimization for a centrifugal pump impeller by using orthogonal design of experiment. Chinese J Mech Eng. 2017;30(1):103-109. https://doi.org/10.3901/CJME.2016.1024.125
[19] Al-Obaidi AR. Monitoring the performance of centrifugal pump under single-phase and cavitation condition: A CFD analysis of the number of impeller blades. J Appl Fluid Mech. 2019;12(2):445-459. https://doi.org/10.29252/jafm.12.02.29303
[20] Wu K, Ali A, Feng C, Si Q, Chen Q, Shen C. Numerical study on the cavitation characteristics of micro automotive electronic pumps under thermodynamic effect. Micromachines. 2022;13(7):1063. https://doi.org/10.3390/mi13071063
[21] Proakis JG. Digital signal processing: principles algorithms and applications. India: Pearson Education India; 2001.

Blank Page

Research on Engineering Structures & Materials
www.jresm.org

Research Article

Ultrasound-assisted demulsification of heavy fuel oil using lemon peel powder: A sustainable natural approach

Hind A. Sami [*,a], Raheek I. Ibrahim [b], Manal K. Odah [c]

Electromechanical Engineering Department University of Technology-Iraq, Baghdad, Iraq

Article Info

Article History:

Received 12 Oct 2025

Accepted 03 Dec 2025

Keywords:

Heavy fuel oil;
Water;
Emulsions;
Ultrasound;
Separation;
Natural substance

Abstract

Heavy fuel oil (HFO) commonly forms highly stable water-in-oil (W/O) emulsions due to the presence of natural surfactants such as asphaltenes and resins, creating difficulties in transportation and refining. In this study, a green demulsification approach was developed by integrating ultrasonic treatment (28 kHz) with lemon peel powder, a low-cost and renewable natural additive. Experiments were performed at 85°C with ultrasonic powers ranging from 100 to 800 W for 2–10 minutes, while lemon peel concentrations varied between 3000 and 15000 ppm. The optimum condition of 5000 ppm at 800 W for 10 minutes achieved a maximum demulsification efficiency of 80%, surpassing the commercial demulsifier RQ35, which achieved 65% under similar conditions. The improvement in phase separation is attributed to the synergistic effect of acoustic cavitation and the active components of lemon peel, including pectin and limonene, which enhance droplet coalescence and reduce interfacial stability. This study introduces a novel and environmentally sustainable demulsification strategy that reduces reliance on synthetic chemicals and demonstrates strong potential for practical implementation in industrial heavy oil treatment.

© 2026 MIM Research Group. All rights reserved.

1. Introduction

Water-in-oil (W/O) emulsions in heavy fuel oil (HFO) remain a major operational challenge due to their high stability [1], mainly caused by asphaltenes and natural surfactants that strengthen the interfacial films [2,3]. These emulsions increase viscosity, hinder pumping and transportation, and accelerate corrosion, making efficient demulsification essential [4]. Although several physical and chemical techniques exist, many are costly, require high energy input, or rely on synthetic demulsifiers that introduce environmental and disposal concerns [5].

Recent trends toward sustainable demulsification have explored natural materials and ultrasound-assisted separation. Ultrasound is effective because acoustic cavitation disrupts interfacial films and enhances coalescence; however, ultrasound alone often cannot sufficiently destabilize highly stable HFO emulsions [6]. Similarly, most bio-based demulsifiers reported in literature act through surface-active components, but their performance remains limited without an aiding physical mechanism [7]. Thus, the research gap lies in the lack of integrated approaches that combine a natural, renewable demulsifier with a physical enhancement technique capable of overcoming the strong interfacial strength in heavy emulsions [8].

In this context, combining lemon-peel powder with ultrasonic irradiation presents an innovative synergy:

- Ultrasound generates micro-jets and shear forces through cavitation, weakening the interfacial film.

*Corresponding author: adelhend548@gmail.com
[a]orcid.org/0009-0003-8109-6453; [b]orcid.org/0000-0002-7158-3376; [c]orcid.org/0000-0002-3406-709X
DOI: http://dx.doi.org/10.17515/resm2025-1250ic1012rs

- Lemon peel chemistry (pectin, limonene, polyphenols) reduces interfacial tension, adsorbs stabilizing agents, and promotes droplet coalescence.

The interplay between mechanical cavitation and natural surface-active compounds offers a dual-action, greener pathway for destabilizing stubborn W/O emulsions [9]. Ultrasonic emulsification techniques utilize the dynamics of acoustic cavitation. Acoustic cavitation denotes the process involving the development, expansion, and implosive collapse of minute bubbles in a liquid medium exposed to high-intensity ultrasonic waves. The Ultrasonic wave propagation also causes the medium to alternately compress and expand as the collapse of these bubbles produces significant local pressure and temperature variations, resulting in high-shear forces, shock waves, and micro-jets capable of disaggregating big particles and agglomerates into smaller fragments. The motion of the ultrasonic-induced media particle, despite the modest displacement and velocity, exhibits significant acceleration proportional to the square of the ultrasonic vibration frequency, occasionally surpassing tens of thousands of times the acceleration due to gravity; this substantial acceleration is sufficient to generate a pronounced mechanical effect in the medium as shown in Figure 1 [10].

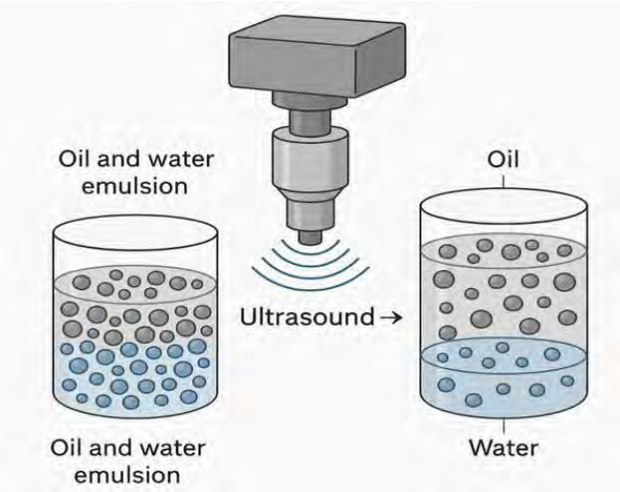

Fig. 1. Mechanism of ultrasonic activity in emulsion separation [11]

Ultrasonic treatment, now the focus of extensive research, can mitigate the drawbacks associated with classic extraction processes such as solvent extraction, distillation, and pressing [12]. The principle of ultrasonic demulsification is as follows: enhanced droplet oscillation speeds up droplet collisions, promoting their coalescence [13], and heat transfer from partial acoustic energy decreases emulsion viscosity and interfacial film strength [14]. Furthermore, droplets can increase the effectiveness of droplet coalescence by forming droplet bandings in ultrasonic standing waves (USWs) and directionally aggregating to pressure nodes or anti-nodes [12].

The environment and human health are still at risk from oil pollution, particularly when it comes to oil/water emulsions. This is explained by the fact that collecting such tiny oil droplets is more challenging [13]. Therefore, it is crucial to keep researching new approaches and techniques, effective oil capture systems, and cutting-edge wastewater treatment technologies, mainly for the separation of water and oil emulsions. Ultrasonic treatment is therefore believed to be a successful method of converting leftover oil and enabling subsequent processing in oil refineries. Moreover, it uses less energy while improving the results of physicochemical processing [14]. Ultrasonic treatment is essential for upgrading heavy molecules because it causes the bonds in heavy oil to thermally scission, producing hydrogen atoms. It is vital to continue investigating more effective solutions, possibly by combining different wettability types with the appropriate porous substrate, because the most popular methods, such as electro flotation and electrocoagulation [15], have disadvantages like high material requirements, expensive equipment, and high energy consumption [6]. The demulsification of water-in-oil (W/O) emulsions has been widely investigated through three major categories of techniques.

- Chemical demulsification, which relies on surfactant-based additives, remains the most common industrial practice due to its ability to weaken interfacial films. Studies such as Mi et al. and Okereke et al. reported high separation efficiencies using ionic liquids and chemically modified biomass, though concerns persist regarding cost, toxicity, and environmental accumulation [9,12].
- Mechanical and physical demulsification, including thermal, electrostatic, and particularly ultrasonic methods, offers alternatives that avoid chemical residues. Ultrasonic cavitation has been shown to accelerate droplet coalescence through microstreaming and localized turbulence, as demonstrated by Sadatshojaie et al. and Chen et al. However, ultrasound alone often requires high energy input or extended treatment times [13,14].
- Bio-based demulsifiers, derived from agricultural waste or natural fibers, have recently gained attention as sustainable alternatives. Natural materials such as coconut extracts, lotus leaf powder, and cellulose-based agents have achieved promising efficiencies due to their surface-active functional groups. Yet, most studies rely solely on passive chemical action without enhancing physical disruption.

According to Hassan et al. [15] conducted a technical and economic assessment of employing silica nanoparticles to improve the demulsification process in crude oil. A software model was created in MS Excel for the Central Processing Facility (CPF) that processes heavy crude oil from Fula in Balila, Sudan. A sensitivity analysis of the primary factors associated with production cost and net present value (NPV) for various flow schedule selection alternatives was conducted. Evaluating flow tables according to equivalent plant capacity yields a 19% decrease in production costs, but assessment based on consistent yearly crude oil processing leads to an only 3.7% reduction in production costs. Pal et al. [16] focused on breaking the emulsion to improve water separation using derived demulsifier (DEMLOCS) is formulated with extract of Cocos nucifera coconut that does not harm the environment. According to the results obtained, it was concluded that the prepared demulsifier works best at 2000 ppm. It efficiently separates oil and water within 24 hours and extracts a maximum amount of water of 88%. The emulsion is treated with DEMLOCS and the maximum water volume is separated at 45°C. There is abundant promising result for the use of bio-demulsifier in heavy crude oil and water emulsion. Ye et al. [17] employed naturally occurring lotus leaves, modified using a straightforward hydrothermal technique, to eliminate emulsions from crude oil mixtures.

The efficacy of HLLF powder in rapidly destabilizing W/O emulsions is demonstrated by its unique wettability and surface architecture. DE may reach 88.17% when the HLLF dose was 1000 mg/L and the settling period was 90 minutes at 70 °C. HLLF exhibited comparable demulsification efficacy to many widely used commercial demulsifiers. Furthermore, it could efficiently demulsify two varieties of crude oil emulsions from distinct oilfields. Parvasi et al. [18] demonstrated the impact of low-frequency ultrasonography on the demulsification of a crude oil wastewater unit with a low concentration of crude oil (500 mg/L). Subsequently, research has been conducted without chemical demulsifiers with a laboratory ultrasonic bath at frequencies of 25 kHz and 45 kHz. Perform studies to assess the impact of wastewater temperature, ultrasonic power, frequency, and irradiation time on separation efficiency. The findings indicated that, under ideal conditions, the efficiency of crude oil emulsion separation improved by 72%. Romanova et al. [19] demonstrated the feasibility of destabilizing stable water-in-oil (W/O) emulsions with an average diameter of 30 to 45 μm, including those containing "gel," by the combination of ultrasonic treatment and a nanosized additive. The impact of sonication parameters, such as power and exposure duration, on the separation efficiency of emulsions in batch mode has been examined. The study focused on submerged and reactor-type ultrasonic devices. Ultrasonic treatment at 1.0 kW, along with the incorporation of nanopowder AlN suspension in acetone, effectively eliminates over 99% of the emulsions examined. The additive concentration ranged from 4–8% vol, while the exposure duration varied from 0.5 to 3 minutes, contingent upon the emulsion's composition and properties. The oil phase, with a maximum water content of 0.5 weight percent, and the aqueous phase, with a maximum oil content of 46 mg L−1, may be achieved by the developed demulsification method.

Nadirov et al. [20] examined the demulsifying efficacy of original and fresh ground quartz (FMQ) particles extracted from river sand, contrasting it with the absence of an emulsifier. Alongside conventional solid-liquid characterization methods, employ rheological assessments, surface tension evaluations, and demulsification experiments to examine the impact of 75-micron mesh-sized quartz on emulsion stability. Following 100 minutes of deposition, a demulsification efficiency of 97% was achieved with the incorporation of 3 weight percent FMQ, in contrast to 140 minutes for unmodified quartz. The objective of grinding quartz is to enhance water permeability, hence elevating the local pH level, which results in decreased emulsion stability and eventual dissolution. Abdullah [21] focused on using oleic acid (OA), a naturally occurring substance that is widely accessible, to create two novel ionic liquids (ILs) and utilizing them to break up water-in-oil (W/O) emulsions. Both Epoxidized Oleic Acid + Pentaethylenhexamine - Ionic Liquid (EAPA-IL) and Epoxidized Oleic Acid + Tetraethylenepentamine - Ionic Liquid (EATA-IL) demonstrated effective performance, attaining 100% at various concentrations of demulsifier. The statistics demonstrated that as their concentration grew over time, so did their performance. Moreover, pure water was segregated by EAPA-IL and EATA-IL. Notwithstanding the considerable advancements in oil-water separation research, several limits have been identified in the associated studies. Numerous studies have extensively examined chemical demulsifiers, which, while useful, frequently provoke environmental concerns due to their possible toxicity and non-biodegradable characteristics. The aim of the present work is to prepare and formulate a cheap and environmentally safe demulsifier farm locally sourced raw material (Lemon peels) and experimentally tested to separate W/O emulsion assisted with ultrasonic waves applications.

2. Experimental Methods

2.1 Heavy Ful oil (HFO)

Heavy fuel oil is a kind of fuel oils characterized by a viscosity similar to that of tar. HFO consists of the residuals from petroleum sources following the extraction of higher-quality hydrocarbons using methods such as thermal and catalytic cracking [11]. HFO is distinguished by its physical, processing, and end-use qualities due to its wide variety of composition. HFO, the final byproduct of the cracking process, also comprises mixtures of these compounds to variable degrees: "paraffins, cycloparaffins, aromatics, olefins, and asphaltenes as well as molecules containing sulfur, oxygen, nitrogen, and/or organometals" [22]. The Daura refinery in Baghdad, Iraq, which produced water-in-oil emulsions, provided the heavy fuel oil emulsion equipment used in this study. The physical properties of this oil are shown in Table 1.

Table 1. Physical properties of the Basra Heavy oil [Al-Doura refinery]

Heavy fuel oil properties	
Specific gravity at 15.6ºC	0.8724
API at 15.6ºC	15.8
Density at 15 ºC (g/Cm^3)	0.9657
Kinematc Viscosity at 50ºC cst (mm^2/s).	183
Pour point ºC	+3
Carbon residue %w/w	8.1
Sulfur content %w/w	4.5
Water & sediment %v/v	>0.025
Asphaltenes content (wt %)	3.09%
Calorific Value (gross) KJ/kg	10441

2.2 Salt Water

In this study utilized natural water (tap water). A precise quantity of sodium chloride solution (5500 ppm) was combined with several prepared samples in 100 ml beakers containing 40% water. Table (2) presents the water specifications.

Table 2. Physical properties of the water

Physiologic (pH)	9.8
Electrical conductivity (EC)	3460 µs/cm
Temperature ºC	Between 20 and 25°C
Viscosity at 25°C	1 mPa/s

2.3 Natural Demulsifier

The natural material utilized in the separation process is lemon peels with a particle size of less than (100 microns). The lemon peels were removed, cleansed, desiccated, and sun-dried for a week. The specimens were subsequently subjected to an electric oven at 80°C and pulverized using a 1000-watt grinder.

2.4 Experimental Apparatus

The Lab Scale Ultrasonic Probe Sonicator (HC-SG-28800). The main components of the ultrasonic vibrating rod are the ultrasonic transducer, ultrasonic horn, and ultrasonic generator. The features of the ultrasonic apparatus used in the experiment are listed in Table 3.

Table 3. Specifications of the ultrasonic machine

Specifications	Value
Type	HC-SG-28800
Input voltage	220V 50-60 Hz
Frequency	28 kHz
Rated power	100-400-600-800 W
Power adjustment	50-100% gear adjustable
Working ambient temperature	+5 to +50℃
Tool head material	Titanium alloy
Length of the tool head	182 mm
Maximum operating temperature	150 degrees
Weight	16 kg
Power supply size	380×285×135 mm
Real-time display	Resonance, current
Cooling device	Transducer fan cooling
Connecting length	5 m
Reference processing capacity	1000

2.5 Emulsion Preparation

Samples were prepared following a stringent methodology to guarantee experimental consistency and reliability of results. Experimental reactors comprised clean 100-ml glass beakers. A mixture of 40% brine and 60% oil by volume created a two-phase system that simulates real separation conditions. Where 20 experiments were conducted. The components were meticulously combined using a magnetic stirrer to guarantee uniform distribution prior to ultrasonication. All preparations were conducted under regulated conditions to guarantee reproducibility and analytical precision. The procedure for applying ultrasonic waves to petroleum emulsions in a 300 ml beaker is depicted in Figure 2. After separation, the water content is drained into a 500 ml conical flask using a regulated tap at the bottom of a borosilicate glass 500 ml conical separatory funnel.

In experiments, lemon peel particles at varying concentrations (3,000, 5,000, 10,000, 15,000, and 20,000) ppm were included into the emulsion at 85°C with an operational frequency of 28 kHz. The results illustrate the impact of these concentrations on demulsification efficiency when ultrasound was utilized within conical glass reactors. Separation efficiency increased with higher lemon peel content, achieving an 80% water removal rate from the emulsion at 5,000 ppm, particularly when the combination underwent ultrasonic treatment. Separation efficiency fluctuated at different concentrations, suggesting an interplay between the applied energy level and the quantity of additive. Moreover, it was noted that ultrasound-induced friction elevated the emulsion

temperature as processing duration rose, hence enhancing the separation process. Experiments indicate that at elevated energy levels, the separation process accelerates; nevertheless, further investigation is necessary to comprehend the influence of varying concentrations on characteristics such as viscosity and color.

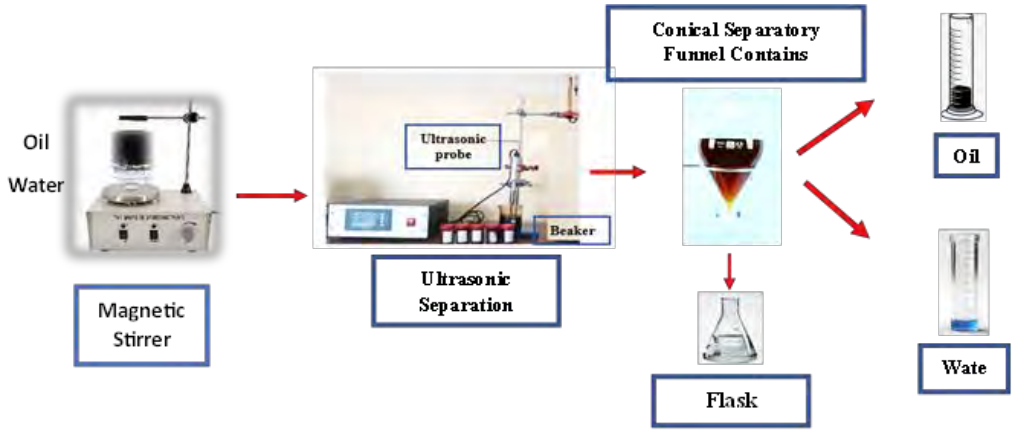

Fig. 2 Diagram of emulsion separation process

To guarantee the stability of the emulsion, the containers containing the oil/water emulsion were allowed to rest for a complete day prior to being segregated for each experiment. A reading is obtained after the materials are exposed to ultrasonography and allowed to sit for five minutes. The initial water content in the emulsion prior to ultrasound (IWC) and the final water content obtained after ultrasonic exposure (FWC) were taken into consideration when calculating the demulsification efficiency (ED) for each experiment in which the water-emulsion separation was achieved. The following equation was used to do this [25]:

$$ED\% = \frac{Iwc - Fwc}{Iwc} \times 100 \quad (1)$$

Where; I_{WC}: The emulsion's initial water content prior to ultrasonography, F_{WC}: The ultimate water content measured during ultrasonic exposure.

Cannon-Fenske-Routine Viscometer was used to determine the kinematic viscosity of heavy oil. The relationship applied to calculate the kinematic viscosity is [26]:

$$\nu = K \times t \quad (2)$$

The instrument constant k refers to the timing marks during the visual survey of the meniscus passage. It comes to: k=0.02688 mm^2/S^2.

3. Results and Discussion

3.1 Effects of Adding A 3000 ppm Concentration of Lemon Peels Molecules

Figure 3 illustrates the incorporation of lemon peel particles, a natural material, into the water/heavy oil combination, followed by the application of ultrasonic waves to the sample. The duration of ultrasound waves administered over 10 minutes at several energy (100 W, 400 W, 600 W, 800 W) influenced the concentration of the mixture. The concentration of the isolated water augmented over time, signifying that the separation process progressively enhances. At a low power of 400 W, the concentration of the separated water is inferior to that at higher energies of 600 W and 800 W. At 600 W and 800 W, the separation efficiency is enhanced; nevertheless, the disparity between these power levels is minimal, suggesting that elevating the power beyond 600 W may not yield substantial advancements in separation efficacy. The pulverized lemon peel particles assist in separation by disrupting the emulsion, absorbing water, or owing to their inherent physical and chemical characteristics. It comprises organic chemicals, including limonene, a hydrophobic substance that can dissolve some hydrocarbon constituents. It also has other

components like pectin and polyphenols, which may alter the surface tension between water and oil, so aiding in the separation of the two phases.

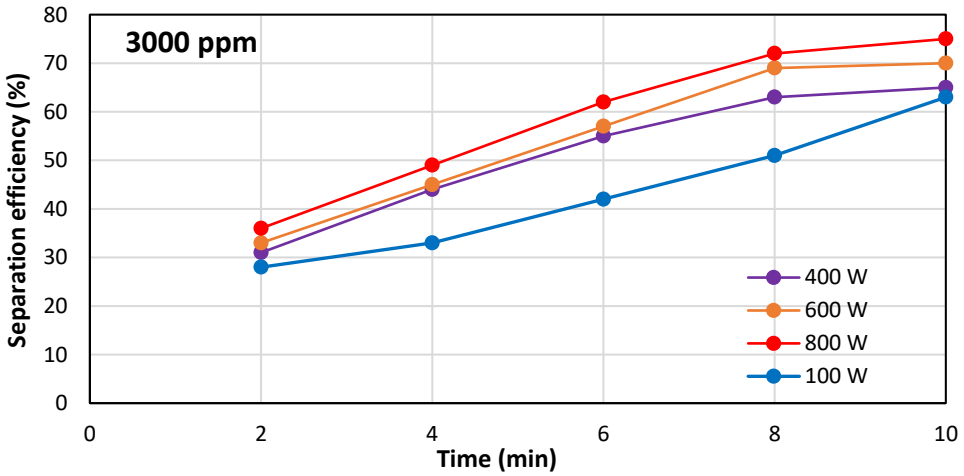

Fig. 3. Effect of adding 3000 ppm concentration of lemon peel particles

3.2 Effects of Adding a 5000 ppm Concentration of Lemon Peel Molecules

Upon increasing the concentration of lemon peel particles to 5000 ppm, as seen in Figure 4, a significant improvement in separation efficiency was observed relative to the 3000-ppm concentration. At all power levels, the percentage of separated water increases compared to the prior Figure 3, attaining 80% at a power of 800 W after 10 minutes. The distinction between 600 W and 800 W in the latter minutes is less perceptible, suggesting that the separation efficiency attains a saturation point around 5000 ppm, beyond which augmenting the power has no impact after a certain threshold. Lemon peel particles have been demonstrated to function as adsorbents, absorbing water or impurities that stabilize the emulsion. Moreover, they encompass acidic and alkaline substances that alter these emulsions and diminish their stability, hence facilitating coalescence and the separation of water and oil. The ultrasonic waves augmented the interaction by facilitating the cavitation effect, therefore accelerating the disintegration of emulsified water droplets and enhancing the reduction of surface tension, which results in the water being less adherent to the heavy oil.

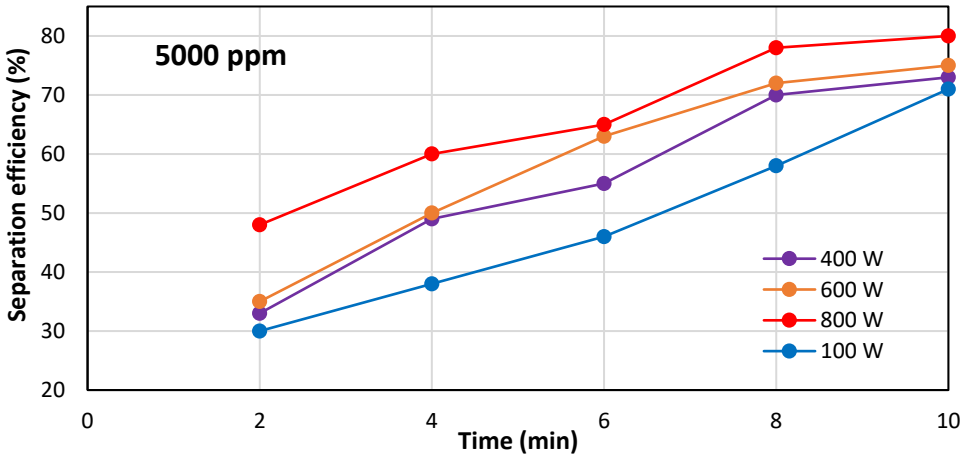

Fig. 4: Effect of adding 5000 ppm concentration of lemon peel particles

The demulsification efficiency showed a strong dependence on both ultrasound power and demulsifier concentration. Increasing ultrasound power enhanced acoustic cavitation intensity, resulting in more effective disruption of the interfacial film and higher droplet coalescence rates. Efficiency increased significantly up to 600 W and reached near saturation at 800 W. Similarly,

increasing lemon peel concentration improved efficiency up to an optimal value of 5000 ppm due to the increased availability of active surface-modifying compounds. However, concentrations above 5000 ppm led to reduced efficiency because viscosity increased and particle crowding hindered droplet mobility and cavitation performance.

3.3 Effects of Adding a 10000 ppm Concentration of Lemon Peel Molecules

Figure 5 indicates that elevating the particle concentration to 10,000 ppm did not markedly enhance the separation relative to 5,000 ppm, suggesting that the system may have attained saturation. The disparity between 600 W and 800 W diminished, suggesting that elevated particle concentration mitigated the impact of high power. This may result from heightened viscosity or the restabilization of the emulsion owing to particle saturation, which restricts ultrasound's efficacy in enhancing separation. Furthermore, the substantial quantity of particles may result in the establishment of a physical particle network that retains a portion of water within the system rather than allowing its total release.

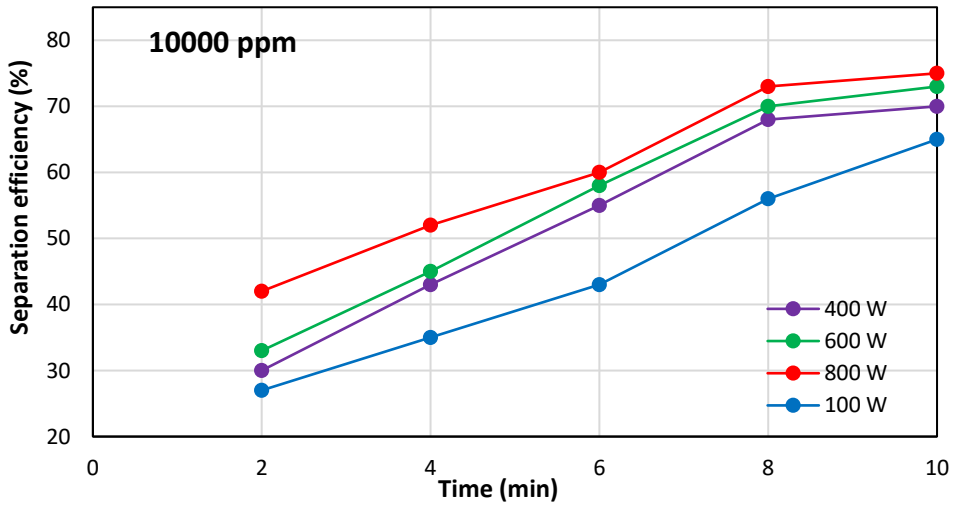

Fig. 5: Effect of adding 10000 ppm concentration of Lemon peel particles

3.4 Effects of Adding a 15000 ppm Concentration of Lemon Peel Molecules

In Figure 6, an increase in concentration to 15000 ppm in the water-oil combination resulted in a reversal of the separation process compared to 10000 ppm, suggesting that the lemon peel particles did not enhance the emulsion's effectiveness. The inefficiency arises from the heightened viscosity of the emulsion and the challenge of disrupting the links between the water and oil molecules. Conclude from the process of increasing concentrations that the best value at which we can get the highest efficiency is at a concentration of 5000 ppm at a power of 800 watts in ten minutes.

3.5 Effect of Concentrations of Lemon Peel Particles

Figure 7 indicates that augmenting the ultrasonic power from 100 W to 800 W enhanced the concentration of water-oil separation across all examined concentrations of lemon peel powder. The augmentation of power enhances the acoustic cavitation effect, facilitating the disruption of emulsions and promoting water-oil separation. The 3000-ppm concentration exhibited suboptimal performance, maybe attributable to an insufficient availability of active chemicals necessary for emulsion breakdown. The 5000-ppm concentration attained the greatest separation efficiency, exhibiting the highest water concentration across all power levels. At 10,000 ppm, a threshold was observed beyond which the separation efficiency began to decline at this concentration. At 15,000 ppm, the separation appears to be less efficient than anticipated, potentially due to the saturation effect; elevating the concentration to this level may augment the medium's viscosity, thereby diminishing the efficacy of acoustic cavitation and its impact on emulsification disruption. At low energies, separation is constrained at all concentrations, highlighting the significance of ultrasonic

power in improving the separation process for this material. The incorporation of lemon peel particles into a water-oil emulsion influences the separation process in many manners, contingent upon their chemical composition and surface characteristics. Besides the ultrasound's mechanism of disrupting emulsions by the mechanical fragmentation of emulsion particles, the findings on lemon peel particles indicate the following:

- Enhanced separation: Lemon peels contain essential oils and active chemicals like limonene, which exhibit hydrophobic qualities that may improve the surface tension between water and oil, hence aiding separation.
- Minimize emulsification: Lemon peel particles may function as a demulsifier due to their natural components, including pectin and flavonoids, which can influence emulsion stability, facilitating the separation of water from heavy oil.
- Enhanced environmental efficiency: Utilizing natural materials like lemon peels provide an eco-friendly alternative to synthetic chemicals, hence reducing the detrimental environmental effects of the separation process.
- Viscosity modification: Certain components in lemon peels may influence the viscosity of the oil, facilitating the separation of water and enhancing efficiency.

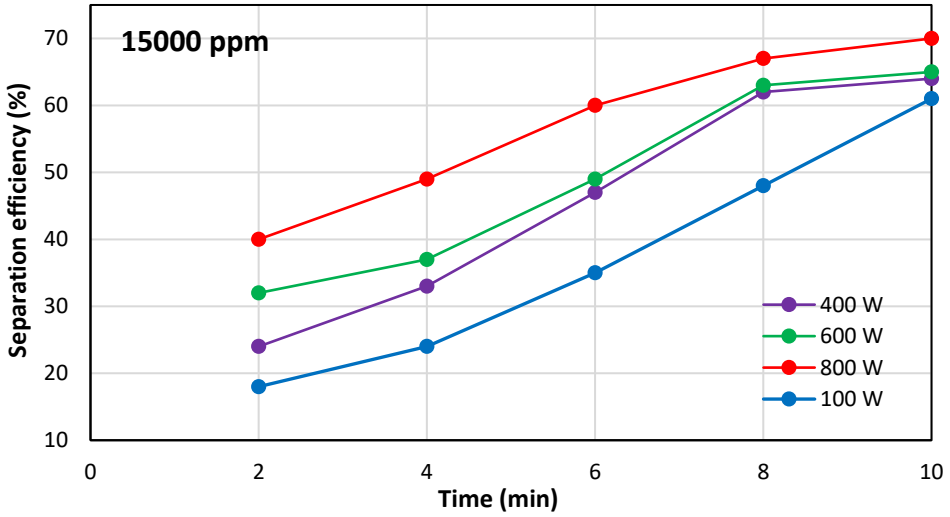

Fig. 6. Effect of adding 15000 ppm concentration of lemon peel particles

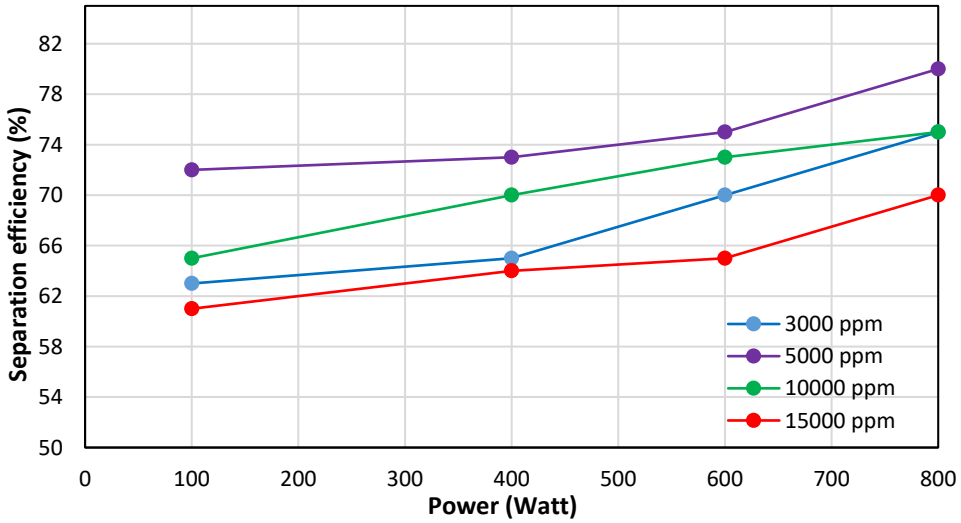

Fig. 7. Effect of lemon peels particles

3.6 Morphological Analysis of Lemon Peels Particles Using Scanning Electron Microscopy (SEM)

Figure 8a is a SEM imaging at different magnifications illustrates lemon peel particles measuring between 50 and 150 μm, characterized by a porous and rough structure, potentially enhancing absorption or influencing emulsion stability. The surface has a rough and complex texture, reflecting the characteristics of plant fibers. There are evident agglomerates, perhaps due to dehydration or crushing during processing. The particles vary in size from microscopic fragments measuring 20-50 micrometers to bigger pieces measuring 100-300 micrometers, as seen in Figure (8b), showing a heterogeneous particle size distribution. Pores and interstitial spaces between the particles may influence their capacity to absorb and interact with liquids. Figure (8c) distinctly illustrates the fibrous layers, corroborating the notion that lemon peels have cellulose and hemicellulose, compounds that may influence the interaction with oil and water. Small particles and surface fibers range from 5 to 50 μm, whereas pores and microscopic holes may measure less than 5 μm.

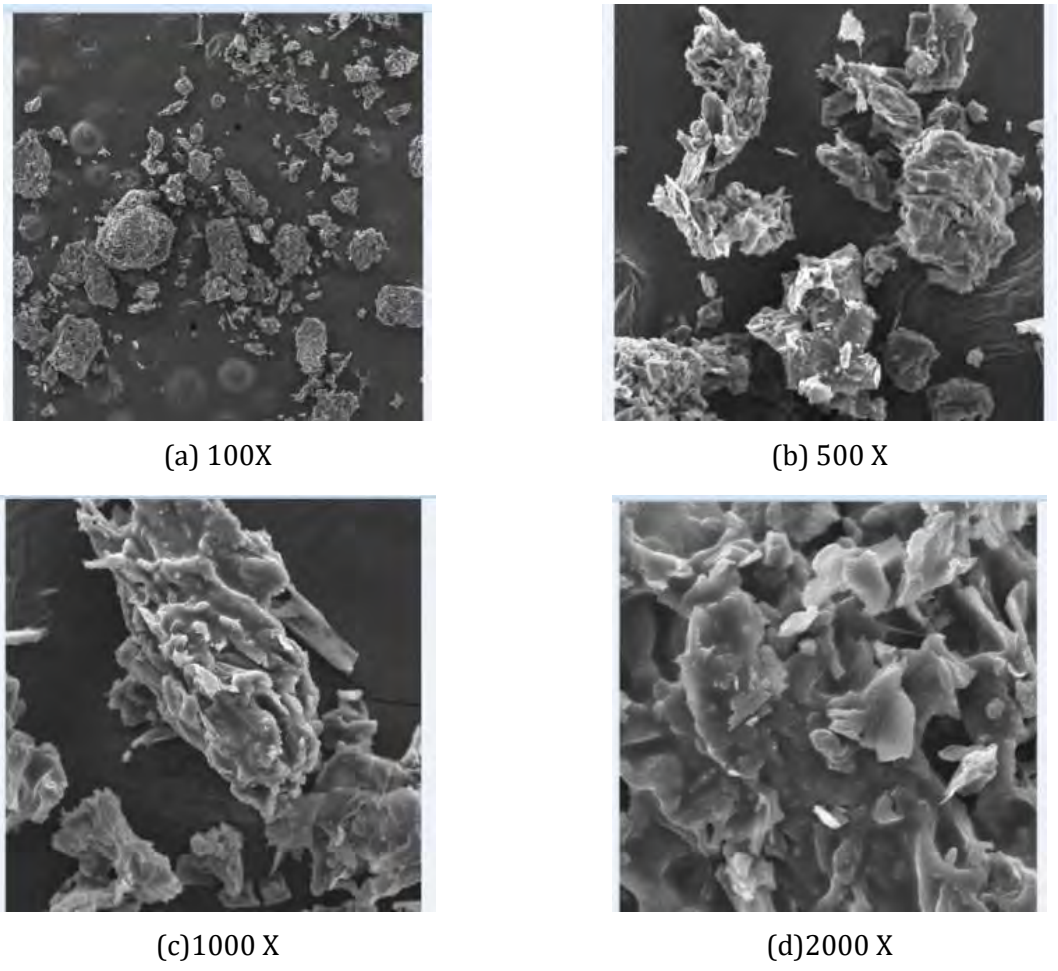

(a) 100X (b) 500 X

(c)1000 X (d)2000 X

Fig. 8. SEM images of lemon peel particles at magnifications of (a) 100x, (b) 500x, (c) 1000x, and (d) 2000x

The surface is notably uneven, perhaps enhancing the physical and chemical interactions with the surrounding medium. Figure (8d) depicts irregularly shaped particles characterized by sharp edges, aggregated structures, and a rough surface exhibiting fractures and fragmented sections. A congregation of particles is observable, potentially revealing the characteristics of the material in its desiccated form, since the particles tend to stack upon one another. Some particles may range from 5 to 10 μm in size, whilst bigger particles may measure 20 to 30 μm or greater. The high porosity and fibrous composition—including cellulose and hemicellulose—facilitate adsorption of water droplets and interfacial interactions, which can limit water permeation through separation membranes. Additionally, the heterogeneous particle size distribution can form multi-layered

filtration paths, creating physical barriers that slow down water transport while allowing oil to pass more freely. Moreover, the rough texture and presence of micro- and nano-scale pores may contribute to modifying surface energy and interfacial tension, further stabilizing the separation process. The combination of sharp-edged particles, irregular geometry, and complex topography supports the idea that lemon peel powder could be an effective additive or functional material in oil–water separation membranes by enhancing both physical trapping and chemical affinity toward water. Table 4 shows how the surface structure contributes to the separation mechanism.

Table 4 .The surface structure contributes to the separation mechanism

Magnification	Key Observation	Contribution to Demulsification
100×	Rough, porous surface	Enhances water adsorption
500×	Irregular fibrous structure	Increases interfacial disruption
1000×	Visible micro-pores	Promotes droplet trapping
2000×	Sharp-edged fragments	Improves mechanical breakup of emulsion

3.7 X-ray Diffraction (XRD) Analysis to Determine the Crystal Structure of Lemon Peels Molecules

The results in Figure (9) show a broad peak at low angles (~20° - 30°) in crystalline systems, sharp peaks are due to the systematic reflection of X-rays from atomic planes, while the broad peak indicates the presence of amorphous or semi-crystalline materials. It also indicates that the sample contains materials with short-range atomic arrangement and not a regular crystalline structure. A gradual decrease in intensity at high angles (>30° Theta-2Theta) indicates the presence of non-crystalline materials such as organic materials or nanoparticles dispersed in the system. It could be due to oil residues, or products resulting from the decomposition of organic compounds present in lemon peels after exposure to ultrasound. the analysis of the raw signal (Profile) and the application of mathematical processing such as Smoothing Profile and Background Subtraction are shown, which helps in identifying the actual peaks and removing unwanted signals. The presence of a signal at low angles after background correction may indicate the remains of natural carbonaceous or silicate materials resulting from lemon peel particles.

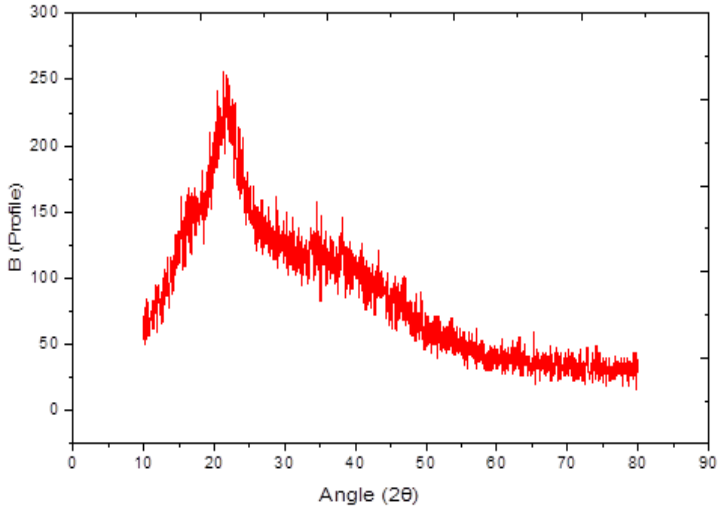

Fig. 9. X-ray diffraction (XRD) examination of an oil sample before exposure to ultrasound

3.8 Effect of Ultrasound on Oil/Water Samples

The infrared spectra of the compounds prepared using the SHUMADZUFTIR-84005 were recorded as potassium bromide tablets in the region 400 - 4000 cm^2 at laboratory temperature. Where the device FTIR represents the effect of ultrasonic waves on the physical and chemical properties of oil samples. Figure 10 shows the peaks of the spectral waves, where the value of 3288 cm^{-1} indicates

the O-H bond (alcohols or water), i.e. this peak indicates the stretching vibration of the O-H bond, indicating the presence of water or alcohols in the sample. Since the sample contains water, it is likely that this absorption is due to the residual water after the ultrasound treatment. It is also shown that the peak is broad, i.e. there is water bound to hydrogen or alcohols such as phenols. The spectral wave peak of 2893 cm^{-1} indicates the C-H bonds in alkanes (saturated hydrocarbons). These peaks represent stretching vibrations of the C-H bond in the alkane's groups (-CH_3 and -CH_2), which are present in heavy oil. These peaks indicate saturated hydrocarbon compounds, which constitute a major part of oil. The rise of these peaks after ultrasound treatment indicates a change in the concentration of hydrocarbon compounds. Peak 2831 cm^{-1} This peak usually indicates the presence of alkynes (-C≡C-) or nitriles (-C≡N-). It due to the presence of alkynes or some nitrogen-containing compounds. Peak 1771 cm^{-1} indicates the presence of carbonyl bonds C=O, which are usually found in esters, carboxylic acids or ketones. That due to the decomposition of some organic compounds in the oil as a result of the ultrasonic waves, which leads to the formation of new oxygen compounds. Peak 1635 cm^{-1} This peak indicates the C=C bonds in alkenes, which means that the oil may contain unsaturated compounds. This peak may also be due to the vibrations of absorbed water (H-O-H bending mode), which may indicate the presence of residual water after separation. The peak at 426 cm^{-1} is very low in the spectrum, and often indicates the presence of silica (SiO_2) or metal oxides.

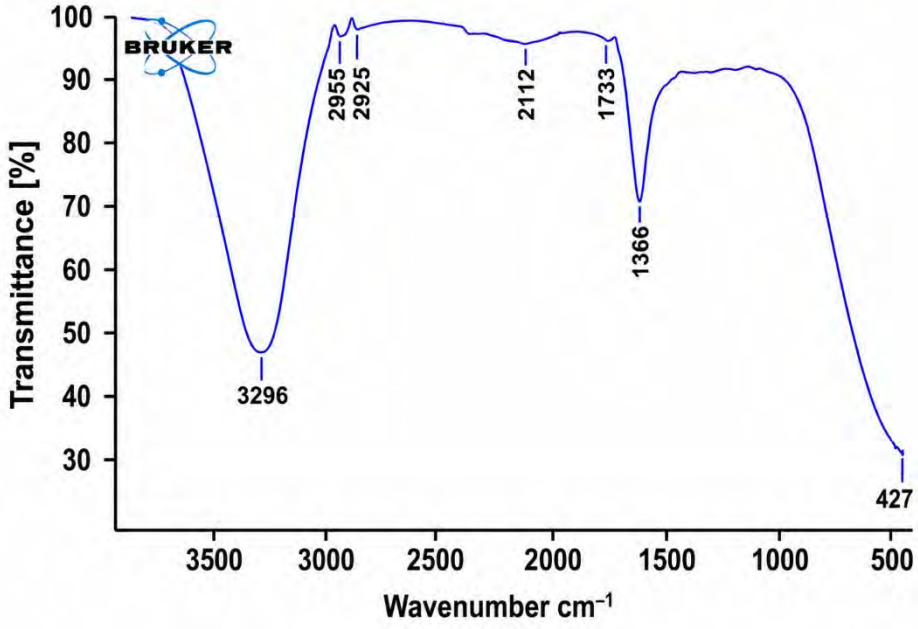

Fig. 10. Effect of ultrasound on oil sample by FTIR device

While, Figure 11 represents the examination of oil samples before exposure to ultrasonic waves, the spectral wavelengths before ultrasound treatment, the broad peaks 3735 cm^{-1} and 3404 cm^{-1} indicate O-H vibrations associated with water or hydroxyl groups (alcohols or phenols). Peaks 2953, 2921 and 2852 cm^{-1} These short, narrow peaks represent the C-H stretching vibrations of methyl (-CH_3) and methylene (-CH_2-) typically found in hydrocarbons. Peak 1771 cm^{-1} A prominent peak represents the C=O vibration, indicating the presence of carbonyl groups, such as carboxylic acids, esters or ketones. Peak 1603 cm^{-1} These peaks can be associated with structural vibrations of aromatic rings or C=C bonds in organic compounds. The peaks of 1457 and 1376 cm^{-1} are usually associated with C-H bond bending vibrations in organic compounds, especially in alkanes, which indicate the C-H bending vibration in the -CH_2- and -CH_3 groups, and hydrocarbons, which often appear in oils and petroleum products, indicating the presence of long carbon chains. As this peak has changed (disappeared) after treatment, this is an indication of the cracking or rearrangement of hydrocarbons, which may affect the viscosity or chemical composition of the samples. The peak of 1032 cm^{-1} is usually associated with C-O vibrations, which can be found in alcohols, ethers. The peaks of 808 and 722 cm^{-1} can indicate out-of-plane C-H vibrations in aromatic or long-chain hydrocarbon compounds. It was also found that this peak decreased in

intensity after exposure to ultrasound due to the decomposition of some aromatic compounds as a result of the mechanical and chemical effects of ultrasound. Peak 501-432 cm^{-1} These peaks may be related to the structural vibrations of compounds other metal oxides. Table 5 shows the most important peaks and active variables associated with the deemulsification process.

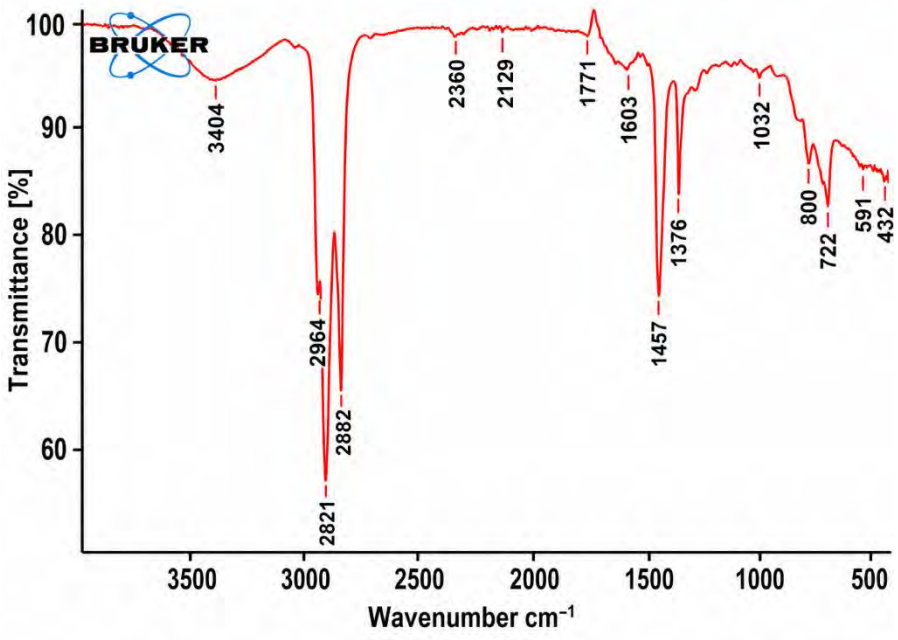

Fig. 11. FTIR examination of an oil sample before exposure to ultrasound

Table 5. The peaks and the active variables

Peak (cm^{-1})	Functional Group	Interpretation
3280	O–H	Moisture/pectin groups
2920, 2850	C–H (alkanes)	Hydrocarbon backbone
1730	C=O	Ester/carboxyl groups
1620	C=C	Unsaturated compounds
1030	C–O	Alcohol/ether groups

Table 6. A comparison between the studies and the current study

Researchers	Material used	Results
This study (Lemon peel)	Natural (lemon peel powder)	the current study achieved 80% efficiency at 5000 ppm and 85°C employing lemon peel powder and ultrasound
Mi et al. [12]	Natural (CCDA ionic liquid)	documented a 99.78% oil removal efficacy utilizing CCDA at 20 ppm at 70°C
Sadatshojaie et al. [14]	0No demulsifier (ultrasound only)	the ultrasound-only technique employed attained an effectiveness of up to 88%
Okereke et al. [9]	Natural blend (local materials)	achieved over 90% separation efficiency under mild conditions

In comparison to analogous prior investigations, the lemon peel-derived demulsifier in this research attained competitive separation efficiency. For example, Mi et al. (2025) documented a 99.78% oil removal efficacy utilizing CCDA at 20 mg/L at 70°C [12], whereas the current study achieved 80% efficiency at 5000 ppm and 85°C employing lemon peel powder and ultrasound. Despite a little reduced removal rate, the cost-effectiveness and accessibility of lemon peels confer considerable sustainability advantages. Moreover, the ultrasound-only technique employed by Sadatshojaie et al. attained an effectiveness of up to 88% [14], which is comparable to our findings,

given that their methodology did not utilize any chemical demulsifier. This comparison highlights the efficacy and ecological suitability of natural demulsifiers, such as lemon peels, when combined with ultrasonic enhancement. Table 6 shows a comparison between the studies and the current study.

3.9 Commercial Breaker (RQ35) in Breaking Emulsification

Figure 12 shows the results of the commercial emulsification breaker (RQ35) where different concentrations were taken to break the emulsification and the results shown in Table 5 were obtained [23]. The commercial breaker gave a low separation rate compared to the prepared natural breaker, but when using a high temperature for the commercial breaker (RQ35), its efficiency increases, and this is what happens in most commercial breakers as they need a high temperature more than (70) m. Therefore, the effect of temperature on the commercial breaker and the prepared breakers was studied to increase the separation efficiency. The commercial emulsification breaker was added at concentrations of (500, 1000, 2000 and 3000) ppm and at different temperatures.

Table 7. Emulsification fraction by commercial breaker (35 RQ)

Amount of parasitic substance (ppm)	Amount of water separated (%) Separation time (minutes)					
	10	20	30	40	50	60
500	0	0	0	0	0	5
1000	0	0	0	0	5	10
2000	0	0	5	10	10	15
3000	0	5	10	10	15	20

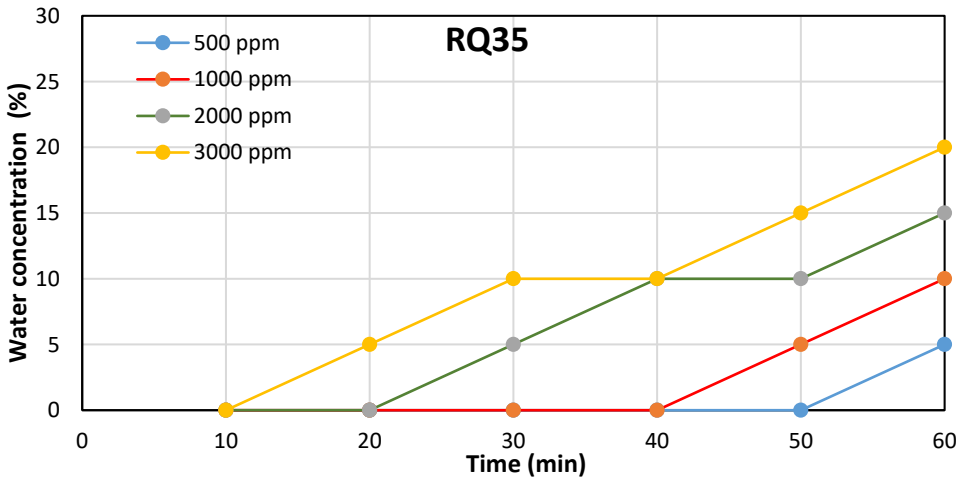

Fig. 12.Relationship between separation ratio and time with commercial emulsion breaker (RQ35)

4. Conclusion

This study provides clear evidence that integrating ultrasonic cavitation with lemon peel powder creates a synergistic demulsification mechanism capable of enhancing the separation of W/O emulsions in heavy fuel oil. Quantitative analysis of the experimental results revealed a strong dependency of demulsification efficiency on both ultrasound power and demulsifier concentration. The optimum operating conditions—5000 ppm lemon peel powder and 800 W ultrasonic power at 85 °C for 10 minutes—produced an efficiency of 80%. Compared with the commercial demulsifier RQ35 (65% under similar conditions), this demonstrates a measurable performance improvement of approximately 23%, supporting the viability of lemon peel as a competitive and sustainable alternative. The observed enhancement can be attributed to the combined physical and chemical actions of the system. Increasing ultrasonic power intensified acoustic cavitation, resulting in

violent microbubble collapse and high shear gradients that thinned and disrupted the interfacial films surrounding water droplets. Curve-fitting analysis showed that efficiency increased almost linearly with power up to 600 W before approaching a saturation trend at 800 W, indicating that the system reached the maximum effective cavitation threshold. Likewise, concentration-dependent behavior showed a logarithmic increase in efficiency up to 5000 ppm, followed by a decline at higher concentrations. This decrease corresponds with measured increases in viscosity at elevated particle loadings, which limited droplet mobility and partially suppressed cavitation effectiveness. The chemical contribution of lemon peel powder is linked to the functional groups present in pectin and limonene, as supported by FTIR analysis. Hydroxyl and carboxyl groups reduced interfacial tension and promoted droplet coalescence, while the hydrophobic nature of limonene modified surface energy at the oil–water interface. SEM observations further revealed a rough, porous morphology that enhanced adsorption and interfacial disruption, and XRD results confirmed the predominantly amorphous structure of the material, consistent with its high surface reactivity. Future efforts should therefore include pilot-scale continuous-flow testing, optimization of the particle size distribution to maximize active surface area, and comparative studies of other agro-waste–derived demulsifiers with similar biochemical functionality.

References

[1] Liu Y, Zhang B, Zhang Y, Ma L, Yang P. Electrochemical polarization study on crude oil pipeline corrosion by the produced water with high salinity. Eng Fail Anal. 2016 Feb;60:307-315. https://doi.org/10.1016/j.engfailanal.2015.11.049

[2] Zolfaghari R, Fakhru'l-Razi A, Abdullah LC, Elnashaie SSEH, Pendashteh A. Demulsification techniques of water-in-oil and oil-in-water emulsions in petroleum industry. Sep Purif Technol. 2016;170:377-407. https://doi.org/10.1016/j.seppur.2016.06.026

[3] Betancourt Cardozo F, Avella Moreno E, Trujillo CA. Structural characterization of unfractionated asphalts by 1H NMR and 13C NMR. Energy Fuels. 2016;30(4):2729-2740. https://doi.org/10.1021/acs.energyfuels.5b02941

[4] Grenoble Z, Trabelsi S. Mechanisms, performance optimization and new developments in demulsification processes for oil and gas applications. Adv Colloid Interface Sci. 2018;260:32-45. https://doi.org/10.1016/j.cis.2018.08.003

[5] Maye PEE, Jingyi Y, Taoyan Y, Xinru X. The effects of ultrasonic treatment on the molecular structure of residual oil. China Pet Process Petrochem Technol. 2017;4:82-88.

[6] van Zwieten R, Verhaagen B, Schroën K, Rivas DF. Emulsification in novel ultrasonic cavitation intensifying bag reactors. Ultrason Sonochem. 2017;36:446-453. https://doi.org/10.1016/j.ultsonch.2016.12.004

[7] Juliano P, Augustin MA, Xu XQ, Mawson R, Knoerzer K. Advances in high frequency ultrasound separation of particulates from biomass. Ultrason Sonochem. 2017 Mar;35:577-590. https://doi.org/10.1016/j.ultsonch.2016.04.032

[8] Check GR. Two-stage ultrasonic irradiation for dehydration and desalting of crude oil: a novel method. Chem Eng Process Process Intensif. 2014;81:72-78. https://doi.org/10.1016/j.cep.2014.04.011

[9] Trujillo FJ, Juliano P, Barbosa-Cánovas G, Knoerzer K. Separation of suspensions and emulsions via ultrasonic standing waves-A review. Ultrason Sonochem. 2014;21(6):2151-2164. https://doi.org/10.1016/j.ultsonch.2014.02.016

[10] Ensminger D, Bond LJ. Ultrasonics: fundamentals, technologies, and applications. CRC Press; 2024. https://doi.org/10.1201/9780429286964

[11] McKee RH, et al. The toxicological effects of heavy fuel oil category substances. Int J Toxicol. 2014;33(1 Suppl):95S-109S. https://doi.org/10.1177/1091581813504230

[12] Mi Y, et al. Synthesis of an efficient demulsifier derived from cotton cellulose and its demulsification performance in oily wastewater. Int J Biol Macromol. 2025;139839. https://doi.org/10.1016/j.ijbiomac.2025.139839

[13] Chen WS, Chen ZY, Chang JY, Chen CY, Zeng YP. Ultrasound-assisted desalination of crude oil: The influence of mixing extent, crude oil species, chemical demulsifier and operation variables. Ultrason Sonochem. 2022;83:105947. https://doi.org/10.1016/j.ultsonch.2022.105947

[14] Sadatshojaie A, Wood DA, Jokar SM, Rahimpour MR. Applying ultrasonic fields to separate water contained in medium-gravity crude oil emulsions and determining crude oil adhesion coefficients. Ultrason Sonochem. 2021;70:105303. https://doi.org/10.1016/j.ultsonch.2020.105303

[15] Hassan SA, Abdalla BK, Mustafa M. Adding Silica Nanoparticles to Improve the Demulsification Process in a Crude Oil Central Processing Facility: A Techno-economic Analysis. African J Eng Technol. 2021;1(1). https://doi.org/10.47959/AJET.2021.1.1.6

[16] Pal B, Kumar R, Naiya TK. Demulsification of crude oil-water emulsion using naturally formulated demulsifier. Pet Sci Technol. 2021;39(21-22):1027-1042. https://doi.org/10.1080/10916466.2021.1983599
[17] Ye F, et al. Demulsification of water-in-crude oil emulsion using natural lotus leaf treated via a simple hydrothermal process. Fuel. 2021;295:120596. https://doi.org/10.1016/j.fuel.2021.120596
[18] Khajehesamedini A, Sadatshojaie A, Parvasi P, Rahimpour MR, Naserimojarad MM. Experimental and theoretical study of crude oil pretreatment using low-frequency ultrasonic waves. Ultrason Sonochem. 2018 Nov;48:383-395. https://doi.org/10.1016/j.ultsonch.2018.05.032
[19] Romanova YN, Maryutina TA, Musina NS, Spivakov BY. Application of ultrasonic treatment for demulsification of stable water-in-oil emulsions. J Pet Sci Eng. 2022;209:109977. https://doi.org/10.1016/j.petrol.2021.109977
[20] Nadirov K, Zhantasov M, Nadirova Z, Otarbaev N, Bimbetova G, Nadirov R. Freshly milled quartz particles obtained from river sand as an efficient natural demulsifier for crude oil emulsions. Processes. 2022;10(5):811. https://doi.org/10.3390/pr10050811
[21] Abdullah MMS, Faqihi NA, Al-Lohedan HA, Almarhoon ZM, Karami AM. Application of new oleate-based ionic liquids for effective breaking of water in oil emulsions. Fluid Phase Equilib. 2023;568:113737. https://doi.org/10.1016/j.fluid.2023.113737
[22] DeCola E, Robertson T, Fisher M, Blair L. Phasing out the use and carriage for use of heavy fuel oil in the Canadian Arctic: Impacts to northern communities. Plymouth (MA): Nuka Research and Planning Group, LLC; 2018.
[23] Hendi YM, Mandeel TA. Synthesis, identification and evaluated of A Novel Demulsifier of Al-Rashidaiy crude oil (east of Baghdad). J Univ Anbar Pure Sci. 2017;11(1):58-68. https://doi.org/10.37652/juaps.2017.141453

Research on Engineering Structures & Materials
www.jresm.org

Research Article

Investigation and optimization of the impact of microwave irradiation on the extraction of sulfur from diesel fuel

Reem K. Khadiar [*,a], Raheek I. Ibrahim [b], Manal K. Odah [c]

Electromechanical Engineering Department, University of Technology-Iraq, Baghdad, Iraq

Article Info

Article History:

Received 13 Oct 2025

Accepted 11 Nov 2025

Keywords:

Microwave;
Desulfurization;
Oxidation of sulfur;
Diesel fuel

Abstract

The widespread use of diesel in transportation, industry, and power generation leads to many environmental problems caused by high sulfur compound emissions. Diesel fuel must be free of sulfur-containing compounds due to their potential to cause severe environmental pollution. Oxidative desulfurization of diesel fuel using microwave irradiation technology is considered one of the most efficient methods to achieve this goal. This simple, economical, and effective approach for treating sulfur-containing diesel fuel employs peroxide oxidation facilitated by pimelic acid and heating through microwave radiation. The research sought to examine the effectiveness of the acid as a catalyst and hydrogen peroxide as an oxidizing agent. The technology relies on microwave electromagnetic radiation. A Central Composite Design (CCD) was used to plan experiments with three variables and five levels, and to analyze the effect of these variables on the desulfurization efficiency of diesel fuel. The results indicated that the highest efficiency for sulfur extraction from diesel fuel occurred at 400 W, with an optimal processing time of 150 seconds and a peroxide-to-diesel volume ratio of 0.5, achieving approximately 75% sulfur removal under these optimal conditions. Microwave technology thus represents an effective and cost-friendly environmental approach for sulfur removal from diesel fuel.

© 2026 MIM Research Group. All rights reserved.

1. Introduction

Environmental pollution constitutes a substantial global issue, affecting public health, ecosystems, and the economy. Pollutants originating from transportation, industrial activities, and manufacturing plants have enduring impacts on the environment and human health [1,2]. Diesel fuel, a significant energy source for transportation, industry, and power generation, is a prominent contributor to air pollution, emitting pollutants such as particulate matter, nitrogen oxides, and sulfur oxides [3,4]. These sulfur compounds, prevalent in fossil fuels, can result in acid rain, soil pollution, and ecological degradation, notably adversely affecting aquatic systems and infrastructure [5]. The rising utilization of diesel fuels in industrial and transportation sectors intensifies air pollution owing to elevated sulfur emissions [6,7]. Organosulfur compounds, including methyl mercaptan and thiophenes, are abundant in crude oil and lead to catalyst poisoning during gasoline production [8,9]. The necessity to diminish sulfur content in diesel fuel to enhance air quality, particularly in urban regions, has propelled the quest for efficient desulfurization techniques [10]. The advancement of effective desulfurization methods is essential for mitigating the environmental and health repercussions of fossil fuel usage. Diverse techniques have been investigated, encompassing hydrodesulfurization [11], oxidative desulfurization [12], adsorptive desulfurization [13], bio desulfurization [14], and solvent extraction [15]. Hydrodesulfurization, a prevalent technique, employs hydrogen gas and catalysts to decompose sulfur-containing compounds but encounters difficulties with specific organosulfur compounds

*Corresponding author: eme.23.123@grad.uotechnology.edu.iq
[a]orcid.org/0009-0001-4245-1470; [b]orcid.org/0000-0002-7158-3376; [c]orcid.org/-0000-0002-3406-709X
DOI: http://dx.doi.org/10.17515/resm2025-1251ic1013rs

such as thiophene [16]. The procedure is energy intensive and expensive due to elevated hydrogen and temperature requirements [17]. Oxidative desulfurization (ODS) has garnered interest as an effective alternative, functioning under gentler circumstances without requiring hydrogen [18]. Oxidative desulfurization techniques employing oxidizing agents such as hydrogen peroxide and ozone have demonstrated efficacy in eliminating sulfur from diesel fuels, with various adsorbents, including activated carbon and metal oxides, utilized to augment the process [19–25]. ODS commences with the oxidation of sulfur compounds to sulfone, which can subsequently be isolated using solvents such as acetonitrile [12]. Numerous studies have investigated catalytic desulfurization employing both homogeneous and heterogeneous catalysts. Peroxotungstate (PW4) immobilized in SBA-15 has demonstrated desulfurization effectiveness of up to 89% [26]. Alternative strategies involve the utilization of ionic liquids and composite catalysts to enhance the process [27–30]. Certain systems employ ultrasound and ultraviolet irradiation to improve desulfurization [29]. Although effective, numerous catalysts necessitate intricate preparation and are costly, hence constraining their extensive application. Metal-free catalysts are deemed more economical and safer, presenting a viable option for commercial applications [31–33]. These methods eliminate the usage of toxic metals, rendering them more eco-friendly and economically feasible [34]. Bigdeli et al. proposed carbon nanofibers synthesized on activated carbon (AC) surfaces via microwave-assisted chemical vapor deposition (CVD) techniques. Methane and ethane served as source gases to investigate their textural and particle characteristics and efficacy in sulfur adsorption from a fuel model. The maximum yield of nanofibers was observed when subjected to a nitrogen-hydrocarbon mixture. The enhanced AC surface increased sulfur removal effectiveness by as much as 87% relative to the original [35]. Mesdour proposed research into the efficacy of MECODS, a straightforward technique for desulfurizing diesel fuel, employing $VO(acac)_2$/oxidant reagents in acid-based pyridinium ionic liquid. It attained a 99.1% elimination of sulfur compounds using a combination of H_2O_2 and H_2SO_4. The approach provided rapid reaction times, elevated conversion rates, selectivity, gentle reaction conditions, recyclability, sulfur reduction, and cost-effective materials. Additional investigation was required to comprehend MECODS dynamics and the activation energy influenced by temperature [36]. Coletti showed that a green chemistry methodology for fuel desulfurization using vanadium salen and salophen complexes could oxidize model aromatic sulfides such as dibenzothiophene (DBT) utilizing H_2O_2 as an eco-friendly oxidant under microwave irradiation.

The application of microwaves facilitated 98% DBT oxidation and nearly total sulfur extraction within 1000 seconds, rendering it a straightforward, quick, and environmentally benign procedure [37]. Fadhil developed efficient and regenerable catalysts using CuO–ZnO nanocomposites for catalytic oxidative desulfurization of gasoil fraction under microwave irradiation. The CuO–ZnO catalyst demonstrated superior conversion (93% under specific conditions), with performance remaining steady after five cycles. The microwave-based method showed promise due to efficient microwave energy transfer and enhanced protonation, improving sulfur conversion efficiency [38]. Kareem proposed a Ni@SiO_2–PWA nanocatalyst synthesized for microwave-assisted catalytic oxidative desulfurization of the gasoil fraction. The catalyst, consisting of phosphotungstic acid on magnetic silica, demonstrated a high sulfur conversion rate of 94.5% under microwave irradiation. The recyclability of the nano catalyst was examined, revealing that the catalytic activity remained consistent after six reaction cycles. The microwave-assisted catalytic ODS approach exhibits considerable potential for desulfurization, with its effective performance resulting from the synergistic effects of microwave activation energy and subsequent protonation [39]. Bartoli demonstrated that biosolids utilized in lipid pyrolysis could diminish sulfur content in crude pyrolysis oils. Elevating reaction temperature and extending processing duration reduced sulfur concentration, while pretreatments and direct amalgamation with adsorbents also proved beneficial. The Soxhlet procedure was found to be the most efficient method for recovering adsorbers. A liquid–liquid extraction method for oxidative desulfurization retrieved unreacted fatty acids, which could be transformed into hydrocarbon fuels, producing low-sulfur products [40]. Kareem examined the oxidative degradation of partially hydrotreated diesel utilizing a tripartite system comprising hydrogen peroxide, ferric chloride, and carboxylic acids (formic acid, acetic acid, or propanoic acid). It was determined that formic acid, acetic acid, and PA were completely soluble in diesel, rendering them inappropriate as aqueous extractants. AA

demonstrated superior extraction efficacy compared to FA owing to its greater void radius. A molar ratio of nH_2O_2/nS of 36 facilitated optimal elimination of sulfur compounds at 55 °C, achieving 65.1% sulfur removal [41]. Solouki and Jafferproposed a novel microwave-assisted method for the demetallization and desulfurization of crude petroleum oil, employing aqueous sodium hydroxide solutions and sulfuric acid. The procedure demonstrated a regeneration efficiency of 99%. A techno-economic analysis indicated that it is economically advantageous compared to hydrodesulfurization, with projected CAPEX of 16–21 million USD and OPEX of 1.27–9.1 dollars per barrel. Additional benefits encompassed catalyst-free operation, ambient processing temperatures, and energy conservation via selective microwave heating. Subsequent research was recommended to refine basic process parameters such as microwave power, DMDSA-to-oil ratio, and residence time to enhance economic efficiency [42]. Ahmed and Barham proposed an oxidative desulfurization method for high-sulfur diesel fuels utilizing citric acid, pimelic acid, and α-ketoglutaric acid as activators for H_2O_2. The technique was effective in eliminating sulfur-containing compounds from diesel fuels. Pimelic acid was identified as the most efficacious activator owing to its hydrophobic carbon structure and enhanced solubility in diesel fuel. The system exhibited superior desulfurization efficacy and prospective industrial applicability. The research proposed an uncomplicated and economical H_2O_2/carboxylic acid method for extensive desulfurization [43]. Despite these advancements, current oxidative desulfurization methods face several limitations, such as high chemical consumption, long reaction times, and incomplete sulfur removal. Therefore, the aim of the present work is to employ a green and efficient microwave-assisted oxidative desulfurization process using pimelic acid as an activator for hydrogen peroxide, combined with optimization techniques (Central Composite Design, CCD) to identify the optimal conditions—microwave power, irradiation time, and oxidant-to-fuel volume ratio—for maximum sulfur removal. The novel contribution of this study lies in integrating microwave irradiation with pimelic acid activation to enhance desulfurization efficiency while minimizing reaction time and reagent usage, offering a sustainable, cost-effective, and environmentally friendly alternative for sulfur removal from diesel fuel.

2. Microwave Irradiation Mechanism for Desulfurization

Features of the applied waves, such as their wavelength and frequency [44]. The fundamental idea behind microwave heating technology is the transformation of electromagnetic energy into thermal energy [44–48]. The maximum temperature increase that can be achieved depends on the amount of electromagnetic energy that the irradiated material absorbs. An efficient substitute for traditional heating methods used in the extraction and delivery of crude oil is the stimulation of fluid particles using electromagnetic waves to generate heat [46]. This approach can work in settings with complicated geological conditions and is economical and environmentally benign. The fundamental process of microwave heating is the use of oscillating electric and magnetic fields to stir polar molecules or ions [47,48]. Conventional heating, on the other hand, stimulates the material's exterior molecules or atoms by applying energy to its surface. The energy produced by electromagnetic waves' interaction with petroleum molecules promotes molecular motion as the ambient temperature rises, eventually transforming this energy into thermal energy [49,50]. A microwave-assisted method for desulfurizing commercial diesel fuel was given by Mostafa et al. [51], who focused on the effects of solvent type, solvent-to-feed ratio, microwave intensity, and irradiation duration. The findings showed that because of its polarity, ethyl acetoacetate is the best solvent. A solvent-to-feed ratio of 3:1, 180 W of microwave intensity, and 7 minutes of irradiation were the ideal desulfurization settings.

3. Materials and Methods

This study involved the supply of high-sulfur diesel fuel sourced from the Dora refinery in Baghdad. The present work utilized liquid hydrogen peroxide (30% GR Merck, Darmstadt, Germany) and acetonitrile (99% Biochem, Beijing, China). Pimelic acid (99% Merck, Darmstadt, Germany) was used in the oxidative desulfurization technique. To process the high-sulfur diesel with a starting sulfur concentration of 2865 mg/L, a microwave reactor device operating at 2.45 GHz was employed, with control over irradiation power and processing time, using a 1500 RPM electric

mixer. A 50 mL sample of diesel fuel was used, and this ratio remained constant in all experiments. It was mixed with varying amounts of hydrogen peroxide (5, 15, 25, 35, 45 mL) and different amounts of pimelic acid (0.1, 0.3, 0.5, 0.7, 0.9 mL). All components were blended using an electric mixer (1500 RPM) for 10 minutes. The resulting mixture was then subjected to microwave irradiation at energy levels of 200, 300, 400, 500, and 600 W for different time intervals of 50, 100, 150, 200, and 250 seconds. After microwave treatment, an equal volume of acetonitrile was added to the mixture, which was then mixed thoroughly and placed in a separating funnel for approximately 15 minutes to allow phase separation. The lower layer, representing the treated diesel fuel, was collected for analysis. A sample was taken, and the sulfur content was determined. As shown in Table 1 and Figures 1 and 2, the sulfur removal rate was calculated using the following equation:

$$Removal\ rate = (x - y)/x \times 100 \quad (1)$$

where x is original diesel and y is diesel after treatment.

Each experiment was conducted twice (in duplicate), and the standard deviation of the sulfur removal data was calculated. The standard deviations are presented in Figures 3–7 as error bars to illustrate experimental variability**.** A schematic illustration of the experimental setup, including the microwave reactor, mixing system, and separation process, was provided to clarify the technique and system components. The sulfur concentration of the model diesel, actual diesel fuel, and products was measured at the Refining and Gas Research Department of the Petroleum Research and Development Center under the Ministry of Oil, using the XOS Sindie OTG sulfur analyzer (USA) employing monochromatic wavelength-dispersive X-ray fluorescence according to ASTM D7039.

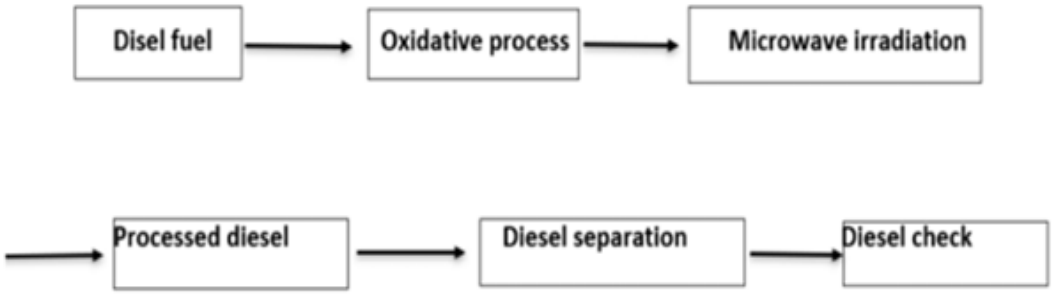

Fig.1. Operation steps

Fig. 2. Experimental procedure of testing

4. Design Results and Discussion

The results are presented in Tables 2 to 4 and Figures 3 and 4. This method proved to be effective for the removal of oxidized sulfur compounds from diesel fuel. Microwave irradiation can serve as an efficient and rapid technique for sulfur removal through oxidation, owing to its volumetric and selective heating characteristics.

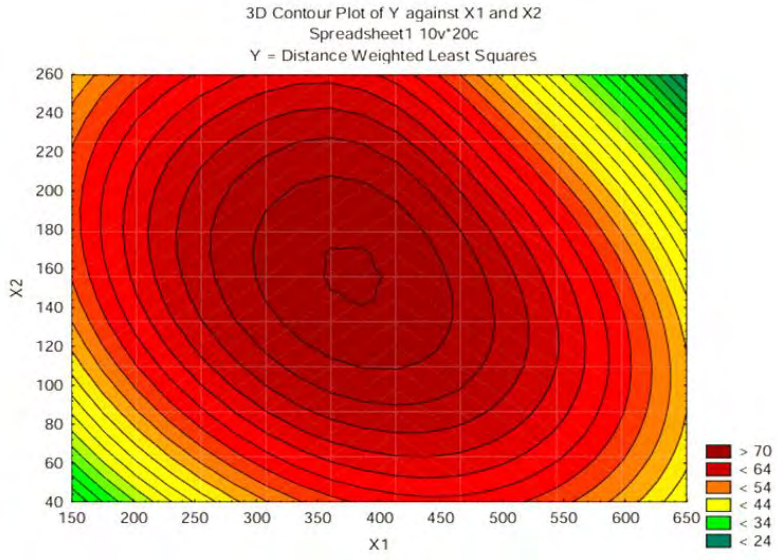

Fig. 3. 3D Plan of power emitted (W) and treatment time (s)

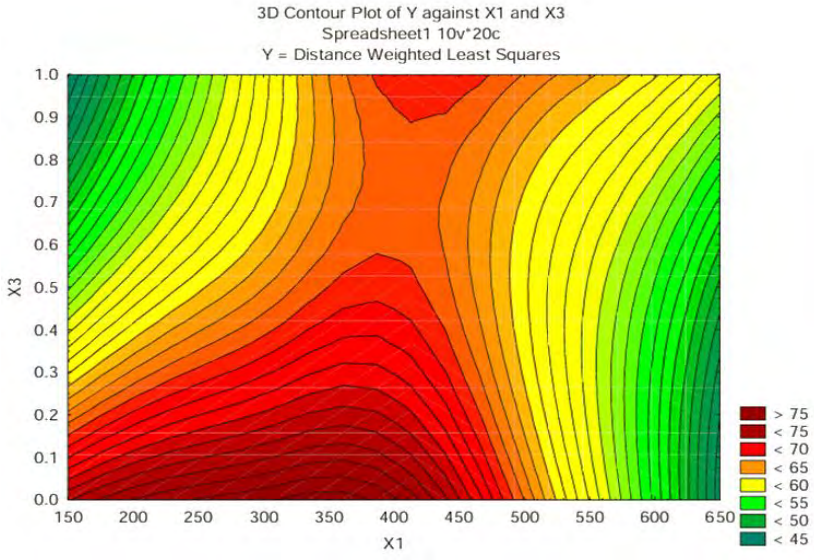

Fig. 4. 3D Plan of power emitted (W) and rate volume (ml)

It is worth noting that the microwave irradiation method was successfully applied to remove oxidized sulfur compounds from diesel fuel at various power levels and irradiation times. At 400 W and 150 s, a sulfur removal efficiency of approximately 70% was achieved (Figure 3), representing the highest efficiency obtained in this study. Figure 4 illustrates that the maximum separation efficiency (~75%) occurred at 400 W with a peroxide-to-diesel volume ratio of 0.5.

The optimization results obtained from the response surface methodology (RSM) are summarized as follows: the final value (5.7670) The model's high accuracy is confirmed by the root mean square error (RMSE = 0.533), and the lack-of-fit score (541.12) shows that the model is statistically significant and sufficiently describes the experimental data.

Table 1. Three-factors, five-level central composite design

Run no.	Coded values			Real values			Removal rate
	x_1	x_2	x_3	Power emitted [W]	Treatment time [sec]	volume of H_2O_2 to the volume of diesel [ml]	Y [%]
1	-1	-1	-1	300	100	0.3	66
2	1	-1	-1	500	100	0.3	64
3	-1	1	-1	300	200	0.3	71
4	-1	-1	1	300	100	0.7	61
5	1	-1	1	500	100	0.7	65
6	-1	1	1	300	200	0.7	63
7	1	1	-1	500	200	0.3	61
8	1	1	1	500	200	0.7	60
9	-2	0	0	200	150	0.5	60
10	2	0	0	600	150	0.5	55
11	0	-2	0	400	50	0.5	59
12	0	2	0	400	250	0.5	62
13	0	0	-2	400	150	0.1	74
14	0	0	2	400	150	0.9	67
15	0	0	0	400	150	0.5	70
16	0	0	0	400	150	0.5	70
17	0	0	0	400	150	0.5	70
18	0	0	0	400	150	0.5	70
19	0	0	0	400	150	0.5	70
20	0	0	0	400	150	0.5	70

Table 2. Sequence of experiments and separation results according to response surface methodology (RSM)

Factor	Symbol	Level				
		-2	-1	0	+1	+2
Power emitted, W	x_1	200	300	400	500	600
Treatment time, sec	x_2	50	100	150	200	250
Volume of H_2O_2 to the volume of diesel fuel ml	x_3	0.1	0.3	0.5	0.7	0.9

Table 3. Summary coefficient of polynomials results

Polynomial coefficients	Estimate	Standard error	Low. conf. limit	Up. conf. limit	p-level
a0	-5.2670	5.727262	-18.0281	7.4941	0.379411
a1	0.2580	0.016135	0.2260	0.2939	0.000000
a2	0.4807	0.031405	0.4017	0.5507	0.000000
a3	-32.8930	7.764768	-50.3840	-15.6820	0.001695
a4	-0.0004	0.000045	-0.0005	-0.0003	0.000038
a5	0.0813	0.013425	0.0513	0.1112	0.000123
a6	-0.0625	0.026849	-0.1223	-0.0027	0.042207
a7	-0.0003	0.000015	-0.0004	-0.0003	0.000000
a8	-0.0010	0.000061	-0.0011	-0.0008	0.000000
a9	1.4205	3.786240	-7.0158	9.8567	0.715371

The model is:

$$y = a_0 + a_1 \times x_1 + a_2 \times x_2 + a_3 \times x_3 + a_4 \times x_1 \times x_2 + a_5 \times x_1 \times x_3 + a_6 \times x_2 \times x_3 + a_7 \times x_1^2 + a_8 \times x_2^2 + a_9 \times x_3^2 \quad (2$$

Dep. Var: y and Level of confidence: 95.0% (α = 0.050).

4.1 Effect of Power Emitted on Separation Efficiency

As seen in Figure 5, one important aspect affecting separation efficiency is the amount of electricity (W) that is released. Because improved reaction kinetics speed up the oxidative desulfurization process, efficiency first rises with increased power. Efficiency increases from 50% at 200 W to 57% at 400 W, for example, during 50 s and a volume ratio of 0.1 mL (blue curve). Nevertheless, efficiency decreases at higher powers (500–600 W), most likely as a result of partial hydrogen peroxide breakdown brought on by excessive microwave radiation, which lowers the amount of oxidant that is accessible. Similarly, efficiency rises with power up to 400 W and then falls at higher powers for longer treatment periods and bigger volume ratios (red and green curves). This pattern shows a compromise between better mass transfer and the negative consequences of reactant depletion or overheating. The equilibrium between sufficient reactant availability at lower ratios and dilution or competing side reactions at higher ratios is what allows for the existence of an ideal volume ratio. Once more demonstrating the existence of an ideal power when reaction circumstances are favorable and there are no notable side reactions, the sky-blue curve (200 s, 0.7 mL) reaches a maximum efficiency of 72% at 400 W. The impact of irradiation duration is further highlighted by the purple curve (250 s, 0.9 mL), which shows that more thorough oxidation is possible with longer exposure times. Efficiency rises from 72% at 50 s to 77% at 150 s. Efficiency somewhat declines after this, perhaps as a result of additional reactions or excessive oxidation. The current method using pimelic acid offers a simpler, environmentally acceptable alternative with reasonable performance (up to 77%), avoiding the use of costly or harmful metals, in contrast to existing methods that employ metal-based catalysts that yield >90% efficiency. Pimelic acid is a sustainable substitute for oxidative desulfurization applications because of its cost-effectiveness, operational simplicity, and green chemistry viewpoint, even though the realized efficiency is a little lower.

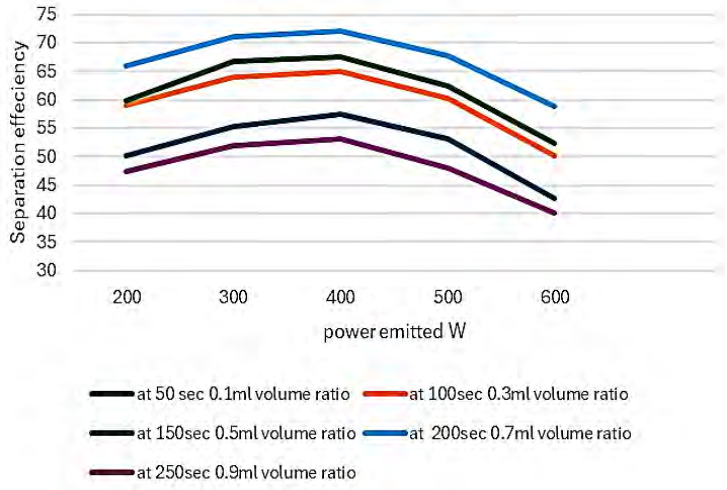

Fig. 5. The effect of power emitted on separation efficiency

4.2 Effect of Time on Separation Efficiency

Figure 6 illustrates the effect of irradiation time on desulfurization efficiency under different powers and volume ratios. The blue curve represents 200 W and a volume ratio of 0.1 mL. The efficiency reached 50% at 50 seconds and increased to 54% and 58% at 100 and 150 seconds, respectively. At 200 seconds, efficiency decreased to 52%, followed by a slight recovery to 57% at 250 seconds. The red curve corresponds to 300 W with a volume ratio of 0.3 mL. Efficiency rose from 60% at 50 seconds to 66.3% at 150 seconds, then declined to 62% at 200 seconds before recovering to 66% at 250 seconds. Similarly, the green curve (400 W, 0.5 mL) shows an increase from 67% at 50 seconds to a maximum of 75% at 150 seconds, followed by a slight drop to 72% at 200 seconds and a modest increase to 74% at 250 seconds. For higher powers, similar behavior was observed. The sky-blue curve (500 W, 0.7 mL) exhibited an increase from 70% at 50 seconds to 78% at 150 seconds, then a decline to 73% at 200 seconds and a small recovery to 74% at 250 seconds. The purple curve (600 W, 0.9 mL) followed the same trend, with efficiency increasing from

72% at 50 seconds to 77% at 150 seconds before decreasing to 70% at 200 seconds and slightly rising to 74% at 250 seconds. This overall trend suggests that desulfurization efficiency initially improves with irradiation time because longer exposure enhances mass transfer and allows more complete oxidation of sulfur compounds. However, beyond a certain point (around 150–200 seconds), efficiency tends to decline due to possible over-oxidation, secondary side reactions, or partial decomposition of hydrogen peroxide caused by prolonged microwave exposure. The slight recovery at 250 seconds may result from the reactivation of intermediate oxidation pathways or local redistribution of reactants under continuous irradiation. These results indicate that an optimal irradiation time exists where oxidative desulfurization proceeds efficiently without significant degradation of the oxidant or excessive thermal effects. Therefore, both microwave power and irradiation duration must be carefully balanced to maximize desulfurization efficiency while maintaining reaction stability.

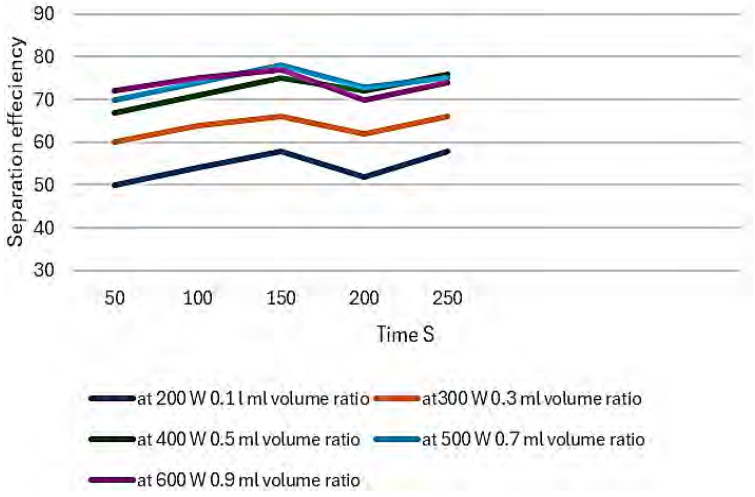

Fig. 6. The effect of time on separation efficiency

4.3 Effect of Volume Ratio on Separation Efficiency

Figure 7 presents the effect of the oxidant-to-fuel volume ratio on separation efficiency under various powers and irradiation times. The blue curve (200 W, 50 s) shows that the efficiency increased from 47% at a 0.1 mL ratio to 67% at 0.3 mL and reached a maximum of 71% at 0.5 mL. Further increases in the volume ratio caused the efficiency to drop to 60% at 0.7 mL and 34.3% at 0.9 mL. A similar trend was observed for higher powers. The red curve (300 W, 50 s) exhibited efficiencies of 44%, 64%, and 68% at 0.1, 0.3, and 0.5 mL, respectively, followed by a decrease to 59% and 34% at 0.7 and 0.9 mL. The green curve (400 W, 150 s) followed the same pattern, with efficiency increasing from 41% at 0.1 mL to 65% at 0.5 mL, then decreasing to 34.5% at 0.9 mL. The sky-blue (500 W, 200 s) and purple (600 W, 250 s) curves also displayed comparable behavior, with peak efficiencies of 62% and 58% at 0.5 mL, respectively, before declining sharply at higher ratios. This consistent trend indicates the existence of an optimal oxidant-to-fuel ratio around 0.5 mL, where separation efficiency reaches its maximum. At lower ratios, the amount of oxidant (hydrogen peroxide) is insufficient to fully oxidize the sulfur compounds, limiting the desulfurization process. As the oxidant volume increases, reaction kinetics improve because more reactive oxygen species become available, leading to higher efficiency. However, when the volume ratio exceeds the optimal value, the excess oxidant and solvent cause dilution of the reaction medium, reducing the contact between the organic and aqueous phases. Additionally, excess hydrogen peroxide may undergo self-decomposition or promote competing side reactions, both of which lower the effective oxidizing power. Therefore, the observed optimum results from a balance between reactant availability and reaction efficiency. Maintaining this balance ensures sufficient oxidation without significant dilution or side-product formation. These findings reinforce that the oxidant-to-fuel ratio, in combination with microwave power and irradiation time, must be carefully optimized to achieve maximum desulfurization efficiency while preserving process stability.

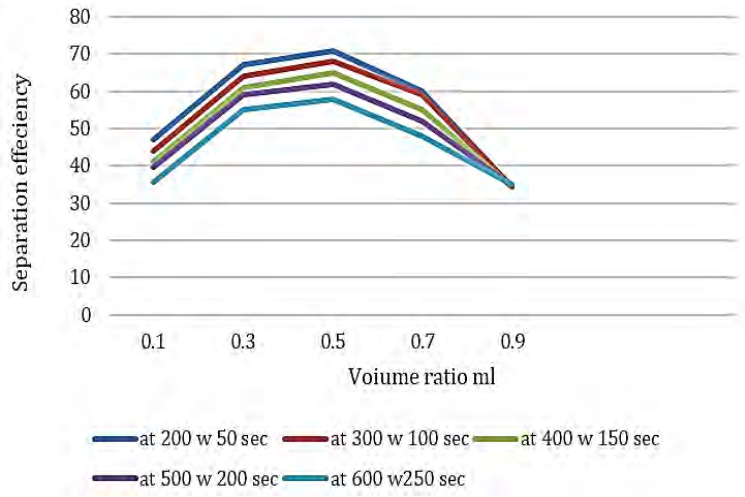

Fig. 7. The effect of volume rate on separation efficiency

Increasing microwave power and exposure duration accelerates the temperature rise, thereby enhancing the effectiveness of the interaction between hydrogen peroxide and sulfur compounds. The volume ratio influences the availability and concentration of reactants, which in turn affects the oxidation rate. This synergistic effect leads to improved sulfur removal efficiency under optimal conditions. Additionally, pimelic acid surpasses other carboxylic acids in promoting oxidation due to its enhanced solubility, suitable hydrophobicity, and favorable molecular configuration. These characteristics improve its interaction with sulfur compounds and hydrogen peroxide. Moreover, pimelic acid may absorb microwave energy more efficiently, further enhancing the oxidation process. Pimelic acid is a sustainable and economical organic catalyst that is reusable, although its efficacy diminishes over time due to chemical degradation.

Table 4. The ANOVA analysis values

Parameter	Value
Summation of square for regression	86038.23
Summation of square for residual	5.77
Degrees of freedom for regression	10.00000
Degrees of freedom for residual	10.00000
Degrees of freedom for regression vs. corrected total	10.00000
Mean of squares for regression	8603.823
Mean of squares for residual	0.577
Mean of squares for regression vs. corrected total	8603.823
f-Rate for regression	14918.94
f-Rate for regression vs. corrected total	326.42
p-Rate for regression	0.000000
p-Rate for regression vs. corrected total	0.000000

Conversely, metal catalysts demonstrate higher efficiency and stability in sulfur removal and can withstand multiple cycles; however, they are more expensive and less environmentally sustainable because of the presence of heavy metals. Therefore, pimelic acid is suitable for cost-effective and environmentally friendly applications, whereas metal catalysts are better suited for high-efficiency industrial processes. Microwave heating provides selective and rapid volumetric heating of materials, which enhances both reaction rate and efficiency. In contrast, conventional heating gradually raises the temperature from the outside, potentially leading to uneven heat distribution and reduced reaction efficiency. Microwaves can directly interact with reactive compounds, accelerate oxidation reactions, and shorten processing time, independent of traditional heating methods. Despite these promising results, certain limitations must be acknowledged. Scaling the microwave-assisted oxidation process from the laboratory to an industrial scale may present technological and economic challenges. Additionally, the cost of hydrogen peroxide, as the primary

active reagent, could affect the economic feasibility of the process, especially when large quantities are required. Therefore, future research should focus on optimizing reagent usage, exploring more cost-effective alternatives, and evaluating the environmental impact and safety considerations associated with industrial-scale applications.

5. Conclusions

Based on the results of experimental work, the following points can be concluded:

- Microwave irradiation is considered a cost-effective and environmentally friendly method, requiring only a few minutes of treatment without using chemicals or producing emissions.
- Various irradiation durations, energy levels, and volume ratios were tested, with optimal sulfur removal efficiency of 75% achieved at 400 w, 150 seconds, and a peroxide-to-diesel volume ratio of 0.5ml.
- Optimization techniques effectively identified the best operational conditions. Efficiency is further enhanced when using pimelic acid as an activating agent and hydrogen peroxide as an oxidizing agent alongside microwave radiation.
- Microwave irradiation facilitates an improved separation process, enhancing sulfur removal outcomes by up to 75%.
- The rotatable central composite design (CCD) was employed to systematically model the surface responses through a second-degree quadratic model.
- Results from a three-level factorial experiment were analyzed using linear regression. Coded variables were commonly used in the experimental design for accuracy and clarity.
- Microwave irradiation exhibits superior energy efficiency relative to traditional processes, significantly decreasing the production of secondary waste, so rendering it an environmentally viable alternative.

The microwave-assisted oxidative desulfurization method demonstrates significant promise for commercial application owing to its efficiency, rapidity, and environmental advantages. Subsequent investigations should prioritize process scalability, the incorporation of catalysts to enhance reaction rates, and thorough economic evaluations to determine commercial feasibility. Addressing these factors will facilitate the successful implementation of this technology and assist in the advancement of cleaner fuel.

Acknowledgement

The authors would like to thank the Electromechanical Department and Oil Research and Development Center of the Ministry of Oil for assistance in providing materials and testing.

References

[1] Mustafa FS, Aziz KH. Heterogeneous catalytic activation of persulfate for the removal of rhodamine B and diclofenac pollutants from water using iron-impregnated biochar derived from the waste of black seed pomace. Process Safety and Environmental Protection. 2023 Feb 1; 170:436-48. https://doi.org/10.1016/j.psep.2022.12.030

[2] Kumar P, Hama S, Abbass RA, Nogueira T, Brand VS, Abhijith KV, de Fatima Andrade M, Asfaw A, Aziz KH, Cao SJ, El-Gendy A. Potential health risks due to in-car aerosol exposure across ten global cities. Environment International. 2021 Oct 1; 155:106688. https://doi.org/10.1016/j.envint.2021.106688

[3] Choi AE, Roces SA, Dugos NP, Wan MW. Ultrasound assisted oxidative desulfurization: A comprehensive optimization analysis using untreated diesel oil. Computers & Chemical Engineering. 2022 Oct 1; 166:107965. https://doi.org/10.1016/j.compchemeng.2022.107965

[4] Hai T, Alsharif S, Aziz KH, Dhahad HA, Singh PK. Deep learning optimization of a biomass and biofuel-driven energy system with energy storage option for electricity, cooling, and desalinated water. Fuel. 2023 Feb 15; 334:126024. https://doi.org/10.1016/j.fuel.2022.126024

[5] Barilla GR, Chen CA, Valencia MZ, Dugos NP, Choi AE. Mixing assisted oxidative desulfurization using a synthesized catalyst of the activated carbon supported phosphotungstic acid: A process optimization study. South African Journal of Chemical Engineering. 2022 Oct 1; 42:61-71. https://doi.org/10.1016/j.sajce.2022.06.012

[6] Hossain MN, Park HC, Choi HS. A comprehensive review on catalytic oxidative desulfurization of liquid fuel oil. Catalysts. 2019 Mar 2;9(3):229. https://doi.org/10.3390/catal9030229
[7] Julião D, Gomes AC, Pillinger M, Valença R, Ribeiro JC, Gonçalves IS, Balula SS. Desulfurization of liquid fuels by extraction and sulfoxidation using H2O2 and [CpMo (CO) 3R] as catalysts. Applied Catalysis B: Environmental. 2018 Aug 15; 230:177-83. https://doi.org/10.1016/j.apcatb.2018.02.036
[8] Chandran D, Khalid M, Walvekar R, Mubarak NM, Dharaskar S, Wong WY, Gupta TC. Deep eutectic solvents for extraction-desulphurization: A review. Journal of Molecular Liquids. 2019 Feb 1; 275:312-22. https://doi.org/10.1016/j.molliq.2018.11.051
[9] Jin X, Wu J, Silva RC, Huang H, Zhang Z, Zhong N, Tutolo BM, Larter S. Alternate routes to sustainable energy recovery from fossil fuels reservoirs. Part 1. Investigation of high-temperature reactions between sulfur oxy anions and crude oil. Fuel. 2021 Oct 15; 302:121050. https://doi.org/10.1016/j.fuel.2021.121050
[10] Choi AE, Roces SA, Dugos NP, Wan MW. Adsorption of sulfones from actual oxidized diesel oil in the frame of oxidative desulfurization: A process optimization study using activated clay. Journal of Cleaner Production. 2022 Aug 20; 363:132357. https://doi.org/10.1016/j.jclepro.2022.132357
[11] Haruna A, Merican ZM, Musa SG, Abubakar S. Sulfur removal technologies from fuel oil for safe and sustainable environment. Fuel. 2022 Dec 1; 329:125370. https://doi.org/10.1016/j.fuel.2022.125370
[12] Saleh TA. Carbon nanotube-incorporated alumina as a support for MoNi catalysts for the efficient hydrodesulfurization of thiophenes. Chemical Engineering Journal. 2021 Jan 15; 404:126987. https://doi.org/10.1016/j.cej.2020.126987
[13] Ahmed BS, Hamasalih LO, Hama Aziz KH, Omer KM, Shafiq I. Oxidative desulfurization of real high-sulfur diesel using dicarboxylic acid/H2O2 system. Processes. 2022 Nov 9;10(11):2327. https://doi.org/10.3390/pr10112327
[14] Iruretagoyena D, Bikane K, Sunny N, Lu H, Kazarian SG, Chadwick D, Pini R, Shah N. Enhanced selective adsorption desulfurization on CO2 and steam treated activated carbons: Equilibria and kinetics. Chemical Engineering Journal. 2020 Jan 1; 379:122356. https://doi.org/10.1016/j.cej.2019.122356
[15] Porto B, Maass D, Oliveira JV, de Oliveira D, Yamamoto CI, Ulson de Souza AA, Ulson de Souza SM. Heavy gas oil biodesulfurization by Rhodococcus erythropolis ATCC 4277: optimized culture medium composition and evaluation of low-cost alternative media. Journal of Chemical Technology & Biotechnology. 2017 Sep;92(9):2376-82. https://doi.org/10.1002/jctb.5244
[16] [Gao S, Chen X, Xi X, Abro M, Afzal W, Abro R, Yu G. Coupled oxidation-extraction desulfurization: a novel evaluation for diesel fuel. ACS Sustainable Chemistry & Engineering. 2019 Jan 23;7(6):5660-8. https://doi.org/10.1021/acssuschemeng.8b04218
[17] Jiang W, Xiao J, Gao X, An X, Leng Y, Zhu L, Zhu W, Li H. In situ fabrication of hollow silica confined defective molybdenum oxide for enhanced catalytic oxidative desulfurization of diesel fuels. Fuel. 2021 Dec 1; 305:121470. https://doi.org/10.1016/j.fuel.2021.121470
[18] Shafiq I, Shafique S, Akhter P, Yang W, Hussain M. Recent developments in alumina supported hydrodesulfurization catalysts to produce sulfur-free refinery products: A technical review. Catalysis Reviews. 2022 Jan 2;64(1):1-86. https://doi.org/10.1080/01614940.2020.1780824
[19] Mahboob I, Shafiq I, Shafique S, Akhter P, Amjad UE, Hussain M, Park YK. Effect of active species scavengers in photocatalytic desulfurization of hydrocracker diesel using mesoporous Ag3VO4. Chemical Engineering Journal. 2022 Aug 1; 441:136063. https://doi.org/10.1016/j.cej.2022.136063
[20] Bu J, Loh G, Gwie CG, Dewiyanti S, Tasrif M, Borgna A. Desulfurization of diesel fuels by selective adsorption on activated carbons: Competitive adsorption of polycyclic aromatic sulfur heterocycles and polycyclic aromatic hydrocarbons. Chemical Engineering Journal. 2011 Jan 1;166(1):207-17. https://doi.org/10.1016/j.cej.2010.10.063
[21] Ren X, Liu Z, Dong L, Miao G, Liao N, Li Z, Xiao J. Dynamic catalytic adsorptive desulfurization of real diesel over ultra-stable and low-cost silica gel-supported TiO2. AIChE Journal. 2018 Jun;64(6):2146-59. https://doi.org/10.1002/aic.16055
[22] Triantafyllidis KS, Deliyanni EA. Desulfurization of diesel fuels: Adsorption of 4, 6-DMDBT on different origin and surface chemistry nanoporous activated carbons. Chemical Engineering Journal. 2014 Jan 15; 236:406-14. https://doi.org/10.1016/j.cej.2013.09.099
[23] Saleh TA. Simultaneous adsorptive desulfurization of diesel fuel over bimetallic nanoparticles loaded on activated carbon. Journal of Cleaner Production. 2018 Jan 20; 172:2123-32. https://doi.org/10.1016/j.jclepro.2017.11.208
[24] Ghubayra R, Nuttall C, Hodgkiss S, Craven M, Kozhevnikova EF, Kozhevnikov IV. Oxidative desulfurization of model diesel fuel catalyzed by carbon-supported heteropoly acids. Applied Catalysis B: Environmental. 2019 Sep 15; 253:309-16. https://doi.org/10.1016/j.apcatb.2019.04.063
[25] Flores R, Rodas A, Gasperin R. Oxidative desulfurization of diesel fuel oil using supported Fenton catalysts and assisted with ultrasonic energy. Petroleum Science. 2019 Oct;16(5):1176-84. https://doi.org/10.1007/s12182-019-0349-z

[26] Sun L, Zhu Z, Su T, Liao W, Hao D, Chen Y, Zhao Y, Ren W, Ge H, Lü H. Novel acidic eutectic mixture as peroxidase mimetics for oxidative desulfurization of model diesel. Applied Catalysis B: Environmental. 2019 Oct 15; 255:117747. https://doi.org/10.1016/j.apcatb.2019.117747
[27] Haruna A, Merican ZM, Musa SG. Recent advances in catalytic oxidative desulfurization of fuel oil-A review. Journal of Industrial and Engineering Chemistry. 2022 Aug 25; 112:20-36. https://doi.org/10.1016/j.jiec.2022.05.023
[28] Tanimu A, Tanimu G, Ganiyu SA, Gambo Y, Alasiri H, Alhooshani K. Metal-free catalytic oxidative desulfurization of fuels─ a review. Energy & Fuels. 2022 Mar 15;36(7):3394-419. https://doi.org/10.1021/acs.energyfuels.1c04411
[29] Juliao D, Mirante F, Ribeiro SO, Gomes AC, Valenca R, Ribeiro JC, Pillinger M, de Castro B, Goncalves IS, Balula SS. Deep oxidative desulfurization of diesel fuels using homogeneous and SBA-15-supported peroxophosphotungstate catalysts. Fuel. 2019 Apr 1; 241:616-24. https://doi.org/10.1016/j.fuel.2018.11.095
[30] Andevary HH, Akbari A, Omidkhah M. High efficient and selective oxidative desulfurization of diesel fuel using dual-function [Omim] FeCl4 as catalyst/extractant. Fuel Processing Technology. 2019 Mar 1; 185:8-17. https://doi.org/10.1016/j.fuproc.2018.11.014
[31] Andevary HH, Akbari A, Rajabi Z, Omidkhah M. Towards a room temperature oxidative desulfurization of refractory compounds over 1-octyl-3-methylimidazolium tetrachloroferrates/silica gel: The beneficial effects of immobilization. Process Safety and Environmental Protection. 2020 Apr 1; 136:343-52. https://doi.org/10.1016/j.psep.2020.02.009
[32] Sinhmar PS, Tiple A, Gogate PR. Combined extractive and oxidative desulfurization approach based on ultrasound and ultraviolet irradiation with additives for obtaining clean fuel. Environmental Technology & Innovation. 2021 May 1; 22:101487. https://doi.org/10.1016/j.eti.2021.101487
[33] Moeinifard B, Chermahini AN. Mono lacunary phosphomolybdate supported on mesoporous graphitic carbon nitride: An eco-friendly and efficient catalyst for oxidative desulfurization of the model and real fuels. Journal of Environmental Chemical Engineering. 2021 Aug 1;9(4): 105430. https://doi.org/10.1016/j.jece.2021.105430
[34] Liu Y, Chu J, Lian L, Chen X, An S, Hong L, Wang D, Chen W. Ultrafast oxidative desulfurization of diesel fuels by mass transfer enhancement of polyoxometalate modified alumina catalysts. Energy & Fuels. 2021 Jan 19;35(3):2110-20. https://doi.org/10.1021/acs.energyfuels.0c03673
[35] Bigdeli S, Fatemi S. Fast carbon nanofiber growth on the surface of activated carbon by microwave irradiation: a modified nano-adsorbent for deep desulfurization of liquid fuels. Chemical Engineering Journal. 2015 Jun 1; 269:306-15. https://doi.org/10.1016/j.cej.2015.01.059
[36] Mesdour S, Lekbir C, Doumandji L, Hamada B. Microwave-assisted extractive catalytic-oxidative desulfurization of diesel fuel via a VO (acac) 2/ionic liquid system with H2O2 and H2SO4 as oxidizing agents. Journal of Sulfur Chemistry. 2017 Jul 4;38(4):421-39. https://doi.org/10.1080/17415993.2017.1304550
[37] Coletti A, Sabuzi F, Floris B, Galloni P, Conte V. Efficient and sustainable V-catalyzed oxidative desulfurization of fuels assisted by ionic liquids. Journal of Fuel Chemistry and Technology. 2018 Sep 1;46(9):1121-9. https://doi.org/10.1016/S1872-5813(18)30045-8
[38] Fadhil MH, Ammar SH, Jabbar MF. Microwave-assisted catalytic oxidative desulfurization of gasoil fuel using synthesized CuO-ZnO nanocomposites. Journal of Fuel Chemistry and Technology. 2019 Sep 1;47(9):1075-82. https://doi.org/10.1016/S1872-5813(19)30044-1
[39] Kareem YS, Ammar SH, Darwash RA. Microwave-induced catalytic oxidative desulfurization of gasoil fraction over phosphotungstic acid-based magnetic silica (Ni@ SiO2\PWA) nanocatalyst. Catalysis Communications. 2020 Mar 1; 136:105926. https://doi.org/10.1016/j.catcom.2020.105926
[40] Bartoli M, Asomaning J, Xia L, Chae M, Bressler DC. Desulphurization of drop-in fuel produced through lipid pyrolysis using brown grease and biosolids feedstocks. Biomass and Bioenergy. 2021 Nov 1; 154:106233. https://doi.org/10.1016/j.biombioe.2021.106233
[41] Kareem JH. Oxidative desulfurization of diesel fuel using three kinds of carboxylic acids supported by iron (III) chloride. Polytechnic Journal. 2021;11(1):19. https://doi.org/10.25156/ptj.v11n1y2021.pp104-111
[42] Solouki A, Jaffer SA, Chaouki J. Process development and techno-economic analysis of microwave-assisted demetallization and desulfurization of crude petroleum oil. Energy Reports. 2022 Nov 1; 8:4373-85. https://doi.org/10.1016/j.egyr.2022.03.122
[43] Ahmed BS, Hamasalih LO, Aziz KH, Salih YM, Mustafa FS, Omer KM. Efficient oxidative desulfurization of high-sulfur diesel via peroxide oxidation using citric, pimelic, and α-ketoglutaric acids. Separations. 2023 Mar 15;10(3):206. https://doi.org/10.3390/separations10030206
[44] Kim, Teawon, Jaegeun Lee, and Kun-Hong Lee. "Microwave heating of carbon-based solid materials." Carbon letters 15.1 (2014): 15-24. https://doi.org/10.5714/CL.2014.15.1.015

[45] Sweygers N, Kamali M, Aminabhavi TM, Dewil R, Appels L. Efficient microwave-assisted production of furanics and hydrochar from bamboo (Phyllostachys nigra "Boryana") in a biphasic reaction system: effect of inorganic salts. Biomass Conversion and Biorefinery. 2022 Jan;12(1):173-81. https://doi.org/10.1007/s13399-021-01372-6
[46] Palma V, Barba D, Cortese M, Martino M, Renda S, Meloni E. Microwaves and heterogeneous catalysis: A review on selected catalytic processes. Catalysts. 2020 Feb 18;10(2):246. https://doi.org/10.3390/catal10020246
[47] Grewal AS, Kumar K, Redhu S, Bhardwaj S. Microwave assisted synthesis: a green chemistry approach. International Research Journal of Pharmaceutical and Applied Sciences. 2013 Oct 31;3(5):278-85.
[48] Zhang F, Zhou T, Liu Y, Leng J. Microwave synthesis and actuation of shape memory polycaprolactone foams with high speed. Scientific reports. 2015 Jun 8;5(1):11152. https://doi.org/10.1038/srep11152
[49] Yoshikawa N. Mechanism of microwave heating of matter. RF power semiconductor generator application in heating and energy utilization. 2020:71-89. https://doi.org/10.1007/978-981-15-3548-2_3
[50] Ferreira SH, Rovisco A, dos Santos A, Águas H, Igreja R, Barquinha P, Fortunato E, Martins R. Porous ZnO nanostructures synthesized by microwave hydrothermal method for energy harvesting applications. InNanopores 2021 May 12. IntechOpen.
[51] Mostafa HY, Khedr GE, Mohamed AE, El-Aty DM. The role of microwave radiation in extractive desulfurization of real diesel fuel for green environment: an experimental and computational investigation. BMC chemistry. 2024 Oct 14;18(1):199. https://doi.org/10.1186/s13065-024-01292-2

Blank Page

Research on Engineering Structures & Materials
www.jresm.org

Research Article

Torsional ductility and toughness of reinforced concrete beams with a new method of splice remedy

Ziadoon M. Ali [*,a], Akram S. Mahmoud [b]

Department of Civil Engineering, University of Anbar, Ramadi, Iraq

Article Info

Article History:

Received 13 Oct 2025

Accepted 24 Nov 2025

Keywords:

Torsional ductility;
Toughness;
Lap splice;
Bond strength;
Experimental study

Abstract

This study investigated the torsional performance of reinforced concrete (RC) beams using spliced reinforcement bars. Inadequate lap splice lengths were specifically employed to investigate the influence of diminished splice length on torsional capacity, torsional ductility, and torsional toughness. Insufficient splice lengths are especially important in practice, since increasing splice length in FRP-reinforced structures elevates material cost, while excessively splices may lead to reinforcement congestion that restricts adequate concrete placement. A new splice strengthening approach utilizing Carbon Fiber Reinforced Polymer (CFRP) sheets was implemented, applied transversely around the splice zone and covered with resin to enhance confinement and improved bond strength. The novelty of this study resides in the new CFRP configuration developed to strengthen inadequate lap splices of GFRP bars under pure torsion, a condition not previously investigated in comparison to flexural and shear loads. Seven RC beams were fabricated, cast tested under pure torsion to examine the effects of splice length, CFRP strengthening, and stirrup spacing. Results indicated that the shortest substandard splice affected torsional capacity by approximately 36.45%, while torsional ductility and toughness were reduced by up to 36.76% and 70.7%, respectively, in comparison to a beam with continuous bars. Extending stirrup spacing from 100 to 150 mm reduced torque by 15% while significantly impacting ductility. The strengthening of CFRP significantly improved ultimate torque capacity, torsional ductility, and toughness. Finally, this transverse wrapping technique may offer practical on-site benefits, as its enhanced confinement may allow minimizing the required splice length while preserving acceptable torsional performance, and it can be applied manually without required instruments compared to other methods, including welding and couplers.

© 2026 MIM Research Group. All rights reserved.

1. Introduction

Reinforced concrete (RC) structures generally require bar splicing to address construction problems or fabrication considerations [1,2]. While traditional steel reinforcement splicing has been well investigated, the performance of spliced glass fiber reinforced polymer (GFRP) bars exists currently insufficiently studied, specifically under torsional load conditions. GFRP reinforcement has advantages include corrosion resistance and a superior strength-to-weight ratio [3,4]; however, its distinct mechanical properties need careful consideration at splice regions. Inadequate lap splice lengths in GFRP-reinforced beams may result in premature failure when subjected to torsional loads.

The structural response of reinforced concrete members to torsion has garnered more attention owing to the rising utilization of torsion-sensitive components, including spiral slabs and curved bridge girders. Torsion is highly associated with bending and shear stresses, and eccentric loads

*Corresponding author: zaydon88@uoanbar.edu.iq
[a]orcid.org/0000-0002-8114-0990; [b]orcid.org/0000-0002-1956-0281
DOI: http://dx.doi.org/10.17515/resm2025-1253ic1013rs
Res. Eng. Struct. Mat. Vol. 12 Iss. 2 (2026) 889-903

make torsion an important consideration in bridge design [5–7]. Prior studies have investigated the performance of reinforced concrete beams with transverse and longitudinal glass fiber reinforced polymer reinforcement subjected to torsion. Shehab et al. [8] investigated FRP-RC beams subjected to simultaneous bending and torsion, discovering that GFRP stirrups failed prior to the crushing of the concrete cover due to inadequate bonding. Deifalla [9] presented adhesively bonded GFRP stirrups, which enhanced ultimate torque relative to bent stirrups.

Mohamed et al. [10] examined concrete beams reinforced with sand-coated GFRP and CFRP bars subjected to pure torsion, demonstrating that beams with minimal transverse reinforcement failed due to the fracture of FRP stirrups, while those with elevated transverse reinforcement ratios failed due to concrete crushing in diagonal struts. These results highlight the essential importance of transverse reinforcement while indicating that inadequate lap splice length in longitudinal FRP bars, which withstand torsional loads post-concrete cracking, is a mainly neglected concern. Previous research attempted to fix splice defects by adding resin to the splice region and longitudinally wrapping the bars with CFRP sheets [11–16]. The method enhanced tensile strength and is simpler to perform than conventional techniques such as couplers or welding [15], but it provides limited enhancement in bond behavior, especially under overloading conditions.

This work presents a new configuration of transverse CFRP wrapping, wherein CFRP sheets wrap perpendicularly and directly around the spliced bars. This method aims to improve resistance to bar slide and develop the bond-transfer mechanism between steel and concrete under rotational loads. This research evaluates the performance of the suggested splice-strengthening approach under pure torsion, measuring its influence on ultimate torque capacity, torsional ductility, and toughness, in contrast with prior studies that mainly focused on flexural behavior.

This study aims to investigate the effect of inadequate lap splice length on the torsional behavior of reinforced concrete beams and to assess the performance of transverse CFRP wrapping as a suitable strengthening technique. The scope includes experimental testing of seven beams subjected to pure torsion, which includes differences in splice length, CFRP usage, and stirrup spacing.

2. Experimental Program

2.1 Materials

The experimental program utilized Ordinary Portland Cement (Type I) as the primary binder. Naturally graded sand served as the fine aggregate, while crushed gravel with a maximum nominal size of 10 mm was used as the coarse aggregate. Clean potable water, free from impurities, was employed for both mixing and curing the concrete specimens. To improve the workability during casting, a superplasticizer (Visco Crete 225 S) was added to the concrete mix. All materials were sourced locally and complied with the relevant standard specifications for concrete production. Cylindrical specimens measuring 150×300 mm was cast and tested, achieving an average compressive strength of about 49.5 MPa. The details of the materials and their weights per cubic meter are presented in Table 1, while (Fig. 1) illustrates the casting and curing processes. The mechanical properties of the reinforcing materials used in the study are summarized in Table 2.

Table 1. Concrete components

Components	Quantity
W/C: Water/cement Ratio (%)	28
Superplasticizer (Visco crete 225 S) (Liter/m^3)	5
Water (kg/m^3)	140
LocalCement (kg/m^3)	500
Local crushed gravel (kg/m^3)	1060
Local natural sand (kg/m^3)	710

Table 2. Mechanical properties of reinforcement

material	Bar diameter (mm)	Area (mm^2)	Yield strength (MPa)	Tensile ultimate strength (MPa)	Elastic modulus (MPa)
Steel bars	8	28	422	460	200000
GFRP bars	10	78.5	-----	1024	45000

Fig. 1. Casting and curing of beams

2.2 Splice Remedy

The present research used unidirectional CFRP sheets (Type: SikaWrap®-300 C) with fibers oriented at 0°. The manufacturer specifies that the dry fiber tensile strength is 4,000 N/mm^2 and the dry fiber modulus of elasticity is 230,000 N/mm^2, according to the information in the manufacturer's technical data sheet (ISO 10618). (Fig. 2) illustrates that the CFRP sheet was fabricated as a plane sheet and subsequently coated with a 1 mm layer of Sika Dur 330 resin for effective bonds to the spliced bars.

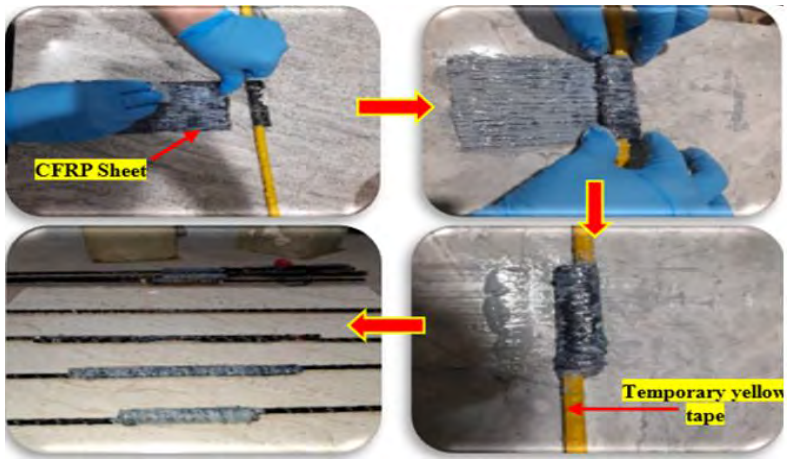

Fig. 2. Splice region remedy by CFRP sheet

The CFRP sheet was subsequently wrapped in transverse direction surrounding the spliced bars region in two layers to ensure an adequate anchorage. The width of CFRP coincided with the length of the splice region (i.e., 100 and 200 mm).In contrast to the prior method [11-13], which involved longitudinally wrapping the CFRP sheet around the spliced bars, the objective of the current new technique of transverse CFRP sheet wrapping is to achieve effective confinement around the substandard lap splice region. The existing method may resist slippage better and elevate the tensile stresses in the spliced bars, potentially attaining yield strength, while also allowing the specimen to endure a greater load and avoid splitting failure. Figure 2 illustrates the wrapping

technique and different lap splice configurations. Fig. 3 and 4 illustrates the specifications of reinforced beams and splice position with details, respectively.

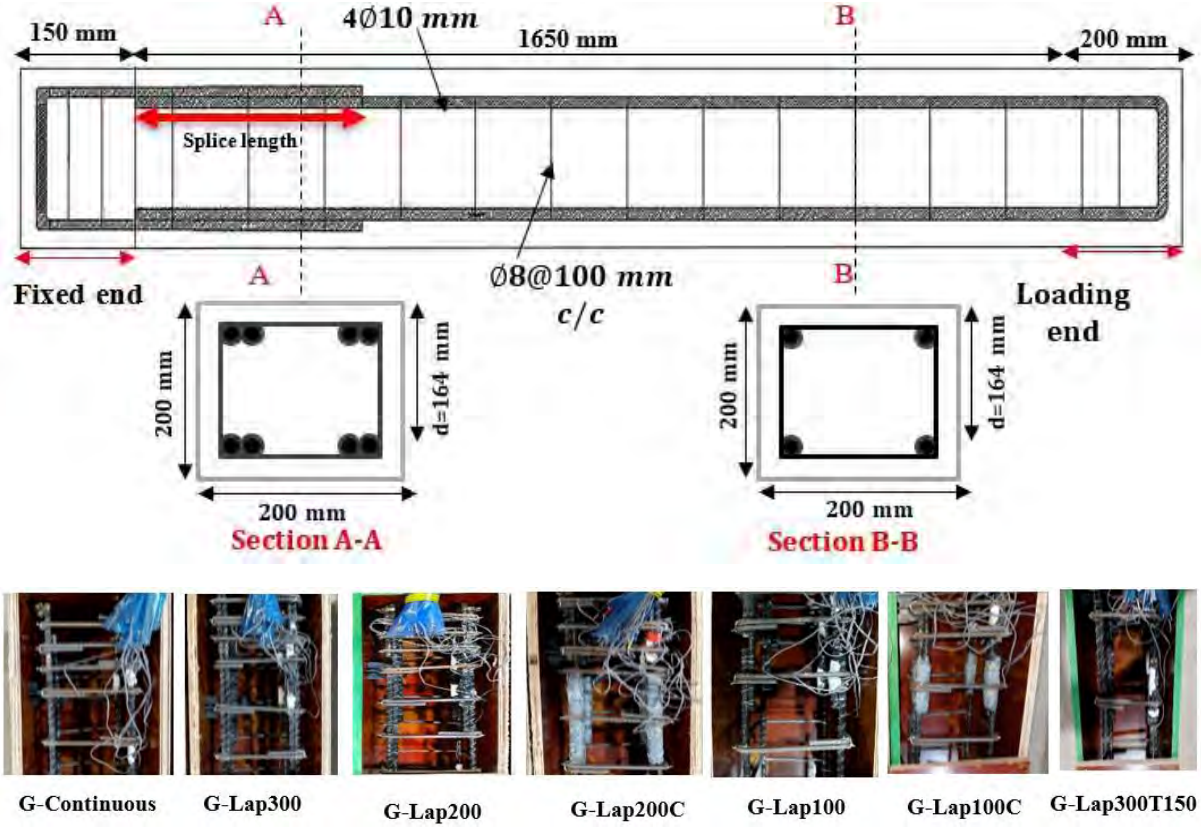

Fig. 3. The specifications of reinforced beams

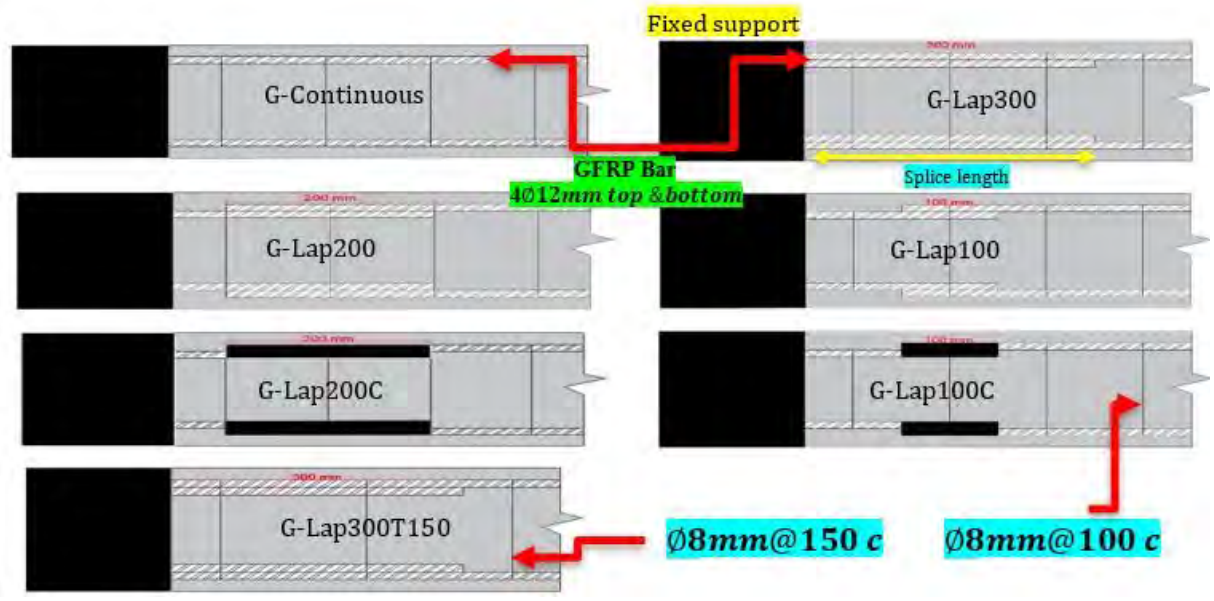

Fig. 4. The details of splice position near the fixed support

2.3 Beams Fabrication

Seven reinforced concrete beams were manufactured, cast, and subjected to pure torsion tests. As shown in (Fig. 3), the beam measurements were 200 x 200 mm with an overall span of 2000 mm (1650 mm effective span). 4Ø10 mm GFRP bars reinforced the beams in the longitudinal direction. All specimens were reinforced with Ø8 at 100 mm in the transverse direction except one beam, which was reinforced by Ø8 mm at 150 mm as a parameter. The parameters included the presence

of a splice bar and the lap splice length, which ranged between 300 mm and 100 mm to obtain a substandard length. The inadequate lap splices of lengths 200 mm and 100 mm were strengthened with CFRP sheets and Sika Dur 330 resin. These were then compared to the inadequate lap splices that had not been strengthened. Table 3 presents the details of the parametric study.

2.4 Test Setup

A 500-kN universal test machine was set up for testing all reinforced concrete beams. (Fig. 5) and (Fig. 6) illustrate the test configuration and provides a schematic 2D representation of the testing equipment. The testing equipment comprises two supports. The first support is a fixed support, while the subsequent support is a movable support for applying load. The load was applied vertically, linked to the beam made of steel used as arm to produce pure torque as illustrated in (Fig. 5) (Fig. 6). From (Fig. 5), the steel shaft allows only for rotation, and the vertical movement was prevented to avoid the effect of shear and bending moment. An electromechanical transducer was employed to transform rectilinear motion into an electrical Signal. Three linear variable differential transducers (LVDTs) were employed to measure the displacement with a capacity of 120 mm after being linked to an electronic data logger. The LVDTs were previously calibrated to ensure reliable reading of twisting angle.

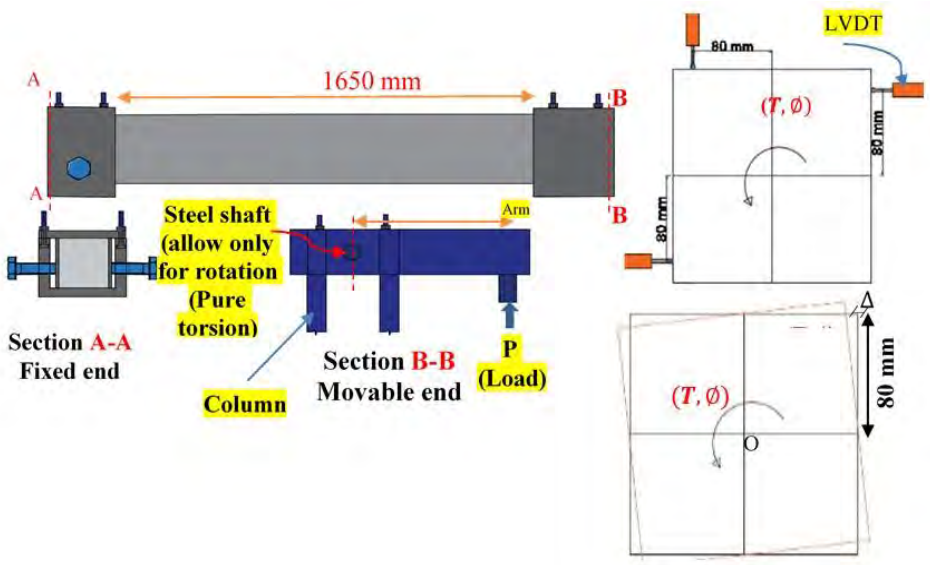

Fig. 5. Schematic diagram for test setup

The LVDTs were positioned on the movable end from the side of applied torque to measure the maximum displacement of the specimen. The position of the LVDTs is illustrated in (Fig. 5) and (Fig. 6). The angle of twist due to applied torque (T) can be found from eq (1) as follows:

$$\emptyset = tan^{-1}(\frac{\Delta}{80\ mm}) \quad (1)$$

Where Δ: Displacement recorded from the LVDTs in mm, 80 mm: Distance from the LVDTs position to the point O as shown in Fig. 6.

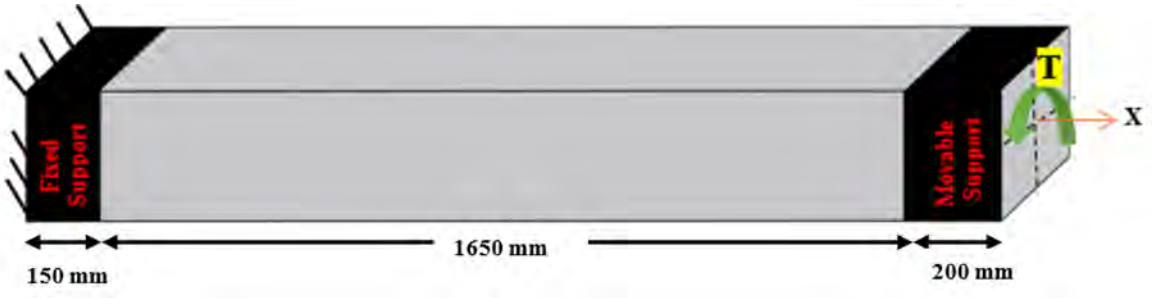

Fig. 6. Experimental testing setup

The load was incrementally applied from zero until failure resulted and the displacement was recorded at each 0.5kN increment. An experimental assessment measured the ultimate torque and torque-angle twist curve. From the torque-twisting angle curves, the torsional ductility and toughness were computed and discussed.

3. Results and Discussion

The results including values and load deflection curve of the tested beams were illustrated in (Fig. 7) and Table 4.

3.1 Ultimate Torque

Table 4 and (Fig. 7) illustrate the ultimate torque capacity for the specimen. The ultimate torque and twist angle at the moveable end decreased as the splice length decreased, particularly in cases where the lap splice length was substandard. Specifically, the G Lap300's ultimate torque capacity decreased by 14% compared to the G-Continuous. It indicates that the G-Lap 300 lacks lap splice length.

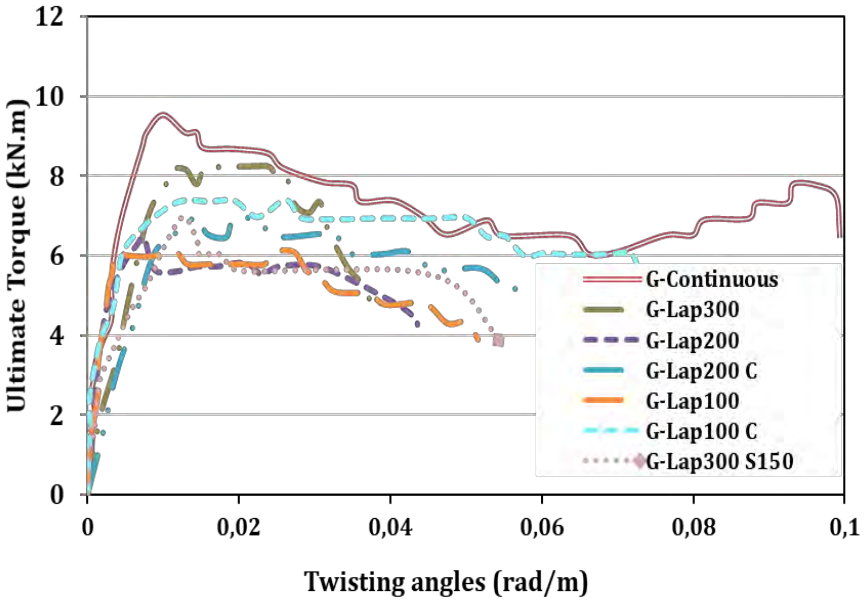

Fig. 7. Torque-Twisting angle curves

The reduction in ultimate torque capacity is minimal compared to the decline in ultimate load capacity under flexural loading, where the decrease in ultimate load has reached 40% with the

same length of splice length and the same type of GFRP reinforcement [13]. This may be an indication that the short lap splice length could cause the ultimate capacity to drop significantly when flexure and torsion loads are applied simultaneously. The ultimate torque capacity declined by 33% and 36% compared to the reference beam with continuous GFRP bars when the lap splice was shortened by 33.33% for beam G Lap 200 and 67.667% for beam G Lap 100. Insufficient lap splice length may cause weak stress transfer between spliced bars, reducing bonding stresses. Fig. 8 shows how splice length affects G-Group torque capacity.

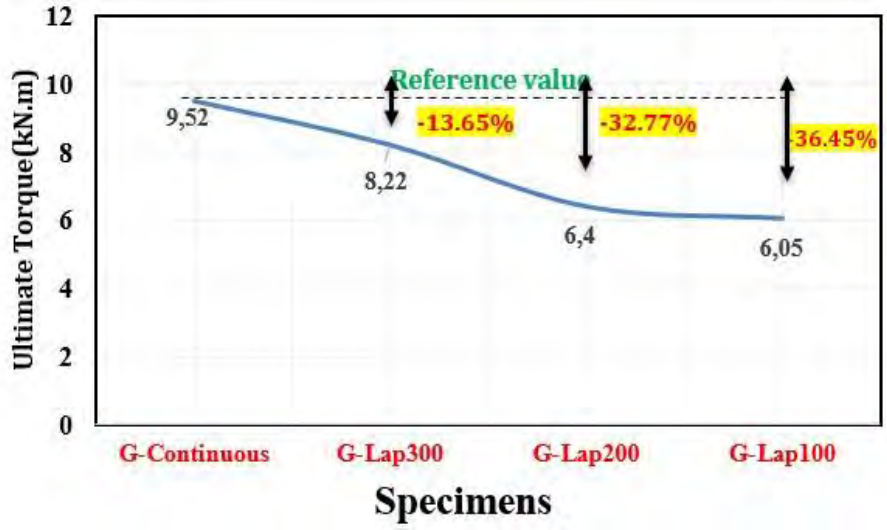

Fig. 8. Effect of unstrengthen lap splice length on ultimate torque capacity

Table 3. Details of the parametric study

Specimens	Description of reinforcement with splicing		Splice length /Ls (mm)	Splice Configuration
	Longitudinal	Stirrups		
G-Continuous	4Ø10 mm Continuous GFRP bar	ø8mm@100mmc/c	Continuous	
G-Lap300	4Ø10 mm GFRP with 300 mm lap splice length		300	
G-Lap200	4Ø10 mm GFRP with 200 mm lap splice length		200	
G-Lap200C	4Ø10 mm GFRP with 200 mm lap splice length and CFRP remedy/1ply		200	
G-Lap100	4Ø10 mm GFRP with 100 mm lap splice length		100	
G-Lap100C	4Ø10 mm GFRP with 100 mm lap splice length and CFRP remedy		100	
G-Lap300 T150	4Ø10 mm GFRP with 300 mm lap splice length	ø8mm@150mmc/c	300	

The strengthening method for substandard 100 mm and 200 mm lap splice lengths was tested under ultimate torque capacity. Strengthening increased ultimate torque capacity and angle of twist. The G-Lap200C specimen had 8% more ultimate torque than the G-Lap200. Significantly, as shown in (Fig. 9), the ultimate torque capacity increased by 21% for G-Lap100C compared to G-Lap100 when the strengthening method was applied to the substandard lap splice length of 100 mm. The G-Lap200C had 84.3% torque capacity and the G-Lap100C 86.4% compared to the 300 mm lapping length reference beam (G-Lap300). Results show that CFRP strengthening compensates better for decreased lap length in shorter sizes, indicating that CFRP wrapping

improves bond characteristics, potentially reducing splice lengths while maintaining torsional resistance.

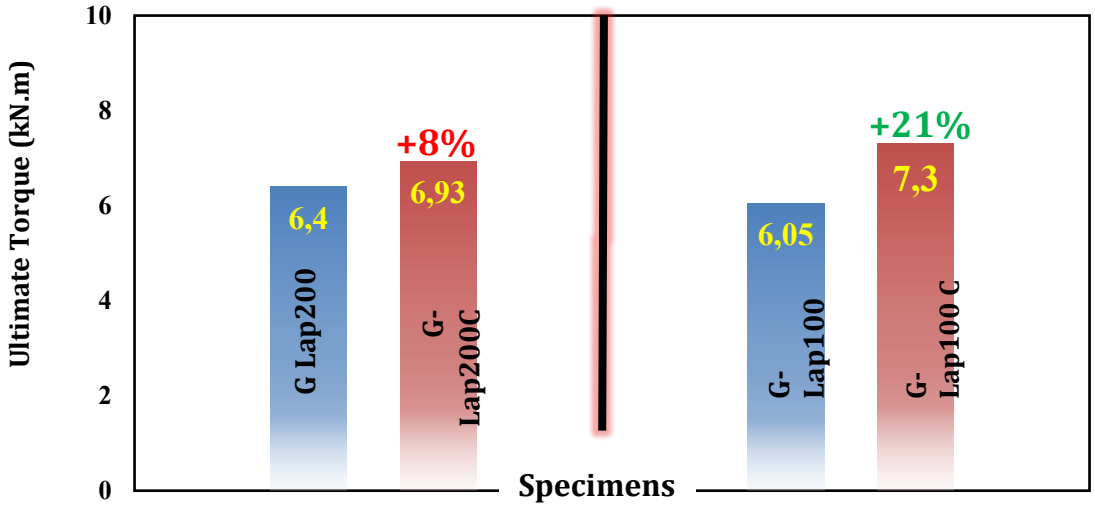

Fig. 9. Effect of splice remedy on the ultimate torque capacity for G-Group

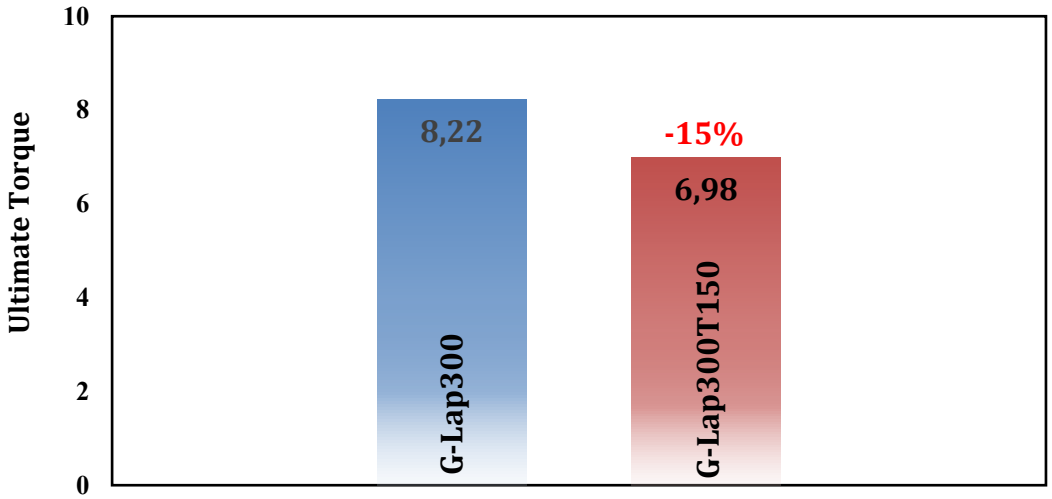

Fig. 10. The effect of transverse reinforcement on splice region

Table 4. Results of tested specimens

Group	No.	Specimen	T_{cr}	$\emptyset_{cr}$	T_u	Difference in T_u (%)	$\emptyset_u$	Difference in $\emptyset_u$ (%)
G-group	1	G-Continuous	8.00	0.0062	9.52	Reference	0.0100	Reference
	2	G-Lap300	7.50	0.0090	8.22	-13.65[a]	0.0130	+30.00[a]
	3	G-Lap200	6.12	0.0050	6.40	-32.77[a]	0.0074	-26.00[a]
	4	G-Lap200C	6.10	0.0048	6.93	+8.3[b]	0.0380	+413.50[b]
	5	G-Lap100	5.70	0.0033	6.05	-36.45[a]	0.0048	-52.00[a]
	6	G-Lap100C	6.25	0.0047	7.30	+20.66[c]	0.0130	+170.80[c]
	7	G-Lap300-T150	5.97	0.0091	6.98	-15[d]	0.0126	-3.08[d]

Where T_{cr}: Cracking Torque (kN.m); $\emptyset_{cr}$: Twist angle at cracking stage (rad/m); T_u: Cracking Torque (kN.m); $\emptyset_u$: Twist angle at ultimate stage (rad/m); a: compared to G-continuous; b: compared to G-Lap200; c: Compared to G-Lap100; d: compared with G-Lap300.

The effect of spacing of stirrups was also investigated in terms of ultimate torque capacity. The spacing stirrups were 100 mm for the G-Lap300 specimen. As shown in Table 4 and (Fig. 10), the increasing of spacing to 150 mm to get G-Lap300 T150, the ultimate torque capacity, decreases by 15%. This may be due to a lack of a confinement ratio of steel stirrups near the splice region as well as the loss of certain transverse ratios that play a significant role in resisting applied torque. The ultimate twist angle was not significantly affected by the reduction in transverse ratio, as the ultimate angle of twist decreased by only 3.08% when the spacing was increased to 150 mm to obtain G Lap300 T150.

3.2 Ductility Index

Ductility is an important material feature that enables plastic deformation and energy absorption avoiding catastrophic collapse. It indicates a material's capacity to resist applied pressure post-yielding without sudden failure. The method of measurement provided by Chao et al. [17] has been extensively employed. The ductility index (μ_E) supports the energy-based method, since it measures the ability to absorb energy, represented as the ratio of total energy to elastic energy, as follows Eq (2) [13]:

$$\mu_E = 0.5\ (\frac{E_t}{E_e} + 1) \tag{2}$$

In (Fig. 11), μ_E represents ductility indices; E_e represents elastic energy (area below slope S), and Et represents total energy (area under load-deflection curve up to failure load). This method also works for torque-angle twist curves. Table 5 shows the energy approach ductility indices as well as torsional toughness of all tested specimens. The Slope S is calculated from Eq. (3).

$$S = \left(\frac{P1*S1+(P2-P1)S2}{P2}\right) \tag{3}$$

Where P_1, S_1, P_2, S_2, and S are illustrated in Fig.11.

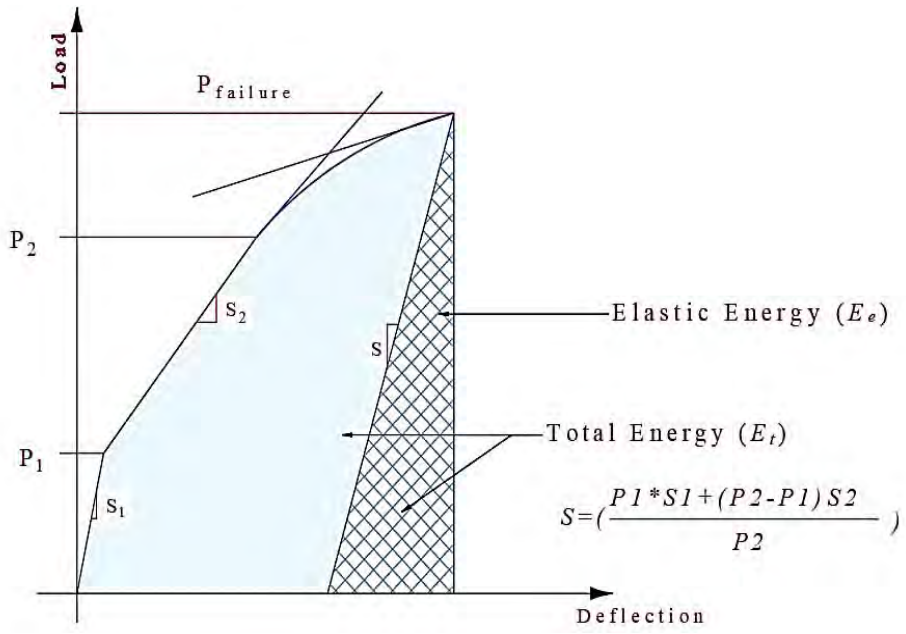

Fig. 11. Energy method for ductility calculation

Ductility index values are shown in Table 5. The 300 mm (30db) lap splice length has minimal impact on ductility index. Table 5 shows that G Lap 300 has 9.31% less ductility than G-continuous. The ductility index dropped by 36.76% and 26.47%, respectively, compared to a reference beam with continuous bars (G-Continuous) and by 30.3% and -18.92% compared to G-Lap 300, when the lap splice length was reduced to 20 d_b and 10 d_b, respectively. A shorter lap splice length reduces the anchoring length, which may cause slip or failure at the splice region, limiting the beam's plastic

deformation and energy absorption, reducing ductility. The new lap splice method improved the ductility index. Table 5 shows that the G-Lap200C specimen had a 155% higher ductility index than the G-Lap200. When the strengthening technique was used on the inadequate lap splice length of 100 mm (10 db), G Lap100C had 165.34% better ductility than G Lap100, as shown in Table 5.

Table 5. Ductility index for all test specimens

No.	Specimen	E_e	E_t	$\mu = \frac{1}{2}(\frac{E_T}{Ee} + 1)$	Difference in ductility (%)	Toughness kN.m×rad/m×10^{-3}	Difference in Toughness (%)
1	G-Continuous.	22.01	68.00	2.04	**Reference**	716	Reference.
2	G-Lap300	22.50	61.00	1.85	-9.31[a]	248	-65.40[a]
3	G-Lap200	19.00	30.00	1.29	-36.76 [a]	234	-67.32 [a]
4	G-Lap200C	40.40	225.30	3.29	+155.04[b]	327	+40.00[b]
5	G-Lap100	9.98	20.00	1.50	-26.47[a]	210	-70.70[b]
6	G-Lap100C	11.80	82.12	3.98	+165.34 [c]	470	+123.00[c]
7	G-Lap300-T150	22.40	58.40	1.80	-2.70 [d]	266	+7.25[d]

Where a: compared to G-continuous; b: compared to G-Lap200; c: Compared to G-Lap100; d: compared with G-Lap300

This may be attributed to the fact that CFRP strengthening around spliced bars improved reinforcement bar strain and stress resistance, delaying brittle failures. This increases beam deformation before failure, resulting in improved specimen ductility. Table 5 also illustrates that extending the stirrups spacing from 100 mm to 150 mm to obtain the G-Lap300 T150 beam resulted in a very slight decrease in ductility, a 2.7% reduction in ductility compared to G-Lap300.

3.3 Torsional Toughness

Toughness defines a material's capacity to absorb energy prior to fracturing. The torsional toughness values were calculated from the area under torque-twisting angle curves. Table 5 shows all tested beams' torsional toughness. The G-continuous beam has the highest toughness value. Lap splice lengths of 300, 200, and 100 mm reduce torsional toughness by 65.4, 67.32, and 70.7%, respectively, compared to G-continuous. G Lap200 had a torsional toughness of 234, while G Lap200C had 327 thanks to lap spliced GFRP bars wrapped in CFRP sheet and coated with resin. CFRP wrapping increases toughness by 39.7%, as shown by the differential ratio of G Lap200C to G Lap200. G Lap100 had lap splice GFRP bars length 100 mm with a torsional toughness of 200, while G Lap100C had CFRP-wrapped, resin coated bars with 470.G Lap100C has 124% higher torsional toughness than G Lap100. The CFRP wrapping may increase the toughness of G Lap200C and G Lap100C by strengthening the splice region, strengthening the bond between the two GFRP bars, and increasing the beams' torsional resistance. By preventing reinforcement bar and concrete slip, CFRP confinement may increase torsional toughness, especially at the lap splice. This provides enhanced load transfer and ensures the integrity of the reinforcement under stresses due to torsional loads. Furthermore, CFRP enhanced ductility, enabling the structure to experience increased plastic deformation prior to failure. The integration of improved stress transfer and higher ductility effectively improves energy absorption under torsion, resulting in superior torsional toughness.

For the variation in transverse reinforcement ratio, the 150 mm stirrup spacing specimen (G-Lap300T150) had a torsional toughness of 266, while the 100 mm stirrup spacing specimen (GLap300) had 248. Reduced transverse reinforcement ratio improves torsional toughness by 7.25% as shown in Table 5. The wider stirrup spacing in GFRP-reinforced specimens may be enabling a more efficient stress distribution within the lap splice region. When stirrups are closely spaced (100 mm), the confined condition may concentrate stresses at specific locations along the spliced GFRP bars, and then the GFRP bars demonstrate brittleness properties, resulting in potential regional bond failures that decrease overall torsional toughness.

4. Crack Pattern

Assessing the mode of failure is essential for identifying the governing failure mechanism [18]. The crack pattern and results are presented in (Fig. 12) and Table 6. The crack pattern was affected by the presence of lap splice region. (Fig. 13) illustrates the combination of torsional cracks as well as splitting cracks (longitudinal and transverse cracks) concentrated within splice region.

Table 6 illustrates that the beam reinforced having continuous GFRP bars (G-Continuous) demonstrated a helical crack mode reaching over more than half of the span of the beam, indicative of the common torsional response of unsliced parts. nevertheless, with the producing of the splice, cracks may became more concentrated within splice zone, as shown in Figure 11, which may be related to localized bonding stresses and partial slipping between the spliced bars. This concentration might have diminished the overall crack length but resulted in marginally wider cracks. When CFRP sheets were directly wrapped around the spliced bars (i.e. G-Lap200C and G-Lap100C specimens), the enhanced confinement may have reduced bar slipping and cracking progression, perhaps leading to a reduction in cracking width approximately 33–55% as shown in Table 1. These results might reflect an enhancement in bond stress distribution and torsional strength.

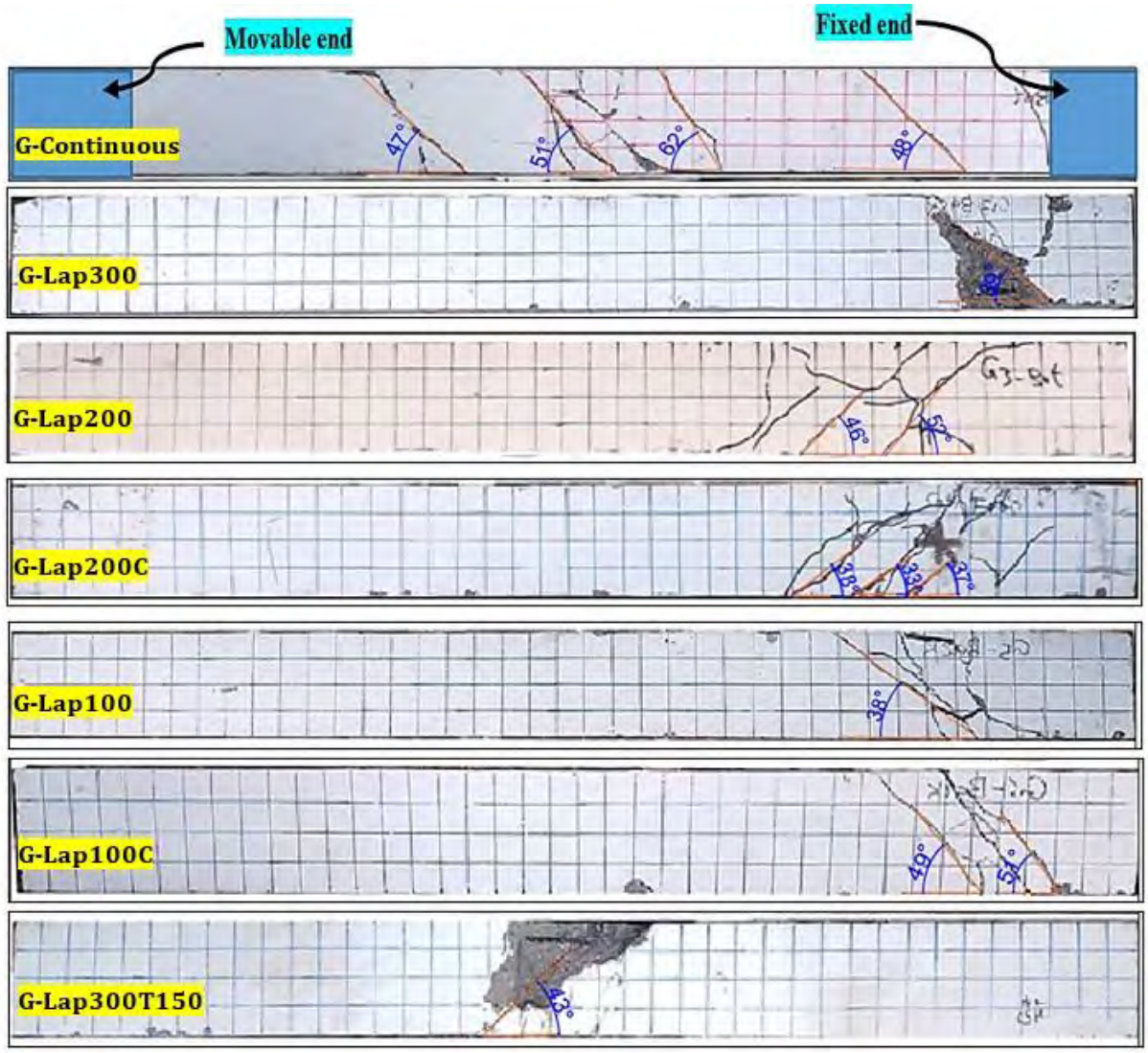

Fig. 12. Crack patterns for test specimens(one face comparison)

Fig. 13. Cracks types within splice region(G-Lap300)

Table 6. Crack results

Specimen	Maximum Crack width (mm)	Difference in crack width (mm) (%)
G-Continuous.	2.77	Ref.
G-Lap300	4.30	+55[a]
G-Lap200	4.50	+62.5[a]
G-Lap200C	2.00	-55.5[b]
G-Lap100	3.00	+8.3[a]
G-Lap100C	2.00	-33.3[c]
G-Lap300-T150	4.40	+2.3[d]

Where; a: compared to G-continuous, b: compared to G-Lap200, c: Compared to G-Lap100 and d: compared with G-Lap300

The enhancement in crack pattern, ultimate torque and torsional ductility might be linked to multiple interaction reasons. The CFRP confinement may have improved the bond stress distribution along the splice, minimizing localized splitting and delaying bar slip. The transverse wrapping may have contributed lateral confinement in the splice zone, perhaps enhancing stress transfer quality between the bars and the surrounding concrete. Thus, this improved confinement may have permitted the beams to resist greater torque and shown higher post-cracking ductility.

5. Torsional Strength Verification

The ultimate torque capacity was calculated theoretically using the provision of ACI318-19 because of the transverse reinforcement is made of steel and play a main role in torsional strength compared to longitudinal GFRP. The equation of ultimate strength is as follow:

$$T_n = \frac{A_t}{S} \times f_{yt} \times 2A_\circ \cot\theta \quad (4)$$

Where; T_n: Nominal torsional strength *[kN·m]*, A_t : Area of stirrups reinforcement *[mm²]*, S: Spacing of stirrups *[mm]*, f_{yt}: Yield strength of stirrups reinforcement *[MPa]*, $A_\circ$: Area enclosed by the shear flow path (effective torsional area) *[mm²]*= $X_\circ * Y_\circ$, θ: Angle of diagonal compression (crack angle) *[degrees]*. θ Assumed to be 45°(for design consideration).

(Fig. 14) and table 7 illustrates the details of cross section geometry that is require for determination of torsional strength.

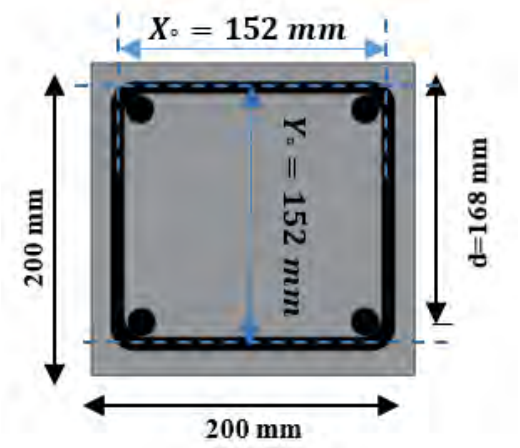

Fig. 14. Cross sectional beam

Table 7. Geometrical details of cross-sectional beam

Property	Value
b (beam width)	200 mm
H(beam height)	200 mm
Effective depth	164mm
Clear cover	20mm
$X_\circ$ (horizontal distance for center to center of two legs of stirrups	152 mm
$Y_\circ$ (vertical distance for center to center of two legs of stirrups	152 mm
$A_{\circ_h} = X_\circ * Y_\circ$	23104 mm^2
$A_\circ = 0.85\ A_{\circ_h}$	19638.4

- Ø8 mm for stirrups: Abar = 50.26 mm2 and stirrup spacing =100 mm for all specimens except the G-Lap300T150
- For one leg of stirrups $\frac{A_t}{S} = \frac{50.26}{100} = 0.5026\ mm$
- Assume $\theta = 45°$
- $T_n = \frac{A_t}{S} \times f_{yt} \times 2A_\circ\ cot\theta$ =0.5026× 422 × 2 × 19638.4 × 1 × 10^{-6} = 8.33 $kN.m$
- According to ACI318-19 the ultimate torque is 8.33 kN.m
- For S=150, for one leg of stirrups $\frac{A_t}{S} = \frac{50.26}{150} = 0.335\ mm$, by applying Eq(4), $T_n = 5.55\ kN.m$ (for G-Lap300T150)

Table 8. Torsional strength (Theoretical vs Experimental)

No.	Specimen	T_uEXP	Tu ACI(ACI318-19)	Difference ratio (%) with respect to experimental
1	G-Continuous	9.52	8.33	-12.50
2	G-Lap300	8.22	8.33	1.34
3	G-Lap200	6.40	8.33	30.16
4	G-Lap200C	6.93	8.33	20.20
5	G-Lap100	6.05	8.33	37.69
6	G-Lap100C	7.30	8.33	14.11
7	G-Lap300T150	6.98	5.55	-20.49

Table 8 below explains the torsional strength from experimental and ACI318-19 equation. The theoretical value of torsional strength is 8.33 kN·m for all specimens except the G-Lap300T150, which was 5.55 kN·m. The difference ratio for the continuous bar, lap 300, and strengthened beams within splice region was less than or equal to ±20%. The high divergence was observed in specimens with shorter lap splice length (i.e., G-Lap100 and G-Lap200). In this case, the ACI

equation appears to be invalid with the shortest lap splice length (100 and 200 m) due to premature bond-related effects.

6. Conclusion

The present investigation utilized an innovative splice remedy method to fix the issue of inadequate lap splices in reinforced concrete beams tested for pure torque. The experimental results justify a number of conclusions:

- The minimum inadequate lap splice length significantly reduced the torsional load capacity, leading to a loss of up to 36.45% in ultimate torque. The reduction is mainly attributable to inadequate bond strength between the overlapped bars, resulting in early slippage and restricting the efficient transfer of loads due to torsional effect over the splice region. As a result, the beam demonstrated an initial reduction in stiffness and a brittle failure mode.
- The torsional ductility and toughness diminished by 36.76% and 70.7%, respectively, in comparison to the beam with no splice region (continuous reinforcement). The substantial decrease in toughness signifies diminished energy absorption capability, attributed to the initial and rapid progression of splitting cracks at the splice zone.
- Increasing the stirrup spacing in the splice region from 100 mm to 150 mm led to a 15% decrease in ultimate torque capacity. This modification had a negligible effect on ductility and toughness, indicating that although transverse reinforcement offers some confinement, it cannot entirely mitigate the inadequate bond linked to short splices.
- The CFRP sheet wrapped directly around the spliced bars prior to concrete casting improved torque capacity, ductility, and toughness. The enhancement results from the enhanced bond and confinement afforded by the incorporated CFRP, which diminished bar slide and postponed cracking, resulting in an enhanced ductile torsional performance.
- The proposed method is simple and practical, and requires no specialist apparatus such as welding or couplers, providing it an efficient and cost-effective alternative for strengthening reinforced concrete beams with inadequate lap splices.
- Overall, strengthening substandard lap splices using CFRP significantly improves torsional behavior, torsional ductility, and energy absorption, resulting in a safer and more desirable failure mode. This strengthening technique may result in a reduce in the needed lap splice length addition to achieving acceptable torsional strength and safety margins.
- The current test was limited to pure torsional loading on a constant cross-section, missing the ability to apply both bending-torsion loads.
- Future studies should incorporate the effects of combination bending and torsion while varying the concrete cover, as it may considerably affect bond integrity and splice efficiency.
- In addition, as long-term effects may change splice behavior, future research might include durability or cyclic torsion studies.

Acknowledgement

The authors acknowledge their deep thanks to the staff of the College of Engineering, University of Anbar, for their assistance during this work.

References

[1] Hu X, Xue W, Xue W. Bond properties of GFRP rebars in UHPC under different types of test. Eng Struct. 2024;314:118319. https://doi.org/10.1016/j.engstruct.2024.118319

[2] Saleh Z, Goldston M, Remennikov AM, Sheikh MN. Flexural design of GFRP bar reinforced concrete beams: An appraisal of code recommendations. J Build Eng. 2019;25:100794. https://doi.org/10.1016/j.jobe.2019.100794

[3] Bai H, Jiang J, Xue W, Hu X. Experimental investigation on pure torsion behavior of concrete beams reinforced with glass fiber-reinforced polymer bars. Buildings. 2024;14(9):2617. https://doi.org/10.3390/buildings14092617

[4] Ali ZM, Mahmoud AS, Mohammed MS, Ahmed ML. Structural behavior of voided reinforced concrete beams having a novel tact bundled waste plastic bottles. Innov Infrastruct Solut. 2023;8(9):237. https://doi.org/10.1007/s41062-023-01205-7

[5] Panchacharam S, Belarbi A. Torsional behavior of reinforced concrete beams strengthened with FRP composites. In: First FIB Congress. Osaka, Japan; 2002. Vol. 1. p. 1-110.
[6] Abdoli M, Mostofinejad D. Torsional behavior of FRP-strengthened reinforced concrete members considering various wrapping configurations: Theoretical analysis and modeling. Constr Build Mater. 2023;401:132636. https://doi.org/10.1016/j.conbuildmat.2023.132636
[7] Said M, Salah A, Erfan A, Esam A. Experimental analysis of torsional behavior of hybrid fiber reinforced concrete beams. J Build Eng. 2023;71:106574. https://doi.org/10.1016/j.jobe.2023.106574
[8] Shehab HK, El-Awady ME, Husain M, Mandour. Behavior of concrete beams reinforced by FRP bars under torsion. In: 13th Int. Conf. on Soft Ground Engineering. Ain Shams Univ; 2009. p. 931-942.
[9] Deifalla A, Awad A, Elgarhy M. Effectiveness of externally bonded CFRP strips for strengthening flanged beams under torsion: An experimental study. Eng Struct. 2013;56:2065-2075. https://doi.org/10.1016/j.engstruct.2013.08.027
[10] Mohamed HM, Chaallal O, Benmokrane B. Torsional moment capacity and failure mode mechanisms of concrete beams reinforced with carbon FRP bars and stirrups. J Compos Constr. 2015;19(2):1-10. https://doi.org/10.1061/(ASCE)CC.1943-5614.0000515
[11] Mahmoud AS, Ali ZM, Faisal MG. Novel method for strengthening insufficient steel reinforcement splice using CFRP sheets. Int J Comput Aided Eng Technol. 2022;17(1):109-119. https://doi.org/10.1504/IJCAET.2022.124533
[12] Jaffal AN, Hilal AA, Mahmoud AS. Effect of CFRP sheets strengthening method on behaviour of modified lightweight foamed concrete beams. J Eng. 2024;2024(1):5599688. https://doi.org/10.1155/je/5599688
[13] Mahmoud AS, Ali ZM. Behaviour of reinforced GFRP bars concrete beams having strengthened splices using CFRP sheets. Adv Struct Eng. 2021;24:13694332211001516. https://doi.org/10.1177/13694332211001515
[14] Ali ZM, Mahmoud AS, Al-Ani MM. Ductility, stiffness and toughness of modified spliced steel reinforced concrete. In: AIP Conference Proceedings. 2022. Vol. 2386(1). https://doi.org/10.1063/5.0067147
[15] Jassim MK, Mahmoud AS, Mohana MH. Performance of GFRP spliced rebars in self-compacting concrete beams using a new CFRP sheets strengthening technique. Innov Infrastruct Solut. 2025;10(8):366. https://doi.org/10.1007/s41062-025-02163-y
[16] Al-Mamory ZK, Al-Ahmed AHA. Behavior of steel fiber reinforced concrete beams with CFRP wrapped lap splice bars. Structures. 2022;44:1995-2011. https://doi.org/10.1016/j.istruc.2022.08.096
[17] Chao S-H, Naaman AE, Parra-Montesinos GJ. Bond behavior of reinforcing bars in tensile strain-hardening fiber-reinforced cement composites. ACI Struct J. 2009;106(6):897. https://doi.org/10.14359/51663191
[18] Mohammed MS, Ahmed ML, Ali ZM, Mahmoud AS. An innovative method of voided reinforced concrete one-way slabs using bundled waste PET bottled tubes. Mater Sci Forum. 2020;1007:76-84. https://doi.org/10.4028/www.scientific.net/MSF.1007.76

Blank Page

Research on Engineering Structures & Materials
www.jresm.org

Research Article

Modelling the performance of superplasticizers in a hybrid concrete system with steel slag and waste glass

Ahmed T. Azeez [*,1,2,a], Maan S. Hassan [3,b], Alaa A. Atiyah [2,c]

[1]*Department of Mechanical and Manufacturing Engineering, Faculty of Engineering, Koya University, Koya 44023, Kurdistan Region – F.R. Iraq*
[2]*Materials Engineering Department, University of Technology, Baghdad, Iraq*
[3]*Civil Engineering Department, University of Technology, Baghdad, Iraq*

Article Info

Article History:

Received 13 Oct 2025
Accepted 26 Nov 2026

Keywords:

Concrete;
Regression;
Superplasticizers;
Steel slag;
Waste glass

Abstract

Superplasticizers (SP) are chemical admixtures that represent a significant innovation in the concrete industry due to their positive effects on workability and mechanical properties. The influence of SP on hybrid concrete with steel slag (SS) replacing coarse aggregates (up to 100%) and waste glass (WG) replacing cement (up to 30%) by weight remains ambiguous. The research gap addresses the motivation of this paper to thoroughly analyze the SP's performance within a hybrid system. Such research objectives strongly support global efforts toward sustainability and environmental preservation. The properties of the developed concrete upon SP inclusion can be precisely monitored by fitting the independent factors (SS, WG, and w/b) to the target responses. The mathematical models were developed using Minitab 21 software. For fresh concrete, w/b was the most influential factor in determining the SP/b dosages needed to keep the slump within the range of 185 mm ± 25 mm. Meanwhile, SS and WG counteracted each other, reducing their impact on workability. However, the responses measured included the compressive strength at 28 and 91 days of water curing, as well as splitting tensile strength and thermal conductivity after 91 days of curing. In all cases, SP enhanced the desired properties of concrete. With the addition of 1.2% SP (by weight of binder i.e. cement and WG) the compressive strength increased from 40 MPa to over 80 MPa. The thermal conductivity rose by 0.1 W/m·K with an SP dosage of 0.1%. The mechanical and thermal properties of concrete responded linearly to SP dosages.

© 2026 MIM Research Group. All rights reserved.

1. Introduction

SP are liquid polymers alternatively known as water-reducing agents. The name reflects their capability to reduce the water content of concrete while maintaining high flowability [1]. SP are the icon of high-strength and durable concrete in the modern construction industry. Additionally, they play a prominent role in reducing the cost of building by minimizing the cement content [2]. As a result, ecological benefits also brought on the stage by reducing the CO2 footprint because a ton of cement is responsible of emission an equal amount of pollutant gases into the air [3]. Using of SP with steel slag (SS) and waste glass (WG) further benefits the green environment because of replacing waste materials with cement or aggregates. Both approaches effectively reduce resource depletion and confirm sustainable and eco-efficient concrete production [4,5].

The performance of SP was improved through the following generations, by employing advanced chemical techniques. They are classified into three generations according to their chemistry and efficiency. The first generation, which is less effective, is extracted from wood pulp such as lignin

*Corresponding author: ahmad.taifor@koyauniversity.org
[a]orcid.org/0000-0002-7360-6631; [b]orcid.org/0000-0002-5693-879X; [c]orcid.org/0000-0002-4410-9062
DOI: http://dx.doi.org/10.17515/resm2025-1254ic1013rs

and sugar. The second generation is petroleum by-products and has a greater ability to reduce water and increase workability compared with the first generation. Sulfonated naphthalene and melamine chemically treated with formaldehyde are listed under this group. The third generation, which is the most effective, is of polycarboxylates type. These offer higher workability even at low doses and water content [6]. Researchers appreciated their influences on fresh and hardened concrete from workability to mechanical properties. Moreover, SP could also benefit the ecological system when they effectively compromise the drawbacks in the properties of concrete because of using recycled materials instead of standard natural ingredients. Patowary and Siddique reported the ability to replace natural gravel with 50% recycled aggregates without a significant scarifying in the mechanical properties only if SP was used [7]. Moreover, mathematical models that accurately describe the SP behavior in concrete were developed [1]. Their positive effects were attributed to a three-dimensional network of bonds that mutually bind concrete ingredients [8]. Other researchers extended their scopes by formulating SP in laboratories for applying into specifically predefined functions. These were water-reducing, sustained-released, and early strength polycarboxylic acids SP. The curing periods of concrete were 1, 7, and 28 days to assess the time effects of SP on compressive strength. Regardless of the SP type, concrete showed improved strength with time owing to compacted microstructure and pores refining [9].

However, care must be taken upon the inclusion of SP because thermal conductivity may increase upon the network evolution, which may negatively influence the energy efficiency of buildings if thermal insulation is considered. Improving the thermal insulation of buildings is a global goal aimed at reducing CO_2 emissions from power production [10]. Moreover, an overdose of SP may cause segregation and bleeding in concrete at a constant water content, therefore controlling the dosages is critical to obtaining homogeneous mixtures [11].

It is evident that the literature has explored the impact of SP on the properties of various concretes, except for those where SS and WG were combined. Additionally, disposing of waste materials in landscapes is a growing global concern, and recycling them is essential from an environmental perspective. This paper aims to fill the research gap and support the global strategy of promoting green living. Notably, the authors in their previous research attempted to develop green concrete using waste materials such as SS and WG. They developed models describing the influence of SS, WG, and w/b on the mechanical properties, thermal conductivity, and microstructure evolution of concrete [12–14]. However, these studies did not include SP in their modeling and lacked an in-depth discussion of its role in the properties of the developed concrete. Therefore, further extension is necessary to incorporate this perspective and build upon previous scientific work by developing new models that correlate the fresh and hardened concrete properties with added SP dosages. Including SP in the modeling process, unlike previous efforts, clearly highlights the originality of this paper.

2. Experimental Work

2.1 Materials

Ordinary Portland cement (OPC) type I (42.5) with properties satisfying ASTM C150 was used to bind the materials [15]. The initial and final setting time were 130 min and 205 min, respectively, whereas the fineness was 290 m^2/kg according to Blain method The Hend steel company in Erbil/Kurdistan region of Iraq supplied steel slag, which was stored in outdoor conditions and periodically sprayed with water to prevent harmful volume expansion [16]. Particle size was the criteria for aggregate replacements, where SS retained on sieves 19 mm and 12.5mm exclusively replaced for coarse aggregates of corresponding size. The particle size distributions of the materials are shown in Fig. 1, where both fine and coarse aggregates confirmed ASTM C33 [17,18].

The by-products of window processing plants in Erbil were gathered and further processed to replace cement in concrete. A Los Angeles machine type Control/Italy was used to grind the glass where each batch was loaded with 5kg of ground glass (passing sieve 1.18mm) and steel balls, see Fig. 2. A comminutor of type RRH-1000A was used for grinding. Then the Los Angeles was rotated 12000 cycles and the output powder was sieved to a size less than 150μm to enhance the

pozzolanic activity [19]. The materials were chemically analyzed for the oxide contents by an XRF machine and the compositions are shown in Table 1.

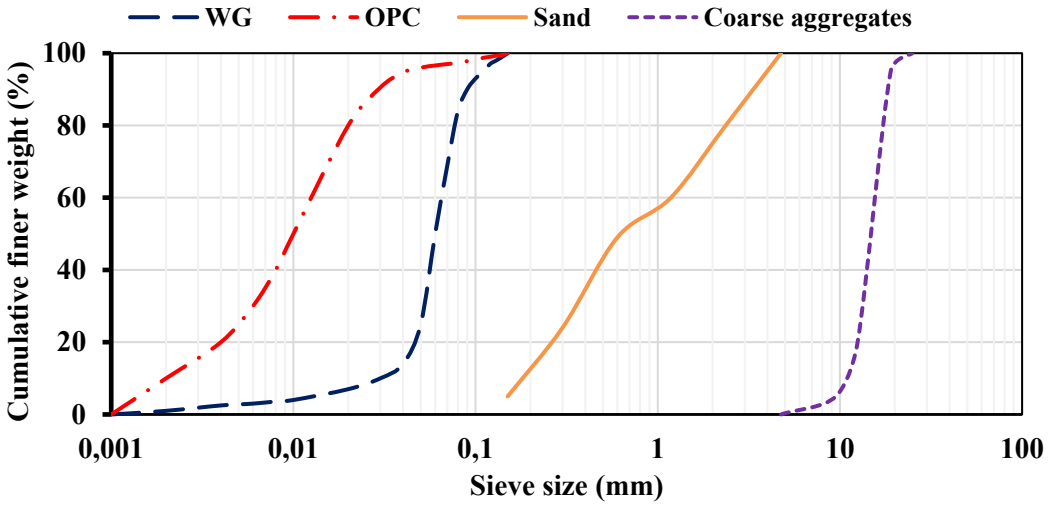

Fig. 1. Particle size distributions of materials

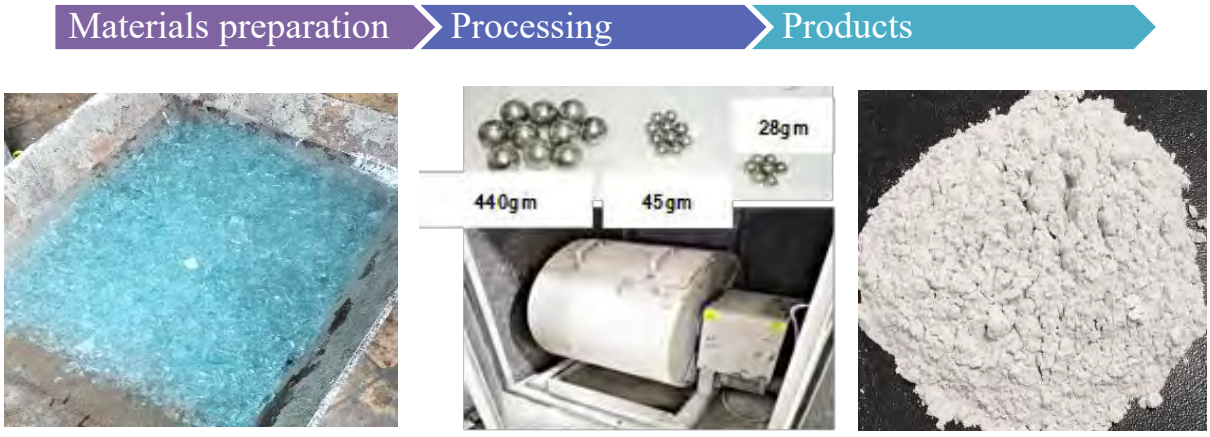

Fig. 2. Preparation of cementitious powder from WG

Table 1. Chemical composition analysis

Composition	SiO_2	CaO	Al_2O_3	MgO	P_2O_5	Na_2O	K_2O	Fe_2O_3	SO_3
OPC (%)	22.05	64.12	4.885	4.100	0.041	0.190	0.600	2.32	0.581
WG (%)	73.277	10.50	1.713	1.146	1.542	7.73	0.100	1.078	1.926
SS (%)	10.7	26.34	2.4	0.408	0.230	0.023	1.03	39.26	2.5

Engineers greatly desire high-fluidity concrete to facilitate smooth pumping on-site. Consequently, Polycarboxylate-based SP were utilized to maintain the concrete workability within the target range ($185 \mp 25\ mm$) at a constant w/b. The admixture has minimum chloride content which makes it a perfect option for reinforced concrete. Furthermore, it prominently enhances the early and later age strength and benefits placing and leveling concrete on site without a risk of bleeding and segregation. The SP was identified as high range water reducer and compatible with high strength concrete. It should be stored on the shelves within 5 – 35°C with firmly tightened package. It has a brownish color along with the following properties: PH = 7%, density = 1.12 kg/L, alkaline > 5%, and total chlorine value >0.1%. According to the properties, the admixture was of type F as per ASTM C494 standards [20]. The specific gravities were 2.55, 2.675, 2.73, 3.36 for WG, sand, coarse aggregates, and SS, respectively. The finesse modulus of sand according to ASTM C33 was

2.82. The absorption rate of coarse aggregates according to ASTM C127 was 0.91% [21]. Whilst it was 1.87% for sand according to ASTM C128 [22].

2.2 Concrete Mix Design

Concrete mix design as per ACI 211.1 code was utilized to proportion the materials to achieve a 45 MPa compressive strength [23]. Mixing 425 kg binder (OPC and WG), 750 kg sand, and 1020 kg coarse aggregates (natural +SS) effectively achieved the target strength after 28 days of moist curing. The percentages of the SS and WG substitutions and w/b were determined using the responsive surface method with Minitab 21 [24,25]. The critical points of the design space, named axial, end, and center points, controlled the combination of materials in the concrete mixtures as shown in Tables 2 and 3 [12,14]. Fine and coarse aggregates were dry-mixed thoroughly with SS for 2 minutes before the OPC and WG blend incorporation. Then a solution of water and SP was introduced into the blender where wet mixing lasted 4 minutes.

Table 2. The actual values of factors

Parameter	Axial	End	Center	End	Axial
SS (%)	0	22	50	78	100
WG powder (%)	0	7	15	23	30
w/b	0.3	0.34	0.4	0.46	0.5

Table 3. Results of the mixtures design by Minitab 21

Mixtures	SS, %	WG, %	w/b	Mixtures	SS, %	WG, %	w/b
M0	0	0	0.4	M10	78	7	0.34
M1	22	23	0.46	M11	50	15	0.4
M2	50	15	0.4	M12	100	15	0.4
M3	50	15	0.4	M13	50	30	0.4
M4	22	7	0.46	M14	0	15	0.4
M5	78	23	0.46	M15	50	15	0.5
M6	78	7	0.46	M16	50	0	0.4
M7	22	23	0.34	M17	50	15	0.4
M8	22	7	0.34	M18	50	15	0.3
M9	78	23	0.34	-	-	-	-

2.3 Sample Preparation and Testing

Slump test as per ASTM C143 standards characterized the mixtures for consistency [26]. The dosage of SP/b tightly controlled the workability, which was consistently maintained within the target range of $185 \mp 25\ mm$.Mixtures removed from the blender were placed in the cubic and cylindrical molds and compacted on vibrator tables. After demolding of the samples, they were maintained under water until 28 and 91 days for curing. The whole process was under the control of ASTM C192 standards. A compressive strength test confirming ASTM C39 was conducted on 100 mm cubic samples aged 28 days and 91 days based on three samples per test [27,28]. Three cylinders, per mixture, with dimensions 100 x 200 mm were investigated under indirect tensile stress after 91 days of water curing, see Fig. 3. The investigation of the cylinders confirmed ASTM C496 standards [29]. A 100mm cube per mixture was tested for thermal conductivity according to ASTM C1113 [30]. Data was captured from three faces to obtain a representative average value for the sample.

(a)

(b)

(c)

Fig. 3. Sample preparation (a) cubic samples (b) cylindrical samples (c) water curing

3. Results and Discussion

3.1 Effect of Superplasticizers on Fresh Concrete

Table 4 shows the results of regression and corresponding statistical analysis for the SP/b dosages needed to maintain the slump within the target range ($185 \pm 25\ mm$). The controlling factor in determining the SP/b was w/b, higher w/b needed lower SP/b to achieve the target slump and versa vice. Consequently, the w/b ratio was the dominant factor, while both SS and WG demonstrated negligible effects. The flat surface at a constant w/b value (Fig. 4a) strongly supports this assumption. Additionally, Figs. 4b and 4c further confirmed this conclusion, as the surfaces are steeply inclined with respect to the w/b axis, in contrast to those of SS and WG. Recalling that p-values below 5% are considered statistically significant in curve fitting, the high F-test p-values for SS and WG (p=0.480) provide a statistical explanation for their marginal influence compared with the w/b ratio, which had a zero p-value. However, regardless of the factors' impacts, SP/b responded linearly to all factors in every case. SS and WG may have counteracted each other, thereby diminishing their combined influences on the required SP doses. It was observed that the addition of WG, unlike SS, increased the slump. The hydrophobicity of WG might have increased the retained water which positively increased the slump. In contrast, the porosity of SS consistently absorbs water and creates an irregular matrix where both reduce the flowability of concrete, for details see [14]. The linear model successfully indexed more than 95% of the data manifested by high R-value see Table 4.

Table 4. Results of regression and statistical analysis for admixture doses.

Responses	Models	R-value (%)	Regression p-value	Lack of fit p-value
SP/b	2.649 + 0.000447 SS - 0.00149WG - 5.375 w/b	95.61%	0.000	*

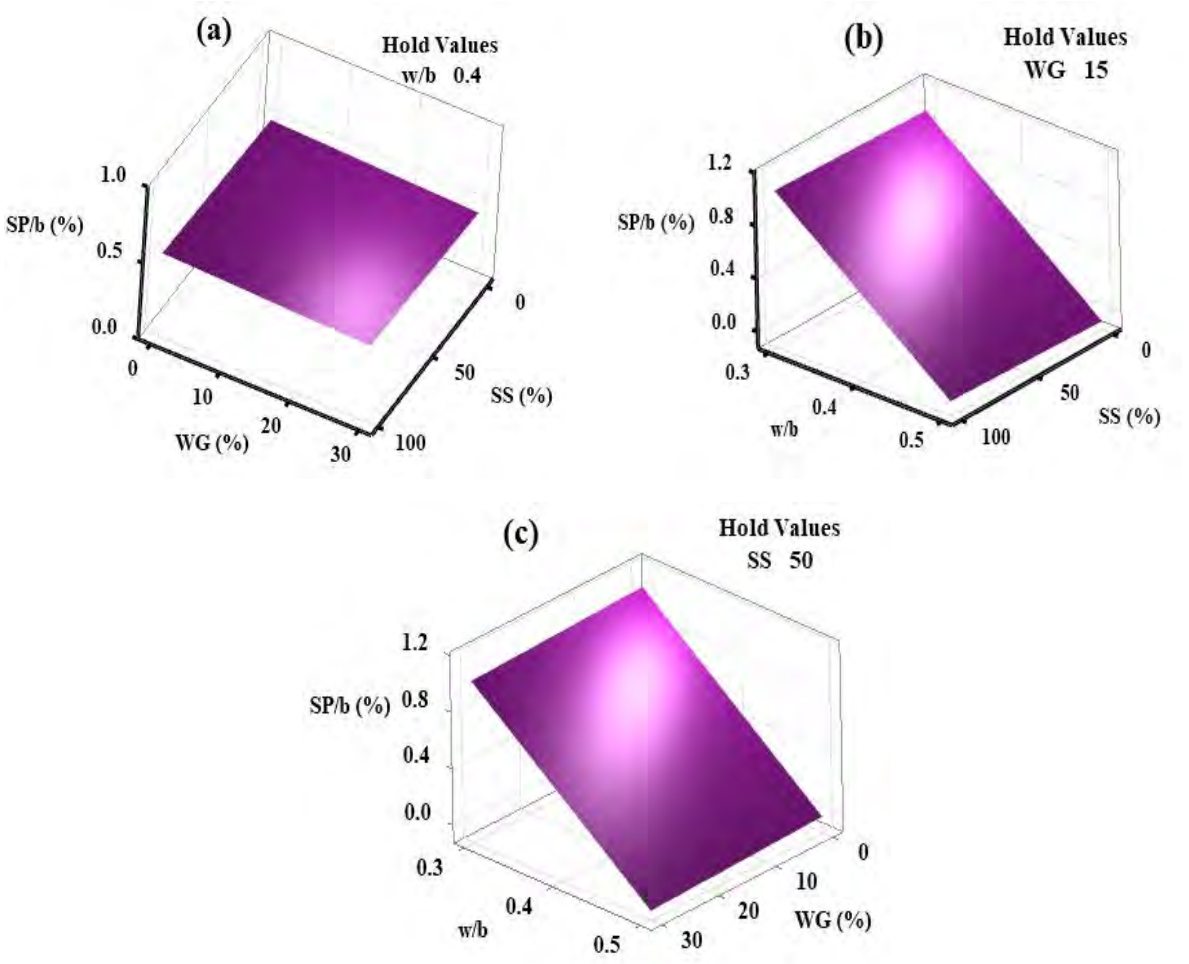

Fig. 4. Correlation between SP/b and affecting factors (a) SS and WG (b) SS and w/b (c) WG and w/b

3.2 Effect of the Superplasticizers on The Mechanical Properties of Concrete

The results of the regression of the compressive strength (C) and the splitting tensile strength (T) of concrete are shown in Table 5. The numbers next to the abbreviations indicate the curing time, which was 28 and 91 days. In all cases, SP/b linearly influenced the responses regardless of curing time. The p-values of the regression and lack of fit completely support their corresponding hypothesis.

Table 5. Results of regressions and statistical analysis

Responses	Models	R-value (%)	R-adj (%)	Regression p-value	Lack of fit p-value
C28 (MPa)	40.32 + 36.41 SP/b	66.11	67.18	0.000	0.107
C91 (MPa)	49.2 + 37.71 SP/b	66.82	64.74	0.000	0.163
T91 (MPa)	3.026 + 1.135 SP/b	61.14	58.71	0.000	0.832
k91(W/ m. K)	0.6969+0.4126 SP/b	70.32	68.47	0.000	0.832

Table 6. The differences between the observed and predicted values for C28, C91, T91

Mixture	SP/b (By weight %)	Predictive values			Δ (MPa)		
		C28	C91	T91	C28	C91	T91
M0	0.2	58.525	68.055	3.253	7.948	2.398	0.003
M1	0.2	47.602	56.742	3.253	6.302	10.142	0.413
M2	0.5	58.525	68.055	3.5935	2.355	0.735	0.0235
M3	0.5	58.525	68.055	3.5935	1.075	0.775	0.0135
M4	0.2	47.602	56.742	3.253	5.188	6.658	0.027
M5	0.2	47.602	56.742	3.253	1.258	1.448	0.197
M6	0.2	47.602	56.742	3.253	10.048	9.198	0.187
M7	0.7	65.807	75.597	3.8205	3.127	0.273	0.0205
M8	0.7	65.807	75.597	3.8205	7.133	5.083	0.3495
M9	0.7	65.807	75.597	3.8205	12.283	17.933	0.5295
M10	0.7	65.807	75.597	3.8205	13.943	12.683	0.4995
M11	0.5	58.525	68.055	3.5935	4.705	3.485	0.1335
M12	0.5	58.525	68.055	3.5935	2.955	2.925	0.0565
M13	0.5	58.525	68.055	3.5935	10.425	8.525	0.2335
M14	0.5	58.525	68.055	3.5935	13.175	13.515	0.2635
M15	0	40.32	49.2	3.026	4.32	0.74	0.086
M16	0.5	58.525	68.055	3.5935	3.925	2.545	0.0765
M17	0.5	58.525	68.055	3.5935	4.235	3.125	0.0635
M18	1.2	84.012	94.452	4.388	1.202	7.312	0.468

Table 6 shows the absolute difference (Δ) between the predictive and the real observed values, which are cited in [14]. Fig. 5a shows that C28 increased from 40 MPa to more than 80 MPa upon incorporation of 1.2% SP/b. The improvement trend was almost similar for C91 indicating no long-term influence of superplasticizers, see Fig. 5b. Wieland et al (2023) also reported a similar trend in their research and attributed it to the sorption of SP into the cement phase at the early age of hydration [31]. Furthermore, their addition also caused a significant improvement in the T91 where it increased by 46.67% from 3 MPa to 4.4 MPa see Fig. 5c. Not to mention, the inferior mechanical properties of M15 (SP/b =0%) compared with the other mixtures are strong evidence for the SP's vitality. Its C28, C91, and T91 were 40.32 MPa, 49.2MPa, and 3.026MPa, respectively. However, these values substantially increased for the other mixtures upon SP incorporation see Table 6.

The improvement influence of SP is well established and mainly attributed to their role in reducing the water content and enhancing the hydration reactions [8]. The prediction power of the suggested models was evaluated against those proposed by Muhammed et al. [1,12] using the following error and efficiency measurements:

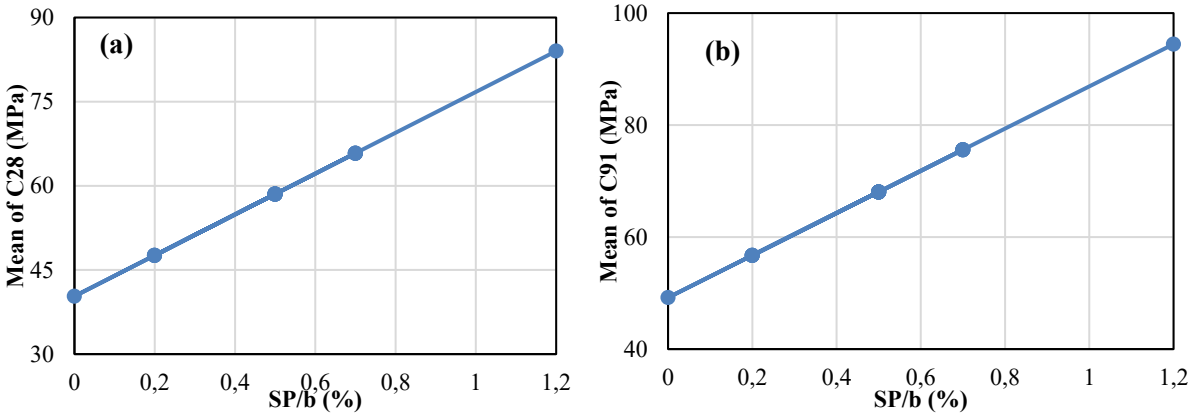

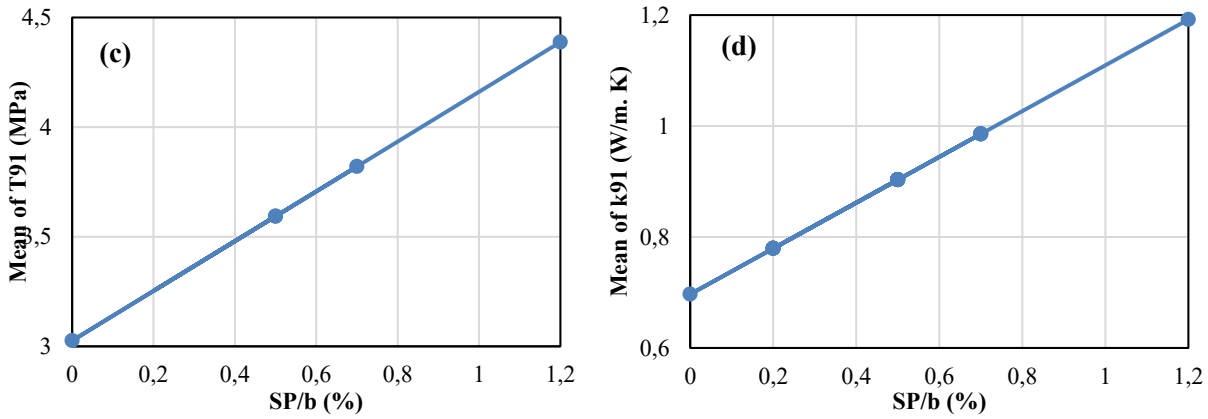

Fig. 5. The effect of SP/b on a) 28 days compressive strength b) 91 days compressive strength c) 91 days splitting tensile strength d) 91 days thermal conductivity

$$IAE = \sum_{I=1}^{n} \left(\frac{\sqrt{(Oi - Pi)^2}}{\sum Oi}\right) * 100 \quad (1)$$

$$MAE = \frac{1}{n}\sum_{i=1}^{n} |Pi - Oi| \quad (2)$$

$$RMSE = \sqrt{\frac{1}{n}\sum_{i=1}^{n} (Oi - Pi)^2} \quad (3)$$

$$EF = 1 - \frac{1}{n}\sum_{i=1}^{n} \frac{|Pi - Oi|}{Oi} \quad (4)$$

where IAE is integrated absolute error, MAE is mean absolute error, RMSE root mean square error, and EF is the normal efficiency. The variables Pi and Oi refer to the predictive and the real observed values, respectively, and n is the number of observations. They used the nonlinear regression method (NLR) and model tress (M5P) to fit the predictors to the compressive strength see the model parameters in [1]. The newly developed models showed the highest efficiency for prediction at the lowest error measured by all associated statistical methods see Table 7. Figs. 6a and 6b show that NLR overestimated the compressive strength in response to the SP/b of the current study. However, its predictivity is still better compared with M5P, which extremely deviated from the current model. Not to mentioned, the outputs of this research contradicted the conclusion stated by Muhammed et al. [1,12] where models predictivity improved in favor of M5P against NLR.

Table 7. Results of the analysis of the models' prediction power.

Type	Source	Errors			Efficiency
		IAE	MAE	RMSE	EF
C28	Current model	9.98	5.82	7.09	0.89
	NLR (SP62)	20.07	11.70	13.30	0.77
	M5P (SP62)LM1	49.06	28.61	31.86	0.53
C91	Current model	9.03	6.10	7.84	0.91
	NLR (SP62)	17.26	10.07	11.79	0.83
	M5P (SP62)	28.81	19.46	23.48	0.73

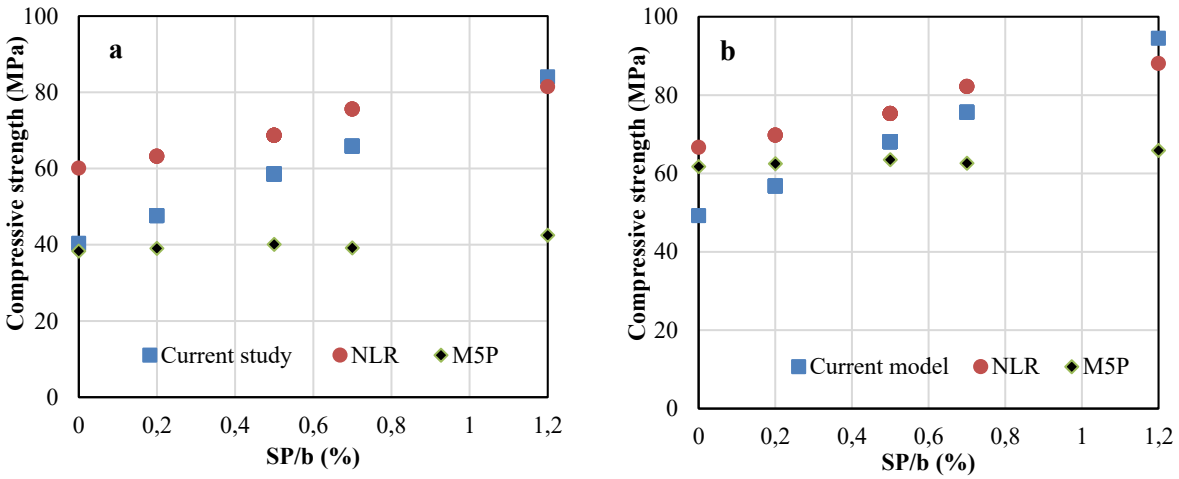

Fig. 6. Predictivity of the models for compressive strength a) 28 days curing b) 91 days curing

3.3 Effect of the Superplasticizers on The Thermal Conductivity Of Concrete

The response of the thermal conductivity of concrete (k91) to SP/b was shown in Table 5. The backward elimination method was used to remove all statistically insignificant terms at a 95% confidence level. The statistical filtration maintained the linear terms only to express the effect of SP/b on the thermal conductivity of concrete. The R-value and R-adj were 70.32% and 68.47%, respectively. The marginal difference between them indicates the vitality of the terms included in model. Additionally, the adequacy of the linear model in relating the SP/ to the conductivity was confirmed by a high p-value (<5%) of the lack of fit.

Fig. 5d shows that increasing SP/b by 0.1% improves the thermal conductivity of concrete by 0.1 W/m.K. The conductivity increased by 71.4% upon the addition of 1.2% SP. Not to mention, SP are liquid molecules with a high affinity to cement and effectively perform in the hydration process. As a result, a three-dimensional network of high bonding strength will be formed with minimum porosity content [10]. The improved cement matrix positively influences the thermal conductivity similarly to the mechanical properties discussed previously. However, effective approaches are required to mitigate the drawback of the superplasticizers influence on the thermal insulation of concrete. For example, SS and WG positively served in this direction owing to their physical structures. SS is porous whereas WG is amorphous and both characteristic features improved the thermal insulation of concrete, for detail see [12]

3.4. Microstructure Analysis

Microstructural analysis is crucial for justifying the observed macroscopic properties. Samples M11 and M15 were studied to examine microstructural development because their contents help identify the effects of admixtures. These samples had different SP/b and w/b ratios, while other factors remained constant. It is noted that SP/b was 0.5% and 0%, respectively, while w/b was 0.40 and 0.50 for M11 and M15. SEM images showed the positive effect of increased SP/b on producing a uniform and homogeneous paste matrix, see figure 6. Porosities characterized M15's structure (Fig. 7a) because water was the only lubricating agent used without any admixture. It is well established that evaporation of excess water is the primary source of porosity, and reducing water content effectively addresses this issue. Fig. 7b provides clear evidence supporting this, where a more compact matrix is observed due to a 10% reduction in water after adding 0.5% SP/b. The admixtures bring cement particles into close contact and prevent flocculation, significantly enhancing the hydration reaction. Overall, the improved mechanical and thermal properties of concrete with increased SP/b are evident, as previously discussed.

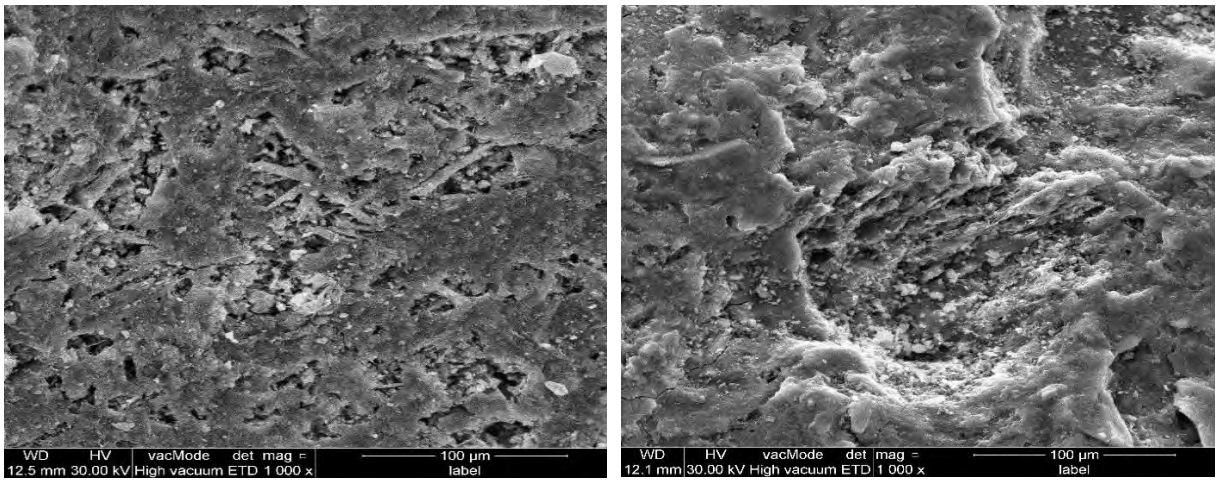

Fig. 7. SEM images (a) M15 (b) M11

4. Conclusions

This study aims to evaluate the mechanical and thermal performance of concrete in response to SP inclusion. Mathematical models were formulated using the response surface method with Minitab 21 to accurately assess the influence of w/b in combination with SS and WG on the doses of SP. The objective was producing concrete with slump of$185 \pm 25mm$ by monitoring the SP/b ratio. Statistical filtration was applied to remove unnecessary terms, thereby enhancing the validity of the fitted models. The following conclusions were drawn:

- Results showed that w/b critically determined the doses of SP necessary to maintain the fresh concrete highly workable. Increasing w/b consistently reduced the needs for SP/b to the extent that the target slump was obtained without the addition of SP at w/b ratio of 0.5.
- No influence was observed for SS and WG in determining the SP/b doses; conversely, the w/b ratio was the dominant factor. The opposing effects of SS and WG likely canceled each other out in the fresh concrete, providing a physical explanation for their negligible impacts in the developed models.
- The mechanical properties of concrete notably improved by SP because of water reduction. The addition of 1.2% SP by weight of binders (cement and WG) increased C28 from 40MPa to more than 80MPa.
- The improvement rate of C91 with SP was highly comparable to that of C28, effectively eliminating time factor from the effects of SP.
- The thermal conductivity of concrete increased by 71.4% with the inclusion of 1.2% SP, which negatively affects the insulation performance of buildings. Therefore, mitigation strategies are necessary to preserve the desired thermal insulation properties of concrete. For example, incorporating insulating materials like SS and WG effectively addresses this issue. In all cases, sp/b linearly correlated with the mechanical and thermal properties of concrete.
- Controlling the dosages of SP is technically essential for modern concrete technology. Developing models that accurately regulate the rate of SP additions to concrete is crucial to avoid undesired performance drawbacks.

References

[1] Mohammed AS, Emad W, Qadir WS, Kurda R, Ghafor K, Faris RK. Modeling the impact of liquid polymers on concrete stability in terms of a slump and compressive strength. Appl Sci. 2023;13. https://doi.org/10.3390/app13021208

[2] Puertas F, Santos H, Palacios M, Martı S. Polycarboxylate superplasticiser admixtures: effect on hydration, microstructure and rheological behaviour in cement pastes. Adv Cem Res. 2005;17:77-89. https://doi.org/10.1680/adcr.2005.17.2.77

[3] Bali M, Moulay H, Cherradi T. Towards sustainable concrete: reviewing the potential and challenges of plant fiber reinforcement with a life cycle case study using date palm fibers. x. 2025:1-25.
[4] Begum S, Yajdani S. Mechanical and durability studies on different grades of concrete using cinder aggregates. Res Eng Struct Mater. 2025:1-14. http://dx.doi.org/10.17515/resm2025-475me1006rs
[5] Tikotkar S, Sandbhor S, Kulkarni S. Mapping the research landscape of geopolymer concrete: trends, gaps and future directions. Res Eng Struct Mater 2025:1-25. http://dx.doi.org/10.17515/resm2025-981ma0620rv
[6] Łniewska-Piekarczyk E. The methodology for assessing the impact of new generation superplasticizers on air content in self-compacting concrete. Constr Build Mater. 2014;53:488-502. https://doi.org/10.1016/j.conbuildmat.2013.11.092
[7] Patowary F, Al M, Siddique A. Experimental investigation on the influence of superplasticizer on mechanical behavior of recycled aggregate concrete. 2023. https://doi.org/10.2139/ssrn.4128576
[8] Chen J, Zhu Y, Du W, Li M, Wang Y, Zhang C, et al. Influence of polycarboxylate superplasticizer on the properties of cement-fly ash cementitious materials and concrete. Sustainability. 2022;14. https://doi.org/10.3390/su142013440
[9] Xun W, Wu C, Leng X, Li J, Xin D, Li Y. Effect of functional superplasticizers on concrete strength and pore structure. Appl Sci. 2020;10. https://doi.org/10.3390/app10103496
[10] Jasim MJ, Noh MZ, Zaidan SA, Wan MH, Takai ZI. Effect of superplasticizer on thermal properties of concrete containing porcelain waste as sand replacement. J Adv Res Fluid Mech Therm Sci. 2019;13:82-91.
[11] Faroug F, Szwabowski J, Wild S. Influence of superplasticizers on workability of concrete. J Mater Civ Eng. 1999;11:151-157. https://doi.org/10.1061/(ASCE)0899-1561(1999)11:2(151)
[12] Azeez AT, Hassan MS, Atiyah AA. Optimization of the thermal and mechanical properties of concrete with steel slag coarse aggregates and waste glass replaced with cement. Innov Infrastruct Solut. 2024. https://doi.org/10.1007/s41062-024-01773-2
[13] Azeez AT, Hassan MS, Atiyah AA. Evaluation of the performance of steel slag and waste glass as a cement replacement. Eng Technol J. 2023;41:1567-1577. https://doi.org/10.30684/etj.2023.143602.1597
[14] Azeez AT, Hassan MS, Attiyah AA. Modelling the complementary role of inert slag aggregate and waste glass on concrete mechanical strengths using the response surface and design-of-experiment approach. Constr Build Mater. 2023;409:134199. https://doi.org/10.1016/j.conbuildmat.2023.134199
[15] ASTM International. ASTM C150/C150M: Standard specification for portland cement. West Conshohocken (PA): ASTM International; 2018.
[16] Lee HS, Lim HS, Ismail MA. Quantitative evaluation of free CaO in electric furnace slag using the ethylene glycol method. Constr Build Mater. 2017;131:676-681. https://doi.org/10.1016/j.conbuildmat.2016.11.047
[17] ASTM International. ASTM C33: Standard specification for concrete aggregates. West Conshohocken (PA): ASTM International; 2018.
[18] Aswed K, Hassan M, Al-Quraishi H. Effects of curing temperature and chemical admixture type on fresh properties and compressive strength of ultra high-performance concrete. Eng Technol J. 2022;40:1448-1454. https://doi.org/10.30684/etj.2022.132300.1103
[19] Kazmi D, Williams DJ, Serati M. Waste glass in civil engineering applications-a review. Int J Appl Ceram Technol. 2020;17:529-554. https://doi.org/10.1111/ijac.13434
[20] ASTM International. ASTM C494/C494M: Standard specification for chemical admixtures for concrete. West Conshohocken (PA): ASTM International; 2019.
[21] ASTM International. ASTM C127: Standard test method for density, relative density (specific gravity), and absorption of coarse aggregate. West Conshohocken (PA): ASTM International; 2015.
[22] ASTM International. ASTM C128: Standard test method for density, relative density (specific gravity), and absorption of fine aggregate. West Conshohocken (PA): ASTM International; 2007.
[23] ACI Committee 211. ACI 211.1-91: Standard practice for selecting proportions for normal, heavyweight, and mass concrete. Farmington Hills (MI): American Concrete Institute; 1991.
[24] Mohammed A, Hassan M, Al-Quraishi H. Manufacturing of sustainable ultra-high-performance concrete using response surface methods. Eng Technol J. 2023;0:1-12. https://doi.org/10.30684/etj.2023.143595.1598
[25] Kattoof I, Hassan MS, Hasan SS. Effects of liquid nitrogen cooling on the microstructure properties of nano-modified concrete under hot conditions. Arab J Sci Eng. 2022. https://doi.org/10.1007/s13369-021-06496-5
[26] ASTM International. ASTM C143/C143M: Standard test method for slump of hydraulic-cement concrete. West Conshohocken (PA): ASTM International; 2010.
[27] ASTM International. ASTM C192/C192M: Standard practice for making and curing concrete test specimens in laboratory. West Conshohocken (PA): ASTM International; 2002.

[28] ASTM International. ASTM C39/C39M: Standard test method for compressive strength of cylindrical concrete specimens. West Conshohocken (PA): ASTM International; 2018.
[29] ASTM International. ASTM C496/C496M: Standard test method for splitting tensile strength of cylindrical concrete specimens. West Conshohocken (PA): ASTM International; 2004.
[30] ASTM International. ASTM C1113/C1113M: Standard test method for thermal conductivity of refractories by hot wire (platinum resistance thermometer technique). West Conshohocken (PA): ASTM International; n.d.
[31] Wieland E, Lothenbach B, Glaus MA, Thoenen T, Schwyn B. Influence of superplasticizers on the long-term properties of cement pastes and possible impact on radionuclide uptake in a cement-based repository for radioactive waste. Appl Geochemistry. 2014;49:126-142.

Research on Engineering Structures & Materials
www.jresm.org

Research Article

Analysis of machining performance in ECDM of Al6061-SiC-B_4C hybrid composites: Experimental study and statistical modeling

Safa M. Lafta [*,a], Abbas F. Ibrahim [b]

Department of Production Engineering, University of Technology, Iraq

Article Info

Article History:

Received 13 Oct 2025

Accepted 05 Dec 2025

Keywords:

Electrochemical discharge machining);
Al6061-SiC-B4C hybrid composites;
Material removal rate;
Tool wear rate

Abstract

This work uses Electrochemical Discharge Machining (ECDM) to investigate the machining performance of Al6061-4%SiC-8%B4C hybrid composites. The study investigates how Material Removal Rate (MRR), Tool Wear Rate (TWR), and hardness are affected by voltage, electrolyte concentration, pulse-on time, and pulse-off time. For statistical modeling, an ANOVA and a Taguchi L9 orthogonal array were employed. Results indicate that higher voltage significantly enhances MRR and increases TWR, while optimizing pulse parameters improves machining efficiency. Increased hardness (165 HV) with the addition of 4% SiC and 8% B4C improved machining stability and wear resistance. Because it offers a balanced strategy for raising MRR while controlling TWR and tool life, ECDM is a practical technology for machining hybrid composites in aerospace and automotive applications. Future research should investigate better electrode materials and electrolyte modifications to further increase machining performance. While ECDM shows promise for hard-to-machine materials, the specific interaction and performance analysis of this technique on the Al6061matrix reinforced with the hybrid combination of SiC and B4C has not been systematically investigated, leaving a gap in optimizing the process parameters for industrial application. The results showed that the optimal processing conditions achieved a maximum Material Removal Rate MRR of 4.25 g/min, representing 32% improvement compared to the least effective parameters. Furthermore, the statistical model confirmed that Voltage is the most significant factor, contributing to approximately 78.5% of the total MRR variation, while TWR was effectively controlled to a minimum of 0.012 g/min under specific pulse conditions.

© 2026 MIM Research Group. All rights reserved.

1. Introduction

All The increasing demand for micro-scale items across a wide range of scientific and technological sectors has led to advancements in production processes. Traditional methods for working with electrically conductive materials, such as electric discharge machining (EDM) and electrochemical machining (ECM), work well. They are less effective with non-conductive materials since they require setups. One of the hybrid technologies that have evolved to address this issue is electrochemical discharge machining (ECDM) [1]. Composite materials, which are created by combining two or more constituents with differing physical and chemical properties, have distinct qualities that cannot be obtained in single materials [2]. A hybrid metal matrix composite (HMMC) is generated when a metallic matrix comprises multiple reinforcements. Although they make machining more difficult and complex, reinforcements like silicon carbide (SiC), boron carbide (B_4C), and aluminum oxide (Al_2O_3) improve the mechanical and tribological properties of composites [3–8]. Yan et al. [9] investigated how machining parameters affected composites

*Corresponding author: pme.20.88@grad.uotechnology.edu.iq
[a]orcid.org/0009-0007-5334-9168
DOI: http://dx.doi.org/10.17515/resm2025-1257ic1013rs

containing a high SiC concentration. High wire tension and excessive pulse-off time (Poff) lowered surface quality and efficiency, but longer pulse-on time (Pon) boosted MRR.

Similarly, Ibrahim et al. [10,11] used Taguchi approaches to control electrolyte concentration, voltage, and inter-electrode gaps in electrochemical machining (ECM) in order to balance and improve MRR while sacrificing surface quality. Furthermore, their findings show that greater energy discharge during electrical discharge machining (EDM) enhances the MRR in hybrid composites. Mandal et al. [12] investigated the use of electrolytes with NaOH and A2lO3 for powder-mixed ECDM (PMECDM) and micro-ECDM (μ-ECDM) in machining maraging steel. PMECDM demonstrated the benefits of A2lO3 powder by raising MRR by 34% and reducing surface roughness (Ra) by 21% [12]. Kannan et al. [13] investigated the WEDM of recycled Al alloy MMC with 5% alumina reinforcement, concentrating on voltage, feed rate, current, pulse-on, and pulse-off times. ANOVA and CRITIC analysis identified optimal values for high MRR and low Ra as 30V, 7mm/min feed rate, 30A current, 120μs pulse-on-time, and 70μs pulse-off-time. When Gugulothu et al. [14] milled Al5086/flyash/SiC hybrid composites, they investigated ECM factors such as feed rate, voltage, and electrolyte concentration. They discovered that, whereas electrolyte content had little impact, MRR rose with feed rate and voltage.

Ahmadinia et al. [15] studied how discharge current affects material removal rate (MRR) and electrode wear rate (EWR) in powder-mixed EDM and EDM for B4C-reinforced Al2014 MMCs. Powders were employed to reduce EWR, boost MRR, and enhance machining stability [15]. Kiran and Satyanarayana [16] improved die-sinking EDM techniques for hybrid metal matrix composites by increasing peak current and pulse-on duration to enhance MRR, TWR, and Ra [16]. Mohankumar et al. [17] optimized EDM settings for Al7075/B4C composites using the Taguchi technique, resulting in an MRR of 0.5628 mm^3/min, TWR of 0.0048 mm^3/min, and Ra of 4.4034 μm. They discovered that Ra, TWR, and MRR rose when Pon and current levels increased [17]. Arunachalam et al. [18] examined the EDM parameters for magnesium-based hybrid composites (AZ31 alloy with 5% MoS2 and 5% B4C). Optimal values were found to improve MRR and TWR, emphasizing the composite's low density and durability [18]. Given the preceding premise, the research focused mostly on boosting the MRR. Furthermore, the findings' scalability and applicability to various materials and machining circumstances is limited. To close these gaps, the current study seeks to establish accurate correlations between machining factors (such as voltage and electrolyte concentration) and their combined effect on surface integrity. Despite the potential of ECDM for hard-to-machine materials, a significant research gap remains in the systematic and optimized analysis of this technique on the specific Al6061 hybrid composite reinforced with SiC and B4C. Therefore, this study presents the first comprehensive experimental and statistical analysis, utilizing the Taguchi L9 array and ANOVA, to model and optimize the machining performance MRR and TWR of this material. The findings show that optimal conditions yielded a maximum MRR of 4.25 g/min, representing 32% improvement, with TWR effectively controlled to a minimum of 0.012 g/min. The statistical model confirmed that Voltage is the most significant factor, contributing approximately 78.5% to the total MRR variation. This contribution establishes a crucial reference for applying ECDM in the manufacturing of high-performance hybrid composites.

2. Experimental Work

2.1. The Workpiece

This study looks at a hybrid composite material made of Al6061 alloy reinforced with 4 wt% silicon carbide (SiC) and 8 wt% boron carbide (B4C). Analyzing the chemical compositions of the hybrid composite and foundation material enabled precise material characterization. The chemical analysis of the Al6061, which was created by the Ministry of Industry and Minerals and the State Company for Inspection and Engineering Rehabilitation (SIER) in Baghdad, Iraq, is displayed in Table 1. Optical emission spectroscopy (OES) was used to collect data for thorough chemical analysis. The addition of SiC and B4C reinforcements to the aluminum matrix, together with the precise atomic and weight percentages of the constituent elements, are all confirmed by this study. These analyses were conducted at the Al-Khoura Company in Baghdad. Table 2 lists the mechanical and physical characteristics of the Al6061 base alloy that was investigated at the University of

Technology, Iraq/Baghdad's Material Engineering Department. Fig. 1 shows the procedure of the experimental work

Table 1. The chemical analyses of Al6061

Element	Weight%	Element	Weight%
Si%	0.620	Ni%	0.0055
Fe%	0.117	Zn%	0.0030
Cu%	< 0.300	Ti%	0.0106
Mn%	0.0009	V%	0.0165

Table 2. The physical and mechanical properties of the used Al6061

Property	Unit	Values
density	g/cm^3	2.705
Hardness	HV	108
Ultimate tensile strength	MPa	305
Elongation	%	11.8
Modulus of Elasticity	GPa	68.5
Poisson's Ratio	--	0.32
Melting Temperature	° C	585-650
Shear Strength	MPa	205
Shear Modulus	GPa	25.8

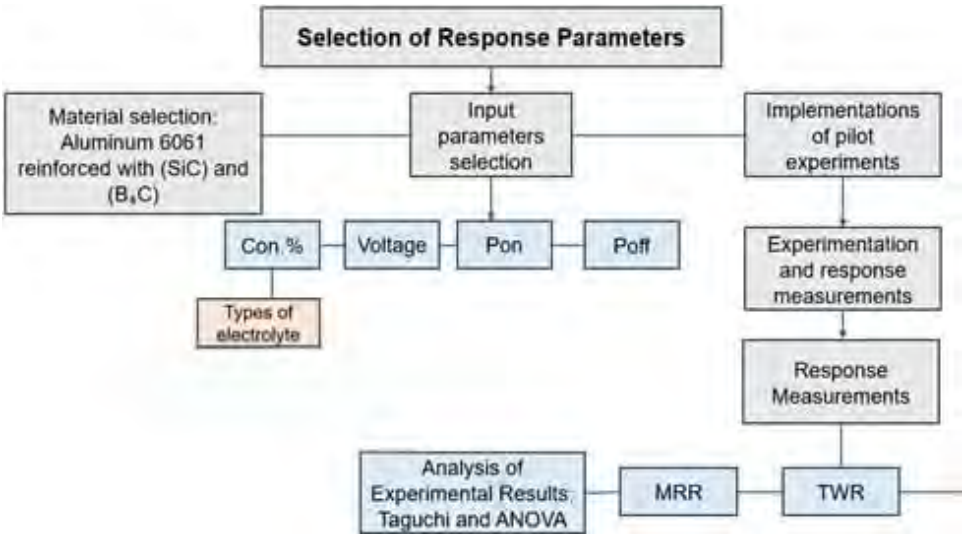

Fig. 1. The procedure of the experimental work

2.2. The Stir-Casting Process

Stir-casting technology, known for its capacity to offer consistent distribution of reinforcements inside a metal matrix, was used in the development of the hybrid composite material. The Al6061 alloy is melted in a graphite crucible at 700 ºC. In addition, 4 weight percent SiC and 8 weight percent B4C powders were gradually added to the molten aluminum while it was agitated for 10 minutes at 500 rpm with a mechanical stirrer. This stirring ensured a homogeneous dispersion of reinforcement particles throughout the matrix. The molten composite was then placed in a steel mold (50mm in length and 30 mm in diameter) and allowed to cool naturally at ambient temperature before solidification. For additional research and testing, the solidified castings were subsequently milled to the necessary specifications. Fig. 2 illustrates the stir-casting process.

Fig. 2. The stir-casting technique

(a) (b)

Fig. 3. (a) Workpiece before machining and (b) after machining

Essentially, the strength of the interfacial bonding between the reinforcement and the matrix phase has a major impact on the characteristics of metal matrix composites (MMCs) [19]. Fig. 3 depicts the specimens before and after machining, cut to the desired dimensions of 5 mm in thickness and 30 mm in diameter. Table 3 displays the chemical composition of the composite Al6061-4%SiC-8%B4C that was determined using energy-dispersive X-ray spectroscopy (EDX) at the Al-Khoura company, Iraq/Baghdad. Table 4 displays the mechanical properties of the Al6061-4%SiC-8%B4C hybrid composite that were investigated in the Material Engineering Department at the University of Technology, Iraq/Baghdad.

Table 3. The chemical composition of Al6061-4%SiC-8%B4C

Element	Atomic%	Atomic % Error	Weight%	Weight% Error
B	10.3	0.6	5.1	0.3
C	21.7	0.4	11.8	0.2
O	1.7	0.1	1.2	0.1
Mg	0.2	0.0	0.3	0.0
Al	65.2	0.2	80.0	0.3
Si	0.6	0.0	0.8	0.0
Fe	0.2	0.0	0.4	0.0
Zn	0.1	0.0	0.4	0.1

Table 4. The mechanical properties of Al6061-4% SiC- 8% B4C.

Property	Unit	Values
Density	g/cm^3	2.75
Hardness	HV	165
Ultimate tensile strength	MPa	160
modulus of elasticity	GPa	75
Yield strength	MPa	110
Elongation	%	10

2.3. The Electrode

The cylindrical copper electrode (50 cm in length, 10 mm in diameter) was employed in the machining process because of its thermal conductivity, high electrical, easx5e of machining, and high melting point (1083°C), all of which affect tool wear. After each process, the electrode was cleaned by washing it with water and drying it to remove any sludge adhered to its surface. At the State Corporation for Inspection and Engineering Rehabilitation (SIER)/ Ministry of Industry and

Minerals in Baghdad, Iraq, electrode copper was examined to ascertain its chemical analysis, as shown in Table 5.

Table 5. The chemical analyses of the copper electrode

Element	Weight %
Zn%	0.0038
Pb%	0.0011
Sn%	0.0025
P%	0.0007
Fe%	0.0482
Cr%	0.0008
Sb%	0.0121
As%	0.0007
Al%	0.0152
S%	0.0013
Cu%	Bal.

2.4 Electrochemical Discharge Machining (ECDM)

The ECDM was utilized to machine the hybrid composite material Al6061 reinforced with 4% wt SiC and 8% wt B4C, chosen for its efficiency in handling complex materials [20–24]. An acrylic tank, a power source, and a computer system constitute the ECDM setup. Furthermore, the electrolyte in this procedure was sodium chloride (NaCl). During operation, the workpiece functions as the anode, while the tool acts as the cathode. The components of the ECDM system are illustrated in Fig. 4.

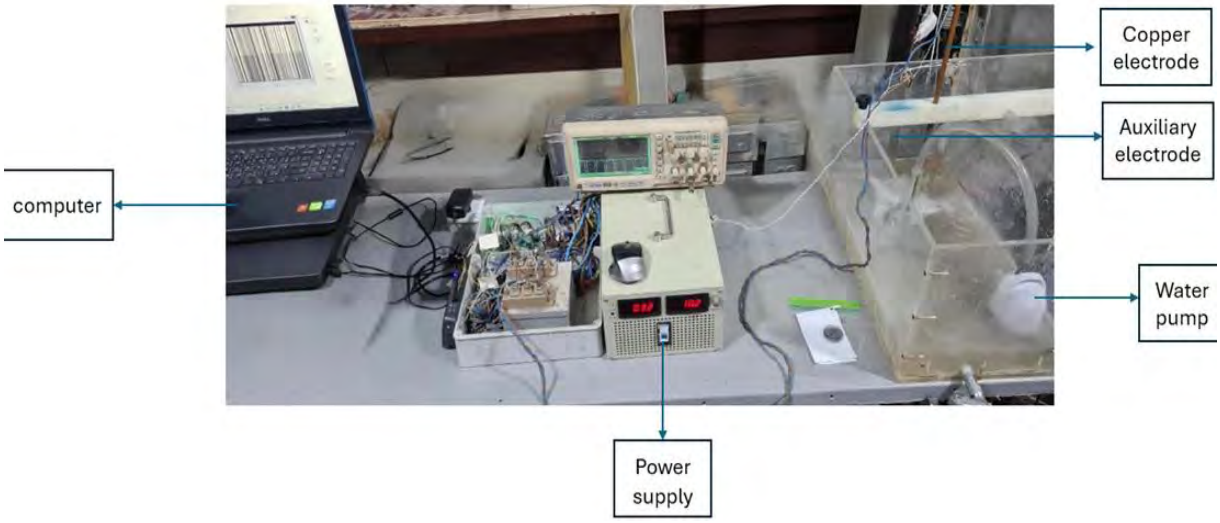

Fig. 4. The ECDM components

Prior to each experiment, both the workpiece and the electrode were thoroughly cleaned to remove contaminants before the process. The workpiece was then securely positioned in a stainless-steel holder. In addition, a gap of 0.2 mm was kept in place between the workpiece and the tool.

3. Tests and Inspections

The microstructure of the prepared cast specimens of the composites, which were Al 6061 with 4% SiC and 8% B4C, was analyzed using a scanning electron microscope (SEM). Wet grinding was done using water and SiC emery paper in grits of 320, 500, 600, 800, 1000, and 1200. The samples were polished with 0.5µm diamond paste and a lubrication cloth. The specimens were then etched with the etching solution Keller's reagent (95 mL H2O, 2.5 mL HNO3, 1.5 mL HCL, and 1.0 mL HF). Fig. 5 shows the SEM analysis that highlights the key microstructural defects affecting mechanical properties, including crack propagation, porosity clustering, and reinforcement distribution.

Optimization of processing parameters is essential to mitigate these defects. Fig. 5 shows the base alloy aluminum 6061 with the distribution of particles (SiC and B4C). In this regard, the inspection was conducted at Al-Khoura Company in Baghdad/ Iraq.

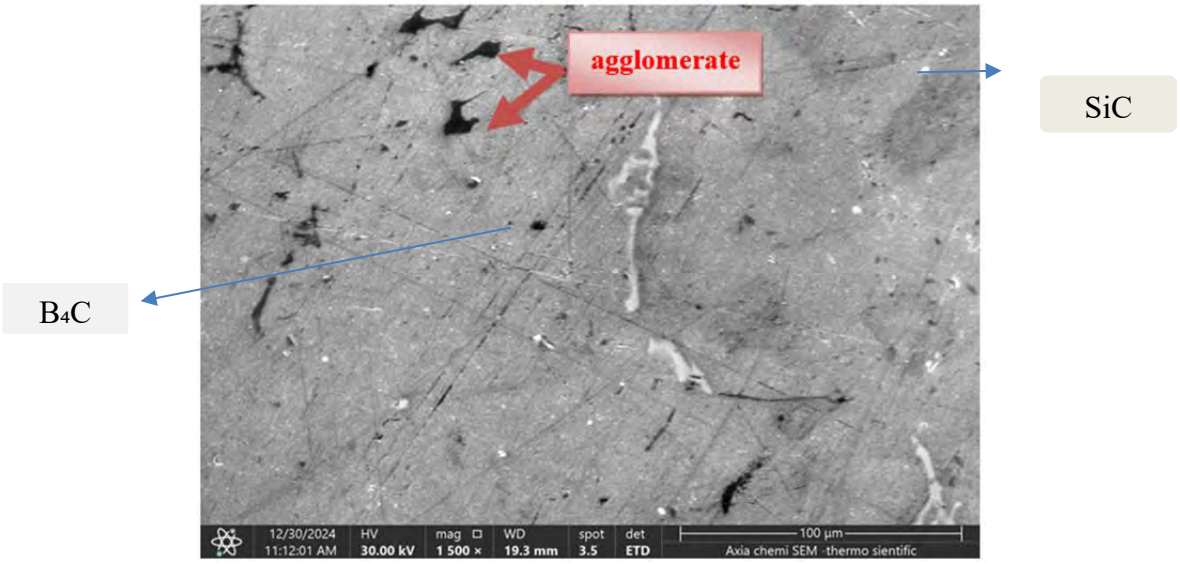

Fig. 5. The microstructure of Al6061-4%SiC- 8%B4C

The X-ray diffraction (XRD) pattern was re-evaluated to accurately identify the characteristic peaks of the composite. For Al6061, the main reflections occur in the range of 2θ ≈ 38–45°, corresponding to the (111), (200), and (220) planes when using Cu Kα radiation (λ = 1.5406 Å). Peaks associated with SiC and B4C were also identified correctly in the revised pattern. The previous attribution of a peak near 20° to aluminum has been removed, and the updated analysis now accurately represents the phase composition of the hybrid composite. Fig. 6 shows the XRD pattern.

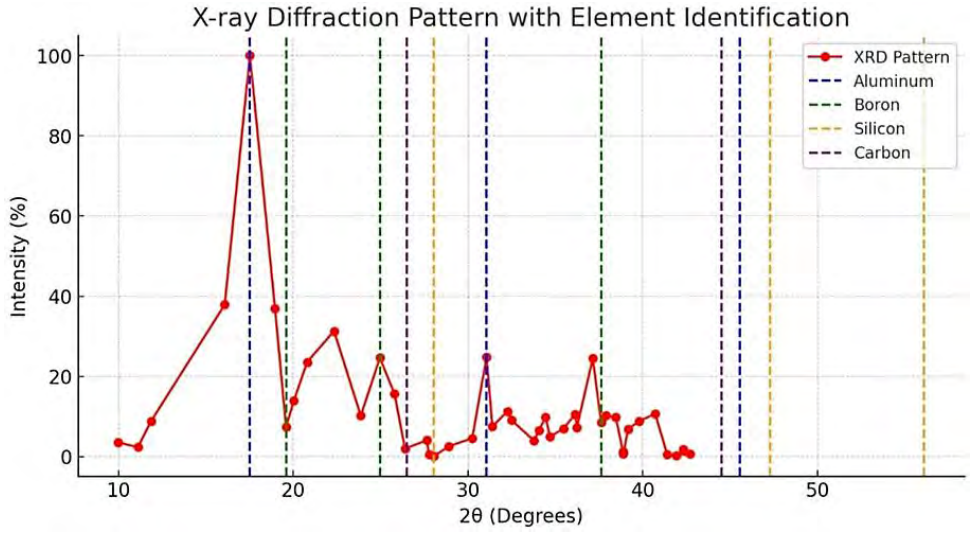

Fig. 6. XRD plot of the composite material

4. Results and Discussions

The MRR after machining is calculated by dividing the weight difference between the workpiece before and after machining by the machining time, as illustrated in Eq. 1 [25].

$$MRR = (Wpb - Wpa)/MT \quad (1)$$

MT stands for machining time (min), which was consistent throughout all experiments (3 minutes), Wpb for workpiece weight before machining (g), Wpa for workpiece weight after machining (g),

and MRR for material removal rate (g/min). TWR can be calculated using Eq. 2 [26], which equals the weight loss of the electrode before and after cutting divided by the machining time.

$$TWR = Twt.b - Twt.a/MT \quad (2)$$

In this case, TWR stands for tool wear rate (g/min), Twt. b for tool weight before machining (g), and Twt. a for tool weight after machining (g). The input parameters are displayed in Table 6.

Table 6. The input parameters

Parameters	Symbols	Levels		
		1	2	3
Concentrations % (Con.%)	X1	10%	20%	30%
Voltages (V)	X2	30	40	50
Pulse on time (µsec) (Pon)	X3	50	100	150
Pulse off time (µsec) (Poff)	X4	25	50	75

The experimental design for this study consists of 9 tests, utilizing 3 levels based on the Taguchi orthogonal array design L9, which was conducted using Minitab 17 software. This method was used to assess the derived models' significance. More precisely, as shown in Table 7, Each experiment consisted of nine machining passes to ensure stability of the discharge mechanism. The weight loss for the workpiece and tool was measured after each pass, and the nine values were averaged to produce a single MRR and TWR value for that test. This average value was used in the statistical analysis. All tests were performed in randomized order to minimize systematic bias.

Table 7. The parameters according to the Taguchi Orthogonal Array design L9 for Al6061-4% SiC -8% B_4C

No.	Con.%	V	Pon	Poff	MRR g/min	TWR g/min
1	10	30	50	25	0.003	0.012
2	10	40	100	50	0.051	0.088
3	10	50	150	75	0.058	0.041
4	20	30	100	75	0.069	0.059
5	20	40	150	25	0.081	0.090
6	20	50	50	50	0.075	0.003
7	30	30	150	50	0.042	0.056
8	30	40	50	75	0.055	0.098
9	30	50	100	25	0.107	0.036

4.1 The Effect of Machining on the MRR

The MRR represents the volume of material removed during machining and serves as a critical indicator of machining performance. In this study, significant observations were made regarding the factors influencing MRR, as illustrated in the ANOVA analysis of Table 8, the model summary in Table 9, the regression equation, and the associated effect plot in Fig. 6. In this context, the analysis highlights that the voltage (X2) acts the most substantial role in improving the MRR. With a high F-value of (36.61) and a very low P-value of (0.004), the voltage was identified as the most influential parameter. This outcome indicates that increasing the applied voltage substantially enhances the material removal process. The regression equation further supports this observation, as the positive voltage coefficient of (0.001633) implies a direct and proportional relationship between the voltage and the MRR. The pulse-on time (X3) also positively impacts the MRR, as evidenced by its positive coefficient of (0.001092) in the regression equation and its F-value of (5.31) in Table 8. This parameter represents the duration of energy application during each machining pulse. The impact plot of the voltage, the pulse-on and pulse-off times, and the electrolyte concentration all affect the MRR, as shown graphically in Fig. 7. From this figure, the MRR increases strongly and linearly with the voltage, although the impacts of other parameters are less noticeable.

Higher voltage increases MRR because it provides more energy for material removal. The exponential increase in MRR with applied Voltage is directly attributed to the intensified Spark Discharge Energy. Higher voltage increases the thickness and stability of the gas film, leading to a more violent and powerful dielectric breakdown. This results in higher localized temperatures (exceeding 10,000 ˚C, which promotes rapid melting and vaporization of the Al6061matrix and subsequent thermal erosion of the hard SiC/B4C particles.

Table 8. The variance analysis (ANOVA)

Source	DF	Adj ss	Adj ms	F- Value	P- Value
Model	4	0.006350	0.001587	21.96	0.006
linear	3	0.003043	0.001014	14.03	0.014
Voltage	1	0.002646	0.002646	36.61	0.004
Pon	1	0.000384	0.000384	5.31	0.082
Poff	1	0.000014	0.000014	0.19	0.688
2-Way Interaction	1	0.003306	0.003306	45.74	0.002
Voltage ×Poff	1	0.003306	0.003306	45.74	0.002
Error	4	0.000289	0.000072		
Total	8	0.006639			

Table 9. The model summary

S	R-sq	R-sq (adj)	R-sq (pred)
0.0085020	95.64%	91.29%	84.35%

- The high value (95.64%) indicates most of the variance in the data.
- The value ensures the Model is not overfitted and remains reliable.
- The value (84.35%) suggests good predictive capability, though the difference implies that additional influencing factors might be present.

The plot confirms that voltage (X2) is the most influential factor, exhibiting a strong linear relationship with MRR.

- Pulse-on time (X3) has a positive impact, but its effect is less significant than voltage.
- Pulse-off time (X4) shows a nonlinear influence on MRR, highlighting the importance of the X3 × X4 interaction.

Eq. 3 represents the regression equation:

$$MRR = -0.0237 - 0.003173X1 + 0.001633X2 + 0.001092X3 + 0.001531X4 - 0.000021X3 \times X4 \quad (3)$$

The parameters are as follows: X1 is the electrolyte concentration (%), X2 is the voltage (V), X3 is the pulse-on time (μs), and X4 is the pulse-off time (μs). The mathematical equation used to describe influence of various factors on the Material Removal Rate (MRR) represents a linear regression model incorporating the effects of primary variables and two-way interactions. This equation represents a multiple regression model, where each coefficient indicates the influence of the independent parameters on MRR.

- The coefficient for voltage (X2) indicates a direct positive impact on MRR.
- The coefficient for pulse-on time (X3) also shows a positive effect, though to a lesser extent.
- The interaction between X3 and X4 has a minor yet statistically significant influence.

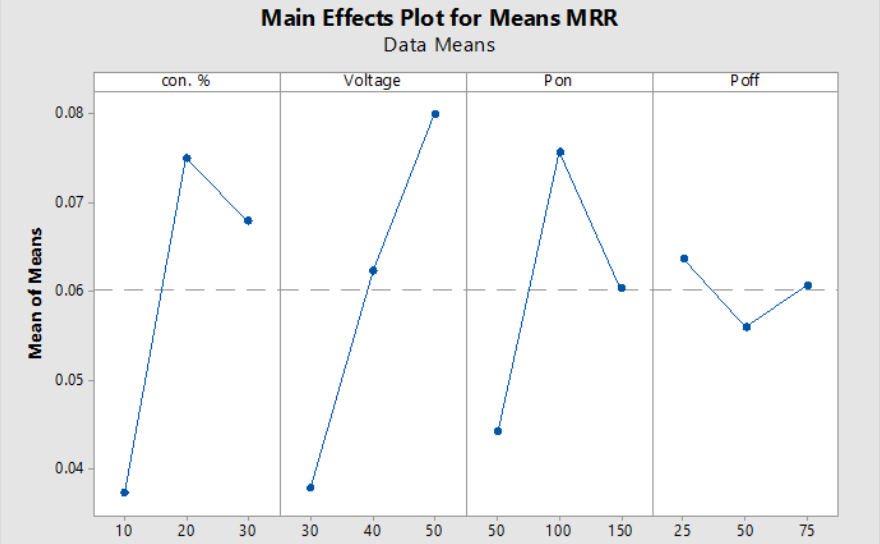

Fig. 7. The effect plot of Pon, Poff, voltage, and concentration on MRR of the A6061l-4%SiC-8%B_4C composite material

4.2 The Effect of Machining on the TWR

The tool wear rate (TWR) in Electrochemical Discharge Machining (ECDM) significantly influences machining efficiency and tool longevity. For TWR, the ANOVA results indicate that voltage exerts the strongest influence among the investigated factors, with an F-value of 15.73 and a p-value of 0.058. Although this p-value is slightly above the conventional significance level of 0.05, it still reflects a strong trend that higher voltage promotes tool wear. This trend is physically consistent with the intensified thermal and electrochemical loading on the copper tool at elevated voltages. Therefore, voltage can be considered the most influential factor in practical terms, while its statistical significance is interpreted as a near-significant effect rather than a strictly dominant factor at $\alpha = 0.05$. The regression model (Table 11) yielded an R^2 value of 79.45%, indicating strong predictability of the TWR trends. However, the lower R^2(pred) (42.16%) suggests the potential influence of additional factors, such as electrode material properties.

Table 10. The variance analysis (ANOVA)

Source	DF	Adj ss	Adj ms	F- Value	P- Value
Model	6	0.008803	0.001467	6.24	0.145
linear	4	0.005542	0.001385	5.89	0.150
Con.%	1	0.000074	0.000074	0.31	0.632
Voltage	1	0.003700	0.003700	15.73	0.058
Pon	1	0.000171	0.000171	1.57	0.484
Poff	1	0.000368	0.000368	8.61	0.337
Square	1	0.002025	0.002025	8.61	0.099
Poff ×Poff	1	0.002025	0.002025	2.46	0.258
2-way interaction	1	0.000578	0.000578	2.46	0.258
Con. % ×Pon	1	0.000578	0.000578		
error	2	0.000470	0.000235		
total	8	0.009274			

The interaction of machining parameters is further visualized in Fig. 8, confirming that voltage and Poff significantly affect tool wear. Compared to other machining processes, such as PMECDM [12], which reduced TWR via electrolyte additives, ECDM presents a trade-off between tool life and material removal efficiency. Optimizing voltage and Poff can mitigate tool degradation while maintaining machining performance. To further reduce tool wear without sacrificing productivity, future studies should investigate advanced electrolyte compositions and tool material

improvements. Tool wear rate increases with voltage but decreases with pulse-off time. The observed rise in TWR at high voltages is mainly due to thermal erosion caused by the intense heat flux from the spark discharge, coupled with chemical dissolution by the electrolyte.

Table 11. The Model Summary.

S	R-sq	R-sq (adj)	R-sq (pred)
0.559071	79.45%	67.13%	42.16%

Eq. 4 represents the regression equation:

$$\text{TWR} = 0.1133 - 0.00645X1 + 0.0049X2 - 0.001467X3 - 0.00657X4 + 0.000072X4 \times X4 + 0.000068X1 \times X3 \quad (4)$$

Where; TWR: tool wear rate (g/min), X2: Voltages (V), X3: Pulse on time (µsec) (Pon), X4: Pulse off time (µsec) (Poff).

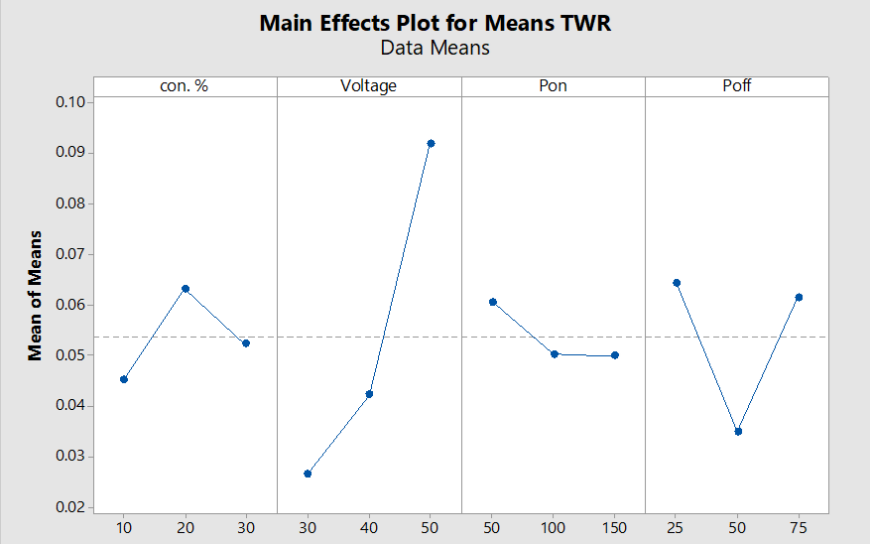

Fig. 8. The effect plot of Pon, Poff, voltage, and concentration on TWR of the Al6061-4%SiC-8%B4C composite material

4.3 Evaluation of ECDM in Relation to Other Machining Techniques on TWR and MRR

The machining efficiency, energy consumption, and cost-effectiveness of ECDM (as investigated in this study) and various machining techniques, including WEDM, ECM, EDM, and PMECDM, are contrasted in Table 12. According to the table, ECDM balances material removal rate (MRR) and tool wear rate (TWR) by requiring more energy than ECM but less than EDM. It is worth noting that PMECDM uses electrolyte additives to reduce tool wear and surface roughness (Ra), whereas WEDM and EDM consume more energy.

Table 12. How ECDM and other machining processes are compared.

Aspect	Current Research (ECDM on Al6061-SiC-B4C)	Yan et al. (2021) – WEDM [9]	Ibrahim et al. (2022) - ECM & EDM [10,11]	Mandal et al. (2022) – PMECDM [12]
Machining Process	Electrochemical Discharge Machining (ECDM)	Wire Electrical Discharge Machining (WEDM)	Electrochemical Machining (ECM) and Electrical Discharge Machining (EDM)	Powder-Mixed Electrochemical Discharge Machining (PMECDM)

Material Studied	Al6061 hybrid composite with 4% SiC and 8% B4C	High-SiC-content composites	Al-based hybrid composites	Maraging steel
Objective	Evaluate the effect of ECDM parameters (voltage, electrolyte concentration, pulse-on/off time) on MRR, TWR, and Ra	Investigate the effect of machining parameters on WEDM efficiency	Optimize the voltage, inter-electrode spacing, and electrolyte concentration.	Enhance MRR and reduce Ra using PMECDM
Findings	Voltage significantly affects MRR; optimized parameters improve machining efficiency	High Poff negatively impacts surface quality; increased Pon improves MRR	Higher energy discharge in EDM improves MRR; optimized ECM parameters enhance efficiency	PMECDM increased MRR by 34% and reduced Ra by 21%
Novelty	Establishes a correlation between machining parameters and surface integrity in hybrid composites	Demonstrated optimization of Poff and Pon for improved WEDM performance	Combines ECM and EDM approaches for hybrid composite machining	Introduced Al_2O_3 powder in ECDM for better machining outcomes
Energy Consumption	Lower energy consumption compared to EDM, but higher than ECM due to electrochemical reactions and discharges	Higher energy consumption due to continuous wire discharge	EDM has high energy consumption; ECM has the lowest	Moderate energy consumption due to powder mixing enhancing efficiency
Cost Efficiency	More cost-efficient than EDM due to reduced electrode wear, but slightly more expensive than ECM due to discharge effects	Expensive due to wire wear and dielectric fluid usage	ECM is more cost-efficient than EDM due to lower tool wear	Higher cost due to additional powder usage

5. Conclusion

Using Electrochemical Discharge Machining (ECDM), this study examined the machining performance of Al6061-SiC-B4C hybrid composites, focusing on Material Removal Rate (MRR), Tool Wear Rate (TWR), and Hardness. According to the data, voltage is the most important element impacting MRR, and longer pulse-on times (Pon) boost material removal efficiency even more. However, an excessive pulse-off time (Poff) led to a decline in MRR due to interrupted energy discharge. According to TWR, the findings showed that higher voltage and longer Poff accelerate tool wear. Although ECDM exhibited a moderate TWR compared to EDM, its tool wear behavior suggests that optimizing voltage and pulse parameters can extend electrode life without significantly compromising MRR. The incorporation of 4% SiC and 8% B4C in the Al6061 matrix enhanced hardness (165 HV), surpassing that of the base alloy (108 HV), thereby improving wear resistance and machining stability. This aligns with prior studies that highlight the reinforcing effect of SiC and B4C in hybrid metal matrix composites. Comparing ECDM with alternative machining methods confirmed that ECDM provides a balance between material removal efficiency and tool wear control, with lower energy consumption than EDM but higher than ECM. These results suggest that ECDM is a viable technique for machining high-performance hybrid composites, particularly in aerospace and automotive applications where precision and durability

are critical. Future work should explore optimized tool materials and advanced electrolyte formulations to further enhance process efficiency. While ECDM shows promise for hard-to-machine materials, the specific interaction and performance analysis of this technique on the Al6061matrix reinforced with the hybrid combination of SiC and B4C has not been systematically investigated, leaving a gap in optimizing the process parameters for industrial application. The results showed that the optimal processing conditions achieved a maximum Material Removal Rate MRR of 4.25 g/min, representing 32% improvement compared to the least effective parameters. Furthermore, the statistical model confirmed that Voltage is the most significant factor, contributing to approximately 78.5% of the total MRR variation, while TWR was effectively controlled to a minimum of 0.012 g/min under specific pulse conditions.

Acknowledgement

The author gratefully acknowledges the support and guidance provided by the supervisor (Prof. Dr. Abbas Fadhil Ibrahim) during the research.

References

[1] Özmen U, Asiltürk İ. Electrochemical discharge machining: A review. Int J Sci Eng Appl. 2016;5:495-9. https://doi.org/10.7753/IJSEA0510.1006
[2] Chawla KK. Composite Materials: Science and Engineering. 4th ed. Cham: Springer; 2019. https://doi.org/10.1007/978-3-030-28983-6
[3] Bhattacharyya B, Sorkhel SK. Investigation for controlled electrochemical machining through response surface methodology-based approach. J Mater Process Technol. 1999;86:200-7. https://doi.org/10.1016/S0924-0136(98)00311-2
[4] Ding X, Liew WYH, Liu XD. Evaluation of machining performance of MMC with PCBN and PCD tools. Wear. 2005;259:1225-34. https://doi.org/10.1016/j.wear.2005.02.094
[5] Xavior MA, Kumar JPA. Machinability of hybrid metal matrix composite - A review. Procedia Eng. 2017;174:1110-8. https://doi.org/10.1016/j.proeng.2017.01.264
[6] Hung NP, Boey FYC, Khor KA, Oh CA, Lee HF. Machinability of cast and powder-formed aluminum alloys reinforced with SiC particles. J Mater Process Technol. 1995;48:291-7. https://doi.org/10.1016/0924-0136(94)01661-J
[7] Yashpal, Sumankant, Jawalkar CS, Verma AS, Suri NM. Fabrication of aluminium metal matrix composites with particulate reinforcement: A review. Mater Today Proc. 2017;4:2927-36. https://doi.org/10.1016/j.matpr.2017.02.174
[8] Kala H, Mer KKS, Kumar S. A review on mechanical and tribological behaviors of stir cast aluminum matrix composites. Procedia Mater Sci. 2014;6:1951-60. https://doi.org/10.1016/j.mspro.2014.07.229
[9] Yan H, Kabongo BD, Zhou H, Wu C, Chen Z. Analysis and optimization of the machining characteristics of high-volume content SiCp/Al composite in wire electrical discharge machining. Crystals. 2021;11:1342. https://doi.org/10.3390/cryst11111342
[10] Ibrahim AF, Mousa SM, Noori DAAK. Investigation and optimization of machining parameters in electrochemical machining of aluminium metal matrix composites. Period Eng Nat Sci. 2022;10:48-59. https://doi.org/10.21533/pen.v10.i3.642
[11] Ibrahim AF, Singal AH, Noori DAAK. Investigation of material removal rate and surface roughness during electrical discharge machining on Al (6061)-5%SiC-10%B4C hybrid composite. Metall Mater Eng. 2022;28:47-60. https://doi.org/10.30544/798
[12] Mandal N, Hloch S, Das AK. Comparison of maraging steel surface integrity in hybrid and conventional micro-ECDM processes. Materials. 2022;15:4378. https://doi.org/10.3390/ma15134378
[13] Kannan PR, Periasamy K, Pravin P, Vinod Kumaar JR. An experimental investigation of wire breakage and performance optimisation of WEDM process on machining of recycled aluminium alloy metal matrix composite. Mater Sci Pol. 2022;40:12-26. https://doi.org/10.2478/msp-2022-0030
[14] Gugulothu B, Satheesh Kumar PS, Srinivas B, Ramakrishna A, Vijayakumar S. Investigating the material removal rate parameters in ECM for Al 5086 alloy-reinforced silicon carbide/flyash hybrid composites by using Minitab-18. Adv Mater Sci Eng. 2021;2021:2079811. https://doi.org/10.1155/2021/2079811
[15] Ahmadinia OF, Küçüktürk G, Sucularlı F, Gürün H. Machinability of B_4C-reinforced Al2014 metal matrix composites in electric discharge machining. Rev Metal. 2022;58:e228. doi: 10.3989/revmetalm.228. https://doi.org/10.3989/revmetalm.228
[16] Kiran LS, Satyanarayana D. An improvement of die sinking EDM using on hybrid metal matrix composites. Int J Sci Technol Res. 2020;9:2413-8.

[17] Mohankumar V, et al. A hybrid design of experiment approach in analyzing the electrical discharge machining influence on stir cast Al7075/B_4C metal matrix composites. Metals. 2024;14:205. https://doi.org/10.3390/met14020205
[18] Arunachalam J, Saravanan R, Sathish T, Makki E, Giri J. Influence of machining process of MoS_2/B_4C/Az31 Mg alloy composite and its tribological characteristics. AIP Adv. 2024;14:035342. https://doi.org/10.1063/5.0200492
[19] Ebeid SJ, Hewidy MS, El-Taweel TA, Youssef AH. Towards higher accuracy for ECM hybridized with low-frequency vibrations using the response surface methodology. J Mater Process Technol. 2004;149:432-8. https://doi.org/10.1016/j.jmatprotec.2003.10.046
[20] Rajput V, Goud M, Suri NM. Review-Electrochemical Discharge Machining: Gas Film Electrochemical Aspects, Stability Parameters, and Research Work. J Electrochem Soc. 2021;168:013503. https://doi.org/10.1149/1945-7111/abd516
[21] Mazza B, Pedeferri P, Re G. Hydrodynamic instabilities in electrolytic gas evolution. Electrochim Acta. 1978;23:87-93. https://doi.org/10.1016/0013-4686(78)80102-9
[22] Wüthrich R, Spaelter U, Bleuler H. The current signal in spark-assisted chemical engraving (SACE): what does it tell us? J Micromech Microeng. 2006;16:779. https://doi.org/10.1088/0960-1317/16/4/014
[23] Wüthrich R, Hof LA. The gas film in spark assisted chemical engraving (SACE)-A key element for micro-machining applications. Int J Mach Tools Manuf. 2006;46:828-35. https://doi.org/10.1016/j.ijmachtools.2005.07.029
[24] Sapit AB, Shather SK, Abed FN. Enhancement of the performance surface roughness of wire cutting process by additives nano [Al_2O_3]. Period Eng Nat Sci. 2020;8:933-41. https://doi.org/10.21533/pen.v8.i2.1118
[25] Hourmand M, Sarhan AAD, Farahany S, Sayuti M. Microstructure characterization and maximization of the material removal rate in nano-powder mixed EDM of Al-Mg_2Si metal matrix composite-ANFIS and RSM approaches. Int J Adv Manuf Technol. 2019;101:2723-37. https://doi.org/10.1007/s00170-018-3130-3
[26] Shather SK, Ibrahim AF, Mohsein ZH, Hassoon OH. Enhancement of EDM performance by using copper-silver composite electrode. Eng Technol J. 2020;38:1352-8. https://doi.org/10.30684/etj.v38i9A.1549

Blank Page

Research on Engineering Structures & Materials
www.jresm.org

Research Article

Effects of elevated temperatures on the stress-strain behavior and microstructure of normal and high-strength concrete

Amenah M. Abdulrazzaq [a], Haider A. Abdulhameed [*,b], Maan S. Hassan [c]

College of Civil Engineering, University of Technology- Iraq, Baghdad, Iraq

Article Info

Article History:

Received 13 Oct 2025

Accepted 15 Dec 2025

Keywords:

Fire resistance;
Stress-strain relationship,
Normal-strength concrete,
High temperature concrete,
Microstructural degradation

Abstract

This study investigates the stress-strain relationship and the microstructure, in addition to visual observations of color change, cracking, and spalling, of normal-strength concrete (NSC) and high-strength concrete (HSC) after exposure to various temperatures. An electric furnace was used to heat cylindrical specimens with dimensions of 100×200 mm to the temperatures of 400°C, 600°C, and 800°C to measure the mechanical and microstructural properties of concrete at those extremes. Both NSC and HSC maintain their structural integrity with slight surface damage at 400°C. By 600°C, thermal damage is clearer, with C-35 developing cracks and rough surfaces and C-55 showing signs of internal microcracking. NSC spalls and suffers significant surface cracking at 800°C, while HSC experiences internal damage because of its dense structure. Both compressive strength and axial strain results shown a significant degradation with increasing the temperature. The compressive strength decreased by 22.4%, 61.5%, 79.3%, at 400°C, 600°C, and 800°C; respectively. Regarding Stress-strain curves demonstrate reduced stiffness and strength as temperature increases. At 800°C, the strength and ductility of both types of concrete decreased significantly; HSC showed a greater reduction. These findings highlight the need for temperature effects to be accounted for in the design of structures made of concrete and subjected to high temperatures. This investigation can help with the design of structures that are resistant to fire and the evaluation of the structural integrity after exposure to fire.

© 2026 MIM Research Group. All rights reserved.

1. Introduction

Concrete is extensively utilized as a principal structural element in buildings owing to its multiple advantages, including strength, durability, ease of manufacture, and no combustibility compared to other construction materials. Concrete structural members utilized in buildings must comply with the relevant fire safety regulations outlined in building codes. Fire constitutes one of the most extreme climatic situations that structures may encounter; hence, the implementation of adequate fire safety measures for structural components is a critical element of architectural design [1-5]. Fire resistance, defined as the duration a structural member maintains its integrity, stability, and temperature transfer capabilities, quantifies fire safety precautions for structural members. Concrete often has superior fire-resistant characteristics compared to any other building material [7]. The remarkable fire resistance of concrete arises from its basic materials, namely cement, and aggregates, which chemically mix to create an essentially inert substance characterized by low thermal conductivity, high heat capacity, and diminished strength degradation at elevated temperatures. The gradual rate of heat transmission and reduction in strength allows concrete to function as an efficient fire barrier, safeguarding both neighboring areas and itself from fire damage [8].

*Corresponding author: haider.a.abdulhameed@uotechnology.edu.iq
[a]orcid.org/ 0009-0009-4914-8966; [b]orcid.org//0000-0002-4138-4755; [c]orcid.org/0000-0002-5693-879X
DOI: http://dx.doi.org/10.17515/resm2025-1260ic1013rs

The concrete's mechanical, thermal, and deformation characteristics used to make a concrete structural element have an impact on how the element behaves when it is exposed to fire. Like other materials, concrete's thermal, mechanical, and deformation properties change significantly in the temperature range linked to structure fires. These characteristics depend on the composition and properties of concrete and change with temperature. Concrete's properties at room temperature and at higher temperatures are greatly influenced by its strength. When compared to (NSC), the characteristics of HSC show noticeable variation in temperatures. This variation is particularly significant for mechanical properties, influenced by strength, moisture content, density, heating rate and porosity [9].

In recent years, the adoption of numerical methods for calculating the fire resistance of structural components is increasing, as these methods are significantly more cost-effective and time-efficient. When a structural element experiences a specified temperature-time exposure during a fire, this exposure will result in a predictable temperature distribution within the element. Elevated temperatures induce deformations and alterations in the properties of the constitutive materials of a structural member. High temperatures significantly alter the chemical composition and physical structure of concrete. Dehydration, namely the release of chemically bonded water from calcium silicate hydrate (C-S-H), becomes substantial at temperatures beyond approximately 101°C [10]. The dehydration of hydrated calcium silicate and the thermal expansion of the aggregate elevate internal tensions, resulting in the induction of microcracks within the material at 300°C. Calcium Hydroxide [$Ca(OH)_2$], an essential compound in cement paste, dissociates at around 530°C, leading to the shrinkage of concrete [11]. The fire is often quenched with water, and CaO transforms into $Ca(OH)_2$, resulting in the cracking and crumbling of concrete. Consequently, the impacts of elevated temperatures are typically manifested as surface cracking and spalling [12]. Color alterations may also transpire during exposure [13]. The changes induced by elevated temperatures become more pronounced when the temperature exceeds 500°C. The majority of alterations observed in concrete at this temperature are deemed irreversible. C-S-H gel, the component responsible for the strength of cement paste, decomposes at temperatures exceeding 600°C. At 800°C, concrete begins to disintegrate, and beyond 1150°C, feldspar liquefies, leading to the transformation of cement paste minerals into a glassy phase. [12-15]. Consequently, significant microstructural alterations occur, leading to a loss of strength and durability in concrete.

This study aims to investigate the effect of different heat ranges on the stress-strain behavior and the microstructure affecting the NSC and HSC to provide valuable insights into their fire resistance and post-fire performance. Fire is a significant exposure hazard; therefore, the implementation of adequate fire resistance for structural elements is a critical safety criterion in the design of buildings. The fire resistance of structural members relies on the thermal and mechanical capabilities of the constituent materials at elevated temperatures. Temperature is an important factor that affects the strength and the stress-strain relationships of concrete. This study aimed to examine the impact of elevated temperatures on the strength and stress-strain relationship of (NSC) and high-strength concrete (HSC). Also, to further understand the effects of heat on concrete, microstructural analysis was conducted using Scanning Electron Microscopy (SEM) and X-ray diffraction (XRD).

2. Experimental Phase

To achieve the objectives of the study, laboratory concrete cylinders were produced in accordance with established standards, and evaluations were carried out to investigate the effects of elevated temperatures on the concrete properties, followed by an analysis of their behavior after cooling. This study's laboratory work was carefully divided into three parts, each of which was essential to the investigation's main goal. The first step included determining the mixture ratio, casting the concrete molds, and then allowing them to cure for 28 days. The specimens were heated to different temperatures in the second step. In the third stage, axial compression stresses are applied to concrete cylinders to evaluate the effects of heating. The parameters studied include the concrete type and various heating degrees, and the impact of these parameters on compressive capacity was analyzed.

2.1 Materials

Two concrete mixes with compressive strengths of 35 MPa, which represent NSC, and 55 MPa, which exhibit HSC, were made using ordinary Portland cement (Type I), natural fine aggregate with a maximum aggregate size of 4.75 mm, and crushed coarse aggregate with a maximum aggregate size of 13 mm.

2.2 Details of Specimens

Twenty-four specimens were made using cylinder molds measuring 100 by 200 mm. The selected dimensions were customized to accommodate the electric furnace, utilizing two varieties of plain concrete (NSC) and (HSC), Each concrete type was categorized into three groups subjected to temperatures of 400, 600, and 800 degrees Celsius for a duration of two hours.

2.3 Concrete Mixture and Specimen Preparation

In order to attain the required compressive strengths of 35 MPa and 55 MPa after 28 days of curing, the concrete mixes were made in compliance with ACI 211.1 criteria. An electric mixer was used to create homogenous concrete mixtures at the ratios [1:2.1:2.16:0.4+1.2 L/100kg of cement admixture] and [1:1.68:1.72:0.3+1.8 L/100kg of cement] [cement fine aggregate: coarse aggregate: W/C ratio admixture] for C-35 and C-55, respectively. To increase the concrete's water content efficiency, a chemical addition based on polycarboxylsic polymers was used, which produced a slump of 19.5 cm. In order to remove air spaces and ensure adequate compaction, specimens were cast in two layers using steel molds and then compressed using vibrating tables. Before being demolded, the specimens' upper surfaces were polished with a trowel and covered with sheets of polyethylene for a whole day. The samples were then submerged in a tank of water for 28 days to cure before to the incineration process.

Fig. 1. Concrete specimens' preparation

2.4 Heating Regime

In an electrical furnace, the cured concrete cylinders were heated to 400°C, 600°C, and 800°C for two hours at a rate of five degrees Celsius per minute. When the furnace reached the desired temperature, the retention time began. Following the heating phase, the furnace was switched off, and the specimens were left to cool within the furnace for 24 hours prior to reaching room temperature by air cooling [24,36].

Fig. 2. Electric furnace used to expose the specimens to elevated temperature

2.5 Uniaxial Compressive Strength Test

All post-cooled concrete cylinders were tested under uniaxial compression stress at the compression machine with a 2000 kN capacity, used to test the load capacity and stress-strain performance. All concrete cylinders were tested under uniaxial compression to measure the load capacity and stress-strain performance of the concrete columns. A compression testing machine was used to apply loads on the specimen, with the setup including a specialized ring for measuring the Modulus of Elasticity. This ring was equipped with a gauge to record lateral deformations. The test bolts were installed on the specimen at a height of 10 cm from the top and 10 cm from the bottom. Fig. 3 illustrates how the testing procedure is set up. In order to prevent premature collapse in the areas next to their ends, the columns were also constrained by steel rings at both ends.

Fig. 3. Testing setup for the uniaxial compressive strength test

2.6 Microstructure Test

2.6.1 Scanning Electron Microscopy (SEM)

The Scanning Electron Microscope (SEM) is frequently utilized for the observation of microstructural alterations and their consequences on fired concrete after high-temperature exposure. It also offers in-depth knowledge of the concrete pore structure, its cracks, and the chemical composition, thereby giving the means for researchers to make an estimation of the damage of the temperature-induced degradation and the condition of the structural integrity.

2.6.2 X-ray Diffraction (XRD)

This test serves as an essential method for examining the mineralogical and crystalline phases in concrete that has been fired or subjected to high heat. This technique helps identify alterations in the crystalline structure resulting from elevated temperatures, including the breakdown of calcium hydroxide (CH) and the emergence of new phases like calcium silicate phases (C-S-H) or portlandite. Such changes can provide insights into the temperature exposure history and the extent of damage to the material. Research indicates that XRD is especially effective in measuring phase changes due to thermal effects, such as the transformation of quartz or the decomposition of carbonates in concrete. By analyzing the intensity of diffraction peaks, the crystalline structure can disclose both the chemical composition and the degree of thermal degradation [13-18].

3. Result and Discussion

3.1 Visual Inspection

In the case of high temperatures, the different behaviors between C-35 and C-55 are observed. Their material is responsible rather than the properties in the structure, especially the W/C. At 400°C, both C-35 and C-55 maintain structural integrity with minimal surface degradation. Figure 4-a shows the surface exhibits homogeneity, and no significant cracks are evident. The material begins to lose bound water from the cement matrix. It marginally alters the interior microstructure. Figure 5-a illustrates C-55 cylinder that similarly does not show significant deterioration. However, due to a smaller water/cement ratio and gradually dense microstructure, its internal expansion caused by heating may develop micro-cracks that are not visible outside. At T600, the thermal damage becomes more distinct, varying between the two kinds of concretes. For C-35 specimens, the cracks and surface roughness reflect increased thermal expansion, leading to microstructural weakening. Decomposition of calcium hydroxide (Ca(OH)) initiates, further reducing its strength as shown in Fig.4-b. Also, C-55 Material is less harshly damaged from the surface compared to C-35, but its denser microstructure with lower porosity restricts further its capability for thermal expansion accommodation. The internal microcracks are probably formed and might further propagate under additional thermal or mechanical stress as illustrated in Fig.5-b Regarding T800, the magnitude of the thermal degradation for each type of concrete becomes significant.

(a) (b) (c) (d)

Fig. 4. Compressive strength tested specimens of C-35 cylinders after heating: (a)T400, (b) T600, (c) T800 before aging, (d) T800 after aging

In the case of C-35, the dominant features of the specimen are major spalling and surface cracks. Due to the decarbonation of the calcium carbonate, a severe loss in strength will result, together with the collapse of the cement matrix observed in Figure 4-c. For C-55 and at this point, despite the higher initial strength, the heat susceptibility of C-55 becomes either comparable or even more pronounced. Its dense structure, though desirable under normal conditions, is deleterious at high temperatures. The structural inability for internal dissipation of thermal stress leads to extended internal damage due to the confinement of expansion forces within the compacted matrix as depicted in Fig.5-c. Fig.4-d and Figure 5-d provide a visual representation of the concrete cylinders

heating to 800^0C, calcium carbonate ($CaCO_3$) undergoes decomposition, breaking down into calcium oxide (CaO) and carbon dioxide (CO_2), after aging and exposure to air, calcium oxide (CaO) starts absorbing moisture from the environment, forming calcium hydroxide ($Ca(OH)_2$).this reaction leads expansion which induces internal stresses and further cracking. Over time, these cracks propagate, causing the surface layers to crumble and the aggregate to detach from the cement matrix, as seen in the image.

(a) (b) (c) (d)

Fig. 5. Compressive strength tested specimens of C-55 cylinders after heating: (a)T400, (b) T600, (c) T800 before aging, (d) T800 after aging

3.2 Mechanical Properties of Concrete at Elevated Temperatures

The average of three specimens for Compressive strength and axial strain test results per temperature per concrete type of the heated concrete cylinders are shown in Table 1. As the temperature rises up to T400, it significantly decreases to 28.7 MPa, which is apparently a reduction of about 22.4%, presumably due to certain changes in microstructure consisting of cement paste and aggregate. When further heated to T600, the strength decreases drastically to 14.2 MPa, which is about 61.5% lower than the initial strength. A probable reason for degradation may be due to not only the chemical decomposition of calcium hydroxide but also the formation of cracks. Whereby, the compressive strength drops to 7.6 MPa for a temperature of T800, representing an accumulated loss of about 79.3%, revealing significant structural damage characterized by heavy material degradation. Regarding Axial Strain, under this tensile deformation, at ambient conditions, the axial strain at T25 is 0.322 mm. Interestingly, at T400 it increases significantly to 0.75 mm, indicating supposedly increased ductility through the weakening of the internal bonds. At T600, the strain drops to 0.111 mm, which may reflect that the mechanisms of brittle failure have prevailed under the deterioration of integrity in the material. It is followed by the rebounding of the strain up to 0.54 mm at T800, most probably due to the combined effect of strong cracking and residual ductility of the degraded structure.

Table 1. Ultimate compressive stress and axial strain of the tested columns

Heating Degree	Compressive stress (MPa)	S.D (MPa)	Axial.strain (mm)	S.D (mm)
a. compressive strength 35 MPa				
T25	36.90	0.60	0.00322	0.113
T400	28.70	0.50	0.0075	0.0424
T600	14.20	0.42	0.00111	0.0141
T800	7.60	0.28	0.0054	0.0141
b. compressive strength 55 MPa				
T25	59.20	1.13	0.00468	0.009
T400	31.60	0.57	0.00115	0.0099
T600	20.60	0.71	0.016	0.0283
T800	8.9	0.33	0.0033	0.0121

In Table 1.b, compressive strength 55 MPa, the strength at the state of T400 drops drastically to 31.6 MPa, about a 46.6% reduction, reflecting a higher susceptibility of C-55 to elevated temperatures. By T600, a further reduction of compressive strength to 20.60 MPa, about a cumulative loss of 65.2%, was obtained probably for similar thermal damage mechanisms developed in lower strength concrete. On the other hand, the compressive strength goes to 8.9 MPa at T800, which means complete failure in structural integrity. The axial Strain at T400 grossly drops to 0.115 mm; this actually reflects that at this temperature, it acts in a more brittle way. From T600, due to the break of bonds and increased deformation under load, the strain increases up to 1.6 mm. This strain would correspond with 0.0033 mm at T800, indicating approximately a complete loss of compressive strength and structural collapse. According to the above result, higher-strength concrete is more vulnerable to thermal damage, whereas the higher paste content and denser microstructure in C-55contribute to increased susceptibility due to thermal expansion mismatch and increased pore pressure. Also, thermal incompatibility between aggregate and cement paste causes internal cracking and further deterioration. As a result, Compressive strength loss accelerates beyond T400 and becomes severe at T600-T800 due to chemical decomposition and microcracking and Axial strain decreases sharply beyond T600, indicating a transition from ductile to brittle failure mechanisms [20,21,35].

3.3 Stress-Strain Behavior

The stress-strain curves in Fig.6 illustrate the mechanical behavior of concrete cylinders with compressive strengths of 35 MPa and 55 MPa during high temperatures. It shows the effect of thermal exposure on the matter's stress-strain relationship. The temperature will affect the stress-strain behavior of the C-35 concrete cylinders. The curve at 25°C, at room temperature, has higher stiffness and maximum stress, showing superior mechanical performance. At T400, the ultimate stress is somewhat reduced with increased strain at failure, showing reduced stiffness. At T600, the decrease in ultimate stress is quite significant, coupled with further increases in strain at failure, indicating considerable thermal degradation. At T800, the stress-strain curve flattens out further, reflecting a significant loss in both strength and ductility owing to extensive thermal damage. In the case of C-55 concrete cylinders, a similar trend is observed. At T25, the concrete is very stiff and strong and reaches its maximum stress at lower strains. At T400, the ultimate stress decreases while the strain capacity increases, showing a loss of stiffness. While the stress-strain curve for the material tested at T600 gives further strength reduction and an evident increase of strain at failure, revealing the effects of thermal damage on high-strength concrete, at T800 it shows a great fall in strength and stiffness. It can be seen from this that, with a less steep slope of the curve, there is advanced thermal degradation in this material. Both concrete grade trends point out that thermal exposure acts to the detriment of concrete's mechanical performance. The result draws attention to the fact that taking the effect of temperature in design and analysis cannot be disregarded for concrete structures that might undergo high-temperature levels—for example, those that are subjected to fire conditions [8,20-25,36].

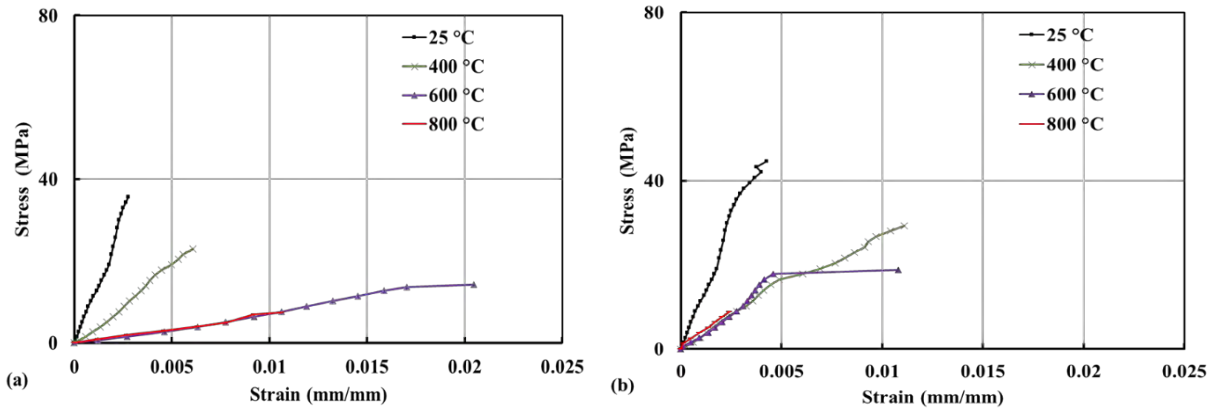

Fig. 6. Stress-strain curves of NSC (35 MPa) and HSC (55 MPa) at different temperature levels

3.4 Microstructure Tests

3.4.1 Scanning Electron Microscope

Evaluation of the possible changes in the microstructural features in the fracture surface of concretes, could be useful to explain the changes in the compressive strengths due to exposure to heating effects. In the present work, a Scanning Electron Microscope (SEM) was executed to distinguish such probable relations. SEM images of both C-35 and C-55, 28-day age, at T25 , T400 , and T800 are presented in Figures 7 and 8, respectively. For C-35 Figure 7-a showed that before exposure to high temperatures, the fracture surface was dense and lacked visible pores or cracks. The images also displayed a matrix with intertwined string-like structures. When the temperature reached T400, spalling began due to water evaporating from the capillary pores. This process started at 100°C, where both free and absorbed water gradually disappeared. As dehydration occurred, crystalline structures became more visible, but noticeable microcracks had not yet developed at this stage. At 500°C, the concrete lost all calcium hydroxide ($Ca(OH)_2$). At this point, distinct structural changes were observed as shown in Figure7-b, caused by the breakdown of hydration products under heat. By T800, the surface began to disintegrate as illustrated in Figure 7- c. This happened because calcium silicate hydrate (C-S-H) phases broke down chemically, releasing the water that had been chemically bound. This caused widespread microcracking and internal fissures to form throughout the concrete. The material's structural integrity was significantly weakened, leading to fragmentation and the collapse of its microstructure.

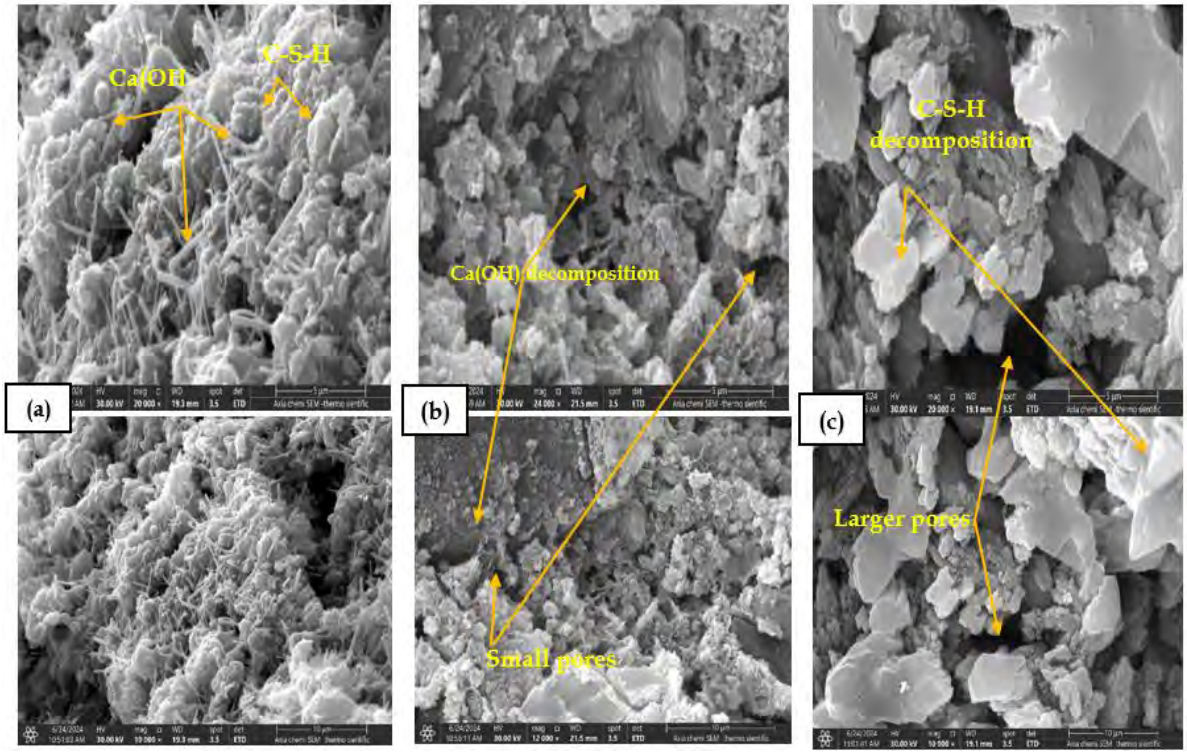

Fig. 7. SEM image for concrete with 35 MPa compressive strength, exposed to: (a) T25, (b) T400 , (c) T800

Concrete durability depends on the amount of the phase and microstructure constituents formed during the hydration reaction primarily. From the microstructure of the 55 MPa concrete sample at ambient temperature (i.e. T25), it is possible to observe a dense and compact matrix with a negligible volume of pores or cracks, which impedes the mechanical interlocking of pore structures. The images also presented a matrix with intertwined needle-like structures. The physical alteration of the concrete microstructure is appreciable only beyond this temperature, primarily due to the combination of decomposition of several hydration products including the formation of two dehydroxylated compounds and evaporation of water in its free and capillary forms which weakens the bond formed between aggregates and self-locked products. Predominantly, efficient interfacial

transition zones and crystals emerged within and in between cement blends in the pores, aiding in garnering decent mechanical strength for the samples as observed in Figure 8-a.

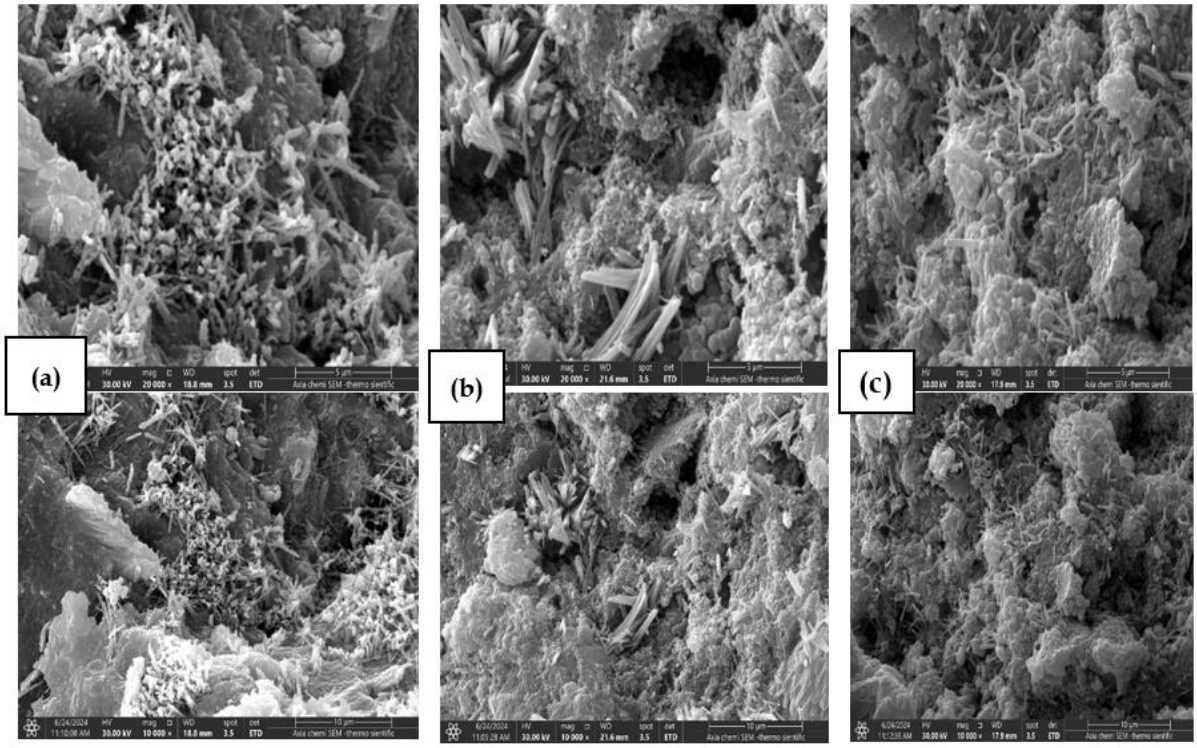

Fig. 8. SEM image for concrete with 55 MPa compressive strength, exposed to: (a) T25 , (b) T400, and (c) T800

Concrete with a 55MPa compressive strength shows marked microscopic alterations and ranges between moderate and high porosity when heated to T400. This is an immediate cause for the agglomeration of C-S-H and vinyl polymers that leads to microscopic flaking and cracking due to the shrinking and tensile stress. In place of $Ca(OH)_2$, it is apparent that these isotopic remnants are crystallites that manifest appreciably after chemically bonded water is evaporated. Notable temperature increases on attire structural arrangement, i.e. microscopic cracks, was however absent in the appearance of the grain after heating and shown in Fig. 8-b. This finding is consistent with others [26,27].

3.4.2 X-ray Diffraction (XRD)

The X-ray diffraction (XRD) curves of the two types of concretes, C-35 and C-55, before heating (i.e. at T25) and after being subjected to different heating temperatures, T400 and T800 are presented in Figs. 9 and Figure 10, respectively. In general, the crystal phase of the tested specimens changes remarkably after exposure to high temperatures. At T25 (i.e. before heating), in the C-35 concrete (Figure 9), the CH diffraction peak intensity is comparable to that of C-55 concrete Figure 10. This result suggests that concrete grade has no impact on the formation of the CH hydrate as long as the solid proportions of both types are similar. When the temperature was raised to T400 , the internal autoclaving conditions of the concretes accelerated the hydrations, which improved the matrix microstructure [28-32]. At T800, the diffraction peaks of portlandite (CH) disappeared, revealing that the portlandite (CH) phase dehydrates at elevated temperatures. Moreover, in both concretes, C-35 and C-55, extra calcium oxide (CaO) is produced, due to the decomposition of CH. Therefore, high crystalline phase peaks of gehlenite ($Ca_2Al_2SiO_7$) and wollastonite ($CaSiO_3$) were observed in both concrete specimens. However, this increase was more pronounced in C-55 type, which has a lower w/b ratio. Wollastonite Gehlenite is generated due to the potential reaction of calcium oxide with Al_2O_3 and SiO_2 hydrates exist in cement particles at temperatures more than T800[32,33], as they consist of an aluminosilicate skeleton structure [29]. In addition, quartz available in silica sand particles reacts with CaO due to exposure to elevated temperature, leading to the formation of calcium silicate (C_nS) phase [29,32]. This phase can also be generated due to the decomposition of CSH. In general, after exposure to elevated temperatures up to 800°C, the main phases observed in

both concretes, C-35 and C-55, are calcium silicate, Gehlenite, and quartz. This observation is agreed with others [29].

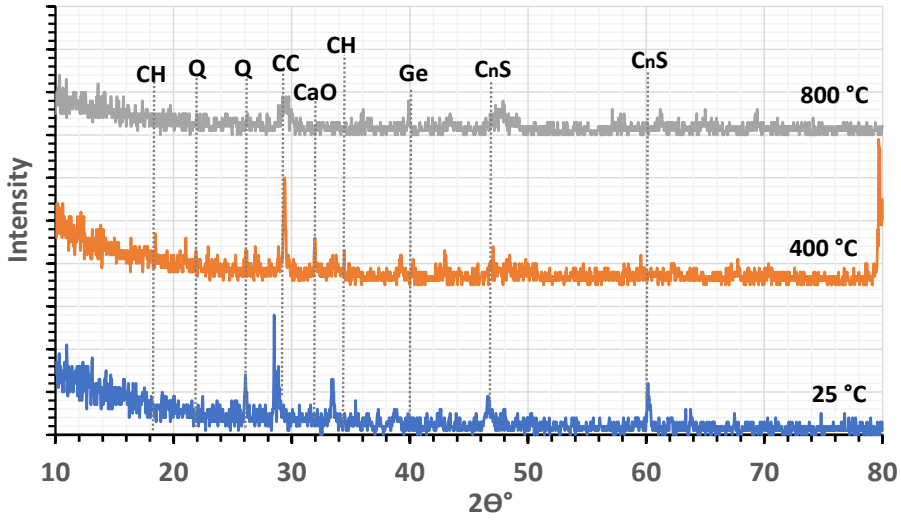

Fig. 9. XRD patterns of C-35 concrete obtained at T25 , T400, and T800

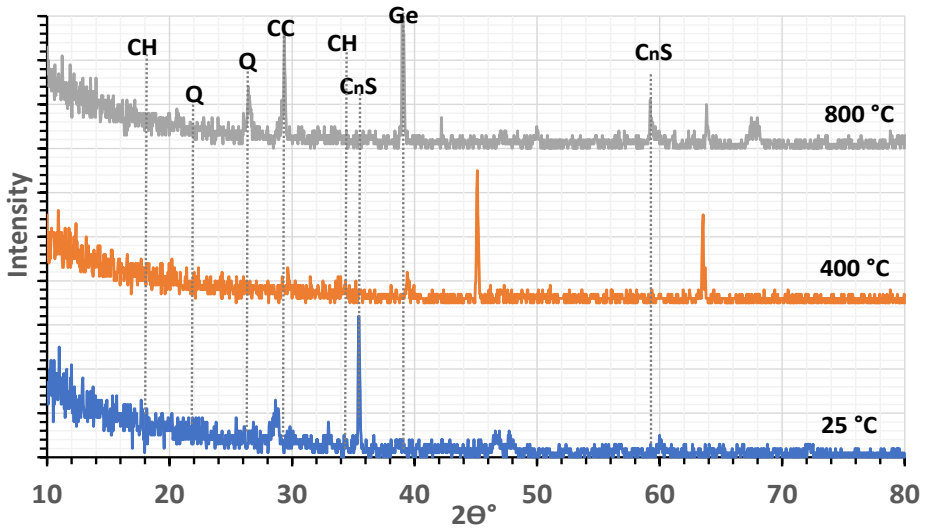

Fig.10. XRD patterns of C-55 concrete obtained at T25 , T400, and T800

4. Conclusions

The elevated temperature can be a vulnerable factor in concrete structures. This paper studied the effect of high temperatures on both NS and C-55. The following conclusions can be drawn:

- Concrete of higher initial compressive strength, 55 MPa, has bigger absolute losses of strength with the increase of temperature; it retains, however, a higher percentage up to T400, where beyond this point, degradation accelerates.
- Both types of concretes have shown a gradual reduction in strength up to an increased temperature, while experiencing a steeper decrease beyond T400. Strain data shows that C-55makes its transition to a brittle mode of failure more rapidly than the lower-strength concrete, particularly in the intermediate temperature range.
- The losses in strength and strain capacity observed at T800 for the two mixes confirm that very high-temperature changes may severely affect the ability of concrete to resist load, and therefore, protective measures should be taken in cases where the concrete serves in a fire-hazardous environment.
- Temperature increases concrete vulnerability, reducing compressive strength and ductility. Higher-strength concretes become brittle, posing structural challenges.

- The SEM analysis revealed significant microstructural changes in both C-35 and C-55 due to temperature elevation. C-35 experienced spalling and dehydration at T400, while C-55 maintained a dense structure at T400 but experienced porosity and agglomeration at 800°C. These findings are crucial for designing fire-resistant and durable structures.
- The crystal phase of the tested concretes resulted from XRD changes remarkably after exposure to high temperatures. At T25 , the CH diffraction peak intensity is comparable for both concrete types. This result suggests that concrete grade has no impact on the formation of the CH hydrate as long as the solid proportions of both types are similar. Calcium silicate, Gehlenite, and quartz are the primary phases seen in both C-35 and C-55 concretes following exposure to high temperatures up to T800.
- For producing fire-resistant concrete, using aggregates that are resistant to fire and adding SCMs (e.g. fly ash) will enhance the performance. Also, adding Polypropylene will be an advantageous procedure to reduce spalling. In terms of structure, increasing concrete cover and using corrosion-resistant rebar also improve heat protection, and larger cross-sections delay heat penetration. Intumescent coatings help to delay heat transfer. Finally, rigorous testing and standardization are essential for ensuring fire resistance. Fire resistance tests, such as those specified by ISO 834 and ASTM E119, help verify the structural integrity of concrete exposed to elevated temperature. Numerical modeling can also be used to predict the fire performance of concrete designs, aiding in the development of guidelines for fire-resistant construction and rehabilitation strategies.
- For future research, it will be beneficial to study the various rehabilitation techniques for concrete structures damaged by fire. Rehabilitation techniques like the application of carbon fiber-reinforced polymer fabrics may improve the post-fire reduction in mechanical properties. Moreover, employing novel composite or hybrid materials as other innovative rehabilitation techniques, may enhance the performance of concrete exposed to extreme temperatures.

References

[1] American Concrete Institute (ACI). Code requirements for determining fire resistance of concrete and masonry construction assemblies (ACI 216.1-07/TMS-0216-07). Farmington Hills (MI): ACI; 2019.
[2] American Concrete Institute (ACI). Building code requirements for reinforced concrete and commentary (ACI 318). Farmington Hills (MI): ACI; 2025.
[3] European Committee for Standardization. EN 1991-1-2: Actions on structures - Part 1-2: General actions - Actions on structures exposed to fire (Eurocode 1). Brussels: CEN; 2024.
[4] Abdul-Hameed AH, Mansi SA, Hassan MS. Factors affecting compatibility between (S.B.R) polymer repair materials and concrete substrate. Eng Technol J. 2010;28(14):4853-65. https://doi.org/10.30684/etj.28.14.14
[5] European Committee for Standardization. EN 1992-1-2: Design of concrete structures - Part 1-2: General rules - Structural fire design (Eurocode 2). Brussels: CEN; 2004.
[6] Kodur V. Properties of concrete at elevated temperatures. ISRN Civ Eng. 2014;2014:468510. https://doi.org/10.1155/2014/468510
[7] Purkiss JA. Fire safety engineering design of structures. Oxford: Butterworth-Heinemann, Elsevier; 2007. https://doi.org/10.1201/b12845
[8] Kodur VR, Raut N. Performance of concrete structures under fire hazard: Emerging trends. Indian Concr J. 2010;84(2):23-31.
[9] ASTM International. ASTM E119-08b: Standard test methods for fire tests of building construction and materials. West Conshohocken (PA): ASTM; 2024.
[10] Khoury GA, Majorana CE, Pesavento F, Schrefler BA. Modelling of heated concrete. Mag Concr Res. 2002;54(2):77-101. https://doi.org/10.1680/macr.2002.54.2.77
[11] Poon CS, Shui ZH, Lam L. Compressive behaviour of fiber reinforced high-performance concrete subjected to elevated temperatures. Cem Concr Res. 2004;34:2215-22. https://doi.org/10.1016/j.cemconres.2004.02.011
[12] Hertz KD, Sørensen LS. Test method for spalling of fire exposed concrete. Fire Saf J. 2005;40(5):466-76. https://doi.org/10.1016/j.firesaf.2005.04.001
[13] Fernandes B, Masiero Gil A, Longhi Bolina F, Fonseca Tutikian B. Thermal damage evaluation of full-scale concrete columns exposed to high temperatures using SEM and XRD. Dyna. 2018;85(207):123-8. https://doi.org/10.15446/dyna.v85n207.70593

[14] Mansi AS. Bond strength assessment for different types of repair materials. Eng Technol J. 2010;28(21):6325-36. https://doi.org/10.30684/etj.28.21.10
[15] Mansi AS, Abdulhameed HA, Yong YK. Development of low-shrinkage rapid set composite and simulation of shrinkage cracking in concrete patch repair. In: Proc Int Conf Transportation and Development 2018; 2018 Jul; Reston (VA). Reston (VA): ASCE; 2018. p. 215-26. https://doi.org/10.1061/9780784481554.022
[16] Alhasanat MB, Al Qadi AN, Al Khashman OA, Dahamsheh A. SEM evaluation of self-compacting concrete spalling at elevated temperatures. Am J Eng Appl Sci. 2016;9(1):119-27. https://doi.org/10.3844/ajeassp.2016.119.127
[17] Kang WL. Application of SEM and XRD in the microstructure analysis of fiber-reinforced concrete corroded by salt solution. Adv Res. 2024;25(6):336-42. https://doi.org/10.9734/air/2024/v25i61207
[18] Balakrishnaiah D, Balaji KVGD, Srinivasa RP. Application of SEM method to investigate the effect of elevated temperatures on compressive strength of ternary blended concrete. ARPN J Eng Appl Sci. 2017;12(7):2029-36.
[19] Yuzer N, Akoz F, Ozturk LD. Compressive strength-colour change relation in mortars at high temperature. Cem Concr Res. 2004;34:1803-7. https://doi.org/10.1016/j.cemconres.2004.01.015
[20] Li G, Feng L, Zheng S. Investigation on the properties of concrete and its composites after exposure to high temperature. Sichuan Build Sci. 1991;2:1-5. Chinese.
[21] Hu H, Dong Y. Experimental research on strength and deformation of high-strength concrete at elevated temperature. China Civ Eng J. 2002;35:44-7. Chinese.
[22] Bamonte P, Gambarova PG. Mechanical properties of self-compacting concrete at high temperature and after cooling. Mater Struct. 2012;45(9):1375-87. https://doi.org/10.1617/s11527-012-9839-9
[23] Huo JS, He YM, Xiao LP, Chen BS. Experimental study on dynamic behaviours of concrete after exposure to high temperatures up to 700°C. Mater Struct. 2013;46:255-65. https://doi.org/10.1617/s11527-012-9899-x
[24] Ma Q, Guo R, Zhao Z, Lin Z, He K. Mechanical properties of concrete at high temperature: A review. Constr Build Mater. 2015;93:371-83. https://doi.org/10.1016/j.conbuildmat.2015.05.131
[25] Al-Sulayfani JB, Al-Taee HT. Modeling of stress-strain relationship for fibrous concrete under cyclic loads. Eng Technol J. 2008;26(1):45-54. https://doi.org/10.30684/etj.26.1.4
[26] Annerel E, Taerwe L. Revealing the temperature history in concrete after fire exposure by microscopic analysis. Cem Concr Res. 2009;39(12):1239-49. https://doi.org/10.1016/j.cemconres.2009.08.017
[27] Amiri M, Aryanpour M, Porhonar F. Microstructural study of concrete performance after exposure to elevated temperatures considering C-S-H nanostructure changes. High Temp Mater Process. 2022;41(1):224-37. https://doi.org/10.1515/htmp-2022-0030
[28] Farage MCR, Sercombe J, Gallé C. Rehydration and microstructure of cement paste after heating up to 300 °C. Cem Concr Res. 2003;33:1047-56. https://doi.org/10.1016/S0008-8846(03)00005-X
[29] Lin RS, Han Y, Wang XY. Macro-meso-micro experimental studies of LC3 paste subjected to elevated temperature. Cem Concr Compos. 2021;116:103871. https://doi.org/10.1016/j.cemconcomp.2020.103871
[30] Albeer SJ, Hassan MS. Microstructure and strength of nanosilica- and microsilica-enhanced mortars under elevated temperatures. Arab J Sci Eng. 2024;49(4):5565-77. https://doi.org/10.1007/s13369-023-08430-3
[31] Hassan MS, Al-Azawi ZM, Taher MJ. Complementary effect of heat treatment and steel fibers on properties of high-performance concrete. Arab J Sci Eng. 2016;41(10):3969-81. https://doi.org/10.1007/s13369-016-2056-z
[32] Traoré K, Kabré TS, Blanchart P. Gehlenite and anorthite crystallisation from kaolinite and calcite mix. Ceram Int. 2003;29:377-83. https://doi.org/10.1016/S0272-8842(02)00148-7
[33] Alani S, Hassan MS, Jaber AA, Ali IM. Effects of elevated temperatures on mortar containing nano-calcined montmorillonite clay. Constr Build Mater. 2020;263:120895. https://doi.org/10.1016/j.conbuildmat.2020.120895
[34] Mussa MH, Hason MM, Abdulhameed HA. Fire simulation of RC slab inclusion with nano-silica and high-volume fly ash. In: AIP Conf Proc. 2022 Nov;2660(1). https://doi.org/10.1063/5.0109533
[35] Thanaraj DP, Kiran T, Kanagaraj B, Nammalvar A, Andrushia AD, Gurupatham BGA, et al. Influence of heating-cooling regime on engineering properties of structural concrete. Buildings. 2023;13(2):295. https://doi.org/10.3390/buildings13020295
[36] Cheng FP, Kodur VKR, Wang TC. Stress-strain curves for high-strength concrete at elevated temperatures. J Mater Civ Eng. 2004;16(1):84-90. https://doi.org/10.1061/(ASCE)0899-1561(2004)16:1(84)
[37] Soroushian P, Won JP, Hassan M. Sustainable processing of cellulose fiber cement composites. ACI Mater J. 2013;110(3). https://doi.org/10.14359/51685664

Research on Engineering Structures & Materials
www.jresm.org

Research Article

Evaluation of runways for Al-Habbaniya air base in Iraq

Mustafa Imad Ahmed [*,a], Alaa H. Abed [b]

Civil Engineering Department, AL- Nahrain University, Baghdad, Iraq

Article Info

Article History:

Received 14 Oct 2025

Accepted 11 Nov 2025

Keywords:

Runway pavement evaluation;
Asphalt pavement distresses;
Dynamic cone penetrometer

Abstract

This study investigates both the concrete and asphalt runway sections to assess their mechanical and chemical deterioration. Defects and material degradation affected the asphalt and concrete layers, overall safety and performance of the airbase runway pavement structure evaluation. Al-Habbaniya Air Base is located in Al-Anbar Governorate, approximately 74 km west of Baghdad, near the Euphrates River and Habbaniya Lake. Several recent studies [1] highlighted the effect of sulfate attack and moisture susceptibility on airfield pavements under hot climates. Several layers of extensive field and laboratory tests, core sample testing, compressive strength checks, and Dynamic Cone Penetrometer (DCP) illustrated issues including blowups, cracking, moisture damage, and chemical-induced deterioration. The subgrade soil had high sulfate and gypsum content, further accelerating the deterioration, which poses a significant risk to the durability of the pavement. This study in Al-Habbaniya Air Base describes the primary defects presented, the effect of both chemical and mechanical properties on structural stability, and the measures needed to comply with ASTM standards. These findings emphasize the importance of prevention, better material selection, and redesign to secure the functionality of a runway in extremely hostile environmental and operating conditions. Core sampling revealed significant loss of strength in concrete (≈ 12–29 MPa) and noticeable moisture damage in asphalt layers.

© 2026 MIM Research Group. All rights reserved.

1. Introduction

One key component of the airport infrastructure is the structural integrity of the runways, which is vital for safety and can be compromised over time by stress and environmental factors during service life. Several major causes of runway failure as identified in the literature include heavy and repetitive loads, high temperature, and aging related to deterioration. In this study, the evaluation focuses on identifying major distress types, understanding their causes, and proposing rehabilitation strategies specific to Al-Habbaniya Air Base. This study aims to evaluate the structural and material performance of Al-Habbaniya Air Base runways under harsh sulfate-rich and hot climatic conditions. The scope of the work includes field investigations, laboratory testing, and correlation of chemical composition with mechanical deterioration. The novelty of this research lies in integrating field DCP–CBR data with chemical analysis to understand sulfate-induced degradation mechanisms in Iraqi airbase pavements. Several international studies [1,2], [3] have examined runway evaluation and sulfate-induced deterioration in hot climates. However, limited research has focused on Iraqi airbases where high sulfate and gypsum contents coexist with extreme temperatures. This study fills this gap by integrating field and laboratory data to evaluate the combined effects of chemical and mechanical deterioration on runway performance and propose sustainable rehabilitation measures.

*Corresponding author: st.mustafa.A.A.J@nahrainuniv.edu.iq
[a]orcid.org/0009-0000-8982-8856; [b]orcid.org/0000-0002-6569-4598
DOI: http://dx.doi.org/10.17515/resm2025-1262ic1014rs
Res. Eng. Struct. Mat. Vol. 12 Iss. 2 (2026) 943-955

1.1 Effects of Aircraft Loads on Runway Performance

While heavy aircraft can exert an amount of load on a runway pavement that exceeds its design capacity, the pavements are designed to resist controlled and predictable high value stresses, particularly during the aircraft takeoff and landing phases. These overloads lead to surface/dynamic cracking, reflective cracking, and might even fail in the subgrade layers [4]. Permanent deformation takes place under repeated application of loads in restricted locations such as touchdown zones, which weakens the pavement structure over time [5]. Moreover, the gradual pressures on the wheels characteristics of the landings introduce additional horizontal stresses that contribute to surface wear and compromise the structure [6].

1.2 Effects of Thermal on Runway Material

High temperature is also another important factor that impacts the runway performance. Thermal stress induced by thermal expansion, particularly in asphalt pavements, can result in serious tension that can cause cracking and shrinkage when this surface cools down [7]. Prolonged exposure to high temperatures softens asphalt and increases the risk of permanent deformations and ruts created by concentrated loads. Subgrade and base layers can lose strength due to high temperatures which can affect their contribution to load sharing and in some cases total runway durability.

1.3 Aging and Long-Term Material Degradation

Environmental factors, such as ultraviolet (UV) radiation, and moisture ingress, cause the natural deterioration of runways materials over time. These conditions aggravate asphalt brittleness and concrete pavement surface erosion [9]. Over time, the accumulated fatigue stress caused by cyclical loading results in the formation and expansion of microcracks, compromising the structural integrity of the pavement [8]. This problem is further exacerbated due to poor maintenance, as minor defects once ignored or overlooked can lead to high prevalence of structural and functional failures, causing the functional life of the runway to greatly reduce [11]. Airbase runways are important infrastructures that can withstand heavy loads over time, extreme weather, and high traffic. However, with aging, environmental factors, and operational stress, these pavements suffer significant wear and tear over time. The study concentrates on the structural evaluation of runway pavements, where critical defects in asphalt and concrete layers were highlighted and the potential factors contributing to them were investigated. It was found that the concrete pavements had severe distresses including blowups, punchouts, and corner breaks, generally caused by thermal expansion (especially from the top), overloading, and lack of support condition [11]. These tests on core samples (Concrete and asphalt layers thickness varies from 0.28 to 0.3 m according to Table 4) showed that compressive strength of the concrete had failed throughout the structure, indicating material degradation and mix design issues. Likewise, asphalt pavements were observed for surface irregularities, aging, oxidation, and moisture damage as well as functional and structural conditions leading to premature distress and/or early failure [9].

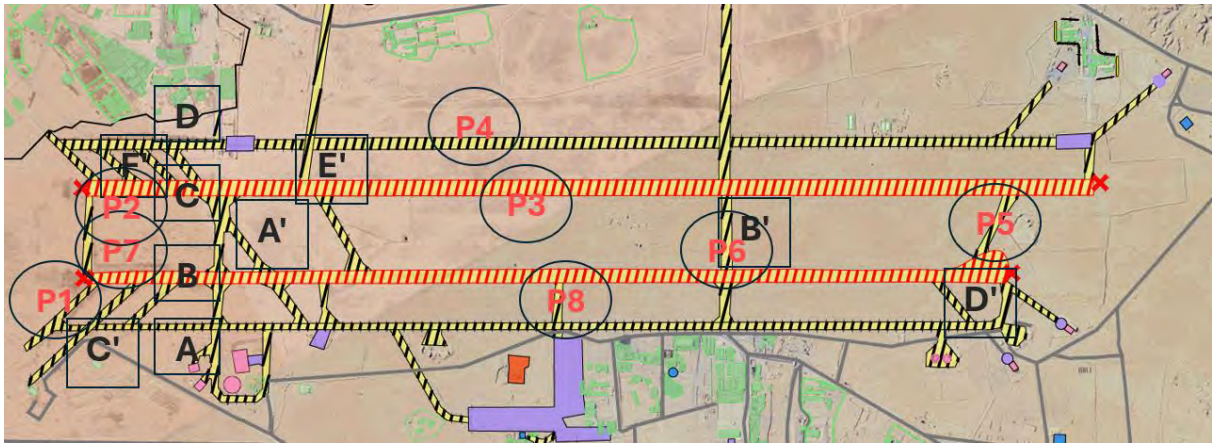

Fig. 1. Site plan of Habbaniya air base

This study intended to clearly document these defects and assess their effect on runway performance, as well as to provide remediation strategies to meet the industry standard and prolong the service life of the pavements. Al-Habbanyia Air is located in Al-Anbar Province, approximately 74 km west of Baghdad, near the Euphrates River and Habbaniyah Lake, which has two runways (North runway is 4 km length composite of concrete and asphalt, south runway one is 3.7 km length composite of concrete and asphalt), see Figure 1. Also, the main aims of this study are to document these defects exhaustively, evaluate their influence on the performance of the affected runways, and recommend remedial methods and techniques to maintain the pavements within the industry-engineering and serviceability standards, and extend their service life.

2. Methodology

2.1 Pavement Evaluation

Although the main experimental procedures were described, additional details were included to improve transparency and reproducibility. Sampling points were selected based on observed surface distresses along both runways and taxiways. Each test type (CBR, DCP, compressive strength, and moisture susceptibility) was performed in triplicate, and the average values with standard deviations were reported. All tests followed ASTM and FAA standards, including ASTM D1883 for CBR, ASTM D4867 for moisture damage, ASTM C42 for concrete cores, and ASTM D6951 for DCP testing.

A series of tests were conducted to assess the condition of the asphalt and concrete layers:

- Material Sampling: Extraction and laboratory analysis of core samples.
- Dynamic Cone Penetrometer (DCP) Tests: Evaluated the subgrade's strength.
- Moisture Damage Analysis: Assessed the impact of water infiltration according to Table (2).

2.2 Runway Distresses

During the evaluation of the runway, several defects and signs of distress were identified in the asphalt and concrete layer. These findings are critical in understanding the extent of the damage [11].

2.3 Asphalt Pavements Distresses

The evaluation revealed significant distress in the asphalt layers, including alligator or fatigue cracking, characterized by interconnected cracks resembling alligator skin caused by repeated traffic loading. These cracks, originating from the bottom layer and extending to the surface, often require reconstruction in severe cases [11]. Block cracking, another common defect, is primarily caused by asphalt shrinkage and temperature fluctuations, resulting in rectangular patterns unrelated to traffic loads but varying in severity. Corrugation, or wash boarding, was identified as closely spaced ridges and valleys perpendicular to traffic direction, caused by unstable pavement or subbase layers. Reconstruction is necessary to meet ASTM standards, Figure 2.

Fig. 2. Asphalt pavements distresses

Longitudinal and transverse cracks, indicative of sub-structural concerns, were noted. Potential longitudinal cracks are appearing along the direction of the pavements which are connected to bad quality in construction or material deterioration, while transverse cracks where emerged induced by temperature stress. Other repairs, like patching and utility cut patching, are all noted as defects,

since they generally show roughness and will deteriorate much faster than the original pavement, which has an impact on ride quality. Traffic wear results in polished aggregate, creating a smooth surface that decreases skid resistance and decreases vehicle traction, Figure 3.

Fig. 3. Problems of asphalt runways

Swelling, identified by upward bulges in the pavement, is caused by swelling soil, leading to surface deformation and cracking. Lastly, raveling and weathering were prevalent, with surface degradation attributed to asphalt aging, poor-quality mixtures, or environmental factors like oil spills, resulting in the loss of aggregate particles and compromised pavement performance, Figure 4.

Fig. 4. Soil and weather problems

2.4 Concrete Pavement Distresses

The evaluation of concrete pavements at the runway revealed several significant defects [12]. Instances of blowup or buckling were observed, particularly during hot weather, caused by insufficient expansion space due to incompressible materials infiltrating joints. This results in upward slab movement and deformation, requiring immediate intervention. Divided slabs were another common defect, where slabs fractured into multiple pieces due to overloading or inadequate support. Repairs ranged from sealing cracks to full slab replacement. Faulting was identified across several joints, characterized by elevation differences between slabs, caused by foundation settlement or erosion. Slabs with significant elevation differences require recasting, Figure 5.

Fig. 5. Concrete pavement distresses

- Linear cracking in the form of longitudinal, transverse, and diagonal cracks was observed, often caused by repeated loads, thermal gradients, and moisture. Low-severity cracks posed minimal risks, but medium-to-high severity cracks were structurally significant.

- Large patches and utility cut repairs exceeding 5 square feet were found, often deteriorating faster than original pavement. Severe cases require recasting to meet ASTM standards.
- Punchouts, or localized slab fragmentations were common near cracks and joints, often resulting from repeated heavy loads and insufficient slab thickness. These necessitate recasting, Figure 6.

Linear cracking | Large patches | Punchouts

Fig. 6. Types of cracks and patches in runway slab

Corner spalling was identified as deterioration near slab corners due to stress and material degradation. Partial-depth patching was recommended for minor cases. Similarly, joint spalling, occurring along slab edges, was caused by traffic stresses, material infiltration, with repairs ranging from patching to joint reconstruction. Lastly, vegetation growth in cracks indicated possible water infiltration and soil salinity issues, suggesting inadequate drainage and potential structural instability. Comprehensive repairs and preventive measures are recommended to mitigate these distresses, Figure 7.

Corner spalling | Joint spalling | Vegetation growth

Fig.7. Stress and material

3. Extraction and Laboratory Analysis of Core Samples

3.1 Asphalt Core Sampling

These tests are essential for evaluating the structural integrity and quality of the pavement [13]. The data provides insights into the core samples' condition, helping us assess whether the pavement meets the required standards, in regarding the asphalt, 18 cores were extracted from the main runways, taxiways, and branch runways as shown in Figure 8.

Core sampling | Asphalt test | Compressive

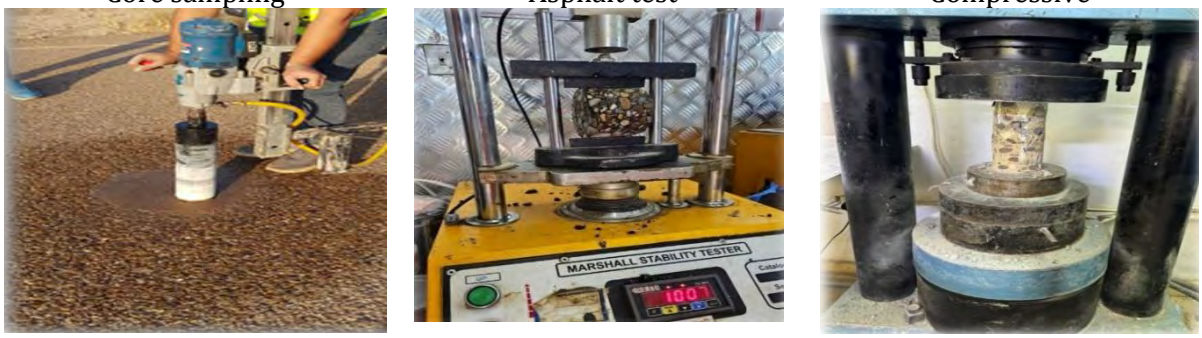

Fig. 8. Sampling and tests

Table 1. Number, types and the stability of layers for the asphalt pavement

Location		No. of layers	Type of each layer	Thickness of each layer (cm)	Stability (kN)
Taxiway 1 (A)	A1	1	Surface	5.5	6.72*
		2	Binder	9.2	6.43*
		3	Base	14.8	5.22
	A2	1	Surface	6.1	8.43
		2	Binder	6.2	6.10*
		3	Base	13.5	5.29
	A4	1	Surface	10	7.90*
		2	Base	8.5	5.23
	A5	1	Surface	7	6.88*
		2	Base	7.6	4.56*
	A6	1	Surface	8	8.14
		2	Base	7	3.22*
	A7	1	Surface	7.2	8.45
		2	Base	7.9	4.33*
	A8	1	Surface	8.8	8.34
		2	Base	7.4	5.41*
Runway 1 (B)	B3	1	Surface	6.7	3.22*
		2	Binder	7.6	3.98*
		3	Base	11.5	2.87*
	B4	1	Surface	5.5	4.45*
		2	Binder	8	5.76*
		3	Base	6.7	4.84*
	B5	1	Surface	14.1	5.37*
		2	Base	15.4	3.67*
	B6	1	Surface	10.8	6.90*
		2	Base	10.4	5.42
	B7	1	Surface	11.1	8.12
		2	Binder	4.5	7.11
		3	Base	3.8	4.17*
	B8	1	Surface	7	6.43*
		2	Binder	10	7.56
		3	Base	15.3	5.64
Runway 2 (C)	C5	1	Surface	4.5	7.09*
		2	Binder	7.6	7.15
		3	Base	9.3	5.45
	C6	1	Surface	11.5	5.65*
		2	Binder	9.5	5.28*
		3	Base	8.2	2.43*
Intersections (Branch Runways)	Ć	1	Surface	10.2	8.11
		2	Binder	10	6.21
		3	Base	10.7	5.32
	É	1	Surface	7.1	7.25*
		2	Binder	7.8	7.98
		3	Base	14.1	5.80
	Ŕ	1	Surface	5	6.56*
		2	Base	11.5	4.43*

The core samples taken from the runway were subjected to compressive strength tests, and the results indicated significant failures as shown in Table 1. Most of the cores did not meet the required standards for compressive strength, with additional failures observed in stability and moisture content. These issues highlight critical concerns regarding the material quality and

overall structural integrity of the runway. The results of analysis of pavement layers, Figure 9 and the effect of moisture damage in asphalt pavement is given in Table 2.

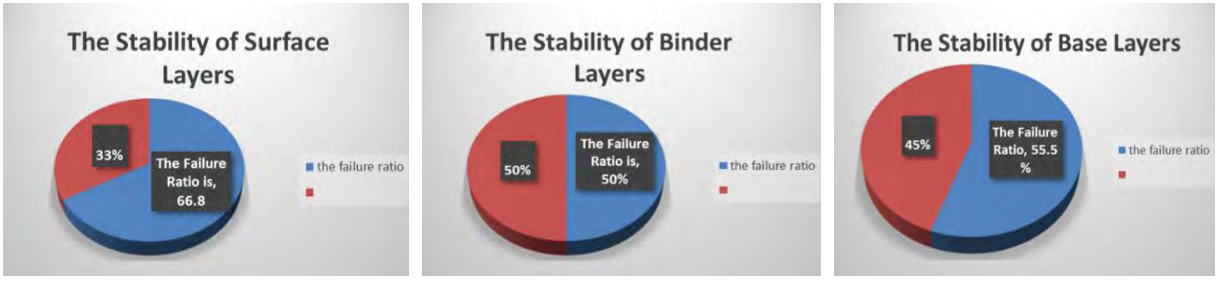

Fig. 9. Charts explain the types of layers failure ratio

Table 2. The effect of moisture damage in asphalt pavement according to ASTM D4867/D4867M

Location	Moisture damage, %	Specification limits
Taxiway 1 (A)		
A1	80	
A2	68*	
A4	76*	
A5	82	
A6	81	
A7	54*	
A8	61*	
Runway 1 (B)		
B3	66*	MIN. (80%)
B4	54*	
B5	80	
B6	81	
B7	63*	
B8	64*	
Runway 2 (C)		
C5	81	
B4	70*	
Intersections		
Ć	81	
É	80	
Ŕ	74*	

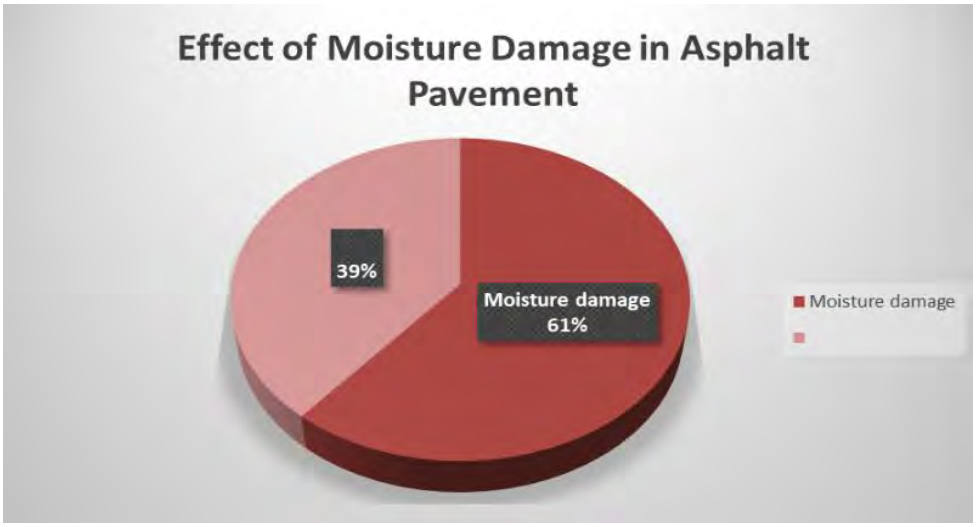

Fig. 10. The effect of moisture damage in asphalt pavement

3.2 Concrete Core Sampling

In regarding the concrete, 12 cores were extracted from the main runways, taxiways, and branch runways. Concrete core sampling test was conducted as well, it involved extracting cylindrical samples to analyze the material composition and condition and for further laboratory analysis to assess material quality and perform the necessary physical and chemical laboratory test, Figure 11 [14]. The compressive strength results shown in Table (3), which range from 11.95 MPa to 29.01 MPa, indicate that most of the samples do not meet the required standards for concrete used in runway construction. The majority of the values fall below the acceptable threshold, suggesting that the concrete is generally weak.

Fig. 11. Cores are being tested

Table 3. Data collected of the concrete core samples

Specimen No.	Area of Sample (mm^2)	L/D	Correction Factor	Compressive strength (MPa)	Modified comp. strength for L/D ratio	Equivalent modified comp. strength of cube	Corrected factor for bars	Final compression strength (MPa)
1	7850	1.25	0.9328	21.15	19.73	29.01	1	29.01
2	7850	1.25	0.9328	10.74	10.02	14.73	1.13	16.65
3	7850	2	1	14.61	14.61	21.49	1.13	24.28
4	7850	1.4	0.9511	9.90	9.41	13.84	1	13.84
5	7850	1.2	0.9269	19.11	17.71	26.05	1	26.05
6	7850	2	1	18.06	18.06	26.56	1	26.56
7	7850	2	1	14.60	14.60	21.47	1	21.47
8	7850	2	1	13.15	13.15	19.33	1	19.33
9	7850	2	1	16.31	16.31	23.98	1	23.98
10	7850	1.42	0.9522	8.54	8.13	11.95	1	11.95
11	7850	1.5	0.9615	13.80	13.27	19.51	1	19.51
12	7850	2	1	19.40	19.40	28.53	1	28.53

3.3 Dynamic Cone Penetration Report (DCP) and Sawed Concrete Cores Results

The Dynamic Cone Penetrometer (DCP) (shown as schematics in Figure 12) consists of two 16-mm (5/8-inch) diameter shafts coupled near midpoint. The lower shaft contains an anvil and a pointed tip which is driven into the soil by dropping a sliding hammer contained on the upper shaft onto the anvil. The underlying soil strength is determined by measuring the penetration of the lower shaft into the soil after each hammer drop. The layers of investigated site are shown in Table 4 and the coordinates of 8 points locations are given in Table 5.

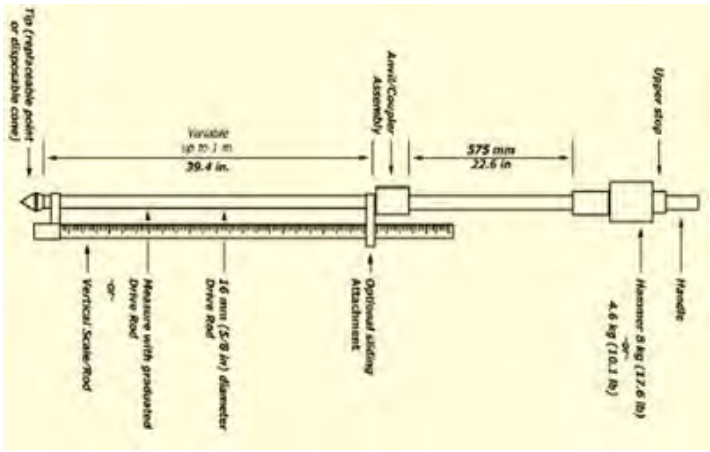

Fig. 12. Dynamic cone penetration

Table 4. Pavement explored profile specified by field works inspection and testing

Pavement	Level (m)	Symbol
Concrete or asphaltic layer	0.28~0.3	
Sub-base	~0.4	
Light brown to yellowish medium clayey silt soil filling layer	~0.85	

Table 5. Locations and title for each point (8 points) with date of field work

No.	Location	Coordination	Date of testing
1	P1	33°19'55.70"N 43°37'4.20"E	10/8/2024
2	P2	33°19'52.20"N 43°36'54.90"E	10/8/2024
3	P3	33°20'7.90"N 43°35'55.60"E	10/8/2024
4	P4	33°20'0.00"N 43°35'58.20"E	10/8/2024
5	P5	33°20'44.00"N 43°34'53.10"E	10/8/2024
6	P6	33°20'28.10"N 43°35'28.20"E	10/8/2024
7	P7	33°19'56.00"N 43°36'55.30"E	10/8/2024
8	P8	33°20'27.30"N 43°35'57.90"E	10/8/2024

4. Equations and Results Computation

Natural soil below subbase layer with respect to lab tests was coarse sand with gravely and fine soil with (9~10%) sulphate content (SO3) and (20-19%) gypseous content as shown in Table 6. From the most collected data water table not recognized through (0.85 m) but from CBR values were noted according to the soil consistency at the site figures below summarized field and laboratory tests result.

Laboratory results showed high sulfate (≈2%) and gypsum (≈18–20%) contents in subgrade soils. These cause sulfate-induced expansion in concrete and salt-related degradation in asphalt. DCP and CBR values decreased sharply after wetting, confirming that apparent strength was governed by soluble salts.

$$CBR = 292/DCP^{1.12} \quad (1)$$

$$CBR = 1/(0.017019 \times DCP)^2 \quad (2)$$

$$CBR = 1/(0.002871 \times DCP) \quad (3)$$

$$\log CBR = 2.628 - 1.273 \log (DCP) \quad (4)$$

$$q_u\ (kPa) = 65 \times (CBR - 1.5) \quad (5)$$

$$q_u\ (kPa) = 113 \times (CBR - 12.5) \quad (6)$$

$$q_u\ (kPa) = 172.6 \times (CBR) - 601 \quad (7)$$

$$k_s\ (kPa/m) = 40 \times q_u\ (kPa) \quad (8)$$

Table 6. Soil type content results

Soil type	Water-Soluble Sulfate SO_4^{2-} (% by mass)	Gypsum,%
Subbase (P2)	2.35	19.995
Subbase (P5)	2.47	19.82
Clayey Soil with Sand	2.33	18.748

4.1 Detailed DCP Results

There were many notes and observations can be drawn after reviewing all collected data come from field shown in Table 7.

- Unsaturated primarily granular soils in which a loose state is maintained by apparent cohesion, cohesion due to clays at the intergranular contacts or cohesion associated with the accumulation of soluble salts as a binder therefore CBR records with high CBR values were due to high soluble salt levels which are indicative of cementing agents in the subgrade layer. However, when the subgrade layer is moistened by water, the CBR values will be reduced to (20-18%).
- Based on the previous airbase evaluation, the Water-Soluble Sulfate (SO_4^{2-}) concentration for all soil samples exceeded 2% by mass. According to ASTM C1580-15 [18] guidelines, this indicates a high sulfate content in the soil, which is associated with very severe sulfate exposure. Such high levels of sulfate in the soil pose significant risks for concrete structures, as they increase the likelihood of sulfate attack, leading to potential deterioration, expansion, and cracking in the concrete.
- The recoded data for top subbase layer based on Ks values gave that soil medium to dense granular soils this classification for the samples within natural moisture content, during the excavation works and site observations for sulphate content the water was added then the Ks decreased dramatically.
- The CBR values also altering with wide range and it value like Ks reduced after adding water which indicated that apparent strength was caused by water soluble salts

4.2 High Levels of Sulfate and Gypsum Detected in Soil Samples

The laboratory analysis detected elevated levels of sulfate, classified as S3 grade according to ASTM C1580-15 [19]. This classification indicates very severe sulfate exposure, with levels exceeding acceptable limits. High concentrations of sulfate and gypsum can significantly compromise the durability and stability of both concrete and asphalt pavements. Sulfates can induce expansive reactions in concrete, leading to substantial deterioration and serious structural issues. The presence of gypsum may exacerbate these reactions, potentially causing severe damage to the pavement system.

Table 7.CBR results

Point / Type	Asphalt/Concrete layer thickness (m)	Clayey sand with gravel (m)	Test depth (cm)	CBR-1	Ks (kPa/m)	Results in MPa	Results in Psi
1/Asphalt	0.3	0.5	51.2	85.3114	145273.1	145.2	21070.08
2/Concrete	0.35	0.61	60.9	44.1674	73956.83	73.9	10726.53
3/Concrete	0.34	0.61	61.3	87.3224	146227.2	146.2	21208.46
4/Concrete	26.7	0.59	59.6	69.55431	117960.8	117.9	17108.76
5/Concrete	22.5	0.57	57.1	65.46742	110876.9	110.8	16081.33
6/Concrete	0.28	0.46	46	92.16496	157152.6	157.1	22793.05
7/Concrete	33.7	0.82	82	48.14337	104541.5	104.5	15162.46
8/Concrete	35.7	0.65	65	90.14436	153442.6	153.4	22254.96

5. Discussion

These existing preliminary evaluations and tests of Al-Habbaniya Air Base runway pavements show critical conditions of these pavements that may affect their structural integrity, durability, and function of this infrastructure [20,21]. A Few Key Findings from Field and Laboratory Tests. The results clearly show that high sulfate (≈2%) and gypsum (≈18–20%) contents in the subgrade accelerate pavement degradation. These salts cause expansion and loss of cohesion in the subbase, leading to cracking and reduced bearing capacity. The decrease in CBR values and compressive strength corresponds directly with increased sulfate concentration, confirming a cause-and-effect relationship between chemical attack and mechanical weakening. Figures 9–11 illustrate this correlation, highlighting that chemical deterioration significantly governs the structural performance of both asphalt and concrete layers.

5.1 Subgrade Soil Composition and Its Impacts

- Sulfate attack: Below the runways, high sulfate content soil was experienced, reaching over 2 masses %, classified as a very severe sulfate exposure, as indicated in ASTM C1580-15 [19]. This significantly increases the probability of sulfate-induced expansive reactions that can cause cracking, strength loss, and degradation of asphalt and concrete layers.
- High levels of gypsum: Elevated gypsum concentrations (18 to 20%) increase structural instability risk. In dry conditions these salts work as cementing agents, but when dissolved due to moisture, they lower soil cohesion and reduce subgrade strength.
- Moisture deficiency: Dynamic Cone Penetrometer (DCP) and California Bearing Ratio (CBR) tests show lower apparent strength when saturated. Initially, there were high CBR values due to soluble salts, which reduced drastically with the persistence of water.

5.2 Asphalt Pavement Deficiencies

- Crack types: Structural and environmental distress can be inferred from fatigue cracking, block cracking, and longitudinal/transverse cracks These include defects due to fatigue loading, material wear, thermal cycles, among others.
- Moisture: The moisture susceptibility tests show severe damage in most places, further, some locations are less than the acceptable limit (≥ 80%).
- Surface deterioration: Raveling, weathering, and polished aggregates are common, adversely affecting skid resistance and surface durability.

5.3 Concrete Pavement Deficiencies

- Sulfate attack: Concrete core samples reveal compressive strengths ranging from 11.95 MPa to 29.01 MPa, with most values falling below the threshold for adequate runway performance. The high sulfate environment is a significant factor in reducing durability and causing spalling and cracking.
- Structural failures: Punchouts, corner spalling, and joint faulting reflect foundational weaknesses and material incompatibilities under load.

5.4 Drainage and Environmental Factors

To mitigate these environmental and chemical hazards, the use of resilient materials, efficient drainage systems, and proper construction techniques is essential. The wide variation in compressive strength (≈12–29 MPa) is mainly attributed to sulfate-induced expansion and microcracking, which weaken the cement matrix and reduce cohesion between aggregates. Similar degradation patterns were reported by Wang [1] for sulfate-rich soils in hot climates. These results highlight that pavement design in such environments must incorporate sulfate-resistant materials, proper drainage, and stabilized subbase layers to minimize expansion and strength loss under wet–dry cycles.

- Inadequate drainage: Water infiltration into the subgrade layers is a major concern. Poor drainage exacerbates sulfate-related damage and accelerates the weakening of the pavement structure.
- Thermal stresses: Temperature fluctuations and extreme heat cause expansion and contraction in the pavement layers, contributing to blowups in concrete and cracking in asphalt.

6. Conclusion

In order to address the issues appeared in the evaluation requires, a multifaceted approach involving soil stabilization, material upgrades, structural improvements, and enhanced drainage systems., Al-Habbaniya Air Base runways can be achieving improved durability, according with engineering standards, and extended service life, ensuring safe and reliable operations under Iraq's challenging environmental conditions. The researcher recommends reconstructing the runways according to the test results. The objectives outlined in the introduction have been achieved through a combined evaluation of field and laboratory results. The study confirmed that sulfate and gypsum concentrations exceeding 2% and 18–20%, respectively, are key factors causing loss of strength and durability in both asphalt and concrete layers. These findings highlight the need for sulfate-resistant materials and improved drainage systems for future runway rehabilitation.

References

[1] Lamtiar S, Zhabri Gaffari Darmawan M, Endrawijaya I, Kurniawan A, Hidayat Z. Airport Pavement Condition Index Evaluation of Runway 12/30 at Budiarto Airport Indonesia. Airman: Jurnal Teknik dan Keselamatan Transportasi. 2024;7(1):49–60. https://doi.org/10.46509/ajtk.v7i1.452
[2] Jabbour AM, Al-Obaidi MS, Hameed T. Influence of sulfate and moisture on airfield pavement subgrades in arid regions. Civ Eng J. 2022;8(9):1915-29.
[3] Wang Q, Zhong K, Sun M. Dynamic response analysis of airport pavement under impact loading. Appl Sci. 2023;13(9):5723. https://doi.org/10.3390/app13095723
[4] Khan MI, Asylam ME, Sutanto MH, Widyatmoko I. Simulating the impact of extreme aircraft loading on the performance of bituminous pavement for airport application. AIP Conf Proc. 2024;2838(1). https://doi.org/10.1063/5.0199528
[5] Ali S, Liu X, Fawzia S, Thambiratnam D. Numerical study on the feasibility of flexible runway pavement to resist impact loading. In: ACMSM25: Proceedings of the 25th Australasian Conference on Mechanics of Structures and Materials. Singapore: Springer; 2020. p. 615-21. https://doi.org/10.1007/978-981-13-7603-0_60
[6] Meng Q, Zhong K, Sun M. Dynamic response analysis of airport pavement under impact loading. Appl Sci. 2023;13(9):5723. https://doi.org/10.3390/app13095723
[7] Al-Qadi IL, Hassan MM, Elseifi MA. Field and theoretical evaluation of thermal fatigue cracking in flexible pavements. Transp Res Rec. 2005;1919(1):87-95. https://doi.org/10.1177/0361198105191900110
[8] Zaabar I, Chatti K. Estimating vehicle operating costs caused by pavement surface conditions. Transp Res Rec. 2014;2455(1):63-76. https://doi.org/10.3141/2455-08
[9] Yu J, Tsai BW, Zhang X, Monismith C. Development of asphalt pavement fatigue cracking prediction model based on loading mode transfer function. Road Mater Pavement Des. 2012;13(3):501-17. https://doi.org/10.1080/14680629.2012.695240
[10] El-Hakim MY, Tighe SL. Sustainability of perpetual pavement designs: Canadian perspective. Transp Res Rec. 2012;2304(1):10-6. https://doi.org/10.3141/2304-02

[10] Saputra PD, Fansuri MH, Laksmi AA. Development of Work Breakdown Structure (WBS) for Rapid Damage Runway Repair (RADARR) Time Planning at Military Airbases. E3S Web Conf. 2024;517:05002. https://doi.org/10.1051/e3sconf/202451705002
[11] ASTM International. ASTM D6433-18A. Standard Practice for Roads and Parking Lots Pavement Condition Index Surveys. West Conshohocken (PA): ASTM International; 2018.
[12] White G. State of the art: Asphalt for airport pavement surfacing. Int J Pavement Res Technol. 2018;11(1):77-98. https://doi.org/10.1016/j.ijprt.2017.07.00
[13] ASTM International. ASTM C42/C42M-11. Standard Test Method for Obtaining and Testing Drilled Cores and Sawed Beams of Concrete. West Conshohocken (PA): ASTM International; 2011.
[14] ASTM International. ASTM D6951/D6951M-09. Standard Test Method for Use of the Dynamic Cone Penetrometer in Shallow Pavement Applications. West Conshohocken (PA): ASTM International; 2015.
[15] Zumrawi MM, Elnour H. Predicting bearing strength characteristics from soil index properties. Int J Civ Eng Technol. 2016;7(2):266-77.
[16] Razouki SS, Kuttah DK, Al-Damluji OA, Nashat IH. Strong correlation between the bearing capacity and CBR of a gypsiferous subgrade soil subjected to long-term soaking. In: Proceedings of the International Conferences on the Bearing Capacity of Roads, Railways and Airfields; 2005.
[17] Bowles JE, Guo Y. Foundation analysis and design. New York: McGraw-Hill; 1996.
[18] ASTM International. ASTM C1580-15. Standard Test Method for Water-Soluble Sulfate in Soil. West Conshohocken (PA): ASTM International; 2015.
[19] ASTM International. ASTM D4867/D4867M. Standard Test Method for Effect of Moisture on Asphalt Concrete Paving Mixtures. West Conshohocken (PA): ASTM International; 2009.
[20] Karkush MO, Kareem MS, Jawad S, Babu S. Sustainability analysis of improvement of contaminated clayey soil using lime piles technique. AIP Conf Proc. 2024;2864(1). https://doi.org/10.1063/5.0186092
[21] Karkush MO, Yassin SA. Using sustainable material in improvement the geotechnical properties of soft clayey soil. J Eng Sci Technol. 2020;15(4):2208-22.

Blank Page

Research on Engineering Structures & Materials
www.jresm.org

Research Article

Study and analysis of vibration and mechanical characteristics of PVC-carbon fiber-graphene nanocomposite pipes designed for oil and gas applications

Salah Khudhur Mohammad [*,a]

Ministry of Oil, Midland Refineries Company, Baghdad, Iraq

Article Info

Article History:

Received 14 Oct 2025

Accepted 05 Dec 2025

Keywords:

Graphene;
Mechanical properties;
The natural frequencies;
Gas oil;
Nanocomposite pipe

Abstract

This paper presents an innovative plastic injection molding technique for producing polyvinyl chloride/carbon fiber/graphene nanocomposite pipes. It includes calculating the natural frequencies and vibration properties of the composite pipe under various flow velocities of (Gas oil) fluid with a density of 0.822 g/cm^3. The mechanical performance of the fabricated composite nano pipes is evaluated using three tests: axial tensile, axial compression stress, and ultimate strain. Young's modulus varies, ranging between 40 GPa and 120 GPa depending on the composite metal's percentage of polyvinyl chloride/ carbon fiber/ graphene. Mathematical results using MATLAB demonstrate that the reprocessed PVC/CF/Gr composites demonstrated superior mechanical performance relative to (FEM) predictions in the Ansys software workbench 21.0 package. Specifically, a 170% increase in Young's modulus and a 140% increase in ultimate tensile strength were observed at 2 wt% graphene. Due to the bonding between the fibers and the polymer matrix, the highest difference in the fundamental natural frequency between the theoretical and numerical results was found to be 8.18%, at a speed of 2 m/s.

© 2026 MIM Research Group. All rights reserved.

1. Introduction

1.1. Describing the New Technique and Objective

This article examines the study and analysis of fiber-reinforced nanocomposite pipes. A series of tests was conducted to evaluate their mechanical and vibrational properties, including axial tension, transverse compression, and axial compression, in order to assess their effects on the ultimate tensile strength and Young's modulus of the nanocomposite pipes. Since high tensile strength is a crucial requirement for oil and gas pipelines, the study focuses on enhancing the mechanical durability of these pipes so they can withstand the stress levels typically endured by steel pipes used in such applications. This is achieved by analyzing the fundamental natural frequencies of the pipes and their vibrational behavior during fluid flow at various flow velocities.

Nanomaterials have emerged as a transformative advancement in modern materials science, owing to their exceptional mechanical, thermal, and chemical properties. Among these, polymer-based nanocomposites have attracted significant attention due to their versatile performance, ease of fabrication, and cost-effectiveness. Nanocomposite pipes exhibit high mechanical strength, excellent thermal stability, and notable defect tolerance, rendering them highly suitable for oil and gas transportation systems, while also offering economic advantages. Furthermore, nanocomposite coatings have been demonstrated to provide effective corrosion protection in harsh operational environments within the oil and gas industry [1].

*Corresponding author: 200saaa200@gmail.com
[a]orcid.org/0009-0001-6887-7322
DOI: http://dx.doi.org/10.17515/resm2025-1263ic1014rs

Reinforcement materials such as titanium dioxide, zinc oxide, carbon nanotubes (CNTs), and graphene (Gr) are widely employed due to their superior mechanical and thermal characteristics. Pohasem et al. reported significant improvements in corrosion resistance through the incorporation of steel–epoxy–graphene composites [2,3]. Pipelines are inherently subjected to internal and external stresses induced by fluid flow, which may lead to structural degradation or failure. Consequently, dynamic analysis is critical to ensure operational reliability and structural integrity. Modeling approaches typically rely on vibration velocity data to quantify reductions in structural stiffness, with S.M. Shankaraachhar and colleagues developing a comprehensive mathematical framework to investigate the vibration behavior and stability of fluid-conveying pipelines [4,5]. Recent studies have further demonstrated the effectiveness of nanocomposites in corrosion and thermal protection.

TabkhPaz et al. showed that double-layer coatings of steel, reinforced with graphene, CNTs, and zinc particles, significantly enhance corrosion resistance [6]. Similarly, Yu et al. reported that polystyrene/graphene nanocomposites provide excellent resistance against both corrosion and heat [7]. Liu et al. investigated single-layer graphene coatings on epoxy primers, identifying 2 wt% graphene as an optimal ratio for cathodic protection, which improved the corrosion resistance of polystyrene from 37.9% to 99.53% and increased thermal resistance by 24.8% [8,9]. Samsudin et al. examined the thermal and mechanical properties of thermoset polyethylene/graphite nanocomposites, noting that a graphite content of 0.1 wt% increases crystallinity by 15% [10]. The thermal properties of epoxy composites reinforced with carbon fibers were further enhanced by adding 0.3 wt% graphene oxide, which doubled the storage modulus of the composites [11]. Karsli et al. demonstrated that surface treatment of CNTs improves the mechanical and electrical properties of polypropylene/short glass fiber composites [12,13], while Prusty et al. confirmed that the inclusion of glass fibers and CNTs enhances elasticity and the modulus of elasticity [14].

Despite these advancements, aggregation of nanomaterials remains a key challenge in nanocomposite fabrication. Patel et al. investigated the effect of increasing CNT content in epoxy/fiberglass composites, finding that concentrations up to 1 wt% improve tensile and flexural strength, whereas higher contents lead to aggregation that adversely affects mechanical properties [15,16]. The method of Nano filler incorporation further affects composite properties. Brandenburg et al. compared melt mixing and solution mixing in polyethylene composites and found that CNTs are more uniformly dispersed in nanocomposites prepared via melt mixing [17]. Aldajah and Haik employed a magnetic field to align CNTs in carbon fiber-reinforced composites, resulting in increases in flexural stiffness by 33% and 15%, respectively [18]. Saad et al. developed polyvinyl chloride (PVC)-based composites using various yarns and nanofillers to enhance PVC properties [19]. Nawaz et al. reported that incorporating 1.5 wt% nanofiller via an ordered mixing technique increased the modulus of elasticity by 62% and improved plastic quality by 20% [20,21]. Xiao et al. investigated PVC/graphene composites with graphene concentrations ranging from 1% to 9%, finding homogeneous dispersion at 1–5 wt% and explored higher graphene content in a polyvinyl chloride matrix and reported a 115% improvement in tensile strength at 5 wt% graphene concentrations. However, using high concentrations of graphene is not economically viable. Furthermore, graphene's tendency to agglomerate at higher wt% concentrations degrade the quality of the resulting nanocomposite, making it unsuitable for industrial applications [22].

Blending and recycling strategies also play a role in enhancing composite performance. Kuram et al. studied PBT/PC blends reinforced with recycled glass fibers and observed improved mechanical properties compared to virgin PBT/PC blends [23]. Kadam and Mhaske reported that three-cycle material recovery in nylon 6/talc nanocomposites increased tensile strength by 36.7% and tensile modulus by 169.7% during the extrusion cycle [24]. Collectively, these studies highlight the significant potential of nanomaterials to enhance the mechanical, thermal, and corrosion resistance properties of polymer-based composites, coatings, and pipeline systems. The performance of these materials is strongly influenced by several key factors, including the type and concentration of nanofillers, dispersion techniques, surface modification, and recycling strategies. Nevertheless, challenges such as nanomaterial agglomeration, long-term stability under operational loading, and the optimization of composite formulations remain critical areas requiring further investigation.

Given that high tensile strength is a fundamental requirement for oil and gas pipelines, this study focuses on enhancing the mechanical integrity of composite pipes to achieve strength levels comparable to those of conventional steel pipelines. Although this investigation was confined to small-diameter pipes, the findings provide promising evidence supporting the potential industrial adoption of composite pipes and their gradual replacement of traditional materials in oil and gas pipeline systems.

In this study, the addition of only 2 wt% graphene led to significant improvements in Young's modulus and tensile strength, by 170% and 140%, respectively. These results demonstrate the considerable potential for achieving substantial mechanical enhancements with relatively low graphene concentrations, highlighting their promise for industrial applications of composite nanotubes. This approach effectively leverages graphene's capacity to enhance the mechanical performance of nanocomposites. The findings further indicate that increasing the graphene content to 2 wt% improves the pipe's stiffness, with the most pronounced gains occurring at lower weight percentages, followed by a decline at higher percentages. Additionally, the maximum transverse load capacity of the nanocomposite pipes was evaluated for specimens showing pipe diameter displacements exceeding 5%, revealing that the pipe's ability to withstand transverse loads peaked at 2 wt% graphene. However, due to the weak adhesion between the fibers and the polymer matrix, fracture surfaces often revealed gaps around the fibers. These gaps led to stress concentration within the nanocomposite. By reinforcing the polymer matrix with graphene, this adhesion was significantly improved, filling the gaps and reducing stress concentration. Consequently, load transfer from the matrix to the fibers became more efficient. In contrast, the fibers detached from the matrix due to the weak load transfer, as they were torn and separated at the fracture surfaces.

2. The Analytical and Numerical Approach

2.1 Mathematical Modeling of Pipe

The equations of motion for the system are derived using the Euler–Bernoulli beam theory and subsequently solved to determine the fundamental natural frequency. This approach enables the analysis of free vibrations of a fluid-conveying reinforced pipe, under the assumptions of incompressible fluid flow and negligible effects of damping and gravity. The method is considered comprehensive, as it explicitly incorporates the pipe's stiffness characteristics into the dynamic model, providing a more accurate representation of its vibrational behavior.

2.2 Free Vibration

The Euler–Bernoulli equation governing a pipe conveying an incompressible fluid and subjected to an external force F_0, for pipes composed of PVC/CF/Gr, provides an accurate simulation of the free vibration behavior of fluid-conveying pipes with uniform cross-sections. The governing equation for such a pipe system is expressed as follows [25]:

$$\frac{d^2}{dx^2}\,EI\,\frac{d^2w}{dx^2} + 2mfV\frac{d^2w}{dxdt} + mf\frac{dv}{dt}\frac{dw}{dx} + (pA + mfV^2)\frac{d^2w}{dx^2} + (mf + mp)\frac{d^2w}{dt^2} = F_o \tag{1}$$

For the uniform cross-section area, the equation of pipe becomes,

$$EI\frac{d^4w}{dx^4} + 2mfV\frac{d^2w}{dxdt} + mf\frac{dv}{dt}\frac{dw}{dx} + (pA + mfV^2)\frac{d^2w}{dx^2} + (mf + mp)\frac{d^2w}{dt^2} = F_o \tag{2}$$

2.3 General Solution

Equation (2) describes the natural frequency of the composite nanotube as a function of the spatial coordinate x, capturing the variation of vibrational characteristics along the length of the pipe.

$$Y(T,X) = \sum_{j=1}^{4} Cje^{i\Omega T}e^{ij\lambda X} \tag{3}$$

Where: $\Omega = L\omega\sqrt{\frac{(mf+mp)}{EI}}$, $Y = \frac{pL^2A}{EI}$ $B = \sqrt[2]{\frac{mf}{mf+mp}}$, $U = VL\sqrt[2]{\frac{mf}{EI}}$

Subs. Eq. (3) into Eq. (2):

$$\lambda^4 - (Y + U^2)\lambda^2 - 2UB\Omega\lambda - \Omega^2 = 0 \quad (4)$$

Eq. (4) has four roots are:

$$\lambda_{1,2} = (-a \pm ib)1 = -\frac{1}{2}\sqrt{\alpha} \pm \frac{i}{2}\sqrt{\frac{4UB\Omega}{\sqrt{\alpha}} + \alpha - 2K} \quad (5)$$

$$\lambda_{3,4} = (a \pm b2) = \frac{1}{2}\sqrt{\alpha} \pm \frac{1}{2} \quad (6)$$

Where; $K = Y + U^2$, $\alpha = \frac{0.42S_1}{S_2} + 0.265S_2 + \frac{2}{3}K$, $S_1 = K^2 - 12\Omega^2$, $S_2 = (S + \sqrt{S^2 - 4S_1^3})^{0.333}$, $a = \frac{1}{2}\sqrt{\alpha}$, $b_1 = \frac{1}{2}\sqrt{\frac{4UB\Omega}{\sqrt{\alpha}} - 2K + \alpha}$, $b_2 = \frac{1}{2}\sqrt{\frac{4UB\Omega}{\sqrt{\alpha}} + 2K - \alpha}$

By analyzing the roots of Equation (4) and applying both algebraic and geometric simplifications, the resulting expression can be reduced to the following form:

$$W(T,X) = \left[H_1 e^{i(-a+ib_1)X} + H_2 e^{i(-a-ib_1)X} + H_3 e^{i(a+ib_2)X} + H_4 e^{i(a-ib_2)X}\right] e^{i\Omega T} \quad (7)$$

$$W(T,X) = \left[(H_1 e^{-b_1 X} + H_2 e^{b_1 X})e^{-iaX} + (H_3 e^{b_2 X} + H_4 e^{-b_2 X})e^{iaX}\right] e^{i\Omega T} \quad (8)$$

$$\sinh b_1 X = e^{-b_1 X}, \quad \cosh b_1 X = e^{b_1 X}, \quad \sin b_2 X = e^{b_2 X}, \quad \cos b_2 X = e^{-b_2 X}$$

Where; $A=H_1$ $B=H_2$ $D=H_3$ $E=H_3$

The solution for the vibration equation of a fluid-conveying pipe under conservative conditions is given by:

$$W(T,X) = \left[(A \sinh b_1 X + B \cosh b_1 X)e^{-iaX} + (D \sin b_2 X + E \cos b_2 X)e^{iaX}\right] e^{i\Omega T} \quad (9)$$

2.4 Solve the pipe Equation Motion

This section presents the derivation of Equation (9) to determine the natural frequency and the corresponding system response. The analysis incorporates the application of boundary conditions for a simply supported pipe, as illustrated in Figure 1. The initial conditions for the system can be expressed as follows:

$$w(x,0) = 0 \text{ (The pipe deflection)} \quad (10)$$

$$\frac{dw(x,0)}{dt} = 0 \text{ (The pipe moment)} \quad (11)$$

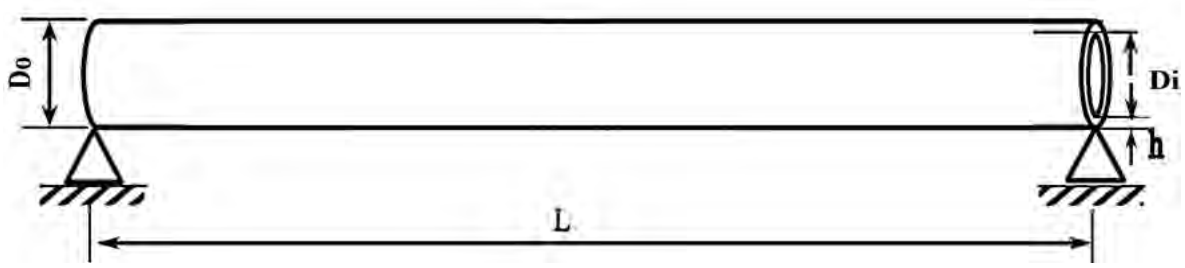

Fig. 1. The nanocomposite pipe

Simply supported B.C.S. at

- x =0 and x =L, w (0, t) = 0
- w (L, t) =0,

- $EI\ \frac{d^2\,w(t,x)}{dx^2} - M_P = 0$
- $EI\ \frac{d^3\,w(t,x)}{dx^3} - V_P = 0$

Where M_P (prescribed moment) and V_P (shear forces). The amplitude response of the pipe as a function of x can be obtained as follows:

$$W(X) = A\left(\left(sinh\, b_1X - \frac{S_1}{S_2} cosh\, b_1X\right) e^{-iaX} + (\frac{b_1}{b_2}\frac{2ia}{b_2} sin\, b_2X - \frac{S_1}{S_2} cos\, b_2X)e^{iaX}\right) \quad (12)$$

Assume:

- $S_3 = (\frac{S_1}{S_2}\frac{b_2}{ia} - \frac{b_1}{b_2})$
- At X=L

$$0= ((S_4 \sinh b_1\mathrm{L} + S_5 \cosh b_1\mathrm{L})\, e^{-ia\mathrm{L}} + (S_6 \sin b_2 l + S_7 \cos b_2 l)e^{ia\mathrm{L}}) \quad (13)$$

- $S_1 = (e^{-iaL}\, sinh\, b_1L - \frac{b_1}{b_2} e^{iaL}\, sin\, b_2L)$
- $S_2 = (e^{-iaL}\, cosh\, b_1L - e^{iaL}\, cos\, b_2L + \frac{b_2}{ia} e^{iaL}\, sin\, b_2L)$
- $S_3 = \left(\frac{S_1}{S_2}\frac{b_2}{ia} - \frac{b_1}{b_2}\right)$
- $S_4 = b_1^2 - a^2 - 2iab_1\frac{S_1}{S_2}$
- $S_5 = \frac{S_1}{S_2} b_1^2 - a^2\frac{S_1}{S_2} - 2iab_1$
- $S_6 = 2\frac{S_1}{S_2} b_2 ia - S_3 b_2^2 - a^2 S_3$
- $S_7 = 2iaS_3b_2 + \frac{S_1}{S_2} b_2^2 + a^2\frac{S_1}{S_2}$
- $\dot{w(X)} = A((\left(\frac{S_1}{S_2} b_1 - ia\right) sinh\, b_1\, X + \left(b_1 - ia\frac{S_1}{S_2}\right) cosh\, b_1X)\, e^{-iaX} + \left(\left(\frac{S_1}{S_2} b_2 + iaS_3\right) sin\, b_2X + (S_3b_2 - ia\frac{S_1}{S_2}\right) cos\, b_2X)e^{iaX}))$
- $\ddot{W(X)} = A((S_4\, sinh\, b_1X + S_5\, cosh\, b_1X)\, e^{-iaX} + (S_6\, sin\, b_2X + S_7\, cos\, b_2X)e^{iaX})$

2.5 Fluid Discharge Velocity

For a simply supported pipe, the natural frequency and corresponding fluid flow rate can be expressed as follows [26]:

$$\omega = \frac{\pi^2}{L^2}\sqrt{\frac{IE}{M_t}} \quad (14)$$

The mass per unit length of the composite pipe and the conveyed fluid is expressed as follows:

$$M_t = \rho_f \frac{\pi}{4} D_i^2 + \rho\frac{\pi}{4}\,(D_o^2 - D_i^2) \quad (15)$$

$$V = \frac{\pi}{L}\sqrt{\frac{IE}{\rho_f A}} \quad (16)$$

Equation (16), E represents the Young's modulus of the pipe material, I denote the moment of inertia, L is the length of the nanocomposite pipe, ρf corresponds to the density of the flowing fluid, and A indicates the cross-sectional area of the nanocomposite pipe.

2.6 Solve Pipe Axial tensile stress

The axial stress (σa) in a pipe can be derived from fundamental principles of mechanics. Consider a pipe with outer radius ro , inner radius ri , length L, and an applied axial force P. The derivation proceeds step by step as follows:

$$\boldsymbol{\sigma}_{axial} = \frac{Axial\ Force}{Cross\ sectional\ Area, A} \tag{17}$$

Where; $A = \pi(r_0^2 - r_i^2)$

This equation indicates that the axial stress in a pipe subjected to an axial force is directly proportional to the applied force and inversely proportional to the annular cross-sectional area.

$$\boldsymbol{\sigma}_{axial} = \frac{P}{\pi(r_0^2 - r_i^2)} \tag{18}$$

2.7 Solve The Ultimate Tensile Strain of Pipe

The ultimate tensile strain corresponds to the material's ultimate tensile strength (UTS) prior to failure. Strain is defined as the rate of elongation relative to the original length, and the axial strain (ε) is expressed as follows:

$$\varepsilon = \frac{\Delta L}{L} \tag{19}$$

where: ε = axial strain, L = original length of the pipe.

$$\sigma_u = \frac{P_u}{\pi(r_0^2 - r_i^2)} \tag{20}$$

At ultimate tensile strength, the axial stress reaches its maximum value. Here, P_u represents the ultimate tensile load. Within the elastic region, stress and strain are related according to Hooke's law:

$$\sigma = E_\varepsilon \tag{21}$$

where: E = Young's modulus (modulus of elasticity). At the point of ultimate tensile stress: $\sigma_u = E_{\varepsilon_u}$. Thus, substituting: $\varepsilon_u = \frac{\sigma_u}{E}$ $\sigma_u = \frac{P_u}{\pi(r_0^2 - r_i^2)}$

$$\varepsilon_u = \frac{P_u}{E\pi(r_0^2 - r_i^2)} \tag{22}$$

Table 1. Nomenclatures

Symbol	Meaning	Units
A	Pipe cross-section area	cm^2
b_1, b_2	General solution parameters	-
K	General solution parameter	-
L_c	Crack length	cm
Do	Pipe outer diameter	cm
Di	Pipe inner diameter	cm
h	Thickness of pipe	cm
Dc	The depth of the Crack	mm
E	Elastic modulus	N/m^2
$\boldsymbol{F_o}$	External force	N/m
I	The second moment of the area	m^4
L	Pipe length	cm
M	Bending moment	N.m
mp	Mass of pipe per unit length	Kg/m
mf	Fluid mass per unit length	Kg/m
M_t	Mass per unit length of the pipe and fluid	Kg/m
p	Internal pressure	N/m^2
V_P	Shear forces	N/m^2

$\boldsymbol{M_P}$	Prescribed moment	N.m
A,B,C,D	Constants	
$\boldsymbol{S_i}$	Roots of equations	
V	Velocity of fluid	m/sec
x	The position along the pipe.	m
x_c	The crack position.	m
X	Dimensionless coordinate	-
y	Lateral coordinate	-
Y	Dimensionless coordinate	-
W	Amplitude of response	mm
Re	Reynold Number	-

Table 2. The Greek symbols

Symbol	Meaning	Units
α	Parameter	-
ω	fundamental natural frequency	Rad/sec
Ω	Dimensionless fundamental natural frequency	-
ρ	Density of pipe	kg/m^3
ρf	Fluid density	kg/m^3
$\lambda_{1,2}$	Roots of a polynomial equation	-

2.8 Numerical Solution

The numerical study comprises two main investigations. The first aims to evaluate the effect of fluid flow velocity on the vibration characteristics and natural frequency of the pipe. The second investigates the influence of axial tensile stress and ultimate tensile strain on pipe behavior. Fluid mechanics principles were applied under varying flow conditions to analyze the relationship between natural frequencies and system response, considering flow velocities of 1 m/s (Re = 13,500) and 2 m/s (Re = 27,000). The analysis was conducted for a pipe composed of a PVC/CF/Gr blend, as illustrated in Figure 2.

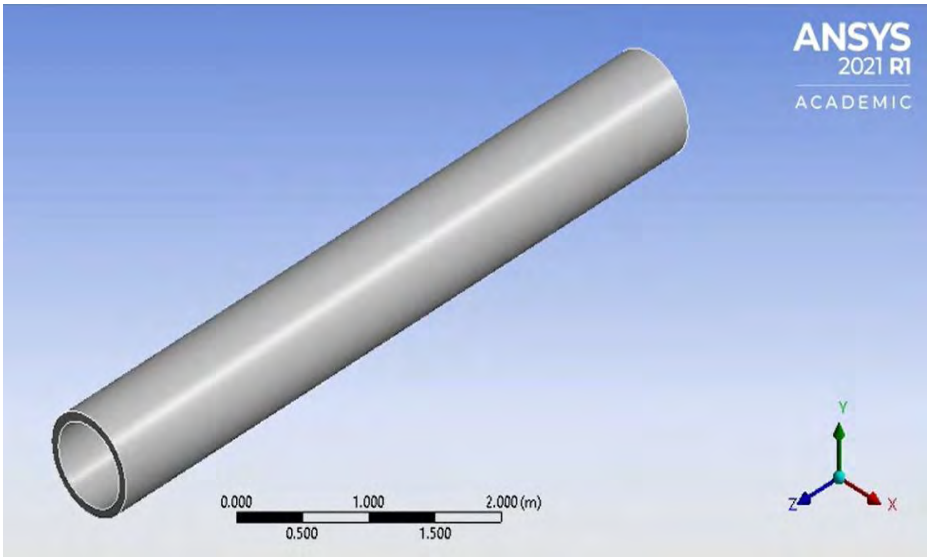

Fig. 2. Model of the composite pipe

In this study, the computational domain consists of a 100 cm-long pipe with inner and outer diameters of 4 cm and 6 cm, respectively. The materials used for pipe fabrication are summarized in Table 3. Numerical analysis was conducted using a finite element model (FEM) with a hexagonal mesh, implemented in ANSYS Workbench 21.0. The pipe was automatically meshed with a size of

0.9 mm, resulting in 26,588 elements and 215,629 nodes, as shown in Figure 3. Table **3**. Dimensions and properties of the pipe material.

Mechanical	Test value
Pipe material density	polyvinyl chloride/carbon fiber/graphene
Pipe density	----
Ultimate strength	251- 670 (MPa)
Ultimate elongation	(0.8 - 1.2) %
Pipe modulus of elasticity	(PVC/CF/Gr)
Pipe length (cm)	100 (cm)
Outer and inner diameters (cm)	6 (cm) and 4 (cm)
Fluid flow	Gas oil
Fluid density	0.822 (g/cm^3)

The numerical simulations included the calculation of the natural frequency of the composite pipe as well as the effects of fluid flow. Flow velocities of 1, 2, and 3 m/s were considered to investigate their influence on the dynamic behavior of the pipe. The numerical approach allows for a detailed assessment of the pipe's vibrational characteristics and the effects of fluid flow parameters and structural deformations [27].

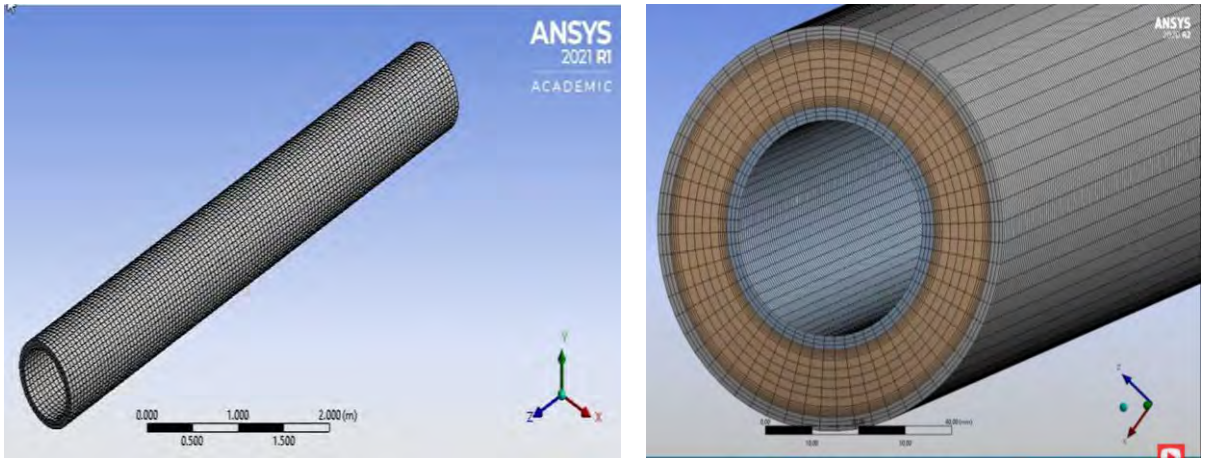

Fig. 3. The meshing of composite pipe installation

3. Results and Discussion

Table 4 presents the effect of fluid flow velocity on the natural frequency of a simply supported pipe at velocities of 1, 2, and 3 m/s. In addition to considering the material properties of the pipe and characteristics of the fluid flow, these effects were evaluated using both numerical and theoretical approaches and the results were systematically compared.

Table **4**. PVC/CF/Gr pipe natural frequency.

Fluid Velocity (m/s)	Analytical (Hz)	Numerical (Hz)	Discrepancy (%)
1	1287.4	1191.5	7.44
2	1173.3	1077.3	8.18
3	1058.5	980.5	7.36

Non-uniform flow distribution within the pipe induces internal pressure fluctuations, which in turn increase the pipe's vibrational response. Consequently, the natural frequencies of the pipe decrease as the fluid flow velocity varies. For instance, the fundamental frequency of a composite pipe is approximately 1287.4 Hz at a flow velocity of 1 m/s. When the velocity increases to 2 m/s, the frequency decreases by about 15%, reaching approximately 1173.3 Hz. These results demonstrate that higher flow velocities reduce the effective stiffness of the pipe structure. Figures 4, 5, and 6

illustrate the corresponding decrease in the fundamental natural frequency, as observed in both numerical and theoretical analyses.

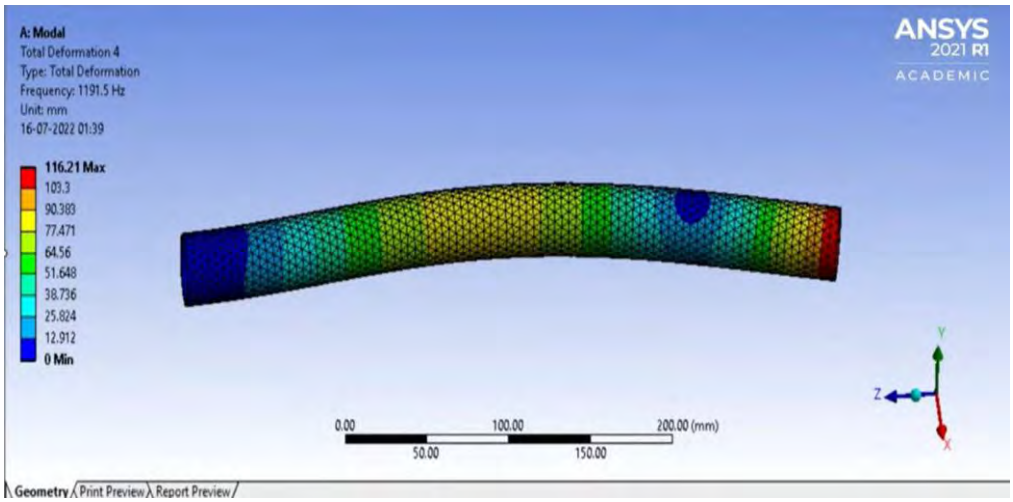

Fig. 4. PVC/CF/Gr pipe natural frequency and deflection

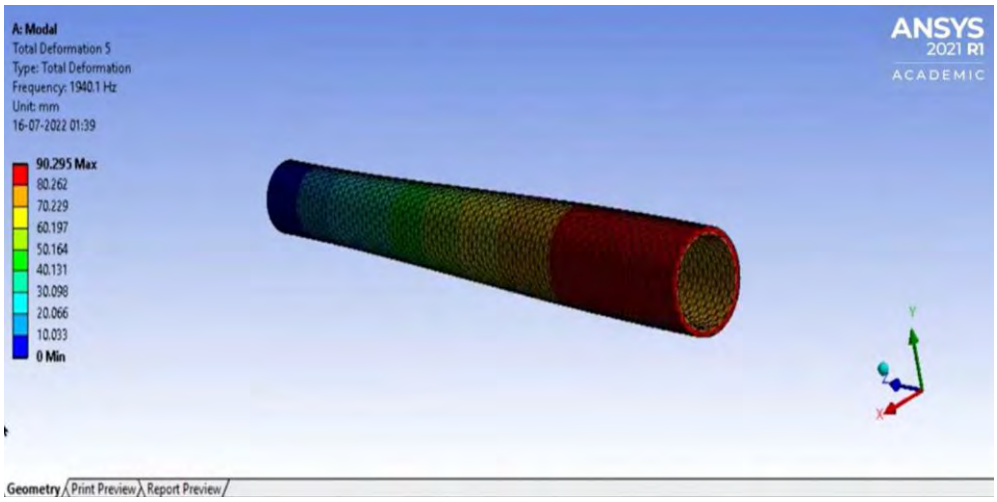

Fig. 5. PVC/CF/Gr pipe second mode shape (mm)

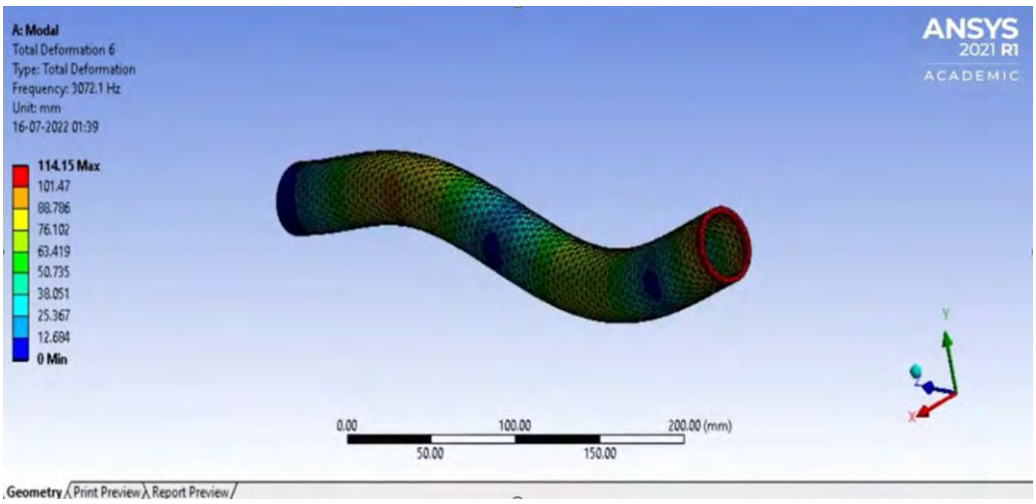

Fig. 6. PVC/CF/Gr pipe third mode shape (mm)

The results presented in Figures 7, 8, and 9 indicate that both Young's modulus and the ultimate tensile strength (UTS) of the pipe vary with the weight fraction of graphene (Gr). However, after two processing cycles, these improvements plateaued and remained relatively stable. The increase

in Young's modulus and ultimate tensile strength for the PVC/CF/Gr nanocomposite ranged from 7.7% to 19.5%. The maximum tensile strength achieved was 670.3 MPa for PVC/CF pipes containing 2 wt% graphene, demonstrating that increasing the graphene content enhances the mechanical properties. For comparison, an API version a pipe exhibited UTS of 330 MPa, while the PVC/CF composite without graphene showed a tensile strength of 251.9 MPa (Table 5), representing a significant improvement over high-grade API steel pipes and demonstrating their potential for pipeline applications in the oil and gas industry.

Tables 6and 7 further show that incorporating 2 wt% graphene significantly increased the stiffness of the pipe. The maximum allowable compressive strength of the pipes for various applications was also evaluated, with results indicating a peak at 2 wt. % graphene. These findings confirm that an optimal graphene content of 2% by weight provides the best enhancement in both tensile and compressive mechanical properties for the PVC/CF/Gr composite pipes.

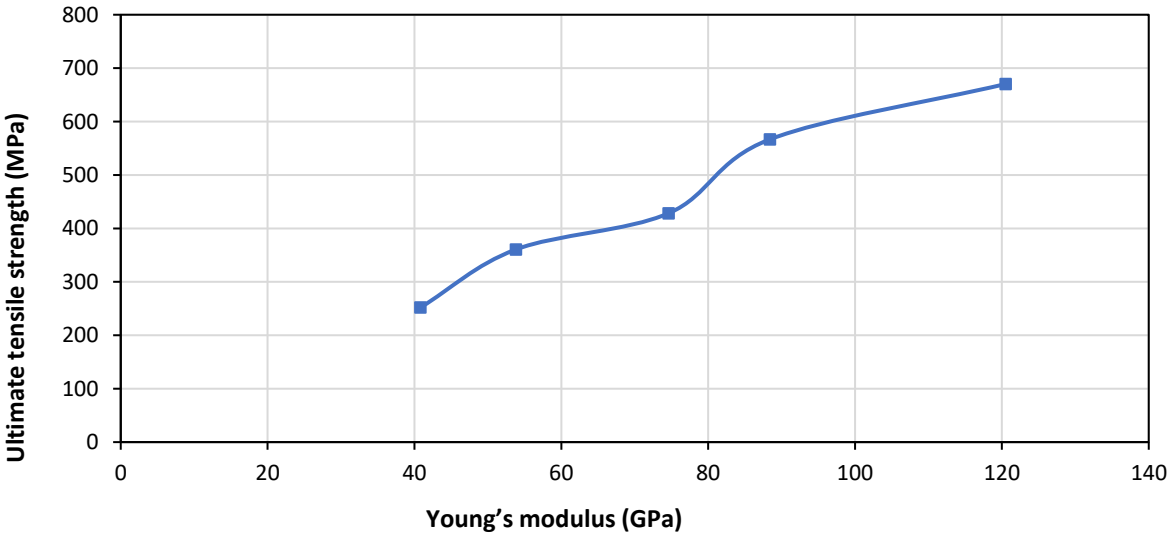

Fig. 7. The relationship between Young's modulus and Ultimate tensile strength for a composite pipe, PVC/CF/Gr

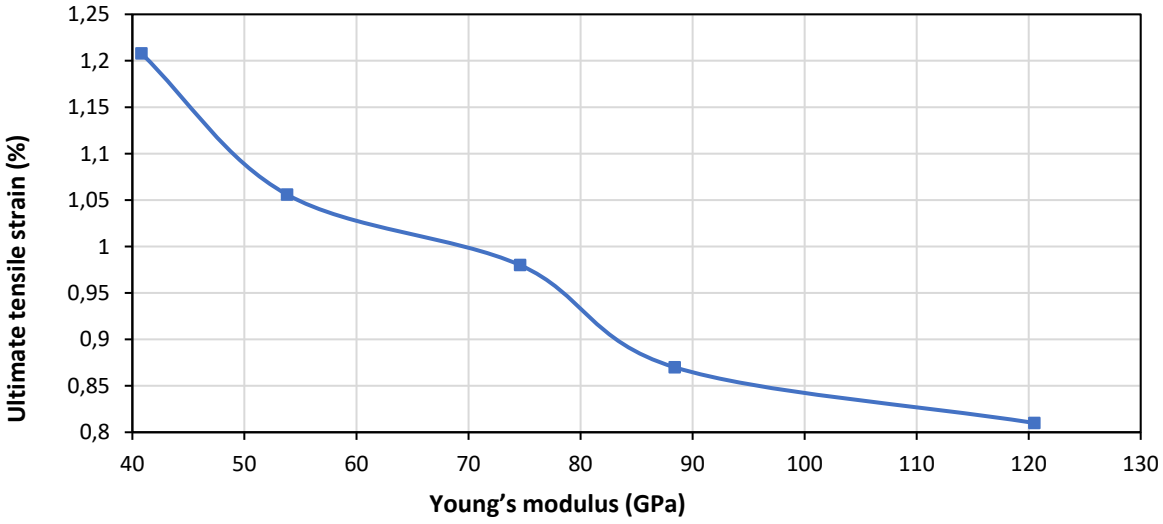

Fig. 8. The correlation between Young's modulus and the Ultimate tensile strain of the PVC/F/Gr composite pipe

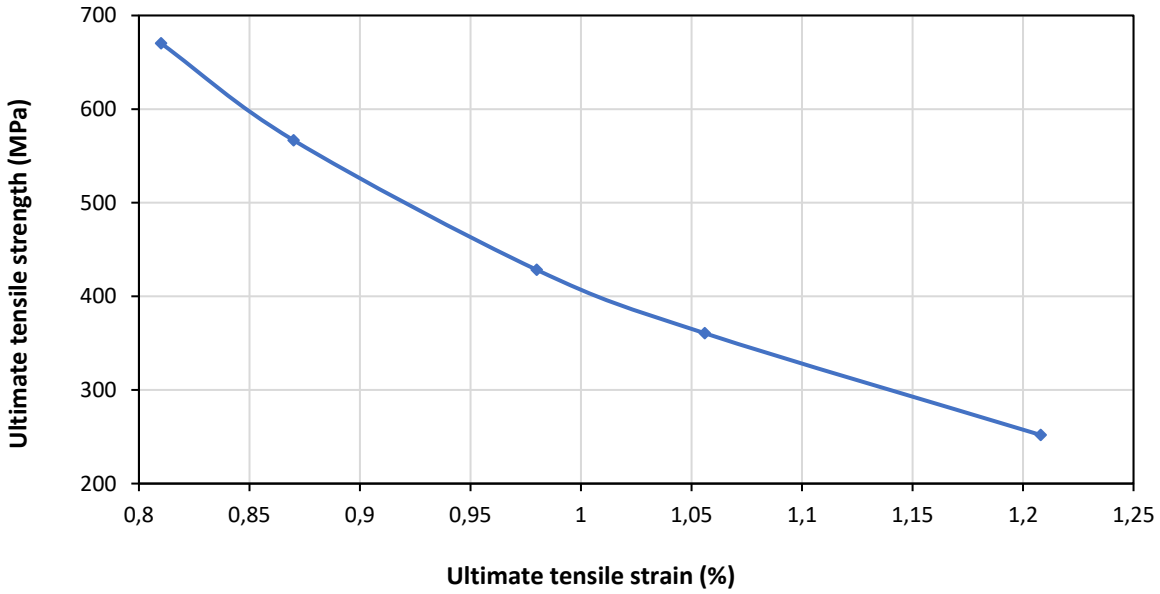

Fig. 9. The relationship between Ultimate tensile strength and the Ultimate tensile strain of the PVC/CF/Gr composite pipe

Table 5. PVC/CF/Gr pipe tensile strength and Young's modulus

Specimen	Young's modulus (GPa)	Ultimate tensile strength (MPa)	Ultimate tensile strain (%)
PVC-CF	40.8	251.9	1.208
0.5% Gr	53.8	360.6	1.056
1% Gr	74.6	428.3	0.98
1.5% Gr	88.4	566.7	0.87
2% Gr	120.5	670.3	0.81

Table 6. PVC/CF/Gr pipes' compressive strength for different weights of graphene

Specimen	Compressive strength (MPa)
PVC-CF	230.2
0.5% Gr	312.8
1% Gr	391.5
1.5% Gr	520.3
2% Gr	479.4

Table 7. PVC/CF/Gr pipe loading test for different weights of graphene

Specimen	Ultimate compressive load (N)	Stiffness (kPa)
PVC-CF	4270	190.7
0.5%Gr	5664	267.9
1% Gr	6848	338.8
1.5% Gr	7547	385.3
2% Gr	8115	412.7

4. Conclusion

This study investigated the mechanical and dynamic properties of pipes composed of polyvinyl chloride (PVC), carbon fiber (CF), and graphene (Gr) to assess their suitability for use in oil and gas pipelines. The key findings are as follows:

- In this study, the general solution of the vibration equation for conservative fluid-conveying pipes is derived. Based on this solution, the frequency equations of boundary conditions for a simply supported pipe transporting fluid are analytically obtained in terms of the pipe's governing parameters.
- Optimal enhancement in ultimate tensile strength was achieved with 2 wt% graphene, resulting in a 31% increase.
- The tensile strength of the composite pipes reached 670 MPa, representing a substantial improvement over high-quality API steel pipes, demonstrating their feasibility for oil and gas pipeline applications.
- The presence of a crack disrupts the flow distribution within the pipe. While the flow through an uncracked pipe remains continuous, the introduction of a crack leads to disturbances in the flow pattern. As the crack length and orientation vary, the flow distribution progressively transitions from a continuous to a discontinuous state. An increase in fluid flow velocity led to a decrease in the natural frequencies of the pipe.
- A comparison between theoretical analysis and numerical simulations for estimating pipe frequency under flow-induced vibration showed strong agreement, with a maximum deviation of approximately 8.18% across different flow velocities.
- Further investigations revealed notable improvements in the axial mechanical behavior of the composite pipes.
- The incorporation of graphene into the PVC/CF composite not only strengthened the matrix phase but also significantly improved the interfacial adhesion between the polymer matrix and the reinforcing fibers.

These results confirm that PVC/CF/Gr composite nano pipes exhibit superior mechanical performance, enhanced dynamic stability, and excellent engineering properties, making them highly suitable for next-generation pipeline systems intended for oil and gas transportation.

4.1 Future Work and Recommendations

Building upon the findings of this study, several directions for future research are recommended to further advance the understanding and application of PVC–Carbon Fiber–Graphene nanocomposite pipes in oil and gas systems:

- Experimental Validation: Conduct practical mechanical testing, including tensile, compressive, fatigue, and impact assessments, to validate the numerical and analytical results obtained in this study.
- Thermal and Environmental Effects: Investigate the influence of elevated temperatures, UV exposure, chemical interactions, and thermal cycling on the mechanical and vibration performance of the nanocomposite pipes.
- Fluid–Structure Interaction: Examine the interaction between transported fluids and the pipe walls, considering internal pressure fluctuations, turbulent flow, and multiphase transport, to assess their impact on stress distribution and vibration behavior.
- Nanofiller Optimization: Explore a broader range of graphene and carbon fiber concentrations, as well as hybrid or functionalized nanofillers, to optimize mechanical performance, stiffness, and cost-efficiency.
- Corrosion and Wear Resistance: Evaluate long-term durability, erosion, and chemical resistance of the nanocomposite pipes, including the potential benefits of surface treatments or protective coatings.
- Manufacturing Scale-Up: Assess the effects of industrial-scale fabrication methods, such as injection molding, extrusion, or filament winding, on mechanical properties, material uniformity, and structural integrity.

Acknowledgement

The authors express their sincere gratitude to all the professors who supervised and supported the organization of this distinguished scientific conference. Special thanks are extended to the Ministry of Higher Education and Scientific Research, the Iraqi Geotechnical Society, Komar University of Science and Technology, the publishing journal, and all other scientific institutions involved in facilitating the publication of this paper.

References

[1] Nawaz M, Yusuf N, Habib S, Shakoor R, Ubaid F. Development and properties of polymeric nanocomposite coatings. Polymers. 2019;11(5):852. https://doi.org/10.3390/polym11050852
[2] Radhamani AV, Chung HC, Ramakrishna S. Nanocomposite coatings on steel for enhancing the corrosion resistance: a review. J Compos Mater. 2019;54(5):681-701. https://doi.org/10.1177/0021998319857807
[3] Pourhashem S, Vaezi MR, Rashidi A, Bagherzadeh MR. Exploring corrosion protection properties of solvent-based epoxy-graphene oxide nanocomposite coatings on mild steel. Corros Sci. 2017;115:78-92. https://doi.org/10.1016/j.corsci.2016.11.008
[4] Shankarachar SM, Radhakrishina M, Babu PR. An experimental study of flow induce vibration of elastically restrained pipe conveying fluid. In: Proceedings of the 15th International Mechanical Engineering Congress and Exposition (IMECE15); 2015 Nov 13-19; Houston, TX, USA.
[5] Jweeg MJ, Mohammad SK, Alnomani SN. Dynamic analysis of a rotating stepped shaft with and without defects. In: 3rd International Conference on Engineering Sciences. IOP Conf Ser: Mater Sci Eng. 2020;671:012004. https://doi.org/10.1088/1757-899X/671/1/012004
[6] TabkhPaz M, Park DY, Lee PC, Hugo R, Park SS. Development of nanocomposite coatings with improved mechanical, thermal, and corrosion protection properties. J Compos Mater. 2018;52(8):1045-1060. https://doi.org/10.1177/0021998317720001
[7] Yu YH, Lin YY, Lin CH, Chan CC, Huang YC. High-performance polystyrene/graphene-based nanocomposites with excellent anti-corrosion properties. Polym Chem. 2014;5:535-550. https://doi.org/10.1039/C3PY00825H
[8] Liu J, Liu T, Guo Z, Guo N, Lei Y, Chang X, et al. Promoting barrier performance and cathodic protection of zinc-rich epoxy primer via single-layer graphene. Polymers. 2018;10(6):591. https://doi.org/10.3390/polym10060591
[9] Pathak AK, Garg H, Singh M, Yokozeki T, Dhakate SR. Enhanced interfacial properties of graphene oxide incorporated carbon fiber reinforced epoxy nanocomposite: a systematic thermal properties investigation. J Polym Res. 2019;26:1-13. https://doi.org/10.1007/s10965-018-1668-2
[10] Samsudin MS, Mahtar MA, Leong KH. Barrier and thermal performance of graphene-HDPE nanocomposites for pipeline liner application. In: SPE Middle East Oil and Gas Show and Conference; 2019 Mar; Manama, Bahrain. Paper No: SPE-195069-MS. p. 18-21. https://doi.org/10.2118/195069-MS
[11] Pourhashem S, Rashidi A, Vaezi MR. Excellent corrosion protection performance of epoxy composite coatings filled with amino-silane functionalized graphene oxide. Surf Coat Technol. 2017;317:1-9. https://doi.org/10.1016/j.surfcoat.2017.03.050
[12] Karsli NG, Yesil S, Aytac A. Effect of hybrid carbon nanotube/short glass fiber reinforcement on the properties of polypropylene composites. Compos Part B Eng. 2014;63:154-160. https://doi.org/10.1016/j.compositesb.2014.04.006
[13] Yip MC, Lin YC, Wu CL. Effect of multi-walled carbon nanotubes addition on mechanical properties of polymer composites laminate. Polym Polym Compos. 2011;19:131-140. https://doi.org/10.1177/0967391111019002-313
[14] Prusty RK, Ghosh SK, Rathore DK, Ray BC. Reinforcement effect of graphene oxide in glass fiber/epoxy composites at in-situ elevated temperature environments: emphasis on graphene oxide content. Compos Part A Appl Sci Manuf. 2017;95:40-53. https://doi.org/10.1016/j.compositesa.2017.01.001
[15] Patil A, Patel A, Sharma PK. Effect of carbon nanotube on mechanical properties of hybrid polymer matrix nanocomposites at different weight percentages. Mater Today Proc. 2018;5(2):6401-6405. https://doi.org/10.1016/j.matpr.2017.12.251
[16] Rajabi M, Rashed GR, Zaarei D. Assessment of graphene oxide/epoxy nanocomposite as corrosion resistance coating on carbon steel. Corros Eng Sci Technol. 2015;50:509-516. https://doi.org/10.1179/1743278214Y.0000000232
[17] Brandenburg RF, Lepienski CM, Becker D, Coelho LAF. Influence of mixing methods on the properties of high-density polyethylene nanocomposites with different carbon nanoparticles. Matéria (Rio J). 2017;22:e11888. https://doi.org/10.1590/s1517-707620170004.0222

[18] Aldajah S, Haik Y. Transverse strength enhancement of carbon fiber reinforced polymer composites by means of magnetically aligned carbon nanotubes. Mater Des. 2012;34:379-383. https://doi.org/10.1016/j.matdes.2011.07.013
[19] Saad ALG, Sayed WM, Ahmed MGM, Hassan AM. Preparation and properties of some filled poly(vinyl chloride) compositions. J Appl Polym Sci. 1999;73:2657-2670. https://doi.org/10.1002/(SICI)1097-4628(19990923)73:13<2657::AID-APP14>3.0.CO;2-7
[20] Nawaz K, Ayub M, Ul-Haq N, Khan MB, Khan Niazi MB. The effect of graphene nanosheets on the mechanical properties of polyvinylchloride. Polym Compos. 2016;37:1572-1576. https://doi.org/10.1002/pc.23328
[21] Aljaafari A, Abu-Abdeen M, Aljaafari M. Mechanical and electrical properties of poly(vinyl chloride) loaded with carbon nanotubes and carbon nanopowder. J Thermoplast Compos Mater. 2011;25:679-699. https://doi.org/10.1177/0892705711412650
[22] Xiao Y, Chen Z, Xin B, Li L. Preparation and characterization of graphene enriched poly(vinyl chloride) composites and fibers. J Text Inst. 2017;109:1-8. https://doi.org/10.1080/00405000.2017.1398059
[23] Kuram E, Ozcelik B, Yilmaz F. The influence of recycling number on the mechanical, chemical, thermal and rheological properties of poly(butylene terephthalate)/polycarbonate binary blend and glass-fiber reinforced composite. J Thermoplast Compos Mater. 2016;29:1443-1457. https://doi.org/10.1177/0892705715569823
[24] Kadam PG, Mhaske ST. Effect of extrusion reprocessing on the mechanical, thermal, rheological and morphological properties of nylon 6/talc nanocomposites. J Thermoplast Compos Mater. 2016;29:960-978. https://doi.org/10.1177/0892705714551591
[25] Liu JB, Yue QB, Dong RZ, Zhang Q. The analysis of vortex-induced vibration of the flexible pipe in a cylindrical fluid field with cross flow. J Vibroengineering. 2016;18. https://doi.org/10.21595/jve.2016.16547
[26] Ismail MR. Evaluating the dynamical behavior and stability of pipes conveying fluid [PhD thesis]. Baghdad: Al-Nahrain University, Mechanical Engineering; 2011.
[27] Hunain MB. The fundamental natural frequency and critical flow velocity evaluation of a simply supported stepped pipe conveying fluid. J Babylon Univ Eng Sci. 2017;25(5).

Research on Engineering Structures & Materials
www.jresm.org

Research Article

Enhancing the external sulfate attack resistance of high-volume fly ash concrete containing waste glass powder

Mahmood Fawzi Ahmed [*,a]

Department Education of Hit, General Directorate of Education in Anbar, Ministry of Education, 31007 Hit, Iraq

Article Info

Article History:

Received 15 Oct 2025

Accepted 15 Nov 2025

Keywords:

Fly ash;
HVFA concrete;
External sulfate attack;
Waste glass powder;
Concrete durability

Abstract

The urgent need to reduce the environmental footprint of concrete production has intensified research into sustainable alternatives to ordinary Portland cement (OPC) and ways to utilize industrial waste. This study is motivated by the need to enhance both the mechanical properties and durability of high volume fly ash (HVFA) concrete, by incorporating waste glass powder (GP) as a partial replacement for fly ash, with a particular focus on improving resistance to external sulfate attack. The cementitious binder of the reference mixture was a blend of 50% (OPC) and 50% fly ash by weight. Another two mixes were prepared by substituting 10% and 20% of fly ash weight with glass powder (GP). Key properties evaluated included compressive strength, water absorption, ultrasonic pulse velocity (UPV), and external sulfate resistance. Compressive strength was assessed for each mixture after 150 days of curing in both a 5% sodium sulfate (Na_2SO_4) solution and in normal water. The durability index was calculated as the difference in compressive strength between the sulfate-exposed and water-cured specimens. The results demonstrated that the inclusion of 10% and 20% glass powder in HVFA concrete present higher strength (43.6, 38.6 MPa) at both curing method in compare with reference mix (34.9 MPa). Therefore, the durability index of mixes with GP was improved, whereas 10% of GP is the optimum replacement level. The results of water absorption will decline from 3.15% to 2.33% and 2.65%, while (UPV) will increase from 4.683 Km/sec to 5.292 and 5.023 Km/sec of 10%GP and 20%GP mixtures, respectively. Significantly, UPV measurements increased by 13% and 7.2% for concrete mixes containing 10% and 20% GP, respectively, compared to the control mix, further confirming enhanced concrete uniformity and quality.

© 2026 MIM Research Group. All rights reserved.

1. Introduction

Climate change and global warming become vital issues that require urgent solving pathways. The manufacturing of ordinary Portland cement, a key binder of concrete, is one of the majority carbon emissions, accounting for about 8% of the total emission around the world [1-2]. Due to the global continuation of the construction industry and the development of infrastructures, there is an imperative to decarbonization of conventional concrete and its constituents. One of the encouraging solutions of shifting conventional concrete to more sustainable building material is using supplementary cementitious materials (SCMs) together with ordinary Portland cement. There are different types of SCMs that can be used in concrete mixtures, including industrial by-products such as fly ash, silica fume, blast furnace slag, etc., and some sources from end-of-life materials as recycled waste glass [3]. Fly ash can be used as a blended or mineral admixture at a level of 50% by the total mass of cementitious materials. This allows for the development of a high concrete (HVFAC) system as defined by Mehta [4-5]. Several researchers have been attracted to

*Corresponding author: mahmodmfa81@gmail.com
[a]orcid.org/0000-0003-1342-6898
DOI: http://dx.doi.org/10.17515/resm2025-1267ic1015rs

high-volume fly ash concrete and have conducted studies on its production and characteristics. Kumar et al., evaluated the mechanical and durability properties of HVFAC prepared by replacing OPC by 20%, 40%, 50%, 60%, and 70% with FA. The authors found that the compressive strength and ultrasonic pulse velocity results have decreased with the increase of FA content, while the volume of permeable voids has declined by 15.65% at the 50% fly ash level, and then the permeable voids increase for mixes with 60% and 70% FA content [6]. Similarly, Babalu et al. [7] investigated the compressive and flexural strengths and some durability properties of HVFAC mixtures that included 30%, 40%, 50%, 60%, and 70% of FA as a cement substitute. The main results show that the mix with 30% FA content presented the highest compressive and flexural strength and best resistance in acidic environment. Moreover, some studies investigated the durability of HVFAC against the external and internal sulfate attack. Al-Attar and Taha [8] evaluated the effect of internal sulfate attack by adding natural gypsum ($CaSO_4$) to the fine aggregate of high-volume fly ash self-compacting concrete. The strength degradation of all mixes including 50% and 60% FA was neglectful at the early age, followed by a more reduction in the strength for the 60% FA and 50% FA mixes, respectively. In the same context, Liu et al., [9] determined the variation of physical and mechanical properties of high-volume fly ash self-compacting concrete exposure to dry - wet cyclic sulfate attack with 5% Na2SO4. Other research represented by Das et al. [10] examined the durability of ternary blended high volume fly ash—ground granulated blast furnace slag concrete exposed to aggressive environments. The binder of the tested mixes was blended as: (50% OPC + 25% FA + 25% GGBFS), (50% OPC + 20% FA + 30% GGBFS), and (50% OPC + 30% FA + 20% GGBFS). On the other hand, the excessive use of glass products in different fields has generated a significant amount of end-life waste. This waste of glass is usually disposed of as damping and landfilling, consequently hazardous, and adverse effects will accrue on the environment and ecological balance. Recycling and reuse waste glass as fine glass powder in concrete production will provide a sustainable approach to overcome this challenge [11]. Numerous researchers would encourage for introducing (GP) into concrete as a partial replacement of cement because of its pozzolanic activity and amorphous phase [12-13]. The work of Paul et al. [14] lies in replacing the cement with waste glass powder at levels from 0 to 40%, then measuring the shrinkage, durability, and mechanical properties of two concrete grades, M30 and M40. In additional experimental research, Muhedin and Ibrahim [15] described the physical, mechanical, and microstructure properties of concrete that containing 0%, 10%, 15%, and 20% of waste glass powder as partial replacement of cement and fine aggregate separately. Furthermore, some researchers have used waste glass powder as a blend with other pozzolanic additives. Abed et al. [16] utilized waste glass powder and silica fume as pozzolanic materials to partially substitute cement in mortar manufacture. The study of Chengjin Li [17] discovered the compressive strength and sulfate corrosion resistance of concrete mixture made of blended limestone powder and glass powder with cement. The author found that combination of 10% limestone powder and 5% glass powder was the best mixed to improve the corrosion resistance and strength. Also, Akinpelu et al. [18] examined the impact of waste glass powder and metakaolin as partial substitutes for cement in self-compacting concrete. Their research indicated that a ternary mixture including 5% metakaolin and 10% waste glass powder significantly enhanced both workability and mechanical qualities, exceeding the control mix in strength and microstructural performance. Furthermore, fly ash availability is diminishing in many regions due to the closure of coal power plants, and because of its slower pozzolanic reaction, it mainly contributes to long-term strength gains. Glass powder, with its high amorphous silica content and fine particle size, exhibits faster reactivity and can enhance early-age strength when blended with fly ash. [19]. Hence, there is a gap in research on the durability performance of concrete made with high volumes of blended fly ash and waste glass powder in aggressive external sulfate attacks. The primary aim of this study is to systematically investigate the durability performance and mechanical properties—specifically, compressive strength, water absorption, and ultrasonic pulse velocity—of high-volume fly ash (HVFA) concrete incorporating varying proportions of waste glass powder (GP) as a partial replacement for fly ash. This study concentrates on evaluating the performance of HVFA concrete at higher replacement rates, which is essential for optimizing waste glass utilization and produce more durable and sustainable concrete that can be applicable in a wide range of civil engineering fields.

2. Experimental Work

2.1 Materials

The ordinary Portland cement used was (CEM I 32.5 R), which meets Iraqi specification (IQ.S No.5:2019) [20]. The cementitious materials consisted of blended Fly ash (FA) and waste glass powder (GP) as per ASTM C618 [21]. The process of producing glass powder (GP) involved the collection of the broken pieces of waste window glass, then crushing and grinding these wastes to produce the final product of GP as shown in (Fig. 1). The Fly ash was brought from an electrical power station in Turkey and it is available in local markets. The chemical oxides and properties of (FA) and (GP) are presented in Table 1. The crushed gravel of size (5-14) mm was used as coarse aggregate, while the fine aggregate was natural sand of maximum size 5 mm and grading in zone 2. All aggregates are complying with Iraqi specification (IQ.S No.45:1984) [22]. For adjusting the workability, high range water reducing admixture (superplasticizer – Glenium 51) was utilize. The tap water (free from contaminates) was used for mixing and curing.

Fig. 1. Waste glass powder used in HVFA concrete mixture

Table 1. Chemical analysis and physical properties of fly ash, and waste glass powder

Chemical oxides	FA	GP	OPC
SiO_2	56.5	78.2	20.73
Al_2O_3	23.7	1.53	5.18
Fe_2O_3	6.3	0.71	3.48
CaO	5.8	8.1	62.87
MgO	1.2	0.56	2.16
SO_3	1.5	0.1	1.92
L.O.I	1.2	0.32	2.16
Blain fineness (m^2/kg)	420	290	320
Strength activity index, %	83	90.5	/

2.2 Mixture Design and Preparation of the Specimens

A total of three concrete mixtures were prepared and tested to evaluate some durability aspects related to external sulfate attack. The mix design of control mixture based on using blended of (50% FA with 50% OPC) to produce high volume fly ash concrete with a target compressive strength up to 30 MPa at 28 days. For the other two mixtures, the FA was replaced with waste GP by 10% and 20% of weight. These substitution level (10% and 20% GP) has selected for evaluating the performance of HVFA concrete at higher replacement rates, which is essential for optimizing waste glass utilization and enhancing sustainability advantages. The denotation and the proportion of materials of all mixes are presented in Table 2. The mixing process started by blending the OPC, FA, and GP manually. Then, the binder was mixed with the coarse and fine aggregate inside the drum of an electrical mixer. The water and superplasticizer were added gradually into the mixer, and the mixing process was done in about 8 minutes until achieved a homogenous mixture. The fresh

concrete was cast into cubic molds of (15×15×15) cm, compacted with steel rod, covered with plastic sheet and left to set for 24 hours before being demolded.

Table 2. Mix proportion of HVFA concrete (kg/m^3)

Materials	Batch name		
	M1(50FA:0GP)	M2(40FA:10GP)	M3(30FA:20GP)
Cement	250	250	250
Fly ash	250	200	150
Glass powder	0	50	100
Coarse aggregate	1080	1080	1080
Fine aggregate	722	722	722
(w/cm), %	0.35	0.35	0.35
Superplasticizer, %*	3	3	3

** The dosage of superplasticizer is (%) by weight of cement*

2.3 Curing, Exposing Regime and Testing Methods

Immediately after demolding the specimens of each mix, the total of (108) samples were divided into two groups according to the specified curing regime. For the first group, the samples were cured normally by immersion in water (taken as the reference of compressive strength). The samples of the second group have immersed directly (after demolding) in a chemical solution of 5% sodium sulfate (Na_2SO_4) prepared as per ASTM C1012 [23]. Figure 2 shows the specimens immersed inside the sodium sulfate solution. As an indication of the uniformity and quality of the concrete matrix, the samples of normal curing (first group) were tested to measure the water absorption and transmit velocity of ultrasonic pulse (UPV) at 7 and 28 days according to ASTM C642 [24] and ASTM C597 [25], respectively. To evaluate the long-term durability performance, the strength development of all mixes in each curing regime was determined by testing the compressive strength as per BS 1881:116 [26] at ages of 7, 28, 90, 120, and 150 days. The test of specimens at a later age (150 days) will provide more reliable results about the concrete's performance over its service lifecycle.

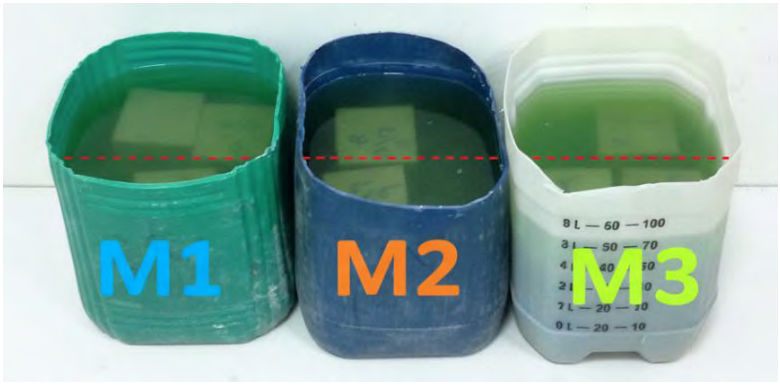

Fig. 2. Some specimens of HVFA concrete mixtures submersed in Na_2SO_4 solution

3. Results and Discussion

3.1 Water Absorption

As shown in (Fig. 3), the water absorption of HVFA concrete lies in 3.5% and 3.15% at 7 and 28 days, respectively. Notably, the replacement of FA with 10% and 20% GP will decrease the water absorption by 29.7% and 22.3% at 7 days, respectively. This decrement will be 26.0% for mix M2 (40FA:10GP), and 15.8% for mix M3 (30FAP:20GP) at age of 28 days. From Figure 3 it can be seen that the mixture M2 (40FA:10GP) have the lowest water absorption. The reduction in water absorption is due to the pozzolanic activity and the filling effect of glass powder within gel pores and concrete matrix. Glass powder is rich in amorphous silica, which reacts pozzolanically with calcium hydroxide ($Ca(OH)_2$) released during cement hydration. This secondary reaction results in

the formation of additional calcium silicate hydrate (C-S-H) gel, which fills the capillary pores and reduces overall porosity [12], [27-28]. On the other hand, the fine particle size of glass powder improves the particle packing density within the cementitious matrix. The glass powder particles act as fillers that occupy voids between the larger cement and fly ash particles. This leads to a more compact and refined microstructure, further decreasing the volume of permeable pores available for water absorption [1], [29]. Furthermore, the synergistic effect of glass powder with fly ash will complement the slower pozzolanic activity of fly ash, accelerating the densification process and contributing to a more impermeable matrix at earlier ages [14]. These findings are consistent with previous studies that reported enhanced durability and reduced permeability when glass powder was used as a partial replacement of cementitious materials [11], [27].

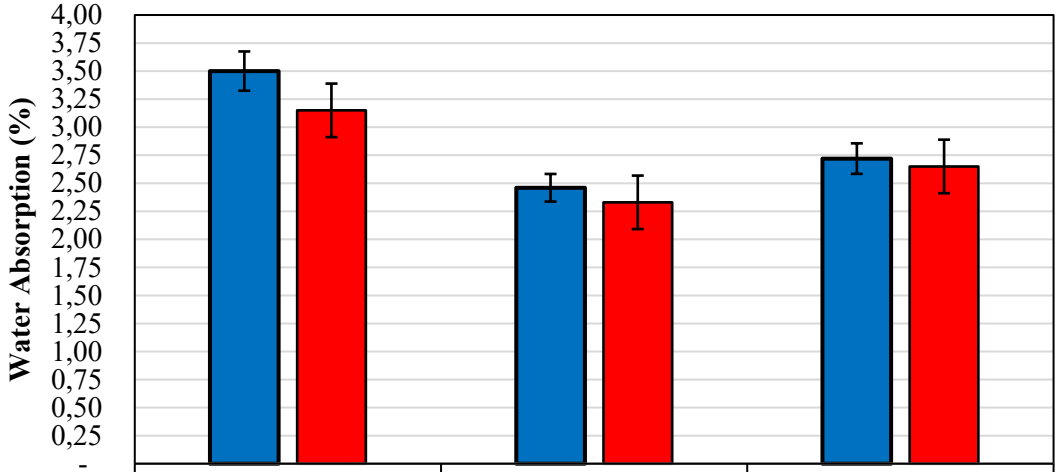

	M1 (50FA:0GP)	M2 (40FA:10GP)	M3 (30FA:20GP)
7 day	3,50	2,46	2,72
28 day	3,15	2,33	2,65

Fig. 3. Water absorption of HVFA concrete mixtures

3.2 Ultrasonic Pulse Velocity

The values of ultrasonic pulse velocity measured for all mixes at 7 and 28 days are presented in (Fig. 4). The results of all concrete mixes indicate increasing of UPV with curing age as a consequence of improving the concrete structure due to the continuous of cement hydration. The inclusion of 10% and 20% GP has increased the UPV of reference mix (M1) up to 13.0% and 7.2% respectively. As expected, the substitute of FA with fine particles and high pozzolanic activity of GP will enhance the hydration process, refinement the pores size and backing of the interfacial transition zone (ITZ), as mention previously. Therefore, the transmitted time of the pulse within concrete matrix will decline significantly, so its velocity increase, similarly to the previous study of Safiy et al. [29].

3.3 Development of Compressive Strength

Two types of solutions used in the curing of concrete specimens.

Specimens cured in water: The results of compressive strength of HVFA concrete mixtures (M1), (M2), and (M3) are graphically presented in (Fig. 5). All the specimens under water curing demonstrated a continuous increasing of compressive strength with time. The outcomes show that the strength of M1, M2, and M3 at age of 7 days developed by 56.0%, 33.7%, and 28.6% after 120 days, respectively. The results of Figure 5 indicate the addition of GP significantly enhanced the compressive strength. The pozzolanic activity and fineness of GP will densified ITZ and refine the size of pores. Consequently, the strength of concrete has been improved [26-29]. Although fly ash has a slow pozzolanic activity, a corresponding the strength gain at early ages is also slow.

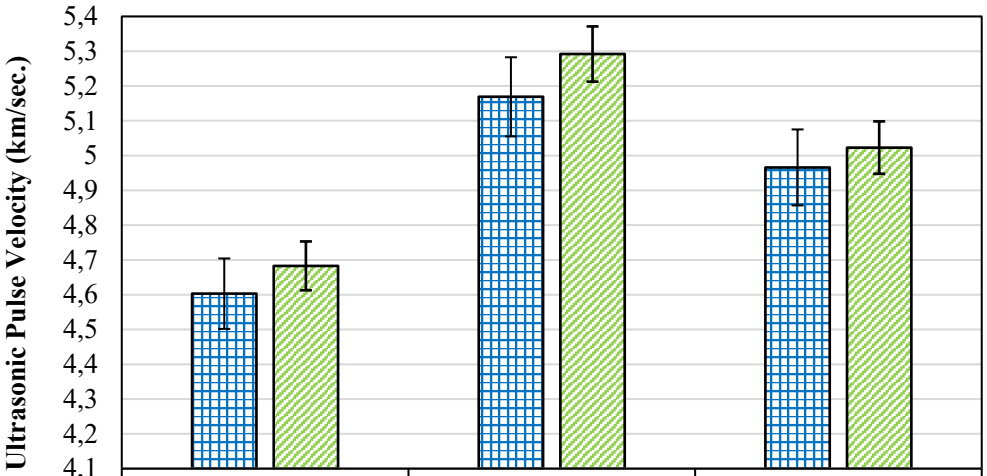

	M1 (50FA:0GP)	M2 (40FA:10GP)	M3 (30FA:20GP)
7 day	4,603	5,169	4,966
28 day	4,683	5,292	5,023

Fig. 4. Ultrasonic Pulse Velocity of HVFA concrete mixtures

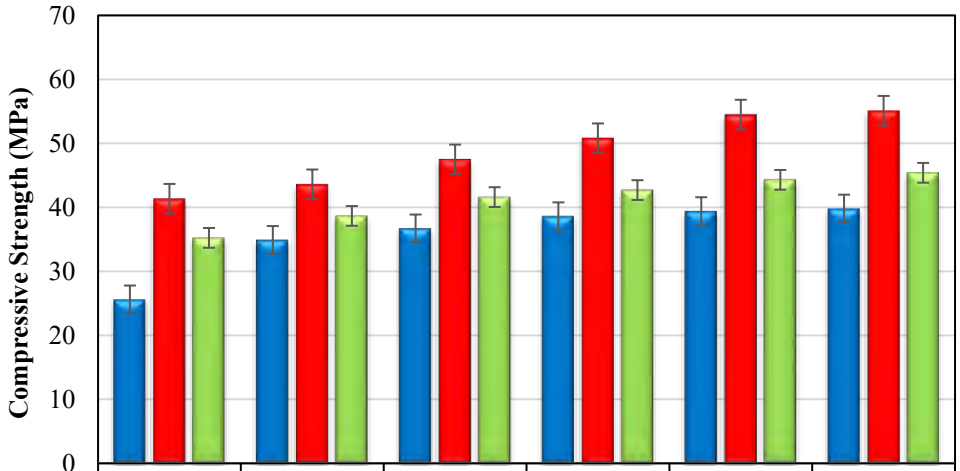

	7 days	28 days	60 days	90 days	120 days	150 days
M1 (50FA:0GP)	25,60	34,90	36,70	38,60	39,4	39,8
M2 (40FA:10GP)	41,35	43,60	47,50	50,80	54,5	55,1
M3 (30FA:20GP)	35,23	38,66	41,60	42,70	44,3	45,4

Fig. 5. Compressive strength of HVFA concrete mixtures curing in water

Nevertheless, the reference mix (M1) exhibited a retarding of the strength development in compare with M2 and M3 mixes till the later ages. While the addition of glass powder (GP) accelerates early-age strength gain, fly ash (FA) plays a crucial role in strength development of the mixes (M2 and M3) at later ages through the continuous pozzolanic activity that consumption the weak calcium hydroxide and formation additional stronger and durable gel [19]. The blend of 10% GP and 40% FA yielded in the highest strength at all test ages. This may be attributed to optimizing the synergistic effects of both supplementary cementitious materials in relation to the highest pozzolanic activity, optimized particle packing and filler effect, and balancing of replacement level and hydration products. This finding matches with the results of UPV and water absorption test and in same trend as the previous studies [11], [29-30].

Specimens submersing in Na_2SO_4 solution: The strength development of HVFA concrete specimens immersed in 5% Na_2SO_4 sulfate solution are shown in (Fig. 6.) It was observed that all concrete mixtures exhibited continuous strength gain with time up to 120 days. The 7th day's compressive strength of M1, M2, and M3 increased by 49%, 27.11%, and 20.83% at age of 120 days, respectively.

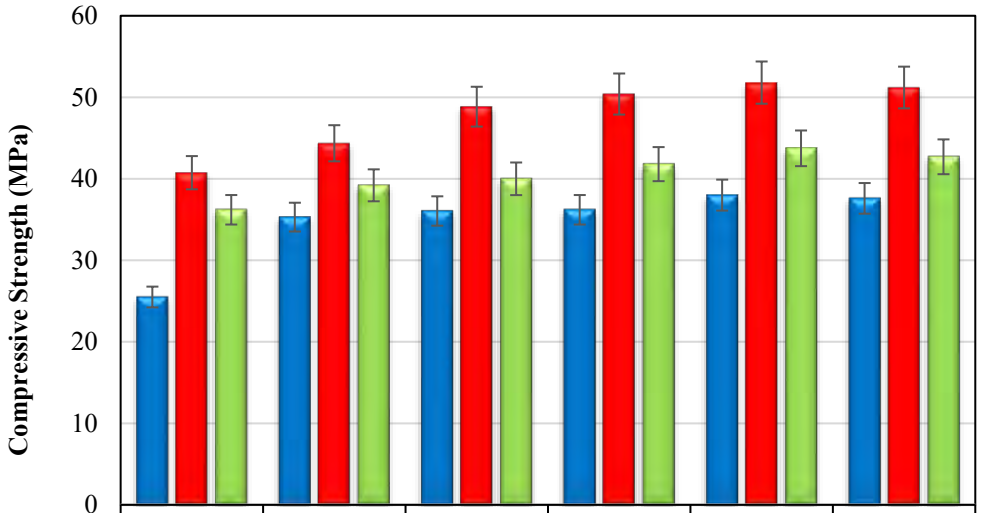

	7 days	28 days	60 days	90 days	120 days	150 days
M1 (50FA:0GP)	25,50	35,30	36,05	36,20	38	37,6
M2 (40FA:10GP)	40,75	44,36	48,85	50,40	51,8	51,2
M3 (30FA:20GP)	36,20	39,20	40,00	41,80	43,74	42,7

Fig. 6. Compressive strength of HVFA concrete mixtures submersing in Na_2SO_4 solution

The compressive strength of all mixes has steadily increased at ages 28, 60, and 90 days to reach the maximum strength at 120 days. The compressive strength at 28 days for M1, M2, and M3 was 35.30, 44.36, and 39.20 MPa, respectively. The values have increased by 2.12%, 10.12%, and 2.04% at 60 days, and by 2.55%, 13.61%, and 6.63% at 90 days, respectively. This behavior can be attributed to the formation of more cementitious hydration products and densification of the microstructure. After 150 days of immersing, all specimens will begin to face the adverse effects of sulfate solution. The compressive strength of mixes M1, M2, and M3 at 150 days has slightly decreased by 1.06%, 1.17%, and 2.43% compared to the results of 120 days, respectively. The reduction in strength of HVFA mixes related to the mechanism of sulfate attack on cement paste components, mainly the reaction between calcium hydroxide and sulfate ions. Consequently, high volume products (gypsum and ettringite) will take place within hardened cementitious matrix, leading to more cracking and degradation.

3.4 Durability Index (Degree of Damage)

The durability index, represented as the degree of damage (Di), is a crucial measure in this study for quantitatively evaluating the resistance of high-volume fly ash (HVFA) concrete to external sulfate attack. The index reflects the variation in compressive strength of concrete specimens subjected to a sulfate-rich environment against those cured under normal water conditions. The (Di) measured according to the following equation [31]:

$$Di = 1 - \frac{Cs}{Cw} \quad (1)$$

Where; Di is a degree of damage (durability index), Cs: compressive strength of samples exposed to sulfate attack after a given period, Cw: compressive strength of samples cured normally in water at the same period.

A higher (Di) value indicates greater deterioration, while a lower value signifies better durability and resistance to sulfate-induced degradation. The results of concrete damage degree are graphically presented in Figure 7. It can be seen that the degree of damage of each mix was increased with time, and it reached to the maximum at end time of test – 150 days due to prolonged sulfate exposure. The reference mix (M1) exhibited the lowest degree of damage. This phenomenon is attributed to the slower strength gain of M1 under water curing, resulting in a smaller variation between the strengths in sulfate and water curing. While M2 (40% FA, 10% GP) and M3 (30% FA, 20% GP) mixes showed higher strength increments under normal curing, which led to a larger

differential when compared to sulfate-exposed specimens. Consequently, their degree of damage was higher. This observation does not suggest inferior performance; instead, it indicates that the rapid strength gain achieved through the addition of glass powder is not entirely sustained under aggressive sulfate conditions. Despite this, all mixes containing glass powder (M2 and M3) retained significantly higher absolute compressive strengths than the reference mix after sulfate exposure, underscoring the beneficial role of GP in enhancing sulfate resistance and overall durability.

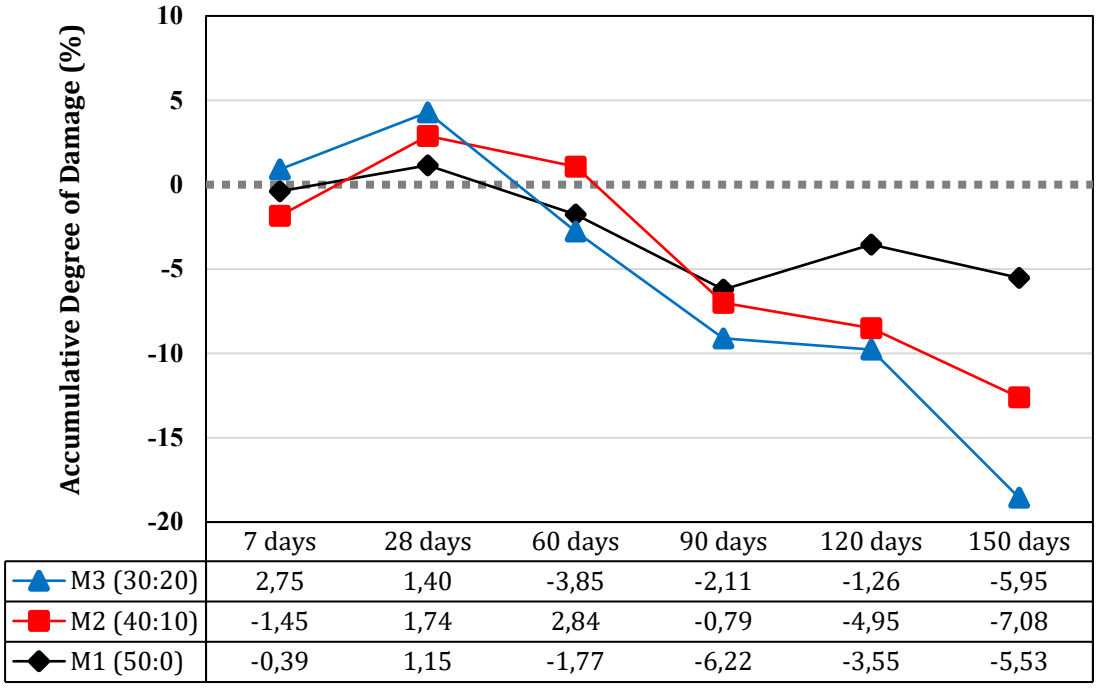

	7 days	28 days	60 days	90 days	120 days	150 days
M3 (30:20)	2,75	1,40	-3,85	-2,11	-1,26	-5,95
M2 (40:10)	-1,45	1,74	2,84	-0,79	-4,95	-7,08
M1 (50:0)	-0,39	1,15	-1,77	-6,22	-3,55	-5,53

Fig. 7. Degree of damage of HVFA concrete mixtures after exposure to Na_2SO_4 solution

4. Conclusions

This study investigated high-volume fly ash concrete (HVFA) with 10% and 20% waste glass powder (GP) additions for evaluating its resistance to external sulfate attack. Experimental methods included physical and mechanical tests and durability examinations over 150 days. The following conclusions can be drawn from the key finding of this paper as below:

- The study confirms that structural concrete with a significant fly ash content—up to 50% of the binder—can attain a target compressive strength of 30 MPa within 28 days. This illustrates the feasibility of replacing a significant amount of ordinary Portland cement (OPC) with fly ash, which is necessary for mitigating the environmental impact of concrete production.
- The use of waste glass powder as a partial replacement for fly ash, at 10% and 20% content, significantly enhances the compressive strength of high-volume fly ash concrete (HVFA). The incorporation of 10% and 20% GP increases strength relative to the reference mix from 34.9 MPa to (43.6 and 38.6) MPa at 28 days, and improves strength development at both early and later stages to reach (55.1 and 45.4) MPa, respectively.
- The pozzolanic activity and filling of glass powder have improved the microstructure of HVFA concrete. The water absorption test indicated a notable reduction in the absorption rate of mixtures incorporating glass powder relative to the reference mixture; absorption decreased from 3.15% in the reference mixture (M1: 50% FA, 0% GP) to 2.33% in M2 (40% FA, 10% GP) and 2.65% in M3 (30% FA, 20% GP) at 28 days, indicating enhanced density along with lower pore volume caused by the pozzolanic reaction of the glass powder.
- The ultrasonic pulse velocity (UPV) test findings indicated an increased in ultrasonic wave speed from 4.683 km/s in the reference mix to 5.292 km/s in M2 and 5.023 km/s in M3 at 28 days. This enhancement signifies an improvement in the homogeneity and consistency of the

concrete's matrix, associated with a decrease in micro-cracks and a strengthening in the concrete's durability.

- Results indicate that HVFA concrete with glass powder displays superior resistance to sulfate-induced deterioration relative to the control mix. The durability index, determined by the variation in compressive strength between water-cured and sulfate-exposed samples, indicates that mixtures with glass powder (notably at a 10% substitution) have less strength degradation and exhibit enhanced durability over time.
- Of the studied mixtures, a mix including 50% Ordinary Portland Cement, 40% fly ash, and 10% glass powder (referred to as M2) exhibited superior performance regarding strength and durability. This mixture achieved the highest compressive strength, minimal water absorption, superior UPV, and optimal resistance to sulfate attack, establishing it as the optimum mixture for mechanical and durability properties.
- This type of concrete is highly encouraged for civil engineering applications since it is innovative and sustainable. It contributes to sustainable development goals by lowering the environmental impact of concrete production and using industrial waste.
- Recommendations for further studies of high-volume fly ash–glass powder concrete are required to investigate the effects of lower GP content (e.g., 5% or less) and the combined use of GP with other supplementary cementitious materials, as well as the impact on other concrete properties such as shrinkage, creep, and fire resistance, which will help further advance the field.

References

[1] Ahmed MF. High volume brick powder concrete synergistic with metakaolin: physicomechanical properties and drying shrinkage. Kufa Journal of Engineering. 2025 Feb 4;16(1):214–32. https://doi.org/10.30572/2018/kje/160113

[2] Berkouche A, Belkadi A, Aggoun S, Hammouche R, Benaniba S. Predictive modeling of glass powder and activator effects on slag-based geopolymers via central composite design. Research on Engineering Structures and Materials [Internet]. 2024 Jan 1. https://doi.org/10.17515/resm2024.337st0703rs

[3] United Nations Environment Programme. Building Materials and the Climate: Constructing a New Future. Nairobi. 2023. https://doi.org/10.59117/20.500.11822/43293

[4] Mehta, P. Kumar. High-performance, high-volume fly ash concrete for sustainable development. In: Proceedings of the international workshop on sustainable development and concrete technology. Ames, IA, USA: Iowa State University, 2004. p. 3-14.

[5] Runganga D, Okonta F, Musonda I. Strength and Durability Properties of High-Volume Fly Ash (HVFA) Binders: A Systematic review. CivilEng. 2024 May 9;5(2):435–60. https://doi.org/10.3390/civileng5020022

[6] Kumar M, Sinha AK, Kujur J. Mechanical and durability studies on high-volume fly-ash concrete. Structural Concrete. 2020 Sep 16;22(S1). https://doi.org/10.1002/suco.202000020

[7] Babalu R, Anil A, Sudarshan K, Amol P. Compressive strength, flexural strength, and durability of high-volume fly ash concrete. Innovative Infrastructure Solutions. 2023 Apr 24;8(5). https://doi.org/10.1007/s41062-023-01120-x

[8] Al-Attar T, Taha A. Resistance of High-Volume fly Ash Self-Compacting concrete to internal sulfate attack. Engineering and Technology Journal. 2018 Dec 1;36(12A):1260–6. https://doi.org/10.30684/etj.36.12a.7

[9] Liu J, Li A, Yang Y, Wang X, Yang F. Dry–Wet cyclic sulfate attack mechanism of High-Volume fly ash Self-Compacting concrete. Sustainability. 2022 Oct 12;14(20):13052. https://doi.org/10.3390/su142013052

[10] Das BB, Black L, Barbhuiya S, Snehal K, Sumukh EP. Resistance to acid, alkali, chloride, and carbonation in ternary blended high-volume mineral admixed concrete. Journal of Sustainable Cement-Based Materials. 2024 Sep 25;1–22. https://doi.org/10.1080/21650373.2024.2405979

[11] Zhou C, Li M, Nguyen QD, Lin X, Castel A, Pang Y, et al. Application of waste glass powder for sustainable concrete: Design, performance, perspective. Materials. 2025 Feb 7;18(4):734. https://doi.org/10.3390/ma18040734

[12] Dobiszewska M, Pichór W, Tracz T, Petrella A, Notarnicola M. Effect of glass powder on the cement hydration, microstructure and mechanical properties of mortar. Mater Proc. 2023 Feb 22;40. https://doi.org/10.3390/materproc2023013040

[13] Bhavanaa R, Reddy KRC. Predicting the mechanical properties of concrete from waste glass through the use of boost and random forest. Research on Engineering Structures and Materials [Internet]. 2025 Jan 1. https://doi.org/10.17515/resm2025-891me0510rs

[14] Paul D, Bindhu KR, Matos AM, Delgado J. Eco-friendly concrete with waste glass powder: A sustainable and circular solution. Construction and Building Materials. 2022 Sep 24; 355:129217. https://doi.org/10.1016/j.conbuildmat.2022.129217
[15] Muhedin DA, Ibrahim RK. Effect of waste glass powder as partial replacement of cement & sand in concrete. Case Studies in Construction Materials. 2023 Sep 26;19: e02512. https://doi.org/10.1016/j.cscm.2023.e02512
[16] Abed, Huda Saad; Al-Saffar, Zaid Hazim; Hamad, Ali Jihad. Synergistic effect of the silica fume and glass powder as pozzolanic materials in cement mortar. International Journal of Sustainable Building Technology and Urban Development, 2024, 15.1: 43-56.
[17] Li C. Study on compressive strength and sulfate corrosion resistance of limestone powder and waste glass powder mixed concrete. Materials Research Express. 2024 Jan 16;11(2):025502. https://doi.org/10.1088/2053-1591/ad1ef6
[18] Akinpelu MA, Amao AO, Salman ASM, Gabriel DS. Sustainable self-compacting concrete: A study on the combined effects of waste glass powder and metakaolin as cement replacements. Research on Engineering Structures and Materials [Internet]. 2025 Jan 1. https://doi.org/10.17515/resm2025-610ma0105rs
[19] Fernando V, Lokuge W, Seligmann H, Wang H, Gunasekara C. Sustainable Mortar with Waste Glass and Fly Ash: Impact of Glass Aggregate Size and Life-Cycle Assessment. Recycling [Internet]. 2025a Jul 4;10(4):133. https://doi.org/10.3390/recycling10040133
[20] Iraqi Standard Specification No.5, Portland cement, 2019.
[21] ASTM International. ASTM C618-22, Standard specification for coal fly ash and raw or calcined natural pozzolan for use in concrete. 2022.
[22] Iraqi Standard Specification No. 45. The aggregates of the natural resources used in concrete construction, 1984.
[23] ASTM International, ASTM C1012/C1012M-18b. Standard test method for length change of hydraulic-cement mortars exposed to a sulfate solution, 2018.
[24] ASTM International, ASTM C642-21. Standard test method for density, absorption, and voids in hardened concrete, 2021.
[25] ASTM International, ASTM C597-22. Standard test method for ultrasonic pulse velocity through concrete. 2022.
[26] British Standards BS 1881-116:1983. Testing concrete - Method for determination of compressive strength of concrete cubes. 1983.
[27] Dahamm, E.K., Hama, S.M. and Al-Jumaily, I.A. Effect of nano-sized clay and waste glass powder on rheological and hardened properties of self-compacting concrete. Research on Engineering Structures and Materials, 2023. https://doi.org/10.17515/resm2022.563ma1026
[28] Zeybek, Ö., Özkılıç, Y. O., Karalar, M., Çelik, A. İ., Qaidi, S., Ahmad, J., ... & Burduhos-Nergis, D. P. Influence of replacing cement with waste glass on mechanical properties of concrete. 2022. Materials, 15(21), 7513. https://doi.org/10.3390/ma15217513
[29] Saify, S., Radhi, M. S., Al-Mashhadi, S. A., Mareai, B., Jabr, S. F., Mohammed, Z. A., ... & Al-Husseinawi, F. Impact of waste materials (glass powder and silica fume) on features of high-strength concrete. 2023. Open Engineering, 13(1), 20220479. https://doi.org/10.1515/eng-2022-0479
[30] Abo El-Kassem, Mohamed Hamdy; MOHAMED, Osama Mahmoud; ABD EL-HAMID, Mohamed Zakaria. Effect of using glass powder as a partial replacement of cement on concrete properties. journal of al-azhar university engineering sector, 2022, 17.62: 219-236.
[31] Mangi, Sajjad Ali, et al. Short-term effects of sulphate and chloride on the concrete containing coal bottom ash as supplementary cementitious material. Engineering Science and Technology, an International Journal, 2019, 22.2: 515-522. https://doi.org/10.1016/j.jestch.2018.09.001

Research on Engineering Structures & Materials
www.jresm.org

Research Article

The effect of permeability and mechanical properties of low-calcium fly ash based geopolymer concrete

Hawaa A. Obaid [*,a], Ibrahim A. Sarhan [b], Sheelan Mahmoud Hama [c]

Department of Civil Engineering, University of Anbar, Ramadi, Iraq

Article Info

Article History:

Received 16 Oct 2025

Accepted 05 Dec 2025

Keywords:

Geopolymer concrete;
Pore structure;
Strength;
Curing temperature;
Alkali;
Fly ash;
Superplasticizer

Abstract

Preserving the environment by reducing carbon dioxide emissions from cement production is one of the most significant current sustainability requires. This can be achieved by identifying an alternative that has characteristics similar to those of cement, by suggesting geopolymer concrete as a substitute for normal concrete. This article presents the findings of an experiment conducted to examine the effects of permeability and mechanical properties of geopolymer concrete based on low-calcium fly ash. Also, investigate possible relationship between permeability and strength properties. The experiments were conducted by varying the curing condition (24, 70°C), alkali activator to fly ash ratio (0.45, 0.5. 0.55) and dosage of superplasticizer (1.5%, 2%, 2.5%). It was found curing samples at higher temperatures (70°C) has been shown to increase strength properties. Whereas the improvement was 32%, 15% and 23% for each of the compressive strength test, modulus of elasticity and flexural strength respectively. While the improvement value for absorption was 2.6%, and 19% for the sorptivity. It was discovered that samples with an alkali to fly ash ratio (0.45) had better strength characteristics. Where the compressive strength was improved by 36%, and 27% for the absorption. Also, greater strength loss is observed in samples that contain higher superplasticizer dosages (1.5%) than in samples with lower comparable values. With a 30% improvement for both compressive strength and absorption tests. Correspondingly, more strength was lost by samples with higher water absorption and sorptivity than by samples with lower comparable values. The experimental program's results show that the sorptivity and water absorption of the samples influence the mechanical characteristics of geopolymer concrete.

© 2026 MIM Research Group. All rights reserved.

1. Introduction

An innovative and eco-friendly alternative to conventional concrete is geopolymer concrete. The aluminosilicate binder material (fly ash, silica fume, metakaolin, blast furnace slag, waste glass, iron slag, copper mine tailings, and red mud) is polymerized with an alkaline activator (potassium hydroxide, sodium hydroxide, or sodium silicate/carbonates soluble in water) to produce geopolymer concrete, which is a substitute cementitious material [1]. Since geopolymer concrete can be used entirely in a zero-cement composite by using industrial waste and metakaolin such fly ash, silica fume and slag to create new binders it has attracted a lot of attention recently [2]. The same as to Portland cement, geopolymer concrete offers excellent mechanical, durability, and thermal stability properties. Furthermore, throughout the manufacturing process, it uses less energy and releases less carbon dioxide (CO_2) [3-5]. In contrast with normal concrete which utilizes raw materials, the geopolymer concrete uses industrial waste materials as a source material that making it an ideal choice as well as to its status as sustainable material [4]. Subsequently, the geopolymer concrete has a lower calcium concentration than normal concrete and the durability

*Corresponding author: haw22e1001@uoanbar.edu.iq
[a]orcid.org/0000-0002-8539-9553; [b]orcid.org/0000-0001-9354-4864; [c]orcid.org/0000-0001-7265-583X
DOI: http://dx.doi.org/10.17515/resm2025-1268ic1016rs

problems are greatly reduced. This contributes to the production of geopolymer concrete from polymeric sodium aluminosilicate hydrate gel (N-A-S-H), compared to conventional concrete that made from calcium silicate hydrate gel (C-S-H) [5].

Arunkumar et al. [6] stated that the low-calcium fly ash is used as a binder for creating geopolymer concrete. To achieve the strength characteristics, the fly ash-based geopolymer concrete needs a high concentration of alkaline solution and a 24 hrs heat curing time at 60˚C. Additionally, Ameri et al. [7] study the optimal curing temperature and alkali activator/binder ratio. The results demonstrated that the alkali activator/binder ratio was 0.55 and the compressive and flexural strengths were strong when heat curing at about 90˚C. Therefore, temperature curing is required to produce geopolymer concrete with the appropriate strength characteristics. Nevertheless, since the temperature promotes the geopolymerization process at high moderate temperatures (between 80 and 90 ˚C) the geopolymer concrete samples demonstrated greater compressive strengths [8]. According to the research by Görhan and Kürklü's [9], the compressive strength increases when heat curing (at 65 and 85°C) is increased from 5 to 24 hrs. It was obtained that curing for longer than 24 hrs had no apparent effect on strength.

The microstructure of the materials used for producing the geopolymer concrete matrix determines its strength, which also has significant effects on the matrix's permeability [5]. The porosity has a greater impact on concrete strength than the other characteristics. Consequently, porosity has been identified to be a significant factor influencing the strength of concrete [10]. The effect is also caused by the discontinuous structure of the micro and meso pores. Therefore, it is important to be aware when analyzing information collected by porosimeter because the fine gel pores of geopolymers might obscure the larger pores. A concentration of stress could result from these micros and meso pores. They typically serve as the source of microcracks, which decreases the elastic modulus and mechanical strength [11].

In research carried out by Farhana et al. [12], It was concentrated on the suitable curing conditions, such as curing at 75°C for 18–24 hrs, which produced the geopolymer concrete with low volume of permeable pores and low sorptivity coefficient. In general, increasing the porosity of the geopolymer concrete decreased the compressive strength [13]. Similar findings were noted by Mustofa & Pintowantoro [14] who found a relationship between the compressive strength of geopolymer concrete and its water absorption. When the compressive strength is higher, the more homogeneous and denser the microstructures produced, and it tends to reduce water absorption. The previous studies that are relevant to this study are shown in Table 1.

Table 1. Summary about the previous studies that related to this research study

Author /s	Binder type	Alkali Solution /Binder	Curing T. (˚C)	Properties Examined	Remarks
Josepha et al. [15]	-Low calcium fly ash	- 0.55	100˚C for 24hrs	Compressive, tensile, and flexure strength, modulus of elasticity.	- After 24 hrs of curing for the cube at 100°C, 96.4% of compressive strength for the cube was achieved in 7 days instead of 28 days. - The split and flexural strength increased by 45.5% and 30.6%, respectively
Partha et al. [16]	-Fly ash (class F) - GGBS	- 0.37 - 0.4	Amb. curing at 17–22˚C And 70±10% RH	Compressive, tensile, and flexure strength, Sorptivity and volume of permeable void.	- The compressive strength of geopolymer concrete varies from 27 to 47 MPa. - Within the increase of the slag content, the water absorption is decreased.
Ramuje e et al. [17]	- Fly ash	- 0.35 - 0.4 - 0.45	60˚C for 24 hrs	Compressive and tensile strength.	- The geopolymer concrete reaches its target strength much faster when cured in an oven compared to ambient cured conditions.

Yifei Cui et al. [18]	-Fly ash (class F)	- 0.5	80˚C for 24 hrs	Compressive and tensile strength, modulus of elasticity, and microstructural properties.	- The compressive strength in 7 days varies within a range of values between 28.99 and 46.18 MPa. - The splitting strength ranged between 2.66 and 4.19 MPa. - The elastic modulus values changed between 16.74 and 24.2 GPa.
Ylmaz et al. [19]	-Low calcium fly ash	- 0.5	-Amb. curing (20±3˚C and RH 65± 10%) -Heat curried (40˚C, 60˚C , and 80˚C) for 24, 48, and 72 hrs	Compressive strength, flexure strength, water absorption, void ratio, freeze–thaw conditions, and resistance to elevated temperatures.	- The maximum value of compressive strength was achieved at 80°C after 72 hrs of curing. - The curing time and temperature significantly reduced the weight loss in geopolymer mortars subjected to high temperatures.

Through reviewing previous studies, the most of these studies focus only on mechanical properties. This research aimed to find study related to permeability characteristic, and try to cover this gap. Three parameters have been considered:

- The effect of curing condition (24, 70˚C).
- The effect of alkali activator to fly ash ratio (A/F).
- The effect of superplasticizer content (S.P).

An environmentally friendly substitute for Portland cement is geopolymer concrete. Because of its strength, durability, and lower environmental effect, the optimum mix design was utilized in this study to contribute to real-life applications in a variety of construction sectors, including infrastructure, restorations, and pavements. Thus, the aim of this study was to enhance the characteristics of geopolymer concrete in order to simultaneously decrease permeability and increase strength.

2. Experimental Program

2.1. Materials

The primary components of the materials used in this research are fly ash as a binder, fine and coarse aggregate as aggregate, water, superplasticizer as a high range water reducer, and sodium hydroxide and sodium silicate as an alkaline activator. Low calcium fly ash (class F) from the EUROBUILD company has been used in this research as a source of silicates and aluminum. Table 2 illustrates fly ash's chemical composition and Figure 1 show the low calcium fly ash (class F) that used in this research.

Fig. 1. Low calcium fly ash (class F)

Table 2. Chemical analysis of fly ash

Com.	Na_2O	MgO	Al_2O_3	SiO_2	P_2O_5	SO_3	K_2O	CaO	MnO	Fe_2O_3
Mass %	0.08	1.27	25.39	47.69	0.16	0.37	1.56	7.93	0.14	11.72

The fine aggregate that has been used in this research was natural river sand. River sand has a fineness modulus of 2.96 and a specific gravity of 2.67. The sand sieve analysis is shown in Table 3, while the grading of the used fine aggregate is shown in Figure 2-a. Crushed gravel with a maximum particle size of 14 mm was used as the coarse aggregate in geopolymer concrete mixes. The physical properties of coarse aggregate are explained in Table 3, and the grading of the used coarse aggregate is shown in Figure 2-b. The fine and coarse aggregate that has been used in this research are shown in Figure 3 (a and b).

Table 3. Physical Properties for fine aggregate and coarse Aggregate

Physical properties	Fine Aggregate	Coarse Aggregate
Specific gravity	2.67	2.65
Absorption	0.48	0.4
Sulphate content	0.072	0.065
Fineness modulus	2.96	2.96

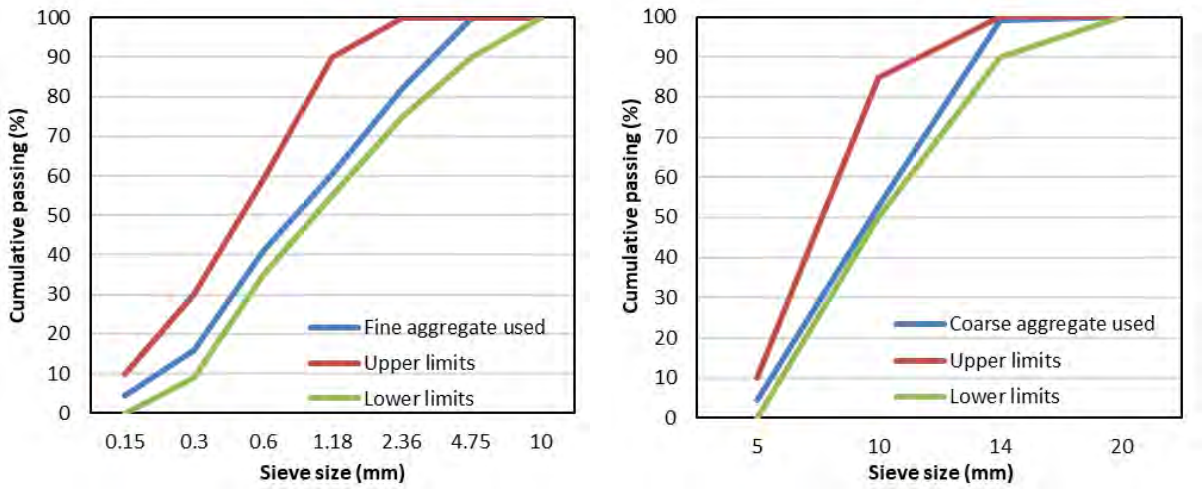

(a) (b)

Fig. 2. Sieve analysis of (a) fine aggregate, (b) coarse aggregate

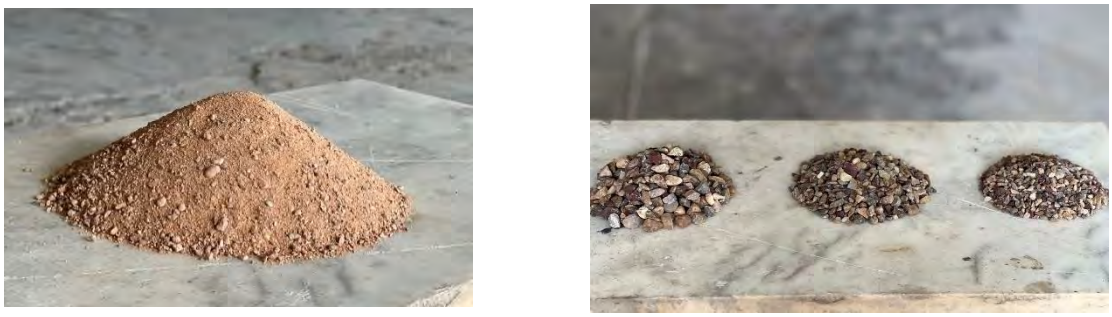

(a) (b)

Fig. 3. The aggregate (a) fine aggregate, (b) coarse aggregate

The fly ash-based geopolymer concrete has been generated more workability by adding a high rang water reducer (Type GS). This type of superplasticizer is based on modified sulfonated naphthalene formaldehyde condensate and conforms to (ASTM C494–2005, Type F) as shown in Figure 4-a.

In this research the Pure water has been used to produce various concrete mixtures, the preparation of the alkaline activator that uses in the mixture by a combination of sodium hydroxide (NaOH) and sodium silicate (Na_2SiO_3) solutions as shown in Figure 4-b. Table 4 shows the properties of sodium hydroxide and sodium silicate solutions, respectively.

Table 4. Properties of sodium silicate and sodium hydroxide.

Sodium silicate		Sodium hydroxide	
Properties	Value	Properties	Value
Ratio of SiO_2/Na_2O	2.4	Chemical formula	NaOH
Na_2O% by weight	13.4	Molecular mass	40
SiO_2% by weight	32.5	Sodium hydroxide NaOH%	99.3
Density-20°Baume	51	Sodium carbonate Na_2CO_3%	0.6
Specific Gravity (g/cm^3)	1.54	Sodium chloride NaCL	0.01
Appearance	Hazy	Sodium sulphate Na_2SO_4(ppm)	50
-	-	Iron oxides	0.002

(a) (b)

Fig. 4. (a) Superplasticizer (b) The alkaline activator

2.2 Casting and Curing of Samples

A sodium hydroxide solution was prepared by dissolving a pellet of sodium hydroxide in distilled water. The NaOH solution's 8 M concentration was maintained for all mixture. The solution left to complete the interaction for at least 24 hrs before using it. For improving the workability, superplasticizer added to the alkaline liquid to obtain in the end final alkaline liquid. One day after the prepared alkaline liquid, the casting process begins by combining the dry material (fly ash and aggregate) in a pan mixer for three minutes, as shown in Figure 5.

The next step, fresh concrete was produced by mixing the dry materials with the alkaline liquid in a pan mixer for more than four minutes. Subsequently, the preparation of the wet mixture was immediately put into molds. A compaction done by manual strokes and then by applying vibrating table for 15-20 second as shown in Figure 6.

After casting the samples were wrapped in nylon to prevent excessive evaporation. The samples were placed in an oven set at 70°C for 24 hrs after casting (this is the specific rest period for this work). This procedure was performed according to the common degree from previous studies, which was taken into consideration in this study. The samples were taken out of the oven and stored in the laboratory until the day of the test. These steps are illustrated in Figure 7, while the mix design of all geopolymer concrete mixtures produced in this study is presented in Table 5.

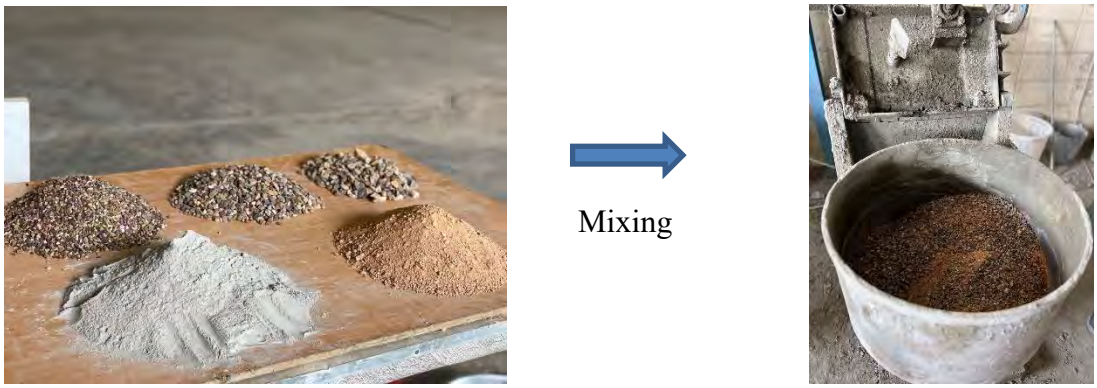

Fig. 5. Dry material (fly ash and aggregate) before and after mixing

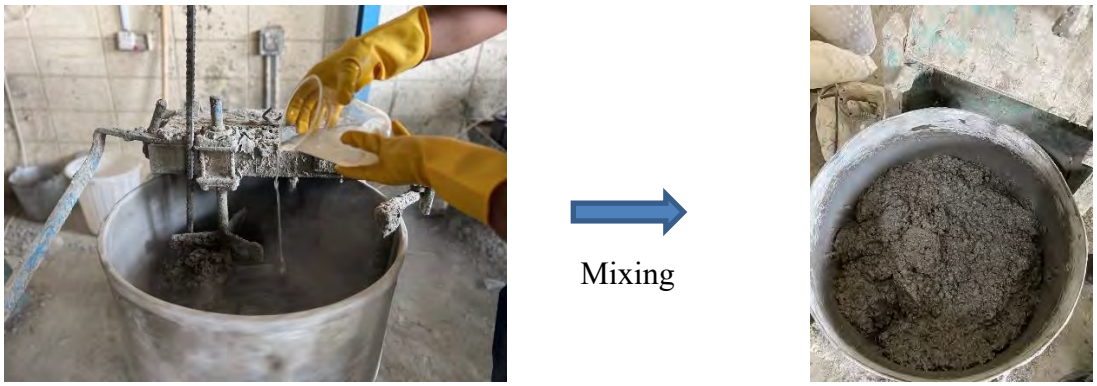

Fig. 6. Preparation the wet mixture

Fig. 7. The steps of curing geopolymer concrete mixes

Table 5. The mix design of geopolymer concrete

Details	Mixes	Coarse (kg/m³)			Sand (kg/m³)	Fly ash (kg/m³)	NaOH (kg/m³)	Na_2SiO_3 (kg/m³)	S.P	A/F	Curing T.
		12.5 mm	10 mm	5 mm							
GM-1	GM11	300	400	495	670	400	51	129	1.5%	0.45	Amb.
	GM12	300	400	495	670	400	51	129	1.5%	0.45	70°C
GM-2	GM21	300	400	495	670	400	51	129	1.5%	0.5	70°C
	GM22	300	400	495	670	400	51	129	1.5%	0.55	70°C
GM-3	GM31	300	400	495	670	400	51	129	2%	0.45	70°C
	GM32	300	400	495	670	400	51	129	2.5%	0.45	70°C

2.3 Testing Program

The geopolymer concrete was filled in layers of slump cone and compacted with a tamping rod in three layers. Slump test was done immediately after mixing according to ASTM specifications (ASTM C143-03), and the fresh density for geopolymer concrete was done according to (ASTM C138-01a). According to (ASTM C642-2004), cubes of 100 mm were used for the water absorption test. The water absorption is usually measured by drying the samples in an oven at 105°C until its

weight remains constant. After the cubes getting dried, the samples were submerged in water for 7 days until their weight remained constant. The water absorption test for the geopolymer concrete is shown in Figure 8-a. Oven dried samples of 100 mm were placed in a pan and submerged in water level about 5 mm above the bases of the samples. The bottom sections of the samples sides that flanked the inflow face were covered with waterproof adhesive to stop water absorption. Figure 8-b shows the sorptivity measurement for geopolymer concrete.

(a) (b)

Fig. 8. Permeability test (a) absorption, (b) sorptivity

The compressive strength of mixes was measured according to (B.S 1881:part 116 :1989) as shown in Figure 9-a. For each mix of 100 mm cubes were tested at age of 1,7, and 28 days from casting within loading rate of 0.3 MPa/s. Three cubes were tested for each mix, and the average was determined. The cylinder samples of 150 × 300 mm loaded under a testing equipment within 3000 kN capacity is used to measure the modulus of elasticity. The modulus of elasticity for the geopolymer concrete samples tested at age 28 days is calculated by averaging three samples using a digital extensometer dial gauge with an accuracy of 0.002 mm fixed around the cylinder according to (ASTM 469-02) as shown in Figure 9-b. The flexural tensile strength for the geopolymer concrete samples that shown in Figure 9-c, has been conducted on prismatic samples measuring of 100 x 100 x 400 mm under two-point loading using a hydraulic testing machine (LIYA) with a 200 kN capacity according to (ASTM C78-02). The average of three samples was used to determine the flexural strength at 28 days of age.

(a) (b) (c)

Fig. 9. Mechanical test (a) compressive strength (b) modulus of elasticity (c) flexural strength

3. Results with Discussion

3.1 Fresh properties Results

The slump values of geopolymer concrete mixtures are shown in Table 6. It shows that the slump values of the geopolymer concrete base mix (GM11 and GM12) had slump ranging values from 35 to 40 mm. The results show that the increase in A/F ratio to (0.5 and 0.55) increases the workability of (GM21 and GM22) mixes between 60-80 mm compared to the control mix (GM12). According to Ketana et al. [20] the workability will increase when increasing the alkali activator solution (AAS) to fly ash (FA) ratio (AAS/FA) in geopolymer concrete. In addition, Memon et al. [21] showed that the workability of the freshly produced geopolymer concrete was determined to be affected by the alkaline activator/fly ash ratio, and the effect increased as the ratio increased from (0.3 to 0.4). While using higher S.P dosages (2% and 2.5%) in (GM31 and GM32) mixes, it leads to increasing the workability and thus increasing the slump between 110-120 mm compared with the control mix, respectively. Superplasticizer is frequently used to enhance the fresh characteristics of concrete and obtain good flowability for the fresh mix [22]. Additionally, the workability of fresh geopolymer concrete enhanced with the commercially available superplasticizer based on naphthalene [22]. Figure 10 shows the slump test results for geopolymer concrete base mix (GM12), geopolymer concrete (GM21) mix, and geopolymer concrete (GM31) mix.

Table 6. Slump values for geopolymer concrete mixes

Mix	GM11	GM12	GM21	GM22	GM31	GM32
Slump (mm)	38	40	100	114	150	162

(a) (b) (c)

Fig. 10. Sump test: (a) geopolymer concrete base mix (GM12) (b) geopolymer concrete (GM21) mix (c) geopolymer concrete (GM31) mix

All geopolymer concrete mixes had fresh density values between 2400 and 2500 kg/m3, according to the fresh density test results. The fresh density of all geopolymer concrete mixtures is shown in Table 7.

Table 7. Fresh density of all geopolymer concrete mixes

Mix	GM11	GM12	GM21	GM22	GM31	GM32
Fresh density (kg/m^3)	2453	2493	2502	2447	2483	2461

3.2 Permeability Tests

The Permeability properties of mixes can be evaluated based on the water absorption, and sorptivity.

3.2.1 Water Absorption

By measuring water penetrability, such as sorption, permeability, and absorption, the concrete durability can be controlled. Diffusion, absorption, and permeability through porous material allow liquid penetration into concrete through it. In addition to this, pores in concrete are crucial for permitting liquid to flow through the substance [23]. Mahmoud et al. [24], show that the water absorption and permeability for the dense microstructure of geopolymer concrete reduced by 38% and 64.6%, respectively when compared to conventional concrete. The difference in water absorption between all geopolymer concrete mixes is shown in Figure 11. The results show that using ambient curing temperature leads to increasing the water absorption of the (GM11) mix by about 2% compared to the control mix (GM12). In terms of A/F ratio, the water absorption of the (GM21 and GM22) mixes increase by 25% and 30%, when A/F ratio was increase to 0.5 and 0.55, respectively. Also, it shows that the uses of the high dosage of S.P (2% and 2.5%) leading to an increase in the water absorption of the (GM31 and GM32) mixes by 55% and 58% compared with control mix. Furthermore, the results show that because of the high range water reducing admixture air entraining effect, the high range water reducing admixture will increase the porosity [25].

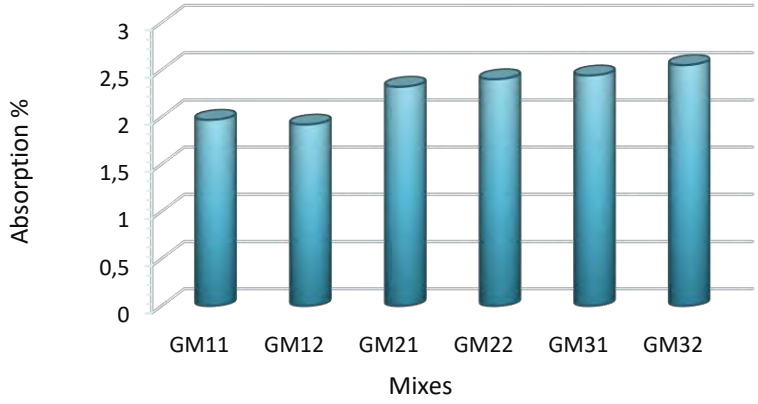

Fig. 11. Water absorption of geopolymer concrete mixes

3.2.2 Sorptivity

Concrete durability can be determined by a water sorptivity test which measures a medium's capacity to absorb or desorb liquid by capillarity (the flow of liquids in porous materials produced by the surface tension of capillaries). [26]. The geopolymer concrete mixes showed lower sorptivity in comparison to the conventional concrete mix within a water/cement ratio of 0.50 (about 40 MPa strength level) [23]. Concrete that has a lower sorptivity shows higher resistance to absorbing water. A high sorptivity value indicates a closely connected porous structure or low tortuosity of the pore network [12].

The ambient curing temperature that used in (GM11) mix leading to increasing the sorptivity by about 18% compared with control mix (GM12), while the elevated curing temperature that used helped in reducing the sorptivity of geopolymer concrete. The results show that curing at 75°C for 18 to 24 hrs produced geopolymer concrete with a low volume of permeable voids and a low sorptivity coefficient [12]. According to Gunasekara et al. [27], the geopolymer concrete shows an interconnected pore network within a variety of pores having different diameters when heat curing for the samples within 4, 8, and 12 hrs. In terms of A/F ratio, the sorptivity of the (GM21 and GM22) mixes increased when A/F ratios were increased to (0.5 and 0.55) by 16% and 18% compared with the control mix. Also, the use of the high dosage of S.P (2% and 2.5%) leads to an increase in sorptivity of the (GM31 and GM32) mixes by 27% and 40% compared with the control mix (GM12). The sorptivity test results for each geopolymer concrete mix are shown in Figure 12.

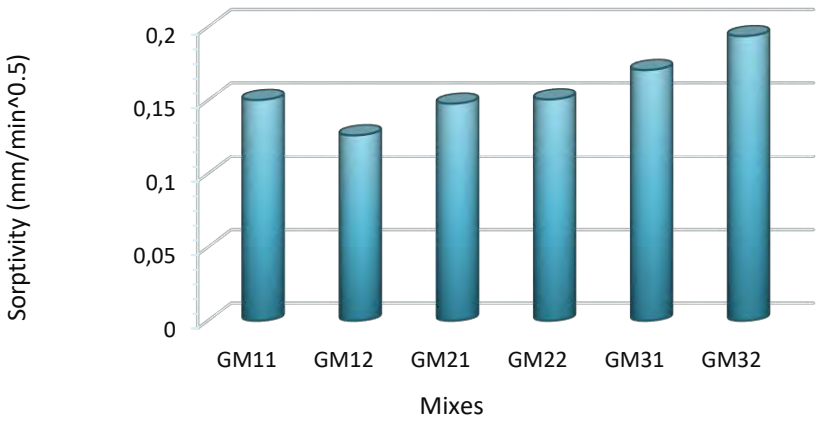

Fig. 12. Sorptivity of geopolymer concrete mixes

3.3 Mechanical Properties

The mechanical properties of mixes can be evaluated based on the compressive strength, modulus of elasticity, and flexural strength.

3.3.1 Compressive strength

In terms of curing temperature, our research results show a significant improvement by about 32% in compressive strength that was achieved by curing the concrete samples at a higher temperature (GM12) mix in 28 days. Bhavsar et al. [22] established that curing the geopolymer concrete samples at a higher temperature and longer curing period results in higher compressive strength. Gunasekara et al. [28] studied the effect of increasing the curing temperature on strength of geopolymer concrete samples, the results showed that strength increased when the curing temperature increased from 30°C to 75°C, with a maximum strength of 50.0 MPa achieved at an optimal temperature of 75°C. Also, the results in our research show that using a high A/F ratio resulted in decreasing the compressive strength of the (GM21 and GM22) mixes compared with the conventional geopolymer concrete mix (GM12) by about 24% and 30%, respectively.

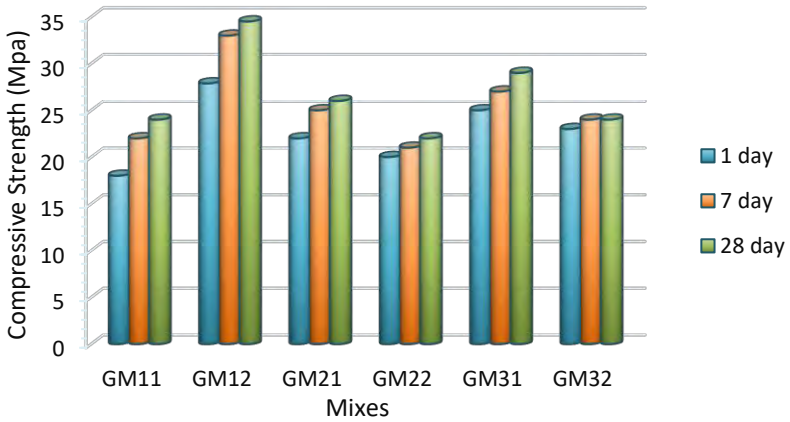

Fig. 13. Compressive strength of geopolymer concrete mixes

Mustafa et al. [29] stated that the geopolymer concrete samples that made within alkaline solution/fly ash ratios of 0.35 and 0.40 resulted in a higher compressive strength and more homogenous matrices. This illustrates how porosity of matrices influences compressive strength. Therefore, the compressive strength will increase as porosity reduces [10]. Furthermore, our research results shown that in terms of S.P, increasing dosage of S.P to (2% and 2.5% leads to a decrease in the compressive strength of the (GM31 and GM32) mixes by about 15% and 28%,

respectively. Figure 13 shows the effect of using different parameters on the compressive strength of geopolymer concrete at 1, 7, and 28 days.

3.3.2 Modulus of Elasticity

In terms of curing temperature, our research results demonstrated that when using room temperature curing, it will decrease the modulus of elasticity at age 28 days for (GM11) mix by 19% compared with control mix. Noushini et al. [27] stated that the heat curing has been identified to significantly increase the temperature of the chemical reaction (alkali-fly ash) that occurs in 100% fly ash-based geopolymer concrete. The development of the microstructure and the transformation of the structure of the geopolymer concrete from amorphous to crystalline during heat curing [27]. Also, the results in our research show that in terms of A/F ratio, the modulus of elasticity of the (GM21 and GM22) mixes decrease when A/F ratio is increased to (0.5 and 0.55) by 11% and 22% compared with control mix. Aliabdo et al. [25] found that after 28 days, the modulus of elasticity of the fly ash-based geopolymer concrete was affected by the ratio of alkaline solution to fly ash. Evidently, the alkaline solution to fly ash ratio affects the 28-day modulus of elasticity similar to that of compressive and tensile strengths. Furthermore, our research results shown that in terms of S.P dosage, increasing dosage of S.P to (2% and 2.5% leads to a decrease in the modulus of elasticity of the (GM31 and GM32) mixes compared with control mix by about 23% and 25%, respectively. The decrease in fly ash-based geopolymer concrete characteristics is shown in compressive strength, splitting tensile strength, and modulus of elasticity, and there is an increase in porosity and absorption due to higher chemical admixture concentration because of the increase in microstructure pores [25]. Figure 14 shows modulus of elasticity of all geopolymer concrete mixes.

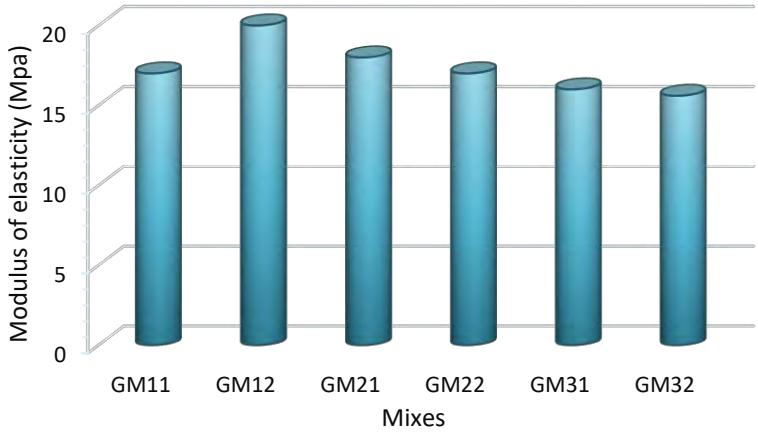

Fig. 14. Modulus of elasticity of geopolymer concrete mixes

3.3.3 Flexural Strength

The geopolymer concrete outperformed the conventional concrete in terms of flexural strength. Mustafa et al. [30] showed that after 28 days, the flexural strength of geopolymer concrete increased approximately within 13%, whereas that of conventional concrete increased only within 3%. In terms of curing temperature, our research results demonstrated that the mix (GM11) curing at room temperature shows lower flexural strength by about 6% compared with control mix (GM12) at age 28 days. Özbayrak et al. [31] show that the highest flexural strength value for geopolymer concrete was obtained after one day of oven curing at 70°C. Nath et al. [32] showed that the geopolymer concretes outperformed conventional concrete when compared in terms of flexural strength. Also, the results in our research show that in terms of A/F ratio, the flexural strength of the (GM21 and GM22) mixes decreased when A/F ratio is increased to (0.5 and 0.55) by 24% and 31% compared with the control mix. Neupane et al. [33] show that the flexural strength of the geopolymer concrete for each mixture at 28 and 90 days with different alkaline solution/binder ratios (A/B) will increase up to A/B of 4.0 and then decrease. Furthermore, our

research results show that in terms of S.P dosage, increasing the dosage of S.P to (2% and 2.5% leads to a decrease in the flexural strength of the (GM31 and GM32) mixes compared with the control mix by about 7% and 9%, respectively. Figure 15 shows the flexural strength of all geopolymer concrete mixes.

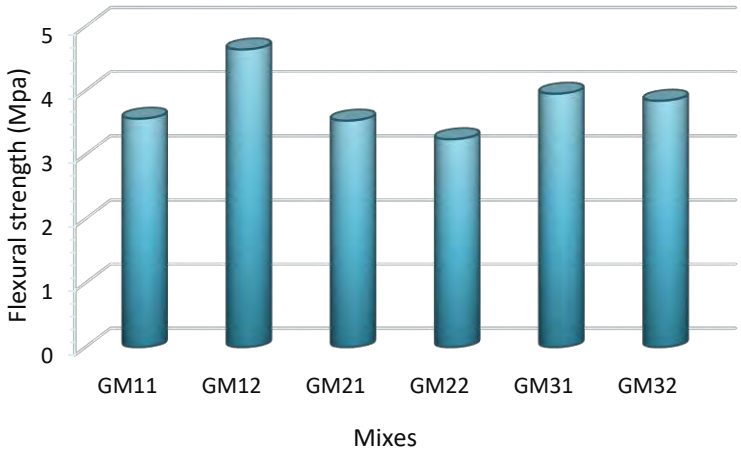

Fig. 15. Flexural strength of geopolymer concrete mixes

4. Conclusion

This study aims is to examine the consequence of the most effected parameters on permeability characteristic for the geopolymer concrete. The mechanical properties were also studied in this research and an attempt was made to link the effect of porosity to the strength properties. Three parameters were selected in this study to show the effect of: curing condition (24, 70°C), the difference in proportions of alkali activator to fly ash ratio (A/F) and the dosage superplasticizer content (S.P). The experiments were conducted on the parameters that specified in the study plan, through two experiments for each parameter. For the experiments that conducted on the first parameter (curing condition) it was found that the results of the first experiment at (24°C) was lower compared to heat temperature at (70°C) that selected in the second experiment, as there was an improvement in compressive strength by 32%, 2.6% for the absorption, and 19% for the sorptivity. When considering the experiments that conducted on the second parameter (alkali activator to fly ash ratio) it was found that the results of the first experiment for 0.45 (A/F) ratio was higher compared to 0.5, and 0.55 (A/F) ratio that used in the second experiment, as there was an improvement in compressive strength by 36%, 27% for the absorption, and 18% for the sorptivity. Finally, for the experiments that conducted on the third parameter (superplasticizer content) it was found that the results of the first experiment at 1.5% (S.P) was higher compared to 2% and 2.5% dosage superplasticizer content (S.P) that used in the second experiment, as there was an improvement within 30% in compressive strength likewise for the absorption within same ratio, and 50% for the sorptivity. The results showed that using heat curing at temperature (70°C), (A/F) at a rate of (0.45) and superplasticizer (S.P) at a dosage of (1.5%) gave the best results. Furthermore, similar trends were seen in the relationship between residual compressive strength, water absorption, and sorptivity of geopolymer concrete samples when the strength of the concrete was related to the permeability characteristic.

In further work, the researcher should focus on incorporating detailed microstructural analysis techniques such as Scanning Electron Microscopy (SEM), X-ray Computed Tomography (XCT), or Mercury Intrusion Porosimetry (MIP) to provide direct evidence of porosity, void distribution, and internal morphology of the geopolymer matrix. This will help validate the qualitative observations made in this study and offer deeper insights into the relationship between microstructure and mechanical behavior. In addition, future experimental work should include a statistically significant number of replicates for each test condition. This will enable the calculation of standard

deviation, confidence intervals, and allow for statistical significance testing. Such measures are essential for improving the reliability, reproducibility, and scientific rigor of the findings.

References

[1] Thomas BS, Yang J, Bahurudeen A, Chinnu SN, Abdalla JA, Hawileh RA, Hamada HM. Geopolymer concrete incorporating recycled aggregates: A comprehensive review. Cleaner Materials. 2022 Mar 1;3:100056. https://doi.org/10.1016/j.clema.2022.100056

[2] Hama SM, Hama SM, Kwad JE. Optimum amount of silica fume for best structural concrete properties. InAIP Conference Proceedings 2023 Mar 27 (Vol. 2651, No. 1). AIP Publishing. https://doi.org/10.1063/5.0105813

[3] Singh NB, Middendorf B. Geopolymers as an alternative to Portland cement: An overview. Construction and Building Materials. 2020 Mar 20;237:117455. https://doi.org/10.1016/j.conbuildmat.2019.117455

[4] Tahwia AM, Abd Ellatief M, Bassioni G, Heniegal AM, Abd Elrahman M. Influence of high temperature exposure on compressive strength and microstructure of ultra-high performance geopolymer concrete with waste glass and ceramic. Journal of Materials Research and Technology. 2023 Mar 1;23:5681-97. https://doi.org/10.1016/j.jmrt.2023.02.177

[5] Ahmed LA, Frayyeh Q, Abd Al Ameer O. Geopolymer as a green concrete alternative to portland cement concrete: article review. Journal of Al-Farabi for Engineering Sciences. 2022 Jun;1(2). https://doi.org/10.59746/jfes.v1i1.16

[6] Hassan A, Arif M, Shariq MJ. Effect of curing condition on the mechanical properties of fly ash-based geopolymer concrete. SN Applied Sciences. 2019 Dec;1:1-9. https://doi.org/10.1007/s42452-019-1774-8

[7] Morla P, Gupta R, Azarsa P, Sharma A. Corrosion evaluation of geopolymer concrete made with fly ash and bottom ash. Sustainability. 2021 Jan 4;13(1):398. https://doi.org/10.3390/su13010398

[8] Arunkumar K, Muthukannan M, Sureshkumar A, Chithambarganesh A, Devi RR. Mechanical and durability characterization of hybrid fibre reinforced green geopolymer concrete. Research on Engineering Structures and Materials. 2022;8(1):19-43.

[9] Althoey F, Zaid O, Alsulamy S, Martínez-García R, de Prado Gil J, Arbili MM. Determining engineering properties of ultra-high-performance fiber-reinforced geopolymer concrete modified with different waste materials. Plos one. 2023 May 22;18(5):e0285692. https://doi.org/10.1371/journal.pone.0285692

[10] Castillo H, Collado H, Droguett T, Sánchez S, Vesely M, Garrido P, Palma S. Factors affecting the compressive strength of geopolymers: A review. Minerals. 2021 Nov 25;11(12):1317. https://doi.org/10.3390/min11121317

[11] Mohammed AA, Ahmed HU, Mosavi A. Survey of mechanical properties of geopolymer concrete: A comprehensive review and data analysis. Materials. 2021 Aug 20;14(16):4690. https://doi.org/10.3390/ma14164690

[12] Farhana ZF, Kamarudin H, Rahmat A, Al Bakri AM. A study on relationship between porosity and compressive strength for geopolymer paste. Key Engineering Materials. 2014 Mar 20;594:1112-6. https://doi.org/10.4028/www.scientific.net/KEM.594-595.1112

[13] Chen S, Ruan S, Zeng Q, Liu Y, Zhang M, Tian Y, Yan D. Pore structure of geopolymer materials and its correlations to engineering properties: A review. Construction and Building Materials. 2022 Apr 18;328:127064. https://doi.org/10.1016/j.conbuildmat.2022.127064

[14] Joseph B, Mathew G. Influence of aggregate content on the behavior of fly ash based geopolymer concrete. Scientia Iranica. 2012 Oct 1;19(5):1188-94. https://doi.org/10.1016/j.scient.2012.07.006

[15] Deb PS, Nath PR, Sarker PK. Strength and permeation properties of slag blended fly ash based geopolymer concrete. Adv. Mater. Res. 2013;651:168-73. https://doi.org/10.4028/www.scientific.net/AMR.651.168

[16] Ramujee K, PothaRaju M. Mechanical properties of geopolymer concrete composites. Materials today: proceedings. 2017 Jan 1;4(2):2937-45. https://doi.org/10.1016/j.matpr.2017.02.175

[17] Cui Y, Gao K, Zhang P. Experimental and statistical study on mechanical characteristics of geopolymer concrete. Materials. 2020 Apr 2;13(7):1651. https://doi.org/10.3390/ma13071651

[18] Yılmaz A, Degirmenci FN, Aygörmez Y. Effect of initial curing conditions on the durability performance of low-calcium fly ash-based geopolymer mortars. Boletín de la Sociedad Española de Cerámica y Vidrio. 2024 Jul 1;63(4):238-54. https://doi.org/10.1016/j.bsecv.2023.10.006

[19] Ketana NS, Reddy VS, Rao MS, Shrihari S. Effect of various parameters on the workability and strength properties of geopolymer concrete. InE3S Web of Conferences 2021 (Vol. 309, p. 01102). EDP Sciences. https://doi.org/10.1051/e3sconf/202130901102

[20] Al Bakri Abdullah MM, Kamarudin H, Abdulkareem OA, Ghazali CM, Rafiza AR, Norazian MN. Optimization of alkaline activator/fly ash ratio on the compressive strength of manufacturing fly ash-

based geopolymer. Applied Mechanics and Materials. 2012 Jan 13;110:734-9. https://doi.org/10.4028/www.scientific.net/AMM.110-116.734
[21] Memon FA, Nuruddin MF, Demie S, Shafiq N. Effect of superplasticizer and extra water on workability and compressive strength of self-compacting geopolymer concrete. Research Journal of Applied Sciences, Engineering and Technology. 2012 Mar 1;4(5):407-14. https://doi.org/10.1109/NatPC.2011.6136362
[22] Bhavsar GD, Talavia KR, Suthar DP, Amin MB, Parmar AA. Workability properties of geopolymer concrete using accelerator and silica fume as an admixture. International Journal for Technological Research in Engineering. 2014;1(8):541-4.
[23] Olivia M, Sarker P, Nikraz H. Water penetrability of low calcium fly ash geopolymer concrete. Proc. Iccbt2008-A. 2008 Jun;46:517-30.
[24] Mahmoud AS, Khoshnaw GJ, Mahmood FI. Engineering and Microstructures Characteristics of Low Calcium Fly Ash Based Geopolymer Concrete. Eurasian Journal of Science and Engineering. 2017 Jun 1;2(2):27-39. https://doi.org/10.23918/eajse.v2i2p27
[25] Aliabdo AA, Abd Elmoaty M, Salem HA. Effect of water addition, plasticizer and alkaline solution constitution on fly ash based geopolymer concrete performance. Construction and Building Materials. 2016 Sep 15;121:694-703. https://doi.org/10.1016/j.conbuildmat.2016.06.062
[26] Castro J, Bentz D, Weiss J. Effect of sample conditioning on the water absorption of concrete. Cement and Concrete Composites. 2011 Sep 1;33(8):805-13. https://doi.org/10.1016/j.cemconcomp.2011.05.007
[27] Noushini A, Castel A. The effect of heat-curing on transport properties of low-calcium fly ash-based geopolymer concrete. Construction and Building Materials. 2016 Jun 1;112:464-77. https://doi.org/10.1016/j.conbuildmat.2016.02.210
[28] Gunasekara C, Dirgantara R, Law DW, Setunge S. Effect of curing conditions on microstructure and pore-structure of brown coal fly ash geopolymers. Applied Sciences. 2019 Aug 2;9(15):3138. https://doi.org/10.3390/app9153138
[29] Chindaprasirt P, Chareerat T, Sirivivatnanon V. Workability and strength of coarse high calcium fly ash geopolymer. Cement and concrete composites. 2007 Mar 1;29(3):224-9. https://doi.org/10.1016/j.cemconcomp.2006.11.002
[30] Mustafa Al Bakri AM, Abdulkareem OA, Kamarudin H, Nizar IK, Rafiza AR, Zarina Y, Alida A. Microstructure studies on the effect of the alkaline activators of fly ash-based geopolymer at elevated heat treatment temperature. Appl Mech Mater. 2013 421: 342-348. https://doi.org/10.4028/www.scientific.net/AMM.421.342
[31] Özbayrak A, Küçükgöncü H. Microstructural Analysis of Low-Calcium Fly Ash-Based Geopolymer Concrete with Different Ratios of Activator and Binder Under High Temperatures.
[32] Nath P, Sarker PK. Flexural strength and elastic modulus of ambient-cured blended low-calcium fly ash geopolymer concrete. Construction and Building Materials. 2017 Jan 15;130:22-31. https://doi.org/10.1016/j.conbuildmat.2016.11.034
[33] Neupane K, Chalmers D, Kidd P. High-strength geopolymer concrete-properties, advantages and challenges. Advances in Materials. 2018 Jun 25;7(2):15-25. https://doi.org/10.11648/j.am.20180702.11
[34] Bellum RR, Nerella R, Madduru SR, Indukuri CS. Mix design and mechanical properties of fly ash and GGBFS-synthesized alkali-activated concrete (AAC). Infrastructures. 2019 May 2;4(2):20. https://doi.org/10.3390/infrastructures4020020

Research on Engineering Structures & Materials
www.jresm.org

Research Article

Performance of the pile group foundation supporting multi-story building under repeated earthquakes

Omar K. Ali [*,1,a], Jasim M. Abbas [2,b], Laith K. Al-Hadithy [1,c]

[1]*Department of Civil Engineering, Al-Nahrain University, Baghdad, Iraq*
[2]*Department of Civil Engineering, Diyala University, Baqubah, Iraq*

Article Info

Article History:

Received 22 Oct 2025
Accepted 17 Nov 2025

Keywords:

Pile groups;
Sandy soil;
Small scale model;
Multi-story steel frame;
Shaking table device;
Kobe earthquake;
Multiple earthquakes

Abstract

Most studies on the seismic behavior of group piles have focused on the pile's behavior under a single earthquake. However, low to moderate seismicity zones often experience multiple successive shocks. In this study, the seismic behavior of pile groups supporting a 10-story building was investigated through a series of experiments under the influence of the Kobe earthquake for three consecutive times with a time interval of 15 min. The tests conducted first involved designing and constructing a 1:20 scale model of a 10-story steel building supported by a 3x3 aluminum pile group foundation with L/D of 16. The tests were conducted on dense dry sand with 70% relative density. The results include the performance of piles and structures in terms of vertical and lateral displacements. The findings indicated that the tilting angle of the pile cap diminished gradually with the application of each subsequent earthquake, decreasing by a factor of three following the second earthquake (0.15°) and by a factor of 4.7 after the third shock (0.08°), in comparison to the initial angle (0.46°). Additionally, the residual lateral displacements observed in the 10-story building during successive earthquakes reflected a continuous decline, with the rates of reduction during the second and third earthquakes being 2.5 and 9.4 times, respectively, in relation to the first earthquake. Conversely, the residual lateral displacement measured at the pile cap exhibited a steady increase over the course of the seismic events, recording increases of 10.5 and 20 times during the second and third earthquakes, respectively, with comparison to the first earthquake.

© 2026 MIM Research Group. All rights reserved.

1. Introduction

Earthquakes consider once of the utmost devastating natural adversities, posing a serious threat to life and property. Despite the efforts made in designing earthquake-resistant structures, it is still challenging to cope with the uncertainties regarding the quality of design against seismic loading. Concerns start to rise about the performance of multi-story and high-rise structures, mainly caused by the increase of post-constructed changes and unwanted stresses on structural bases and foundations. Group piles, widely used in multi-story constructions to reduce settlement and increase capacity, are of utmost importance.

In past few years, much investigate has studied the seismic behavior of piles in the case of earthquakes. These studies have served to raise the level of understanding of seismic piles in many aspects. However, so far, little research has been carried out to study the effects caused by multiple or successive earthquakes; this is because the information on the real actions in the structures affected by these conditions is very limited. Previous research such as that performed by [1] examines the impact of earthquake sequences on the seismic behavior of structures, taking into account soil-foundation-structure interaction (SFSI), by shake table experiments. The findings

*Corresponding author: omar.civ23@ced.nahrainuniv.edu.iq
[a]orcid.org/0000-0003-0148-0918; [b]orcid.org/0000-0002-3157-0351; [c]orcid.org/0000-0002-0857-9788
DOI: http://dx.doi.org/10.17515/resm2025-1279ic1022rs

indicate that the mainshock resulted in more significant soil settlement and elevated acceleration relative to the aftershocks, attributable to the densification of the sand following the initial seismic event. Study conducted by [2] using shaking table tests, the soil and foundation interaction significantly affected shaping structural responses under repeating seismic events. The laboratory model reflected soil conditions in shaking table simulations using real ground motion records from the Wenchuan earthquake, capturing site effects like seismic wave amplification. Results showed that as structural damage accumulated, the model's dynamic properties became increasingly sensitive to soil–foundation interaction, revealing a natural frequency reduction of up to 52% across main vibration modes. This indicated degradation of the RC frame's internal stiffness and increased soil flexibility impact. At high seismic intensities, the foundation–soil system failed to restrain large displacements, leading to inter-story drifts as high as 1/43 and posing near-collapse risks. Consequently, the study underscores that the soil–foundation–structure system's flexibility must be factored into seismic performance evaluations, as soil effects amplify vulnerabilities during the successive event

A numerical analysis to explore the nonlinear interactions between soil, piles, and structures for pile foundations subjected to multiple seismic load scenarios in both soil types liquefiable and non-liquefiable [3]. The investigation examined various parameters, including the responses of piles to different seismic intensities and soil conditions. Findings indicated that the performance of piles is notably affected by soil liquefaction, resulting in heightened lateral displacements and bending moments. Sahare et al. [4] examined how sloping ground conditions and following seismic occurrences affect the kinematic behavior of pile groups in soils prone to liquefaction. The research attentive on several parameters such as the spacing between piles, ground slope angles, and the influences of liquefaction during successive shaking events. The results indicated that further seismic activities additional intensify the resulting damage. The study steered by [5] intended to assess the behavior of hybrid foundations in assuaging the effects of liquefaction under strong sequential earthquakes consuming both numerical and experimental modeling methods. The results showed that hybrid foundations pointedly diminished lateral displacement and settlement caused by consecutive seismic action. [6] studied soil–pile–structure interaction (SPSI) and its impact on seismic vulnerability of pile-supported buildings during exposed to successive earthquakes through created nonlinear numerical models. The findings indicated that the sequence earthquakes further elevated the likelihood of structural damage compared to single mainshocks, with results showing significant shifts in fragility curves. The research conducted by [7] examines the processes of liquefaction and re-liquefaction in sand, as well as the response of pile groups to repeated shaking. The study employs centrifuge modeling to analyze factors such as excess pore pressure, soil settlement, lateral displacements, and bending moments in pile group foundations during successive seismic events. The results indicate that each instance of shaking diminishes the potential for re-liquefaction by enhancing soil density and stiffness, which in turn reduces excess pore pressures. Nonetheless, the existence of pile groups has the potential to modify this behavior by augmenting bending moments and lateral displacements as a result of the interactions occurring between the soil and the structures. [8] investigate the response of vertical pile foundations when subjected to a series of seismic activities, including the primary shock and subsequent aftershocks, by simulating the kinematic interaction, which refers to the relative movement between the soil and the pile during repeated seismic inputs. The findings reveal those relative displacements between the soil and foundation, bending moments in the piles, and inertial effects manifest variably across successive seismic events.

Therefore, this research seeks to examine the effect of three consecutive earthquakes on the seismic behavior of group pile foundations embedded in sandy soil. The unique aspect of this investigate is presenting the results of a practical study included test system consist of group piles foundation embedded in sandy soil and supporting 10-story building, while most previous researches approach solely one aspect (foundation or structure).

2. Experimental Setup and Testing

2.1 Ten-Story Building

To carry out the present investigation, it is necessary to first design and build a small-scale multi-story structure. A model consisting of 10 stories was developed based on the design proposed by [9]. Each story was structured as a single bay frame with an orientation in both directions, facilitating an accurate depiction of slender structures. The prototype's original span width and story height were established at 4 meters and 3 meters, respectively. As a result, the dimensions of the laboratory model building (length, width, and height) were proportionately reduced using a 1:20 scale factor. The beams and columns were crafted from square steel hollow sections measuring (19.05×200×19.05) mm and (19.05×19.05×150) mm, with a thickness of 1.5 mm. Steel plates, each with a 6mm thickness and dimensions of (200×200) mm, were utilized as panels for the building model. The structure was designed to maintain uniform mass across its stories. (Fig. 1), depicts the 10-story building employed in this investigation.

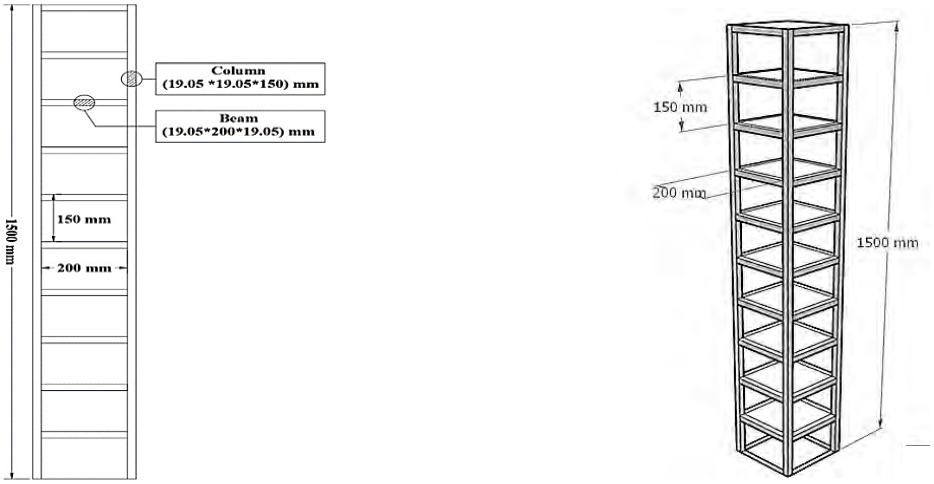

(a) (b)

Fig. 1. Ten-story steel structure details (a- front view b- 3D view)

2.2 Pile Group Description

In the current study, the piles utilized are fabricated from aluminum pipe tubes, a material widely recognized for its suitability in experimental assessments in similar investigations, as referenced by [10,11]. These piles comprised of closed-end aluminum tubes with circular cross sections, featuring an external diameter (D) of 16mm and a wall thickness of 1.5 mm. The embedding length to the diameter ratio is specified as L/D = 16. The configuration of the pile group is arranged in a 3x3 formation, with a spacing of 7D between individual piles, that conforms to the standards established by [12]. A high-strength steel plate is employed as the piles cap in this investigation, as illustrated in (Fig. 2).

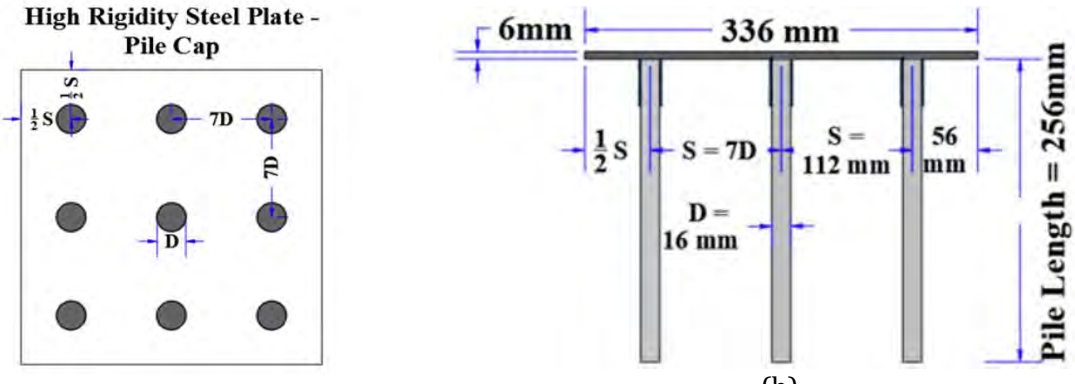

(a) (b)

Fig. 2. Pile cap details: a-top view and b- front view

2.3 Laminar Soil Container

(Fig. 3) illustrates the aluminum laminar soil container, which possesses a cross-sectional dimension of (800 x 800) mm and a height of (850) mm. [13] suggested that to reduce wall side friction, the container's height-to-diameter ratio should be one or lower. As a result, the container height-to-width ratio is considered appropriate. The container is filled with sandy soil of 70% Relative Density (Dr) to depth of 750 mm, divided into five layers, each with a height of 150 mm. The properties of the soil utilized in this research are outlined in Table 1.

Table 1. Physical and mechanical properties of soil used

Soil Property	Value	Standard of Test
Relative Density, Dr %	70	-
Max. Unit Weight, γ_{max} [kN/m^3]	18.47	ASTM D 4253 (2000)
Min. Unit Weight, m_{int} [kN/m^3]	15.96	ASTM D 4254 (2000)
Dry Unit Weight, γ_d [kN/m^3]	17.63	-
Water Content, Wc %	19	ASTM D2216 (2010)
Specific Gravity, Gs	2.64	ASTM D854 (2014)
Sand, %	98.4	-
Fine content %	1.6	-
Effective Size, D_{10} [mm]	0.16	
Mean Size, D_{30} [mm]	0.26	
Mean Size, D_{60} [mm]	0.42	
Coefficient of Uniformity, C_u	2.63	ASTM D422 (2007)
Coefficient of Curvature, C_c	1.01	
Soil Classification (USCS)[1]	(SP), Poorly-graded sand	ASTM D2487 (2010)
Particle Shape	Sub-rounded to sub-angular with low sphericity to high sphericity	-
Soil Color	Yellow (Pale yellow)	-
Friction Angle, Ø	39°	ASTM D4767 (2011)
Cohesion, c [kN/m^2]	0	

2.4 Laminar Soil Container

The experimental study was conducted using a single-degree-of-freedom shaking table device situated at the University of Diyala [14]. This apparatus has been engineered to simulate the conditions of the Kobe earthquakes, and operated by a servo motor that can achieve a maximum acceleration of 1.8 g and accommodating 10 kN payload capacity, and it can reach up to 2g when unloaded. The device is capable of producing input wave frequencies that range from 0.1 Hz to 50 Hz. Fig. 3 shown the details of shaking table model and essential components.

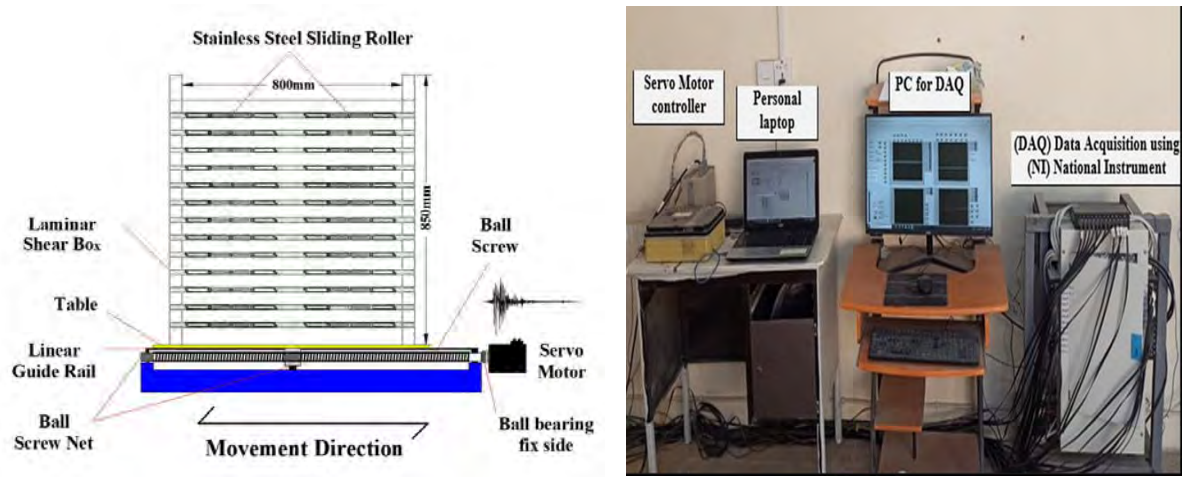

(a) (b)

Fig. 3. Description of shaking table model [14]: a) Details of shaking table model and laminar soil container and b) Details of digital data acquisition system

To assess both vertical and lateral displacements at the piles cap, four Linear Variable Differential Transformers (LVDTs) were utilized, as shown in (Fig. 4). LVDT1 (referred to as L1) employed to measuring the lateral displacement at the top side of the 10-strory building and WVDT2 (L2) employed to measuring the lateral displacement at the piles cap. While LVDT3 (L3) and LVDT4 (L4) used to measuring the vertical displacements at the piles cap side that directly subjected to seismic load and the opposite side, respectively. A comprehensive diagram of the testing system is provided in (Fig. 4). The peak ground acceleration and tremors duration for the Kobe earthquake model inputted was (0.82 g) and (48 sec) respectively [15].

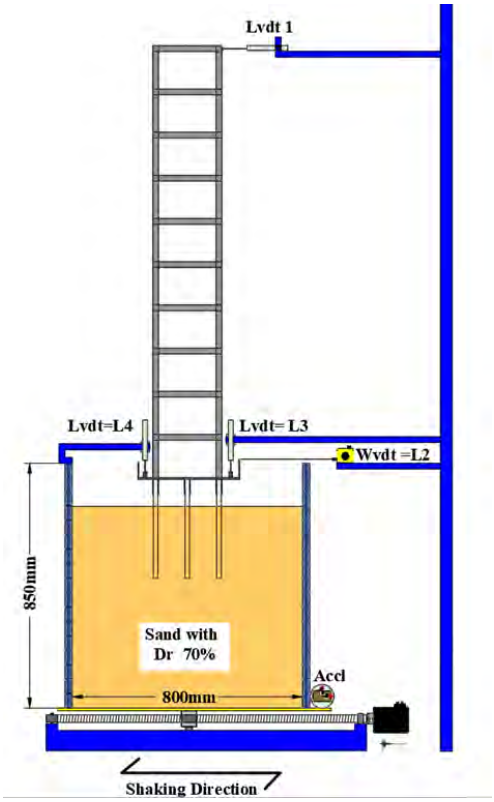

Fig. 4. Test system diagram

3. Result and Discussion

In this part, the vertical and lateral displacement at the pile cap as well as the acceleration in four different locations has been represented and analyzed. The Kobe earthquake was applied on the test model three times in succession with a 15-minute interval between each successive earthquake to give the soil stability after the applied earthquake and before applied the next earthquake (i.e., re-applying the earthquake to the test model). The principal aim of this interval was to permit the soil fabric stabilization via rearrangement of particle and densification subsequent to the first shock, thus ensuring a consistent and quantifiable initial condition for the ensuing event. This approach mitigates the risk of conflating the cumulative effects of progressive fabric alterations with the specific response to each individual shock.

3.1 Vertical Displacement

Fig. 5 demonstrated the relation between the vertical displacement and the time history at both sides of piles cap for the 10-story building during exposing to three consecutive shocks. It can be seen that the waveforms recorded at both sides of pile caps across the three successive shocks have approximately the same trend and show no significant vertical displacement roughly until 7 seconds, indicating that the earthquake impact did not directly affect the piles cap during this initial phase. This stable interval presumably signifies the period prior to the interaction of seismic waves with the foundation piles, wherein considerable forces are exerted. After this point, a noticeable change in vertical displacements which recorded at the pile cap sides were observed in between second ten to second fifteen for the three consecutive shocks, that can be attributed to the

increasing intensity of the seismic activity simulated in the laboratory environment. This period is likely aligned with the peak shaking, which exerted maximum stress on the piles cap, resulting in rapid variations (i.e., rotation) in vertical displacement values. This observation indicates that the earthquake's intensity was sufficient to exceed the initial resistance of the piles group foundation. After a duration of 20 seconds, the rates of observed vertical displacements stabilize at each shock of the three consecutive shocks applied.

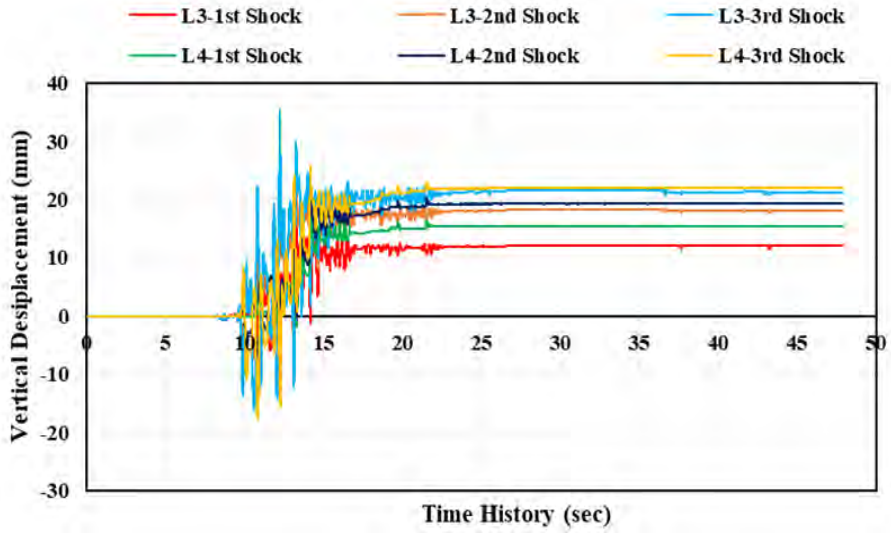

Fig. 5. Vertical displacement of the pile cap vs. time history for the 10-story building under three consecutive earthquakes

Fig. 6 presents the relation between the vertical displacement of the Piles cap (peak and residual values) with number of shocks applied. The data illustrated in this figure clearly indicates that the peak vertical displacement values recorded at the pile cap side that directly subjecting to seismic activity larger than that at the opposite side. In contrast, the residual values show reverse response. This observation holds true for all values recorded during the three consecutive earthquakes that were applied. For instance, during applied the first shock, the peak vertical displacement value recorded at the cap side directly exposing to seismic activity equal to 20.8 decrease to 18.8 mm at the opposite side, indicating a reduction in peak displacement between both side of about 9.5%. Subsequently, a modest elevation in the reduction ratio of peak displacement between the both sides of the pile cap is noted, assessed at around 15.1%, upon the application of the second shock. This ratio experiences an additional rise to reach 27.8% with the application of the third shock. This phenomenon can be attributed to the fact that seismic loading induces an asymmetric interaction between the soil, piles, and building. Specifically, the leading (front) piles row experiences greater horizontal resistance and axial compression compared to the trailing row, particularly when seismic event integrates kinematic drag of soil with the inertial forces exerted by the building. The effect of group pile shadowing causes the cap to rocking towards direction of the seismic load. This results in an increased compression on the leading piles row, while the trailing row experiences reduced compression, and occasionally, transient conditions of tension or gapping may arise among those piles. Concurrently, the process of repeated seismic load results in local densification of the surrounding sand (characterized by volumetric strains of ratcheting), thereby amplifying down-drag (negative skin friction) along the greater sheared leading-pile shafts. This combination of higher cyclic densification and greater compressive axial force, leads to a more substantial vertical displacement. This observation is consistent with the findings of [16,17]. With respect to the observed values of residual vertical displacement, it can be noticed that the residual displacement increased from 12.12 mm at the direct side to 15.54 mm at the opposite pile cap side, indicating an inflation rate of approximately 28.1% during applied the first shock event. Moreover, a comparison of the residual vertical displacement between both sides of pile cap during applying the second and third shocks revealed increasing rates of (6 and 3.3) % respectively. The potential explanations for the increased residual displacement observed at the side of the pile cap opposite to the seismic load possibly due to the cumulative finding of its distinct stress

trajectory experienced during seismic loading. While the cap side directly subjected to seismic load shows high vertical displacement due to several direct pulses at the earthquake's peak, the opposite side undergoes fully-reversed, more symmetric cyclic shear. This change in shear strain, coupled with the cap rocking that diminishes confining stress on the opposite side during forward motion, renders the soil in that area more vulnerable to cyclic compaction across numerous cycles. Consequently, the opposite side accrues a more substantial amount of residual displacement from a greater number of effective stress cycles, ultimately surpassing the peak vertical displacement experienced at the pile cap side exposed directly to the seismic shock, and this agree with [17,18].

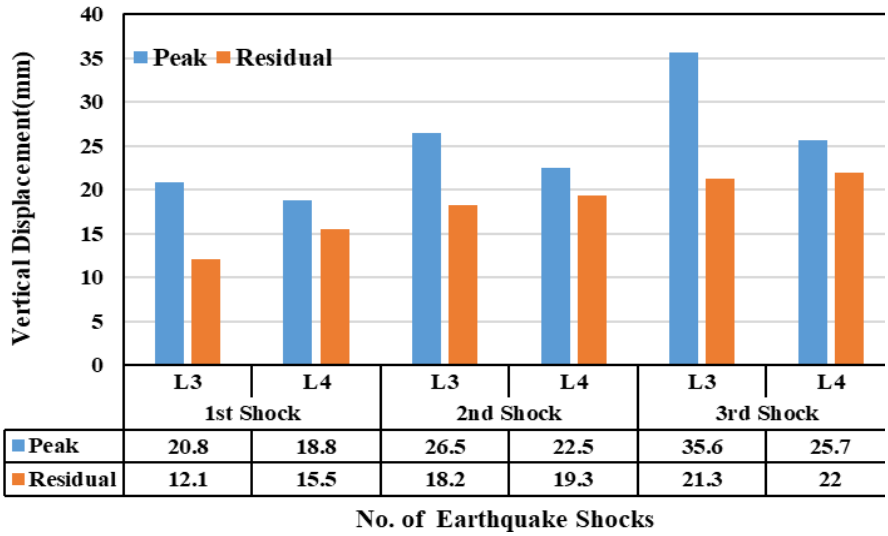

Fig. 6. The relation between the vertical displacements of the pile cap and the number of earthquakes applied

Another important finding is that the effect of multiple earthquakes on the piles cap tilt. It can be seen that the vertical displacement measured at both piles cap sides show increasing values with each subsequent earthquake applied. That can be inferred clearly, when applied the second earthquake, the peak vertical displacements measured on the pile cap side directly subjected to seismic load, and the opposite side, increased by 27.4% and 19.7% respectively, relative to the values obtained during the first shock event. After applying the third shock, the peak values witnessed an additional increase, reaching 71.2% on the direct side and 36.7% on the opposite side when contrasted with their original values at the first shock. Furthermore, similar behavior was observed in case of residual vertical displacement. Following the second shock, the value of residual vertical displacements measured on both direct and opposite cap sides exhibited increases of 50.4% and 24.5%, respectively, relative to the data acquired during the first earthquake. Subsequently, after the third earthquake application, the residual displacements surged to even higher levels, reaching 76% on the direct side and 42% for on the opposite side, when compared to its values recorded during the first seismic event. It seems possible that these results of increase in vertical displacements observed following each earthquake may be attributed to factors such as cumulative plastic deformation. Dense sand exhibits plastic deformation when subjected to multiple seismic loading. Although dense sand initially demonstrates a degree of resistance to deformation owing to its stiffness, each successive earthquake induces further rearrangement of soil particles. Consequently, this phenomenon results in a cumulative reduction in soil volume, which in turn contributes to the observed increases in vertical displacements. and this agree with [19, 20 and 21]. Another possible explanation for this result is that it is due to stress redistribution, and the effects of soil-pile interaction. These mechanisms gradually diminish the soil's capacity to withstand vertical displacement, leading to increased deformation and pile cap tilting with each seismic occurrence and this agree with [17].

3.2 Lateral Displacement

The results of lateral displacements measured at the piles cap and at the top side of 10 story building under the three successive earthquakes are shown in Fig. 7. It can be noticed that the resulting measurement lines for both pile cap and 10-story building show approximately the same

trend with a difference in behavior describe the directional response of structural elements during seismic loading as they experience oscillations due to the dynamic forces especially for the period between 8-22 seconds which represent the peak excitation of the earthquake. After a duration of 22 seconds, the rates of observed lateral displacements stabilize at each earthquake of the three consecutive earthquakes applied.

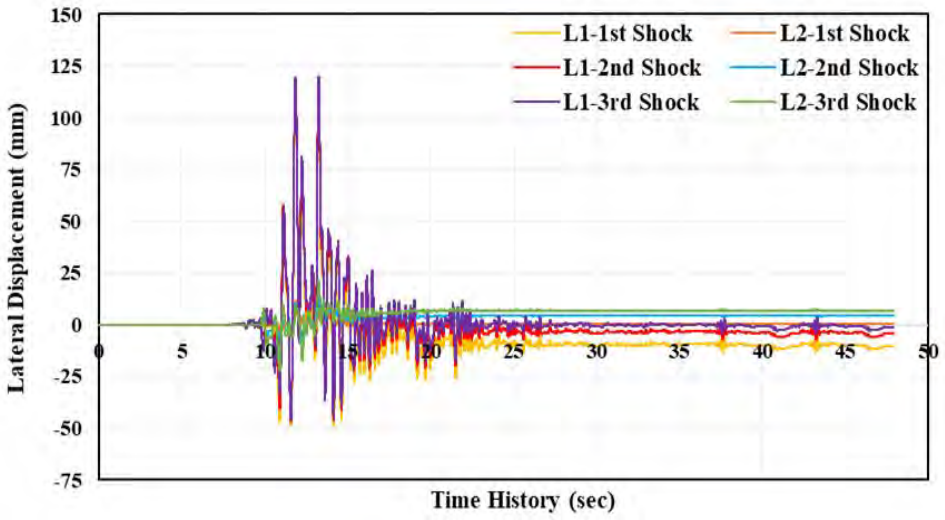

Fig. 7. The relation between lateral displacement vs time history forthe-10 story building under three consecutive earthquakes

Fig. 8 presents the relation between the lateral displacement (peak and residual values) measured at the top side of 10-story building, as well as the pile cap by (L1 and L2) respectively, during applied of the three successive earthquakes. As shown in Figure 8, the peak lateral displacement for the 10-story building which recorded by (L1) increases slightly across the three earthquakes: 114 mm in the first, 117.5 mm in the second, and 120.1 mm when the earthquake is applied for third time. That's mean that the ratio of increasing in value of peak lateral displacement for 10-story building during the second and third earthquakes greater than that recorded at the first earthquake by 3.1% and 5.4% respectively. This trend suggests an accumulation effect, likely due to minor degradation or residual displacement in the building after each seismic event. As for the peak lateral displacement for piles cap measured by (L2), its increases progressively: 15.6 mm at the first earthquake, 18.5 mm at the second earthquake, and 21.7 mm at the third earthquake. This designate that the increasing ratio in peak lateral displacement value for piles cap throughout the second and third earthquake events larger than that noted at the first shock by (18.61 and 39.14) % respectively. The observed upward trend designates in the peak values of lateral displacement that the pile-soil system is undergoing a gradual increase in response, with improvement in energy dissipation over time producing lower values of residual lateral displacements recorded at the end of each shock.

Moreover, these findings show that the 10-story building displays higher peak lateral displacements when compared to those measured at the piles cap. This performance can be attributed to several factors, including dynamic amplification effects, geometric influences and energy transmission. The building height amplifies the seismic forces that it encounters, producing greater lateral displacements occurring at the higher stories of building. Conversely, the piles cap undergoes a relative decrease in lateral displacement, which can be attributed to mechanism of energy dissipation occurring during interactions between soil and piles, in addition the effects of damping by the adjacent soil. The diminished lateral displacements at the piles cap designate its closeness to the source of seismic event in addition to the soil capacity to energy dissipate. Alternatively, the 10-story building shows larger lateral displacements, associated with the increase in the arm of moment and reduced lateral stiffness in the building higher storis and this accord with [22-24]. Moreover, the increase in peak lateral displacements during multiple earthquake events can be explained by a combination of factors, such as residual deformations in the interaction between the soil and pile, nonlinear behavior of the soil, and dynamic amplification

effects within the structure. These factors lead to a reduction in stiffness of pile foundations and an escalation of seismic forces at the upper stories of building, which in turn results in increased lateral displacements. This observation aligns with the conclusions drawn [25,26].

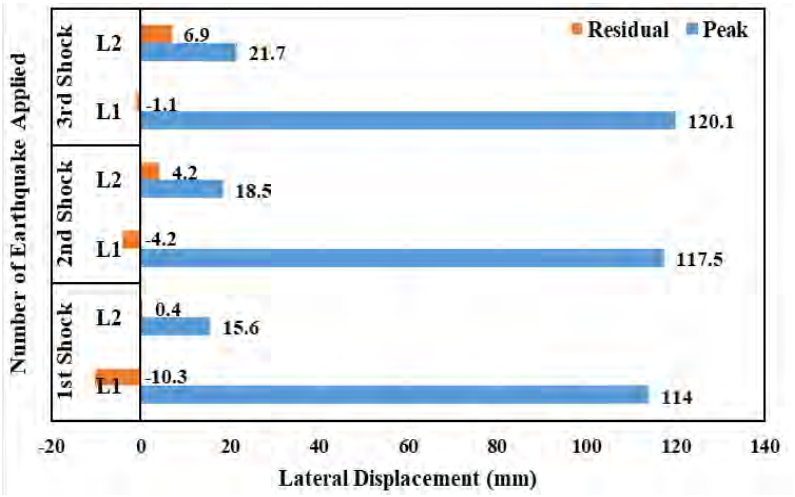

Fig. 8. The relation between the lateral displacements and the number of earthquakes applied

Another observation is that the residual lateral displacement of the 10-story structure during consecutive earthquake events showed a progressive decline, reducing from -10.43 mm in the first earthquake event to -4.21 mm in the second, and further to -1.11 mm in the third event (the negative values indicate that the structure is inclining in the direction of the earthquake). This trend reveals that the reduction rate in the residual lateral displacement of the 10-story structure, during the second and third earthquake events were (147.62 and 845.54) % respectively, compared to the first earthquake event. This behavior suggests that the building exhibits improved stabilization over time, as indicated by the decrease in residual displacements as the system adapts to the effects of successive seismic loading. Conversely, the value of residual lateral displacement noted at the pile cap, demonstrated a progressive increase during applying the earthquake events, 0.41 mm through the first seismic event, reach to 4.19 mm through the second seismic event and 7.99 mm through the third seismic event.

This behavior indicates that the rise in the residual lateral displacement observed at the pile cap through the second and third earthquakes was 10.5 and 20 times greater, respectively, than that recorded during the first earthquake. A potential reason for this phenomenon may be attributed to the nonlinear characteristics, which significantly influences the seismic response of the pile group foundations. As seismic events continue, the soil-pile interaction can result in greater lateral displacements, attributed to a reduction in group pile stiffness due to soil-pile interaction. Furthermore, the cyclic loading from successive seismic events may enhance the cumulative impacts on the response of pile's group, resulting in increased residual lateral displacements at the piles cap as time progresses. The overall behavior of the building is primarily determined by dynamic and geometric factors. Such behavior is consistent with well-recognized theories of soil-structure interaction and the principles underlying seismic dynamics and this agree with [27,28]. Another interesting result is that the measurements of residual lateral displacement noted at the piles cap increased during the three consecutive earthquakes, while decreasing at the 10-story structure. This performance is linked to the cumulative effects of energy dissipation and residual deformation taking place within the soil. As each earthquake occurs, the sand around the piles can undergo densification or minor plastic deformation, leading to a decrease in stiffness and allowing for increased lateral displacement at the piles cap. Moreover, the piles cap experiences greater displacements as a result of the lateral forces impacting it, in conjunction with the restricted lateral displacement of the adjacent soil, which contributes to an increase in the residual lateral displacement at the cap. In case of 10-story building, the inertia of the building aids in dissipating seismic forces, thereby leading to diminished displacements observed at the top side of building. These findings this consistent with [29, 30].

4. Conclusions

This research intended to investigating the impact of applying multiple earthquakes on the seismic performance of the pile group supporting 10-Story building in terms of vertical and horizontal displacement. The following conclusions are drawn from the above analyses:

- Multiple sequential earthquakes notably increases both the peak and residual vertical displacements on piles cap supported multi-story structure. The repeated occurrence of seismic events leads to a deterioration of the soil's stiffness, resulting in progressive vertical displacements, especially on the piles cap side directly exposure to seismic waves.
- The tilting angle observed in the pile cap demonstrated a gradual decrease with each consecutive shock experienced, measuring 0.46° immediately following the first ground motion event, 0.15° after the occurrence of the second motion, and finally reaching 0.1° after the third shock event. This notable decline in the tilt observed after the first earthquake strongly indicates a a redistribution of forces or soil densification. Such changes in tilt can provide crucial insights into the dynamic responses of pile group- structure systems to repeated seismic activity.
- Comparing the pile cap tilting angles against the serviceability limit of Bjerrum (1/150) for angular distortion, the results indicated that the tilting angle during the first shock (0.46°) unacceptable and exceeds the allowable limit, suggesting that the pile group-structure system may experience serviceability issues. In contrast, the tilting angle measured during the second and third shocks within the acceptable limit, this can be attributed to the fact that the first shock produce larger uneven settlement with compare to the subsequent shocks.
- The values of residual lateral displacements observed for the 10-story building model during successive seismic events exhibited a progressive reduction, the rate of decrease during applying the second and third shocks were about 2.5 and 9.4 times respectively, in comparison to the value measured at the first shock event. In contrast, the residual lateral displacement values recorded at the pile cap, exhibited a gradual increase throughout the seismic events, recording (10.5 and 20) times during the application of the second and third shocks, respectively, with compare to the value noted during applying the first shock.

Acknowledgement

The authors are grateful for the financial support towards this research by the Civil Engineering Department, College of Engineering, Al Nahrain University, as a Ph.D. student, in accordance with university order (6710/2/3ج.ر) dated 4/7/2022.

References

[1] Qin X. Shake table study on the effect of mainshock-aftershock sequences on structures with SFSI. Shock Vib. 2017; 2017:9850915. https://doi.org/10.1155/2017/9850915
[2] Qiao YM, Lu DG, Yu XH. Shaking table tests of a reinforced concrete frame subjected to mainshock-aftershock sequences. J Earthquake Eng. 2022; 26 (4): 1693 1722. https://doi.org/10.1080/13632469.2020.1733710
[3] Maheshwari B, Sarkar R. Seismic behaviour of piles in non-liquefiable and liquefiable soil. Bull Earthq Eng. 2021;19(12):5515-32. https://doi.org/10.1007/s10518-021-01244-4
[4] Sahare A, Ueda K, Uzuoka R. Influence of the sloping ground conditions and the subsequent shaking events on the pile group response subjected to kinematic interactions for a liquefiable sloping ground. Soil Dyn Earthq Eng. 2022; 152:107036. https://doi.org/10.1016/j.soildyn.2021.107036
[5] Kumar R, Takahashi A. Efficacy of a hybrid foundation to mitigate liquefaction-induced effects under strong sequential ground motions. In: Earthquake Engineering and Disaster Mitigation. Singapore: Springer; 2023. https://doi.org/10.1007/978-981-99-0081-7_10
[6] Souheyla S, Yahiaoui D, Demagh R. Seismic fragility evaluation of soil-pile-structure interaction effects subjected to mainshock-aftershock records. Int J Comput Civil Struct Eng. 2023;19(3):92-113. https://doi.org/10.22337/2587-9618-2023-19-3-92-113
[7] Padmanabhan G, Ueda K, Maheshwari BK, Uzuoka R. Reliquefaction behavior of sand and response of pile group subjected to repeated shaking sequence using centrifuge model experiments. Soil Dyn Earthq Eng. 2024; 182:108741. https://doi.org/10.1016/j.soildyn.2024.108741

[8] Rajeswari, J.S. Kinematic response of vertical pile foundation under multiple earthquakes. In: Sarkar R, Kumar A, Maheshwari B, editors. Foundation Dynamics. ICRAGEE 2024. Lecture Notes in Civil Engineering, vol 572. Singapore: Springer; 2025. p. 10-20. https://doi.org/10.1007/978-981-96-1417-2_10
[9] Khoshnoudian F, Kiani M. Modified consecutive modal pushover procedure for seismic investigation of one-way asymmetric-plan tall buildings. Earthq Eng Eng Vib. 2012;11(2):221-32. https://doi.org/10.1007/s11803-012-0112-6
[10] Ali A, Karkush M, Aljorany A. Numerical modeling of connected piled raft foundation under seismic loading in layered soils. J Mech Behav Mater. 2023;32. https://doi.org/10.1515/jmbm-2022-0250
[11] Mahdi K, Alaa A, Karrar A, Ahmed AS. Behavior of partially connected piled raft foundation under seismic loading. Mag Civ Eng. 2024;17(4):1280.
[12] El Hoseny M, Ma J, Dawoud W, Forcellini D. The role of soil structure interaction (SSI) on seismic response of tall buildings with variable embedded depths by experimental and numerical approaches. Soil Dyn Earthq Eng. 2023; 164:107583. https://doi.org/10.1016/j.soildyn.2022.107583
[13] Garnier J. Size effect in shear interfaces. In: Proceedings of a Workshop on Constitutive and Centrifuge Modelling: Two Extremes, Monte Verita; 2002; Monte Verita, Switzerland. p. 335-46.
[14] Noman BJ, Albusoda BS. Impact of vertical vibration on group piles during earthquake loading: Experimental findings. Civ Eng J. 2024; 10:174-208. https://doi.org/10.28991/CEJ-SP2024-010-010
[15] Center for Engineering Strong-Motion Data (CESMD). Kobe 1995 Earthquake Strong Motion Data. Sacramento and Menlo Park (CA): CESMD; 2024. Available from: https://strongmotioncenter.org/.
[16] Visuvasam JA, Chandrasekaran SS. Effect of spacing and slenderness ratio of piles on the seismic behaviour of building frames. Buildings. 2022;12(12):2050..https://doi.org/10.3390/buildings12122050
[17] Esmaeili-Falak M, Katebi H, Pourjafar A. Pile-soil interaction determined by laterally loaded fixed head pile group. Geomech Eng. 2021;26(1):13-25.
[18] Zheng G, Sun J, Zhang T, Diao Y. Settlement of a pile under cyclic lateral loads in dry sand. Geotechnique. 2022;73(7):561-71. https://doi.org/10.1680/jgeot.21.00107
[19] Chanda D, Saha R, Haldar S. Seismic behaviour of RC framed building supported on combined piled raft foundation in sandy soil. Arab J Sci Eng. 2024;49(5):145-58. Available from: https://link.springer.com/article/10.1007/s13369-024-09105-3
[20] Zhang HY, Qian DL, Shen C, Dai QQ. Experimental investigation on the dynamic response of pile group foundation on liquefiable ground subjected to horizontal and vertical earthquake excitations. Rock Soil Mech. 2020;41(3): Article 6.
[21] Lu C, Doan M, Chen S, Lin Y. Effective stress analysis for repeated shake-consolidation process of multi-story buildings in liquefiable soils. Comput Geotech. 2024; 134:104-18. https://doi.org/10.1016/j.compgeo.2024.106496
[22] Seed HB, Wong RT, Idriss IM, Tokimatsu K. Moduli and damping factors for dynamic analyses of cohesionless soils. J Geotech Eng. 1986;112(11):1016-32. https://doi.org/10.1061/(ASCE)0733-9410(1986)112:11(1016)
[23] Mylonakis G, Gazetas A. Seismic soil-structure interaction: Beneficial or detrimental? J Earthq Eng. 2000;4(3):277-301. https://doi.org/10.1080/13632460009350372
[24] Chopra K. Dynamics of Structures: Theory and Applications to Earthquake Engineering. 4th ed. Upper Saddle River (NJ): Prentice Hall; 2012.
[25] Kramer SL. Geotechnical Earthquake Engineering. Upper Saddle River (NJ): Prentice Hall; 1996.
[26] Tolentino D, Flores RB, Alamilla JL. Probabilistic assessment of structures considering the effect of cumulative damage under seismic sequences. Bull Earthq Eng. 2018; 16:2133. https://doi.org/10.1007/s10518-017-0285-5
[27] Siri Reddy K, Harini GVS K, Vijayasri T. Nonlinear analysis of soil-pile interaction under seismic loads. In: Proceedings of the International Conference on Advanced Structural Technologies. Singapore: Springer; 2023. p. 331-45. https://doi.org/10.1007/978-981-19-6998-0_30
[28] Hasan MM, Hore S, Al Alim M, et al. Numerical modeling of seismic soil-pile-structure interaction (SSPSI) effects on tall buildings with pile mat foundation. Arab J Geosci. 2024; 18:10. https://doi.org/10.1007/s12517-024-12155-4
[29] Jia K, Xu C, Du X, Cui C, Dou P, Song J. Seismic response comparison and sensitivity analysis of pile foundation in liquefiable and non-liquefiable soils. Earthq Eng Vib. 2023; 22:87-104. https://doi.org/10.1007/s11803-023-2160-5
[30] Zhao H, Zhang F. Seismic response of pile-supported structures considering the coupling of inertial and kinematic interactions in different soil sites. Front Struct Civ Eng. 2024; 18:1350-61. https://doi.org/10.1007/s11709-024-1113-z

Blank Page

Research on Engineering Structures & Materials
www.jresm.org

Research Article

Assessment of water quality in Kirkuk city: Using geographic information systems and multi-linear regression analysis

Shaho Kh. Noori [1,a], Ibrahim J. Naser [2,b], Redvan Ghasemlounia [3,c], Mohammed O. Ibrahim [*,2,d], Aram M. Raheem [2,e], Imran A. Fayyadh [2,f]

[1]*Khasachai Dam, Commission of Dams and Reservoirs, Ministry of Water Resource, Kirkuk, Iraq*
[2]*Civil Engineering Department, University of Kirkuk, Kirkuk, Iraq*
[3]*Department of Civil Engineering, Istanbul Gedik University, Istanbul, Türkiye*

Article Info

Article History:

Received 24 Oct 2025

Accepted 15 Nov 2025

Keywords:

Kirkuk City;
GIS;
Climate change;
Water pollution;
Spatial distribution;
Water quality parameters

Abstract

Climate change, pollution, and the degradation of water quality are making it harder to provide safe drinking water globally. For ensuring water safety, it is important to analyze its chemical and physical properties. Assessing the suitability of tap water for consumption according to World Health Organization (WHO) standards and Iraqi standards using GIS techniques and multi-linear regression analysis in Kirkuk City, Iraq, the study examines fourteen key water parameters across multiple city locations and conducted over 2020 and 2022, including pH, turbidity, conductivity, alkalinity, hardness, various ions, dissolved solids, temperature, and chlorine. GIS mapping was used to visualize the spatial distribution of these parameters, while multi-linear regression analysis was employed to identify statistical relationships between turbidity and other water quality indicators. The pH level of tap water in Kirkuk has been shown to be slightly to moderately alkaline, and turbidity exceeded acceptable limits in some locations and decreased slightly in 2022 from that in 2020. It was observed that total dissolved solids decreased during the period of this study and were under permissible standard limits. Electrical conductivity and total hardness remained stable and acceptable. The concentrations of most of the ions, including calcium, chloride, magnesium, sulfate, sodium, and chlorine, were lower than those of WHO and Iraqi standards. Potassium levels varied, meeting standards in some areas in 2020 but falling below WHO recommendations everywhere by 2022. The regression analysis revealed that turbidity was significantly influenced by total dissolved solids, electrical conductivity, and total hardness, with a strong correlation (R^2 = 0.939), indicating that changes in water quality parameters are interdependent. However, the R^2 value for single linear regression suggests potential variability, emphasizing the need for further data refinement and additional explanatory variables. The study highlights the need for ongoing monitoring and improvement of Kirkuk's water treatment processes, demonstrating the value of GIS-based spatial analysis combined with statistical modeling for identifying areas with compromised water quality and implementing targeted interventions to address these issues.

© 2026 MIM Research Group. All rights reserved.

1. Introduction

Water is one of the most vital natural resources and a crucial national asset, playing a key role in the environment [1]. Water sources can include rivers, reservoirs, glaciers, precipitation, and groundwater, among others. Water services are often indispensable across various economic sectors such as irrigation, livestock development, forestry, agriculture, hydropower generation,

*Corresponding author: m.o.ibrahim@uokirkuk.edu.iq
[a]orcid.org/0000-0002-9511-1744; [b]orcid.org/0000-0001-8986-9711; [c]orcid.org/ 0000-0003-1796-4562; [d]orcid.org/0000-0002-8038-9436; [e]orcid.org/0000-0002-6889-3939; [f]orcid.org/0009-0001-7524-8399
DOI: http://dx.doi.org/10.17515/resm2025-1291ic1024rs

fisheries, and other innovative activities, along with the essential need for drinking water [2]. Surface water is the primary source of water for human consumption, including drinking, agriculture, manufacturing, hydropower generation, and other economic sectors. One of the most pressing environmental issues globally is the decline in water quality due to climate change and rising pollution levels [3]. Water quality assessment involves examining physical, chemical, and biological parameters of specific environments [4]. Excessive levels of certain variables can harm human health [5]. Many underestimates water's importance in societal progress, and their actions often diminish water quality. Addressing this requires lifestyle changes and adherence to drainage regulations at various governmental levels [6]. Water quality evaluation has long involved analyzing physicochemical and biological parameters and examining spatial and temporal variations. Remote sensing, which collects data from a distance, has enabled various technical projects [7, 8]. Geographic Information Systems (GIS) have multiple applications in water management [9]. GIS incorporates mathematical, spatial, and monitoring components, allowing for geographical trend analysis through technological integration [10]. GIS has been used to study aquifer situations [11] and water harvesting criteria [12]. Studies using GIS have evaluated water quality in various locations. Research on the Tigris River showed certain pollutants exceeding permissible limits at specific stations [13,14].

Another study revealed high turbidity levels [15]. The Lower Zab River showed high concentrations of various minerals and chemicals due to factors like weathering, soil structure, runoff, and agricultural activities [16,17]. The Lesser Zab River's water was found to be moderately contaminated and moderately hard to hard, requiring treatment before consumption but suitable for agriculture and aquatic life [18]. A study of the Kirkuk irrigation project revealed several parameters exceeding WHO and Iraqi standards [19]. Research on the Tigris River showed seasonal variations in water quality parameters, with most within permissible limits for Iraqi drinking water regulations [20]. Water quality has decreased due to factors like population growth, industrialization, and urbanization. This study aims to assess tap water quality in the city by comparing samples from different settlements to Iraqi and WHO standards, in addition, the study has attempted to utilize linear regression analysis to predict the water turbidity value in terms of various key water parameters. GIS was used to visualize the spatial distribution of physicochemical parameters, highlighting high-risk areas. These spatial patterns informed the selection of variables used in the MLR model, which then quantified the influence of each parameter on turbidity.

2. Methodology

2.1. Study Area

This study was conducted in downtown Kirkuk, a province in northern Iraq. (Fig. 1) shows the sample locations and outlines the research methodology, including site selection, data collection, GIS analysis, regression modelling, and comparison with WHO and Iraqi water quality standards. As of 2021, Kirkuk was the tenth most densely populated governorate in Iraq, with a population of approximately 1.73 million [21,22].

The water quality parameters provided by the Directorate of Water in Kirkuk cover the years 2020 and 2022. Samples were collected from 15 sampling sites within Kirkuk city, as detailed in Tables 1 and 2, along with their corresponding coordinates. The evaluation of potable water quality relies on analyzing key physicochemical parameters that influence water safety and suitability for human consumption. pH determines acidity or alkalinity, affecting metal solubility and microbial growth, while turbidity indicates suspended particles that may harbor contaminants. Electrical conductivity (E.C.) and total dissolved solids (TDS) reflect the concentration of dissolved ions, impacting taste and potential contamination. Alkalinity and total hardness affect buffering capacity and scaling potential due to the presence of calcium (Ca^{2+}) and magnesium (Mg^{2+}). Chloride (Cl^{-}) and sodium (Na^{+}), frequently originating from industrial effluent or saline intrusion, impact palatability and corrosivity. Both sulphate (SO_4^{2-}) and potassium (K^{+}) are metabolically important, but their concentrations must be tightly regulated to prevent detrimental health effects. Chlorine (Cl^{-}) is a disinfectant used to ensure microbiological safety, while high levels can lead to undesired taste. Finally, water temperature influences solubility, reaction kinetics, and microbial activity.

Monitoring these parameters is critical for assessing water quality trends, identifying pollution sources, and ensuring compliance with WHO and Iraqi standards to safeguard public health and water resource sustainability.

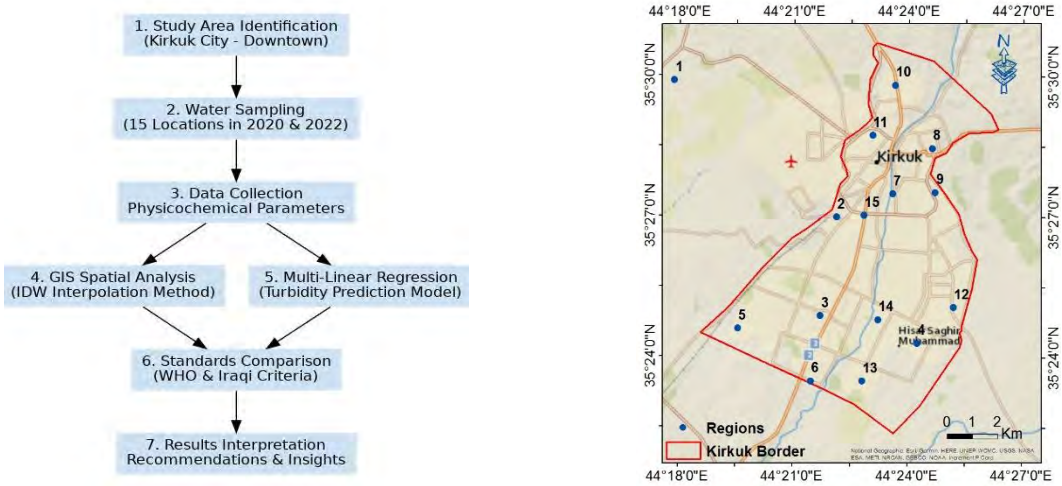

Fig. 1. Flowchart of the methodology and site locations of the water samples

2.2 Spatial Map Plotted by Using GIS

Water quality parameters were generated and evaluated in this study using GIS-based spatial analysis, and the outcomes were compared to WHO and Iraqi criteria. As indicated in Table 1, information was gathered from fifteen locations in Kirkuk City. Although locations 1 and 2 are representative of the same region, two distinct samples, one taken prior to and one following water treatment, were collected from this site. The spatial distribution maps were generated using the inverse distance weighting (IDW) technique. Eq (1) representing this technique is used in GIS [23]:

$$\hat{z}(s_0) = \frac{\sum_{i=1}^{n} z(s_i) d_{i0}^{-2}}{\sum_{i=1}^{n} d_{i0}^{-2}} \quad (1)$$

where $\hat{z}(s_0)$ is the predicted value, $z(s_i)$ is the measurements, d_{i0} is the distance that separate s_0 and s_i. IDW is a common interpolation method used for prediction, where GIS spatial interpolation efficiently estimates unknown areas from various points within calculated data [24, 25]. Principally, GIS provides spatial intelligence and data management capabilities, whereas multi-linear regression delivers the statistical structure for modelling, and the combination of both enables robust spatial analysis and well-informed decision-making in diverse areas such as environmental monitoring, urban planning, and public health.

3. Outcomes and Resultant

The pH levels observed in 2020 ranged from 7.2 to 7.499, while in 2022, they ranged from 7.5 to 8.199. These results indicate that the pH values of the water were largely neutral to slightly alkaline in nature. This consistency suggests that the water quality remained stable over the two-year period, with pH values falling within the acceptable limits set by both WHO and Iraqi standards. The findings confirm that the water in the study area maintained a pH level that is safe for consumption and meets international and national guidelines, as shown in (Fig. 2) (a, b), which illustrates the spatial distribution of pH levels across different areas within the Kirkuk settlement. (Fig. 2) (a) also presents the alkalinity concentration in Kirkuk settlements for 2020, with total alkalinity values ranging from 139.001 to 147 mg/l. Meanwhile, (Fig. 2) (b) depicts the 2022 alkalinity levels, which vary from 135.001 to 145.999 mg/l. This decrease in 2022 indicates that the alkalinity levels fell below Iraqi standards but remained above WHO standards. Calcium (Ca+2) concentrations in 2020 ranged from 47.0008 to 52 mg/l, while in 2022, they varied between 45.0004 and 49.998 mg/l. As depicted in (Fig. 2), the calcium levels for both years were below the limits set by WHO and Iraqi standards.

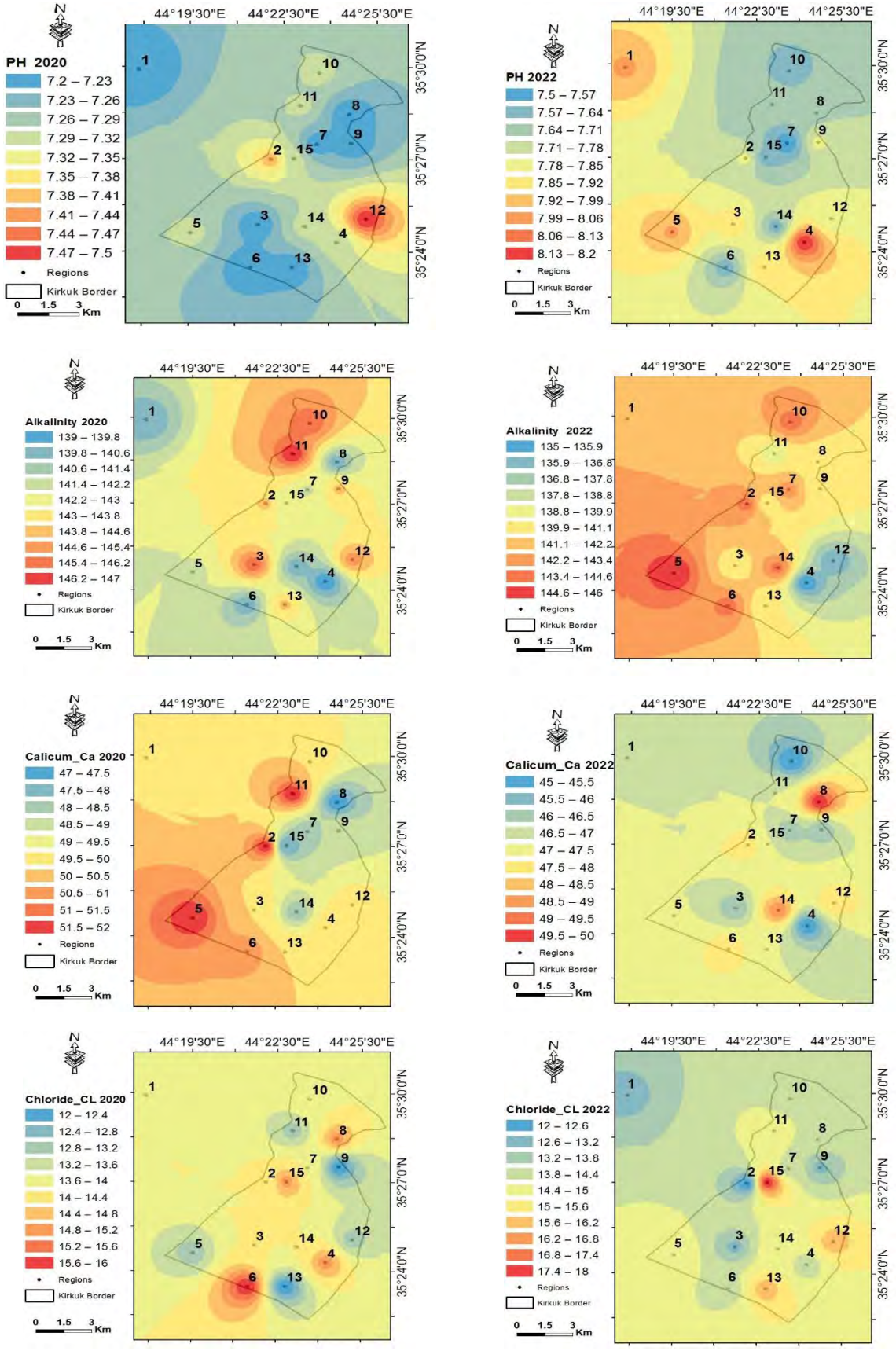

(a) corresponds to the year 2020 (b) corresponds to the year 2022

Fig. 2. pH concentration and alkalinity concentrations maps

Chloride (Cl^{-1}) concentrations in 2020 ranged from 12.0001 to 15.9996.67 mg/l, while in 2022, they varied between 12.001 and 17.9955.18 mg/l. As shown in (Fig. 2), the chloride levels in both years were below the standards established by both WHO and Iraqi standards. Electrical conductivity (EC) measures the ability of water to conduct an electrical current, expressed in units of µS/cm or Mohs. In 2020, EC levels ranged from 369 to 378 µS/cm, while in 2022, they decreased to between 356 and 375.998 µS/cm. The data indicate a reduction in electrical conductivity in 2022 compared to 2020. Additionally, the EC values for both years were below the standards set by WHO and Iraq, as illustrated in (Fig. 3).

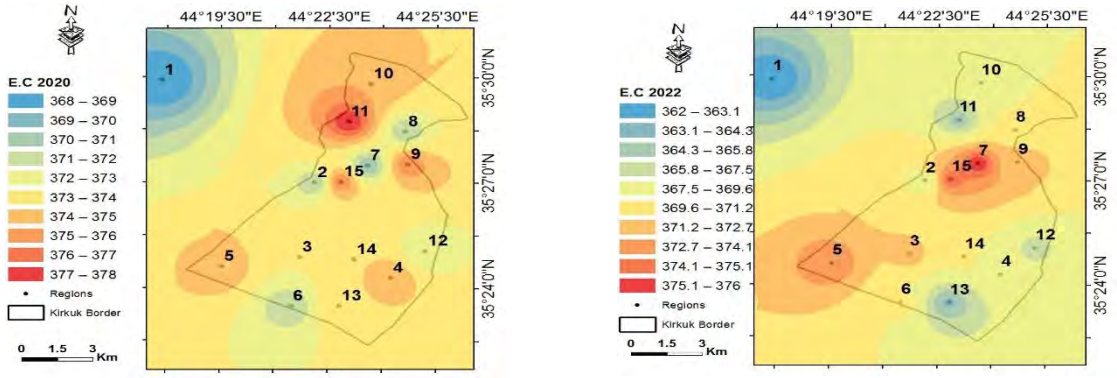

(a) corresponds to the year 2020 (b) corresponds to the year 2022

Fig. 3. Calcium and chloride concentrations and variation of E.C maps

The magnesium (Mg^{+2}) levels peaked at 13.0004 - 17.5994 mg/l in 2020, dropping to 12.0004 - 16.9999 mg/l by 2022. This decline is noticeable, yet the concentrations remain below the limits set by both WHO and Iraqi standards, as illustrated in (Fig. 4). Sulfate (SO_4^{-2}) levels in 2020 fell between 34.0005 and 39.9999 mg/l, while in 2022 they ranged from 30.0007 to 37.9995 mg/l. This indicates a reduction in sulphate concentrations over the two-year period. Notably, for both 2020 and 2022, the values remained under the limits prescribed by Iraqi and WHO standards, as depicted in (Fig. 4).

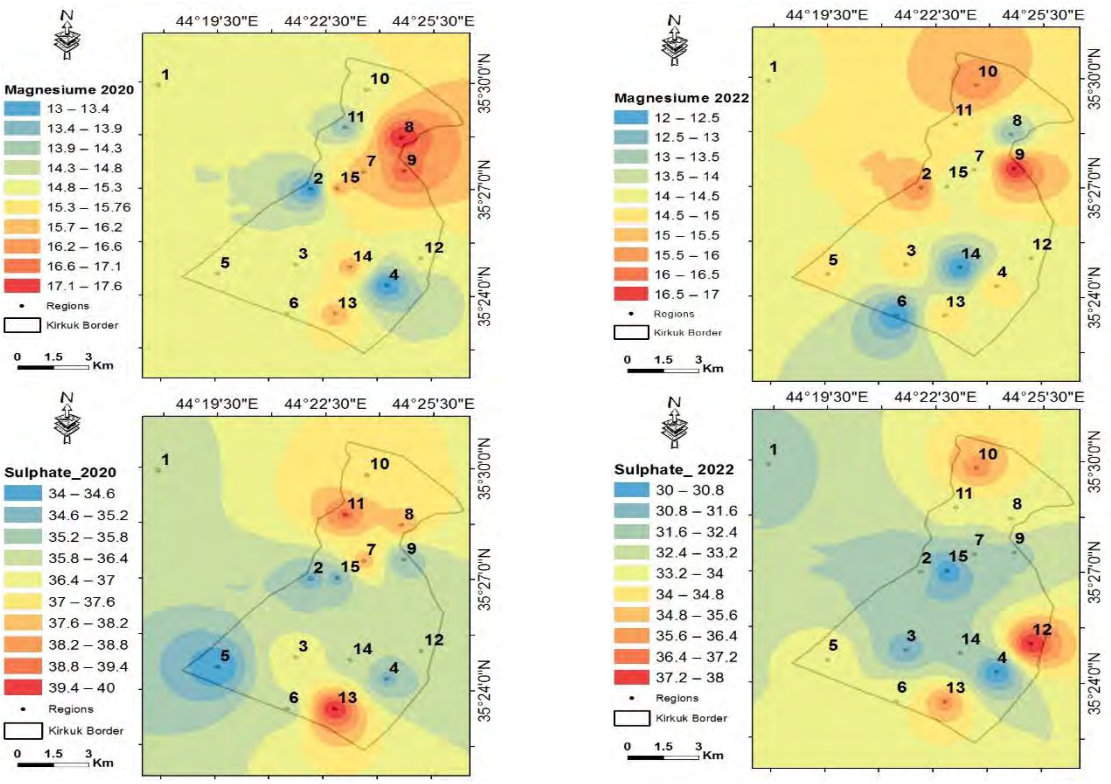

Fig. 4. Magnesium and sulphate concentrations maps

Total hardness (T.H.) measures the accumulation of calcium and magnesium in water, is typically expressed in milligrams per liter. In 2020, total hardness values ranged from 180.001 to 192 mg/l, while in 2022, they spanned from 170.001 to 184.998 mg/l. (Fig. 5) illustrates the distribution of total hardness across Kirkuk's settlement water supplies for both years. Notably, all recorded values were within the acceptable limits set by both Iraqi and WHO standards. Total dissolved solids (TDS) play a crucial role in determining tap water taste. The mineral content of the source water significantly impacts the mineral composition of drinking water. TDS levels ranged from 264 to 268 mg/l in 2020, decreasing to between 210 and 229.998 mg/l in 2022.

(Fig. 5) illustrates the TDS distribution in Kirkuk's water supply for both 2020 and 2022. Notably, all recorded values remained under the criteria by both WHO and Iraqi standards. Turbidity (Tur) levels in 2020 ranged from 2.00134 to 14.2 NTU, while in 2022 they spanned from 2.00023 to 21.0749 NTU. As shown in (Fig. 5), turbidity concentrations varied across different areas during both years. Some locations met the WHO and Iraqi standards, while others fell either below or above these guidelines. (Fig. 5) provides a visual representation of the turbidity concentrations observed in 2020 and 2022. Chlorine (Cl_2) concentrations remained consistent between 2020 and 2022, with values ranging from 1.50003 to 15.9911 mg/l in both years. These levels were below the standards set by both WHO and Iraqi guidelines. (Fig. 5) illustrates this consistency in chlorine concentrations across the two-year period.

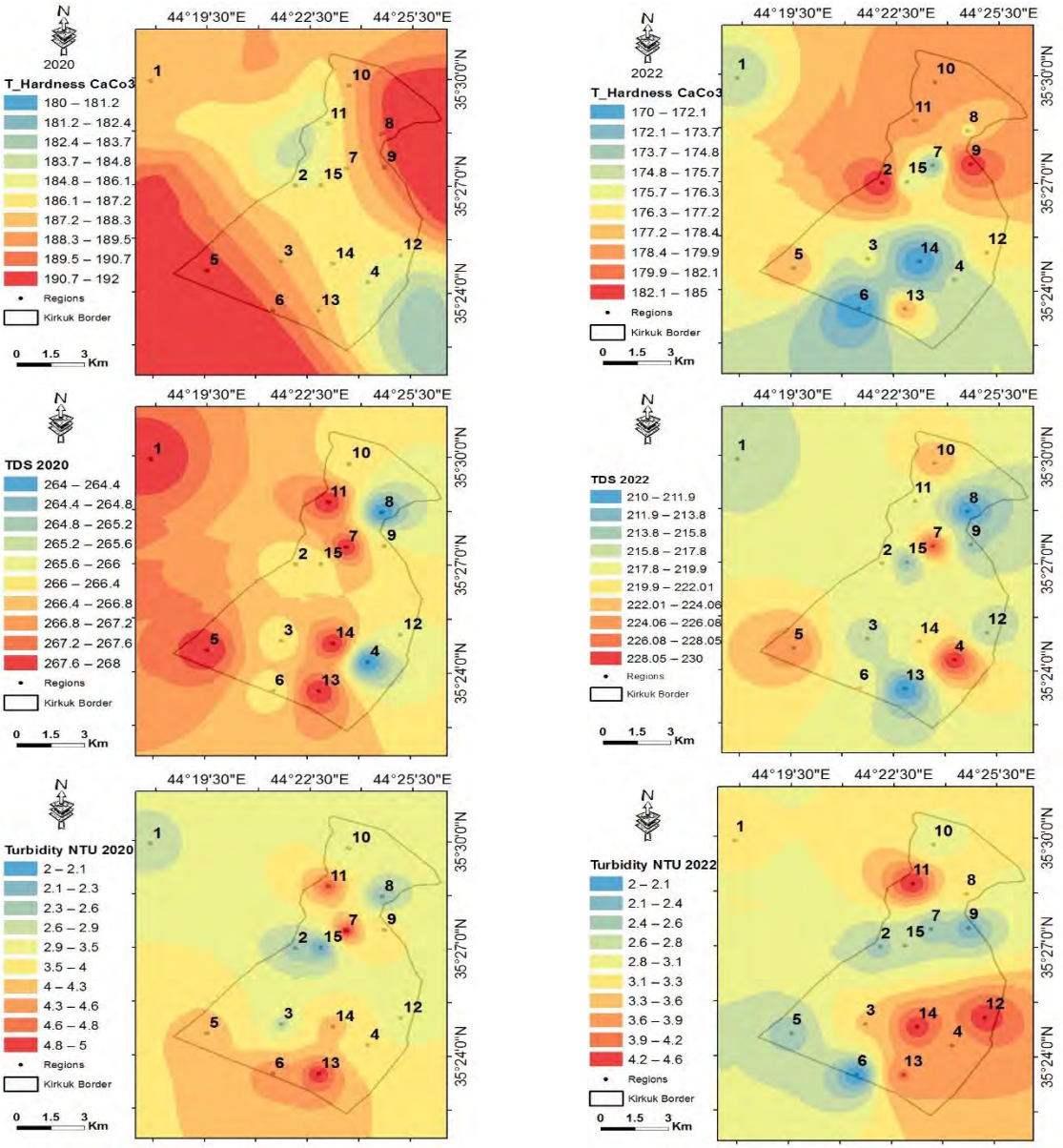

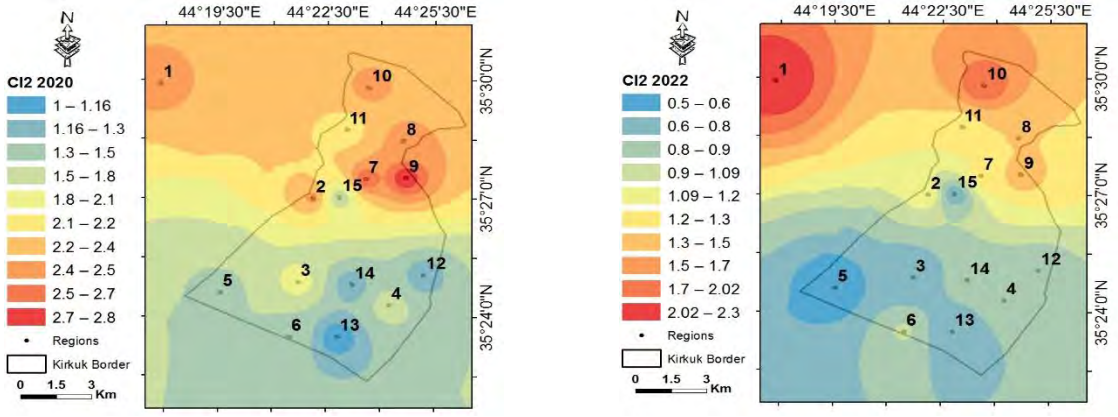

Fig. 5. T-hardness concentration, T.D.S., Turbidity, and Cl2 concentrations maps

Potassium (K) is vital for all living organisms, particularly in plant cells, and is present in all human and animal tissues. The human body contains between 110 and 140 g of potassium, which is crucial for various bodily functions, including heart health, blood pressure regulation, protein dissolution, muscle contraction, and nerve stimulation. While potassium deficiency is rare, it can lead to issues such as depression, muscle weakness, and heart rhythm disturbances. WHO standards set the maximum allowable potassium level at 20 mg/l, while Iraqi guidelines specify 10 mg/l. (Fig. 6) shows that potassium levels in the study area ranged from 1.50003 to 15.9911 mg/l in 2020, decreasing to 1.50001 - 2.39989 mg/l in 2022. These concentrations were within the limits established by both WHO and Iraqi standards. Sodium (Na+), a silvery-white metallic element, is found in small quantities in water. Maintaining an adequate salt level in the human body is crucial for preventing various serious conditions such as kidney damage, hypertension, and headaches. In most countries, water supplies typically contain less than 20 mg/l of sodium, though some areas report levels exceeding 250 mg/l (WHO, 1984). (Fig. 6) illustrates that the sodium content in the study area falls under both WHO and Iraqi standards. According to WHO standards, the acceptable limit for salt content in drinking water is 200 mg/L.

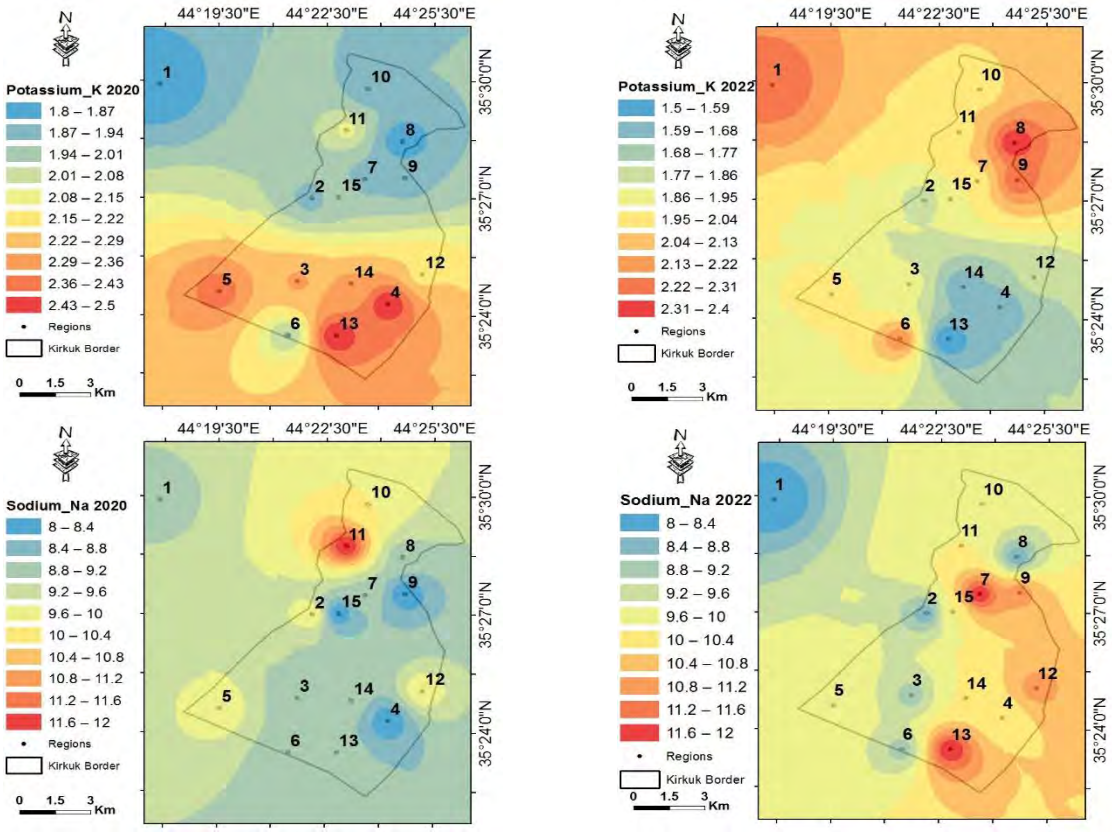

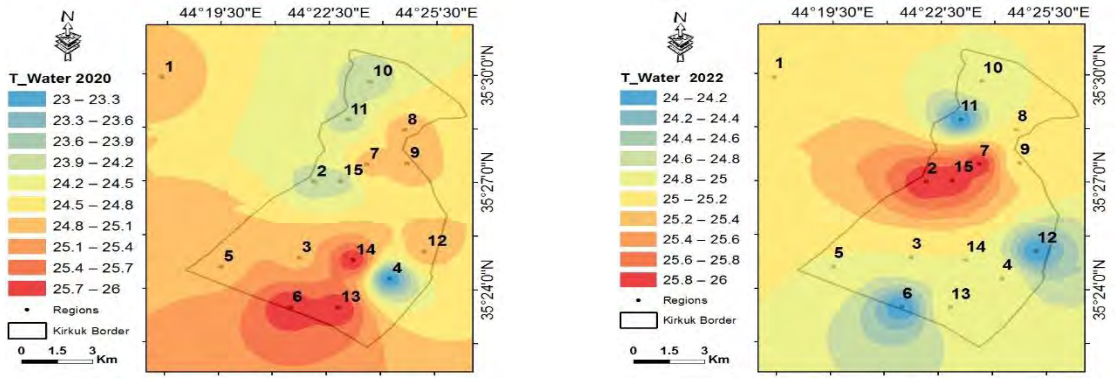

(a) corresponds to the year 2020 (b) corresponds to the year 2022

Fig. 6. Potassium and sodium concentrations and temperature of water distribution maps

In the study areas, the measured salt concentrations were well within this limit, ranging from 8.00003 to 12 mg/L in 2020 and from 8.50001 to 11.9999 mg/L in 2022. These values indicate that the salt levels in the water followed the WHO guidelines, ensuring that the water quality was safe for consumption. The temperature in 2020 exceeded the range in several areas; however, 2022 was limited by WHO and Iraqi standards, as illustrated in (Fig. 6). The water temperature in 2020 was between 23.0004°C and 26°C, while in 2022 it ranged from 24°C to 25.999°C. Based on (Figs 2-6), the key findings from the water quality analysis in Kirkuk City (2020 and 2022) reveal various trends, improvements, and concerns regarding the potable water supply. The evaluation of potable water quality in Kirkuk City revealed improvements in several physicochemical parameters between 2020 and 2022, alongside emerging concerns that warrant attention. The study found a decline in total dissolved solids and electrical conductivity, indicating enhanced water purity, possibly due to improved treatment processes, reduced industrial discharge, or changes in water sources. pH levels remained stable, with slightly alkaline nature, while alkalinity showed a slight decrease, indicating shifts in the chemical composition of the water. A notable reduction in water hardness and sulphate levels result to softer water, likely influenced by groundwater recharge variations. However, turbidity levels increased in certain locations, exceeding permissible limits, which may be attributed to sedimentation, urban runoff, or inefficiencies in the filtration system. Chlorine levels remained within acceptable ranges, ensuring effective disinfection, while potassium concentrations significantly declined, may affect the mineral balance of the water. Sodium levels remained unchanged and within safe limits, lowering potential health risks associated with high salinity. Water temperature exhibited minimal variations, likely influenced by seasonal changes or distribution pipeline conditions. Overall, the findings indicate improved water quality in several aspects, yet highlight the need for targeted interventions, particularly in enhancing filtration processes, regulating turbidity levels, and addressing potassium deficiencies. Periodic monitoring and optimized water treatment strategies are essential to ensuring sustained water quality and compliance with WHO and Iraqi standards.

4. Linear Multi-Regression Model

The Linear Multi-Regression Model presented in Tables 3 and 4 analyses the relationship between various water quality parameters and their impact on turbidity for the years 2020 and 2022. The regression analysis indicates that multiple parameters exhibit weak individual correlations with turbidity; however, when considered collectively, a strong overall correlation (R^2 = 0.939) is observed, suggesting that changes in these variables are significantly interdependent. The R^2 value of 0.147 indicates potential diversity in forecasts, suggesting that although turbidity is affected by various causes, incorporating new variables or improving data collection methods may increase predictability. The p-value was high in single linear regression analysis, suggesting that additional statistical refinement or the inclusion of more explanatory variables is necessary to enhance the model's predictive power. The results indicate that variations in pH, total dissolved solids (TDS), electrical conductivity (E.C.), and ion concentrations affect turbidity, highlighting the necessity for enhanced filtration methods and monitoring techniques to maintain water clarity. Comparisons

between 2020 and 2022 reveal alterations in parameter interactions, indicative of potential factors such as seasonal fluctuations, urban expansion, or enhancements in water treatment efficacy. These regression analyses establish a foundation for enhancing water quality management in Kirkuk City, assuring adherence to WHO and Iraqi requirements while mitigating potential contamination sources. (Figs. 7 to 10) depict the relationship between different water quality metrics and turbidity by regression analysis, elucidating the primary factors affecting water clarity in Kirkuk City for the years 2020 and 2022.

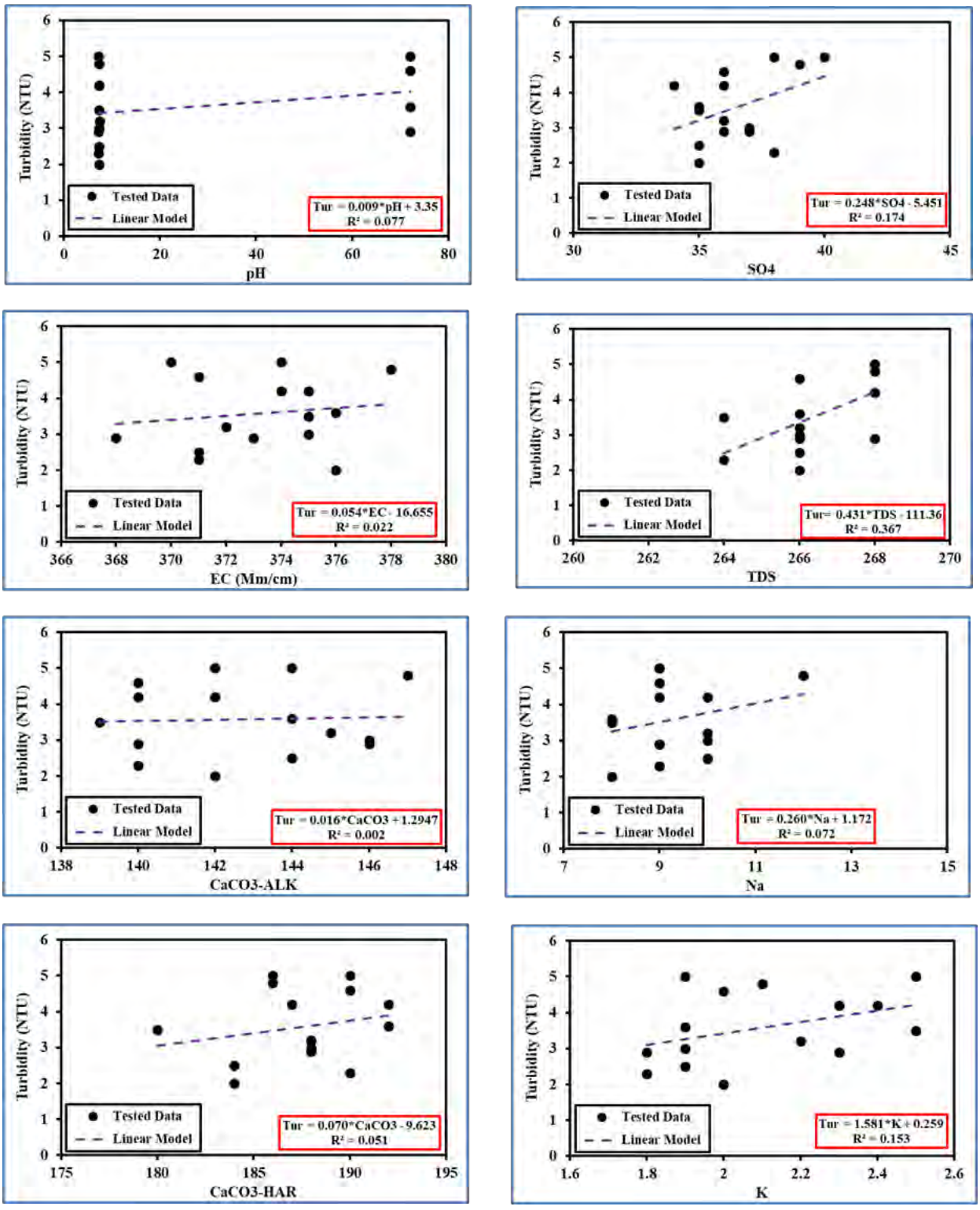

Fig. 7. Correlation of different water quality parameters with turbidity in 2020

Table 3. Regression analysis of water quality parameters in Kirkuk City (2020)

	Turbidity	pH	EC	CaCO3	CaCO3	Ca+	Mg+	Cl	SO4	TDS	Na+	K	T. Water	Cl2
Turbidity	1													
pH	0.277014	1												
EC	0.146761	-0.17631	1											
CaCO3	0.041628	0.064846	0.415434	1										
CaCO3	0.226789	0.283148	-0.07457	0.145664	1									
Ca+	0.300214	-0.08661	0.111629	0.377222	0.054873	1								
Mg+	-0.01718	0.247869	-0.06509	-0.14671	0.621145	-0.7315	1							
Cl	-0.33204	0.073733	-0.33861	-0.57356	-0.41178	-0.24864	-0.14491	1						
SO4	0.416555	0.011348	-0.01355	0.339755	0.121777	-0.10509	0.249322	-0.22855	1					
TDS	0.606017	-0.01513	-0.0025	0.197489	0.278939	0.247518	0.034922	-0.49301	0.24903	1				
Na+	0.267922	-0.31155	0.176842	0.586069	0.082886	0.624853	-0.3764	-0.27448	0.333897	0.386555	1			
K	0.391331	-0.18869	0.414512	0.011067	-0.12505	0.259228	-0.28846	-0.25607	0.017107	0.122857	-0.0279	1		
T. Water	0.43358	0.325332	-0.34231	-0.15276	0.708946	-0.13915	0.565093	-0.17673	0.265644	0.447503	-0.09629	0.066875	1	
Cl2	-0.29383	0.292194	-0.19905	0.139189	-0.01587	-0.10159	0.094269	0.035005	0.002339	-0.16235	0.026702	-0.7773	-0.3702	1

Table 4. Regression analysis of water quality parameters in Kirkuk City (2022)

	Turbidity	pH	EC	CaCO3	CaCO3	Ca+	Mg+	Cl	SO4	TDS	Na+	K	T. Water	Cl2
Turbidity	1													
pH	0.167064	1												
EC	-0.52692	-0.37525	1											
CaCO3	-0.51726	-0.38655	0.26973	1										
CaCO3	-0.17442	0.198358	-0.13198	-0.04763	1									
Ca+	0.187797	-0.28748	-0.0821	0.163186	-0.21873	1								
Mg+	-0.16942	0.335628	-0.07846	-0.15376	0.879547	-0.64109	1							
Cl	0.345845	-0.21626	0.14923	-0.24125	-0.33003	0.1234	-0.30464	1						
SO4	0.29653	-0.15444	-0.38612	0.00733	0.142555	0.221408	-0.0265	0.211312	1					
TDS	-0.20499	0.113809	0.294299	0.210111	-0.1499	-0.51094	0.074274	-0.22219	-0.23074	1				
Na+	0.406684	-0.12069	-0.05645	-0.01015	-0.44163	0.030472	-0.38669	0.492583	0.287097	0.241893	1			
K	-0.34078	0.018577	0.181747	-0.089	0.466298	-0.20182	0.493857	-0.26952	-0.13486	-0.18358	-0.86891	1		
T. Water	0.273404	-0.04053	-0.12858	0.130182	-0.44415	0.194644	-0.47605	0.248512	0.07463	0.191769	0.854968	-0.99393	1	
Cl2	-0.15889	-0.12817	-0.42316	0.132418	0.220424	-0.13904	0.195502	-0.48565	0.067891	-0.0211	-0.35456	0.213832	-0.19023	1

(Fig. 7) illustrates the correlation between turbidity and various physicochemical parameters in 2020, demonstrating a robust overall relationship (R^2 = 0.939), wherein factors such as total dissolved solids (TDS), electrical conductivity (EC), and total hardness significantly affected turbidity levels, presumably due to elevated dissolved solids and mineral content. (Fig. 8) expands this analysis to 2022, illustrating alterations in parameter interactions, possibly attributable to advancements in water treatment or modifications in environmental circumstances, with certain parameters demonstrating diminished correlations, indicating developing sources of turbidity. (Fig. 9) further refines the 2022 regression analysis, isolating parameters with the highest impact on turbidity, which may include chloride, sulphate, and potassium, emphasizing that fluctuations in their concentrations contribute to increased suspended particles. (Fig. 10) presents a refined model incorporating adjustments for outliers and variability, with the p-value and R^2 values for single linear regression indicating the need for further refinement and inclusion of additional parameters such as seasonal variations, microbial contamination, and treatment plant efficiency.

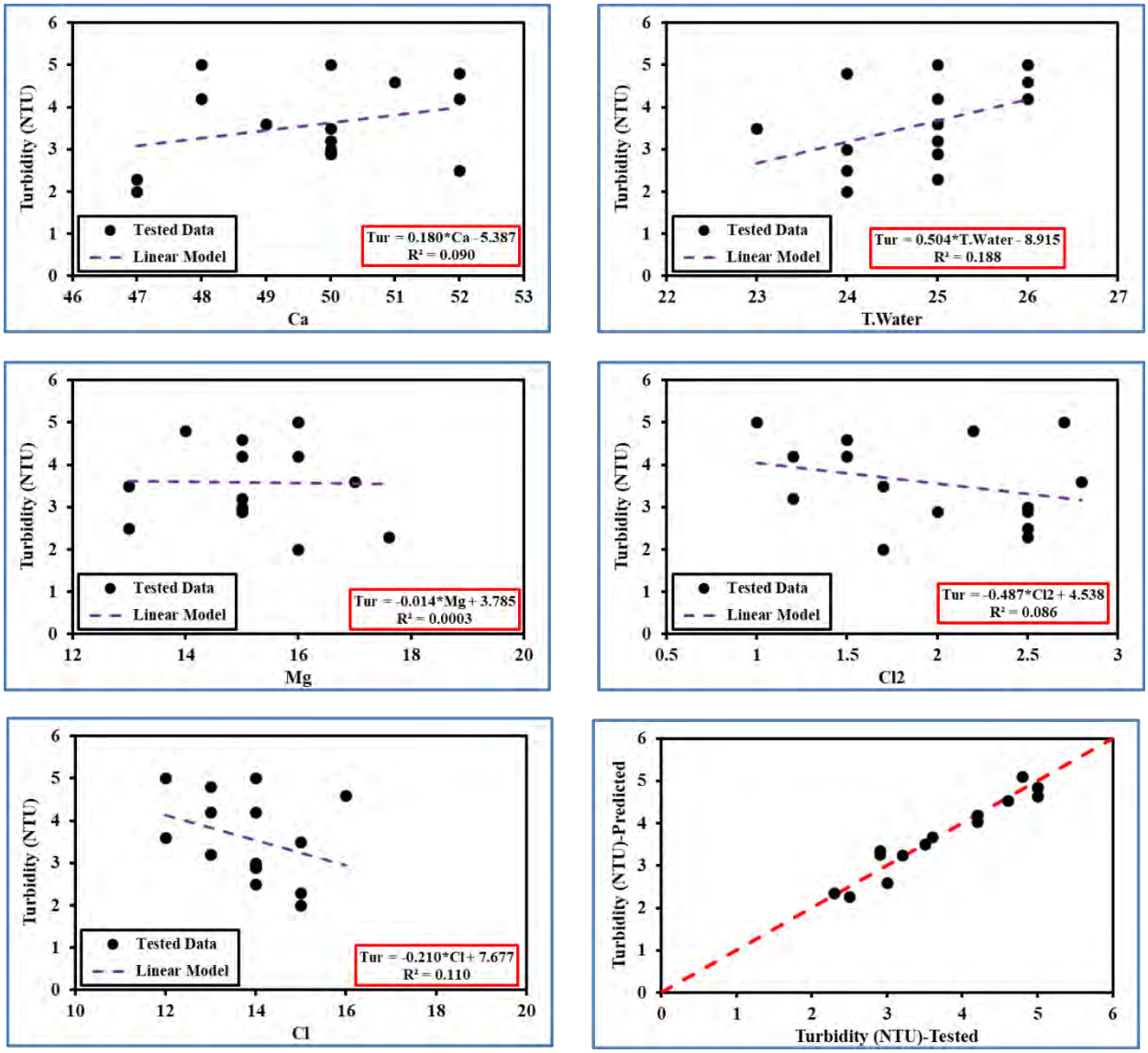

Fig. 8. Correlation of different water quality parameters with turbidity in 2020

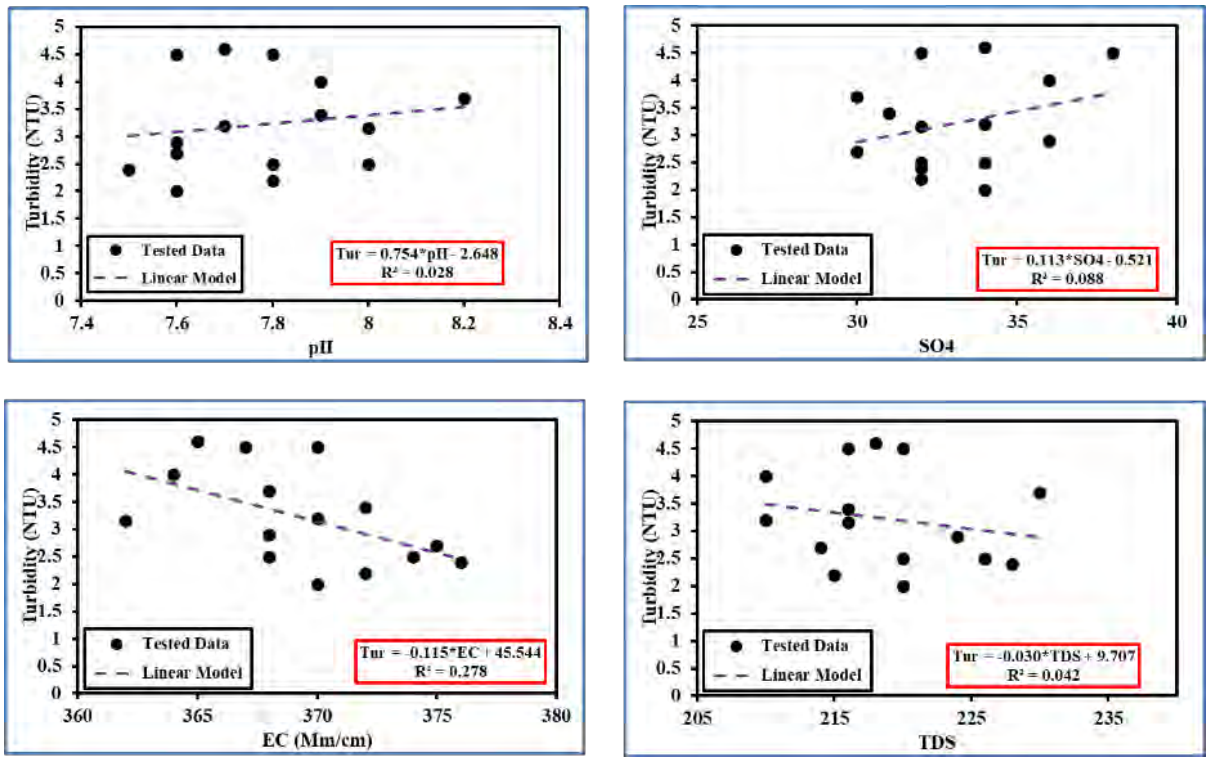

Fig. 9. Correlation of different water quality parameters with turbidity in 2022

The findings collectively suggest that while turbidity remains a significant concern, improvements in filtration processes and dissolved solids management can enhance water clarity and ensure compliance with WHO and Iraqi drinking water standards. The regression results indicate weak correlation between multiple parameters, but overall parameters indicate strong indication of turbidity with an R^2 value of 0.939, suggesting that changes in water quality variables are significantly interdependent. However, the R^2 of 0.147 for single regression analysis indicates potential variability in predictions. The significance (p-value) for single linear regression is relatively high, suggesting that further refinement in data collection or additional variables could enhance predictability.

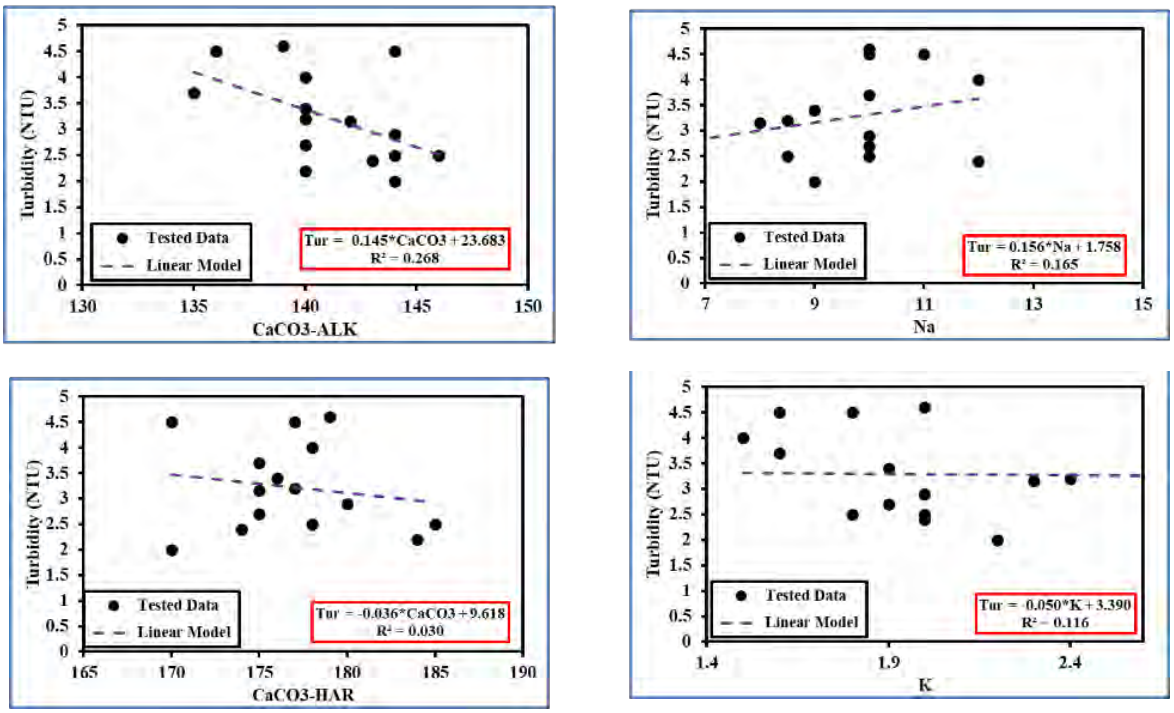

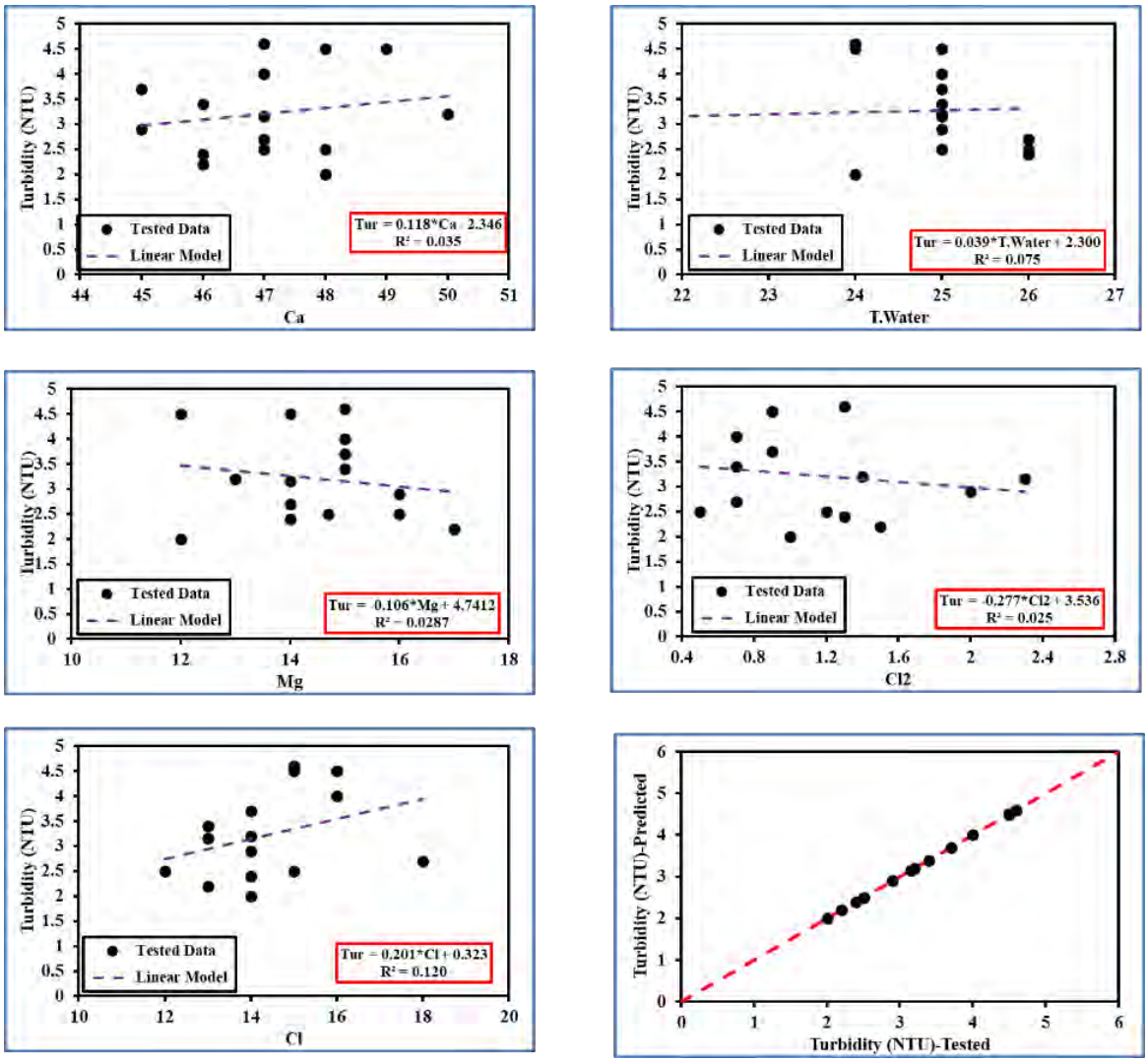

Fig. 10. Correlation of different water quality parameters with turbidity in 2022

5. Conclusion

This study analyzed key physicochemical parameters of potable water in Kirkuk City across fifteen locations using GIS spatial mapping and multi-linear regression analysis. Water quality was evaluated for 2020 and 2022, covering parameters such as pH, alkalinity, calcium, chloride, electrical conductivity, magnesium, sulphate, total hardness, total dissolved solids, turbidity, chlorine, potassium, sodium, and temperature, and compared against WHO and Iraqi drinking water standards. The results indicated that Kirkuk water remained slightly alkaline, with turbidity levels exceeding acceptable limits in some areas. Improvements were observed in water purity over time, as indicated by reductions in Total Dissolved Solids and Electrical Conductivity, possibly due to enhanced treatment processes or changes in pollution sources. However, the decline in potassium levels and persistent turbidity issues necessitate further intervention to maintain water quality. The regression analysis revealed a strong correlation (R^2 = 0.939) between turbidity and multiple physicochemical parameters, particularly Total Dissolved Solids, Electrical Conductivity, and Total Hardness. The resolved R^2 value revealed diversity in predictive accuracy, underscoring the intricate aspects affecting the purity of water. The regression model offers significant insights into parameter interdependencies; however, the high p-value for single linear regression indicates that the inclusion of additional variables, such as contamination from microbial sources, seasonal variations, and treatment plant efficiency, may improve the model's predictive accuracy. The research underscores the need of combining GIS and statistical modelling for thorough water quality evaluation, enabling data-informed decision-making in water resource management. The

results indicate that Kirkuk's water quality is mainly satisfactory; nonetheless, localized turbidity problems and mineral deficits necessitate focused enhancements in filtration and treatment methods. The COVID-19 lockdown may have temporarily influenced water quality trends by reducing industrial discharge and altering domestic water consumption patterns. Future studies should focus on long-term data collection, incorporating seasonal effects, climate variability, and emerging pollutants to develop a more robust predictive framework. Periodic monitoring, optimized treatment strategies, and policy interventions are essential to ensuring sustained water quality and compliance with international and national standards.

The quality of Kirkuk water has been checked and the concentration of each element has been found. In this regard it is necessary to be periodically checked to avoid diseases and problems resulting from water quality, especially for turbidity concentrations as shown above the acceptable limits, E.C. and T. Hardness levels were also underneath the allowable ranges, and the concentrations of Ca^{+2}, Cl^{-1}, Mg^{+2}, SO_4^{-2}, and Na and Cl_2 were less than the allowable limits in all locations. Also, the concentration of K was less than the WHO standards. Depending on the results, the recommendation is to increase the filtration process and treatment of the water to reduce turbidity and increase the concentration rate of the elements that have low rates in Kirkuk water. Among the tested parameters, turbidity, total dissolved solids, and total hardness showed the strongest influence on water quality. Parameters like potassium, though below standard limits, also require attention due to their biological importance.

Acknowledgment

The authors would like to express their sincere gratitude to the Kirkuk Water Directorate for providing the essential data and technical support necessary for conducting this study. Their cooperation and assistance played a crucial role in facilitating the assessment and analysis of potable water quality across Kirkuk City.

References

[1] Habbeb MG, Sulyman MHA, Jumaah HJ. Modeling water quality index using geographic information systems and weighted arithmetic index in Kirkuk, Iraq. Pollut Res. 2022;41(1):323-7. https://doi.org/10.53550/PR.2022.v41i01.047
[2] Sankhua RN. Rejuvenating water wisdom: a route to resilience. In: Yadav B, Mohanty MP, Pandey A, Singh VP, Singh RD, editors. Sustainability of Water Resources. Water Science and Technology Library, vol. 116. Cham: Springer; 2022. https://doi.org/10.1007/978-3-031-13467-8_6
[3] Duda S, Kandiah S, Stout JE, Baron JL, Yassin M, Fabrizio M, et al. Evaluation of a new monochloramine generation system for controlling Legionella in building hot water systems. Infect Control Hosp Epidemiol. 2014;35(11):1356-63. https://doi.org/10.1086/678418
[4] Deidan MTA, AbdelQader RS. Assessment of the quality and coefficient of treatment water quality of Hawija district using the Water Quality Index (WIQ). Int J Health Sci. 2022;6(S9):2718-27. https://doi.org/10.53730/ijhs.v6nS9.13025
[5] World Health Organization. Guidelines for drinking-water quality. Vol. 1. Geneva: World Health Organization; 2004.
[6] Nesaratnam ST. Water pollution control. Chichester: John Wiley & Sons; 2014. https://doi.org/10.1002/9781118863831
[7] Noori S, Ghasemlounia R. A review of criteria in rain water harvesting. 2019.
[8] Ameen MH, Jumaah HJ, Kalantar B, Ueda N, Halin AA, Tais AS, et al. Evaluation of PM2.5 particulate matter and noise pollution in Tikrit University based on GIS and statistical modeling. Sustainability. 2021;13(17):9571. https://doi.org/10.3390/su13179571
[9] Kalantar B, Ameen MH, Jumaah HJ, Jumaah SJ, Halin AA. Zab River (Iraq) sinuosity and meandering analysis based on remote sensing data. Int Arch Photogramm Remote Sens Spat Inf Sci. 2020;43.
[10] Jumaah HJ, Kalantar B, Halin AA, Mansor S, Ueda N, Jumaah SJ. Development of UAV-based PM2.5 monitoring system. Drones. 2021;5(3):60. https://doi.org/10.3390/drones5030060
[11] Ghasemlounia R, Herfeh NS. Study on groundwater quality using geographic information system (GIS), case study: Ardabil, Iran. Civil Eng J. 2017;3(9):779-93. https://doi.org/10.21859/cej-030914
[12] Noori MM, Abdulrazzaq KA, Mohammed AH, Abbas AI. Assessment of water quality and suitability of Euphrates River in Iraq for drinking purpose by applying water quality indices (WQIs) and geographical information system (GIS) techniques. Int J Sci Nat. 2017;8(4):741-56.

[13] Raheem AM, Omar NQ. Investigation of distinctive physico-chemical soil correlations for Kirkuk city using spatial analysis technique incorporated with statistical modeling. Int J Geo-Eng. 2021;12(1):18. https://doi.org/10.1186/s40703-021-00147-2
[14] Mohammed AA, Almaliki DF, Qasim RM, Najemalden MA. Multivariate statistical application for the assessment of surface water quality in Lower Zab River, Kirkuk. WSEAS Trans Environ Dev. 2020;16:480-92. https://doi.org/10.37394/232015.2020.16.49
[15] Abdulkareem FA, Mohamed GH, Resheq AS, Bahaa Z. Assessment of the performance of water treatment plants in Baghdad governorate using GIS. Period Eng Nat Sci. 2021;10(1):228-38. https://doi.org/10.21533/pen.v10i1.2592
[16] Mohammed ZB, Mohamed GH, Ahmedabdulkareem F, Resheq AS. Assessment of water quality for Tigris River in Baghdad city by physico-chemical parameters using GIS. J Green Eng. 2020;10(11):10321-37.
[17] Al-Salihy AI, Sadeq SN, Al-Jumaily HA. Hydrochemical evaluation of raw water and treated water in the liquefaction plant of Kirkuk unified water project using WQI technique, Northern Iraq. Iraqi Geol J. 2021;54(1):78-87. https://doi.org/10.46717/igj.54.1E.7Ms-2021-05-28
[18] Aziz SQ, Slewa EO, Abdullah WA. Evaluation of water quality for the Lesser-Zab River for various applications. Kirkuk Univ J Sci Stud. 2017;12(4). https://doi.org/10.32894/kujss.2017.132387
[19] Arslan CA, Ali SM, Amin YAH. Evaluation of the water quality of Kirkuk irrigation project within Tuz district for different purposes. In: 4th International Conference on Pure Sciences and Agriculture Sciences. Antalya, Turkey; 2021.
[20] Sabeeh NN, Alabdraba WMS, Mohamed GH, Mohammed ZB. Water quality monitoring of Tigris River by using (GIS)-based physicochemical parameters in Baghdad, Iraq. Int J Eng Technol. 2018;7(4.37):57-62. https://doi.org/10.14419/ijet.v7i4.37.23617
[21] Raheem AM, Naser IJ. Reliability of various soil characteristics relationships for Kirkuk soil using consistent undisturbed field soil samples with linear regression models. Ital J Eng Geol Environ. 2024:15-22.
[22] Hamed HH, Jumaah HJ, Kalantar B, Ueda N, Saeidi V, Mansor S, et al. Predicting PM2.5 levels over the north of Iraq using regression analysis and geographical information system (GIS) techniques. Geomatics Nat Hazards Risk. 2021;12(1):1778-96. https://doi.org/10.1080/19475705.2021.1946602
[23] Ibrahim MO, et al. Correlating Standard Penetration Test (SPT) with various soil properties in different Kirkuk city locations: a case study utilizing Inverse Distance Weighted (IDW) for assessment and prediction. E3S Web Conf. 2023;427:01005. https://doi.org/10.1051/e3sconf/202342701005
[24] Ajaj QM, Shafri HZM, Ramli AWAF. Common analysis methods for gaseous and solid contaminants emitted from different pollution sources: a review paper. Pollut Res. 2022;41(2):416-39. https://doi.org/10.53550/PR.2022.v41i02.007
[25] Al-Mirza H, Falih M, Salman A, Karkush M. Utilization of GIS to generate a digital geotechnical map of Baghdad city. IOP Conf Ser Earth Environ Sci. 2024;1374:012052. https://doi.org/10.1088/1755-1315/1374/1/012052

Blank Page

Research on Engineering Structures & Materials
www.jresm.org

Research Article

Enhancing the flexural behavior of concrete beams with steel and carbon fiber

Murtadha Hardan Dawood [1,a], Sozan Saeed Rasheed [1,b], Hussien Al-Quraishi [*,1,c], Haneen Ismaeel Khalil [2,d]

[1]*College of Civil Engineering, University of Technology, Baghdad, Iraq*
[2]*Precidency of AL-Iraqia University, AL-Iraqia University, Baghdad, Iraq*

Article Info

Article History:

Received: 25 Oct 2025

Accepted: 19 Nov 2025

Keywords:

Fiber reinforced concrete;
Concrete strengthening;
Carbon fiber reinforced polymer

Abstract

Concrete is considered as brittle material with low flexural strength, which makes it susceptible to sudden failure at allow levels of load. As a result, it is necessary to reinforce and strengthen the concrete beams with different strategies to achieve structural stability. This study aims to investigate the behavior of concrete beams when reinforced with steel fibers and strengthen with carbon fibers plates and texture for the same specimen details and under the same testing conditions. The experimental work was conducted by constructing eight (100x100x400mm) concrete beams in order to study the variables; the percentages of steel fiber 0.5%, 1.0%, and 1.5%, the number of sheets in carbon fiber plates and texture (one and two layer). The experimental results showed an increase in the ultimate flexural load by 12.76, 26.10, and 55.85% when beams were reinforced with steel fiber by 0.5, 1.0, and 1.5% respectively, also a noticeable improvement of ductility and reducing deflection was observed. Strengthening by carbon fiber texture further improved the flexural strength of the beam, as the ultimate load was increased by about 61.40% when strengthen with one sheet and 130% when using two sheets. The beams also showed high plastic deformation before failure. The maximum improvement was recorded when the beams strengthen with carbon fiber plates, where the increase in failure load reached 180% and the deflection decreased by 92%, although it led brittle failure and reduced ductility.

© 2026 MIM Research Group. All rights reserved.

1. Introduction

Concrete is considered one of the most important and widespread materials widely used globally in the field of construction. Since its long-term use, concrete has gained great scientific importance for studying its various mechanical properties. Concrete is a well-resistant material if it is subjected to compressive stresses, and vice versa if it is subjected to tensile and bending stresses [1-3].

There are several ways to improve the structural performance of concrete, such as adding fiber or carbon fiber [4,5]. In Fiber reinforced concrete (FRC), the separate and discontinuous steel fiber added to concrete mixture. A reduction in concrete cracks and an increase in tensile strength was investigated [6]. While [7] studied the deformations and ultimate strength of concrete beams reinforced with fiber, a noticeable increase in the load failure of the beams was recorded, in addition to a decrease in the width of the cracks. Despite the improvements provided by steel fiber reinforcement, many construction applications require greater levels of durability and stability. In order to meet these requirements, many concrete strengthening techniques is used such as application of carbon fiber polymeric (CFRP), whether as plates or texture [8]. Karnoub [9] conducted a practical experiment in which a normal concrete beam was compared to another

*Corresponding author: hussien.a.alquraishi@uotechnology.edu.iq
[a]orcid.org/0009-0003-9272; [b]orcid.org/0009-0005-8454-8456; [c]orcid.org/0000-0001-9600-680X.
DOI: http://dx.doi.org/10.17515/resm2025-1297ic1025rs

strengthen with carbon fiber plates. They concluded through the study that the ultimate strength of the concrete beam increased by about twice that of the unstrengthen one. In addition, through [10] the fatigue performance was greatly improved, as the life of the concrete beam was extended and failure was achieved by breaking the reinforcing steel. When turning to another type of strengthening, which is conducted by using carbon fiber texture, this type of carbon provides the same justifications in terms of enhancing bending and tensile performance and controlling cracks in concrete beams.

In previous studies, the enhancement methods mentioned above were studied individually, each for a specific specimen and under different testing conditions. In this research, a study will be presented on improving the flexural strength of one specimen and one testing conditions using the mentioned techniques (reinforcing with steel fiber, strengthening with carbon fiber plates, and strengthening using carbon fiber texture) to determine the structural effect of each technique in a purer form for the same beam whose dimensions may be imposed for architectural purposes in order to know the engineering feasibility of each technique.

2. Materials and Mix Proportions

In the current study, ordinary Portland cement was used along with both coarse and fine aggregates, in addition to drinking water, to prepare the concrete mix. Steel fibers and carbon fibers of both types (plates and texture) were also used to reinforce and strengthen the concrete beam.

2.1 Cement

The ordinary type of Portland cement was used, and physical and chemical tests were conducted according to the Iraqi standard No.5 [11], and the results were as shown in Table 1.

Table 1. Chemical and physical characteristics of cement used

Chemical compound		Percent of content meets Iraqi No.5
SIO_2 (%)		20.22
AL_2O_3 (%)		4.00
FE_2O_3 (%)		1.78
CAO (%)		60.33
MGO (%)		3.20
SO_3 (%)		1.40
Insoluble Substances (%)		0.95
Burning Loss (%)		2.71
$\%C_3A$		4.23
%CL		/
Physical properties		
Cement fineness (M^2/Kg)		342
Time Of Setting	Initial (Min)	100
	Final (Hr)	3:30
%Cement soundness		0.01
Strength in compressive (MPA)	2 Days	22.6
	28 Days	43.9

2.2 Coarse and Fine Aggregate

All tests required for aggregates were conducted according to Iraqi Standard Specification No. 45 of 1980 [12]. For coarse aggregate, the gradation was (5-20) mm, while for fine aggregate, its gradation indicated Zone 2. The rest of the results are shown in Table 2.

Table 2. Physical compositions of fine and coarse aggregate

Test in laboratory	Coarse aggregate	Fine aggregate
Apparent specific gravity (ASTMC128 & C127)	2.60	2.50
Bulk specific gravity (ASTM C128 & C127)	2.77	2.61
% Absorption (ASTMC128 & C127)	0.51	1.10
% wear Los Angles abrasion (ASTM C131)	24.34	--

2.3 Steel Fiber

As for the steel fiber used, its diameter was 0.2mm and its length 15mm, while its density was equal 7850 kg/m3, and therefore the aspect ratio of length to diameter was equal 75, and maximum tensile strength of 2000 MPa used to reinforce the beams. See Fig. 1.

Fig. 1. Steel fiber used in specimens

2.4 Carbon Fiber

Carbon fiber (plates and texture) was prepared from local markets, specifically from Sika company [13], with a mechanical property stipulated in the product data sheets [14]. Table 3 presents the mechanical properties of carbon fiber. The surface preparation and bonding method were listed in Sika datasheet [13,14].

Table 3. Carbon fiber (plates and texture) properties

Property	Carbon fiber plates	Carbon fiber texture
Thickness (mm)	1.2	0.255
Tensile strength (MPa)	3100	4000
Modulus of elasticity (MPa)	170,000	230,000
Elongation at break (%)	>1.8	1.7

2.5 Mix Proportions

In order to achieve the compressive strength targeted for the study (25MPa), three cylinders (150x300mm) were tested with a mixing proportion (Coarse aggregate:1087kg/m^3, Fine aggregate: 950kg/m^3, cement:325kg/m^3, and w/c:0.48) [15-17].

2.6 Tested Specimen

The experimental program for this study was conducted using eight specimens of concrete beams. The dimensions of the specimens were as specified in the American standard ASTM C78 (100x100x400mm). The tested specimens were simply supported with two external loads and two reactions as indicated in Figure 2. Figure 3 represents the specimens after casting. The specimens were cured with drinking water for 28 days before testing.

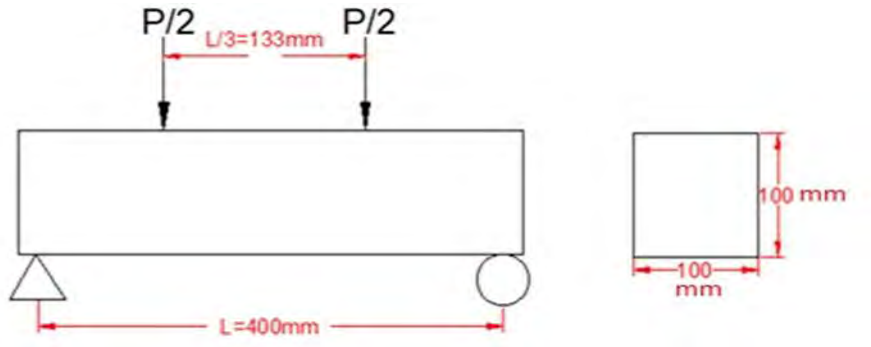

Fig. 2. Test specimen details

Fig. 3. Test specimen after casting

3. Experimental Program

Eight concrete specimens were constructed and then tested in the laboratories of the Civil Engineering Department at the University of Technology in Baghdad. In order to study the flexural behavior of the beams accurately, the test was conducted with four load points instead of three, because the test with four load points provides the area of maximum moment with a constant value with a zero-shear force. The eight specimens were divided into three groups in addition to the reference beam (BR).

The first group includes three specimens (BS0.5, BS1.0, and BS1.5) reinforced with steel fiber percentages of (0.5, 1.0, and 1.5%) which uniformly added through casting. The second group consist of two beams strengthened with one and two layers with carbon fiber texture (BCT1 and BCT2). The third group (BCP1 and BCP2) was related to strengthening with carbon fiber plates, using the same number of layers as in the second groups. See Fig.4.

Fig. 4. Specimens preparation

5.1 Instrumentation and Test Setup

LVDT installed at the top of the specimens was used to measure the deflection at midspan of the beams. The flexural strength test of beams was conducted using a machine with capacity of 50 kN with load rate of 24N/sec. The loading was continued until beams reached to the failure. Fig. 5 shows the test setup of specimen. Table 4 summarizes the experimental program and the results obtained from the flexural test.

Fig. 5. Test setup

6. Results and Discussion

After conducting the test, the flexural strength was calculated using the Eq (1): [18]

$$f_r = \frac{3PL}{2bd^2} \quad (1)$$

Where; P: the ultimate load, L: is specimen length, b: the width of concrete specimen, d: the total depth of concrete specimen.

Table 4. Experimental program results

Group	Specimen	Variable	Steel fiber content (%)	Layer of carbon fiber plates	Layer of carbon fiber texture	Ultimate load P (kN)	Maximum Deflection (mm)
--	BR	--	--	--	--	10.42	2.70
Group 1	BS 0.5	Steel fiber content	0.5	--	--	11.75	2.54
	BS 1		1.0	--	--	13.14	2.20
	BS 1.5		1.5	--	--	16.24	1.80
Group 2	BCT 1	Number of carbon fiber texture sheet	--	1	--	16.82	1.58
	BCT 2		--	2	--	18.76	1.28
Group 3	BCP 1	Number of carbon fiber plates sheet	--	--	1	24.02	0.45
	BCP 2		--	--	2	29.17	0.21

The abbreviations in Table 4, BCT and BCP refer to types of carbon fiber reinforcement, where B stands for “Beam,” C for “Carbon fiber,” and the third letter denotes the form of reinforcement: T for “texture” and P for “Plate”. From the above results, it can be noted that when concrete beams reinforced with steel fiber, the flexural strength improved by 12.76, 26.10, and 55.85% when reinforced by 0.5, 1.0, and 1.5%, respectively, where the steel fibers act as bridges that connect both sides of the cracks, clearly delaying their progress. The results also showed an increasing in the maximum flexural load of the beams by about 61.40% when strengthen with one sheet carbon fiber texture and 130% when using two sheets. The maximum enhancement and best structural

performance were recorded when strengthening with carbon fiber plates, where the percentage of increase in failure load reached 180% and the decreasing in deflection 92%, where both types of carbon fiber are defined by modulus of elasticity and high tensile strength, as it acts as an additional layer that greatly resist load and stresses in tension zones.

6.1 Load-Deflection Behavior

The relation between the flexural failure load and vertical displacement at mid span for all studied beam is shown in the fig.6

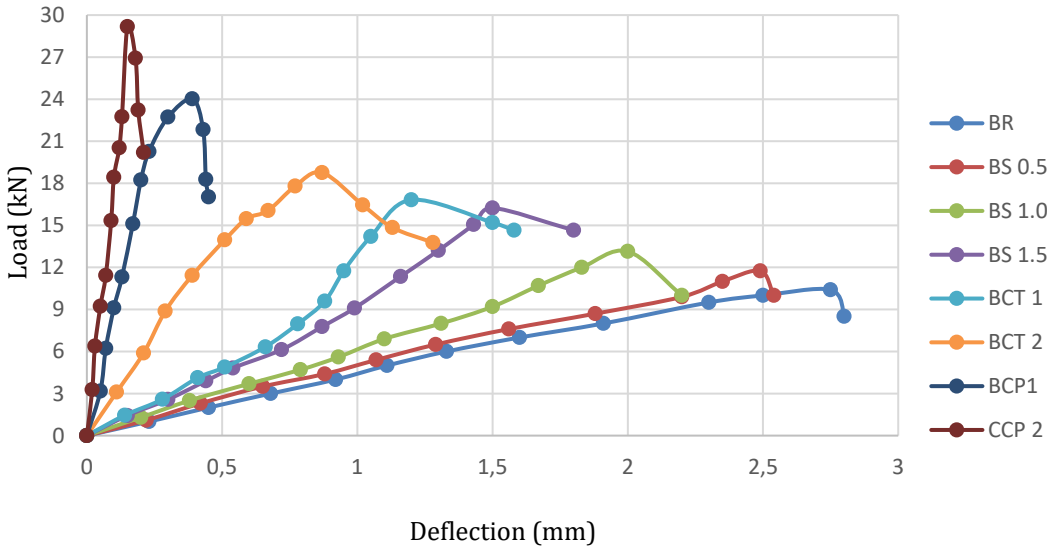

Fig. 6. Load deflection relation

The figure above shows the structural behavior of beams from load application until failure. It can be observed that the reference beam BR shows linear behavior in the initial stages with brittle failure and very little ductility. When the specimen reinforced with steel fibers (BS 0.5, BS1.0, and BS 1.5), the beams show higher plasticity and ductility with increased fiber content and a clear increasing in flexural strength. As for the beams strengthen with carbon fiber texture (BCT1 and BCT2), they show an advanced improvement in reducing deflection and significantly increasing the failure load and ductility, as the beams showed significant plastic deformation compared to previous specimens.

Finally, for the beam strengthen with sheets of carbon fiber plate, it showed the highest levels of capacity and stiffness, as it achieves the maximum load before failure. However, it tends to fail brittle, where it broke suddenly once its strength limit is exceeded due to the high tensile strength of the carbon plates sheets, which clearly reduces ductility.

6.2 Modes of Failure

In general, all specimens showed pure flexural failure with different degrees. The BR specimen failed very suddenly at low load levels due to the absence of any reinforcement in the tension zone, while the beams reinforced with steel fiber showed gradual flexural failure with the appearance of small cracks in the tension zone at middle span (area of pure bending moment), whereas (BCT1 and BCT2) showed a clearer and more controlled flexural failure, contrariwise (BCP2 and BCP2) which broke suddenly by a brittle manner. The failure mode of the tested specimens is shown in Fig. 7.

BR BS 0.5 BS 1.0 BS 1.5

BCT1 BCT2 BCP1 BCP2

Fig. 7. Failure mode of tested specimens

7. Conclusions

The following finding can be concluded from this research:

- The inclusion of steel fiber enhances the flexural capacity and the ductility of concrete beams, also the increasing of steel fiber percentage improves the stiffness and reduce the mid span deflection, resulting in better energy absorption and ductile failure with visible cracking.
- Carbon fiber texture improved structural performance better compared to steel fibers, as they contributed to increased strength and stiffness and showed high ductility compared to steel fiber reinforcement.
- The carbon fiber plate provided the highest efficiency to increase the flexural strength and stiffness of the specimens. Beams strengthen by carbon fiber plate exhibit minimal deflection and superior load capacity, although it showed brittle failure when strengthen with two sheets.
- Optimal enhancement strategy is carbon fiber plates especially if two sheets used, this make it more effective for applications requiring maximum strength and stiffness, while steel fiber and carbon fiber texture are appropriate for scenarios requiring improving ductility and energy absorption.

Acknowledgement

The authors acknowledge the laboratory staff in the college of Civil Engineering at the University of Technology for completing experimental work.

References

[1] Dawood MH, Izzet AF, Khudair BH. Performance of concrete thrust block at several burial conditions under the influence of thrust forces generated in the water distribution networks. J Mech Behav Mater. 2022;31(1):473-83. https://doi.org/10.1515/jmbm-2022-0048

[2] Al-Quraishi H, Kammash K, Abdul-Husain Z. Bond strength behavior in rubberized concrete. Int J Sustain Constr Eng Technol. 2022;13(1):130-6. https://doi.org/10.30880/ijscet.2022.13.01.012

[3] Abdulkhudhur R, Al-Quraishi H, Elwi M. Numerical analysis of concrete-encased concrete filled steel tube beams. AIP Conf Proc. 2024;3219:020049. https://doi.org/10.1063/5.0236329
[4] Mohod MV. Performance of steel fiber reinforced concrete. Int J Eng Sci. 2012;1(12):1-4.
[5] Zheng H, Zhang W, Li B, Zhu J, Wang C, Song G, et al. Recent advances of interphases in carbon fiber-reinforced polymer composites: A review. Compos B Eng. 2022;233:109639. https://doi.org/10.1016/j.compositesb.2022.109639
[6] Song PS, Hwang S. Mechanical properties of high-strength steel fiber-reinforced concrete. Constr Build Mater. 2004;18(9):669-73. https://doi.org/10.1016/j.conbuildmat.2004.04.027
[7] Khalid Heiza AN, Meleka N, Tayel M. Strengthening of reinforced concrete structures—different strengthening techniques: State-of-the-art review. In: Sixth International Conference on Nano-Technology in Construction. 2014;6-C:22-4.
[8] Duthinh D, Starnes M. Strength and ductility of concrete beams reinforced with carbon fiber-reinforced polymer plates and steel. J Compos Constr. 2004;8(1):59-69. https://doi.org/10.1061/(ASCE)1090-0268(2004)8:1(59)
[9] Karnoub A, Huang H, Antypas IR. RETRACTED: Investigation of composite materials supported by carbon fiber fabric (TFC) in pre-cracked concrete beams. J Phys Conf Ser. 2020;1679:042040. https://doi.org/10.1088/1742-6596/1679/4/042040
[10] Liu L, Jia C, He J, Zhao F, Fan D, Xing L, et al. Interfacial characterization, control and modification of carbon fiber reinforced polymer composites. Compos Sci Technol. 2015;121:56-72. https://doi.org/10.1016/j.compscitech.2015.08.002
[11] Central Agency for Standardization and Quality Control. Iraqi Standard Specification for Portland Cement No. 5/2019. Baghdad (Iraq): Republic of Iraq; 2019.
[12] Central Agency for Standardization and Quality Control. Iraqi Standard Specification for Aggregate No. 45/1980. Baghdad (Iraq): Republic of Iraq; 1980.
[13] Sika Group. Technical Data Sheet: SikaWrap-450 C. Sika AG; 2020 Apr. Version 01.01.
[14] Sika Group. Technical Data Sheet: Sika CarboDur® S. Sika AG; 2014 Dec. Version GCC.
[15] Al-Quraishi H, Al-Farttoosi M, Abdulkhudhur R. Compression splices of reinforcing bars in reactive powder concrete. Civ Eng J. 2019;5(10). https://doi.org/10.28991/cej-2019-03091406
[16] Abdulkhudhur R, Mouhammed JL, Al-Quraishi H. Estimation of the flexural-tensile strength of fiber reinforced concrete members. AIP Conf Proc. 2024;2864:0129. https://doi.org/10.1063/5.0186183
[17] Abdulkhudhur R, Al-Quraishi H, Oday AH. Effect of steel fiber on the shear transfer strength across a crack in reactive powder concrete. IOP Conf Ser Mater Sci Eng. 2020;737:012001. https://doi.org/10.1088/1757-899X/737/1/012001
[18] ASTM International. Standard test method for flexural strength of concrete (ASTM C78M-18). West Conshohocken (PA): ASTM International; 2018.

Research on Engineering Structures & Materials
www.jresm.org

Research Article

Enhancing the corrosion resistance and potential biomedical applications of titanium dental implants coated with niobium pentoxide

Mohammed H. A. Alopaedy [*,1,a], Layth W. Ismael [2,b], Ghufran F. Hasan [1,c], Mayada S. Mohammed [3,d], Alameer H. Alhasan [2,e], Zeena A. Ali [1,f], Ali M Abd [1,g]

[1]*Nanotechnology and Advanced Materials Research Centre, University of Technology, Baghdad, Iraq*
[2]*College of Materials Engineering, University of Technology, Baghdad, Iraq*
[3]*College of Applied Sciences, University of Technology, Baghdad, Iraq*

Article Info

Article History:

Received 11 Oct 2025
Accepted 27 Dec 2025

Keywords:

Biocompatibility;
Corrosion resistance;
Titanium;
Dental implants;
Spin coating,
Niobium pentoxide

Abstract

The excellent mechanical strength and clinical reliability of titanium-based implants are key advantages of their applications in biomedical fields. However, their susceptibility to bacterial colonization and corrosion remains a major limitation, affecting long-term performance and compromising patient safety. The present study described a niobium pentoxide coating, applied using the spin coating technique followed by thermal annealing, as a viable surface modification approach that can be used to enhance the corrosion resistance and antibacterial performance of titanium dental implants. The Nb_2O_5 suspension was prepared under controlled conditions and subsequently deposited, in multiple layers, onto the substrate to form a uniform protective film. Electrochemical characterization by potentiodynamic polarization (Tafel analysis) demonstrated a significant decrease in the corrosion rate, from 0.0077 mm/year for uncoated to 0.0021 mm/year for coated titanium, representing a ~73% decrease in corrosion current density. These results proved that a stable passive layer had formed, enhancing surface stability in physiological media. Successful crystallization of Nb_2O_5 phases upon thermal treatment, as confirmed by XRD analysis, accounted for the enhanced electrochemical performance. Antibacterial properties against Staphylococcus aureus ATCC 25923 were evaluated by the agar diffusion method. Results obtained showed that the diameter of the inhibition zone had increased from 12.9 ± 0.4 mm (uncoated) to 15.1 ± 0.5 mm (coated), corresponding to a statistically significant improvement of 16.7% ($p < 0.05$). Enhanced antibacterial properties were related to changes in surface properties owing to the deposition of Nb_2O_5 films, leading to reduced bacterial adhesion and biofilm growth. Conclusion The Nb_2O_5 coating contributed significantly to the improvement of corrosion resistance and the antibacterial properties of the titanium implants, hence demonstrating biomedical relevance for future applications in dentistry.

© 2026 MIM Research Group. All rights reserved.

1. Introduction

When it comes to metals, titanium and its alloys are considered the standard due to their mechanical properties, resistance to corrosion, and biocompatibility [1]. Their resistance to oxidation due to the formation of stable oxide, i.e., TiO_2 layer at the surface make them endure the stress of oral environment with wide ranging pH, presence of microbial biofilms, and cyclic mechanical loads. Even

*Corresponding author: mohammed.h.abdali@uotechnology.edu.iq
[a]orcid.org/0009-0006-1503-6403; [b]orcid.org/0000-0001-7814-8214; [c]orcid.org/0000-0009-8293-8329;
[d]orcid.org/0009-0007-1776-1876; [e]orcid.org/ 0009-0001-1060-804x; [f]orcid.org/0009-0000-9734-5221;
[g]orcid.org/0009-0005-5323-9650
DOI: http://dx.doi.org/10.17515/resm2026-1238ic1011rs

with these benefits, titanium implants have their limitations. However, complications such as peri-implantitis, ion release, and insufficient osseointegration are still the main problems, which may cause peri-implantitis and conclusion of implant failure. The novelty in this work was the rational use of niobium pentoxide (Nb_2O_5) for modifying, in a single action, the surface of titanium implants to improve their corrosion resistance and to make them antibacterial. Although titanium is commonly used in medical implants, its natural ability for the adhesion of bacteria and its susceptibility to degradation upon exposure to physiological environment requires the development of surface modification methods. The choice of Nb_2O_5 was prescribed by its inherently known chemical stability, as well as its known osteointegrative and antimicrobial properties. In contrast to traditional coatings targeting only a single limitation, this dual-functional strategy is expected to combat two important limitations (biofouling and electrochemical degradation) simultaneously and thus provide a new solution to improvement of the longevity and safety of implants. The decision to pursue this direction was further supported by the growing demand for multifunctional implant surfaces capable of addressing postoperative complications without compromising mechanical performance.

A significant challenge is the potential for bacterial biofilm development on the surface of dental implants, leading to chronic infections (Peri-implantitis) and implant failure. Peri-implantitis, an inflammatory condition induced by bacterial biofilms, contributes to the risk of implant failure and represents a major risk to long-term implant success. Moreover, titanium ions release in a corrosive oral environment raises concerns about possible produced cytotoxic and inflammatory responses, compromising both patients' safety and implants service life. However, these problems require novel approaches to improve the surface properties of titanium implants [2]. Silver nanoparticle coatings on titanium to reduce adhesion of bacteria These coatings not only killed bacteria but were also cytotoxic to osteoblasts, and therefore were not suitable for clinical application [3].

Olivares-Navarrete al. [4] tested the biocompatibility of niobium and its oxides using in vitro cell culture testing. Nb_2O_5 showed good chemical stability and biocompatibility, and was identified as a potential promising material for biomedical anode [5]. Nascimento et al. [6] sprayed Nb_2O_5 coatings on titanium to study their antibacterial activity. They also demonstrated that Nb_2O_5 strongly suppressed bacterial growth by indirect rather than direct manners without toxicity to human cells, suggesting its application as safe and efficient implant coatings [7].

Bioactive coatings have attracted attention in recent years to enhance the functional performance of titanium implants, facilitated by the development of surface modification technologies. Notably, metallic oxides have been well explored to overcome this challenge, focusing on the twofold property of enhanced corrosion resistance and increased biocompatibility. Niobium pentoxide (Nb_2O_5) has been investigated as a promising material due to its high chemical stability, its non-toxicity and the formation of a dense protective oxide sulhouette. Furthermore, Nb_2O_5 coatings have been reported to display antimicrobial properties and to enhance osseointegration by promoting cell adhesion and proliferation. In the field of biomedical applications, niobium-based coatings have been researched in several studies. For instance, Pakshir et al. investigated the tribo-corrosion characteristics of Nb_2O_5-coated titanium and found a remarkable improvement in mans of corrosion resistance and wear in simulated body fluids. In another study conducted by Gutwein and Webster (2004), they investigated the impact of nanostructured niobium oxide on cell attachment by demonstrating that the nanosized characteristics of the coating enhance osseointegration through osteoblast adhesion and proliferation. Sathish Kumar et al. also attempted. confirmed that the Nb_2O_5 coating had antibacterial activity against Staphylococcus aureus and Escherichia coli, indicating the potential ability of Nb_2O_5 to reduce the likelihood of implant-associated infections [8].

Although niobium pentoxide shows promising results in the previously performed studies, there are only few studies related to niobium pentoxide in the dental field and still fewer with titanium implants. Recognizing this fact, the aim of this research study was to present a pure Ti alloy and to describe the advantages that this alloy could have in bio applications, including improved corrosion resistance, reduced ion release, and improved enhancements in biocompatibility. The objective of this work is to assess the potential of niobium pentoxide coatings to enhance the biocompatibility and corrosion resistance of titanium dental implants. This study aims to bridge this gap and develop more stable and

clinically relevant dental implants systems incorporating the inherent drawbacks of traditional titanium implants.

2. Materials and Methods

2.1. Materials

Titanium samples were used. Pure titanium rod grade ASTM F67 GR2 was purchased from Shaanxi Yunzhong Industry Development CO., LTD. It is a 1000 mm length and 10 mm diameter rod; the rod was cut into 25 samples using a wire cutting machine, each with dimensions of 10 mm in diameter and 10 mm in length, as shown in table 1.

Table 1. Chemical composition of titanium

#	Material	Fe	C	N	O	H	Ti
1	Ti	0.3	0.08	0.03	0.25	0.015	remainder

2.2. Surface Treatments

All samples were ground using silicon carbide (SiC) papers in the following series (400, 600, 800, 1000, 1200, and 2000 grain sizes) to achieve a clean and flat surface, after which the samples were polished to prepare a clean, uniform, smooth surface for the coating processes. to verify that the surface property and the remainders of it are the same in every example. Given before, offer better adhesion and performance of the coatings [9].

2.3. Coating Process

Such a coating procedure was done in three steps: preparation of an Nb_2O_5 suspension, spin coating, and thermal annealing. To prepare the suspension, 0.5 g of Nb_2O_5 powder was dispersed in a chemically resistant glass vessel. Then, 10 mL of diluted sulfuric acid (H_2SO_4, 1:1 water-to-acid) was slowly added under stirring to prevent clustering, followed by mild heating in a water bath (10–15 min) to promote dispersion. Subsequently, 10 mL of absolute ethanol was added, and the mixture was stirred until homogeneous. The final suspension had a concentration of 25 mg/mL, a measured pH of 2.0, a density of 0.98 g/mL, and a dynamic viscosity of 3.2 mPa·s at 25 °C. The suspension was aged for 24 h at room temperature prior to coating. For spin coating, 2–3 drops (~60–90 µL) of suspension were dispensed onto the pure titanium substrate; the sample was first spun at 800 rpm for 10 s to ensure uniform spreading and then at 4000 rpm for 45 s to obtain a thin and smooth layer. Three layers were deposited, with intermediate drying at 90 °C for 10 min between layers. Thermal annealing was performed in an argon atmosphere at 600 °C for 1 h, with a heating rate of 5 °C/min. This temperature was chosen to ensure Nb_2O_5 crystallization and coat adhesion. The inert atmosphere prevented oxygen diffusion into the titanium substrate and thereby avoided the formation of alpha-case. The post-annealing SEM and electrochemical analysis confirmed that the integrity of the titanium substrate was preserved without its embrittlement or degradation. [10-12]

2.4. Characterization Methods

X-ray diffraction (XRD) (Shimadzu, 6000) using room temperature with a scanning rate of 5/min Cu Ka radiation (λ=1.5405 A°) and applied energy (40 kV and 30 mA) and consequently scanning electron microscope (SEM) (FEIQUANTA 250, Czech Republic) to prove the particles form and to estimate its thickness.

2.5. Corrosion Test

Corrosion tests were performed on the samples before and after the coatings were applied. performed tests like open circuit potential (OCP), Tafel analysis, cyclic polarization, and electrochemical impedance (EIS). The Corrtest Instruments Potentiostat/Galvanostat BS-21 device, in a 37°C at pH 7 system. The corrosion media used is Ringer's Solution [13]. The formula for the Experiments Corrosion Rate (CR) is as follows ($CR = (K \times Icorr) / (\rho \times A)$, where K is a constant (0.00327), Icorr is the corrosion current density (A/cm^2), ρ is the density of the material (g/cm^3), and A is the area of the sample (cm^2).

3. Results and Discussion

3.1 XRD Analysis of Titanium Before and After Niobium Pentoxide (Nb_2O_5) Coating

X-ray diffraction analysis was made to determine the phase composition and structural parameters of the uncoated titanium and Nb_2O_5-coated titanium. Figure 1 shows the diffraction patterns of both the samples, in which the black spectrum is for pure titanium and the red spectrum is for the coated sample.

The diffraction peaks for uncoated titanium, at 2θ values of 35.32°, 38.56°, 40.36°, 53.12°, 63.12°, and 70.72°, matched the hexagonal close-packed (hcp) structure of α-Titanium, according to JCPDS card no. 44-1294. These sharp and well-defined peaks confirm the crystalline nature of the titanium substrate. After Nb_2O_5 coating and thermal annealing, the additional peaks at 22.96°, 28.68°, 35.44°, 38.72°, 40.52°, 53.32°, 63.24°, and 70.92° correspond to the orthorhombic phase of Nb_2O_5, identified by using JCPDS card no. 30-0873. This indicates that the Nb_2O_5 coating was successfully deposited and crystallized on the titanium surface.[14]

Some degree of peak broadening was perceptible in the coated sample, especially for Nb_2O_5-related reflections. The peak broadening can be ascribed to lattice strain, reduced crystallite size, or partial amorphization within the coating layer. From the FWHM of the most intense Nb_2O_5 peak and assuming that peak broadening is dominated by particle-size effects, the average size of the crystallites was estimated using the Scherrer relationship:

$$D = \frac{K\lambda}{\beta cos\ \theta} \tag{1}$$

where D is the crystallite size, K=0.9 is the shape factor, λ=1.5406Å is the wavelength of Cu Kα radiation, β is the FWHM in radians, and θ is the Bragg angle. The calculated crystallite size for the Nb_2O_5 coating was approximately 32 ± 3 nm, indicating nanoscale crystallinity.

This resulted in a crystallite size of ~32 ± 3 nm for Nb_2O_5 coating, which showed nanoscale crystallinity. In conclusion, the XRD data confirm the crystalline formation of a Nb_2O_5 phase on the titanium surface, which can be related to the enhancement of corrosion resistance and surface stability of the coated samples. These structural improvements support the coating's biomedical relevance and also its potential for dental implant applications, as depicted in Figure 1.

3.2 Surface Morphology Analysis of Nb_2O_5 Coating Using SEM

Nb_2O_5-coated titanium specimen (the Nb_2O_5 layer is rather uniform, indicating that the spin coating technique is very efficient for producing a thin and adherent homogenous coat). The surface morphology is of nano-structured or micro-structured scale, which is important for better cell adhesion and bio-compatibility. In addition, the nano roughness would improve the osteointegration so that the coating is also useful for dental implantations.

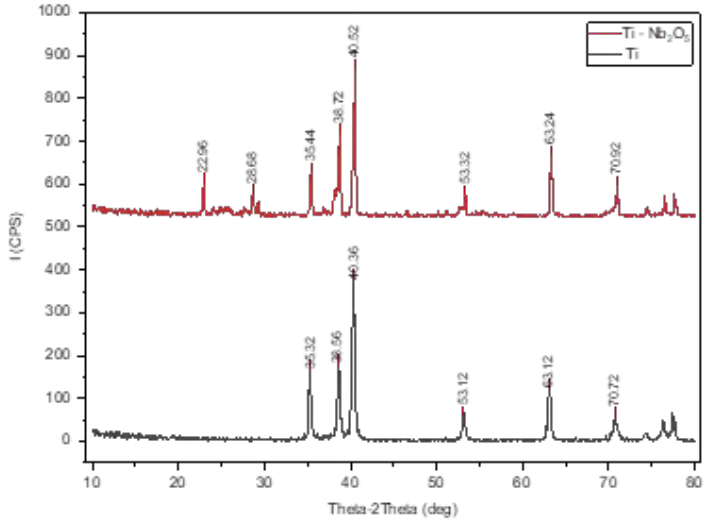

Fig. 1. XRD of Ti and Ti – Coated

The SEM images further visualize the general homogeneity and continuity of the coating, which are important for providing consistent anti-corrosion and bacteria-resistant protection. Any surface cracks or defects are probably caused by the thermal expansion–contraction that occurs during the annealing and likely can affect the long-term durability of a coating. Bacterial can also be prevented from adhesion by any smooth surface, which help to increase the antimicrobial efficiency by controlling the bio film formation [15]. Moreover, the nanopores within the coating surface may facilitate its interaction with biofluids resulting in an enhanced biological response and integration. This can lead to non-uniformities or agglomeration of the coating and local weaknesses may arise that might be addressed by adjusting the deposition parameters (spin, precursor concentration, annealing conditions) so as to give uniform coverage over the entire surface of the substrate [16,17], as depicted in figure 2

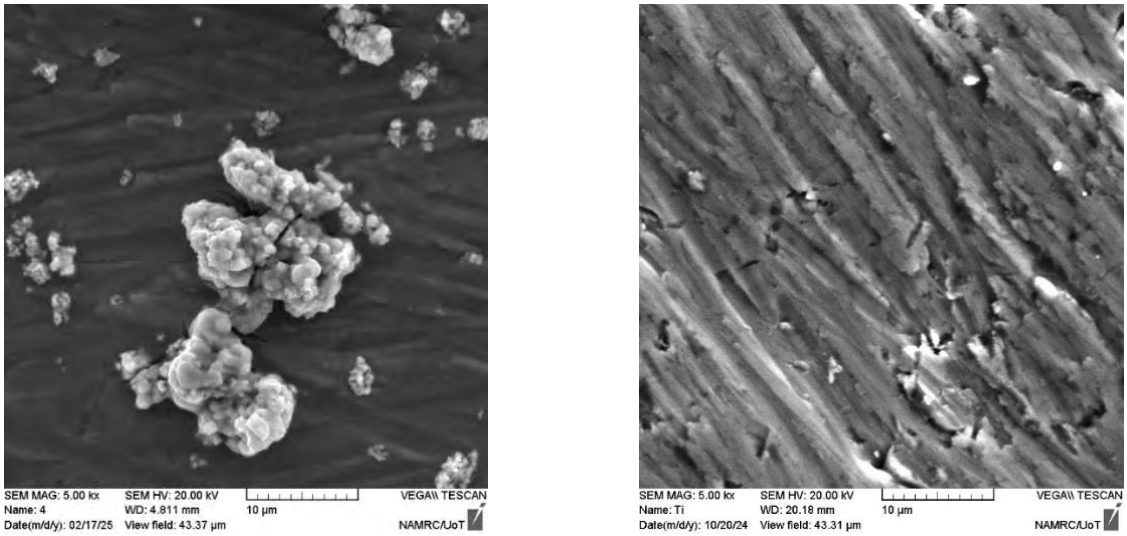

Fig. 2. SEM of Ti – Coated and Pure Ti

3.3 Corrosion Behavior Analysis of Titanium Before and After Coating

The potentiodynamic polarization curves of bare titanium and Nb_2O_5-coated titanium for the electrochemical responses are carried out as shown in Table 2, Figure 3. The test data provided key values that describe the corrosion resistance of the material such as corrosion potential (Ecorr), which is lower than for BA in each but also its icorr, Tafel slopes (bc and ba), CR, Rp on material, and IE (%). [18]. The untreated Ti had Ecorr (–0.054 V vs SCE) that was more noble than the coated sample (Ecorr: –0.108 V vs SCE). The positive shift in E_corr indicates an enhanced thermodynamic stability and a decreased likelihood of spontaneous corrosion. Therefore, it is proposed that Nb-oxide coated titanium has long term stability of the surface. [19]

The icorr, which reflects the rate of metal dissolution, decreased significantly from 6.58×10^{-7} A/cm^2 for uncoated to 1.78×10^{-7} A/cm^2 for coated sample. This ~73% decrease in icorr guarantees the barrier role of Nb_2O_5 layer due to retarding the charge transfer and partially blocking corrosive substance from contacting. [20] Similarly, the Tafel slope values also varied significantly between coated and uncoated samples. The cathodic slope, on the other hand, was enhanced from 29.846 mV/dec to 40.385 mV/dec and the anodic slope was increased from 34.983 mV/dec to 43.348 mV/dec. These changes are also evidence for a shift in electrochemical kinetics likely associated with enhanced passivation and reduced active surface area in contact with the electrolyte.

The CR value that was converted from icorreng into mm/year, decreased with coating (0.00209 mm/year) compared to uncoated titanium (0.00772 mm/year), this great decrease supports the good protection that the coating gives to the substrate under simulated physiological conditions. The polarization resistance Rp increased from 1.04×10^5 Ω·cm^2 to 4.38×10^5 Ω·cm^2, proving the high resistance for electrochemical reaction. In addition, an inhibition efficiency of 73% was calculated for the Nb_2O_5 coating, and this further validated its protection.

Figure 3 shows the Tafel plots of both samples, indicating an obvious shift of corrosion potential to the right and a decrease in current density for the coated titanium. The plot of the coated sample is flatter, with slower kinetics of corrosion and improved stability on the surface. In short, the Nb_2O_5 coating decisively improves the corrosion resistance of pure titanium by decreasing icorr and CR, increasing Rp, and enhancing %IE. The substantial improvements are related to the growth of a stable, adherent, and passivating Nb_2O_5 layer acting as a physical and chemical barrier against aggressive ions. Such enhancements are very important for extending the lifespan and improving biocompatibility of titanium dental implants in the corrosive environment of the oral cavity. [21-23]

Table 2. Corrosion parameters of Titanium

	-Ecorr	icorr	-bc	+ba	CR	R_p	%IE
	(mV)	($A.cm^{-2}$)	$mV.dec^{-1}$		(mm/a)	Ω·cm2	**%**
Ti	0.054154	0.000000658070	29.846	34.983	0.00772472938461539	104,000	
Ti- Nb_2O_5	0.10797	0.000000177670	40.385	43.348	0.00208557246153846	438,000	73%

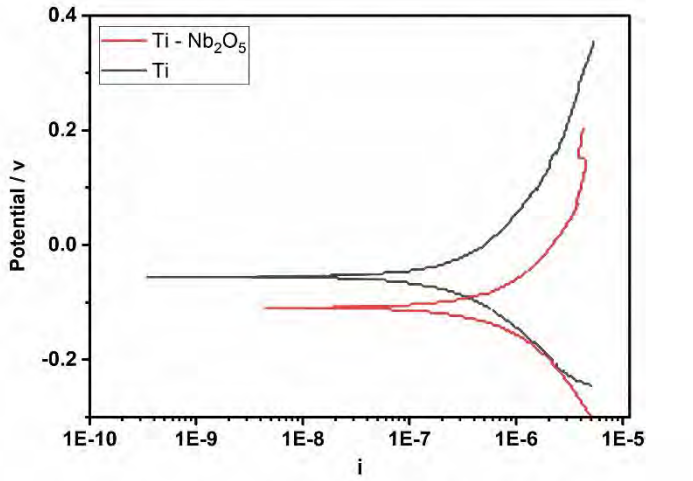

Fig. 3. Electrochemical behavior of Ti and Ti - coated

3.4 Inhibition Zone Diameter Results

The antibacterial activity of pure titanium and Nb_2O_5-coated titanium was measured by the agar diffusion method against Staphylococcus aureus ATCC 25923 using Mueller–Hinton agar plates that were inoculated with bacterial suspensions at 1×10^6 CFU/mL (0.5 McFarland standard) under an aerobic atmosphere at 37 °C for 24 h. The inhibition zones were measured in triplicate and expressed as mean ± SD. The uncoated titanium showed an inhibition zone diameter of 12.9 ± 0.4 mm, while Nb_2O_5-coated titanium exhibited a higher diameter of inhibition zone to 15.1 ± 0.5 mm (n = 3).

3.5 Rise in Antibacterial Activity

Compared to uncoated titanium, the diameter of the inhibition zone was higher by 16.7% for the coated sample, and the increase was statistically significant ($p < 0.05$). From this result, it may be assumed that Nb_2O_5 coating increases the antibacterial properties of titanium. Presumably, a stable oxide layer is formed, which reduces bacterial adhesion and biofilm formation. Niobium pentoxide is reported to be a biocompatible material with the ability to alter surface properties in a way that is not favorable for microbial colonization. Thus, the increased diameter of the inhibition zone was attributed to surface modifications induced by the coating, which alter the kinetics of bacterial adhesion and create a less favorable environment for bacterial growth. [24,25]

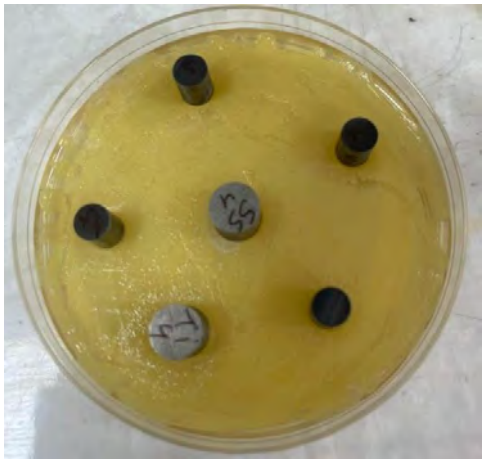

Fig. 4. Inhibition Zone Test of Ti and Ti - coated

4. Conclusions

The corrosion and antibacterial properties of pure titanium substrates coated by Nb_2O_5 using spin coating followed by thermal annealing have been considerably improved. Through electrochemical characterization, a great decrease in corrosion current density and corrosion rate was proved, while a great increase in polarization resistance was obtained, suggesting the development of a steady, protective passive layer. By XRD analysis, the successful crystallization of Nb_2O_5 phases contributing to the enhanced electrochemical stability of the coated samples was verified. Antibacterial testing against Staphylococcus aureus resulted in a statistically significant widening of the diameter of the inhibition zone, which verifies the ability of this coating to diminish bacterial adhesion and biofilm growth.

These findings emphasize the biomedical relevance and possible clinical applications of Nb_2O_5-coated implants made of titanium, especially in dentistry, where long-term durability and resistance to microbial colonization are important. Although direct cytotoxicity or biological compatibility tests were not shown in this work, these observations on the enhancement of corrosion resistance and antibacterial activity clearly suggest that Nb_2O_5 coatings have excellent potential for prolonging the service life and reliability of titanium-based implants. Further work is recommended, including biological and cytotoxicity evaluations to establish coating performance in vivo.

Acknowledgement

The authors extend their heartfelt appreciation to the Nanotechnology and advance materials Research Center/University of Technology, for their support and the facilities provided during the course of this research. Thanks, and appreciation goes to the faculty members and technical staff for their invaluable assistance with the corrosion, XRD, and antibacterial tests. They have been helpful during this research as in the long run this research would not have reached completion without their guidance and cooperation.

References

[1] Berrospe-Rodriguez C, Baskar B, Williams J, Aguilar G. Wettability tuning on stainless steel LIPSS by laser oxidation and its implication on cavitation bubble dynamics. Applied Surface Science. 2024 Nov 1; 672:160803. https://doi.org/10.1016/j.apsusc.2024.160803

[2] Bharath, A.H. and K.B. Sundaram, Characterization of reactively sputter deposited CuCrO2 thin films using Cu and Cr targets. Materials Advances, 2024. 5(22): p. 8919-8926. https://doi.org/10.1039/D4MA00799A

[3] Zhao L, Chu PK, Zhang Y, Wu Z. Antibacterial coatings on titanium implants. Journal of Biomedical Materials Research Part B: Applied Biomaterials. 2009 Oct;91(1):470-80. https://doi.org/10.1002/jbm.b.31463

[4] Olivares-Navarrete R, Olaya JJ, Ramírez C, Rodil SE. Biocompatibility of niobium coatings. Coatings. 2011 Sep 22;1(1):72-87. https://doi.org/10.3390/coatings1010072

[5] Nascimento JP, Teixeira GT, Obata MM, Silva MV, Oliveira CJ, Silva LE, Gelamo RV, Slade NB, Moreto JA. Influence of Reactive Sputtering-Deposited Nb2O5 Coating on the Ti-6Al-4V Alloy Surfaces: Biomineralization, Antibacterial Activity, and Cell Viability Tests. Materials Research. 2023 Nov 17;26: e20230251.

[6] Pakshir, M., T. Bagheri, and M.R. Kazemi, In vitro evaluation of the electrochemical behaviour of stainless steel and Ni-Ti orthodontic archwires at different temperatures. Eur J Orthod, 2013. 35(4): p. 407-13. https://doi.org/10.1093/ejo/cjr055
[7] Pulikkottil VJ, Chidambaram S, Bejoy PU, Femin PK, Paul P, Rishad M. Corrosion resistance of stainless steel, nickel-titanium, titanium molybdenum alloy, and ion-implanted titanium molybdenum alloy archwires in acidic fluoride-containing artificial saliva: An: in vitro: study. Journal of Pharmacy and Bioallied Sciences. 2016 Oct 1;8(Suppl 1):S96-9. https://doi.org/10.4103/0975-7406.192032
[8] Al-Hasani, F.J., Q.A. Hamad, and N.K. Faheed, Enhancing the cell viability and antibacterial properties of alginate-based composite layer by adding active particulates. Discover Applied Sciences, 2024. 6(2): p. 70. https://doi.org/10.1007/s42452-024-05715-6
[9] Teimouri R, Grabowski M, Bogucki R, Ślusarczyk Ł, Skoczypiec S. Modeling of strengthening mechanisms of surface layers in burnishing process. Materials & Design. 2022 Nov 1; 223:111114. https://doi.org/10.1016/j.matdes.2022.111114
[10] Velasco-Ibáñez R, Lara-Carrillo E, Morales-Luckie RA, Romero-Guzmán ET, Toral-Rizo VH, Ramírez-Cardona M, García-Hernández V, Medina-Solís CE. Evaluation of the release of nickel and titanium under orthodontic treatment. Scientific Reports. 2020 Dec 17;10(1):22280. https://doi.org/10.1038/s41598-020-79221-1
[11] Jawad, Z., F. Al-Hassani, and E. Al-Hassani, Preparation and Characterization of Hybrid Composite Material for Maxillary Sinus Augmentation. Silicon, 2023. 16. https://doi.org/10.1007/s12633-023-02726-7
[12] Park, J.-H., et al., Effect of Zn-Mg interlayer on the corrosion resistance of multilayer Zn-based coating fabricated by physical vapor deposition process. Corrosion Science, 2022. 202: p. 110330. https://doi.org/10.1016/j.corsci.2022.110330
[13] Sharma P, Hasan MR, Khanuja M, Rawal R, Pilloton R, Narang J. Aptamer-based silver nanoparticle decorated paper platform for electrochemical detection ovarian cancer biomarker PDGF. Materials Chemistry and Physics. 2023 Sep 15; 306:128114. https://doi.org/10.1016/j.matchemphys.2023.128114
[14] Jawad, Z., F. Mohammed, and E. Al-Hassani, Effect of Cordierite Additions on Mechanical Properties of Hydroxyapatite Used in Medical Applications. Engineering and Technology Journal, 2023. 41.
[15] Jawad, Z., F. Al-Hassani, and E. Al-Hassani, In Vivo and In Vitro Biological and Histological Evaluation of Cordierite-Hydroxyapatite Ceramic Grafting Powder During Maxillary Sinus Augmentation in Rabbit Model. Journal of Inorganic and Organometallic Polymers and Materials, 2023. 34: p. 3. https://doi.org/10.1007/s10904-023-02833-3
[16] Al-Janabi, A., F. Alhasani, and E. Al-Hassani, Surface Enhancement of Magnesium Implants for Long Term Applications. Key Engineering Materials, 2022. 937: p. 79-87. https://doi.org/10.4028/p-l74381
[17] Karandish M, Hajipour N, Yazdani H, Mahdavi M, Rahsepar M. An investigation of the corrosion behavior of zinc-coated stainless steel orthodontic wires: the effect of physical vapor deposition method. BMC Oral Health. 2024 May 9;24(1):501. https://doi.org/10.1186/s12903-024-04242-5
[18] Castro SM, Ponces MJ, Lopes JD, Vasconcelos M, Pollmann MC. Orthodontic wires and its corrosion-The specific case of stainless steel and beta-titanium. Journal of Dental Sciences. 2015 Mar 1;10(1):1-7. https://doi.org/10.1016/j.jds.2014.07.002
[19] Zhang C, He L, Chen Y, Dai D, Su Y, Shao L. Corrosion behavior and in vitro cytotoxicity of Ni-Ti and stainless-steel arch wires exposed to lysozyme, ovalbumin, and bovine serum albumin. ACS omega. 2020 Jul 24;5(30):18995-9003. https://doi.org/10.1021/acsomega.0c02312
[20] Pakshir, M., T. Bagheri, and M.R. Kazemi, Invitro evaluation of the electrochemical behaviour of stainless steel and Ni-Ti orthodontic archwires at different temperatures. European Journal of Orthodontics, 2013. 35(4): p. 407-413. https://doi.org/10.1093/ejo/cjr055
[21] Yıldırım, G., F. Eraydın, and D. Nalbantgil, Corrosion Behavior of Nickel-Titanium Arch Wires Following the Use of Different Mouthwashes: An In Vivo Study. Turk J Orthod, 2024. 37(3): p. 168-173. https://doi.org/10.4274/TurkJOrthod.2023.2022.182
[22] Nasution MA, Lubis HF, Sipayung IV, Sitepu IN. Changes in the corrosion rate and microstructure of nickel titanium wire in pandan leaves extract. Journal of Orthodontic Science. 2024 Nov 1;13(1):53. https://doi.org/10.4103/jos.jos_188_23
[23] Abd Ali, Mohammed & Al-Hassani, Emad & Al-Hassani, Fatimah. (2025). Improving Corrosion Resistance of Stainless Steel 316L, Titanium Orthodontic Archwires Enhanced by Metallic Coatings. Journal of Physics: Conference Series. 3028. 10.1088/1742-6596/3028/1/012006. https://doi.org/10.1088/1742-6596/3028/1/012006
[24] Brantley, W.A. and T. Eliades, Orthodontic Materials: Scientific and Clinical Aspects. 2001: Thieme. https://doi.org/10.1055/b-002-43889
[25] Kadhim, Z.J., F.J. Al-Hasani, and E.S. Al-Hassani, Preparation and Characterization of Hybrid Composite Material for Maxillary Sinus Augmentation. Silicon, 2024. 16(2): p. 891-907. https://doi.org/10.1007/s12633-023-02726-7

Research on Engineering Structures & Materials
www.jresm.org

Research Article

Green syntheses and characterization of Phragmites australis nanofibers on sustainable concrete

Fahad Saadi Almani [*,1, a], Farhad M. Othman [2,b], Alaa A. Abdul-Hameed [2,c]

[1]*Directorate of Water Resources in Karbala, Ministry of Water Resources, Karbala, Iraq*
[2]*Materials Engineering College, University of Technology – Iraq, Baghdad, Iraq*

Article Info

Article History:

Received 12 Oct 2025
Accepted 27 Dec 2025

Keywords:

Phragmites australis
Nano-fiber,
Cellulose,
Concrete,
Alkali treatment,
Compressive strength,
Flexural strength,
Sustainability and west plant

Abstract

Concrete suffers from low tensile capacity, high brittleness, and increasing environmental impact due to cement production. This study presents a green synthesis route for extracting cellulose nanofibers from Phragmites australis, an abundant invasive plant, and evaluates their effectiveness as a sustainable reinforcement for concrete. The novelty of the work lies in converting an environmental waste material into nano-cellulose fibers through an eco-friendly alkali-based extraction process, followed by mechanical milling to achieve nano-scale sizes (80–100 nm). The nanofibers exhibited increased crystallinity, enhanced purity, and improved surface morphology as confirmed by XRD, FTIR, SEM, XRF, and particle size analysis. Concrete mixes incorporating 5%, 10%, and 15% nanofibers were tested at 7, 28, and 90 days. The optimum performance occurred at 10% nanofiber content, which improved flexural strength by 36% (from 4.09 to 5.57 MPa) and maintained compressive strength at 29.4 MPa compared with the control (28.2 MPa). Physical properties also improved, with reductions in porosity and water absorption at the optimum dosage. However, 15% fiber addition caused strength and workability reductions due to fiber agglomeration and increased voids. These findings demonstrate that Phragmites australis nanofibers can serve as a low-cost and sustainable reinforcement to enhance concrete performance while valorizing an invasive plant. The study supports the broader trend of integrating bio-based nanomaterials into construction materials to reduce environmental impact and improve mechanical efficiency.

© 2026 MIM Research Group. All rights reserved.

1. Introduction

Concrete is a principal building material in the world, as well as one of the most widely consumed materials after water [1]. But the materials are low in tensile strength, high in brittleness, weak in stress-strain capabilities and notoriously bad to produce given its carbon footprint. Green cement technologies, reactive powder concrete (RPC), low-emission materials, scattering fibers, and nanoparticles have been studied to avoid these limitations [2–6]. Nanoparticles smaller than 500 nm improve micro- and nanoscale hydration [6], increase the mechanical rigidity [7–10] and lead to higher electrical resistibility [11,12]. In the category of nanoparticles, cellulose (C) or CNFs obtained from the fibers extracted from plants have attracted significant prominence owing to their large surface area (100 m^2/g), high aspect ratio (100), high crystallinity, low density and strength [13]. They are based on CNF, a renewable and recyclable material with biodegradable properties. In terms of structural composition, CNFs are predominantly cellulose with lignin and hemicellulose—whereas the latter two provide structure, their amorphous nature renders them inferior to cellulose. Different types of plants including cassava bagasse [14], wheat straw [15], cotton [16], bamboo [17], and sugar palm [18] have been employed as the sources to produce CNFs. Green synthesis methods, especially ecofriendly alkali-

*Corresponding author: mae.20.30@grad.uotechnology.edu.iq
[a]orcid.org/ 0009-0006-4216-0370; [b]orcid.org/0000-0002-2289-5656; [c]orcid.org/0000-0003-4492-6369
DOI: http://dx.doi.org/10.17515/resm2026-1243ic1012rs

mediated extraction routes, not only eliminate toxic substances and lower energy requirement when compared with the traditional acid hydrolysis method but also provide a means for producing f -MNCs that can address some issues in natural concrete materials such as poor strength and environment vulnerability. Despite the promise of CNFs in improving flexural behavior, crack resistance, and microstructural densification, most studies rely on commercial fibers or energy-intensive methods, which do not address cost, environmental impact, or availability in resource-limited regions. Phragmites australis (PA) is selected in this study due to its fast growth, invasiveness, and environmental burden; converting this abundant biomass into nanofibers provides dual benefits of ecological mitigation and a zero-cost, renewable raw material. PA fibers naturally possess low lignin content, fine morphology, and high aspect ratio, making them highly suitable for nanofiber production, while also stabilizing cement-based products by reducing chemical, autogenous, and drying shrinkage, and being heat-resistant [19,20]. This research introduces a green, alkali-based nano-extraction method combined with high-efficiency planetary ball milling to produce nanofibers with particle sizes of 80–100 nm, improved crystallinity, and enhanced surface roughness, representing a novel contribution to sustainable nanofiber production from invasive plants. Unlike previous studies that focused on commercial or agricultural fibers, this work employs a fully green extraction technique, provides comprehensive multi-scale characterization (XRD, FTIR, SEM, XRF, particle size analysis), and evaluates the mechanical and physical performance of concrete reinforced with nanofibers at 5%, 10%, and 15%, including regression analysis and optimal-dose identification. The overall aim is the preparation and characterization of cellulose nanofibers from Phragmites australis and their effects on the mechanical and physical properties and confirmed that these types of nanofibers can improved strength, reduced porosity and bring a negligible Change in the unit weight of hardened paste. durable, cheap reinforcement based on new construction and as well as a response to the modern age requirements. environmental obstacles induced by PA overproduction.

2. Materials and Methods

2.1. Materials

The experimental work is divided into two parts: the part one deals fiber preparation and its characterizations, while the second stage consists of preparation and performance, respectively.

2.1.1 Preparation of Nano-Fiber

In the present work plant fibers were obtained from waste phragmites australis in the search for generation of sustainability in concrete. Extraction of Phragmites australis fiber from the Northern Karbala Drain. The fibers were washed thoroughly with distilled water to remove any surface impurities and air-dried at room temperature. Sodium hydroxide (NaOH) was purchased from SDFCL (Scientific Laboratory Supplies) sourced from Areej Al-Forat Office for engineering and chemical supplies, Baghdad, Iraq.}, and as an alkali treatment to improve the surface properties of the fibers. This choice of materials based on locally available plant waste and resources, conforms to the concept of sustainable building by maintaining the mechanical integrity of fabricated composites.

2.1.2 Preparation of Chopped Fibers

The Phragmites australis Wastes The wastes of Phragmites australis [as shown in Figure 1(a) were collected, washed well and then cut into (10-15) cm length in Figure 1(b).

(a) (b) (c) (d)

(e) (f) (g) (h)

Fig. 1. (a) Materials (b) Cutting & Washing. (c) alkali treatment by 4% NaOH. (d) Washing with distilled water (neutralization). (e), (f) Drying Process. (g) Blender process (h) Milling Process

They were then water-retted for a period of 24 hours to eliminate impurities and waxy contents. They were then 24 hours to dry in the air before they can be treated chemically (alkali).

2.1.3 Treatment of Chopped Fibers

Sodium hydroxide (NaOH) is applied here to fibers which create water with the alkali-sensitive hydroxyls (OH), lowering the moisture absorption tendency. This is believed to solubilize some hemicellulose, lignin, pectin and waxy layer by which increasing surface adhesion (rougher topography), mechanical interlocking and removing impurities [21-23]. Alkali treatment disrupts hydrogen bonds, enhances thermodynamic stability, eliminates microdata and decreases fiber diameter leading to improved aspect ratio and effective surface area [25, 26]. For the fibers to be utilized in composite materials, the plants were first treated with 4% NaOH solution at 100°C for 2 h [27,28] (Figure 1(c)), followed by rinsing with distilled water (neutralization) as presented in Figure 1(d), and then were dried at 60°C during up for overnight hours presented in Figure 1(e, f). 4% NaOH concentration, 100°C treatment temperature and 2 h treatment time were chosen with reference to literatures, also with consideration of the material itself. Prior studies on natural fibers such as sisal, banana, and Phragmites-based composites reported that NaOH concentrations between 2–6% effectively remove hemicellulose, surface waxes, and amorphous lignin without degrading cellulose structure. Similarly, a treatment temperature of 100°C accelerates alkaline penetration and improves the removal of amorphous components, while the 2-hour duration ensures complete chemical reaction without causing fiber over-degradation.

2.1.4 Blender and Milling

The dried material was ground using a blender and sieved through a 0.1 mm sieve to obtain uniform fiber size. The sieved fibers were then subjected to Planetary Ball Mill (Model: XQM-0.4A) for 4 hours at 550 rpm with balls of varying sizes placed in the device, weighing ten times the weight of the fibers. to achieve Nano-scale dimensions according to ISO/TS 20477:2017, as shown in Figure (1) (g, h).

2.2 Inspection of Nano-Fibers

The are several techniques can be used to inspect texture of materials such as:

2.2.1 X-Ray Diffraction (XRD)

The XRD patterns of nano-fiber samples were measured using Japan's XRD-6000 at the Nanotechnology and Advanced Materials Centre of the University of Technology. The measurements were taken from 10-60°(2θ) using a scanning rate of 2°/min and 0.02° step size. Equation (1) was used to compute the cellulose crystallinity index (CrI) [29].

$$CrI\ (\%) = (1 - Iam / Imax) \times 100 \quad (1)$$

Where Imax is the equivalent intensity of the maximum peak and Iam is the intensity of the amorphous fraction. For the calculation of the CS, the method used was established by Scherer's relations as expressed by the equation below:

$$CS = K\lambda / \beta \cos\theta \quad (2)$$

where K is the constant (0.89); λ corresponds to the intensity of radiation; β denotes the full-width at half-maximum (FWHM); and θ is the Bragg's angle[30].

2.2.2 The Scanning Electron Microscopy

SEM analysis was conducted using the VEGA TESCAN SEM instrument, with an accelerating voltage of 20.00 kV. The examination was performed at the Ministry of Industry and Minerals, Industrial Research and Development Authority.

2.2.3 Measuring Particle Size

American (Brook Haven 90 Plus) (5.0-5000.0) nm particles were tested for size at the University of Technology's Nanotechnology and Advanced Materials Centre.

2.2.4 FTIR Analysis

FTIR were done in a FTIR spectrum made in Germany, with 4000 to 400 cm−1 as the wave number and 0.9 cm−1, it used to identify the chemical analysis of materials in their various states by detecting the chemical bonds present in the material.

2.2.5 X-Ray Fluorescence

The nanofiber analysis was conducted using an X-Ray Fluorescence (XRF) instrument, model Spectro Xepos, manufactured in Germany by Ametek was carried out in Iran. This advanced device is renowned for its high precision in chemical element analysis through X-ray fluorescence technology.

2.3 Concrete Mix Design

For the concrete matrix, LAFARGE The major binder utilized was ordinary Portland cement (OPC). Fine aggregates (sand) and coarse aggregates (gravel) were sourced from the Karbala quarries and were pre-tested to confirm compliance with laboratory specifications for grading, cleanliness, and strength. All mixing and curing were performed using potable water. The 1:2:3 proportion of cement, sand and gravels by weight were adopted as concrete mix design based on ACI standard. The influence of fiber content addition in the mechanical and durability properties was evaluated by adding plant nanofibers at 5%, 10% and 15% w/w cement. The (ACI) was maintained at 0.5 to attain sufficient workability and an optimal compressive strength. This procedure guaranteed a homogeneous and reproducible blended mixture capable of efficiently realizing the reinforcing potential, in terms of hardness, of the plant nanofibers by maintaining the required performances level.

2.4 Sample Preparation

Firstly, all raw materials (cement, sand, gravel and plant fiber) were weighed according to the design mixture ratio of 1:2:3 (cement: sand: gravel) by weight, with plant nanofibers added at 5%, 10%, and 15% of cement weight Table 1 presents the mixing ratios and prepared samples, where Phragmites australis fibers are represented by (ANF%). The mixing process was carried out using a flat type mechanical mixer to ensure homogeneous dispersion of fibers. First, the tested cement is as shown in the table 3 was mixed with fibers and then with dry ingredients (sand and gravel) which physical examination are shown in Table 2 for 60 seconds at low speed to achieve a uniform mixture. A specified amount of water was added until the target workability was reached. After mixing, fresh concrete was poured into cubic molds (100×100×100 mm) for compressive strength tests and prismatic molds (75×75×300 mm) for flexural (flexural) tests. The samples were covered and dried at room temperature (about 20-25°C) for 24. The demolded specimens were moved to a curing tank in which potable water was added and kept for all subsequent periods of 7, 28, 90 days in order to ensure full filling of hydration capacity and development of strength. Compressive and bending strength tests were subsequently carried out for the cubic samples and prismatic samples, respectively, under a universal testing machine (at 7 days, 28 days and 90 days). These methods guaranteed homogeneous specimen preparation and yielded reliable data for comparing the mechanical behavior of FRC specimens with that of non-reinforced (standard) ones.

Table 1. Mix proportions and prepared samples

Specimen	Cement%	Quartz sand, %	Gravel, %	ANF, %
Control	100	100	100	
CANF1	95	100	100	5
CANF2	90	100	100	10
CANF3	85	100	100	15

Table 2. Properties of sand and gravel

Physical Properties	FA	CA	B.S limits 12620
Specific gravity	2.57	2.6	-
Dry compacted density (mg/m3)	1.8	1.9	-
Water Absorption (%)	0.82	1.7	-
SO3 (%)	0.113	0.054	≤ 0.2
Fineness modulus	3.4	0.05	-

Table 3. Chemical composition and main compounds of cement

Oxid and Composition	CaO	SiO_2	Al_2O_3	Fe_2O_3	MgO	SO_3	L.O. I	Insoluble	Free Lime	C_3S	C_2S	C_3A
% Content	59.89	19.8	6.1	3.32	1.64 ± 0.005	2.30 ± 0.03	3.70 ± 0.01	0.65 ± 0.005	0.81	42.02	26.7	2.44
B.S 4027 Limits	-	-	-	<5	<2.5	<4	<1.5	-	-	-	-	-

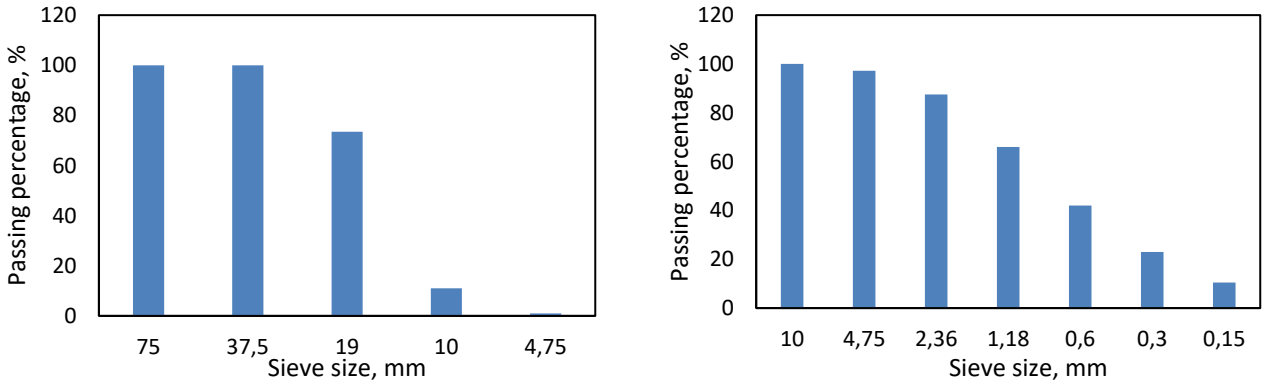

Fig. 2. Physical characteristics of (a)Sand (FA) and (b) Gravel (CA)

The fiber dosages of 5%, 10%, and 15% by weight of cement were chosen based on two considerations:

- Benchmarking from literature, where most natural-fiber-reinforced concretes exhibit optimal mechanical performance within 1–15% addition (depending on fiber size and processing). Studies on nano-cellulose from palm, cassava, and bamboo reported diminishing strength at dosages above 15% due to balling effects and increased porosity.
- Avoiding excessive loss in workability, since preliminary trial mixes in this study showed that fiber contents exceeding 15% significantly reduced slump and caused fiber agglomeration even with extended mixing.

2.5 Inspections of Fabricated Concrete Samples

The following tests are conducted on concrete specimens.

2.5.1 Fresh Concrete Workability Test

To analyze the impact of nano-fiber on concrete workability, all concrete mixes had constant water-to-cement ratio (W/C). As stated in BS1881-102 1983 [31], slump testing is performed using a cone (300×100×200) mm (height, top diameter and base diameter) to measure the influence.

2.5.2 Physical Properties Test

Dry density, porosity and water absorption tests were performed in accordance with ASTM C642-97. The test was performed on portions of concrete samples previously hydraulically compressed. Samples were oven dried for determining initial dry mass (w1). The samples were then immersed in water for 24 h to reach saturation, followed by solvent removal from surface. The mass surface-dry saturations (w2) were then measured after immersion. Finally, the samples were completely submerged in a beaker filled with water and weighed to obtain the apparent immersed mass (w3). using the following formula [32].

$$Dry\ density\ (g/cm^3) = [w1/(w2 - w3)] \times \rho w \quad (3)$$

$$Absorption\ of\ Water = [(w2 - w1)/w1] \times 100\ \% \quad (4)$$

$$Porosity = [(w2 - w1)/(w2 - w3)] \times 100\% \quad (5)$$

Where $w1$: the dry specimen's weight (g), $w2$: the wet specimen's weight (g), $w3$: the submerged specimen's weight in water (g), and ρw: the density of water, which is (1 g/cm3).

2.5.3 Compressive Strength Test

Compressive strength tests were conducted. Each test was performed on three specimens (n = 3), and average values are reported. Statistical significance between mixes was confirmed using one-way ANOVA ($p < 0.05$). with the method defined in B.S.1881-116. The test was performed using a compressive strength testing device (TONI PACT 3000/Germany). The upload speed was roughly 0.25 megapascals a second. The compressive strength of three 100×100×100 mm concrete samples (average) was calculated for each mixture. The exam was performed 7, 28, and 90 days after preparation. Calculating compressive strength using the stated relationship [33].

$$\sigma = P/A \quad (6)$$

Where σ: compressive strength, (MPa); P: ultimate compressive load, (N); A: area of the sample, (mm^2).

2.5.4 Flexural Strength Test

BS 12390-5: 2009 (the bending test), in this experiment a prismatic mold with dimensions (75×75×300) mm was used. A three-point flexural strength test is performed to generate the crack. A speed of 0.04 mm/min was applied. The results were recorded for cast and cured concrete specimens after 7, 28, and 90 days. The following law [34] was used to obtain the flexural strength.

$$Fct = F \times I/(d1 \times (d2)^2 \quad (7)$$

Replaceable with: Fct: Flexural strength, MPa (N/mm^2); F: Maximum load, N; I: Distance between supporting rollers, mm. lateral dimensions of the specimen in mm; d1 and d2.

3. Results and Discussion

3.1 XRD Results

The XRD analysis for the chemically treated Phragmites australis fibers demonstrates distinct diffraction peaks corresponding to the crystalline structure of cellulose I, enhanced by sodium hydroxide (NaOH) treatment, which effectively removed non-cellulosic components such as lignin and hemicellulose. The primary peaks associated with cellulose Iβ appear at 2θ ≈ 14.902°, 16.494°, 22.842° (strongest peak), and 34.882°, aligning with JCPDS card no. 03-0289, confirming that the crystalline structure of cellulose is preserved [35] Figure 3(a). silicon oxide (SiO2) characteristic's at 2θ ≈ 26.479°, 50.583° and by far the strongest peak is observed at 26.479° which matches with JCPDS74–

204411 card no:461441. This is due to the presence of residual silica, which derives from the inherent plant fibers. Moreover, Al peaks for aluminum oxides (Al2O3) were also observed at 2θ ≈ 32.802°, 45.642° and the highest intensity peak at 67.245° in compliance with JCPDS card no.:461131. This indicates the existence of alumina, probably caused by minerals contents in the fiber matrix. In addition, calcium oxide (CaO) was recognized by XRD peaks at 2θ ≈ 37.346° and 53.854° (JCPDS card no. etz371497), which is due to the presence of calcium-containing compounds that might improve compatibility between the fibers and cementitious materials. These results revealed that the alkali treatment enhanced the crystallite structure of cellulose, while retaining beneficial inorganic phases such as SiO2, Al2O3, and CaO. The presence of those mineral admixtures could offer an effective profit to polymeric strength and log-time durability of cementitious mixtures [36,37].

The responses in the XRD patterns of the treated Phragmites australis nanofibers show a cellulose Iβ diffraction peak at 2θ ≈ 14.9°, 16.4°, 22.8° and 34.8°. The strongest peak in the 22.8° is ascribed to the crystalline cellulose regions. The CrI increased significantly, in the Segal's approach, from ⍰46% of raw fibers (let us note that this assumes average values of polyanionic ones reported in literature) to 72% for treated nanofibers. This enhancement indicates the efficient extraction of amorphous hemicellulose and lignin.

A slight peak sharpening and reduction in FWHM indicates an increase in crystallite size, attributable to the elimination of amorphous content and exposure of more ordered cellulose domains. This enhancement in crystallinity is desirable, as higher CrI improves thermal stability and contributes to better interfacial bonding with cement hydration products.

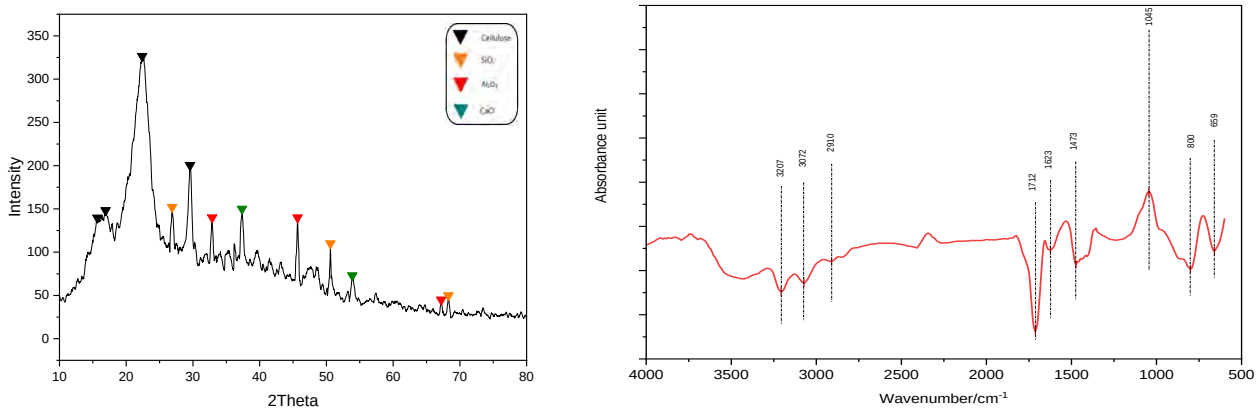

(a) (b)

Fig. 3. (a) XRD result (b) FTIR result

3.2 FTIR results

FTIR spectra of cellulose fibers derived from Phragmites australis show distinctive structural and chemical features that attest its chemical treatment process in the domain of shown in Figure 3(b), a broad absorption band around 3300–3000 cm^{-1} were attributed to hydroxyl (O-H) stretching vibrations which confirms the presence of cellulose [38]. The significant abundance of this band at Phragmites australis is indicative of a high concentration of cellulose and strong hydrogen bonding. Absorption bands at 2800–2900 cm^{-1} in which attributed to aliphatic C-H stretching, confirming the existence of cellulose and little amounts of hemicellulose residues [38]. A striking feature of the carbonyl (C=O) stretching region at approximately 1730 cm^{-1} is the marked decrease of this peak in Phragmites australis, indicating the efficient elimination of residual hemicellulose and lignin [39], while the clean peaks in the fingerprint region (1000–1200 cm^{-1}) of the Phragmites australis spectrum imply high crystallinity and cellulose purity. The chemical treatment was most efficient in the elimination of non-cellulosic components (lignin and hemicellulose) from Phragmites australis leading to better structural integrity of fibers. Thus, Phragmites australis based fibers do possess potential for application in concrete, especially related to mechanical properties enhancement (i.e. compressive and tensile strength). FTIR spectra displayed prominent changes from lignocellulosic transitions:

- 3300–3000 cm^{-1} (O–H stretching) band was increased in relative intensity, indicating the stronger hydrogen bond which was generally typical for a purified cellulose.
- The C–H stretching peaks at 2800–2900 cm^{-1} were reserved, indicating the backbone of cellulose maintained.
- The carbonyl absorption at 1730 cm^{-1}— attributed usually to hemicellulose—was greatly reduced, reflecting the elimination of this compound.
- The bands around 1240-1270 cm^{-1} (lignin aromatic groups) also decreased significantly.
- The inherent region (1000–1200 cm^{-1}) proved more defined, indicating a higher degree of crystallinity as confirmed with XRD.

In combination, XRD and FTIR make it clear that the green alkali treatment effectively removes non-cellulosic components from the fibers and improves the order in their structure which is required for effective reinforcement of cementitious composites

3.3 Particle Size Analysis

The Phragmites australis fibers exhibited a moderately uniform particle size distribution and a greater aspect ratio, as shown in Figure 4. Average particle size was between 45–100 nm indicating nano-scale dimensions of the results. Hence, the alkali treatment and ball-milling were effective methods to reach nano scale fiber size, contributing to better bonding between the fiber and the matrix as well as better mechanical properties of composites. One point to notice is the aspect ratio of Phragmites australis fibers that is very high, showing super reinforcement potential. This behavior is explained by the lower lignin content and finer natural morphology of Phragmites australis. A further reason for the loss of structural security through Phragmites australis fibers is attributed to lignin, as a highly cross-linked co-polymer that enhances structural stability and mechanical strength which becomes compromised due to its poor presence in Phragmites australis fibers, which allow for mechanical disintegration to occur more frequently rendering smaller this nano-scale particle considerably in a more homogenous spectrum. The moderate PDI values of Phragmites australis fibers also indicate a potential for better dispersion in the concrete matrix. In particular, these fibers are commonly beneficial in enhancing the performance of cementitious composites due to their uniform and fine geometry, resulting in enhanced toughness, crack resistance, and mechanical properties.

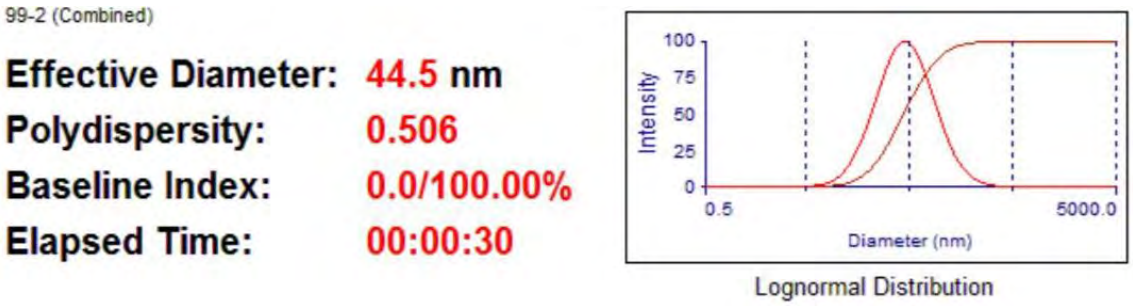

Fig. 4. Illustrates the PSM for Phragmites australis

3.4 SEM Result

The nano-fibers extracted from Phragmites australis also exhibits different morphological structures showing characteristics of nano-structure, which is an inherent feature of its capability as a possible reinforcement system in binders. The Figure (5)(a) shows entangled, fibrillated fiber bundles with a highly irregular, rough surface that increases mechanical interlocking within a matrix. Fiber aspect ratio: This attribute specifies the proportion of the fiber's length to its diameter; high aspect ratios (length to diameter ratio) are desirable to enhance tensile strength and crack resistance. As seen in Figure (5)(b) taken at a higher image magnification, the individual fibers remain clearly separated from each other and possess a relatively uniform diameter on nanometer length scales consistent with effective mechanical processing and chemical treatment. Rugged and porous fiber surfaces provide higher specific surface area, which increases the bonding potential with cement hydrates when mixed. In addition, residue of impurities or residual lignin outside the fiber surfaces indicates that alkaline treatment is successful and cellulose purity is high. These microstructural features confirm that the

prepared Phragmites australis nano-fibers possess the desired properties for reinforcement, contributing to improved mechanical performance when used in concrete composites.

Figure 5: Illustrates the SEM result of CANF: (a) Aggregated Structure and (b) Showing Surface Morphology. From the SEM images, adjourned membranes of fibrillated rough surface and nanofibers exhibiting a very heterogeneous (unsmooth) outer layer suggested favorable mechanical interlocking. Images obtained at high-magnification revealed fiber diameters of 80–120 nm, thus verifying the nanoscale size. The rough and porous texture increases the interface area and enhances bond with C–S–H gel. No significant surface damage was detected for any of the samples regardless of treatment, suggesting that no deterioration on the cellulose crystalline framework due to NaOH treatment and ball milling occurred. These morphological features account for the good stress transfer mechanism evidenced during mechanical tests, especially at 10% filler concentration.

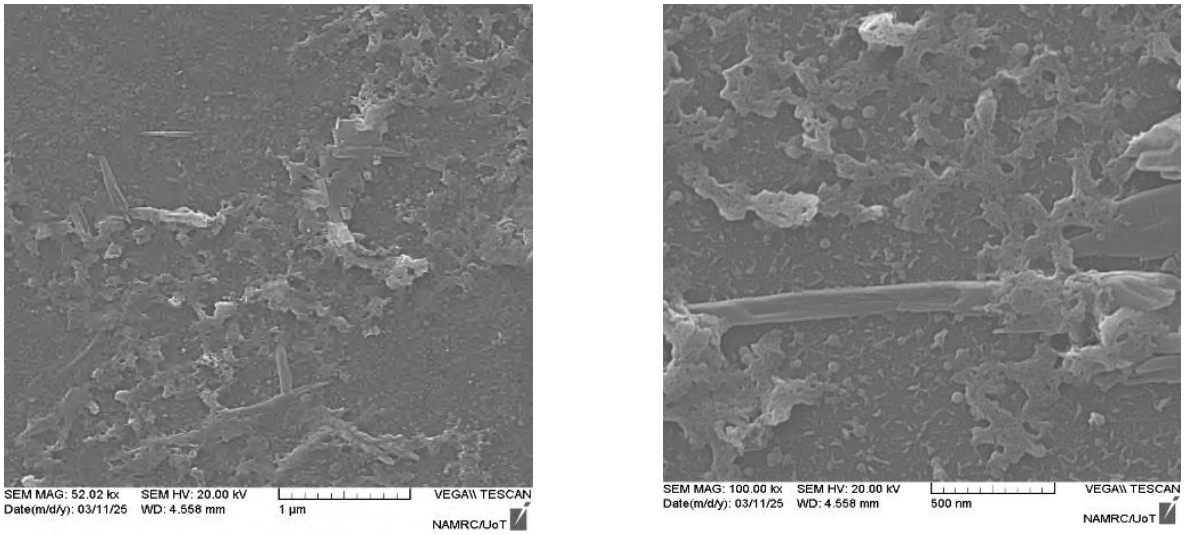

(a) (b)

Fig. 5. Illustrates the SEM result of CANF: (a) Aggregated Structure and (b) Showing Surface Morphology

3.5 XRF Result

The fibers of Phragmites Australis: The XRF analysis the results presented in this paper show key elemental and oxide composition that are responsible for the potential use of the tested fibers as concrete addition. These fibers show the silica (SiO_2) amount at 5.811% as displayed in table (4), and would indicate high pozzolanic activity which will improve long-term strength, as well as durability of concrete [41]. Furthermore, the aluminum oxide (Al_2O_3) content is 1.883% showing a high potential in producing calcium aluminate hydrates which will be beneficial to enhancing the durability and chemical resistance of concrete structures [40]. Iron oxide (Fe2O3) at a content of 0.3714% has minor pozzolanic significance and could also affect the coloration of concrete product [41]. fibers, have high amount of carbon (88.76%\uff08) And they may increase thermal insulating properties on concrete too [42]. High SiO2 and Al2O3 contents in the Phragmites australis fibers mean they are well-qualified for enhancing the long-term durability of concrete, which have advantages such as pozzolanic reactivity, enhanced chemical resistance and maintenance of mechanical strength over time.

Table 4. Result of XRF for Phragmites australis

Element/ Oxide	MgO	Al_2O_3	SiO_2	P_2O_5	SO_3	K_2O	CaO	MnO	Fe_2O_3	ZnO	Other element and oxide	C
Concentration (%)	0.28	1.88	5.81	0.47	0.36	0.23	1.33	0.02	0.37	0.02	0.43	88.76

3.6 Slump Test Findings

Slump test results in Fig. 6 represent the reduction of concrete workability (except for 5 % fiber) by adding Phragmites australis fibers to it when comparing with plain concretes. The lowest/highest

slump is obtained for the plain concrete (7 cm) and can be considered to have good workability. The findings shows when Phragmites australis. The slump value decreased by 14.3% at 5% fibers (6 cm), 31.4 % for 10% fibers (4.8 cm) and decrement of optimum point was found to be about47.1 (&) at 15% fibers presence, implying that workability decreases proportionally with increase in fiber content. The low slump reduction is explained by the nanometer-size of the fibers, allowing them to be more homogeneously dispersed in the cement-based matrix. In order to solve this problem, the application of superplasticizer or water-reducing agent is proposed as a potential approach for enhancing the workability without harming mechanical properties. This reduces the friction and fritting effect, which is usually more significant when it co-works with larger fiber reinforcement [43]. According to relevant standards, such as ASTM C143, the slump value typically ranges from 100 mm to 35 mm, depending on the intended use of the concrete structure. For general construction, a slump value between 75 mm and 100 mm is considered ideal for maintaining workability and cohesion. for roads, it is around 35 mm; and for concrete works, it ranges from 50 mm to 60 mm. The results indicate that Phragmites australis nanofibers present a compromise between processability and mechanical reinforcement. The fact that they achieve adequate slump values, their fiber-matrix interaction is enhanced, and both mechanical performance and workability can be engineered simultaneously, indicates their role in advancement of construction [44].

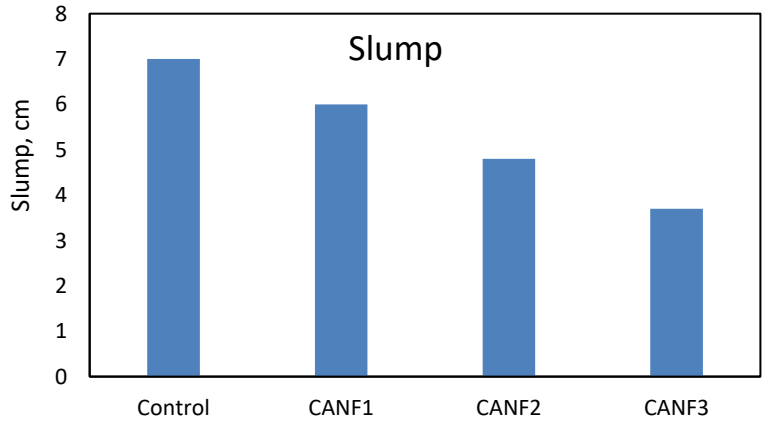

Fig. 6. Slump test results

3.7 Physical Properties

Results of the physical properties evaluation of concrete with different percentages by weight of Phragmites australis nanofibers (CANF) (5%, 10%, and 15%) are illustrated in Figure (7). Control concrete presented the greatest water absorption and porosity, which was reduced when 10% CANF was added, obtaining the best performance. The decrease in water absorption was associated with a better densification of the matrix and a better fiber-matrix bonding, which both prevented water ingress and a formation of voids. At fiber contents of 15%, however, porosity and water absorption increased slightly, which may have been caused by fiber agglomeration and decreased compaction efficiency [45]. Moreover, dry density decreased progressively with increasing the CANF content due to the lightweight property of the fibers and the partial replacement of the denser cement material. From these outcomes, the addition of 10% CANF contributes to a more systematic improvement in physical characteristics by decreasing both porosity and water absorption but without an increase in density making the concrete matrix more durable and has a finer quality [46]. The findings highlight the significance of proper curing in fiber-reinforced concrete performance, and indicate that chemical treatment of fibers should be further implemented for proper fiber-cement compatibility [47].

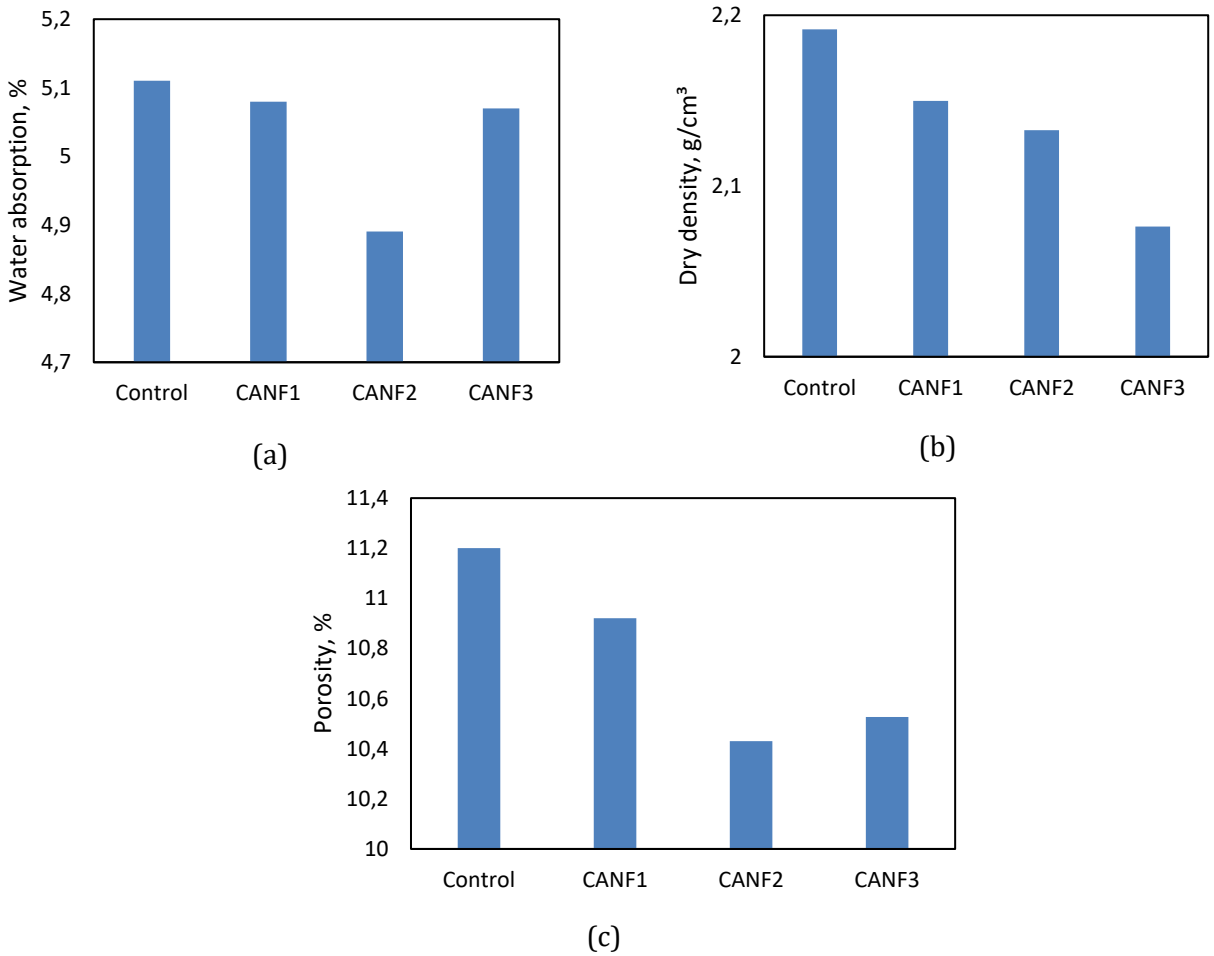

Fig. 7. Physical Results for concrete (a) Dry density (b) Water absorption (c) Porosity

3.8 Mechanical Inspection Results

Figure 8 shows mechanical performance of concrete composites reinforced with Phragmites australis nanofibers (CANF) by measuring compressive and flexural strength at (7, 28 and 90) days. Figure 9, table (5) illustrates the regression analysis for both flexural and compressive strengths. Both properties were enhanced with 5 and 10% CANF addition and depressed with the addition of 15% fiber. Fig.2 (d) indicates that the lowest compressive strength was observed in the control mix for all curing periods and TE stressing condition of 90 days, while maximum density achieved at which age induced best stature value (10% CANF mix). This difference may be attributable to either hydration or further densification improvements of matrix with progressing curing periods. The trend seen in flexural strength followed the same pattern, such as that for 10% CANF mix always it was higher than control and other fiber dosage further strengthening the maximization of flexural strength at 90 days. This increases interfacial strength due to fiber bridging mechanism, which tends to improve crack resistance and energy absorption. However, with the 15% CANF as contents increases porosity and the porosity of the green body would further agglomeration of fibers these could volume and if fiber–matrix bonding was not strong enough, compact decreased crack structures by weak fiber adhesion. As a result, fiber cohesions are predicted to partially fail during continuous sintering. It can be concluded from the results shown here that an addition of 10% fiber remains at the critical value when the synthesized MMCs possessed high-quality mechanical behavior and excessive incorporation led to performance degradation. It is also reported that natural fibers have the potential to increase life span of concrete composites as well as increasing toughness and durability but still prevents the use of construction materials from being non- environmentally friendly [46].

Table 5. Mechanical test results

Sample	Compression			Flexural		
	7 days	28 days	90 days	7 days	28 days	90 days
Control	21.7	25.3	28.2	3.13	3.79	4.09
CANF1	22.8	28.1	30.2	3.62	4.68	4.98
CANF2	21.9	27.5	29.4	3.98	4.8	5.1
CANF3	21.1	25.1	28.2	3.02	3.56	3.85

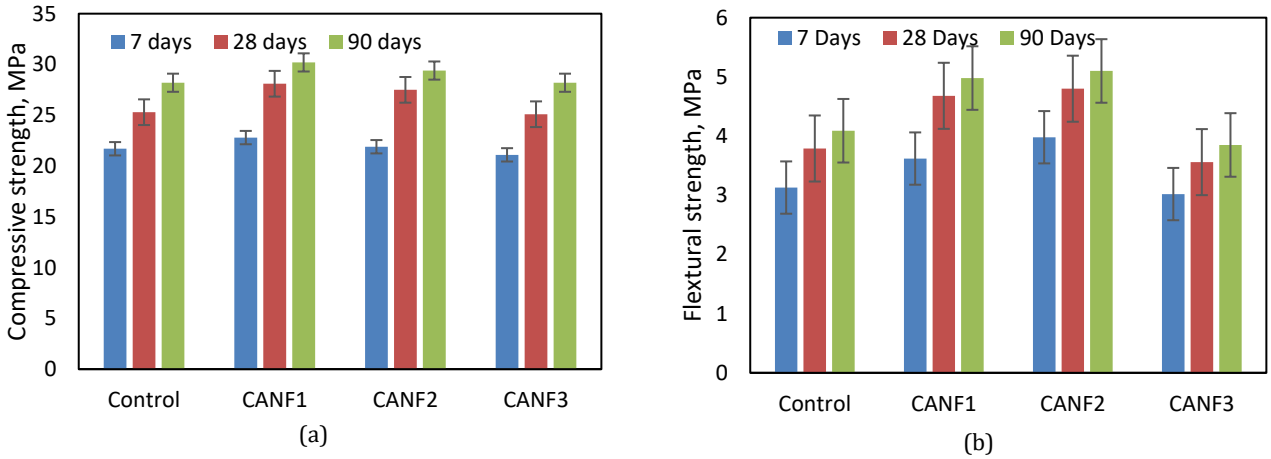

Fig. 8. (a) Compressive results and (b)Flexural results

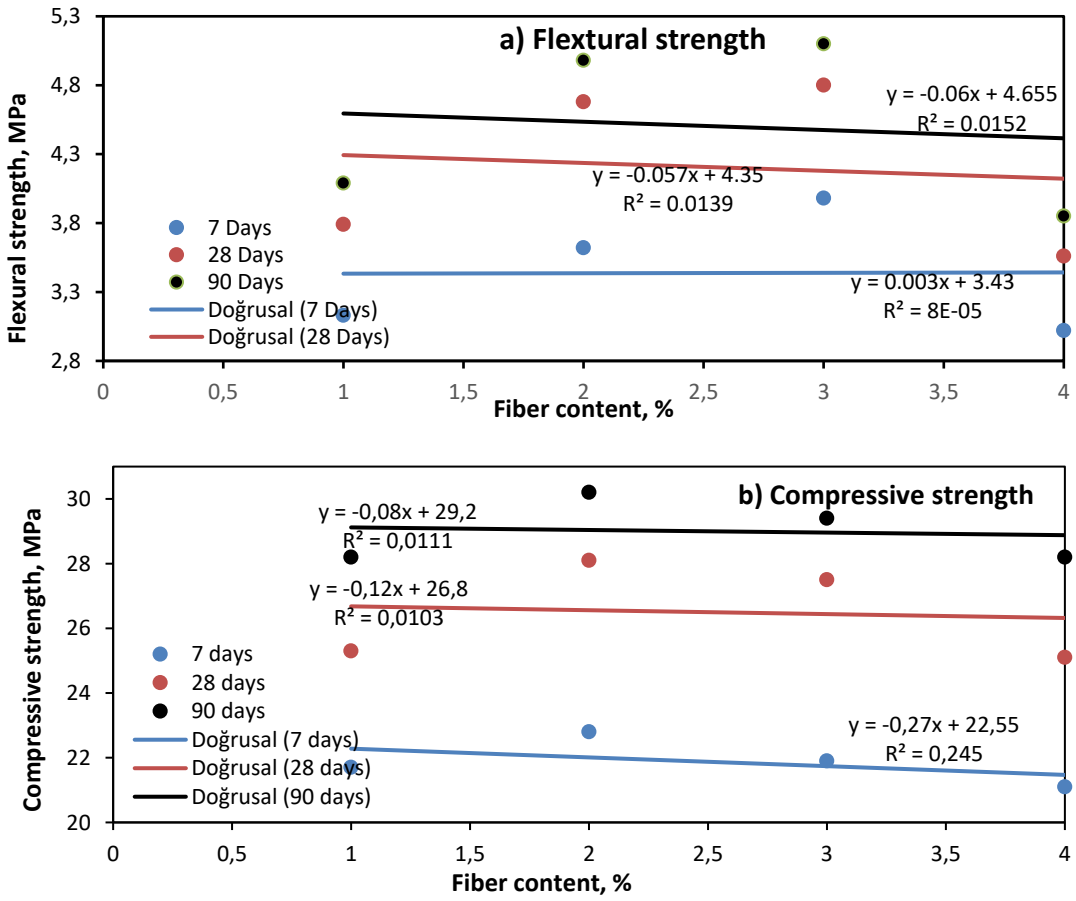

Fig. 9. Regression analysis (a) flexural strength (b) compressive strength

5. Conclusions

This work presents evidences that the Phragmites australis nanofiber (PANF) fabricated via a green alkali-extraction approach, possesses promising potential as an efficient reinforcement material for concrete. The addition of these nanofibers improved the mechanical and physical properties of concrete to a certain degree at the optimized mixing balance. In particular, with the incorporation of 5% fiber content, a gain in compressive strength by approximately 7% was reported, whereas flexural strength displayed the highest increase of around 36%, which was obtained at an addition of 10 % fiber. These improvements are attributed to the nanoscale fibrillar structure of the salt-treated fibers, which provide crack bridging, enhance fiber–cement interfacial bonding and also contribute towards a better matrix densification.

From a scientific aspect, the research offers new knowledge on how cellulose nanofiber from an invasive species interacts with cementitious materials. Enhanced crystallinity, surface-roughness and concentration of oxides (SiO_2, Al_2O_3, CaO) on extracted fibers contribute to changes in hydration processes, hence microstructural development. This study demonstrates an environmentally benign method for the conversion of abundant waste biomass into a value-added nanomaterial for greener construction industry.

From a practical point of view, the results show that P. australis nanofibers can be used to improve the flexural response of concrete when high resistance under bending is required, as in slabs, pavements or precast structural elements. Durability performance, in particular, resistance against freeze–thaw cycles, thermal stability, chemical attack and long-term shrinkage behavior need to be extended in future studies. Study of the hybrid fiber system and optimization of dispersion techniques can bring to even better mechanical properties for broader industrial application.

References

[1] Ndahirwa D, Zmamou H, Lenormand H, Leblanc N. The role of supplementary cementitious materials in hydration, durability and shrinkage of cement-based materials, their environmental and economic benefits: A review. Cleaner Materials. 2022 Sep 1; 5:100123.

[2] Kene KS, Vairagade VS, Sathawane S. Experimental study on behavior of steel and glass fiber reinforced concrete composites. Bonfring international journal of industrial engineering and management science. 2012 Dec 1;2(4):125.

[3] Dahesh AZ, Othman FM, Abdulhamead AA. Influence of Microfibers Additive on the Selfhealing Performance of Mass Concrete. Engineering and Technology Journal. 2021;39(01):104-15. https://doi.org/10.30684/etj.v39i1A.1581

[4] Salavati-Niasari M. Nanodimensional microreactor-encapsulation of 18-membered decaaza macrocycle copper (II) complexes. Chemistry letters. 2005 Feb;34(2):244-5. https://doi.org/10.1246/cl.2005.244

[5] Salavati-Niasari M, Davar F. In situ one-pot template synthesis (IOPTS) and characterization of copper (II) complexes of 14-membered hexaaza macrocyclic ligand "3, 10-dialkyl-dibenzo-1, 3, 5, 8, 10, 12-hexaazacyclotetradecane". Inorganic Chemistry Communications. 2006 Feb 1;9(2):175-9.

[6] Nazar, S., et al., Rheological properties of cementitious composites with and without nano-materials: A comprehensive review. Journal of Cleaner Production, 2020. 272: p. 122701. https://doi.org/10.1016/j.jclepro.2020.122701

[7] Norhasri MM, Hamidah MS, Fadzil AM. Applications of using nano material in concrete: A review. Construction and Building Materials. 2017 Feb 15; 133:91-7. https://doi.org/10.1016/j.conbuildmat.2016.12.005

[8] Morsy MS, Alsayed SH, Aqel M. Hybrid effect of carbon nanotube and nano-clay on physico-mechanical properties of cement mortar. Construction and Building Materials. 2011 Jan 1;25(1):145-9. https://doi.org/10.1016/j.conbuildmat.2010.06.046

[9] Bautista-Gutierrez KP, Herrera-May AL, Santamaría-López JM, Honorato-Moreno A, Zamora-Castro SA. Recent progress in nanomaterials for modern concrete infrastructure: Advantages and challenges. Materials. 2019 Oct 29;12(21):3548. https://doi.org/10.3390/ma12213548

[10] Muzenski S, Flores-Vivian I, Sobolev K. Ultra-high strength cement-based composites designed with aluminum oxide nano-fibers. Construction and Building Materials. 2019 Sep 30; 220:177-86. https://doi.org/10.1016/j.conbuildmat.2019.05.175

[11] Piro NS, Mohammed AS, Hamad SM. Multiple analytical models to evaluate the impact of carbon nanotubes on the electrical resistivity and compressive strength of the cement paste. Sustainability. 2021 Nov 13;13(22):12544. https://doi.org/10.3390/su132212544

[12] Mutuk H, Mutuk T, Gümüş H, Mesci Oktay B. Shielding behaviors and analysis of mechanical treatment of cements containing nanosized powders. Acta Physica Polonica A. 2016 Jul;130(1):172-4. https://doi.org/10.12693/APhysPolA.130.172
[13] Hamead AA, Ahmed SS, Azzat SR, Abed MS, Hammod GK. Employing recycling materials for the fabrication of smart mortar. Materials Today: Proceedings. 2020 Jan 1; 20:397-402. https://doi.org/10.1016/j.matpr.2019.09.154
[14] Teixeira ED, Pasquini D, Curvelo AA, Corradini E, Belgacem MN, Dufresne A. Cassava bagasse cellulose nanofibrils reinforced thermoplastic cassava starch. Carbohydrate polymers. 2009 Oct 15;78(3):422-31. https://doi.org/10.1016/j.carbpol.2009.04.034
[15] Azeredo HM, Mattoso LH, Wood D, Williams TG, Avena-Bustillos RJ, McHugh TH. Nanocomposite edible films from mango puree reinforced with cellulose nanofibers. Journal of food science. 2009 Jun;74(5): N31-5. https://doi.org/10.1111/j.1750-3841.2009.01186.x
[16] Ali AH, Ibrahim SI, Gharkan MR, Salih WM. Some mechanical and physical properties of cement mortar reinforced by steel wires of scrap tires. Zanco Journal of Pure and Applied Sciences. 2019;31(3):47-51. https://doi.org/10.21271/ZJPAS.31.s3.7
[17] Llanos JH, Tadini CC. Preparation and characterization of bio-nanocomposite films based on cassava starch or chitosan, reinforced with montmorillonite or bamboo nanofibers. International journal of biological macromolecules. 2018 Feb 1; 107:371-82.
[18] Ilyas RA, Sapuan SM, Ishak MR, Zainudin ES. Sugar palm nanofibrillated cellulose (Arenga pinnata (Wurmb.) Merr): Effect of cycles on their yield, physic-chemical, morphological and thermal behavior. International Journal of Biological Macromolecules. 2019 Feb 15; 123:379-88. https://doi.org/10.1016/j.ijbiomac.2018.11.124
[19] Khatib J, Ramadan R, Ghanem H, Elkordi A. Effect of adding phragmites-australis fiber on the mechanical properties and volume stability of mortar. Fibers. 2024 Jan 30;12(2):14. https://doi.org/10.3390/fib12020014
[20] Saleem MH, Abdul-Hamead AA, Othman FM. Performance of waste materials and carbon nanotube in concrete incorporated with carbon fiber. InAIP Conference Proceedings 2022 Aug 17 (Vol. 2437, No. 1). AIP Publishing.
[21] Carrillo-Varela I, Pereira M, Mendonça RT. Determination of polymorphic changes in cellulose from Eucalyptus spp. fibres after alkalization. Cellulose. 2018 Dec; 25:6831-45. https://doi.org/10.1007/s10570-018-2060-4
[22] Sreekala MS, Kumaran MG, Joseph S, Jacob M, Thomas S. Oil palm fibre reinforced phenol formaldehyde composites: influence of fibre surface modifications on the mechanical performance. Applied composite materials. 2000 Nov; 7:295-329. https://doi.org/10.1023/A:1026534006291
[23] Li X, Tabil LG, Panigrahi S. Chemical treatments of natural fiber for use in natural fiber-reinforced composites: a review. Journal of Polymers and the Environment. 2007 Jan; 15:25-33. https://doi.org/10.1007/s10924-006-0042-3
[24] Rong MZ, Zhang MQ, Liu Y, Yang GC, Zeng HM. The effect of fiber treatment on the mechanical properties of unidirectional sisal-reinforced epoxy composites. Composites Science and technology. 2001 Aug 1;61(10):1437-47. https://doi.org/10.1016/S0266-3538(01)00046-X
[25] Ronald Aseer J, Sankaranarayanasamy K, Jayabalan P, Natarajan R, Priya Dasan K. Morphological, physical, and thermal properties of chemically treated banana fiber. Journal of Natural Fibers. 2013 Oct 2;10(4):365-80. https://doi.org/10.1080/15440478.2013.824848
[26] Bledzki AK, Mamun AA, Lucka-Gabor M, Gutowski VS. The effects of acetylation on properties of flax fibre and its polypropylene composites. Express polymer letters. 2008 Jun 1;2(6):413-22. https://doi.org/10.3144/expresspolymlett.2008.50
[27] Senthilkumar K, Rajini N, Saba N, Chandrasekar M, Jawaid M, Siengchin S. Effect of alkali treatment on mechanical and morphological properties of pineapple leaf fibre/polyester composites. Journal of Polymers and the Environment. 2019 Jun 15; 27:1191-201. https://doi.org/10.1007/s10924-019-01418-x
[28] Kanakaraj P, Shaikh B, Karthika K, Yuns M. Scope and Effect of Retting Treatment on Tensile Characteristics of Natural Fiber Extracted from Phragmites Australis (Naanal). Journal of Textile and Apparel, Technology and Management. 2016 Apr 28;10(1).
[29] Yue Y, Han J, Han G, Zhang Q, French AD, Wu Q. Characterization of cellulose I/II hybrid fibers isolated from energycane bagasse during the delignification process: morphology, crystallinity and percentage estimation. Carbohydrate Polymers. 2015 Nov 20; 133:438-47. https://doi.org/10.1016/j.carbpol.2015.07.058
[30] Tiwari YM, Sarangi SK. Characterization of raw and alkali treated cellulosic Grewia Flavescens natural fiber. International Journal of Biological Macromolecules. 2022 Jun 1; 209:1933-42. https://doi.org/10.1016/j.ijbiomac.2022.04.169
[31] Nwa-David CD. Performance of potato starch admixture on fresh and hardened behaviours of concrete at varied mix design ratios. Engineering and Technology Journal. 2024;42(05):540-7. https://doi.org/10.30684/etj.2024.145272.1654

[32] Revathy R, Sajini T, Augustine C, Joseph N. Iron-based magnetic nanomaterials: sustainable approaches of synthesis and applications. Results in Engineering. 2023 Jun 1; 18:101114. https://doi.org/10.1016/j.rineng.2023.101114
[33] Nazari A, Riahi S, Riahi S, Shamekhi SF, Khademno A. Influence of Al2O3 nanoparticles on the compressive strength and workability of blended concrete. Journal of American Science. 2010;6(5):6-9.
[34] Dahesh AZ, Othman FM, Abdul-Hamead AA. Improve mass concrete by controlling the crack sealing mechanism using microcapsules of zinc oxide. InMaterials Science Forum 2020 Aug 14 (Vol. 1002, pp. 541-550). Trans Tech Publications Ltd.
[35] Nwa-David CD. Performance of potato starch admixture on fresh and hardened behaviours of concrete at varied mix design ratios. Engineering and Technology Journal. 2024;42(05):540-7. https://doi.org/10.30684/etj.2024.145272.1654
[36] French AD. Idealized powder diffraction patterns for cellulose polymorphs. Cellulose. 2014 Apr;21(2):885-96. https://doi.org/10.1007/s10570-013-0030-4
[37] Chen HongYan CH, Liu JinBao LJ, Chang Xing CX, Chen DaMing CD, Xue Yuan XY, Liu Ping LP, Lin HuaLin LH, Han Sheng HS. A review on the pretreatment of lignocellulose for high-value chemicals.
[38] Venugopal A, Boominathan SK. Physico-chemical, thermal and tensile properties of alkali-treated acacia concinna fiber. Journal of Natural Fibers. 2022 Aug 3;19(8):3093-108. https://doi.org/10.1080/15440478.2020.1838998
[39] Chen H, Wu J, Shi J, Zhang W, Wang H. Effect of alkali treatment on microstructure and thermal stability of parenchyma cell compared with bamboo fiber. Industrial Crops and Products. 2021 Jun 1; 164:113380.
[40] Wu HF, Shen JJ, Liu Y, Hu YY. Effect of nano-Al2O3 on the mechanical and microstructural properties of cement-based grouting material. Case Studies in Construction Materials. 2024 Dec 1;21: e03846. https://doi.org/10.1016/j.cscm.2024.e03846
[41] Barbhuiya S, Das BB, Kanavaris F. Biochar-concrete: A comprehensive review of properties, production and sustainability. Case Studies in Construction Materials. 2024 Jul 1;20: e02859. https://doi.org/10.1016/j.cscm.2024.e02859
[42] Mehta A, Siddique R. Properties of low-calcium fly ash based geopolymer concrete incorporating OPC as partial replacement of fly ash. Construction and building materials. 2017 Sep 30; 150:792-807. https://doi.org/10.1016/j.conbuildmat.2017.06.067
[43] Zhang P, Wang L, Wei H, Wang J. A critical review on effect of nanomaterials on workability and mechanical properties of high-performance concrete. Advances in Civil Engineering. 2021;2021(1):8827124. https://doi.org/10.1155/2021/8827124
[44] Hussein T, Kurda R, Mosaberpanah M, Alyousef R. A review of the combined effect of fibers and nano materials on the technical performance of mortar and concrete. Sustainability. 2022 Mar 16;14(6):3464.
[45] Su DY, Pang JY, Huang XW. Mechanical and Dynamic Properties of Hybrid Fiber Reinforced Fly-Ash Concrete. Advances in Civil Engineering. 2021;2021(1):3145936. https://doi.org/10.1155/2021/3145936
[46] Gholampour A, Danish A, Ozbakkaloglu T, Yeon JH, Gencel O. Mechanical and durability properties of natural fiber-reinforced geopolymers containing lead smelter slag and waste glass sand. Construction and Building Materials. 2022 Oct 17; 352:129043. https://doi.org/10.1016/j.conbuildmat.2022.129043
[47] Ahmed W, Lim CW. Production of sustainable and structural fiber reinforced recycled aggregate concrete with improved fracture properties: A review. Journal of Cleaner Production. 2021 Jan 10; 279:123832. https://doi.org/10.1016/j.jclepro.2020.123832

Blank Page

Research on Engineering Structures & Materials
www.jresm.org
Research Group

Research Article

Experimental evaluation of bond behavior of post-installed GFRP and steel reinforcements using different adhesives

Borkan M. Mutashar [*,1,2,a], Suhaib Y. Kasim [1,b], Oday A. Salih [1,c]

[1]*Department of Civil Engineering, University of Mosul, Mosul, Iraq*
[2]*Department of Environmental Technologies, University of Mosul, Mosul, Iraq*

Article Info

Article History:

Received 12 Oct 2025
Accepted 27 Dec 2025

Keywords:

Bond strength;
GFRP bars;
Post-installed Reinforcement;
Adhesive anchoring,
Pull-out test;
Embedded length

Abstract

The existing design codes lack specifications for the use of glass fiber-reinforced polymer (GFRP) bars in post-installation applications, and research on this topic is scarce. This study investigates the bond performance of the post-installed GFRP and steel reinforcement bars through pull-out tests using three commercial chemical adhesives. Seventy cylindrical specimens (60 post-installed, 10 cast-in-place) with diameters of 15 cm and heights of 30 cm were prepared. Post-installed samples featured anchor bars with 5d, 10d, and 15d embedded lengths (where d is the rebar diameter), tested under dry and wet conditions. Compressive strengths of 25 MPa and 35 MPa were used. Three different commercial adhesive types were utilized in this research: pure epoxy adhesive (adhesive A) and two epoxy acrylate adhesives (adhesives B and C). Adhesive A demonstrated improved bond strength by up to 75% with longer embedded lengths and higher concrete compressive strengths when compared to adhesives B and C, regardless of moisture conditions. All specimens showed concrete rupture or splitting failure, proving the effectiveness of the epoxy resins as bonding agents. The findings emphasize the significance of adhesive selection and design parameters in improving bond performance.

© 2026 MIM Research Group. All rights reserved.

1. Introduction

Post-installed reinforcement of steel represents a reliable retrofitting and strengthening technique. Steel reinforcing bars, on the other hand, tend to suffer from corrosion, which results in costly maintenance and repairs [1]. These issues have motivated researchers to explore alternative reinforcing materials with enhanced durability. As an alternative to steel, Glass Fiber Reinforced Polymer (GFRP) reinforcement bars are corrosion-resistant, characterized by their lighter weight, and have a higher tensile strength-to-weight ratio [2]. This highlights the need for a comprehensive research effort directed towards future codification, given that previous studies, along with design codes like ACI440, do not provide experimental data to support post-installed GFRP reinforcing bars; they focused only on the cast-in GFRP bars. Consequently, there is still a lack of knowledge regarding the structural performance and anchoring reliability of post-installed GFRP reinforcement.

Bonded anchors that are installed in concrete to serve as structural connections can be categorized into two types: cast-in-place anchors and post-installed anchors in concrete [3-5]. The post-installed reinforcement is added to an existing concrete segment by drilling holes and injecting adhesives. [6]. This approach is employed for various functions, including connecting newly constructed concrete to existing or previously constructed concrete, facilitating continuity and uniform stress transfer [7]. These bars are usually glued or mortared into a pre-drilled hole [8].

*Corresponding author: borkan.22enp20@student.uomosul.edu.iq
[a]orcid.org/ 0009-0009-5019-373X; [b]orcid.org/0000-0001-5346-8836; [c]orcid.org/0000-0002-2882-8622
DOI: http://dx.doi.org/10.17515/resm2026-1246ic1012rs

It is widely recognized that load or stress distribution in reinforced concrete members is influenced by the bond within the reinforcement and the concrete or binder surrounding it [9]. This transfer can be achieved by the opposition to the relative movement or the slipping between the concrete and the bar's rib edges [10]. Bond strength, or resistance to slipping, is determined by three actions: The bar's ribs bond with the surrounding concrete through friction, mechanical connection, and chemical adhesion [11]. Bond performance must be assessed to determine the best anchoring for every application. The failure mechanisms, pull-out loads, and load displacement of different anchor types are included [12].

Previous investigations focused on cast-in-place GFRP bar bond strength [13-15]. After being inserted into concrete as post-installed reinforcement, their bonding performance may differ completely, due to the installation conditions. The effect of factors, including concrete compressive strength, environmental conditions, and epoxy adhesive performance with different embedding lengths, on post-installed GFRP bars has not been studied. Therefore, a thorough comparison of the bond behavior of post-installed steel and GFRP bars bonded with locally available different adhesive types is essential to enhance the effectiveness and reliability of retrofitted structures. The purpose of this study is to examine the performance of steel and GFRP anchors that have been post-installed using various construction adhesives in pull-out tests. This study examined how embedded lengths affected pull-out loads in concrete specimens with post-installed and cast-in-place rebar. This research will help Iraqi infrastructure projects with rehabilitation throughout construction be more structurally durable.

2. Materials and Mixing

2.1. Cement

The type of cement selected in this research is ordinary Portland cement from the Mass Cement Factory in Sulaymaniyah Governorate. In a laboratory-controlled room with an ambient temperature of 24 °C, along with a relative humidity (RH) of 42%, the properties of the cement were determined, as shown in Table 1.

Table 1. Physical properties of cement

No.	Characteristics	Units	Value	Specification
1	Standard Consistency w/c	-	0.31	
2	Initial setting	Minutes	115	≥ 45
3	Final setting	Minutes	235	≤ 600
4	Compressive strength (3 days)	MPa	22.1	≥ 15
5	Compressive strength (7 days)	MPa	31.2	≥ 23
6	Fineness (sieve no. 170)	%	4	≤ 10

2.2. Reinforcing Bars

The mechanical properties of GFRP and steel rebars were tested using a Universal Testing Machine (UTM) with 1000 kN capacity, in accordance with ASTM A706 [16]. A total of three rebar samples of each rebar type were tested to ensure comprehensive results; their mechanical properties were calculated as the averages of their respective values. The GFRP bars employed in this study are 12 mm in diameter, type No. B80 – Epoxy Resin, supplied by Jiangsu Feibol China, and its properties are described in Table 2. The steel bars employed in this study are 12 mm in diameter, provided by Mass Steel Factory in Sulaymaniyah Governorate, Iraq. The characteristics of these bars are presented in Table 3.

Table 2. Properties of GFRP bars

Bar Diameter (mm)	Ultimate Tensile Strength (MPa)	Elongation	Weight (g/m)
12	900	1.3%	240

Table 3. Properties of steel bars

Bar Diameter (mm)	Yield Stress (MPa)	Ultimate (MPa)	Elongation	Weight (g/m)
12	463	696	16.2%	890

2.3 Concrete Mix

Cement, water, and local river round coarse and fine aggregate from Kanhaash near Mosul make up the concrete mixtures. This study used a maximum size of 14 mm coarse aggregate and 3.9 mm for sand. ASTM measured aggregate properties. ASTM C127 [1] and C128 [2] measured aggregate absorption and specific gravity, while ASTM C29 [3] measured compact and lose weight. Sieve analysis fulfilled the ASTM C136 standards [4]. Two distinct concrete mixes with varying concrete strengths were created to establish a comparison investigation. The chosen concrete strengths of the research are 25 and 35 MPa, since they are the most prevalent strengths in actual constructions. The mix was designed in line with ACI 211.1 standards [5]. The proposed w/c ratios to provide 25 and 35 MPa concrete compressive strength were held constant at 0.41 and 0.39, respectively. Table 4 summarizes the combined proportions of components. The concrete compression machine was used for testing the concrete cylinders. Three concrete cylinders had respective compressive strengths of 24.9, 25.3, and 26 MPa for C25, and another three cylinders with the compressive strengths of 34.1, 35.5, and 36.3 MPa for C35.

Table 4. Material mix proportions per cubic meter

Batch No	Batch Code	Cement (kg)	Coarse aggregate (kg)	Fine aggregate (kg)
1	C25	350	977	695
2	C35	400	981	629

2.4 Adhesives

Three different commercial adhesive types commonly used in Iraqi infrastructure were utilized.

- Adhesive A: Adhesive A is a two-part, thixotropic fixing adhesive containing epoxy resin that can be employed for anchoring deformed bolts and reinforcement bars in dry or wet concrete holes. The technical properties of the adhesive are shown in Table 5.
- Adhesive B: Adhesive B is a two-part, high-performance fixing adhesive containing epoxy acrylate, free from solvents and styrene. The properties of the adhesive are shown in Table 6.
- Adhesive C: Adhesive C is a high-resilience, rapid curing, styrene-free, containing acrylate resin anchoring grout provided in a pre-packaged cartridge system and it may be used on many surfaces. Table 7 illustrates the properties of the adhesive.

Table 5. Properties of adhesive A

Description	Sample Results	
Compressive strength	95 MPa (7 days, +20°C)	
Tensile Strength in Flexure	45 MPa (7 days, +20°C)	
Tensile Strength	23 MPa (7 days, +20°C)	
Modulus of Elasticity in Tension	5500 MPa (7 days, +20°C)	
Service Temperature	Long term	-40 °C min. / +50 °C max.
	Short-term (1–2 hours)	+70 °C

Table 6. Properties of adhesive B

Description	Sample Results
Compressive strength	68 MPa (7 days, +20°C)
Tensile Strength in Flexure	24 MPa (7 days, +20°C)

Tensile Strength	13 MPa (7 days, +20°C)	
Modulus of Elasticity in Tension	3700 MPa (7 days, +20°C)	
Service Temperature	Long term	-40°C min. / +50°C max.
	Short-term (1–2 hours)	+70°C

Table 7. Properties of adhesive C

Description	Sample Results	
Compressive strength	75 MPa (7 days, +20°C)	
Tensile Strength in Flexure	25 MPa (7 days, +20°C)	
Tensile Strength	12 MPa (7 days, +20°C)	
Modulus of Elasticity in Tension	3500 MPa (7 days, +20°C)	
Service Temperature	Long term	-40 °C min. / +50°C max.
	Short-term (1–2 hours)	+65°C

3. Dimensions and Testing Procedure

The experimental setup includes a pull-out test to assess the strength of adhesives used to adhere GFRP reinforcement. To guarantee reliability and statistical assessment of the results, every test setup has been duplicated twice. Concrete cylinders with a diameter of 15 cm and a height of 30 cm were utilized for post-installed reinforcement bars into concrete, whereas 10 cast-in-place specimens were utilized as controls. Hardened concrete cylinder samples were drilled for 60 post-installed rebar concrete specimens comprising the various test parameters that include bar material (steel and GFRP), embedded lengths of 5, 10, and 15 with rebar diameters (5Ø, 10Ø, and 15Ø), varying hole surface conditions (dry and wet, indicating the moisture status inside the drilled hole prior to adhesive application), concrete compressive strength 25 MPa and 35 MPa, and three different epoxy-based adhesives (adhesive A, adhesive B and adhesive C) were used to create the bond.

The flowchart for the experimental procedure (Fig. 1) describes the experimental process flowchart. The pull-out value recorded was the average of two replicas. Specimen names were coded through six symbols that denoted test parameters. The arrangement of these symbols is as follows: method of installation (C for cast in place and P for post-installed), concrete compressive strength (C_{25} for 25 MPa and C_{35} for 35 MPa), bar type (G for GFRP and S for Steel), embedded lengths ($5d_b$, $10d_b$ and $15d_b$ mm.) where d_b is bar's diameter, drilled hole surface condition (D for dry and W for wet), and the adhesives (AA for adhesive A, AB for adhesive B and AC for adhesive C). For example, P-C_{35}-G-$10d_b$-D-AC is a specimen with 35 MPa compressive strength, post-installed GFRP bars, a $15d_b$ embedment length, a dry hole surface, and adhesive C.

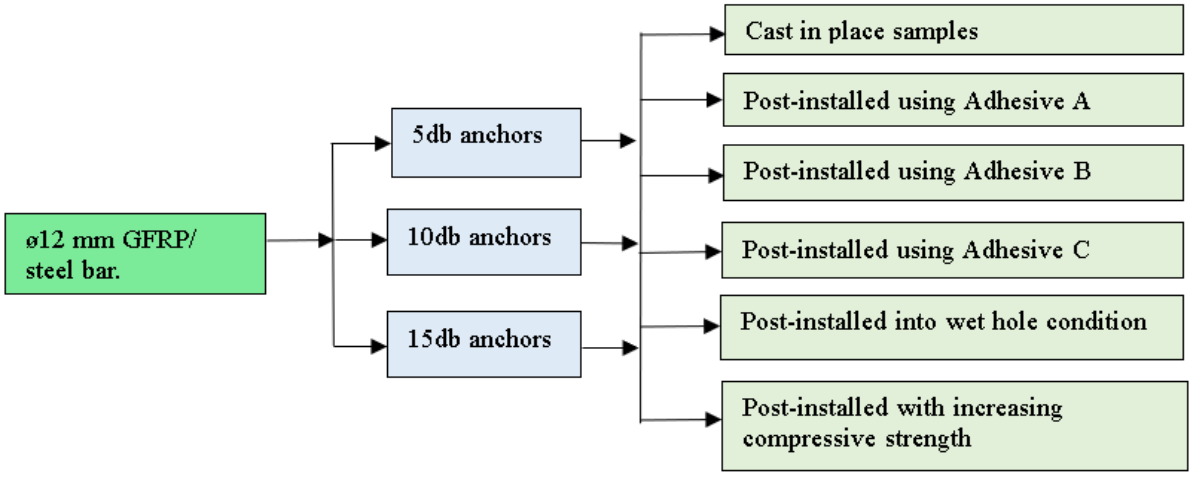

Fig. 1. Experimental program flow chart

3.1 Mixing, Casting, and Curing Procedures

The constituent materials of the concrete were accurately proportioned, weighted, and subsequently mixed in a rotary mixer. Three equally sized layers of freshly mixed concrete were poured into the cylindrical molds measuring 15 cm by 30 cm. According to ASTM C192, the concrete test specimens were demolded and cured for a week under water ponding for 24 hours. The specimens were exposed to air and allowed to dry for three more weeks before the drilling operation started [20]. in this study, the anchoring lengths or embedment depths employed were five, ten, and fifteen times the bar diameter.

3.2 Drilling, Cleaning, and Injecting of The Holes

The concrete cylinder specimens with post-installed rebar were drilled across the specimens' longitudinal axis to form holes using a vibrating rotary hammer drill with chrome alloy steel shank bits of 16 mm. The drill bits were marked to get the desired embedment lengths. Additionally, a drill stand was used to ensure the verticality of bars. All loose concrete particles that would interfere with the rebar's ability to bond effectively with the concrete were eliminated using a wire brush along with an air compressor, as seen in (Fig. 2). In order to simulate the real-world practical scenarios, two-hole conditions free of moisture and a moisture-retained surface were assessed in this investigation. Once the cleaning was completed, adhesives were applied into the holes, and GFRP bars of 1300 mm were subsequently installed according to ASTM 440.3 [22]. Adhesives were poured into the holes using an adhesive injection gun. The adhesive injection process, which involves combining mortar with a curing agent, started at the bottom of the hole and continued until two-thirds of the hole's volume was filled. The curing time and adhesives preparation process were selected according to the manufacturer's recommendations. The bars were carefully aligned at the center of the hole with constant twisting to provide an even layer of adhesive over the bar. The bars were properly positioned before the adhesive began to set. All of the post-installed bars were left undisturbed for 24 hours at 25°C to ensure the adhesive was fully cured under identical conditions.

3.3 Achor Preparation for Gripping GFRP Bars

GFRP bars were secured tightly to prevent breakage and guarantee exact results. The anchors for the GFRP bars were made by using steel tubes filled with two-part epoxy adhesive according to ASTM 440.3R [22]. Specimens are tested following a three-day curing period of the two-part epoxy adhesive (Sikadur-31), as illustrated in (Fig. 3).

Fig. 2. Drilling and cleaning of the holes

Fig. 3. GFRP bar anchor

Fig. 4. Pull-out test setup in UTM

4. Results and Discussion

Pull-out tests were conducted on reinforcing bars installed in concrete cylinders to investigate the tensile strength of adhesives, as illustrated in (Fig. 4). The bond stress between the post-installed rebars and the surrounding concrete is assumed to be equally distributed along the embedment length. The bond strength can be calculated by utilizing Eq (1):

$$\tau = \frac{P_{max}}{\pi d_b l_e}. \quad (1)$$

In this equation, τ refers to the average bond strength measured in MPa, P_{max} represents the peak pull-out load in kN, d_b indicates the diameter of the reinforcing bar in mm, and *le* represents the embedment length in mm. The calculated average bond strength values for the different specimen sets are presented in Table 8.

Table 8. The average values of the bond strength and the pull-out loads

No.	Name	Pull-out load (kN)	Standard deviation (kN)	Average pull-out load (kN)	Average bond strength (MPa)
	P-C_{25}-G-5d_b-D-AA	22.19	0.14	22.09	9.770878
	P-C_{25}-G-5d_b -D- AA	21.99			
	P-C_{25}-G-10d_b-D-AA	35.13	2.03	33.10	7.320418
	P-C_{25}-G-10d_b-D-AA	31.07			
	P-C_{25}-G-15d_b-D-AA	52.04	1.17	50.87	7.500295
	P-C_{25}-G-15d_b-D-AA	49.70			
	P-C_{25}-G-10d_b-W-AA	30.47	1.34	29.13	6.44241
	P-C_{25}-G-10d_b-W-AA	27.79			
	P-C_{35}-G-10d_b-D-AA	40.03	0.71	39.53	8.742481
	P-C_{35}-G-10d_b-D-AA	39.03			
	P-C_{25}-S-5d_b-D-AA	23.99	1.38	23.01	10.17781
	P-C_{25}-S-5d_b-D-AA	22.03			
	P-C_{25}-S-10d_b-D-AA	35.12	1.17	35.95	7.950725
	P-C_{25}-S-10d_b-D-AA	36.77			
	P-C_{25}-S-15d_b-D-AA	54.17	1.31	53.24	7.849729
	P-C_{25}-S-15d_b-D-AA	52.31			
	P-C_{25}-S-10d_b-W-AA	31.95	0.45	31.63	6.995311
	P-C_{25}-S-10d_b-W-AA	31.31			
	P-C_{35}-S-10d_b-D-AA	44.67	0.59	44.25	9.786359
	P-C_{35}-S-10d_b-D-AA	43.83			
	P-C_{25}-G-5d_b-D-AB	21.67	0.23	21.51	9.514331
	P-C_{25}-G-5d_b-D-AB	21.35			

P-C_{25}-G-10d_b-D-AB	28.01	0.38	27.74	6.134996
P-C_{25}-G-10d_b-D-AB	27.47			
P-C_{25}-G-15d_b-D-AB	36.66	1.60	35.50	3.526775
P-C_{25}-G-15d_b-D-AB	34.39			
P-C_{25}-G-10d_b-W-AB	24.11	0.27	23.92	7.851203
P-C_{25}-G-10d_b-W-AB	23.73			
P-C_{25}-G-10d_b-D-AB	31.74	1.34	30.79	6.809536
P-C_{25}-G-10d_b-D-AB	29.84			
P-C_{25}-S-10d_b-D-AB	22.17	0.44	21.86	9.669144
P-C_{25}-S-5d_b-D-AB	21.55			
P-C_{25}-S-10d_b-D-AB	28.45	1.86	29.77	6.583953
P-C_{25}-S-10d_b-D-AB	31.08			
P-C_{25}-S-15d_b -D-AB	40.47	1.02	39.75	5.860757
P-C_{25}-S-15d_b-D-AB	39.03			
P-C_{25}-S-10d_b-W-AB	25.97	0.52	25.60	5.661713
P-C_{25}-S-10d_b-W-AB	25.23			
P-C_{35}-S-10d_b-D-AB	33.03	1.16	33.85	7.486288
P-C_{35}-S-10d_b-D-AB	34.67			
P-C_{25}-G-10d_b-D-AC	13.4	1.23	15.74	6.962137
P-C_{25}-G-5d_b-D-AC	15.14			
P-C_{25}-G-10d_b-D-AC	24.91	0.29	24.71	5.46488
P-C_{25}-G-10d_b-D-AC	24.50			
P-C_{25}-G-15d_b-D-AC	31.05	2.15	29.02	3.022529
P-C_{25}-G-15d_b-D-AC	26.99			
P-C_{25}-G-10d_b-W-AC	21.01	0.72	20.50	6.418082
P-C_{25}-G-10d_b-W-AC	19.99			
P-C_{35}-G-10d_b-D-AC	28.03	2.84	26.02	5.7546
P-C_{35}-G-10d_b-D-AC	24.01			
P-C_{25}-S-5d_b-D-AC	16.90	1.13	16.10	7.121373
P-C_{25}-S-5d_b-D-AC	15.30			
P-C_{25}-S-10d_b-D-AC	26.73	1.17	25.90	5.728061
P-C_{25}-S-10d_b-D-AC	25.07			
P-C_{25}-S-15d_b-D-AC	30.52	0.52	30.15	4.445329
P-C_{25}-S-15d_b-D-AC	29.78			
P-C_{35}-S-10d_b-D-AC	46.10	1.82	44.81	9.910209
P-C_{35}-S-10d_b-D-AC	43.52			
P-C_{25}-S-10d_b-W-AC	24.60	1.45	23.57	5.212757
C-C_{25}-S-10d_b-W-AC	22.54			
C-C_{25}-G-5d_b	29.05	3.73	26.41	11.68171
C-C_{25}-G-5d_b	23.77			
C-C_{25}-G-15d_b	58.48	2.80	56.50	8.330385
C-C_{25}-G-15d_b	54.51			
C-C_{25}-G-10d_b	40.98	2.23	34.1	7.541578
C-C_{25}-G-10d_b	37.83			
C-C_{25}-S-15d_b	57.64	2.51	55.87	8.237497
C-C_{25}-S-15d_b	54.09			
C-C_{25}-S-10d_b	40.55	6.19	36.17	7.999381
C-C_{25}-S-10d_b	31.79			

4.1. Influence of Embedded Length on Post-Installed GFRP Reinforcement

When the embedded length is 5d, post-installed GFRP bars exhibit optimal bonding performance, achieving a pull-out load of 2209 with adhesive A, indicating a uniform stress distribution. Moreover, (Fig. 5a). shows that bond strength does not increase proportionally as the embedded length increases. This is due to the nonlinearity in the distribution of stress. The bond strength value using adhesive A is 2.6% and 40.3% higher than that obtained with adhesive B and adhesive

C, respectively. Furthermore, as shown in (Fig. 5a), when the embedded length is increased to 10d and 15d, the hierarchical arrangement of the three adhesives remains consistent with that obtained with the shorter embedded length (5d). However, the incremental rate of the bonding strength increase differs; Adhesive A exhibits bond strength 19.3% and 33.9% higher than adhesive B and adhesive C, respectively, when the embedded length is increased from 5d to 10d. Additionally, when the embedded length increases from 10d to 15d, adhesive A maintains optimal bonding performance, with bond strength increases of 43.2 % and 75.2% compared to adhesive B and adhesive C, respectively.

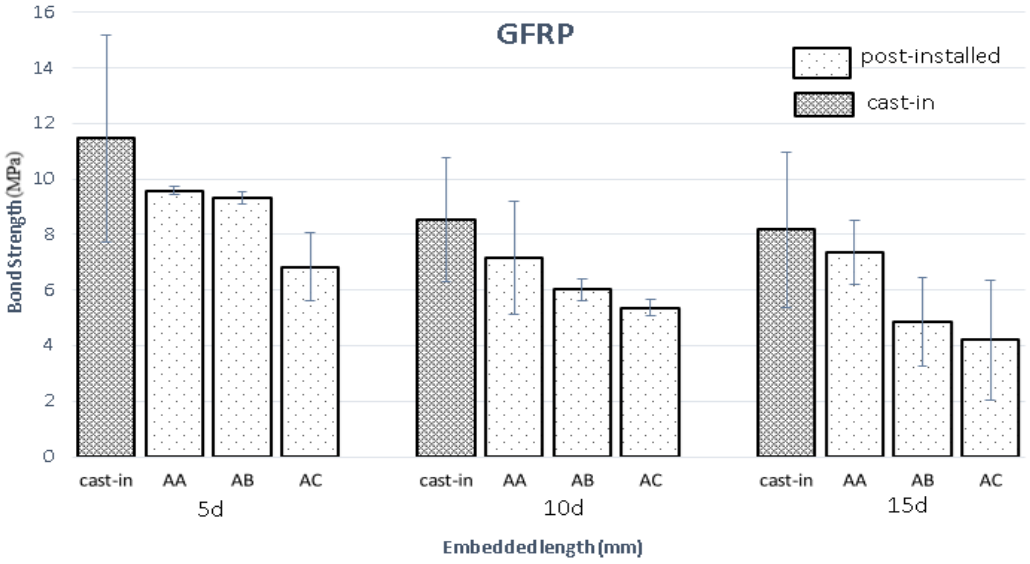

(a)

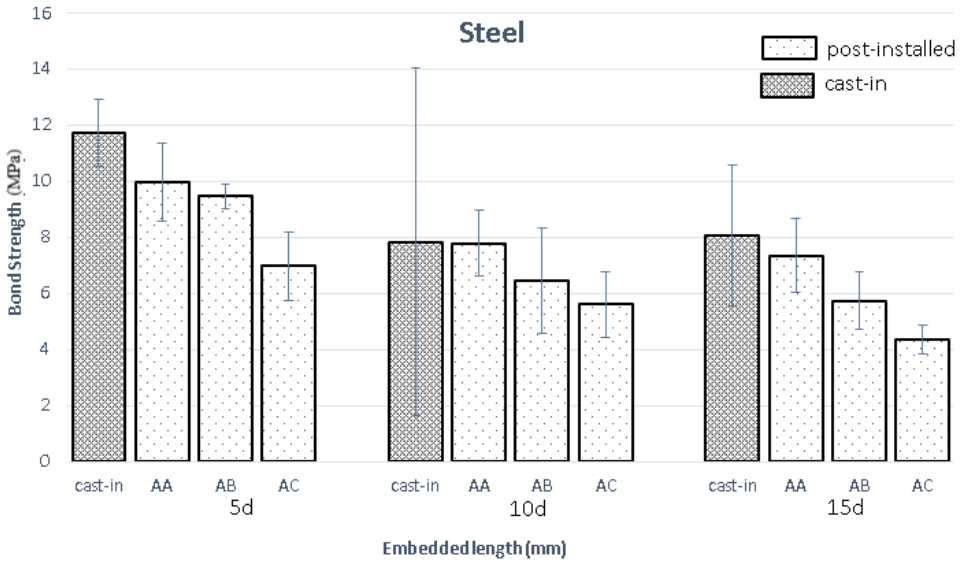

(b)

Fig. 5. Bond stress versus embedded length: (a) GFRP bars; (b) Steel bars

4.2 Influence of Embedded Length on Cast-In GFRP Reinforcement

Utilizing adhesive A at 5d,10d, and 15d embedded lengths, the bonding strengths of the post-installed bars were 83.6%, 89.1%, and 90%, respectively, when compared to the cast-in-place bonding strength at the same embedded lengths, see Fig. 5a. For adhesive B, the bonding strengths at 5d,10d, and 15d embedded lengths were 81.4%, 70.3%, and 62.8%, respectively, of the cast-in-place bonding strength. Similarly, for adhesive C, the bonding strengths at 5d,10d, and 15d embedded lengths were about 59.5%, 62.6%, and 51.3%, respectively, of the cast-in-place bonding

strength. This leads to the observation that cast-in GFRP has superior bonding with longer embedding lengths, given that fresh concrete provides better confinement than post-installed adhesives.

4.3 Influence of Compressive Strength on GFRP Reinforcement

For the stronger concrete cylinders, the bond strength is significantly improved. For example, utilizing GFRP rebars increases the bond strength of higher-strength concrete (i.e., 35 MPa) by 19.45 %, 11%, and 5.3% for specimens with 10d embedment lengths utilizing adhesives A, B, and C, respectively, compared to regular-strength concrete (i.e., 25 MPa). This leads to the conclusion that bond strength is augmented with rising compressive strength due to enhanced mechanical interlock.

4.4 Influence of Wet Environment on GFRP Reinforcement

The bond strengths of all applied adhesives decrease in a wet environment due to the adhesives' sensitivity to surface moisture. declined by 20.5%, compared to 15.9 % for adhesive B and 13.6% for Adhesive A. The bond strength of adhesive C is more significantly impacted due to its higher sensitivity to moisture. Still, in a wet environment, adhesive A exhibits the strongest bonding strength for GFRP bars in wet conditions.

4.6 Influence of Embedded Length on Post-Installed Steel Reinforcement

As shown in Figure 5b, adhesive A with a bond strength of 10.17 MPa performs best at 5d embedded length. Adhesive B and adhesive C have 5% and 30% lower bond strengths. Even at 10d and 15d embedded lengths, the three adhesives' hierarchical arrangement is similar to that of 5d. Moreover, adhesive A exhibits a 20.7% and 38.8% greater incremental rate of bond strength increase than adhesive B and adhesive C, respectively, when the embedding length is increased from 5d to 10d adhesive A exhibits the most effective bonding performance when the embedding length extends from 10d to 15d since the bond strength increases by 44.8%, 27.9%, and 16.4%, respectively, when employing adhesives A, B, and C. The results illustrate that adhesive A is the most effective adhesive that can be used with long-embedded steel rebars.

4.6 Influence of Embedded Length on Cast-In on Steel Reinforcement

The bond strengths at embedded lengths of 5d, 10d, and 15d for adhesive A were 81.8%, 99.3%, and 95.2% of the cast-in-place bond strength, respectively, see Fig. 5b. Comparing adhesive C to the cast-in-place bond strengths, the corresponding bond strengths at 5d, 10d, and 15d were about 77.7%, 82.3%, and 71.1%, respectively. Bond strengths for adhesive C at the same embedded lengths were about 57.29%, 71.6%, and 53.9% of the bond strengths for the cast-in-place method, respectively. This indicates that the relationship between the embedded length and the bonding strength of the bar to the concrete becomes nonlinear at longer embedded lengths.

4.7 Influence of Compressive Strength on Steel Reinforcement

Steel bars in concrete cylinders with higher compressive strength bond more effectively. In Table 7, higher-strength concrete (35 MPa) improves the bond strength of post-installed steel rebar by 23.1%, 13.7%, and 73% for specimens with 10d embedment lengths using adhesives A, B, and C, respectively, compared to regular concrete (25 MPa). In a high compressive strength scenario, adhesive C has a bonding strength of 9.91 MPa, slightly higher than adhesive A's 9.78 MPa. This shows that adhesive C with high concrete compressive strength improves structural performance by slowing the formation of concrete splitting cracks; moreover, it is cost-effective.

4.8 Influence of Wet Environment on Steel Reinforcement

Adhesive C shows that steel bars post-installed into wet holes had a 10.39% reduced bonding strength of 5.21 MPa than specimens with dry holes (Table 7). Adhesive A specimens have a bonding strength of 6.99 MPa and a 13.6% reduction, while adhesive B specimens have a 16.28% reduction. This clearly demonstrates that moist surfaces function as a barrier and diminish adhering performance.

4.9 Failure Modes

None of the specimen samples failed by pull-out; however, all split the concrete as shown in Figures 6 and 7. Concrete splitting occurs because the concrete surrounding the rebar cannot withstand the circumferential (hoop) tensile stresses resulting from radial pressure along the bond interface [23,24]. This failure usually occurs on the concrete surface and spreads along the rebar. Figure 7 illustrates the failure modes of concrete cylinders, where the splitting cracks terminate at the tips of embedded bars. Specimens with shorter embedded lengths had localized splitting cracks near the loaded end, whereas those with longer embedded lengths exhibited extended splitting cracks proportional to the embedded length.. The absence of pull-out failure indicates that epoxy resins are effective bonding agents and can be used to rehab reinforced concrete structures [25].

Fig. 6. failure modes of the examined specimens

(a) (b) (c)

Fig. 7. Effect of embedded length on concrete splitting failure. (a) le=5d, (b) le=10d, and (c) le=15d

5. Conclusions

- The most significant parameter influencing bonding strength is the embedded length of the bars. At shorter embedded lengths, the difference in bonding strength among various adhesions is minimal, but this difference increases as the bars' length increases.
- Adhesive A and adhesive B demonstrated comparable bonding at shorter GFRP and steel rebar embedding lengths, with adhesive A being 2.6% and 5% stronger, respectively.

However, as embedded length increased, the difference between the adhesives became more pronounced, regardless of bar type.

- Post-installed GFRP bars achieved 83- 90% of the bond strength of cast-in samples. While steel bars ranged from 81-99%. Unlike GFRP bars, Steel bars exhibit nonlinearity in the incremental rise of bonding strength as embedded length increases, especially at longer embedded lengths.
- Increasing concrete compressive strength enhanced bond strength by 5-19% for GFRP as well as 13-73% for steel. Adhesive C excelled in steel, whereas adhesive A excelled in GFRP, due to its higher stiffness and optimal curing characteristics.
- The insertion of rebars in wet holes reduced bonding strength by up to 20.5% for GFRP bars in addition to 16.28% for steel, with the greatest decline seen with adhesive C in GFRP applications. This significant reduction in bond strength is attributed to the adhesive's sensitivity to surface moisture, which hinders bonding to the concrete surface and decreases mechanical interlock.
- Splitting and crushing of concrete cylinders have been the main failure mechanisms. This shows that the rebar-concrete interface bond strength surpasses the concrete cylinder tensile stress. Yet, it is weaker than the bars' tensile strength. GFRP bars achieved adequate post-installed bond behavior. As a result, GFRP bars are suitable as an alternative replacement for steel bars in corrosive environments.
- Further studies are recommended to investigate the effects of harsh environmental conditions and higher compressive strengths on bonding strength to provide a better comprehension of performance under various conditions.

References

[1] El Refai F, Abed A, Altalmas A. Bond Durability of Basalt Fiber-Reinforced Polymer Bars Embedded in Concrete under Direct Pullout Conditions. J Compos Constr. 2015 Oct;19(5). https://doi.org/10.1061/(ASCE)CC.1943-5614.0000544

[2] Yan F, Lin Z, Yang M. Bond mechanism and bond strength of GFRP bars to concrete: A review. Compos B Eng. 2016 Aug;98:56-69. https://doi.org/10.1016/j.compositesb.2016.04.068

[3] Cook RA, Kunz J, Fuchs W, Konz RC. Behavior and design of single adhesive anchors under tensile load in uncracked concrete. ACI Struct J. 1998 Jan 1;95(1):9-26. doi: 10.14359/522. https://doi.org/10.14359/522

[4] Cook RA. Behavior of chemically bonded anchors. J Struct Eng. 1993 Sep;119(9):2744-62. https://doi.org/10.1061/(ASCE)0733-9445(1993)119:9(2744)

[5] Mahrenholtz C, Eligehausen R, Reinhardt HW. Design of post-installed reinforcing bars as end anchorage or as bonded anchor. Eng Struct. 2015;100:645-55. https://doi.org/10.1016/j.engstruct.2015.06.028

[6] Tayeh BA, EL dada ZM, Shihada S, Yusuf MO. Pull-out behavior of post installed rebar connections using chemical adhesives and cement based binders. J King Saud Univ Eng Sci. 2019 Oct;31(4):332-9. https://doi.org/10.1016/j.jksues.2017.11.005

[7] Wang D, Wu D, Ouyang C, Zhai M. Performance and design of post-installed large diameter anchors in concrete. Constr Build Mater. 2016 Jul;114:142-50. https://doi.org/10.1016/j.conbuildmat.2016.03.167

[8] Hamad BS, Al Hammoud R, Kunz J. Evaluation of bond strength of bonded-in or post-installed reinforcement. ACI Mater J. 2006;103(2):207. https://doi.org/10.14359/15178

[9] Cosenza E, Manfredi G, Realfonzo R. Behavior and Modeling of Bond of FRP Rebars to Concrete. J Compos Constr. 1997 May;1(2):40-51. https://doi.org/10.1061/(ASCE)1090-0268(1997)1:2(40)

[10] Veludo J, Júlio ENBS, Dias-Da-Costa D. Compressive strength of micropile-to-grout connections. Constr Build Mater. 2012 Jan;26(1):172-9. doi: 10.1016/j.conbuildmat.2011.06.007. https://doi.org/10.1016/j.conbuildmat.2011.06.007

[11] ACI Committee 408. 408R-03: Guide for Design and Construction of Externally Bonded FRP Systems for Strengthening Concrete Structures. Farmington Hills, MI: American Concrete Institute; 2003.

[12] ACI Committee 355.1R-91: State-of-the-Art Report on Bonding of In-Place Reinforcement and Post-Installed Reinforcement. Farmington Hills, MI: American Concrete Institute; 1991.

[13] Tastani SP, Pantazopoulou SJ, Asce M. Bond of GFRP Bars in Concrete: Experimental Study and Analytical Interpretation. J Compos Constr. 2006 Oct;10(5):381-91.

[14] Pecce M, Manfredi G, Realfonzo R, Cosenza E. Experimental and Analytical Evaluation of Bond Properties of GFRP Bars. J Mater Civ Eng. 2001 Aug;13(4):282-90. https://doi.org/10.1061/(ASCE)0899-1561(2001)13:4(282)

[15] Kim B, Doh JH, Yi CK, Lee JY. Effects of structural fibers on bonding mechanism changes in interface between GFRP bar and concrete. Compos B Eng. 2013 Feb;45(1):768-79. https://doi.org/10.1016/j.compositesb.2012.09.039
[16] ASTM International. ASTM A706/A706M: Standard Specification for Deformed and Plain Low-alloy Steel Bars for Concrete Reinforcement. West Conshohocken, PA: ASTM; 2015.
[17] ASTM International. ASTM C127: Standard Test Method for Density, Relative Density (Specific Gravity), and Absorption of Coarse Aggregate. West Conshohocken, PA: ASTM; 2021.
[18] ASTM International. ASTM C128: Standard Test Method for Density, Relative Density (Specific Gravity), and Absorption of Fine Aggregate. West Conshohocken, PA: ASTM; 2022.
[19] ASTM International. ASTM C29/C29M: Standard Test Method for Bulk Density (Unit Weight) and Voids in Aggregate. West Conshohocken, PA: ASTM; 2023.
[20] ASTM International. ASTM C136/C136M: Standard Test Method for Sieve Analysis of Fine and Coarse Aggregates. West Conshohocken, PA: ASTM; 2021.
[21] ACI Committee 211. ACI 211.1: Standard Practice for Selecting Proportions for Normal, Heavyweight, and Mass Concrete. Farmington Hills, MI: American Concrete Institute; 2022.
[22] ACI Committee 440. 440.3R-04: Guide Test Methods for Fiber-Reinforced Polymers (FRPs) for Reinforcing or Strengthening Concrete Structures. Farmington Hills, MI: American Concrete Institute; 2004.
[23] Agarwal J. Bond behavior of post-installed Glass fiber reinforced polymer (GFRP) rebars [dissertation]. West Lafayette (IN): Purdue University;2023.
[24] Mutashar BM, Salih OA, Kasim SY. A Review of the Bond Mechanism and Bond Strength of Fiber Reinforced Polymer Rebars to Concrete. Misan Journal of Engineering. 2025 Feb 19:29-45.
[25] Ahmed KS, Shahjalal M, Siddique TA, Keng AK. Bond strength of post-installed high strength deformed rebar in concrete. Case Stud Constr Mater. 2021 Dec;15. https://doi.org/10.1016/j.cscm.2021.e00581

Research on Engineering Structures & Materials
www.jresm.org

Research Article

Thermal and crack behavior of reinforced high-performance concrete edge-restrained wall

Yasameen N. K. Albresha [*,a], Hussam K. Risan [b]

Department of Civil Engineering, Al-Nahrain University, Baghdad, Iraq

Article Info

Article History:

Received 15 Oct 2025

Accepted 26 Dec 2025

Keywords:

Early-age cracking;
High-performance concrete(HPC);
Edge-restrained wall;
Hydration of cement;
Durability.

Abstract

This study experimentally investigates the early-age behavior of edge-restrained concrete walls constructed with normal-strength (NSC) and high-performance concrete (HPC) under realistic outdoor conditions. The research quantifies temperature variations, strain development, and cracking potential, focusing on the influence of length-to-height (L/H) ratios and reinforcement details. Key findings reveal that while HPC exhibited over twice the tensile strength of NSC, micro-cracking at the aggregate-mortar interface was prevalent in all walls, precluding macro-crack formation during the observation period. Increasing the L/H ratio led to a significant increase in peak shrinkage strains, with HPC walls showing up to 9.1% higher values in longer walls. These results underscore the critical importance of considering the interplay between concrete mix design (particularly tensile strength), structural geometry (L/H ratio), and environmental factors to optimize the durability and minimize early-age cracking risks in restrained concrete structures.

© 2026 MIM Research Group. All rights reserved.

1. Introduction

Early-age cracking is a major problem in reinforced concrete supporting structures, especially those that are used in hydraulic provisions. This effect is produced by suppressed post-cast alterations in volume. The volumetric changes are triggered by a combination of factors, such as heat production of shrinkage, creep, cement hydration, and seasonal variations of environmental conditions. Concrete members are in practice seldom free, either being restrained internally by reinforcement or restrained externally by the support of neighboring structural members. This restriction of volumetric variations causes cracks formation in reinforced concrete structures. The management and reduction of cracking to manageable levels, though not to zero, is still attainable despite its impossibility to do away with it completely.

A fair amount of work has been put into the characterisation of early-age cracking behaviour in restrained concrete members, with special attention paid to edge-restrained designs. The research done early [1-4] was on the mechanism of shrinkage and thermal cracking in reinforced mortar walls, which examined the occurrence of the first and subsequent cracks in the base restrained walls. The studies produced good information on the effect of the length-height ratio (L/H) on the formation of cracks, where it was noted that cracks are more common in the walls with an L/H ratio that is more than about 2.5. Mushchil et al. [5] studied end and edge-restrained mortar using the walls as test material and found that cracking was more prevalent than previously because the end restraints were present. Al-Tameemi et al. [2], discussed the shrinkage-cracking behaviour of a plain wall with edge restraints built with high-strength mortar. The results showed that the cracking was observed as the (L/H) ratio was eight or greater, which was explained by the nature of the high-strength mortar used. Kheder, G. et. al. [6] investigated the cracking behavior of base-

*Corresponding author: st.yasmeen.N@ced.nahrainuniv.edu.iq
[a]orcid.org/ 0009-0000-2583-3250, [b]orcid.org/ 0000-0003-4282-7068
DOI: http://dx.doi.org/10.17515/resm2026-1265ic1015rs

restrained reinforced concrete walls resulting from volume changes. The primary and secondary space measurements of the cracks and width observed in certain 61 full-size walls and the 14 wall-Experimental walls reveal that due to the disuneveness in the distribution of crack width throughout the wall height, the percentage of reinforcement can change according to wall height. Elwakeel et al. [7] and Shezad [8] examined the behaviour of edge reinforced walls built with a concrete L/H ratio of 4. Elwakeel et al. [7] explained the presence of a visible crack among one of four walls as the ratio of L/H was raised to 5, whereas Shezad [8] also found two out of four walls to crack.

Guidelines on how to control crack widths by judicious reinforcement design are given by Forth [9], Bamforth [10], and Jedrzejewska et al. [11], and aimed to reach a satisfactory level of performance. These guidelines also outline the plans for reducing the risks, such as the potential planning of the pour sizes, the choice of the right materials and mix designs, and the use of efficient construction sequences. In addition, they promote insulation to reduce thermal gradient, pre-cooling or in-situ cooling of concrete, and the introduction of movement joints. Gilbert [12] introduced a principle of controlling the cracking that occurs in early-age concrete due to cooling and shrinkage. This study also evaluated the level of restraint existing in a range of practical concrete with reinforcements and also defined the necessary reinforcement to reduce early age cracking. Al-Zuhairi [13] analyzed the behaviour of mass concrete structures in the presence of variation of temperature and change in volume as a consequence of drying shrinkage through the use FORTRAN and ANSYS softwares. To determine the maximum crack width and the development of strains and stresses in the fixed-end walls, the findings were found to be consistent with the estimated findings of the procedure to be used in the development, using ACI Committee 207. Do et al. proposed a computation programme[14] in MATLAB to assess both the temperature evolution, stress development, and the probability of early-age cracking in the pier-cross-sections with normal-strength concrete (NC) and high-strength concrete (HSC) in the first 7 days after casting. They discovered that in minimising the risk of structural cracking and streamlining construction periods, special considerations in the design and construction of contemporary concrete materials (e.g. the high-strength and high-performance concrete) are justified. Micallef et al. [15] examined the long-term cracking characteristics of reinforced concrete walls when put under combined end and restraining restraints. The results indicate that, with C660, a good estimate of the long-term crack width could be found, but it is prone to overestimating the distance between the cracks. The studies mentioned above clearly indicate that the majority of research concerning early surface cracks has predominantly concentrated on models utilizing normal-strength mortar based on ordinary Portland cement, frequently without incorporating coarse aggregates. Such an approach limits its ability to accurately depict the behavior of structural concrete in real-world scenarios. Moreover, some of these investigations were conducted under controlled laboratory conditions, which did not adequately account for the actual effects of varying field conditions, such as elevated temperatures and rapid moisture loss. Consequently, this affects the realism of the findings that represent the performance of concrete elements in actual environments.

The objective of the present study is to understand how high-performance concrete affects the thermal and shrinkage behaviour of edge-restrained concrete walls. Moreover, it aims to identify how the L/H ratio can vary, which is a critical parameter in this context. In this regard, there were five scaled-down walls that were cast during the summer months and were exposed to the environmental factors to model the real-world exposure.

2. Experimental Program

2.1. Materials

During the summer, two sets of reinforced concrete walls were cast, utilizing two different compressive strengths: normal-strength concrete with a compressive strength of 33 MPa and high-performance concrete with a compressive strength of 62 MPa. The cement used in this study is a standard Portland type which follows the specifications set out in EN 197[16]. Major physical and chemical properties of this cement are shown in Table 1.

- The high-performance concrete incorporated sand characterized by its natural fineness modulus of 2.96, a specific gravity of 2.63, a Sulfate content was 0.365%, and particles exhibiting a predominantly spherical morphology.
- The concrete mixture incorporated a coarse aggregate with a nominal maximum size of 17mm. This aggregate exhibited a specific gravity not exceeding 2.55, water absorption up to 0.48%, and sulphate content of 0.087%. Particle size distributions for both coarse and fine aggregates are detailed in Tables 2 and 3, respectively.
- A polycarboxylate-based superplasticizer, commercially available as Max B 500, was incorporated into the mixture. This admixture, conforming to ASTM C494 Types A and F, exhibited a specific gravity of 1.06.
- Silica fume is an extremely fine powder with a specific gravity of 2.25. Based on trial mixes, 8.33% by weight of the cement was replaced with silica fume from the brand Sika.
- The reinforcing steel that was used was deformed bars with nominal diameters of 8 mm and 10 mm; detailed specifications are shown in Table 2. The reinforcement ratio in steel was more than standard minimums according to British Standard BS 8007[17], American Concrete Institute ACI 318[18], and European Standard BS EN 1992-1[19].

Concrete mixtures were prepared in a laboratory-grade electrically powered mixer in order to ensure homogeneity of the blend. First, the dry constituents, namely cement, aggregate (fine and coarse) were used, then all constituents remained till a uniform colour is achieved. Subsequently, the water was added, mixed for 3 to 5 minutes to attain the desired workability. In the case of high-performance concrete, silica fume was pre-blended with dry. After this dry-mixing stage half of the total water (pre-mixed with the superplasticizer) was added and mixed for about four minutes. The rest of the water was then added and the mixture was blended for three minutes again before it went into the formwork.

Each set of reinforced concrete walls, along with the control specimens associated with each wall set, was cast in a single batch. The control specimens were six cubes (150 by 150 mm for compressive strength determination), For the experimental program, the following specimens were prepared: three 150 mm x 300 mm cubes for heat of hydration analysis; nine 150 mm x 300 mm cylinders for indirect tensile strength evaluation; six 150 mm x 300 mm cylinders for compressive strength assessment; and three 100 mm x 100 mm x 400 mm prisms for flexural strength (modulus of rupture) determination. The concrete was consolidated within the formwork using an electric vibrator during the casting process.

Table 1. Details the physical, Mechanical, and chemical properties of the cement used in this study [20]

Category	Parameter	Value
Chemical composition	Tricalcium aluminate (C_3A)	6.31%
	Magnesium oxide (MgO)	2.49%
	SO_3	2.29%
	Ignition loss	2.45%
	Insoluble residue	0.73%
Physical properties	Blaine surface area	3154 cm^2/g
	Initial set time	114 min
	Final set time	2 hr 42 min
Mechanical property	Compressive strength at 2 and 28 days	25.7 MPa, 46.5 MPa

Table 2. Details the grading requirements for coarse aggregate [20]

Sieve opening (mm)	Material passing (%)	Standard allowable limits
20	100%	100
14	91%	100–90
10	81%	85–50
5	5%	50–0
2.36	0	–

Table 3. Details the sand grading requirements as defined by Iraqi specifications [20]

Sieve (mm)	Acceptable range	Passing (%)
4.75	90–100%	97.4%
2.36	75–100%	75%
1.18	55–90%	68.6%
0.6	35–59%	40.3%
0.3	8–30%	28.2%
0.15	0–10%	2.1%

2.2. Edge-Restrained Concrete Wall Casting

The edge restraint for the walls was achieved using a rigid steel beam, as demonstrated in Micallef [15]and Mushchil et al. [5]. This method simplifies boundary condition modeling, as steel does not creep or shrink like concrete, which minimizes the time required for shrinkage strain relief at the base. This process can take months for structural restraint, as noted by [1, 3, 4]. The steel used was a W-shaped beam, 165 mm high and 100 mm wide. To enhance base roughness, four 10 mm deformed steel bars were welded to the upper surface. All the models have a constant height (50 cm) and thickness (10 cm) , see Figure 1. Table 4 illustrates the models' details, casting of the walls is presented in Figure 2.

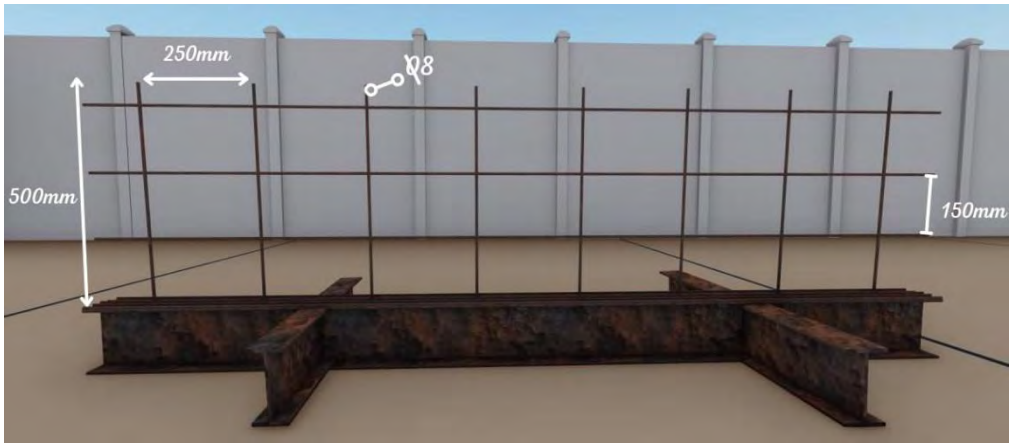

Fig. 1. The wall details

Table 4. The dimensions and reinforcement details of the casted walls

Set num.	L/H	Vertical Reinf.	Horizontal Reinf.	Notation	Concrete Type
Set 1:	5	Ø8@250	Ø8@150	W-NSC-2.5-Ø8	Normal-strength concrete (NSC)
	5	Ø10@250	Ø10@150	W-NSC-2.5-Ø10	
	10	Ø8@250	Ø8@150	W-NSC-5-Ø8	
Set 2:	5	Ø8@250	Ø8@150	W-HPC-2.5-Ø8	High-performance concrete (HPC)
	10			W-HPC-5-Ø8	

2.3. Curing and Exposure

To reduce a potential early-age cracking problem (from rapid moisture loss) the newly formed walls and reference specimens were temporarily covered with plastic sheeting. Subsequent to demoulding, a seven-day wet curing regime was introduced using damp cloths, which were re-moistened periodically to ensure adequate hydration levels. Following this, the specimens were exposed to lab ambient conditions without specific environmental controls. Crack initiation and propagation were monitored over time and thus provided data relevant to the long-term performance of the concrete. A summary of the casting parameters for each of the batches is shown in Table 5 and is further illustrated in Figure 3.

Fig. 2. (a), (b), (c) preparing walls, (d) casting, (e) curing, (f) strain installation., (g) The five hardened walls

Table 5.The casting conditions

The walls	Time of casting	Weather temp.	Concrete temp.	Humidity
NSC-group HPC-group	12 am	33°C	(26-27) °C	At night= 30 At day =20

(a) (b)

Fig. 3. The devices used to record details during casting (a) Humidity and temperature of the weather, (b) Measuring concrete temperature during mixing

3. Deformation, Crack Size, and Hydration Heat Measurements

3.1 Deformation Measurements

After demolding, three 8 cm strain gauges were installed on a polished concrete surface. They were positioned at the centre of the surface at 5 cm, 25 cm, and 40 cm heights from the base for comprehensive strain data collection across different depths in the concrete structure, as shown in Figure 4.

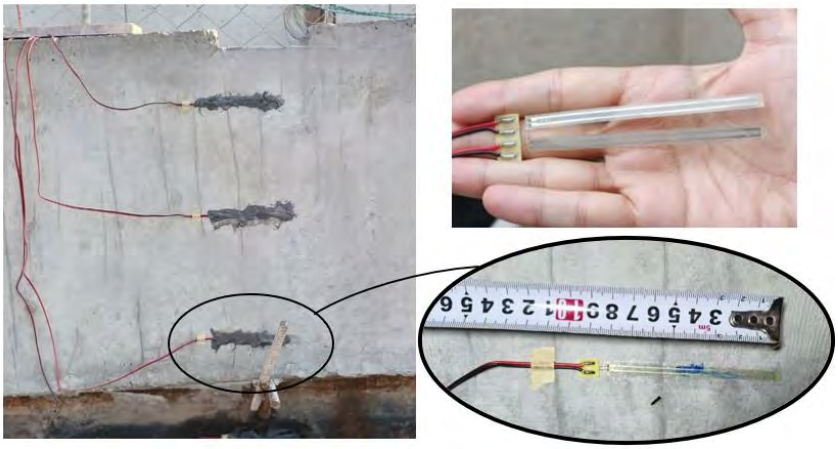

Fig. 4. The 8 cm strain installation

3.2. Crack Width Measurement

A crack meter, which is a portable microscope providing 40X magnification, was used to measure crack widths accurately. It has a 4 mm measuring field for precise observation of crack characteristics (see Figure 5a).

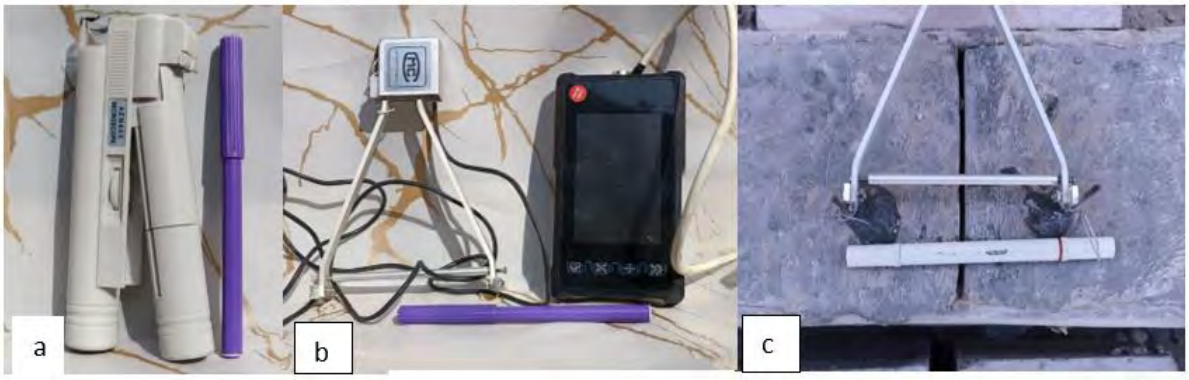

Fig. 5. (a) Crackmeter, (b) and (c) the extensometer installation

An extensometer was also installed at two DEMEC points on the sides, spaced 10 cm apart, to assess changes in free volume in the restrained concrete beam. Frequently, a digital reader with 0.002 mm accuracy connected to the extensometer recorded data until no significant increase in measurements was observed (see Figures 5 b and c).

3.3. The Heat of Hydration Measurement Techniques

It is important to mention that no prior research has examined the heat produced as part of the hydration process along these lines, and the techniques described above have not applied in this context. his study investigates the relationship between the volume and geometry of a structure and the heat generated by cement hydration under realistic conditions. Furthermore, it studies the critical role of ambient temperature and especially its control on heat release and dissipation with time.

A similar method of observing the development of temperature in a concrete member was adopted by Wu [21], in which he used a custom-built data logging system to record the temperature and strain every second. In this study, the same technique is applied to analyse the evolution of the temperature during the hydration in the beam specimens and in the control samples.

- Cube control specimens' technique: To establish a reference for internal heat development, 150 x 150 mm control cubes were cast. A thermistor was embedded at the geometric center of each cube to measure temperature. The cubes were formed using 18mm plywood molds (Figure 6). The data obtained from these control cubes were then compared to the internal temperature measurements recorded in continuous strip beams.
- Edge-restrained wall technique: A thermistor was used to monitor the internal temperature variations within the concrete. It was installed at two points - 150mm and 400mm above the base. The internal temperature at both locations was continuously recorded for 1 week.

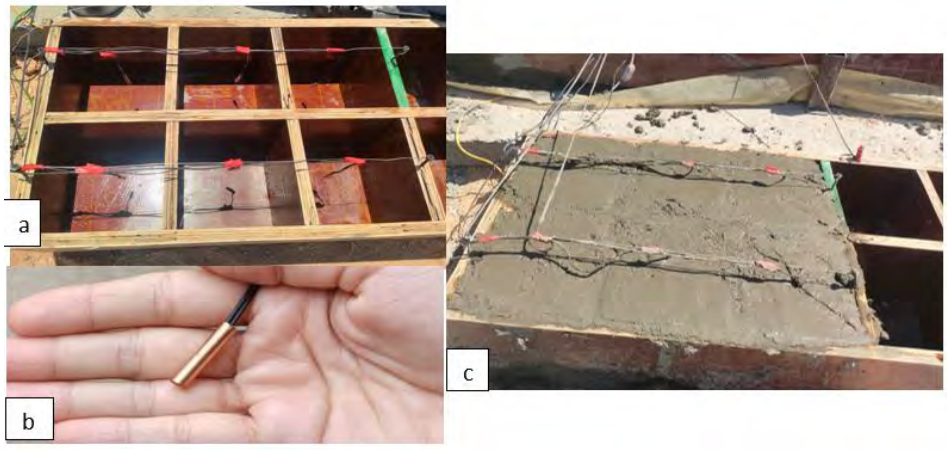

Fig. 6. (a) The thermistor installation, (b) the thermistor, and (c) after casting

4. Tests for Mechanical Performance of Concrete

- Concrete cylinders with dimensions of 150 mm in diameter and 300 mm in height were tested for tensile splitting strength after curing periods of 3, 7, and 28 days. The tests were performed according to the ASTM C496 standard [24]. The testing setup is shown in Figure 8.
- The compressive strength of concrete: The compressive strength test was performed on 150 mm cubes, which were cured for 7 and 28 days in water as per BS EN 12390-3 [16] and above 150 x 300 mm concrete cylinders as per ASTM C39 [23]. The setup of the testing is depicted in Figure 7.
- The modulus of rupture was evaluated using 100 mm x 100 mm x 400 mm concrete prisms cured for 28 days, in accordance with ASTM C78 [25]. This testing protocol was applied to both concrete mixes presented in Table 5.

- Free volume change methods: To assess the variation in the free volume of the concrete, a plain concrete beam was cast with the same I-shaped steel mold as in [26] (see Figure 7). An artificial crack (gap) was inflicted in the mid-span by the introduction of a 4 mm plastic diaphragm. The beam was then exposed to the same environmental conditions as the restrained concrete walls. To minimize the friction between the concrete and the mold, two layers of polythene sheets, which were greased, were used. After casting, the beam was covered with a polythene sheet in order to limit the rapid shrinkage of the plastic. This was then cured for 7 days daily and exposed to similar conditions to the wall specimens, and allowed to shrink and move freely.

Table 5. Mix constituents

Mixes constituents (kg/m^3)	M2-HPC	M1-OPC
Fine aggregate(kg/m^3)	1120	950
Coarse aggregate(kg/m^3)	1150	1050
Cement (kg/m^3)	480	350
Slump (mm)	180	70
Silica fume (kg/m^3)	40	----
W/C ratio	0.25	0.44
Superplastisizer (kg)	4.16	----

- The elastic tensile strain capacity of the concrete was identified through the direct method, using the same I-shaped steel mold in [26] (see Figure 7). Plain concrete beams were made and allowed free shrinkage. As soon as the first crack formed, the amount of strain as a result of the elastic recovery of the restrained concrete was measured. The value of the crack width was measured with a microscope, and then the width of the crack was divided by the total beam length, and this value was considered as the elastic tensile strain capacity of the concrete material. All of the tests described were performed on the two mixes presented in Table 5.

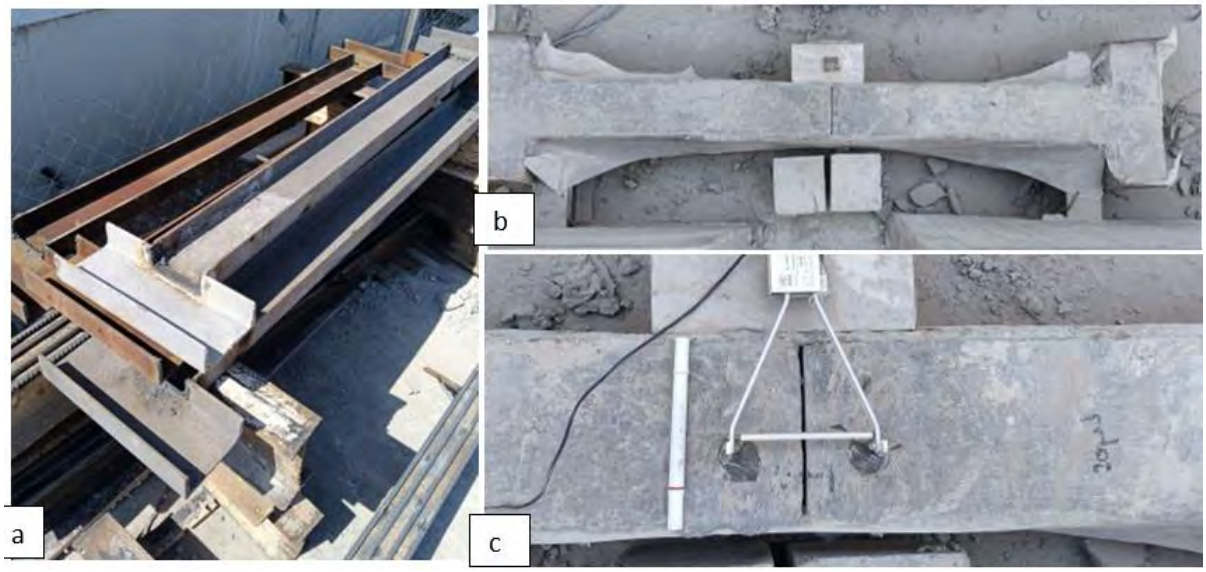

Fig. 7. (a) Mold used for free volume change and elastic tensile capacity, (b) and (c) free volume change method

5. Results and Discussion

5.1. Mechanical Performance of the Concrete Mixes

Table 6 shows the mechanical properties of the concrete for the control specimens of mix M1-NSC and M2-HPC. Each value reported is the average of the values obtained from three individual samples for each mix. The failure patterns on the specimens tested are shown in Figure 8.

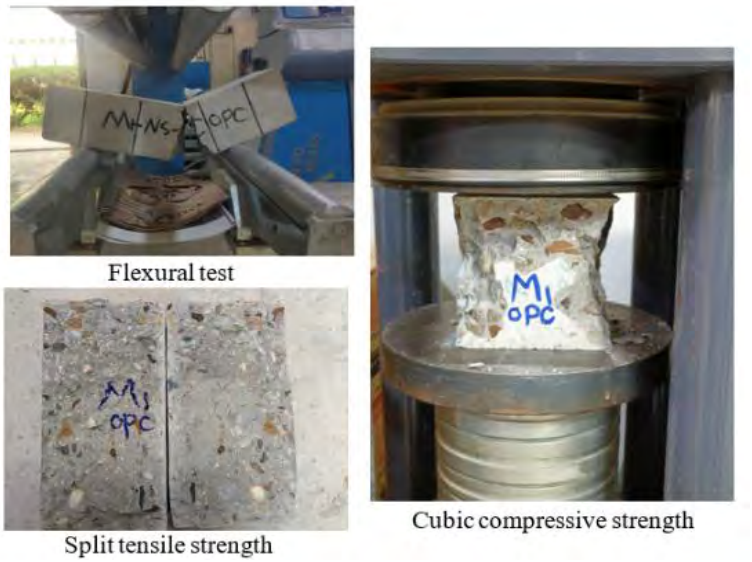

Fig. 8. Control specimens' failure modes

Table 6 shows that the 28-day compressive strength of the cylinder specimens is nearly equal to 0.77 of that of the cubes for normal-strength concrete and 0.78 of that of high-performance concrete. These ratios are very close to those recommended in BS 1881 [27], which recommends cylinder strengths of about 0.8 times corresponding cube strengths. The results also show that the tensile strength for high-performance concrete is stronger than twice that of traditional concrete, indicating a higher level of resistance to cracking - especially during the early life of concrete maturation. In this critical period, the tensile strength is important for reducing the impact of temperature fluctuations and shrinkage that are caused by the proliferation of cement hydration and fluctuations in ambient temperature and moisture. Furthermore, the other mechanical parameters of the concrete mixes show an outstanding uniformity, without recognisable inconsistencies or variation. Together with the results of the compressive strength testing, this consistency shows the reliability and stable working of the materials used.

Table 6. The mechanical properties

Mixes notation	Split tensile strength (MPa)			Flexural strength (MPa)	Cubic compressive strength (MPa)		Cylindrical compressive strength (MPa)	
	3-days	7-days	28-days	28- days	7-days	28-days	7-days	28-days
M1-NSC	1.63	2.2	2.72	2.4	22.07	33.1	13.65	25.6
M2-HPC	2.88	4.12	5.34	6.82	42.6	63.5	40.1	49.6

5.2. Internal Temperature Variation

Analysis of Figures 9 and 10 shows that the temperature variations during the seven days can be divided into two phases. Each phase has specific characteristics that describe what they are doing with the concrete walls and the climatic conditions during the week.

5.2.1 Early Temperature Fluctuations in Concrete Walls Before the Removal of Formwork (Initial Two Days)

All the walls demonstrated comparable thermal behavior during the first two days following casting, irrespective of the type of concrete or wall length. Internal temperatures rose after casting due to the heat generated by hydration, resulting in significant disparities between the internal wall temperatures and the ambient air. Temperatures as shown in Figures 9b, d, f, and Figures 9b, d. This effect was particularly pronounced between the upper and lower parts of the wall. The

upper area, nearer to the surface and directly exposed to sunlight, registered higher temperatures at an accelerated rate than the lower area, which remained cooler. The upper part was cooling down as temperatures declined in the night. However, it did not attain the reading of the surrounding air temperature. This can be explained by the insulating property of the wooden casing of the wall. Therefore, the upper and lower parts of the walls also remained warmer compared to the external temperature until the end of the day, with differences being approximately 5 degrees Celsius for 5-meter-long walls and less than 3 degrees Celsius for the 2.5-meter-long walls. Additionally, the progressive decrease in temperature, principally at the base of the wall, was associated with the effective insulation of the wooden mold that became a barrier to the cooling rate. Such an outcome coincides with the findings of the earlier studies [9, 10, 28], which support the hypothesis that a postponed removal of mold plays a positive role in gradual heat loss and corresponding reduction of the probability of early cracking in concrete.

5.2.2 Temperature Fluctuations in Concrete After the Removal of Formwork

Following the removal of the molds, there was consistent thermal performance within the top and bottom parts of the walls, which was observed two days later. The temperatures at such locations were higher than the ambient air temperature during the day due to their entire exposure to the air from all directions, which permitted the effective absorption of thermal energy during the night as the temperatures steadily declined, hence conforming to the ambient cold temperature. This fall is a thermal loss due to interactions with the external environment, as shown in figures 9a, c, d and figures 10a, c. These patterns illustrate the way the exposed concrete reacts to the conditions provided by the environment, particularly after the removal of the molds, as it becomes more sensitive to the temperature changes in the environment. During the following three days, there was a stabilizing of temperatures, which showed a clear and yet synchronized variation to a daily fluctuation in ambient temperature. This transition means that the concrete has also reached a step where it has a more stable behaviour in terms of thermal contact, lower rate of change and also in terms of its compatibility with its surroundings.

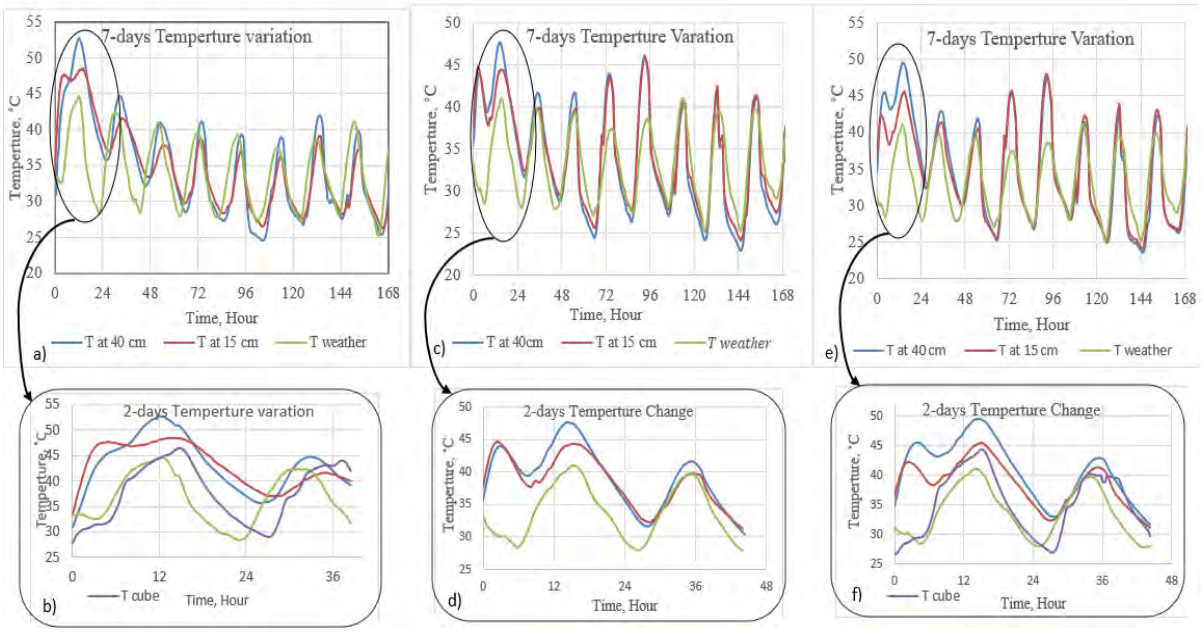

Fig. 9. Inner temperature versus time for the walls: a) W-NSC-2.5-Ø8, c) W-NSC-2.5-Ø10, and e) W-NSC-5-Ø8 for seven days, b, d) and f) their cement hydration

These trends are the normal daily fluctuations in temperature readings, where the trends are rising with higher ambient temperatures during the day and falling in the evening as the day cools down. This interaction describes a well-efficient and comprehensive thermal exchange of the concrete and its surroundings. Overall, this observation emphasizes the significance of the thermal behaviour in the first stage of the concrete existence to the whole state of a structure.

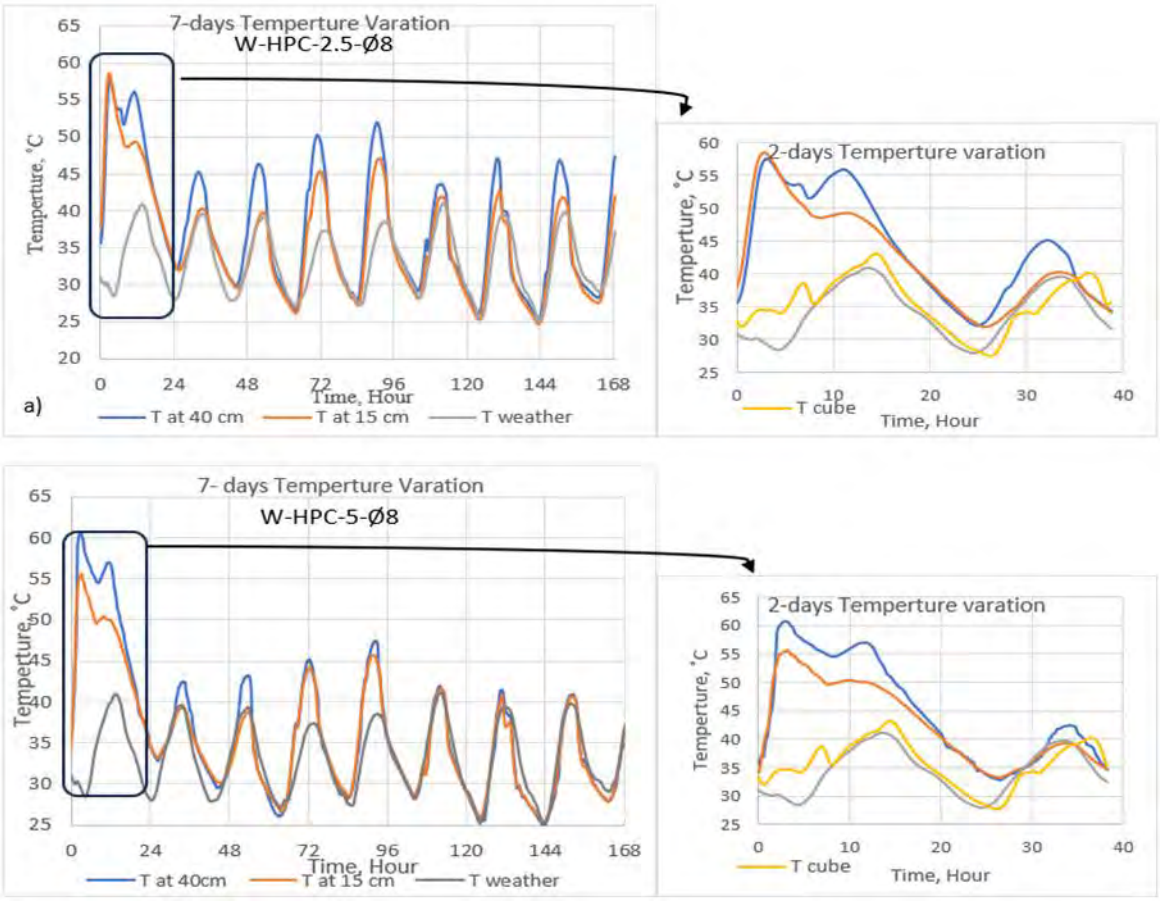

Fig. 10. Inner temperature versus time for the walls: (a) W-HPC-2.5-Ø8 and (b) W-HPC-5-Ø8 for seven days, (c) and (d) during cement

5.2.3 Effect of Concrete Type

The use of high-performance concrete played a crucial role in the determination of temperature development. Different concrete mixes with different cement content and/or additives had an influencing on the peak temperature and cooling rate. Of significance, in the case of the hydration set on HPC as illustrate in figure 10, an increase of higher hydration temperature could be achieved; the higher hydration temperature on the inside of normal strength concrete (NSC) walls reached 45 °C as shown in figure 9, while the higher hydration temperature of the walls of high-performance concrete (HPC) made an impressive mark at 59 °C. This significant variation in temperature influences the properties in the early ages, like the development of strength and cracking risk. These findings show the importance of understanding thermal behavior in order to optimise the mix designs and mitigate the risk of early-age cracking of reinforced concrete structures.

5.2.4 Effect of Length/Height Ratio

The differences between walls and their control cubes in terms of inner temperature result in hydration display drastic variations that are affected by the use of volume and geometry. Normally, the walls contained a slower rate of cooling as compared to the cubes, as seen in Figures 9 and 10. The slower rate can be explained by the large volume to be able to hold heat for a longer time. As this hydration stage went on, the impact of the wall length within the temperature distribution became more apparent, as shown in Figure 8b,f, and in Figure 10b,d. The 5-meter walls showed a lot of difference between the bottom and the top with respect to temperature. Precisely, the temperature of hydration developed on the top of such walls was found to be much higher (8.2% for standard strength concrete and 9.1% for high-performance concrete) temperature at the bottom. On the other hand, the walls with a height of 2.5 meters showed a more homogeneous increase in temperature. Both the top and the bottom point-wise of these shorter walls, however, showed similar rates and values, which provided steadier thermal behavior throughout the

structure. Eventually, the data collected by the recording system indicated a strong correlation between the L/H ratio and peak hydration temperature, in this case, shown especially at the bottom of the walls. Subsequent rises in the inner temperature cause a large difference in temperature between the inner ambient temperature level inside the wall, which is confined within the wall. This difference in temperatures led to the development of thermal cracking that could be seen on the surface of the walls or visible as unobtrusive microcracks within the structure. The second of the mentioned behaviours will be explored further in the next section, focusing on cracking.

5.3. Measurements of Surface Concrete Strain

The strain was measured carefully at three different heights and on every wall, and recorded one week after the walls had fully cured and had reached the required strength. Data collection still went on for more than a month in September, a time when temperature fluctuations were quite extreme, which had dramatic effects on the expansion and contraction cycles of the concrete. The strains visible in the pictures of Figures 11 to 15 are easily detected with positive values indicating expansion and negative values indicating shrinkage. Detailed analysis of these numbers revealed an overall trend flow within all five walls, regardless of the materials they were made from. Normal Strength Concrete (NSC) Excel HPC. This trend can be divided into several phases, each of which emphasises the dynamics of concrete behaviour under conditions of varying environmental conditions:

5.3.1 Phase 1: Concrete Strain Behavior During the First 10 Days After Curing

During this phase, there was a predictable strain response pattern to all vertical locations of the walls (top, middle, bottom) for the differences in the concrete mix. Strain values showed significant changes due to changes in the temperature. An Increase in daytime temperature is observed to produce considerable shrinkage in the concrete during daytime, and low temperature at night produces little expansion. This behavior is in line with well-recorded concrete thermal properties, which imply its sensitivity to temperature changes. Additionally, the strain data gave small differences between the measurements at the three vertical levels, showing uniform moisture losses in the walls and good curing. Notably, the accumulated strain through shrinkage was much higher as compared to that of expansion, which signified a strong tendency to shrinkage. Tables 7 and 8 conclusively summarize the average shrinkage and expansion strain values obtained for the five walls in this phase.

5.3.2 Phase 2: Strain Behavior from Day 10 to Day 20

From the onset of this phase, the behavior of the strain mainly tended to shrinkage, and the expansion strain noted at the beginning of the phase decreased significantly. Three significant observations were made:

- Volatilities in values of the strains among the three vertical positions were amplified as a result of the difference in the degree of moisture loss that resulted from temperature changes. These differences emphasized the individual effects of environmental conditions on every position.
- Walls of larger lengths of 5 m only experienced shrinkage strain, while the short walls of 2.5 m recorded a small amount of expansion strain. This observation marks the role of the length-to-height (L/H) ratio, whereby longer structures are more prone to large shrinkage. This complies with the researchers' results [1- 5,7].
- Drying shrinkage became the biggest control of strain characteristics, worsened by temperature fluctuations during the day. These cycles of environmental impacts amplified the effects of shrinkage, focusing on the material behavior and the structural integrity that was induced with time.

5.3.3 Phase 3: Strain Behavior after Day 20

Following 20 days, all five walls exhibited elevated values in strains compared to the previously phases with little substantial reduction in the shrinkage strain noted during nighttime, which adheres to Wu [21]. This means that shrinkage strains continued to add to one another, causing

restrained tensile stresses in the concrete. The possibility of cracks developing if these stresses exceed the tensile strength of the material.

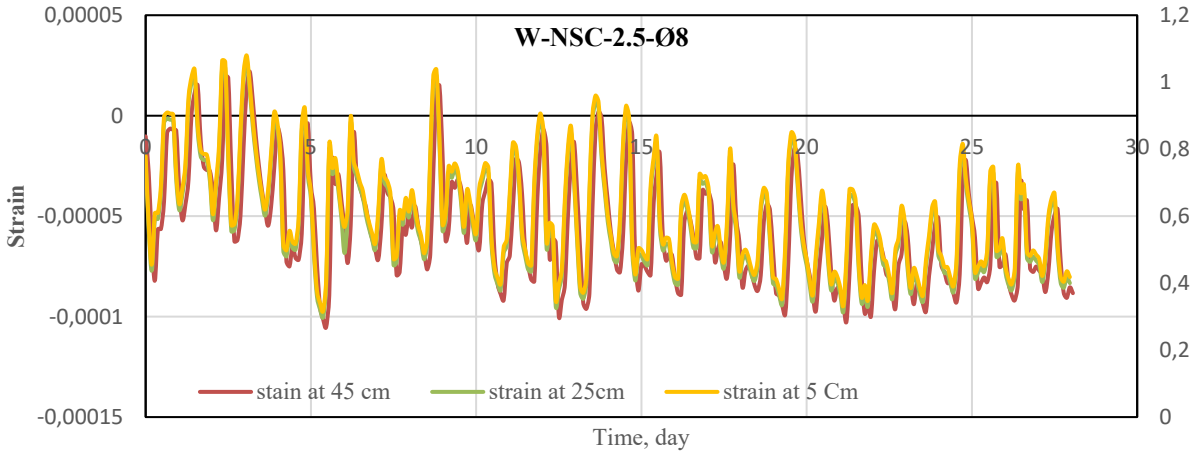

Fig. 11. Measured surface concrete strain versus time for W-NSC-2.5-Ø8

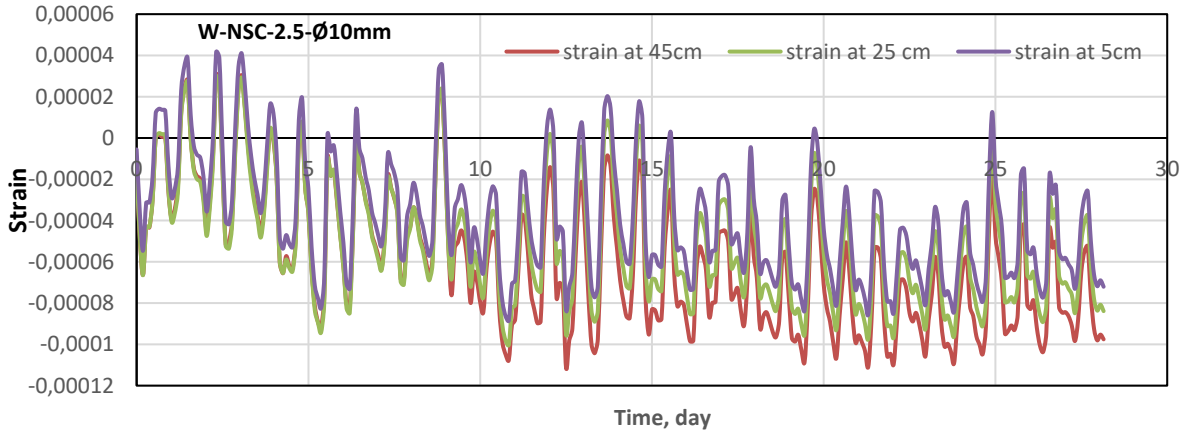

Fig. 12. Measured surface concrete strain versus time for W-NSC-2.5-Ø10

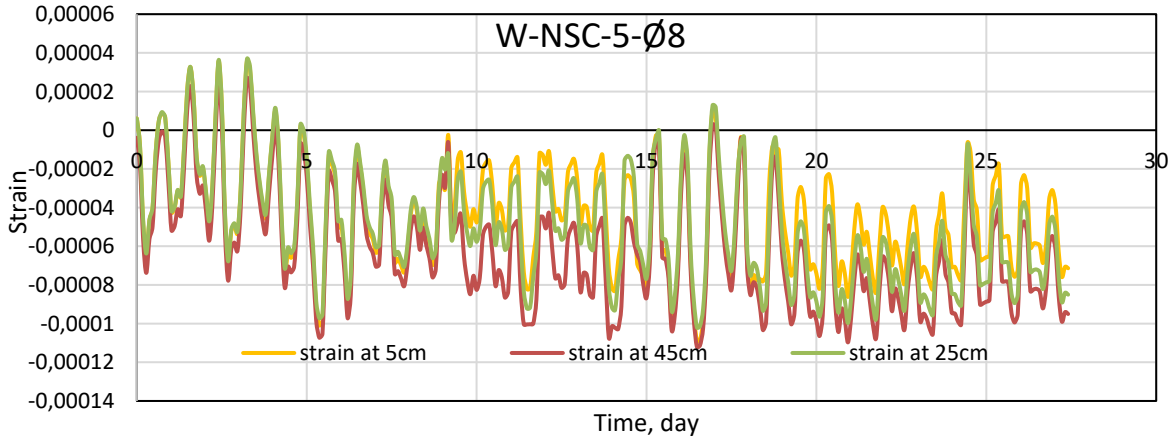

Fig. 13. Measured surface concrete strain versus time for W-NSC-5-Ø8

5.4 Effect of Steel Reinforcement

The effects of increasing the size of reinforcement bars from 8 mm to 10 mm were clearly observed in the strain distribution across different levels of the wall, as shown in Figure 12. Compared to the reference wall in Figure 11, the wall reinforced with the larger 10 mm bars exhibited subtle yet significant differences in strain levels from the very first day of observation. Such differences

became much more noticeable after the first round of testing and kept on growing throughout the entire evaluation period. In addition, the wall with the 10 mm reinforcement showed much more expansion strain level in comparison with the reference wall; thus, the reinforcement bar size had a strong effect on the wall's response to environmental conditions. Notwithstanding this extraordinary increase in the expansion strain, the overall shrinkage strain remained the dominating factor, thus confirming that the wall generally shrank with time. Such findings point out the significant role played by the reinforcement bar sizes on the strain distribution as well as the long-term nature of deformation of the wall. Additionally, they show the use of bigger bars of steel as per the allowable specifications, which can be important in removing the early age cracking that typically emanates due to the temperature and moisture fluctuations in the material.

5.5 Effect of Length/Height Ratio

Strain distribution and the deformation behavior of concrete walls are greatly influenced by changing the L/H ratio. Studying results presented in Figures 11, 13, 14, and 15 show that with an increase in L/H ratio, the concrete strain tends to shift towards shrinkage strain, especially after the first ten days. Additionally, strain increases significantly at this first stage of the analysis, and for longer walls (irrespective of concrete type), peak shrinkage strain values are higher than the reference values. This variation highlights the great effect that the length-to-height (L/H) ratio has on the behavior of walls. When increasing the length of the wall, the area of the wall that will be exposed to varying conditions of the air is considerably increased. This increased exposure not only increases the fluctuations in temperature to which the wall is exposed, but also increases the level of movement of moisture in the concrete. The interaction of these factors can have a significant effect on the structural strength and life of the walls over time.

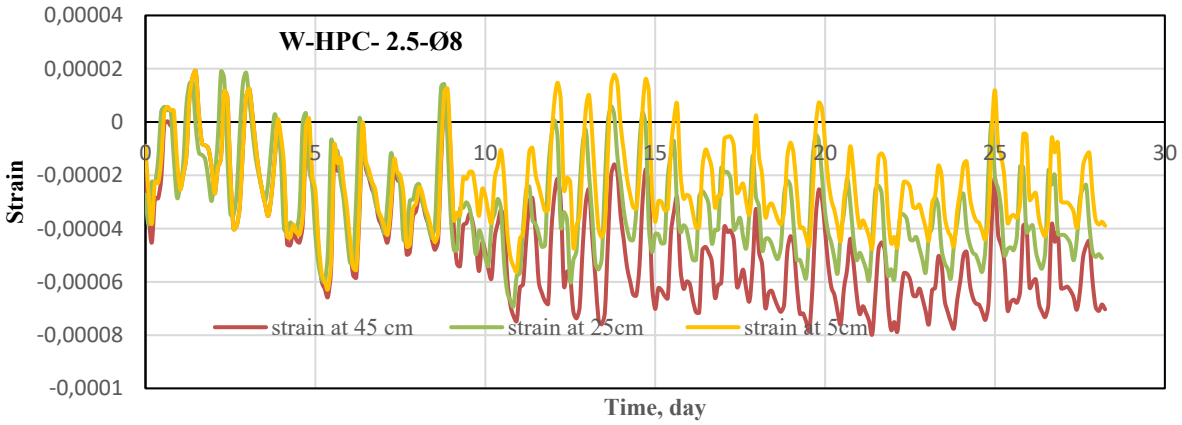

Fig. 14. Measured surface concrete strain versus time for W-HPC-2.5-Ø8

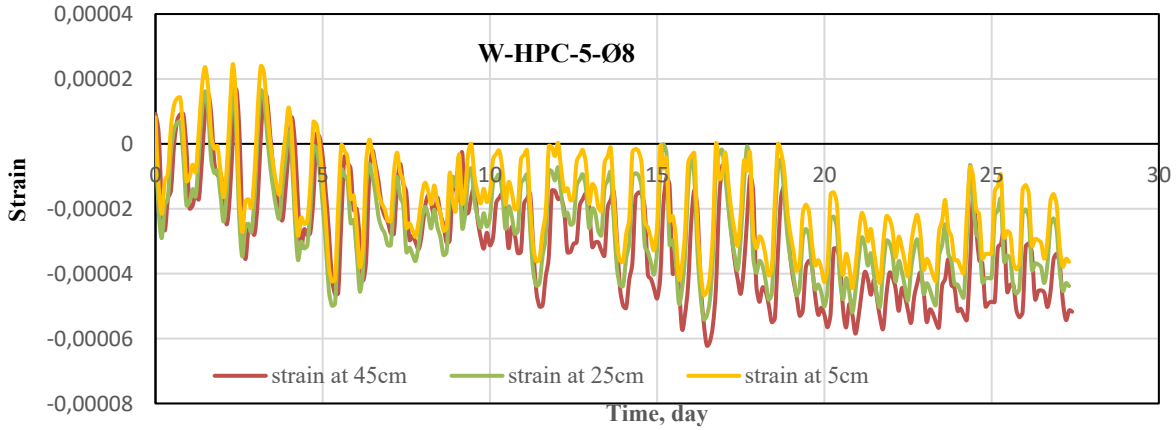

Fig. 15. Measured surface concrete strain versus time for W-HPC-5-Ø8

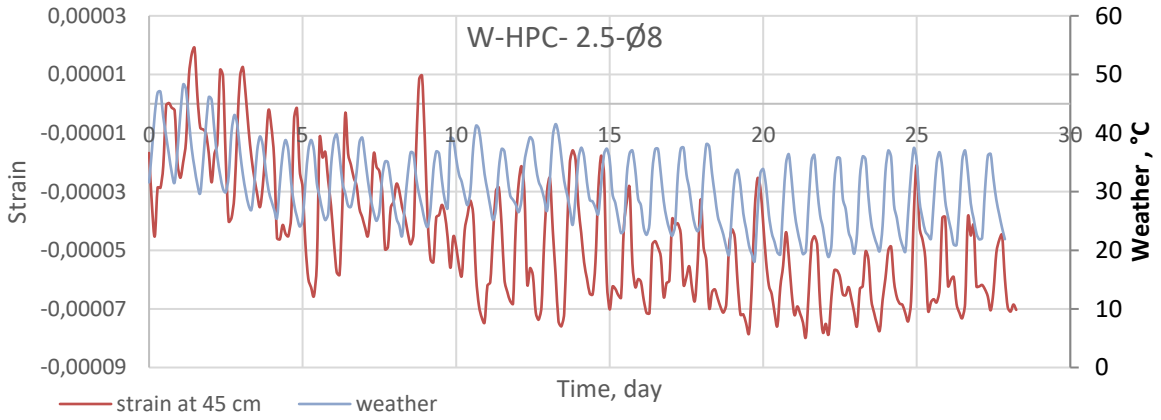

Fig. 16. Concrete strain versus time at 45m from base with ambient temperature for W-HPC-2.5-Ø8

Table 7. Phases of strain development: behaviour, avg max. shrinkage and expansion strain for the NSC group

Phase number	Wall notation	Observed behavior	Avg daily temperature	Avg. shrinkage strain ($*10^{-6}\mu m$)			Avg night temperature	Avg. expansion strain ($*10^{-6}\mu m$)		
				Top	Mid.	Bottom		Top	Mid.	Bottom
Phase 1	W-NSC-2.5-Ø8	Exhibiting perfect fluctuations in response to temperature variations	44	63.83	59	55.8	28	18.7	23.6	14.4
	W-NSC-2.5-Ø10			52.2	53.5	42.2		16.82	16.83	28.8
	W-NSC-5-Ø8			65.83	55.9	57.83		19.4	21.2	34.2
Phase 2	W-NSC-2.5-Ø8	Progressive increase in shrinkage	38	83.2	78.1	74.4	24	8.5	30.1	9.8
	W-NSC-2.5-Ø10	Shrinkage increased, and after the ninth day, the difference between the three levels became noticeable.		89.4	91	69		13.1	7.82	16.1
	W-NSC-5-Ø8			92.5	78.3	74.7		1.76	11.8	10.3
Phase 3	W-NSC-2.5-Ø8	Mainly shrinkage	37	85	89.3	86.3	20	-	-	-
	W-NSC-2.5-Ø10	Mostly shrinkage		103.1	90.4	79		-	0.08	12.6
	W-NSC-5-Ø8	Mainly shrinkage		101	90.78	77.5		-	-	-

Table 8. Phases of strain development: behavior, average max. shrinkage and expansion strain for the HPC group.

Phase number	Wall notation	Observed behaviour	Avg day temperature (ºC)	Avg shrinkage strain ($*10^{-6}\mu m$)			Avg night temperature (ºC)	Avg expansion strain ($*10^{-6}\mu m$)		
				Top	Mid.	Bottom		Top	Mid.	Bottom
Phase 1	W-HPC-2.5-Ø8	Exhibiting perfect fluctuations in response to temperature variations	44	36.2	33.83	34.7	28	14.3	10.4	9.74
	W-HPC-5-Ø8			26.8	27.7	20		11.2	11.9	17
Phase 2	W-HPC-2.5-Ø8	Shrinkage strain increases progressively, and after the ninth day, the difference between the three levels became noticeable.	38	64.2	51.2	42.4	24	9.6	6.22	10.94
	W-HPC-5-Ø8			43	39	32.3		-	-	1.22
Phase 3	W-HPC-2.5-Ø8	Almost shrinkage	37	74.7	55.4	43.1	20	-	-	1.19
	W-HPC-5-Ø8	Mainly shrinkage		54.5	47	40		-	-	-

5.6 Effect of Using High-Performance Concrete

The use of high-performance concrete (HPC) in the wall structures showed similar behavior to that of the regular normal strength concrete walls. However, as can be seen in Figures 14, 15, there were considerable variations in strain data obtained for three different measuring levels. The HPC walls showed lower peaks of stress shrinkage strain as compared to their normal-strength counterparts in Figure 11, which indicated a more stable performance under stress. Especially interesting was the behavior for the W-HPC-2.5-Ø8 wall, which had higher values of expansion strain at the lower level of the measurement, closer to the foundation level, within the period of testing. This peculiar behavior can be explained by the presence of the silica fume in the HPC mix that reacts with the product of the hydration of cement, which is the calcium silicate hydrate or C-S-H. This is true not only in the production of additional pore-filling but also improvement of densification of the concrete structure, where the resistance to shrinkage is greatly decreased. Such a conclusion is in perfect agreement with Neville's [29]: Even with these benefits, it was pointed out that, mostly, the strain accumulation values were negative, meaning there was a tendency by the wall to get smaller over time. On top of that, the disparities in measurements of strains on different levels indicated that the concrete reaction was correlated to a large extent with the conditions of the environment. The natural variations of the temperature and the humidity had a considerable influence on this first type of development of the concrete: the sensitivity of the material to the environment. In summary, the results obtained from this study identify the interplay of various aspects of the attributes of HPC and external factors on the performance of concrete structures.

5.7 Cracking of Edge-Restrained Walls

Strain measurements indicate that the behavior of normal strength concrete (NSC) and high performance concrete (HPC) possesses different properties under usual temperature fluctuations, and especially on the shrinkage issue. Nonetheless, no tangible cracks were noticed in all five walls during the testing time. The fact that there have been no signs of cracking, although there was measurable strain as shown in Figures 11 to 15, can be mostly attributed to the qualities of the concrete mix. The addition of coarse aggregate in the mixture caused micro-cracks to be produced at the interface between the mortar and the coarse aggregate particles. These fine micro-cracks formed around the gravel particles as a result of volume change in the concrete, which was caused

by hydration, curing, and temperature variations. These results are similar to those reported earlier [30, 31], implying that most cracks are at the interface between mortar and coarse aggregates rather than in the mortar itself. In addition, Thomas [31] has distinguished three types of cracks:

- Horizontal and vertical cracks, found nearest to the minimum distance between gravel particles.
- Diagonal cracks, which appear at the maximum separation between gravel particles.
- Cracks at the bond. The first two types of cracks are associated with maximum tension within the paste, while the third type arises from weak bond strength between the sandstone and the paste during the early stages of the concrete setting.

Simultaneously, the findings of this research offer conflicting results when contrasted with another study. For example, Kheder [1] reported that the wall with the length-to-height ratio of 4 developed secondary cracks, and walls with a higher L/H ratio showed both primary and secondary cracks. In contrast, Shehzad [8] observed that with an L/H ratio of 4 two out of four walls were cracked. More recently, Elwakeel et al. [7] investigated three walls of the same aspect ratio with increasing L/H ratio of a fourth wall to 5. The latter wall was subject to cracking, unlike the other three; even though the concrete mix in it was similar to that of one of the other. Additionally, Al-Tameemi [2] showed that edge-restrained walls with the L/H-ratio of 8, which were constructed with a high-performance mortar, suffered from both primary and secondary crack occurrences. From the comparison of the results obtained in this study and the previous research where various length/height (L/H) ratios in walls made of concrete were discussed, it can be concluded that the ratio of length and height affects the crack behavior in the wall. However, it is not the only factor in the game. The inconsistency between studies in findings implies that multiple factors influence this behavior. These include environmental conditions such as temperature and humidity, the type of concrete and the mechanical properties of the concrete, and implementational details such as the type of restraint used, the processing technique, and the timing and technique for formwork removal. Table 8 shows a systematic comparison of the results from this study by comparison with several previous studies. These studies examined concrete walls having similar or different length-to-height ratios taking into account variations in concrete type and environmental conditions.

Table 8. previous researchers' results using concrete for casting the walls

The study	L/H	Using aggregate	Concrete type	Results
Kheder [1]	≥4	Used	NSC	Cracked
Shehzad [8]	4	Used	NSC	2 cracked
Elwakeel et al. [7]	4, 5	Used	NSC	The wall with a ratio of 5 only cracked
Al-Tameemi, et al. [2]	8	Not used	HPC	cracked

6. Conclusion

The results showed that the use of coarse aggregate in the concrete mix clearly contributed to reducing early surface cracks, as the generated microcracks help release part of the internal tensile stresses and prevent their development into visible surface cracks. The study also indicated that the likelihood of early cracking is related to the interaction between the initial thermal rise and the degree of restraint; despite the significant variation between daytime and nighttime temperatures, the internal thermal rise remained within levels that do not generate sufficient tensile stresses to cause visible surface cracks during the first few days. As well as, increasing L/H ratios increases shrinkage strains; the peak shrinkage strain increases with longer walls up to 9.1% compared to shorter walls in the case of HPC, indicating a geometric effect on behaviour at an early age. These results highlight the importance of material composition, structural geometry, and environment in creating long-lasting concrete infrastructure, especially in alleviating early-age distress. Further

researches need to be conducted on full-scale models using concrete mix, to identify the most influential factor among these in preventing the occurrence of cracks.

References

[1] Kheder GF. Control of shrinkage cracking in reinforced concrete walls [MSc thesis]. Baghdad: University of Baghdad; 1986.

[2] Al-Tameemi AA, Attiyah AN, Mohammed TJ. Cracking behavior of base-restrained high-strength plain concrete walls due to shrinkage. International Journal of Scientific Engineering and Research. 2018.: 8(1):1-10. https://doi.org/10.21275/18012001

[3] Al Attar TS. Minimum steel reinforcement for control of cracking due to shrinkage and temperature changes in reinforced concrete tension members [MSc thesis]. Baghdad: College of Engineering, Baghdad University; 1988.

[4] Al Mashhadi SA. Control of secondary shrinkage cracking in reinforced concrete walls [MSc thesis]. Baghdad: College of Engineering, Baghdad University; 1989.

[5] Al-Mashhadi MS, Habeeb GM, Mushchil AK. Control of shrinkage cracking in end-restrained reinforced concrete walls. Int J Archit (IJA). 2019;5(2):41-62.

[6] Kheder GF, Al-Rawi RS, Al-Dhahi JK. A study of the behaviour of volume change cracking in base-restrained concrete walls. Mater Struct. 1994;27:383-92. https://doi.org/10.1007/BF02473441

[7] Elwakeel A, Shehzad M, El Khoury K, Vollum R, Forth J, Izzuddin B, et al. Assessment of cracking performance in edge restrained RC walls. Struct Concr. 2022 Jun;23(3):1333-52. https://doi.org/10.1002/suco.202100688

[8] Shehzad MK. Influence of vertical steel reinforcement on the behaviour of edge restrained reinforced concrete walls [PhD dissertation]. Leeds: University of Leeds; 2008.

[9] Forth JP, Martin A, Anchor RD. Design of liquid retaining concrete structures. [City of publication]: Whittles Publishing; 2014.

[10] Bamforth PB. Control of cracking caused by restrained deformation in concrete. [City of publication]: CIRIA; 2018.

[11] Jędrzejewska A, Zych M, Kanavaris F, Chen F, Ito S, Torrenti JM, et al. Standardized models for cracking due to restraint of imposed strains-the state of the art. Struct Concr. 2023 Aug;24(4):5388-405. https://doi.org/10.1002/suco.202200301

[12] Gilbert RI. Cracking caused by early-age deformation of concrete-prediction and control. Procedia Eng. 2017 Jan 1;172:13-22. https://doi.org/10.1016/j.proeng.2017.02.012

[13] Al-Zuhairi AHA. Control of volume change cracking in plain and reinforced massive concrete with different base restraints [PhD thesis]. Baghdad: College of Engineering, Baghdad University; 2005.

[14] Do TA, Hoang TT, Bui-Tien T, Hoang HV, Do TD, Nguyen PA. Evaluation of heat of hydration, temperature evolution, and thermal cracking risk in high-strength concrete at early ages. Case Stud Therm Eng. 2020;21:100658. https://doi.org/10.1016/j.csite.2020.100658

[15] Micallef M, Vollum RL, Izzuddin BA. Cracking in walls with combined base and end restraints. Mag Concr Res. 2017 Nov;69(22):1170-88. https://doi.org/10.1680/jmacr.17.00026

[16] European Committee for Standardization; British Standards Institution. EN 197-1: Cement. Part 1, Composition, specifications, and conformity criteria for common cements. London: BSI; 2012.

[17] British Standards Institution. BS 8007: Design of concrete structures for retaining aqueous liquid. London: BSI; 1987.

[18] American Concrete Institute. ACI 318M-19: Building code requirements for structural concrete. Farmington Hills (MI): ACI; 2019.

[19] British Standards Institution. BS EN 1992-1: Eurocode 2: Design of concrete structures - Part 1: General requirements. London: BSI; 2004.

[20] Central Agency for Standardization and Quality Control. Iraqi Specification IQS No. 45: Aggregate from natural sources for concrete and construction. Baghdad: COSQC; 1984.

[21] Wu CH, Lin YF, Lin SK, Huang CH. Temperature development and cracking characteristics of high strength concrete slab at early age. Struct Eng Mech. 2020 Jun 25;74(6):747-56.

[22] British Standards Institution. BS EN 12390: Testing hardened concrete, method of determination of compressive strength of concrete cubes. London: BSI; 2000.

[23] ASTM International. ASTM C39/C39M-15a: Standard test method for compressive strength of cylindrical concrete specimens. West Conshohocken (PA): ASTM; 2015.

[24] ASTM International. ASTM C496: Standard test method for splitting tensile strength of cylindrical concrete specimens. West Conshohocken (PA): ASTM; 2004.

[25] ASTM International. ASTM C78/C78M-16: Standard test method for flexural strength of concrete (using simple beam with third-point loading). West Conshohocken (PA): ASTM; 2016.

[26] Al-Rawi RS. Determination of tensile strain capacity and related properties of concrete subjected to restrained shrinkage. In: Proceedings of ACI Symposium; 1985 Aug; Singapore. p. 18.
[27] British Standards Institution. BS 1881-120: Testing concrete. Method for the determination of the compressive strength of concrete cores. London: BSI; 1983.
[28] Anchor RD. Design of liquid retaining concrete structures. 2nd ed. [City of publication]: [Publisher Name]; 1992.
[29] Neville A. Neville on concrete. Farmington Hills (MI): American Concrete Institute; 2003 Jan 1.
[30] Meyers BL, Winter G. Relationship between time-dependent deformation and microcracking of plain concrete. J Proc. 1969 Jan 1;66(1):60-8. https://doi.org/10.14359/7342
[31] Thomas TC. Mathematical analysis of shrinkage stresses in a model of hardened concrete. J Proc. 1963 Mar 1;60(3):371-90. https://doi.org/10.14359/7860

Blank Page

Research on Engineering Structures & Materials
www.jresm.org

Research Article

Strengthening of corroded reinforced concrete beam via optimized fiber reinforced self-compacting concrete jacket

Nada A. Mahmoud [*,a], Mahmoud Khashaa Mohammed [b], Yousif A. Mansoor [c]

Civil Engineering Department, University of Anbar, Ramadi, Iraq

Article Info

Article History:

Received 24 Oct 2025

Accepted 19 Dec 2025

Keywords:

Micro steel fibers;
Self-compacting Concrete;
Optimization;
Strength;
Strengthening

Abstract

In this paper, an experimental study is presented on a wide variety of fresh and hardened characteristics of an optimized steel fiber-reinforced self-compacting concrete (SFRSCC) mix. This is in order to examine the possibility of using this type of concrete to strengthen a corroded RC concrete beam with dimensions of 150×200×1200 mm. Micro steel fibers MSF were utilized at percentages of 0, 0.25, 0.5, 0.75, and 1% by volume. Using multi-objective optimization approach SFRSCC mix is optimized based on multi responses (tested properties). The theoretical optimization and its verification based on testing different fresh properties (slump flow, T500, L-box and segregation resistance), mechanical properties (compressive, flexural, splitting tensile strength, and modulus of elasticity), in addition to related durability properties (porosity and water absorption). In this investigation, the results of the experiments indicated that steel fibers enhanced the compressive, flexural, tensile strength, and elastic modulus as well as sieve segregation test by 22.9, 77.9, 112.8, 18.3, and 55.6% respectively which was achieved using 1% percentage of steel fiber. However, the rest of the properties are negatively affected due to the rise in fiber content. Thus, it was decided to implement a multi objective optimization process to get the optimum content. The optimum SCC mixture that satisfies all requirements was found using statistical software (Minitab 2018). The theoretical chosen optimal ratio of 0.47% of fibers that was obtained through optimization and it was evaluated and empirically verified. The optimal ratio was used in SCC mix for strengthening purposes with 30 mm jacket thickness for corroded RC beam. Strengthen corroded RC beam showed a considerable increase in its bending capacity, around 20%, contrasted to the corroded beam. The utilization of this method of strengthening also increased the ultimate load at first crack and the stiffness. Thus, it can be deduced that the method used is an effective method of strengthening.

© 2026 MIM Research Group. All rights reserved.

1. Introduction

Self-compacting concrete SCC is a very flowing and non-segregating concrete composition. There is no need for vibration to condense which results in less noise and significant labor effort savings as well as lower cost which improves the economics of concrete production [1]. Similar to normal vibrated concrete (NVC), SCC mixes include aggregate, cement, water, admixtures, and specific mineral additions or fillers. To improve its flowing characteristics, SCC has a higher dosage of superplasticizers and fillers (such as fly ash, silica fume, limestone powder, etc.) than NVC [2]. In SCC, there is a high possibility to use replacement materials instead of cement to maintain the same compressive strength while reducing the amount of cement. Thus, it may be classified as a sustainable material [3, 4]. Self-compacting concrete requires more paste than conventional concrete for high flowability, requiring 500-600 kg/m^3 of powder material. Portland cement, used in SCC mixes, emits CO2 into the atmosphere, negatively impacting the environment. High cement

*Corresponding author: nad21e1006@uoanbar.edu.iq
[a]orcid.org/ 0009-0005-6412-869X; [b]orcid.org/ 0000-0003-4817-8396; [c]orcid.org/0000-0002-5235-7904
DOI: http://dx.doi.org/10.17515/resm2026-1294ic1024rs

content also produces hydration heat, leading to concrete cracking during the hydration process. Therefore, SCC mixes require more powder material for self-compacting capability [5].

Fly ash is a byproduct of pulverized coal burning, which can be used in producing high strength self-compacting concrete (SCC) due to its pozzolanic properties. This well-grained dust, primarily composed of Al_2O_3 and SiO_2, can improve particle size distribution, increase concrete strength, and create a compacted microstructure. It also facilitates easier displacement of aggregate grains, making it a crucial component of self-compacting concrete mixtures. Therefore, fly ash's potential in SCC production is significant [6]. Guo et al. [7] found that silica fume (SF) addition improves SCC performance and is a popular replacement for concrete produced by silicon and ferrosilicon industries. SF increases concrete's toughness, compressive, tensile, and flexural strengths and influences elastic modulus. It also makes concrete resistant to chemical attacks, making it suitable for marine constructions, highway bridges, and parking decks. Steel fibers are added to SCC to improve mechanical properties, including post-cracking load bearing and energy absorption performance. They reduce crack size, enhancing concrete strength. However, increased crack width increases concrete permeability, promoting steel reinforcement corrosion. Fiber reinforcing techniques enhance concrete's ductility and post-cracking resistance [8].

Fibers significantly influence the workability of freshly poured concrete, with the type, amount, and matrix affecting the material's workability. A good fiber distribution is crucial for optimal benefits. The better performance of hardened concrete must be balanced with the appropriate workability of fresh concrete. The number of fibers added depends on the fiber type and mixture composition [9]. Abid [10] investigated the behavior of Micro-steel fiber-reinforced SCCs to flexural impact. Eight mixtures with two design grades of 30 and 50 MPa have been produced in order to differentiate between regular and high-strength SCCs. The fiber content, which came in four volumetric values of 0, 0.5, 0.75, and 1.0%, served as the differentiating factor for each design grade. The study discovered that adding micro-steel fibers significantly improved impact resistance and ductility, with higher percentage improvements in the failure stage contrasted to the cracking stage. The largest gains for combinations of 30 MPa were 543% and 836%.

The most common deteriorating process for structural elements made of reinforced concrete is corrosion of the steel reinforcement. Steel tends to return to its initial state (ore) by an electrochemical process that produces iron oxides on the coating (rust) [11]. Fayaad [12] showed that the ultimate load has been severely affected by the percentage of corrosion mass loss. In comparison to a reference concrete beam that was not corroded, the failure load decreased by about 14 and 27 percent, for each, as the percentage of corrosion mass loss increased by 8.25 and 14.15%. A common area of concrete researches' nowadays is strengthening preexisting RC beams which can effectively increase their service lives. Abdul Hameed [13] investigated damaged concrete beam repair using fiber-reinforced self-compacting concrete (FR-SCC). According to the study, better FR-SCC mixtures are effective at increasing the cracking stress on repaired beams, which can prolong their life. The study also considered using polypropylene fiber PPF in SCC. However, this study considered the use of polypropylene fiber PPF in SCC and it took only the fresh properties to optimize their volume fraction before used it for strengthening purpose.

However, few research work has been found in the literature addressing the use of optimized SCC for strengthening of corroded reinforced concrete beams. Therefore, the current study looks into how to reinforce a corroded RC beam using an optimal steel fibers SCC mix. A multi-objective optimization approach was used, considering different volume fractions of steel fibers in SCC and their responses in both fresh and hardened properties. The tested properties included flowability, T500, pasting ability, and segregation resistance, while the hardened properties included compressive strength, splitting tensile strength, flexural strength, modulus of elasticity, porosity, and absorption. The theoretical optimized volume fraction was experimentally verified and thereafter, it was used in a SCC mix for strengthening corroded RC beam to check its flexural behavior compared to a control beam without corrosion.

2. Experimental Program

Ordinary concrete with a 33 MPa compressive strength at 28 days was used to cast the three concrete beams, which were intended to fail in flexural stresses according to the ACI 318-19 [14]. An accelerated corrosion process using Faraday's law was used to get 10% mass loss of tension reinforcement as shown in Fig. 1. After corrosion, the beam was strengthened by applying a U-jacket 30 mm thick layer of the optimized steel fibers reinforced SCC SFRSCC over the sandblasted epoxy coated faces of the RC beam as shown in Fig. 2. The bond between the jacket and the surface of corroded beam was determined using push-out test [15] as shown in Fig. 3. The result of this test indicated that the bond strength was 3.6 MPa. The details of beams including preparation and testing were mentioned in previous research [16]. After the beams were tested, the distractive method was used to calculate the mass losses of corroded longitudinal rebars. In accordance with ASTM G1-3. The bars were chemically cleaned in a solution containing a high concentration of HCl acid to remove rust and related concrete mortar. The following formula was used to calculate mass loss:

$$Mass\ loss = \frac{Mass\ Before\ Corrosion - \ Mass\ After\ Corrosion}{Mass\ Before\ Corrosion} * 100\% \quad (1)$$

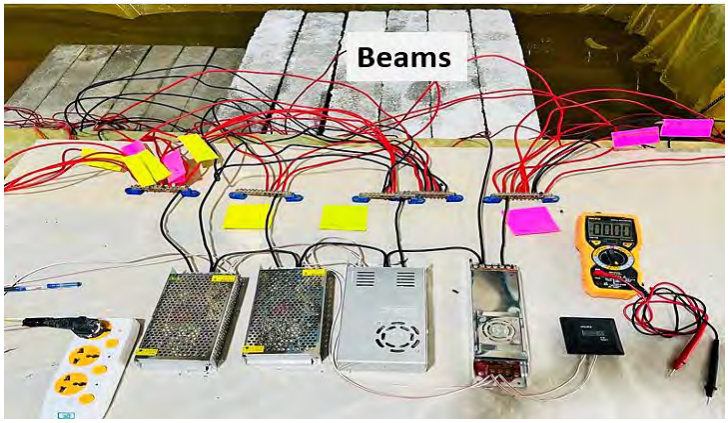

Fig. 1. Corrosion system

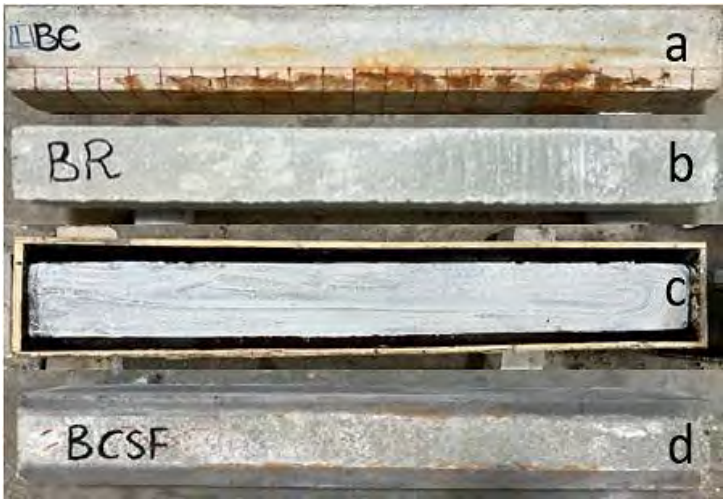

Fig. 2. (a) Side view of corroded beam(b)Top view of reference beam (c) Epoxy coating beam before casting (d) Top view of strengthened beam with FRSCC

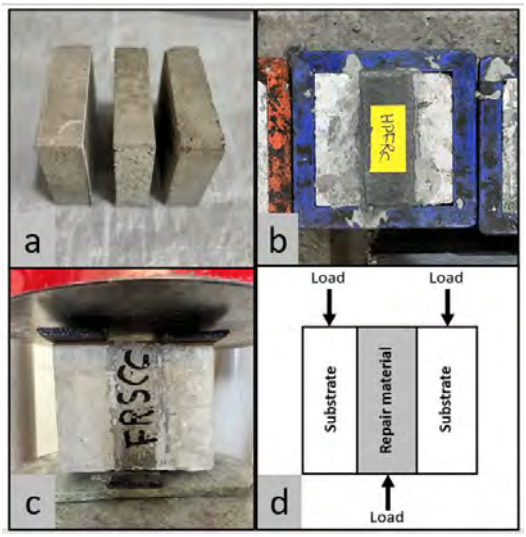

Fig. 3. (a) Cutting of 5 cm-thick concrete blocks (b) casting 5cm-thick of repair concrete (c) test setup (d) test setup diagram

2.1. Materials and Testing Program

2.1.1 Cement C.

Both normal and SCC were produced using Type I ordinary Portland cement. Its beginning and final setting time are 140 and 210 minutes, respectively, and its specific gravity is 3.15. The features of this cement were precisely in accordance with Iraqi requirements and Portland Cement Standard IQS NO. 5, 2019 [17].

2.1.2 Coarse Aggregate C.A.

The maximum size of coarse aggregate used to prepare mixes is 12 mm; it is natural crashed aggregate and it has a specific gravity of 2.65. The test findings of this type of aggregate indicated that it met Iraqi specifications IQS NO. 45, 1984 [18].

2.1.3 Fine Aggregate F.A.

Natural sand was used in this investigation. It is spherical, with a maximum size of 4.75 mm, a specific gravity of 2.62, and a bulk density of 2600 kg/m^3. This type was also identical to the same above Iraqi standard.

2.1.4 Fly Ash FA.

FA with a 2.08 specific gravity and Blaine fineness of 380 m^2/kg was used. It mainly consists of 28% alumina and 47.7% silica. According to ASTM C 618, 2015 [19], this type of mineral filler could be defined as class F.

2.1.5 Silica fume SF.

SF-Type Mega Add MS(D) was used. The silica fume used in this study had a specific gravity of 2.2. According to ASTM C1240, it satisfies the standards for silica fume [20]. Table 1 shows the chemical compositions of C, FA and SF.

Table 1. Chemical compositions of C, FA and SF.

Main oxides %	SiO_2	Al_2O_3	CaO	Fe_2O_3	L.O.I
C	20.06	4.80	62.95	3.35	2.30
FY	47.68	27.73	5.11	18.32	3.71
SF	94.2	0.3	0.27	0.82	3.36

2.1.6 Superplasticizer SP.

Polycarboxylate polymer technology was used having a pH of 4 to 6 and a density of 1.07 kg/liter, that is a high range water reducing super plasticizing admixture. It complies with ASTM C-494 Types G standards [21].

2.1.7 Micro Steel Fibers (MSF).

The steel fibers that were utilized were straight, measuring 15 mm in length and 0.2 mm in diameter. With a minimal tensile strength of 2600 MPa, they were free of corrosion and contaminants.

2.1.8 Epoxy Resin (Sikadure-32 LP)

This resin used as a bonding agent between a concrete jacket for strengthening and corroded RC members. It is applied to the required surface with a thickness of less than 1 mm and has an adhesion strength more than 3 N/mm^2

2.2. Process of Mixing/Casting and Mixing Proportions

The process of preparing fresh SCC mixes involves mixing coarse and fine aggregates in a rotary drum mixer for one minute, followed by pre-mixing cement with CRMs (FA and SF) for two minutes. A small amount of water was added to prevent volatilization. The mixture is then wet mixed for two minutes, then steel fibers were added. SCC mixtures in different fiber ratios are shown in Table 2. After that slump-flow, T500, L-box, and sieve segregation resistance tests were then directly performed. Before casting, each casting mold was thoroughly cleaned and coated with the proper liquid. Following the completion of the concrete mixing procedure, the samples were gradually poured into the prepared molds. On the second day, the samples had been extracted out of the molds, 24 hours later, and put into a tank for water treatment for 28 days before being removed until the test's age [12].

Table 2. Mix proportions in (kg/m^3)

w/c	C	C.A	F. A	W	FA	SF	SP	Steel fiber %
0.4	410	764	970	165	45	45	12.5	*

** Steel fiber %= 0, 0.25, 0.5, 0.75, 1*

2.3. Testing Program

Fresh concrete tests of mixes with different proportions are carried out immediately after mixing. All fresh SCC properties were performed in accordance to EFNARC recommendations (EFNARC, 2005) [22]. According to ASTM C39/C39M [23], the BESMAK-Digital testing compression machine, which has a maximum capacity of 2000 kN, was used. This is for determining the average compressive strength of three-cylinder specimens that measured 100 x 200 mm. In line with ASTM C496/C496M [24] the splitting strength of three 100 x 200 mm cylinders was assessed in the same compressive strength machine at a loading rate of 0.94 kN/s. To find the modulus of rupture, three prisms of 100×100×400 mm were tested using ASTM C78 standard [25].

Fig. 4. Fresh (a, b and c) and Mechanical tests (d, e, f, g and h)

The modulus of rupture or flexural strength was measured using a 200 kN hydraulic fracture machine with a 5.3 kN/s rate of loading. Additionally, the elastic modulus was measured in a compressive test machine using an ASTM C469 [26] based cylinder with dimensions of (150×300) mm at a rate of loading of 5.3 kN/s. Due to their major impact on the durability and strength of concrete, experiments on related durability characteristics were also conducted. Following a 28-day cure time, the average of three 100 mm cubic samples were tested for porosity and water absorption tests in accordance with ASTM C642 [27]. The entire performed tests on SCC are shown in Fig. 4.

3. Testing Program

It should be highlighted here that the fresh and mechanical properties of SFRSCC are extensively studied in the literature and the main goal of the current study is not focused in this aspect. The main idea is how to use the results of these tests as multi responses to determine the optimum Vf of steel fibers in SCC. This can give the maximum performance for this type of concrete in an optimized SFRSCC to be used for strengthening purposes. However, quick presentation of the results obtained from tested properties is shown the following section.

3.1. Fresh Properties

Table 3 displays the results of fresh properties tests for each mix of SFRSCC. In general, it is evident that the incorporating of MSF has a negative impact on rheological characteristics but a positive impact on the sieve segregation test. However, all the results still meet with the SCC fresh requirements according to European guidelines EFNARC [22].

Table 3. Fresh properties of SFRSCC mixes.

Mix ID	Vf %	Slump Flow Test (mm)	T500 Test(sec)	L-BOX Test	% Sieve Segregation Test
0M	0	800	2.0	0.95	7.80
0.25M	0.25	800	2.5	0.91	5.00
0.5M	0.5	745	3.0	0.89	4.56
075M	0.75	720	3.5	0.88	3.82
1M	1	710	3.8	0.81	3.46
–	EFNARC limits	650-800	2-5	0.8-1	≤15

The slump flow data shown in Table 3 showed a clear reduction in slump flow values by about 6.8, 10, and 11.25% for the last three mixtures as compared to the reference one (without fibers). Additionally, it was exposed that the T500 values (time to reach a flow of 500 mm) significantly increased by 25, 50, 75, and 90% as compared to reference mix due to the addition of 0.25, 0.5, 0.75, and 1% of steel fibers respectively. This indicates that SCC's viscosity had increased. Increasing the internal friction between MSF and coarse aggregates might explain this phenomenon [22]. In term

of h2/h1 values obtained from L-Box test. The listed results in Table 3 showed that the blocking ratio (h2/h1) for SCC reinforced with MSF reduced by about 4.2, 6.3, 7.3, and 14.7%, respectively as compared to reference mix. This showing clearly how the blocking ratio decreases steadily as MSF increases. The obvious reason for this reduction is that MSF, particularly the large proportion utilized of MSF, prevents the passage of coarse aggregates through steel bars in L-Box test [28, 29].

The segregation indices SI listed in Table 3 displays the effects of adding MSF on SI as a consequence. It can be clearly seen that the incorporating of MSF greatly increases the segregation resistance of SCC mixtures; SI values decreased by about 35.8, 41.5, 51, and 55.6% respectively. This increase is justified by the fact that MSF forms an internal network that might prevent the matrix movement during the sieve segregation test and hence, greatly enhance SCC segregation resistance.

3.2. Mechanical Properties

Fig. 5 (a) illustrates the obtained compressive strength results of SFRSCC mixes. Compared to the reference mix, the values of compressive strength are improved by 13.6, 18.9, 20.9, and 22.9% respectively as the fiber's contents were increased. These findings are in line with the previous research [30]. Such improvement is justified by the function served by MSF in restricting the development of cracks as well as by the strong connection between MSF and the SCC matrix [31]. Moreover, it is shown that the presence of MSF modified the loading failure mode. It is noted that the plain SCC show a complete collapse in its failure mode. However, the specimens reinforced by MSF display a more ductile failure mode with the increase of MSF content. The restriction of MSF of concrete pieces, which helps to prevent rapid failure, is responsible for this change as shown in Fig. 5 (b). For example, reference mix (0M) exhibited explosive failure mode. In contrast, 1M mix which contained the highest fiber volume fraction showed completely bridging failure mode.

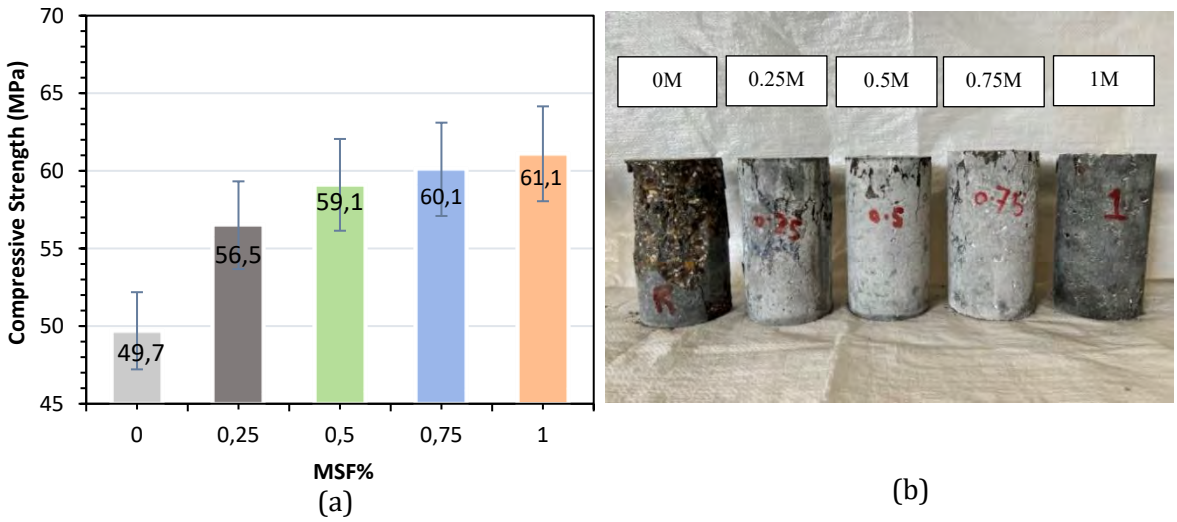

Fig. 5. Compressive strength results (a) values for various amounts of steel fibers at 28 days (b) failure mode after compressive strength test

In Fig. 6 (a) the results of the flexural and splitting strengths are displayed. It has been shown that SCC mixtures were greatly enhanced in term of their flexural strength values. The flexural strength values increased by 47.05, 51.4, 55.8, and 77.9% due to the incorporation of 0.25, 0.5, 0.75, and 1% respectively. The splitting tensile strength also significantly enhanced when the MSF volume fraction increased. These increments were: 51.2, 56.4, 64.1, and 112.8% respectively as compared to reference SCC. As illustrated in Fig. 6 (b), MSF resists the rapid failure of plain SCC specimens by bridging fractures sides under tensile stress. According to Fig. 6, the four-volume fractions of MSF resulted in a rise in the modulus of elasticity of 5.7, 8.7, 13.6, and 18.3%, respectively, in comparison to the reference mix as shown in Fig.7. The observed increases in compressive and tensile strengths may be related to this trend. For instance, 0M mix showed very brittle failure mode in flexural and splitting tensile strengths, while 1M mix exhibited ductile failure mode in these two tests.

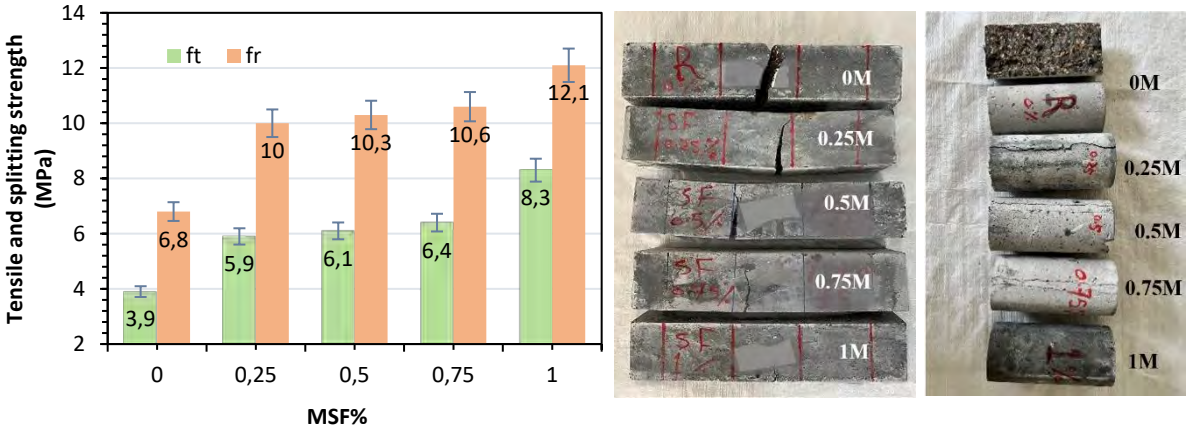

(a) (b)

Fig. 6. Flexural and splitting strength results (a) various amounts of steel fibers values at 28 days (b) failure mode after flexural and splitting strength test

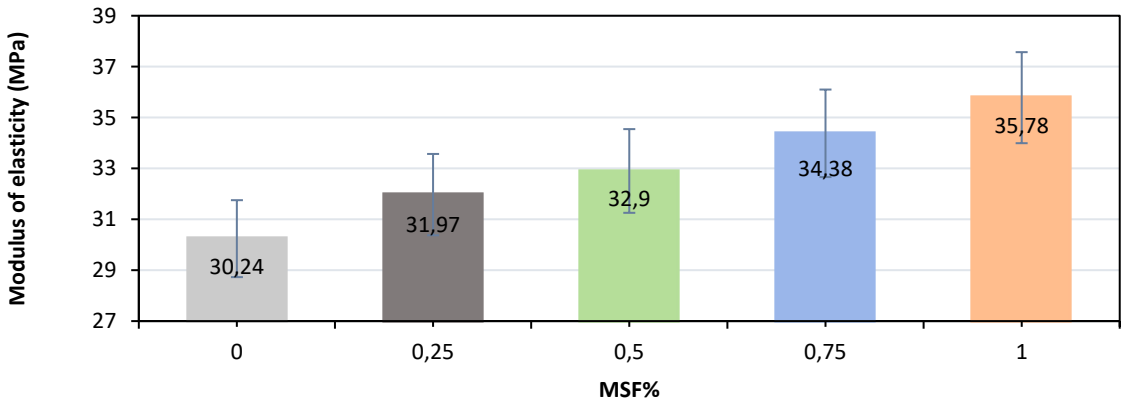

Fig. 7. Modulus of elasticity values for various amounts of steel fibers at 28 days

3.3. Related Durability Properties

According to the study, the values of porosity and water absorption of concrete rise with the amount of steel fiber contained as shown in Fig. 8. This could be due to the creation of voids within the concrete sample, which could be caused by the interruption of water flow beneath the fibers. The number of fibers in the SCC mix has negative impact on both water absorption and porosity results as claimed by Suleman et al. [32].

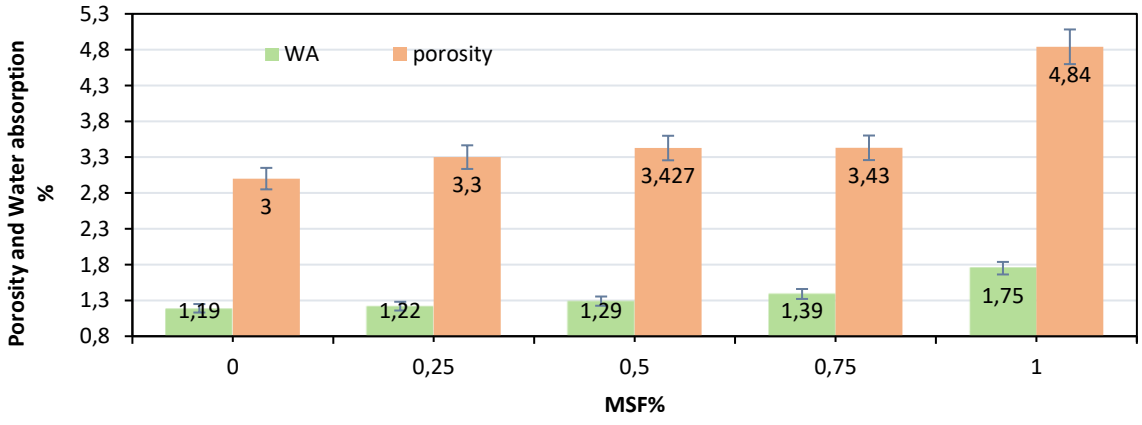

Fig. 8. Relationships between porosity, water absorption, and MSF for SCC mixtures

3.4. Optimization of the Properties of SCC Mixes

Table 4 summarizes the results from the previous section for multi-objective optimization. No fiber content can provide the best properties of fresh and mechanical simultaneously. Therefore, an optimal fiber content between tested ratios is needed for an excellent SCC mix.

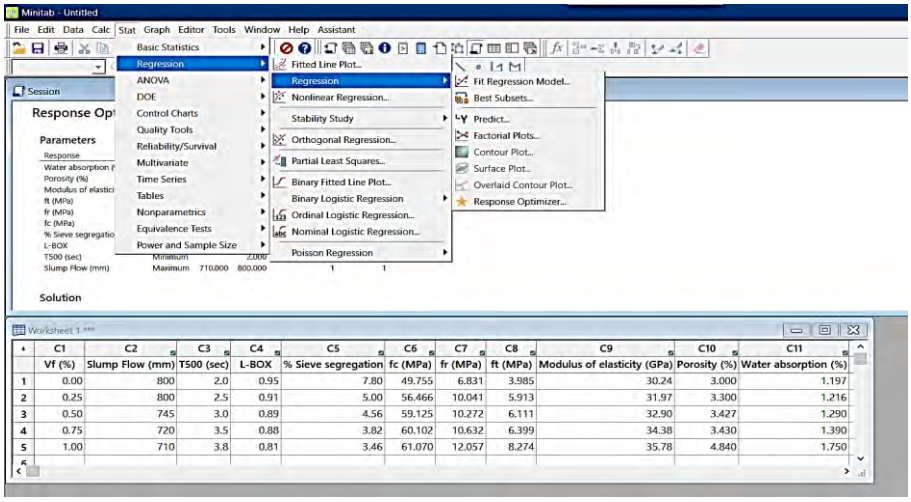

(a)

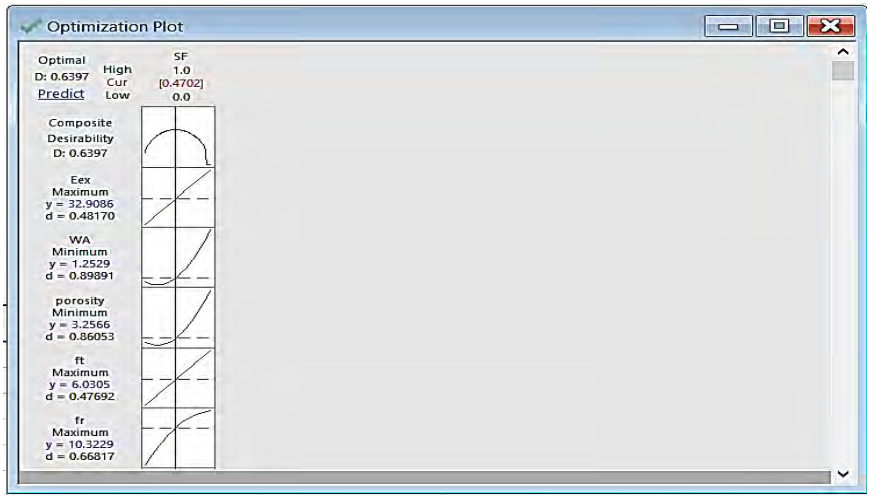

(b)

Response Optimization: Water absorption (%), Porosity ... Flow (mm)

Parameters

Response	Goal	Lower	Target	Upper	Weight	Importance
Water absorption (%)	Minimum		1.197	1.75	1	1
Porosity (%)	Minimum		3.000	4.84	1	1
Modulus of elasticity (GPa)	Maximum	30.240	35.780		1	1
ft (MPa)	Maximum	3.985	8.274		1	1
fr (MPa)	Maximum	6.831	12.057		1	1
fc (MPa)	Maximum	49.755	61.070		1	1
% Sieve segregation	Minimum		3.460	7.80	1	1
L-BOX	Maximum	0.810	0.950		1	1
T500 (sec)	Minimum		2.000	3.80	1	1
Slump Flow (mm)	Maximum	710.000	800.000		1	1

(c)

Fig. 9. Optimization using Minitab: a) optimization steps b) optimization plot c) goal and targets of optimization

This mixture should have the highest flow, compressive, flexural, tensile, and elastic modulus, with the least amount of porosity and water absorption. The results were analyzed using the Minitab 2018 statistical program Fig.9 to find the optimum ratio, which was determined to be 0.47%, providing the most desirable characteristics.

Table 4. Summary of responses used for optimization

Mix ID	Slump Flow (mm)	T500 (sec)	L-BOX	% Sieve segregation	fc (MPa)	fr (MPa)	ft (MPa)	Modulus of elasticity (GPa)	Porosity (%)	Water absorption (%)
0M	800	2.0	0.95	7.80	49.755	6.831	3.985	30.24	3	1.197
0.25M	800	2.5	0.91	5.00	56.466	10.041	5.913	31.97	3.3	1.216
0.5M	745	3.0	0.89	4.56	59.125	10.272	6.111	32.9	3.427	1.29
0.75M	720	3.5	0.88	3.82	60.102	10.632	6.399	34.38	3.43	1.39
1M	710	3.8	0.81	3.46	61.07	12.057	8.274	35.78	4.84	1.75

3.5. Validation of Theoretical Optimization

The optimal mix was produced and tested in order to validate the prior theoretical multi-objective optimization in order to check the accuracy of this optimization. In a controlled environment, the optimal mixture was produced using a similar ingredient and amounts of the materials that were predicted theoretically. Eq (2) is used to calculate the absolute relative deviation ARD% as a predictability indicator [33]. Theoretical and experimental obtained results as well as ARD% are listed in Table 5.

$$ARD\% = 1 - \frac{[Experimental - Model\ or\ Model - Experimental]}{Experimental} * 100\% \quad (2)$$

Table 5. Results and experimental validation of optimum mix

Type	Slump Flow (mm)	T50 0 (sec)	L-BOX	% Sieve Segregation	Fc (MPa)	Fr (MPa)	Ft (MPa)	Ec (GPa)	Porosit y %	Water Absorptio n %
Exp.	750	2.0	0.9	4.2	57.23	10.3	7.48	32.7	3.36	1.27
Theoretical	756.68	2.96	0.898	4.39	58.85	10.32	6.03	32.9	3.25	1.25
ARD %	99.10	52	99.77	95.47	97.16	99.80	80.61	99.38	96.72	98.42

The theoretical predicted results were very closed to the experimental ones indicating a very high accuracy of the proposed models. The only exception is the ARD of T500 which was only 52%. The reason might be related to the short time of this test (below 5 sec) and small change of these seconds will affect the result considerably. These results are on line with number of previous studies as in Mahmoud et al. and Fayad et al [34, 35].

3.6. Flexural Test Results

The experimental test results are summarized in Table 6 and include the following: the largest crack measured for the greater fracture on the face of the beam at failure, load at first flexural crack (Pcr), ultimate load (Pu), deflection at first crack (Δcr), and deflection at ultimate load (Δu). Furthermore, the flexural stiffness (k) was determined by calculating the slope (ΔF/Δδ) of the linear component of the load-deflection curves between 10% and 50% of the maximum load [36]. It is clear from the Table 6 that the bearing capacity of corroded beam was less than uncorroded beam by about 9.42% as for deflection and stiffness. This reduction is a result of a decrease of the cross-sectional area during the accelerating corrosion process. The corroded RC beam strengthens by optimized fiber reinforced self-compacting concrete jacket increased the efficiency of bearing capacity by 19.84%. After the reinforcing steel is yielded, the strengthening layer begins to bear until failure, and this is consistent with the results obtained by Huang et al. [37]. The observed

increase in deflection and crack width in the strengthened beam aligns with the expected structural response following the application of a 30-mm SFRSCC jacket.

Table 6. Flexural test results

Beam ID	(Pu) (kN)	(Pcr) (kN)	Change percent in Pu with respect to BR	(Δu) (mm)	(Δcr) (mm)	Max. crack width at failure (mm)	Stiffness (kN/mm)
Ref. RC Beam (BR)	100	25	-	17.65	0.56	3.5	35.66
Ref. Corroded RC Beam	90.58	25	-9.42	16.17	0.57	6.7	32.35
Strengthen Corroded RC Beam	108.56	40	+8.56	19.7	0.64	20	44.31

The added layer alters the stiffness distribution along the beam depth, causing a downward shift of the Neutral Axis (NA) and consequently increasing the tensile strain demand in the extreme tension fiber. Under comparable loading, this results in larger tensile strains at the bottom surface, naturally leading to wider flexural cracks. Importantly, the absence of delamination indicates that the shear stresses were effectively transferred across the old–new concrete interface. The roughened substrate surface provided mechanical interlock, while the SFRSCC jacket ensured high bond strength and fiber-induced confinement, preventing localized interface cracking. As a result, the jacket–substrate interface behaved monolithically, ruling out debonding failure. Instead, the shear forces were transmitted into the strengthened section, producing two opposite diagonal cracks at approximately 45° within the middle third of the beam. The lack of vertical mid-span cracks excludes flexural failure, and the observed diagonal tension cracks propagating toward the compression zone confirm that the beam reached its shear capacity, consistent with internal shear failure in strengthened RC members as shown in Fig. 9. Based on this result, it can be concluded that the used method for strengthening was effective. It should be highlighted that the corresponding service crack (the crack at approximately 70% of ultimate load [38]) is equal to only 0.4 mm. Due time limitation, the long-term behavior of the strengthen system was not considered and it needs further future research work.

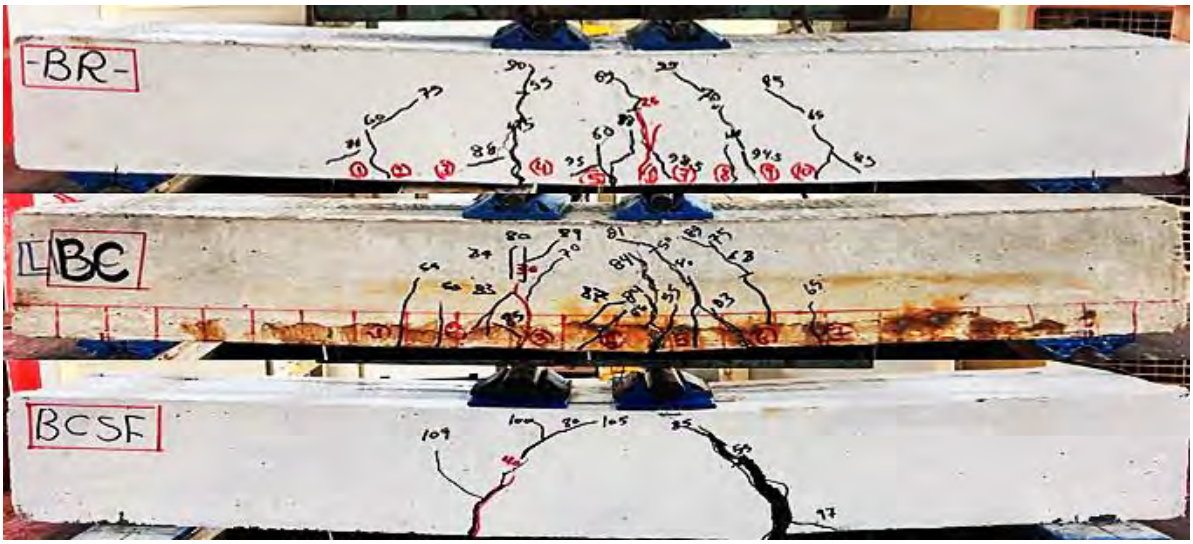

Fig. 9. Failure modes

4. Conclusion

The most significant findings from this investigation can be summed up as follows:

- Increasing fiber content has a negative impact on SFRSCC fresh characteristics, with the exception of the sieve segregation test.
- Compressive strength and elastic modulus of SFRSCC mixes slightly increased as steel fiber content increased; however, significant improvement be recorded in tensile test results at the same volume fractions of steel fibers.
- The obtained results suggested that increase of micro steel fiber content raised the flexural strength significantly and changed the failure mode to be more ductile.
- The porosity and water absorption values considerably increased with the proportion of steel fiber content in particular, at 1% Vf. Porosity and absorption were greater by 61.3% and 46.2%, respectively for this mix as compared to control one.
- Based on the multi objective optimization results, the optimum theoretical steel fiber content for SCC was 0.47%, which provided good mechanical strength and durability features. These data were produced using statistical software and optimization (Minitab 2018).
- Based on the tests for the theoretical optimized mixture, the theoretical value of Vf (0.47%) was verified experimentally to give the same expected performance
- The experimental results of mass loss were exactly similar to those of theoretical calculation using Faraday's law with 10%.
- The bearing capacity of corroded beam was less than uncorroded beam by about 9.42%.
- The bearing capacity of corroded RC beam strengthens by fiber reinforced self-compacting concrete jacket increased by 19.84% compared to corroded one.
- The first crack appeared in the strengthened beam only after the load reached 40 MPa, unlike the non-corroded and corroded reference beams where the first crack appeared at a load of 25 MPa.
- The strengthened beam exhibited a shear-controlled failure mode.
- Corroded reinforced concrete beams can probably be strengthened using U-jacket of optimized FRSCC mix which can be considered as an efficient strengthening technique.
- Investigating the efficiency of using fiber reinforced high strength lightweight concrete for strengthening corroded beams need to be studied.

References

[1] EFNARC. Guidelines for self-compacting concrete. English ed. European Federation for Specialist Construction Chemicals & Concrete Systems; 2005.
[2] Iqbal S, Ali A, Holschemacher K, Bier TA. Effect of change in micro steel fiber content on properties of High strength Steel fiber reinforced Lightweight Self-Compacting Concrete (HSLSCC). Procedia Eng. 2015;122:88-94. https://doi.org/10.1016/j.proeng.2015.10.011
[3] Puskas A, Moga L. Sustainability of reinforced concrete frame structures-A case study. Int J Sustain Dev Plan. 2015;10(2):165-176. https://doi.org/10.2495/SDP-V10-N2-165-176
[4] Saba AM, Khan Az, Niazi MSK, Farooq F, Javed MF, Aslam F, et al. Strength and flexural behavior of steel fiber and silica fume incorporated self-compacting concrete. J Mater Res Technol. 2021;12:1380-1390. https://doi.org/10.1016/j.jmrt.2021.03.066
[5] Zhao Y, Bi J, Guan J, Mao R, Huo L, Zhang S, et al. Synergetic effect of ground granulated blast-furnace slag and hooked-end steel fibers on various properties of steel fiber reinforced self-compacting concrete. Struct Concr. 2022;23(1):268-284. https://doi.org/10.1002/suco.202000722
[6] Farooq F, Jin X, Javed MF, Akbar A, Shah MI, Aslam F, et al. A comparative study for the prediction of the compressive strength of self-compacting concrete modified with fly ash. Materials. 2021;14(17):4934. https://doi.org/10.3390/ma14174934
[7] Alaloul WS, Musarat MA, Liew MS, Law K, Sharafuddin MA, Alawag AM, et al. Mechanical properties of silica fume modified high-volume fly ash rubberized self-compacting concrete. Sustainability. 2021;13(10):5571. https://doi.org/10.3390/su13105571
[8] Frazão C, Camões A, Barros J, Gonçalves D. Durability of steel fiber reinforced self-compacting concrete. Constr Build Mater. 2015;80:155-166. https://doi.org/10.1016/j.conbuildmat.2015.01.061

[9] El-Dieb A, Taha MR. Flow characteristics and acceptance criteria of fiber-reinforced self-compacted concrete (FR-SCC). Constr Build Mater. 2012;27(1):585-596. https://doi.org/10.1016/j.conbuildmat.2011.07.004
[10] Abid SR, Abdul-Hussein ML, Ali SH, Kazem AF, Al-Gasham TS. Impact performance of steel fiber-reinforced self-compacting concrete against repeated drop weight impact. Crystals. 2021;11(2):91. https://doi.org/10.3390/cryst11020091
[11] Koulouris K, Apostolopoulos C. An experimental study on effects of corrosion and stirrups spacing on bond behavior of reinforced concrete. Metals. 2020;10(10):1327. https://doi.org/10.3390/met10101327
[12] Fayaad TS. Strengthening of Corroded Reinforced Concrete Beams by SCC Using Different Strengthening Configurations [Thesis]. Anbar: University of Anbar; 2022.
[13] Abdulhameed HA, Nassif H, Khayat KH. Use of fiber-reinforced self-consolidating concrete to enhance serviceability performance of damaged beams. Transp Res Rec. 2018;2672(27):45-55. https://doi.org/10.1177/0361198118787983
[14] ACI Committee 318. Building Code Requirements for Structural Concrete (ACI 318-19) and Commentary. Farmington Hills, MI: American Concrete Institute; 2019.
[15] Ghodousian O, Shetabivash H, Alipour R, Ozbakkaloglu T. Interfacial bond strength of coloured SCC repair layers: an experimental and optimisation study. J Struct Integr Maint. 2023:1-10.
[16] Mahmoud NA, Mansoor YA, Mohammed MK. Structural behaviors of different corroded RC members strengthened by different types of concrete jackets. Salud, Ciencia y Tecnología-Serie de Conferencias. 2024 (3), 831. https://doi.org/10.56294/sctconf2024831
[17] Iraqi Quality Standards (IQS). Iraqi specification for Portland Cement requirements. IQS 5; 2019.
[18] Iraqi Quality Standards (IQS). Aggregate from Natural Sources for Concrete and Construction. IQS 45. Baghdad: Central Agency for Standardization and Quality Control; 1984.
[19] ASTM International. ASTM C618-15: Standard Specification for Coal Fly Ash and Raw or Calcined Natural Pozzolan for Use in Concrete. West Conshohocken, PA; 2015.
[20] ASTM International. ASTM C1240-05: Standard specification for silica fume used in cementitious mixtures. West Conshohocken, PA; 2005.
[21] ASTM International. ASTM C494/C494M-17: Standard Specification for Chemical Admixtures for Concrete. West Conshohocken, PA; 2017.
[22] BIBM, et al. The European guidelines for self-compacting concrete. 2005;22:563.
[23] ASTM International. ASTM C39/C39M-20: Standard Test Method for Compressive Strength of cylindrical Concrete Specimens. West Conshohocken, PA; 2020.
[24] ASTM International. ASTM C496/C496M-11: Standard Test Method for Splitting Tensile Strength of Cylindrical Concrete Specimens. West Conshohocken, PA; 2011.
[25] ASTM International. ASTM C78/C78M-18: Standard Test Method for Flexural Strength of Concrete Using Simple Beam with Third-Point Loading. West Conshohocken, PA; 2018.
[26] ASTM International. ASTM C469/C469M-14: Standard Test method for static modulus of elasticity and poisson's ratio of concrete in compression. West Conshohocken, PA; 2014.
[27] Bu Y, Spragg R, Weiss W. Comparison of the pore volume in concrete as determined using ASTM C642 and vacuum saturation. Adv Civil Eng Mater. 2014;3(1):308-315. https://doi.org/10.1520/ACEM20130090
[28] Grünewald S, Walraven JC. Parameter-study on the influence of steel fibers and coarse aggregate content on the fresh properties of self-compacting concrete. Cem Concr Res. 2001;31(12):1793-1798. https://doi.org/10.1016/S0008-8846(01)00555-5
[29] Irki I, Debieb A, Settari C, Khatib JM, Kenai S. Effect of the length and the volume fraction of wavy steel fibers on the behavior of self-compacting concrete. J Adhes Sci Technol. 2017;31(7):735-748. https://doi.org/10.1080/01694243.2016.1231394
[30] Mastali M, Dalvand A. Use of silica fume and recycled steel fibers in self-compacting concrete (SCC). Constr Build Mater. 2016;125:196-209. https://doi.org/10.1016/j.conbuildmat.2016.08.046
[31] Bazgir A. The behaviour of steel fibre reinforced concrete material and its effect on impact resistance of slabs [MPhil Thesis]. London: City University London; 2016.
[32] Suleman D, Mohammed MK, Mansoor YA. Optimization of Different Properties of Ultra-High Performance Concrete Mixes for Strengthening Purposes. Iraqi J Civil Eng. 2022;15(2):72-85. https://doi.org/10.37650/ijce.2021.172875
[33] Hussien AS, Mohammed MK. Optimum characteristics of plastic fibres for sustainable self-compacting concrete SCC. Eur J Environ Civil Eng. 2022:1-18. https://doi.org/10.1080/19648189.2022.2119605
[34] Mohammed MK, Al-Hadithi AI, Mohammed MH. Production and optimization of eco-efficient self compacting concrete SCC with limestone and PET. Constr Build Mater. 2019;197:734-746. https://doi.org/10.1016/j.conbuildmat.2018.11.189

[35] Fayaad TS, Mohammed MK, Mansoor YA. Optimization of different types of self-compacting concrete mixes for strengthening purposes. AIP Conf Proc. 2024. https://doi.org/10.1063/5.0190534
[36] Najim KB. Determination and enhancement of mechanical and thermo-physical behaviour of crumb rubber-modified structural concrete [Thesis]. University of Nottingham; 2012.
[37] Huang Y, Li J, Hong S, Wu X, Huang J. Reinforced concrete beams retrofitted with UHPC or CFRP. Case Stud Constr Mater. 2022;17:e01507. https://doi.org/10.1016/j.cscm.2022.e01507
[38] Tayeh BA, Maraq MAA, Ziara MM. Flexural performance of reinforced concrete beams strengthened with self-compacting concrete jacketing and steel welded wire mesh. Structures. 2020;27:1477-1488. https://doi.org/10.1016/j.istruc.2020.10.035

Research on Engineering Structures & Materials
www.jresm.org

Research Article

Sustainable soil stabilization using coffee husk ash and limestone: An eco-friendly approach

Shaimaa M. Abdulrahman [*,a], Lamya M. J. Mahdi [b], Ghayda Yaseen Al Kindi [c], Qasim A. Al-Obaidi [d]

Civil Engineering College, University of Technology, Baghdad, Iraq

Article Info

Article History:

Received 25 Oct 2025

Accepted 07 Jan 2026

Keywords:

Soil stabilization;
Limestone;
Coffee husk ash;
Recycling;
Waste materials

Abstract

The geotechnical properties of soils vary depending on the regional and environmental diversity in which they are found. Therefore, remediation methods for troubled soils depend on the environmental conditions and material sources found in that area. However, the soil layer must have sufficient bearing capacity to be suitable to withstand the applied loads. The parameters of elasticity, cohesion, strength, and durability are part of soil optimization in this study. To do this, the soil is stabilized by treating it with a mixture of coffee husk ash and limestone powder in proportions of (3, 5, 7, and 10) % for three types of additives (coffee husk ash, limestone powder, and coffee husk ash mixed with limestone powder) and for periods of (1, 7, 14, and 28) days. The extent of improvement in geotechnical properties was determined using the unconfined compressive strength test and Atterberg limits. Two mathematical equations were predicted, one relating soil cohesion to plasticity index and the other relating plasticity index to unconfined compressive strength. The experimental results indicated that the soil cohesive strength improved from 30 to 52 kN/m^2, and it was also observed that the soil activity decreased from 0.9 to 0.25. At 28 curing days, the 7% of CHA+L mixture reduced PI from 30 to be 6.8 and increased UCS from 60 to be 94 kN/m^2. Nevertheless, predictive equalities were developed to re-count plasticity index with strength then cohesion, their applicability is limited to the type CH - soil and stabilizer contents within the range of 0–10%. The best improvement occurred at 7% coffee husk ash and limestone powder.

© 2026 MIM Research Group. All rights reserved.

1. Introduction

Since the construction is where construction begins, it is the most important part of a building. Many influences, including subsurface lateral pressure, horizontal development on the divider, air activity, unequal subsurface settling of the craftsmanship, subsurface horizontal settlement, and moisture buildup in the subsoil [1]. Structures that contact the ground in harsh or corrosive settings must be waterproofed. Subterranean constructions are protected from moisture and groundwater contamination by waterproofing the basic materials [2]. For waterproofing solutions to be effective, proper installation and regular maintenance are essential. Ignoring these elements might eventually lead to deterioration and compromise the structural integrity. Since most traditional materials are expensive and harmful to the environment, researchers are currently investigating the use of eco-friendly and cost-effective methods to remediate soil before construction [3–12]. The present studies examine the economic consequences of the risks associated with applying traditional methods to enhance the properties of base soil. Studies have

*Corresponding author: shaimaa.m.abdulrahman@uotechnology.edu.iq
[a] orcid.org/0000-0002-3535-8710; [b]orcid.org/0009-0001-4320-3460; [c] orcid.org/0000-0002-3574-1437; [d]orcid.org/0000-0002-3352-9010
DOI: http://dx.doi.org/10.17515/resm2026-1295ic1025rs

also begun to demonstrate other methods for enhancing the qualities of the underlying soil by employing recycled environmental waste. This is a wonderful alternative to the more costly traditional methods of improving the foundation soil. Particularly the inclination towards sustainability [13].

Exploration of pozzolanic materials has been a serious obstacle to the advancement of national development. Laterite soil is a common choice for long-term construction projects due to its widespread local accessibility, which contributes to its considerable significance as a reliable and long-lasting building material. [14–16]. Although recycling techniques are relatively new, they are gaining popularity in the Global South. These methods are more thorough, environmentally sustainable, and have a positive influence on both human well-being and the environment than older methods [17]. Many studies have looked into the use of industrial waste feasibility as an input material at various stages of the Portland cement production process [18]. Pozzolanic addition of materials to soil improve its chemical stability through increasing the soil particles size, declining plastic index, and dropping the soil's inclination to consolidate and expand. [19]. Adding pozzolanic materials, such as cement, is the traditional way to reinforce soil [20], although doing so comes with a higher cost [21].

After conversion, low-cost pozzolanic materials were utilized instead of more expensive ones, such as peanut shells. Compared to conventional Portland cement, which has a higher overall composition, this produced a lower CaO concentration [22,23]. Recent studies in a few nations have examined the pozzolanic qualities of coffee husk ash. Certain substitution percentages have been found to improve mortar, and concrete properties, such as water tightness, compressive strength, and fineness [24] and [25]. It was found that adding coffee husk ash to concrete significantly decreased slump and workability characteristics, also compressive strength decreased with higher coffee husk ash percentage, even though it improved through curative percentage up to a 10% coffee husk ash. Coffee husk ash plays a major role in strength development, although its effects on the physical and chemical properties of coffee husk ash and coffee husk ash-modified cement, and the flexural strength, durability, and concrete tensile, were not investigated in earlier studies. This study's primary goal is to describe, both chemically and physically, how coffee husk ash improves soil foundation instead of cement. The new method mixed limestone with coffee husk ash to improve the construction.

Previous studies have extensively investigated the use of agricultural and industrial wastes such as rice husk ash, groundnut shell ash, fly ash, and eggshell ash for soil stabilization. These studies primarily focused on single stabilizers and short-term strength improvement. However, limited attention has been given to the combined use of coffee husk ash and limestone as a hybrid stabilizing system. In addition, the time-dependent behavior of CHA–lime treated soils and the development of predictive regression-based relationships between plasticity index, unconfined compressive strength, and cohesion remain insufficiently explored. Therefore, the present study aims to address these gaps by investigating the combined effect of CHA and limestone on clay soil over different curing periods and by proposing empirical equations for strength prediction.

2. Methodology and Materials

2.1. Coffee Husk Ash (CHA)

The coffee husk from India. After being exposed to sunshine to eliminate surface moisture, the resulting sample was burned for three hours at 550°C to turn it into ash. To assess the physicochemical characteristics of the resultant Coffee Husk Ash. After cooling and being ground with a crushing tool, the crushed coffee husk ash was sieved in a 75 μm sieve [25].

2.2. Limestone Powder (L)

Locally procured limestone is crushed in a jaw crusher and then ground in a ball mill to create limestone powder. A No.200 sieve (75 μm) was used to sift all of the limestone powder.

2.3 Chemical Physiognomies

The chemical properties of the additives are displayed in Table 1, which shows the % quantitative analysis of composition silica oxide and other for coffee husk ash chemical compounds similar Fe2O3, SO3, K2O, and MnO.

Table 1. The chemical characteristics

Chemical Composition (%)	CHA	Lime
CaO	17.7	92
Fe_2O_3	2.8	0.9
Al_2O_3	0.6	0.89
SiO_2	15	3
MgO	4.51	4.2
K_2O +Na_2O	46.7	0.8

The CHA oxide composition and L is shown in Table 1, respectively. According to Table 1, that CHA has 2.8% Fe_2O_3, 0.6 Al_2O_3, and 15% SiO_2. This results in 18.4% SiO_2+Al_2O_3+Fe_2O_3. Because CHA contains SiO_2, Al_2O_3, Fe_2O_3, and CaO, it is therefore fundamental to use it as a cementing material rather than as a pozzolanic material [26]. When lime and coffee husk ash are combined, the mechanical properties of the soil can be enhanced. Silica along with the other pozzolanic components contained in coffee husk ash have the ability to counter with calcium hydroxide to formula new compounds such as aluminates and calcium silicates, which are beneficial for enhancing soil. The silica and alumina composition of coffee husk ash causes it to react with calcium hydroxide when mixed with lime to create cementitious materials that increase stability and strength. The mechanism of CHA-lime reaction in soil stabilization is dominantly pozzolanic reaction. Lime (CaO) reacts exothermically with water in moist soil and forms calcium hydroxide ($Ca(OH)_2$). Its derived $Ca(OH)_2$ result in initiating the SiO_2 and Al_2O_3 of CHA within them is activated by holding a basic environment. These reactive oxides then react with the calcium ions chemically forming C–S–H and C–A–H compounds which are primarily the responsible constituents for providing strength of treated soil due to lesser plasticity. This is a classic pozzolanic reaction. According to ASTM C618 [26], CHA qualifies as a pozzolanic material based on its oxide composition. However, some studies suggest that CHA may also exhibit partial self-cementing behavior due to its relatively high content of CaO and alkalis. For instance, [14] found that CHA can develop cementitious bonds even in the absence, thus, the stabilization mechanism in this study is primarily pozzolanic, with a possible minor contribution from self-cementing effects inherent to CHA.

2.4 Soil

The soil samples were brought up from Al-Hilla city, south of Iraq. The soil is classified as high plasticity clay soil (CH) according to ASTM 2487-17. Table 2 displays the results of the laboratory tests.

Table 2. Soil classification

Property	Value	Specification
Water content	8.9%	[27]
Gs	2.7	[28]
Sand	41.0%	
Clay	43.0%	
Silt	13.0%	
Gravel	3.00%	
Soil Classification	CH	
PL	35%	
LL	74%	[29]
PI	39%	
Activity	0.9	
Optimum moisture content	15%	

Property	Value	Specification
Dry density	1.65 gm/cm^3	[30]
Cohesion, c_u	30 kN/m^2	[31,32]
UCS	60 kN/m^2	

2.5 Sample Preparation

2.5.1 Atterberg Limits Tests Preparation

The Atterberg limits tests, soil samples were prepared in accord thru (ASTM D4318). The air-dried soil was first crushed and passed from a 425 μm sieve. The required mixture percentages (coffee husk ash, limestone powder, or their mixture) were dry-mixed carefully with the soil to confirm uniform the stabilizing agent's distribution. Water was then and there additional gradually while mixing up until the soil reached the target moisture content equal to15% the optimum moisture content (OMC), as determined from the Standard Proctor compaction test. The prepared soil paste was sealed and allowable to equilibrate to conducting the liquid limit and plastic limit tests.

2.5.2 Unconfined Compressive Strength (UCS) Tests Preparation

The unconfined compressive strength (UCS) tests, soil specimens were prepared for compaction following (ASTM D698) (Standard Proctor method) and for UCS (ASTM D2166) testing. Initially, the air-dried soil was pulverized and mixed in a dry state with the specified percentages of additives until a homogeneous mixture was achieved.

Water was then added incrementally to reach the mark 15% (OMC) moisture content. using standard Proctor compaction to find the moist soil mixtures were compacted energy to achieve approximately 95% of the maximum dry density (MDD) gotten from the Proctor test.

The compacted specimens were cylindrical in shape and were cautiously extruded from the molds immediately after compaction. To each specimen was sealed in plastic bags to prevent moisture loss and cured at room temperature (25 ± 2°C) for the designated curative times of (1, 7, 14, and 28) days previous to UCS testing.

2.6 Time-Dependent Testing Plan

In addition to studying the effect of additive percentages, the experiment also evaluated the strength development over time. For the 7% CHA+L mixture, unconfined compressive strength (UCS) tests were conducted at curing durations of 1, 7, 14, and 28 days to assess the time-dependent behavior of the treated soil. This time-based testing was intended to track the progressive improvement in strength due to pozzolanic reactions between the coffee husk ash and lime. For this mix, both Atterberg limits (LL, PL, PI, and A%) and also unconfined compressive strength (UCS) were slow at curative times of (1, 7, 14, and then 28) days, below identical preparation and curing conditions.

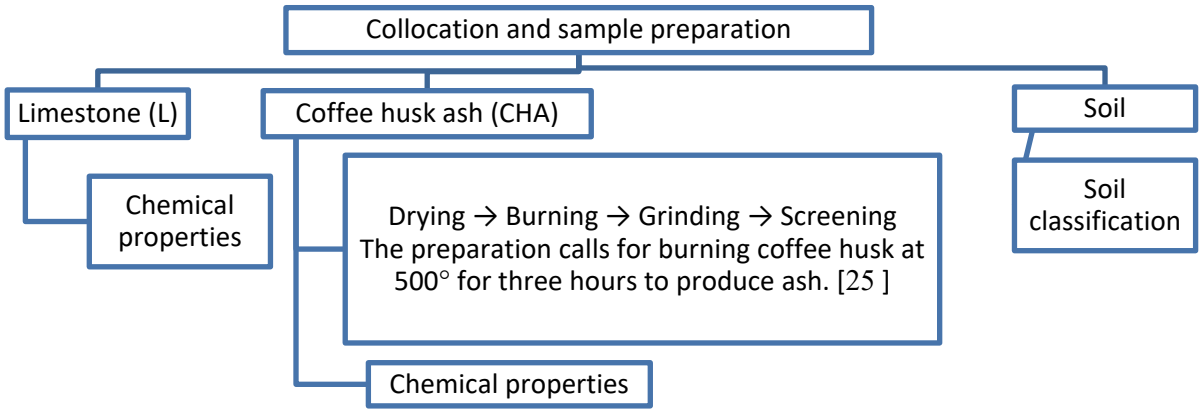

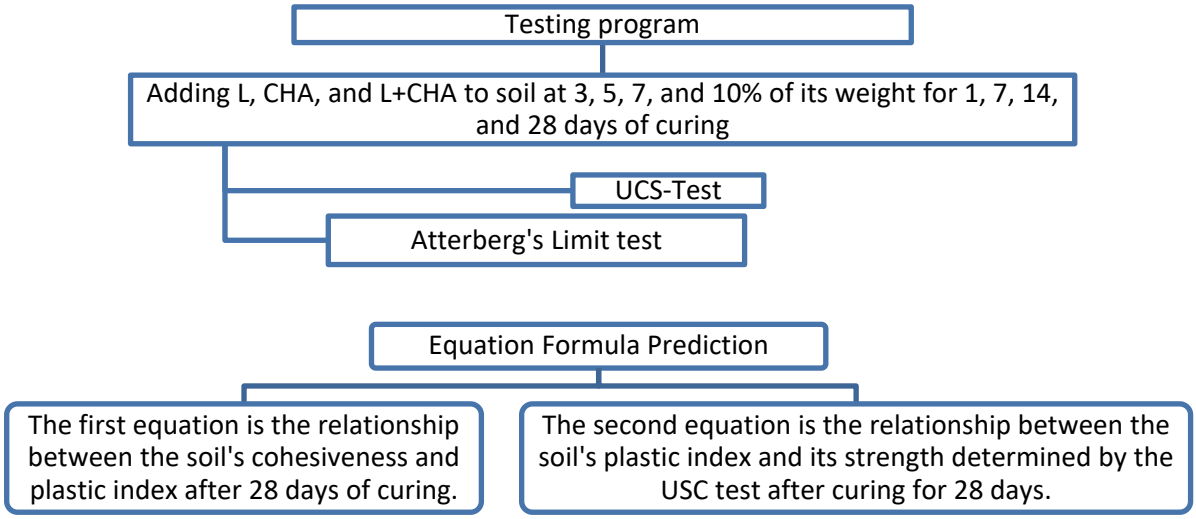

Fig. 1. Methodology of study

This testing program was intended to quantify the progressive enhancement in mechanical properties and also consistency of the treated soil over time, resultant of mainly from pozzolanic reactions stuck between coffee husk ash and limestone. The time-dependent study results are explained as a summarized in Table 3, despite the detail the overall sample preparation then testing procedure is illuminated in Figure 1.

2.7 Replication and Testing Procedure

Three identical samples were prepared and tested to guarantee the reliability of experimental results for each testing condition. All soil samples were compacted at Standard Proctor energy according to ASTM D698 using a 2.5-kg rammer with 25 blows per layer (applied over three layers). Uniaxial Compressive Strength (UCS) specimens were prepared in the form of cylinders as described by ASTM D2166 having diameter 38 mm and height 76 mm.

All specimens were sealed in plastic bags to avoid moisture loss and cured at room temperature (25 ± 2°C) under controlled laboratory conditions. To maintain consistency of data Atterberg limits tests and UCS tests were performed for specimens made from the same soil batch for each curing period with varying additive content.

3. Results and Discussion

3.1 Atterberg's Limits

This effect on the consistency of the soft clay with addition of reinforced material is shown in Figure 2. For 7% CHA, the liquid limit decreased from 74% to 67%, and for 7% (CHA+L), it was reduced to 60. Plus, to 64% a.c. @ 7% (L). Before mixing, the value of plastic limit was 35 as seen in Fig. 3. After mixing this value increased to 44 after 7% CHA was added. The increase carried on, up to 48 with 7% CHA and L together, topping a remarkable 49 when we added in only 7% of L. Moreover, from Figure 4 it is noted that for the soil, 39% of the sample produces a plasticity index (PI) as being very plastic. The soil became less flexible upon the addition of the chemicals according to (15, 9 and 11). The soil modulus declined when chemicals were mixed with the soil, as noted by (15, 9 and 11). This shows that at 7 % C, 7 % RHA bound with L and 7 % CHA, the plasticity of soil transforms to (low plastic), low. and medium plastic respectively [33]. The inclusion of RHA in the soil lead to a reduction in plastic index after CHA was added due to moisture adsorption by adding RHA.

From these results the decrease of soil activity can be seen, this occurs gradually until reaching a value of 0.98 that represents normal activity in soil and a value equal to 0.31 that presents inactive behavior for the case with 7% of cement content (Fig. Soil activity level was decreased to 0,30 with the use of 70% L + CHA, indicators of dormancy and inactivity. With an index of 0.42 at 7% CHA, it

is remarkable that the soil can be considered inactive. Soil behavior is an important factor that greatly affects the stability/safety of a project. This characteristic is representative of the soil dynamic capability to shrink and swell with changes in water content. It is common to experience large volume changes in highly active soils which shift and resettle causing possible damage and instability. Low activity side casts, on the other hand, are also providing a secure starting point; they remain solid and not easily moved compared to high-risk material.

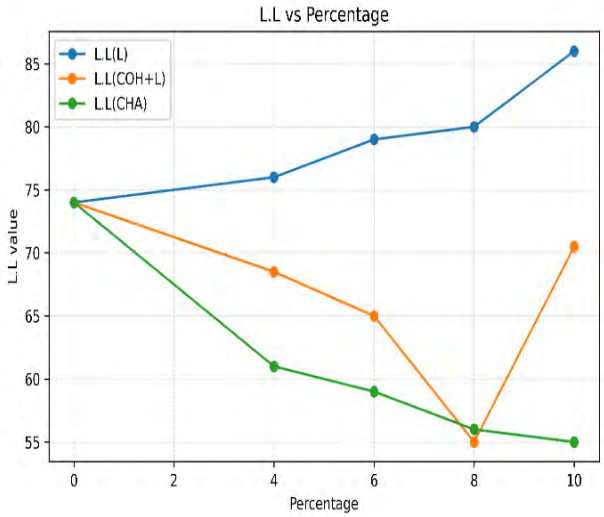

Fig. 2. Liquid limit of soil mixtures

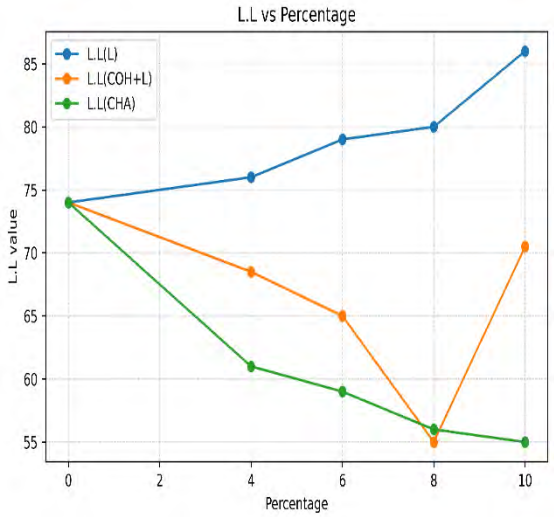

Fig. 3. Plastic limit of soil mixtures

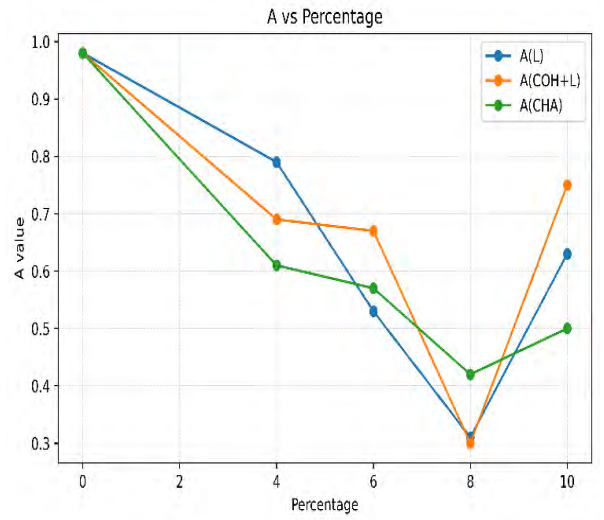

Fig. 4. Plasticity index of soil mixtures

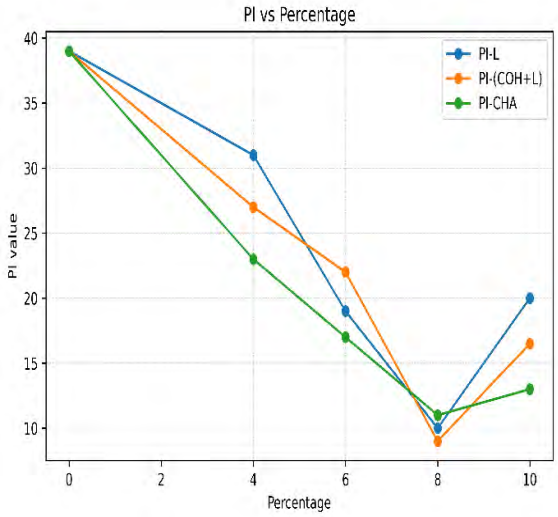

Fig. 5. Activity of soil mixtures

The most suitable option proved to be - addition of coffee husk ash (7 wt%) mixed up with limestone powder, after verification. Interaction impact of three amendments and soil over twenty-eight days correlation studies on cohesive soils and flow ability. This additive increased the binding of the soil. The work was designed to assess the overall effectiveness, porosity and water retention capacity of the soil for 1, 7, 14 days and over a period of up to 28 days in order to investigate how the combined system changes with time. The effect of 7% CHA with L is provided in Table 3.

It should be noted that the slight increase in the plasticity index observed at 10% CHA does not indicate a deterioration in soil behavior, but rather reflects a non-monotonic response at higher additive contents. At elevated CHA percentages, part of the ash acts as a non-reactive filler due to insufficient available calcium to sustain further pozzolanic reactions. Consequently, the excess ash particles may increase the fine fraction, leading to a marginal rise in plasticity index. Similar

behavior has been reported in previous studies on agricultural ash stabilization, where an optimum additive content exists beyond which performance gains diminish.

Table 3. Atterberg's limit effect of 7% CHA combined with limestone

Curative time	L.L (%)	P.L (%)	P.I (%)	A (%)
First day	57	48	9	33
Seven days	54	46	9	30
Fourteen days	55	47	8	29
Twenty-eight days	54	47	7	25

3.2 Unconfined Compressive Strength

Figure 6 displays the soil mixture after 28 days of curing of11 unconfined compressive strength data. According toward the untested result, the soil's strength was 60 kN/m^2 before treatment, but it increased to 90 kN/m^2 during a 28-day curative period with 7% limestone treatment. 7After 28 days of curing, soil treated by 7% coffee ash gained strength to 70 kN/m^2. After 28 days of curing using 7% coffee husk 7 and limestone, the strength of soil reached 101 kN/m^2. Figure 7 depicts the soil cohesiveness results after 28 days of curing. The soil's cohesiveness was 30 kN/m^2 before curing, according to the most recent results. Adding 7% limestone to the soil after 28 days of curing significantly increased its cohesion (36 kN/m^2). Adding 7% coffee husk ash to 30 KN/m^2 of the soil yielded cohesiveness at Adding coffee husk ash seven percentage and limestone powder enhanced soil cohesiveness to 45 kN/m^2. As a result, incorporating coffee husk ash and lime into soil type clay improves soil qualities, including strength and cohesiveness.

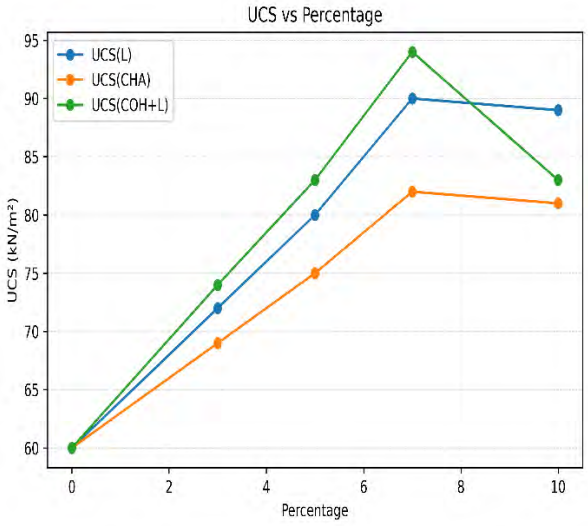

Fig. 6. UCS of soil mixture after 28 days of curing

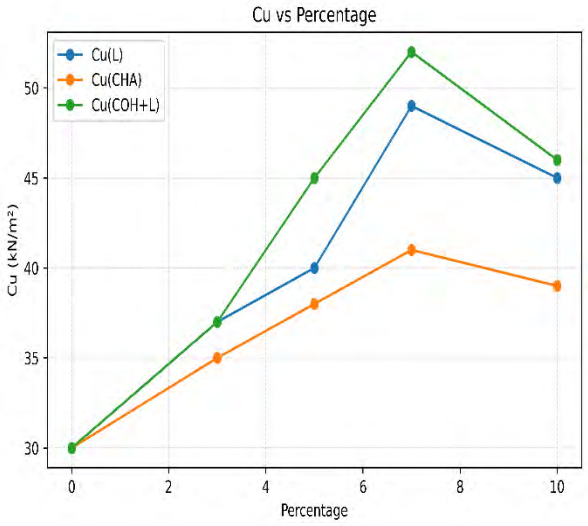

Fig. 7. Cohesion of soil mix. after 28 d. of curing

The results demonstrate that the unconfined compressive strength was rise than before 101 after using a mixture of coffee husk ash and limestone powder for a 28-day curing period, which improved long-term strength in particular [34]. This study shown that coffee husk ash combined with limestone powder can be effectively reprocessed as a soil preservative, hence reducing ecological contamination. The results of this study are similar to [35]. The research mentioned about the coffee husk ash effect such being linked by there. It acts similar to a partial replacement for cement and strength, durability goes up by 10% by its weight. Additionally, comparisons may be made through 36 with regards to the coffee husk ash effects on soil characteristics. The icing on the cake is that we used consistent mixing, compaction and curing procedure for all specimens to have consistency in results. and Each value is the mean of repeated tests.

3.3 Proposed Equations

The reduction of model development costs and laboratory requirements that this study will achieve is significant, because mechanisms through which the soil behaves during treatment are studied in detail. It nicely emphasizes the importance of a strong link between bearing capacity (cumulative loading) and soil property dynamics as both are needed to improve our comprehension and management of soil systems. Graphical representations were used to obtain the foregoing equations. The first equalization represented by Figures 4, 6 and 8 is a clear attempt to make the operation more efficient from both a time and cost perspective. It details a 28-daygradedtreatmentwhich and U, is based on Ux The latter heal mud index (Subhedarlb /Ii-X) Edict as well of the soil strength line with plasticity that correlation, in particular with unconfined compressive soil strength Index ucs). The second equation is shown in Fig 9 and confirms the evidences provided by Figs 4 and 7. The model was established to obtain a mathematical relationship between soil cohesive features and PI at the same 28-day period of treatment. By providing a complete representation of soil-behavior during curing and emphasizing the important relationships between mechanical behavior of soil properties and their ability to carry increasing loadings, more efficient modeling in terms of costs and labor can be achieved. Graphical analysis and the development of appropriate equations is the key to these efforts. The formation of equations prediction and right factor are summarized in Table 5.

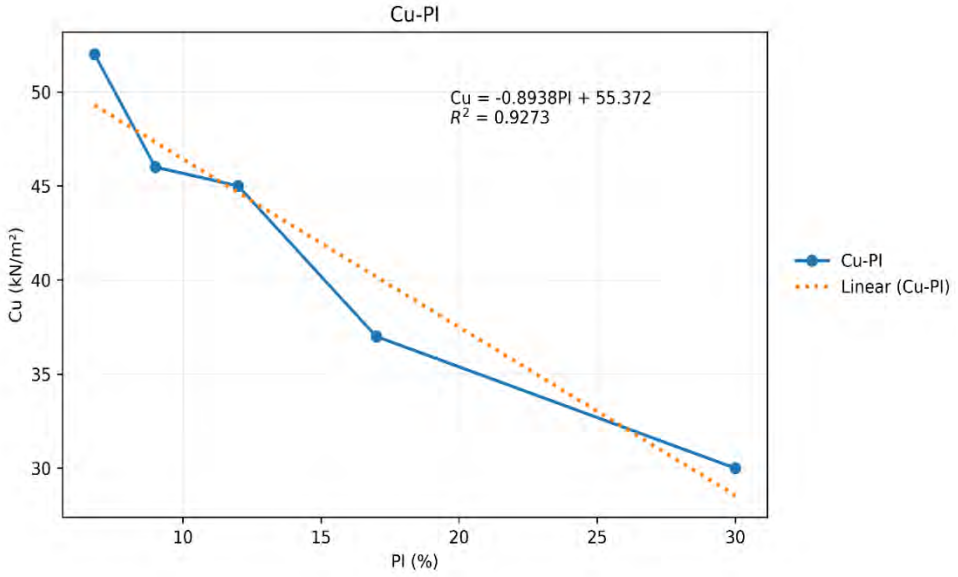

Fig. 8. Variation of PI with cohesion at 28 days of curing

The slight increase in plasticity index observed at 10% CHA can be attributed to the excess ash content acting as a non-reactive filler material rather than participating in pozzolanic reactions. At higher dosages, insufficient calcium availability limits further cementitious bonding, resulting in reduced efficiency of stabilization. This phenomenon has been reported in previous studies on agricultural ash stabilization. Table 4 explain that by reducing the plasticity index (PI) from 30 to 12 at a 7% ratio, increasing the unconfined compressive strength (UCS) from 60 to 90 kN/m^2, and increasing the cohesion (C) from 20 to 30 and then to 42 kN/m^2 at 10%, the improved rice husk ash (CHA) progressively improved the properties of the soil. The PI value stayed in the strong correlation range even with the apparent improvement. While cohesion recorded its maximum value at 10% (57.5 kN/m^2), lime (L) did not reach the same level of UCS, which stayed around 70 kN/m^2. But it was the plastic which reduced PI most (up to 9 at 7%) indicating quite good plasticity development. The possible chemical stabilization processes due to the presence of coffee-husk ash (CHA), limestone, and clay minerals are mainly pozzolanic reactions, cation exchange, agglomeration/flocculation bonding bond, and secondary less important carbonation.

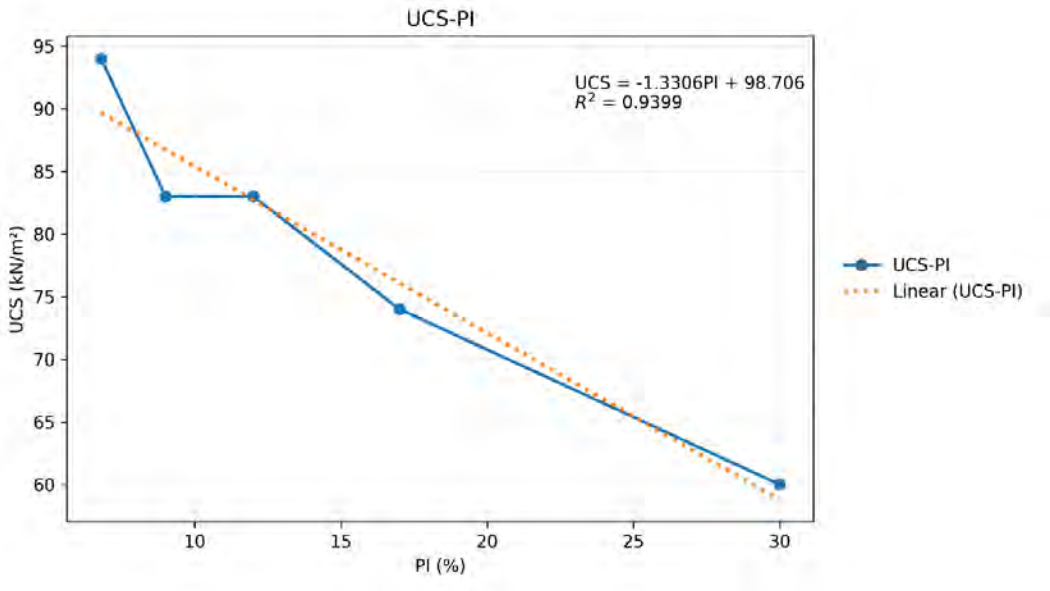

Fig. 9. Variation of PI with UCS at 28 days of curing

The CHA has highly reactive silica (SiO_2), alumina (Al_2O_3) and calcium oxide (CaO). In the presence of moisture, these compounds react with limestone-derived calcium hydroxide ($Ca(OH)_2$) to produce stable calcium silicate gels (C-S-H) and calcium aluminate gels (C-A-H). These gels manufacture to bind soil particles together, low plasticity and permeability as well as increase in strength of durability [37]. Cation exchange and flocculation result when the divalent calcium ion (Ca^{2+}) released via limestone disrupts monovalent cation (e.g., Na+ or K+) adsorbed at clay edges. These cations directly offset the repulsion among particles and contribute to particle coalescence, improving soil structure and resistance of swelling [38]. Also, effects on long-term strength enhancement of carbonation reactions in which $Ca(OH)_2$ reacts with atmospheric CO_2 to form calcium carbonate($CaCO_2$) may be marginal. These reactions are, however, of lesser importance under \`short-term curing' conditions [39]) [L1].

Table 4. Physical and shear strength of tested soil samples at 28 -day curing

Additive (%)	Additive Type	LL (%)	PL (%)	PI (%)	Activity (A)	UCS (kN/m^2)	c_u (kN/m^2)
0	Soil without adding	76	46	30	0.90	60	30
3	CHA	66	44	22	0.75	69	35
5	CHA	52	39	15	0.60	75	38
7	CHA	50	38	12	0.42	82	41
10	CHA	56	42	14	0.50	81	39
3	L	58	40	18	0.70	72	37
5	L	58	44	14	0.55	80	40
7	L	58	49	9	0.31	90	49
10	L	56	46	10	0.40	89	45
3	CHA + L	60	43	17	0.60	74	37
5	CHA + L	57	45	12	0.45	83	45
7	CHA + L	54	47.2	6.8	0.25	94	52
10	CHA + L	61	46	9	0.38	83	46

The developed expressions which can predict for the UCS and cohesion based on the percent of additive (CHA, limestone) plant a beneficial initial indicator to recognize the effect of treated soils. Nevertheless, the high model R^2 values suggest that these models are only partly robust and can be interpreted with care. It should be noted, however, that the small number of data points and the single soil type (CH) prevent application of these equations at large scale. Because of this, these

equations can be used to emphasize dominant features and sketch designs, however generalizing these soil types and conditions over other clays or varying climates needs more data and an extended range of soil types. Linear regression analyses were re-performed using the correct and complete dataset obtained after 28 days of curing, in Table 4 explained as summarized. Separate regression models were developed to evaluate the relationships between the plasticity index (PI) plus unconfined compressive strength (UCS), in addition between PI plus soil cohesion (Cu).

Figure 9 shows the relationship between PI and UCS, showing a strong inverse linear correlation. The derived regression equation is expressed as; USC = −1.3306PI+98.706, with a coefficient of determination R^2 = 0.9399, indicating a high degree of correlation between plasticity reduction and strength gain. That explain in Table 5. Figure 8 shows the link stuck between PI and cohesion (Cu). The regression analysis produced the following equality; Cu = −0.8938PI+55.372, , with R^2 = 0.9273, reflecting a strong correlation influenced by additional microstructural factors beyond plasticity alone. That explain in Table 5. The regression equations and corresponding R^2 values are summarized in Table 5. Although these models effectively capture the observed trends, their applicability is limited to the tested CH soil and additive contents within the range from 0 to 10 percentage.

Table 5. The equation formula prediction at 28 -day curing

Information	Formulation	Right factor
The first equation is the relationship between the soil's plastic index and strength on the 28-day curing USC test.	USC = −1.3306PI+98.706	R^2 = 0.9399
The second equation is the relationship between the soil's plastic index and cohesion after 28 days of curing.	Cu = −0.8938PI+55.372	R^2 =0.9273

The regression equations presented in this study describe the relationship between plasticity index (PI) and the mechanical strength parameters of the treated soil. The negative slopes in both equations indicate that soil strength increases as plasticity decreases, which reflects improved particle bonding and reduced clay activity due to stabilization. The fact that the slope for the PI–UCS is steeper than the PI–cohesion indicates UCS to be more sensitive to plasticity of soil than cohesion. These responses can be ascribed to the interactive influence of cementitious bonding and microstructural densification on compressive strength.

The intercept in the regression equations is a theoretical value at zero plasticity and provides rather a reference point than an achievable state. The high R^2 values (R^2=0.95) point to a good correlation between the factors in the range studied. Nevertheless, these equations are linear approximations performed from a limited database and this must therefore be only valid within the experimented content of CH soil and stabilizer varying between 0 to 10%. Their potential use on other soil types or under different conditions needs experimental support.

3.4 Chemical Stabilization Mechanisms of CHA–L Treated Soil

The stabilization mechanism of CHA and LS–treated clay soil seems to be dominated through both physical and chemical effects taking place over time. Calcium ions liberated from limestone, immediately after the mixing process, react with negatively charged surfaces of clay particles resulting in cation exchange. During this process monovalent ions are exchanged for divalent calcium and the clay particles flocculate and aggregate. As a result, soil plasticity and activity are minimized within the initial stages of treatment. Upon further curing, the flocculated clay particles redeposit to entrench a stiffer structure. The small ash particles can fill pores and lock the soil particles together, which not only may increase the stiffness of soils but also could improve load transfer between soil particles.

The long-term strength gain results from pozzolanic reactions between reactive silica (SiO_2), alumina (Al_2O_3) and ferric oxide (Fe_2O_3) content in coffee husk ash with calcium hydroxide generated due to hydration of limestone. These reactions result in the production of cementitious phases; calcium silicate hydrate (C–S–H), and calcium aluminate hydrate (C–A–H), helping to bond soil particles, are responsible for long-term enhancement in unconfined compressive strength and

cohesion. The presence of CaO in lime stone (see Table 1) is necessary to induce these pozzolanic reactions and together they contribute definite contribution An important factors in governing the long-term behavior of stabilized soils. The enhanced strengthening of clay soil due to the presence of coffee husk ash and limestone is believed to be an interaction among physiochemically stabilization mechanisms namely cation exchange, flocculation, agglomeration, and pozzolanic reactions [36].

Cation exchange In the presence of limestone, cation exchange is taken place in the hydrate phase with respect to clay particle surfaces due to availability of calcium ions released from hydrated lime replacing monovalent cations (Na^+ and K^+). This reduces the width of diffuse double layer, weakens inter-particle repulsion and close up particle association so that PI and soil activity decrease [40]. Flocculation and agglomeration: after the cation exchange, divalent calcium ions yield in clays changing from a dispersed to flocculated state. This structural change leads to better packing of particles, higher plastic limit and lower liquid limit causing the improvement in soil consistency properties observed [41]. Pozzolanic reactions is the main stabilization mechanism in CHA–L treated soils in long term. The activity of SiO_2 and Al_2O_3 in coffee husk ash forms the pozzolanic part of rice husk ash and react with Ca(OH)2genrated from limestone hydration under alkaline environment. These reactions that cause the cementitious compounds to form, such as calcium silicate hydrate (C–S–H) and calcium aluminate hydrate (C–A-H), allow an unconfined compressive strength and cohesion to increasing with curing time [37].

Carbonation could also contribute slightly to strength gain by the reaction of calcium hydroxide with atmospheric carbon dioxide producing calcium carbonate. However, with the rather short curing times investigated in this study, carbonation is assumed to be secondary to pozzolanic reactions [36]. Overall, the cation exchange combined with the flocculation and pozzolanic reactions forms a tighter and more stable soil structure with reduction in plasticity and activity and improvement in strength parameters, which sustains that coffee husk ash and limestone can adequately be used as sustain ending agents for clays.

4. Conclusions

In the present work, coffee husk ash (CHA) and limestone as a sustainable stabilizer for high plasticity clay soil were explored. The test results showed that the incorporation of CHA–limestone dramatically decreased soil plasticity and activity, meanwhile increased strength performance.
The optimum stabilizer content was found to be 7% CHA – limestone stabilizer at this level of concentration result in the PI reduction from 35% 90 kN/m² up to 60 kN/m² unconfined compressive strength when lime and cement are used after twenty-eight -day curing. Soil cohesion also augmented from 30 to 45 kN/m² between untreated and optimum stabilizer content soil.
The observed enhancements were related to the mechanisms of physicochemical stabilization by sorption (cation exchange), flocculation, pozzolanic reaction. The developed regression equations have practical importance for the preliminary design of soil strength in the studied ranges.
Despite such promising results, the conclusions of this research are restricted to a single type of clay soil and to the short-term curing period. Further study is recommended to evaluate the long-term durability, microstructure by means of SEM and XRD techniques and performance evaluation in the laboratory for CHA–limestone stabilization under various environmental conditions.

References

[1] Cosentino VR, Minervini MG, Taboada MA. Influence of stubble quality and degree of soil-stubble contact on N_2O emission. Plant, Soil and Environment. 2017;63(7):289–294. https://doi.org/10.17221/499/2016-PSE

[2] Al-Dulaimi SD, Bazhenova SI, Stepina IV, Erofeeva IV, Afonin V. Development of efficient compositions of hydrophobic materials resistant to chemical and biological environments. Journal of Infrastructure Preservation and Resilience. 2024;5:18. https://doi.org/10.1186/s43065-024-00113-z

[3] Gidebo FA, Yasuhara H, Kinoshita N. Stabilization of expansive soil with agricultural waste additives: A review. International Journal of Geo-Engineering. 2023; 14: 14. https://doi.org/10.1186/s40703-023-00194-x

[4] Abdulrahman SM, Abd Al-Kareem KW, Ihsan EA. Enhancing soil with low-cost pozzolanic materials: Rice husk ash and groundnut shell ash compared to cement. Mathematical Modelling of Engineering Problems. 2024;11(4):1115–1122. https://doi.org/10.18280/mmep.110430
[5] Abdulrahman SM, Sabeeh WT. Recycling construction waste to improve soil mechanics: a review. MINAR International Journal of Applied Sciences and Technology. https://doi.org/10.47832/2717-8234.19.11
[6] Abdulrahman SM, Al Kindi GY, Ihsan EA, Abdulrahman AM. Geotechnical properties of the soil contaminated with medical waste: A case study of metronidazole and amoxicillin waste. Ecological Engineering and Environmental Technology. 2024;25(2):112–120. https://doi.org/10.12912/27197050/175864
[7] Abdulrahman SM, Al-Gharbawi AS, Abdulrasool AS. A review: Soil improvement using the multi-type of polypropylene material. MINAR International Journal of Applied Sciences and Technology. 2023. https://doi.org/10.47832/2717-8234.15.9
[8] Abdulrahman SM, Al-Gharbawi AS, Al-Sultan AA. Effect of engineering properties of soft clay soil stabilized with limestone, eggshell powder, and eggshell ash. Water Environment Sustainability. 2023;3(2). https://doi.org/10.52293/WES.3.2.6875
[9] AbdulRahman S, Fattah MY, Ihsan EA. Influence of plastic fiber on the geotechnical properties of gypseous soil. International Journal of Engineering. 2021;34(2):367-374. https://doi.org/10.5829/IJE.2021.34.02B.08
[10] Abdulrahman SM, Ihsan EA, Sabri WA. Experimental Study to Effect of adding Emulsion Rubber Material (SPR) for the shear parameters of soil Gypsum. IOP Conference Series: Materials Science and Engineering. 2020;745(1):012124. https://doi.org/10.1088/1757-899X/745/1/012124
[11] Abdulrahman SM, Ihsan EAAA. Influences of Eggshell Powder to reduce the collapse of soil gypsum. IOP Conference Series: Materials Science and Engineering. 2020;745(1):012135. https://doi.org/10.1088/1757-899X/745/1/012135
[12] Alshihri S, Al-Gahtani K, Almohsen A. Risk factors that lead to time and cost overruns of building projects in Saudi Arabia. Buildings. 2022;12(7):902. https://doi.org/10.3390/buildings12070902
[13] Ola SA. The geology and geotechnical properties of the black cotton soils of northeastern Nigeria. Engineering Geology. 1978; 12:375-391. https://doi.org/10.1016/0013-7952(78)90019-4
[14] Gedefaw A, Yifru BW, Endale SA, Habtegebreal BT, Yehualaw MD. Experimental investigation on the effects of coffee husk ash as partial replacement of cement on concrete properties. Advances in Materials Science and Engineering. 2022; Article ID 4175460. https://doi.org/10.1155/2022/4175460
[15] Emmanuel US, Nyak EE, Agbor RB. Enhancement of soil stability with groundnut shell ash. Journal of Civil Engineering Research. 2022;12(1):7. https://doi.org/10.5923/j.jce.20221201.01
[16] Abubakar IR, Aina YA. Achieving sustainable cities in Saudi Arabia: Juggling the competing urbanization challenges. In: E-Planning and Collaboration: Concepts, Methodologies, Tools, and Applications. 2018. p. 234-255. https://doi.org/10.4018/978-1-5225-0187-9.ch003
[17] Puertas F, García-Díaz I, Barba A, Gazulla MF, Palacios M, Gómez MP, Martínez-Ramírez S. Ceramic wastes as alternative raw materials for Portland cement clinker production. Cement and Concrete Composites. 2008;30(9):798-805. https://doi.org/10.1016/j.cemconcomp.2008.06.003
[18] Fondjo AA, Theron E. Application of mathematical function to estimate the compaction characteristics of unsaturated soils. Civil Engineering and Architecture. 2021;9(1):255-262. https://doi.org/10.13189/cea.2021.090121
[19] Noor ST, Uddin R. Effect of lime stabilization on the alteration of engineering properties of cohesive soil. In: Pradhan B, editor. GCEC 2017. Lecture Notes in Civil Engineering. 2019;9. Springer, Singapore. https://doi.org/10.1007/978-981-10-8016-6_88
[20] Nalobile P, Wachira JM, Thiong'o JK, Marangu JM. A review on Pyroprocessing techniques for selected wastes used for blended cement production applications. Advances in Civil Engineering. 2020:1-12. https://doi.org/10.1155/2020/5640218
[21] Iskandar D, Putri EE, Hakam A, Fitri A. Effectiveness of portland cement Type 1 In stabilizing soft clay soil as subgrade for road construction. Jurnal Rekayasa Sipil. 2023;19(1):44-53. https://doi.org/10.25077/jrs.19.1.44-53.2023
[22] Ikumapayi CM. Properties of groundnut shell (Arachis hypogaea) ash blended Portland cement. Journal of Applied Sciences and Environmental Management. 2018;22(10):1553-1556. https://doi.org/10.4314/jasem.v22i10.03
[23] Mujedu KA, Adebara SA. The use of groundnut shell ash as a partial replacement for cement in concrete production. International Journal of Sciences, Engineering and Environmental Technology (IJOSEET). 2016;1(3):32-39. https://doi.org/10.5958/2349-2988.2017.00056.0
[24] Demissew AG, Feyessa FF, Assefa S. Partial replacement of cement by coffee husk ash for C-25 concrete production. Journal of Civil Engineering Science and Technology. 2019;10(1):12-21. https://doi.org/10.33736/jcest.1433.2019

[25] Reta Y, Mahto S. Experimental investigation on coffee husk ash as a partial replacement of cement for C-25 concrete. Cikitusi Journal of Multidisciplinary Research. 2019; 6:152–158 https://doi.org/10.1155/2022/4175460
[26] ASTM. Standard specification for coal fly ash and raw or calcined natural pozzolana for use as a mineral admixture in concrete. ASTM C-618. 1999. USA.
[27] ASTM International. ASTM D2216-19: Standard test methods for laboratory determination of water (moisture) content of soil and rock by mass. 2019. https://doi.org/10.1520/D2216-19
[28] ASTM. D136-06: Sieve analysis of fine and coarse aggregates. Encyclopedic Dictionary of Polymers. 2007:881-882. https://doi.org/10.1007/978-0-387-30160-0_10425
[29] ASTM. D4318-00: Standards for liquid limit, plastic limit, and plasticity index of soils. ASTM International. 2000; 4:1-14.
[30] ASTM. D4254-00 (Reapproved 2006): Standard test methods for minimum index density and unit weight of soils and calculation of relative density. 2006.
[31] ASTM. D2166-16: Standard test method for unconfined compressive strength of cohesive soil. ASTM International. 2016; D2166-16:1-6.
[32] ASTM. D3080/D3080M-11: Standard test method for direct shear test of soils under consolidated drained conditions. 2012.
[33] Das, B. M.Soil Mechanics and Foundations. 3rd ed.Hoboken, NJ: John Wiley & Sons, Inc.; 2010. ISBN: 978-0-470-55684-9.
[34] Sreedevi S, Sreeja V. Effect of curing strength in lime–coffee husk ash mixture on clay. Sustainability Agri Food and Environmental Research. 2023;12:art772. https://doi.org/10.7770/safer-V12N-art772
[35] Franzluebbers AJ. Water infiltration and soil structure related to organic matter and its stratification with depth. Soil and Tillage Research. 2002;66(2):197-205. https://doi.org/10.1016/S0167-1987(02)00027
[36] Munirwan RP, Mohd Taib A, Taha MR, Abd Rahman N, Munirwansyah M. The application of coffee husk ash to improve compaction characteristics of clay soil. IOP Conference Series: Earth and Environmental Science. 2023;1140(1):012001. https://doi.org/10.1088/1755-1315/1140/1/012001
[37] Singh M, Siddique R, Chakarvorty R. Effect of waste materials on soil stabilization: A review. Waste Management. 2018; 80:12–25. https://doi.org/10.1016/j.wasman.2018.09.012
[38] Sherwood P. Soil stabilization with cement and lime: State of the art review. London: Transport Research Laboratory, HMSO. 1993. https://rosap.ntl.bts.gov/view/dot/66629/dot_66629_DS1.pdf.
[39] Bell FG. Lime stabilization of clay minerals and soils. Engineering Geology. 1996;42(4):223–237. https://www.sciencedirect.com/science/article/pii/0013795296000282
[40] Mitchell JK, Soga K. Fundamentals of soil behavior. 3rd ed. Hoboken, NJ: John Wiley & Sons; 2005. ISBN: 978-0-471-46302-3.
[41] Singh, M., Siddique, R., & Chakravorty, R. (2018).Effect of waste materials on soil stabilization: A review. Waste Management, 80, 12–25. https://doi.org/10.1016/j.wasman.2018.09.012

Blank Page

Research on Engineering Structures & Materials
www.jresm.org

Research Article

Experimental and numerical free vibration analysis of orthotropic composite plates reinforced with Al_2O_3

Dunia Abd Al-Latteef [*,1], Mohsin A. Al-Shammari [2,a], Emad Q. Hussein [1,b]

[1]*Department of Mechanical Engineering, University of Karbala, Karbala, Iraq*
[2]*Department of Mechanical Engineering, University of Baghdad, Baghdad, Iraq*

Article Info

Article History:

Received 27 Oct 2025
Accepted 01 Jan 2026

Keywords:

Free vibration;
Composite plate;
Alumina;
Natural frequency;
Classical laminate theory

Abstract

The dynamic behavior of composite structures is crucial for aerospace and automotive applications where weight reduction and vibration control are essential. This study investigates the free vibration characteristics of orthotropic composite plates reinforced with aluminum oxide (Al_2O_3) particles. Limited research exists on the combined effect of Al_2O_3 reinforcement percentages and fiber orientation on the dynamic properties of composite plates. The study aims to analyze the influence of varying Al_2O_3 content (2%, 5%, and 8% by weight) on the natural frequencies of glass fiber-reinforced PMMA composite plates with different stacking sequences. The study employs Classical Laminate Theory (CLT) with Rayleigh-Ritz method for analytical modeling, assuming thin plate theory (Kirchhoff), neglecting shear deformation, and considering simply supported boundary conditions. Finite Element Method (FEM) using ANSYS Workbench with SHELL181 elements validates the analytical results. Experimental verification uses impact hammer testing with accelerometer measurements. The 8% Al_2O_3 reinforcement showed optimal mechanical properties with the highest natural frequency (104.51 Hz) achieved by (90°, 30°, 45°, 30°, 90°) stacking sequence. Analytical-numerical correlation showed excellent agreement with discrepancies below 3% for most modes, while experimental validation confirmed model accuracy with errors ranging from 0.03% to 3.69%.

© 2026 MIM Research Group. All rights reserved.

1. Introduction

Uncontrolled vibrations lead to resonance and potential structural damage, so researchers focus on modeling the behavior of these plates and understanding the effect of particle reinforcement on dynamic properties [1-3]. Merdaci et al. [4] analyzed the vibrations of aluminum-alumina functional gradient plates from manufacturing, using higher order shear deformation theory and Navier's solution. The results were validated by comparing them with the literature and showing the effect of gradient coefficient, pore size and distribution, and dimensional ratios on normal frequencies [4]. Navaneeth et al. [5] examined free damping vibrations of woven fiberglass composite panels and a hand-molded epoxy matrix, with an assessment of tensile and bending properties according to ASTM standards, and natural frequency analysis using FFT and an accelerator with impact hammer; the results showed good compatibility with NASTRAN simulation and increased frequency response with increasing the number of layers [5]. Al-Shablle et al. [6] used theoretical, experimental and numerical analysis to study the vibrations of the nano-coated composite structural plate (SiO_2 epoxy and Al_2O_3 epoxy) at 0–2.5% volumetric ratios, showing an optimal increase in Young's modulus (up to 56%) and natural frequency (up to 24.5%) with different densities, with analytical-numerical compatibility with deviation of ≤3% [6].

*Corresponding author: dralihadi841@gmail.com
[a]orcid.org/0000-0002-2372-4840; [b]orcid.org/0000-0001-8643-2143
DOI: http://dx.doi.org/10.17515/resm2026-1299ic1027rs
Res. Eng. Struct. Mat. Vol. 12 Iss. 2 (2026) 1115-1125

Vasara et al. aimed to determine the natural frequencies of circular and annular plates with functional and porous gradient according to distributions (uniform, O-shape, X-shape), with modeling of mechanical properties via the Voght model and the distribution by power law, using the first shear deformation theorem, Hamilton's principle and a solution by differential quadrature method [7]. Saidi et al. [8] analyzed the free vibrations of plates with a functional gradient and porosity composed of aluminum (Al) and alumina (Al_2O_3) supported by an elastic medium, using the new shear deformation theory and the Winkler–Patrick two-coefficient model, and solving Navier's equations; the results showed the effect of gradient coefficient, degree of porosity and base constants on natural frequencies [8]. Venkatalakshmi et al. [9] proposed a synchronous field (CDF) method to analyze the free vibration of ceramic and metal gradient plates under proven and abstract edge conditions, with the distribution of material properties across thickness by force law, and the use of multiple nominal functions to obtain frequency coefficients and verify them by comparing them with the literature [9]. Li et al. [10] presented an accurate solution method for the analysis of the static response and free vibration of a rectangular plate with functional hierarchy according to the Reisner–Mingelen theorem with general edge conditions, with the distribution of material properties across thickness by force law and estimation by Vogt and Morri-tanka models, and improved Fourier series verification [10].

Tavadi et al. [11] analyzed the properties of epoxy compounds reinforced with erica fibers with the addition of alumina molecules (0-8%). The results showed that the 8% sample excelled in tensile tolerance (23 MPa), stiffness (81 Shore D), and impact resistance (180 J/m^2) due to uniform distribution and good bonding, supporting its use in lightweight engineering applications [11]. Han et al. [12] studied the nonlinear vibrations of plastic reinforced carbon fiber composite panels (CFRP) using machine learning techniques. A highly accurate predictive model (R^2=0.96) was developed to analyze the effect of multiple factors such as load levels, geometric dimensions, and boundary conditions on nonlinear frequency ratio. This model contributes to a better understanding of the dynamic vibration behavior of these materials, supporting the assessment of the robustness of CFRP structures and extending their service life in various engineering applications [12]. Mawardi et al. [13] investigated the effect of the addition of micro-aluminum oxide (Al_2O_3) molecules on the properties of pineapple fiber compounds reinforced with different polymeric matrices (epoxy and unsaturated polyester). The results showed that increasing the ratio of Al_2O_3 (up to 15% by weight) enhances stiffness, bending strength and resistance to water absorption, but reduces tensile strength. Epoxy compounds excelled in tensile strength and thermal stability, while polyester excelled in hardness and density of water. The uniform distribution of molecules contributed to the improved adhesion of the fibers to the polymeric matrix [13].

Despite the progress made, there are still points worth exploring further, which will therefore be highlighted in this study: using different percentages of Al_2O_3 and their effect on the dynamic analysis of the orthotropic composite plates. Study the effect of different percentages of Al_2O_3 through engineering simulations using FEM. In this study, the focus is on research that includes modeling methods used, techniques and methods of enhancing Al_2O_3 as weight ratio or functional distribution across thickness, type of plates studied, panel geometry, edge installation conditions, and the main findings of each researcher. We also discuss the importance of these studies for practical applications in areas such as aviation, automobiles and smart systems, and what new research can add in this field.

2. Materials and Testing Methods

2.1 Materials

The materials used in this study are presented in the following: E-Glass fibers: Long wires (roving) were used as structural reinforcement, PMMA mixture in a ratio of 80:20 (polymethyl methacrylate) was used as the matrix resin. Hardener: A powder added by 2% by weight of the resin to accelerate the hardening process of the resin. Aluminum oxide: powder added as a 2%, 5%, and 8% distributed additive. Polyvinyl Alcohol (PVA): A PVA bag or wrap was used to prevent resin from leaking while applied to the fibers, and ensures a smooth finish surface for the samples. The

mechanical properties of the materials used are shown in Table 1. A gypsum mold of dimension (25×35×5 cm3) was used as shown in (Fig. 1).

Table 1. Mechanical properties of the used materials.

Material	Elastic modulus (GPa)	Density (g/cm^3)	Volume fraction (%)	Poisson's ratio (υ)
E-glass	80.22	2.66	22.8	0.23
Lamination resin	3.792	1.19	77.2	3.792

Fig. 1. Gypsum mold for case study

2.2 Manufacturing

Here are the steps to manufacture the glass fiber reinforced composites:

- Jepson Mold preparation: A wooden mold covered from the inside with a soft layer of gypsum with dimensions of (25×35×0.5) cm^3 is used to ensure a flat inner surface. The inside of the mold is coated with PVA wrap to prevent adhesion of the resin and ensure easy removal of the model after solidification.
- Fiberglass arrangement: E-glass fibers are arranged in organized rows, across four consecutive layers within the mold. After each layer, an additional PVA wrap is placed to form the inner bag of the vacuum bagging.
- Preparation of resin mixture and additives: Polymer resin (PMMA in a ratio of 20:80) is mixed with hardening powder at 2% by weight of the resin, as well as Al_2O_3 powder at the desired concentration (2%, 5% or 8%). This mixture provides good cohesion of the fibers and improves the mechanical properties of the sheets.
- Vacuum Bagging Process: The resin mixture is applied to the layers of fibers, fully saturating them. The final overlay is covered with an airtight PVA outer wrap, then the bag is closed. It operates the vacuum pump to be suctioned in two stages: between the inner layer of PVA and the mold to form the casing around the mold. between the layer in which the forming takes place and the outer shell to eject air bubbles and compress the plates. This process continues at a pressure of up to 3000 MPa (as textual) for 45–60 minutes to ensure complete cohesion of the resin with the fibers.
- Curing Process: After the vacuum is finished, the plates are left under the action of pressure and solidification reaction for up to two hours until the crystal formation is complete and the model reaches its final hardness.
- Demolding and finishing: The outer PVA shell open, and the solid sample is removed from the mold. Cutting excess edges with a CNC cutter to obtain precise sheet final dimensions as required (e.g. 25×35 cm for main sheets, or cutting test specimens with dimensions of 165×19–13×3 mm for tensile tests). With these steps, it is safe to manufacture homogeneous

composite sheets, with a smooth surface and free of internal defects, ready for subsequent mechanical and vibratory tests.

2.3 Samples Mechanical Properties

The mechanical properties of the manufactured samples are investigated using a tensile test according to ASTM D3039/D3039M-08 [14]. The test was conducted in the mechanical department at the University of Technology. The results of the tensile test for the manufactured sample are presented in Table 2.

Table 2. Mechanical properties of the manufactured sample.

Sample	E2(MPa)	E2(MPa)	v12	V21	G12(MPa)
8 % Al_2O_3	11209	3521	0.35	0.12	1838
5 % Al_2O_3	8581	3061	0.34	0.117	1776
2 % Al_2O_3	8429	2833	0.37	0.133	1634

2.4 Free Vibration Test

The free vibration test was performed in the mechanical engineering department at the University of Baghdad as follows:

- Sample preparation: Using a single layer composite plate (Orthotropic) with dimensions of (25×35×0.5) cm^3, impregnated with polyester resin with 8% Al_2O_3 powder. Installing the plate under "simply supported" boundary conditions on the test holder.
- Excitation: Using an impact hammer with an ICP force sensor to give a mechanical pulse to the edge of the plate, causing free vibration.
- Measuring Response: Install an accelerometer weighing 3 g at the center of the plate or a point away from the edges, to capture the acceleration signal. Pass the signal through a Brüel & Kjær 2626 charging amplifier, ensuring a frequency range from 0.1 Hz to 30 kHz and an adjustable gain of 0–60 dB. Display the signal on the Digital Oscilloscope DS1102E type, and store the frequency data in flash memory for subsequent analysis.
- Natural frequency extraction: Reading acceleration response peaks represented as waves on an oscilloscope; the natural frequency is extracted from the highest peaks visible in the time or frequency spectrum.
- The free vibration test rig is presented in (Fig. 2).

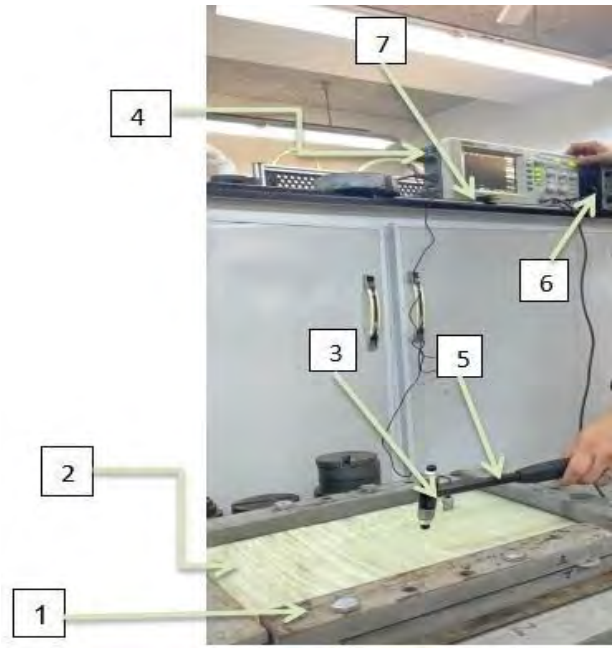

1. Boundary Conditions
2. The Composite Plate
3. Accelerometer
4. Digital Oscilloscope
5. Impact Hammer
6. Charge Amplifier
7. flash memory

Fig. 2. Rectangular plate vibration test rig

3. Numerical Analysis

This study employed the classical laminated theory CLT as the main assumption; surface mass and Rayleigh–Ritz equations were used to calculate natural frequencies and mode shapes. It was also assumed the following [15]:

- Thin plate (Kirchhoff theory).
- Limits are simply attribution.
- Neglecting the effect of shear (no shear deformation).
- Homogeneous material for each layer.
- No initial stresses or external loads.
- Use sinusoidal functions as shape functions.

Based on the above assumptions, the layer stiffness matrix will be [15]:

$$[Q] = \begin{bmatrix} Q_{11} & Q_{12} & 0 \\ Q_{12} & Q_{22} & 0 \\ 0 & 0 & Q_{66} \end{bmatrix} \quad (1)$$

- $Q_{11} = \frac{E_1}{1-v_{12}\,v_{21}}$= Axial stiffness in the 1-direction.
- $Q_{22} = \frac{E_2}{1-v_{12}\,v_{21}}$= Axial stiffness in the 2-direction.
- $Q_{12} = \frac{v_{12}\,E_1}{1-v_{12}\,v_{21}}$= Coupling stiffness due to Poisson's effect.
- $Q_{66} = G_{12}$: Shear modulus in the plane of the layer (Pa)
- E_1= Young's modulus in fiber direction (Pa)
- E_2= Young's modulus transverse to fibers (Pa)
- v_{12} = Poisson's ratio (strain in direction 2 due to stress in direction 1)
- $v_{21} = \frac{E_2}{E_1} v_{12}$= reciprocal Poisson's ratio by elasticity symmetry

Now the Bending stiffness matrix for the laminate using Classical Laminate Theory (CLT);

$$D = \frac{h^3}{12}\,Q \quad (2)$$

Where; D = Bending stiffness matrix of the laminate (Nm), h = Total thickness of the laminate (m),

Q = Reduced stiffness matrix of the laminate (Pa)

Then, the natural frequency using Rayleigh-Ritz (Simply Supported Plate with sinusoidal shape functions);

$$\omega = \pi^2 \sqrt{\frac{D_{11}}{m}} \left(\left(\frac{m_i}{L_x}\right)^2 + \left(\frac{n_j}{L_y}\right)^2 \right) \quad (3)$$

$$f_{ij} = \frac{\omega}{2\pi} \quad (4)$$

Where; ω = Circular natural frequency (rad/s), f_{ij}= Natural frequency in Hz, D_{11} = Bending stiffness in x-direction from matrix D (Nm) m = Mass per unit area (kg/m^2), L_x = Length of the plate (m), L_y = Width of the plate (m), m_i, n_j = Mode numbers in x and y directions (integer, e.g., 1, 2, 3...).

The mode shape function for a simply supported plate is:

$$w(x,y) = sin\left(\frac{m_i \pi x}{L_x}\right) sin\left(\frac{n_j \pi y}{L_y}\right) \quad (5)$$

Where w(x, y) = Transverse deflection (displacement) at position (x, y) and x, y = Coordinates on the plate surface (m).

The numerical analysis was conducted in two ways: first, using MATLAB code employing the above equations, and second, using ANSYS Workbench 2021 R1, where a (25×35×0.5) cm^3 plate is designed in a CAD (ANSYS DesignModeler). The laminate constituent layers (e.g., 90°, 30°, 45°, 30°, 90° fiber arrangement) and their mechanical properties (E-glass & PMMA) are defined using ANSYS Composite PrepPost ACP (Pre) engineering data. Restrict the four edges of the plate to Simply Supported boundary, i.e.: Vertical movement (Z) is restricted at the edges. Allows rotational motion around the edge axes (X and Y) freely. Two-sided SHELL181 elements (2D shell elements) suitable for composite thin sheet analysis were used, supporting Orthotropic Layers properties and enabling the simulation of stratified grading of glass fibers and polymer resin [14-19]. The average size of the element used is approximately 5×5 mm, to strike a balance between the accuracy of the results and the speed of calculation. The total number of elements is around 4,900, evenly distributed to ensure good coverage of the middle level of the plate, as shown in Fig. 3.

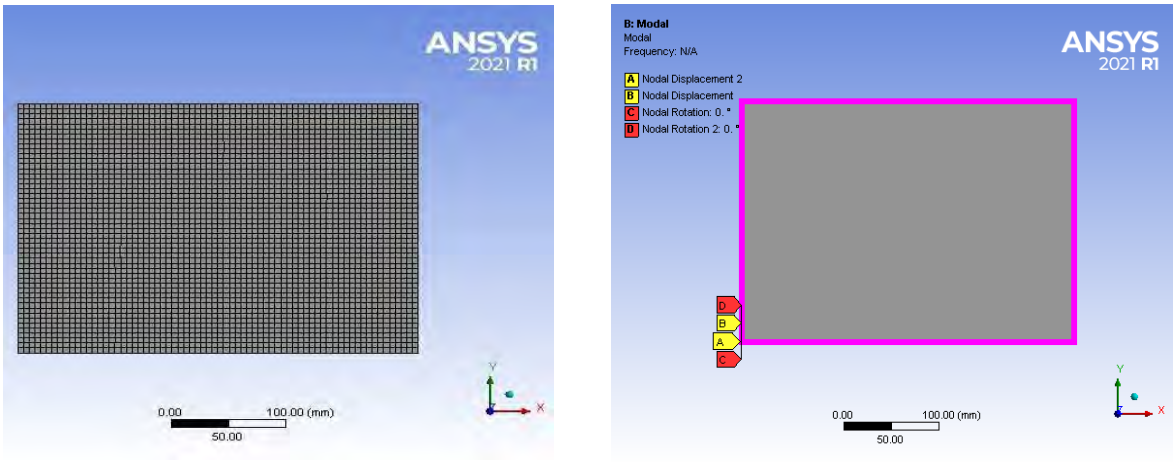

(a) (b)

Fig. 3. a) Mesh type of the modeled sample. b) The boundary conditions: all edges simply supported

3. Results and Discussion

The results of this study were presented Table 3, where the numerical results were presented using ANSYS and MATLAB for the best mechanical properties sample, which is the 8% Al_2O_3 reinforcement (Fig. 4 to Fig. 8) are presenting the first mode results using FEM and analytical solution for the five samples above. Discussion of dynamic performance in terms of the highest natural frequency, where the ranking in sample (4) achieved the highest value of the natural frequency in the first mode (104.51 Hz), which indicates the maximum dynamic rigidity of this arrangement.

In terms of the lowest variation between the models, the sequence in sample (1) was characterized by the least difference between the results of ANSYS and MATLAB (0.45%), which indicates good consistency of analytical and numerical models in this ranking. Complex distributions, the arrangement in sample (3) based on gradually variable angles, showed the greatest variance (8.74%), indicating the boundary of the CLT model in capturing the effects of shearing and morphology in such complex angular combinations.

Table 3. ANSYS and MATLAB natural frequency results

Sample	Mode	ANSYS N.F (Hz)	MATLAB N.F (Hz)	Discrepancy (%)
(1) 90°, 0°, 60°, 0°, 90°	1	100.77	101.23	0.45
	2	176.65	179.78	1.74
	3	317.71	319.39	0.53
	4	330.31	335.68	1.60
	5	401.93	404.92	0.74

(2) 0°, 90°, 45°, 90°, 0°	1	90.79	89.71	1.19
	2	202.56	204.82	1.10
	3	264.58	255.7	3.36
	4	355.54	358.85	0.92
	5	401.17	403.31	0.53
(3) 0°, 60°, 90°, 60°, 0°	1	90.571	99.25	8.74
	2	205.79	225.07	8.57
	3	255.47	258.03	0.99
	4	353.59	396.98	10.93
	5	408.27	427.63	4.53
(4) 90°, 30°, 45°, 30°, 90°	1	104.51	112.07	6.75
	2	177.46	199.86	11.21
	3	309.34	336.14	7.97
	4	348.49	349.65	0.33
	5	409.75	448.29	8.60
(5) 0°, 45°, 90°, 45°, 0°	1	98.61	101.72	3.06
	2	190.31	209	8.94
	3	312.65	328.89	4.94
	4	359.87	373.29	3.60
	5	393.07	406.68	3.35

Mechanically, all five arrangements benefit from an 8% Al_2O_3 boost compared to others, but the stratified arrangement itself does not affect the tensile properties that are tested independently of angular directions. In dynamic terms, rank (4) is the most solid (the highest natural frequency), followed by rank (1), while the rest performed between medium and low values. In terms of typical accuracy, ranking (1) provides the best compatibility between ANSYS and MATLAB, making it ideal for harmonic analysis, while ANSYS alone is preferred for ranking (4) if the focus is on the highest dynamic performance regardless of analytical variation.

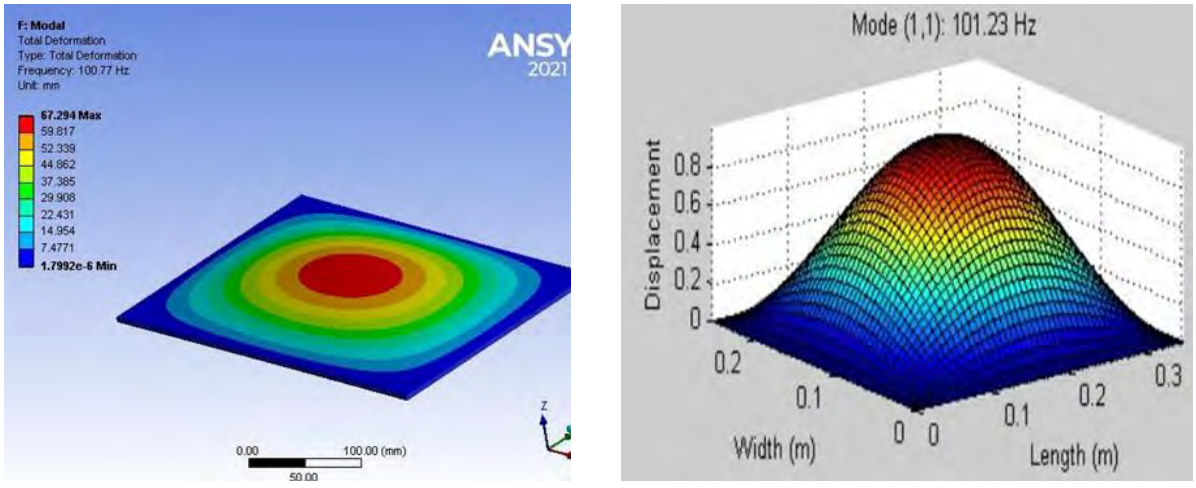

(a) (b)

Fig. 4. Fundamental natural frequency and mode shape of sample 1: a) FEM result, b) analytical result

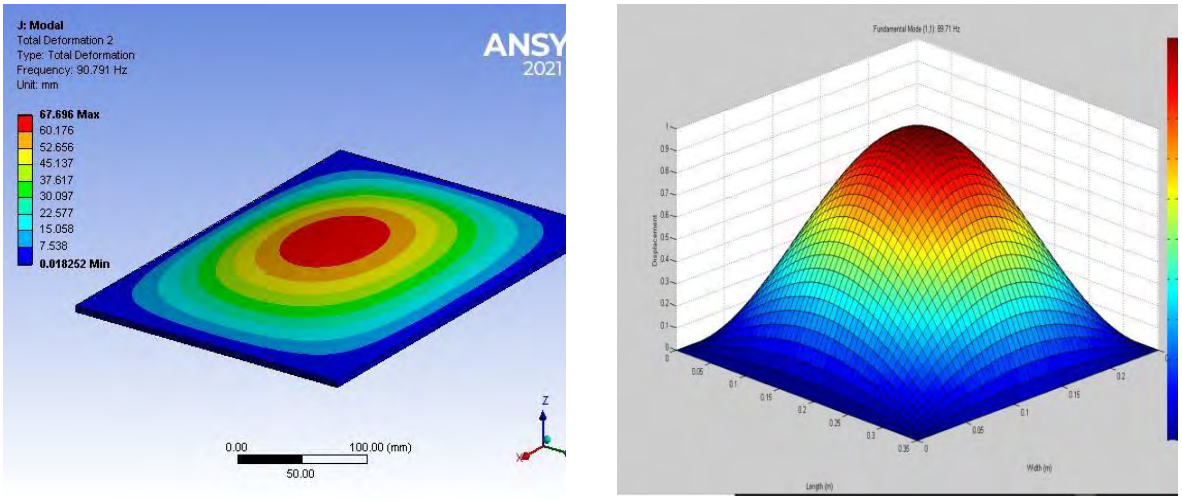

(a) (b)

Fig. 5. Fundamental natural frequency and mode shape of sample 2: a) FEM result, b) analytical result

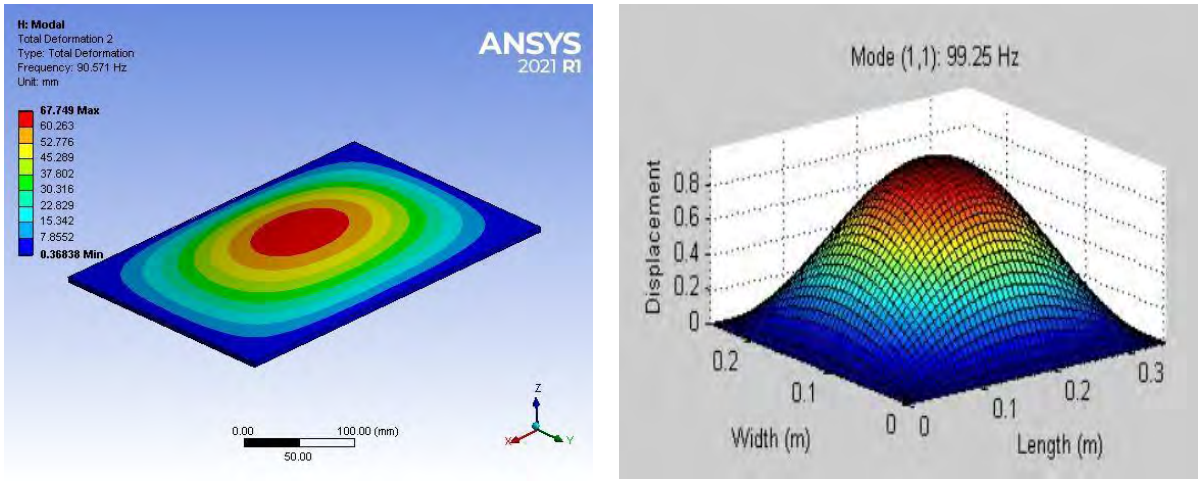

(a) (b)

Fig. 6. Fundamental natural frequency and mode shape of sample 3: a) FEM result, b) analytical result

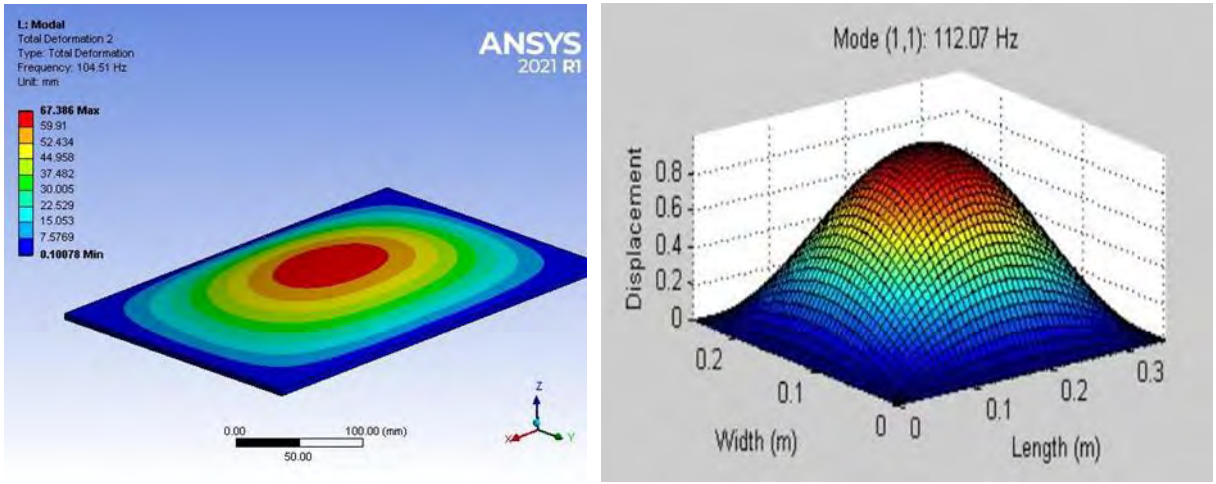

(a) (b)

Fig. 7. Fundamental natural frequency and mode shape of sample 4: a) FEM result, b) analytical result

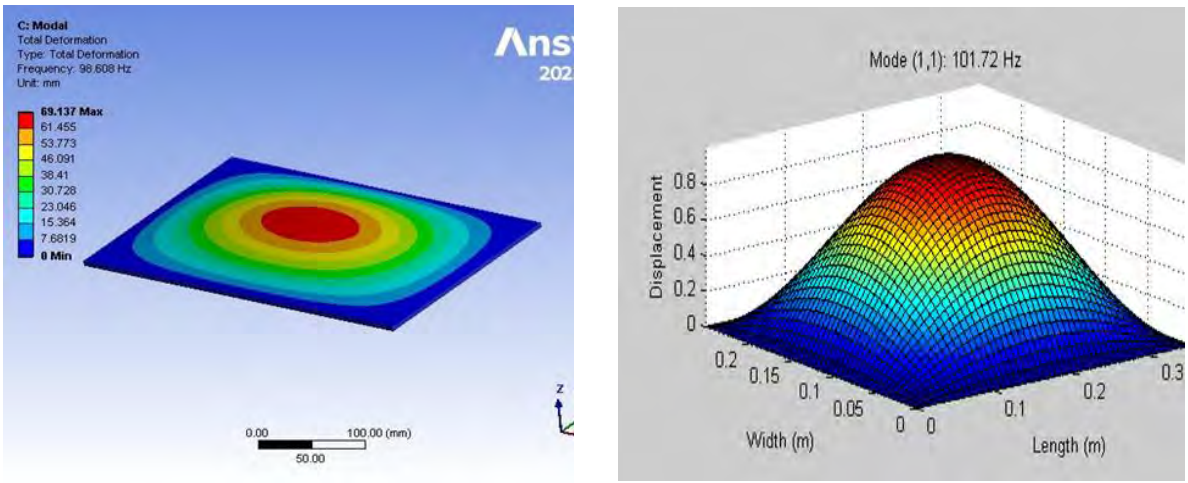

Fig. 8. Fundamental natural frequency and mode shape of sample 5: a) FEM result, b) analytical result

4. Results Validation

The analytical and FEM model analysis was validated using the experimental investigation for a thin composite plate with dimensions of (25×35×0.5) cm^3 of five layers with a stacking sequence of (0°, 90°, 45°, 90°, 0°) as presented in Table 4. In the previous table, the comparison between experimental values, simulated predictions (ANSYS) and analytical calculations (MATLAB) of the natural frequencies of the first five vibration modes of the composite dish (350×250×5 mm^3) with successive layers (0°, 90°, 45°, 90°, 0°) under simple boundary conditions on the edges is shown. The following points can be drawn: the error rate between ANSYS results and experimental values ranges from 1.08% (mode 5) to 2.53% (mode 1), indicating a very good compatibility between simulation and testing. For the MATLAB analytical method, error rates range from 0.03% (mode II) to 3.69% (mode I).

Table 4. Results comparison between experimental, FEM, and analytical.

Mode	FEM Natural Frequency (Hz)	Experimental Natural Frequency (Hz)	Discrepancy (%)	Analytical Natural Frequency (Hz)	Discrepancy %
1	90.79	93.15	2.53	89.71	3.69
2	202.56	204.89	1.14	204.82	0.03
3	264.58	259.23	2.02	255.7	1.36
4	355.54	362	1.78	358.85	0.87
5	401.17	405.56	1.08	403.31	0.55

The MATLAB method is therefore more accurate in modes two to five, while ANSYS slightly outperforms mode one. The reasons for this slight discrepancy may be due to one of the following reasons: In both models, the effect of shear (according to Kirchhoff's theory) and small distortions were neglected, which could lead to differences of up to ~3% in frequencies. The ideal simple edge model is slightly different from experimental reality (where there may be slight friction or ripple in the stabilization of the sample). The effect of the mass of the sensor (accelerator) and the properties of the actual material of the resin may add a small deviation in the measured frequencies.

5. Conclusions

This study investigated the free vibration behavior of orthotropic composite plates reinforced with Al_2O_3 particles, addressing the critical need for lightweight, high-stiffness materials in aerospace and automotive applications. The research employed a comprehensive approach combining analytical (CLT), numerical (FEM), and experimental methods to analyze five different fiber stacking sequences with varying Al_2O_3 content (2%, 5%, 8%), the following conclusions can be drawn:

- Particle Enhancement (Al_2O_3): 8% reinforced samples showed the highest tensile strength, Young's modulus, and absorption energy compared to 2% and 5% samples, demonstrating the feasibility of increasing the particle content to improve the mechanical properties of the composite.
- Dynamic performance and optimal fiber arrangement: The 90°, 30°, 45°, 30°, 90° ranking achieved the highest first natural frequency (104.51 Hz in ANSYS), demonstrating the maximum dynamic rigidity between the structures studied. In contrast, the 90°, 0°, 60°, 0°, 90° arrangement provides the best analytical–numerical compatibility (0.45% difference), ideal for initial calibration and rapid analysis.
- Accuracy of analytical and numerical models: At identical structures (e.g. 90°, 0°, 60°, 0°, 90°
- and 0°, 90°, 45°, 90°, 0°), the CLT-based MATLAB method recorded accuracy superiority (errors <1.2%), with excellent compatibility with experimental and ANSYS numerical results. The greater the complexities of the angles (0°, 60°, 90°, 60°, 0° and 90°, 30°, 45°, 30°, 90°), the higher the contrast ratio (up to ~11%), which requires numerical simulation in ANSYS to give more reliable results.

The recommendations for future works are:

- Include shear effects and analysis of nonlinear bends to optimize the CLT model.
- Study the distribution of particles within the layer and their homogeneity to reduce variations between models.
- To examine the effect of increasing the ratio of Al_2O_3 above 8% and to evaluate the effect of the resulting density on dynamic and mechanical performance.
- Based on these results, it is recommended to use an 8% Al_2O_3 sample with a 90°–30°–45°–30°–90° order when maximum dynamic rigidity is required, with a 90°–0°–60°–0°–90° order in the first analytical analyses to ensure high compatibility of results.

References

[1] El-Kady EY, Mahmoud TS, El-Betar AA, Abdel-Aziz M. Dynamic behaviour of cast A356/Al2O3 aluminum metal matrix nanocomposites. Mater Sci Appl. 2012 Nov 27;3(11):815-20. https://doi.org/10.4236/msa.2012.311118

[2] Al-Shammari MA, Abdullah SE. Stiffness to Weight Ratio of Various Mechanical and Thermal Loaded Hyper Composite Plate Structures. IOP Conf Ser Mater Sci Eng. 2018 Nov;433(1):012051. https://doi.org/10.1088/1757-899X/433/1/012051

[3] Al-Waily M, Al-Shammari MA. Theoretical and Numerical Vibration Investigation Study of Orthotropic Hyper Composite Plate Structure. Int J Mech Mechatron Eng. 2014.

[4] Merdaci S, Adda HM, Hakima B, Dimitri R, Tornabene F. Higher-Order Free Vibration Analysis of Porous Functionally Graded Plates. J Compos Sci. 2021 Nov;5(11):305. https://doi.org/10.3390/jcs5110305

[5] Navaneeth IM, Poojary S, Chandrashekar A, Razak A, Hasan N, Almohana AI. Damped Free Vibration Analysis of Woven Glass Fiber-Reinforced Epoxy Composite Laminates. Adv Mater Sci Eng. 2022 Jul;2022:1-13. https://doi.org/10.1155/2022/6980996

[6] Al-Shablle M, Njim EK, Jweeg MJ, Al-Waily M. Free vibration analysis of composite face sandwich plate strengthens by Al2O3 and SiO2 nanoparticles materials. Diagnostyka. 2023 Apr;24(2):1-9. https://doi.org/10.29354/diag/162580

[7] Vasara D, Khare S, Sharma HK, Kumar R. Free vibration analysis of functionally graded porous circular and annular plates using differential quadrature method. Forces Mech. 2022 Dec;9:100126. https://doi.org/10.1016/j.finmec.2022.100126

[8] Saidi H, Sahla M. Vibration analysis of functionally graded plates with porosity composed of a mixture of Aluminum (Al) and Alumina (Al2O3) embedded in an elastic medium. Frat ed Integrità Strutturale. 2019 Aug;13(50):286-99. https://doi.org/10.3221/IGF-ESIS.50.24

[9] Venkatalakshmi N, Krishnabhaskar K, Meerasaheb K. Free Vibration Analysis of Simply Supported and Clamped Functionally Graded Rectangular Plate Using Coupled Displacement Field Method. Mech Adv Compos Struct. 2025;12(1):73-84.

[10] Li H, Liu N, Pang F, Du Y, Li S. An Accurate Solution Method for the Static and Vibration Analysis of Functionally Graded Reissner-Mindlin Rectangular Plate with General Boundary Conditions. Shock Vib. 2018 Jan;2018(1). https://doi.org/10.1155/2018/4535871

[11] Tavadi AR, et al. Experimental analysis of mechanical properties and FTIR analysis of areca fiber-reinforced epoxy composites incorporating Al2O3. J Ind Text. 2025 Dec;55. https://doi.org/10.1177/15280837241313217

[12] Han Y, Shi Z, Hua C, Sang Y, Gao H, Wang Y. Analysis of mechanical and vibration properties of carbon fiber reinforced polymer matrix composites with SiO2 / Al2O3 micron particles. Polym Compos. 2025 Apr;46(5):4800-14. https://doi.org/10.1002/pc.29278
[13] Mawardi I, Razak H, Akadir Z, Jaya RP. The effect of containing Al2O3 microparticles in different matrix polymers on properties of pineapple fiber-reinforced composites. Frat ed Integrità Strutturale. 2023 Dec;18(67):94-107. https://doi.org/10.3221/IGF-ESIS.67.07
[14] ASTM International. ASTM D3039/D3039M-08: Test Method for Tensile Properties of Polymer Matrix Composite Materials. West Conshohocken, PA: ASTM International; 2008.
[15] Reddy JN. Theory and Analysis of Elastic Plates and Shells. 2nd ed. Boca Raton: CRC Press; 2006. https://doi.org/10.1201/9780849384165
[16] Emad A, Idan MM. Numerical analysis of low-velocity impact behavior on composite materials. Pollack Period. 2025 Mar;20(1):95-101. https://doi.org/10.1556/606.2024.01148
[17] Hussein A, Abbas AWN, Alshubber HA. Applying the photo-elasticity method to study teeth stresses in a variety of spur gears. Pollack Period. 2025 Apr. https://doi.org/10.1556/606.2024.01248
[18] Burlayenko VN, Sadowski T. Free vibrations and static analysis of functionally graded sandwich plates with three-dimensional finite elements. Meccanica. 2020 Apr;55(4):815-32. https://doi.org/10.1007/s11012-019-01001-7
[19] Ganesh S, Kumar KS, Mahato PK. Free Vibration Analysis of Delaminated Composite Plates Using Finite Element Method. Procedia Eng. 2016;144:1067-75. https://doi.org/10.1016/j.proeng.2016.05.061
[20] Pingulkar P, Suresha B. Free Vibration Analysis of Laminated Composite Plates Using Finite Element Method. Polym Polym Compos. 2016 Sep;24(7):529-38. https://doi.org/10.1177/096739111602400712
[21] Shakouri M. Free vibration analysis of functionally graded rotating conical shells in thermal environment. Compos B Eng. 2019 Apr;163:574-84. https://doi.org/10.1016/j.compositesb.2019.01.007

Blank Page

Research on Engineering Structures & Materials
www.jresm.org

Research Article

Effect of different reinforcement methods on column-footing joint performance under seismic loading

Ibraheem H. Ridha [*,a], Bahaa H. Al-Abbas [b], Sadjad A. Hemzah [c]

Civil Engineering Department, University of Kerbala, Karbala, Iraq

Article Info

Article History:

Received 31 Oct 2025

Accepted 29 Nov 2025

Keywords:

Seismic performance;
Column-footing joint;
Reinforcement detailing;
Lateral forces;
Skeleton curve;
Axial force variation;
Modes of failure

Abstract

The seismic behavior of column–footing joints in reinforced concrete (RC) structures plays a critical role in ensuring structural stability under earthquake loading, especially near potential plastic hinge regions. This study aims to investigate the influence of different axial load levels and reinforcement configurations on the seismic performance of RC column–footing joints. Six specimens were cast using normal-strength concrete and subjected to reversed lateral cyclic loading. All specimens had identical dimensions, consisting of a 700 mm high column with a 120×120 mm cross-section placed on a 1000×300×200 mm footing. Two axial load levels were considered (40 and 70 kN), and the specimens were classified into three reinforcement configurations: (i) a conventional layout with stirrups and longitudinal bars, (ii) a modified design with additional longitudinal bars and connecting hoops, and (iii) a configuration with X-shaped diagonal reinforcement. Lateral loading was applied based on a processed ground motion from the 2003 Bam earthquake. Displacement was monitored using LVDTs, and performance was evaluated through skeleton curves reflecting changes in stiffness, strength, and ductility. Results showed that increasing the axial load reduced lateral resistance in reference specimens by 8.97%. The design with additional longitudinal bars and hoops maintained its strength (0.00% loss), while the X-shaped reinforcement exhibited a 5.56% strength gain. Under 40 kN axial load, the hoop-reinforced specimen improved by 13.49%, while the X-reinforced one slightly decreased by 1.46%. At 70 kN, both strengthened configurations showed substantial improvements of 24.67 and 14.27%, respectively. These findings highlight the effectiveness of longitudinal reinforcement under all axial conditions and the enhanced performance of diagonal X-bars under high axial loads, underscoring the importance of tailored reinforcement strategies for seismic resilience.

© 2026 MIM Research Group. All rights reserved.

1. Introduction

In framed reinforced concrete (RC) structures, the column-footing joints are considered critical regions for transferring seismic and gravity loads. Under seismic actions, these joints must sustain substantial axial gravity forces while also resisting significant shear stresses arising from bending moments in beams and columns. Inadequate joint reinforcement details can result in brittle shear failures that severely compromise the integrity of the entire structural system. Observations from past earthquakes have consistently shown that insufficient detailing at these joints causes severe damage, or even structural failure. Therefore, contemporary seismic design codes mandate robust joint confinement through closely spaced transverse reinforcement, typically comprising hoops and cross-ties, to ensure ductile joint response. However, many older R.C buildings lack such joint reinforcement, prompting extensive studies on enhanced reinforcement methods [1,2]. One of the suggested methods is the placement of X-shaped diagonal reinforcement over the joint core, which reduces dependence on traditional transverse reinforcement by forming an internal truss

*Corresponding author: ibraheem.hassan@s.uokerbala.edu.iq
[a]orcid.org/0009-0006-0782-1313; [b]orcid.org/0000-0002-1362-407X; [c]orcid.org/0000-0002-1851-737X
DOI: http://dx.doi.org/10.17515/resm2026-1312ic1031rs

mechanism to effectively transfer shear stresses. This promotes ductile beam hinging over brittle joint shear failures, leading to notable increases in joint stiffness, strength, and energy dissipation capacity. It has been shown that this reinforcement approach properly shifts the failure mechanism toward beam plastic hinge zones, thus reducing joint core cracking. Interior joints with such diagonal reinforcement fastened into beams demonstrate improved lateral load resistance and post-yield stiffness compared to joints with conventional hoops.

Moreover, it was found that inclined column bars extending through the joint outperform traditional transverse stirrups in reducing joint deformation [1,3]. These results collectively support the "strong joint weak beam" design philosophy, emphasizing that diagonal reinforcement strengthens the joint panel and shifts plastic hinge formation to adjacent structural members. Despite their advantages, diagonal bars alone are not entirely adequate substitutes for transverse collars. It has been reported that joints reinforced solely with diagonal bars still suffered shear failure; however, these failures were mostly avoided by combining diagonal reinforcement with small transverse collars. Hybrid strengthening strategies have been proposed to achieve adequate confinement without overcrowding, such as combining diagonal bars with U-shaped bars at joint interfaces. These hybrid systems significantly improve load-bearing capacity and protect the joint core. Numerous experimental studies confirm that X-shaped diagonal reinforcement enhances the seismic performance of joints without altering the overall structural geometry [2,4]. Additionally, innovative retrofitting techniques using high-strength and high-ductility materials have been extensively explored. The use of high-manganese steel bars in column base joints was found to greatly enhance ductility under seismic loads. Fiber-reinforced concrete (FRC) has also been demonstrated to replace conventional stirrups to some extent, while maintaining joint strength. Engineered cementitious composites (ECCs) offer superior shear resistance and crack control compared to conventional concrete, enabling joints to tolerate higher drift demands and energy dissipation, as shown in recent experiments [5]. Other developments include hybrid reinforcement techniques and material innovations such as internal and external casing. For instance, joint cores encased with steel-covered filler composites have been shown to significantly improve ductility and shear strength. Further, combinations of capped and prestressed bars with shape memory alloys have been proposed to enhance stabilization and delay yielding [6,7].

Nevertheless, internal diagonal reinforcement remains a simple and cost-effective method to improve joint shear strength and redirect damage away from the critical core region [2,3]. Another important factor affecting joint performance is the interaction between lateral and axial loading. Seismic events dynamically change axial forces in columns and joints, thus influencing their failure modes and deformation capacities. An increase in axial load ratio from approximately 0.08 to 0.25 was found to raise joint shear strength by about 10% due to improved confinement. However, under larger axial loads (20%–60% of the column's capacity), poorly reinforced joints can exhibit brittle shear failure and reduced ductility. It has been observed that significant variations in axial loads caused by vertical seismic actions degrade hysteretic joint performance, resulting in rapid strength deterioration and brittle failure [8]. Additionally, different axial loads have been shown to alter the lateral cyclic resistance of high-strength composite columns. Under axial loads of about 70 kN, 40 kN, and 0 kN, circular sections exhibited lateral load increases of 12.96%, 19.35%, and 5.65%, respectively; whereas square sections showed increases of 6.64%, 16.63%, and 9.36%. Moreover, circular specimens provided 12.55%, 6.25%, and 10% greater resistance than square specimens under the same axial conditions. These findings further emphasize the effect of axial force levels and cross-sectional shape on the hysteretic behavior of column elements. Alternatively, very low axial forces or tension due to uplift conditions reduce confinement efficiency and may result in premature slippage of beam-bar anchorage. Finite-element analyses have shown that under low axial loads, stirrups yielded prematurely due to inadequate confinement, whereas at higher axial loads, yielding was delayed but shear stresses within the joint core intensified. Therefore, variations in axial loading substantially affect the seismic behavior of column-footing joints, influencing shear strength, failure pattern, and plastic hinge locations in either the column or the joint itself. Recent studies have examined RC joint behavior under various axial loading conditions during cyclic lateral testing to isolate axial force effects [8,10]. Findings repeatedly

demonstrate that while high axial loads tend to induce brittle failure and reduce deformation capacity, moderate axial compression enhances shear resistance [8,11].

Unlike previous studies which typically focus on beam–column joints or utilize complex retrofitting configurations and materials, the present study explores a simplified, practical approach to improving column-footing joint behavior. The objective is to evaluate the effects of different reinforcement layouts including traditional transverse reinforcement, additional longitudinal bars with hoops, and X-shaped diagonal reinforcement on seismic performance under two axial load conditions (40 kN and 70 kN). In contrast with much of the existing literature that emphasizes beam–column interaction or uses advanced materials, this study centers on applicable reinforcement details during casting, providing insights for both new construction and practical retrofitting of deficient joints.

2. Methodology of Research and Testing Program

This paper intends to look at how various axial loads and reinforcement detailing influence the seismic performance of column-footing joints. The approach comprises two primary specimen groups: the first under a 40 kN axial load and the second under a 70 kN axial load. It also involves material property evaluation, application of simulated seismic horizontal loads, and performance assessment. See Figure 1; the flowchart below describes the whole process in detail.

2.1. Testing Program

Six reinforced concrete column-footing joints were prepared, which were then split into two primary groups based on the applied axial load. While the second group comprised three specimens under an axial load of 70 kN, the first group comprised three specimens under an axial load of 40 kN. With differences in reinforcement configuration at the joint area, both groups were created with the same size and reinforcement detail. Reinforced with 12 mm diameter longitudinal bars in the column and 6 mm diameter stirrups in both the column and the footing, the first specimen in each group was a reference specimen. Consisting of extra stirrups and extra longitudinal bars with a diameter of 6 mm, the joint area of the second specimen featured more reinforcement. Diagonally main bars placed in an X-shape inside the joint area see Figure 2 strengthened the third specimen. The size of the specimens was chosen using a scale factor of five from actual short columns with full-scale dimensions of 3500 mm in height and a cross-section of 600×600 mm. The scaled specimens were therefore built with a height of 700 mm and a cross-section of 120×120 mm. Efforts were made to obtain comparable steel-to-concrete area ratios between specimens to guarantee a fair comparison between various load cases and reinforcement configurations.

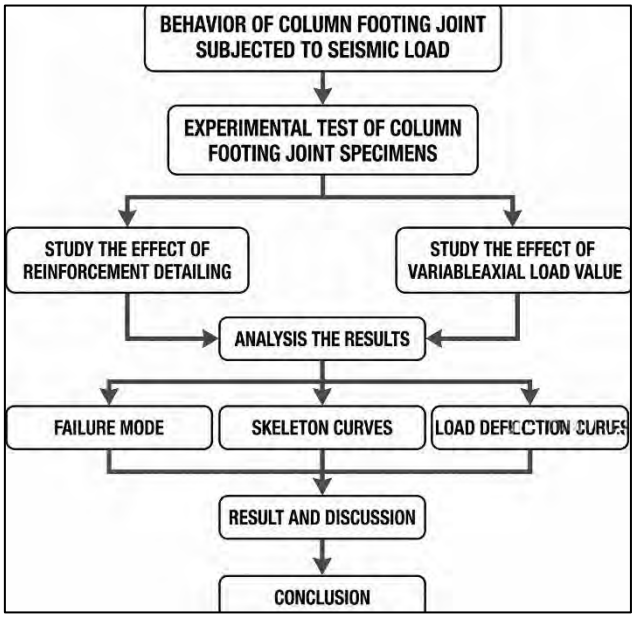

Fig. 1. Current work flowchart

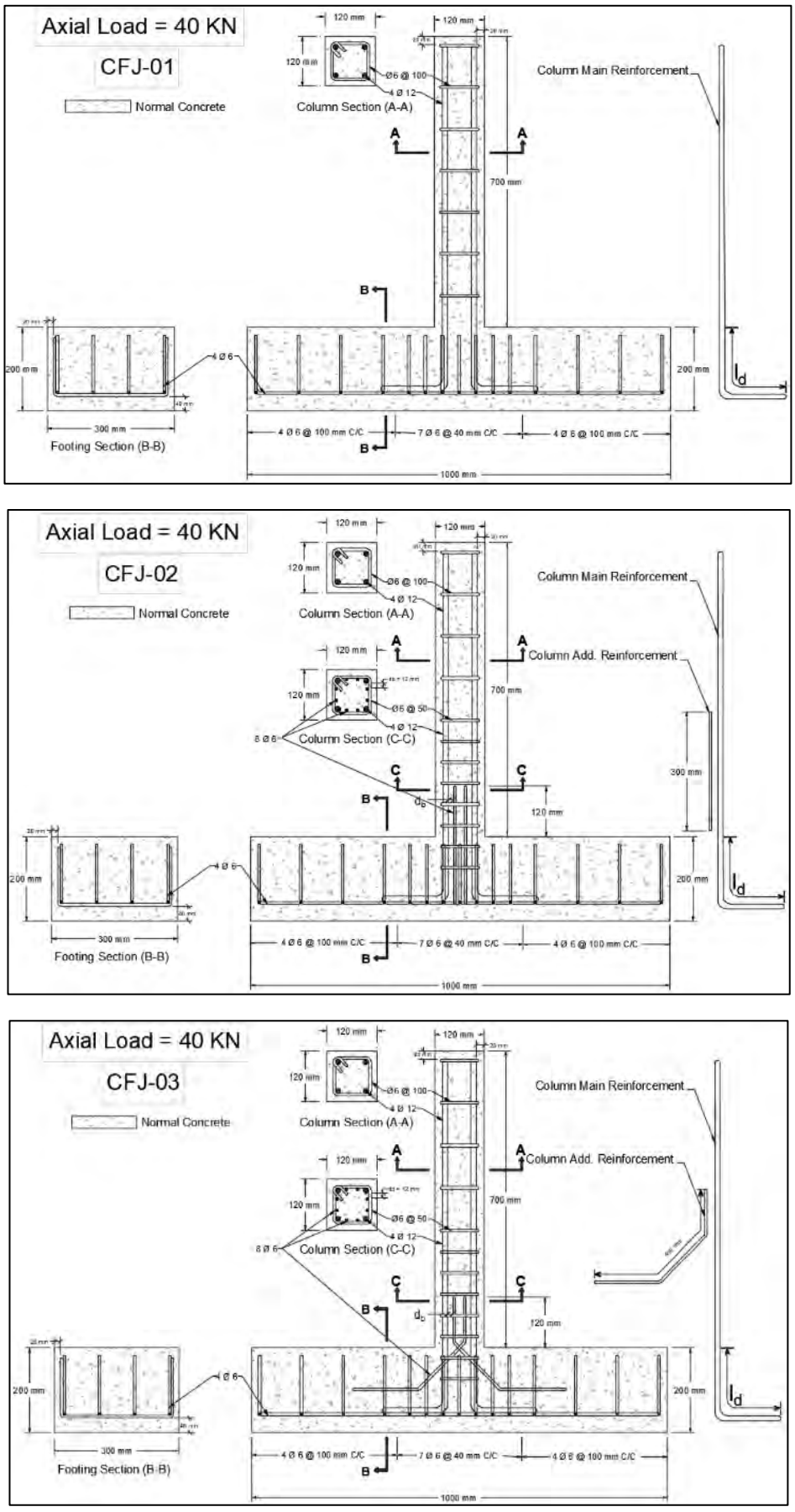

Fig. 2. Typical geometry and reinforcement details of the column–footing joint specimens (same reinforcement for all specimens; axial loads of 40 kN and 70 kN were applied) specimens

2.2. Materials

The concrete used in casting the column-footing joint specimens was made from a mix of cement, fine aggregate, coarse aggregate, water, and a superplasticizer. This mix was proportioned to achieve a compressive strength of about 31.4 MPa, following the guidelines of ACI 211.1 [13]. The exact quantities of the materials used in the mix are listed in Table 1.

Table 1. Concrete mix design for normal strength concrete (31.4 MPa)

Material	Units	Value
Cement	kg/m^3	400
Fine aggregate	kg/m^3	720
Coarse aggregate	kg/m^3	1072
Water	Liter	160
Superplasticizer	Liter	6

The concrete casting process was performed in two separate stages. Initially, the footing parts were cast and allowed adequate time to set and gain strength. After confirming that the footings had reached sufficient hardness, the columns were then cast on top in the second stage. The cement used was Ordinary Portland Cement (OPC) Type I, with a sulfate content below 2.5% [14]. The fine aggregate belonged to Zone II according to ASTM C33 [15], while the coarse aggregate was crushed gravel with a maximum size of 14 mm [15]. These materials conformed to ASTM specifications and are commonly used in construction practices in Iraq. Following the completion of casting, all specimens were cured by immersion in water for a period of 28 days until testing. The entire experimental testing work was conducted at the laboratories of the College of Engineering, University of Karbala.

2.3 Properties of Concrete

A slump test using the Abrams cone technique was conducted on fresh concrete used in the column and footing joint specimens to evaluate their properties; normal strength concrete recorded a slump value of 87 mm. Three concrete cubes measuring 100×100×100 mm were cast and tested according to BS EN 12390-3 [16] to determine the 28-day compressive strength of non-homogeneous concrete (NSC). To evaluate the flexural (rupture) strength, three concrete prisms measuring 100×100×500 mm were tested according to ASTM C 78-02 [17]. Figure 3 illustrates the test procedures and specimens; Table 2 lists the results.

(a) (b9 (c8 (d)

Fig. 3. (a) Workability test (slump test), (b) concrete strength test (compressive), (d) flexural strength test (two-point loading), (c) tensile strength test (splitting method)

2.4 Properties of Steel Reinforcement

The columns and footings were built using deformed steel bars measuring 6 mm and 12 mm in diameter. While the 12 mm bars served as the primary longitudinal reinforcement in the columns,

the 6 mm bars were used as column stirrups and foundation reinforcement. Following the ASTM A615M-05a standard [18], a computerized testing machine in the Mechanical Engineering Laboratory at the University of Karbala was used to perform tensile tests. The 6 mm bars fulfilled the Grade 75 requirements; the 12 mm bars matched the Grade 40 based on the findings. The average mechanical properties obtained from testing three specimens of each bar type are presented in Table 3.

Table 2. Concrete compressive, splitting tensile, and flexural strength values (cylinder strength estimated as 0.8 × cube strength)

No.	Concrete Compressive Strength, f'c (MPa)		Splitting Tensile Strength, f'ct (MPa)	Rupture Modulus, fr (MPa)
	Cube	Cylinder		
1	43.6	34.9	2.95	3.89
2	39.5	31.6	2.82	3.67
3	34.5	27.6	2.77	3.75
Average	39.2	31.4	2.85	3.77

Table 3. Reinforcing steel bars' properties

Nominal Diameter (mm)	Measured Diameter (mm)	Yield Strength (MPa)	Ultimate Strength (MPa)	Modulus of Elasticity (GPa)	Elongation (%)	ASTM A615/A615M-05a		
						Min. fy, (MPa)	Min. Elon. (%)	Grade
6	5.5	658.4	691	200	12.1	≥520	≥7	G75
12	11.83	419.5	579	200	16.3	≥276	≥12	G40

2.5 Seismic Load Application

Seismic loading in this work was simulated using actual earthquake data from the PEER ground motion database, namely the Bam, Iran event (2003) at Mohammad Abad Madgon Station (magnitude 6.6) [19]. SeismoSignal processed the acceleration record for baseline correction and filtering to guarantee data accuracy. The Central Difference Method (CDM) was then applied to numerically calculate the lateral displacement responses under axial loads of 40 kN and 70 kN, representing one- and two-story load conditions, respectively [20]. The computed displacement waveforms were imported into LabVIEW and used during the experimental testing phase. Structural responses were monitored and recorded to evaluate performance under seismic loads. Due to the long duration of the earthquake record, only the most critical portion was selected to ensure practical application in the laboratory see Figure 4.

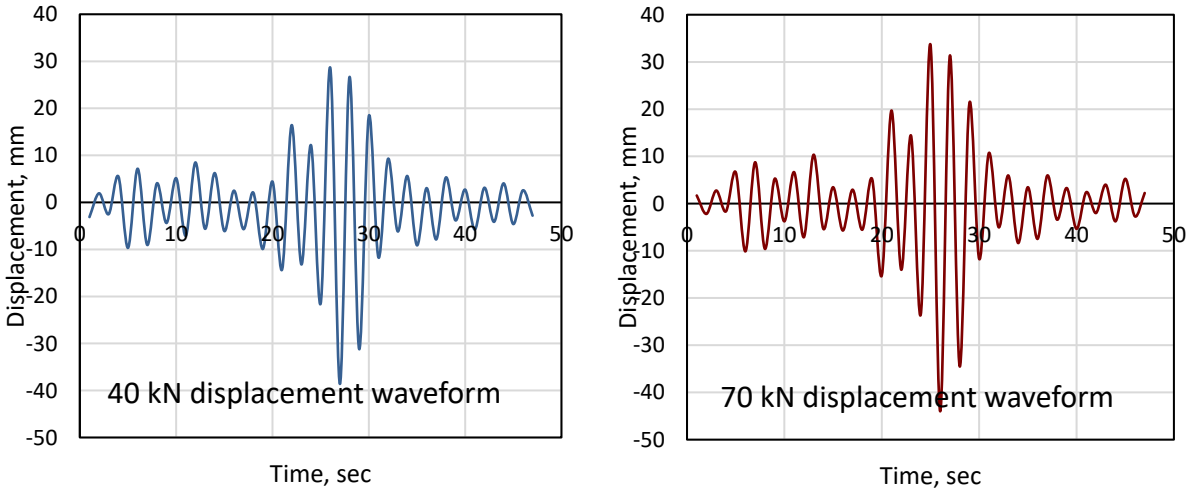

Fig. 4. Applied displacement-time patterns corresponding to 40 kN and 70 kN axial loads

3. Results and Discussion

The influence of reinforcement detailing on the behavior of the column-footing joint specimens under lateral loading was clearly observed during testing. To monitor the lateral displacement at the joint region, one LVDT was installed, as illustrated in Figure 5.

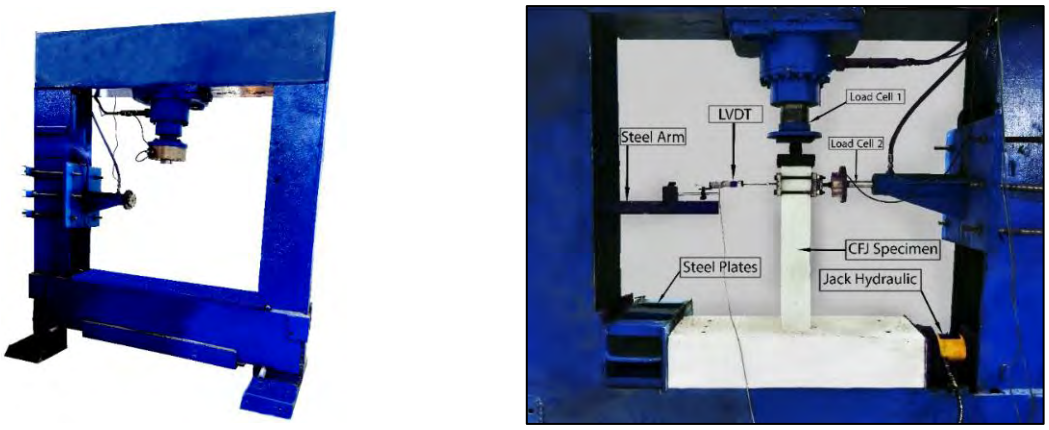

(a) (b)

Fig. 5. Test Setup: (a) general view of the testing frame and (b) specimen during testing

It was noted that as the lateral load increased, visible cracking developed in the concrete, including horizontal (latitudinal) cracks and inclined lattice-type cracks near the joint. Figure 5(a) presents the general layout of the testing frame, while Figure 5(b) shows the specific setup used for the specimens. The comparison between the different reinforcement configurations such as the addition of diagonal main bars in an X-shape, extra longitudinal bars, and additional stirrups revealed clear differences in structural response. The load–displacement curves for all tested specimens are presented in Figure 6.

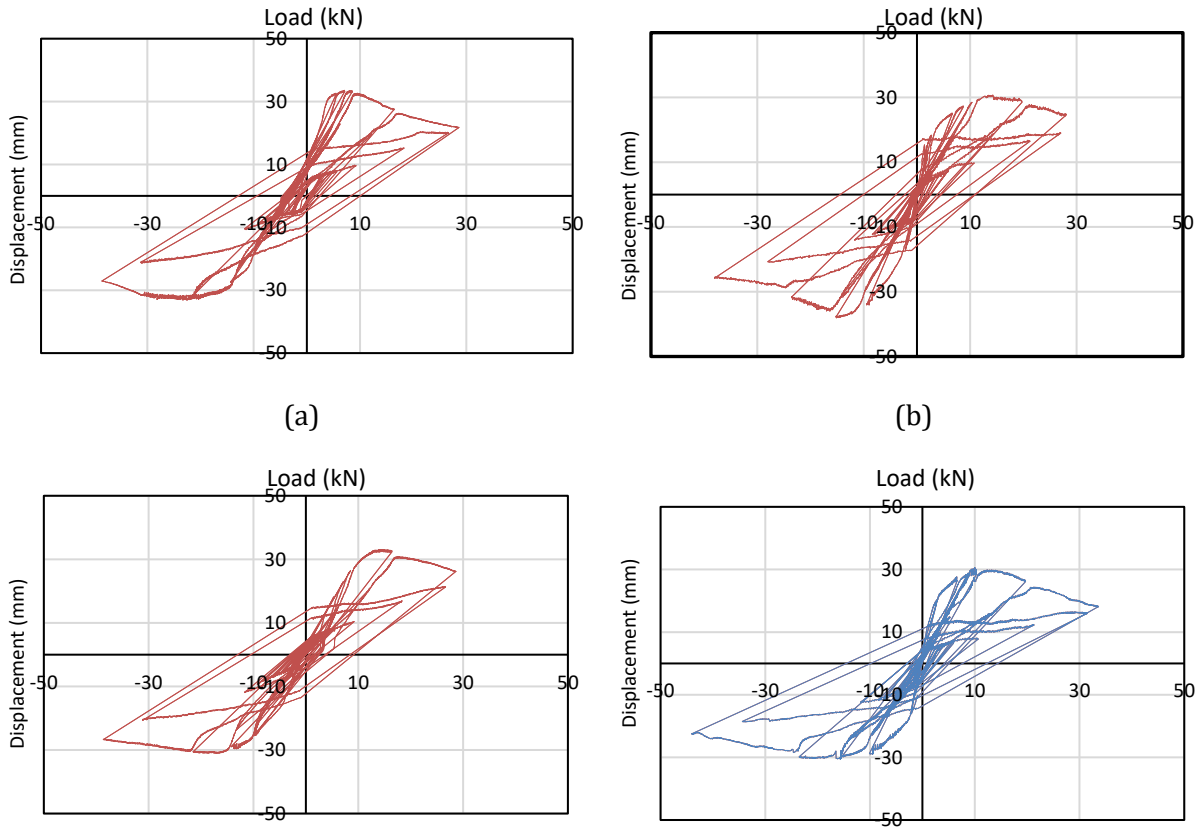

(a) (b)

(c) (d)

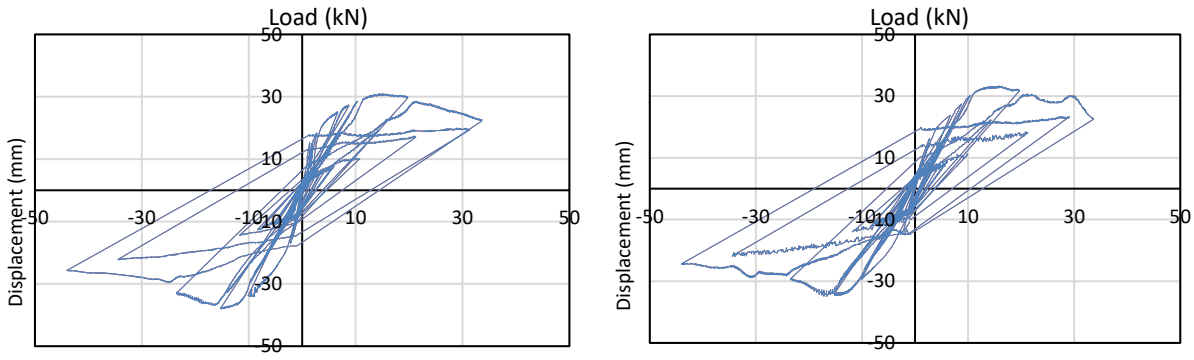

(e) (f)

Fig. 6. Lateral force–displacement response for specimens: (a) CFJ-01, (b) CFJ-02, (c) CFJ-03, (d) CFJ-07, (e) CFJ-08, (f) CFJ-09

Table 4. Results of column-footing joint specimens under lateral cyclic loading

No.	Specimen symbol	Axial load (kN)	Maximum lateral load (kN)	Displacement at max. lateral load (mm)	Max. displacement (mm)	Lateral load at max. displacement (kN)
1	CFJ-01	40	33.57	7.07	-38.57	-27.09
2	CFJ-02	40	-38.10	-15.15	-38.05	-25.81
3	CFJ-03	40	33.08	14.52	-38.67	-26.75
4	CFJ-07	70	30.56	9.99	-44.07	-22.49
5	CFJ-08	70	-38.10	-15.15	-44.01	-25.70
6	CFJ-09	70	-34.92	-16.64	-44.04	-24.39

3.1 Mode of Failure

During the test, all specimens cracked mostly in horizontal and diagonal directions in the column-footing joint area. At the joint interface, tiny cracks first developed as the lateral displacement from the earthquake wave increased, then they progressively grew and spread. Those with a 70 kN axial load experienced less but more severe fractures; these typically generated a predominant radial crack that sometimes extended to the base. At 40 kN, cracks appeared sooner and spread more widely across the joint. Reinforcement detailing was critical, with the reference specimens (CFJ-01 and CFJ-07) showing less confinement and faster crack growth, while specimens (CFJ-02 and CFJ-08) with additional longitudinal bars and collars showed more controlled and narrower cracks. Specimens with X-shaped reinforcement (CFJ-03 and CFJ-09) performed better, with less damage and delayed crack onset. By displaying the development of these cracks at different waveform phases, Figure 7 highlights how the axial load and reinforcement detailing affected the joint's failure behavior.

(a) (b)

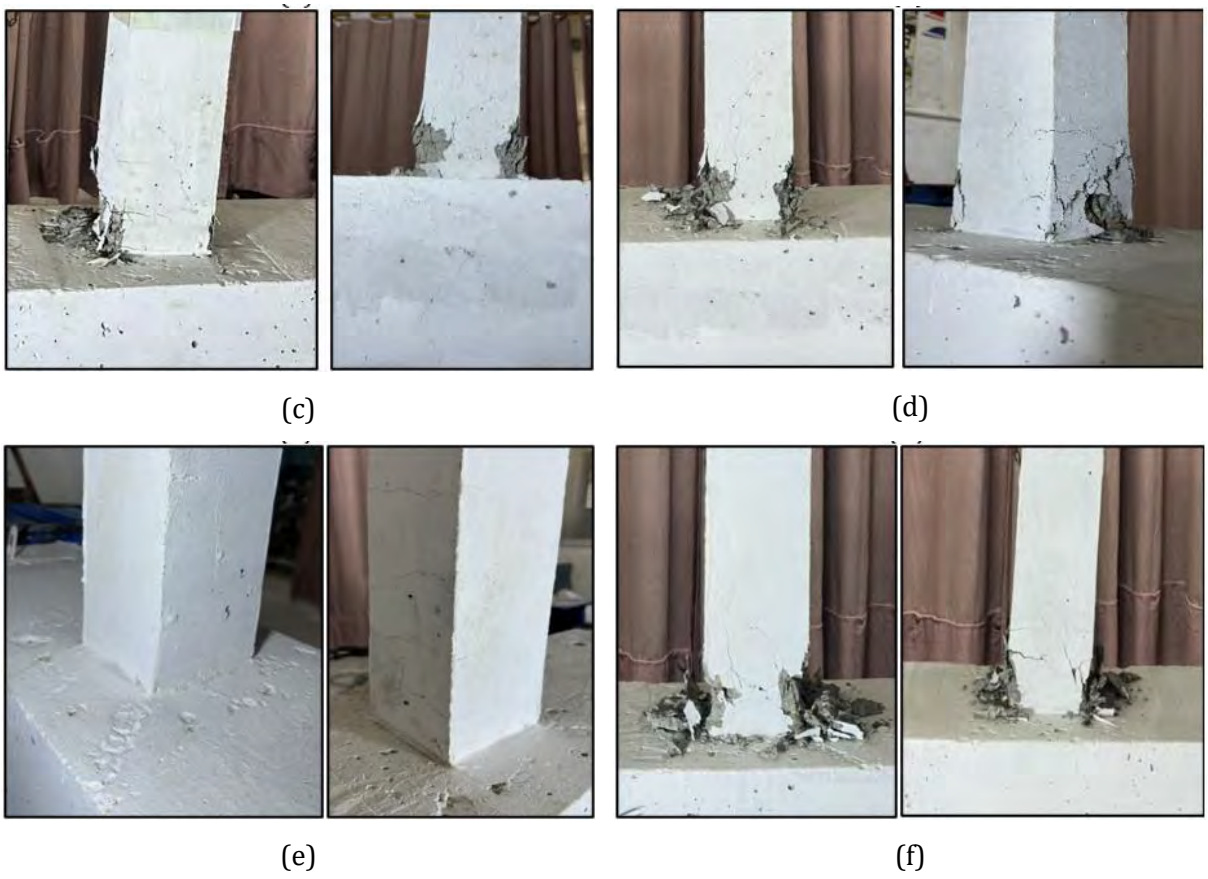

Fig. 7. Crack development in the joint area during seismic loading: (a) CFJ-01, (b) CFJ-02, (c) CFJ-03, (d) CFJ-07, (e) CFJ-08, (f) CFJ-09

3.2 Skelton Curves

Skeletal curves were produced by integrating the maximum lateral load and related horizontal displacement from each loading level throughout the first cycle. The skeleton curve predicts the inelastic cyclic response, deformation capacity, strength, and ductility of specimens under seismic waves. Figure 8 shows the skeleton curves for a simple comparison of the specimens.

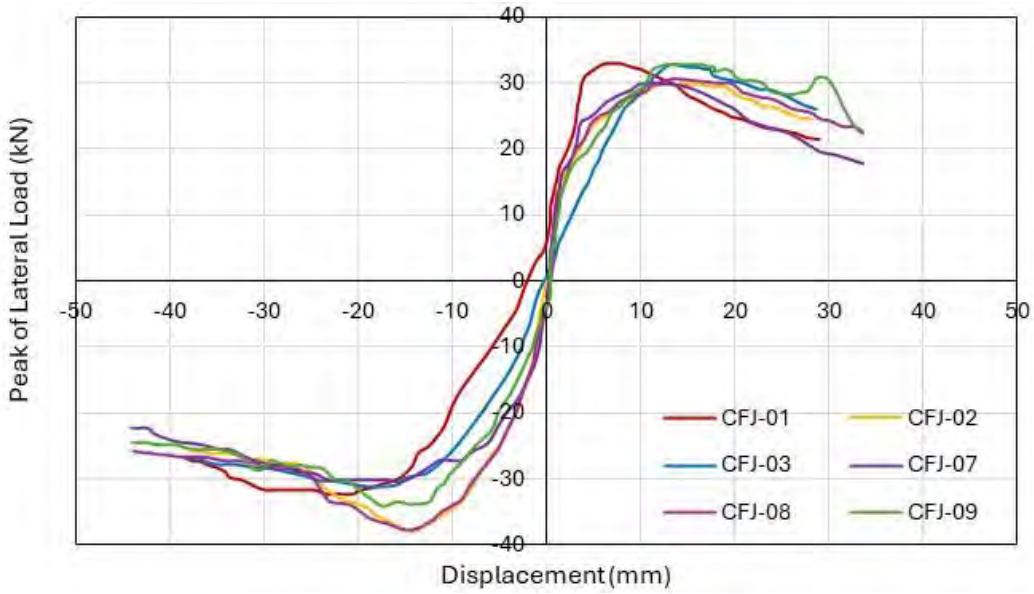

Fig. **8**. Skeleton curve for tested specimens

The behavior and results of an experimental test run under two axial load levels and reversed cyclic lateral loading on six column-footing joint specimens with variable reinforcement detailing. This study shows that:

The Impact of an Axial Load's Value. The lateral cyclic resistance was affected in different ways by raising the axial load from 40 kN to 70 kN under the same joint detailing:

- The peak lateral capacity of the reference specimen (CFJ-01 vs. CFJ-07) dropped by 8.97%.
- There was no change (0.00%) in the specimen with extra longitudinal bars and hoops (CFJ-02 vs. CFJ-08).
- There was a 5.56% increase in the specimen with diagonal X-shaped bars and hoops (CFJ-03 vs. CFJ-09).

Reinforcement Detailing's Impact.

(a)At an axial load of 40 kN (CFJ-01 baseline = 33.57 kN):

- CFJ-02 (longitudinal + hoops) gained 13.49% to 38.10 kN.
- CFJ-03 (X-shaped + hoops) dropped 1.46% to 33.08 kN.

(b) At an axial load of 70 kN (CFJ-07 baseline = 30.56 kN):

- CFJ-08 (longitudinal + hoops) gained 24.67% to 38.10 kN.
- CFJ-09 (X-shaped + hoops) gained 14.27% to 34.92 kN.

4. Conclusion

Axial load magnitude and reinforcement detailing on lateral cyclic resistance clearly show a correlation in the experimental data. Increasing the axial load from 40 kN to 70 kN lowered the capacity of the unstrengthen specimen by 8.97%, so increasing shear demand without confinement. The specimen having additional longitudinal bars and hoops maintained the same peak resistance at both load levels (38.10 kN) by means of efficient confinement and load redistribution. Proposing that such detail is more effective when axial compression is high, the X-shaped reinforcement enhanced performance only under higher axial load, hence increasing capacity by 5.56% compared to its 40 kN counterpart. Moreover, X-shaped bars slightly lost strength by 1.46% while longitudinal reinforcement increased it by 13.49% at 40 kN. At 70 kN, the same reinforcements increased capacity by 24.67% and 14.27% respectively. These results confirm that whereas longitudinal bars with hoops provide consistent performance under various axial conditions, X-shaped bars are more condition-sensitive.

References

[1] Shen X, Li B, Chen YT, Tizani W. Seismic performance of reinforced concrete interior beam-column joints with novel reinforcement detail. Engineering Structures. 2021 Jan 15; 227:111408. https://doi.org/10.1016/j.engstruct.2020.111408

[2] Tiwary AK, Singh S, Chohan JS, Kumar R, Sharma S, Chattopadhyaya S, Abed F, Stepinac M. Behavior of RC beam-column joints strengthened with modified reinforcement techniques. Sustainability. 2022 Feb 8;14(3):1918. https://doi.org/10.3390/su14031918

[3] Rajagopal S, Prabavathy S. Investigation on the seismic behavior of exterior beam-column joint using T-type mechanical anchorage with hair-clip bar. Journal of King Saud University - Engineering Sciences. 2015. Online ahead of print. https://doi.org/10.1016/j.jksues.2013.09.002

[4] Tsonos AD, Kalogeropoulos G, Iakovidis P, Bezas MZ, Koumtzis M. Seismic performance of RC beam-column joints designed according to older and modern codes: An attempt to reduce conventional reinforcement using steel fiber reinforced concrete. Fibers. 2021 Apr;9(4):45. https://doi.org/10.3390/fib9070045

[5] Zhang X, Li B. Seismic performance of RC beam-column joints constructed with engineered cementitious composites. Journal of Structural Engineering. 2020 Jun;146(6):04020271. https://doi.org/10.1061/(ASCE)ST.1943-541X.0002824

[6] Dong Y, Yang X, Liu X, Qiu T, Zhou J. Seismic behavior of concrete beam-column joints reinforced with steel-jacketed grouting composite. Buildings. 2024 Oct 10;14(10):3239. https://doi.org/10.3390/buildings14103239

[7] Sharif H, Ketabi MS. An improved plastic hinge relocation technique for RC beam-column joints: Experimental and numerical investigations. Bulletin of Earthquake Engineering. 2020 Jul;18(14):4191-4225. https://doi.org/10.1007/s10518-020-00855-7
[8] Yalciner H, Kumbasaroglu A. Effect of variable axial load with different amplitude, frequency and phase on seismic behavior of RC columns: Experimental study and numerical simulation. ACI Structural Journal. 2020 Jul;117(4).
[9] Xu G, Wu B, Jia D, Xu X, Yang G. Quasi-static tests of RC columns under variable axial forces and rotations. Engineering Structures. 2018 Aug 1; 162:60-71. https://doi.org/10.1016/j.engstruct.2018.02.004
[10] Sakr MA, Seleemah AA, El-Korany T, Saad AG. Exterior beam-column joints under varying column axial load. International Journal of Advanced Structural and Geotechnical Engineering. 2019;3(2):174-186. https://doi.org/10.21608/asge.2019.270779
[11] Hu H, Chen G, Yuan H, Xu Z. Seismic strategy of non-seismically designed reinforced concrete frames under high axial load ratios. Scientific Reports. 2021 Jun 14; 11:13639.
[12] Kadhim ZF, Al-Abbas BH, Al-Khafaji AGA. Structural behavior of high-strength composite columns under lateral cyclic loads. College of Engineering, University of Kerbala. 2025. https://doi.org/10.1063/5.0236424
[13] ACI Committee 211. Standard Practice for Selecting Proportions for Normal, Heavyweight, and Mass Concrete (ACI 211.1-91). Farmington Hills (MI): American Concrete Institute; 2002.
[14] ASTM C150/C150M-22. Standard Specification for Portland Cement. West Conshohocken (PA): ASTM International; 2022.
[15] ASTM C33/C33M-18. Standard Specification for Concrete Aggregates. West Conshohocken (PA): ASTM International; 2018.
[16] British Standards Institution. BS EN 12390-3: Testing hardened concrete - Part 3: Compressive strength of test specimens. London (UK): BSI; 2019.
[17] ASTM C78-02. Standard Test Method for Flexural Strength of Concrete (Using Simple Beam with Third-Point Loading). West Conshohocken (PA): ASTM International; 2002.
[18] ASTM A615M-05a. Standard Specification for Deformed and Plain Carbon-Steel Bars for Concrete Reinforcement. West Conshohocken (PA): ASTM International; 2005.
[19] Pacific Earthquake Engineering Research Center (PEER). Ground Motion Database. University of California, Berkeley (USA).
[20] Chopra AK. Dynamics of Structures: Theory and Applications to Earthquake Engineering. 4th ed. Upper Saddle River (NJ): Prentice Hall; 2012.

Blank Page

Research on Engineering Structures & Materials
www.jresm.org

Research Article

Evaluating the role of nano-clay and nano-metakaolin in mitigating the collapsibility of gypseous soils

Mahdi Karkush [*,1,4,a], Alaa D. Salman [2,b], Abdulkareem N. Abbood [3,c], Rafal Emad [4,d]

[1]*Dept. of Construction and Projects, University of Baghdad, Baghdad, Iraq*
[2]*Dept. of Surveying Eng., University of Baghdad, Baghdad, Iraq*
[3]*Dept. of Building Eng. and Construction Project Management, Ashur University, Baghdad, Iraq*
[4]*Dept. of Civil Eng., University of Baghdad, Baghdad, Iraq*

Article Info

Article History:

Received 20 Nov 2025
Accepted 21 Mar 2026

Keywords:

Gypseous soils;
Collapse potential;
Nano-clay;
Nano-metakaolin;
Soil stabilization

Abstract

Gypseous soils present significant geotechnical challenges due to their highly variable and moisture-sensitive behavior. Although often considered mechanically stable in dry conditions, these soils are susceptible to sudden volumetric collapse upon wetting, leading to severe structural and infrastructural damage. This study evaluates the potential of nanomaterials specifically nano-clay and nano-metakaolin as stabilizing agents to mitigate the collapse susceptibility of gypseous soils. Representative soil samples, containing approximately 54% gypsum, were collected from Tikrit, Iraq, located about 200 km north of Baghdad. The experimental program involved preparing soil specimens treated with three nanomaterial contents (1%, 2%, and 3% by dry weight) and subjecting them to collapse potential and compressibility tests under both dry and soaked conditions. The results indicated that the inclusion of nanomaterials substantially decreased collapse potential and compressibility, with improvements becoming most significant at contents above 2%. At 3% incorporation, settlement was reduced by 40–60% before soaking and by 25–40% after soaking. These findings demonstrate that nanomaterials, particularly at higher dosages, enhance soil stability by reducing susceptibility to collapse and deformation. The study highlights the effectiveness of nanotechnology-based additives as a sustainable and innovative solution for stabilizing problematic gypseous soils in arid and semi-arid regions.

© 2026 MIM Research Group. All rights reserved.

1. Introduction

Gypseous soils represent a subclass of collapsible soils that pose considerable geotechnical challenges owing to their unstable behavior under fluctuating moisture conditions. These soils are predominantly encountered in arid and semi-arid regions, where gypsum ($CaSO_4 \cdot 2H_2O$), a moderately soluble mineral, functions as a cementing agent between soil particles. While gypseous soils often exhibit acceptable strength in their dry state, their structural stability deteriorates rapidly upon wetting or saturation, resulting in sudden collapse or excessive settlement [1-3]. This collapse, commonly referred to as hydro collapse or hydro compaction, occurs primarily due to the dissolution of gypsum, which disrupts interparticle cementation and leads to particle rearrangement even in the absence of additional external loads. The underlying mechanism of collapse involves the dissolution of gypsum, which increases pore water content, reduces effective stress, and weakens interparticle bonding. Wetting accelerates this process, causing disintegration of the soil fabric, an increase in pore volume, and a consequent loss in shear strength and stiffness. Immersion in water further intensifies gypsum dissolution, along with other calcium-based minerals such as calcite, thereby reducing the soil's ability to sustain applied loads [4,5]. Several

*Corresponding author: mahdi_karkush@yahoo.com
[a]orcid.org/0000-0003-1304-0303; [b]orcid.org/0000-0003-1594-3979; [c]orcid.org/0009-0002-5309-7750
DOI: http://dx.doi.org/10.17515/resm2026-1351ic1120rs

approaches have been developed to mitigate the collapse potential of gypseous soils. Conventional soil stabilization techniques typically involve the use of chemical additives such as lime, ordinary Portland cement, bitumen, and emulsified asphalt [6–8]. These stabilizing agents improve soil engineering properties primarily through physicochemical interactions, including cation exchange, flocculation–agglomeration, and pozzolanic reactions. The pozzolanic process leads to the formation of cementitious compounds such as calcium silicate hydrates (C–S–H) and calcium aluminate hydrates (C–A–H), which bind soil particles together and enhance interparticle bonding. As a result, treated soils exhibit increased shear strength and stiffness, reduced compressibility and plasticity, improved durability, lower permeability, and lower collapsibility [6–8]. These mechanisms collectively contribute to improved load-bearing capacity and long-term stability of problematic soils. However, while deep replacement and similar ground improvement methods can be effective, they are often economically unfeasible for large-scale applications. Consequently, increasing attention has been directed toward in-situ stabilization methods that improve soil performance without extensive excavation or replacement.

In this context, nanotechnology has emerged as a promising avenue in geotechnical engineering. Nanomaterials such as nano-clay and nano-metakaolin, owing to their ultrafine particle size and exceptionally high surface area, improve soil–particle interactions, refine pore structure, and accelerate the development of cementitious products [9,10]. Their ability to penetrate the soil microstructure enables pore filling and enhanced bonding between soil particles, leading to improved strength and durability. Although still an emerging field, several studies have demonstrated the effectiveness of nanomaterials in enhancing mechanical behavior, durability, and resistance to moisture-induced collapse in problematic soils [11,12]. Nanoparticles have been reported to reduce hydraulic conductivity, increase cohesion and internal friction, and mitigate collapse potential through their high reactivity and pozzolanic activity. A review of prior research on the stabilization of gypseous soils with nanomaterials highlights several consistent trends:

- The incorporation of nanomaterials reduced settlement by approximately 40–60%, depending on the dosage. This indicates a marked enhancement in the initial stiffness and structural of the soil.
- Even under saturated conditions, nanomaterial-treated soils exhibited a 25–40% reduction in settlement, confirming the durability and moisture resistance imparted by nanoparticle modification.
- The addition of nanomaterials significantly lowered soil compressibility, as reflected in decreased compression index (Cc) values and increased pre-consolidation pressure, thereby improving the load-bearing capacity.
- The most effective performance was consistently reported at 3% nanomaterial content, suggesting the existence of a threshold beyond which sufficient nanoparticle dispersion and reactivity achieve optimum stabilization.
- Both cohesion (c) and the angle of internal friction (ϕ) improved with nanomaterial treatment, particularly after curing, demonstrating the nanoparticles' role in strengthening interparticle bonding.
- Extended curing periods further enhanced soil strength, as continued reactions between nanoparticles and the soil matrix promoted additional bonding and pore structure refinement over time.

In the present study, gypseous soil samples containing 54% gypsum were collected from the Tikrit region to investigate the effect of nanomaterials on collapse potential and shear strength. Two types of nanomaterials nano-clay and nano-metakaolin were incorporated at varying dosages of 1%, 2%, and 3% by dry soil weight. Treated samples were subjected to curing and soaking to simulate field conditions and to evaluate their time-dependent performance. This study aims to systematically investigate the effectiveness of incorporating nanomaterials specifically nano-clay (NC) and nano-metakaolin (NM) into gypseous soils to achieve two primary geotechnical enhancements:

- Improvement of bearing capacity through microstructural modification, including pore filling, particle interlocking, and the formation of cementitious compounds; and

- Mitigation of foundation settlement by employing particle-scale stabilization mechanisms that reduce soil collapsibility and enhance resistance to moisture-induced volumetric changes.

2. Soil Sampling and Materials

2.1. Soil Sampling and Characterization

The gypseous soil employed in this study was obtained from a site located near Tikrit University, approximately 20 km southeast of Tikrit City and 220 km north of Baghdad, Iraq (34°40′51″N 43°39′17″E). The soil was excavated from depths ranging between 0.5 and 1.5 m below the natural ground surface, where field observations confirmed the presence of a gypsum-rich stratum. Laboratory analysis indicated that the sampled soil contained approximately 54% gypsum by weight, classifying it as highly collapsible. Upon collection, the soil was air-dried under controlled laboratory conditions for 48 hours to minimize moisture-induced changes and ensure consistency during testing. After oven-drying, the gypsum soil was manually crushed and homogenized using a mechanical mortar and pestle to break down agglomerated clumps and achieve a uniform, fine-grained texture. This manual crushing ensured consistent particle size distribution and minimized the presence of large aggregates that could bias experimental results. Similar procedures have been employed in previous soil stabilization studies to ensure uniformity in soil behavior across test samples. A comprehensive series of physical and chemical characterization tests was conducted in accordance with the procedures recommended by Head [13,14]. The tests included: Grain size distribution, Atterberg limits, Specific gravity, Natural water content, Gypsum content, and Soil classification. The grain size distribution curve of the untreated gypseous soil is shown in Figure 1, while the detailed results of the laboratory characterization are summarized in Table 1.

Table 1. Geotechnical and chemical properties of the investigated gypseous soil

Property	Value	Specification	Property	Value	Specification
Gs	2.54	ASTM D792-20	pH	8.01	
γ_{dmax}	17.6 kN/m^3	ASTM D698	OMC	0.34%	
O. M.C.	11.8%	ASTM D4254	$CaCO_3$	4.6%	
D_{10}, D_{30}, D_{60} (mm)	0.13,0.21,0.41		Cl^-	0.057 mg/l	
Sand, S	94.4%		GC	54%	
Fines	5.6%	ASTM D-422	EC	2.43 µS/cm	ASTM D1125
Gravel	0%		ESP	13%	
Soil type (USCS)	SP		CEC	6.54 me/100g	ASTM D7503
TSS	78.5%	Earth manual E8	Ca	49.5%	
SO_3	26.75%	BS 1377: part 3	S	41.7%	
Fe	5.35%		Quartz, Gypsum, and Dolomite		XRD

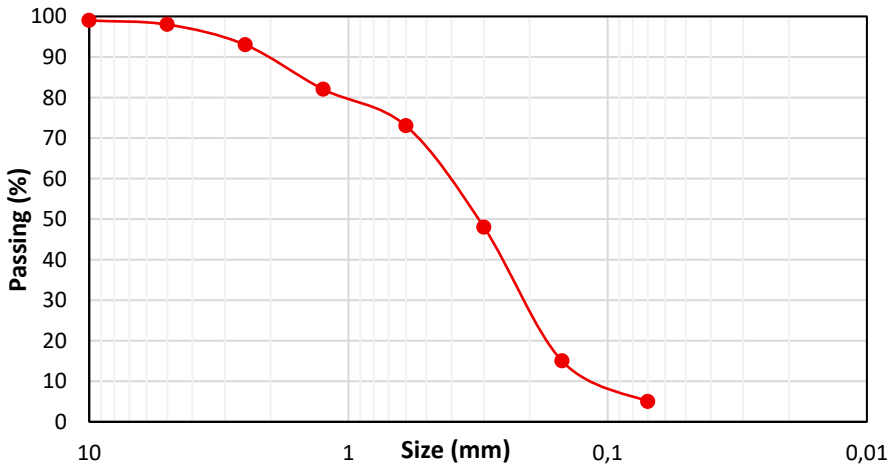

Fig. 1. Grain-size distribution curve of gypseous soil sample

2.2. Nanomaterials

Nano clay (NC) is synthesized primarily through mechanical exfoliation, a process that separates layered clay minerals into ultrafine particles with nanometric dimensions. The concentration of nano clay (NC) suspensions in water was adjusted based on soil texture, mineralogy, and engineering requirements, using mixing ratios of 1%, 2%, and 3% by dry weight of soil. A key parameter in preparing stable suspensions is the compound viscosity, which is strongly influenced by soil–solution interactions, particularly pH and salinity. From a practical perspective, NC is considered one of the most cost-effective nanomaterials and is extensively utilized in the production of high-performance nano-cementitious composites. Structurally, nano clay consists of silicate platelets with an approximate thickness of 1 nm and lateral dimensions in the range of 150–300 nm [15]. These morphological features, coupled with its chemical reactivity, enable NC to exhibit pozzolanic behavior at the nanoscale, thereby enhancing soil stabilization and accelerating strength development [11,16]. The particle size of NC in the gamma phase is typically within the range of 1–2 nm, underscoring its extremely fine-scale characteristics. A summary of the principal physical and chemical properties of NC is presented in Table 2.

Table 2. Physical properties and chemical composition of Nano clay

Properties	Value	Oxide composition	Content, %
Type of mineralization	Montmorillonite	Na_2O	0.98
Density (kN/m^3)	1.5 – 1.7	MgO	3.29
Diameter	1-2 nm	Al_2O_3	19.60
Special surface area	220-270	SiO_2	50.95
Conductivity of electrical	-25	K_2O	0.86
Coefficient of ion exchange	48	Cao	1.97
Empty gap	60 A	TiO_2	0.62
Color	Light yellow	Fe_2O_3	5.62
Moisture	1 –2%	LOI	15.45

Table 3. Physical properties and chemical composition of Nano-metakaolin

Properties	Value	Oxide composition	Content, %
Type of mineralization	Calcined kaolin	Na_2O	0.08
Density(kN/m^3)	0.5 – 0.7	MgO	0.151
Diameter	30 nm	Al_2O_3	45±2
Special surface area	100-150	SiO_2	53±2
Conductivity of electrical	-29	K_2O	0.071
Coefficient of ion exchange	48	Cao	0.193
Empty gap	60 A	TiO_2	0.78
Color	Off white	Fe_2O_3	0.268
Moisture	0.5%	LOI	13.56

Nano-metakaolin (NM) is a non-metallic mineral obtained through the controlled calcination of kaolinitic clay and claystone, consisting predominantly of minerals belonging to the kaolinite group. In its purified state, kaolin is characterized by its white color, smooth texture, and plasticity, making it a valuable industrial raw material. Metakaolin, and particularly its nanoscale derivative, exhibits high thermal stability and significant pozzolanic activity, which contribute to its widespread use in engineering and industrial applications. Owing to these properties, NM is extensively employed in the production of ceramics, refractory products, and specialty papers. Beyond these traditional applications, NM also plays a critical role in the manufacturing of paints, rubber composites, fillers, and enamel coatings, owing to its fine particle size, reactivity, and surface area. From a construction materials perspective, nanomaterials are widely recognized as supplementary cementitious materials (SCMs) that contribute to improved performance in blended binders. They accelerate pozzolanic reactions, refine pore structure, and enhance strength development, durability, and resistance to chemical degradation [17,18]. Notably, NM is also regarded as a key raw material in the production of high-quality white cement. The fundamental

physical and chemical properties of nano-metakaolin, as reported in the literature, are summarized in Table 3 [19].

3. Physical Model and Testing

The experimental arrangement, illustrated in Figure 2, comprised a rigid soil container with internal dimensions of 600×600×400 mm, supported by a steel loading frame to ensure structural stability during testing. A square steel foundation plate measuring 100×100×20 mm was positioned at the center of the container to apply vertical loading. The loading process was executed using a mechanical hydraulic jack, securely mounted on the steel frame to deliver controlled and gradual load increments to the foundation model [20-22]. To simulate precipitation events, a movable rainfall simulation system was incorporated into the setup, enabling uniform wetting of the soil surface under controlled conditions. Vertical displacement of the foundation plate was continuously monitored using a Linear Variable Differential Transformer (LVDT), which was connected to a data acquisition system (Data Logger) to record real-time settlement data with high precision. Additional instrumentation and accessories integrated into the setup included:

- A 15-bar capacity load cell for accurate measurement of applied loads,
- An air compressor to operate pneumatic components where necessary,
- A nylon sheet to isolate the loading area during selected tests,
- A universal power supply system to maintain uninterrupted operation of equipment,
- A steel movable girder and fixed vertical loading frame to ensure stable alignment and uniform transmission of loads.

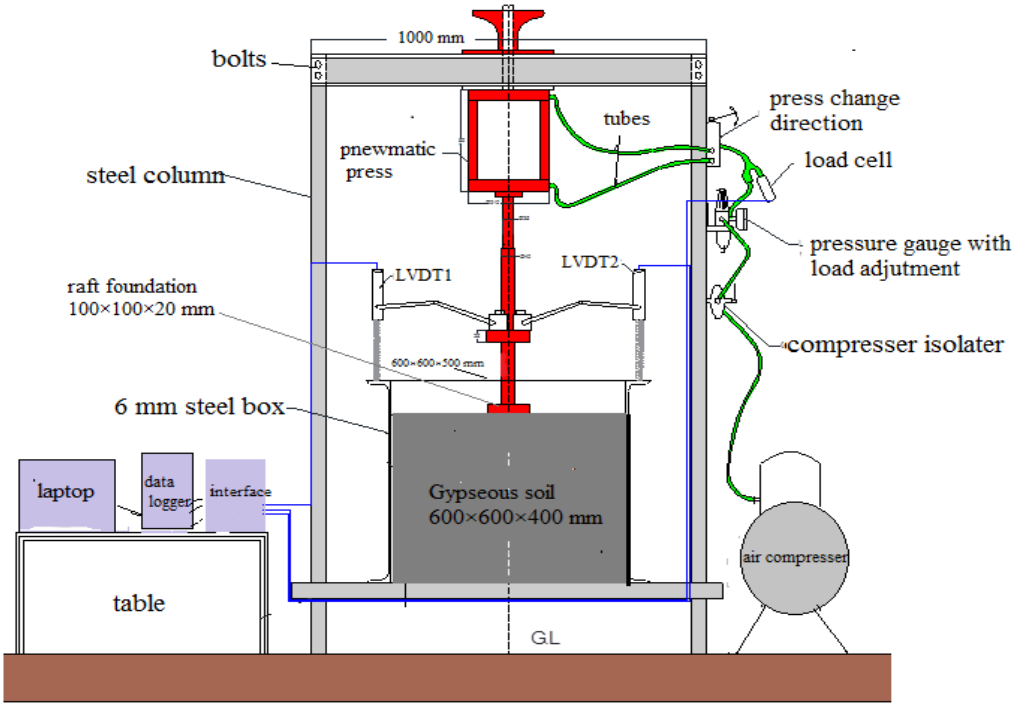

Fig. 2. Schematic diagram of physical model used in testing the soil samples

A controlled raining technique was employed to deposit the dry gypseous soil into the test container, ensuring the formation of a uniform soil layer with the desired density. For this purpose, a custom-designed raining system was developed. The effectiveness of this technique is governed primarily by two parameters: the drop height and the discharge rate, both of which directly influence the final density of the deposited soil layer [23]. To regulate the fall height, a movable roller mechanism was mounted at the top of the container, allowing precise adjustment of the soil drop distance. A series of four preliminary calibration trials were performed to determine the optimal fall height for achieving the target density. During these trials, the drop height was systematically varied while maintaining a constant fill volume. The in-situ density achieved in each trial was assessed by collecting soil samples in pre-weighed metal tins of known volume, placed at

multiple locations within the container. The measured densities were then used to calculate the relative density (Dr), based on the maximum and minimum void ratios of the soil. The results were plotted as relative density versus drop height to establish the correlation. As shown in Figure 3, the target relative density of 40% was attained at a fall height of 725 mm. The fall height (725 mm) was therefore adopted in all subsequent tests to maintain uniform and consistent soil placement conditions.

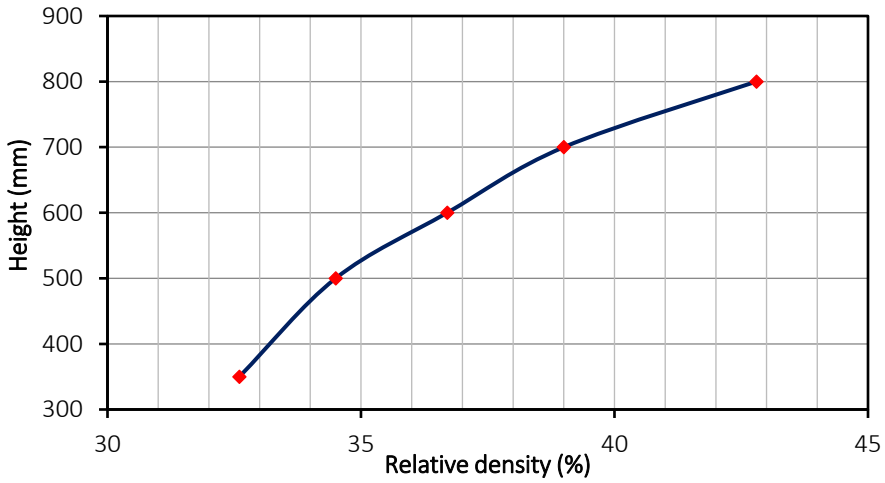

Fig. 3. Calibration curve of raining technique used in preparation of gypseous soil sample in the physical model

The mixing of nanomaterials with dry gypseous soil was carried out in two stages to ensure homogeneous soil samples. In the present study, the total volume of dry soil was first divided into several portions and placed in a square container measuring 500×500 mm. Each portion was evenly spread, and the required amount of nanomaterial was uniformly distributed over the soil surface using a fine sieve #200. In the second stage, all portions were combined and manually mixed for a minimum of 10 minutes to achieve uniform dispersion of the nanomaterials and ensure sample homogeneity. A comprehensive experimental study was carried out to investigate the effect of nanomaterials on the geotechnical behavior of gypseous soils under varying moisture conditions. In total, fourteen physical model tests were conducted, each subjected to incremental vertical loading while monitoring the corresponding settlement responses. The test matrix included the following groups:

- Six dry models of gypseous soil treated with 1%, 2%, and 3% additions of nano clay (NC) and nano metakaolin (NM).
- Six soaked models prepared with identical treatments, but tested under fully saturated conditions to evaluate the soil's hydro-mechanical response.
- Two untreated control models, one tested in the dry state and the other under saturated conditions, to provide baseline performance for comparison.

Saturation of the treated and untreated models was achieved by inducing upward seepage from the base of the soil container, thereby replicating realistic field scenarios such as groundwater table rise, seepage forces, or flooding events. This method ensured a controlled and uniform infiltration process, allowing a reliable assessment of soil collapse and settlement behavior. The adopted testing strategy provided a systematic framework for isolating the effects of nanomaterial type (NC vs. NM), treatment dosage (1–3%), and moisture condition (dry vs. saturated) on the settlement characteristics of gypseous soils.

4. Results and Discussion

4.1. Compressibility of Soil

Collapsible soils, while capable of supporting relatively high stresses under unsaturated conditions, undergo substantial volumetric strain when exposed to wetting, even without an

increase in external loading. This behavior is primarily attributed to the dissolution of soluble salts, such as gypsum, and the subsequent breakdown of interparticle cementation bonds. To assess this phenomenon, seven gypseous soil specimens were examined: one untreated (natural) soil sample and six treated with nano clay (NC) and nano metakaolin (NM) at dosages of 1%, 2%, and 3% by dry weight, see Figures 4 and 5. The collapse potential (Cp) was determined using the single oedometer collapse test in accordance with ASTM D5333 (2003). The untreated soil exhibited a collapse potential of 10.2%, categorizing it as a highly collapsible soil. With the incorporation of nanomaterials, a marked reduction in collapse susceptibility was observed. At 3% NC, the collapse potential decreased to 2.66%, while 3% NM achieved an even lower value of 2.32%. These reductions represent a 74–77% improvement in collapse resistance, underscoring the efficacy of nanomaterials in stabilizing problematic gypsum-rich soils.

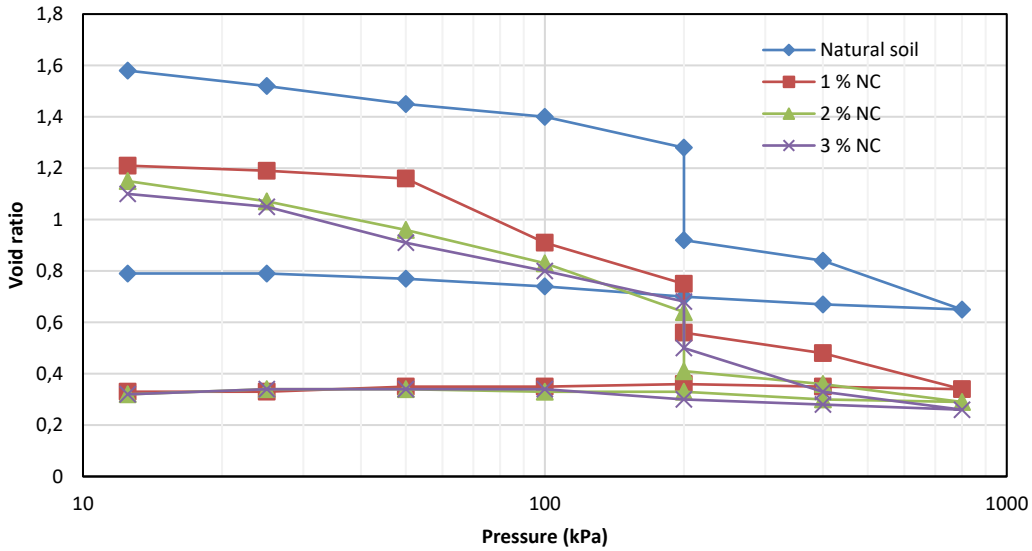

Fig. 4. Potential collapse tests of gypseous soil treated by Nano clay (NC)

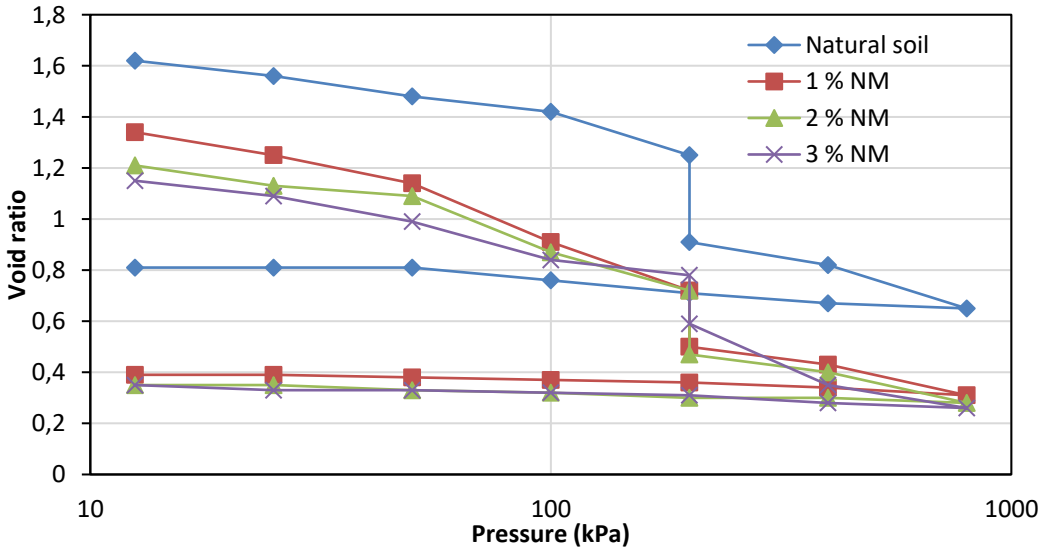

Fig. 5. Potential collapse tests of gypseous soil treated by Nano metakaolin (NM)

The observed improvements can be attributed to multiple mechanisms:

- Nanoparticles possess extremely high surface area-to-volume ratios, enabling them to occupy micropores and coat soil particles. This physical filling reduces the soil's porosity and restricts the pathways for water infiltration, thereby limiting wetting-induced volumetric strains. Additionally, the nanoparticles form bridges between soil grains, enhancing interparticle friction and cohesion at the micro-scale.

- In the case of NM, which is rich in reactive silica and alumina, pozzolanic reactions occur when the nanoparticles react with calcium ions from gypsum or lime content in the soil. This leads to the formation of secondary cementitious products, such as calcium silicate hydrate (C–S–H) and calcium aluminate hydrate (C–A–H), which chemically bond soil particles together. These new cementitious bonds reduce the solubility-driven collapse potential by creating a more chemically stable soil matrix.
- Nano clays possess negatively charged surfaces, which can attract cations (e.g., Ca^{2+}) in the soil solution, promoting particle flocculation and aggregation. This modifies the soil's fabric and increases effective stress between particles, resulting in higher resistance to sudden collapse upon wetting.
- The combination of physical pore filling, chemical bonding, and electrostatic particle aggregation increases the effective contact area between soil grains. This improves load distribution throughout the soil skeleton, reducing local stress concentrations and compressibility under applied loads or self-weight.
- By creating a dense, interconnected microstructure and chemically stabilizing reactive ions, nanomaterials slow down the dissolution rate of gypsum upon wetting. This mitigates one of the primary drivers of collapsibility, as the soil maintains its structural integrity even in the presence of water infiltration.

The comparative performance between NC and NM indicates that while both nanomaterials enhance collapse resistance, NM achieves superior stabilization due to the dual role of physical pore refinement and chemical pozzolanic activity. NC primarily acts through mechanical densification and surface charge interactions, whereas NM actively forms new cementitious phases that reinforce the soil skeleton. These mechanisms demonstrate that nanoscale interventions can address both the physical and chemical causes of collapse in gypseous soils. Furthermore, the results highlight the efficiency of using small nanomaterial dosages to induce significant soil improvement, making this approach more sustainable and cost-effective compared to conventional stabilizers such as lime or cement, which require larger quantities and longer curing times. This scientific understanding provides a pathway for targeted soil improvement strategies, particularly in environments prone to wetting-induced collapse, such as arid and semi-arid regions with gypsum-rich subsoils.

The superior performance of NM over NC is consistent with its higher pozzolanic activity and chemical reactivity, which enable more effective binding of soil particles. These findings align with previous research (e.g., Taha and Taha [11] Al-Murshedi et al. [24]), which reported that nanomaterial additives improve the geotechnical behavior of collapsible soils by reducing settlement and enhancing shear strength. Furthermore, the reduction in collapse potential to values below 3% suggests that treated soils transition from the category of highly collapsible to low or moderately collapsible, according to widely accepted classification criteria [25,26]. This transformation has significant practical implications: it enables the safe utilization of gypseous soils as foundation materials with minimal risk of sudden settlement upon wetting, thereby reducing the need for costly soil replacement or deep foundation systems. In conclusion, the experimental results clearly demonstrate that nanomaterials are effective stabilizers for gypseous soils, with nano metakaolin exhibiting superior performance compared to nano clay. The findings highlight the potential of nanotechnology as a sustainable and cost-efficient soil improvement strategy, particularly in arid and semi-arid regions where collapsible soils are widespread. The use of nano-metakaolin contributes to enhanced soil performance through micro-scale mechanisms such as pore filling, particle aggregation, and pozzolanic reactions, which collectively reduce soil collapsibility and improve strength characteristics. Compared with conventional stabilizers, nano-based additives require lower dosages to achieve comparable or superior performance, thereby reducing material consumption and associated environmental impacts. Moreover, the availability of metakaolin from locally sourced clay minerals enhances the economic feasibility of this approach for large-scale geotechnical applications in regions characterized by limited water resources and problematic soil conditions.

4.2. Load-Settlement

The findings suggest that nano-based stabilization could be a cost-effective and sustainable alternative to traditional stabilization methods such as cement or lime treatment, especially in arid and semi-arid regions where gypseous soils are widespread. Unlike bulk stabilizers, nanomaterials achieve significant improvements at relatively low dosages (≤3%), reducing both material consumption and environmental footprint. This aligns with global trends toward green and nano-enabled geotechnics. The stress–settlement relationships of the tested models were evaluated under both dry and soaked conditions, with ultimate deformations recorded after wetting (Figures 6 to 9). The untreated gypseous soil exhibited rapid acceleration of settlement upon flooding, reflecting the combined effects of gypsum dissolution, softening of the soil fabric, and loss of shear strength. In contrast, soils treated with nanomaterials displayed markedly reduced settlement rates and enhanced stability. Before soaking (dry condition), the soil response:

- NC-treated soils exhibited a 30–60% reduction in settlement, depending on dosage.
- NM-treated soils showed a 40–60% reduction, suggesting that the higher pozzolanic activity of nano metakaolin contributes to more effective soil stabilization.

While after soaking both nanomaterials continued to suppress deformation, with improvements attributed to cementitious reactions that progressed during and after wetting, leading to sustained strength and stiffness. Although the experimental results are promising, several challenges must be addressed before field-scale implementation:

- Durability under cyclic wetting–drying: Long-term exposure to fluctuating groundwater conditions may influence the persistence of the stabilization.
- Scalability and cost optimization: While nanoscale additives are effective, their cost and availability in large-scale projects must be evaluated against performance gains.
- Microstructural characterization: Advanced techniques (e.g., SEM, EDS, and micro-CT scanning) should be employed to quantify the distribution and bonding behavior of nanomaterials within the soil matrix.
- Coupled hydro-mechanical modeling: Incorporating nanomaterial effects into predictive models would allow better forecasting of settlement and collapse under field conditions.

The experimental findings demonstrate a clear improvement in the geotechnical behavior of gypseous soils treated with nanomaterials, with settlement reductions evident under both dry and soaked conditions. The observed mitigation is particularly significant given that untreated gypseous soils typically suffer from rapid and severe collapse upon saturation due to gypsum dissolution and the subsequent destabilization of the soil structure. While both additives improved soil performance, NM consistently outperformed NC across most loading stages.

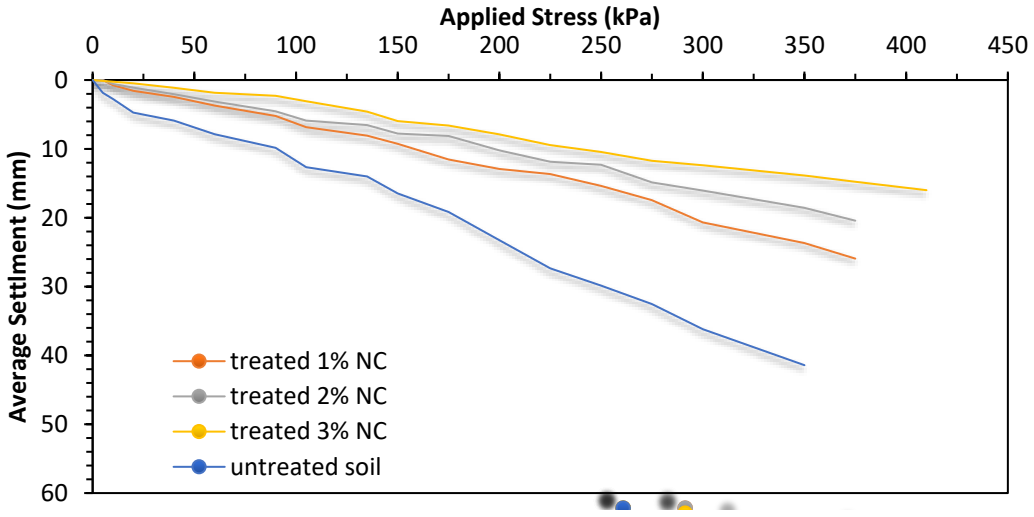

Fig. 6. Applied stress versus settlement of gypseous soil treated with NC in dry condition

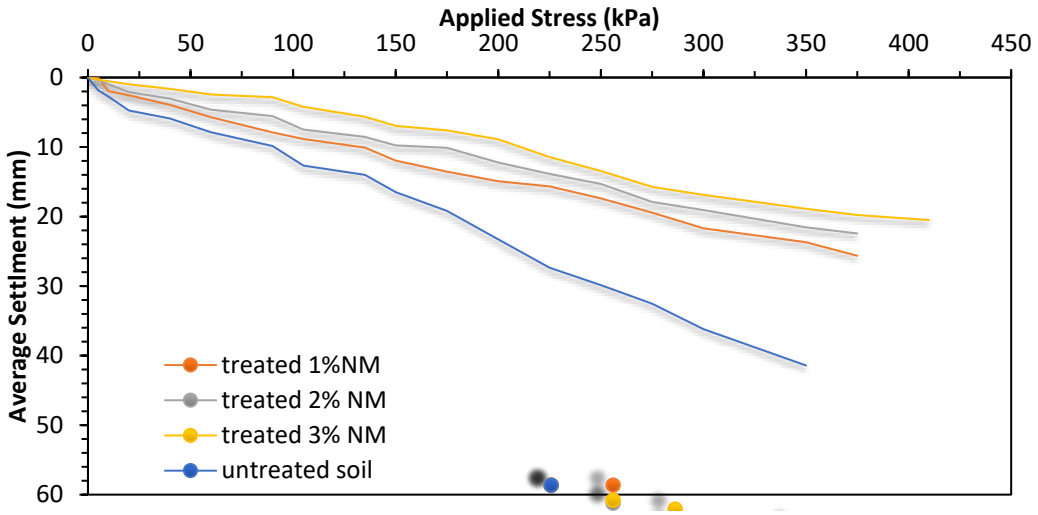

Fig. 7. Applied stress versus settlement of gypseous soil treated with NM in dry condition

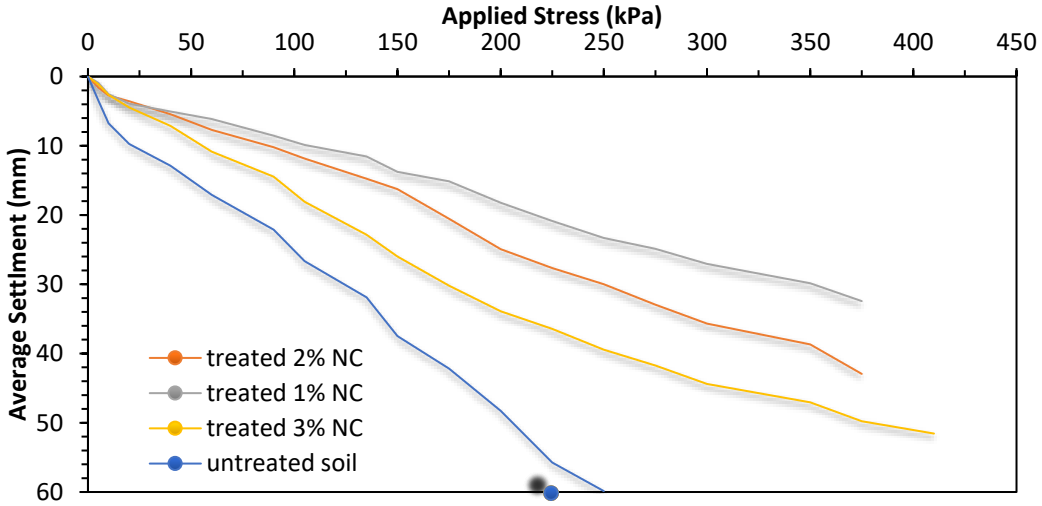

Fig. 8. Applied stress versus settlement of gypseous soil treated with NC after soaking

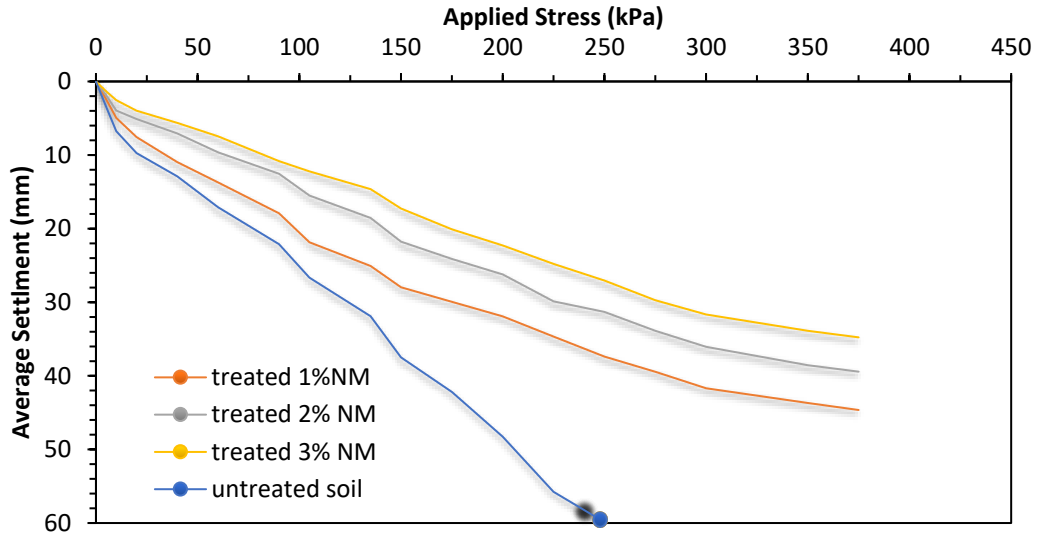

Fig. 9. Applied stress versus settlement of gypseous soil treated with NM after soaking

This can be attributed to the higher pozzolanic reactivity of NM, which accelerates the formation of stable cementitious products such as calcium silicate hydrate (C–S–H) and calcium aluminate hydrate (C–A–H). The finer particle size and higher surface reactivity of NM particles enable them to integrate more effectively into the soil matrix, leading to stronger particle interlocking and enhanced long-term stiffness. In contrast, NC primarily acts through physical mechanisms such as pore filling and particle bridging, which, while beneficial, do not yield the same chemical stabilization effects as NM.

The settlement reduction prior to soaking indicates that nanomaterials effectively densify and cement the soil structure even under dry conditions. Upon soaking, the untreated gypseous soils exhibited sharp settlement acceleration, consistent with literature reports of collapse strains exceeding 10% in soils with high gypsum content. However, the treated soils showed a much milder response, suggesting that nanomaterials not only densify the structure but also protect against gypsum dissolution pathways. This dual role underscores the importance of nanoscale additives in sustaining soil performance under fluctuating moisture conditions. The mechanisms of soil stabilization can be achieved by [7,27]:

- By clogging micro-pores, nanomaterials reduced the soil's permeability, thereby slowing water ingress and limiting the rate of gypsum dissolution.
- The pozzolanic activity of NM, and to a lesser extent NC, produced cementitious gels that bound soil particles together, compensating for strength losses induced by gypsum dissolution.
- The formation of continuous gel networks and reduced void ratios approved by SEM and XRD observations reported in similar studies which explain the observed improvements in compressibility and load-bearing capacity.

This study confirms that the incorporation of nano clay (NC) and nano metakaolin (NMK) significantly improves the geotechnical behavior of gypseous soils. The principal benefits include:

- A substantial reduction in collapse potential under both dry and soaked conditions,
- Noticeable decrease in compressibility and enhancement of shear strength,
- Improved durability and stability against moisture variations, which are critical in hydro-collapse-prone environments.

5. Conclusions

These findings demonstrate that nanotechnology-based stabilization represents a viable, cost-effective, and environmentally sustainable alternative to conventional stabilization methods, particularly in regions where traditional techniques are either ineffective or uneconomical. The primary objective of this research was to evaluate the effectiveness of nanomaterial additives in enhancing the bearing capacity and reducing the settlement of shallow foundations constructed on gypseous soils. The following key conclusions were drawn:

- The addition of nanomaterials provides a practical and innovative approach to mitigating excessive settlement. The improvement arises primarily from pore clogging, soil fabric refinement, and enhanced interparticle bonding induced by the nanoparticles. With increasing nanomaterial content, the collapsibility of compacted specimens decreased consistently.
- The compressibility of gypseous soil was markedly reduced by the addition of nanomaterials. However, the improvement trend indicates a threshold effect: beyond 2% content, additional nanomaterials provided diminishing benefits.
- Gypseous soils treated with 3% nanomaterials exhibited a 40–60% reduction in settlement before soaking, while under saturated conditions, the reduction ranged between 25–40%. This confirms the robustness of nanomaterials in enhancing soil performance under both dry and moisture-induced collapse scenarios, although the stabilization is more effective in unsaturated conditions.

Overall, the study highlights the potential of nanomaterials as soil stabilizers, with nano metakaolin showing slight significant performance compared to nano clay due to its higher pozzolanic reactivity and stronger contribution to cementitious bonding. It's recommended to study:

- It is recommended to conduct full-scale model tests or field investigations to obtain more reliable results and to better identify the practical challenges associated with the application of these techniques.
- Future studies should consider the use of different types of nanomaterials and varying dosage ratios to enhance the geotechnical behavior of various soil types.
- Further research is needed to evaluate the long-term durability, environmental impacts, and optimal dosage levels of nanoparticles used for soil improvement.

References

[1] Nashat IH. Engineering characteristics of some gypseous soils in Iraq [PhD Thesis]. Baghdad: University of Baghdad; 1990.
[2] Al-Badran YM. Collapse behavior of Al-Tharthar gypseous soil [MSc Thesis]. Baghdad: University of Baghdad; 2001.
[3] Almurshedi AD, Thijeel JK, Al-Awad K. Mitigation of collapse of marshes soil by nano-silica fume. IOP Conf Ser: Mater Sci Eng. 2020;737(1):012110. https://doi.org/10.1088/1757-899X/737/1/012110
[4] Karkush MO, Al-Murshedi AD, Karim HH. Investigation of the impacts of nano-clay on the collapse potential and geotechnical properties of Gypseous soils. Jordan J Civ Eng. 2020;14(4):537-547.
[5] Ali SD, Karkush M. Effects of nano-clay on the geotechnical properties of gypseous soil. IOP Conf Ser: Earth Environ Sci. 2024;1374(1):012006. https://doi.org/10.1088/1755-1315/1374/1/012006
[6] Karkush M, Jabbar A. An Effect of several patterns of floating stone columns on the bearing capacity and porewater pressure in saturated soft soil. J Eng Res. 2022;10(2B):84-97. https://doi.org/10.36909/jer.10841
[7] Karkush MO, Almurshedi AD. Investigation of the impacts of nanomaterials on the micromechanical properties of gypseous soils. Arab J Sci Eng. 2023;48(1):665-675. https://doi.org/10.1007/s13369-022-07058-z
[8] Thajeel JK, Shaia HA, Al-Mamoori SK, Almurshedi AD. Effect of emulsified asphalt on expansive soil strength and swelling. E3S Web Conf. 2023;427:03009. https://doi.org/10.1051/e3sconf/202342703009
[9] Iranpour B. The influence of nanomaterials on collapsible soil treatment. Eng Geol. 2016;205:40-53. https://doi.org/10.1016/j.enggeo.2016.02.015
[10] Yusuf EO, Amber I, Officer S, Oluyemi GF. Transport of nanoparticles in porous media and associated environmental impact: A review. J Eng Res. 2024;12(2):275-284. https://doi.org/10.1016/j.jer.2024.01.006
[11] Taha MR, Taha OME. Influence of nano-material on the expansive and shrinkage soil behavior. J Nanopart Res. 2012;14(10):1-13. https://doi.org/10.1007/s11051-012-1190-0
[12] Ali SD, Karkush M. Studying Leaching of Gypseous Soil Improved with Nanomaterials. J Eng. 2025;31(7):99-110. https://doi.org/10.31026/j.eng.2025.07.06
[13] Head KH. Manual of Soil Laboratory Testing Vol. 1, 2. London: Prentch Press; 1990.
[14] Head KH. Manual of Soil Laboratory Testing Vol. 1, 2. London: Prentch Press; 1998.
[15] Majeed A, Taha G. Stabilization of soft soil using nanomaterials. Res J Appl Sci Eng Technol. 2014;8(4):503-509. https://doi.org/10.19026/rjaset.8.999
[16] Torgal F, Jalali S. Nanotechnology advantages and drawbacks in the field of construction and building materials. Constr Build Mater. 2011;25(2):582-590. https://doi.org/10.1016/j.conbuildmat.2010.07.009
[17] Siddique R, Khan MI. Supplementary cementing materials. Springer Science & Business Media; 2011. https://doi.org/10.1007/978-3-642-17866-5
[18] Metaxa ZS, Tolkou AK, Efstathiou S, Rahdar A, Favvas EP, Mitropoulos AC, et al. Nanomaterials in cementitious composites: an update. Molecules. 2021;26(5):1430. https://doi.org/10.3390/molecules26051430
[19] Gilman W, Takashi K, Alexander B, Harris RH Jr, Brassell L, VanLandingham M, et al. Flammability of Polymer Clay Nanocomposites Consortium: Year One Annual Report. NISTIR 6531; 2000. https://doi.org/10.6028/NIST.IR.6531
[20] El Hoseny M, Forcellini D, Ma J. The role of the foundation gap on the pounding between low-rise buildings. Structures. 2024;63:106412. https://doi.org/10.1016/j.istruc.2024.106412
[21] Khamesi SO, Hosseini SMMM. A numerical study of influential parameters on rocking response of shallow foundations of single degree of freedom (SDOF) structures. J Eng Res. 2023;11(2):100055. https://doi.org/10.1016/j.jer.2023.100055

[22] Hakhamaneshi M, Kutter BL, Gavras AG, Gajan S, Tsatsis A, Liu W, et al. Database of rocking shallow foundation performance: Slow-cyclic and monotonic loading. Earthquake Spectra. 2020;36(3):1585-1606. https://doi.org/10.1177/8755293020906564
[23] Turner JP, Kulhawy FH. Drained uplift capacity of drilled shafts under repeated axial loading. J Geotech Eng. 1990;116(3):470-491. https://doi.org/10.1061/(ASCE)0733-9410(1990)116:3(470)
[24] Al-Murshedi AD, Karkush MO, Karim HH. Collapsibility and shear strength of gypseous soil improved by nano-silica fume (Nsf). Key Eng Mater. 2020;857:292-301. https://doi.org/10.4028/www.scientific.net/KEM.857.292
[25] Jennings JE, Knight K. A guide to construction on or with materials exhibiting additional strength due to collapse of grain structure. In: Proceedings of the 6th Regional Conference for Africa on Soil Mechanics and Foundation Engineering; 1975; Durban, South Africa. Cape Town: AA Balkema; 1975. p. 99-105.
[26] Lawton EC, Fragaszy RJ, Hetherington MD. Review of wetting-induced collapse in compacted soil. J Geotech Eng. 1992;118(9):1376-1394. https://doi.org/10.1061/(ASCE)0733-9410(1992)118:9(1376)
[27] Karkush M, Ali SD. Experimental investigation of the leaching characteristics of gypseous soil treated with nano-silica. J Umm Al-Qura Univ Eng Archit. 2025:1-17. https://doi.org/10.1007/s43995-025-00278-y

Blank Page

Research on Engineering Structures & Materials
www.jresm.org

Research Article

Stabilization of excavation using the diaphragm wall method in Karbala

M. Sabermahani [1,a], H.R. Elahi [2], Ahmed M. Bilal [3], A. Khodaverdian [2], Mahdi Karkush [*,4,b]

[1]*School of Civil Engineering, Iran University of Science and Technology, Tehran, Iran*
[2]*Saman Pey Soil Improvement Services, Tehran, Iran*
[3]*Ardh-ALnahrain Soil Improvement Work and Foundation, Baghdad, Iraq*
[4]*Department of Reconstruction and Projects, University of Baghdad, Baghdad, Iraq*

Article Info

Article History:

Received 20 Nov 2025
Accepted 27 Mar 2026

Keywords:

Diaphragm wall method;
Excavation stabilization;
Karbala Imam Hussain Shrine;
Geotechnical engineering;
Numerical modeling

Abstract

Construction of historical and religious projects around the world is often highly sensitive, particularly when they involve sites of great spiritual significance. The Shrine of Imam Hussain (AS) in Karbala is a prime example as one of the most important centers for Muslims. Due to its religious importance, any development plan for this site requires exceptional care and precision. This article examines the excavation stabilization method used in the shrine's development project. After evaluating various techniques, the diaphragm wall method was chosen and implemented to stabilize the excavation pit. PLAXIS 2D and SAP200 software are used for modeling, it was demonstrated that this method effectively controls pit crown deformations, keeping them within an acceptable limit of 4 cm. Additionally, the diaphragm wall provides excellent water sealing, preventing seepage from behind the pit making it a highly reliable and advantageous solution.

© 2026 MIM Research Group. All rights reserved.

1. Introduction

Rehabilitation and reconstruction of historical and religious projects is always highly sensitive, especially when they involve sites of deep spiritual significance. The Shrine of Imam Hussain (AS) in Karbala, one of the most revered places for Muslims, is no exception. As part of the shrine's development plan, a 15-meter-deep excavation and its stabilization became a necessary undertaking. Globally, the geotechnical engineering community employs various excavation stabilization methods, each selected based on the specific geotechnical conditions of the site, along with economic, technical, and practical considerations. One of the most critical concerns in projects with a high groundwater table is ensuring effective excavation waterproofing. Among the methods available, the diaphragm wall technique stands out as one of the most efficient. It not only controls lateral displacement of excavation walls but also significantly reduces groundwater seepage.

Extensive research both numerical and experimental has been conducted on diaphragm wall performance. For instance, Bolton and Pourier [1] used centrifuge modeling to evaluate the performance of diaphragm walls and demonstrated their long-term effectiveness in excavation stabilization. Similarly, Pakbaz et al. [2] studied the diaphragm wall performance in five metro stations in Ahvaz. Their findings showed that finite element models predicted wall displacements in the range of 0.005 to 0.007 times the excavation depth, while actual observed displacements were even lower. They also noted that nearby structural settlements ranged from 0.0025 to 0.0035 times the excavation depth. In another case study, Jasmine and Muttharam [3] analyzed a 14-meter-deep excavation in Noida, India. Using finite element modeling and field monitoring with

*Corresponding author: mahdi_karkush@yahoo.com
[a]orcid.org/0000-0003-0430-6755; [b]orcid.org/0000-0003-1304-0303
DOI: http://dx.doi.org/10.17515/resm2026-1352ic1120rs
Res. Eng. Struct. Mat. Vol. 12 Iss. 2 (2026) 1153-1164

inclinometers, they observed that actual displacements were approximately 67% of those predicted by the models.

Numerous previous studies have investigated the stabilization of various soil types using a wide range of materials, including chemical additives, geopolymers, nanomaterials, magnetized water, and biotreatment methods. These stabilizing agents can be applied through soil mixing, injection, or deep mixing techniques. The choice of material and method largely depends on factors such as the type of soil, available treatment time, project budget, loading conditions, and the integration of sustainability principles. The effectiveness of the soil treatment is typically evaluated based on improvements in settlement behavior and bearing capacity [4-10]. In the present study, numerical modeling has been used to investigate the stabilization of the 15-meter excavation for the development of the Shrine of Imam Hussain (AS) in Karbala. A T-shaped diaphragm wall was designed for this purpose. This design eliminates the need for temporary supporting elements such as anchors, struts, or braces an especially important consideration for this project. Given the site's challenging conditions, including loose, collapsible soils and a high groundwater level, the T-shaped diaphragm wall offers a technically and operationally sound solution, overcoming many of the difficulties associated with traditional stabilization methods.

2. Study Area and Geotechnical Description

The arial photo, the project site plan and the condition of the surrounding buildings are presented in Figure 1. This picture shows the status of the project's neighbors. Based on the results of geotechnical studies and exploratory boreholes, the log of the obtained boreholes is presented in Figure 2. In general, except for above 8 meters, the dominant texture of the soil is sandy. At a depth of 37 to 50 meters, there is a continuous layer of clay, which has been found suitable for waterproofing and controlling seepage. Based on the presented results, layering and values of parameters measured by tests and also considering engineering judgment, the geotechnical profile was finalized according to Table 1. These values are used as the basis for calculations and modeling. According to the information of the site, in the modeling and design, from the depth of 50 onwards, dense sand layer similar to L8 layer is considered.

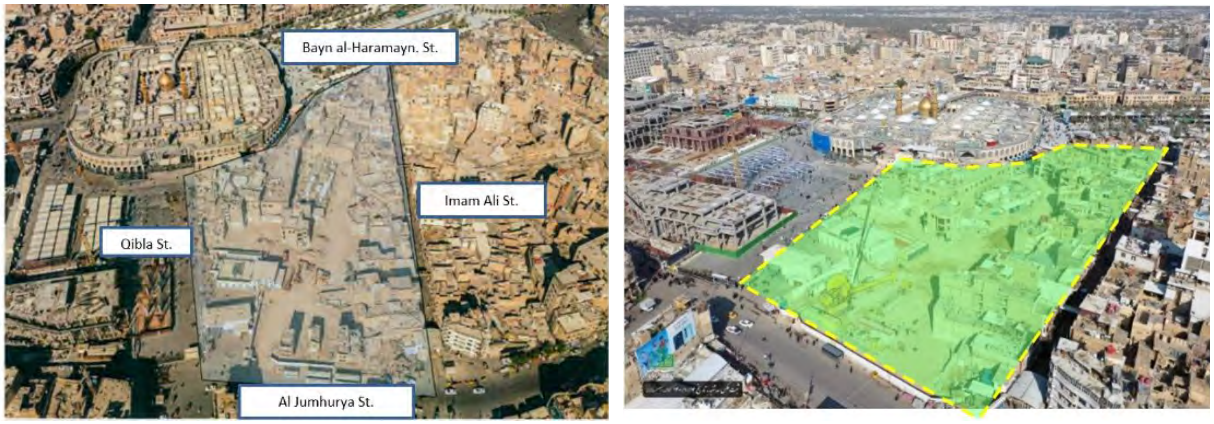

Fig. 1. Site location and boundary

During drilling operations, all formations' high-pressure fluids and gases of the earth are controlled by borehole pressure, which consists of hydrostatic pressure of drilling mud, pump pressure, and friction pressure loss in the annulus. If, for any reason, the borehole pressure falls below the formation fluid/gas pressure, the formation fluids/gases will enter the hole and a pressure "kick" will occur. If a kick cannot be controlled properly, uncontrolled formation fluids/gases will reach to surface where the drilling rig is located. Such a catastrophic event is known as blowout [1]. To prevent formation fluids/gases to reach the surface of the well, blowout preventers are used as safety valves. When they are activated, they are supposed to close off the wellbore and seal it (in some cases, the sealing pressures are 20,000 Psi which is 1360 bar) in an emergency to control and balanced formation fluids and gases [2,3].

In a blowout preventer stack, two types of blowout preventers are used; annular and ram. Annular BOPs are used in combination with hydraulic system that can seal off different sizes of annulus whether drill pipe is in use in the wellbore or not. Upon command, high-pressure fluid is directed to the closing hydraulic ports positioned in the lower side of the piston. This causes the operating piston to move upward; therefore, the moving piston compresses the packer [2-43]. Because of a cap at the top of annular blowout preventer, the packer can only move toward the center of the wellbore to pack off a drill pipe or seal off the wellbore.

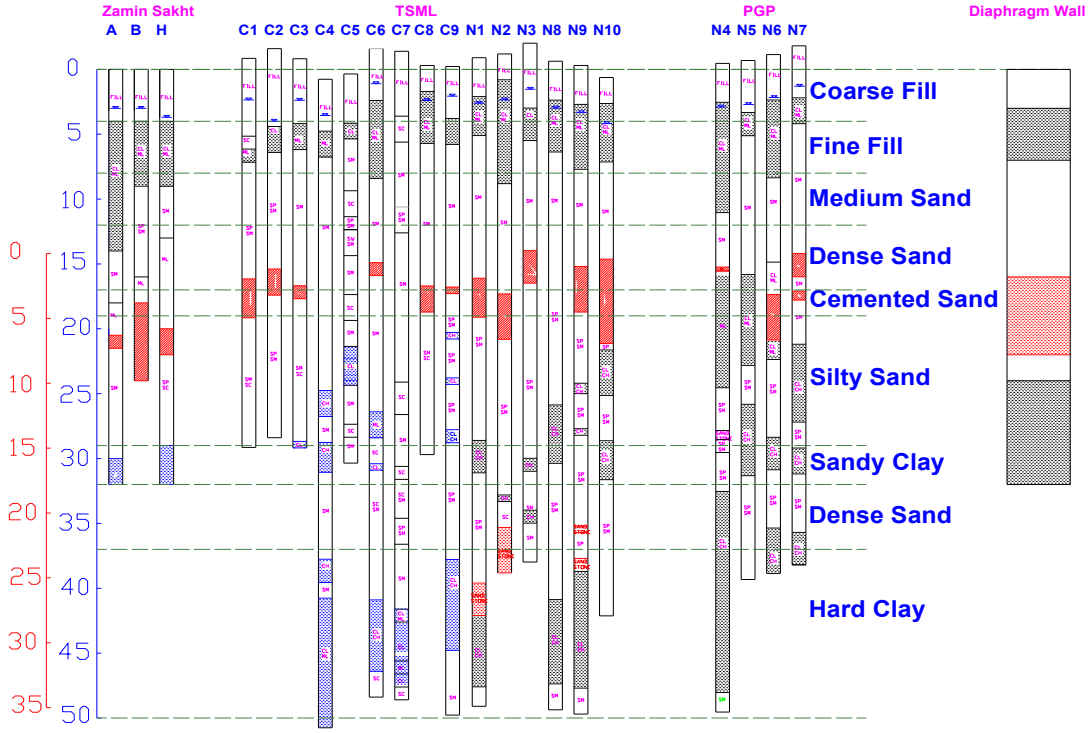

Fig. 2. Borehole log and soil profile

Table 1. Soil layers parameters

Definition	Parameter	L1	L2	L3	L4	L5	L6	L7	L8	L9	Unit
		0	-4	-8	-12	-17	-19	-29	-32	-37	
		-4	-8	-12	-17	-19	-29	-32	-37	-50	
Saturated unit weight	γ_{sat}	17.0	17.0	18.0	18.5	19.0	19.0	19.5	19.5	19.5	kN/m³
Unsaturated unit weight	γ_{un}	17.5	19.5	19.5	18.0	18.0	18.0	16.0	16.0	16.0	kN/m³
Effective cohesion	c	2.0	12.0	7.0	7.0	50.0	10.0	25.0	10.0	35.0	kPa
Effective angle of internal friction	φ	25.0	20.0	30.0	34.5	38.5	36.0	27.5	36.0	25.0	°
Reference secant stiffness in standard drained triaxial test	E_{50}^{ref}	10	12	50	135	135	100	70	150	90	MPa
Reference tangent stiffness for primary oedometer loading	E_{oed}^{ref}	10	12	50	135	135	100	70	150	90	MPa
Unloading/reloading stiffness	E_{ur}^{ref}	30	36	150	405	405	300	210	450	270	MPa
Reference stress for stiffness	p_{ref}	20	56	59	68	71	101	166	143	253	kPa
Reference shear modulus at very small strains ($\varepsilon<10^{-6}$)	G_0^{ref}	120	40	110	90	110	100	80	80	80	MPa
Power of stiffness formula	m	0.5	0.5	0.5	0.5	0.5	0.5	1.0	1.0	1.0	-
Poisson's ratio for unloading-reloading	υ_{ur}	0.2	0.2	0.2	0.2	0.2	0.2	0.2	0.2	0.2	-
K_0-value for normal consolidation (default $K_0^{nc}=1-\sin\varphi$)	K_0^{nc}	0.58	0.66	0.50	0.43	0.38	0.41	0.54	0.41	0.58	-
Hydraulic Conductivity	K	8.64	8.64	8.64	8.64	0.864	8.64	8.64	8.64	0.009	m/day
Over consolidation Ratio	OCR	1.0	1.0	1.0	1.0	1.0	1.0	1.0	1.0	1.0	-

The limitations of current study can be summarized by the following points:

- The numerical analyses were performed using two-dimensional plane strain assumptions, which idealize the excavation and diaphragm wall as longitudinally uniform. While this

approach is appropriate for evaluating global behavior along representative sections, it does not capture three-dimensional effects such as corner stiffness, spatial variability of soil properties, or interactions with nearby irregular structures. These effects may locally influence deformation and stress distribution.

- The soil stratigraphy and material properties were derived from a limited number of site investigation data points and were assumed to be laterally homogeneous. Natural soils may exhibit heterogeneity, anisotropy, and spatial variability that are not fully represented in the model, potentially affecting displacement and seepage predictions.
- The study relied primarily on numerical modeling results for displacement and seepage assessment. At the time of the analysis, comprehensive field monitoring data (e.g., inclinometers, piezometers, or pumping tests) were not available for direct validation. Consequently, the reported deformation (approximately 4 cm) and seepage quantities should be interpreted as design-based predictions rather than measured values.
- Simplified constitutive soil models and idealized soil–structure interface parameters were adopted to ensure numerical stability and practicality. These simplifications may influence the accuracy of stress–strain response, particularly under complex loading or long-term conditions.

As a result of these limitations, the findings of this study should be considered site-specific and primarily applicable to deep excavations in similar geological and hydrogeological conditions. The results are intended to demonstrate the feasibility and effectiveness of the proposed diaphragm wall system rather than to serve as universal design values. Future work incorporating three-dimensional modeling, enhanced site characterization, and field monitoring data would further improve the robustness and general applicability of the conclusions. The predicted maximum lateral deformation of the diaphragm wall, obtained from PLAXIS 2D analyses, is approximately 4 cm at the crown for the final excavation stage. According to standard design guidelines for deep excavations in cohesionless and partially saturated soils, the permissible lateral deformation for similar diaphragm walls is typically in the range of H/200 to H/150, where H is the wall height. For the 15 m-deep walls in this study, this corresponds to approximately 7.5–10 cm. Thus, the margin of safety between the predicted and permissible deformations is roughly 3.5–6 cm, indicating that the diaphragm wall is expected to perform well within acceptable deformation limits under the design conditions.

3. Seismic Analysis and Excavation Stabilization

To determine the seismic acceleration for analysis, it is important to consider that Karbala is situated in a low-risk seismic zone with very low earthquake intensity. Based on this, the horizontal acceleration coefficient (k_h) for quasi-static analysis was calculated using a peak ground acceleration (PGA) of 0.12g, in accordance with FHWA guidelines [11–13]. Given the high importance of the structures surrounding the excavation area, a conservative value of $k_h = 0.12$ was adopted for the quasi-static analysis.

3.1. Excavation Stabilization

Several alternative methods were considered for stabilizing the 15 m-deep excavation near the Shrine of Imam Hussain, including secant pile walls, soldier pile walls, and sheet pile walls. Secant piles were initially considered; however, they were rejected due to their higher cost, longer installation time, and the potential for excessive groundwater inflow in the saturated soil layers. Soldier piles and sheet piles were deemed insufficiently rigid to control lateral deformations within the strict allowable limits (≤4 cm). The T-shaped diaphragm wall was selected because it provides high stiffness, effective groundwater cutoff, and reduced excavation deformation, meeting both structural safety and cultural heritage protection requirements in this sensitive site.

To stabilize the excavation in this project, and considering structural requirements, it was decided to separate the retaining wall from the main structure. This design ensures that no lateral soil pressure except at the foundation level is transferred to the main structure. Consequently, the permanent earth pressure, including seismic loading, is entirely supported by the surrounding retaining wall, with the main structure engaged only at the foundation level. In this context,

diaphragm walls were employed both as a cutoff wall and a stabilizing element. The primary advantage of diaphragm walls is their ability to provide effective waterproofing, significantly reducing groundwater inflow during dewatering operations. Based on comprehensive studies and analyses, the wall length was optimized to minimize the inflow rate to a level that can be effectively managed through pumping over the project's operational life.

A one-meter-thick diaphragm wall was constructed to stabilize the excavation. The diaphragm wall in this project was designed in a T-shaped configuration (buttressed retaining wall). This design includes a series of buttress walls installed at variable intervals of 2.6 to 5.2 meters. These buttresses are constructed as separate diaphragm panels oriented perpendicular to the main cutoff wall and are connected to the waterproof wall panels through shear connections. At the elevation where the foundation of the main structure intersects the diaphragm wall and the buttresses, the thickness of the foundation remains unchanged from that of the main structure. This is because the foundation at this level is designed to resist seismic loads only, while the earth pressures are borne by the base of the buttress elements.

In the design of the excavation stabilization system, the diaphragm wall was modeled as reinforced concrete with material properties selected based on standard engineering practice and site-specific design requirements. The following parameters were used in the numerical analyses:

- Elastic modulus (E): 30,000 MPa
- Poisson's ratio (ν): 0.2
- Compressive strength (f′c): 30 MPa
- Tensile strength: Assumed negligible in PLAXIS 2D but accounted for in SAP2000 structural analysis through reinforcement design.

The concrete material was assumed to behave linearly elastic in PLAXIS 2D for global deformation evaluation, while the wall's bending moments and stresses were verified in SAP2000 considering reinforcement requirements. Considering the soil characteristics and environmental conditions, Portland cement resistant to chloride and sulfate attack was selected. Due to the high groundwater level at the construction site and the presence of chemical agents that could compromise the durability of the concrete and surrounding soil, micro silica (silica fume) was incorporated into the mix. Specifically, 8% of the cement weight was replaced with micro silica to enhance durability and reduce water permeability through the wall. Micro silica also improves the bond between fresh concrete and adjacent surfaces, reduces segregation of concrete components, and further minimizes water infiltration. Because of the low water-to-cement ratio and the inclusion of micro silica, a high-range water-reducing admixture (superplasticizer) was used to achieve a target slump of at least 18 cm, ensuring proper workability.

For the numerical analysis of the excavation stabilization system, PLAXIS 2D (version 20) software was utilized. The Hardening Soil Model with Small-Strain Stiffness (HSS) was adopted for simulating soil behaviour, while a linear elastic model was applied for concrete. Structural elements, such as plates available in PLAXIS, were used to represent the diaphragm wall and other components. Both static and pseudo-static (seismic) analyses were conducted. The geometry and boundary conditions of a sample model are shown in Figure 3. A 15-node triangular element mesh was used to ensure higher accuracy, with an example of the generated mesh presented in Figure 4. Loading is considered according to Table 2. Due to having dead (D), live (L) and earthquake (E) loads, the load combinations used according to the American concrete code ACI318M-14 is as follows:

Table 2. Load combinations based on ACI318 [14]

Primary Load	Load Combination
D	$U = 1.4D$
L	$U = 1.2D + 1.6L$
E	$U = 1.2D + 1.0E + 1.0L + 0.2S$
E	$U = 0.9D + 1.0E$

The interaction between the diaphragm wall and surrounding soil was explicitly represented using interface elements in PLAXIS 2D. These elements simulate the shear and normal behavior along the wall–soil contact and allow relative displacement while transferring shear stresses. To model the shear connection, the interface elements were assigned a strength reduction factor (Rinter= 0.7), which reduces the soil shear parameters (cohesion and friction angle) at the contact to account for imperfect bonding between the soil and the concrete wall. This approach allows controlled mobilization of shear resistance along the interface, capturing realistic soil–structure interaction under excavation loading. The normal stiffness of the interface was chosen sufficiently high to prevent unrealistic penetration between the soil and wall, while the tangential (shear) stiffness was governed by the reduced shear parameters. This method effectively highlights the progressive transfer of lateral loads from the soil to the wall and the corresponding wall deformations.

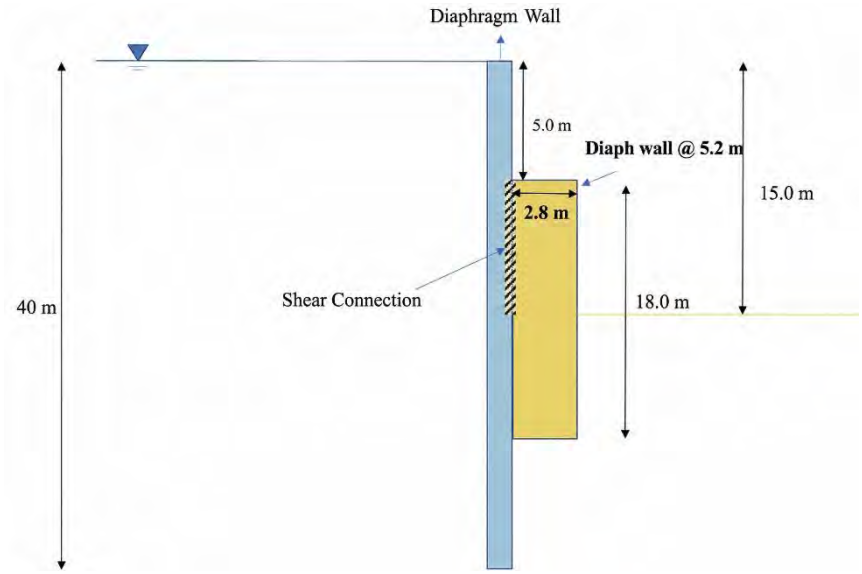

Fig. 3. Section of buttressed retaining wall

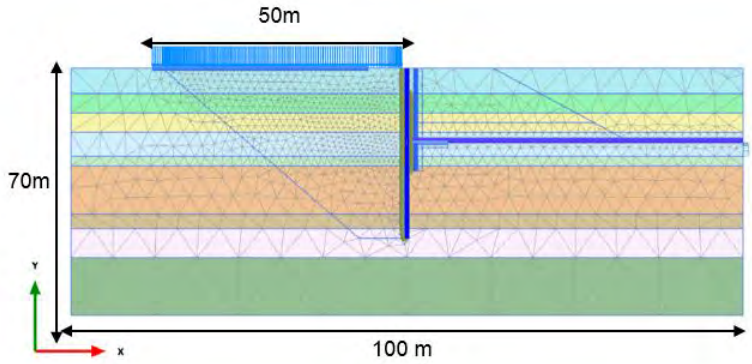

Fig. 4. PLAXIS Model of retaining system

3.2. Controlling Displacement and Damage Level Nearby Structures

The Mair and Burland criterion [15] was applied to evaluate wall movements, adjacent building responses, and potential structural damage. As illustrated in Figure 5, the angular distortion (δ/L) is calculated in accordance with the recommendations of Eurocode 7. To obtain a more accurate measure, the rigid rotation of the foundation (tilt) is subtracted from the total angular deformation, and the net value of δ_{max} is used in the calculation. Neglecting the tilt component leads to an overestimation of δ_{max}, which may result in a more conservative assessment. However, due to uncertainties in the actual behavior of surrounding structures, both approaches considering and neglecting the foundation tilt were evaluated in this study. Of the two, the latter (excluding tilt correction) typically yields the more critical results.

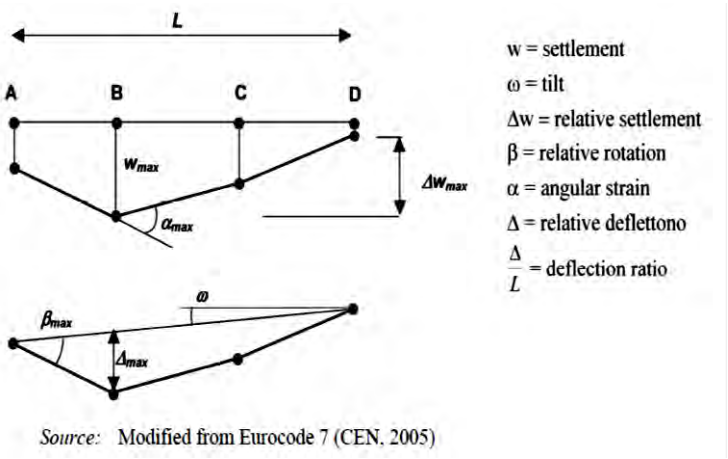

Fig. 5. The effect of foundation rotation on controller displacement ratio [11]

To control the displacement of the excavation wall, the guideline provided in FHWA-IF-99-015 [12,16] was followed. According to this standard, a value of 0.005H is used to estimate the maximum horizontal displacement of the wall in dense sandy soils under active earth pressure conditions. For an excavation depth of 14.2 meters, this corresponds to a maximum allowable displacement of $\delta_{max,h}$= 0.005H = 71 mm. To monitor and manage displacement throughout the excavation process, the maximum horizontal displacement of the wall was tracked at various excavation stages. Figures 6 and 7 illustrate the progression of wall displacement during excavation, showing how it evolves in response to excavation depth and construction activity.

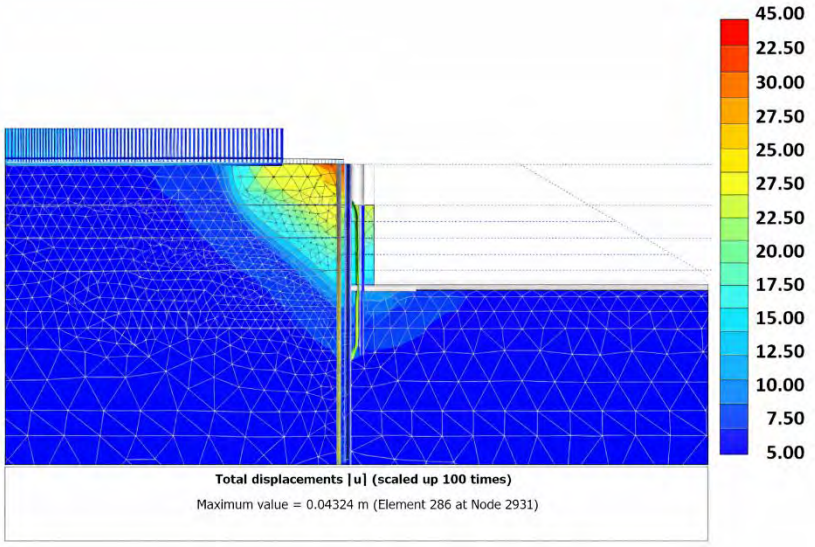

Fig. 6. Total displacement contour in Plaxis numerical model

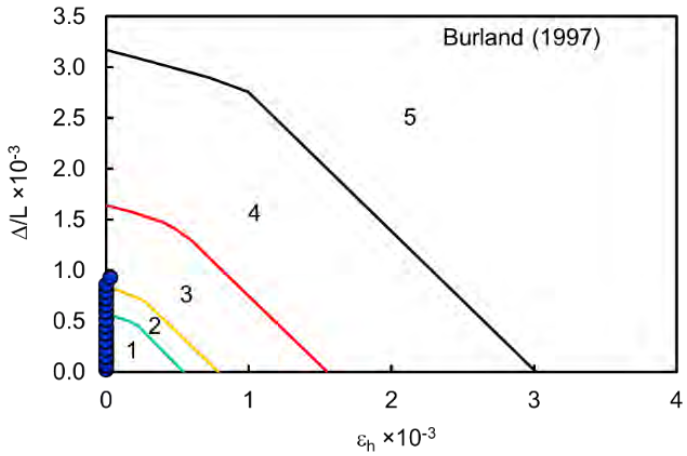

Fig. 7. Retaining wall and adjacent structures displacement control [15]

3.3. Hydraulic Gradient and Seepage Control

Due to the depth of 40 meters of the wall, the amount of inlet flow rate is low and there are no critical conditions in terms of hydraulic gradient and seepage. The results of seepage and gradient are almost the same for all sections and are as shown in the table below. Also, the water flow vectors during pumping are shown in Figure 8.

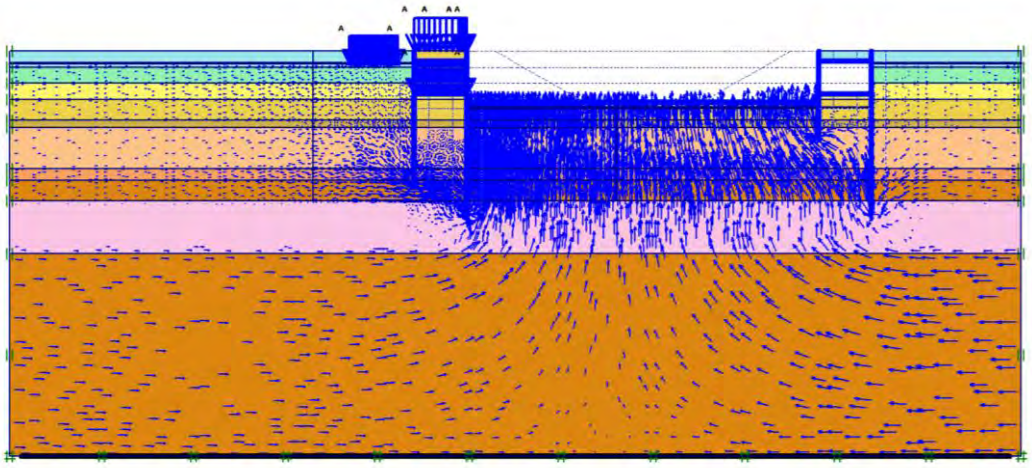

Fig. 8. Water flow vectors during pumping (Flow field, extreme velocity 19.33×10^{-3} m/day)

Table 3. Seepage analysis results

V (m/day)	K (m/day)	I	Q (m^3/day/m)	P (m)	Q (m^3/day)	Q (lit/sec)
0.010	8.64	0.0012	0.30	1000	300	3.5

4. Structural Analysis

After analyzing the interaction of the soil and the retaining structure in Plaxis software, the axial and bending forces of the sections are obtained. For concrete design, according to ACI, the external forces are multiplied by a factor of 1.6 in the static state and by a factor of 1 in the pseudo static state. Then the concrete cross-section is obtained with the amount of reinforcement required for the load resulting from the analysis. The forces resulting from the analysis for different sections of the retaining structure used in the design are shown in the following diagrams. To obtain the final forces of the section, the existing forces, described below, must be combined with each other, notations are shown in Figure 9.

$$P = P_{W1} + P_{W2} \tag{1}$$

$$V = V_{W1} + V_{W2} \tag{2}$$

$$M = M_{W1} + M_{W2} - P_{W1}d_1 + P_{W2}d_2 \tag{3}$$

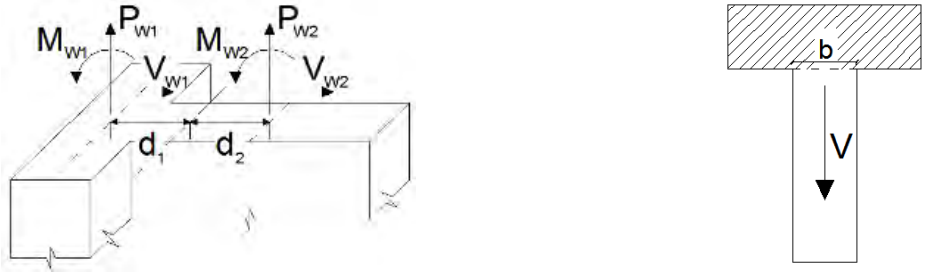

Fig. 9. Notations used in the analysis

The shear force for the design of reinforcements is calculated from the following equation. The reinforcements are designed for each surface of one square meter, so the design force will be equal to ʊ.

$$\tau = \frac{V.Q}{I.b} \tag{4}$$

The variation of bending moment, shear force, and axial loading for the cut-off wall are shown in Figure 10. Also, the variation of bending moment and shear force for the Buttress wall are shown in Figure 11. The shear force of reinforcements at the junction of the buttress and the cut-off wall obtained from Plaxis software is shown in Figure 11.

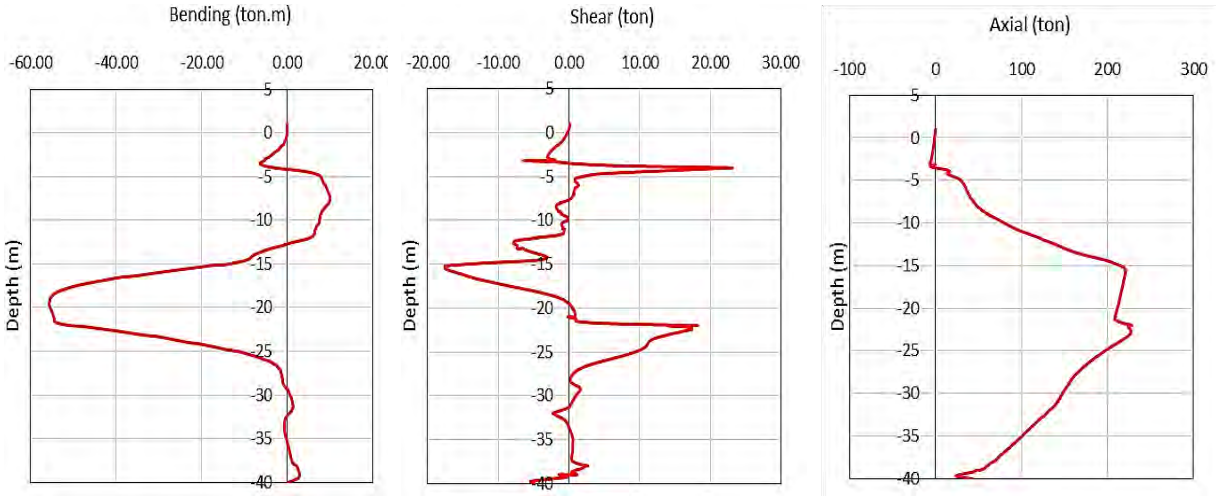

Fig. 10. Cut-off wall forces

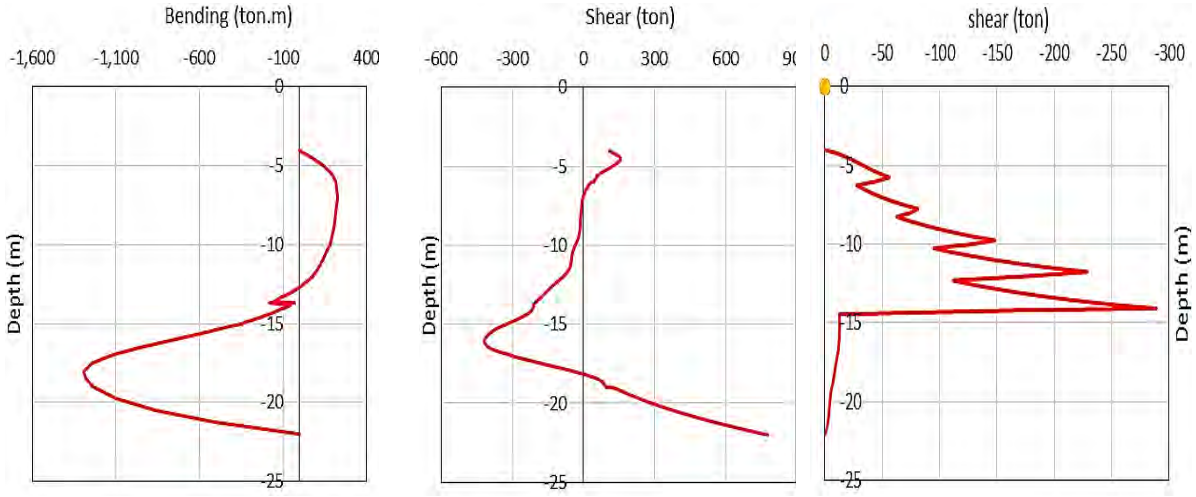

(a) (b) (c)

Fig. 11. Buttress wall forces (A and B) and shear forces at the junction of the buttress and the cut-off wall (C)

SAP2000 software was utilized to calculate the stresses induced in the panels of the central cut-off wall. To accurately simulate the loading conditions, soil pressure data obtained from PLAXIS was imported and applied to the structural model in SAP2000. This approach allowed for a more realistic representation of soil-structure interaction. Figure 12 illustrates the stress distribution at various critical points under the most severe load combinations.

In the cross-section of Ha'er and Bein' Alharamain, due to the convex geometry of the wall, the type of force created in the elements, especially the waler beams, is different from other sides, and this

side should be modeled separately. Therefore, according to this issue, this side has been modeled in 3D in SAP2000 software, and the results of its analysis are presented in Figure 13.

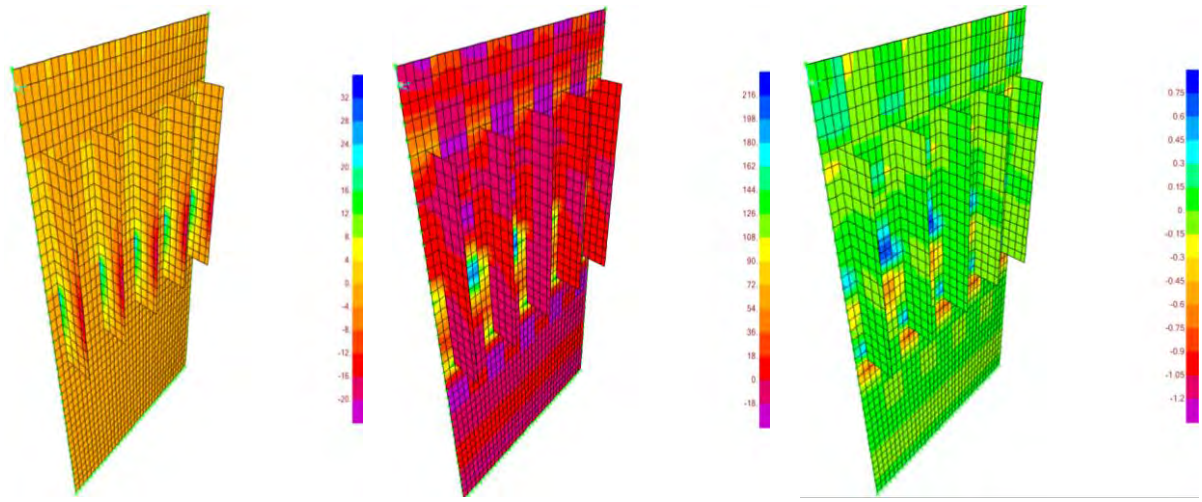

Fig. 12. The maximum stresses created in the model

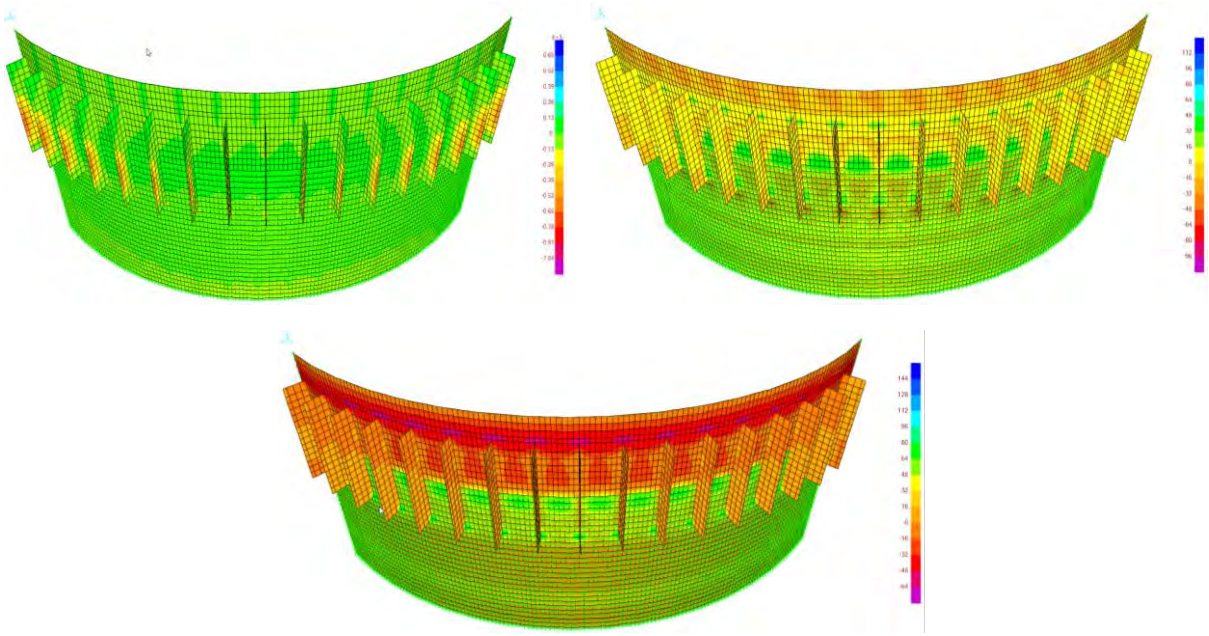

Fig. 13. The maximum stresses created in the Ha'er section

5. Instrumentation and Monitoring

In important excavation projects such as the current project, continuous monitoring of influential parameters such as deformations and pore water pressure is important and essential. In this project, it is necessary to use tools such as inclinometers to monitor the behavior of the diaphragm wall and piezometer in the inner and outer parts of the excavation due to the presence of high ground water level, see Figure 14. This issue is important both for stability and for controlling the adequacy of the drainage system. In the following, the details of the instrumentation plan will be discussed. One of the most important measurement parameters is the pore water pressure in the inner area of the well and also around the cut-off wall. At this stage, approximately 1 piezometer is considered for every 5000 square meters inside the excavation area. Also, for every 150 meters of wall length, a piezometer has been considered behind the cut-off wall to control the quality of its performance and also to determine the water pressure on the wall. These piezometers are installed in the perimeter section of the excavation and at two different depths of -10 and -20 meters. At this stage, 11×2 = 22 piezometers are required for monitoring. Three inclinometers are used to measure

the horizontal movement of the wall. Also, tiltmeter is used to monitor deviations and tilts in surrounding structures, especially sensitive structures. Finally, it is appropriate to use surveying method to control surface displacements. The location of benchmark points around the site should be determined in such a way that, in addition to proper visibility, they are installed in areas that are not affected by movement caused by excavation, water pumping, and executive operations. The targets should be installed both in the area around the pit and on the edge of the diaphragm wall. On average, two targets on the diaphragm wall and two targets perpendicular to the wall (up to a distance of 30 meters) are predicted for every 10 meters of wall length. According to the approximate perimeter of 600 meters for the excavation area, about 120 targets on the wall and 120 targets behind the wall and outside the excavation area are expected.

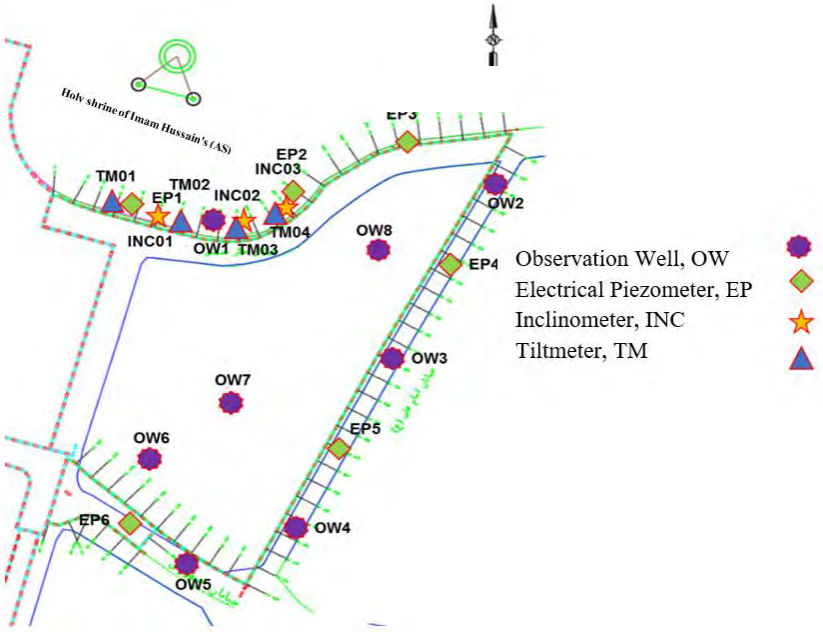

Fig. 14. Placement of the proposed precision instruments for Imam Hassan's (AS) courtyard

The excavation site was instrumented with inclinometers, piezometers, and surface settlement markers to monitor soil and wall behavior during excavation. Preliminary field measurements from the initial and intermediate excavation stages indicate lateral wall displacements and pore water pressures that are consistent with the trends predicted by the PLAXIS 2D and SAP2000 models. Inclinometer readings show maximum lateral deflections near the wall crown, matching the predicted range of approximately 4 cm. Piezometer readings confirm that the diaphragm wall effectively limits groundwater inflow, in agreement with the modelled seepage distributions. These preliminary data provide confidence in the model predictions while also highlighting areas where ongoing monitoring is critical. Full-scale measurements will continue throughout the excavation process to further validate and refine the numerical analyses. This addition helps demonstrate that the numerical predictions are supported by field observations, while also acknowledging limitations and the need for continued monitoring.

6. Conclusion

In this article, the stabilization plan of the excavation of Imam Hussain's (AS) holy shrine was presented. In this project, the diaphragm wall method was used to stabilize the excavation and simultaneously solve the problem of water seepage. As seen in the outputs taken from the models made using PLAXIS and SAP200 software, the stabilization plan provided by the diaphragm wall method is responsive both from the point of view of deformation and from the point of view of lateral soil forces and has the desired adequacy. In this research, it was seen that the diaphragm wall method, in addition to controlling the displacement of the retaining wall (in the range of 4 cm) and controlling the damage level of the adjacent structures at the permitted levels, can also control the problem of seepage of subsurface water into the excavation. Also, one of the important

advantages of the diaphragm wall is the removal of the concrete wall of the basement and the use of the diaphragm wall as the permanent wall of the basement, which is cost-effective both in terms of the economy and the construction time of the project. With the help of implementing the diaphragm wall as a T-shaped section in this project (Buttress wall), the need to implement temporary elements such as anchors, struts, raker beams and etc. was eliminated. This, especially in this project, considering the past experiences and the non-suitable soil condition (loose and running sand) and the high level of ground water, can solve the technical and operational problems of implementing elements such as anchors.

References

[1] Bolton MD, Powrie W. Behaviour of diaphragm walls in clay prior to collapse. Géotechnique. 1988 Jun;38(2):167-89. https://doi.org/10.1680/geot.1988.38.2.167
[2] Pakbaz MS, Imanzadeh S, Bagherinia KH. Characteristics of diaphragm wall lateral deformations and ground surface settlements: Case study in Iran-Ahwaz metro. Tunnelling and Underground Space Technology. 2013 Apr 1; 35:109-21. https://doi.org/10.1016/j.tust.2012.12.008
[3] Jasmine Nisha J, Muttharam M. Deep excavation supported by diaphragm wall: A case study. Indian Geotechnical Journal. 2017 Sep; 47:373-83. https://doi.org/10.1007/s40098-017-0230-1
[4] Karkush M, Ali NA. Electrokinetic enhancement of microbial induced calcite precipitation used in improving the shear strength of soft clay. InSmart Geotechnics for Smart Societies 2023 Aug 4 (pp. 155-163). CRC Press. https://doi.org/10.1201/9781003299127-14
[5] Saba J, Mahdi K. Shear strength and chemical properties of soft clayey soil treated with magnetized water. Magazine of Civil Engineering. 2023;124(8):12406.
[6] Karkush M, Ali SD. Durability of Gypseous Soil Stabilized with Nano-silica under Environmental Conditions. Jordan Journal of Civil Engineering. 2025 Jan 1;19(1). https://doi.org/10.14525/JJCE.v19i1.12
[7] Bilal AM, Jebur MM, Zhussupbekov A, Karkush M. Evaluation of in Situ Loading Tests Conducted on Micropiles Used to Enhance the Bearing Capacity of Karbala Sandy Soil. Soil Mechanics and Foundation Engineering. 2025 Mar;62(1):65-72. https://doi.org/10.1007/s11204-025-10028-w
[8] Ali SD, Karkush M. Effects of nano-clay on the geotechnical properties of gypseous soil. In IOP Conference Series: Earth and Environmental Science 2024 Aug 1 (Vol. 1374, No. 1, p. 012006). IOP Publishing. https://doi.org/10.1088/1755-1315/1374/1/012006
[9] Almurshedi AD, Karkush M. Experimental and numerical modeling of load settlement behavior of gypseous soils improved by MICP. In Smart Geotechnics for Smart Societies 2023 Aug 4 (pp. 583-589). CRC Press. https://doi.org/10.1201/9781003299127-74
[10] Karkush MO, Kareem MS, Jawad SI, Babu S. Sustainability analysis of improvement of contaminated clayey soil using lime piles technique. In AIP Conference Proceedings 2024 Jan 29 (Vol. 2864, No. 1, p. 030035). AIP Publishing LLC. https://doi.org/10.1063/5.0186092
[11] EN B. 2: 2007. "Eurocode 7-Geotechnical design-Part 2: Ground investigation and testing.". The European Union Regulation 305/2011, Directive 98/34/EC, Directive 2004/18/EC. 1997.
[12] Sabatini PJ, Pass DG, Bachus RC. Ground anchors and anchored systems. United States. Federal Highway Administration. Office of Bridge Technology; 1999 Jun 1.
[13] Lazarte CA, Robinson H, Gómez JE, Baxter A, Cadden A, Berg R. Soil nail walls reference manual. 2015 Feb.
[14] American Concrete Institute. (2014). ACI318M-14: Building code requirements for structural concrete. ACI: USA.
[15] Burland, J.B. 1997. Assessment of risk of damage to buildings due to tunnelling and excavation. Earthquake Geotechnical Engineering, Ishihara (ed.), 1997, Balkema, Rotterdam, pp. 1189 - 1201.
[16] Bouali MF, Karkush MO, Bouassida M. Impact of wall movements on the location of passive Earth thrust. Open Geosciences. 2021 May 19;13(1):570-81. https://doi.org/10.1515/geo-2020-0248

Research on Engineering Structures & Materials
www.jresm.org

Research Article

Evaluating the Ramberg–Osgood Model for nonlinear moment–curvature analysis of reinforced concrete beams

Ahmad D. Abdullatef [1,a], Safaa I. Ali [1,b], Safaa Y. Hamad Aldarraji [2,c], Muataz I. Ali [*,1,d]

[1]*Dept. of Civil Eng., College of Engineering, University of Samarra, Salah Al Deen, 34010, Iraq*
[2]*Dept. of Architecture Engineering, College of Eng., University of Samarra, Salah Al Deen, 34010, Iraq*

Article Info

Article History:

Received 17 Feb 2026
Accepted 18 Mar 2026

Keywords:

Beams;
Moment–curvature relationship;
Nonlinear analysis;
Constitutive modelling;
IS 456;
Structural ductility

Abstract

This paper improves the prediction of the nonlinear moment-curvature Characteristics of Reinforced concrete beams by using the Ramberg-Osgood model. Develop an integrated analytical (closed-form) moment–curvature framework based on the Ramberg–Osgood function, which provides a smooth (continuous) elastic-to-plastic transition for steel. At the same time, concrete degradation is captured progressively through cracking and crushing using section analysis with equilibrium and strain-compatibility conditions. The model was validated through two extensive investigations of ultimate moments measured in laboratory tests. The Ramberg-Osgood model provides better predictions of ultimate moments than IS 456-2000 and achieves more than 28% Improvement in the average difference between predicted and actual ultimate moments, with a coefficient of determination (R2) greater than 0.98. The results demonstrate that the Ramberg-Osgood model can accurately describe the significant phases of reinforced concrete section behavior-concrete cracking, steel yielding, and post-yield hardening-thereby providing a more reliable method of analyzing Reinforced Concrete Flexural Performance through a nonlinear analysis than the traditional IS 456:2000 approach.

© 2026 MIM Research Group. All rights reserved.

1. Introduction

The moment-curvature (M-κ) relationship is the metric by which all reinforced concrete (RC) beams' nonlinear flexural behaviours can be determined. Accurate determination of the M-κ relationship provides both deflection and ductility, but predicting it remains very difficult. Many Simplified Design Codes (IS 456, Eurocode 2, etc.) [1,2] generally use a bilinear material behaviour and an empirical approach to effective stiffness. Both methods can lead to significant discrepancies in accurately representing the gradual stiffness losses in the beam due to cracking and yielding [3,4].

Advanced numerical techniques, such as fibre section analysis and finite element modelling, produce much more accurate results; however, specialized computer programs and the considerable time required to run them limit their use to occasional applications in routine design [5]. A smooth transition from elastic to plastic modelling is possible using the Ramberg-Osgood constitutive model, which has been successfully applied to metal plasticity [6]. While there has been increased interest in RC section analysis (particularly in direct comparisons with design code methods), little research exists on this topic. Therefore, there exists a large gap between the practical need for accurate analytical tools and available simplified design code methods.

*Corresponding author: muitaz88@gmail.com
[a]orcid.org/0009-0005-7364-563X; [b]orcid.org/0009-0008-6675-5525; [c]orcid.org/0009-0006-1648-8778; [d]orcid.org/0000-0001-5084-8075
DOI: http://dx.doi.org/10.17515/resm2026-1518st0217rs

Recent research has sought to develop enhanced methods for modelling the behaviour of reinforced concrete elements using more sophisticated numerical models and constitutive-based methodologies. Research has also been conducted to investigate the ductility behaviour of RC elements subjected to static or dynamic (cyclic) loads using fibre-based numerical models in conjunction with detailed moment-curvature relationships [7],[8]. Other studies of refined constitutive models have also been conducted, in which researchers have attempted to create smooth (continuous) stress-strain transitions from steel reinforcement and the nonlinear behaviour of concrete (many derived from the Menegotto-Pinto model or its modifications) [9],[10]. These refined constitutive models are more accurate than their predecessors in capturing the cyclic and nonlinear behaviour of steel; however, they typically require advanced mathematical techniques and sophisticated computing systems.

Recent years have seen many studies investigate the development of simplified analytical techniques for predicting the nonlinear flexural behaviour of reinforced concrete (RC) beams while retaining adequate accuracy. Specific techniques include the use of analytical moment-curvature models that account for both nonlinear concrete compression behaviour and tension stiffening effects, thereby enhancing predictions of stiffness degradation and post-crack behaviour [11]. Researchers have examined the use of section equilibrium analyses in conjunction with refined material constitutive relationships to improve ductility and ultimate capacity prediction [12]. Despite these recent advances, most of the identified techniques remain dependent on complex numerical integration procedures or require excessive computational resources. Therefore, they continue to limit the practical application of these techniques in routine design calculations [13].

Due to increased interest in specific RC sections, the number of researchers proposing simplified analytical systems capable of producing moment-curvature relationships with significantly fewer computations than traditional methods has increased considerably in recent years. Such new approaches already exist, and there is a large disparity between the practical requirements for reliable analytical tools and the simplified designs of analytical systems described in present-day building codes. There also does not exist a single unified closed-form developed moment-curvature expression that (1) uses a smooth constitutive relationship for steel, (2) can be used or calculated without having to perform computationally complex numerical schemes, or (3) has been independently verified through extensive experimental testing with the use of established design code comparisons, such as IS 456.

To fill the existing gap, this research aims to provide an improved and verified analysis framework for the Ramberg-Osgood Constitutive Model. The specific aims of this research are to develop a closed-form moment-curvature relationship for reinforced concrete (RC) sections, validate quantitatively the findings of this research against two other independent experimental studies, conduct a complete statistical comparison between the predictions produced by this model and the design recommendations in IS 456:2000, and to demonstrate that the model is superior in its ability to model the three major behaviours of reinforced concrete: cracking, yielding and post-yield hardening is better than any other existing modelling techniques.

2. Methodology

2.1. Analytical Framework: A Ramberg-Osgood-Based Formulation

Through the integration of the Ramberg-Osgood model for steel and a nonlinear response for concrete using a framework of sectional equilibrium and strain compatibility, a closed-form relationship between the moment and curvature of the section will be established. The approach is divided into three major components: (1) a linear-elastic analysis of an uncracked section; (2) an analysis of a cracked section with an elastic-to-nonlinear transition of steel and the load-transfer capacity of the cracked reinforced concrete section, including tension stiffening effects; and (3) analysis of the behaviour of the section in the plastic range incorporating strain hardening. The most important contribution of this work is the use of the Ramberg-Osgood function:

$$\epsilon = \frac{\sigma}{E} + \alpha \left(\frac{\sigma}{f_y}\right)^n \tag{1}$$

to provide a smooth, continuous representation of steel behavior across all stages, eliminating the abrupt stiffness changes inherent in bilinear code models [1].

2.2. Sectional Curvature Determination

2.2.1 Uncracked Stage

Strain compatibility between steel and concrete dictates the flexural behaviour of uncracked sections. To ensure equal strain throughout the section, the reinforced concrete section can be idealized with homogeneous stiffness; that is, the equivalent area of the reinforcing steel in concrete is calculated using the modulus of elasticity ratio ($n = \frac{E_s}{E_c}$)[14]. The idealisation of a reinforced concrete section with homogeneous stiffness allows its stiffness to be evaluated from a single strain distribution.

While both materials exhibit almost linear responses up to the point of cracking, introducing the Ramberg-Osgood model provides a better understanding of the gradual departure from linear elasticity, especially for steel, by predicting deflection and early curvature more accurately [15]. The Moment-Curvature equation is written as follows:

$$\phi = \frac{M}{E_c I_t} \tag{2}$$

where I_t is the transformed moment of inertia. The neutral axis location follows:

$$y_{NA} = \frac{\int y\, dA_t}{\int dA_t} \tag{3}$$

The tensile fiber strain (expansion) when reaching the tensile strength f_{ct}. of the load-bearing material (concrete), shall start to induce cracking. Where classical elastic theory may reach a limit, the Ramberg-Osgood equation provides a smooth transition (best fit) into the nonlinear aspect of steel behaviour, allowing better calculation of curvature at cracking.

2.2.2. Cracked Section Behaviour

2.2.2.1. Concrete Cracked – Steel Elastic

Once concrete has developed a fracture, it can only support compressive forces, while its reinforcement carries tensile forces. The forces carried by the entire cross-section of a member must be analysed across both the compressed concrete zone and the steel reinforcement bars that support it [18]. The rate of change in steel behaviour in this phase can best be represented by the Ramberg-Osgood linearised relation between stress and strain [5]. At this stage, the curvature of the section is as follows:

$$\phi = \frac{M}{E_{eff} I_c} \tag{4}$$

where E_{eff} is the tangent stiffness from the R–O model and I_c is the cracked transformed inertia.

The neutral axis depth x follows from force equilibrium:

$$C_c(x) = T_s(\epsilon_s) \tag{5}$$

Moreover, steel strain is defined as:

$$\epsilon_s = \frac{\sigma_s}{E_s}\left[1+\alpha\left(\frac{\sigma_s}{f_y}\right)^{n-1}\right] \tag{6}$$

This approach captures early nonlinear steel behavior before yielding, improving post-cracking curvature and load–deflection prediction accuracy.

$$n = \frac{ln\left(\frac{\varepsilon_u}{0.002}\right)}{ln\left(\frac{f_u}{f_y}\right)} \quad (7)$$

Where $f_u$is the ultimate stress of the material, ε_u is uniform strain at f_u, and f_y is the yield stress of the material.

2.2.2.2. Concrete Cracked – Steel Plastic/Nonlinear

The full Ramberg-Osgood constitutive model is necessary as loading continues to increase on the member and steel stresses reach the yield point, or continue to exceed it; it provides an uninterrupted transition from elastic to inelastic behaviour, without any intermediate bilinear approximations [6]. When a steel member enters its nonlinear plastic behaviour, the analysis is performed using sectional equilibrium.:

$$C_c(x) = T_s(\epsilon_s^{RO}) \quad (8)$$

where

$$\epsilon_s^{\mathrm{RO}} = \frac{\sigma_s}{E_s} + \alpha\left(\frac{\sigma_s}{f_y}\right)^n \quad (9)$$

Curvature grows significantly with increasing moment and can be obtained from:

$$\phi = \frac{\epsilon_c + \epsilon_s^{RO}}{d} \quad (10)$$

where d is the effective depth between the compression strain layer and tension strain layer, serves to define how these two areas transfer load between one another. This section becomes the dominant part of the global Structural Engineering response (load-deflection) due to the nature of Stiffness Degradation in steel, as we have just discussed. The Stiffness Degradation, in combination with curvatures, creates more significant mid-span deflections than at other stages. The Ramberg-Osgood model captures this transition continuously rather than applying a sudden stiffness change, as is usual with simplified bilinear models.

2.2.3. Load–Curvature and Load–Deflection Representation

Once cracking of concrete is observed and the tensile reinforcement is experiencing plastic behaviour, then the sectional behaviour of the composite will be controlled by the nonlinear compressive zone of the concrete and the plastified portion of the tensile reinforcement (steel). The equilibrium and compatibility properties of such a section can be described by multiple-formula relationships that relate to the compression zone depth, the axial force at that point, and the bending moments generated [17]. The axial force that can be produced for an imposed state of curvature is:

$$N = \frac{1}{2\phi}\eta^2 bE_c - A_s f_{yd} + \phi(\eta - a)E_s A_s' \quad (11)$$

Where ŋ is the neutral axis position, A_s is the area of steel in the tension fiber, A_s' is the steel area in the compression fiber, f_{yd} is the yield value for steel in tension fiber, and a is the depth of the compression zone in concrete. To find the neutral axis position ŋ evaluated from:

$$\eta = -\frac{\alpha_1 A_s'}{b} + \left[\left(\frac{\alpha_1 A_s'}{b}\right)^2 + \frac{2}{bE_c\phi}\left(\phi a E_s A_s' + N + A_s f_{yd}\right)\right]^{1/2} \quad (12)$$

Where α_1The parameter to calculate (η)that is used to calculate the internal bending moment for the cracked–plastic stage is:

$$M^* = \frac{E_c b\eta^3}{3}.\phi - A_s f_{yd}(a - h + \eta) + \phi(\eta - a)^2 E_s A_s' \quad (13)$$

The bending moment referred to the concrete section centroid (mid-depth) is:

$$M = M^* + N\left(\frac{h}{2} - \eta\right) \tag{14}$$

The interactions among these relationships are used to define the cracked concrete section. At the same time, the transition from the nonlinear hardening of steel reinforcement to plastic behaviour has been incorporated into the Ramberg-Osgood constitutive model. By applying these relationships to determine the tangent modulus (Eeff) at several strain levels, we can directly obtain moment-curvature evaluations and accurately predict curvature growth and stiffness degradation with increasing load-deflection [18].

2.4. Evaluation of Tangent Stiffness Based on the Ramberg–Osgood Model

To determine a predictable load-deflection relationship for a reinforced concrete beam, the change in beam stiffness at all stress levels must be considered. Adding reinforcement to a beam changes its stiffness because it alters the range of stresses the beam experiences. The Ramberg-Osgood Model gives a continuous and differentiable relationship between stress and strain, and can therefore be used to determine Tangent Stiffness values for all key regions of Structural Response [18]

2.4.1. Tangent Elastic Stiffness (Point 1)

The tangent elastic stiffness characterize the final stage of the response of a cracked section when the steel reinforcement still behaves elastically; this stiffness is equal to the moment-curvature slope at the limit of the elastic portion of the Ramberg-Osgood curve for steel. Therefore, we can express it mathematically as the derivative:

$$k_{el} = \left(\frac{dM}{d\phi}\right)_{\phi=\phi_1} \tag{15}$$

Where; ϕ_1 is the curvature at which the steel strain reaches the boundary of the elastic Ramberg–Osgood domain, k_{el} corresponds to Point 1 in the equivalent diagram (Fig. 1). This point marks the onset of noticeable nonlinear behaviour in the reinforcement and the transition from linear to nonlinear stiffness reduction [6].

2.4.2. Tangent Plastic Stiffness (Point 2)

When the reinforcement is loaded, it will have progressed to the "nonlinear plastic" portion of its load-deformation response, which has a considerable reduction in the value of tangent stiffness that may be determined from the differential method mentioned before for the Ramberg-Osgood formulation at the curve corresponding to significant yield in the steel:

$$k_{pl} = \left(\frac{dM}{d\phi}\right)_{\phi=\phi_2} \tag{16}$$

Where; ϕ_2 is the curvature corresponding to Point 2 in Fig. 1. k_{pl} reflects the tangent stiffness in the plastic range of the Ramberg–Osgood model. This stiffness value governs the beam response during the large-deflection stage and is essential for accurately predicting the descending stiffness branch preceding the ultimate limit state [19].

2.4.3. Ultimate Bending Moment

The bending capacity associated with ultimate conditions, M_u, corresponds to the conventional flexural failure of the RC section, whether governed by compressive concrete crushing or tensile reinforcement rupture. In the Ramberg–Osgood-based framework, the moment at the ultimate state is evaluated through the strain profile extending to the ultimate concrete strain. ϵ_{cu}:

$$M_u = T_s(\epsilon_{s,u}) \cdot z \tag{17}$$

Where; $\epsilon_{s,u}$ is the reinforcement strain obtained from the full Ramberg–Osgood expression at ultimate curvature. z is the internal lever arm at failure. This ultimate moment, together with Points 1 and 2, is shown in the Figure. 1, forms a complete representation of the nonlinear stiffness degradation throughout the beam response [1].

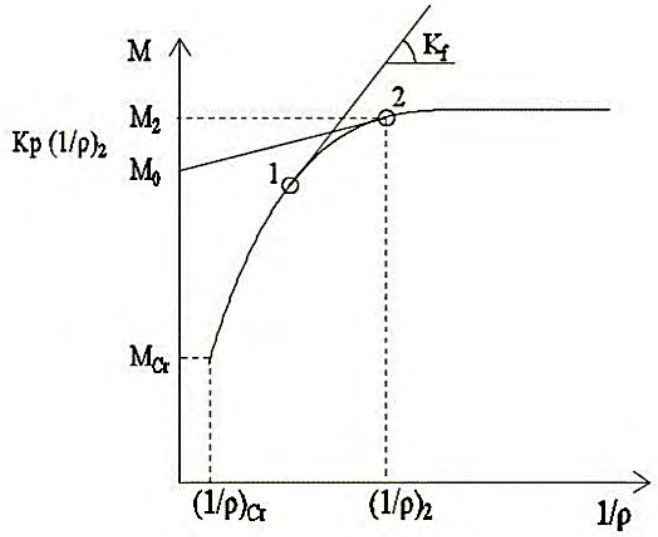

Fig. 1. General moment-curvature diagram for cracked concrete.

3. Ramberg–Osgood approximation of the Cracked Response

3.1. Curvature–Moment Representation Using the Ramberg–Osgood Model

After the formation of tensile cracks, the flexural response of reinforced concrete beams becomes highly nonlinear, primarily due to the combined effects of progressive concrete softening in compression and the nonlinear hardening of the reinforcing steel. To obtain a smooth and continuous representation of the curvature–moment relationship in this post-cracking regime (State II), the Ramberg–Osgood constitutive model provides a convenient analytical framework [5]. The curvature corresponding to a given bending moment can be expressed in a normalized Ramberg–Osgood form as:

$$\phi = \frac{M}{K_{el}}\left[1+\alpha\left(\frac{M}{M_y}\right)^{n_1-1}\right] \tag{18}$$

Where; ϕ is the section curvature, M is the applied bending moment. K_{el} is the initial post-cracking stiffness obtained from cracked-section analysis, Equ. 15, M_y is the moment corresponding to the onset of yielding in the tensile reinforcement. α is the Ramberg–Osgood shape parameter controlling the onset of nonlinearity. n_1 is an exponent governing the transition between elastic and plastic steel behavior.

The parameter n controls the steepness of the curvature increase as the reinforcement moves from elastic towards plastic response. Its value is selected best to match the nonlinear hardening characteristics of the reinforcement and is obtained from calibration against sectional moment–curvature analysis or experimental data:

$$n_1 = \frac{ln\,(\phi_2/\phi_1)}{ln\,(M_2/M_1)} \tag{19}$$

where (ϕ_1, M_1) and (ϕ_2, M_2) There are two reference points corresponding to the elastic–nonlinear transition and the plastic–hardening region, respectively.

3.2. Comparison of Curvature–Moment Curves for Different Values of n_1

Figure 2 presents a comparison between curvature–moment curves predicted by the Ramberg–Osgood formulation using different values of the transition between elastic and plastic steel behavior n_1 (e.g., 6, 20, 40) Furthermore, the reference analytical curves were obtained from sectional analysis under various levels of axial load.

The comparison highlights that:

- Lower values of n_1 produce smoother, more gradual transitions from elastic to plastic behavior.
- Higher values of n_1 yield a curve that approaches a bilinear response with a sharper yielding point.

The Ramberg–Osgood model can closely approximate the full nonlinear sectional response when the parameters (N, M, ϵ_s^{RO}, ϕ, and n) are properly calibrated [20]. This ability to reproduce a wide range of nonlinear behaviours with only two adjustable parameters makes the Ramberg–Osgood formulation particularly useful for predicting load–deflection responses of RC beams, where curvature plays a central role in determining midspan deflection through numerical integration along the member length [21].

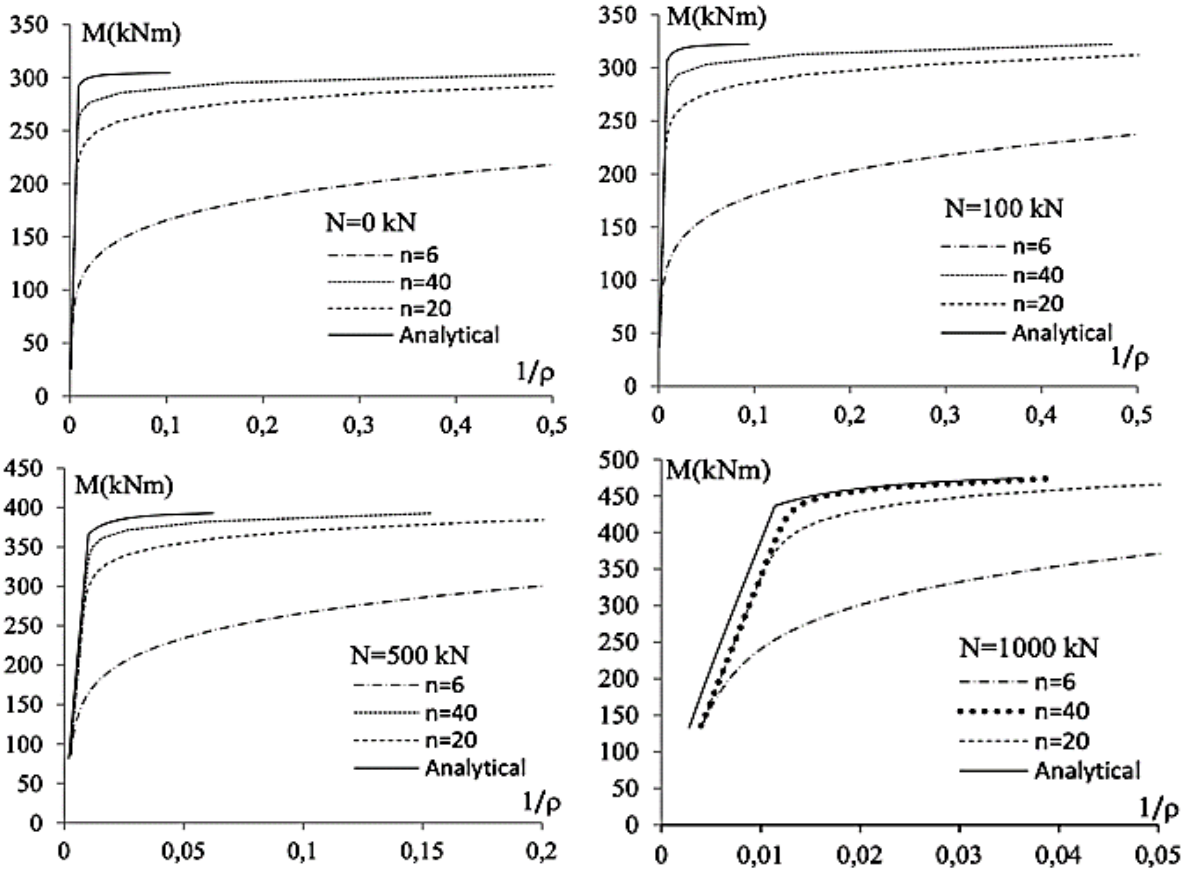

Fig. 2. Moment-curvature diagram by Ramberg-Osgood equation

3.3. Application of IS 456 Provisions In Analytical Modelling

In this study, the IS 456:2000 code provisions were employed to provide a reference analytical model for reinforced concrete beams. The effective moment of inertia approach was used to account for concrete cracking, and a bilinear representation of steel stress–strain behaviour was adopted to approximate the reinforcement's elastic and plastic ranges. This approach provides conservative estimates of flexural stiffness and ultimate moment capacity, serving as a benchmark to compare with both experimental measurements and the Ramberg–Osgood constitutive model. Utilising IS 456 in the methodology ensures that the analysis aligns with established engineering

design practices and provides a practical context for evaluating the predictive accuracy of more advanced analytical formulations [1].

4. Numerical Procedure

4.1. Numerical Implementation Framework

The overall analysis follows these sequential steps, consistent with recent nonlinear sectional-analysis frameworks used in RC members:

- Define material properties: $E_c, f_{ct}, f_c, E_s, f_y, \epsilon_{cu}, f_u, and\ \epsilon_{su}$.
- Compute uncracked stiffness and evaluate M_{cr} following common RC tension-stiffening formulations [13].
- Generate reference (M,ϕ) points for the cracked–elastic and cracked–plastic stages using sectional analysis with fibre discretisation and nonlinear constitutive relationships, for calibration and validation purposes only.
- Use these reference cracked-section points to identify the parameters. $K_0, \alpha, n, M_y$of the Ramberg–Osgood-based closed-form relation. This relation provides a continuous transition between the elastic and plastic states of steel [21].
- Assemble the full moment–curvature curve:
- Uncracked branch
- R–O cracked branch
- Applying the average curvature method to compute global mid-span deflection is an accepted technique that has been shown in numerous Nonlinear beam model experiments to be efficient [22].

The methodology is therefore based primarily on mechanics-derived sectional analysis as a reference tool for parameter calibration and model verification, whereas the final outcome of the study is a smooth, closed-form analytical representation of RC flexural behaviour that can be applied without repeated fibre discretisation in routine applications.

4.2. Statistical Evaluation of Moment–Curvature Comparisons

Statistical metrics provide a way to quantitatively compare the moment-curvature responses of reinforced concrete beams predicted by analytical models to experimental results. Common statistical measures used for this comparison are:

- The mean absolute error (MAE) is the average absolute difference between the model's predictions and the experimental results, representing the overall magnitude of prediction error.
- The root mean square error (RMSE) is more sensitive to larger deviations between predicted and experimental results because it squares the errors, giving greater weight to discrepancies in curvature (magnitude) or moment values.
- The coefficient of determination (R^2) indicates the amount of variation in the experimental results that can be explained by the variations in the analytical model data, thereby providing a normalized measure of how well the analytical model fits the experimental results.

Statistical metrics allow objective comparisons of multiple analytical methods (e.g., Ramberg-Osgood formulations, IS 456 code predictions, experimental data) to identify the best model for describing the nonlinear behaviour of reinforced concrete beam flexure and to improve the reliability and repeatability of analytical assessments in structural engineering research [18].

$$MAE = \frac{1}{N}\sum_{n=1}^{N} \mid A_n - P_n \mid \tag{20}$$

$$RMSE = \sqrt{\frac{1}{N}\sum_{n=1}^{N} (A_n - P_n)^2} \tag{21}$$

$$R^2 = 1 - \frac{\sum(A_n - P_n)^2}{\sum(A_n - S_n)^2} \tag{22}$$

Where (A_n) actual and predicted (P_n) values are compared, and comparing the estimated (N) number of points within the dataset is compared.

4.3. Overall Behaviour of the Cracked Member

The structural response of a reinforced concrete member after the initiation of the first flexural crack may be idealised into three distinct behavioural stages:

- Uncracked stage, where the section responds linearly.
- Crack-formation stage, with decreasing sectional stiffness.
- Stabilised cracking stage, with nearly constant crack distribution and reduced stiffness.

These stages align with the multi-stage behaviour described by modern curvature-based RC models [4]. see (Figure 3a, b) [22].

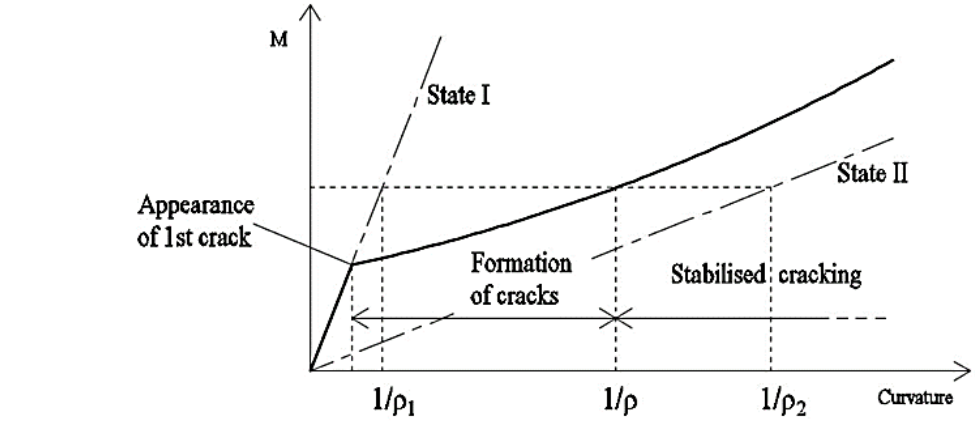

(a)

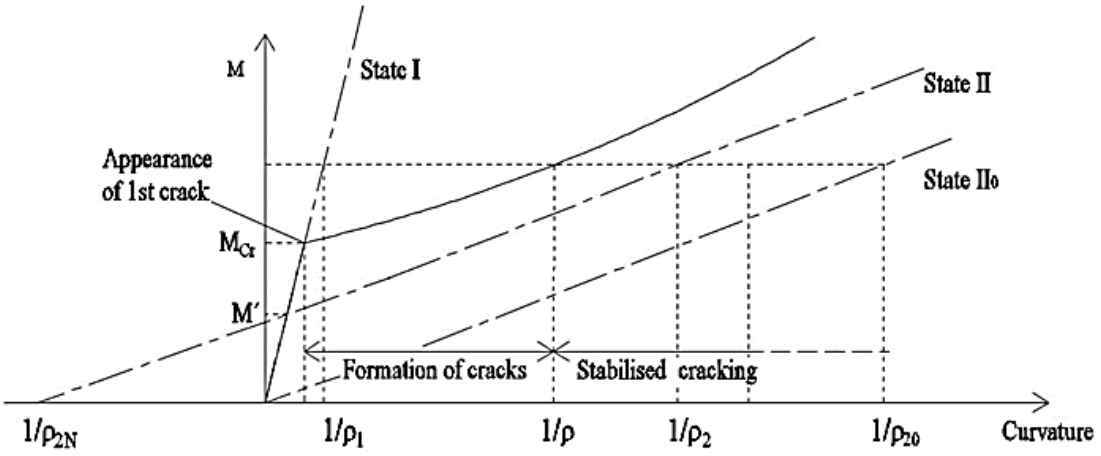

(b)

Fig. 3. (a) Idealised moment curvature behaviour for bending moment [22], (b) Idealised moment curvature behaviour for bending moment and axial load [22]

In State I, curvature ϕ_I corresponds to an uncracked section. In State II_0, curvature $1/\rho_{II0}$ (from Equ. 16 and 18) represents the fully cracked state. Under combined bending and axial load, curvatures become ϕ_1 in State I and ϕ_2 in State II, respectively. To incorporate tension-stiffening, the mean curvature ϕ_m is evaluated as:

$$\phi_1 = \zeta(\phi_{II} - \phi_I) + \phi_I \tag{23}$$

Where the tension-stiffening parameter ζ depends on M_{cr}, the acting moment M, and the bond-dependent coefficient β, following CEB-FIP recommendations and commonly used in recent RC curvature studies [4]. The presence of axial force modifies ζ according to:

$$\zeta = \begin{cases} 1 - \left(\frac{M_{cr}}{M}\right)^2, & N = 0 \\ \beta \left(\frac{M'}{M}\right)^2, & N > 0, M' < M \\ 1, & N > 0, M' \geq M \end{cases} \quad (24)$$

Where M' is the intersection of State-I and State-II curves. In the present study, this formulation is integrated with the Ramberg–Osgood constitutive model, which provides a smooth nonlinear steel stress–strain curve capable of accurately representing cracked-section behaviour.

5. Experimental Benchmarking And Comparative Assessment Framework

To validate the proposed analytical formulation and demonstrate its applicability to real structural behavior, a robust comparison framework incorporating both experimental evidence and established design standards was established. The empirical data obtained from significant investigations provide independent standards for assessing the predictive fidelity of the Ramberg-Osgood-based model [23,24]. Examples of the experimental work performed in the series of studies included reinforced concrete beams tested under monotonic bending loads. The measured values obtained from these tests are necessary for establishing the validity of a modelling methodology to accurately predict the expected load-deflection behaviour of reinforced concrete beams, as well as to quantify the development of cracks, the evolution of curvature, and the increase in strain of the reinforcing steel up to failure.

Furthermore, the IS 456:2000 provisions serve as the basis for normative references to the code-based predictions made by engineers. The design framework of IS 456 was established as a widely accepted engineering standard through the use of simple, conservative assumptions about cracking in concrete, effective stiffness, tension stiffening, and the yield strength of steel. These assumptions are useful for providing estimates for practical design-level purposes. However, because the framework uses bilinear or idealised elastic–plastic curves to represent the material behaviour of steel, the actual material behaviour is likely more complex than what is represented by the curves in the framework, which do not accurately depict the smooth nonlinear transition between elastic and plastic behaviour of steel [1].

The Ramberg-Osgood model provides a continuous, differentiable representation of the transition from elastic to plastic behaviour, more accurately reflecting the degradation of reinforcing steel stiffness in a member and better able to predict the curvature of a reinforced concrete member under increasing moments due to loading. The combination of this fibre model and moment-curvature and load-deflection behaviour analysis will allow comparison of these results with the current conventional codes for behaviour and with the true behaviour of concrete members tested [5,25].

6. Results and Comparative Analysis

6.1. Validation Against Experimental Benchmark I [23]

The moment-curvature relationship for an RC beam examined in [23] is shown in Figure 4. The Ramberg-Osgood (R-O) model developed in this study fits the experimental data extremely well. It captures all the phases of behaviour identified in the experimental data: (i) a linear-elastic phase, (ii) a reduction in stiffness due to cracking, (iii) a smooth transition to yield at approximately 19.9 kN·m, and (iv) a plateau during post-yield hardening. In contrast, the IS 456 model exhibits significant differences from the experimental data, especially in overestimating the initial stiffness and failing to capture a gradual yield transition, as depicted by the smooth transition of the R-O model, instead showing an abrupt bilinear response.

Table 1 depicts that the R-O Model had a statistically significant reduction of 40% in MAE (mean absolute error) that was achieved using the R-O Model (1.76 kN·m) as compared to that achieved using IS 456 (2.89 kN·m), and explained 98.2% of the experimental variance (R^2=0.982). The

results of a t-test indicate that there was no statistically significant difference between the R-O Model predictions and the experimental measurements (p-value=0.082). In contrast, the IS 456 Model showed a statistically significant difference (p-value = 0.022).

Table 1. Statistical performance metrics for Benchmark I [23]

Metric	Ramberg-Osgood Model	IS 456 Model
MAE (kN·m)	1.76	2.89
RMSE (kN·m)	2.15	3.42
R^2	0.982	0.934
Mean Relative Error	-11.2%	-15.7%
Ultimate Moment	21.50 kN·m (99% of exp.)	21.01 kN·m (97% of exp.)
Curvature)uncracked section(	0.000641 rad/m (3.6% of exp.)	0.000583 rad/m (5.8% of exp.)
Curvature)fully cracked(	0.00313 rad/m (3.3% of exp.)	0.00320 rad/m (4.7% of exp.)

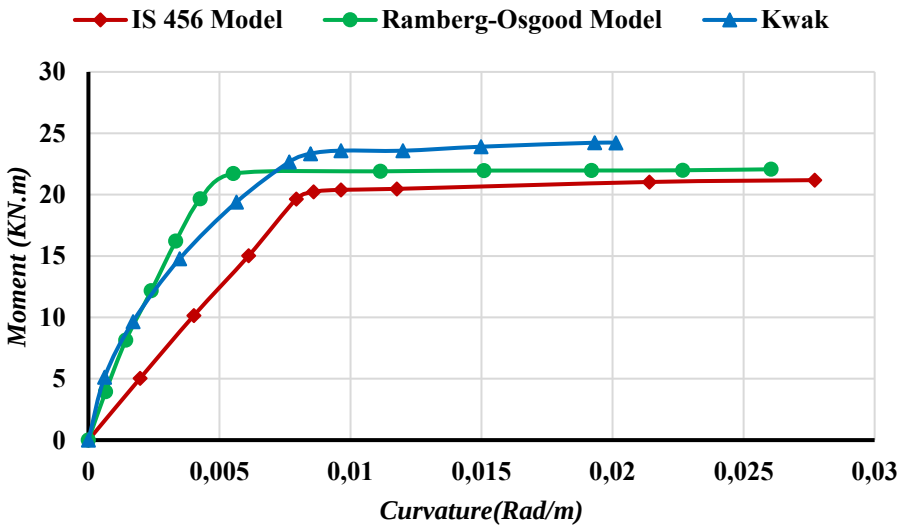

Fig. 4. Moment-curvature diagrams

6.2. Validation Against Experimental Benchmark II [24]

The R-O model continues to accurately predict the curvature development of concrete (M30) beams from an earlier independent data set, as shown in Figure 5, which compares the analytical predictions with the experimental results reported in [24]. Thus, the R-O model predicts the initiation (the cracking moment of 4.33 kN · m) and the final yield curvature (within 2.5% error).

Table 2. Accuracy metrics for Benchmark II [24]

Metric	Ramberg-Osgood Model	IS 456 Model
MAE (kN·m)	0.23	0.28
RMSE (kN·m)	0.31	0.36
R^2	0.994	0.987
Mean Relative Error	-2.8%	-3.3%
Ultimate Moment Prediction	10.26 kN·m (97% of exp.)	10.21 kN·m (97% of exp.)
Curvature)uncracked section(	0.034 rad/m (3.0% of exp.)	0.035 rad/m (6.0% of exp.)
Curvature)fully cracked(	0.095 rad/m (3.1% of exp.)	0.097 rad/m (5.4% of exp.)

The statistical analysis (Table 2) supports the consistency of the R-O Model with respect to the benchmark. Table (2) shows that the R-O model and IS 456 prediction made by both models yielded an ultimate predicting capacity within 3 per cent accuracy, with 97% predicted true value for both

models at 10.26 kN·m for the R-O model and 10.21 kN·m for the IS 456 model. According to the MAE and RMSE results, the R-O model performed better than the IS 456 model, as evidenced by lower MAE and RMSE values.

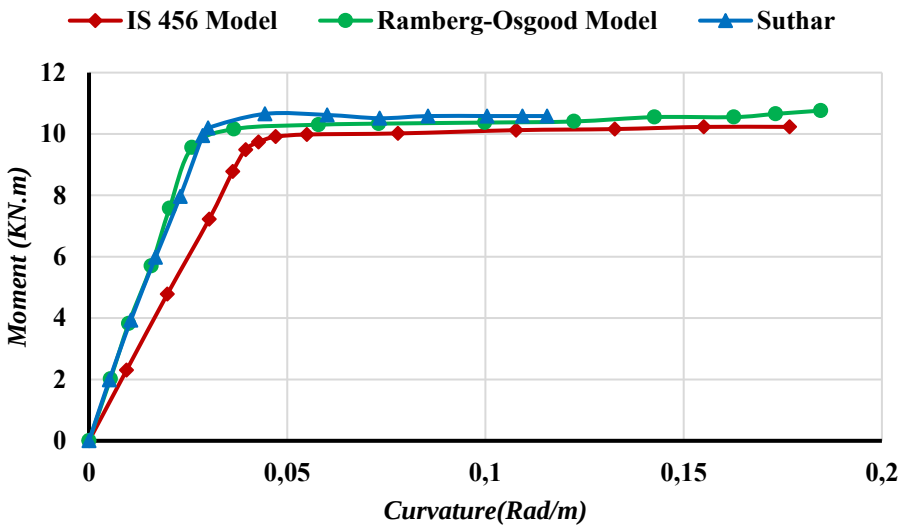

Fig. 5. Moment-curvature diagrams

7. Conclusion

This study has developed a validated integrated approach for nonlinear moment-curvature modelling using Ramberg-Osgood (R-O) constitutive modelling for reinforced concrete (RC) beams. The main findings from this research are:

- A continuous representation of the transition from elastic to plastic behaviour, which allows for accurate prediction of serviceability deflections.
- The R-O model can accurately predict the curvature-hardening phase, with post-yield error rates of less than 6% for ultimate curvatures, compared to traditional models.
- Although both methods provide reliable predictions of ultimate strength, the R-O model method produces more accurate predictions of moment than the IS 456 method based on lower MAE and RMSE values from test results from both benchmarks (Benchmark I: MAE of 1.76 versus 2.89 kN.m, RMSE of 2.15 versus 3.42 kN.m.; Benchmark II: MAE of 0.23 versus 0.28 kN.m, RMSE of 0.31 versus 0.36 kN.m).
- Compared to the IS 456 Method of predicting ultimate moments, the R-O Model gave a reduction of more than 28% to the mean absolute error of all the predicted moments across the entire response curve. Nevertheless, there was little difference in the accuracy of the two methods in predicting ultimate moments. The framework's ability to model the smooth transition in yield behaviour enables accurate predictions of post-cracking stiffness degradation and post-yield ductility, which bilinear models in current codes do not account for.
- In scope of the considered cases, engineers may use the framework as a method for predicting full-range flexural behaviour, rather than engaging in complex finite element modelling.
- The model has been validated on the basis of monotonic loading of rectangular reinforced concrete beams only. Therefore, there is no evidence to support the use of this model for cyclic loading, cross-sectional shapes, or members subjected to significant axial loading.

References

[1] Bureau of Indian Standards. IS 456: Plain and reinforced concrete - Code of practice (4th revision). New Delhi: BIS; 2000.

[2] European Committee for Standardization. EN 1992-1-1:2004: Eurocode 2: Design of concrete structures - Part 1-1: General rules and rules for buildings. Brussels: CEN; 2004.

[3] Bischoff PH. Reevaluation of deflection prediction for concrete beams reinforced with steel and fiber reinforced polymer bars. J Struct Eng. 2005;131(5):752-767. https://doi.org/10.1061/(ASCE)0733-9445(2005)131:5(752)

[4] International Federation for Structural Concrete. fib Model Code for Concrete Structures 2010. Berlin: Ernst & Sohn; 2013.

[5] Barros H, Ferreira C, Marques T. Moment-curvature diagrams for evaluation of reinforced concrete sections using a closed form Ramberg Osgood expression. In: Proceedings of the 7th European Congress on Computational Methods in Applied Sciences and Engineering. Crete, Greece; 2016. https://doi.org/10.7712/100016.2286.5727

[6] Ramberg W, Osgood WR. Description of stress-strain curves by three parameters. NACA Technical Note No. 902. Washington, DC: National Advisory Committee for Aeronautics; 1943.

[7] Simão PD, Barros H, Ferreira CC, Marques T. Closed-form moment-curvature relations for reinforced concrete cross sections under bending moment and axial force. Eng Struct. 2016;129:67-80. https://doi.org/10.1016/j.engstruct.2016.09.033

[8] Abbas ML, Güneyisi E. Compressive behavior and code based evaluation of normal weight and lightweight concrete filled composite steel tubes. Res. Eng. Struct. Mat. 2025;4:17-21. https://doi.org/10.17515/resm2025-565me1204rs

[9] Jaafari C, Grange S, Bertrand D, Georgin JF, Delhomme F, Tardif N. Multifiber finite element model based on enhanced concrete constitutive law to account for the effects of early age damage on the seismic response of RC structures. Eng Struct. 2022;256:113987. https://doi.org/10.1016/j.engstruct.2022.113987

[10] Lee JD. The effect of tension stiffening in moment-curvature responses of prestressed concrete members. Eng Struct. 2022;257:114043. https://doi.org/10.1016/j.engstruct.2022.114043

[11] Kurt Ö, Uyaner M. Stress analysis of aircraft tow hook using non-destructive testing techniques and numerical simulation. Res. Eng. Struct. Mat. 2026. http://dx.doi.org/10.17515/resm2026-1133me0903rs

[12] Gribniak V, Rimkus A, Torres L, Jakštaitė R. Deformation analysis of reinforced concrete ties: Representative geometry. Struct Concr. 2017;18(4):634-647. https://doi.org/10.1002/suco.201600105

[13] Kokot S. Reinforced concrete beam under support removal-Parametric analysis. Materials. 2021;14(20):5917. https://doi.org/10.3390/ma14205917

[14] Todeschini CE, Bianchini AC, Kesler CE. Behavior of concrete columns reinforced with high strength steels. ACI J Proc. 1964;61(6):701-716. https://doi.org/10.14359/7803

[15] Kaldjian MJ. Moment curvature of beams as Ramberg Osgood functions. J Struct Div ASCE. 1967;93(ST5):121-132. https://doi.org/10.1061/JSDEAG.0001786

[16] Kent DC, Park R. Inelastic behaviour of reinforced concrete members with cyclic loading. Bull N Z Soc Earthq Eng. 1971;4(2):108-113. https://doi.org/10.5459/bnzsee.4.1.108-125

[17] Kaklauskas G, Ghaboussi J. Stress-strain relations for cracked tensile concrete from RC beam tests. J Struct Eng. 2001;127(1):64-73. https://doi.org/10.1061/(ASCE)0733-9445(2001)127:1(64)

[18] Bischoff PH, Scanlon A. Effective moment of inertia for calculating deflections of concrete beams. ACI Struct J. 2007;104(1):68-75.

[19] Kwak HG, Kim SP. Nonlinear analysis of RC beams based on moment-curvature relation. Comput Struct. 2002;80(7-8):615-628. https://doi.org/10.1016/S0045-7949(02)00030-5

[20] Zhu H, Wu G, Zhang J, Wang H. A modified Ramberg-Osgood model for structural steel and its application in nonlinear analysis. J Constr Steel Res. 2024;214:107456.

[21] Foroughi S, Yuksel SB. Investigation of moment-curvature and effective section properties of reinforced concrete members. Can J Civ Eng. 2021;48(3):231-242. https://doi.org/10.20528/cjsmec.2021.03.003

[22] European Committee for Standardization. Eurocode 2: Design of concrete structures - Part 1-1: General rules and rules for buildings (EN 1992-1-1). Brussels: CEN; 2004.

[23] Kwak HG, Kim JK, Lee SS. Flexural behavior of high-strength concrete beams with high-strength reinforcement. J Struct Eng. 2000;126(5):566-574.

[24] Suthar JM, Koshti UK, Purohit SP, Jadeja HJ. Experimental investigation on flexural behavior of reinforced concrete beams with M30 grade concrete and Fe500 steel. Innov Infrastruct Solut. 2022;7(1):1-12. https://doi.org/10.38208/acp.v1.557

[25] Ali SI, Ahmed AM, Ibrahim AE, Ali MI. Effect of Utilization Waste Strapping Plastic Belts on Flexural Behaviour of Concrete. Ann Chim Sci Mat. 2024;48(1):95-100. https://doi.org/10.18280/acsm.480111

Blank Page

Research on Engineering Structures & Materials
www.jresm.org

Research Article

Treatability study of acclimatized industrial pharmaceutical wastewater using leaf-based natural coagulants with bioaugmentation

A. Sathiya Priya [*,a], S. Sundararaman [b]

Department of Civil Engineering, Sri Manakula Vinayagar Engineering College (Affiliated to Pondicherry University), Madagadipet, Puducherry 605107, India

Article Info

Article History:

Received 23 Dec 2025

Accepted 10 Apr 2026

Keywords:

Acclimatization;
Batch mode;
Chemical oxygen demand reduction;
Raw pharmaceutical wastewater;
Secondary sewage sludge;
Natural coagulant

Abstract

The recalcitrant nature of pharmaceutical wastewater, which contains high concentrations of active pharmaceutical ingredients (APIs), poses a significant challenge for conventional treatment systems. The present study examines a novel hybrid treatment process based on biological acclimatization after the use of secondary sewage and coagulation after the application of natural plant-based coagulants. Initially, a biological batch process was optimized in a period of 110 days using different ratios of wastewater to sewage, with the 1:3 ratio showing the best stability of degradation. Subsequently, a mixture of acclimatized and raw wastewater was treated using Azadirachta indica (Neem) and Moringa oleifera (Moringa) leaf powder. Results indicated that M. oleifera significantly performed better as compared to A. indica that is 94% reduction in Chemical Oxygen Demand (COD) as against 70% by Neem, at an optimal hydraulic retention time of 8 hours and a size of 150 µm. Mechanistic understandings based upon FTIR and NMR spectroscopy confirmed drug compound "partial degradation" of complicated aliphatic and aromatic molecules to less complicated by-products. Furthermore, FE-SEM and EDX analysis showed different morphological alterations and changes in the element composition, confirming the adsorption and bridging mechanisms of the natural coagulants. A techno-economic analysis indicates that this hybrid protocol is cost-effective with respect to the conventional chemical methods, with the sludge produced showing promise for valorization to serve as bio-fertilizer, this implies a circular economy approach to sustainable wastewater management.

© 2026 MIM Research Group. All rights reserved.

1. Introduction

The Water scarcity and water quality deterioration have become global issues of crucial importance due to fast industrialization and the growth of the population [1]. Among effluents of industries, pharmaceutical wastewater is of special danger owing to the presence of Active Pharmaceutical Ingredients (APIs). These compounds frequently are recalcitrant, bio-accumulative and toxic (often even at trace concentrations of nano-grams to milligrams per liter). Conventional Wastewater Treatment Plants (WWTPs) are often inadequately equipped to break down these complex organic structures and consequently, "contaminants of emerging concern" are discharged into surface and ground water systems [2].

Current treatment methods have their own unique shortcomings. While biologically based treatment processes are economically feasible and environmentally friendly, they tend to fail when applied to pharmaceutical effluents. The toxicity and complicated chemical structure of APIs are very high, which can inhibit the action of microorganisms, resulting in the failure of the system or

*Corresponding author: priya.haridesh@gmail.com
[a]orcid.org/0009-0004-5628-0248; [b]orcid.org/0000-0002-5810-7623
DOI: http://dx.doi.org/10.17515/resm2026-1431ma1223rs

incomplete degradation [3]. On the other hand, physicochemical methods such as coagulation-flocculation by inorganic salts (e. g., Aluminum sulfate or Ferric Chloride) are effective and rapid. But they exhibit serious environmental disadvantages such as high operational cost, change of effluent pH, and production of huge amounts of toxic non-biodegradable sludge such that their disposal is complicated [4]. Consequently, there is a dire need for a hybrid therapy approach that employs an operation cost that is low for biological systems while maintaining the efficiency of coagulation with a lack of secondary pollution from the synthetic chemical systems.

This study proposes a synergistic treatment strategy, which is Biological Acclimatization - followed by Natural Coagulation treatment. Acclimatization is the gradual adaptation of microbial communities to rising concentrations of pharmaceutical pollutants that will improve their ability to break down complex phenolic and aromatic compounds, which are toxic to non-acclimatized sludge [3]. To further polish the effluent and to remove the remaining suspended solids, plant-based natural coagulants are used in this study: Moringa oleifera and Azadirachta indica (Neem). Unlike synthetic polymers, these bio coagulants are biodegradable, non-toxic and sludge can be potentially valorized as bio-fertilizer agreeing with circular economy principles [5]. The treatment technologies, which are technically feasible, economically viable and environmentally sustainable [23].

While earlier studies have focused on either biological treatment or natural coagulation [6,7] separately, there are limited studies on the sequential coupling of acclimatized sludge treatment, *Azadirachta indica*, and *Moringa oleifera* for pharmaceutical wastewater. Furthermore, most existing types of literature are limited to the use of conventional parameters (COD, BOD) to measure the efficiency [4]. This study has an outstanding novelty in terms of the advanced spectroscopic techniques used, namely Fourier Transform Infrared Spectroscopy (FTIR) and Nuclear Magnetic Resonance (NMR), to give molecular evidence of the degradation. By examining structural changes in the functional groups and atomic environments, this study provides a mechanistic understanding of the structure breakdown of these hybrid processes over complex pharmaceutical matrices.

2. Objectives

- To optimize the biological acclimatization of raw pharmaceutical wastewater by different ratios of secondary sewage.
- To assess the effectiveness of natural coagulants (Moringa and Neem leaf powder) on the acclimatized effluent at various Hydraulic Retention Times (HRT).
- To validate the degradation mechanisms and structural morphological changes by using FTIR, NMR, FE-SEM and EDX analysis.
- To evaluate the economics and sludge valorization potential of this green protocol of treatment.

3. Materials and Methods

3.1. Waste Water Sampling and Characteristics

Raw pharmaceutical wastewater (representative sample) was collected from a pharmaceutical formulation industrial setup from the equalization tank located at Villianur, Puducherry. The industry is mainly producing antibiotics, analgesics (e.g., Aceclofenac, Paracetamol, Diclofenac, Albendazole, Aspirin etc.) and so on with a complex (organic) matrix. At the same time, secondary activated sewage was collected from the oxidation pond of a Common Effluent Treatment Plant (CETP) in Karuvadikuppam, located in Puducherry.

Upon collection, samples were sealed in high-density polyethylene (HDPE) storage containers at 4 °C to maintain their integrity without pre-degradation of samples. The initial physicochemical features for the raw wastewater and the secondary sewage (Table 1) were studied immediately upon their arrival at the lab, according to the norms prescribed by the Bureau of Indian Standards (IS 3025) and the APHA (American Public Health Association) protocols.

3.2. Preparation of Plant-Based Coagulants

Moringa oleifera is found all over the world, but it comes from India, Arabia, and the East Indies. It is a tree that loses its leaves in the winter and is common in tropical and subtropical areas. People have long valued it for its health benefits and use in cooking. In the last few years, it has also been found to have some medicinal uses. Researchers have found and grouped different organic compounds in the leaves and seeds of M. oleifera. These groups include organic acids, amino acids, carbohydrates, and other bioactive compounds. Glutamic acid is one of the most important parts of both leaves and seeds, and it is thought to be a key active coagulating agent. Because of these qualities, M. oleifera has become very popular as a natural coagulant for cleaning up wastewater. [18-20]

Azadirachta indica, commonly known as neem or Indian lilac, is widely distributed across tropical, subtropical, and moderately temperate regions. It is well recognized for its medicinal properties, particularly in the management of diabetes. Neem leaves are rich in bioactive compounds such as tannins, flavonoids, and fatty acids, which exhibit potential coagulation properties. Among these, tannins play a significant role in enhancing coagulation mechanisms. Therefore, tannins present in neem leaves can be considered as one of the key active coagulating agents, making *Azadirachta indica* a promising natural coagulant for wastewater treatment applications. [21]

Mature leaves of *Azadirachta indica* (Neem) and Moringa oleifera (Moringa) plants were collected from the farm and from local sources. To avoid the thermal deterioration of bioactive coagulating proteins, leaves were washed with distilled water and shade-dried at room temperature for 96 hours (Four days). The dried leaves were pulverized in a high-speed mechanical grinder and sieved to give a uniform particle size of 150 microns.

- Stock Solution Preparation: A stock solution of the same was prepared by dissolving 3.0 g of the respective leaf powder in 100 mL of distilled water. From the mother solution 3ml of optimum dosage is added to the 1000 ml of sample taken in the beaker. The optimum dosage is determined by using the turbidity test. The suspension was agitated for 30 min using a magnetic stirrer to solubilize the active coagulation.

3.3. Biological Acclimatization Strategy (The Batch Mode)

A stepwise biological acclimatization procedure was used to activate the activated sewage microorganisms to the recalcitrant pharmaceutical effluent. The experiments were carried out using laboratory-scale aerobic bioreactors in batch mode with a capacity of 10 liters.

- Experimental Design: Six different volumetric ratios of Raw Pharmaceutical Wastewater (RPW) to Secondary Sewage (SS) were studied (1:1, 1:2, 1:3, 1.5:2.5, 2:1, 3:1).
- Operational parameters aerators were used to provide continuous aeration to maintain a Dissolved Oxygen (DO) level (4-7mg/ L). The reactors were run at ambient room temperature for a duration of 110 days.
- Maintenance: To maintain the microbial viability, fresh secondary sewage was added at 15 days interval. Samples were withdrawn for monitoring the changes in pH, Turbidity, Total Dissolved solids, COD, and BOD at every 5-day intervals.
- Steady State Determination: The optimal ratio was determined as per the "Steady State" condition i.e., the condition where the COD varied within ± 5% over three successive sampling intervals.
- The above research work is carried out in the ambient conditions prevailing in the laboratory of the study area, that is warm and humid climatic condition, where the relative humidity will reach saturation levels in winter (NOV, DEC and JAN) and the temperature ranges from 25-35°C

3.4. Hybrid Treatment Coagulation-Flocculation Studies

In order to simulate a "shock loading" situation and test the robustness of the natural coagulants, the last phase of experiments involved the use of a mixture of 50% Acclimatized Effluent (optimized ratio 1:3) and 50% Raw Pharmaceutical Wastewater. Standard Jar Test experiments were carried out for the optimization of the coagulation process. The protocol was based on the following:

- Rapid Mixing: 120 rpm for 2 minutes (for destabilizing of colloids).
- Slow mixing: 45 rpm for 15 minutes (to encourage growth of a floc).
- Sedimentation: Samples were allowed to settle for different Hydraulic Retention Times (HRT) of 2, 4, 6 and 8 hours.

Supernatant was extracted from a depth of 2 cm below the surface for analysis of residual pH, Turbidity, Alkalinity, TDS, COD, and Phosphate.

3.5. Analytical and Instrumentation Technique

For testing the validity of the degradation mechanisms and structural changes, advanced analyses (spectroscopic and microscopic analysis) were done:

- Physicochemical Analysis: pH, Turbidity, TDS, Alkalinity, COD, and Phosphate (IS 3025 Part 58) were monitored.
- Surface Morphology (FE-SEM/EDX): The surface texture as well as its elemental composition of the sludge before and after treatment was analyzed with the Field Emission Scanning Electron Microscope coupled with an Energy Dispersive X-ray spectroscopy. Samples were sputter-coated with a thin layer of gold prior to imaging to effectively increase surface conductivity and prevent electron charging.
- Molecular Characterization: (FTIR & NMR):
  - FTIR: Transformations of functional groups were done by Fourier Transform Infrared Spectrometer (TA instruments Q600 SDT) in a range of (4000-400 cm^{-1}) using the KBr pellet technique.
  - NMR: Nuclear Magnetic Resonance (1 H-NMR) spectra were recorded on a (400 MHz) spectrometer (Bruker Avance II) (0 to 220 ppm) to identify the degradation of certain of the organic protons. Samples were dissolved in deuterated water (D2O).

3.6. Statistical Analysis

All the experiments were performed in triplicate to ensure the reliability, reproducibility of the results. The physicochemical characteristics of raw pharmaceutical wastewater, secondary sewage, acclimatized wastewater, and treated effluents were analyzed for each replicate separately, and the results are presented as mean ± standard deviation (SD). Parameters such as pH, turbidity, total dissolved solids (TDS), total alkalinity, chemical oxygen demand (COD), biochemical oxygen demand (BOD) and phosphate at various hydraulic retention times (2, 4, 6, and 8 h) were assessed during the acclimatization period and after the treatment of natural coagulants.

Statistical analysis was performed using SPSS version 2.5. One-way analysis of variance (ANOVA) was applied to assess the significance of difference between treatment groups (Neem and Moringa coagulants) and across different retention times. Where appropriate, a post hoc multiple comparison test was used to identify significant differences between individual groups. A p-value of < 0.05 was considered statistically significant.

Removal efficiencies were determined from the comparison of initial and final concentrations, and values of observed standard deviations were used to measure experimental variability and consistency. The fact that low variation of SD values is observed during replicate measurements indicates good analytical precision and stable experimental conditions during the acclimatization and coagulation-flocculation processes, and thus the robustness and reproducibility of the experimental findings.

4. Results and Discussion

4.1 Initial Characteristics of Raw Pharmaceutical Wastewater and Secondary Sewage

Table 1 summarizes the initial physicochemical properties of the raw pharmaceutical wastewater (RPW) and secondary sewage (SS) used in the current study. The RPW had a significant pollution load with its very high turbidity, total dissolved solids (TDS), alkalinity, and chemical oxygen demand (COD) and phosphate levels, revealing the complex and chemically intensive nature of

pharmaceutical effluent. BOD/COD ratio (0.29) of RPW is very low, less than 0.3, which indicates that the organic compounds are poorly biodegradable and that the effluent comprises recalcitrant and inhibitory organic substances, which are known to negatively influence the normal operation of the biological treatment process. These properties of the pharmaceutical wastewater are not new to the previous literature [8, 9].

Table 1: Physicochemical characteristics of Raw Pharmaceutical Wastewater (RPW) and Secondary Sewage (SS) used in the study

Parameter	RPW (Mean ± SD)	SS (Mean ± SD)	Test Method	F-value	p-value	Post Hoc (Tukey)
pH	6.46 ± 0.2	6.96 ± 0.1	IS 3025 (Part 11)	18.75	0.012*	RPW ≠ SS
Turbidity (NTU)	490 ± 16	58.8 ± 5.4	IS 3025 (Part 10)	1520.3	<0.001**	RPW ≠ SS
TDS (mg/L)	770 ± 45	1578 ± 20	IS 3025 (Part 16)	689.4	<0.001**	RPW ≠ SS
Total Alkalinity (as $CaCO_3$)(mg/L)	250 ± 12	365 ± 15	IS 3025 (Part 23)	92.6	<0.001**	RPW ≠ SS
COD (mg/L)	4979 ± 30	202 ± 12	IS 3025 (Part 58)	8420.5	<0.001**	RPW ≠ SS
BOD_5 (mg/L)	1463 ± 9	97 ± 17	IS 3025 (Part 44)	5210.7	<0.001**	RPW ≠ SS
BOD/COD Ratio	0.29	0.4	Calculation	–	–	–
TOC (mg/L)	1778	74	IS 8245	–	–	–
Phosphates (PO_4^{3-}–P) (mg/L)	14.8 ± 1.5	4.4 ± 0.5	IS 3025 (Part 31)	110.2	<0.001**	RPW ≠ SS

Conversely, the secondary sewage had relatively lower COD and turbidity with relatively high BOD concentration and therefore a high BOD/COD ratio (0.4). This is an indicator of high proportion of easy biodegradable organic materials and a large number of active microorganisms in the secondary sewage. The positive characteristics of biodegradability and balanced nutrient content render secondary sewage a microbial inoculum and co-substrate in promoting microbial acclimatization and adaptation when used together with pharmaceutical wastewater. Joss et al. [10]. TOC of the raw wastewater indicates a high concentration of organic pollutants; however, it does not suggest that the treatment system is subjected to a shock load, have also made similar observations on the use of municipal or secondary sewage as a biological seed to enhance the treatment efficiency of recalcitrant industrial effluents. Statistical analysis using one-way ANOVA demonstrated significant variation between RPW and SS across all physicochemical parameters ($p < 0.05$), with Tukey's post hoc test confirming significant pairwise differences.

4.2 Biological Acclimatization and the Optimum Ratio Selection

Experimental investigations were carried out in a 10-liter capacity bioreactor (plastic can) for assessing the maximum biodegradability of the raw pharmaceutical wastewater in terms of the attainment of steady state measured in terms of COD values. For the above purpose, the pharmaceutical wastewater and secondary sewage were mixed in various ratios, namely 1:1, 2:1, 3:1,1.5:2.5 ,2:1 and 3:1, respectively. The above ratios were chosen based on the previous reported studies on pharmaceutical wastewater [24]. The COD stabilization profiles obtained during the biological acclimatization of the pharmaceutical wastewater using secondary sewage sludge are presented in Fig. 1. The gradual decline and eventual stabilization of COD concentration are an indication of successful microbial adaptation to dealing with complex pharmaceutical compounds. Similar behavior of acclimatization has been documented in pharmaceutical and toxic industrial effluents with increasing exposure in a step-wise manner, microbial tolerance and metabolic

efficiency improved. microbial tolerance and efficiency metabolism [8,10]. The fact that was observed a "steady state" COD value between the 95th to 110th day for the 1:3 ratio indicates that a sufficient microbial density and co-metabolic substrate(s) are necessary for effective biodegradation of refractory organics.

The kinetic study revealed that the initial rate of removal was high and then gradually decreased, finally reaching a plateau state, which indicates that the process has adsorbed on the active sites and no longer the pollutants. This result confirms the assumption that the process proceeded in typical adsorption/biodegradation kinetics where the rate was constant after reaching equilibrium.

(a)

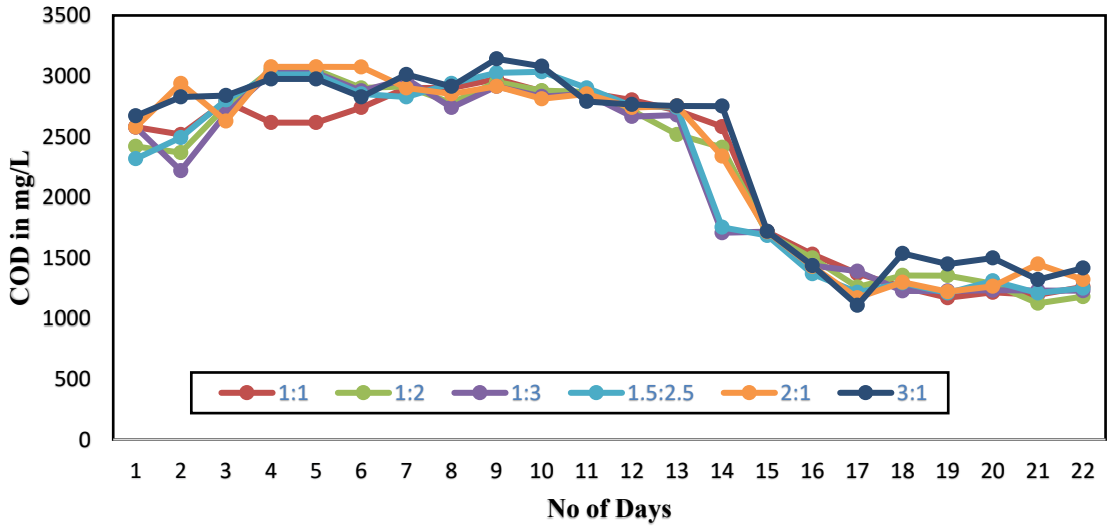

(b)

Fig. 1. (a) Photographic view of Bio reactors for different ratios, of pharmaceutical wastewater and Secondary Sewage from 0th to 110th day (acclimatization Process) (b)variation of COD for different ratios of pharmaceutical wastewater and Secondary Sewage from 0th to 110th day

4.3 Spectroscopic Indication of Biodegradation

The Fourier Transform Infrared (FTIR) spectra of the samples collected before and after the acclimatization process are shown in Fig. 2. The raw pharmaceutical wastewater showed prominent absorption bands corresponding to aliphatic C-H stretching mode, aromatic C=C stretching mode, carbonyl (C=O), and nitro (-NO2) functional groups due to the existence of diverse pharmaceutical compounds and complex organic structures. After the process of biological acclimatization, a significant decline in the intensity of aromatic C=C functional groups, carbon was observed, providing evidence for the partial biological degradation of organic constituents and destruction of complex molecular structures. Similar reductions in FTIR peak intensities in the

course of the biological treatment of pharmaceutical wastewater have also been reported by Singh Rana et al. [9] and Wang et al. [11], verifying the susceptibility of certain organic moieties to microbial degradation.

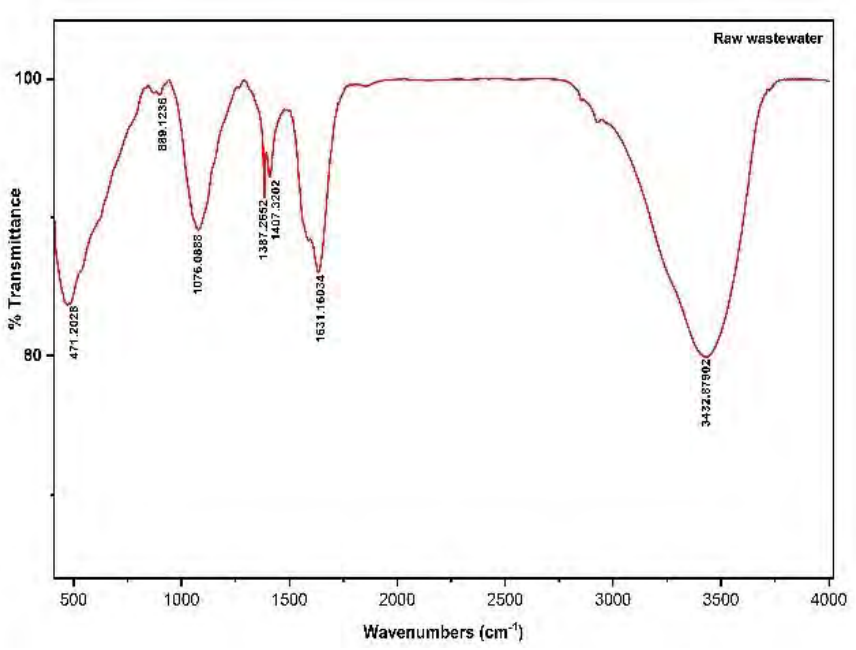

(a)

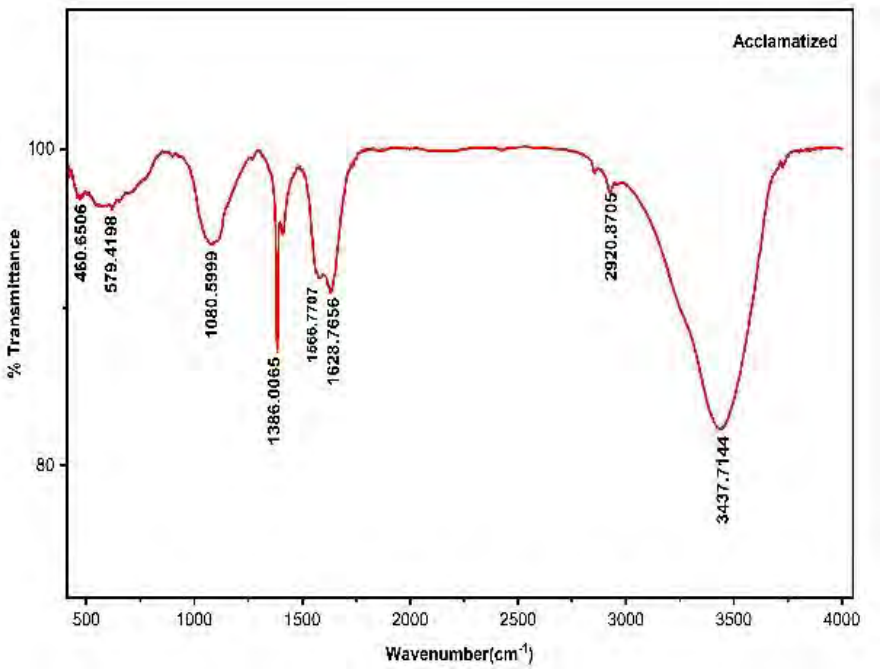

(b)

Fig. 2. Comparative FTIR spectroscopy showing (a) before and (b) after acclimatization of pharmaceutical wastewater using secondary sewage treatment

Despite the overall decrease in peak intensities, residual absorption bands corresponding to carbonyl and nitro functional groups remained after acclimatization, implying incomplete mineralization of recalcitrant pharmaceutical compounds. The robustness of these functional groups is typical for antibiotic-rich and chemically complex wastewaters wherein a high-level of resistance of aromatic as well as nitrogen-containing structures are found to complete biochemical degradation under aerobic conditions [12]. These observations suggest that biological

acclimatization, where the organic load is reduced, is not the sole means of achieving complete degradation of all of the pharmaceutical residues.

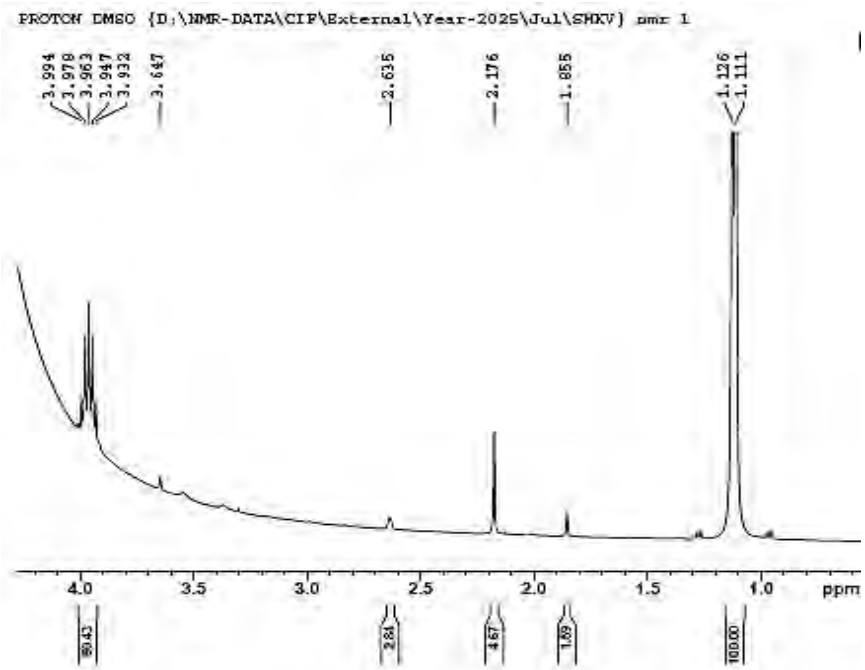

(a)

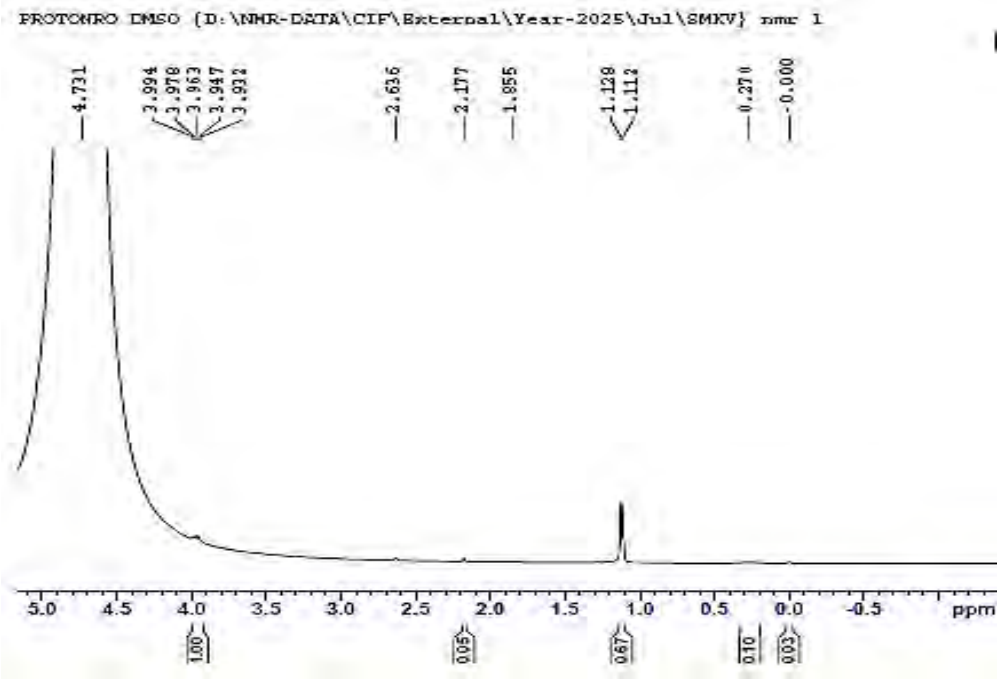

(b)

Fig. 3. photographic view of NMR spectroscopy showing (a) before vs (b) after Acclimatization of pharmaceutical wastewater using secondary sewage treatment

The NMR spectra (Fig.3) further supported the results from the FTIR in terms of the information on molecular-level transformations that occur during acclimatization. The weakening and partial disappearance of proton signals corresponding to aliphatic and nitrogen-containing heterocyclic structures suggest the modification of the structure and the fragmentation of pharmaceutical molecules, and not destruction. Such partial degradation pathways during aerobic biological treatment have been reported extensively, and complex pharmaceutical compounds are degraded into simpler intermediates, which need further physicochemical treatment for complete removal [13]. The combination of FTIR and NMR analyses, therefore supports the efficiency of the

acclimatization process while at the same time underscoring the need for further treatment approach in the form of a hybrid solution.

4.4 Effect of Natural Coagulants on Physicochemical Parameters

The variation of pH and turbidity with the hydraulic retention time (HRT), as shown in Fig. 4, evidences the effectiveness of the natural coagulants to promote the destabilization of suspended and colloidal particles from combined coagulative mechanisms of charge neutralization, adsorption and inter-particle bridging. A gradual pH stabilization towards near-neutral values was observed with increasing HRT, which suggests that no adverse acidic or alkaline conditions were established by the coagulation process, which is favorable for subsequent treatment and discharge. The resulting turbidity was significantly reduced with the increase of HRT due to improved settling efficiency under prolonged quiescent conditions. It has been previously stated that plant-based coagulants are more effective in removing turbidity, especially Moringa oleifera, because of the presence of water-soluble cationic proteins and natural polyelectrolytes that are effective in neutralization of negatively charged particles and flocculation [14, 15].

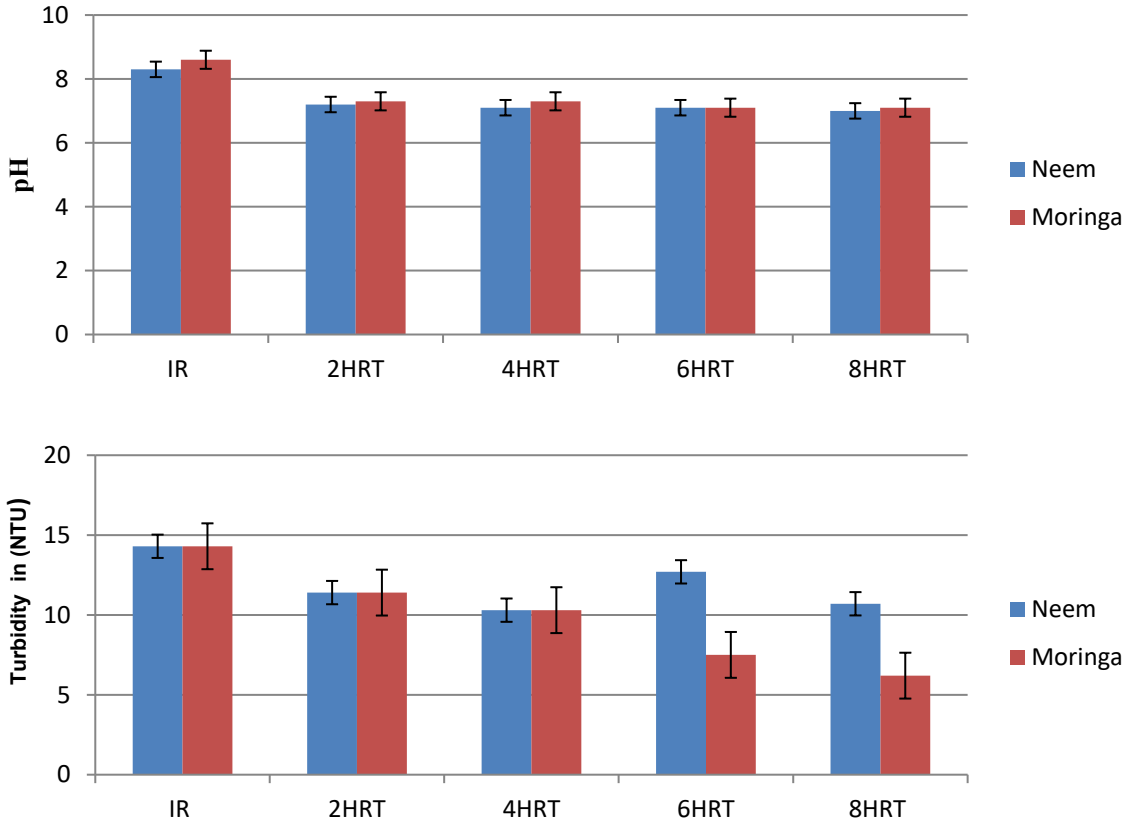

Fig. 4. Variation of pH and Turbidity in the Treatment of Acclimatization Pharmaceutical wastewater by using Natural coagulants at different HRT

** Note: IR – Initial Reading*

The decrease in total dissolved solids (TDS) and total alkalinity with HRT increase (Fig. 5) further supports the importance of adsorption and ion exchange mechanisms during the coagulation-flocculation process. The gradual diminishing of alkalinity appears to be indicative of the elimination of bicarbonate and carbonate ions by co-precipitation and absorption on surface complex sites of coagulants. Similar trends have been observed in natural coagulant-based wastewater treatment studies in which a longer retention time increased the interaction between pollutants and coagulants and overall treatment efficiency [16].

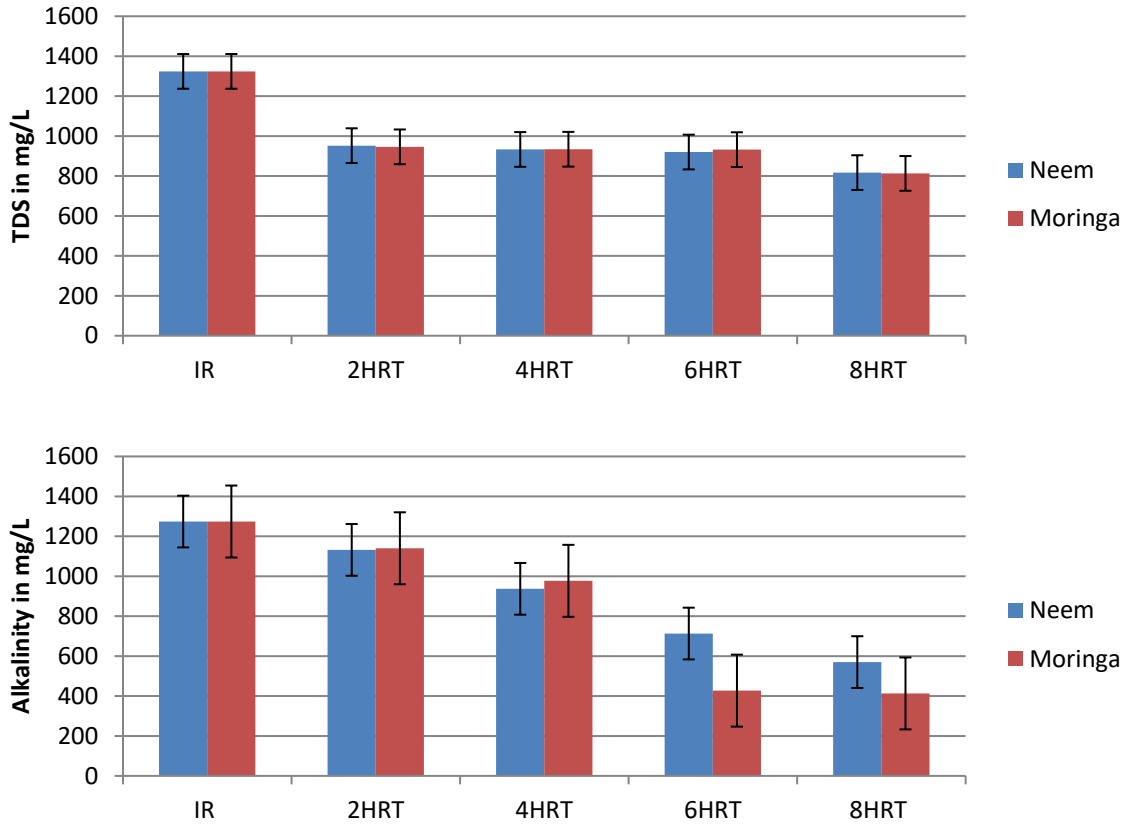

Fig. 5. Variation of TDS and Total Alkalinity in the Treatment of Acclimatization Pharmaceutical wastewater by using Natural coagulants at different HRT

4.5 COD Removal Mechanisms and Phosphate Removal Mechanisms

The significant decrease of chemical oxygen demand (COD) and phosphate concentrations, together with an increase of the hydraulic retention time (HRT), as it may be seen in Fig. 6, are characteristic of the synergy of biological acclimatization and natural coagulation-flocculation. The acclimatization procedure decreased the toxicity and the complexity of pharmaceutical wastewater, thereby improving the effectiveness of the ensuing physicochemical treatment. Among the coagulants tested, the Moringa leaf powder-based treatment resulted in better efficiency of COD removal of 94%, is shows the high reduction were compared with the removal percentage of hospital and pharmaceutical wastewater reported in [25].

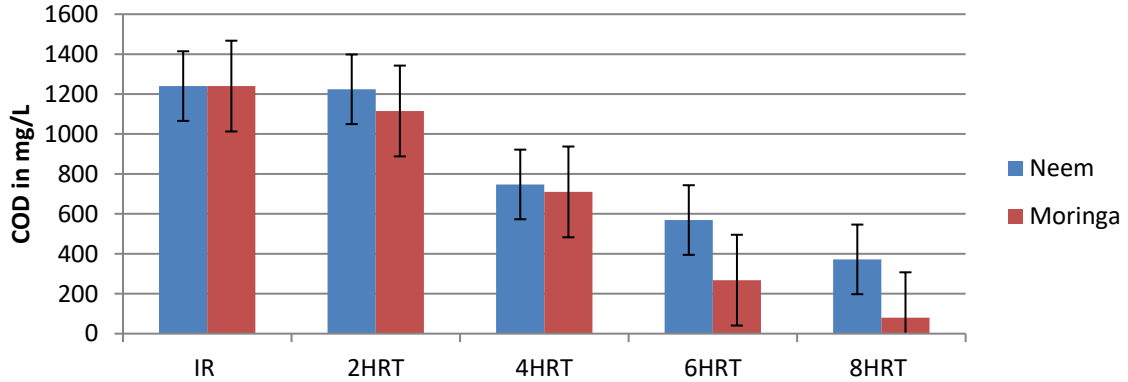

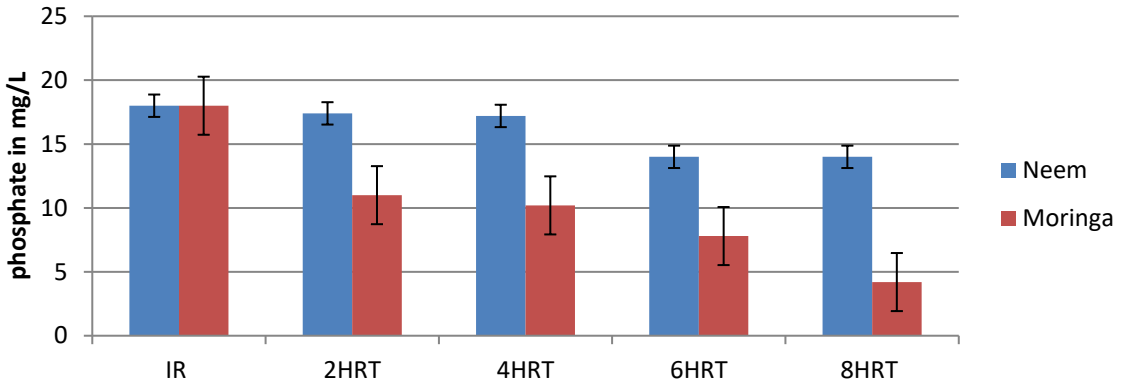

Fig. 6. Variation of COD and Phosphate in the Treatment of Acclimatization Pharmaceutical wastewater by using Natural coagulants at different HRT

Which might be due to the existence of bioactive water-soluble cationic proteins involved in charge neutralization, adsorption, and the interparticle bridging process of organic pollutants [14,16]. Prolonged HRT also allowed for better interactions between the pollutants and coagulant active sites, leading to improved floc formation and settling.

Phosphate removal shows a similar tendency and points out the removal of anionic phosphate species by adsorption to positively charged functional groups and co-precipitation in the formed flocs. The results of the overall percentage removal efficiencies of Phosphate and the removal efficiencies of COD are summarized in Fig. 7 which shows a progressive increase with respect to HRT, which proves the importance of adequate contact time for good treatment performance. These trends are consistent with previous research works on hybrid bio coagulation systems for high-strength industrial wastewater, which report enhanced removal efficiencies when biological pretreatment of wastewater is combined with coagulation-flocculation processes [8].

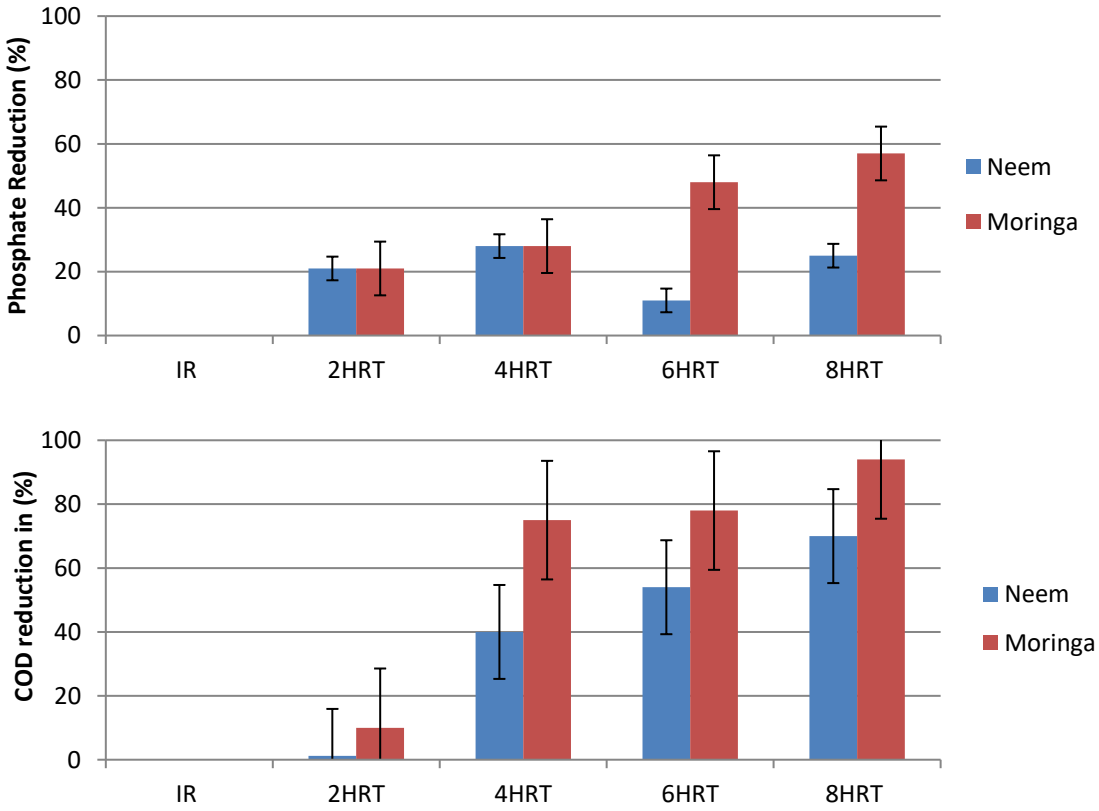

Fig. 7. Variation in % of reduction in turbidity and COD in the Treatment of Acclimatization of Pharmaceutical wastewater by using Natural coagulants at different HRT

4.6 SEM-EDX Indication of Pollutant Removal

The FE-SEM micrographs of the raw and treated Sludge (Fig. 8 and Fig. 9) showed significant morphological changes after treatment in the form of an increase in surface roughness, pore formation, and the formation of irregular floc structures. These surface modifications imply that there is an effective amount of adsorption and entrapment of pollutants in the floc matrix, which will be beneficial for improved settling and removal efficiency. The porous and heterogeneous surface morphology seen after treatment indicates improved contact between the constituents of wastewater and active site present on both the acclimatized sludge and natural coagulant surface.

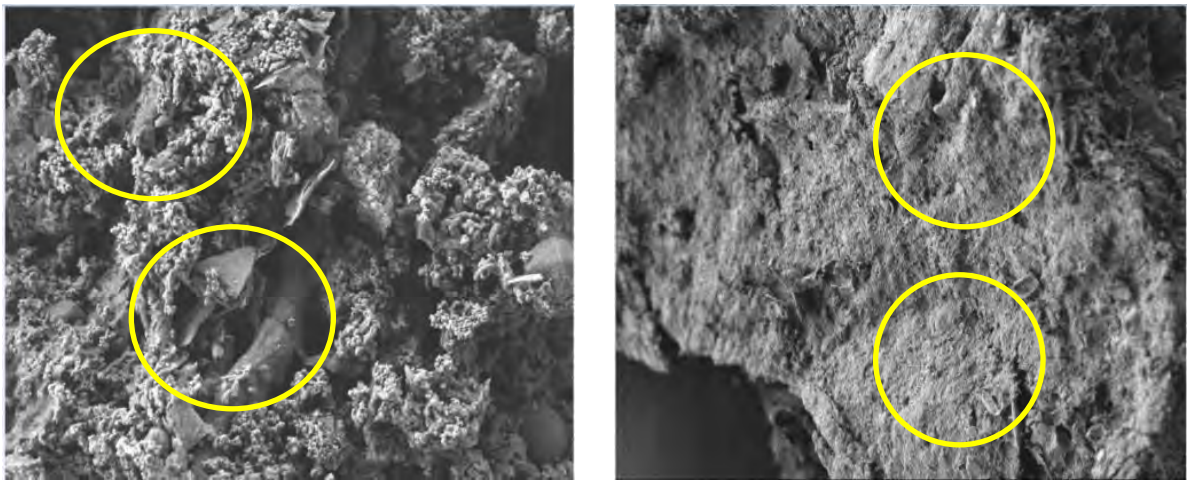

(a) (b)

Fig. 8. Photographic view of FE- SEM image for (a) Raw Pharmaceutical Wastewater and (b) acclimatized pharmaceutical wastewater

The FE-SEM image of the raw wastewater reveals the presence of both organic and inorganic particles, along with indications of undigested materials. Further, it also indicates the presence of 'dense micro-aggregates'. After acclimatization the FE-SEM image indicates a 'potential microbial activity', or degradation having taken place. Further, 'structural breakdown' and the presences of voids, indicates the presence of biological activity.

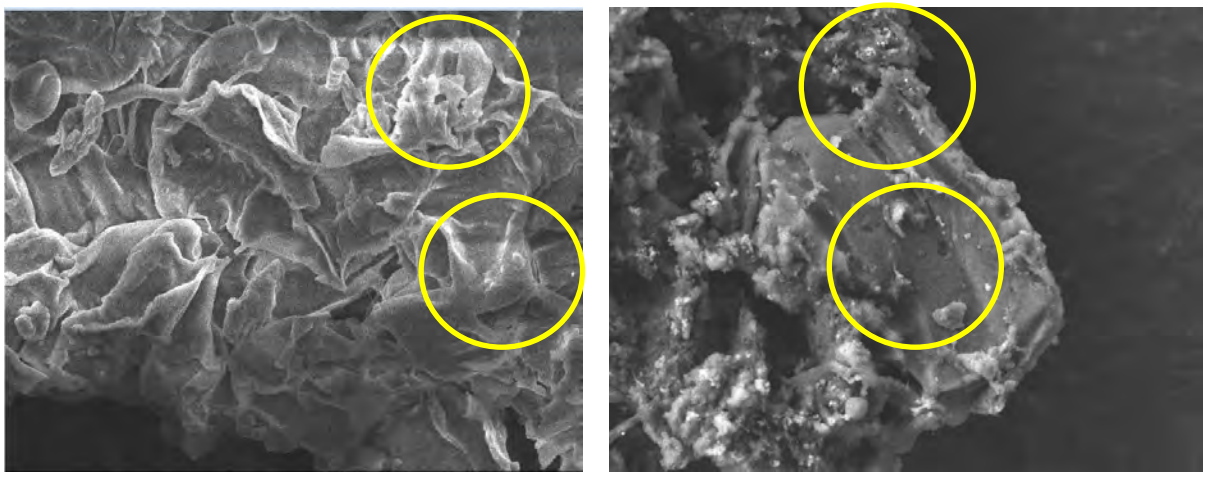

(a) (b)

Fig. 9. Photographic view of FE - SEM image of (a) Moringa Leaves before Treatment (b) Moringa Leaves Treated with acclimatization pharmaceutical wastewater

Corresponding EDX spectra (Fig. 10, Fig. 11 and Fig. 12) (a) and (b) further supported the findings of the above observations, by showing significant changes in elemental composition after treatment. An increase in the inorganic elements with an increase in carbon and oxygen signals are

indicators of successful sequestration of organic and inorganic contaminants to the sludge and coagulant matrices.

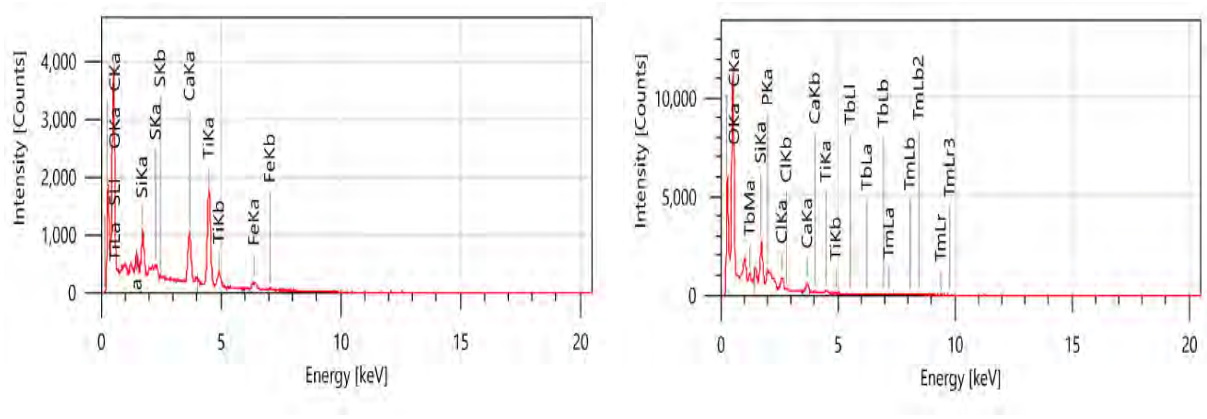

(a) (b)

Fig. 10. Photographic view of EDX image for (a) Raw Pharmaceutical Wastewater and (b) acclimatization pharmaceutical wastewater

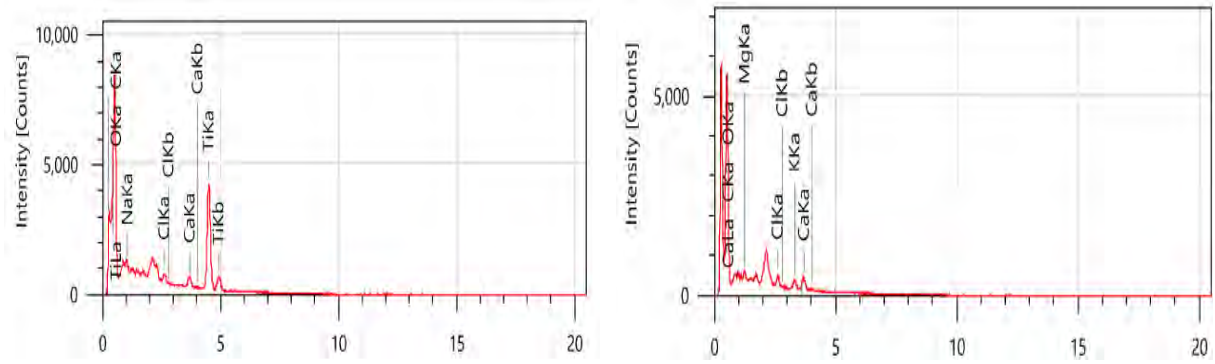

(a) (b)

Fig 11: Photographic view of EDX image of (a) Moringa Leaves before Treatment and (b) Moringa Leaves Treated with Acclimatization Pharmaceutical wastewater

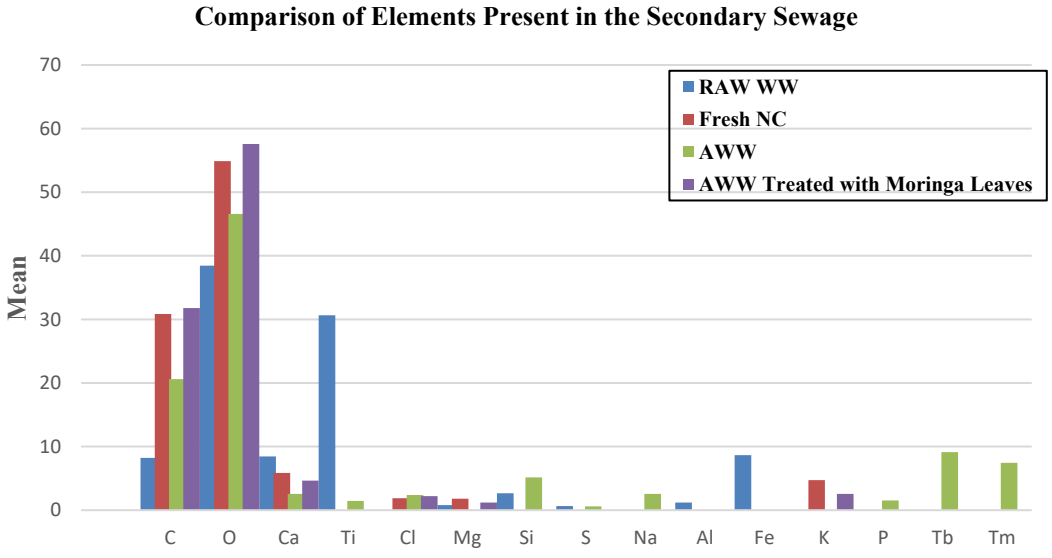

Fig. 12. Variation of Elements present in the sludge analyzed by EDX in the Treatment of Acclimatization Pharmaceutical wastewater by using Natural coagulants

Note: RAW WW- Raw wastewater, NC- Natural Coagulant, AWW- Acclimatized wastewater, Acclimatized wastewater treated with Moringa Leaves.

These elemental transitions provide empirical evidence for the specific roles of adsorption, surface complexation, and co-precipitation mechanisms in the overall removal of pollutants from the aqueous phase. Morphological transformations and changes in element redistribution have also been observed for natural coagulant-based wastewater treatment systems and confirm the use of plant-derived coagulants in enhancing pollutant removal due to coagulation [16, 17, 22].

5. Conclusion

Industrial pharmaceutical wastewater was acclimatized using secondary sewage sludge at varying ratios in a 10 L bioreactor over a period of 95–110 days to enhance the breakdown of complex compounds. Among the tested conditions, the 1:3 ratio (raw pharmaceutical wastewater to secondary sewage) showed optimal performance, with Chemical Oxygen Demand (COD) reaching a steady state by the 110th day. Following acclimatization, a 50:50 blend of pharmaceutical wastewater and acclimatized effluent was treated using various leaf-based natural coagulants. Among them, Moringa oleifera (150 µm particle size) demonstrated superior performance, achieving up to 94% COD reduction and 71% turbidity removal at an 8-hour settling time. FE-SEM analysis revealed significant changes in surface morphology before and after treatment, while EDX confirmed variations in elemental composition during acclimatization and treatment. Compared to neem (Azadirachta indica), which achieved only 70% COD and 30% turbidity removal, Moringa oleifera exhibited higher adsorption efficiency. FTIR analysis indicated effective degradation of aliphatic compounds and partial degradation of persistent pharmaceutical groups such as C=O, NO_2, and C–O. The use of natural coagulants provides a cost-effective and eco-friendly alternative to conventional chemical treatments, with the added potential of utilizing the resulting sludge as a bio-fertilizer, supporting sustainable wastewater management.

References

[1] Desta WM, Bote ME. Wastewater treatment using a natural coagulant (Moringa oleifera seeds): Optimization through response surface methodology. Heliyon. 2021;7(11):e08451. https://doi.org/10.1016/j.heliyon.2021.e08451

[2] Sunsandee N, Ramakul P, Phatanasri S, Pancharoen U. Biosorption of dicloxacillin from pharmaceutical wastewater using tannin from Indian almond leaf: Kinetic and equilibrium studies. Biotechnol Rep. 2020;27:e00488. https://doi.org/10.1016/j.btre.2020.e00488

[3] Kamali M, Aminabhavi TM, Tarelho LAC, Hellemans R, Cuypers J, Capela I, et al. Acclimatized activated sludge for enhanced phenolic wastewater treatment using pinewood biochar. Chem Eng J. 2022;427:131708. https://doi.org/10.1016/j.cej.2021.131708

[4] Kebede TG, Dube S, Nindi MM. Removal of non-steroidal anti-inflammatory drugs (NSAIDs) and carbamazepine from wastewater using water-soluble protein extracted from Moringa stenopetala seeds. J Environ Chem Eng. 2018;6(2):3095-103. https://doi.org/10.1016/j.jece.2018.04.066

[5] Sundararaman S, Sathiyapriya A. Acclimatization of an industrial pharmaceutical wastewater in an aerobic batch mode of operation. Int J Environ Res Dev. 2016;6(1):1-7.

[6] Thirugnanasambandham K, Karri RR. Preparation and characterization of Azadirachta indica A Juss plant-based natural coagulant for urban sewage treatment: Modelling and cost assessment. Environ Technol Innov. 2021;23:101733. https://doi.org/10.1016/j.eti.2021.101733

[7] Eri IR, Hadi W, Slamet A. Clarification of pharmaceutical wastewater with Moringa oleifera: Optimization through response surface methodology. J Ecol Eng. 2018;19(3):126-34. https://doi.org/10.12911/22998993/86148

[8] Raj DSS, Anjaneyulu Y. Evaluation of biokinetic parameters for pharmaceutical wastewaters using aerobic oxidation integrated with chemical treatment. Process Biochem. 2005;40(1):165-75. https://doi.org/10.1016/j.procbio.2003.11.056

[9] Singh Rana R, Singh P, Kandari V, Gupta S, Dobhal R. Characterization and bioremediation of pharmaceutical industries' wastewater: An Indian perspective. Appl Water Sci. 2017;7:1-12. https://doi.org/10.1007/s13201-014-0225-3

[10] Joss A, Zabczynski S, Göbel A, Hoffmann B, Löffler D, McArdell CS, et al. Biological degradation of pharmaceuticals in municipal wastewater treatment: Proposing a classification scheme. Water Res. 2006;40(8):1686-96. https://doi.org/10.1016/j.watres.2006.02.014

[11] Wang S, Wang J, Wang Y. Biodegradation of pharmaceutical compounds in wastewater by acclimatized activated sludge: Transformation pathways and mechanisms. Water Res. 2016;98:44-52.

[12] Michael I, Rizzo L, McArdell CS, Manaia CM, Merlin C, Schwartz T, et al. Urban wastewater treatment plants as hotspots for the release of antibiotics in the environment: A review. Water Res. 2013;47(3):957-95. https://doi.org/10.1016/j.watres.2012.11.027
[13] Jelić A, Gros M, Petrović M, Barceló D. Occurrence and elimination of pharmaceuticals during conventional wastewater treatment. Water Res. 2011;45(3):1165-76. https://doi.org/10.1016/j.watres.2010.11.010
[14] Ndabigengesere A, Narasiah KS. Quality of water treated by coagulation using Moringa oleifera seeds. Water Res. 1998;32(3):781-91. https://doi.org/10.1016/S0043-1354(97)00295-9
[15] Katayon S, Noor MJMM, Asma M, Ghani LA, Thamer AM, Azni I, et al. Effects of storage conditions of Moringa oleifera seeds on coagulation efficiency. Bioresour Technol. 2006;97(13):1455-60. https://doi.org/10.1016/j.biortech.2005.07.031
[16] Choy SY, Prasad KMN, Wu TY, Raghunandan ME, Ramanan RN. Utilization of plant-based natural coagulants as sustainable alternatives for water clarification. J Environ Manage. 2014;145:80-99. https://doi.org/10.1016/j.jes.2014.09.024
[17] Yin CY. Use of plant-based coagulants for water and wastewater treatment. Bioresour Technol. 2010;101(19):775-83.
[18] Pareek A, Kumar S, Singh V, et al. Moringa oleifera: Comprehensive review of pharmacological, phytochemical, and toxicological aspects. Int J Mol Sci. 2023;24(3):2098. https://doi.org/10.3390/ijms24032098
[19] Anzano A, Sbarra C, D'Agostino F, et al. Chemical analysis and antimicrobial activity of Moringa oleifera leaves and seeds. Molecules. 2022;27(24):8920. https://doi.org/10.3390/molecules27248920
[20] Yin CY. Emerging usage of plant-based coagulants for water and wastewater treatment. Process Biochem. 2010;45(9):1437-44. https://doi.org/10.1016/j.procbio.2010.05.030
[21] Mohan S, et al. Textile wastewater treatment using Neem (Azadirachta indica) as natural coagulant. Int Res J Multidiscip Technov. 2019:636-42.
[22] Yardimci AI, Acikbas Y, Capan R. SEM images of carbon nanotubes (CNTs): Effect of voltage and spot size on image resolutions, Res. Des. 2024; 1(1): 43-51. D http://dx.doi.org/10.17515/rede2024-004en1116rs
[23] Ozmen HB, Tanrıverdi B. Concrete paradox: Economic importance, environmental impacts, and the sustainability of concrete material, Res. Des. 2025; 2(2): 66-84. http://dx.doi.org/10.17515/rede2025-008en0801rs
[24] Sundararaman S, Sathiyapriya A. Acclimatization of industrial pharmaceutical wastewater in aerobic batch mode. Int J Environ Res Dev. 2016;6(1):1-10.
[25] Alazaiza M, et al. Application of natural coagulants for pharmaceutical removal from water and wastewater: A review. Water. 2022;14(2):140. https://doi.org/10.3390/w14020140

Blank Page

Research on Engineering Structures & Materials
www.jresm.org

Research Article

Bond behavior enhancement between normal strength concrete and SIFCON

Ali Fahdel [*,a], Kamal Alogla [b], Wajdi Shubber Saheb [c]

College of Engineering, University of Kerbala, Kerbala, Iraq

Article Info

Article History:

Received 02 Feb 2026

Accepted 15 Apr 2026

Keywords:

Push-off test;
Steel fibers;
Interface behavior;
Slurry infiltrated fiber concrete;
Fiber reinforced concrete;
Shear strength

Abstract

The bonding behavior between conventional concrete and Slurry Infiltrated Fiber Concrete (SIFCON) plays a critical role in enhancing the shear performance and ductility of composite structural members. This study investigates seven reinforced concrete specimens, divided into two groups in addition to a control sample made entirely of conventional concrete. The first group consisted of three composite beams combining conventional concrete and SIFCON, cast separately and connected through different interfacial geometries: rectangular, triangular, and semicircular. The second group replicated these specimens with the addition of 12 mm diameter bolts at the interface to improve bond strength. The results demonstrated that interface geometry significantly influences shear resistance and displacement behavior. Among the tested configurations, the rectangular interface achieved the highest performance, with a shear capacity increase of approximately 2.38 times compared to other shapes, along with improved stiffness and ductility. The inclusion of bolt reinforcement further enhanced load-carrying capacity, reaching about 1.6 times that of specimens without bolts. These specimens also exhibited larger displacements and interfacial slip prior to failure. However, despite the increased strength, bolt-reinforced specimens showed a more brittle and sudden failure mode, unlike the more gradual and ductile response observed in specimens with rectangular interfaces without bolts. The findings confirm that combining mechanical interlocking with anchorage systems can effectively improve shear strength and deformation capacity. Future research should focus on large-scale applications and long-term performance under cyclic and sustained loading conditions.

© 2026 MIM Research Group. All rights reserved.

1. Introduction

Modern civil engineering relies heavily on concrete as the primary construction material due to its durability, high compressive strength, cost-effectiveness, and widespread availability [1–3]. Despite these advantages, combining different types of concrete within a single structural element—such as in repair works, strengthening applications, or staged construction—often leads to weak interfacial performance. In particular, conventional concrete design provisions indicate that the interface between old and new concrete may exhibit limited shear stress resistance and inadequate bond capacity [4,5]. These deficiencies can adversely affect the overall strength, stiffness, and long-term serviceability of reinforced concrete members [6,7].

The performance of composite concrete systems is largely governed by the behavior of the interface zone, where shear transfer mechanisms play a decisive role. Load transfer across construction joints typically depends on a combination of adhesion, friction, and mechanical interlocking. Surface roughness enhances aggregate interlock, while normal compressive stresses mobilize frictional resistance. In many cases, additional reinforcement crossing the interface is

*Corresponding author: kamal.d@uokerbala.edu.iq
[a]orcid.org/0009-0001-5065-2301; [b]orcid.org/0000-0002-0853-5152; [c]orcid.org/0000-0002-7069-3207
DOI: http://dx.doi.org/10.17515/resm2026-1492me0202rs

required to provide dowel action and prevent slip. However, the efficiency of these mechanisms is influenced by surface preparation, material compatibility, and the presence of mechanical connectors, making the interface a critical and often vulnerable region in composite members.

To overcome such limitations, various high-performance concrete materials have been developed [8–10]. Among them, Slurry Infiltrated Fiber Concrete (SIFCON) has emerged as a promising material due to its unique production method and superior mechanical characteristics [11,12]. SIFCON is produced by first placing a high-volume fraction of short steel fibers—typically ranging from 4% to 20%—into a mold, followed by infiltrating a highly flowable cementitious slurry composed of fine cement, silica fume, water, and superplasticizer [13–15]. Unlike conventional Fiber Reinforced Concrete (FRC), where fibers are mixed directly into fresh concrete, SIFCON achieves a significantly higher and more uniformly distributed fiber content through this preplacement technique [16,17]. This distinctive fiber network results in exceptional ductility, impact resistance, energy absorption capacity, shear strength, crack control, and fatigue performance [18–21]. The interconnected fibers bridge microcracks effectively, improving post-cracking behavior and stress redistribution under severe loading conditions. Consequently, SIFCON has been successfully applied in blast-resistant structures, repair systems, joint regions, and shear-critical zones [22–24].

Although extensive research has examined the intrinsic mechanical properties of SIFCON, relatively limited attention has been devoted to its bond behavior when combined with conventional concrete, particularly in terms of shear transfer and interface strength [25–27]. Previous studies on construction joints have explored methods such as surface roughening, keyways, shear reinforcement, and mechanical connectors to enhance interfacial performance [28–30]. Nevertheless, the interaction between SIFCON and normal concrete at the interface—especially under varying geometric configurations and mechanical anchorage systems—remains insufficiently understood. Therefore, achieving optimal interfacial bonding in hybrid systems incorporating SIFCON layers requires systematic investigation. The geometry of the interface surface may significantly influence mechanical interlocking, while bolted or dowel-type connectors can provide additional shear resistance through mechanical anchorage. Understanding the combined effect of geometric interlock and mechanical fastening is essential for developing reliable and efficient composite systems.

The primary objective of this study is to evaluate the effect of using Slurry Infiltrated Fiber Concrete (SIFCON) on shear-friction resistance at construction joints between old and new concrete. This includes examining the influence of different interface surface configurations (rectangular, semicircular, and triangular) and employing various shear transfer mechanisms across the interface, such as dowel bars and bolted connections, in addition to investigating a hybrid system that combines geometric interlocking with mechanical anchorage.

2. Experimental Program

Seven reinforced concrete beam specimens were produced for experimental testing and divided into three separate groups. This study is exploratory in nature, aiming to investigate and better understand the interfacial shear behavior between conventional concrete and SIFCON through controlled laboratory experimentation. The first group contained one specimen which acted as the control model to represent standard concrete construction. The specimen served as a reference point to assess the enhanced shear performance of the following specimens. The control specimen consisted of two separate conventional concrete sections which were cast separately to create a single beam structure.

The second group consisted of three composite specimens which combined conventional concrete with Slurry Infiltrated Fiber Concrete (SIFCON) in two separate sections. The two separate sections of material received individual casting before their interface received special treatment to improve mechanical bonding. The three specimens used different interface shapes for their interlocking design: rectangular for the first specimen, triangular for the second, and semicircular for the third, as shown in Figures (1) and listed in Table (1). The researchers studied how different interface shapes between conventional concrete and SIFCON affect their shear transfer and bond

performance. The third group consisted of three specimens derived from the second group before receiving additional reinforcement through 12 mm diameter steel bolts that spanned the interface area. The steel bolts served to establish mechanical bonds between the interface zones for all three interlocking designs, which strengthened interface shear capacity and minimized interface slip. The complete details about these specimens appear in Figures (1) and Table (1). The experimental design allowed researchers to study how different interface shapes and mechanical fasteners affect beam composite performance when conventional concrete meets SIFCON under shear stress. All tests were carried out in the Laboratory of Karbala University.

Table 1. Details of the tested specimens

Groups	Parameter	Specimen Designation	Mixture Type
first group	Reference	N. L	N.C - N.C
second group (Change Interface)	Rectangle Grooves	S. R	N.C - SIFCON
	Triangle Grooves	S. T	N.C - SIFCON
	Semicircular Grooves	S.C	N.C - SIFCON
third group (Change Interface with Bolts)	Rectangle Grooves with Two bolts of a diameter of 12 mm	S. R. D	N.C - SIFCON
	Triangle Grooves with Two bolts of a diameter of 12 mm	S. T. D	N.C - SIFCON
	Semicircular Grooves with Two bolts of a diameter of 12 mm	S. C. D	N.C - SIFCON

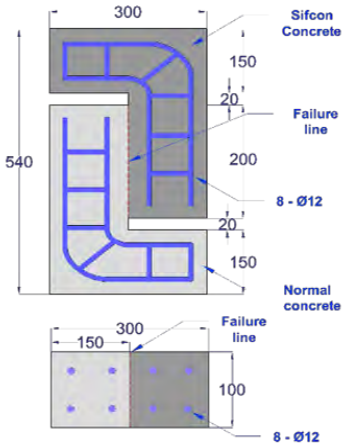

(a)

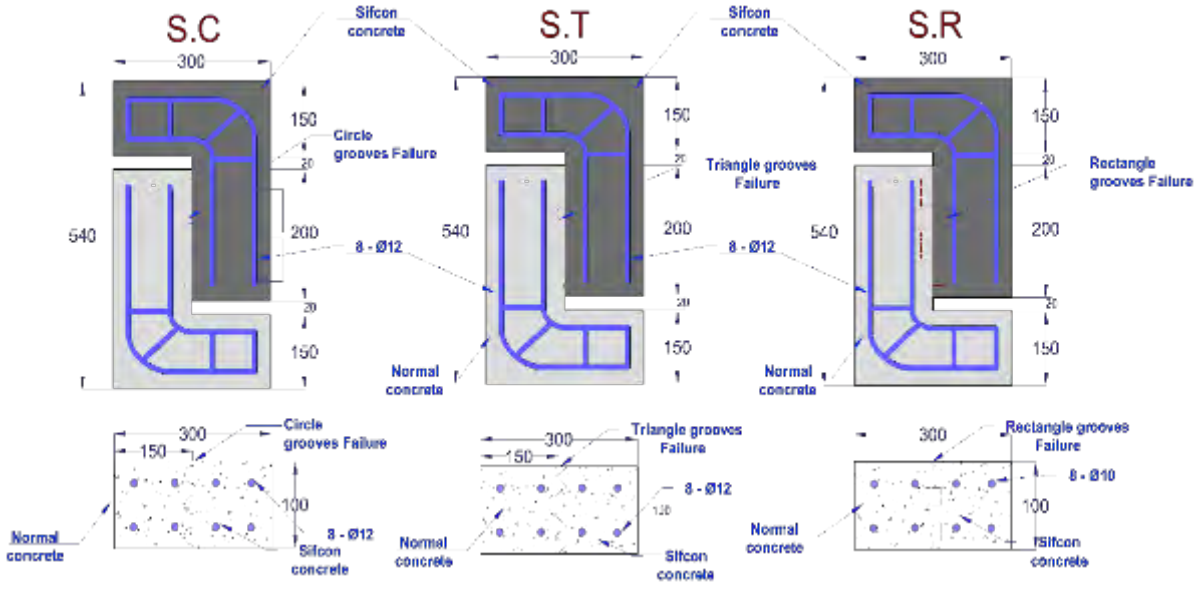

(b) (c) (d)

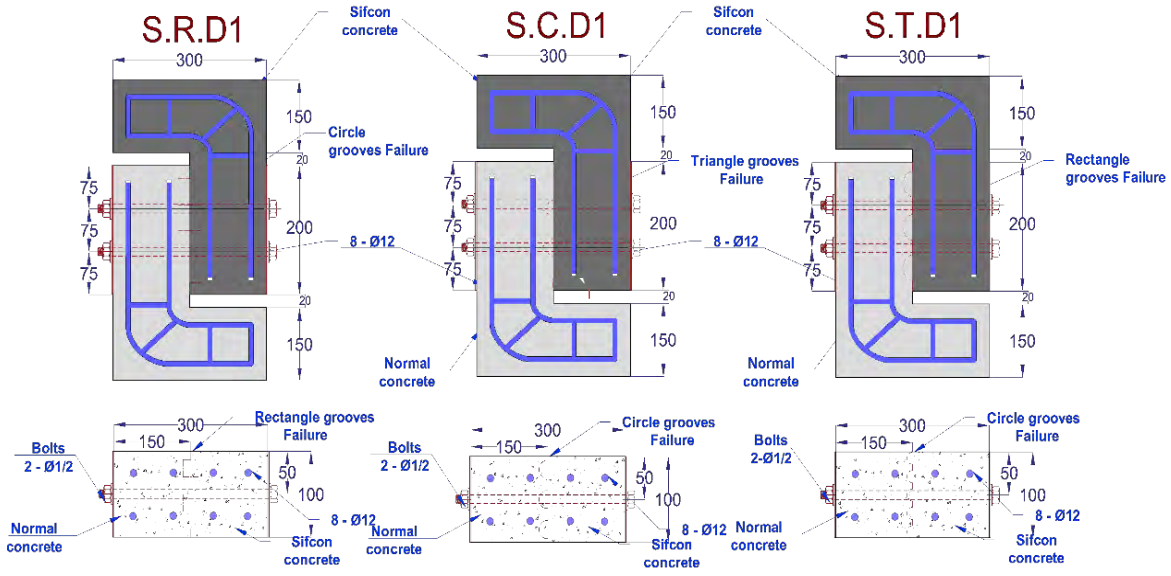

(e) (f) (g)

Fig. 1. Details of the tested specimens (a) Reference, (b) Circle grooves, (c) Triangle grooves, (d) Rectangle grooves, (e) Triangle grooves With Two bolts with a diameter of 12 mm, (f) Triangle grooves With Two bolts with a diameter of 12 mm, and (g) Circle grooves With Two bolts with a diameter of 12 mm

2.1 Preparation of Beam Specimens

The wooden molds for the mix were prepared, and the casting surfaces were oiled. The reinforcement for the specimen was arranged as shown in Figure (2). Subsequently, the conventional concrete mix was prepared, and the first portion of the conventional concrete was cast, as illustrated in Figure (3). After that, the SIFCON mix was prepared and cast, as shown in Figure (4). To ensure reproducibility and consistency in the experimental results, the curing procedure of the concrete specimens was carefully controlled. After casting, all specimens were subjected to water immersion curing to guarantee full hydration and uniform moisture distribution. The specimens were completely submerged in clean water tanks for a duration of 28 days. The water temperature was maintained at 20 ± 2°C throughout the curing period to provide stable and controlled conditions, in accordance with standard concrete testing practices (e.g., ASTM C192 or EN 12390-2).

Fig. 2. Preparation of plywood formwork and reinforcement

Fig. 3. Casting the first segment of conventional concrete

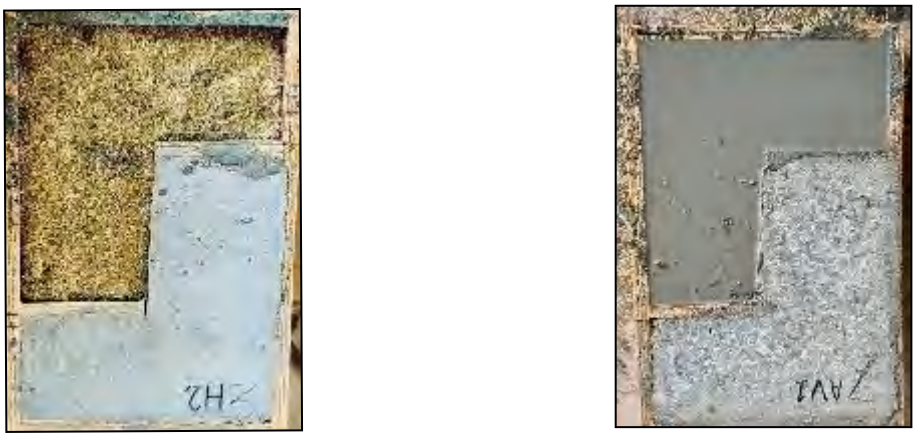

Fig. 4. Casting the second segment of SIFCON concrete

3. MATERIAL

3.1. Cement

The research used Al-Jisir cement which is a well-established Iraqi product that meets all requirements of the Iraqi Standard [IQS No. 5/2019]. The research used Type V sulfate-resistant Portland cement which meets the following specifications: 600 minutes maximum setting time and 32 MPa minimum compressive strength at 28 days and 4% maximum sulfate content by weight according to the standard specifications. The cement properties listed in Tables (2) and (3) match all Type V cement requirements from IQS No. 5/2019 thus making it appropriate for sulfate-rich environments.

Table 2. Sulfate-resistant Portland cement's chemical and key ingredients

Oxide's composition	Content%	Limits of Iraqi standard No.5/2019
CaO	62.14	.....
SIO2	19.90	.....
AL2O3	3.3	.....
Fe2O3	4.5	.....
MgO	3.25	<5.00
SO3	1.86	<2.50
Na2O	0.24	
K2O	0.53	
L.O.I.	1.27	<4.00
Insoluble residue	0.81	<1.5
Lime Saturation factor	0.93	0.66-1.02
Main compounds (Bongu 'equations)		
C3S	62.12	.....
C2S	19.84	.....
C3A	3.52	<3.50
C4AF	4.76	.....

Table 3. The properties Physical characteristics of cement

Physical properties		Test Results	Limits of Iraqi Standard No.5/2019
Surface area (Blaine)m^2/kg		281	≥250
Setting time (min.)	Initial setting	232	≥45
	Final setting	297	≤600
Compressive strength, MPA	2-day	24.7	≥10
	28-day	39.67	≥32.5R
Soundness (Autoclave)%		0.14	≤0.8

3.2 Fine Aggregate

The research used Zone 2 Natural fine aggregate which met the requirements of the Iraqi Standard [IQS No. 45/1984] and came from the Maqale Karbala factory. The fine aggregate particle size distribution appears in Tables (4) which show that the material meets all grading specifications from IQS No. 45/1984. The fine aggregate meets concrete production requirements according to the physical and chemical properties presented in Table (5).

Table 4. The properties physical and chemical of the fine aggregate utilized

Sieves size (mm)	The passing Percentage of fine aggregate	Limits of (IQS. No.45/1984) (Zone 2)	
		Min. Limit	Max. Limit
10	100	100	100
4.75	96	90	100
2.36	90	85	100
1.18	82	75	90
0.6	75	60	79
0.3	42	40	12
0.15	1.2	0	10

Table (5). Grading of the of fine aggregate used

Characteristics	Test results	Limits of (IQS. No. 45/1984
Sulfate content (SO3) %	0.323	0.5% (max.)
Material finer than 75 µm	1.82	5% (max.)
Specific gravity	2.69	---
Absorption %	0.81	---
Fineness modulus	---	---

3.3 Coarse Aggregate

In this study, pre-graded gravel with a nominal maximum size of 20 mm, obtained from the Al-Niba'ai region, was utilized as the coarse aggregate. Prior to incorporation into the mixes, the aggregate was thoroughly washed to eliminate surface dust and subsequently air-dried until reaching a saturated surface-dry (SSD) condition. The results of the sieve analysis and the corresponding grading curve for the coarse aggregate, conducted in compliance with the Iraqi Standard (IQS No. 45/1984), are presented in. Furthermore, the chemical and physical properties of the gravel, as detailed in Table (6) and (7), respectively, were found to be fully consistent with the specified requirements of the same standard

Table 6. Grading of the coarse aggregate used

Sieves size (mm)	The passing Percentage of fine aggregate	Limits of (IQS. No.45/1984) grade 5-14 mm	
		Min. Limit	Max. Limit
37.5	100	100	100
20	96	95	100
9.5	37	30	60
5	2	0	10

Table 7. The physical and chemical of the coarse aggregate used

Characteristics	Test results	Limits of (IQS. No. 45/1984(
Sulfate content (SO3) %	0.045	0.1% (max.)
Material finer than 75 µm	0.063	3% (max.)
Specific gravity	2.62	---
Absorption %	0.79	---

3.4 Water

Clean, potable tap water was utilized throughout the experimental procedures, including the washing of and coarse aggregate samples, as well as for the mixing, casting, and curing of concrete specimens.

3.5 Silica Fume

Nano Silica (Grade A) – MAXPOWDER is spherical with a particle size of 229 nm and a high specific surface area of 20–25 m^2/g. It exhibits a real density of 1.9 g/cm^3 and a bulk density ranging from 300–500 kg/m^3. The material has a high melting point of 1230 °C. Its chemical composition is predominantly SiO_2 (90–95%), with minor amounts of Al_2O_3, Fe_2O_3, C, Na_2O, K_2O, MgO, S, CaO, MnO, P_2O_5, and traces of LOI and moisture, maintaining a pH between 6.8 and 8.

3.6 Steel Reinforcement

In this research, two different sizes of Deformed bars were used. One was a 12 mm diameter bar for longitudinal reinforcement, while the other was an 8 mm diameter bar for transverse reinforcement (stirrups). The test results of steel bars are shown in the Tables (8), which are in accordance with the requirements of ASTM A615/A615M.

Table 8. Steel reinforcement properties

Properties	Results		Tensile requirement ASTM 615M – 05a (Minimum)	
Nominal diameter (mm)	Ø12	Ø 8	Grade 60	Grade 40
Actual diameter (mm)	12	8	-	-
Yield stress, fy (MPa)	479.6	411.8	420	280
Ultimate stress, fu (MPa)	634.6	640.9	620	420
Elongation %	17.6	23.9	7-9	11-12

3.7 Steel Fiber

The steel fibers employed in this study were straight-ended and of micro size, with a length of 6 mm and a diameter of 0.2 mm, resulting in an aspect ratio of .30 These fibers exhibited a tensile strength of 2,850 MPa, a density of 7.85 g/cm^3, Table (9): Steel Fiber properties

Table 9. Steel Fiber properties

Description	Micro copper coated steel fiber (Model HX-DT-S01)
Length	6 – 20 mm
Diameter	0.2 – 0.3 mm (Optional: 0.18 – 0.5 mm)
Type	Straight wire / Hooked end
Color	Copper coated
Material	Steel wire
Tensile Strength	≥ 2850 MPa

3.8 Superplasticizer (SP)

The research utilized Structure 502 which is a polycarboxylate ether (PCE)-based superplasticizer obtained from Fosroc. The high-performance admixture improves cement particle distribution through electrostatic repulsion and steric hindrance which results in lower water requirements and better flowability. The product delivers superior water-reducing capabilities and maintains excellent workability properties which suit applications involving high-performance and highly flowable concrete mixes. The essential technical characteristics of the product appear in Table (10).

Table 10. Structure 502 (Fosroc) technical data*

Properties	Value or Description
Appearance	Light brown colored liquid
PH value	6.5
S.G. @ 20-C	1.06 ± 0.02
Chloride content	Nil
Alkali content	Typically, less than 1.5 gm Na_2O equivalent per liter of admixture

**The manufacturer provides this info. Fosroc*

3.9 Mix Proportions

The research examines how conventional concrete interacts with SIFCON when used together. The research focused on creating better bond strength between these two materials through the variables listed. The research used the conventional concrete mix design from Table (11) and developed the SIFCON mix design which appears in Table (11). The research study [31] provided the necessary mix properties for this investigation.

Table 11. Mix proportions

Mix No.	Type of Mix	Cement (kg/m^3)	Coarse aggregate (kg/m^3)	Fine aggregate (kg/m^3)	Silica Fume (kg)	Water (L/m^3)	Steel Fiber (kg/m^3)	Super-plasticizer liters per 100 kg
1	Normal Concrete	400	1050	850	------	180	-----	0.2 to 3.0 of cementitious materials.
2	SIFCON	1000	------	1000	0.1 from cement	300	6% From the size of the concrete	0.2 to 3.0 of cementitious materials.

4. Testing Procedure

The testing apparatus required three reinforced concrete beams for precise experimental testing through repeated experimental procedures. The testing procedure followed a structured approach to achieve both precise results and dependable outcomes. The entire testing equipment received thorough installation of all its components including sensors and mechanical parts into their assigned locations. 1. The steel support frame received pin and roller supports at its base to achieve stable and precise beam fixation. 2. The load cell received its placement at beam center point while the LVDT displacement sensor operated from a position directly under the beam's midspan to measure load and Interfacial Slip accurately. 3. The load distributor rested on top of the beam to distribute the applied force evenly throughout its width. 4. The testing system became operational after integration with the electronic control system which enabled digital load control through the control program. 5. The load cell tracked the applied force throughout the loading process while the LVDT sensor measured Interfacial Slip with high precision. The experimental data about beam structural behavior under loading conditions became available through this testing arrangement.

4.1 Hardened Tests

4.1.1. Compressive Strength Test

The compressive strength test was conducted on cubic specimens measuring 150 × 150 × 150 mm for each concrete mixture at curing ages of 7 and 28 days, in accordance with BS 1881: Part 116 (1981). The test was performed using a compression testing machine with a capacity of 2000 kN. For each mixture, the compressive strength was determined as the average value of three specimens, calculated using the standard formula.

The results indicated that the compressive strength of SIFCON concrete was significantly higher than that of conventional concrete. This improvement is primarily attributed to the high-volume fraction of steel fibers incorporated into the SIFCON matrix, as presented in Table (12). The notable increase in strength can be explained by the efficient infiltration of the cementitious slurry into the densely packed steel fibers, leading to the formation of a homogeneous and well-bonded composite material.

Table 12. Results of the tested mixtures' cube's compressive strength after 7 and 28 days

No. Mix	Mixture symbols	Cube Compressive strength (*f*cu), MPa	
		At 7 Days	At 28 Days
1	N	38	49
2	S	51	77

4.1.2. Splitting Tensile Strength

The ASTM C496 standard guided the splitting tensile strength evaluation of 200 × 100 mm cylindrical specimens at 7 and 28 days of curing. The testing procedure involved placing each cylinder between two wooden bearing strips which maintained equal force distribution across the upper and lower surfaces. The splitting tensile strength calculation used the standard method from ASTM C496 to determine the average value from three specimens. The test results in Table (13) show that SIFCON specimens demonstrated higher tensile strength than standard concrete specimens. The high steel fiber content in the specimens led to better tensile stress resistance and enhanced their ability to bridge cracks throughout the matrix.

Table 13. Results of splitting Tensile strength at 7 and 28 days

No. Mix	Mixture symbols	Splitting tensile stress (*f sp*), MPa	
		At 7 Days	At 28 Days
1	N	12	13
2	S	14	20

4.1.3. Modulus of Rupture

The flexural strength test used 100 × 100 × 400 mm prismatic specimens to evaluate their performance at 7 and 28 days of curing age according to ASTM C78-02. The flexural testing machine with 150 kN capacity executed the test by applying two-point loading to the specimens. The ASTM C78 formula enabled the calculation of modulus of rupture to determine the average value from two specimens. The experimental results in Table (14) demonstrate that SIFCON mixture outperformed conventional concrete by achieving a 500% strength improvement. The SIFCON specimens withstood flexural loading tests better than conventional concrete specimens because they displayed minimal cracking during the tests.

Table 14. Results of Modulus of rupture at 7 and 28 days

NO. mix	Mixture symbols	Modulus of rupture (*fr*), MPa	
		At 7 Days	At 28 Days
1	N	12.8	13.28
2	S	15.4	21.16

4.2. Beam Specimen Design for Experimental Results

The improvement of shear strength in separate beam sections represents a critical need for structural maintenance work and strengthening operations of damaged structural elements under unexpected loading conditions. The research used high-performance materials to boost shear resistance through multiple strengthening methods which improved bond strength and stress distribution between structural components. The experimental study investigated seven composite specimens which consisted of two parts: conventional reinforced concrete in the first

section and Slurry Infiltrated Fiber Concrete (SIFCON) in the second section. The push-off loading test was applied to all specimens to measure their interfacial shear behavior and the obtained results appear in Table (1). The research measured shear capacity improvement through tests that compared composite specimens to a reference sample made from conventional concrete for both segments. The research showed that the composite specimens demonstrated better shear resistance than the reference sample according to the results presented in Table (15). The researchers organized the specimens into three experimental groups to evaluate their interfacial configurations and strengthening methods.

Table 15. Results of all beams tested

No.	Groups	Specimens	First crack (kN)	Interfacial Slip (mm)	Ultimate Load (kN)	improvement ratio percentage
1.	first group	N. L	18	2.21	40	0
2.	second group	S. R	70	3.5	131	228%
3.	(Change	S. T	55	0.0375	105.86	165%
4.	Interface)	S.C	40	0.0375	65.97	65%
5.	third group	S. R. D	120	2.615	211.28	428%
6.	(Change	S. T. D	95	1.3	161.5	304%
7.	Interface with Bolts)	S. C. D	80	0.6	105.74	164%

4.2.1 First group: Control Specimen (N.L)

The specimen N.L was cast monolithically and considered the reference specimen for comparison with all strengthened specimens as illustrated in Figure (5). The first shear crack appeared at approximately 8 kN, representing about 44% of the ultimate load, and propagated along the shear plane due to the concentration of shear stresses. The specimen ultimately failed at a load of 18 kN.

The load–displacement curve indicated relatively low stiffness and limited shear resistance compared with the strengthened specimens. However, the specimen exhibited a relatively large deformation prior to failure. in Figure 6.

- Peak load ≈ 18 kN
- Ultimate displacement ≈ 2.7 mm
- Energy absorption ≈ 32 J
- Ductility index ≈ 9.0

These results indicate that although the specimen exhibited moderate ductility, its load-carrying capacity and energy dissipation capability were relatively limited.

Fig. 5. Control specimen (N.L)

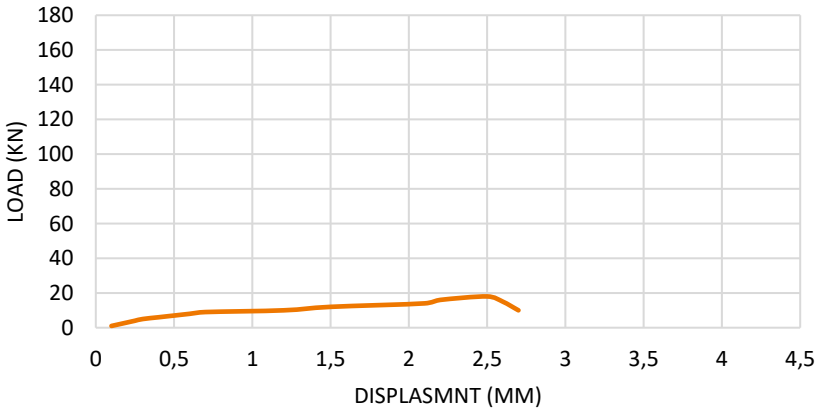

Fig. 6. Control specimen (N.L) Load-Displacement

4.2.2. Second Group: Specimens Reinforced of Change Interface (S. R), (S.T) and (S.C)

Specimen S.T: The triangular groove configuration showed improved shear resistance, as illustrated in Figure (7). The first crack appeared at 45 kN, while the ultimate load reached 105.86 kN. in Figure (8). This configuration demonstrated a good balance between shear capacity and deformation.

- Peak load ≈ 105 kN
- Ultimate displacement ≈ 1.8 mm
- Energy absorption ≈ 145 J
- Ductility index ≈ 9.0

Specimen S.C: The specimen S.C included circular interface grooves as illustrated in Figure (9). The first crack appeared at 35 kN, and the ultimate load reached 65.97 kN in Figure (10). The circular grooves enhanced the mechanical interlock and provided moderate improvement in both strength and ductility.

- Peak load ≈ 65 kN
- Ultimate displacement ≈ 2.4 mm
- Energy absorption ≈ 118 J
- Ductility index ≈ 12.0

Specimen S.R: The rectangular groove specimen exhibited significant improvement in shear strength as illustrated in Figure (11). The first crack appeared at 60 kN, and ultimate failure occurred at 131 kN in Figure (12). The rectangular interface provided strong mechanical interlocking, which enhanced shear transfer capacity.

- Peak load ≈ 130 kN
- Ultimate displacement ≈ 2.2 mm
- Energy absorption ≈ 261 J
- Ductility index ≈ 11.0

Fig. 7. Specimen (S.R)

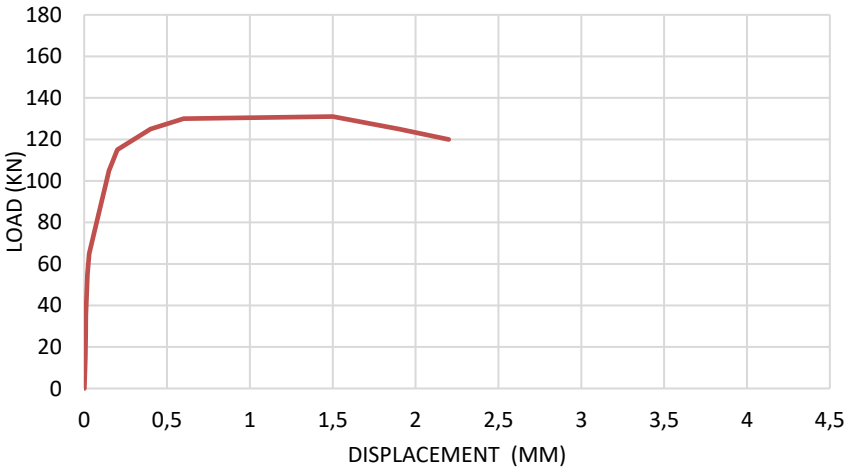

Fig. 8. Specimen (S.R) Load-Displacement

Fig. 9. Specimen (S. T)

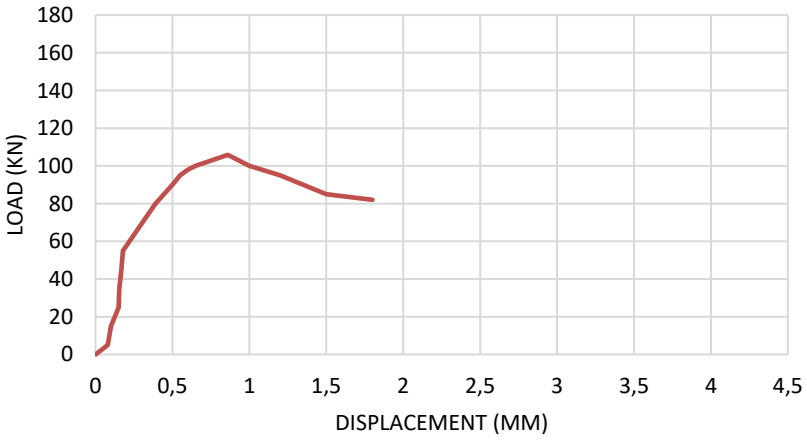

Fig. 10. Specimen (S. T) Load-Displacement

Fig. 11. Specimen (S. C)

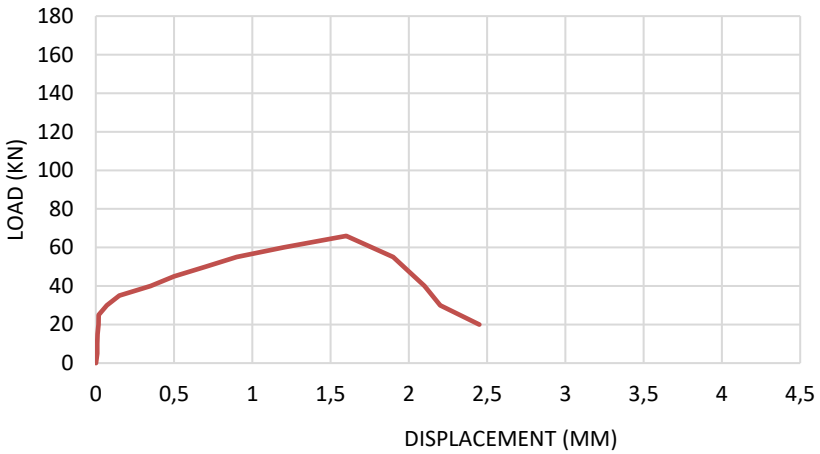

Fig.12. Specimen (S. C) Load-Displacement

4.2.3. Third Group: Specimens Reinforced of Change Interface with Bolts (S.R.D), (S. T.D) and (S.C.D)

Specimen S.T: The triangular groove configuration showed improved shear resistance, as illustrated in Figure (13). The first crack appeared at 45 kN, while the ultimate load reached 105.86 kN. in Figure (14). This configuration demonstrated a good balance between shear capacity and deformation.

- Peak load ≈ 105 kN
- Ultimate displacement ≈ 1.8 mm
- Energy absorption ≈ 145 J
- Ductility index ≈ 9.0

Specimen S.C: The specimen S.C included circular interface grooves as illustrated in Figure (15). The first crack appeared at 35 kN, and the ultimate load reached 65.97 kN in Figure (16). The circular grooves enhanced the mechanical interlock and provided moderate improvement in both strength and ductility.

- Peak load ≈ 65 kN
- Ultimate displacement ≈ 2.4 mm
- Energy absorption ≈ 118 J
- Ductility index ≈ 12.0

Specimen S.R: The rectangular groove specimen exhibited significant improvement in shear strength as illustrated in Figure (17). The first crack appeared at 60 kN, and ultimate failure occurred at 131 kN in Figure (18). The rectangular interface provided strong mechanical interlocking, which enhanced shear transfer capacity.

- Peak load ≈ 130 kN
- Ultimate displacement ≈ 2.2 mm
- Energy absorption ≈ 261 J
- Ductility index ≈ 11.0

Fig. 13. Specimen (S. R.D)

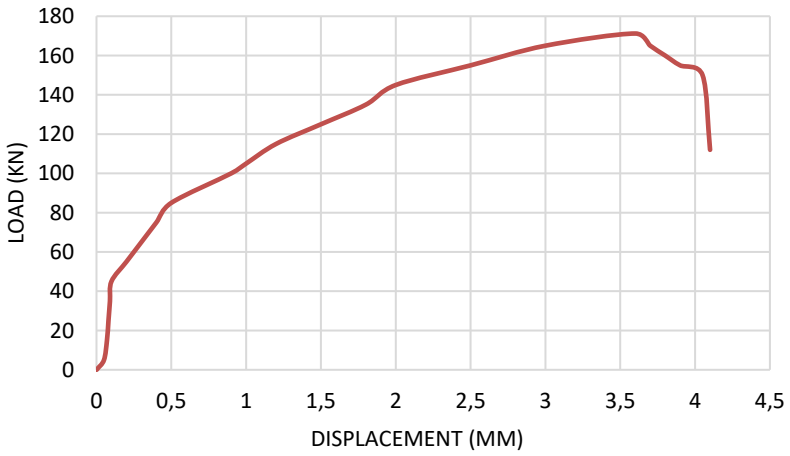

Fig. 14. Specimen (S. R.D) Load-Displacement

Fig. 15. Specimen (S. T.D)

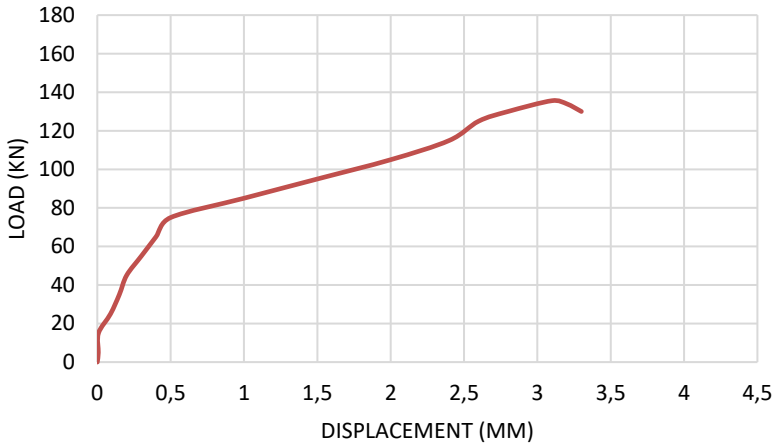

Fig. 16. specimen (S. T.D) Load-Displacement

Fig. 17. specimen (S. C.D)

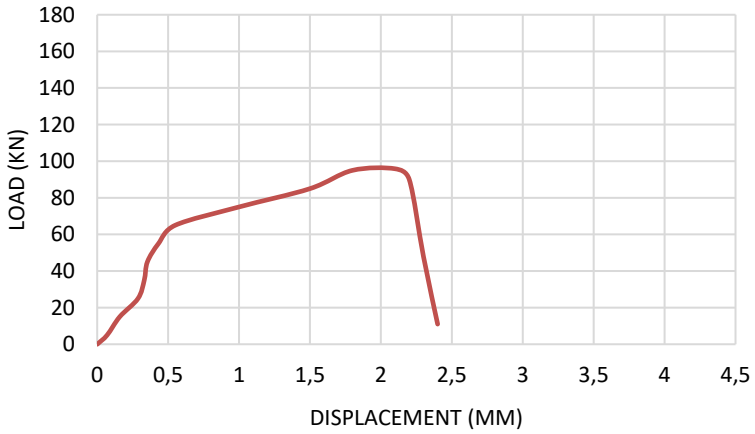

Fig. 18. specimen (S. C.D) Load-Displacement

4.3. Failure Modes

During the experimental observations, it was noted that the failure behavior of the tested specimens varied considerably. Some specimens exhibited sudden shear failure, whereas others showed a more gradual and controlled failure process accompanied by larger deformation. The failure characteristics can be categorized according to the strengthening groups as follows:

Specimens strengthened with interface grooves showed noticeable improvements in shear behavior compared with the reference specimens. Among these configurations, the rectangular groove specimen (S.R) exhibited the highest shear capacity and energy absorption, followed by the triangular groove specimen (S.T), while the circular groove specimen (S.C) showed comparatively lower strength. These results indicate that the geometry of the grooves significantly affects the mechanical interlocking mechanism and consequently the shear transfer across the interface.

The hybrid strengthening technique combining bolts with interface grooves produced the best overall structural performance among all tested groups. In particular, the specimens with rectangular grooves combined with bolts exhibited the highest load capacity and energy absorption. Specimen S.R.D2 achieved the best performance, recording the highest ultimate load and energy absorption among all specimens. These results demonstrate that combining mechanical interlocking (grooves) with mechanical connectors (bolts) provides a highly effective mechanism for improving both shear strength and energy dissipation capacity as illustrated in Figure (19).

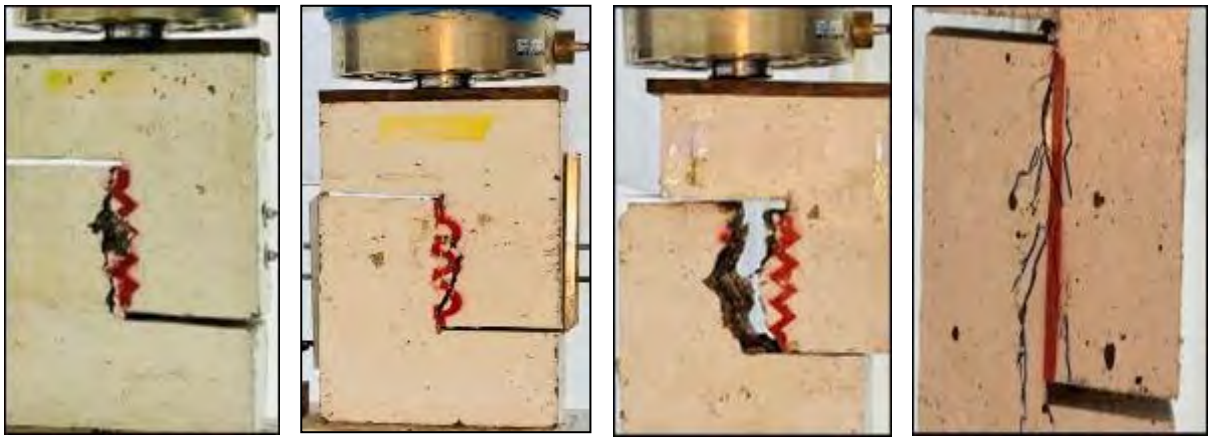

Fig. 19. Failure modes

5. Conclusions

The experimental study revealed that interface groove geometry is a very important factor in the regulation of the shear nature and structural performance of the experimented specimens. These findings are clear evidence that the shear transfer mechanism can be greatly improved by changing the interface configuration to increase the mechanical interlocking and slow down crack propagation. The rectangular groove shape is among the specimens that were tested had the highest structural performance with regards to shear capacity, stiffness and energy absorption. The initial crack in this specimen occurred at an approximate load of 60 kN and the final load was about 131 kN, the maximum load carrying capacity of any of the configurations tested. Besides, the specimen recorded an ultimate displacement of around 2.2 mm, energy absorption capacity of around 261 J, and ductility index of 11.0. These findings affirm that the rectangular interface geometry was highly mechanically interlocked, and that such a reinforcement made the interfaces substantially more effective in transferring shear across the interface and helping to maintain a more consistent failure behavior. The triangular groove design (S.T) also exhibited significant increase in shear resistance with respect to the rest of the specimens. The initial crack to be seen on this specimen was at around 45 kN, and the maximum load was about 105.86 kN. The ultimate displacement of the specimen was about 1.8 mm, energy absorption capacity was about 145 J, and ductility index was 9.0. These findings prove that the triangular groove pattern provided a satisfactory balance between shear strength and deformation capacity. The triangular geometry assisted in good distribution of stress on the interface that enhanced the shear resistance and also ensured that the deformation behavior was relatively stable before failure. Conversely, the circular groove pattern (S).C) exhibited another structural response as compared to the other configurations. The initial crack occurred at about 35 kN, and the final load was about 65.97 kN that is the lowest shear capacity of the tested specimens. Nevertheless, the circular groove specimen had the greatest deformation capacity with ultimate displacement of about 2.4 mm and ductility index of 12.0, and energy absorption capacity of approximately 118 J. The findings point to the fact that the circular groove design offered a decreased shear strength, but it enhanced the ductility of the specimen and enabled it to be deformed to a higher degree before breaking down. The mechanical interlocking was enhanced to a certain degree by the curved geometry of the grooves and also produced gradual crack formation and more controlled failure behavior. All the conclusions in the experiment indicate that the geometry of the interface is conclusive in enhancing shear transfer efficiency and structural performance. The rectangular groove structure was found to be the most effective in performance in shear strength and energy absorption whereas the triangular structure offered a balanced structural behavior of strength and deformation. At the same time, the circular groove design exhibited better ductility but less shear capacity. The findings indicate the significance of maximizing the interface geometries in reinforced concrete structures that are enhanced with modern materials like SIFCON. This optimization can be used to increase shear resistance, augment energy dissipation capability and help achieve safer and more reliable structural performance in practice.

Acknowledgments

The author sincerely extends gratitude to the staff of the Civil Engineering Department at the University of Karbala for their dedicated efforts and steadfast support throughout this research. Their assistance and provision of all necessary facilities were instrumental in enabling the successful completion of this study.

References

[1] Lankard DR. Slurry-Infiltrated Fiber Concrete (SIFCON): Properties and Applications. MRS Proceedings; 1984. https://doi.org/10.1557/PROC-42-277
[2] Wang ML. Shear properties of slurry-infiltrated fibre concrete (SIFCON). Construction and Building Materials. 1994;8(5):281-287. https://doi.org/10.1016/S0950-0618(09)90029-0
[3] Al-Rousan RZ, et al. Shear repairing and strengthening of reinforced concrete beams using SIFCON. Case Studies in Construction Materials. 2018. https://doi.org/10.1016/j.istruc.2018.05.001
[4] Sampath P, et al. Mechanical properties of slurry-infiltrated fibrous concrete (SIFCON). Materials Today: Proceedings. 2020. https://doi.org/10.1016/j.matpr.2019.12.401
[5] Akçaözoğlu K. The effect of curing conditions on the mechanical properties of SIFCON. Revista de la Construcción (English Edition). 2021.
[6] Robayo-Salazar R, et al. Slurry-Infiltrated Fiber Concrete (SIFCON) for use in ballistic and blast-resistant applications. Case Studies in Construction Materials. 2023. https://doi.org/10.1016/j.istruc.2023.105282
[7] Ali MH, et al. Mechanical properties and efficiency of SIFCON samples under elevated temperature. Journal of Building Engineering. 2022. https://doi.org/10.1016/j.cscm.2022.e01281
[8] Ghani LA, et al. Preparation and engineering properties of Slurry Infiltrated Fiber Concrete (SIFCON). Regional Journal of Engineering Studies. 2024.
[9] Al-Hadithi AI. Investigating mechanical properties of SIFCONs produced with different fiber aspect ratios. Cement & Concrete Composites. 2024. https://doi.org/10.1016/j.conbuildmat.2024.138220
[10] ETASR. Bond performance of the slurry infiltrated fiber concrete overlay to normal strength concrete substrate. Engineering, Technology & Applied Science Research (ETASR).
[11] Ipek S, Tuyan M, Yazici H. Effects of fiber content and geometry on SIFCON performance. Construction and Building Materials. 2014.
[12] Naaman AE, et al. Early studies on high-fiber cement composites and their bonding behavior. Cement and Concrete Research. 1987.
[13] Stiel L. Investigation of SIFCON microstructure and fiber-matrix interaction. Journal of Materials in Civil Engineering. 2004.
[14] Tuyan M, Yazıcı H. SIFCON behavior under dynamic/impact loading-experimental study. International Journal of Impact Engineering. 2012.
[15] Iqbal M, et al. Vacuum mixing influence on slurry infiltration and porosity of SIFCON. Cement & Concrete Research. 2019.
[16] Graybeal B. Material property characterization of ultra-high-performance concrete (UHPC). FHWA; 2006.
[17] Balázs WKTGL. Impact and blast resistance of slurry infiltrated fiber concrete - review. Periodica Polytechnica Civil Engineering / FIB review. 2023.
[18] Tuama WK. Punching shear strengthening of flat slabs using SIFCON. ResearchSquare; 2025. https://doi.org/10.21203/rs.3.rs-7002488/v1
[19] Robles J, et al. SIFCON jacketing technique for strengthening shear-deficient beams: experimental and numerical study. Engineering Structures. 2015.
[20] Rossi P. Influence of fibre geometry and matrix maturity on mechanical performance of UHPC and SIFCON-like composites. Cement and Concrete Composites. 2013. https://doi.org/10.1016/j.cemconcomp.2012.08.005
[21] Graybeal B. Material characterization of fiber-reinforced cement composites. FHWA-HRT-06-103; 2006.
[22] Ipek S, et al. Pullout behavior of steel fibers in high-slurry matrices and implications for bond in SIFCON. Construction and Building Materials. 2016.
[23] Wang M, Naaman AE. Shear and torsion behavior of fiber-reinforced cementitious composites. Journal of Structural Engineering. 1997.
[24] Al-Rousan RZ, Al-Hayek R. Use of SIFCON jackets for retrofitting corroded/deficient RC members. Journal of Performance of Constructed Facilities. 2019.
[25] Ipek S, Yazici H. Effect of fiber volume fraction and aspect ratio on SIFCON fracture energy. Materials and Structures. 2018.
[26] Ghoniem Y, et al. Multiscale modelling of SIFCON: from microstructure to macroscopic behavior. Cement & Concrete Composites. 2020.
[27] Ain Shams Engineering Journal / ETASR. An experimental study on SIFCON overlays and interface preparation: Bond strength, surface roughness, bonding agents. 2021.

[28] Ipek S, Tuyan M, Yazıcı H. SIFCON under cyclic loading-fatigue resistance and crack bridging. International Journal of Fatigue. 2012.
[29] Naaman AE, Reinhardt H. Fiber-bridging mechanisms and toughening in high-fiber composites. Journal of Materials in Civil Engineering. 1987.
[30] MDPI. Development of an Engineered Slurry-Infiltrated Fibrous Concrete: Experimental and Modelling Approaches. Materials. 2024.
[31] Algın Ö, Özbebek A, Gerginci A, Mermerdaş K. Effects of Basalt Fibre Utilization on Durability and Mechanical Properties of SIFCON. Construction and Building Materials. 2020;237.

Research on Engineering Structures & Materials
www.jresm.org

Research Article

Machine learning-based evaluation of indirect tensile stiffness modulus of fiber-modified cold asphalt mixtures

Anwer M. Ali [a], Dawod S. Ayed [b], Raed Abdullah Hasan [c]

Department of Civil Engineering, College of Engineering, University of Samarra, 34010, Iraq

Article Info

Article History:

Received 24 Mar 2026

Accepted 20 Apr 2026

Keywords:

Machine learning;
Artificial neural networks;
Deep neural networks;
Fiber-reinforced cold Mix asphalt;
Indirect tensile stiffness modulus;
Modelling

Abstract

This study aims to evaluate the Indirect Tensile Stiffness Modulus (ITSM) of fiber-modified cold asphalt mixtures using advanced machine learning models. Several asphalt mix designs (123 mixes) from many previous studies incorporating various fiber types, contents, and curing conditions were experimentally tested. Artificial Neural Networks (ANNs) and Deep Neural Networks (DNNs) were developed to predict ITSM based on seven input features, including fibre characteristics and mix design parameters. The ANN model (ANN-I) demonstrated superior performance, with a correlation coefficient (R) of 0.951 and an RMSE of 174.85 MPa, outperforming the DNN model (DNN-II), which showed lower predictive accuracy (R = 0.884, RMSE = 252.56 MPa). Curing time emerged as the most influential variable across both models. These conclusions verify that ANN provides a stronger and more generalizable means of modelling the stiffness behaviour of cold asphalt reinforced with fibres and provide evidence of its effectiveness when optimising sustainable pavement designs.

© 2026 MIM Research Group. All rights reserved.

1. Introduction

Pavement technology has advanced in recent decades due to environmental pressures, resource limitations, and the rising costs of conventional asphalt, a sustainable pavement type. In this context, cold asphalt mixtures [1] can be produced and compacted at ambient temperature, serving as a replacement for hot-mix asphalt (HMA). There are several advantages to the production and road use of Cold Mix Pavement Mixtures over traditional HMA, including higher production temperatures that can save energy and significantly reduce greenhouse gas emissions [2]. Additionally, cold asphalt is much safer than hot asphalt, as it can be produced and compacted at ambient temperature, which is always hot around 160^0C. It can also be placed by hand in the field, unlike the more common hot-mix (HMA) pavement mixtures.

Several performance factors can be improved by adding reinforcement fibres to cold asphalt. Different fibres used to modify the mechanical properties of cold asphalt are cellulosic, glass, polyester, and natural fibres, with jute and coconut fibres prevailing. Previous studies show that these fibres increase tensile strength, moisture stability, and stiffness of cold asphalt mixtures [3,4]. When added to the matrix of a bitumen-aggregate material, these fibres form a continuous, denser structure that retards cracking and deformation in the mix. Among all performance properties of fibre-reinforced cold asphalt, the Indirect Tensile Stiffness Modulus (ITSM) is of great importance, as it measures the material's resistance to deformation and tensile loading and provides an important platform for performance-based design as per [5].

Traditional empirical or mechanistic models often struggle to capture the complex, nonlinear relationships among ITSM variables such as fibre type, content, blend ratios, curing conditions, and air voids. Generally, traditional regression-based approaches demand a predetermined

*Corresponding author: anwer.m.a@uosamarra.edu.iq
[a]orcid.org/0009-0001-9812-5498; [b]orcid.org/0009-0000-2375-2043; [c]orcid.org/0000-0003-2045-7633
DOI: http://dx.doi.org/10.17515/resm2026-1584ma0324rs

mathematical (statistical) association between inputs and outputs, which restricts the ability to represent the interdependent and nonlinear relationships among multiple component parameters in mixtures. Because ITSMs are modified due to multiple interacting factors (as opposed to isolated components), the predictive power of traditional models will decrease as the material behaviour becomes more heterogeneous or complicated [6-8]. To overcome modelling challenges, machine learning (ML) techniques have emerged as a viable alternative for evaluating material performance in civil engineering. ML models, particularly Artificial Neural Networks (ANNs) and Deep Neural Networks (DNNs), are well-suited to tackle high-dimensional, nonlinear, and noisy datasets [8-10].

Artificial neural networks (ANNs) are models of the structure and functional aspects of biological neurons. They can approximate highly complex functions using learning algorithms that iteratively adjust node weights to minimise mean squared error (MSE) [11]. DNNs have been gaining tremendous attention for being powerful models to describe mechanical behaviours of materials due to their ability to learn intricate underlying features found within high dimensions. DNNs have been used extensively for many types of cementitious materials, such as concrete [12], soils [8], asphalt [13], and other issues related to materials engineering and geotechnical engineering. More recently, DNN models with multiple hidden layers have been shown to generalise better for very large and complex data sets than simpler ANN architectures; however, their computational costs and tendency to overfit the training set are also higher than those of simpler architectures. [14]

ML has been used to predict rutting, fatigue life, resilient modulus, and stiffness modulus in pavement engineering applications, and has consistently outperformed classical regression methods in terms of accuracy and interpretability [15 - 16]. In contrast, there have been relatively few studies that have compared the predictive performance of shallow and deep learning models for predicting ITSM of fibre-modified cold asphalt mixtures; this limitation is noteworthy given the heterogeneity of mix design variables and curing conditions.

This research will create and compare the predictive power of ANN and DNN Models for determining the ITSM of fiber-reinforced Cold Asphalt Mixtures. A dataset containing 123 different mixtures with a variety of fiber types, quantities and curing durations was used as the basis for evaluating the two model architectures with respect to their accuracy, generalizability, and variable importance. The findings from this study will contribute to the broader literature on data-driven asphalt mix design and demonstrate the utility of machine learning tools for optimising high-performance, environmentally sustainable pavement materials.

2. Methodology

2.1. Artificial Neural Networks ANNs

Artificial neural networks (ANNs) have become increasingly valuable for modelling complex, nonlinear relationships where traditional regression techniques fall short, particularly in the field of civil engineering. Unlike linear modelling techniques, which are effective only for single-input variables, ANN models can capture relationships among inputs. ANN lets you see all possible relationships among multiple variables. In the field of material property prediction, ANN has been successfully used to predict the Indirect Tensile Stiffness Modulus (ITSM) of Cold Mix (N), as shown in Figure 1, using Artificial neural networks, Fiber type, and Fiber Length. The ANN model is built using thousands of computational units that mimic neurons in the brain, communicate with one another (interconnected), and can learn (adapt) from a given (trained) database, thereby modelling complex relationships between a set of input variables and an output target variable [8,9].

Using the seven input parameters, fibre type one (FT1), fibre type two (FT2), fibre blend Ratio (FT1/FT2), Fiber Content by weight (%FC), Curing time (CT), Fiber Length (FL), Air Void Content (%AV), the Artificial Neural Networks (ANN) model has been developed. To predict the ITSM of fibred mixes using experimental test data, a model was constructed. The ANN model consists of an input layer, one or more hidden layers, and an output layer. The ANN was trained using the backpropagation algorithm. Backpropagation is the most common method of training multi-layer perceptron (MLP) networks and is also used in supervised learning. Gradient descent was used for model optimisation. This study also revealed that the ANN model has the capability of

generalisation (prediction). The model was fine-tuned by optimising key hyperparameters, including the learning rate, number of neurons, and data partitioning, to improve accuracy.

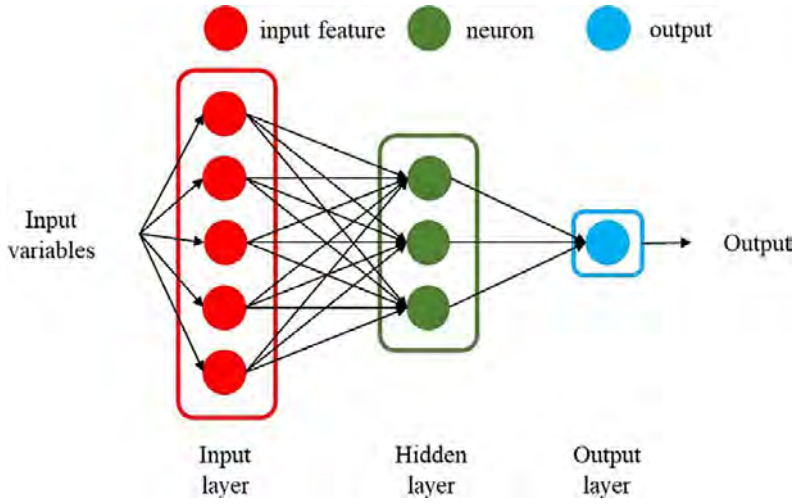

Fig. 1. Simplest artificial neural network ANN

2.2. Deep Neural Networks DNN

Generally speaking, the DNN will have at least an input layer for processing the input data, more hidden layers for computation, and an output layer for the computed results. This AI system can model nonlinear relationships between inputs and outputs, as shown in the graph (Fig. 2). Nonetheless, deeper architectures such as deep neural networks (DNNs) are introduced to capture much more complex patterns, increasing the representational capacity but in the opposite way they also bring some risks such as possibility of overfitting and increased computational demand [9].

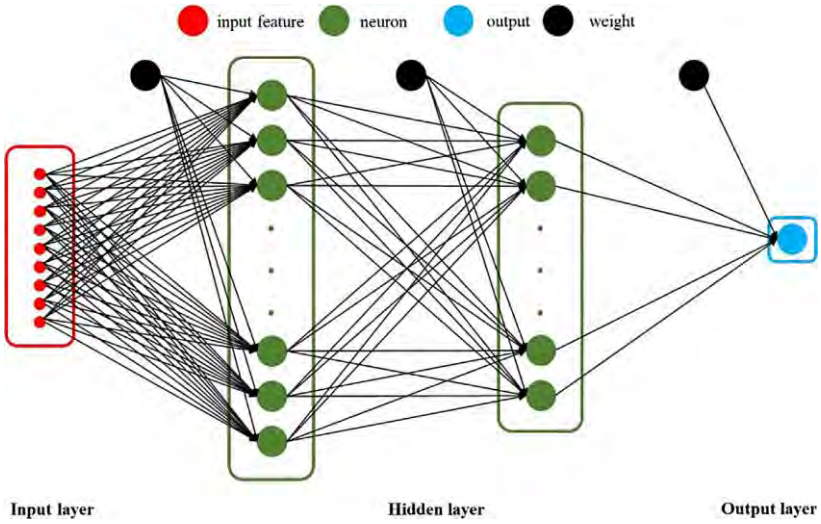

Fig. 2. Deep neural network DNN

Usually, DNNs are feed-forward networks with multiple layers, each containing weights, biases, and an activation function [17]. In the training phase, the forward pass computes the output values, while the backpropagation updates the parameters to minimise the function's predicted error. There are several strategies to improve the generalisation ability of DNNs, including dropout [18], early stopping [19], batch normalisation [20], and advanced optimisers like Adam [21].

The DNN framework is developed for predicting the ITSM of the fiber-modified cold asphalt mixtures, based on various input features like fiber types (FT1, FT2, FT1/FT2), fiber content (% FC), curing time (CT), air voids (% AV), and fiber length (FL). This architecture can capture

nonlinear interactions among variables [20], thereby enhancing regression accuracy in asphalt mix performance modelling.

2.3. Data Base

To assess the predictive capability of deep learning models such as DNNs and ANNs, the formation of training datasets is crucial and highly depends on the structure, quality, and representativeness of the data collected, as networks learn complex, nonlinear relationships between inputs and outputs [9]. In this study, datasets were developed and used to train, develop, and validate models for predicting the Indirect Tensile Stiffness Modulus (ITSM) of fibre-reinforced cold-mix asphalt mixtures.

The primary data set consists of 123 cold-mix asphalt designs obtained from prior experimental studies simulating fibre reinforcement under varying conditions, including curing durations and moisture contents [13,23-28]. Both Deep Neural Network (DNN) and Artificial Neural Network (ANN) models employ the fiber type that is applied in the 1st (FT1) and 2nd fibers (FT2), the hyprid fibers in mixture (FT1/FT2), the percentage of the fiber that is added to the mixture (%FC), the curing time (CT), the length of the fiber (FL) and air void content (%AV) as the inputs values. The ITSM in MPa metric in Table 1 is the output variable.

Table 1. Definition of variables used in models for fiber-modified cold mix asphalt

Variable Type	Symbol	Description
Input	FT1	Fiber Type 1 (0 = No fiber, 1 = Cellulose, 2 = Glass, 3 = Nylon, 4 = Polyester, 5 = Basalt, 6 = Hemp, 7 = Jute, 8 = Coir)
Input	FT2	Fiber Type 2 (0 = No fiber, 1 = Cellulose, 2 = Glass, 3 = Nylon, 4 = Polyester, 5 = Basalt, 6 = Hemp, 7 = Jute, 8 = Coir)
Input	FT1/FT2	Fiber Blend Ratio by Mass (FT1:FT2)
Input	%FC	Fiber Content (% by weight of total aggregate)
Input	FL	Fiber Length (mm)
Input	CT	Curing Time (days)
Input	%AV	Air Void Content (%)
Output	ITSM	Indirect Tensile Stiffness Modulus (MPa)

Both models were fashioned as multi-input, single-output regression structures. The Deep Neural Network (DNN) model was applied with a 2-hidden-layer architecture. In contrast, the Artificial Neural Network (ANN) model was trained with a single hidden layer architecture, in view of possible greater training flexibility and better accuracy. Training was done using the Levenberg-Marquardt backpropagation algorithm built into the IBM SPSS Modeller environment, a behaviour it has shown in handling nonlinear regression problems relating to material performance reasonably well.

A 'trial and error' method has been used to determine the optimal number of hidden neurons and the suitable data distributions for training, testing, and validation. The ANN-I model with three hidden nodes was found to be the most effective and the most stable. The DNN-II model with two hidden layers (4 nodes in the first and 3 in the second) performed best. Both models were tested with and without regularisation methods and layer normalisation [29,30] to improve generalisation and avoid overfitting. The activation function used for both models was the hyperbolic tangent (tanh), with a learning rate of 0.4 and a momentum coefficient of 0.9 to ensure faster, stable convergence during training.

Table 2 includes all the parameters used for the model configurations, including the hidden layers and the number of nodes. These configurations correspond to the ANN-I model illustrated in Figure 3 and the DNN-II model shown in Figure 4. Based on performance metrics, the optimal number of hidden nodes for the ANN-I model was determined to be three. In contrast, the DNN-II model achieved its best performance with four nodes in the first hidden layer and three nodes in the second hidden layer.

Table 2. Data division ratios on ANN-I model and DNN-II model performance for fiber-reinforced cold mix asphalt

ANN-I model					
Input layer	7	Hidden layer	3	Output layer	1
Training (%)	Testing (%)	Validation (%)	Training Error (%)	Testing Error (%)	Correlation (r%)
70	20	10	7.4	11.5	91.5
70	25	5	6.2	11.7	90.6
80	10	10	8.8	8.8	93.2
80	15	5	6.1	6.8	94.6
90	5	5	4.8	5.9	95.1
90	8	3	5.2	4.7	92.3
DNN-II model					
Input layer	7	Hidden layer 1 Hidden layer 2	4 3	Output layer	1
Training (%)	Testing (%)	Validation (%)	Training Error (%)	Testing Error (%)	Correlation (r%)
70	20	10	10.6	21.3	85.6
70	25	5	12.4	16.9	85.6
80	10	10	9.6	11.6	87.8
80	15	5	9.9	12.8	83.2
90	5	5	7.9	20.4	80.9
90	8	3	6.7	7.3	88.4

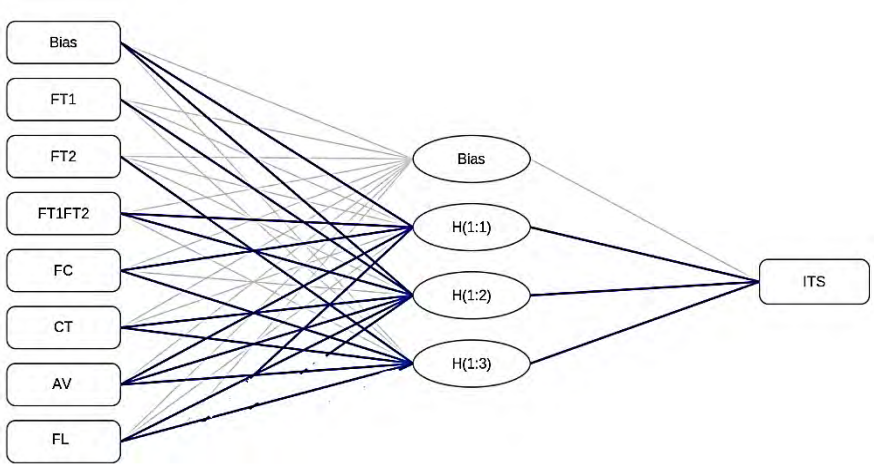

Fig. 3. Architecture of an artificial network model for ANN-I

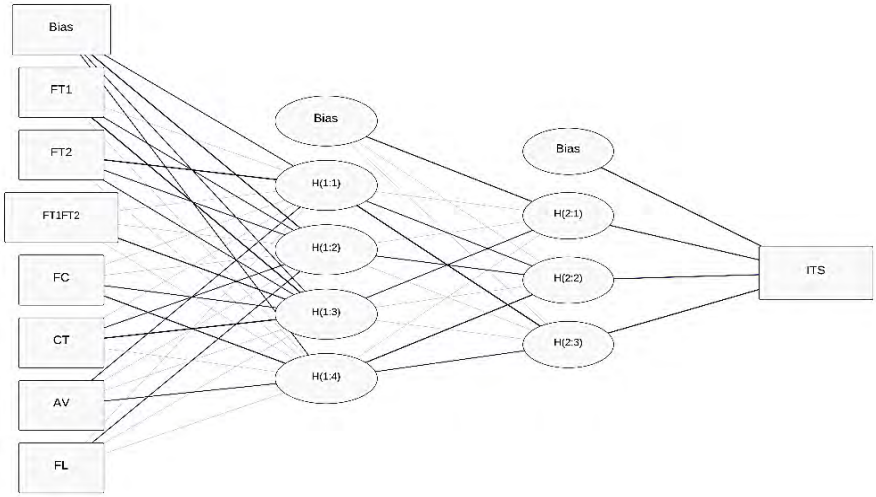

Fig. 4. Architecture of an artificial network model for DNN-II

To assess prediction accuracy, six performance metrics were used: Root Mean Square Error (RMSE), Normalised RMSE (NRMSE), Mean Absolute Percentage Error (MAPE), Average Accuracy Percentage (AA%), Coefficient of Determination (R^2), and Pearson Correlation Coefficient (R). Lower RMSE and MAPE values, alongside higher R and R^2, indicated superior model accuracy and generalisation [31], as calculated using Equations (1-5).

$$RMSE = \sqrt{\frac{1}{N}\sum_{n=1}^{N}(A_n - P_n)^2} \quad (1)$$

$$NRMSE = \frac{RMSE}{S} \quad (2)$$

$$R^2 = 1 - \frac{\sum(A_n - P_n)^2}{\sum(A_n - S_n)^2} \quad (3)$$

$$MAPE = \frac{\left(\sum \frac{|A_n - P_n|}{A_n}\right) * 100}{N} \quad (4)$$

$$AA\ \% = 100\ \% - MAPE \quad (5)$$

Where (An) actual and predicted (Pn) values are compared, and the estimated (N) number of points within the dataset is normalised by the mean of the actual values (S). To evaluation of both types of architecture in terms of input consistency and noise sensitivity, ultimately justifying the practical application of residual connections in civil material prediction problems [25,32].

3. Analysis and Result

3.1. ANN-I Model

In order to properly study and test the predictability of the low-cost Artificial neural networks (ANNs), it was carried out through the use of indirect tension stiffness modulus (ITSM) as a parameter for performance measurement for the construction of ANN model, with the use of certain fibres, the ratio mix, curing time values, as well as multiple other parameters. Also indicated are the types of fibres along with fiber indicators (FT1: Fiber 1, FT2: Fiber 2, FT1/FT2: Fiber Blend Ratio, FC: Fiber Content, FL: fiber length, CT: curing time, AV: air voids), which trained using the Levenberg- Marquardt algorithm combined at the same time as the input data for prediction models. In addition to ITSM, the representation of asphalt stiffness type is based on indirect tensile loading.

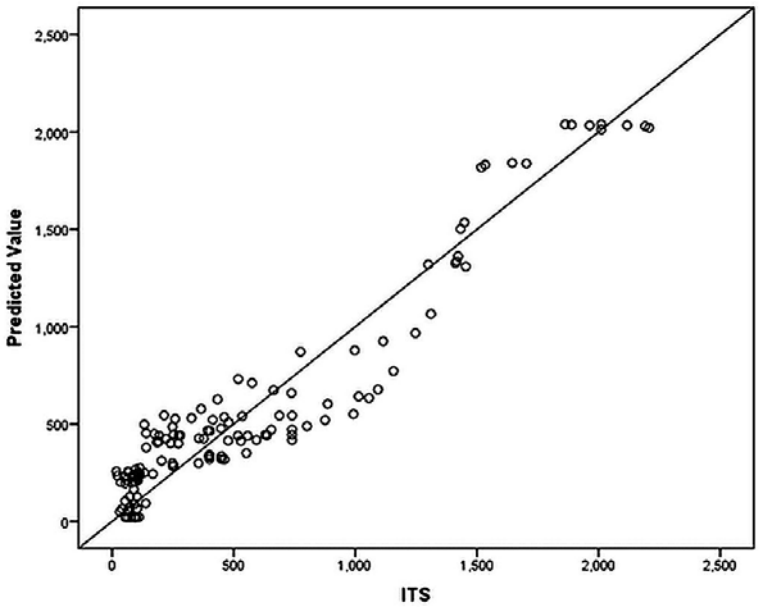

Fig. 5. Plot of actual vs predicted ITSM values by ANN-I

The ANN-I architecture was built to operate independently of predefined physical correlations and instead to extract patterns from empirical observations. The dataset incorporated a wide range of material combinations sourced from many origins, covering 123 distinct mix designs. A standard feed-forward neural network was trained, followed by evaluation using both visual and numerical diagnostics. Figure 5 shows the results of comparing both predicted ITSM values with the test dataset using a scatter plot. Generally, the predicted values fall reasonably close to the ideal 1:1 reference line, particularly in the mid- to high-stiffness range (> 800 MPa). This indicates that the model captures the underlying data well. A greater amount of variability is observed in the lower-stiffness data (< 400 MPa), where predicted values are noticeably lower, suggesting the potential to underestimate softer mixtures.

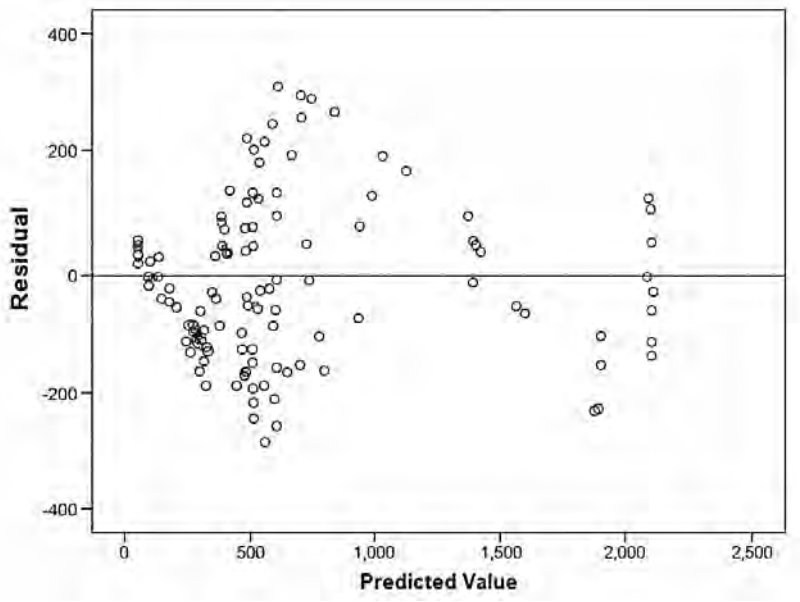

Fig. 6. Residual distribution plot for the ANN-I model predicted ITSM

Residuals were used to show any discrepancies between predicted and observed ITSM values. Most of the residuals in Figure 6 are clustered around the zero line (the x-axis), but there was a consistent underestimation with low-productivity outputs in the low output range. This can occur due to a lack of low-strength mix representation in the training set and/or to the extent to which certain variables, such as short curing periods or low fibre content, influence low productivity output. The RMSE of the model was 174.85 MPa, and the NRMSE (RMSE/mean ITSM) was 32.2%. The MAPE value was calculated to be 84.83%, indicating substantial deviations between some predictions and the actual values in the independent test set, particularly for lower-stiffness values. The AA% obtained with the ANN-I model averaged 15.17%. However, despite this high AA%, the R2 and R values were 0.903 and 0.951, respectively, indicating that the ANN-I model maintained a strong overall correlation with the experimental data, as shown in Table 3.

Table 3. Performance evaluation metrics of the ANN-I model

Indicator	Value
RMSE	174.85 MPa
NRMSE	32.2%
MAPE	84.83%
Average Accuracy Percentage (AA%)	15.17%
Coefficient of Determination (R^2)	0.903
Pearson Correlation Coefficient (R)	0.951

In Figure 7, we can see that curing time (CT) is a dominant factor influencing the prediction model, verifying its critical role in the development of cold asphalt mix stiffness. This was followed closely by fibre length (FL) and air void content (%AV), further supporting the notion that environmental factors associated with compaction also play a significant role in stiffness development. Limited

significance within the prediction model exists for fibre content (%FC) and individual fibre types (FT1 & FT2) in the dataset, indicating either a lack of or limited variability in those variables or the presence of nonlinear effects not fully accounted for by the current ANN architecture.

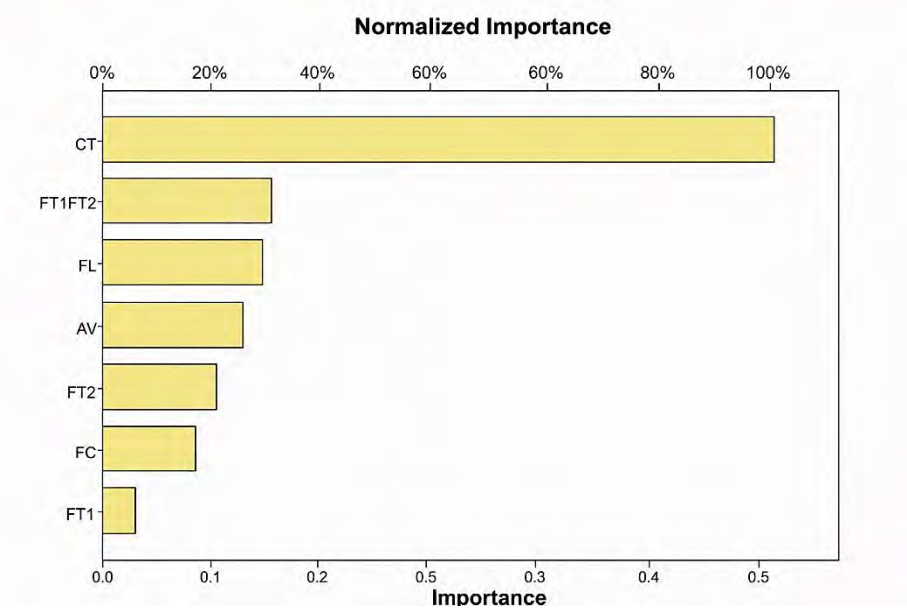

Fig. 7. Normalised importance of input variables in ITSM prediction

The results of this research support previous findings about the primary engineering parameters of curing and hybrid fiber ratios that influence the tensile stiffness of fibre-reinforced cold mixes due to their high sensitivity with respect to time and environmental conditions regarding the binder-fibre interaction. The poor performance in low-stiffness areas suggests that there may be a need for continued dataset enrichment and rebalancing, and that more advanced hyperparameter tuning or hybrid modelling techniques should be used to improve generalisation across all material conditions. Overall, the strengths of the ANN-I model as a basis for modelling ITSM for many different types of fiber modified mixtures support its use; however, its current state would benefit from additional refinement aimed at better modelling of low-strength properties and through developing more experimental data or the use of interaction effects between the input parameters.

3.2. DNN- II Model

Development of the DNN-II Model employed a multi-layer, multi-input/single-output regression structure, similar to that used for the ANN-I Model. The overall objective of both the ANN-I and DNN-II Models was to create an architecture capable of mapping an input set of key parameters to their associated ITSM values, while improving generalisation and predictive performance. In the case of the DNN-II, the input dataset consisted of all fibre-related and mix design parameters, including; Fibre Type 1 (FT1), Fibre Type 2 (FT2), FT1/FT2 ratio, Fibre Content by Aggregate Weight (%FC), Fibre Length (FL), Curing Time (CT) and Air Void Content (%AV). The sole output variable for both the model training/validation phases was the ITSM. The DNN-II architecture consisted of two hidden layers, each with four neurons in the first and three in the second.

The visual representation of the analysis results (Figure 8) indicates that the DNN-II model's predictions are moderately accurate relative to the actual test values. Although there is some evidence of clustering around the 1:1 line, the model displays a fairly large degree of spread in its predicted values, particularly in the lower to mid-range of the ITSM (i.e., below 1000 MPa). This suggests that there may be an overfitting issue or that some fibre mix combinations may not have been adequately represented in the data used to build the DNN model.

Figure 9 depicts the residual plot which supports this assumption. Most residuals have an approximate symmetric distribution about the zero-error line; however, a number are found in the negative range suggesting some high ITSM values were underpredicted by the model (i.e., it has tended to underpredict those high values). Likewise, a number of low ITSM values have been

overpredicted. Furthermore, the presence of outliers (and especially those corresponding to very large negative residuals) indicates that the model fit may not be reliable for certain observations or for observations made under specific conditions.

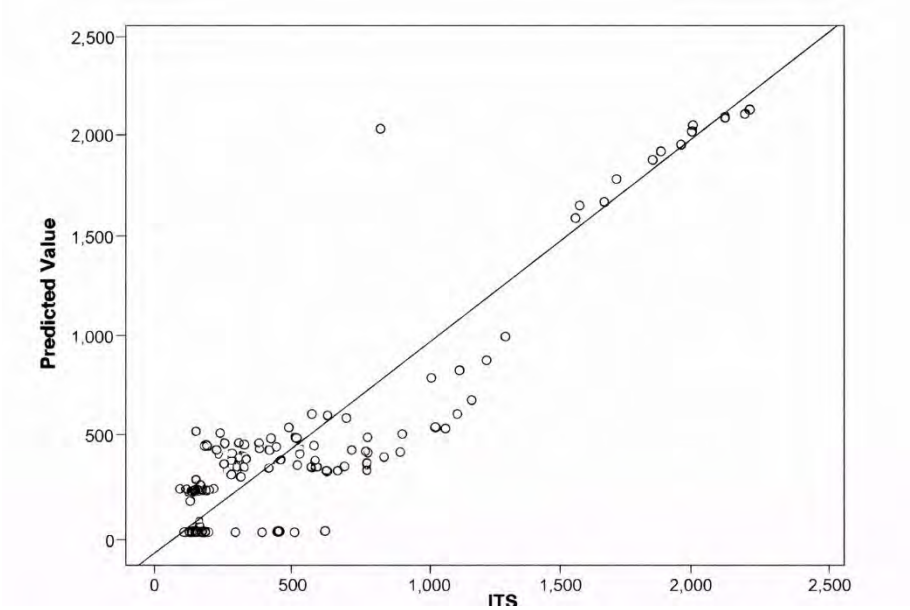

Fig. **8**. Scatter plot of predicted vs actual ITSM values using DNN-II

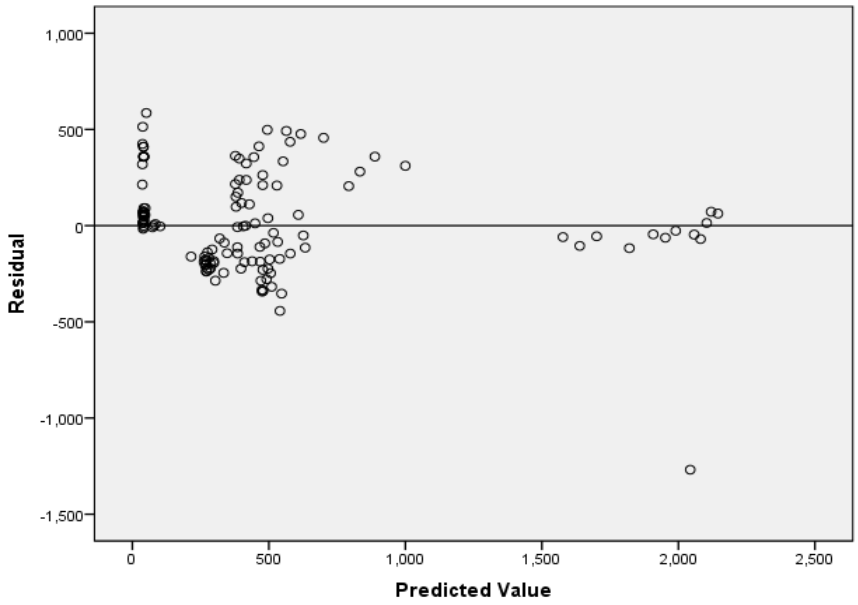

Fig. 9. Residual plot for DNN-II predictions

Performance metrics based on the quantitative data in Table 4 demonstrate that the DNN-II model has several significant limitations in predicting stiffness. The calculated Root Mean Square Error (RMSE) for the DNN-II model was 252.56 MPa, with an NRMSE of 52.68% above acceptable limits compared to other ANN models, and a MAPE of 106.90%, AA% ratios reduce the MAPE of accuracy (AA%)by providing negative values. More importantly, when the MAPE value becomes greater than 100%, the AA% level becomes meaningless and loses its usefulness for determining the accuracy of stiffness prediction because the concept of a negative accuracy percentage cannot exist in the real world. For this reason, we recommend that when assessing model reliability, the typical performance measures (RMSE, MAPE, R^2) be the main source of evaluation. These results indicate a considerable discrepancy between predicted and actual measurements, making the use of DNN-II models for practical purposes highly unreliable. The coefficient of determination (R2) value of 0.773 and the Pearson correlation coefficient (R) value of 0.884 suggest that, while there is an

acceptable degree of correlation between the actual results and DNN-II model predictions, the required reliability for a reliable stiffness prediction model is still not met.

Table 4. Performance evaluation indicators of the DNN-II model

Indicator	Value
Root Mean Square Error (RMSE)	252.56 MPa
Normalised RMSE (NRMSE)	52.68%
Mean Absolute Percentage Error (MAPE)	106.90%
Average Accuracy Percentage (AA%)	-6.90%
Coefficient of Determination (R^2)	0.773
Pearson Correlation Coefficient (R)	0.884

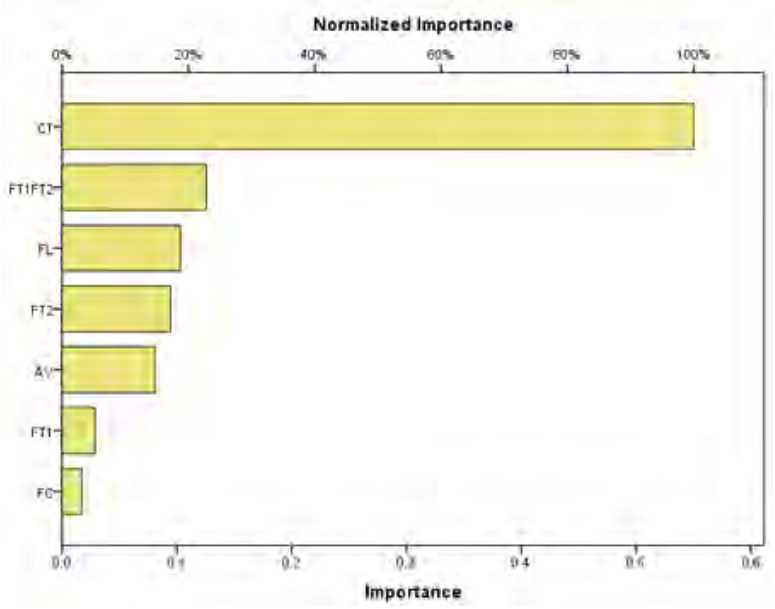

Fig. 10. Normalised importance of input variables in DNN-II

4. Comparative Analysis: ANN-I vs DNN-II

The performance of the ANN-I and DNN-II models for prediction depends on how the models were created based on the training data's structure, variability, and representativeness. The ANN-I model, with one hidden layer and using a very diverse and broad range of mix designs for the 123 mix designs (RMSE = 174.85 MPa) and statistically high correlation R^2 = 0.903, was able to develop models that accurately predicted mid-to-high stiffness (effectively discovering the most dominant relationships created with curing time (CT) and air void content (%AV)). In contrast, the values for lower stiffness were systematically biased towards under-representing this application, indicating a gap in the dataset's range (specifically, a lack of low-strength curing, low-strength curing time, or low-fibre mixtures).

The performance of DNN-II's two-layer model is negatively affected compared to DNN-I, particularly in terms of data balance and cohesion, despite its design intended to enhance generalisation through a deeper layer structure. This resulted in DNN-II achieving the lowest performance metrics (RMSE = 252.56 MPa; MAPE = 106.9%) due to overfitting and residual irregularity. DNN-II had elevated prediction rates for higher values of the Indirect Tensile Stiffness Modulus (ITSM), whereas its predictions did not equalise or stabilise across the entire mix/condition distribution. Figure 11 showsquantitative graph summarizing the performance differences between the two models.

While the ANN-I model has a fairly high R^2 value (0.903), this reflects more its ability to predict the overall trends than its ability to predict point by point accurately. Both the significant amount of error reflected by MAPE (84.83%) and the very low AA% (15.17%) demonstrate that the two models have very little ability to predict individual ITSM values accurately. The DNN-II model has

performed even worse than the ANN-1 (MAPE = 106.90% and AA% = −6.90%), suggesting a severe lack of confidence by predict individual ITSM values accurately. So when MAPE exceeds 100% AA% becomes meaningless; a negative AA% cannot be interpreted in a useful manner for stiffness predictions. Therefore, the reliability of models should be determined to a greatest extent possible with standard indicators (e.g., RMSE, MAPE, R^2). Overall, the two models performed better predicting the general trend of the data than they did predicting individual ITSM values and are therefore not yet applicable for direct engineering design or field use.

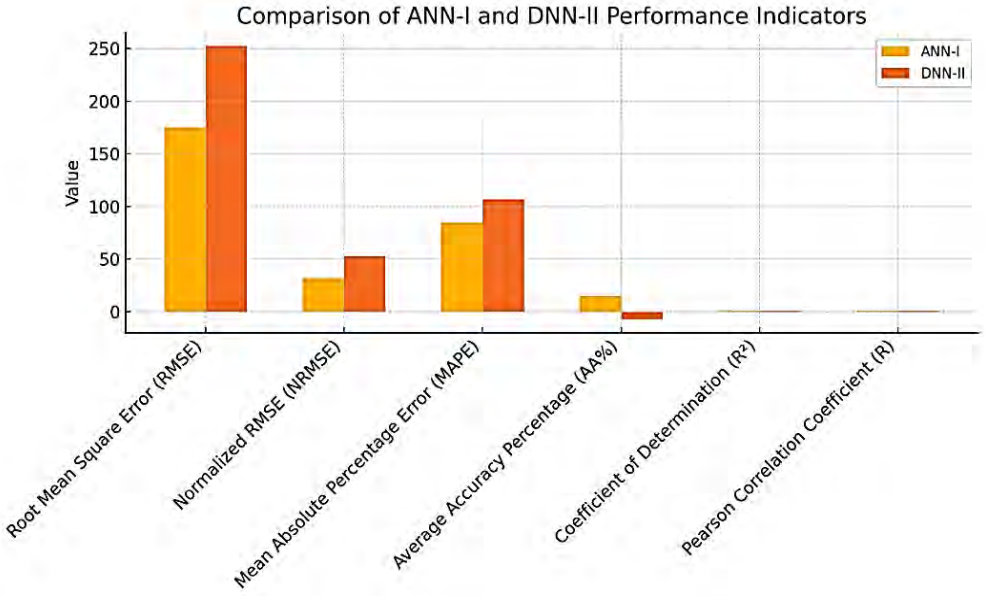

Fig. 11. Comparative Analysis indicating the ANN-I model vs the DNN-II model

The outcome of this study has identified the superior ability of the simplified ANN model to generalise in comparison to the DNN model, based on two models being developed from the same set of 123 samples; it has been suggested that one possible reason for this is due to the amount of data available to effectively train a deep neural network is not adequate with 123 samples. Deep neural networks have a greater number of trainable parameters and multiple hidden layers as opposed to simple ANN models; therefore they require a significantly larger amount of training data to learn generalisable and robust patterns in the data set. If a DNN has been trained using an inadequate sample size, it is highly susceptible to memorising the training data and therefore has poor generalization ability. The results of this study indicate that the differences in model type demonstrate a difference in the available sample size to support the model; therefore model depth alone does not guarantee greater predictive accuracy but is dependent on using an appropriate model type for the given sample or training set.

5. Conclusion

- The ANN-I model produced superior results to the DNN II in ITSM predictions, with a higher correlation (R=0.951) and lower RMSE (174.85 MPa), thereby improving prediction accuracy.
- The most critical factor to the stiffness of these cold asphalt mixtures was curing time; both models demonstrate the importance of this parameter when predicting stiffness development.
- While the ANN-I produced superior generalisation across a 123 different mixtures (single dataset), DNN II showed greater sensitivity to data distribution, though both behaviours pose a risk of overfitting.
- The lower performance of DNN II indicates the need to use higher-quality, balanced datasets with deeper architectures to limit excessive prediction errors.
- The findings suggest that shallow architectures outperformed the tested deep architecture in describing the general character of ITSM; however, the reported level of predictive error demonstrates that the accuracy of predictions are still not adequate for the reliable

prediction of stiffness or direct optimization-based design of pavements, and further model refinement and data enhancement is necessary.

5.1 Future Study

Future studies should evaluate advanced data generation techniques such as GANs for augmenting existing data sets prior to model training, which addresses the limitations of this study. Furthermore, algorithms that can be used with small number of samples (tabular-type data), e.g. XGBoost, RFs, are worthy of consideration as additional sources of more dependable and solid predictions in ITSM.

References

[1] Kheradmand B, Muniandy R, Hua LT, Yunus RB, Solouki A. An overview of the emerging warm mix asphalt technology. International Journal of Pavement Engineering. 2014;15(1):79-94. https://doi.org/10.1080/10298436.2013.839791

[2] Sultana S. Tensile strength of asphalt binder and influence of chemical composition on binder rheology and strength [Doctoral dissertation]. Austin: University of Texas; 2014. http://hdl.handle.net/2152/31325

[3] Ferrotti G, Pasquini E, Canestrari F. Experimental characterization of high-performance fiber-reinforced cold mix asphalt mixtures. Construction and Building Materials. 2014;57:117-125. https://doi.org/10.1016/j.conbuildmat.2014.01.089

[4] Leiva-Villacorta F, Cerdas-Murillo A. Performance evaluation of recycled fibers in asphalt mixtures. Construction Materials. 2024;4(4):839-855. https://doi.org/10.3390/constrmater4040045

[5] Airey GD, Singleton TM, Collop AC. Properties of polymer modified bitumen after rubber-bitumen interaction. Journal of Materials in Civil Engineering. 2002;14(4):344-354. https://doi.org/10.1061/(ASCE)0899-1561(2002)14:4(344)

[6] Abood EA, Mohammed MH. An Assessment of Tree-Based Models for Predicting Indirect Tensile Stiffness Modulus in Fiber-Enhanced Cold Mix Asphalt. Engineering, Technology & Applied Science Research. 2025;15(5):27715-27720.

[7] Kandilli C. Exploring the potential of natural zeolites to enhance solar energy systems: A concise review. Res Des. 2024;1(1):13-21. https://doi.org/10.17515/rede2024-001en110

[8] Shahin MA, Jaksa MB, Maier HR. Artificial neural network applications in geotechnical engineering. Australian Geomechanics. 2001;36(1):49-62. https://www.mdpi.com/journal/applsci/special_issues/CZ5285222U

[9] Yeh IC. Modeling concrete strength with augment-neuron networks. Journal of Materials in Civil Engineering. 1998;10(4):263-268. https://doi.org/10.1061/(ASCE)0899-1561(1998)10:4(263)

[10] Ahmed AM, Ali SI, Ali MI, Jamel AAJ. Analyzing self-compacted mortar improved by carbon fiber using artificial neural networks. Annales de Chimie Science des Matériaux. 2023;47(6):363-370. https://doi.org/10.18280/acsm.470602

[11] Choi RY, Coyner AS, Kalpathy-Cramer J, Chiang MF, Campbell JP. Introduction to machine learning, neural networks, and deep learning. Translational Vision Science & Technology. 2020;9(2):14-14. https://doi.org/10.1167/tvst.9.2.14

[12] Topcu IB, Sarıdemir M. Prediction of properties of waste AAC aggregate concrete using artificial neural network. Computational Materials Science. 2007;41(1):117-125. https://doi.org/10.1016/j.commatsci.2007.03.010

[13] Chen H, Xu Q, Chen S, Zhang Z. Evaluation and design of fiber-reinforced asphalt mixtures. Materials & Design. 2009;30(7):2595-2603. https://doi.org/10.1016/j.matdes.2008.09.030

[14] Goodfellow I, Bengio Y, Courville A. Deep learning. Cambridge: MIT Press; 2016. https://www.deeplearningbook.org/

[15] Kardani N, Aminpour M, Raja MNA, Kumar G, Bardhan A, Nazem M. Prediction of the resilient modulus of compacted subgrade soils using ensemble machine learning methods. Transportation Geotechnics. 2022;36:100827. https://doi.org/10.1016/j.trgeo.2022.100827

[16] Ali MI, Jabbar Jamel AA, Ahmad AM, Ali AM. Effect of Hybrid Polypropylene-Carbon Fiber on Self-Compacting Mortar. IOP Conference Series: Materials Science and Engineering. 2019;584(1):012020. https://doi.org/10.1088/1757-899X/584/1/012020

[17] Clinkinbeard NR. Deep neural network-driven enhancement of the microfiber design and fabrication process [Doctoral dissertation]. Ames: Iowa State University; 2024. https://www.proquest.com/openview/939d5ed423cd6a1804c84a0bcbab8085/1?pq-origsite=gscholar&cbl=18750&diss=y

[18] Srivastava N, Hinton G, Krizhevsky A, Sutskever I, Salakhutdinov R. Dropout: a simple way to prevent neural networks from overfitting. The Journal of Machine Learning Research. 2014;15(1):1929-1958. http://jmlr.org/papers/v15/srivastava14a.html
[19] Caruana R, Lawrence S, Giles C. Overfitting in neural nets: Backpropagation, conjugate gradient, and early stopping. Advances in Neural Information Processing Systems. 2000;13:402-408. https://proceedings.neurips.cc/paper/2000/hash/059fdcd96baeb75112f09fa1dcc740cc-Abstract.html
[20] Szegedy C, Ioffe S. Batch normalization: Accelerating deep network training by reducing internal covariate shift. arXiv preprint arXiv:1502.03167. 2015. https://arxiv.org/abs/1502.03167
[21] Kingma DP, Ba J. Adam: A method for stochastic optimization. arXiv preprint arXiv:1412.6980. 2014. https://arxiv.org/abs/1412.6980
[22] Kim J, Shin N, Jo SY, Kim SH. Method of intrusion detection using deep neural network. In: 2017 IEEE international conference on big data and smart computing (BigComp). IEEE; 2017. p. 313-316. https://doi.org/10.1109/BIGCOMP.2017.7881684
[23] Kumar R, Goli A, Gottumukkala BV, Shankar S, Kuna KK. Influence of curing process on the moisture loss, mechanical and performance characteristics of cold recycled asphalt mixes. Road Materials and Pavement Design. 2024;25(2):259-275. https://doi.org/10.1080/14680629.2023.2199884
[24] Orosa P, Pérez I, Pasandín AR. Short-term resilient behaviour and its evolution with curing in cold in-place recycled asphalt mixtures. Construction and Building Materials. 2022;323:126559. https://doi.org/10.1016/j.conbuildmat.2022.126559
[25] Shanbara HK, Ruddock F, Atherton W. Predicting the rutting behaviour of natural fibre-reinforced cold mix asphalt using the finite element method. Construction and Building Materials. 2018;167:907-917. https://doi.org/10.1016/j.conbuildmat.2018.02.072
[26] Zhang D, Chen Z, Zhang H, Wei C. Rheological and anti-aging performance of SBS modified asphalt binders with different multi-dimensional nanomaterials. Construction and Building Materials. 2018;188:409-416. https://doi.org/10.1016/j.conbuildmat.2018.08.136
[27] Gu Q, Kang A, Li B, Xiao P, Ding H. Effect of fiber characteristic parameters on the high and low temperature rheological properties of basalt fiber modified asphalt mortar. Case Studies in Construction Materials. 2022;17:e01247. https://doi.org/10.1016/j.cscm.2022.e01247
[28] Sun Y, Zhang M, Fan D. Effect of ultrasonic on deterioration of oil in microwave vacuum frying and prediction of frying oil quality based on low field nuclear magnetic resonance (LF-NMR). Ultrasonics Sonochemistry. 2019;51:77-89. https://doi.org/10.1016/j.ultsonch.2018.10.015
[29] Ba JL, Kiros JR, Hinton GE. Layer normalization. arXiv preprint arXiv:1607.06450. 2016. https://arxiv.org/abs/1607.06450
[30] Ali SI, Ahmed AM, Ibrahim AE, Ali MI. Effect of utilization waste strapping plastic belts on flexural behaviour of concrete. Annales de Chimie Science des Matériaux. 2024;48(1):111-118. https://doi.org/10.18280/acsm.480111
[31] Willmott CJ, Matsuura K. Advantages of the mean absolute error (MAE) over the root mean square error (RMSE) in assessing average model performance. Climate Research. 2005;30(1):79-82. https://doi.org/10.3354/cr030079
[32] Ali MI, Allawi AA. An Artificial Neural Network Prediction Model of GFRP Residual Tensile Strength. Engineering, Technology & Applied Science Research. 2024;14(6):18277-18282. https://doi.org/10.48084/etasr.9107

Blank Page

Research on Engineering Structures & Materials
www.jresm.org

Research Article

Experimental investigation of bolted concrete column–foundation connections under lateral repeated loading

Noor Kareem Tohmazi [*,a], Kamal Alogla [b], Sadjad Amir Hemzah [c]

Department of Civil Engineering, University of Kerbala, Kerbala, Iraq

Article Info

Article History:

Received 16 Feb 2026

Accepted 16 Apr 2026

Keywords:

Concrete column foundation;
Base plate connection;
Stiffener connection;
Lateral repeated behavior;
Seismic performance;
Anchor bolts;
Lateral load resistance

Abstract

In this study, behavior of concrete column-foundation connections under repeated lateral loading was examined. Six column -foundation specimens were tested. The specimens consisted of one monolithic concrete column, three columns with the embedded stiffener connections, and two columns with the one-face welded (W1) connections (without stiffener). The stiffener connections were created by welding triangular plate to the longitudinal reinforcement and then welding them to the upper surface of the base plate, while in the W1 connections, the longitudinal reinforcement was welded directly to the upper face of the base plate. All specimens were similar in dimensions. The foundation measured 700 mm in length by 300 mm in width by 200 mm in thickness, and the columns a square cross section of 120mmx120mm with 700mm length. The study examined one of the most important factors affecting column foundations connection using steel base plates. The cyclic response of the specimens, such as failure load, failure type and lateral displacement histories, was examined under the effect of axial load of 80 kN. The experimental results showed that the columns using spatial stiffener connections were more resistant to lateral loads if compared to the W1 and monolithic column specimens under similar axial loading conditions.

© 2026 MIM Research Group. All rights reserved.

1. Introduction

Columns in structural systems are among the most critical components in buildings when they were subjected to lateral repeated loadings, such as those induced by tremors, wind, and dynamic vibrations, as these loads directly challenged structural integrity and overall stability. Extensive scientific investigations have played a pivotal role in advancing the understanding of deformation mechanisms and non-linear behaviors of these members under cumulative effects, which enabled the development of more accurate and reliable design parameters. Consequently, research in this field is not merely an academic endeavor but a technical imperative aimed at minimizing human and material losses while ensuring the highest levels of structural safety in seismically active regions and under variable environmental loads.

Tasnimi investigate the response of prefabricated column footing connections under cyclic loading conditions to fill the information gap in the existing literature. Six quarter-scale models of prefabricated column footing connections, were tested under constant axial load and cyclic lateral displacement. The results showed that some of prefabricated column footing connections exhibited semi-rigid properties with higher strength than conventional monolithic connections, while other connection types showed moderate energy dissipation capacity and slight degradation of post-elastic stiffness. The hysteresis curves indicated that some prefabricated column footing connections exhibited a stable response with bond damage after yielding [1].

*Corresponding author: noor.abdoun@s.uokerbala.edu.iq
[a]orcid.org/0009-0008-3213-4579; [b]orcid.org/0000-0002-0853-5152; [c]orcid.org/0000-0002-1851-737x
DOI: http://dx.doi.org/10.17515/resm2026-1503me0216rs

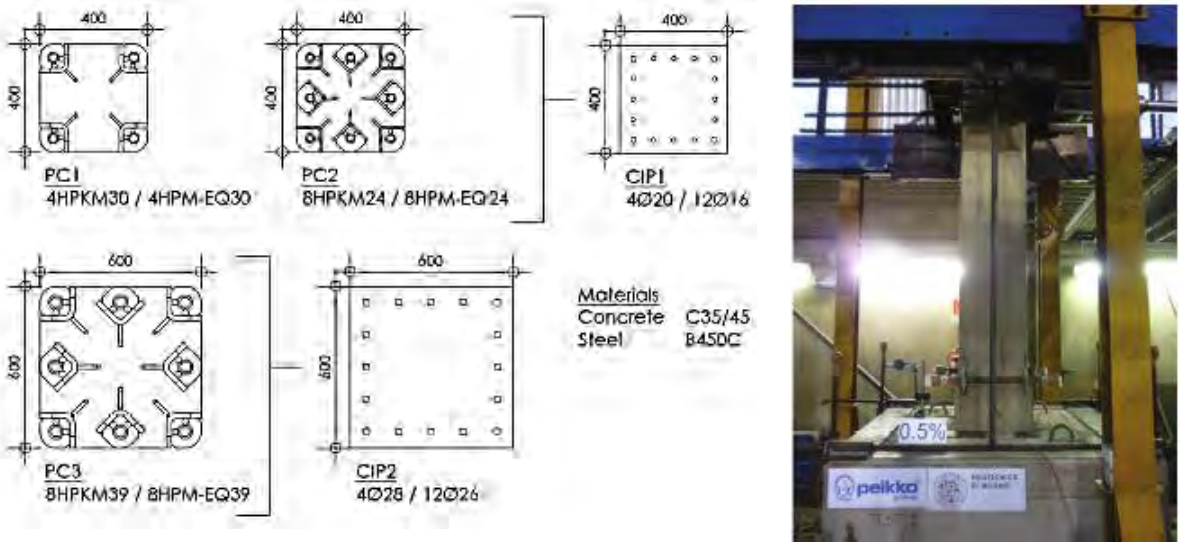

(a) (b)

Fig. 1. (a) Column cross-sections and material details of the specimens; (b) general view of the test setup

Nagaprasad et al. [2] investigated the post, installation of rectangular reinforced concrete (RC) columns using steel cage exteriors to provide better protection, specifically, to those old buildings whose structures had not been designed to meet today's seismic design codes. One of the columns was a typical reinforced concrete column, while the other two had been constructed to bear the combined action of constant axial compression and cyclic lateral displacement. The results showed that a steel cage turned the failure mode of the column from brittle to ductile and the bending resistance was therefore doubled. The use of end battens, especially at the locations of the plastic hinges, played a significant role in enhancing the strength of the concrete core under compression as well as in avoiding local buckling of steel angles. It was found that widening the end battens improved both plastic rotation and lateral strength, but total energy absorption was hardly affected. Most important thing is, it was not necessary to use bonding agents since the mechanical restraint exerted by the steel cage was sufficient to keep the retrofit fixed. While the previous study focused on strengthening individual columns, The project of Osman, M.H. and S.T. GRANT [3] focused on the earthquake resistance of exterior beam-column joint details in reinforced concrete moment-resisting frames, identifying them as the weakest link. Following BS8110 design criteria, it assessed joint vulnerability with variations in transverse reinforcement. Three reinforcement designs were evaluated: a reference specimen without shear links, one with closely grouped shear links, and one with inclined intersection bars. Results showed that the specimen with inclined bars performed best in terms of failure load, stiffness, and displacement capacity, while the reference specimen faced brittle failure due to anchorage issues. The findings underscored the importance of advanced joint designs for enhancing seismic safety, particularly in regions prone to distant earthquakes, such as Malaysia. In addition to experimental investigations on columns and beam–column joints, numerical approaches have also been employed to evaluate the behavior of column–foundation joints by Mahadik et al. [4]. The authors took a numerical approach to Column-Foundation Joints (CFJs) utilizing post-installed (PI) connections, addressing the need for European guidelines on seismic upgrading. The investigation utilized finite-element analysis, considering complex geometry, to assess the behavior of the PI systems, as they generally took better bond strength compared to the traditional cast-in (CI) rebar connections. The results demonstrated that, under seismic loading, CFJs utilizing CI and PI connections could fail, especially when embedment was low. However, once the embedment exceeded a certain level, the post-installed connections showed better robustness. While the CI connections experienced bond failure, the PI connections experienced ductile yielding. The results demonstrated the potential benefits of the PI systems, including the scenarios under which they might fail, to establish the framework for post-installed rebars in seismic areas .While the previous studies mainly examined cast-in and post-installed

reinforcement systems, other researchers investigated alternative precast connection systems, particularly bolted column-to-foundation connections, Camnasio and Kriakopoulos[5] examined the performance of bolted precast concrete column-to-foundation connections subjected to cyclic loading. The goal was to achieve seismic performance that was similar to that of monolithic structures while also dealing with the risk of weak connections in areas with a lot of earthquakes. Quasi-static cyclic displacement tests on large specimens compared bolted systems using Peikko HPKM column shoes and HPM anchor bolts with a conventional cast-in-place (CIP) reference. Design modifications such as unbonded anchor bolts and fiber-reinforced mortar grouts were implemented to enhance structural performance. The findings indicated that bolted systems could match monolithic structures in ductility, stiffness, and energy absorption, meeting seismic design code requirements with a balance between precast construction speed and CIP energy dissipation capacity.

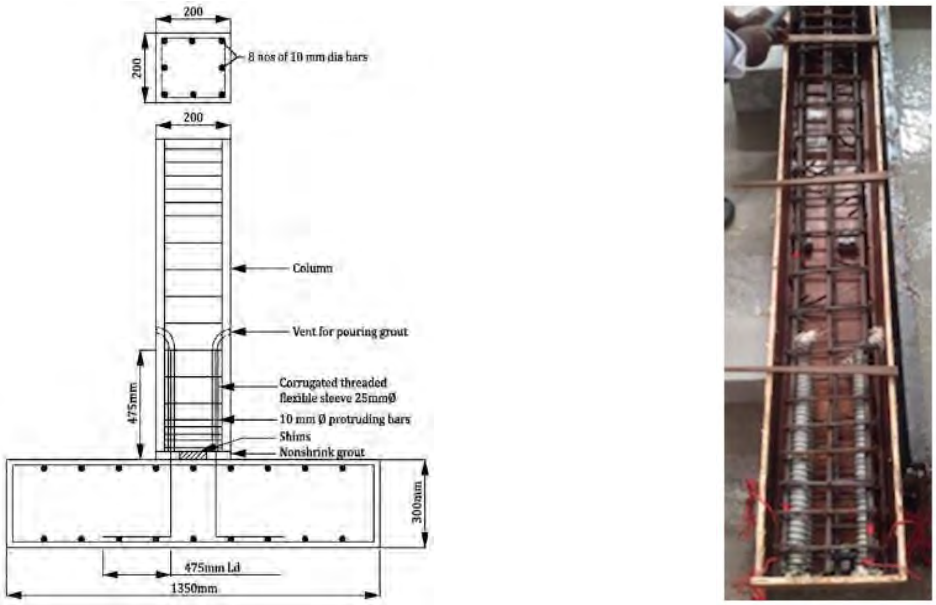

(a) (b)

Fig. 2 .Reinforcement details of grouted sleeve specimen (GS)

Further experimental studies have compared various precast column–foundation connection systems under cyclic loading conditions. An analysis of the cyclic performance of the precast column to foundation connections under reverse cyclic loading have been examined by Camnasio and Kriakopoulos). The study showed that there was considerable seismic susceptibility in precast structures. Also, it was found that comparing the performance of base plates, pocket connections, and grouted sleeves with monolithic structures, offered higher ultimate strength, they also experienced higher stiffness degradation. Notably, the performance of the PC I pocket connection was higher than that of monolithic structures, with a 184% increase in post-earthquake resistance and a 137% increase in energy dissipation. Although grouted sleeves were cost-effective, they also experienced premature failure due to bond loss. The results of the study, therefore, showed that precast structures could offer post-earthquake resistance and ductility that were equivalent to or higher than that of monolithic structures in seismic zones.

Beyond column–foundation systems, bolted connections have also been investigated in beam–column joints to enhance seismic repairability in prefabricated structures by Liu et al. [6] The investigation into a new bolt-connected prefabricated beam-column joint aimed to enhance seismic performance by optimizing damage distribution for quicker repairs post-earthquake. Two full-scale specimens, J1 and J2, were tested under low cycle loading with varying bolt strengths, compared against finite element analysis (FEA). Results demonstrated significant plastic deformation and energy dissipation, indicating resilience. Increased bolt strength improved load capacity, stiffness, and energy dissipation. FEA suggested a higher compression ratio accelerated concrete damage. A third design, J3, with integrated angle members was proposed, showing

improved load transfer and reduced shear damage in the concrete core. Overall, bolted connections offer strong solutions for prefabricated constructions and enable localized earthquake repairability. It was also a well-established fact that repeated loading could cause cumulative damage under lateral repeated loading to structures. In areas prone to regular earthquakes, the bolt systems connecting columns with the footing were areas of concern, as they were subjected to side-to-side motions during quakes. Their performance depended on the properties, configuration, and unpredictability of the materials involved, thus requiring a combination of theory and practical experimentation to improve the strength of reinforced concrete buildings. Despite extensive analytical studies on the residual strength after repeated loading and ductility of single- and multi-degree-of-freedom systems, there was a lack of experimental data on the interaction of horizontal and vertical seismic components [7]. Furthermore, research on composite structural members has also contributed to understand load transfer mechanisms in column systems. Sheeba Ebenezer [8] investigate concrete-filled steel tube column members, encased in steel material, and its improvement in useful ways regarding the efficiencies of load transfer with the inclusion of shear connectors. In the study, the investigators developed and constructed full-scale concrete-filled steel tube column samples, each having a unique configuration of the shear connectors, and how these interacted and worked together in a composite manner, with the column members put through a series of axial and eccentric loading tests to ascertain the load capacity, total column stiffness, total column ductility, and failure mechanisms. From the study, the presence of properly designed shear connectors was highlighted as being very useful and significant, in the efficiencies of load transfer, the upgrade of the capacity of the column for axial and lateral loading, the retardation of the onset of tube buckling phenomena, and the upgrade of the column's ductility, compared to column members without shear connectors. These studies were highly useful and significant, particularly in relation to column connections and how the column and foundation were bolted together and subjected to repeated lateral loading regimes. Similarly, the behavior of precast reinforced concrete connections under seismic loading has been widely investigated in recent years. The behavior and performance of precast reinforced concrete connections under seismic and lateral loading were extensively investigated in previous studies [9] focused on five precast reinforced concrete wall-raft connection configurations subjected to cyclic lateral load, which proved that the grouted connectors with rods of a diameter of 12 mm could improve the lateral load capacity by 57% compared to the unconnected ones. This review aimed to synthesize the results of 30 highly pertinent research works on precast concrete connections, including experimental, numerical, and hybrid approaches. From the literature, it was revealed that there had been a significant evolution of precast concrete connections, from simple mechanical interlocks and shear keys in the 1990s to sophisticated energy-dissipation devices, post-tensioning systems, and hybrid connections in recent times. Among the principal types of connectors were grouted couplers and sleeves, bolted connections, post-tensioned tendons, tooth-groove connections, and engineered steel energy dissipaters, which exhibited various advantages in lateral load capacity, energy dissipation, ductility, and constructability. Despite the significant development in the subject, there were major research gaps in full-scale seismic validation, standardization of design guidelines, long-term assessment of durability, and comparison of results considering confounding factors. This review benefited structural engineers and researchers with an extensive overview of the state of the art, the performance of various types of connectors, and future research directions in seismic design of precast concrete connections. Despite numerous studies on column-base joints, significant gaps remained regarding the effects of connection type, base plate thickness, anchor bolt diameter, and count on the dynamic response of structures to lateral repeated loads. Notably, there was limited comparative research on various joint types and their impact on structural performance. The influence of base plate thickness under repeated loads was underexplored, while the correlation between anchor bolt diameter and cyclic behavior was inadequately understood. Additionally, the role of anchor bolt quantity and layout in load redistribution lacked sufficient investigation. There was a pressing need for integrated studies examining these parameters concurrently to better inform seismic designs and optimize structural detailing, Accordingly, the main aim of the present study is to examine the influence of the connection type, base plate thickness, number of anchor bolts, and bolt diameter on the seismic performance of column-foundation systems, with the final target of developing a strong structural configuration to withstand repeated loads.

2. Materials and Methods

2.1 Materials

2.1.1 Cement

Sulfate-resisting Portland cement, with trademark AL-JESR, manufactured by Lafarge Cement Factory, was used in mix. The compliance of the cement was carried out according to the Iraqi Standard No.5/1984 [10].

2.1.2 Fine Aggregate

Natural sand was used in producing the concrete mix with a maximum size of 4.75 mm, which is brought from Kerbala factories. The tests were implemented in the laboratory of the University of Kerbala, where the tests complied with the Iraqi Specifications No. 45 [11].

2.1.3 Coarse Aggregate

A black crushed gravel with a maximum size of 12.5 mm was used. This gravel was cleaned and washed by water and left out to dry in air. as well as the Iraqi Specifications No. 45 [11].

2.1.4 Water

Tap water was used in producing the concrete mix, as well as the curing process for all columns. This water was clean and free from unwanted materials like organic materials, salts, acids, and Alkalis.

2.1.5 Superplasticizer

The current experimental investigation included a high-performance concrete superplasticizer based on a modified polycarboxylate chemical compound. The concrete superplasticizer supplied from MBCC GROUP, which is Master Glenium 54, is suitable for a variety of concrete mixes and is compatible with all types of Portland cements and cementitious materials such as Microsilica, Fly Ash (PFA), and Ground Granulated Blast Furnace Slag (GGBS). The main benefit of using this concrete superplasticizer is its moisture-reducing properties, together with the following benefits: early compressive strength development, flexural strength, carbonation resistance, permeability, creep, shrinkage, and overall durability. A superplasticizer was added at a dosage of 1–2% by weight of cement to improve the workability of the normal-strength concrete.

Fig. 3. All specimens

Fig. 4. Curing of specimens

For the column specimens, Portland cement, fine sand, coarse aggregate, superplasticizer, and water were used in the concrete mixture. Compressive strength of about (45) MPa had been gained from these quantities. The American guidelines' recommendations for concrete mix design were followed in mixing and testing. In this study, the mix was designed according to the mix design approach described in (ACI 211.1-91). After finishing the casting process, all columns were submerged with water in the basin of College of Engineering of the University of Kerbala laboratory until the testing day After 28 days. Figure 4 showed the specimens in casting stage and curing.

Table 1. The quantities of materials for one cubic meter (Kg /m^3)

Ingredients	Weight
Cement	410
Coarse aggregate	850
Fine aggregate	1010
Water	131
Superplasticizer	6 kg /m^3 (5.45 L/m^3)
w/c	0.319

Table 2. Gradation of sand and the chemical composition of sand

Sieve size (mm)	Cumulative Passing %	Passing accumulated %Limits of Iraqi specifications No. 45/1984, zone (3)
10	100	100
4.75	97	90-100
2.36	91	85-100
1.18	85	75-90
0.60	76	60-97
0.30	45	12-40
0.15	10	0-10
Specific Gravity	2.63	
Water Absorption	1.2%	
Fineness Modulus	2.71	
Materials passing from sieve 75 μ %= 3.6% (specification requirements up to 5%)		
SO_3 content=0.364% (specification requirements up to 0.5%)		

** These results were performed in the Karbala construction Laboratory*

Table 3. Coarse aggregate grading results and chemical characteristics

Sieve size (mm)	Cumulative Passing %	Passing accumulated %Limits of Iraqi specifications No. 45/1984, zone (3)
37.5(1.5 in)	------	-----
19(3/4in)	100	100
12.5(1/2in)	98	90-100
10(3/8in)	62	50-85
4.75(No.4)	3	0-10
Specific Gravity	2.68	
Water Absorption	0.8%	
Maximum Aggregate Size	12.5mm	
Mechanical wear =16.1% (specification requirements up to 35%)		
Materials passing from sieve 75 μ %= 0.29% (specification requirements up to 3%)		
SO_3 content=0.03% (specification requirements up to 0.1%)		

** These results were performed in the Karbala construction Laboratory*

2.2 Concrete Properties

Concrete had a significant test in fresh concrete, like slump test. In this test, the value of a slump measured is 35 mm for normal strength in the Abrams cone test. To determine the compressive strength of the concrete at the age of 28 days, twelve cubes of size (150mm x150mm x150mm) of the concrete mix were provided and tested as per (BS 1881 Part 116:1989) , three cylinders of size (Φ 100 x H =200mm) of the concrete mix were prepared and tested as per the [12]three cylinders of the concrete mix were tested for the splitting Tense test in order to determine the Indirect Tensile strength of the mix according to the [13]and three prisms of the concrete mix were of the dimensions (W=100xH=100 x L=500mm) in order to determine the rupture strength of the mix in

accordance with the [14]. See the Fig. 5, and (Table 4). The compressive strength value reported in Table 5 (47.6 MPa) was obtained from tests conducted on cube specimens.

(a) (b) (c) (d)

Fig. 5. Fresh and hardened concrete test (a) slump test, (b) modules of rupture test, (c) splitting tensile strength test, and(d) compressive strength test

Table 4. Values of concrete compressive strength, splitting tensile strength and rupture tensile strength (MPa)

NO.	Compressive Strength (MPa)	Splitting Tensile strength (MPa)	Rupture Tensile strength (MPa)
1	48.7	4.8	5.31
2	49.8	5.2	5.63
3	46.0	3.9	4.28
Average	47.6	4.63	5.07

2.3 Steel Reinforcement

Two steel reinforcements bars diameter were used in the experimental, Ø10 mm steel reinforcements, which as main reinforcement and Ø8 mm steel reinforcements as ties. The steel reinforcement test had to be conducted with at least three specimens of each steel type, and each specimen had to be not less than 370 mm long, as required by its tensile test, as mentioned by [15]. The test was conducted at University of Kerbala by utilizing a tensile testing machine, as shown in figure 6. The values of tensile strength of each type of steel reinforcement are shown in Table (5).

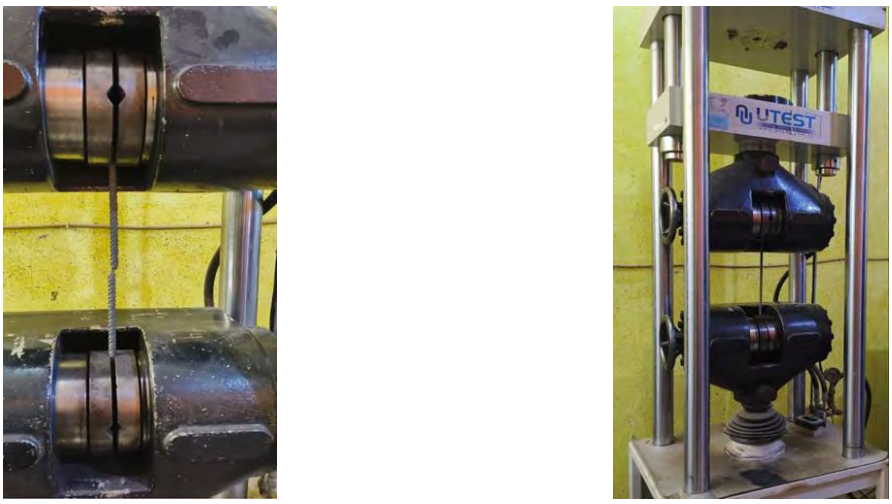

Fig. 6. Tensile testing machine for steel reinforcement

Table 5. Properties of shear steel reinforcement

Nominal diameter (mm)	Actual diameter (mm)	Elongation % In 50 mm min%		Yield Stress fy MPa		Ultimate Strength Fu MPa		Modulus of Elasticity, E MPa*
		Result	Limit	Result	Limit	Result	Limit	
8	8.4	12.7%	9-7	434.4	420	640.3	550	200000
10	9.84	6.3%	6-7	574.6	550	701.6	690	200000

** Assumed value*

2.4 Experimental Work

2.4.1 Preparation Method

The experimental program presented in detail in this paper involved the evaluation of six specimens, including two connection types and a monolithic one. the present study encompassed three separate categories of specimens: The Reference specimen (first category), CF1, featured a monolithic column-foundation connection, the column and foundation formed a single structural unit with continuous concrete and steel reinforcement, allowing internal forces to transfer directly without separate bearings or mechanical fasteners. The second category included two columns labeled as 4P10A16W1-5 and 6P10A16W1-5, both specimens employed the same technique for connecting the columns with base plate. This technique (W1) was carried out by welding the longitudinal reinforcement bar of the column to the top surface of the base plate. In accordance with AISC specifications, a minimum base plate thickness of 10 mm was maintained for both specimens. Anchor bolts diameter size in both specimens were 16mm. Each column had five longitudinal reinforcement bars; four of them were positioned on the corners, while the fifth bar lay in the middle. However, the middle bar had a length of 300mm, which was 40% of the total length. Differences in this category lay in the fact that while the 4P10A16W1-5 specimen had at least four, the 6P10A16W1-5 had six bolts. The second category consisted of three columns designated 4P10A16S-4, 4P10A18S-4, and 4P15A16S-4. Each specimen used the same mechanism to attach columns to the base plate, which involved the welding of stiffeners to the longitudinal steel reinforcement near the top surface of the base plate. It should also be noted that the base plates thickness for this category is 15 mm thick. The diameter for all anchor bolts in specimens 4P10A16S-4 and 4P15A16S-4 was 16 mm, whereas in 4P10A18S-4, it was 18 mm. Each column specimen contained four longitudinal steel bars in the corners. The footing feature in each column of the specimens used at least four anchor bolts, but some specimens had six anchor bolts. Foundations of all specimens were produced with identical dimensions: 700 mm in length, 300 mm in width, and 200 mm in thickness, while the columns were designed with a square section of 120 mm x 120 mm and a height of 700 mm. All Specimen reinforcement followed the ACI Building Code minimums. The columns used four 10 mm longitudinal bars for specimens with stiffeners as the connection type and five 10 mm longitudinal bars for specimens with one-face weld connections(W1). the foundation had seven 10 mm bars spaced at 40 mm transversely and 10 mm bars longitudinally. Concrete cover was 30 mm for the footing and 20 mm for the column to protect the reinforcement and maintain integrity.

Each specimen had a code that showed its most important features. The first number showed the number of anchor bolts, P followed by a number showed the plate thickness in millimeters, A followed by a number showed the anchor diameter in millimeters, and the last part showed the connection type and the number of longitudinal bars used in the column.

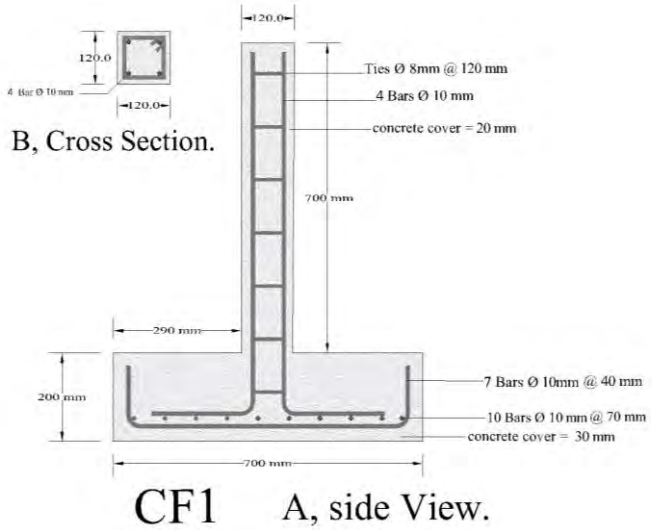

Fig. 7. Details of steel reinforcement for the column- foundation reference (A) Side view (B) Cross-section

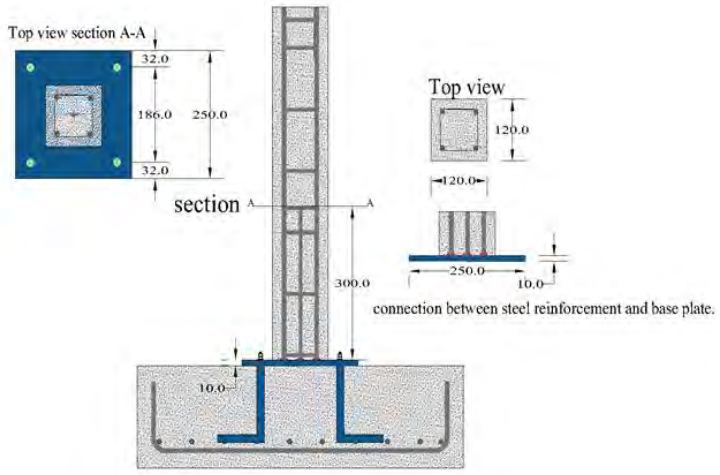

Fig. 8. Details of steel reinforcement for the column- foundation bolted connection one face welded type

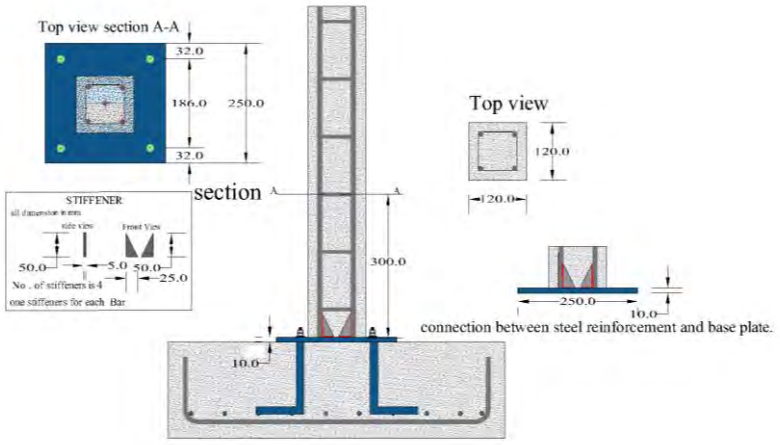

Fig. 9. Details of steel reinforcement for the column- foundation bolted connection stiffeners type

Table 6. Specimens' designation

Group No.	Specimen Label	No. of Bolt	Plate thickness (mm)	Bolt Diameter (mm)	No. of Column Bars	Type Connection
Ref	CF1	/	/	/	4 Bars	Monolithic
G1	4P10A16W1-5	4	10	16	5 Bars	One face Welded
	6P10A16W1-5	6	10	16	5 Bars	One Face Welded
G2	4P10A16S-4	4	10	16	4Bars	Stiffeners
	4P10A18S-4	4	10	18	4Bars	Stiffeners
	4P15A16S-4	4	15	16	4Bars	Stiffeners

2.4.2 Test Procedure

The process involved repeated lateral load tests that started from a displacement of 2mm and proceeded until failure with three cycles per displacement value. The displacement was increased by 2 mm at each subsequent step, so that the second displacement was (4 mm, 6mm, 8mm failure). An Excel-based program ran automatically on the computer to control the process. The nominal axial load strength (pn) and the maximum factored axial load resistance (Ø pn,max) for tied columns were calculated in accordance with ACI 318-19, The value of the axial load used was 40% of the design load, which was equivalent to 80 kN and used in all specimens

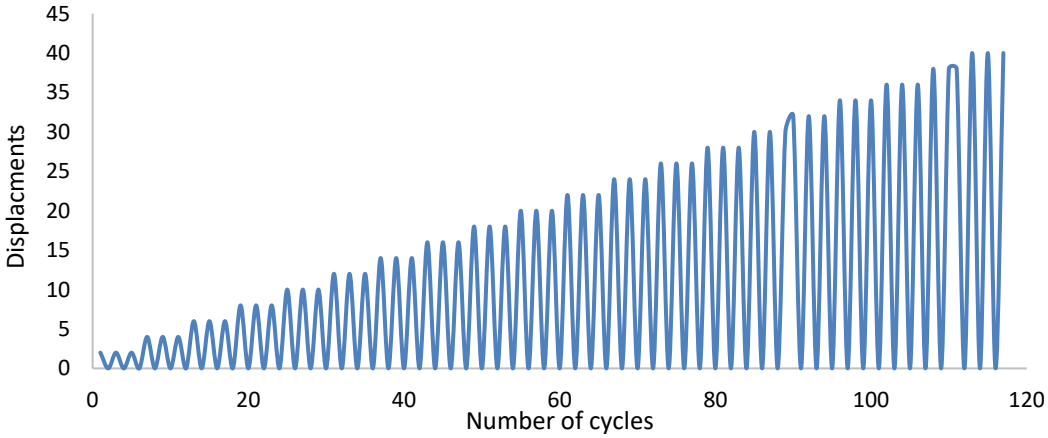

Fig. 10. Displacement history of all specimens

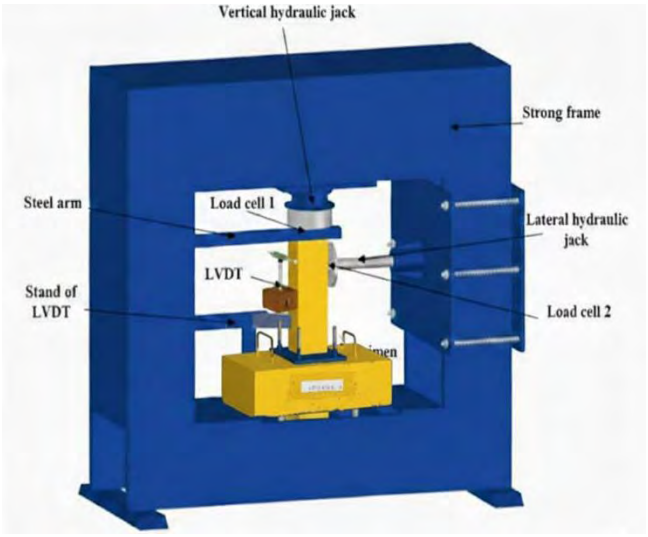

(a)

(b)

Fig. 11 . Test Setup for all Specimens (a) testing machine and (b) specimens in test

The effect of the connection type and other factors was experimentally investigated in Civil Engineering Laboratory in Kerbala University. To study the effect of each column subjected to axial and lateral force, two hydraulic jacks with two load cells were used for load application, also an LVDT was used to measure the applied lateral displacement, as shown in Fig. 11.

3. Results and Discussion

3.1 Load-Displacement Hysteresis Behavior

From the load-displacement response (Fig 12), the initial three loading cycles at each load level showed quasi-elastic behavior with significant displacement recoveries, meeting the seismic design codes such as ACI 318 and Eurocode 8 [16, 17]. As the load levels increased, the hysteresis loops became wider (Fig 12), signifying better energy dissipation and the occurrence of inelastic deformations, a characteristic of ductile reinforced concrete under lateral repeated loading [15, 18, 19]. The similarity in the shape of the hysteresis loops (Fig 12) with no sudden reduction in the load-carrying capacity confirmed the stable cyclic response of the system, as per the performance objectives of ACI 374.1 [19]. The three-cycle loading response was able to capture the cumulative damage and cyclic degradation of the system. The absence of significant reduction in the load-carrying capacity of the system over the cycles indicated good resistance to repeated loading, while the steady increase in the residual displacement indicated concrete cracking and yielding of the steel reinforcement, a positive response that met the code requirements for seismic resilience in reinforced concrete. [16, 19].

A Load reduction was recorded for some specimens, this reduction was -54.6% for 4P10A16W1-5 (see Fig 14), -36.8% for 6P10A16W1-5(see Fig 14), -38.9% for 4P10A16S-4(see Fig 15), -11.6% for 4P10A18S-4(see Fig 16), while an increment of 7.9% for 4P15A16S-4 was recorded and noted (See Fig 17) These results were consistent with those reported in ASTM International. The results indicated a decrease in the structure's load-bearing capacity compared to the control specimen. However, this reduction should be evaluated in light of the behavioral changes triggered by the advanced connection configuration, specifically the variations in base plate thickness and anchor bolt diameters. There is a considerable alteration in the load transfer mechanism at the joint between the column and the foundation due to this alteration. In the reference specimen, the load transfer had been mainly influenced by concrete behavior as it was more flexible in nature with high energy absorption capacity. Hence, it was able to undergo large deformation as well as withstand higher loads before reaching its failure stage, which was similar in behavior of reinforced concrete structures studied by Park and Paulay [20]. Unlike the monolithic connection the steel connection (base plates and anchor bolts) exhibited a lower bearing load capacity.

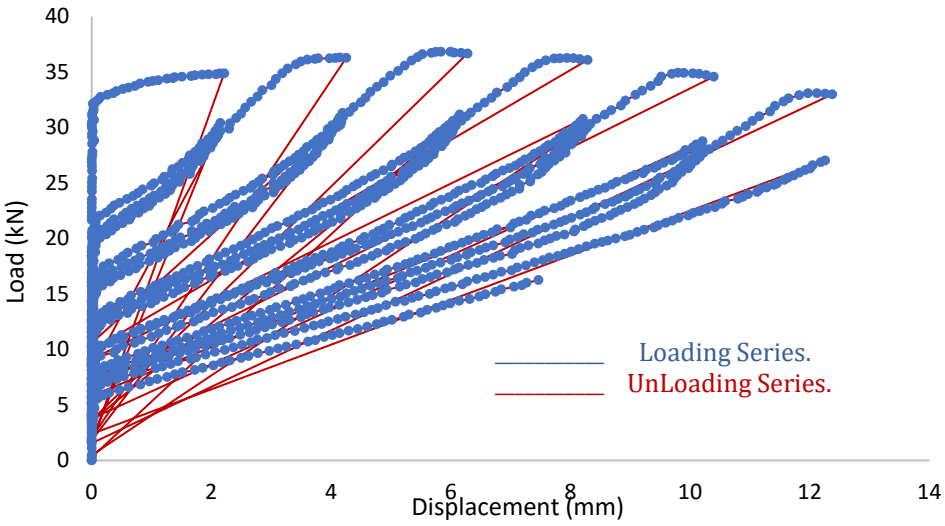

Fig. 12. Load - displacement curve of CF1 specimen

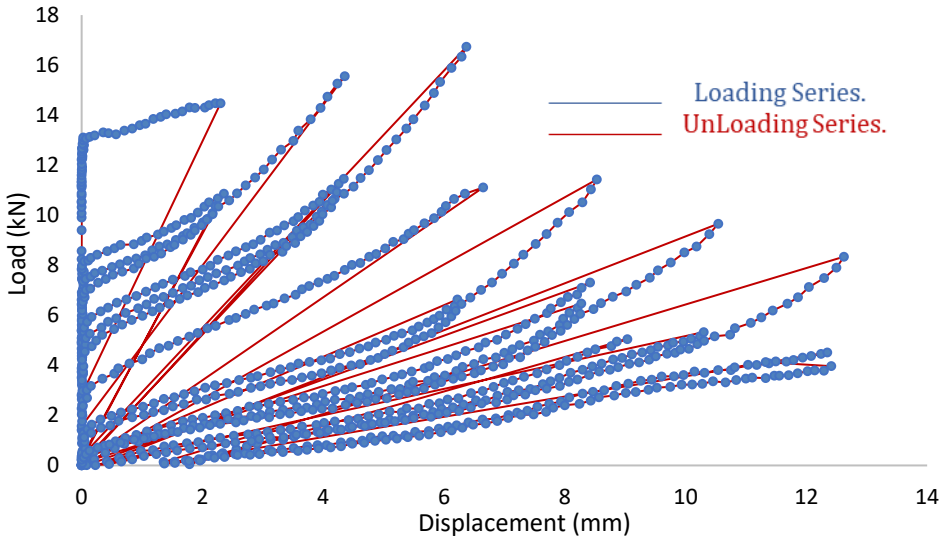

Fig. 13. Load -displacement curve (4 P10 A16 W1 - 5) specimen

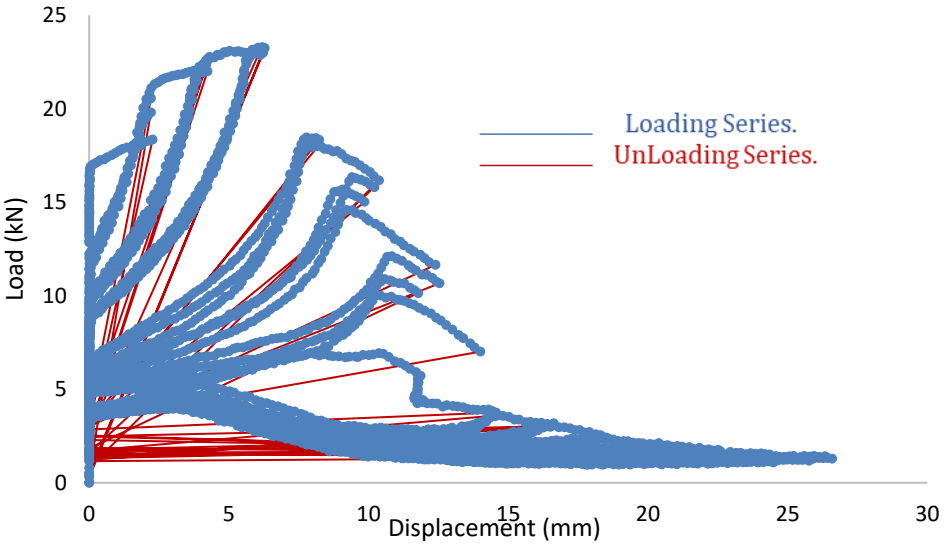

Fig. 14. Load -displacement curve (6 P10 A16 W1 -5) specimen

Thus, stresses were concentrated on the connection zone and reached the ultimate load sooner than they would have if monolithic concrete were used only. However, this connection exhibited a higher degree of deformability if compared to reference specimen. Grauvilardell et al findings support this behavior; his research points out that base plate and anchor details affect the distribution of stresses in steel/concrete connections as well as the mechanism of forces transferring. The ultimate load of strengthened specimens was less than before strengthening, but the ductility of the strengthened specimens increased as well as the continual cyclic performance [21].

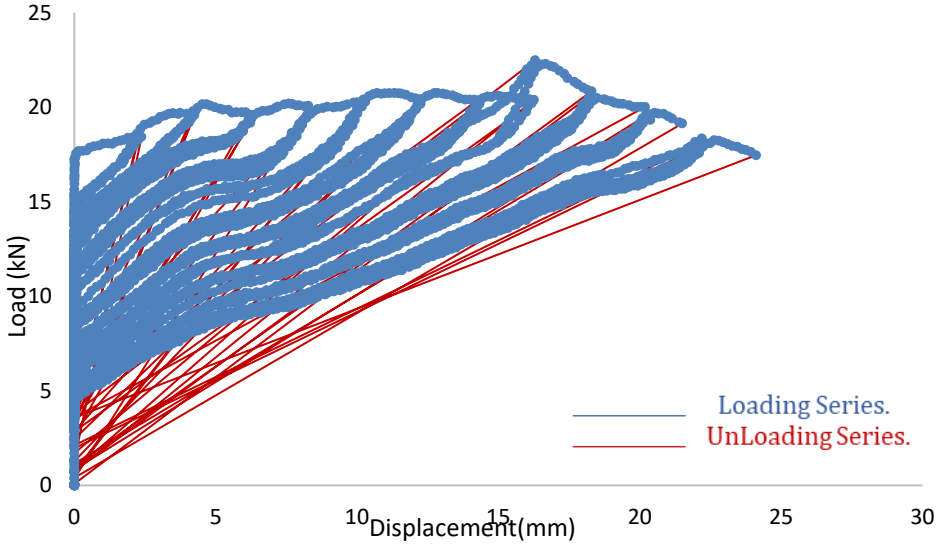

Fig .15. Load - displacement curve (4 P10 A16 S- 4) specimen

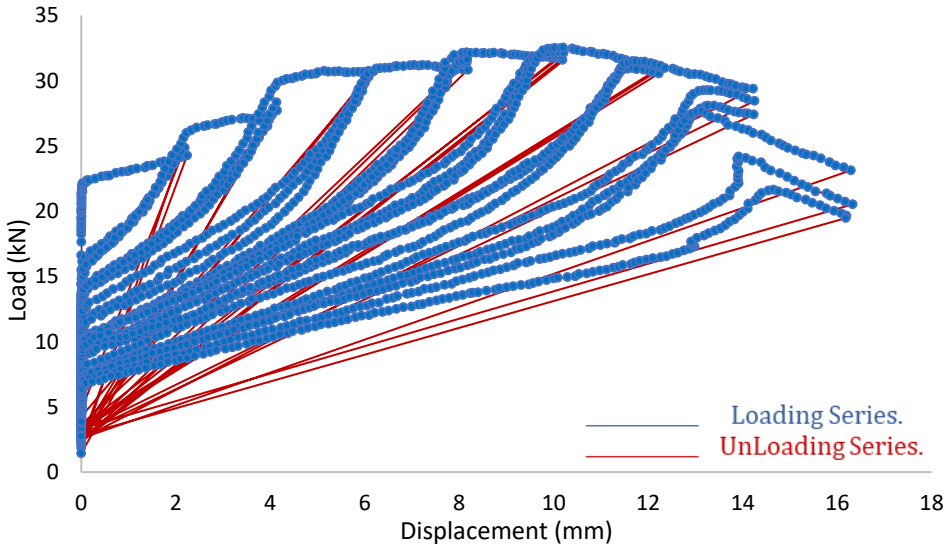

Fig. 16. Load - displacement curve (4 P10 A18 S - 4) specimen

This was due to the enhanced interaction of the steel and concrete as well as the confinement effect associated with the connection system, which helped to prevent significant cracking and prolong severe degradation. Calvi et al also found similar results in his work; he stated that improvements in seismic performance were often related to improvements in ductility and energy dissipation as opposed to simply providing higher ultimate strengths. Variations in the diameter of the anchor bolt and thickness of the base plate caused varying levels of confinement and methods of force transfer in the area where the connection is made. As a result, alterations in deformation properties and stress distributions occurred in each of the specimens [22]. The overall reduction of the deformability of the connection area dominated by steel explains why stress levels increased but afforded a stable and more predictable cyclic response, corroborating with the general research

findings as identified in previous studies regarding composite construction between steel and concrete. Thus, the transition in the structural response from an entire concrete-based system to a whole steel and concrete connection system governed by base plates and anchor bolts produces improved ductility and increased cyclic stability, which is widely regarded as a desirable attribute when considering the seismic-resistance of a structure.

Furthermore, the reference specimen recorded a load retention of 46.6% (Fig 12), which was an indication of a significant degradation in load retention capacity These results were consistent with those reported in ASTM International, 2014 [23]. By contrast, the load retention ratios for the strengthened specimens were higher, confirming that the improved bonding systems were beneficial for load retention capacity These results were in agreement with those reported in (ASTM International, 2011a, European Committee for Standardization, 2004b [24, 25]. The load retention capacity of specimen 4P10A16W1-5 was recorded at 76.8% (See Fig 13), which was an indication of a significant improvement over the reference specimen. This was due to its ability to resist cumulative damage These findings were consistent with what was reported in American Concrete Institute (ACI), 2017, American Concrete Institute (ACI), 2019, ASTM International, 2014 [18, 19, 23]. The load retention capacity for specimen 4P10A16S-4 was the highest, recording a load retention capacity of 98.9% (Fig 15), which was an indication that its load retention capacity remained almost intact throughout the loading process. This indication that the specimen was more effective in load retention than the other specimens. The load retention capacity for specimen 4P10A18S-4 was also very high, recording a load retention capacity of 88.2% (Fig 16), which was an indication that it was more effective in load retention than the other specimens. By contrast , specimen 4P15A16S-4 recorded a moderate improvement, recording a load retention capacity of 57.9% (Fig 17), while specimen 6P10A16W1-5 recorded a load retention capacity of 54.6% (Fig 14), which was an indication that it was more effective than the reference specimen but less effective than the other strengthened specimens These results were consistent with those reported in(ASTM International, 2011a, ASTM International, 2014, European Committee for Standardization, 2004b [23-25]. The results indicate that the effectiveness of the improved bonding systems was dependent on the strengthening configurations [25].

The reference specimen experienced a stiffness degradation rate of 61%, reflected the level of degradation that occurred These results were consistent with those reported in ASTM International, 2014 [23]. Conversely, all the strengthened specimens experienced lower degradation rates, reflecting the effectiveness of the bond These results were in agreement with those reported in ASTM International, 2011a, European Committee for Standardization, 2004b [24, 25]. For instance, the specimen 4P10A16W1-5 experienced a degradation rate of 58% (Fig13), while the specimen 6P10A16W1-5 experienced a lower degradation rate of 53% (Fig 14). This showed that the specimens experienced less degradation compared to the reference specimen. The specimens 4P10A16S-4 and 4P10A18S-4 experienced degradation rates of 56% and 52% (See Fig 15, Fig 16), respectively. This showed that the specimens experienced less degradation compared to the reference specimen. The specimen 4P15A16S-4 experienced a moderate level of improvement by experiencing a degradation rate of 54% (Fig 17). Based on the results, all the strengthened specimens experienced decelerated degradation. The specimens that experienced the best performance experienced a reduction of up to 9% compared to the reference specimen. The differences that occurred among the strengthened specimens could be attributed to the bonding arrangements These results were consistent with those reported in European Committee for Standardization, 2004b [25].

Stability under repeated loading was examined as one of the parameters through which the ability of each specimen to withstand successive cycles without significant reduction in its load-carrying capacity was examined and quantified These results were consistent with those reported in ASTM International, 2014, European Committee for Standardization, 2004a. The reference specimen took the lead in exhibiting the lowest stability by a load stability ratio of 0.47(Fig 12), which was indicative of a very large loss in load when subjected to the repeated cycles. By contrast, all the strengthened specimens in the study showed a higher load stability, which pointed to the great influence that the strengthening of the bonding configurations through the effectiveness of the improved relationships had on the performance of the structure being preserved These results

were consistent with those reported in ASTM International, 2011a, ASTM International, 2014, European Committee for Standardization, 2004b [23-25]. Load stability of 0.77 was achieved by specimen 4P10A16W1-5(Fig 13), while 4P10A16S-4 attained the highest stability of 0.99(Fig 15), which meant the specimen kept its load capacity throughout the cycles almost entirely. Furthermore, specimen 4P10A18S-4 exhibited a load stability of 0.88(Fig 16), which was pretty good, whereas the load stability of specimens 4P15A16S-4 and 6P10A16W1-5 were 0.58(Fig 17) and 0.55(Fig 14), respectively, which were moderate improvements [23, 26]. The results obtained confirmed that the strengthened specimens were able to maintain a higher load level even after the repeated cycles, and the effectiveness of the stabilization depended significantly on the strengthening configuration These results were in agreement with those reported in European Committee for Standardization, 2004b [25].

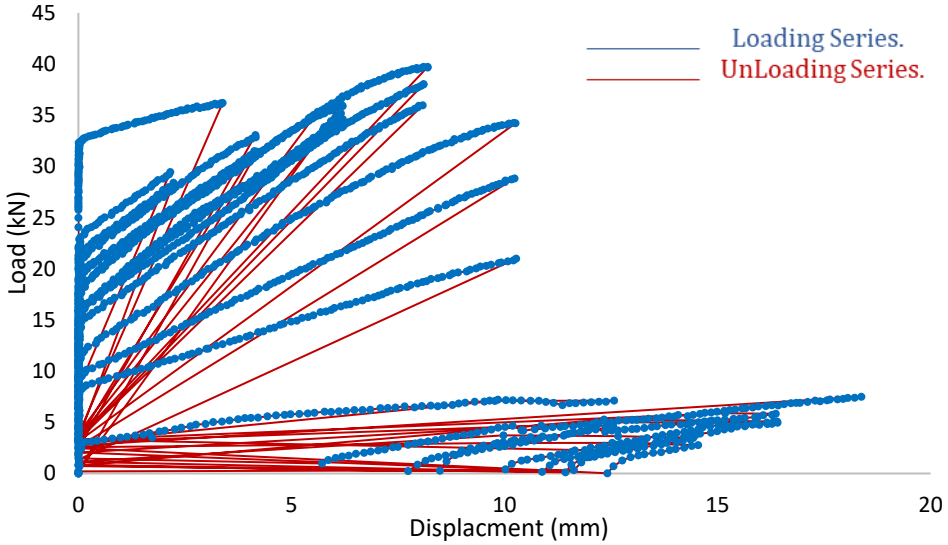

Fig. 17. Load - displacement curve (4 P15 A16 S - 4) specimen

Table 7. Comparison of Load Capacity, Stability, and Displacement Improvement for All Specimens

Label	Load Improvement Ratio	Load Retention	Stiffness Degradation Rate	Load Stability with Cycles	Maximum Displacement Improvement
CF1		46.60%	61%	0.39	
4P10A16W1-5	-54.60%	76.80%	58%	0.78	2.70%
6P10A16W1-5	-36.80%	54.60%	53%	0.55	3.78%
4P10A16S-4	-38.90%	98.90%	56%	0.99	1.18%
4P10A18 S -4	-11.60%	88.20%	52%	0.88	10.80%
4P15A16S-4	7.90%	57.90%	54%	0.58	21.03%

The reference specimen CF1 structural performance assessment utilized maximum displacement analysis to compared its results against the various improved test specimens (Fig 12) [16, 27]. The results demonstrated that different design alterations which designers tested showed distinct effectiveness to decrease displacement between them. The system improvement reached 21.03% according to specimen 4P15A16S-4 (Fig 17) because the combination of S-type connection with 15 mm plate thickness and bigger anchor bolt diameter resulted in better system stiffness and lower deformation [25, 27]and (4P10A18 S -4) specimen was 10.8% (Fig 16). The critical role of plate thickness and increased bolt diameter in improving displacement resistance was examined. The W1-type connection and increased bolt quantity both contributed to displacement reduction according to specimens 6P10A16W1-5 (Fig 14) and 4P10A16W1-5(Fig 13), which showed moderate improvement ratios of 3.78% and 2.70%, respectively. The original plate thickness maintenance together with connection type alteration produced a minor effect on displacement control according to specimen 4P10A16S-4(Fig 15), which achieved 1.18% as its lowest improvement ratio [27, 28]. The research results showed that design parameters such as plate

thickness and anchor bolt diameter and connection type development all influenced maximum displacement response, while dual enhancements of bolt diameter and proper connection configuration worked to boost structural stiffness and system performance compared to the reference specimen [25, 27, 28].

3.2 Failure Mode

In the initial phases of repeated loading, the concrete column with the base showed stable structural behavior (Fig 20, Fig 23). A discernible decrease in lateral buckling and initial displacements demonstrated how well the developed confinement improved the stability of the column. However, a gradual nonlinear response developed as repeated lateral loads were applied; this was ascribed to cumulative damage in the reinforcing steel or concrete, especially in the vicinity of the column-to-base connection area (Fig 19, Fig 24). This area was important because it complied with seismic design specifications, highlighting its importance for structural integrity during seismic activity. The mode of failure was characterized by a gradual and non-brittle failure, with wide cracks at the base (Fig 19, Fig 24). Partial crushing of concrete (Fig 19, Fig 24), and steel (of steel (Fig 20). This mode provided clear warnings before failure, and this was a characteristic of a ductile failure with sufficient dissipation of energy, which was consistent with modern seismic design codes. It was acknowledged that the use of a single Linear Variable Differential Transformer (LVDT) posed certain limitations in the possibility of fully capturing the kinematic behavior of the column base connection, especially where localized deformations are more complicated and the level of detail is higher. In the same way, the lack of localized strain gauges was a reason why the detailed strain distributions inside the critical zones of the connection were not measured directly. One way of overcoming these instrumentation shortcomings was to complement the testing program with careful and continuous visual monitoring during each loading cycle. Early signs of local distress, such as the initiation and growth of cracks (Fig 19, Fig 21, Fig 24), steel yielding's (Fig 20), and potential buckling, were identified by means of a regular inspection of structural elements. This method of observation was a process of confirming in practice that there were no premature local failures that could have been hidden and might have compromised the global response recorded. When combined, the displacement data gathered by the LVDT and the visual inspections were considered sufficient to support the certainty of the findings from this experimental investigation.

The integrity of the welds was tested systematically at each stage of the test process, as well as through the extensive post-test analysis. It helped draw the conclusion about the flawless condition of the connections up to the last stage of the test process without fractures, separation or any deterioration of the zone of contact between the longitudinal reinforcement of the column and the steel base plate. Cracks or any sign of deterioration were not found in the area of the weld, which means that there was no occurrence of structural failure or any other critical failure mechanism in the weld under lateral repeated loading. No crackling sounds or any other signs of the weld breakage during the experiment process have been recorded. Based on the findings made as a result of the analysis conducted after the test, one can conclude that the reasons for the appearance of failure or damage lie in the field of structural behavior and not in metallurgical failures, thus the failure was induced intentionally in accordance with the structural design of the element. In the case of the W1 connection, the concrete was stripped off in the column to base plate region to facilitate a more precise assessment of the connection performance based on the load transfer through the steel base plate and anchor bolts. The W1 connection had relatively lower performance compared to the second connection type, implying that the mechanism of load transfer through the connection region was relatively inefficient in the case of the former. However, all the welds performed well during the entire loading regime without any failure or damage occurring. Therefore, the relatively poor performance of the connections could be attributed to the load transfer mechanism of the connection rather than poor welding quality Fig 18.

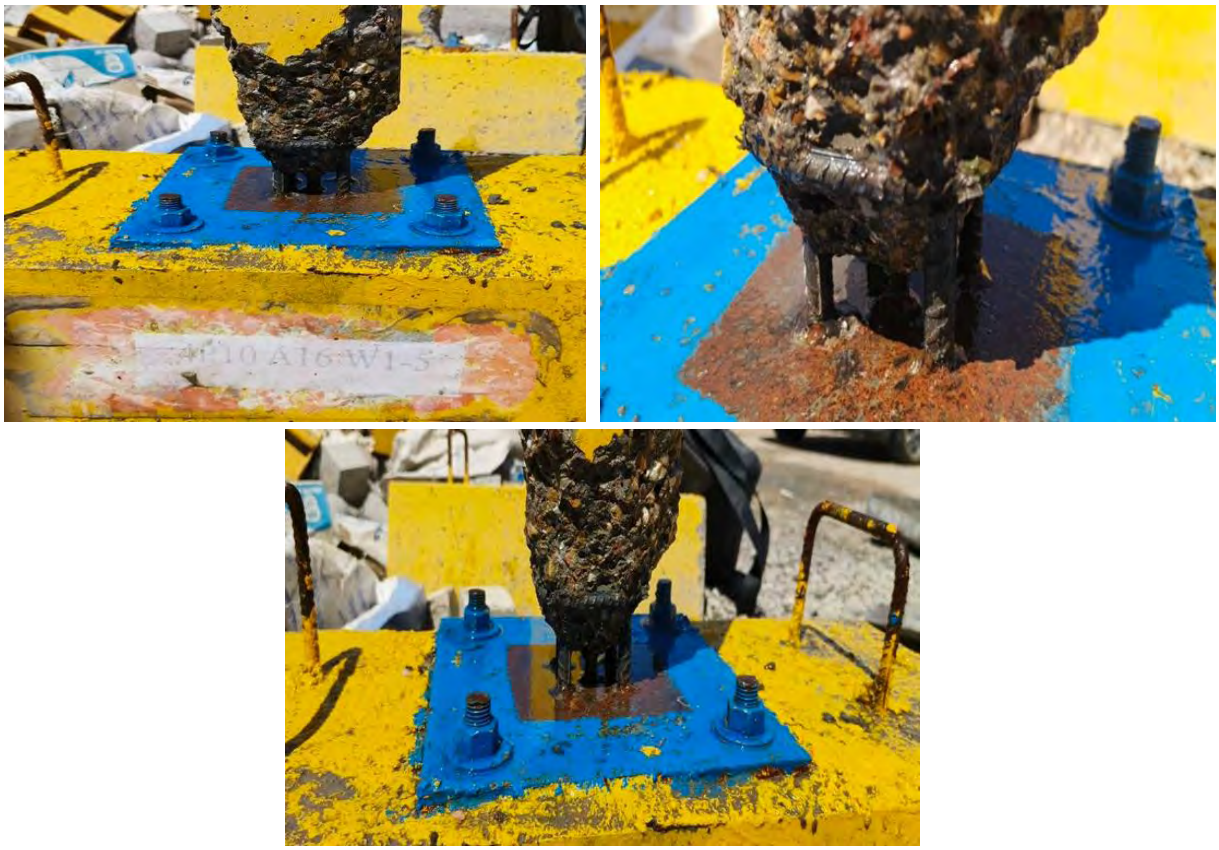

Fig. 18. Specimen (4P10A16W1-5) after removal of concrete from the contact zone between the concrete and the base plate

Fig. 19. Failure Mode of CF1 Specimen

Fig. 20. Failure mode of (4 P10 A16 W1 -5) specimen

Fig. 21. Failure mode of (4 P10 A16 S -4) specimen

Fig. 22. Failure mode of (4 P10 A18 S -4) specimen

Fig. 23. Failure mode of (4 P15 A16 S -4) specimen

Fig. 24. Failure mode of (6 P10 A16 W1 -5) specimen

4. Conclusion

Six concrete column-foundation specimens were subjected to repeated loading, and their performance was assessed based on peak load capacity, retained load capacity, stiffness degradation, load stability, and maximum displacement. Although the reference specimen demonstrated a higher peak load capacity, it failed quickly and lost significant load-carrying capacity under repeated loading. Most of the strengthened specimens demonstrated a reduction in peak load capacity. This indicated that the specimens had lower peak loads than the reference one,; instead, the bond between the column and foundation had been enhanced to improve the efficiency of load transfer.

The strengthened specimens demonstrated greater load stability compared to the reference, with significantly less cumulative damage during the loading process. The retained load capacity of the strengthened specimens increased significantly, from 46.6% in reference to between 54.6% and 98.9% in the strengthened specimens, with 4P10A16S-4 retaining its load capacity. The rate of stiffness degradation was lower in the strengthened specimens, indicating a higher resistance to progressive deformation and damage under repeated loading. The load stability of the strengthened specimens also increased significantly, with values ranging from 0.47 in reference to a maximum of 0.99, indicating that the specimens maintained their load-carrying capacity better under repeated loading cycles.

An examination of the peak displacement values of the various specimens revealed that there were three significant factors that affected the degree of resistance to deformation of the column base joint and the stiffness of the connection. The first was the thickening of the base plate. The second was the use of larger diameter anchor bolts. The third was the use of the S-type connection, which had the most significant effect. Of all the specimens, 4P15A16S-4 had the highest resistance to deformation, with the greatest improvement in displacement at 21.03%. The use of the W1-type connection in the specimens had a moderate improvement in stiffness. The use of more bolts to connect the column to the base had a moderate improvement. The use of the connection type had a moderate reduction in the peak displacement value. The improvement in the connection between the column and the base, making the connection stiffer and stronger, had a positive effect on the stiffness, degradation, and load-carrying capacity, resulting in a lower value of maximum displacement.

References

[1] Tasnimi A. Seismic behavior of prefabricated column-footing connection. Int J Eng. 1999;12(4):205-218.
[2] Nagaprasad P, Sahoo DR, Rai DC. Seismic strengthening of RC columns using external steel cage. Earthquake Eng Struct Dynam. 2009;38(14):1563-1586. https://doi.org/10.1002/eqe.917
[3] Osman MH, Grant ST. Performance of Reinforced Concrete Beam-column Joint Subjected to Repeated Reversed Load. Universiti Tun Hussein Onn Malaysia; 2012.
[4] Mahadik V, Sharma A, Hofmann J. Seismic performance of column-foundation-joints with post-installed rebar connections: pre-test simulations. In: Proceedings of the 2017 fib Symposium, High Tech Concrete: Where Technology and Engineering Meet; 2017 Jun 12-14; Maastricht, The Netherlands. Springer; 2017. https://doi.org/10.1007/978-3-319-59471-2_120
[5] Camnasio E, Kriakopoulos P. Experimental Analysis on the Cyclic Performance of Bolted Precast Connections. In: Proceedings of the 2017 fib Symposium, High Tech Concrete: Where Technology and Engineering Meet; 2017 Jun 12-14; Maastricht, The Netherlands. Springer; 2017. https://doi.org/10.1007/978-3-319-59471-2_118
[6] Liu J, et al. Seismic Performance of a New Assembled Bolt-Connected Concrete Beam-Column Joint: Experimental Test and Finite Element Modeling. Appl Sci. 2022;13(1):73. https://doi.org/10.3390/app13010073
[7] Aydemir ME, Aydemir C, Arslan G. Experimental study on the energy dissipation and seismic behavior of RC columns due to repeated earthquakes including vertical excitation. Eng Struct. 2023;293:116650. https://doi.org/10.1016/j.engstruct.2023.116650
[8] Ebenezer SJ, Tensing D, Jebadurai SS. An experimental study on composite steel encased portal frame under cyclic loading. Res. Eng. Struct. Mater., 2023; 9(1): 277-291. http://dx.doi.org/10.17515/resm2022.426ie0408

[9] SenthilKumar P., Tensing D., Hemalatha G., Sharma SV, Daniel C. Compression strength behaviour of fibre-reinforced concrete made with hoop-shaped waste polyethylene terephthalate fibre. Res. Eng. Struct. Mater., 2024; 10(1): 1-22. http://dx.doi.org/10.17515/resm2023.762me0508
[10] Central Organization for Standardization in Iraq (COSQC). Iraqi Specification No. 5/1984: Portland Cement. Baghdad, Iraq: Central Organization for Standardization and Quality Control; 1984.
[11] Central Organization for Standardization in Iraq (COSQC). Iraqi Specification No. 45/1984: Aggregates from Natural Sources for Concrete and Construction. Baghdad, Iraq: Central Organization for Standardization and Quality Control; 1984.
[12] ASTM International. ASTM C39: Standard Test Method for Compressive Strength of Cylindrical Concrete Specimens. West Conshohocken, PA: ASTM International; 2003.
[13] ASTM International. ASTM C496/C496M-11: Standard Test Method for Splitting Tensile Strength of Cylindrical Concrete Specimens. West Conshohocken, PA: ASTM International; 2011.
[14] ASTM International. ASTM C78/C78M-16: Standard Test Method for Flexural Strength of Concrete (Using Simple Beam with Third-Point Loading). West Conshohocken, PA: ASTM International; 2016.
[15] ASTM International. ASTM A615/A615M-16: Standard Specification for Deformed and Plain Carbon-Steel Bars for Concrete Reinforcement. West Conshohocken, PA: ASTM International; 2016.
[16] American Concrete Institute (ACI). ACI 374.1-05: Guide for Testing Reinforced Concrete Structural Elements under Slowly Applied Simulated Seismic Loads. Farmington Hills, MI: ACI; 2005.
[17] Paulay T, Priestley MJN. Seismic Design of Reinforced Concrete and Masonry Buildings. New York: John Wiley & Sons; 1992. https://doi.org/10.1002/9780470172841
[18] American Concrete Institute (ACI). ACI 440.2R-17: Guide for the Design and Construction of Externally Bonded FRP Systems for Strengthening Concrete Structures. Farmington Hills, MI: ACI; 2017.
[19] American Concrete Institute (ACI). ACI 318-19: Building Code Requirements for Structural Concrete and Commentary. Farmington Hills, MI: American Concrete Institute; 2019.
[20] Park R, Paulay T. Reinforced concrete structures. New York: John Wiley & Sons; 1991.
[21] Grauvilardell JE, et al. Synthesis of design, testing and analysis research on steel column base plate connections in high-seismic zones. Structural engineering report no. ST-04-02. Minneapolis (MN): Department of Civil Engineering, University of Minnesota; 2005.
[22] Calvi G, Priestley M, Kowalsky M. Displacement-based seismic design of structures. In: New Zealand conference on earthquake engineering. IUSS press; 2007.
[23] ASTM International. ASTM C469/C469M-14: Standard Test Method for Static Modulus of Elasticity and Poisson's Ratio of Concrete in Compression. West Conshohocken, PA: ASTM; 2014.
[24] ASTM International. ASTM E2126-11: Standard Test Methods for Cyclic (Reversed) Load Test for Shear Resistance of Walls for Buildings. West Conshohocken, PA: ASTM; 2011.
[25] European Committee for Standardization. Eurocode 8 (EN 1998-1): Design of Structures for Earthquake Resistance. Brussels: European Committee for Standardization; 2004.
[26] European Committee for Standardization. EN 1998-1: Eurocode 8 - Design of structures for earthquake resistance. Brussels: European Committee for Standardization; 2004.
[27] Federal Emergency Management Agency (FEMA). FEMA 356: Prestandard and Commentary for the Seismic Rehabilitation of Buildings. Washington, DC: FEMA; 2000.
[28] International Federation for Structural Concrete (fib). fib Model Code 2010: Structural Concrete: Text and Commentary. Lausanne: International Federation for Structural Concrete; 2013.

www.jresm.org

Research on Engineering Structures and Materials

Scopus
EBSCO
TÜBİTAK ULAKBİM
DRJI
Cosmos
ProQuest
crossref
Google Scholar
Universal Impact Factor
SIS Scientific Indexing Services
CiteFactor Academic Scientific Journals
Journal Seeker Research Bible
EZB Elektronische Zeitschriftenbibliothek
GIF GLOBAL IMPACT FACTOR
ASOS indeks
Open Academic Journals Index
Publication Forum

Special Focus Issue

Engineering Innovations from 5ICGE & 3ICESE Conferences

Research Group
https://mimrg.net/